STEEL HEAT TREATMENT HANDBOOK
Second Edition

STEEL HEAT TREATMENT

METALLURGY AND TECHNOLOGIES

REVIEWED
By Abrianto Akuan at 9:03 am, Jan 18, 2009

STEEL HEAT TREATMENT HANDBOOK

Second Edition

George E. Totten, Ph.D., FASM

STEEL HEAT TREATMENT
METALLURGY AND TECHNOLOGIES

STEEL HEAT TREATMENT
EQUIPMENT AND PROCESS DESIGN

STEEL HEAT TREATMENT HANDBOOK
Second Edition

STEEL HEAT TREATMENT

METALLURGY AND TECHNOLOGIES

EDITED BY
George E. Totten, Ph.D., FASM

Portland State University
Portland, Oregon, U.S.A.

Taylor & Francis
Taylor & Francis Group
Boca Raton London New York

CRC is an imprint of the Taylor & Francis Group,
an informa business

Cover figure: Microstructure due to slow and fast cooling of a steel weld.

The micrograph shows the microstructure of a steel weld showing the solidification structure and solid-state decomposition of austenite to martensite. The lower part of the micrograph shows columnar delta-ferrite solidification with interdendritic-regions of transformed austenite formed during slow cooling. The top part of the microstructure shows large platelets of martensite formed due to rapid cooling. (From Babu S. S., J. M. Vitek, T. Palmer, J. W. Elmer, S. A. David. Nonequilibrium phase selection during weld solidification of Fe-C-Mn-Al steels, *Proceedings of the Solidification Processes and Microstructures,* A symposium in honor of Prof. W. Kurz, TMS Annual Meeting, Charlotte, NC, March 2004. Courtesy of Oak Ridge National Laboratory.)

CRC Press
Taylor & Francis Group
6000 Broken Sound Parkway NW, Suite 300
Boca Raton, FL 33487-2742

Printed in the United States of America on acid-free paper
10 9 8 7 6 5 4 3 2 1

International Standard Book Number-10: 0-8493-8455-9 (Hardcover) 0-8493-8455-9 (Hardcover)
International Standard Book Number-13: 978-0-8493-8455-4 (Hardcover) 978-0-8493-8455-4 (Hardcover)

Library of Congress Cataloging-in-Publication Data

Steel heat treatment : metallurgy and technologies / George E. Totten, editor.
p. cm.
Includes bibliographical references and index.
ISBN-13: 978-0-8493-8455-4 (alk. paper)
ISBN-10: 0-8493-8455-9 (alk. paper)
1. Steel--Heat treatment. I. Totten, George E. II. Title.

TN751.S687 2006
672.3'6--dc22 2006023584

Visit the Taylor & Francis Web site at
http://www.taylorandfrancis.com

and the CRC Press Web site at
http://www.crcpress.com

Preface

The first edition of the *Steel Heat Treatment Handbook* was initially released in 1997. The objective of that book was to provide the reader with well-referenced information on the subjects covered with sufficient depth and breadth to serve as either an advanced undergraduate or graduate level text on heat treatment or as a continuing handbook reference for the designer or practicing engineer. However, since the initial release of the first edition of the *Steel Heat Treatment Handbook*, there have been various advancements in the field that needed to be addressed to assure up-to-date coverage of the topic. This text, *Steel Heat Treatment: Metallurgy and Technologies*, is part of a revision of the earlier text. Some of the chapters in this text are updated revisions of the earlier book and others are completely new chapters or revisions. These chapters include:

Chapter 1. Steel Nomenclature (Revision)
Chapter 2. Classification and Mechanisms of Steel Transformations (New Chapter)
Chapter 3. Fundamental Concepts in Steel Heat Treatment (Minor Revisions)
Chapter 4. Effects of Alloying Elements on the Heat Treatment of Steel (Minor Revisions)
Chapter 5. Hardenability (Minor Revisions)
Chapter 6. Steel Heat Treatment (Minor Revisions)
Chapter 7. Heat Treatment with Gaseous Atmospheres (Revision)
Chapter 8. Nitriding Techniques, Ferritic Nitrocarburizing, and Austenitic Nitrocarburizing Techniques and Methods (Revision)
Chapter 9. Quenching and Quenching Technology (Revision)
Chapter 10. Distortion of Heat-Treated Components (New Chapter)
Chapter 11. Tool Steels (New Chapter)
Chapter 12. Stainless Steel Heat Treatment (New Chapter)
Chapter 13. Heat Treatment of Powder Metallurgy Steel Components (New Chapter)

Approximately a third of the book is new and a third of the book is significantly revised versus the first edition of the *Steel Heat Treatment Handbook*. This new text is current with respect to heat treatment technology at this point at the beginning of the 21st century and is considerably broader in coverage but with the same depth and thoroughness that characterized the first edition.

Unfortunately, my close friend, colleague and mentor, Dr. Maurice A.H. Howes, who helped to bring the first edition of *Steel Heat Treatment Handbook* into fruition was unable to assist in the preparation of this second edition. However, I have endeavored to keep the same consistency and rigor of coverage as well as be true to the original vision that we had for this text as a way of serving the heat treatment industry so that this book will be a value resource to the reader in the future.

George E. Totten, Ph.D., FASM
Portland State University
Portland, Oregon

Editor

George E. Totten, Ph.D. is president of G.E. Totten & Associates, LLC in Seattle, Washington and a visiting professor of materials science at Portland State University. He is coeditor of a number of books including *Steel Heat Treatment Handbook*, *Handbook of Aluminum*, *Handbook of Hydraulic Fluid Technology*, *Mechanical Tribology*, and *Surface Modification and Mechanisms* (all titles of CRC Press), as well as the author or coauthor of over 400 technical papers, patents, and books on lubrication, hydraulics, and thermal processing. He is a Fellow of ASM International, SAE International, and the International Federation for Heat Treatment and Surface Engineering (IFHTSE), and a member of other professional organizations including ACS, ASME, and ASTM. He formerly served as president of IFHTSE. He earned B.S. and M.S. degrees from Fairleigh Dickinson University, Teaneck, New Jersey and a Ph.D. degree from New York University, New York.

Contributors

S.S. Babu
Edison Welding Institute
Columbus, Ohio

Elhachmi Essadiqi
CANMET, Materials Technology Laboratory
Ottawa, ON, Canada

Johann Grosch
Institut fuer Werkstofftechnik
Technische Universitaet
Berlin, Germany

Božidar Liščić
Faculty of Mechanical Engineering and Naval Architecture
University of Zabreb
Zabreb, Croatia

Guoquan Liu
Beijing University of Science and Technology
Beijing, China

Michiharu Narazaki
Utsunomiya University
Utsunomiya, Japan

Arnold R. Ness
Bradley University
Peoria, Illinois

Joseph W. Newkirk
University of Missouri-Rolla,
Rolla, Missouri

Angelo Fernando Padilha
University of Sao Paulo
Sao Paulo, Brazil

Ronald Lesley Plaut
University of Sao Paulo
Sao Paulo, Brazil

David Pye
Pye Metallurgical Consulting, Inc.
Meadville, Pennsylvania

Paulo Rangel Rios
Fluminense Federal University
V. Redonda, Brazil

Anil Kumar Sinha
AKS Associates
Fort Wayne, Indiana

Anton Stich
Technical University of Munich
Munich, Germany

Alexey V. Sverdlin
Bradley University
Peoria, Illinois

Hans M. Tensi
Technical University of Munich
Munich, Germany

Sanjay N. Thakur
Hazen Powder Parts, LLC
Hazen, Arkansas

George E. Totten
Portland State University
Portland, Oregon

Chengjian Wu
Beijing University of Science and Technology
Beijing, China

Contents

Chapter 1 Steel Nomenclature

Anil Kumar Sinha, Chengjian Wu, and Guoquan Liu

Chapter 2 Classification and Mechanisms of Steel Transformation

S.S. Babu

Chapter 3 Fundamental Concepts in Steel Heat Treatment

Alexey V. Sverdlin and Arnold R. Ness

Chapter 4 Effects of Alloying Elements on the Heat Treatment of Steel

Alexey V. Sverdlin and Arnold R. Ness

Chapter 5 Hardenability

Božidar Liščić

Chapter 6 Steel Heat Treatment

Božidar Liščić

Chapter 7 Heat Treatment with Gaseous Atmospheres

Johann Grosch

Chapter 8 Nitriding Techniques, Ferritic Nitrocarburizing, and Austenitic Nitrocarburizing Techniques and Methods

David Pye

Chapter 9 Quenching and Quenching Technology

Hans M. Tensi, Anton Stich, and George E. Totten

Chapter 10 Distortion of Heat-Treated Components

Michiharu Narazaki and George E. Totten

Chapter 11 Tool Steels

Elhachmi Essadiqi

Chapter 12 Stainless Steel Heat Treatment

Angelo Fernando Padilha, Ronald Lesley Plaut, and Paulo Rangel Rios

Chapter 13 Heat Treatment of Powder Metallurgy Steel Components

Joseph W. Newkirk and Sanjay N. Thakur

Appendices

Appendix 1 Common Conversion Constants

Appendix 2 Temperature Conversion Table

Appendix 3 Volume Conversion Table

Appendix 4 Hardness Conversion Tables: Hardened Steel and Hard Alloys

Appendix 5 Recommended MIL 6875 Specification Steel Heat Treatment Conditions

Appendix 6 Colors of Hardening and Tempering Heats

Appendix 7 Weight Tables for Steel Bars

1 Steel Nomenclature

Anil Kumar Sinha, Chengjian Wu, and Guoquan Liu

CONTENTS

1.1 Introduction 2
1.2 Effects of Alloying Elements 2
1.2.1 Carbon 3
1.2.2 Manganese 3
1.2.3 Silicon 4
1.2.4 Phosphorus 4
1.2.5 Sulfur 4
1.2.6 Aluminum 5
1.2.7 Nitrogen 5
1.2.8 Chromium 5
1.2.9 Nickel 5
1.2.10 Molybdenum 5
1.2.11 Tungsten 6
1.2.12 Vanadium 6
1.2.13 Niobium and Tantalum 6
1.2.14 Titanium 6
1.2.15 Rare Earth Metals 7
1.2.16 Cobalt 7
1.2.17 Copper 7
1.2.18 Boron 7
1.2.19 Zirconium 8
1.2.20 Lead 8
1.2.21 Tin 8
1.2.22 Antimony 8
1.2.23 Calcium 8
1.3 Classification of Steels 8
1.3.1 Types of Steels Based on Deoxidation Practice 9
1.3.1.1 Killed Steels 9
1.3.1.2 Semikilled Steels 10
1.3.1.3 Rimmed Steels 10
1.3.1.4 Capped Steels 11
1.3.2 Quality Descriptors and Classifications 11
1.3.3 Classification of Steel Based on Chemical Composition 13
1.3.3.1 Carbon and Carbon–Manganese Steels 13
1.3.3.2 Low-Alloy Steels 17
1.3.3.3 High-Strength Low-Alloy Steels 24
1.3.3.4 Tool Steels 27
1.3.3.5 Stainless Steels 33

1.3.3.6 Maraging Steels 44
1.4 Designations for Steels 45
1.4.1 SAE-AISI Designations 46
1.4.1.1 Carbon and Alloy Steels 46
1.4.1.2 HSLA Steels 47
1.4.1.3 Formerly Listed SAE Steels 47
1.4.2 UNS Designations 47
1.5 Specifications for Steels 50
1.5.1 ASTM (ASME) Specifications 50
1.5.2 AMS Specifications 51
1.5.3 Military and Federal Specifications 51
1.5.4 API Specifications 54
1.5.5 ANSI Specifications 66
1.5.6 AWS Specifications 66
1.6 International Specifications and Designations 66
1.6.1 ISO Designations 66
1.6.1.1 The Designation for Steels with Yield Strength 66
1.6.1.2 The Designation for Steels with Chemical Composition 84
1.6.2 GB Designations (State Standards of China) 85
1.6.3 DIN Standards 86
1.6.4 JIS Standards 86
1.6.5 BS Standards 86
1.6.6 AFNOR Standards 86
References 87

1.1 INTRODUCTION

According to the iron–carbon phase diagram [1–3], all binary Fe–C alloys containing less than about 2.11 wt% carbon* are classified as steels, and all those containing higher carbon content are termed cast iron. When alloying elements are added to obtain the desired properties, the carbon content used to distinguish steels from cast iron would vary from 2.11 wt%.

Steels are the most complex and widely used engineering materials because of (1) the abundance of iron in the Earth's crust, (2) the high melting temperature of iron (1534°C), (3) a range of mechanical properties, such as moderate (200–300 MPa) yield strength with excellent ductility to in excess of 1400 MPa yield stress with fracture toughness up to 100 MPa m^{-2}, and (4) associated microstructures produced by solid-state phase transformations by varying the cooling rate from the austenitic condition [4].

This chapter describes the effects of alloying elements on the properties and characteristics of steels, reviews the various systems used to classify steels, and provides extensive tabular data relating to the designation of steels.

1.2 EFFECTS OF ALLOYING ELEMENTS

Steels contain alloying elements and impurities that must be associated with austenite, ferrite, and cementite. The combined effects of alloying elements and heat treatment produce an enormous variety of microstructures and properties. Given the limited scope of this chapter, it

*This figure varies slightly depending on the source. It is commonly taken as 2.11 wt% [1] or 2.06 wt% [2], while it is calculated thermodynamically as 2.14 wt% [3].

would be difficult to include a detailed survey of the effects of alloying elements on the iron–carbon equilibrium diagram, allotropic transformations, and forming of new phases. This complicated subject, which lies in the domain of ferrous physical metallurgy, has been reviewed extensively in Chapter 2 of this handbook and elsewhere in the literature [4,5,8–12].

In this section, the effects of various elements on steelmaking (deoxidation) practices and steel characteristics will be briefly outlined. It should be noted that the effects of a single alloying element on either practice or characteristics is modified by the influence of other elements. The interaction of alloying elements must be considered [5].

According to the effect on matrix, alloying elements can be divided into two categories:

1. By expending the γ-field, and encouraging the formation of austenite, such as Ni, Co, Mn, Cu, C, and N (these elements are called austenite stabilizers)
2. By contracting the γ-field, and encouraging the formation of ferrite, such as Si, Cr, W, Mo, P, Al, Sn, Sb, As, Zr, Nb, B, S, and Ce (these elements are called ferrite stabilizers)

Alloying elements can be divided into two categories according to the interaction with carbon in steel:

1. Carbide-forming elements, such as Mn, Cr, Mo, W, V, Nb, Ti, and Zr. They go into solid solution in cementite at low concentrations. At higher concentrations, they form more stable alloy carbides, though Mn only dissolves in cementite.
2. Noncarbide-forming elements, such as Ni, Co, Cu, Si, P, and Al. They are free from carbide in steels, and normally found in the matrix [5,11,12].

To simplify the discussion, the effects of various alloying elements listed below are summarized separately.

1.2.1 Carbon

The amount of carbon (C) required in the finished steel limits the type of steel that can be made. As the C content of rimmed steels increases, surface quality deteriorates. Killed steels in the approximate range of 0.15–0.30% C may have poorer surface quality and require special processing to attain surface quality comparable to steels with higher or lower C contents.

Carbon has a moderate tendency for macrosegregation during solidification, and it is often more significant than that of any other alloying elements. Carbon has a strong tendency to segregate at the defects in steels (such as grain boundaries and dislocations). Carbide-forming elements may interact with carbon and form alloy carbides. Carbon is the main hardening element in all steels except the austenitic precipitation hardening (PH) stainless steels, managing steels, and interstitial-free (IF) steels. The strengthening effect of C in steels consists of solid solution strengthening and carbide dispersion strengthening. As the C content in steel increases, strength increases, but ductility and weldability decrease [4,5].

1.2.2 Manganese

Manganese (Mn) is present in virtually all steels in amounts of 0.30% or more [13]. Manganese is essentially a deoxidizer and a desulfurizer [14]. It has a lesser tendency for macrosegregation than any of the common elements. Steels above 0.60% Mn cannot be readily rimmed. Manganese is beneficial to surface quality in all carbon ranges (with the exception of extremely low-carbon rimmed steels) and reduction in the risk of red-shortness. Manganese favorably affects forgeability and weldability.

Manganese is a weak carbide former, only dissolving in cementite, and forms alloying cementite in steels [5]. Manganese is an austenite former as a result of the open γ-phase field. Large quantities (>2% Mn) result in an increased tendency toward cracking and distortion during quenching [4,5,15]. The presence of alloying element Mn in steels enhances the impurities such as P, Sn, Sb, and As segregating to grain boundaries and induces temper embrittlement [5].

1.2.3 Silicon

Silicon (Si) is one of the principal deoxidizers used in steelmaking; therefore, silicon content also determines the type of steel produced. Killed carbon steels may contain Si up to a maximum of 0.60%. Semikilled steels may contain moderate amounts of Si. For example, in rimmed steel, the Si content is generally less than 0.10%.

Silicon dissolves completely in ferrite, when silicon content is below 0.30%, increasing its strength without greatly decreasing ductility. Beyond 0.40% Si, a marked decrease in ductility is noticed in plain carbon steels [4].

If combined with Mn or Mo, silicon may produce greater hardenability of steels [5]. Due to the addition of Si, stress corrosion can be eliminated in Cr–Ni austenitic steels. In heat-treated steels, Si is an important alloy element, and increases hardenability, wear resistance, elastic limit and yield strength, and scale resistance in heat-resistant steels [5,15]. Si is a noncarbide former, and free from cementite or carbides; it dissolves in martensite and retards the decomposition of alloying martensite up to 300°C.

1.2.4 Phosphorus

Phosphorus (P) segregates during solidification, but to a lesser extent than C and S. Phosphorus dissolves in ferrite and increases the strength of steels. As the amount of P increases, the ductility and impact toughness of steels decrease, and raises the cold-shortness [4,5].

Phosphorus has a very strong tendency to segregate at the grain boundaries, and causes the temper embrittlement of alloying steels, especially in Mn, Cr, Mn–Si, Cr–Ni, and Cr–Mn steels. Phosphorus also increases the hardenability and retards the decomposition of martensite-like Si in steels [5]. High P content is often specified in low-carbon free-machining steels to improve machinability. In low-alloy structural steels containing ~0.1% C, P increases strength and atmospheric corrosion resistance. In austenitic Cr–Ni steels, the addition of P can cause precipitation effects and an increase in yield points [15]. In strong oxidizing agent, P causes grain boundary corrosion in austenitic stainless steels after solid solution treatment as a result of the segregation of P at grain boundaries [5].

1.2.5 Sulfur

Increased amounts of sulfur (S) can cause red- or hot-shortness due to the low-melting sulfide eutectics surrounding the grain in reticular fashion [15,16]. Sulfur has a detrimental effect on transverse ductility, notch impact toughness, weldability, and surface quality (particularly in the lower carbon and lower manganese steels), but has a slight effect on longitudinal mechanical properties.

Sulfur has a very strong tendency to segregate at grain boundaries and causes reduction of hot ductility in alloy steels. However, sulfur in the range of 0.08–0.33% is intentionally added to free-machining steels for increased machinability [5,17] .

Sulfur improves the fatigue life of bearing steels [18], because (1) the thermal coefficient on MnS inclusion is higher than that of matrix, but the thermal coefficient of oxide inclusions is lower than that of matrix, (2) MnS inclusions coat or cover oxides (such as

alumina, silicate, and spinel), thereby reducing the tensile stresses in the surrounding matrix [5,10,19].

1.2.6 Aluminum

Aluminum (Al) is widely used as a deoxidizer and a grain refiner [9]. As Al forms very hard nitrides with nitrogen, it is usually an alloying element in nitriding steels. It increases scaling resistance and is therefore often added to heat-resistant steels and alloys. In precipitation-hardening stainless steels, Al can be used as an alloying element, causing precipitation-hardening reaction. Aluminum is also used in maraging steels. Aluminum increases the corrosion resistance in low-carbon corrosion-resisting steels. Of all the alloying elements, Al is one of the most effective elements in controlling grain growth prior to quenching.

Aluminum has the drawback of a tendency to promote graphitization.

1.2.7 Nitrogen

Nitrogen (N) is one of the important elements in expanded γ-field group. It can expand and stabilize the austenitic structure, and partly substitute Ni in austenitic steels. If the nitride-forming elements V, Nb, and Ti are added to high-strength low-alloy (HSLA) steels, fine nitrides and carbonitrides will form during controlled rolling and controlled cooling. Nitrogen can be used as an alloying element in microalloying steels or austenitic stainless steels, causing precipitation or solid solution strengthening [5]. Nitrogen induces strain aging, quench aging, and blue brittleness in low-carbon steels.

1.2.8 Chromium

Chromium (Cr) is a medium carbide former. In the low Cr/C ratio range, only alloyed cementite $(Fe,Cr)_3C$ forms. If the Cr/C ratio rises, chromium carbides $(Cr,Fe)_7C_3$ or $(Cr,Fe)_{23}C_6$ or both, would appear. Chromium increases hardenability, corrosion and oxidation resistance of steels, improves high-temperature strength and high-pressure hydrogenation properties, and enhances abrasion resistance in high-carbon grades. Chromium carbides are hard and wear-resistant and increase the edge-holding quality. Complex chromium–iron carbides slowly go into solution in austenite; therefore, a longer time at temperature is necessary to allow solution to take place before quenching is accomplished [5,6,14]. Chromium is the most important alloying element in steels. The addition of Cr in steels enhances the impurities, such as P, Sn, Sb, and As, segregating to grain boundaries and induces temper embrittlement.

1.2.9 Nickel

Nickel (Ni) is a noncarbide-forming element in steels. As a result of the open γ-phase field, Ni is an austenite-forming element [5,11,15]. Nickel raises hardenability. In combination with Ni, Cr and Mo, it produce greater hardenability, impact toughness, and fatigue resistance in steels [5,10,11,18]. Nickel dissolving in ferrite improves toughness, decreases $FATT_{50\%}$ (°C), even at the subzero temperatures [20]. Nickel raises the corrosion resistance of Cr–Ni austenitic stainless steels in nonoxidizing acid medium.

1.2.10 Molybdenum

Molybdenum (Mo) is a pronounced carbide former. It dissolves slightly in cementite, while molybdenum carbides will form when the Mo content in steel is high enough. Molybdenum can induce secondary hardening during the tempering of quenched steels and improves the creep strength of low-alloy steels at elevated temperatures.

The addition of Mo produces fine-grained steels, increases hardenability, and improves fatigue strength. Alloy steels containing 0.20–0.40% Mo or V display a delayed temper embrittlement, but cannot eliminate it. Molybdenum increases corrosion resistance and is used to a great extent in high-alloy Cr ferritic stainless steels and with Cr–Ni austenitic stainless steels. High Mo contents reduce the stainless steel's susceptibility to pitting [5,15]. Molybdenum has a very strong solid solution strengthening in austenitic alloys at elevated temperatures. Molybdenum is a very important alloying element for alloy steels.

1.2.11 Tungsten

Tungsten (W) is a strong carbide former. The behavior of W is very similar to Mo in steels. Tungsten slightly dissolves in cementite. As the content of W increases in alloy steels, W forms very hard, abrasion-resistant carbides, and can induce secondary hardening during the tempering of quenched steels. It promotes hot strength and red-hardness and thus cutting ability. It prevents grain growth at high temperature. W and Mo are the main alloying elements in high-speed steels [5,13]. However, W and Mo impair scaling resistance.

1.2.12 Vanadium

Vanadium (V) is a very strong carbide former. Very small amounts of V dissolve in cementite. It dissolves in austenite, strongly increasing hardenability, but the undissolved vanadium carbides decrease hardenability [5]. Vanadium is a grain refiner, and imparts strength and toughness. Fine vanadium carbides and nitrides give a strong dispersion hardening effect in microalloyed steels after controlled rolling and controlled cooling. Vanadium provides a very strong secondary hardening effect on tempering, therefore it raises hot-hardness and thus cutting ability in high-speed steels. Vanadium increases fatigue strength and improves notch sensitivity.

Vanadium increases wear resistance, edge-holding quality, and high-temperature strength. It is therefore used mainly as an additional alloying element in high-speed, hot-forging, and creep-resistant steels. It promotes the weldability of heat-treatable steels. The presence of V retards the rate of tempering embrittlement in Mo-bearing steels.

1.2.13 Niobium and Tantalum

Niobium (Nb) and tantalum (Ta) are very strong carbide and nitride formers. Small amounts of Nb can form fine nitrides or carbonitrides and refine the grains, therefore increasing the yield strength of steels. Niobium is widely used in microalloying steels to obtain high strength and good toughness through controlled rolling and controlled cooling practices. A 0.03% Nb in austenite can increase the yield strength of medium-carbon steel by 150 MPa. Niobium-containing nonquenched and tempered steels, including microalloyed medium-carbon steels and low-carbon bainite (martensite) steels, offer a greatly improved combination of strength and toughness. Niobium is a stabilizer in Cr–Ni austenitic steels to eliminate intergranular corrosion.

1.2.14 Titanium

Titanium (Ti) is a very strong carbide and nitride former. The effects of Ti are similar to those of Nb and V, but titanium carbides and nitrides are more stable than those of Nb and V. It is widely used in austenitic stainless steels as a carbide former for stabilization to eliminate intergranular corrosion. By the addition of Ti, intermetallic compounds are formed in maraging steels, causing age hardening. Titanium increases creep rupture strength through formation of special nitrides and tends significantly to segregation and banding [15].

Ti, Nb, and V are effective grain inhibitors because their nitrides and carbides are quite stable and difficult to dissolve in austenite. If Ti, Nb, and V dissolve in austenite, the hardenability of alloy steels may increase strongly due to the presence of Mn and Cr in steels. Mn and Cr decrease the stability of Ti-, Nb-, and V-carbides in steels [5].

1.2.15 Rare Earth Metals

Rare earth metals (REMs) constitute the IIIB group of 17 elements in the periodic table. They are scandium (Sc) of the fourth period, yttrium (Y) of the fifth period, and the lanthanides of the sixth period, which include the elements, lanthanum (La), cerium (Ce), praseodymium (Pr), neodymium (Nd), promethium (Pm), samarium (Sm), europium (Eu), gadolinium (Gd), terbium (Tb), dysprosium (Dy), holmium (Ho), erbium (Er), thulium (Tm; Tu), ytterbium (Yb), and lutecium (or lutecium, Lu). Their chemical and physical properties are similar. They generally coexist and are difficult to separate in ore beneficiation and metal extraction so they are usually supplied as a mixture and used in various mixture states in metallurgical industries. REMs are strong deoxidizers and desulfurizers, and they also react with the low-melting elements, such as antimony (Sb), tin (Sn), arsenic (As), and phosphorus (P), forming high-melting compounds and preventing them from causing the red-shortness and temper embrittlement [21,22]. The effects of REM on shape control and modification of inclusions would improve transversal plasticity and toughness, hot ductility, fatigue strength, and machinability. REMs tend strongly to segregate at the grain boundaries and increase the hardenability of steels [21,23].

1.2.16 Cobalt

Cobalt (Co) is a noncarbide former in steels. It decreases hardenability of carbon steels, but by addition of Cr, it increases hardenability of Cr–Mo alloy steels. Cobalt raises the martensitic transformation temperature of M_s (°C) and decreases the amount of retained austenite in alloy steels. Cobalt promotes the precipitation hardening [5]. It inhibits grain growth at high temperature and significantly improves the retention of temper and high-temperature strength, resulting in an increase in tool life. The use of Co is generally restricted to high-speed steels, hot-forming tool steels, maraging steels, and creep-resistant and high-temperature materials [13,15].

1.2.17 Copper

Copper (Cu) addition has a moderate tendency to segregate. Above 0.30% Cu can cause precipitation hardening. It increases hardenability. If Cu is present in appreciable amounts, it is detrimental to hot-working operations. It is detrimental to surface quality and exaggerates the surface defects inherent in resulfurized steels. However, Cu improves the atmospheric corrosion resistance (when in excess of 0.20%) and the tensile properties in alloy and low-alloy steels, and reportedly helps the adhesion of paint [6,14]. In austenitic stainless steels, a Cu content above 1% results in improved resistance to H_2SO_4 and HCl and stress corrosion [5,15].

1.2.18 Boron

Boron (B), in very small amounts (0.0005–0.0035%), has a starting effect on the hardenability of steels due to the strong tendency to segregate at grain boundaries. The segregation of B in steels is a nonequilibrium segregation. It also improves the hardenability of other alloying elements. It is used as a very economical substitute for some of the more expensive elements. The beneficial effects of B are only apparent with lower- and medium-carbon steels, with no real increase in hardenability above 0.6% C [14]. The weldability of boron-alloyed steels is another reason for their use. However, large amounts of B result in brittle, unworkable steels.

1.2.19 Zirconium

Zirconium (Zr) is added to killed HSLA steels to obtain improvement in inclusion characteristics, particularly sulfide inclusions, where modifications of inclusion shape improve ductility in transverse bending. It increases the life of heat-conducting materials. It is also a strong carbide former and produces a contracted austenite phase field [5,15].

1.2.20 Lead

Lead (Pb) is sometimes added (in the range of 0.2–0.5%) to carbon and alloy steels through mechanical dispersion during teeming to improve machinability.

1.2.21 Tin

Tin (Sn) in relatively small amounts is harmful to steels. It has a very strong tendency to segregate at grain boundaries and induces temper embrittlement in alloy steels. It has a detrimental effect on the surface quality of continuous cast billets containing small amounts of Cu [24]. Small amounts of Sn and Cu also decrease the hot ductility of steels in the austenite + ferrite region [25].

1.2.22 Antimony

Antimony (Sb) has a strong tendency to segregate during the freezing process, and has a detrimental effect on the surface quality of continuous cast billets. It also has a very strong tendency to segregate at grain boundaries and cause temper embrittlement in alloy steels.

1.2.23 Calcium

Calcium (Ca) is a strong deoxidizer; silicocalcium is used usually in steelmaking. The combination of Ca, Al, and Si forms low-melting oxides in steelmaking, and improves machinability.

1.3 CLASSIFICATION OF STEELS

Steels can be classified by different systems depending on [4,6,8]:

1. Compositions, such as carbon (or nonalloy), low-alloy, and alloy steels
2. Manufacturing methods, such as converter, electric furnace, or electroslag remelting methods
3. Application or main characteristic, such as structural, tool, stainless steel, or heat-resistant steels
4. Finishing methods, such as hot rolling, cold rolling, casting, or controlled rolling and controlled cooling
5. Product shape, such as bar, plate, strip, tubing, or structural shape
6. Oxidation practice employed, such as rimmed, killed, semikilled, and capped steels
7. Microstructure, such as ferritic, pearlitic, martensitic, and austenitic (Figure 1.1)
8. Required strength level, as specified in the American Society for Testing and Materials (ASTM) standards
9. Heat treatment, such as annealing, quenching and tempering, air cooling (normalization), and thermomechanical processing
10. Quality descriptors and classifications, such as forging quality and commercial quality

Among the above classification systems, chemical composition is the most widely used basis for designation and is given due emphasis in this chapter. Classification systems based on oxidation practice, application, and quality descriptors are also briefly discussed.

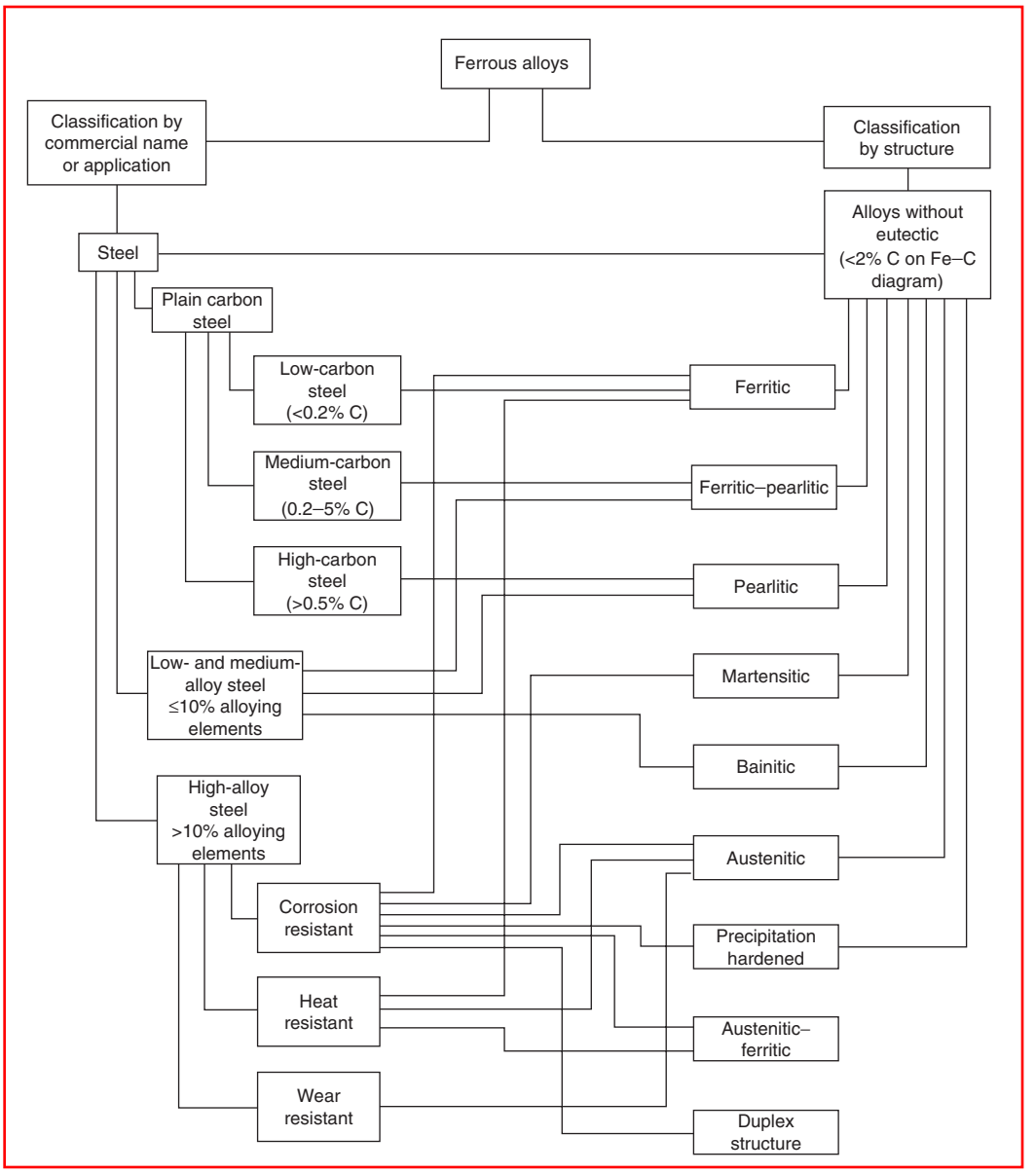

FIGURE 1.1 Classification of steels. (Courtesy of D.M. Stefanescu, University of Alabama, Tuscaloosa, AL. Slightly modified by the present authors.)

1.3.1 Types of Steels Based on Deoxidation Practice

Steels, when cast into ingots, can be classified into four types according to the deoxidation practice or, alternatively, by the amount of gas evolved during solidification. These four types are called killed, semikilled, capped, and rimmed steels [6,8].

1.3.1.1 Killed Steels

Killed steel is a type of steel from which there is practically no evolution of gas during solidification of the ingot after pouring, because of the complete deoxidation, and formation of pipe in the upper central portion of the ingot, which is later cut off and discarded. All alloy steels, most

low-alloy steels, and many carbon steels are usually killed. The continuous casting billets are also killed. The essential quality criterion is soundness [26–28]. Killed steel is characterized by a homogeneous structure and even distribution of chemical compositions and properties.

Killed steel is produced by the use of a deoxidizer such as Al and a ferroalloy of Mn or Si; However, calcium silicide and other special deoxidizers are sometimes used.

1.3.1.2 Semikilled Steels

Gas evolution is not completely suppressed by deoxidizing additions in semikilled steel, because it is partially deoxidized. There is a greater degree of gas evolution than in killed steel, but less than in capped or rimmed steel. An ingot skin of considerable thickness is formed before the beginning of gas evolution. A correctly deoxidized semikilled steel ingot does not have a pipe but does have well-scattered large blow holes in the top-center half of the ingot; however, the blow holes weld shut during rolling of the ingot. Semikilled steels generally have a carbon content in the range of 0.15–0.30%. They find a wide range of uses in structural shapes, skelp, and pipe applications. The main features of semikilled steels are UJ variable degrees of uniformity in composition, which are intermediate between those of killed and rimmed steels and less segregation than rimmed steel, and (2) a pronounced tendency for positive chemical segregation at the top center of the ingot (Figure 1.2).

1.3.1.3 Rimmed Steels

Rimmed steel is characterized by a great degree of gas evolution during solidification in the mold and a marked difference in chemical composition across the section and from the top to the bottom of the ingot (Figure 1.2). These result in the formation of an outer ingot skin or rim of relatively pure iron and an inner liquid (core) portion of the ingot with higher concentrations of alloying and residual elements, especially C, N, S, and P, having lower melting temperature. The higher purity zone at the surface is preserved during rolling [28]. Rimmed ingots are best suited for the manufacture of many products, such as plates, sheets, wires, tubes, and shapes, where good surface or ductility is required [28].

The technology of producing rimmed steels limits the maximum content of C and Mn, and the steel does not retain any significant amount of highly oxidizable elements such as Al, Si, or Ti. Rimmed steels are cheaper than killed or semikilled steels for only a small addition of deoxidizer is required and is formed without top scrap.

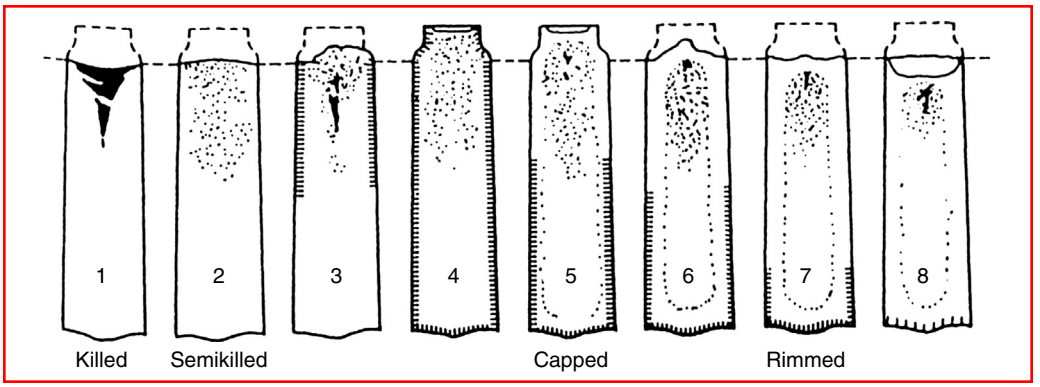

FIGURE 1.2 Eight typical conditions of commercial steel ingots, cast in identical bottle-top molds, in relation to the degree of suppression of gas evolution. The dotted line denotes the height to which the steel originally was poured in each ingot mold. Based on the carbon, and more significantly, the oxygen content of the steel, the ingot structures range from that of a completely killed ingot (No. 1) to that of a violently rimmed ingot (No. 8). (From W.D. Landford and H.E. McGannon, Eds., *The Making, Shaping, and Treating of Steel*, 10th ed., U.S. Steel, Pittsburgh, PA, 1985.)

1.3.1.4 Capped Steels

Capped steel is a type of steel with characteristics similar to those of a rimmed steel but to a degree intermediate between that of rimmed and semikilled steels. Less deoxidizer is used to produce a capped ingot than to produce a semikilled ingot [29]. This induces a controlled rimming action when the ingot is cast. The gas entrapped during solidification is excess of that required to counteract normal shrinkage, resulting in a tendency for the steel to rise in the mold.

Capping is a variation of rimmed steel practice. The capping operation confines the time of gas evolution and prevents the formation of an excessive number of gas voids within the ingot. The capped ingot process is usually applied to steels with carbon contents greater than 0.15% that are used for sheet, strip, tin plate, skelp, wire, and bars.

Mechanically capped steel is poured into bottle-top molds using a heavy cast iron cap to seal the top of the ingot and to stop the rimming action [29]. Chemically capped steel is cast in open-top molds. The capping is accomplished by the addition of Al or ferrosilicon to the top of the ingot, causing the steel at the top surface to solidify rapidly. The top portion of the ingot is cropped and discarded.

1.3.2 Quality Descriptors and Classifications

Quality descriptors are names applied to various steel products to indicate that a particular product possesses certain characteristics that make it especially well suited for specific applications or fabrication processes. The quality designations and descriptors for various carbon steel products and alloy steel plates are listed in Table 1.1. Forging quality and cold extrusion quality descriptors for carbon steels are self-explanatory. However, others are not explicit; for example, merchant quality hot-rolled carbon steel bars are made for noncritical applications requiring modest strength and mild bending or forming but not requiring forging or heat-treating operations. The quality classification for one steel commodity is not necessarily extended to subsequent products made from the same commodity; for example, standard quality cold-finished bars are produced from special quality hot-rolled carbon steel bars. Alloy steel plate qualities are described by structural, drawing, cold working, pressure vessel, and aircraft qualities [27].

The various physical and mechanical characteristics indicated by a quality descriptor result from the combined effects of several factors such as (1) the degree of internal soundness, (2) the relative uniformity of chemical composition, (3) the number, size, and distribution of nonmetallic inclusions, (4) the relative freedom from harmful surface imperfections, (5) extensive testing during manufacture, (6) the size of the discard cropped from the ingot, and (7) hardenability requirements. Control of these factors during manufacture is essential to achieve mill products with the desired characteristics. The degree of control over these and other related factors is another segment of information conveyed by the quality descriptor.

Some, but not all, of the basic quality descriptors may be modified by one or more additional requirements as may be appropriate, namely macroetch test, special discard, restricted chemical composition, maximum incidental (residual) alloying elements, austenitic grain size, and special hardenability. These limitations could be applied forging quality alloy steel bars but not to merchant quality bars.

Understanding the various quality descriptors is difficult because most of the prerequisites for qualifying steel for a specific descriptor are subjective. Only limitations on chemical composition ranges, residual alloying elements, nonmetallic inclusion count, austenitic grain size, and special hardenability are quantifiable. The subjective evaluation of the other attributes depends on the experience and the skill of the individuals who make the evaluation. Although the use of these subjective quality descriptors might appear impractical and imprecise, steel products made to meet the requirements of a specific quality descriptor can be relied upon to have those characteristics necessary for that product to be used in the suggested application or fabrication operation [6].

TABLE 1.1
Quality Descriptions[a] of Carbon and Alloy Steels

Carbon Steels

Semifinished for forging
- Forging quality
- Special hardenability
- Special internal soundness
- Nonmetallic inclusion requirement
- Special surface

Carbon steel structural sections
- Structural quality

Carbon steel plates
- Regular quality
- Structural quality
- Cold-drawing quality
- Cold-pressing quality
- Cold-flanging quality
- Forging quality
- Pressure vessel quality

Hot-rolled carbon steel bars
- Merchant quality
- Special quality
  - Special hardenability
  - Special internal soundness
  - Nonmetallic inclusion requirement
  - Special surface
- Scrapless nut quality
- Axle shaft quality
- Cold extrusion quality
- Cold-heading and cold-forging quality

Cold-finished carbon steel bars
- Standard quality
  - Special hardenability
  - Special internal soundness
  - Nonmetallic inclusion requirement
  - Special surface
- Cold-heading and cold-forging quality
- Cold extrusion quality

Hot-rolled sheets
- Commercial quality
- Drawing quality
- Drawing quality special killed
- Structural quality

Cold-rolled sheets
- Commercial quality
- Drawing quality
- Drawing quality special killed
- Structural quality

Porcelain enameling sheets
- Commercial quality
- Drawing quality
- Drawing quality special killed

Long terne sheets
- Commercial quality
- Drawing quality
- Drawing quality special killed
- Structural quality

Galvanized sheets
- Commercial quality
- Drawing quality
- Drawing quality special killed
- Lock-forming quality

Electrolytic zinc coated sheets
- Commercial quality
- Drawing quality
- Drawing quality special killed
- Structural quality

Hot-rolled strip
- Commercial quality
- Drawing quality
- Drawing quality special killed
- Structural quality

Cold-rolled strip
- Specific quality descriptions are not

Mill products
- Specific quality descriptions are not applicable to tin mill products

Carbon steel wire
- Industrial quality wire
- Cold extrusion wires
- Heading, forging, and roll-threading wires
- Mechanical spring wires
- Upholstery spring construction wires
- Welding wire

Carbon steel flut wire
- Stitching wire
- Stapling wire

Carbon steel pipe

Structural tubing

Line pipe

Oil country tubular goods

Steel specialty tubular products
- Pressure tubing
- Mechanical tubing
- Aircraft tubing

Hot-rolled carbon steel wire rods
- Industrial quality
- Rods for manufacture of wire intended for electric welded chain
- Rods for heading, forging, and roll-threading wire
- Rods for lock washer wire
- Rods for scrapless nut wire
- Rods for upholstery spring wire
- Rods for welding wire

Alloy Steels

Alloy steel plates
- Drawing quality
- Pressure vessel quality
- Structural quality
- Aircraft physical quality

Hot-rolled alloy steel bars
- Regular quality
- Aircraft quality or steel subject to magnetic particle inspection
- Axle shaft quality
- Bearing quality
- Cold-heading quality
- Special cold-heading quality
- Rifle barrel quality, gun quality, shell or A.P. shot quality

Alloy steel wire
- Aircraft quality
- Bearing quality
- Special surface quality

Cold-finished alloy steel bars
- Regular quality
- Aircraft quality or steel subject to magnetic particle inspection
- Axle shaft quality
- Bearing shaft quality
- Cold-heading quality
- Special cold-heading quality
- Rifle barrel quality, gun quality, shell or A.P. shot quality

Line pipe

Oil country tubular goods

Steel specialty tubular goods
- Pressure tubing
- Mechanical tubing
- Stainless and heat-resisting pipe, pressure

TABLE 1.1 (Continued)
Quality Descriptions[a] of Carbon and Alloy Steels

Carbon Steels	Alloy Steels
provided in cold-rolled strip because this product is largely produced for specific and use	tubing, and mechanical tubing Aircraft tubing pipe

[a]In the case of certain qualities, P and S are usually finished to lower limits than the specified maximum.
Source: From H. Okamoto, C–Fe, in *Binary Alloy Phase Diagrams*, 2nd ed., T.B. Massalski, Ed., ASM International, Materials Park, OH, 1990, pp. 842–848.

1.3.3 Classification of Steel Based on Chemical Composition

1.3.3.1 Carbon and Carbon–Manganese Steels

In addition to carbon, plain carbon steels contain the following other elements: Mn up to 1.65%, S up to 0.05%, P up to 0.04%, Si up to 0.60%, and Cu up to 0.60%. The effects of each of these elements in plain carbon steels have been summarized in Section 1.2.

Carbon steel can be classified according to various deoxidation processes (see Section 1.3.1). Deoxidation practice and steelmaking process will have an effect on the characteristics and properties of the steel (see Section 1.2). However, variations in C content have the greatest effect on mechanical properties, with C additions leading to increased hardness and strength. As such, carbon steels are generally grouped according to their C content. In general, carbon steels contain up to 2% total alloying elements and can be subdivided into low-carbon, medium-carbon, high-carbon, and ultrahigh-carbon (UHC) steels; each of these designations is discussed below.

As a group, carbon steels constitute the most frequently used steel. Table 1.2 lists various grades of standard carbon and low-alloy steels with the Society of Automotive Engineers and American Iron and Steel Institute (SAE-AISI) designations. Table 1.3 shows some representative standard carbon steel compositions with SAE-AISI and the corresponding Unified Numbering System (UNS) designations [6,8,30].

Low-carbon steels contain up to 0.25% C. The largest category of this class is flat-rolled products (sheet or strip), usually in the cold-rolled or subcritical annealed condition and usually with final temper-rolling treatment. The carbon content for high formability and high drawability steels is very low (<0.10% C) with up to 0.40% Mn. These lower carbon steels are used in automobile body panels, tin plates, appliances, and wire products.

The low-carbon steels (0.10–0.25% C) have increased strength and hardness and reduced formability compared to the lowest carbon group. They are designated as carburizing or case-hardening steels [9]. Selection of these grades for carburizing applications depends on the nature of the part, the properties required, and the processing practices preferred. An increase of carbon content of the base steel results in greater core hardness with a given quench. However, an increase in Mn increases the hardenability of both the core and the case.

A typical application for carburized plain carbon steel is for parts with hard wear-resistant surface but without any need for increased mechanical properties in the core, e.g., small shafts, plunges, or highly loaded gearing [8]. Rolled structural steels in the form of plates and

TABLE 1.2
SAE-AISI Designation System for Carbon and Low-Alloy Steels

Numerals and Digits	Type of Steel and Nominal Alloy Content (%)
Carbon steels	
10xx[a]	Plain carbon (Mn 1.00 max)
11xx	Resulfurized
12xx	Resulfurized and rephosphorized
15xx	Plain carbon (max Mn range: 1.00–1.65)
Manganese steels	
13xx	Mn 1.75
Nickel steels	
23xx	Ni 3.50
25xx	Ni 5.00
Nickel–chromium steels	
31xx	Ni 1.25; Cr 0.65 and 0.80
32xx	Ni 1.75; Cr 1.07
33xx	Ni 3.50; Cr 1.50 and 1.57
34xx	Ni 3.00; Cr 0.77
Molybdenum steels	
40xx	Mo 0.20 and 0.25
44xx	Mo 0.40 and 0.52
Chromium–molybdenum steels	
41xx	Cr 0.50, 0.80, and 0.95; Mo 0.12, 0.20, 0.25, and 0.30
Nickel–chromium–molybdenum steels	
43xx	Ni 1.82; Cr 0.50 and 0.80; Mo 0.25
43BVxx	Ni 1.82; Cr 0.50; Mo 0.12 and 0.25; V 0.03 min
47xx	Ni 1.05; Cr 0.45; Mo 0.20 and 0.35
81xx	Ni 0.30; Cr 0.40; Mo 0.12
86xx	Ni 0.55; Cr 0.50; Mo 0.20
87xx	Ni 0.55; Cr 0.50; Mo 0.25
88xx	Ni 0.55; Cr 0.50; Mo 0.35
93xx	Ni 3.25; Cr 1.20; Mo 0.12
94xx	Ni 0.45; Cr 0.40; Mo 0.12
97xx	Ni 0.55; Cr 0.20; Mo 0.20
98xx	Ni 1.00; Cr 0.80; Mo 0.25
Nickel–molybdenum steels	
46xx	Ni 0.85 and 1.82; Mo 0.20 and 0.25
48xx	Ni 3.50; Mo 0.25
Chromium steels	
50xx	Cr 0.27, 0.40, 0.50, and 0.65
51xx	Cr 0.80, 0.87, 0.92, 0.95, 1.00, and 1.05
Chromium (bearing) steels	
50xxx	Cr 0.50 } C 1.00
51xxx	Cr 1.02 min } C 1.00
52xxx	Cr 1.45 } C 1.00
Chromium–vanadium steels	
61xx	Cr 0.60, 0.80, and 0.95; V 0.10 and 0.15 min
Tungsten–chromium steel	
72xx	W 1.75; Cr 0.75
Silicon–manganese steels	
92xx	Si 1.40 and 2.00; Mn 0.65, 0.82, and 0.85; Cr 0 and 0.65
High-strength low-alloy steels	
9xx	Various SAE grades
Boron steels	
xxBxx	B denotes boron steel
Leaded steels	
xxLxx	L denotes leaded steel

[a]The xx in the last two digits of these designations indicates that the carbon content (in hundredths of a percent) is to be inserted.

Source: From Courtesy of ASM International, Materials Park, OH. With permission.

TABLE 1.3
Standard Carbon Steel Compositions with SAE-AISI and Corresponding UNS Designations

Plain Carbon Steel (Nonresulfurized, 1.0% Mn Max)[a]

UNS Number	SAE-AISI Number	Cast or Heat Chemical Ranges and Limits (%)[a]			
		C	Mn	P max	S max
G10060	1006	0.08 max	0.45 max	0.040	0.050
G10080	1008	0.10 max	0.50 max	0.040	0.050
G10090	1009	0.15 max	0.60 max	0.040	0.050
G10100	1010	0.08–0.13	0.30–0.60	0.040	0.050
G10120	1012	0.10–0.15	0.30–0.60	0.040	0.050
G10150	1015	0.12–0.18	0.30–0.60	0.040	0.050
G10160	1016	0.12–0.18	0.60–0.90	0.040	0.050
G10170	1017	0.14–0.20	0.30–0.60	0.040	0.050
G10180	1018	0.14–0.20	0.60–0.90	0.040	0.050
G10190	1019	0.14–0.20	0.70–1.00	0.040	0.050
G10200	1020	0.17–0.23	0.30–0.60	0.040	0.050
G10210	1021	0.17–0.23	0.60–0.90	0.040	0.050
G10220	1022	0.17–0.23	0.70–1.00	0.040	0.050
G10230	1023	0.19–0.25	0.30–0.60	0.040	0.050
G10250	1025	0.22–0.28	0.30–0.60	0.040	0.050
G10260	1026	0.22–0.28	0.60–0.90	0.040	0.050
G10300	1030	0.27–0.34	0.60–0.90	0.040	0.050
G10330	1033	0.29–0.36	0.70–1.00	0.040	0.050
G10350	1035	0.31–0.38	0.60–0.90	0.040	0.050
G10370	1037	0.31–0.38	0.70–1.00	0.040	0.050
G10380	1038	0.34–0.42	0.60–0.90	0.040	0.050
G10390	1039	0.36–0.44	0.70–1.00	0.040	0.050
G10400	1040	0.36–0.44	0.60–0.90	0.040	0.050
G10420	1042	0.39–0.47	0.60–0.90	0.040	0.050
G10430	1043	0.39–0.47	0.70–1.00	0.040	0.050
G10450	1045	0.42–0.50	0.60–0.90	0.040	0.050
G10490	1049	0.45–0.53	0.60–0.90	0.040	0.050
G10500	1050	0.47–0.55	0.60–0.90	0.040	0.050
G10550	1055	0.52–0.60	0.60–0.90	0.040	0.050
G10600	1060	0.55–0.66	0.60–0.90	0.040	0.050
G10640	1064	0.59–0.70	0.50–0.80	0.040	0.050
G10650	1065	0.59–0.70	0.60–0.90	0.040	0.050
G10700	1070	0.65–0.76	0.60–0.90	0.040	0.050
G10740	1074	0.69–0.80	0.50–0.80	0.040	0.050
G10750	1075	0.69–0.80	0.40–0.70	0.040	0.050
G10780	1078	0.72–0.86	0.30–0.60	0.040	0.050
G10800	1080	0.74–0.88	0.60–0.90	0.040	0.050
G10840	1084	0.80–0.94	0.60–0.90	0.040	0.050
G10850	1085	0.80–0.94	0.70–1.00	0.040	0.050
G10860	1086	0.80–0.94	0.30–0.50	0.040	0.050
G10900	1090	0.84–0.98	0.60–0.90	0.040	0.050
G10950	1095	0.90–1.04	0.30–0.50	0.040	0.050

Continued

TABLE 1.3 (Continued)
Standard Carbon Steel Compositions with SAE-AISI and Corresponding UNS Designations

Free-Cutting (Resulfurized) Carbon Steel Compositions[a]

UNS Number	SAE-AISI Number	Cast or Heat Chemical Ranges and Limits (%)			
		C	Mn	P max	S
G11080	1108	0.08–0.13	0.50–0.80	0.040	0.08–0.13
G11100	1110	0.08–0.13	0.30–0.60	0.040	0.08–0.13
G11170	1117	0.14–0.20	1.00–1.30	0.040	0.08–0.13
G11180	1118	0.14–0.20	1.30–1.60	0.040	0.08–0.13
G11370	1137	0.32–0.39	1.35–1.65	0.040	0.08–0.13
G11390	1139	0.35–0.43	1.35–1.65	0.040	0.13–0.20
G11400	1140	0.37–0.44	0.70–1.00	0.040	0.08–0.13
G11410	1141	0.37–0.45	1.35–1.65	0.040	0.08–0.13
G11440	1144	0.40–0.48	1.35–1.65	0.040	0.24–0.33
G11460	1146	0.42–0.49	0.70–1.00	0.040	0.08–0.13
G11S10	1151	0.48–0.55	0.70–1.00	0.040	0.08–0.13

Standard Resulfurized and Rephosphorized Carbon Steels[a]

UNS Number	SAE-AISI Number	Cast or Heat Chemical Ranges and Limits, %(a)				
		C max	Mn	P	S	Pb
Gl2110	1211	0.13	0.60–0.90	0.07–0.12	0.10–0.15	—
G12120	1212	0.13	0.70–1.00	0.07–0.12	0.16–0.23	—
G12130	1213	0.13	0.70–1.00	0.07–0.12	0.24–0.33	—
G12150	1215	0.09	0.75–1.05	0.04–0.09	0.26–0.35	—
G12144	12L14[b]	0.15	0.85–1.15	0.04–0.09	0.26–0.35	0.15–0.35

Standard Nonresulfurized Carbon Steels (Over 1.0% Manganese)

UNS Number	SAE-AISI Number	Cast or Heat Chemical Ranges and Limits, %			
		C	Mn	P max	S max
G15130	1513	0.10–0.16	1.10–1.40	0.040	0.050
G15220	1522	0.18–0.24	1.10–1.40	0.040	0.050
G15240	1524	0.19–0.25	1.35–1.65	0.040	0.050
G15260	1526	0.22–0.29	1.10–1.40	0.040	0.050
G15270	1527	0.22–0.29	1.20–1.50	0.040	0.050
G15360	1536	0.30–0.37	1.20–1.50	0.040	0.050
G15410	1541	0.36–0.44	1.35–1.65	0.040	0.050
G15480	1548	0.44–0.52	1.10–1.40	0.040	0.050
G15510	1551	0.45–0.56	0.85–1.15	0.040	0.050
G15520	1552	0.47–0.55	1.20–1.50	0.040	0.050
G15610	1561	0.55–0.65	0.75–1.05	0.040	0.050
G15660	1566	0.60–0.71	0.85–1.15	0.040	0.050

Applicable to semifinished products for forging, hot-rolled and cold-finished bars, wire rods, and seamless tubing.
[a]It is not common practice to produce the 12xx series of steels to specified limits for silicon because of its adverse effect on machinability.
[b]Contains 0.15–0.35% lead; other steels listed here can be produced with similar amounts of lead.
Source: From *Numbering System, Chemical Composition, 1993 SAE Handbook*, Vol. 1, Materials Society of Automotive Engineers, Warrendale, PA, pp. 1.01–1.189.

sections containing ~0.25% C, with up to 1.5% Mn and Al are used if improved toughness is required. When used for stampings, forgings, seamless tubes, and boilerplate, Al addition should be avoided. An important type of this category is the low-carbon free-cutting steels containing up to 0.15% C and up to 1.2% Mn, a minimum of Si and up to 0.35% S with or without 0.30% Pb. These steels are suited for automotive mass production manufacturing methods [4].

Medium-carbon steels containing 0.30–0.55% C and 0.60–1.65% Mn are used where higher mechanical properties are desired. They are usually hardened and strengthened by heat treatment or by cold work. Low-carbon and manganese steels in this group find wide applications for certain types of cold-formed parts that need annealing, normalizing, or quenching and tempering treatment before use. The higher carbon grades are often cold drawn to specific mechanical properties for use without heat treatment for some applications.

All of these steels can be used for forgings, and their selection is dependent on the section size and the mechanical properties needed after heat treatment [8]. These grades, generally produced as killed steels, are used for a wide range of applications that include automobile parts for body, engines, suspensions, steering, engine torque converter, and transmission [31]. Some Pb or S additions make them free-cutting grades, whereas Al addition produces grain refinement and improved toughness. In general, steels containing 0.40–0.60% C are used as rails, railway wheels, tires, and axles.

High-carbon steels containing 0.55–1.00% C and 0.30–0.90% Mn have more restricted applications than the medium-carbon steels because of higher production cost and poor formability (or ductility) and weldability. High-carbon steels find applications in the spring industry (as light and thicker plat springs, laminated springs, and heavier coiled springs), farm implement industry (as plow beams, plowshares, scraper blades, discs, mowers, knives, and harrow teeth), and high-strength wires where improved wear characteristics and higher strength than those attainable with lower carbon grades are needed.

UHC steels are experimental plain carbon steels with 1.0–2.1% C (15–32 vol% cementite) [32–34]. Optimum superplastic elongation has been found at about 1.6% C content [9]. These steels have the capability of emerging as important technological materials because they exhibit superplasticity. The superplastic behavior of these materials is attributed to the structure consisting of uniform distribution of very fine, spherical, discontinuous particles (0.1–1.5 μm diameter) in a very fine-grained ferrite matrix (0.5–2.0 μm diameter) that can be readily achieved by any of the four thermomechanical treatment routes described elsewhere [4].

1.3.3.2 Low-Alloy Steels

Alloy steels may be defined as those steels that owe their improved properties to the presence of one or more special elements or to the presence of large proportions of elements such as Mn and Si than are ordinarily present in carbon steels [26]. Alloy steels contain Mn, Si, or Cu in quantities greater than the maximum limits (e.g., 1.65% Mn, 0.60% Si, and 0.60% Cu) of carbon steels, or they contain special ranges or minimums of one or more alloying elements. However, in some countries Mn, Si, or Cu as an alloy element in low-alloy and alloy steels is only greater than 1.00% Mn, 0.50% Si, or 0.10% Cu [7].

The alloying elements increase the mechanical and fabrication properties. Broadly, alloy steels can be divided into (1) low-alloy steels containing less than 5 wt% total noncarbon alloy addition, (2) medium-alloy steels containing 5–10 wt% total noncarbon alloy addition, and (3) high-alloy steels with more than 10 wt% total noncarbon alloy addition. Table 1.4 lists some low-alloy steel compositions with SAE-AISI and corresponding UNS designations.

Low-alloy steels constitute a group of steels that exhibit superior mechanical properties compared to plain carbon steels as the result of addition of such alloying elements as Ni, Cr, and Mo. For many low-alloy steels, the main function of the alloying elements is to increase

TABLE 1.4
Low-Alloy Steel Compositions Applicable to Billets, Blooms, Slabs, and Hot-Rolled and Cold-Finished Bars (Slightly Wider Ranges of Compositions Apply to Plates)

UNS Number	SAE Number	Corresponding AISI Number	Ladle Chemical Composition Limits (%)[a]								
			C	Mn	P	S	Si	Ni	Cr	Mo	V
G13300	1330	1330	0.28–0.33	1.60–1.90	0.035	0.040	0.15–0.35	—	—	—	—
G13350	1335	1335	0.33–0.38	1.60–1.90	0.035	0.040	0.15–0.35	—	—	—	—
G13400	1340	1340	0.38–0.43	1.60–1.90	0.035	0.040	0.15–0.35	—	—	—	—
G13450	1345	1345	0.43–0.48	1.60–1.90	0.035	0.040	0.15–0.35	—	—	—	—
G40230	4023	4023	0.20–0.25	0.70–0.90	0.035	0.040	0.15–0.35	—	—		
G40240	4024	4024	0.20–0.25	0.70–0.90	0.035	0.035–0.050	0.15–0.35	—	—	0.20–0.30	—
G40270	4027	4027	0.25–0.30	0.70–0.90	0.035	0.040	0.15–0.35	—	—	0.20–0.30	—
G40280	4028	4028	0.25–0.30	0.70–0.90	0.035	0.035–0.050	0.15–0.35	—	—	0.20–0.30	—
G40320	4032	—	0.30–0.35	0.70–0.90	0.035	0.040	0.15–0.35	—	—	0.20–0.30	—
G40370	4037	4037	0.35–0.40	0.70–0.90	0.035	0.040	0.15–0.35	—	—	0.20–0.30	—
G40420	4042	—	0.40–0.45	0.70–0.90	0.035	0.040	0.15–0.35	—	—	0.20–0.30	—
G40470	4047	4047	0.45–0.50	0.70–0.90	0.035	0.040	0.15–0.35	—	—	0.20–0.30	—
G41180	4118	4118	0.18–0.23	0.70–0.90	0.035	0.040	0.15–0.35	—	0.40–0.60	0.08–0.15	—
G41300	4130	4130	0.28–0.33	0.40–0.60	0.035	0.040	0.15–0.35	—	0.80–1.10	0.15–0.25	—
G41350	4135	—	0.33–0.38	0.70–0.90	0.035	0.040	0.15–0.35	—	0.80–1.10	0.15–0.25	—
G41370	4137	4137	0.35–0.40	0.70–0.90	0.035	0.040	0.15–0.35	—	0.80–1.10	0.15–0.25	—
G41400	4140	4140	0.38–0.43	0.75–1.00	0.035	0.040	0.15–0.35	—	0.80–1.10	0.15–0.25	—
G41420	4142	4142	0.40–0.45	0.75–1.00	0.035	0.040	0.15–0.35	—	0.80–1.10	0.15–0.25	—
G41450	4145	4145	0.41–0.48	0.75–1.00	0.035	0.040	0.15–0.35	—	0.80–1.10	0.15–0.25	—
G41470	4147	4147	0.45–0.50	0.75–1.00	0.035	0.040	0.15–0.35	—	0.80–1.10	0.15–0.25	—
G41500	4150	4150	0.48–0.53	0.75–1.00	0.035	0.040	0.15–0.35	—	0.80–1.10	0.15–0.25	—
G41610	4161	4161	0.56–0.64	0.75–1.00	0.035	0.040	0.15–0.35	—	0.70–0.90	0.25–0.35	—
G43200	4320	4320	0.17–0.22	0.45–0.65	0.035	0.040	0.15–0.35	1.65–2.00	0.40–0.60	0.20–0.30	—
G43400	4340	4340	0.38–0.43	0.60–0.80	0.035	0.040	0.15–0.35	1.65–2.00	0.70–0.90	0.20–0.30	—
G43406	E4340[b]	E4340	0.38–0.43	0.65–0.85	0.025	0.025	0.15–0.35	1.65–2.00	0.70–0.90	0.20–0.30	—
G44220	4422	—	0.20–0.25	0.70–0.90	0.035	0.040	0.15–0.35	—	—	0.35–0.45	—
G44270	4427	—	0.24–0.29	0.70–0.90	0.035	0.040	0.15–0.35	—	—	0.35–0.45	—

G46150	4615	4615	0.13–0.18	0.45–0.65	0.035	0.040	0.15–0.25	1.65–2.00	—	0.20–0.30	—
G46170	4617	—	0.15–0.20	0.45–0.65	0.035	0.040	0.15–0.35	1.65–2.00	—	0.20–0.30	—
G46200	4620	4620	0.17–0.22	0.45–0.65	0.035	0.040	0.15–0.35	1.65–2.00	—	0.20–0.30	—
G46260	4626	4626	0.24–0.29	0.45–0.65	0.035	0.040 max	0.15–0.35	0.70–1.00	—	0.15–0.25	—
G47180	4718	4718	0.16–0.21	0.70–0.90	—	—	—	0.90–1.20	0.35–0.55	0.30–0.40	—
G47200	4720	4720	0.17–0.22	0.50–0.70	0.035	0.040	0.15–0.35	0.90–1.20	0.35–0.55	0.15–0.25	—
G48150	4815	4815	0.13–0.18	0.40–0.60	0.035	0.040	0.15–0.35	3.25–3.75	—	0.20–0.30	—
G48170	4817	4817	0.15–0.20	0.40–0.60	0.035	0.040	0.15–0.35	3.25–3.75	—	0.20–0.30	—
G48200	4820	4820	0.18–0.23	0.50–0.70	0.035	0.040	0.15–0.35	3.23–3.75	—	0.20–0.30	—
G50401	50B40[c]	—	0.38–0.43	0.75–1.00	0.035	0.040	0.15–0.35	—	0.40–0.60	—	—
G50441	50B44[c]	50B44	0.43–0.48	0.75–1.00	0.035	0.040	0.15–0.35	—	0.40–0.60	—	—
G50460	5O46	—	0.43–0.48	0.75–1.00	0.035	0.040	0.15–0.35	—	0.20–0.35	—	—
G50461	50B46[c]	50B46	0.44–0.49	0.75–1.00	0.035	0.040	0.15–0.35	—	0.20–0.35	—	—
G50501	50B50[c]	50B50	0.48–0.53	0.75–1.00	0.035	0.040	0.15–0.35	—	0.40–0.60	—	—
G50600	5060	—	0.56–0.64	0.75–1.00	0.035	0.040	0.15–0.35	—	0.40–0.60	—	—
G50601	50B60[c]	50B60	0.56–0.64	0.75–1.00	0.035	0.040	0.15–0.35	—	0.40–0.60	—	—
G51150	5115	—	0.13–0.18	0.70–0.90	0.035	0.040	0.15–0.35	—	0.70–0.90	—	—
G51170	5117	5117	0.15–0.20	0.70–1.90	0.040	0.040	0.15–0.35	—	0.70–0.90	—	—
G51200	5120	5120	0.17–0.22	0.70–0.90	0.035	0.040	0.15–0.35	—	0.70–0.90	—	—
G51300	5130	5130	0.28–0.33	0.70–0.90	0.035	0.040	0.15–0.35	—	0.80–1.10	—	—
G51320	5132	5132	0.30–0.35	0.60–0.80	0.035	0.040	0.15–0.35	—	0.75–1.00	—	—
G51350	5135	5135	0.33–0.38	0.60–0.80	0.035	0.040	0.15–3.35	—	0.80–1.05	—	—
G51400	5140	5140	0.38–0.43	0.70–0.90	0.035	0.040	0.15–0.35	—	0.70–0.90	—	—
G51470	5147	5147	0.46–0.51	0.70–0.95	0.035	0.040	0.15–0.35	—	0.85–1.15	—	—
G51500	5150	5150	0.48–0.53	0.70–0.90	0.035	0.040	0.15–0.35	—	0.70–0.90	—	—
G51550	5155	5155	0.51–0.59	0.70–0.90	0.035	0.040	0.15–0.35	—	0.70–0.90	—	—
G51600	5160	5160	0.56–0.64	0.75–1.00	0.035	0.040	0.15–0.35	—	0.70–0.90	—	—
G51601	51B60[c]	51B60	0.56–0.64	0.75–1.00	0.035	0.040	0.15–0.35	—	0.70–0.90	—	—
G50986	50100[b]	—	0.98–1.10	0.25–0.45	0.025	0.025	0.15–0.35	—	0.40–0.60	—	—
G51986	51100[b]	E51100	0.98–1.10	0.25–0.45	0.025	0.025	0.15–0.35	—	0.90–1.15	—	—
G52986	52100[b]	E52100	0.98–1.10	0.25–0.45	0.025	0.025	0.15–0.35	—	1.30–1.60	—	—

Continued

TABLE 1.4 (Continued)
Low-Alloy Steel Compositions Applicable to Billets, Blooms, Slabs, and Hot-Rolled and Cold-Finished Bars (Slightly Wider Ranges of Compositions Apply to Plates)

UNS Number	SAE Number	Corresponding AISI Number	Ladle Chemical Composition Limits (%)[a]								
			C	Mn	P	S	Si	Ni	Cr	Mo	V
G61180	6118	6118	0.16–0.21	0.50–0.70	0.035	0.040	0.15–0.35	—	0.50–0.70	—	0.10–0.15
G61500	6150	6150	0.48–0.53	0.70–0.90	0.035	0.040	0.15–0.35	—	0.80–1.10	—	0.15 min
G81150	8115	8115	0.13–0.18	0.70–0.90	0.035	0.040	0.15–0.35	0.20–0.40	0.30–0.50	0.08–0.15	—
G81451	81B45[c]	81B45	0.43–0.48	0.75–1.00	0.035	0.040	0.15–0.35	0.20–0.40	0.35–0.55	0.08–0.15	—
G86150	8615	8615	0.13–0.18	0.70–0.90	0.035	0.040	0.15–0.35	0.40–0.70	0.40–0.60	0.15–0.25	—
G86170	8617	8617	0.15–0.20	0.70–0.90	0.035	0.040	0.15–0.35	0.40–0.70	0.40–0.60	0.15–0.25	—
G86200	8620	8620	0.18–0.23	0.70–0.90	0.035	0.040	0.15–0.35	0.40–0.70	0.40–0.60	0.15–0.25	—
G86220	8622	8622	0.20–0.25	0.70–0.90	0.035	0.040	0.15–0.35	0.40–0.70	0.40–0.60	0.15–0.25	—
G86250	8625	8625	0.23–0.28	0.70–0.90	0.035	0.040	0.15–0.35	0.40–0.70	0.40–0.60	0.15–0.25	—
G86270	8627	8627	0.25–0.30	0.70–0.90	0.035	0.040	0.15–0.35	0.40–0.70	0.40–0.60	0.15–0.25	—
G86300	8630	8630	0.28–0.33	0.70–0.90	0.035	0.040	0.15–0.35	0.40–0.70	0.40–0.60	0.15–0.25	—
G86370	8637	8637	0.35–0.40	0.75–1.00	0.035	0.040	0.15–0.35	0.40–0.70	0.40–0.60	0.15–0.25	—
G86400	8640	8640	0.38–0.43	0.75–1.00	0.035	0.040	0.15–0.35	0.4O–0.70	0.40–0.60	0.15–0.25	—

G86420	8642		8642	0.40–0.45	0.75–1.00	0.035	0.040	0.15–0.35	0.40–0.70	0.40–0.60	0.15–0.25	—
G86450	8645		8645	0.43–0.48	0.75–1.00	0.035	0.040	0.15–0.35	0.40–0.70	0.40–0.60	0.15–0.25	—
G86451	86B45[c]	—		0.43–0.48	0.75–1.00	0.035	0.040	0.15–0.35	0.40–0.70	0.40–0.60	0.15–0.25	—
G86500	8650	—		0.48–0.53	0.75–1.00	0.035	0.040	0.15–0.35	0.40–0.70	0.40–0.60	0.15–0.25	—
G86550	8655		8655	0.51–0.59	0.75–1.00	0.035	0.040	0.15–0.35	0.40–0.70	0.40–0.60	0.15–0.25	—
G86600	8660	—		0.56–0.64	0.75–1.00	0.035	0.040	0.15–0.35	0.40–0.70	0.40–0.60	0.15–0.25	—
G87200	8720		8720	0.18–0.23	0.70–0.90	0.035	0.040	0.15–0.35	0.40–0.70	0.40–0.60	0.20–0.30	—
G87400	8740		8740	0.38–0.43	0.75–1.00	0.035	0.040	0.15–0.35	0.40–0.70	0.40–0.60	0.20–0.30	—
G88220	8822		8822	0.20–0.25	0.75–1.00	0.035	0.040	0.15–0.35	0.40–0.70	0.40–0.60	0.30–0.40	—
G92540	9254		—	0.51–0.59	0.60–0.80	0.035	0.040	1.20–1.60	—	0.60–0.80	—	—
G92600	9260		9260	0.56–0.64	0.75–1.00	0.035	0.040	1.80–2.20	—	—	—	—
G93106	9310[b]	—		0.08–0.13	0.45–0.65	0.025	0.025	0.15–0.35	3.00–3.50	1.00–1.40	0.08–0.15	—
G94151	94B15[c]	—		0.13–0.18	0.75–1.00	0.035	0.04	0.15–0.35	0.30–0.60	0.30–0.50	0.08–0.15	—
G94171	94B17[c]	94B17		0.15–0.20	0.75–1.00	0.035	0.04	0.15–0.35	0.30–0.60	0.30–0.50	0.08–0.15	—
G94301	94B30[c]	94B30		0.28–0.33	0.75–1.00	0.035	0.04	0.15–0.35	0.30–0.60	0.30–0.50	0.08–0.15	—

[a]Small quantities of certain elements that are not specified or required may be found in alloy steels. These elements are to be considered as incidental and are acceptable to the following maximum amount, copper to 0.35%, nickel to 0.25%, chromium to 0.20%, and molybdenum to 0.06%.

[b]Electric furnace steel.

[c]Boron content is 0.0005–0.003%.

Source: From *Numbering System, Chemical Composition, 1993 SAE Handbook*, Vol. 1, Materials Society of Automotive Engineers, Warrendale, PA, pp. 1.01–1.189.

the hardenability in order to optimize the strength and toughness after heat treatment. In some instances, however, alloying elements are used to reduce environmental degradation under certain specified conditions.

Low-alloy steels can be classified according to: (1) chemical composition such as nickel steels, nickel–chromium steels, molybdenum steels, chromium–molybdenum steels, and so forth, based on the principal alloying elements present and as described in Table 1.2, (2) heat treatment such as quenched and tempered, normalized and tempered, annealed and so on, and (3) weldability.

Because of the large variety of chemical compositions possible and the fact that some steels are employed in more than one heat-treated conditions some overlap exists among the low-alloy steel classifications. However, these grades can be divided into four major groups such as (1) low-carbon quenched and tempered (QT) steels, (2) medium-carbon ultrahigh-strength steels, (3) bearing steels, and (4) heat-resistant Cr–Mo steels (see Table 1.5).

Low-carbon QT steels (also called low-carbon martensitic steels) are characterized by relatively high yield strength with a minimum yield strength of 690 MPa (100 ksi) and good notch toughness, ductility, corrosion resistance, or weldability. The chemical compositions of low-carbon QT steels are listed in Table 1.5. These steels are not included in SAE-AISI classification. However, they are covered by ASTM designations, and a few steels, such as HY-80 and HY-100, are included in military (MIL) specifications. The steels listed are primarily available in the form of plate, sheet, bar, structural shape, or forged products. They are extensively used for a wide variety of applications such as pressure vessels, earth-moving, and mining equipment and as major members of large steel structures. They are also used for cold-headed and cold-forged parts as fasteners or pins and heat-treated to the desired properties [26].

Medium-carbon ultrahigh-strength steels are structural steels with very high strength. These steels exhibit a minimum yield strength of 1380 MPa (200 ksi). Table 1.5 lists typical compositions such as SAE-AISI 4130, high-strength 4140, deeper hardening higher-strength 4340, 300M (a modification of 4340 steel with increased Si content (1.6%) to raise the third transformation temperature of tempering and prevent temper embrittlement of martensite) and Ladish D-6a and Ladish D-6ac steels (another modification of 4340 with grain refiner V and higher C, Cr, and Mo contents, developed for aircraft and missile structural applications). Other less prominent steels that may be included in this family are SAE-AISI 6150 steel (a tough shock-resistant, shallow-hardening Cr–V steel with high fatigue and impact resistance in the heat-treated conditions) and 8640 steel (an oil-hardening steel exhibiting properties similar to those of 4340 steel) [35]. Product forms include billet, bar, rod, forgings, plate, sheet, tubing, and welding wire.

These steels are used for gears, aircraft landing gear, airframe parts, pressure vessels, bolts, springs, screws, axles, studs, fasteners, machinery parts, connecting rods, crankshafts, piston rods, oil well drilling bits, high-pressure tubing, flanges, wrenches, sprockets, etc. [35].

Bearing steels used for ball and roller bearing applications comprise low-carbon (0.10–0.20% C) case-hardened steels and high-carbon (~1% C) through-hardened or surface-induction hardened steels (see Table 1.5). Many of these steels are covered by SAE-AISI designations.

Chromium–molybdenum heat-resistant steels contain 0.5–9% Cr, 0.5–1.0% Mo, and usually less than 0.20% C. They are ordinarily supplied in the normalized and tempered, quenched and tempered, or annealed condition. Cr–Mo steels are extensively used in oil refineries, oil and gas industries, chemical industries, electric power generating stations and fossil fuel and nuclear power plants for piping, heat exchangers, superheater tubes, and pressure vessels. Various product shapes and corresponding ASTM specifications for these steels are provided in Table 1.6. Nominal chemical compositions are given in Table 1.7.

TABLE 1.5
Chemical Compositions for Typical Low-Alloy Steels

Steel	Composition, wt%[a]								
	C	Si	Mn	P	S	Ni	Cr	Mo	Other
Low-carbon quenched and tempered steels									
A 514/A 517 grade A	0.15–0.21	0.40–0.80	0.80–1.10	0.035	0.04	—	0.50–0.80	0.18–0.28	0.05–0.15 Zn[b] 0.0025 B
A 514/A 517 grade F	0.10–0.20	0.15–0.35	0.60–1.00	0.035	0.04	0.70–1.00	0.40–0.65	0.40–0.60	0.03–0.08 V 0.15–0.50 Cu 0.0005–0.005 B
A 514/A 517 grade R	0.15–0.20	0.20–0.35	0.85–1.15	0.035	0.04	0.90–1.10	0.35–0.65	0.15–0.25	0.03–0.08 V
A 533 type A	0.25	0.15–0.40	1.15–1.50	0.035	0.04	—	—	0.45–0.60	—
A 533 type C	0.25	0.15–0.40	1.15–1.50	0.035	0.04	0.70–1.00	—	0.45–0.60	—
HY-80	0.12–0.18	0.15–0.35	0.10–0.40	0.025	0.025	2.00–3.25	1.00–1.80	0.20–0.60	0.25 Cu 0.03 V 0.02 Ti
HY-100	0.12–0.20	0.15–0.35	0.10–0.40	0.025	0.025	2.25–3.50	1.00–1.80	0.20–0.60	0.25 Cu 0.03 V 0.02 Ti
Medium-carbon ultrahigh-strength steels									
4130	0.28–0.33	0.20–0.35	0.40–0.60	—	—	—	0.80–1.10	0.15–0.25	—
4340	0.38–0.43	0.20–0.35	0.60–0.80	—	—	1.65–2.00	0.70–0.90	0.20–0.30	—
300M	0.40–0.46	1.45–1.80	0.65–0.90	—	—	1.65–2.00	0.70–0.95	0.30–0.45	0.05 V min
D-6a	0.42–0.48	0.15–0.30	0.60–0.90	—	—	0.40–0.70	0.90–1.20	0.90–1.10	0.05–0.10 V
Carburizing bearing steels									
4118	0.18–0.23	0.15–0.30	0.70–0.90	0.035	0.040	—	0.40–0.60	0.08–0.18	—
5120	0.17–0.22	0.15–0.30	0.70–0.90	0.035	0.040	—	0.70–0.90	—	—
3310	0.08–0.13	0.20–0.35	0.45–0.60	0.025	0.025	3.25–3.75	1.40–1.75	—	—
Through-hardened bearing steels									
52100	0.98–1.10	0.15–0.30	0.25–0.45	0.025	0.025	—	1.30–1.60	—	—
A 485 grade 1	0.90–1.05	0.45–0.75	0.95–1.25	0.025	0.025	0.25	0.90–1.20	0.10	0.35 Cu
A 485 grade 3	0.95–1.10	0.15–0.35	0.65–0.90	0.025	0.025	0.25	1.10–1.50	0.20–0.30	0.35 Cu

[a]Single values represent the maximum allowable.

[b]Zirconium may be replaced by cerium. When cerium is added, the cerium/sulfur ratio should be approximately 1.5:1, based on heat analysis.

Source: From Anon., *ASM Handbook*, 10th ed., Vol. 1, ASM International, Materials Park, OH, 1990, pp. 140–194.

TABLE 1.6
ASTM Specifications for Chromium–Molybdenum Steel Product Forms

Type	Forgings	Tubes	Pipe	Castings	Plate
$^1/_2$Cr–$^1/_2$Mo	A 182-F2	—	A 335-P2	—	A 387-Gr2
			A 369-FP2		
			A 426-CP2		
1Cr–$^1/_2$Mo	A 182-F12	—	A 335-P12	—	A 387-Gr12
	A 336-F12		A 369-FP12		
		A 426-CP12			
1$^1/_4$Cr–$^1/_2$Mo	A 182-F11	A 199-T11	A 335-P11	A 217-WC6	A 387-Gr11
	A 336-F11/F11A	A 200-T11	A 369-FP11	A 356-Gr6	
	A 541-C11C	A 213-T11	A 426-CP11	A 389-C23	
2$^1/_4$Cr–1Mo	A 182-F22/F22a	A 199-T22	A 335-P22	A 217-WC9	A 387-Gr22
	A 336-F22/F22A	A 200-T22	A 369-FP22	A 356-Gr10	A 542
	A 541-C22C/22D	A 213-T22	A 426-CP22		
3Cr–1Mo	A 182-F21	A 199-T21	A 335-P21	—	A 387-Gr21
	A 336-F21/F21A	A 200-T21	A 369-FP21		
		A 213-T21	A 426-CP21		
3Cr–1MoV	A 182-F21b	—	—	—	—
5Cr–$^1/_2$Mo	A 182-F5/F5a	A 199-T5	A 335-P5	A 217-C5	A 387-Gr5
	A 336-F5/F5A	A 200-T5	A 369-FP5		
	A 473-501/502	A 213-T5	A 426-CP5		
5Cr–$^1/_2$MoSi	—	A 213-T5b	A 335-P5b	—	—
			A 426-CP5b		
5Cr–$^1/_2$MoTi	—	A 213-T5c	A 335-P5c	—	—
7Cr–$^1/_2$Mo	A 182-F7	A 199-T7	A 335-P7	—	A 387-Gr7
	A 473-501A	A 200-T7	A 369-FP7		
		A 213-T7	A 426-CP7		
9Cr–1Mo	A 182-F9	A 199-T9	A 335-P9	A 217-C12	A 387-Gr9
	A 336-F9	A 200-T9	A 369-FP9		
	A 473-501B	A 213-T9	A 426-CP9		

Source: From Anon., *ASM Handbook*, 10th ed., Vol. 1, ASM International, Materials Park, OH, 1990, pp. 140–194.

1.3.3.3 High-Strength Low-Alloy Steels

A general description of HSLA steel is as that containing: (1) low carbon (0.03–0.25%) content to obtain good toughness, formability, and weldability, (2) one or more of the strong carbide-forming microalloying elements (MAEs) (e.g., V, Nb, or Ti), (3) a group of solid solution strengthening elements (e.g., Mn up to 2.0% and Si), and (4) one or more of the additional MAEs (e.g., Ca, Zr) and the rare earth elements, particularly Ce and La, for sulfide inclusion shape control and increasing toughness [4,5,21,22,36,37]. In many other HSLA steels, small amounts of Ni, Cr, Cu, and particularly Mo are also present, which increase atmospheric corrosion resistance and hardenability. A very fine ferrite grain structure in the final product produced by a combination of controlled rolling and controlled cooling with an optimum utilization of microalloying additions, in HSLA steels, is an important factor in simultaneously increasing strength and toughness and decreasing the ductile–brittle transition temperature (to as low as -70°C). Carbides (NbC, VC, TiC), nitrides (TiN, NbN, AlN), and carbonitrides (e.g., V(C,N), Nb(C,N), (Nb,V) CN, (Nb,Ti) CN) are the dispersed second-phase particles that act as grain size refiners or dispersive strengthening phases in HSLA steels.

TABLE 1.7
Nominal Chemical Compositions for Heat-Resistant Chromium–Molybdenum Steels

Type	UNS Designation	Composition (%)[a]						
		C	Mn	S	P	Si	Cr	Mo
$^1/_2$Cr–$^1/_2$Mo	K12122	0.10–0.20	0.30–0.80	0.040	0.040	0.10–0.60	0.50–0.80	0.45–0.65
1Cr–$^1/_2$Mo	K11562	0.15	0.30–0.60	0.045	0.045	0.50	0.80–1.25	0.45–0.65
1$^1/_4$Cr–$^1/_2$Mo	K11597	0.15	0.30–0.60	0.030	0.030	0.50–1.00	1.00–1.50	0.45–0 65
1$^1/_4$Cr–$^1/_2$Mo	K11592	0.10–0.20	0.30–0.80	0.040	0.040	0.50–1.00	1.00–1.50	0.45–0.65
2$^1/_4$Cr–1Mo	K21590	0.15	0.30–0.60	0.040	0.040	0.50	2.00–2.50	0.87–1.13
3Cr–1Mo	K31545	0.15	0.30–0.60	0.030	0.030	0.50	2.65–3.35	0.80–1.06
3Cr–1MoV[b]	K31830	0.18	0.30–0.60	0.020	0.020	0.10	2.75–3.25	0.90–1.10
5Cr–$^1/_2$Mo	K41545	0.15	0.30–0.60	0.030	0.030	0.50	4.00–6.00	0.45–0.65
7Cr–$^1/_2$Mo	K61595	0.15	0.30–0.60	0.030	0.030	0.50–1.00	6.00–8.00	0.45–0.65
9Cr–1Mo	K90941	0.15	0.30–0.60	0.030	0.030	0.50–1.00	8.00–10.00	0.90–1.10
9Cr–1MoV[c]	—	0.08–0.12	0.30–0.60	0.010	0.020	0.20–0.50	8.00–9.00	0.85–1.05

[a]Single values are maximums.
[b]Also contains 0.02–0.030% V, 0.001–0.003% B, and 0.015–0.035% Ti.
[c]Also contains 0.40% Ni, 0.18–0.25% V, 0.06–0.10% Nb, 0.03–0.07% N, and 0.04% Al.
Source: From Anon., *ASM Handbook*, 10th ed., Vol. 1, ASM International, Materials Park, OH, 1990, pp. 140–194.

HSLA steels are successfully used as ship, plate, bar, structural sections, and forged bar products, and find applications in several diverse fields such as oil and gas pipelines; in the automotive, agricultural, and pressure vessel industries, in offshore structures and platforms and in the constructions of crane, bridges, buildings, shipbuildings, railroad, tank cars, and power transmission and TV towers [36].

1.3.3.3.1 Classification of HSLA Steels

Several special terms are used to describe various types of HSLA steels [37–39]:

1. *Weathering steels*: Steels containing ~0.1% C, 0.2–0.5% Cu, 0.5–1.0% Mn, 0.05–0.15% P, 0.15–0.90% Si, and sometimes containing Cr and Ni, exhibiting superior atmospheric corrosion resistance. Typical applications include railroad cars, bridges, and unpainted buildings.
2. *Control-rolled steels*: Steels designated to develop a highly deformed austenite structure by hot rolling (according to a predetermined rolling schedule) that will transform to a very fine equiaxed ferrite structure on cooling.
3. *Pearlite-reduced steels*: Steels strengthened by very fine-grained ferrite and precipitation hardening but with low carbon content, and therefore exhibiting little or no pearlite in the microstructure.
4. *Microalloyed steels*: Conventional HSLA steels containing V, Ti, or Nb, as defined above. They exhibit discontinuous yielding behavior.
5. *Acicular ferrite steels*: Very low-carbon (typically 0.03–0.06%) steels with enough hardenability (by Mn, Mo, Nb, and B additions) to transform on cooling to a very fine, high-strength acicular ferrite structure rather than the usual polygonal ferrite structure. In addition to high strength and good toughness, these steels have continuous yielding behavior.
6. *Low-carbon bainite steels*: Steels are strengthened by bainite, with very fine grains and precipitations. They contain 0.02–0.2% C, 0.6–1.6% Mn, 0.3–0.6% Mo, and MAEs (such as V, Nb, Ti, and B), usually containing 0.4–0.7% Cr. The yield strength of these steels is higher than 490 MPa, with good toughness [5].
7. *Low-carbon martensite steels*: Steels are strengthened by martensite with high hardenability (by addition of Mo, Mn, Cr, Nb, and B) and fine grains (by Nb addition). These steels contain 0.05–0.25% C, 1.5–2.0% Mn, 0.20–0.50 Mo, and MAEs (such as Nb, Ti, V, and B). Some steels containing small amounts of Ni, Cr, and Cu, after rolling or forging, and directly quenching and tempering attain a low-carbon martensite structure with high yield strength (760–1100 MPa), high toughness (CVN 50–130 J), and superior fatigue strength [5,40,41].
8. *Dual-phase steels*: Steels comprising essentially fine dispersion of hard strong martensite but sometimes also retained austenite or even bainite in a soft and fine-grained ferrite matrix. The volume function of martensite is about 20–30%. Steels are characterized by continuous yielding (i.e., no yield point elongation), low yield stress (the YS/UTS ratio being around 0.50), high UTS, superior formability, and rapid initial work-hardening rate. Additionally, they possess greater resistance to onset of necking (i.e., plastic instability) in the uniaxial sheet material forming process to provide large uniform strain [42–45]. Table 1.8 lists HSLA steels according to chemical composition and minimum machining property requirements.

TABLE 1.8
Composition Ranges and Limits for SAE HSLA Steels

SAE Designation[b]	Heat Composition Limits (%)[a] C max	Mn max	P max
942X	0.21	1.35	0.04
945A	0.15	1.00	0.04
945C	0.23	1.40	0.04
945X	0.22	1.35	0.04
950A	0.15	1.30	0.04
950B	0.22	1.30	0.04
950C	0.25	1.60	0.04
950D	0.15	1.00	0.15
950X	0.23	1.35	0.04
955X	0.25	1.35	0.04
960X	0.26	1.45	0.04
965X	0.26	1.45	0.04
970X	0.26	1.65	0.04
980X	0.26	1.65	0.04

[a]Maximum contents of sulfur and silicon for all grades: 0.050% S, 0.90% Si.
[b]Second and third digits of designation indicate minimum yield strength in ksi. Suffix X indicates that the steel contains niobium, vanadium, nitrogen, or other alloying elements. A second suffix K indicates that the steel is produced fully killed using fine-grain practice; otherwise, the steel is produced semikilled.
Source: From *Numbering System, Chemical Composition, 1993 SAE Handbook*, Vol. 1, Materials Society of Automotive Engineers, Warrendale, PA, pp. 1.01–1.189.

1.3.3.4 Tool Steels

A tool steel is any steel used to shape other metals by cutting, forming, machining, battering, or die casting or to shape and cut wood, paper, rock, or concrete. Hence tool steels are designed to have high hardness and durability under severe service conditions. They comprise a wide range from plain carbon steels with up to 1.2% C without appreciable amounts of alloying elements to the highly alloyed steels in which alloying additions reach 50%. Although some carbon tool steels and low-alloy tool steels have a wide range of carbon content, most of the higher alloy tool steels have a comparatively narrow carbon range. A mixed classification system is used to classify tool steels based on the use, composition, special mechanical properties, or method of heat treatment.

According to AISI specification, there are nine main groups of wrought tool steels. Table 1.9 lists the compositions of these tool steels with corresponding designated symbols [46], which are discussed herein.

High-speed steels are used for applications requiring long life at relatively high operating temperatures such as for heavy cuts or high-speed machining. High-speed steels are the most important alloy tool steels because of their very high hardness and good wear assistance in the heat-treated condition and their ability to retain high hardness and the elevated temperatures often encountered during the operation of the tool at high cutting speeds. This red- or hot-hardness property is an important feature of a high-speed steel [47,48].

TABLE 1.9
Composition Limits of Principal Types of Tool Steels

Designation		Composition[a] (%)								
AISI	UNS	C	Mn	Si	Cr	Ni	Mo	W	V	Co
Molybdenum high-speed steels										
M1	T11301	0.78–0.88	0.15–0.40	0.20–0.50	3.50–4.00	0.30 max	8.20–9.20	1.40–2.10	1.00–1.35	—
M2	T11302	0.78–0.88; 0.95–1.05	0.15–0.40	0.20–0.45	3.75–4.50	0.30 max	4.50–5.50	5.50–6.75	1.75–2.20	—
M3 class 1	T11313	1.00–1.10	0.15–0.40	0.20–0.45	3.75–4.50	0.30 max	4.75–6.50	5.00–6.75	2.25–2.75	—
M3 class 2	T11323	1.15–125	0.15–0.40	0.20–0.45	3.75–4.50	0.30 max	4.75–6.50	5.00–6.75	2.75–3.75	—
M4	T11304	1.25–1.40	0.15–0.40	0.20–0.45	3.75–4.75	0.30 max	4.25–5.50	5.25–6.50	3.75–4.50	—
M7	T11307	0.97–1.05	0.15–0.40	0.20–0.55	3.50–4.00	0.30 max	8.20–9.20	1.40–2.10	1.75–2.25	—
M10	T11310	0.84–0.94; 0.95–1.05	0.10–0.40	0.20–0.45	3.75–4.50	0.30 max	7.75–8.50	—	1.80–2.20	—
M30	T11330	0.75–0.85	0.15–0.40	0.20–0.45	3.50–4.25	0.30 max	7.75–9.00	1.30–2.30	1.00–1.40	4.50–5.50
M33	T11333	0.85–0.92	0.15–0.40	0.15–0.50	3.50–4.00	0.30 max	9.00–10.00	1.30–2.10	1.00–1.35	7.75–8.75
M34	T11334	0.85–0.92	0.15–0.40	0.20–0.45	3.50–4.00	0.30 max	7.75–9.20	1.40–2.10	1.90–2.30	7.75–8.75
M35	T11335	0.82–0.88	0.15–0.40	0.20–0.45	3.75–4.50	0.30 max	4.50–5.50	5.50–6.75	1.75–2.20	4.50–5.50
M36	T11336	0.80–0.90	0.15–0.40	0.20–0.45	3.75–4.50	0.30 max	4.50–5.50	5.50–6.50	1.75–2.25	7.75–8.75
M41	T11341	1.05–1.15	0.20–0.60	0.15–0.50	3.75–4.50	0.30 max	3.25–4.25	6.25–7.00	1.75–2.25	4.75–5.75
M42	T11342	1.05–1.15	0.15–0.40	0.15–0.65	3.50–4.25	0.30 max	9.00–10.00	1.15–1.85	0.95–1.35	7.75–8.75
M43	T11343	1.15–1.25	0.20–0.40	0.15–0.65	3.50–4.25	0.30 max	7.50–8.50	2.25–3.00	1.50–1.75	7.75–8.75
M44	T11344	1.10–1.20	0.20–0.40	0.30–0.55	4.00–4.75	0.30 max	6.00–7.00	5.00–5.75	1.85–2.20	11.00–12.25
M46	T11346	1.22–1.30	0.20–0.40	0.40–0.65	3.70–4.20	0.30 max	8.00–8.50	1.90–2.20	3.00–3.30	7.80–8.80
M47	T11347	1.05–1.15	0.15–0.40	0.20–0.45	3.50–4.00	0.30 max	9.25–10.00	1.30–1.80	1.15–1.35	4.75–5.25
M48	T11348	1.42–1.52	0.15–0.40	0.15–0.40	3.50–4.00	0.30 max	4.75–5.50	9.50–10.50	2.75–3.25	8.00–10.00
M62	T11362	1.25–1.35	0.15–0.40	0.15–0.40	3.50–4.00	0.30 max	10.00–11.00	5.75–6.50	1.80–2.10	—
Tungsten high-speed steels										
T1	T12001	0.65–0.80	0.10–0.40	0.20–0.40	3.75–4.50	0.30 max	—	17.25–18.75	0.90–1.30	—
T2	T12002	0.80–0.90	0.20–0.40	0.20–0.40	3.75–4.50	0.30 max	1.00 max	17.50–19.00	1.80–2.40	—
T4	T12004	0.70–0.80	0.10–0.40	0.20–0.40	3.75–4.50	0.30 max	0.40–1.00	17.50–19.00	0.80–1.20	4.25–5.75
T5	T12005	0.75–0.85	0.20–0.40	0.20–0.40	3.75–5.00	0.30 max	0.50–1.25	17.50–19.00	1.80–2.40	7.00–9.50
T6	T12006	0.75–0.85	0.20–0.40	0.20–0.40	4.00–4.75	0.30 max	0.40–1.00	18.50–21.00	1.50–2.10	11.00–13.00
T8	T12008	0.75–0.85	0.26–0.40	0.20–0.40	3.75–4.50	0.30 max	0.40–1.00	13.25–14.75	1.80–2.40	4.25–5.75
T15	T12015	1.50–1.60	0.15–0.40	0.15–0.40	3.75–5.00	0.30 max	1.00 max	11.75–13.00	4.50–5.25	4.75–5.25

Intermediate high-speed steels										
M50	T11350	0.78–0.88	0.15–0.45	0.20–0.60	3.75–4.50	0.30 max	3.90–4.75	—	0.80–1.25	—
M52	T11352	0.85–0.95	0.15–0.45	0.20–0.60	3.50–4.30	0.30 max	4.00–4.90	0.75–1.50	1.65–2.25	—
Chromium hot-work steels										
H10	T20810	0.35–0.45	0.25–0.70	0.80–1.20	3.00–3.75	0.30 max	2.00–3.00	—	0.25–0.75	—
H11	T20811	0.33–0.43	0.20–0.50	0.80–1.20	4.75–5.50	0.30 max	1.10–1.60	—	0.30–0.60	—
H12	T20812	0.30–0.40	0.20–0.50	0.80–1.20	4.75–5.50	0.30 max	1.25–1.75	1.00–1.70	0.50 max	—
H13	T20813	0.32–0.45	0.20–0.50	0.80–1.20	4.75–5.50	0.30 max	1.10–1.75	—	0.80–1.20	—
H14	T20814	0.35–0.45	0.20–0.50	0.80–1.20	4.75–5.50	0.30 max	—	4.00–5.25	—	—
H19	T20819	0.32–0.45	0.20–0.50	0.20–0.50	4.00–4.75	0.30 max	0.30–0.55	3.75–4.50	1.75–2.20	4.00–4.50
Tungsten hot-work steels										
H21	T20821	0.26–0.36	0.15–0.40	0.15–0.50	3.00–3.75	0.30 max	—	8.50–10.00	0.30–0.60	—
H22	T20822	0.30–0.40	0.15–0.40	0.15–0.40	1.75–3.75	0.30 max	—	10.00–11.75	0.25–0.50	—
H23	T20823	0.25–0.35	0.15–0.40	0.15–0.60	11.00–12.75	0.30 max	—	11.00–12.75	0.75–1.25	—
H24	T20824	0.42–0.53	0.15–0.40	0.15–0.40	2.50–3.50	0.30 max	—	14.00–16.00	0.40–0.60	—
H25	T20825	0.22–0.32	0.15–0.40	0.15–0.40	3.75–4.50	0.30 max	—	14.00–16.00	0.40–0.60	—
H26	T20826	0.45–0.55[b]	0.15–0.40	0.15–0.40	3.75–4.50	0.30 max	—	17.25–19.00	0.75–1.25	—
Molybdenum hot-work steels										
H42	T20842	0.55–0.70[b]	0.15–0.40	—	3.75–4.50	0.30 max	4.50–5.50	5.50–6.75	1.75–2.20	—
Air-hardening, medium-alloy, cold-work steels										
A2	T30102	0.95–1.05	1.00 max	0.50 max	4.75–5.50	0.30 max	0.90–1.40	—	0.15–0.50	—
A3	T30103	1.20–1.30	0.40–0.60	0.50 max	4.75–5.50	0.30 max	0.90–1.40	—	0.80–1.40	—
A4	T30104	0.95–1.05	1.80–2.20	0.50 max	0.90–2.20	0.30 max	0.90–1.40	—	—	—
A6	T30106	0.65–0.75	1.80–2.50	0.50 max	0.90–1.20	0.30 max	0.90–1.40	—	—	—
A7	T30107	2.00–2.85	0.80 max	0.50 max	5.00–5.75	0.30 max	0.90–1.40	0.50–1.50	3.90–5.15	—
A8	T30108	0.50–0.60	0.50 max	0.75–1.10	4.75–5.50	0.30 max	1.15–1.65	1.00–1.50	—	—
A9	T30109	0.45–0.55	0.50 max	0.95–1.15	4.75–5.50	1.25–1.75	1.30–1.80	—	0.80–1.40	—
Al0	T30110	1.25–1.50[c]	1.60–2.10	1.00–1.50	—	1.55–2.05	1.25–1.75		—	—
High-carbon, high-chromium, cold-work steels										
D2	T30402	1.40–1.60	0.60 max	0.60 max	11.00–13.00	0.30 max	0.70–1.20	—	1.10 max	—
D3	T30403	2.00–2.35	0.60 max	0.60 max	11.00–13.50	0.30 max	—	1.00 max	1.00 max	—
D4	T30404	2.05–2.40	0.60 max	0.60 max	11.00–13.00	0.30 max	0.70–1.20	—	1.00 max	—
D5	T30405	1.40–1.60	0.60 max	0.60 max	11.00–13.00	0.30 max	0.70–1.20	—	1.00 max	2.50–3.50
D7	T304O7	2.15–2.50	0.60 max	0.60 max	11.50–13.50	0.30 max	0.70–1.20	—	3.80–4.40	—

Continued

TABLE 1.9 (Continued)
Composition Limits of Principal Types of Tool Steels

Designation		Composition[a] (%)								
AISI	UNS	C	Mn	Si	Cr	Ni	Mo	W	V	Co
Oil-hardening cold-work steels										
O1	T31501	0.85–1.00	1.00–1.40	0.50 max	0.40–0.60	0.30 max	—	0.40–0.60	0.30 max	—
O2	T31502	0.85–0.95	1.40–1.80	0.50 max	0.50 max	0.30 max	0.30 max	—	0.30 max	—
O6	T31506	1.25–1.55[c]	0.30–1.10	0.55–1.50	0.30 max	0.30 max	0.20–0.30	—	—	—
O7	T31507	1.10–1.30	1.00 max	0.60 max	0.35–0.85	0.30 max	0.30 max	1.00–2.00	0.40 max	—
Shock-resisting steels										
S1	T41901	0.40–0.55	0.10–0.40	0.15–1.20	1.00–1.80	0.30 max	0.50 max	1.50–3.00	0.15–0.30	—
S2	T41902	0.40–0.55	0.30–0.50	0.90–1.20	—	0.30 max	0.30–0.60	—	0.50 max	—
S5	T41905	0.50–0.65	0.60–1.00	1.75–2.25	0.50 max	—	0.20–1.35	—	0.35 max	—
S6	T41906	0.40–0.50	1.20–1.50	2.00–2.50	1.20–1.50	—	0.30–0.50	—	0.20–0.40	—
S7	T41907	0.45–0.55	0.20–0.90	0.20–1.00	3.00–3.50	—	1.30–1.80	—	0.20–0.30[d]	—
Low-alloy special-purpose tool steels										
L2	T61202	0.45–1.00[b]	0.10–0.90	0.50 max	0.70–1.20	—	0.25 max	—	0.10–0.30	—
L6	T61206	0.65–0.75	0.25–0.80	0.50 max	0.60–1.20	1.25–2.00	0.50 max	—	0.20–0.30[d]	—

Low-carbon mold steels										
P2	T51602	0.10 max	0.10–0.40	0.10–0.40	0.75–1.25	0.10–4.50	0.15–0.40	—	—	—
P3	T51603	0.10 max	0.20–0.60	0.40 max	0.40–0.75	1.00–1.50	—	—	—	—
P4	T51604	0.12 max	0.20–0.60	0.10–0.40	4.00–5.25	—	0.40–1.00	—	—	—
P5	T51605	0.10 max	0.20–0.60	0.40 max	2.00–2.50	0.35 max	—	—	—	—
P6	T51606	0.05–0.15	0.35–0.70	0.10–0.40	1.25–1.75	3.25–3.75	—	—	—	—
P20	T51620	0.28–0.40	0.60–1.00	0.20–0.80	1.40–2.00	—	0.30–0.55	—	—	—
P21	T51621	0.18–0.22	0.20–0.40	0.20–0.40	0.50 max	3.90–4.25	—	—	0.15–0.25	1.05–1.25Al
Water-hardening tool steels										
W1	T72301	0.70–1.50[e]	0.10–0.40	0.10–0.40	0.15 max	0.20 max	0.10 max	0.15 max	0.10 max	—
W2	T72302	0.85–1.50[e]	0.10–0.40	0.10–0.40	0.15 max	0.20 max	0.10 max	0.15 max	0.15–0.35	—
W5	T72305	1.05–1.15	0.10–0.40	0.10–0.40	0.40–0.60	0.20 max	0.10 max	0.15 max	0.10 max	—

[a]All steels except group W contain 0.25 max Cu, 0.03 max P, and 0.03 max S; group W steels contain 0.20 max Cu, 0.025 max P, and 0.025 max S. Where specified, sulfur may be increased to 0.06 to 0.15% to improve machinability of group A, D, H, M, and T steels.
[b]Available in several carbon ranges.
[c]Contains free graphite in the microstructure.
[d]Optional.
[e]Specified carbon ranges are designated by suffix numbers.
Source: From A.M. Bayer and L.R. Walton, in *ASM Handbook*, 10th ed., Vol. 1, ASM International, Materials, Park, OH, 1990, pp. 757–779.

High-speed steels are grouped into molybdenum type M and tungsten type T. Type M tool steels contain Mo, W, Cr, V, Mo, and C as the major alloying elements, while type T tool steels contain W, Cr, V, Mo, Co, and C as the main alloying elements. In the United States, type M steels account for 95% of the high-speed steels produced. There is also a subgroup consisting of intermediate high-speed steels in the M group. The most popular grades among molybdenum types are M1, M2, M4, M7, M10, and M42, while those among tungsten types are T1 and T15.

The main advantage of type M steels is their lower initial cost (approximately 40% cheaper than that of similar type T steels), but they are more susceptible to decarburizing, thereby necessitating better temperature control than type T steels. By using salt baths and sometimes surface coatings, decarburization can be controlled. The mechanical properties of type M and type T steels are similar except that type M steels have slightly greater toughness than type T steels at the same hardness level [4].

Hot-work tool steels (AISI series) fall into three major groups: (1) chromium-base, types H1–H19, (2) tungsten-base, types H20–H39, and (3) molybdenum-base, types H40–H59. The distinction is based on the principal alloying additions; however, all classes have medium carbon content and Cr content varying from 1.75 to 12.75%. Among these steels, H11, H12, H13 are produced in large quantities. These steels possess good red-hardness and retain high hardness (~50 Rc) after prolonged exposures at 500–550°C. They are used extensively for hot-work applications, which include parts for aluminum and magnesium die casting and extrusion, plastic injection molding, and compression and transfer molds [47].

Cold-work tool steels comprise three categories: (1) air-hardening, medium-alloy tool steels (AISI A series), (2) high-chromium tool steels (AISI D series), and (3) oil-hardening tool steels (AISI O series). AISI A series tool steels have high hardenability and harden readily on air cooling. In the air-hardened and tempered condition, they are suitable for applications where improved toughness and reasonably good abrasion resistance are required such as for forming, blanking, and drawing dies. The most popular grade is A2. AISI D series tool steels possess excellent wear resistance and nondeforming properties, thereby making them very useful as cold-work die steels. They find applications in blanking and cold-forming dies, drawing and lamination dies, thread-rolling dies, shear and slitter blades, forming rolls, and so forth. Among these steels, D2 is by far the most popular grade [47]. AISI O series tool steels are used for blanking, coining, drawing, and forming dies and punches, shear blades, gauges, and chuck jaws after oil quenching and tempering [47]. Among these grades, O1 is the most widely used.

Shock-resisting tool steels (AISI S series) are used where repetitive impact stresses are encountered such as in hammers, chipping and cold chisels, rivet sets, punches, driver bits, stamps, and shear blades in quenched and tempered conditions. In these steels, high toughness is the major concern and hardness the secondary concern. Among these grades, S5 and S7 are perhaps the most widely used.

Low-alloy special-purpose tool steels (AISI series) are similar in composition to the W-type tool steels, except that the addition of Cr and other elements render greater hardenability and wear-resistance properties, type L6 and the low-carbon version of L2 are commonly used for a large number of machine parts.

Mold steels (AISI P series) are mostly used in low-temperature die casting dies and in molds for the injection or compression molding of plastics [46].

Water-hardening tool steels (AISI W series): Among the three compositions listed, W1 is the most widely used as cutting tools, punches, dies, files, reamers, taps, drills, razors, wood-working tools, and surgical instruments in the quenched and tempered condition.

1.3.3.5 Stainless Steels

Stainless steels may be defined as complex alloy steels containing a minimum of 10.5% Cr with or without other elements to produce austenitic, ferritic, duplex (ferritic–austenitic), martensitic, and precipitation-hardening grades. AISI uses a three-digit code for stainless steels. Table 1.10 and Table 1.11 list the compositions of standard and nonstandard stainless steels, respectively, with the corresponding designated symbols, which are discussed below [49].

Austenitic stainless steels constitute about 65–70% of the total U.S. stainless steel production and have occupied a dominant position because of their higher corrosion resistance such as strength and toughness at both elevated and ambient temperatures, excellent cryogenic properties, esthetic appeal, and varying specific combination and properties that can be obtained by different compositions within the group [50].

In general, austenitic stainless steels are Fe–Cr–Ni–C and Fe–Cr–Mn–Ni–N alloys containing 16–26% Cr, 0.75–19.0% Mn, 1–40% Ni, 0.03–0.35% C, and sufficient N to stabilize austenite at room and elevated temperatures. The 2xx series (Cr–Mn–Ni) steels contain N, 5.5–15.5% Mn, and up to 6% Ni, the 3xx (Cr–Ni) types contain higher amounts of Ni and up to 2% Mn. Mo, Cu, and Si may be added to increase corrosion resistance. Ti and Nb may be added to decrease the sensitivity of intergranular corrosion. The addition of Mo and N may increase halide-pitting resistance; Si and Cu may be added to increase resistance to stress corrosion cracking. S and Se may be added to certain series to enhance machinability. Nitrogen is added to increase yield strength.

Broadly, austenitic stainless steels can be classified into ten groups [4,51]. These classifications are not straightforward because of the overlapping effects.

Ferrite stainless steels contain essentially 10.5–30% Cr with additions of Mn and Si and occasionally Mo, Ni, Al, Ti, or Nb to confer particular characteristics. As they remain ferritic at room and elevated temperatures, they cannot be hardened by heat treatment. The ductile–brittle transition temperature of ferrite stainless steels is higher than room temperature; if $C+N < 0.0015$ wt%, the transition temperature can be kept well below the room temperature. These extra-low interstitial ferritic stainless steels have good ductility and toughness. The yield strength of ferritic stainless steels in the annealed condition is usually in the range 275–415 MPa (40–60 ksi). They are used because of their good ductility, good resistance to general liquid corrosion, and high-temperature oxidation, resistance to pitting and stress corrosion cracking, and generally lower cost than the austenitic grades [10]. As in the ferritic grade, S and Se may be added to improve machinability.

The standard ferrite stainless steels are types 405, 409, 429, 430, 430F, 430F–Se, 434, 436, 439, 444, and 446 (Table 1.10). In addition, high-quality ferrite stainless steels are types E-Brite 26-1, MoNiT (25-4-4), AL29-4c, and AL29-4-2 (Table 1.11).

Duplex stainless steels contain 18–29% Cr, 2.5–8.5% Ni, and 1–4% Mo, up to 2.5% Mn, up to 2% Si, and up to 0.35% N. They possess a mixed structure of ferrite and austenite. The volume fractions of ferrite and austenite vary between 0.3 and 0.7 in a duplex structure. The ratio of the ferrite and austenitic determines the properties of duplex stainless steels. The yield strength increases with increasing ferrite content. The ultimate tensile strength rises to a maximum at 70–80% ferrite, then decreases as the ferrite goes to 100%. Compared to austenitic grades, they can offer improved yield strength (about two to three times greater) and greater resistance to stress corrosion cracking, but the deep drawability is less than austenitic grades. Compared to ferritic grades, they can provide improved toughness, formability, and weldability. The duplex stainless steels can be embrittled due to the formability α' and σ phases. In general, duplex stainless steels cannot be used in the temperature range from 300 to 950°C.

Types AISI 329 and Carpenter 7-Mo and 7-Mo-Plus (UNS S32950) are the more popular duplex steels (Table 1.10 and Table 1.11). The new type SAF2507 contains ultralow carbon

TABLE 1.10
Compositions of Standard Stainless Steels

Type	UNS Designation	Composition (%)[a]							
		C	Mn	Si	Cr	Ni	P	S	Other
Austenitic types									
201	S20100	0.15	5.5–7.5	1.00	16.0–18.0	3.5–5.5	0.06	0.03	0.25 N
202	S20200	0.15	7.5–10.0	1.00	17.0–19.0	4.0–6.0	0.06	0.03	0.25 N
205	S20500	0.12–0.25	14.0–15.5	1.00	16.5–18.0	1.0–1.75	0.06	0.03	0.32–0.40 N
301	S30100	0.15	2.00	1.00	16.0–18.0	6.0–8.0	0.045	0.03	—
302	S30200	0.15	2.00	1.00	17.0–19.0	8.0–10.0	0.045	0.03	—
302B	S30215	0.15	2.00	2.0–3.0	17.0–19.0	8.0–10.0	0.045	0.03	—
303	S30300	0.15	2.00	1.00	17.0–19.0	8.0–10.0	0.2	0.15 min	0.6 Mo[b]
303Se	S30323	0.15	2.00	1.00	17.0–19.0	8.0–10.0	0.2	0.06	0.15 min Se
304	S30400	0.08	2.00	1.00	18.0–20.0	8.0–10.5	0.045	0.03	—
304H	S30409	0.04–0.10	2.00	1.00	18.0–20.0	8.0–10.5	0.045	0.03	—
304L	S30403	0.03	2.00	1.00	18.0–20.0	8.0–12.0	0.045	0.03	—
304LN	S30453	0.03	2.00	1.00	18.0–20.0	8.0–12.0	0.045	0.03	0.10–0.16 N
302Cu	S30430	0.08	2.00	1.00	17.0–19.0	8.0–10.0	0.045	0.03	3.0–4.0 Cu
304N	S30451	0.08	2.00	1.00	18.0–20.0	8.0–10.5	0.045	0.03	0.10–0.16 N
305	S30500	0.12	2.00	1.00	17.0–19.0	10.5–13.0	0.045	0.03	—
308	S30800	0.08	2.00	1.00	19.0–21.0	10.0–12.0	0.045	0.03	—
309	S30900	0.20	2.00	1.00	22.0–24.0	12.0–15.0	0.045	0.03	—
309S	S30908	0.08	2.00	1.00	22.0–24.0	12.0–15.0	0.045	0.03	—
310	S31000	0.25	2.00	1.50	24.0–26.0	19.0–22.0	0.045	0.03	—
310S	S31008	0.08	2.00	1.50	24.0–26.0	19.0–22.0	0.045	0.03	—
314	S31400	0.25	2.00	1.5–3.0	23.0–26.0	19.0–22.0	0.045	0.03	—
316	S31600	0.08	2.00	1.00	16.0–18.0	10.0–14.0	0.045	0.03	2.0–3.0 Mo
316F	S31620	0.08	2.00	1.00	16.0–18.0	10.0–14.0	0.20	0.10 min	1.75–2.5 Mo
316H	S31609	0.04–0.10	2.00	1.00	16.0–18.0	10.0–14.0	0.045	0.03	2.0–3.0 Mo
316L	S31603	0.03	2.00	1.00	16.0–18.0	10.0–14.0	0.045	0.03	2.0–3.0 Mo
316LN	S31653	0.03	2.00	1.00	16.0–18.0	10.0–14.0	0.045	0.03	2.0–3.0 Mo; 0.10–0.16N
316N	S31651	0.08	2.00	1.00	16.0–18.0	10.0–14.0	0.045	0.03	2.0–3.0 Mo; 0.10–0.16 N

317	S31700	0.08	2.00	1.00	18.0–20.0	11.0–15.0	0.045	0.03	3.0–4.0 Mo
317L	S31703	0.03	2.00	1.00	18.0–20.0	11.0–15.0	0.045	0.03	3.0–4.0 Mo
321	S32100	0.08	2.00	1.00	17.0–19.0	9.0–12.0	0.045	0.03	5 × %C min Ti
321H	S32109	0.04–0.10	2.00	1.00	17.0–19.0	9.0–12.0	0.045	0.03	5 × %C min Ti
330	N08330	0.08	2.00	0.75–1.5	17.0–20.0	34.0–37.0	0.04	0.03	—
347	S34700	0.08	2.00	1.00	17.0–19.0	9.0–13.0	0.045	0.03	10 × %C min Nb
347H	S34709	0.04–0.10	2.00	1.00	17.0–19.0	9.0–13.0	0.045	0.03	8 × %C min–1.0 max Nb
348	S34800	0.08	2.00	1.00	17.0–19.0	9.0–13.0	0.045	0.03	0.2 Co; 10 × %C min Nb; 0.10 Ta
348H	S34809	0.04–0.10	2.00	1.00	17.0–19.0	9.0–13.0	0.045	0.03	0.2 Co; 8 × %C min–1.0 max Nb; 0.10 Ta
384	S38400	0.08	2.00	1.00	15.0–17.0	17.0–19.0	0.045	0.03	—
Ferritic types									
405	S40500	0.08	1.00	1.00	11.5–14.5	—	0.04	0.03	0.10–0.30 A1
409	S40900	0.08	1.00	1.00	10.5–11.75	0.5	0.045	0.045	6 × %C min–0.75 max Ti
429	S42900	0.12	1.00	1.00	14.0–16.0	—	0.04	0.03	—
430	S43000	0.12	1.00	1.00	16.0–18.0	—	0.04	0.03	—
430F	S43020	0.12	1.25	1.00	16.0–18.0	—	0.06	0.15 min	0.6 Mo[b]
430FSe	S43023	0.12	1.25	1.00	16.0–18.0	—	0.06	0.06	0.15 min Se
434	S43400	0.12	1.00	1.00	16.0–18.0	—	0.04	0.03	0.75–1.25 Mo
436	S43600	0.12	1.00	1.00	16.0–18.0	—	0.04	0.03	0.75–1.25 Mo; 5 × %C min–0.70 max Nb
439	S43035	0.07	1.00	1.00	17.0–19.0	0.50	0.04	0.03	0.15 Al; 12 × %C min–1.10 Ti
442	S44200	0.2	1.00	1.00	18.0–23.0	—	0.04	0.03	
444	S44400	0.025	1.00	1.00	17.5–19.5	1.00	0.04	0.03	1.75–2.50 Mo; 0.025 N; 0.2 + 4 (%C + %N) min–0.8 max (Ti + Nb)
446	S44600	0.20	1.50	1.00	23.0–27.0	—	0.04	0.03	0.25 N

Continued

TABLE 1.10 (Continued)
Compositions of Standard Stainless Steels

Type	UNS Designation	Composition (%)[a] C	Mn	Si	Cr	Ni	P	S	Other
Duplex (ferritic–austenitic) type									
329	S32900	0.20	1.00	0.75	23.0–28.0	2.50–5.00	0.04	0.03	1.00–2.00 Mo
Martensitic types									
403	S40300	0.15	1.00	0.50	11.5–13.0	—	0.04	0.03	—
410	S41000	0.15	1.00	1.00	11.5–13.5	—	0.04	0.03	—
414	S41400	0.15	1.00	1.00	11.5–13.5	1.25–2.50	0.04	0.03	—
416	S41600	0.15	1.25	1.00	12.0–14.0	—	0.06	0.15 min	0.6 Mo[b]
416Se	S41623	0.15	1.25	1.00	12.0–14.0	—	0.06	0.06	0.15 min Se
420	S42000	0.15 min	1.00	1.00	12.0–14.0	—	0.04	0.03	—
420F	S42020	0.15 min	1.25	1.00	12.0–14.0	—	0.06	0.15 min	0.6 Mo[b]
422	S42200	0.20–0.25	1.00	0.75	11.5–13.5	0.5–1.0	0.04	0.03	0.75–1.25 Mo; 0.75–1.25 W; 0.15–0.3 V
431	S43100	0.20	1.00	1.00	15.0–17.0	1.25–2.50	0.04	0.03	—
440A	S44002	0.60–0.75	1.00	1.00	16.0–18.0	—	0.04	0.03	0.75 Mo
440B	S44003	0.75–0.95	1.00	1.00	16.0–18.0	—	0.04	0.03	0.75 Mo
440C	S44004	0.95–1.20	1.00	1.00	16.0–18.0	—	0.04	0.03	0.75 Mo
Precipitation-hardening types									
PH13-8Mo	S13800	0.05	0.20	0.10	12.25–13.25	7.5–8.5	0.01	0.008	2.0–2.5 Mo; 0.90–1.35 Al; 0.01 N
15-5PH	S15500	0.07	1.00	1.00	14.0–15.5	3.5–5.5	0.04	0.03	2.5–4.5 Cu; 0.15–0.45 Nb
17-4PH	S17400	0.07	1.00	1.00	15.5–17.5	3.0–5.0	0.04	0.03	3.0–5.0 Cu; 0.15–0.45 Nb
17-7PH	S17700	0.09	1.00	1.00	16.0–18.0	6.5–7.75	0.04	0.04	0.75–1.5 Al

[a]Single values are maximum values unless otherwise indicated.
[b]Optional.
Source: From S.D. Washko and G. Aggen, in *ASM Handbook*, 10th ed., Vol. 1, ASM International, Materials Park, OH, 1990, pp. 841–907.

TABLE 1.11
Compositions of Nonstandard Stainless Steels

Designation[a]	UNS Designation	Composition (%)[b] C	Ma	Si	Cr	Ni	P	S	Other
Austenitic stainless steels									
Gall-Tough	S20161	0.15	4.00–6.00	3.00–4.00	15.00–18.00	4.00–6.00	0.040	0.040	0.08–0.20 N
203 EZ (XM-II)	S20300	0.08	5.0–6.5	1.00	16.0–18.0	5.0–6.5	0.040	0.18–0.35	0.5 Mo; 1.75–2.25 Cu
Nitronic 50 (XM-19)	S20910	0.06	4.0–6.0	1.00	20.5–23.5	11.5–13.5	0.040	0.030	1.5–3.0 Mo; 0.2–0.4 N; 0.1–0.3 Nb; 0.1–0.3 V
Tenelon (XM-31)	S21400	0.12	14.5–16.0	0.3–1.0	7.0–18.5	0.75	0.045	0.030	0.35 N
Cryogenic Tenelon (XM-14)	S21460	0.12	14.0–16.0	1.00	7.0–19.0	5.0–6.0	0.060	0.030	0.35–0.50 N
Esshete 1250	S21500	0.15	5.5–7.0	1.20	14.0–16.0	9.0–11.0	0.040	0.030	0.003–0.009 B; 0.75–1.25 Nb; 0.15–0.40 V
Type 216 (XM-17)	S21600	0.08	7.5–9.0	1.00	17.5–22.0	5.0–7.0	0.045	0.030	2.0–3.0 Mo; 0.25–0.50 N
Type 216 L (XM-18)	S21603	0.03	7.5–9.0	1.00	17.5–22.0	7.5–9.0	0.045	0.030	2.0–3.0 Mo; 0.25–0.50 N
Nitronic 60	S21800	0.10	7.0–9.0	3.5–4.5	16.0–18.0	8.0–9.0	0.040	0.030	0.08–0.18 N
Nitronic 40 (XM-10)	S21900	0.08	8.0–10.0	1.00	19.0–21.5	5.5–7.5	0.060	0.030	0.15–0.40 N
21-6-9 LC	S21904	0.04	8.00–10.00	1.00	19.00–21.50	5.50–7.50	0.060	0.030	0.15–0.40 N
Nitronic 33 (18-3-Mn)	S24000	0.08	11.50–14.50	1.00	17.00–19.00	2.50–3.75	0.060	0.030	0.20–0.40 N
Nitronic 32 (18-2-Mn)	S24100	0.15	11.00–14.00	1.00	16.50–19.50	0.50–2.50	0.060	0.030	0.20–0.45 N
18-18 Plus	S28200	0.15	17.0–19.0	1.00	17.5–19.5	—	0.045	0.030	0.5–1.5 Mo; 0.5–1.5 Cu; 0.4–0.6 N
303 Plus X (XM-5)	S30310	0.15	2.5–4.5	1.00	17.0–19.0	7.0–10.0	0.020	0.25 min	0.6 Mo
MVMA[c]	S30415	0.05	0.60	1.30	18.5	9.50	—	—	0.15 N; 0.04 Ce
304Bl[d]	S30424	0.08	2.00	0.75	18.00–20.00	12.00–15.00	0.045	0.030	0.10 N; 1.00–1.25 B

Continued

TABLE 1.11 (Continued)
Compositions of Nonstandard Stainless Steels

Designation[a]	UNS Designation	Composition (%)[b] C	Ma	Si	Cr	Ni	P	S	Other
304 HN (XM-21)	S30452	0.04–0.10	2.00	1.00	18.0–20.0	8.0–10.5	0.045	0.030	0.16–0.30 N
Cronifer 1815 LCSi	S30600	0.018	2.00	3.7–4.3	17.0–18.5	14.0–15.5	0.020	0.020	0.2 Mo
RA 85 H[c]	S30615	0.20	0.80	3.50	18.5	14.50	—	—	1.0 Al
253 MA	S30815	0.05–0.l0	0.80	1.4–2.0	20.0–22.0	10.0–12.0	0.040	0.030	0.14–0.20 N; 0.03–0.08 Ce; 1.0 Al
Type 309 S Cb	S30940	0.08	2.00	1.00	22.0–24.0	12.0–15.0	0.045	0.030	10 × %C min to 1.10 max Nb
Type 310 Cb	S31040	0.08	2.00	1.50	24.0–26.0	19.0–22.0	0.045	0.030	l0 × %C min to 1.10 max Nb + Ta
254 SMO	S31254	0.020	1.00	0.80	19.50–20.50	17.50–18.50	0.030	0.010	6.00–6.50 Mo; 0.50–1.00 Cu; 0.180–0.220 N
Type 316 Ti	S31635	0.08	2.00	1.00	16.0–18.0	10.0–14.0	0.045	0.030	5 × %(C + N) min to 0.70 max Ti; 2.0–3.0 Mo; 0.10 N
Type 316 Cb	S31640	0.08	2.00	1.00	16.0–18.0	10.0–14.0	0.045	0.030	10 × %C min to 1.10 max Nb + Ta; 2.0–3.0 Mo; 0.10 N
Type 316 HQ	—	0.030	2.00	1.00	16.00–18.25	10.00–14.00	0.030	0.015	3.00–4.00 Cu; 2.00–3.00 Mo
Type 317 LM	S31725	0.03	2.00	1.00	18.0–20.0	13.5–17.5	0.045	0.030	4.0–5.0 Mo; 0.10 N
17-14-4 LN	S31726	0.03	2.00	0.75	17.0–20.0	13.5–17.5	0.045	0.030	4.0–5.0 Mo; 0.10–0.20 N
Type 317 LN	S31753	0.03	2.00	1.00	18.0–20.0	11.0–15.0	0.030	0.030	0.10–0.22 N
Type 370	S37000	0.03–0.05	1.65–2.35	0.5–1.0	12.5–14.5	14.5–16.5	0.040	0.010	1.5–2.5 Mo;

									0.1–0.4 Ti; 0.005 N; 0.05 Co
18-18-2 (XM-15)	S38100	0.08	2.00	1.5–2.5	17.0–19.0	17.5–18.5	0.030	0.030	—
19-9 DL	S63198	0.28–0.35	0.75–1.50	0.03–0.8	18.0–21.0	8.0–11.0	0.040	0.030	1.0–1.75 Mo; 0.1–0.35 Ti; 1.0–1.75 W; 0.25–0.60 Nb
20Cb-3	N08020	0.07	2.00	1.00	19.0–21.0	32.0–38.0	0.045	0.035	2.0–3.0 Mo; 3.0–4.0 Cu; 8 × %C min to 1.00 max Nb
20Mo-4	N08024	0.03	1.00	0.50	22.5–25.0	35.0–40.0	0.035	0.035	3.50–5.00 Mo; 0.50–1.50 Cu; 0.15–0.35 Nb
20Mo-6	N08026	0.03	1.00	0.50	22.00–26.00	33.00–37.20	0.03	0.03	5.00–6.70 Mo; 2.00–4.00 Cu
Sanicro 28	N08028	0.02	2.00	1.00	26.0–28.0	29.5–32.5	0.020	0.015	3.0–4.0 Mo; 0.6–1.4 Cu
AL-6X	N08366	0.035	2.00	1.00	20.0–22.0	23.5–25.5	0.030	0.030	6.0–7.0 Mo
AL-6XN	N08367	0.030	2.00	1.00	20.0–22.0	23.50–25.50	0.040	0.030	6.00–7.00 Mo; 0.18–0.25 N
JS-700	N08700	0.04	2.00	1.00	19.0–23.0	24.0–26.0	0.040	0.030	4.3–5.0 Mo; 8 × %C min to 0.5 max Nb; 0.5 Cu; 0.005 Pb; 0.035 S
Type 332	N08800	0.01	1.50	1.00	19.0–23.0	30.0–35.0	0.045	0.015	0.15–0.60 Ti; 0.15–0.60 Al
904L	N08904	0.02	2.00	1.00	19.0–23.0	23.0–28.0	0.045	0.035	4.0–5.0 Mo: 1.0–2.0 Cu
Cronifer 1925 hMo	N08925	0.02	1.00	0.50	24.0–26.0	19.0–21.0	0.045	0.030	6.0–7.0 Mo; 0.8–1.5 Cu; 0.10–0.20 N

Continued

TABLE 1.11 (Continued)
Compositions of Nonstandard Stainless Steels

Designation[a]	UNS Designation	Composition (%)[b] C	Ma	Si	Cr	Ni	P	S	Other
Cronifer 2328	—	0.04	0.75	0.75	22.0–24.0	26.0–28.0	0.030	0.015	2.5–3.5 Cu; 0.4–0.7 Ti; 2.5–3.0 Mo
Ferritic stainless steels									
18-2 FM (XM-34)	S18200	0.08	1.25–2.50	1.00	17.5–19.5	—	0.040	0.15 min	1.5–2.5 Mo
Type 430 Ti	S43036	0.10	1.00	1.00	16.0–19.5	0.75	0.040	0.030	5 × %C min to 0.75 max Ti
Type 441	S44100	0.03	1.00	1.00	17.5–19.5	1.00	0.040	0.040	0.3 + 9 × (%C) min to 0.90 max Nb; 0.1–0.5 Ti; 0.03 N
E-Brite 26-1	S44627	0.01	0.40	0.40	25.0–27.0	0.50	0.020	0.020	0.75–1.5 Mo; 0.05–0.2 Nb; 0.015 N; 0.2 Cu
MoNiT (25-4-4)	S44635	0.025	1.00	0.75	24.5–26.0	3.5–4.5	0.040	0.030	3.5–4.5 Mo; 0.2 + 4 (%C + %N) min to 0.8 max (Ti + Nb); 0.035 N
Sea-Cure (SC-1)	S44660	0.025	1.00	1.00	25.0–27.0	1.5–3.5	0.040	0.030	2.5–3.5 Mo; 0.2 + 4 (%C + %N) min to 0.8 max (Ti + Nb); 0.035 N
AL29-4C	S44735	0.030	1.00	1.00	28.0–30.0	1.00	0.040	0.030	3.60–4.20 Mo; 0.20–1.00 Ti + Nb and 6 (%C + %N) min Ti + Nb; 0.045 N
AL29-4-2	S44800	0.01	0.30	0.20	28.0–30.0	2.0–2.5	0.025	0.020	3.5–4.2 Mo; 0.15 Cu; 0.02 N; 0.025 max (%C + %N)

18 SR(c)	—	0.04	0.30	1.03	18.0	—	—	—	2.0 A1; 0.4 Ti
12 SR(c)	—	0.02	—	0.50	12.0	—	—	—	1.2 Al; 0.3 Ti
406	—	0.06	1.00	0.50	12.0–14.0	0.50	0.040	0.030	2.75–4.25 Al; 0.6 Ti
408 Cb	—	0.03	0.2–0.5	0.2–0.5	11.75–12.25	0.45	0.030	0.020	0.75–1.25 Al; 0.65–0.75 Nb; 0.3–0.5 Ti; 0.03 N
ALFA IV	—	0.03	0.50	0.60	19.0–21.0	0.45	0.035	0.005	4.75–5.25 Al; 0.005–0.035 Ce; 0.03 N
Sealmet 1	—	0.08	0.5–0.8	0.3–0.6	28.0–29.0	0.40	0.030	0.015	0.04 N
Duplex stainless steels									
44LN	S31200	0.030	2.00	1.00	24.0–26.0	5.50–6.50	0.045	0.030	1.20–2.00 Mo; 0.14–0.20 N
DP-3	S31260	0.030	1.00	0.75	24.0–26.0	5.50–7.50	0.030	0.030	2.50–3.50 Mo; 0.20–0.80 Cu; 0.10–0.30 N; 0.10–0.50 W
3RE60	S31500	0.030	1.20–2.00	1.40–2.00	18.00–19.00	4.25–5.25	0.030	0.030	2.50–3.00 Mo
2205	S31803	0.030	2.00	1.00	21.0–23.0	4.50–6.50	0.030	0.020	2.50–3.50 Mo; 0.08–0.20 N
2304	S32304	0.030	2.50	1.0	21.5–24.5	3.0–5.5	0.040	0.040	0.05–0.60 Mo; 0.05–0.60 Cu; 0.05–0.20 N
Uranus 50	S32404	0.04	2.00	1.0	20.5–22.5	5.5–8.5	0.030	0.010	2.0–3.0 Mo; 1.0–2.0 Cu; 0.20 N
Ferralium 255	S32550	0.04	1.50	1.00	24.0–27.0	4.50–6.50	0.04	0.03	2.00–4.00 Mo; 1.50–2.50 Cu; 0.10–0.25 N
7-Mo-PlUS	S32950	0.03	2.00	0.60	26.0–29.0	3.50–5.20	0.035	0.010	1.00–2.50 Mo; 0.15–0.35 N
Martensitic stainless steels									
Type 410 S	S41008	0.08	1.00	1.00	11.5–13.5	0.60	0.040	0.030	—
Type 410 Cb (XM-30)	S41040	0.15	1.00	1.00	11.5–13.5	—	0.040	0.030	0.05–0.20 Nb

Continued

TABLE 1.11 (Continued)
Compositions of Nonstandard Stainless Steels

Designation[a]	UNS Designation	Composition (%)[b] C	Ma	Si	Cr	Ni	P	S	Other
E4	S41050	0.04	1.00	1.00	10.5–12.5	0.60–1.1	0.045	0.030	0.10 N
CA6NM	S41500	0.05	0.5–1.0	0.60	11.5–14.0	3.5–5.5	0.030	0.030	0.5–1.0 Mo
416 Plus X (XM-6)	S41610	0.15	1.5–2.5	1.00	12.0–14.0	—	0.060	0.15 min	0.6 Mo
Type 418 (Greek Ascolloy)	S41800	0.15–0.20	0.50	0.50	12.0–14.0	1.8–2.2	0.040	0.030	2.5–3.5 W
TrimRite	S42010	0.15–0.30	1.00	1.00	13.5–15.0	0.25–1.00	0.040	0.030	0.40–1.00 Mo
Type 420 F–Se	S42023	0.3–0.4	1.25	1.00	12.0–14.0	—	0.060	0.060	0.15 min Se; 0.6 Zr; 0.6 Cu
Lapelloy	S42300	0.27–0.32	0.95–1.35	0.50	11.0–12.0	0.50	0.025	0.025	2.5–3.0 Mo; 0.2–0.3 V
Type 440 F	S44020	0.95–1.20	1.25	1.00	16.0–18.0	0.75	0.040	0.10–0.35	0.08 N
Type 440 F–Se	S44023	0.95–1.20	1.25	1.00	16.0–18.0	0.75	0.040	0.030	0.15 min Se; 0.60 Mo

Precipitation-hardening stainless steels									
PH14-4Mo	S14800	0.05	1.00	1.00	13.75–15.0	7.75–8.75	0.015	0.010	2.0–3.0 Mo; 0.75–1.50 Al
PH15-7Mo (Type 632)	S15700	0.09	1.00	1.00	14.0–16.0	6.5–7.75	0.040	0.030	2.0–3.0 Mo; 0.75–1.5 Al
AM-350 (Type 633)	S35000	0.07–0.11	0.5–1.25	0.50	16.0–17.0	4.0–5.0	0.040	0.030	2.5–3.25 Mo; 0.07–0.13 N
AM-355 (Type 634)	S35500	0.10–0.15	0.5–1.25	0.50	15.0–16.0	4.0–5.0	0.040	0.030	2.5–3.25 Mo; 0.07–0.13 N
Custom 450 (XM-25)	S45000	0.05	1.00	1.00	14.0–16.0	5.0–7.0	0.030	0.030	1.25–1.75 Cu; 0.5–1.0 Mo; 8 × %C min Nb
Custom 455 (XM-16)	S45500	0.05	0.50	0.50	11.0–12.5	7.5–9.5	0.040	0.030	1.5–2.5 Cu; 0.8–1.4 Ti; 0.1–0.5 Nb; 0.5 Mo

[a]XM designations in this column are ASTM designations for the listed alloy.
[b]Single values are maximum values unless otherwise indicated.
[c]Nominal compositions.
[d]UNS designation has not been specified. This designation appears in ASTM A 887 and merely indicates the form to be used.
Source: From S.D. Washko and G. Aggen, in *ASM Handbook*, 10th ed., Vol. 1, ASM International, Materials Park, OH, 1990, pp. 841–907.

content (0.01–0.02% C), high Mo content (about 4% Mo), and high N content (about 0.3% N). This new type duplex steel gives the excellent resistance to pitting corrosion.

Duplex stainless steels find applications as welded pipe products for handling wet and dry CO_2 and sour gas and oil products in the petrochemical industry, as welded tubing for heat exchanges, for handling chloride-containing coolants, and for handling hot brines and organic chemicals in the chemical, electric, and other industries [4].

Martensitic stainless steels contain 11.5–18% Cr, 0.08–1.20% C, and other alloying elements less than 2 to 3%. They can be hardened and tempered to yield strength in the range of 550–1900 MPa (80–275 ksi). The Cr content provides these steels with such high hardenability that they can be air hardened even in large sections. If they are to be heat treated for maximum strength, the amount of δ-ferrite should be minimized [10].

The standard martensitic grades are types 403, 410, 414, 416, 416Se, 420, 422, 431, 440A, 440B, and 440C (Table 1.10). They are used in manifold stud bolts, heat control shafts, steam valves, Bourdon tubes, gun mounts, water pump parts, carburetor parts, wire cutter blades, garden shears, cutlery, paint spray nozzles, glass and plastic molds, bomb shackle parts, drive screws, aircraft bolting, cable terminals, diesel engine pump parts, instrument parts, crankshaft counterweight pins, valve trim, ball bearings, and races.

PH stainless steels are high-strength alloys with appreciable ductility and good corrosion resistance that are developed by a simple heat treatment comprising martensite formation and low-temperature aging (or tempering) treatment; the latter heat treatment step may be applied after fabrication. PH stainless steels can have a matrix structure of either austenite or martensite. Alloy elements added to form precipitates are Mo, Cu, Al, Ti, Nb, and N. PH stainless steels may be divided into three broad groups: (1) martensitic type, (2) semiaustenitic type, and (3) austenitic type (Table 1.10 and Table 1.11). A majority of these steels are classified by a three-digit number in the AISI 400 series or by a five-digit UNS designation. However, most of them are better known by their trade names or their manufacturer. All steels are available in sheet, strip, plate, bar, and wire.

Martensitic PH stainless steels (also called single-treatment alloys) are most widely used and include 17-4PH (AISI 430 or UNS S17400), stainless W (AISI 635 or UNS S17400), 15-5PH (UNS S15500), PH13-8Mo (UNS S13800), and Custom 450 (UNS S45000). These steels have a predominantly austenitic structure at the solution-annealing temperature, but they undergo an austenitic-to-martensite transformation during cooling to room temperature. These steels can be readily welded [49].

Semiaustenitic PH stainless steels (also called double-treatment alloys) were developed for increased formability before the hardening treatment. Important alloys are 17-7PH (UNS S17700) and PH15-7Mo (UNS S15700). These alloys are completely austenite in the as-quenched condition after solution annealing (which displays good toughness and ductility in the cold-forming operations), and eventually martensite can be obtained by conditioning treatment or thermomechanical treatment. Ultrahigh strength can be obtained in these steels by combinations of cold working and aging.

Austenitic PH stainless steels possess austenitic structures in both the solution annealed and aged conditions. The most important steels in this class include A-286 (AISI 600 or UNS S66286), 17-10P, and 14–17Cu–Mo alloys. Of these grades, A-286 is the most extensively used in the aerospace applications.

1.3.3.6 Maraging Steels

Maraging steels are a specific class of carbon-free (or small amounts) ultrahigh-strength steels that derive their strength not from carbon but from precipitation of intermetallic

TABLE 1.12
Nominal Compositions of Commercial Maraging Steels

Grade	Composition (%)[a]					
	Ni	Mo	Co	Ti	Al	Nb
Standard grades						
18Ni(200)	18	3.3	8.5	0.2	0.1	—
18Ni(250)	18	5.0	8.5	0.4	0.1	—
18Ni(300)	18	5.0	9.0	0.7	0.1	—
18Ni(350)	18	4.2[b]	12.5	1.6	0.1	—
18Ni(Cast)	17	4.6	10.0	0.3	0.1	—
12-5-3(180)[c]	12	3	—	0.2	0.3	—
Cobalt-free and low-cobalt bearing grades						
Cobalt-free 18Ni(200)	18.5	3.0	—	0.7	0.1	—
Cobalt-free 18Ni(250)	18.5	3.0	—	1.4	0.1	—
Low-cobalt 18Ni(250)	18.5	2.6	2.0	1.2	0.1	0.1
Cobalt-free 18Ni(300)	18.5	4.0	—	1.85	0.1	—

[a]All grades contain no more than 0.03% C.
[b]Some producers use a combination of 4.8% Mo and 1.4% Ti, nominal.
[c]Contains 5% Cr.
Source: From K. Rohrbach and M. Schmidt, in *ASM Handbook*, 10th ed., Vol. 1, ASM International, Materials Park, OH, 1990, pp. 793–800.

compounds and martensitic transformation [5,50–52]. The commonly available maraging steels contain 10–19% Ni, 0–18% Co, 3–14% Mo, 0.2–1.6% Ti, 0.1–0.2% Al, and some intermetallic compounds are Ni_3Ti, Ni_3Mo, Fe_2Mo, etc. Since these steels develop very high strength by martensitic transformation and subsequent age-hardening, they are termed maraging steels [53].

There are four types of maraging steels, namely 200, 250, 300, and 350; the number refers to the ultimate tensile strength in ksi (kpsi). The tensile strength is based on the Ti content, which varies between 0.2 and 1.85%. Table 1.12 lists the compositions of these grades [54]. In these grades, C content is maintained at a very low level (<0.03%); the sum of Si and Mn is lower (0.2%); and P and S contents are also very small (<0.005 and <0.008%, respectively) [4].

Maraging steels have found applications where lightweight structures with ultrahigh strength and high toughness are essential and cost is not a major concern. Maraging steels have been extensively used in two general types of applications:

1. Aerospace and aircraft industry for critical components such as missile cases, load cells, helicopter flexible drive shafts, jet engine drive shafts, and landing gear
2. Tool manufacturing industries for stub shafts, flexible drive shafts, splined shafts, springs, plastic molds, hot-forging dies, aluminum and zinc die casting dies, cold-heading dies and cases, diesel fuel pump pins, router bits, clutch disks, gears in the machine tools, carbide die holders, autofrettage equipment, etc.

1.4 DESIGNATIONS FOR STEELS

A designation is the specific identification of each grade, type, or class of steel by a number, letter, symbol, name, or suitable combination thereof unique to a certain steel. It is used in a

specific document as well as in a particular country. In the steel industries, these terms have very specific uses: grade is used to describe chemical composition; type is used to denote deoxidation practice; and class is used to indicate some other attributes such as tensile strength level or surface quality [8].

In ASTM specifications, however, these terms are used somewhat interchangeably. For example, in ASTM A 434, grade identifies chemical composition and class indicates tensile properties. In ASTM A 515, grade describes strength level; the maximum carbon content allowed by the specification is dependent on both the plate thickness and the strength level. In ASTM A 533, type indicates chemical analysis, while class denotes strength level. In ASTM A 302, grade identifies requirements for both chemical composition and tensile properties. ASTM A 514 and A 517 are specifications for high-strength quenched and tempered alloy steel plate for structural and pressure vessel applications, respectively; each has a number of grades for identifying the chemical composition that is capable of developing the required mechanical properties. However, all grades of both designations have the same composition limits.

By far the most widely used basis for classification and designation of steels is the chemical composition. The most commonly used system of designating carbon and alloy steels in the United States is that of the AISI and SAE numerical designations. The UNS is also increasingly employed. Other designations used in the specialized fields include Aerospace Materials Specification (AMS) and American Petroleum Institute (API) designation. These designation systems are discussed below.

1.4.1 SAE-AISI Designations

As stated above, the SAE-AISI system is the most widely used designation for carbon and alloy steels. The SAE-AISI system is applied to semifinished forgings, hot-rolled and cold-finished bars, wire rod, seamless tubular goods, structural shapes, plates, sheet, strip, and welded tubing. Table 1.2 lists the SAE-AISI system of numerical designations for both carbon and low-alloy steels.

1.4.1.1 Carbon and Alloy Steels

With few exceptions, the SAE-AISI system uses a four-digit number to designate carbon and alloy steels that is specific for chemical composition ranges. Certain types of alloy steels are designated by five digits (numerals). Table 1.2 shows an abbreviated listing of four-digit designations of the SAE-AISI carbon and alloy steels. The first digit, 1, of this designation indicates a carbon steel; i.e., carbon steels comprise 1xxx groups in the SAE-AISI system and are subdivided into four series due to the variance in certain fundamental properties among them. Thus, the plain carbon steels comprise 10xx series (containing 1.00% Mn maximum); resulfurized carbon steels comprise the 11xx series; resulfurized and rephosphorized carbon steels comprise the 12xx series; and nonresulfurized high-manganese (up to 1.65%) carbon steels are produced for applications requiring good machinability.

Carbon and alloy steel designations showing the letter B inserted between the second and third digits indicate that the steel has 0.0005–0.003% boron. Likewise, the letter L inserted between the second and third digits indicates that the steel has 0.15–0.35% lead for enhanced machinability. Sometimes the prefix M is used for merchant quality steels and the suffix H is used to comply with specific hardenability requirements. In alloy steels, the prefix letter E is used to designate steels that are produced by the electric furnace process.

The major alloying element in an alloy steel is indicated by the first two digits of the designation (Table 1.2). Thus, a first digit of 2 denotes a nickel steel; 3, a nickel–chromium

steel; 4, a molybdenum, chromium–molybdenum, nickel–molybdenum, or nickel–chromium–molybdenum steel; 5, a chromium steel; 6, a chromium–vanadium steel; 7, a tungsten–chromium steel; 8, a nickel–chromium–molybdenum steel; and 9, a silicon–manganese steel or a nickel–chromium–molybdenum steel. In the case of a simple alloy steel, the second digit represents the approximate percentage of the predominant alloying element. For example, 2520 grade indicates a nickel steel of approximately 5% Ni (and 0.2% carbon).

The last two digits of four-numeral designations and the last three digits of five-numeral designations indicate the approximate carbon content of the allowable carbon range in hundredths of a percent. For example, 1020 steel indicates a plain carbon steel with an approximate mean of 0.20% carbon, varying within acceptable carbon limits of 0.18 and 0.23%. Similarly, 4340 steels are Ni–Cr–Mo steels and contain an approximate mean of 0.40% carbon, varying within an allowable carbon range of 0.38–0.43%, and 51100 steel is a chromium steel with an approximate mean of 1.00% carbon, varying within an acceptable carbon range of 0.98–1.10% [4,30,55].

Potential standard steels are listed in SAE J1081 and Table 1.13. They are experimental steels to which no regular AISI-SAE designations have been assigned. The numbers consist of the prefix PS followed by a sequential number starting with 1. Some were developed to minimize the amount of nickel and others to enhance a particular attribute of a standard grade of alloy steel [30].

1.4.1.2 HSLA Steels

Several grades of HSLA steels have been described in the SAE Recommended Practice J410. Their chemical composition and minimum mechanical property requirements are provided in Table 1.8 [30].

1.4.1.3 Formerly Listed SAE Steels

A number of grades of carbon and alloy steels have been excluded from the list of standard SAE steels because of their inadequate applications. A detailed list of formerly used SAE carbon and alloy steels is given in SAE J1249, and producers of these steels should be contacted for their availability.

1.4.2 UNS Designations

The UNS has been developed by the ASTM E 527, the SAE J1086, and several other technical societies, trade associations, and U.S. government agencies [29]. A UNS number, which is a designation of chemical composition and not a specification, is assigned to each chemical composition of the standard carbon and alloy steel grades for which controlling limits have been established by the SAE-AISI [26,30,56].

The UNS designation consists of a single-letter prefix followed by five numerals (digits). The letters denote the broad class of alloys; the numerals define specific alloys within that class. The prefix letter G signifies standard grades of carbon and alloy steels; the prefix letter H indicates standard grades that meet certain hardenability requirement limits (SAE-AISI H steels); the prefix T includes tool steels, wrought and cast; the prefix letter S relates to heat- and corrosion-resistant steels (including stainless steel), valve steels, and iron-base super-alloys; the prefix letter J is used for cast steels (except tool steels); the prefix letter K identifies miscellaneous steels and ferrous alloys; and the prefix W denotes welding filler metals (for example, W00001–W59999 series represent a wide variety of steel compositions) [56]. The first four digits of the UNS number usually correspond to the standard SAE-AISI designations, while the last digit (except zero) of the five-numeral series denotes some additional

TABLE 1.13
SAE Potential Standard Steel Compositions

	Ladle Chemical Composition Limits (wt %)								
SAE PS Number[a]	C	Mn	P max	S max	Si	Ni	Cr	Mo	B
PS 10	0.19–0.24	0.95–1.25	0.035	0.040	0.15–0.35	0.20–0.40	0.25–0.40	0.05–0.10	—
PS 15	0.18–0.23	0.90–1.20	0.035	0.040	0.15–0.35	—	0.40–0.60	0.13–0.20	—
PS 16	0.20–0.25	0.90–1.20	0.035	0.040	0.15–0.35	—	0.40–0.60	0.13–0.20	—
PS 17	0.23–0.28	0.90–1.20	0.035	0.040	0.15–0.35	—	0.40–0.60	0.13–0.20	—
PS 18	0.25–0.30	0.90–1.20	0.035	0.040	0.15–0.35	—	0.40–0.60	0.13–0.20	—
PS 19	0.18–0.23	0.90–1.20	0.035	0.040	0.15–0.35	—	0.40–0.60	0.08–0.15	0.0005–0.003
PS 20	0.13–0.18	0.90–1.20	0.035	0.040	0.15–0.35	—	0.40–0.60	0.13–0.20	—
PS 21	0.15–0.20	0.90–1.20	0.035	0.040	0.15–0.35	—	0.40–0.60	0.13–0.20	—
PS 24	0.18–0.23	0.75–1.00	0.035	0.040	0.15–0.35	—	0.45–0.65	0.20–0.30	—
PS 30	0.13–0.18	0.70–0.90	0.035	0.040	0.15–0.35	0.70–1.00	0.45–0.65	0.45–0.60	—
PS 31	0.15–0.20	0.70–0.90	0.035	0.040	0.15–0.35	0.70–1.00	0.45–0.65	0.45–0.60	—
PS 32	0.18–0.23	0.70–0.90	0.035	0.040	0.15–0.35	0.70–1.00	0.45–0.65	0.45–0.60	—
PS 33[b]	0.17–0.24	0.85–1.25	0.035	0.040	0.15–0.35	0.20 min	0.20 min	0.05 min	—
PS 34	0.28–0.33	0.90–1.20	0.035	0.040	0.15–0.35	—	0.40–0.60	0.13–0.20	—
PS 36	0.38–0.43	0.90–1.20	0.035	0.040	0.15–0.35	—	0.45–0.65	0.13–0.20	—

PS 38	0.43–0.48	0.90–1.20	0.035	0.040	0.15–0.35	—	0.45–0.65	0.13–0.20	—
PS 39	0.48–0.53	0.90–1.20	0.035	0.040	0.15–0.35	—	0.45–0.65	0.13–0.20	—
PS 40	0.51–0.59	0.90–1.20	0.035	0.040	0.15–0.35	—	0.45–0.65	0.13–0.20	—
PS 54	0.19–0.25	0.70–1.05	0.035	0.040	0.15–0.35	—	0.40–0.70	0.05 min	—
PS 55	0.15–0.20	0.70–1.00	0.035	0.040	0.15–0.35	1.65–2.00	0.45–0.65	0.65–0.80	—
PS 56	0.080–0.13	0.70–1.00	0.035	0.040	0.15–0.35	1.65–2.00	0.45–0.65	0.65–0.80	—
PS 57	0.08 max	1.25 max	0.040	0.15–0.35	1.00 max	—	17.00–19.00	1.75–2.25	—
PS 58	0.16–0.21	1.00–1.30	0.035	0.040	0.15–0.35	—	0.45–0.65	—	—
PS 59	0.18–0.23	1.00–1.30	0.035	0.040	0.15–0.35	—	0.70–0.90	—	—
PS 61	0.23–0.28	1.00–1.30	0.035	0.040	0.15–0.35	—	0.70–0.90	—	—
PS 63	0.31–0.38	0.75–1.10	0.035	0.040	0.15–0.35	—	0.45–0.65	—	0.0005–0.003
PS 64	0.16–0.21	1.00–1.30	0.035	0.040	0.15–0.35	—	0.70–0.90	—	—
PS 65	0.21–0.26	1.00–1.30	0.035	0.040	0.15–0.35	—	0.70–0.90	—	—
PS 66[c]	0.16–0.21	0.40–0.70	0.035	0.040	0.15–0.35	1.65–2.00	0.45–0.75	0.08–0.15	—
PS 67	0.42–0.49	0.80–1.20	0.035	0.040	0.15–0.35	—	0.85–1.20	0.25–0.35	—

[a]Some PS steels may be supplied to a hardenability requirement.

[b]Supplied to a hardenability requirement of 15 HRC points within the range of 23–43 HRC at J4 ($^4/_{16}$ in. distance from quenched end), subject to agreement between producer and user.

[c]PS 66 has a vanadium content of 0.10–0.15%.

Source: From *Numbering System, Chemical Composition, 1993 SAE Handbook*, Vol. 1, Materials Society of Automotive Engineers, Warrendale, PA, pp. 1.01–1.189.

composition requirements, such as boron, lead, or nonstandard chemical ranges. Table 1.3 and Table 1.4 list the UNS numbers corresponding to SAE-AISI numbers for various standard carbon and alloy steels, respectively, with composition ranges.

1.5 SPECIFICATIONS FOR STEELS

A specification is typically an acronym or abbreviation for a standards organization plus a specific written statement of both technical and commercial requirements that a product must satisfy. It is a document that restrains or controls procurement and is issued by that standards organization. All material specifications contain general and specific information [57]. Any reasonably adequate specification will furnish the information about the items stated below [6,8].

The scope of the document may include product classification, required size range, condition, and any comments on product processing considered helpful to either the supplier or the user. An informative title and a statement of the required form may be employed instead of a scope item.

Chemical composition may be described, or it may be denoted by a well-known designation based on chemical composition. The SAE-AISI designations are normally used.

A quality statement covering any appropriate quality descriptor and whatever additional prerequisites might be necessary. It may also include the type of steel and the steelmaking processes allowed.

Quantitative requirements recognize permissible composition ranges and all physical and mechanical properties necessary to characterize the material. Testing methods employed to check these properties should also be included or reference made to standard test methods. This section should only address those properties that are vital for the intended application.

Additional requirements can cover surface preparation, special tolerances, and edge finish on flat-rolled products as well as special packaging, identification, and loading instructions.

Engineering societies, trade associations, and institutes whose members make, specify, or purchase steel products publish standard specifications; many of them are well recognized and highly respected. Some of the notable specification-writing groups or standard organizations in the United States are listed below. It is clear from these names that a particular specification-writing group is limited to its own specialized field.

Organization	Acronym
Association of American Railroads	AAR
American Bureau of Shipbuilding	ABS
Aerospace Materials Specification (of SAE)	AMS
American National Standards Institute	ANSI
American Petroleum Institute	API
American Railway Engineering Association	AREA
American Society of Mechanical Engineers	ASME
American Society for Testing and Materials	ASTM
American Welding Society	AWS
Society of Automotive Engineers	SAE

1.5.1 ASTM (ASME) SPECIFICATIONS

The most widely used standard specifications for steel in the United States are those published by ASTM, many of which are complete specifications, usually adequate for procurement

purposes. These specifications frequently apply to specific products, which are usually oriented toward the performance of the fabricated end product. They begin with the prefix ASTM, followed by letter A, identifying a ferrous material, then a number indicating the actual specification, which may be followed by letters or numbers subdividing the material by analysis. The AISI code is sometimes used for this purpose. Finally the year of origin is mentioned. A letter T after this denotes a tentative specification. Generally, each specification includes a steel in a specific form or for a special purpose rather than by analysis.

ASTM specifications represent a consensus drawn from producers, specifiers, fabricators, and users of steel mill products. In many cases, the dimensions, tolerances, limits, and restrictions in the ASTM specifications are the same as the corresponding items of the standard practices in the AISI steel product manuals. Many of the ASTM specifications have been adopted by the American Society of Mechanical Engineers (ASME) with slight or no modifications. ASME uses the prefix S with the ASTM specifications; for example, ASME SA 213 and ASTM A 213 are the same.

Steel products can be distinguished by the ASTM specification number, which denotes their method of production. Sometimes, citing the ASTM specification is not sufficient to completely identify a steel product. For example, A 434 is a specification used for heat-treated (hardened and tempered) alloy steel bars. To fully identify steel bars indicated by this specification, the grade/AISI-SAE designation and class (the required strength level) must also be quoted. The ASTM specification A 434 also covers, by reference, two standards for test methods (A 370 for mechanical testing and E 112 for grain size determination) and A 29 specifying general requirements for bar products.

SAE-AISI designations for the chemical compositions of carbon and alloy steels are sometimes included in the ASTM specifications for bars, wires, and billets for forging. Some ASTM specifications for sheet products incorporate SAE-AISI designations for chemical composition. ASTM specifications for plates and structural shapes normally specify the limits and ranges of chemical composition directly without the SAE-AISI designations. Table 1.14 incorporates a list of some ASTM specifications that include SAE-AISI designations for compositions of different steel grades.

1.5.2 AMS Specifications

AMS, published by SAE, are procurement documents, not design specifications. The majority of the AMS pertain to materials intended for aerospace applications. These specifications generally include mechanical property requirements and limits that are significantly more severe than those for materials or steel grades with identical compositions but meant for nonaerospace applications. Their compliance will ensure procurement of a specific form and condition or a specific material (or steel grade) or process. Table 1.15 and Table 1.16 show the AMS designations of carbon and alloy steels, respectively, indicating the chemical composition, title of specification (covering specific form, chemical composition, process, and condition), and equivalent UNS number, nearest proprietary or AISI-SAE grade, and similar MIL or federal (FED) specifications [58].

1.5.3 Military and Federal Specifications

MIL specifications and standards are produced and adopted by the U.S. Department of Defense. MIL specifications are used to define materials, products, and services. MIL standards provide procedures for design, manufacturing, and testing instead of giving only a particular material description. MIL specifications begin with the prefix MIL, followed by a

TABLE 1.14
ASTM Specifications That Cover SAE-AISI Designations

A 29	Carbon and alloy steel bars, hot rolled and cold finished	A 510	Carbon steel wire rods and coarse round wire	A 646	Premium quality alloy steel blooms and billets for aircraft and aerospace forgings
A 108	Standard quality cold-finished carbon steel bars	A 534	Carburizing steels for antifriction bearings	A 659	Commercial quality hot-rolled carbon steel sheet and strip
A 295	High carbon–chromium ball and roller bearing steel	A 535	Special quality ball and roller bearing steel	A 682	Cold-rolled spring quality carbon steel strip, generic
A 304	Alloy steel bars having hardenability requirements	A 544	Scrapless nut quality carbon steel wire	A 684	Untempered cold-rolled high-carbon steel strip
A 322	Hot-rolled alloy steel bars	A 545	Cold-heading quality carbon steel wire for machine screws	A 689	Carbon and alloy steel bars for springs
A 331	Cold-finished alloy steel bars	A 546	Cold-heading quality medium high carbon steel wire for hexagon-head bolts	A 711	Carbon and alloy steel blooms, billets, and slabs for forging
A 434	Hot-rolled or cold-finished quenched and tempered alloy steel bars	A 547	Cold-heading quality alloy steel wire for hexagon-head bolts	A 713	High-carbon spring steel wire for heat-treated components
A 505	Hot-rolled and cold-rolled alloy steel sheet and strip	A 548	Cold-heading quality carbon steel wire for tapping or sheet metal screws	A 752	Alloy steel wire rods and coarse round wire
A 506	Regular quality hot-rolled and cold-rolled alloy steel sheet and strip	A 549	Cold-heading quality carbon steel wire for wood screws	A 827	Carbon steel plates for forging and similar applications
A 507	Drawing quality hot-rolled and cold-rolled alloy steel sheet and strip	A 575	Merchant quality hot-rolled carbon steel bars	A 829	Structural quality alloy steel plates
		A 576	Special quality hot-rolled carbon steel bars	A 830	Structural quality carbon steel plates

Source: From Anon., Carbon and alloy steels, SAE J411, *1993 SAE Handbook*, Vol. 1, Materials Society of Automotive Engineers, Warrendale, PA, pp. 2.01–2.04.

TABLE 1.15
AMS Number, Title of Specification, and Equivalent UNS Number, Proprietary/AISI-SAE Alloy, and Similar Specification for Wrought Carbon Steels

AMS No.	Title of Specification	UNS No.	Alloy	Similar Specification
5100H	Bars, screw stock, free machining, cold drawn	G12120	1212	
5020C	Bars, forgings, and tubing, 1.5Mn 0.25Pb (0.32–0.39C), free cutting	G11374	111.37	
5022L	Bars, forgings, and tubing, 0.14–0.20C, free cutting	G11170	1117	
5024F	Bars, forgings, and tubing, 1.5Mn (0.32–0.39C), free cutting	G11370	1137	
5027C	Wire, welding, 1.05Cr 0.55Ni 1.0Mo 0.07V (0.26–0.32C), vacuum melted, environment-controlled packaging	K24728	D6AC	
5028B	Wire, welding, 1.05Cr 0.55Ni 1.0Mo 0.07V (0.34–0.40C), vacuum melted, environment-controlled packaging	K23725	D6AC	
5029B	Wire, welding, 0.78Cr l.8Ni 0.35Mo 0.20V (0.33–0.38C), vacuum melted, environment-controlled packaging	K23577		
5030F	Wire, welding, 0.06 carbon maximum	K00606		
5031C	Welding electrodes, covered, steel, 0.07–0.15C	W06013	S6013	FED-QQ-E-450, Type 6013
5032E	Wire, 0.18–0.23C, annealed	G10200	1020	FED-QQ-W-461
5036G	Sheet and strip, aluminum coated, low carbon			MIL-S-4174, Type 1, Grade B
5040J	Sheet and strip, 0.15 carbon maximum, deep drawing grade	G10100	1010	
5042J	Sheet and strip, 0.15 carbon maximum, forming grade	G10100	1010	
5044G	Sheet and strip, 0.15 carbon maximum, half hard temper	G10100	1010	
5045F	Sheet and strip, 0.25 carbon maximum, hard temper	G10200	1020	
5046A	Sheet, strip, and plate, annealed	G10200 G10250	1020 1025	MIL-S-7952
5047D	Sheet and strip, 0.08–0.13C, Al killed, deep-forming grade	G10100	1010	
5050J	Tubing, seamless, 0.15 carbon maximum, annealed	G10100	1010	
5053G	Tubing, welded, 0.13 carbon maximum, annealed	G10100	1010	
5060F	Bars, forgings, and tubing, 0.13–0.18C	G10150	1015	
5061D	Bars and wire, low carbon	K00802		
5062E	Bars, forgings, tubing, sheet, strip, and plate, low carbon	K02508		
5069E	Bars, forgings, and tubing, 0.15–0.20C	G10180	1018	
5070G	Bars and forgings, 0.18–0.23C	G10220	1022	
5075E	Tubing, seamless, 0.22–0.28C, cold drawn and stress relieved	G10250	1025	MIL-T-5066
5077E	Tubing, welded, 0.22–0.28C, normalized or stress relieved	G10250	1025	MIL-T-5066
5080H	Bars, forgings, and tubing, 0.31–0.38C	G10350	1035	

Continued

TABLE 1.15 (Continued)
AMS Number, Title of Specification, and Equivalent UNS Number, Proprietary/AISI-SAE Alloy, and Similar Specification for Wrought Carbon Steels

AMS No.	Title of Specification	UNS No.	Alloy	Similar Specification
5082E	Tubing, seamless, 0.31–0.38C, stress relieved	G10350	1035	
5085D	Sheet, strip, and plate, 0.47–0.55C, annealed	G10500	1050	
5110F	Wire, carbon, spring temper, cold drawn, 0.75–0.88C	G10800	1080	
5112J	Wire, spring quality music wire, 0.70–1.00C, cold drawn	G10900	1090	
5115G	Wire, valve spring quality, 0.60–0.75C, hardened and tempered	G10700	1070	
5120J	Strip, 0.68–0.80C	G10740	1074	
5121G	Sheet and strip, 0.90–1.40C	G10950	1095	MIL-S-7947
5122G	Strip, 0.90–1.04C, hard temper	G10950	1095	MIL-S-7947, hard temper
5132G	Bars, 0.90–1.30C	G10950	1095	

Source: From *Specification for Drill Pipe, API Specification 5D*, 3rd ed., August 1, 1992, American Petroleum Institute, Washington, D.C.

code letter that represents the first letter of the title for the item, followed by hyphen and then the serial numbers or digits. Some examples of MIL specifications for steels with corresponding AMS numbers, UNS numbers, and nearest proprietary or AISI-SAE grades are listed in Table 1.15 and Table 1.16.

Federal (QQ) specifications are identical to the MIL, except that they are provided by the General Services Administration (GSA) and are used by federal agencies as well as by MIL establishments when there are no separate MIL specifications available. Federal specifications begin with the prefix FED-QQ, followed by the letter and code numbers. Examples of federal specifications for steels with equivalent UNS numbers in parentheses are FED-QQ-S-700 (C10300); FED-QQ-S-700 (C1085) (G10850); FED-QQ-S-763 (309) (S30900); and FED-QQ-S-766 (316L) (S31603) [56] (see Table 1.16).

1.5.4 API Specifications

The API fosters the development standards, codes, and safe practices within the petroleum industry. The API standard appears with the prefix API before the specification. For example, API Spec 5D covers all grades of seamless drill pipe (for use in drilling and producing operations), process of manufacture, chemical composition and mechanical property requirements, testing and inspection methods, and requirements for dimensions, weights, and lengths [59]. API Spec 5L covers all grades of seamless and welded steel line pipe and requirements for dimensions, weight, lengths, strengths, threaded ends, plain ends, belled ends, and thread protectors, and testing and inspection methods. This specification includes A25, A, B, X42, X46, X52, X56, X60, X65, X70, and X80 grades, and grades intermediate to grade X42 and higher. It provides the standards for pipe suitable for use in conveying gas, water, and oil on both the oil and natural gas industries [60]. API Spec 5LC covers seamless, centrifugal cast, and welded corrosion-resistant alloy line pipe (austenitic stainless steels, martensitic stainless steels,

TABLE 1.16
AMS Number, Title of Specification, and Equivalent UNS Number, Nearest Proprietary or AISI-SAE Grade, and Similar Specification for Wrought Alloy Steels

AMS No.	Title of Specification	UNS No.	Alloy	Similar Specification
6250H	Bars, forgings, and tubing, 1.5Cr 3.5Ni (0.07–0.13C)	K44910	3310	MIL-S-7393, Composition I
6255A	Bars, forgings, and tubing, 1.1Si 1.45Cr 1.0Mo 0.08A1 (0.16–0.22C), premium air quality, double vacuum melted	K21940	CBS 600	
6256A	Bars, forgings, and tubing, 1.0Cr 3.0Ni 4.5Mo 0.08A1 0.38V (0.10–0.16C), premium air quality, double vacuum melted	K71350	CBS 1000M	
6257	Bars, forgings, and tubing, 1.6Si 0.82Cr 1.8Ni 0.40Mo 0.08V (0.40–0.44C), consumable Electrode vacuum remelted, normalized and tempered			
6260L	Bars, forgings, and tubing, carburizing grade, 1.2Cr 3.2Ni 0.12Mo (0.07–0.13C)	G93106	9310	
6263H	Bars, forgings, and tubing, carburizing grade, 1.2Cr 3.2Ni 0.12Mo (0.11–0.17C)	G93150	9315	
6264G	Bars, forgings, and tubing, carburizing grade, 3.2Ni 1.2Cr 0.12Mo (0.14–0.20C)	K44414	9317	
6265H	Bars, forgings, and tubing, 1.2Cr 3.25Ni (0.07–0.13C), vacuum consumable electrode remelted	G93106	9310	
6266G	Bars, forgings, and tubing, 0.50Cr 1.82Ni 0.25Mo 0.003B 0.06V (0.08–0.13C)	K21028	43BV12	
6267D	Bars, forgings, and tubing, 1.2Cr 3.25Ni 0.12Mo (0.07–0.13C), electroslag remelted or vacuum remelted, consumable electrode	G93106	9310	
6270L	Bars, forgings, and tubing, 0.5Cr 0.55Ni 0.20Mo (0.11–0.17C)	G86150	8615	
6272H	Bars, forgings, and tubing, 0.50Cr 0.55Ni 0.20Mo (0.15–0.20C)	G86170	8617	
6274L	Bars, forgings, and tubing, 0.50Cr 0.55Ni 0.20Mo (0.18–0.23C)	G86200	8620	
6275F	Bars, forgings, and tubing, 0.40Cr 0.45Ni 0.12Mo 0.002B (0.15–0.20C)	G94171	94B17	
6276F	Bars, forgings, and tubing, 0.50Cr 0.55Ni 0.20Mo (0.18–0.23C), consumable electrode vacuum melted	G86200	8620	

Continued

TABLE 1.16 (Continued)
AMS Number, Title of Specification, and Equivalent UNS Number, Nearest Proprietary or AISI-SAE Grade, and Similar Specification for Wrought Alloy Steels

AMS No.	Title of Specification	UNS No.	Alloy	Similar Specification
6277D	Bars, forgings, and tubing, 0.50Cr 0.55Ni 0.20Mo (0.18–0.23C), vacuum arc or electroslag remelted	G86200	8620	
6278A	Bars, forgings, and tubing, 4.1Cr 3.4Ni 4.2Mo 1.2V (0.11–0.15C), premium aircraft quality for bearing applications, double vacuum melted			
6280H	Bars, forgings, and rings, 0.50Cr 0.55Ni 0.20Mo (0.28–0.33C)	G86300	8630	MIL-S-6050
6281G	Tubing, mechanical, 0.50Cr 0.55Ni 0.20Mo (0.28–0.33C)	G86300	8630	
6282G	Tubing, mechanical, 0.50Cr 0.55Ni 0.25Mo (0.33–0.38C)	G87350	8735	
6290F	Bars and forgings, carburizing grade, 1.8Ni 0.25Mo (0.11–0.17C)	G46150	4615	MIL-S-7493, Composition 4615
6292F	Bars and forgings, carburizing grade, 1.8Ni 0.25Mo (0.14–0.20C)	G46170	4617	MIL-S-7493 Composition 4617
6294F	Bars and forgings, carburizing grade, 1.8Ni 0.25Mo (0.17–0.22C)	G46200	4620	
6299C	Bars, forgings, and tubing, 0.50Cr 1.8Ni 0.25Mo (0.17–0.23C)	H43200	4320H	
6300C	Bars and forgings, 0.25Mo (0.35–0.40C)	G40370	4037	
6302E	Bars, forgings, and tubing, low alloy, heat resistant, 0.65Si 1.25Cr 0.50Mo 0.25V (0.28–0.33C)	K23015	17-22A(S)	
6303E	Bars and forgings, low alloy, heat resistant, 0.65Si 1.25Cr 0.50Mo 0.85V (0.25–0.30C)	K22770	17-22A(V)	
6304G	Bars, forgings, and tubing, low alloy, heat resistant, 0.95Cr 0.55Mo 0.30V (0.40–0.50C)	K14675	17-22A	MIL-S-24502
MAM				
6304	Bars, forgings, and tubing, low alloy, heat resistant, 0.95Cr 0.55Mo 0.30V (0.40–0.50C)	K14675	17-22A	MIL-S-24502
6305B	Bars, forgings, and tubing, low alloy, heat resistant, 0.95Cr 0.55Mo 0.30V (0.40–0.50C), vacuum arc remelted	K14675	17–22A	

Continued

TABLE 1.16 (Continued)
AMS Number, Title of Specification, and Equivalent UNS Number, Nearest Proprietary or AISI-SAE Grade, and Similar Specification for Wrought Alloy Steels

AMS No.	Title of Specification	UNS No.	Alloy	Similar Specification
6308A	Bars and forgings, 0.90Si 1.0Cr 2.0Ni 3.2Mo 2.0Cu 0.10V (0.07–0.13C), vacuum arc or electroslag remelted	K71040	Pyrowear, alloy 53	
6312E	Bars, forgings, and tubing, 1.8Ni 0.25Mo (0.38–0.43C)	K22440	4640	
6317F	Bars and forgings, 1.8Ni 0.25Mo (0.38–0.43C), heat treated, 125 ksi (862 MPa) tensile strength	K22400	4640	
6320J	Bars, forgings, and rings, 0.50Cr 0.55Ni 0.25Mo (0.33–0.38C)	G87350	8735	
6321D	Bars, forgings, and tubing, 0.42Cr 0.30Ni 0.12Mo 0.003B (0.38–0.43C)	K03810	81B40	
6322K	Bars, forgings, and rings, 0.50Cr 0.55Ni 0.25Mo (0.38–0.43C)	G87400	8740	MIL-S-6049
6323H	Tubing, mechanical, 0.50Cr 0.55Ni 0.25Mo (0.38–0.43C)	G87400	8740	
6324E	Bars, forgings, and tubing, 0.65Cr 0.70Ni 0.25Mo (0.38–0.43C)	K11640	8740 Mod	
6325F	Bars and forgings, 0.50Cr 0.55Ni 0.25Mo (0.38–0.43C), heat treated, 105 ksi (724 MPa) tensile strength	G8740	8740	MIL-S-6049
6327G	Bars and forgings, 0.50Cr 0.55Ni 0.25Mo (0.38–0.43C), heat treated, 125 ksi (862 MPa) tensile strength	G8740	8740	MIL-S-6049
6328H	Bars, forgings, and tubing, 0.50Cr 0.55Ni 0.25Mo (0.48–0.53C)	K13550	8750	
6330E	Bars, forgings, and tubing, 0.65Cr 1.25Ni (0.33–0.38C)	K22033		
6331	Wire, welding, 0.50Cr 0.55Ni 0.20Mo (0.33–0.38C), vacuum melted, environment controlled packaging	G87350	8735	
6342H	Bars, forgings, and tubing, 0.80Cr 1.0Ni 0.25Mo (0.38–0.43C)	G98400	9840	
6348A	Bars, 0.95Cr 0.20Mo (0.28–0.33C), normalized	G41300	4130	MIL-S-6758
6349B	Bars, 0.95Cr 0.20Mo (0.38–0.43C), normalized	G41400	4140	MIL-S-5626
6350H	Sheet, strip, and plate, 0.95Cr 0.20Mo (0.28–0.33C)	G41300	4130	MIL-S-18729
6351E	Sheet, strip, and plate, 0.95Cr 0.20Mo (0.28–0.33C), spheroidized	G41300	4130	
6352F	Sheet, strip, and plate, 0.95Cr 0.20Mo (0.33–0.38C)	G41350	4135	

Continued

TABLE 1.16 (Continued)
AMS Number, Title of Specification, and Equivalent UNS Number, Nearest Proprietary or AISI-SAE Grade, and Similar Specification for Wrought Alloy Steels

AMS No.	Title of Specification	UNS No.	Alloy	Similar Specification
6354D	Sheet, strip, and plate, 0.75Si 0.62Cr 0.20Mo 0.10Zr (0.10–0.17C)	K11914	NAX 9115-AC	
6356D	Sheet, strip, and plate, 0.95Cr 0.20Mo (0.30–0.35C)	G41320	4132	
6357G	Sheet, strip, and plate, 0.50Cr 0.55Ni 0.25Mo (0.33–0.38C)	G87350	8735	
6358F	Sheet, strip, and plate, 0.50Cr 0.55Ni 0.25Mo (0.38–0.43C)	G87400	8740	
6359F	Sheet, strip, and plate, 0.80Cr 1.8Ni 0.25Mo (0.38–0.43C)	G43400	4340	
6360J	Tubing, seamless, 0.95Cr 0.20Mo (0.28–0.33C), normalized or stress relieved	G41300	4130	MIL-T-6736 Condition N
6361C	Tubing, seamless round, 0.95Cr 0.20Mo (0.28–0.33C), 125 ksi (860 MPa) tensile strength	G41300	4130	MIL-T-6736
6362D	Tubing, seamless, 0.95Cr 0.20Mo (0.28–0.33C), 150 ksi (1034 MPa) tensile strength	G41300	4130	MIL-T-6736 Condition HT
6365H	Tubing, seamless, 0.95Cr 0.20Mo (0.33–0.38C), normalized or stress relieved	G41350	4135	MIL-T-6735
6370K	Bars, forgings, and rings, 0.95Cr 0.20Mo (0.28–0.33C)	G41300	4130	MIL-S-6758
6371H	Tubing, mechanical, 0.95Cr 0.20Mo (0.28–0.33C)	G41300	4130	MIL-T-6736
6372H	Tubing, mechanical, 0.95Cr 0.20Mo (0.33–0.38C)	G41350	4135	
6373C	Tubing, welded, 0.95Cr 0.20Mo (0.28–0.33C)	G41300	4130	MIL-T-6736
6374A	Tubing, seam-free, round, 0.95Cr 0.20Mo (0.28–0.33C), 95 ksi (655 MPa) tensile strength	G41300	4130	
6375	Wire, welding, 0.50Cr 0.55Ni 0.20Mo (0.18–0.23C), vacuum melted, environment controlled packaging	G86200	8620	
6378E	Bars, 1.0Cr 0.20Mo 0.045Se (0.39–0.48C), die drawn, 130 ksi (896 MPa) yield strength, free machining	K11542	4142H Mod	
6379A	Bars, die drawn, 0.95Cr 0.20Mo 0.05Te (0.40–0.53C), tempered, 165 ksi (1140 MPa) yield strength	K11546	4140 Mod	
6381E	Tubing, mechanical, 0.95Cr 0.20Mo (0.38–0.43C)	G41400	4140	

Continued

TABLE 1.16 (Continued)
AMS Number, Title of Specification, and Equivalent UNS Number, Nearest Proprietary or AISI-SAE Grade, and Similar Specification for Wrought Alloy Steels

AMS No.	Title of Specification	UNS No.	Alloy	Similar Specification
6382K	Bars, forgings, and rings, 0.95Cr 0.20Mo (0.38–0.43C)	G41400	4140	MIL-S-5626
6385E	Sheet, strip, and plate, low alloy, heat resistant, 1.25Cr 0.50Mo 0.65Si 0.25V (0.27–0.33C)	K23015	17–22A/S	
6386B	Sheet and plate, heat treated, 90 ksi and 100 ksi yield strength	K11856	—	
6390C	Tubing, mechanical, 0.95Cr 0.20Mo (0.38–0.43C)	G41400	4140	
6395D	Sheet, strip, and plate, 0.95Cr 0.20Mo (0.38–0.43C)	G41400	4140	
6396B	Sheet, strip, and plate, 0.80Cr 1.8Ni 0.25Mo (0.49–0.55C), annealed	K22950		
6406C	Sheet, strip, and plate, 2.1Cr 0.58Mo 1.6Si 0.05V (0.41–0.46C), annealed	K34378	X200	
6407E	Bars, forgings, and tubing, 1.2Cr 2.0Ni 0.45Mo (0.27–0.33C)	K33020	IIS-220	
6408	Bars and forgings, tool, hotwork, 5.2Cr 1.5Mo 1.0V (0.35–0.45C), electroslag remelted (ESR) or consumable electrode vacuum arc remelted (VAR), annealed	T20813	H-13	
6409	Bars, forgings, and tubing, 0.80Cr 1.8Ni 0.25Mo (0.38–0.43C), special aircraft quality cleanliness, normalized and tempered	G43400	4340	MIL-S-5000
6411D	Bars, forgings, and tubing, 0.88Cr 1.8Ni 0.42Mo 0.08V (0.28–0.33C), consumable electrode remelted	K23080	4340 Mod	
6412J	Bars and forgings, 0.80Cr 1.8Ni 0.25Mo (0.35–0.40C)	G43370	4337	
6413H	Tubing, mechanical, 0.80Cr 1.8Ni 0.25Mo (0.35–0.40C)	G43370	4337	
6414F	Bars, forgings, and tubing, 0.80Cr 1.8Ni 0.25Mo (0.38–0.43C), vacuum consumable electrode remelted	G43400	4340	
6415M MAM	Bars, forgings, and tubing, 0.80Cr 1.8Ni 0.25Mo (0.38–0.43C)	G43400	4340	MIL-S-5000
6415	Bars, forgings, and tubing, 0.80Cr 1.8Ni 0.25Mo (0.38–0.43C)	G43400	4340	MIL-S-5000
6417D	Bars, forgings, and tubing, 0.82Cr 1.8Ni 0.40Mo 1.6Si 0.08V (0.38–0.43C), consumable electrode remelted	K44220	300M	

Continued

TABLE 1.16 (Continued)
AMS Number, Title of Specification, and Equivalent UNS Number, Nearest Proprietary or AISI-SAE Grade, and Similar Specification for Wrought Alloy Steels

AMS No.	Title of Specification	UNS No.	Alloy	Similar Specification
6418G	Bars, forgings, tubing, and rings, 0.30Cr 1.8Ni 0.40Mo 1.3Mn 1.5Si (0.23–0.28C)	K32550	Hy-Tuf	MIL-S-7108
6419C	Bars, forgings, and tubing, 0.82Cr 1.8Ni 0.40Mo 0.08V 1.6Si (0.40–0.45C), consumable electrode vacuum remelted	K44220	300M	MIL-S-8844
6421C	Bars, forgings, and tubing, 0.80Cr 0.85Ni 0.20Mo 0.003B (0.35–0.40C)	—	98B37 Mod	
6422F	Bars, forgings, and tubing, 0.80Cr 0.85Ni 0.20Mo 0.003B 0.04V (0.38–0.43C)	K11940	98BV40 Mod	
6423D	Bars, forgings, and tubing, 0.92Cr 0.75Ni 0.52Mo 0.003B 0.04V (0.40–0.46C)	K24336	98BV40 Mod	
6424B	Bars, forgings, and tubing, 0.80Cr 1.8Ni 0.25Mo (0.49–0.55C)	K22950	—	
6425	Bars, forgings, and tubing, 0.30Cr 1.8Ni 0.40Mo 1.4Mn 1.5Si (0.23–0.28C), consumable vacuum electrode remelted	K32550	Hy-Tuf	
6426D	Bars, forging, and tubing, 1.0Cr 0.58Mo 0.75Si (0.80–0.90C), consumable electrode melted	K18597	52CB	
6427H	Bars, forgings, and tubing, 0.88Cr 1.8Ni 0.42Mo 0.08V (0.28–0.33C)	K23080	4330 Mod	
6428D	Bars, forgings, and tubing, 0.80Cr 1.8Ni 0.35Mo 0.20V (0.32–0.38C)	K23477	4335 Mod	
6429D	Bars, forgings, tubing, and rings, 0.78Cr 1.8Ni 0.35Mo 0.20V (0.33–0.38C), consumable electrode vacuum melted	K33517	4335 Mod	
6430D	Bars, forgings, tubing, and rings, 0.78Cr 1.8Ni 0.35Mo 0.20V 0.75Mn (0.32–0.38C)	K33517	4335 Mod	
6431J	Bars, forgings, and tubing, 1.05Cr 0.55Ni 1.0Mo 0.11V (0.45–0.50C), consumable electrode vacuum melted	K24728	D6	MIL-S-8949
6432A	Bars, forgings, and tubing, 1.05Cr 0.55Ni 1.0Mo 0.12V (0.43–0.49C)	K24728	D6A	
6433D	Sheet, strip, and plate, 0.80Cr 1.8Ni 0.35Mo 0.20V 0.75Mn (0.33–0.38C)	K33517	4335 Mod	

Continued

TABLE 1.16 (Continued)
AMS Number, Title of Specification, and Equivalent UNS Number, Nearest Proprietary or AISI-SAE Grade, and Similar Specification for Wrought Alloy Steels

AMS No.	Title of Specification	UNS No.	Alloy	Similar Specification
6434D	Sheet, strip, and plate, 0.78Cr 1.8Ni 0.35Mo 0.20V (0.33–0.38C)	K33517	4335 Mod	
6435C	Sheet, strip, and plate, 0.78Cr 1.8Ni 0.35Mo 0.20V (0.33–0.38C), vacuum consumable electrode melted, annealed	K33517	4335 Mod	
6436B	Sheet, strip, and plate, low alloy, heat resistant, 0.65Si 1.25Cr 0.50Mo 0.85V (0.25–0.30C), annealed	K22770	17–22A(V)	
6437D	Sheet, strip, and plate, 5.0Cr 1.3Mo 0.50V (0.38–0.43C)	T20811	H-H	
6438D	Sheet, strip, and plate, 1.05Cr 0.55Ni 1.0Mo 0.12V (0.45–0.50C), consumable electrode vacuum melted	K24728	D6	
6439B	Sheet, strip, and Plate, 1.05Cr 0.55Ni 1.0Mo 0.12V (0.42–0.48C), consumable electrode vacuum melted, annealed	K24728	D6AC	MIL-S-8949
6440J	Bars, forgings, and tubing, 1.45Cr (0.98–1.10C), for bearing applications	G52986	52100	
6442E	Bars and forgings, 0.50Cr (0.98–1.10C), for bearing applications	G50986	50100	MIL-S-7420
6443E	Bars, forgings, and tubing, 1.0Cr (0.98–1.10C), consumable electrode vacuum melted	G51986	51100	
6444H	Bars, forgings, and tubing, 1.45Cr (0.98–1.10C), premium aircraft quality, consumable electrode vacuum melted	G52986	52100	
6445E	Bars, forgings, and tubing, 1.05Cr 1.1Mn (0.92–1.02C), consumable electrode vacuum melted	K22097	51100 Mod	
6446C	Bars, forgings, and tubing, 1.0Cr (0.98–1.10C), electroslag remelted	G51986	51100	
6447D	Bars, forgings, and tubing, 1.4Cr (0.98–1.10C), electroslag remelted	G52986	52100	
6448F	Bars, forgings, and tubing, 0.95Cr 0.22V (0.48–0.53C)	G61500	6150	MIL-S-8503
6449C	Bars, forgings, and tubing, 1.0Cr (0.98–1.10C), for bearing applications	G51986	51100	MIL-S-7420

Continued

TABLE 1.16 (Continued)
AMS Number, Title of Specification, and Equivalent UNS Number, Nearest Proprietary or AISI-SAE Grade, and Similar Specification for Wrought Alloy Steels

AMS No.	Title of Specification	UNS No.	Alloy	Similar Specification
6450F	Wire, spring, 0.95Cr 0.22V (0.48–0.53C), annealed and cold drawn	G61500	6150	
6451A	Wire, spring, 1.4Si 0.65Cr (0.51–0.59C), oil tempered	G92540	9254	
6452A	Wire, welding, 0.95Cr 0.20Mo (0.38–0.43C), vacuum melted, environment controlled packaging	G43406	E4340	MIL-R-5632, Type II
6453	Wire, welding, 0.30 Cr 1.8Ni 0.40Mo (0.23–0.28C), vacuum melted, environment controlled packaging	K 32550	Hy-Tuf	
6454B	Sheet, strip, and plate, 1.8Ni 0.8Cr 0.25Mo (0.38–0.43C), consumable electrode melted	G43400	4340	
6455G	Sheet, strip, and plate, 0.95Cr 0.22V (0.48–0.53C)	G61500	6150	MIL-S-18731
6456A	Wire, welding, 0.8Cr 1.8Ni 0.25Mo (0.35–0.40C), vacuum melted, environment controlled packaging		4340 Mod	MIL-R-5632, Type III
6457A	Wire, welding, 0.95Cr 0.20Mo (0.28–0.33C), vacuum melted, environment controlled packaging	K13147	4130	MIL-R-5632, Type I
6458F	Wire, welding, 1.25Cr 0.50Mo 0.30V 0.65Si (0.28–0.33C), vacuum melted, environment controlled packaging	K23015	17–22A(S)	
6459B	Wire welding, 1.0Cr 1.0Mo 0.12V (0.18–0.23C), vacuum induction melted	K22720		
6460D	Wire, welding, 0.62Cr 0.20Mo 0.75Si 0.10Zr (0.10–0.17C)	K11365	NAX-915-AC	
6461G	Wire, welding, 0.95Cr 0.20V (0.28–0.33C), vacuum melted, environment controlled packaging	K13148	6130	
6462F	Wire, welding, 0.95Cr 0.20V (0.28–0.33C)	K13149	6130	
6463B	Wire, welding, 18.5Ni 8.5Co 5.2Mo 0.72Ti 0.10A1, vacuum environment controlled packaging	K93130	Mar 300	
6464E	Electrodes, welding, covered, 1.05Mo 0.20V (0.06–0.12C)	W10013	10013 (AWS)	MIL-E-6843, Class E-10013

Continued

TABLE 1.16 (Continued)
AMS Number, Title of Specification, and Equivalent UNS Number, Nearest Proprietary or AISI-SAE Grade, and Similar Specification for Wrought Alloy Steels

AMS No.	Title of Specification	UNS No.	Alloy	Similar Specification
6465B	Wire, welding, 2.0Cr 10Ni 8.0Co 1.0Mo 0.02A1 0.06V (0.10–0.14C), vacuum melted, environment controlled pakaging	K91971	HY-180	
6466D	Wire, welding, corrosion resistant, 5.2Cr 0.55Mo	S50280	Type 502	
6467C	Electrode, welding, covered, 5Cr 0.55Mo	W50210	Type 502	
6468B	Wire, welding, 1.0Cr 3.8Co 0.45Mo 0.08V (0.14–0.17C), vacuum melted, environment controlled packaging	K91461	HP 9-4-20	
6469A	Wire, welding, 1.75Mn 0.80Cr 2.8Ni 0.85Mo (0.09–0.12C), vacuum melted, environment controlled packaging	—	—	
6470J	Bars, forgings, and tubing, nitriding grade, 1.6Cr 0.35Mo 1.1A1 (0.38–0.43C)	K24065	135 Mod	MIL-S-6709
6471D	Bars, forgings, and tubing, nitriding grade, 1.6Cr 0.35Mo 1.2A1 (0.38–0.43C), consumable electrode vacuum melted	K24065	135 Mod	
6472C	Bars and forgings, nitriding grade, 1.6Cr 0.35Mo 1.1 A1 (0.38–0.43C), hardened and tempered, 112 ksi (772 MPa) tensile strength	K24065	135 Mod	MIL-S-6709
6473	Wire, welding, 0.88Cr 1.8Ni 1.6Co 0.42Mo 0.08V (0.28–0.33C), vacuum melted, environment controlled packaging			
6475F	Bars, forgings, and tubing, nitriding grade, 1.1Cr 3.5Ni 0.25Mo 1.25A1 (0.21–0.26C)	K52355		
6476	Bars, forgings, and tubing, 0.50Cr 0.12Mo (0.89–1.01C), for bearing applications			
6477	Bars, forgings, and tubing, 0.80Cr (0.90–1.03C), for bearing applications			
6485G	Bars and forgings, 5.0Cr 1.3Mo 0.50V (0.38–0.43C)	T20811	H-11	FED-QQ-T-570 Class H-11
6487G	Bars and forgings, 5.0Cr 1.3Mo 0.50V (0.38–0.43C), consumable electrode vacuum melted	T20811	H-11	
6488E	Bars and forgings, 5.0Cr 1.3Mo 0.5V (0.38–0.43C)	T20811	H-11	

Continued

TABLE 1.16 (Continued)
AMS Number, Title of Specification, and Equivalent UNS Number, Nearest Proprietary or AISI-SAE Grade, and Similar Specification for Wrought Alloy Steels

AMS No.	Title of Specification	UNS No.	Alloy	Similar Specification
6490D	Bars, forgings, and tubing, 4.0Cr 4.2Mo 1.0V (0.77–0.85C), premium aircraft quality for bearing applications, consumable electrode vacuum melted	T11350	M-50	
6491A	Bars, forgings, and tubing, 4.1Cr 4.2Mo 1.0V (0.80–0.85C), premium aircraft quality for bearing applications, Double vacuum melted	T11350	M-50	
6501A	Wire, welding, maraging steel, 18Ni 8.0Co 4.9Mo 0.40Ti 0.10A1, vacuum induction melted, environment controlled packaging	K92890	Maraging 250	
6512C	Bars, forgings, tubing, and rings, 18Ni 7.8Co 4.9Mo 0.40Ti 0.10A1, consumable electrode melted, annealed	K92890	Maraging 250	MIL-S-46850 Type III, Grade
6514C	Bars, forgings, tubing, and rings, Maraging, 18.5Ni 9Co 4.9Mo 0.65Ti 0.10A1, consumable electrode melted, annealed	K93120	Maraging 300	MIL-S-46850 Type 300 MIL-S-13881, Type II, Class I
6518A	Sheet, strip, and plate, maraging, 19Ni 3.0Mo 1.4Ti 0.10A1, double vacuum melted, solution heat treated			
6519A	Bars, forgings, tubing, and rings, maraging, 19Ni 3.0Mo 1.4Ti 0.10A1, double vacuum melted, annealed			
6520B	Sheet, strip, and plate, maraging 250, 18Ni 7.8Co 4.9Mo 0.40Ti 0.10A1, consumable electrode melted, Solution heat treated	K92890	Maraging 250	
6521A	Sheet, strip, and plate, 18.5NI 9.0Co 4.9Mo 0.65Ti 0.10A1, consumable electrode melted, solution heat treated	K93120	Maraging 300	MIL-S-46850 Grade 300
6522A	plate, 2.0Cr 10Ni 14Co 1.0Mo (0.13–0.17C), vacuum melted, normalized and overaged	K92571	AF-1410	
6523C	Sheet, strip, and plate, 0.75Cr 9.0Ni 4.5Co 1.0Mo 0.09V (0.17–0.23C), vacuum consumable electrode melted, annealed	K91472	HP 9–4–20	

Continued

TABLE 1.16 (Continued)
AMS Number, Title of Specification, and Equivalent UNS Number, Nearest Proprietary or AISI-SAE Grade, and Similar Specification for Wrought Alloy Steels

AMS No.	Title of Specification	UNS No.	Alloy	Similar Specification
6524C	Wire, welding, 1.0Cr 7.5Ni 4.5Co 1.0Mo 0.09V (0.29–0.34C), consumable electrode vacuum melted	K91313	HP 9–4–30	
6525A	Bars, forgings, tubing, and rings, 0.75Cr 9.0Ni 4.5Co 1.0Mo 0.09V (0.17–0.23C), consumable electrode vacuum melted	K91472	HP 9–4–20	
6526C	Bars, forgings, tubing, and rings, 1.0Cr 7.5Ni 4.5Co 1.0Mo 0.09V (0.29–0.34C), consumable electrode vacuum melted, annealed	K91283	HP 9–4–30	
6527B	Bars and forgings, 2.0Cr 10Ni 14Co 1.0Mo (0.15–0.19C), vacuum melted, normalized and overaged	K92571	AF 1410	
6528	Bars, 0.95Cr 0.20Mo (0.28–0.33C), special aircraft quality cleanliness, normalized	G41300	4130	
6529	Bars, 0.95Cr 0.20Mo (0.38–0.43C), special aircraft quality cleanliness, normalized	G41400	4140	
6530H	Tubing, seamless, 0.50Ni 0.55Cr 0.20Mo (0.28–0.33C)	G86300	8630	
6532	Bars and forgings, 3.1Cr 11.5Ni 13.5Co 1.2Mo (0.21–0.25C), vacuum melted, annealed	K92580	Aermet 100	
6533	Wire, welding, 2.0Cr 10Ni 14Co 1.9Mo (0.13–0.17C), vacuum melted, environment controlled packaging	K92571	AF 1410	
6535G	Tubing, seamless, 0.50Cr 0.55Ni 0.20Mo (0.28–0.33C)	G86300	8630	
6543B	Bars and forgings, 2.0Cr 10Ni 8.0Co 1.0Mo (0.10–0.14C), double vacuum melted, solution heat treated	K92571	AF 1410	
6544B	Plate, maraging, 2.0Cr 10Ni 8.0Co 1.0Mo (0.10–0.14C), double vacuum melted, heat treated	K91970		
6546D	Sheet, strip, and plate, 0.48Cr 0.80Ni 4.0Co 0.48Mo 0.09V (0.24–0.30C), consumable electrode melted, annealed	K91122	HP 9–4–25	
6550H	Tubing, Welded, 0.55Cr 0.50Ni 0.20Mo (0.28–0.33C)	G86300	8630	MIL-T-6734

Source: From 1994 SAE AMS Index, Society of Automotive Engineers, Warrendale, PA.

duplex stainless steels, and nickel-base alloys), dimensions, weights, process of manufacture, chemical and mechanical property requirements, and testing and inspection methods [61]. API Spec 5LD covers seamless, centrifugal cast, and welded clad steel line pipe and lined steel pipe with increased corrosion-resistant properties. The clad and lined steel line pipes are composed of a base metal outside and a corrosion resistent alloy (CRA) layer inside the pipe; the base material conforms to API Spec 5L, except as modified in the API Spec 5LC document. This specification provides standards for pipe with improved corrosion resistance suitable for use in conveying gas, water, and oil in both the oil and natural gas industries [62].

1.5.5 ANSI Specifications

ANSI standard begins with the prefix ANSI, followed by an alphanumeric code with an uppercase letter, subsequently followed by one to three digits and additional digits that are separated by decimal points. ANSI standards can also have a standard developer's acronym in the title. Examples are ANSI H35.2, ANSI A156.2, ANSI B18.2.3.6M, ANSI/ASME NQ2-1989, ANSI/API Spec 5CT-1992, ANSI/API Spec 5D-1992, ANSI/API Spec 5L-1992, and ANSI/API Spec 5LC-1991 [57,60–62].

1.5.6 AWS Specifications

AWS standards are used to support welding design, testing, quality assurance, and other related joining functions. These standards begin with the prefix AWS followed by the letter and numerals with decimal point. Examples of AWS specifications with corresponding AISI-SAE or proprietary grade and UNS number in parentheses are AWS A5.1 (E6010, W06010), AWS A5.2 (RG65, WK00065), and AWS A5.5 (E9018-D3, W19118).

1.6 INTERNATIONAL SPECIFICATIONS AND DESIGNATIONS

Since steelmaking technology is available worldwide, familiarity with international specifications and designations for steels is necessary. Table 1.17 cross-references SAE steels with those of a selected group of international specifications and designations, which are described in the following paragraphs. More elaborate information on cross-referencing is available in Refs. [7,15,57,63].

1.6.1 ISO Designations

The International Organization for Standardization (ISO) system has standard designation for steel.

1.6.1.1 The Designation for Steels with Yield Strength

The designations are preceded by the letter and followed by yield strength value (MPa). The prefix of nonalloy structural steel is letter S, for example, S235. The prefix of nonalloy engineering steel is letter E, for example, E235. The numbers indicate the yield strength $\geq$235 MPa.

The method of HSLA steels is equivalent to nonalloy engineering steels. The lower limit of yield strength is 355–690 MPa, for example, E355, . . . , . . . , E690, where E355 and E690 are different steel grades.

TABLE 1.17
Cross-Reference to Steels

United States (SAE)	Fed. R. of Germany (DIN)	Japan (JIS)	United Kingdom (BS)	France (AFNOR NF)	China (GB)	ISO
Carbon steels						
1005	1.0288, D5-2 1.0303, QSt32-2 1.0312, D5-1 1.0314, D6-2 1.0393, ED3 1.0394, ED4 1.1012, RFe120	—	970 015A03	—	05F	—
1006	1.0311, D7-1 1.0313, D8-2 1.0317, RSD4 1.0321, St23 1.0334, StW23 1.0335, StW24 1.0354, St14Cu3 1.0391, EK2 1.0392, EK4 1.1009, Ck7	—	970 030A04 970 040A04 970 050A04	A35-564 XC6FF	—	—
1008	1.0010, D9 1.0318, St28 1.0320, St22 1.0322, USD8 1.0326, RSt28 1.0330, St2, St12 1.0333, St3, St13 1.0331, RoSt2 1.0332, StW22 1.0336, USt4, USt14 1.0337, RoSt4 1.0344, St12Cu3 1.0347, RRSt13 1.0357, USt28 1.0359, RRSt23 1.0375, Feinstblech T57, T61, T65, T70 1.0385, Weissblech T57, T61, T65, T70 1.0744, 6P10 1.0746, 6P20 1.1116, USD6	G3445 STKM11A (11A)	1449 3CR 1449 3CS 1449 3HR 1449 3HS 1717 ERW101 3606 261	A35-551 XC10 XC6 XC6FF	08F 08 08A1	CC8X
1010	1.0204, UQSt36 1.0301, C10 1.0328, USD10 1.0349, RSD9	G4051 S10C G4051 S9Ck	1449 40F30, 43F35, 46F40, 50F45,	A33-101 AF34 CC10 C10	10F 10	C10 CE10 C11x

Continued

TABLE 1.17 (Continued)
Cross-Reference to Steels

United States (SAE)	Fed. R. of Germany (DIN)	Japan (JIS)	United Kingdom (BS)	France (AFNOR NF)	China (GB)	ISO
	1.1121, Ck10 1.1122, Cq10		60F55, 68F62, 75F70 (available in HR, HS, CS conditions) 1449 4HR, 4HS, 4CR, 4CS 970 040A10 (En2A, En2A/1, En2B) 970 045A10, 045M10 (En32A) 970 050A10 970 060A10 980 CEW1			
1012	1.0439, RSD13	G4051 S12C	1449 12HS, 12CS 1501 141-360 970 040A12 (En2A, En2A/1, En2B) 970 050A12 970 060A12	A33-101 AF37 A35-551 XC12 C12	—	—
1013	1.0036, USt37-2 1.0037, St37-2 1.0038, RSt37-2 1.0055, USt34-1 1.0057, RSt34-1 1.0116, St37-3 1.0218, RSt41-2 1.0219, St41-3 1.0307, StE210.7 1.0309, St35.4 1.0315, St37.8 1.0319, RRStE210.7 1.0356, TTSt35 1.0417 1.0457, StE240.7	—	3059 360 3061 360 3603 360	A35-551 XC12 CC12	—	—
1015	1.0401, C15 1.1132, CQ15 1.1135, Ck16A1	G4051 F15Ck G4051 S15C	970 040A15 970 050A15 970 060A15	XC15	15	C15 C15E4 C15M2

Continued

TABLE 1.17 (Continued)
Cross-Reference to Steels

United States (SAE)	Fed. R. of Germany (DIN)	Japan (JIS)	United Kingdom (BS)	France (AFNOR NF)	China (GB)	ISO
	1.1140, Cm15 1.1141, Ck15 1.1144 1.1148, Ck15A1		970 080A15, 080M15 970 173H16			
1016	1.0419, RS144.2 1.0467, 15Mn3 1.0468, 15Mn3A1 1.1142, GS-Ck16	—	3059 440 3606 440 970 080A15, 080M15 970 170H15 970 173H16		15Mn	—
1017	—	G4051 S17C	1449 17HS, 17CS 970 040A17 970 050A17 970 060A17	A35-551 XC18 A35-552 XC18 A35-566 XC18 A35-553 XC18S A35-554 XC18S	—	—
1018	1.0453, C16.8	—	970 080A17	A33-101 AF42 C20		
1019	—	—	—	—		
1020	1.0402, C22 1.0414, D20-2 1.0427, C22.3 1.0460, C22.8 1.1149, Cm22 1.1151, Ck22	G4051 S20C G4051 S20CK	970 040A20 970 050A20 (En2C, En2D) 970 060A20	A35-551 XC18 A35-552 XC18 A35-566 XC18 A35-553 C20 A35-553XC18S A35-554XC18S CC20	20	C20 CC21K
1021	—	—	970 070M20 970 080A20	A35-551 21B3 A35-552 21B3 A35-553 21B3 A35-557 21B3 A35-566 21B3	—	—
1022	1.0432, C21 1.0469, 21Mn4 1.0482, 19Mn5 1.1133, 20Mn5, GS-20Mn5 1.1134, Ck19	—	3111 Type 9 970 120M19 970 170H20	A35-551 20MB5 A35-552 20 MB5 A35-553 20MB5 A35-556 20MB5 A35-557 20MB5 A35-566 20MB5 A35-566 20M5	20Mn	—

Continued

TABLE 1.17 (Continued)
Cross-Reference to Steels

United States (SAE)	Fed. R. of Germany (DIN)	Japan (JIS)	United Kingdom (BS)	France (AFNOR NF)	China (GB)	ISO
1023	1.1150, Ck22.8 1.1152, Cq22	G4051 S22C	1449 2HS, 22CS 970 040A22 (En2C, En2D) 970 050A22 970 060A22 970 080A22	—	—	—
1025	1.0406, C25 1.0415, D25-2, D26-2 1.1158, Ck25	G4051 S25C	—	A35-552 XC25 A35-566 XC25	25	C25 C25E4 C25M2
1026	1.1155, GS-Ck25 1.1156, GS-Ck24	—	970 070M26 970 080A25 970 080A27	—	25Mn	—
1029	1.0562, 28Mn4	G3445 STKM15A (15A), STKM15C (15C) G4051 S28C	970 060A27 970 080A27 (En5A)	A33-101 AF50 CC28 C30	—	—
1030	1.0528, C30 1.0530, D30-2 1.1178, Ck30 1.1179, Cm30 1.1811, G-31Mn4	G4051 S30C	1449 30HS, 30CS 970 060A30 970 080A30 (En5B) 970 080M30 (En5)	A35-552 XC32 A35-553 XC32	30	C30 C30
1035	1.0501, C35 1.0516, D35-2 1.1172, Cq35 1.1173, Ck34 1.1180, Cm35 1.1181, Ck35	G4051 S35C	1717 CDS105/106 970 060A35 970 080A32 (En5C) 970 080A35 (En8A) 980 CFS6	A33-101 AF55 A35-553 C35 A35-553 XC38 A35-554 XC38 XC35 XC38TS C35	35	C35 C35E4 C35M2
1037	1.0520, 31Mn4 1.0561, 36Mn4	G4051 S35C	3111 type 10 970 080M36 970 170H36	—	35Mn	—
1038	No international equivalents					
1039	1.1190, Ck42A1	—	970 060A40 970 080A40 (En8C) 970 080M40 (En8)	40M5 A35-552 XC38H2 A35-553 38MB5	40Mn	—

Continued

TABLE 1.17 (Continued)
Cross-Reference to Steels

United States (SAE)	Fed. R. of Germany (DIN)	Japan (JIS)	United Kingdom (BS)	France (AFNOR NF)	China (GB)	ISO
			970 170H41	A35-556 38MB5 A35-557 XC38H2 XC42, XC42TS		
1040	1.0511, C40 1.0541, D40-2 1.1186, Ck40 1.1189, Cm40	G4051 S40C	1287 1449 40HS, 40CS 3146 Class 1 Grade C 3146 Class 8 970 060A40 970 080A40 (En8C) 970 080M40 (En8)	A33-101 AF60 C40	40	C40 C40E4 C40M2
1042	1.0517, D45-2	G4051 S43C	970 060A42 970 080A42 (En8D)	A35-552 XC42H1 A35-553 C40 CC45 XC42, XC42TS	—	—
1043	1.0558, GS-60.3	G4051 S43C	970 060A42 970 080A42 (En8D) 970 080M46	A35-552 XC42H2	—	—
1044	1.0517, D45-2	—	—	—	—	—
1045	1.0503, C45 1.1184, Ck46 1.1191, Ck45, GS-Ck45 1.1192, Cq45 1.1194, Cq45 1.1201, Cm45 1.1193, Cf45	G4051 S45C G5111 SCC5	970 060A47 970 080A47 970 080M46	A33-101 AF65 A35-552 XC48H1 A35-553 XC45 A35-554 XC48 XC48TS C45	45	C45 C45E4 C45M2
1046	1.0503, C45 1.0519, 45MnAl 1.1159, GS-46Mn4	—	3100 AW2 970 080M46	45M4TS A35-552 XC48H1 A35-552 XC48H2 XC48TS	45Mn	—
1049	—	G3445 STKM17A (17A) G3445 STKM17C (17C)	970 060A47 970 080A47	A35-552 XC48H1 A35-554 XC48 XC48TS	—	—

Continued

TABLE 1.17 (Continued)
Cross-Reference to Steels

United States (SAE)	Fed. R. of Germany (DIN)	Japan (JIS)	United Kingdom (BS)	France (AFNOR NF)	China (GB)	ISO
1050	1.0540, C50 1.1202, D53-3 1.1206, Ck50 1.1210, Ck53 1.1213, Cf53 1.1219, Cf54 1.1241, Cm50	G4051 S50C G4051 S53C	1549 50HS 1549 50CS 970 060A52 970 080A52 (En43C) 970 080M50 (En43A)	A35-553 XC50	50	C50 C50E4 C50M2
1053	1.1210, Ck53 1.1213, Cf53 1.1219, Cf54	G4051 S53C	970 080A52 (En43C)	52M4TS A35-553 XC54	50Mn	—
1055	1.0518, D55-2 1.0535, C35 1.1202, D53-3 1.1203, Ck55 1.1209, Cm55 1.1210, Ck53 1.1213, Cf53 1.1219, Cf54 1.1220, D55-3 1.1820, C55W	G4051 S53C G4051 S55C	3100 AW3 970 060A57 970 070M55 970 080A52 (En43C) 970 080A57	A33-101 AF70 A35-552 XC55H1 A35-552 XC55H2 A35-553 XC54 XC55 C55	55	C55 C55E4
1059	1.0609, D58-2 1.0610, D60-2 1.0611, D63-2 1.1212, D58-3 1.1222, D63-3 1.1228, D60-3	—	970 060A62	A35-553 XC60	—	—
1060	1.0601, C60 1.0642, 60Mn3 1.1221, Ck60 1.1223, Cm60 1.1740, C60W	G4051 S58C	1449 60HS 1449 60CS 970 060A57 970 080A57	A35-553 XC60	60	C60 C60E4 C60M2
1064	1.0611, D63-2 1.0612, D65-2 1.0613, D68-2 1.1222, D63-3 1.1236, D65-3	—	970 060A62 970 080A62 (En43D)	—	—	SL, SM
1065	1.0627, C68 1.0640, 64Mn3 1.1230, Federstahldraht FD 1.1233 1.1240, 65Mn4 1.1250, Federstahldraht VD 1.1260, 66Mn4	—	970 060A67 970 080A67 (En43E)	XC65	65	Type DC

Continued

TABLE 1.17 (Continued)
Cross-Reference to Steels

United States (SAE)	Fed. R. of Germany (DIN)	Japan (JIS)	United Kingdom (BS)	France (AFNOR NF)	China (GB)	ISO
1069	1.0615, D70-2 1.0617, D73-2 1.0627, C68 1.1232, D68-3 1.1237 1.1249, Cf70 1.1251, D70-3 1.1520, C70W1 1.1620, C70W2	—	—	A35-553 XC68 XC70	70	—
1070	1.0603, C67 1.0643, 70Mn3 1.1231, Ck67	—	1449 70HS, 70CS 970 060A72 970 070A72 (En42) 970 080A72	XC70	70	Type DC
1074	1.0605, C75 1.0645, 76Mn3 1.0655, C74 1.1242, D73-3	—	970 070A72 (En42) 970 080A72	A35-553 XC75 XC70	75	—
1075	1.0614, D75-2 1.0617, D73-2 1.0620, D78-2 1.1242, D73-3 1.1252, D78-3 1.1253, D75-3	—	—	A35-553-XC75 XC70	75	—
1078	1.0620, D78-2 1.0622, D80-2 1.0626, D83-2 1.1252, D78-3 1.1253, D75-3 1.1255, D80-3 1.1262, D83-3 1.1525, C80W1	G4801 SUP3	970 060A78	XC80	—	—
1080	1.1259, 80Mn4 1.1265 D85-2	—	1449 80HS, 80CS 970 060A78 970 060A83 970 070A78 970 080A78 970 080A83	XC80	80	—
1084	1.1830, C85W	—	970 060A86 970 080A86	XC85		
1085	1.0647, 85Mn3 1.1273, 90Mn4 1.1819, 90Mn4	—	970 080A83	—	85	—

Continued

TABLE 1.17 (Continued)
Cross-Reference to Steels

United States (SAE)	Fed. R. of Germany (DIN)	Japan (JIS)	United Kingdom (BS)	France (AFNOR NF)	China (GB)	ISO
1086	1.0616, C85, D85-2 1.0626, D83-2 1.0628, D88-2 1.1262, D83-3 1.1265, D85-3 1.1269, Ck85 1.1272, D88-3	—	970 050A86	A35-553 XC90	85	Type DC
1090	1.1273, 90Mn4 1.1819, 90Mn4 1.1282, D95S3	—	1449 95HS 1449 95CS 970 060A96	—	T9A	—
1095	1.0618, D95-2 1.1274, Ck 101 1.1275, Ck100 1.1282, D95S3 1.1291, MK97 1.1545, C105W1 1.1645, C105W2	G4801 SUP4	1449 95HS 1449 95CS 970 060A99	A35-553 XC100	T10	—
1140	No international equivalents					
1141	—	G4804 SUM42	970 212A42 (En8DM) 970 216A42	A35-562 45MF4	Y40Mn	44SMn28
1144	1.0727, 45S20	G4804 SUM43	970 212A42 (En8DM) 970 212M44 970 216M44 970 225M44 970 226M44	A35-562 45MF6	—	44SMn28
1146	1.0727, 45S20	—	970 212M44	45MF4	—	—
1151	1.0728, 60S20 1.0729, 70S20	—	—	—	—	—
Resulfurized/rephosphorized carbon steels						
1211	No international equivalents					
1212	1.0711, 9S20 1.0721, 10S20 1.1011, RFe160K	G4804 SUM21	—	10F2 12MF4 S200	—	9S20
1213	1.0715, 9SMn28 1.0736, 9SMn36 1.0740, 9SMn40	G4804 SUM22	970 220M07 (En1A) 970 230M07 970 240M07 (En1A)	A35-561 S250 S250	—	—
1215	1.0736, 9SMn36	G4804 SUM23	970 240M07 (En1B)	A35-561 S300	—	—
12L14	—	—	—	—	Y15Pb	11SMnPb28

Continued

TABLE 1.17 (Continued)
Cross-Reference to Steels

United States (SAE)	Fed. R. of Germany (DIN)	Japan (JIS)	United Kingdom (BS)	France (AFNOR NF)	China (GB)	ISO
Alloy steels						
1330	—	—	—	—	30Mn2	28Mn6
1335	1.5069, 36Mn7	—	—	—	35Mn2	36Mn6
1340	1.5223, 42MnV7	—	—	—	40Mn2	42Mn6
1345	1.0625, StSch90C 1.0912, 46Mn7 1.0913, 50Mn7 1.0915, 50MnV7 1.5085, 51Mn7 1.5225, 51MnV7	—	—	—	45Mn2	
4023	1.5416, 20Mo3	—	—	—	—	—
4024	1.5416, 20Mo3	—	—	—	—	—
4027	1.5419, 22Mo4	—	—	—	—	—
4028	—	—	970 605M30	—	—	—
4032	1.5411	G5111 SCMnM3	970 605A32 970 605H32 970 605M30 970 605M36 (En16)	—	—	—
4037	1.2382, 43MnSiMo4 1.5412, GS-40MnMo4 3 1.5432, 42MnMo7	—	3111 Type 2/1 3111 Type 2/2 970 605A37 970 605H37	—	—	36Mo3E
4042	1.2382, 43MnSiMo4 1.5432, 42MnMo7	—	—	—	—	—
4047	No international equivalents					
4118	1.7211, 23CrMoB4 1.7264, 20CrMo5	G4052 SCM15H G4105 SCM21H G4052 SCM418H G4105 SCM418H	970 708H20 970 708M20	—	G20 CrMo	18CrMo4 18CrMo4E
4130	—	G4105 SCM1 G4105 SCM432 G4105 SCM2 G4105 SCM430 G4106 SCM2	1717 CDS110 970 708A30	A35-552 30CD4 A35-556 30CD4 A35-557 30CD4	30CrMo 30CrMoA	—
4135	1.2330, 35CrMo4 1.7220, 34CrMo4 1.7220, GS- 34CrMo4 1.7226, 34CrMoS4 1.7231, 33CrMo4	G4054 SCM3H G4054 SCM435H G4105 SCM1 G4105 SCM432 G4105 SCM3 G4105 SCM435	970 708A37 970 708H37	35CD4 A35-552 35CD4 A35-553 35CD4 A35-556 35CD4 A35-557 34CD4	35CrMo 35CrMoV	34CrMo4 34CrMo4E 34CrMoS4

Continued

TABLE 1.17 (Continued)
Cross-Reference to Steels

United States (SAE)	Fed. R. of Germany (DIN)	Japan (JIS)	United Kingdom (BS)	France (AFNOR NF)	China (GB)	ISO
4137	1.7225, GS-42CrMo4	G4052 SCM4H G4052 SCM440H G4105 SCM4	3100 type 5 970 708A37 970 708H37 970 709A37	40CD4 42CD4 A35-552 38CD4 A35-557 38CD4	—	—
Carbon–manganese steels						
1513	1.0424, Schiffbaustahl CS:DS 1.0479, 13Mn6 1.0496, 12Mn6 1.0513, Schiffbaustahl A32 1.0514, Schiffbaustahl B32 1.0515, Schiffbaustahl E32 1.0549 1.0579 1.0583, Schiffbaustahl A36 1.0584, Schiffbaustahl D36 1.0589, Schiffbaustahl E 36 1.0599 1.8941, QStE260N 1.8945, QStE340N 1.8950, QStE380N	—	1449 40/30 HR 1449 40/30 HS 1449 40/30 CS 1453 A2 2772 150M12 970 125A15 970 130M15 970 130M15 (En201)	12M5 A33-101 AF50-S A35-501 E35-4 A35-501 E36-2 A35-501 E36-3	15Mn	—
1522	1.0471, 21MnS15 1.0529, StE350-Z2 1.1120, GS-20Mn5 1.1138, GS-21 Mn5 1.1169, 20Mn6 1.8970, StE385.7 1.8972, StE415.7 1.8978 1.8979	G4106 SMn21	1503 221–460 1503 223–409 1503 224–490 3146 CLA2 980 CFS7	A35-551 20MB5 A35-552 20M5 A35-556 20M5 A35-552 20MB5 A35-553 20MB5 A35-556 20MB5 A35-557 20MB5 A35-566 20MB5	20Mn	—

Continued

TABLE 1.17 (Continued)
Cross-Reference to Steels

United States (SAE)	Fed. R. of Germany (DIN)	Japan (JIS)	United Kingdom (BS)	France (AFNOR NF)	China (GB)	ISO
1524	1.0499, 21Mn6A1 1.1133, 20Mn5, GS-20Mn5 1.1160, 22Mn6	G4106 SMn21 G5111 SCMn1	1456 Grade A 970 150M19 (En14A, En14B) 970 175H23 980 CDS9, CDS10	—	20Mn2	—
1526	—	—	970 120M28	A35-566 25MS5	25Mn	—
1527	1.0412, 27MnSi5 1.1161, 26Mn5 1.1165, 30Mn5 1.1165, GS-30Mn5 1.1170, 28Mn6	G5111 SCMn2	1453 A3 1456 Grade B1, Grade B2 3100 A5 3100 A6 970 150M28 (En14A, En14B)	—	30Mn	—
1536	1.0561, 36Mn4 1.1165, 30Mn5 1.1165, GS-30Mn5 1.1166, 34Mn5 1.1167, 36Mn5, GS-36Mn5 1.1813, G-35Mn5	G4052 SMn1H G4052 SMn433H G4106 SMn1 G4106 SMn433 G5111 SCMn2 G5111 SCMn3	1045 3100 A5, A6 970 120M36 (En15B) 970 150M36 (En15)	A35-552 32M5 A35-552 38MB5 A35-553 38MB5 A35-556 38MB5 A35-557 38MB5	35Mn	—
1541	1.0563, E 1.0564, N-80 1.1127, 36Mn6 1.1168, GS-40Mn5	G4106 SMn2, SMn438 G4052 SMn2H, SMn438H G4106 SMn3, SMn443 G4052 SMn3H, SMn443H G5111 SCMn5	970 135M44 970 150M40	40M5 45M5 A35-552 40M6	40Mn2	SL, SM
1548	1.1128, 46Mn5 1.1159, GS-46Mn4	—	—	—	45Mn	SL, SM
1551	1.0542, StSch80	—	—	24M4TS		SL, SM
1552	1.0624, StSch90B 1.1226, 52Mn5	—	—	55M5	50Mn2	SL, SM
1561	1.0908, 60SiMn5	—	—	—	60Mn	SL, SM
1566	1.1233 1.1240, 65Mn4 1.1260, 66Mn7	—	—	—	65Mn	—

Continued

TABLE 1.17 (Continued)
Cross-Reference to Steels

United States (SAE)	Fed. R. of Germany (DIN)	Japan (JIS)	United Kingdom (BS)	France (AFNOR NF)	China (GB)	ISO
Resulfurized carbon steels						
1108	1.0700, U7S10 1.0702, U10S10	G4804 SUM12	—	A35-562 10F1	—	10S20
1110	1.0703, R10S10	G4804 SUM11	—	—	—	—
1117	—	G4804 SUM31	970 210A15 970 210M17 (En32M) 970 214A15 970 214M15 (En202)	—	Y20	—
1118	—	—	970 214M15 (En201)	—	—	—
1137	—	G4804 SUM41	970 212M36 (En8M) 970 216M36 (En15AM) 970 225M36	35MF4 A35-562 35MF6	Y35	—
1139	1.0726, 35S20	—	970 212A37 (En8BM) 970 212M36 (En8M) 970 216M36 (En15AM) 970 225M36	35MF4 A35-562 35MF6	—	—
4140	1.3563, 43CrMo4 1.7223, 41CrMo4 1.7225, 42CrMo4 1.7225, GS-42CrMo4 1.7227, 42CrMoS4	G4052 SCM4H G4052 SCM440H G4103 SNCM4 G4105 SCM4 G4105 SCM440	3100 Type 5 4670 711M40 970 708A40 970 708A42 (En19C) 970 708H42 970 708M40 970 709A40 970 709M40	40CD4 A35-552 42CD4, 42CDTS A35-553 42CD4, 42CDTS A35-556 42CD4, 42CDTS A35-557 42CD4, 42CDTS	42CrMo	42CrMo4 42CrMo4E 42CrMoS4
4142	1.3563, 43CrMo4 1.7223, 41CrMo4	—	970 708A42 (En19C) 970 708H42 970 709A42	40CD4 A35-552 42CD4, 42CDTS A35-553 42CD4, 42CDTS A35-556 42CD4, 42CDTS A35-557 42CD4, 42CDTS	42CrMo 40CrMnMo	42CrMo4

Continued

TABLE 1.17 (Continued)
Cross-Reference to Steels

United States (SAE)	Fed. R. of Germany (DIN)	Japan (JIS)	United Kingdom (BS)	France (AFNOR NF)	China (GB)	ISO
4145	1.2332, 47CrMo4	G4052 SCM5H G4052 SCM445H G4105 SCM5, SCM445	970 708H45	A35-553 45SCD6 A35-552 45SCD6	—	—
4147	1.2332, 47CrMo4 1.3565, 48CrMo4 1.7228, 50CrMo4 1.7228, GS-50CrMo4 1.7230, 50CrMoPb4 1.7328, 49CrMo4	G4052 SCM5H G4052 SCM445H G4105 SCM5, SCM445	970 708A47	A35-552 45SCD6 A35-553 45SCD6 A35-571 50SCD6	—	—
4150	1.3565, 48CrMo4 1.7238, 49CrMo4 1.7228, 50CrMo4 1.7228, GS-50CrMo4 1.7230, 50CrMoPb4 1.7238, 49CrMo4	—	—	A35-571 50SCD6	—	50CrMo4
4161	1.7229, 61CrMo4 1.7266, GS-58CrMnMo4 GS-58CrMnMo4 4 3	G4801 SUP13	3100 BW4 3146 CLA12 Grade C	—	—	—
4320	—	G4103 SNCM23 G4103 SNCM420 G4103 SNCM420H	—	20NCD7 A35-565 18NCD4 A35-565 20NCD7		
4340	1.6565, 40NiCrMo6	G4103 SNCM8 G4103 SNCM439 G4108 SNB23-1-5 G4108 SNB24-1-5	4670 818M40 970 2S.119	—		
	40CrNiMoA 45CrNiMo VA	36CrNiMo6				
E4340	1.6562, 40NiCrMo 7 3	—	970 2S.119	—		
	45CrNiMo VA 40CrNiMoA	—				
4422	1.5419, 22Mo	—	—	23D5		
4427	No international equivalent					

Continued

TABLE 1.17 (Continued)
Cross-Reference to Steels

United States (SAE)	Fed. R. of Germany (DIN)	Japan (JIS)	United Kingdom (BS)	France (AFNOR NF)	China (GB)	ISO
4615	—	—	—	15ND8	—	—
4617	—	—	970 665A17 970 665H17 970 665M17 (En34)	—	—	—
4620	—	—	970 665A19 970 665H20 970 665M20	2ND8	—	—
4626	—	—	970 665A24 (En35B)	—	—	—
4718	No international equivalent					
4720	—	—	—	18NCD4	—	—
4815	No international equivalent					
4817	No international equivalent					
4820	No international equivalent					
50B40	1.7003, 38Cr2 1.7023, 28CrS2	G4052 SMnC3H G4052 SMnC443H G4106 SMnC3 G4106 SMnC443 G5111 SCMnCr4	—	A35-552 38C2 A35-556 38C2 A35-557 38C2 A35-552 42C2 A35-556 42C2 A35-557 42C2	—	—
50B44	—	—	—	45C2	—	—
5046	1.3561, 44Cr2	—	—	—	—	—
50B46	No international equivalent					
50B50	1.7138, 52MnCrB3	—	—	55C2	—	—
5060	1.2101, 62SiMnCr4	—	970 526M60 (EnH)	61SC7 A35-552 60SC7	—	—
5115	1.7131, 16MnCr5, GS-16MnCr5 1.7139, 16MnCrS5 1.7142, 16MnCrPb5 1.7160, 16MnCrB5	G4052 SCr21H G4052 SCr415H G4104 SCr21 G4104 SCr415	970 527A17 970 527H17 970 527M17	16MC5 A35-551 16MC5	15Cr 15CrMn	—

Continued

TABLE 1.17 (Continued)
Cross-Reference to Steels

United States (SAE)	Fed. R. of Germany (DIN)	Japan (JIS)	United Kingdom (BS)	France (AFNOR NF)	China (GB)	ISO
5117	1.3521, 17MnCr5 1.7016, 17Cr3 1.7131, 16MnCr5, GS-16MnCr5 1.7139, 16MnCrS5 1.7142, 16MnCrPb5 1.7168, 18MnCrB5	—	—	18Cr4 A35-551 16MC5	—	—
5120	1.2162, 21MnCr5 1.3523, 19MnCr5 1.7027, 20Cr4 1.7028, 20Cr5 4 1.7121, 20CrMnS3 3 1.7146, 20MnCrPb5 1.7147, GS-20MnCr5 1.7149, 20MnCrS5	G4052 SCr22H G4052 SCr420H G4052 SMn21H G4052 SMn421H G4104 SCr22 G4104 SCr420	—	A35-551 20MC5 A35-552 20MC5	20Cr 20CrMn	20Cr4 20MnCr5 20Cr4E 20CrS4
5130	1.8401, 30MnCrTi4	G4052 SCr2H G4052 SCr430H G4104 SCr2 G4104 SCr430	970 530A30 (En18A) 970 530H30	28C4	30Cr	—
5132	1.7033, 34Cr4 1.7037, 34CrS4	G4104 SCr3 G4104 SCr435	970 530A32 (En18B) 970 530A36 (En18C) 970 530H32	A35-552 32C4 A35-553 32C4 A35-556 32C4 A35-557 32C4	—	—
5135	1.7034, 37Cr4 1.7038, 37CrS4 1.7043, 38Cr4	G4052 SCr3H G4052 SCr435H	3111 Type 3 970 530A36 (En 18C) 970 530H36	38C4 A35-552 38Cr4 A35-553 38Cr4 A35-556 38Cr4 A35-557 38Cr4	35Cr	34Cr4 34CrS4
5140	1.7035, 41Cr4 1.7039, 41CrS4 1.7045, 42Cr4	G4052 SCr4H G4052 SCr440H G4104 SCr4 G4104 SCr440	3111 Type 3 970 2S.117 970 530A40 (En 18D) 970 530H40 970 530M40	A35-552 42C4 A35-557 42C4 A35-556 42C4	40Cr 38Cr	41Cr4 41CrS4 41Cr4E

Continued

TABLE 1.17 (Continued)
Cross-Reference to Steels

United States (SAE)	Fed. R. of Germany (DIN)	Japan (JIS)	United Kingdom (BS)	France (AFNOR NF)	China (GB)	ISO
5147	1.7145, GS-50CrMn4 4	—	3100 BW2 3100 BW3 3146 CLA12 Grade A 3146 CLA12 Grade B	50C 4	45Cr	—
5150	1.7145, GS-50CrMn4 4 1.8404, 60MnCrTi4	—	3100 BW2 3100 BW3 3146 CLA12 Grade A 3146 CLA12 Grade B	—	50Cr	—
5155	1.7176, 55Cr3	G4801 SUP11 G4801 SUP9	—	A35-571 55C3	55CrMnA	—
5160	1.2125, 65MnCr4	G4801 SUP9A	970 527A60 (En48) 970 527H60	—	60CrMnA	—
51B60	—	—	—	—	60CrMnBA	—
E50100	1.2018, 95Cr1 1.3501, 100Cr2	—	—	A35-565 100C2	GCr6	—
E51100	1.2057, 105Cr4 1.2109, 125CrSi5 1.2127, 105MnCr4 1.3503, 105Cr4	—	—	—	GCr9	—
E52100	1.2059, 120Cr5 1.2060, 105Cr5 1.2067, 100Cr6 1.3505, 100Cr6 1.3503, 105Cr4 1.3514, 101Cr6 1.3520, 100CrMn6	—	970 534A99 (En31) 970 535A99 (En31)	—	GCr15	1
6118	No international equivalents	G4801 SUP10	970 735A 50 (En47)	A35-552 50CV4	50CrVA	50CrV4
6150	1.8159, GS-50Cr V4		970 S.204	A35-553 50CV4 A35-571 50CVA		
8115	No international equivalents					
81B45	No international equivalents					
8615	—	—	—	15NCD2 15NCD4	—	—
8617	—	—	970 805A17 970 805H17 970 805M17 (En 361)	18NCD4 18NCD6	—	—

Continued

TABLE 1.17 (Continued)
Cross-Reference to Steels

United States (SAE)	Fed. R. of Germany (DIN)	Japan (JIS)	United Kingdom (BS)	France (AFNOR NF)	China (GB)	ISO
8620	1.6522, 20NiCrMo2 1.6523, 21NiCrMo2 1.6526, 21NiCrMoS2 1.6543, 21NiCrMo2 2	G4052 SNCM21H G4052 SNCM220H G4103 SNCM21 G4103 SNCM220	2772 806M20 970 805A20 970 805H20 970 805M20 (En362)	18NCD4 20NCD2 A35-551 19NCDB2 A35-552 19NCDB2 A35-551 20NCD2 A35-553 20NCD2 A35-565 20NCD2 A35-566 20NCD2	20CrNiMo G20CrNiMo	20NiCrMo2 20NiCrMo2E 20NiCrMoS2
8622	1.6541, 23MnNiCrMo5 2	—	2772 806M22 970 805A22 970 805H22 970 805M22	23NCDB4 A35-556 23MNCD5 A35-556 23NCDB2 A35-566 22NCD2		
8625	—	—	970 805H25 970 805M25	25NCD4 A35-556 25MNCD6 A35-566 25MNDC6	—	—
8627	No international equivalents					
8630	1.6545, 30NiCrMo2 2	—	—	30NCD2	—	—
8637	—	—	970 945M38 (En100)	40NCD3	—	—
8640	1.6546, 40NiCrMo2 2	—	3111 Type 7, 2S.147 970 945A40 (En 100C)	40NCD2 40NCD2TS 40NCD3TS 40NCD3	—	41CrNiMo2E
8642	No international equivalents					
8645	No international equivalents					
86B45	No international equivalents					

Continued

TABLE 1.17 (Continued)
Cross-Reference to Steels

United States (SAE)	Fed. R. of Germany (DIN)	Japan (JIS)	United Kingdom (BS)	France (AFNOR NF)	China (GB)	ISO
8650	No international equivalents					
8655	No international equivalents					
8660	—	—	970 805A60 970 805H60	—	—	—
8720	No international equivalents					
8740	1.6546, 40NiCrMo2 2	—	3111 Type 7, 2S.147	40NCD2 40NCD2TS 40NCD3TS	—	—
8822	No international equivalents					
9254	—	—	—	—	—	56SiCr7
9260	—	G4801 SUP7	970 250A58 (En45A) 970 250A61 (En45A)	60S7 61S7	60Si2Mn 60Si2MnA	59Si7 61SiCr7
E9310	1.6657, 14NiCrMo1 3 4 G10CrNi3Mo	—	970 832H13 970 832M13 (En36C) S.157	16NCD13		—
94B15	No international equivalents					
94B17	No international equivalents					
94B30	No international equivalents					

Source: From Anon., Classification and designation of carbon and low-alloy steels, *ASM Handbook*, 10th ed., Vol. 1, ASM International, Materials Park, OH, 1990, pp. 140–194; H. Lin, G. Lin, and Y. Ma, Eds., *Designation and Trade Name Handbook of Steels Worldwide*, mechanical Industry Press, Beijing, 1997.

1.6.1.2 The Designation for Steels with Chemical Composition

The prefix of nonalloy heat-treatable steel is C, and followed by numerical value. The numerical value is 100 times of the average of carbon content, for example, C25 is the steel containing an approximate mean of 0.25% C. The additional suffix EX or MX indicated the quality steel or the high quality steel.

The designation for structural alloy steels and spring steels are similar to that of DIN systems. For example, 36CrNiMo4 contains 0.36% C and alloy elements, such as Cr, Ni, and Mo, the number 4 is the product of multiplier of the amount of first alloy element (here Cr).

The designation for bearing steels is indicated by a numeric code. Types 1–5 represent high-carbon chromium-bearing steels (fully hardened hearing steels), Types 10–16 are the surface-hardened bearing steels, Types 20–21 denote stainless-bearing steels, and Types 30–32 are the high-temperature bearing steels. Stainless steels are also indicated by a numeric code. For example, the ferritic stainless steels include Type 1Ti, 1, 2, 8, . . . , martensitic stainless steels include Type 3, 4, 5, . . . , austenitic stainless steels include Types 10–24 and A2–A4, etc.

Heat-resistant steels are indicated with prefix letter H and followed by numeric code. For example, types H1–H7 are ferritic steels and types H10–H18 are austenitic steels.

Nonalloy tool steels are preceded by the prefix letters TC and followed by a numeric code, which indicates 100 times of the average of the carbon content.

The designation for alloy tool steels is equivalent to that of alloy structural steels. High-speed steels are preceded by the prefix letters HS and followed by a numeric code, which indicates the percentage content of alloy elements of W, Mo, V, and Co. For example, HS 2-9-1-8 indicates that steel contains 2% W, 9% Mo, 1% V, and 8% Co, respectively. High-speed steel free from Mo uses numeric 0. If a high-speed steel were free from Co, then 0 would not be added. For example, tungsten high-speed steel HS 18-0-1 contains 18% W, 0% Mo, 1% V, and 0% Co. Some steels of ISO designations are provided in Table 1.17.

1.6.2 GB Designations (State Standards of China)

The state standard of China for steels is called Guojia Biaozhun, abbreviated as GB. The GB designations for nonalloy common steels and HSLA steels use the prefix letter Q, followed by the yield strength value (MPa). For example, Q235, Q345, Q390 denote nonalloy common steels and HSLA steels with their yield strength 235, 345, and 390 MPa, respectively.

Nonalloy structural steels and alloy structural steels are represented by numeric codes, which are 100 times of the average carbon content. For example, numeric code 45 shows the steel containing 0.45% C. Alloy elements in steel use the descriptive code with chemical symbols, and followed by its average content. As the average content is less than 1.5%, it is indicated only with the chemical symbol, for example, 34CrNi3Mo containing 0.30–0.40% C, 0.70–1.10% Cr, 2.75–3.25% Ni, and 0.25–0.40% Mo.

Nonalloy tool steels are represented by the prefix letter T, followed by numeric codes, which are ten times of the average carbon content. For example, T8 means the steel contains an average carbon content about 0.80%. When the average carbon content is more than 1.0% in alloy tool steels, the steel grade would not indicate the carbon content; but the average content is less than 1.0%, it uses numeric code ten times carbon content. For example, CrMn steel contains 1.30–1.50% C, 1.30–1.60% Cr, 0.45–0.75% Mn, and 9Mn2V steel contains 0.85–0.95% C, 1.70–2.00% Mn, 0.10 to 0.25% V. The descriptive method for the alloy element is the same in alloy structural steels.

Carbon content is not indicated in high-speed steels, and only uses the descriptive code with chemical symbols and followed by alloy element content. For example, tungsten high-speed steel 18-4-1 (T1) is represented by W18Cr4V, and W–Mo high-speed steel 6-5-4-2 (M2) is indicated by W6Mo5Cr4V2.

They are represented by a numeric code, which indicates ten times of the carbon content and followed by chemical symbols of alloy elements with their content in stainless steels and heat-resistant steels, but microalloy elements only show the chemical symbols. For example, steel 9Cr18MoV contains 0.85–0.95% C, 17–19% Cr, 0.0–1.3% Mo, 0.07–0.12% V. If the carbon content is less than 0.03 or 0.08%, 00 or 0 would be used for the steel designations, respectively, such as 00Cr18Ni10 and 0Cr13.

1.6.3 DIN Standards

DIN standards are developed by Deutsches Institut fuer Normung in Germany. All German steel standards and specifications are represented by the letters DIN and followed by an alphanumeric or a numeric code. An uppercase letter sometimes precedes this code. German designations are reported in one of the following two methods. One method uses the descriptive code with chemical symbols and numbers in the designation. The second, called the Werkstoff number, uses numbers only, with a decimal after the first digit. There are four figures after the decimal point, the first two of which are used to identify the alloy, and the last two the quantity. Most steels are covered by the significant figure 1, but some have no significant figure before the decimal point. Examples of both methods are provided in Table 1.17, which cross-references DIN designations and indicates chemical composition for DIN steels. However, standards for heat-resistant steels are prefixed with the letter SEW (Stahl-Eisen-Werkstoff Blaetter, steel-iron material sheets). Examples of DIN designations in both methods with equivalent UNS numbers in parentheses are as follows: DIN 40NiCrMo6 or DIN 1.6565 (G43400) is a Ni–Cr–Mo steel that contains 0.35–0.45% C, 0.9–1.4% Cr, 0.5–0.7% Mn, 0.2–0.3% Mo, 1.4–1.7% Ni, 0.035% S, and 0.15–0.35% Si; DIN 17200 1.1149 or DIN 17200 Cm22 (G10200) is a nonresulfurized carbon steel containing 0.17–0.24% C, 0.3–0.6% Mn, 0.035 max P, 0.02–0.035% S, and 0.4% max Si.

1.6.4 JIS Standards

JIS standards are developed by the Japanese Industrial Standards Committee (JISC) in Tokyo, Japan. The specifications begin with the prefix JIS, followed by a letter G for carbon and low-alloy steels. This is followed by a space and series of numbers and letters indicating the particular steel. JIS designations are provided in Table 1.17. As examples of JIS designations with equivalent UNS-AISI numbers in parentheses, JIS G3445 STKM11A (G10080) is a low-carbon tube steel containing 0.12% C, 0.35% Si, 0.60% Mn, 0.04% P, and 0.04% S; JIS G3445 STK 17A (G10490) is a medium-carbon nonresulfurized steel containing 0.45–0.55% C, 0.40–1.0% Mn, 0.04% P, 0.04% S, and 0.04% Si; JIS G4403 SKH2 (AISI T1 grade) is a tungsten high-speed tool steel containing 0.73–0.83% C, 3.8–4.5% Cr, 0.4% Mn, 0.4% Si, 0.8–1.2% V, and 17–19% W; and JIS G4403 SKH59 (AISI M42 grade) is a molybdenum ultrahard high-speed tool steel containing 1–1.15% C, 7.5–8.5% Co, 3.5–4.5% Cr, 0.4% max Mn, 9–10% Mo, 0.5% max Si, 0.9–1.4% V, 1.2–1.9% W, 0.25% max Ni, 0.03% max P, 0.03% max S, and 0.25% Cu.

1.6.5 BS Standards

BS standards are developed by the British Standards Institute (BSI) in London, England. The letters BS precede the standard numerical code, and, like JIS standards, each British designation covers a product form and an alloy code. Table 1.17 lists steels identified by British standards. Some example of BS designations with equivalent AISI designations in parentheses are given: BS 970 708A30 (4130) is a Cr–Mo low-alloy steel containing 0.28–0.33% C, 0.9–1.2% Cr, 0.4–0.6% Mn, 0.15–0.25% Mo, 0.035% P, 0.04% S, and 0.1–0.35% Si; and BS 970 304S15 (304) is a wrought austenitic stainless steel (sheet, strip, plate) containing 0.06% C, 17.5–19% Cr, 0.5–2.0% Mn, 8–11% Ni, 0.05% P, 0.03% S, and 0.2–1.0% Si.

1.6.6 AFNOR Standards

AFNOR standards are developed by the Association Française de Normalisation in Paris, France. The AFNOR standards, which are given in Table 1.17, usually begin with the letters

NF, followed by an alphanumeric code constituting an uppercase letter followed by a series of digits, which are subsequently followed by an alphanumeric sequence. For example, resulfurized (free-cutting) steel is listed in AFNOR NF A35–562 standard or specification, and 35MF6 designation (equivalent to SAE 1137) represents the steel bar containing 0.33–0.39% C, 1.30–1.70% Mn, 0.10–0.40% Si, 0.040% P, and 0.09–0.13% S; whereas 45MF4 designation (equivalent to SAE 1146) contains 0.42–0.49% C, 0.8–1.1% Mn, 0.1–0.4% Si, 0.04% max P, 0.09–0.13% S. Similarly, AFNOR NF A35-573 Z6CN 18.09 is a wrought (SAE 304) stainless steel (sheet, strip, plate) and contains 0.07% C, 17–19% Cr, 2% Mn, 8–10% Ni, 0.04% P, 0.03% S, and 1% Si.

REFERENCES

1. J.R. Davis, Ed., *Concise Metals Engineering Data Book*, ASM International, Materials Park, OH, 1997, p. 44.
2. W.M. Garrison, Jr., Steels: classification, in *Encyclopedia of Materials: Science and Technology*, K.H.J. Buschow, R.W. Cahn, M.C. Flemings, B. Ilschner, E.J. Kramer, and S. Mahajan, Eds., Elsevier, Amsterdam, 2001, pp. 8840–8843.
3. H. Okamoto, C–Fe, in *Binary Alloy Phase Diagrams*, 2nd ed., T.B. Massalski, Ed., ASM International, Materials Park, OH, 1990, pp. 842–848.
4. A.K. Sinha, *Ferrous Physical Metallurgy*, Butterworths, London, 1989.
5. S. Zhang and C. Wu, *Ferrous Materials*, Metallurgical Industry Press, Beijing, 1992.
6. Anon., Classification and designation of carbon and low-alloy steels, *ASM Handbook*, 10th ed., Vol. 1, ASM International, Materials Park, OH, 1990, pp. 140–194.
7. H. Lin, G. Lin, and Y. Ma, Eds., *Designation and Trade Name Handbook of Steels Worldwide*, Mechanical Industry Press, Beijing, 1997.
8. Anon., Carbon and alloy steels, SAE J411, *1993 SAE Handbook*, Vol. 1, Materials Society of Automotive Engineers, Warrendale, PA, pp. 2.01–2.04.
9. G. Krauss, *Steels—Heat Treatment and Processing Principles*, ASM International, Materials Park, OH, 1990.
10. W.C. Leslie, *The Physical Metallurgy of Steels*, McGraw-Hill, New York, 1981.
11. E.C. Bain and H.W. Paxton, *Alloying Elements in Steel*, American Society for Metals, Cleveland, OH, 1966.
12. R.W.K. Honeycombe, *Steels—Microstructure and Properties*, Adward Arnold, London, 1982.
13. H.E. Boyer, in *Fundamentals of Ferrous Metallurgy*, Course 11, Lesson 12, Materials Engineering Institute, ASM International, Materials Park, OH, 1981.
14. R.B. Ross, *Metallic Materials Specification Handbook*, 4th ed., Chapman & Hall, London, 1992.
15. C.W. Wegst, *Stahlschlüssel* (*Key to Steel*), Verlag Stahlschlüssel Wegst GmbH, 1992.
16. W.J. McG. Tegart and A. Gittins, in *Sulfide Inclusions in Steel*, J.T. Deabradillo and E. Snape, Eds., American Society for Metals, Cleveland, OH, 1975, p. 198.
17. C.W. Kovach, in *Sulfide Inclusions in Steel*, J.T. Deabradillo and E. Snape, Eds., American Society for Metals, Cleveland, OH, 1975, p. 459.
18. C.M. Lyne and A. Kazak, *Trans. ASM 61*: 10 (1968).
19. D. Brovoksbank and K.W. Andraws, *JISI 206*: 595 (1968).
20. N.S. Stoloff, in *Fracture Vol. VI*, *Fracture of Metals*, H. Liebowitz, Ed., Academic Press, New York, 1969.
21. J. Yu, Z. Yu, and C. Wu, *J. Metals 40*(*5*): 26–31 (1988).
22. S. Zhang and C. Wu, in *Proceedings of 3rd International Congress on Heat Treatment of Materials*, Shanghai, 1983, pp. 3.25–3.36.
23. T.Y. Hsu (Zuyao Xu), *ISIJ Int. 38*: 1153–1164 (1998).
24. M.J.U.T. Van Wijngaarden and G.P. Visagie, in *Proceedings of the 79th Steelmaking Conference*, Vol. 79, Pittsburgh Meeting, March 24–27, pp. 627–631.
25. H. Matsuka, K. Osawa, M. Ono, and M. Ohmura, *ISIJ Int. 37*: 255–262 (1997).

26. W.D. Landford and H.E. McGannon, Eds., *The Making, Shaping, and Treating of Steel*, 10th ed., U.S. Steel, Pittsburgh, PA, 1985.
27. *Steel Products Manual: Plates; Rolled Floor Plates: Carbon, High Strength Low Alloy, and Alloy Steel*, American Iron and Steel Institute, Washington, D.C., 1985.
28. E. Hornbogen, in *Physical Metallurgy*, R.W. Cahn and P. Haasen, Eds., Elsevier, New York, 1983, pp. 1075–1138.
29. J.D. Smith, in *Fundamentals of Ferrous Metallurgy*, Course 11, Lessons 2 and 5, Materials Engineering Institute, ASM International, Materials Park, OH, 1979.
30. *Numbering System, Chemical Composition, 1993 SAE Handbook, Vol. 1, Materials*, Society of Automotive Engineers, Warrendale, PA, pp. 1.01–1.189.
31. W.F. Smith, *Structure and Properties of Engineering Alloys*, McGraw-Hill, New York, 1981.
32. O.D. Sherby, B. Walser, C.M. Young, and E.M. Cady, *Scr. Metall. 9*: 596 (1975).
33. E.S. Kayali, H. Sunada, T. Oyama, J. Wadsworth, and O.D. Sherby, *J. Mater. Sci. 14*: 2688–2692 (1979).
34. D.W. Kum, T. Oyama, O.D. Sherby, O.A. Ruano, and J. Wadsworth, *Superplastic Forming,* Conference Proceedings, 1984, American Society for Metals, Cleveland, OH, 1985, pp. 32–42.
35. T.A. Phillip, in *ASM Handbook*, 10th ed., Vol. 1, ASM International, Materials Park, OH, 1990, pp. 430–448.
36. A.K. Sinha, in *Production of Iron/Steel and High Quality Product Mix* (Conf. Proc. 1991), ASM International, Materials Park, OH, 1992, pp. 195–206.
37. L.F. Porter and P.E. Repas, *J. Metals 34*(4): 14–21 (1982).
38. L.F. Porter, in *Encyclopaedia of Materials Science and Engineering*, Pergamon Press, Oxford, 1986, pp. 2157–2162.
39. H. Zhang, in *Chinese Encyclopedia of Metallurgy, Metallic Materials*, Metallurgical Industry Press, Beijing, 2001, pp. 152–154.
40. P. Charlier and L. Bacher, *Proc. Seventh Int. Conf. Strength of Metals and Alloys*, Vol. 2, Montreal, Canada, August 12–16, 1986, Pergamon Press, Oxford, p. 1019.
41. P. Charlier and A. Guimier, *Proc. Int. Sem. Automotive Steels*, Moscow, April 19–21, 1988, p. 167.
42. A.H. Nakagawa and G. Thomas, *Metall. Trans. 16A*: 831–840 (1985).
43. D.Z. Yang, E.L. Brown, D.K. Matlock, and G. Krauss, *Metall. Trans. 16A*: 1523–1526 (1985).
44. R.C. Davies, *Metall. Trans. 10A*: 113–118 (1979).
45. A.R. Marder, *Metall. Trans. 13A*: 85–92 (1982).
46. A.M. Bayer and L.R. Walton, in *ASM Handbook*, 10th ed., Vol. 1, ASM International, Materials Park, OH, 1990, pp. 757–779.
47. M.G.H. Wells, in *Encyclopaedia of Materials Science and Engineering*, Pergamon Press, Oxford, 1986, pp. 5115–5120.
48. R. Higgins, *Engineering Metallurgy*, 5th ed., Krieger, Malabar, FL, 1983.
49. S.D. Washko and G. Aggen, in *ASM Handbook*, 10th ed., Vol. 1, ASM International, Materials Park, OH, 1990, pp. 841–907.
50. R.F. Decker, J.T. Each, and A.J. Goldman, *Trans. ASM 55*: 58 (1962).
51. S. Floreen, *Met. Rev. 13*: 115–128 (1968).
52. S. Floreen, in *Encyclopaedia of Materials Science and Engineering*, Pergamon Press, Oxford, 1986, pp. 5171–5177.
53. T. Morrison, *Metall. Mater. Technol. 8*: 80–85 (1976).
54. K. Rohrbach and M. Schmidt, in *ASM Handbook*, 10th ed., Vol. 1, ASM International, Materials Park, OH, 1990, pp. 793–800.
55. *Heat Treater's Guide—Standard Practices and Procedures for Steel*, ASM, Cleveland, OH, 1982.
56. *Metals and Alloys in the Unified Numbering System*, 6th ed., Society of Automotive Engineers, Warrendale, PA, 1993.
57. *Worldwide Guide to Equivalent Irons and Steels*, ASM International, Materials Park, OH, 1992.
58. *1994 SAE AMS Index*, Society of Automotive Engineers, Warrendale, PA.
59. *Specification for Drill Pipe, API Specification 5D*, 3rd ed., August 1, 1992, American Petroleum Institute, Washington, D.C.
60. *Specification for Line Pipe, API Specification 5L*, 40th ed., November 1, 1992, American Petroleum Institute, Washington, D.C.

61. *Specification for CRA Line Pipe, API Specification 5LC*, 2nd ed., August 1, 1991, American Petroleum Institute, Washington, D.C.
62. *1994 Publications, Programs & Services*, American Petroleum Institute, Washington, D.C.
63. D.L. Potts and J.G. Gensure, *International Metallic Materials Cross-Reference*, Genium Publishing, New York, 1989.

2 Classification and Mechanisms of Steel Transformation*

S.S. Babu

CONTENTS

2.1 Introduction 91
2.2 Phase Transformation Mechanisms 92
2.3 Microstructure Evolution during Austenite Decomposition 96
2.3.1 Allotriomorphic Ferrite 96
2.3.2 Widmanstätten Ferrite 97
2.3.3 Bainite 99
2.3.4 Pearlite 101
2.3.5 Martensite 103
2.4 Microstructure Evolution during Reheating 106
2.4.1 Tempered Martensite 107
2.4.1.1 Carbon Segregation and Aging of Martensite 107
2.4.1.2 First Stage of Tempering 107
2.4.1.3 Second Stage of Tempering 107
2.4.1.4 Third Stage of Tempering 108
2.4.1.5 Fourth Stage of Tempering 108
2.4.2 Austenite Formation 109
2.5 Summary of Steel Microstructure Evolution 109
2.6 Prediction of Microstructure Evolution during Heat Treatment 110
2.6.1 Calculation of Multicomponent Multiphase Diagrams 112
2.6.2 Calculation of Diffusion-Controlled Growth 113
2.7 Summary 116
2.8 Acknowledgments 118
References 118

2.1 INTRODUCTION

The microstructure of steels consists of a spatial arrangement of crystalline aggregates of different phases. The size, shape, distribution, composition, and crystal structure of these phases essentially control the final properties of any given steel, including hardness, strength, ductility, impact toughness, and creep strength. Steel is the most versatile alloy among all the industrial alloys. It exhibits a diverse range of microstructures that possess different combinations of strengths and toughnesses. In a majority of the steels, this versatility is made possible

* The submitted manuscript has been authored by a contractor of the U.S. Government under contract DE-AC05-00OR22725. Accordingly, the U.S. Government retains a nonexclusive, royalty-free license to publish or reproduce the published form of this contribution, or allow others to do so, for U.S. Government purposes.

by modifying the decomposition of a high-temperature δ-ferrite (body-centered cubic [bcc] crystal structure) to high-temperature austenite phase (face-centered cubic [fcc] crystal structure) and then decomposition of austenite to a low-temperature α-ferrite (bcc) phase by changing the composition and cooling rate. In low-alloy steels, the most important phase change is from austenite to α-ferrite. For example, for a given composition of low-alloy steel, a ferrite–pearlite microstructure can be obtained by slow cooling. With an increase in cooling rate, Widmantstätten or upper bainite microstructure can be obtained from austenite. With a further increase in the cooling rate, a hard martensite microstructure can be obtained. Pearlite contains a lamellar aggregate of ferrite and cementite phases, upper bainite contains ferrite platelets separated by austenite or carbides, and martensite contains carbon-supersaturated ferrite platelets with a high density of dislocations or twin boundaries.

Another feature of steels is that all of the above microstructures are far from equilibrium (i.e., the equilibrium microstructure at room temperature is a mixture of ferrite and graphite). The ferrite–pearlite microstructure, which contains ferrite + orthorhombic cementite lamella, is the closest to the equilibrium of the above structures. In contrast, the martensite microstructure has a body-centered tetragonal (bct) crystal structure with supersaturated carbon and is the farthest from equilibrium. Therefore, tempering martensite at high temperature can be used to attain intermediate-phase mixtures that are closer to final equilibrium, thus providing another methodology to control the microstructure and properties of the steel. The methods of controlling steel microstructure through alloy modification and heat treatment have been followed by metallurgists and this will continue to be the goal of material scientists. The focus of this chapter is to extend this approach to new classes of steels without trial and error experimentation to heat treatment based on the mechanisms of phase transformations.

Over the decades, mechanisms of phase transformations that occur in steel have been illustrated in a simple Fe–C metastable diagram (Figure 2.1) that describes the stability regions for ferrite, austenite, and cementite structures. On cooling from the liquid region, the first phase to solidify is δ-ferrite. With continued cooling, the δ-ferrite transforms to γ-austenite. With further cooling, the austenite transforms to α-ferrite and cementite. Basic and applied research in the past has led to a fundamental understanding of these structural changes and their relationship to microstructure evolution in alloys ranging from simple Fe–C systems to complex Fe–C–X steels (where X stands for many different substitutional alloying elements, including manganese, nickel, chromium, silicon, and molybdenum). The relationships between crystal structure changes, the interface structure, the phase morphologies (i.e., ferrite or bainite), and the distribution of alloying elements between phases are understood. In addition, computational thermodynamic and kinetic tools have been developed to the extent that it is possible to predict transformation kinetics quantitatively as a function of steel composition. In this chapter, a framework to classify transformation mechanisms is introduced. Then, the steel microstructures are classified and discussed based on this framework. Finally, a brief introduction is given to the application of computational thermodynamics and kinetics to describe phase transformations in low-alloy steels.

2.2 PHASE TRANSFORMATION MECHANISMS

The various phase transformations that occur in steels can be classified according to a thermodynamic basis, a microstructural basis, and a mechanistic basis [1]:

1. The thermodynamic basis classifies the phase transformation based on the derivatives of the Gibbs free energy (G) of the system with temperature change at a constant pressure. If the first derivative shows a discontinuity at a transformation temperature, it is called first-order transformation. For example, the transformation of a solid to a

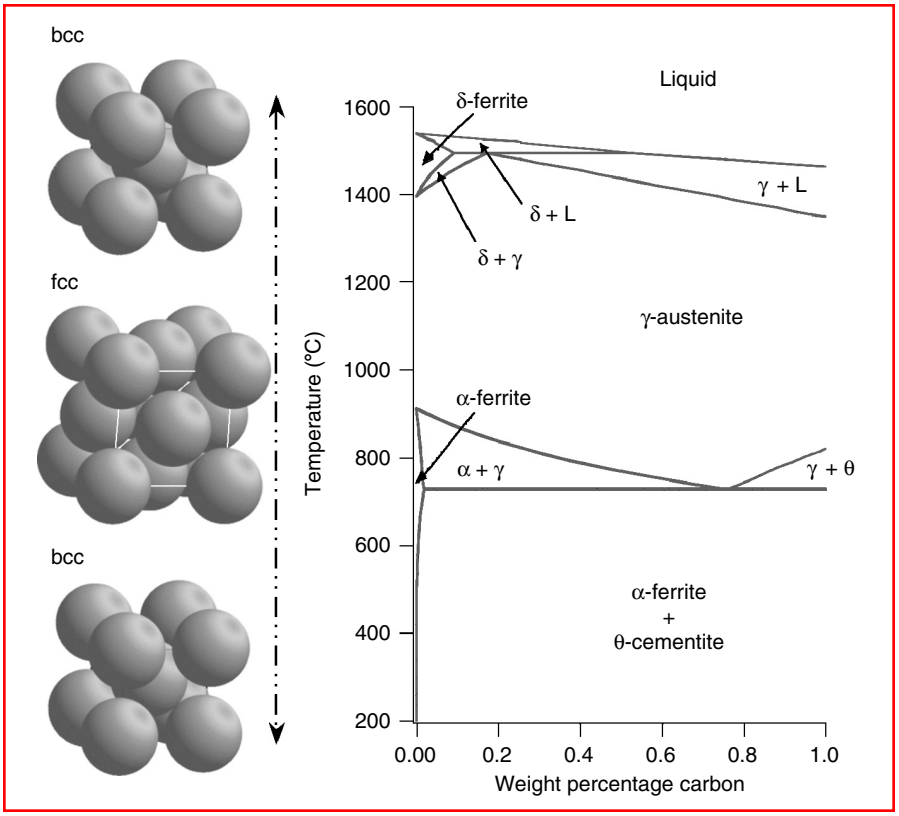

FIGURE 2.1 Illustration of body-centered cubic (bcc) ferrite and face-centered cubic (fcc) austenite with a calculated metastable Fe–C binary diagram showing the phase stability of austenite, ferrite, and cementite.

liquid of pure metal at melting temperature is a first-order transformation. Similarly, in other systems, with continued differentiation of G, and the phase transformation is classified as the nth order if the discontinuity shows up after n differentiations $(\mathrm{d}^n G/\mathrm{d}T^n)_P$. An example of a second-order transition is the ordering of the bcc ferrite phase in an Fe–Al system.

2. The microstructural basis relates to the origin of a product phase from a parent phase. If the product phase forms everywhere within a sample without the need for any nucleation, it is classified as a homogeneous transformation. If the product phase forms as a small entity with a sharp interface and if it grows into the product phase, it is classified as a heterogeneous transformation through a nucleation and growth process. Microstructural evolution in steel is predominantly a heterogeneous transformation.
3. The mechanistic basis relates to the way the crystal structure change is achieved during transformation. The heterogeneous transformation in a material can occur by three mechanisms [2]: (a) athermal growth through glissile interfaces (e.g., austenite to martensite formation), (b) thermally activated growth (e.g., pearlite formation from austenite), and (c) growth controlled by heat transport (e.g., solidification). Details of each subclassification of growth mechanisms have been discussed by Christian [2] and are shown in Figure 2.2.

In summary, the transformation in metals and alloys can be classified based on thermodynamic, microstructural, or growth mechanisms. The heterogeneous transformation can be

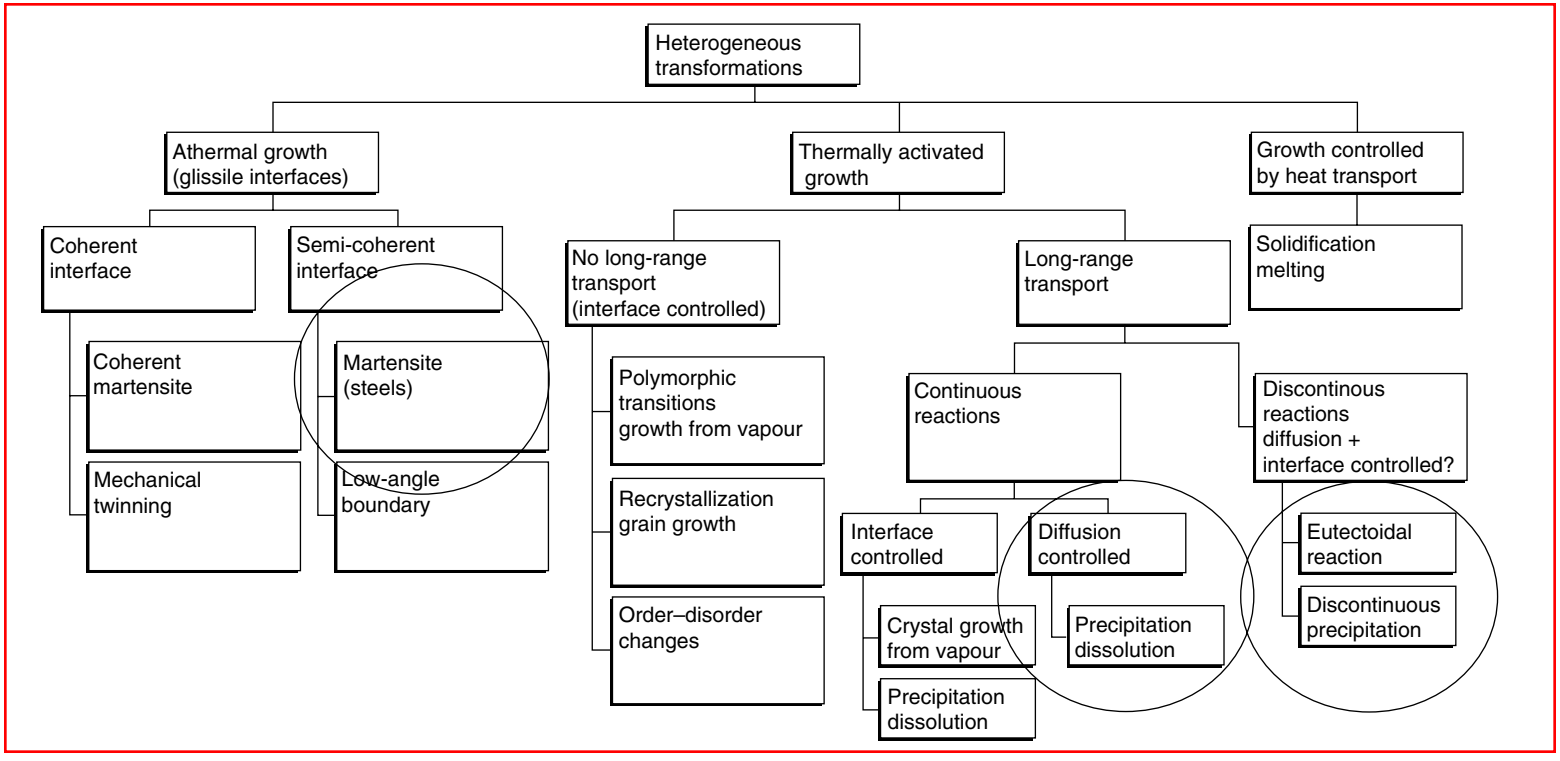

FIGURE 2.2 Classification of heterogeneous transformation based on mechanisms of growth. Most relevant phase transformation mechanisms for steel heat treatment are encircled. (Adapted from J.W. Christian, *The Theory of Transformations* in *Metals and Alloys*, 2nd ed., Part 1, Pergamon Press, Oxford, 1981, p. 9.)

controlled by glissile interface motion, thermally activated interface movement, or heat transport. The relevant mechanism for steel microstructure evolution during heat treatment is a heterogeneous phase transformation involving glissile interface (displacive) or long-range transport (reconstructive).

The reconstructive transformation involves mixing of atoms on either side of the parent and product phase interface through diffusion. The displacive transformation involves coordinated atom motion in the parent phase to change the parent crystal structure to the product crystal structure. These reconstructive and displacive transformation mechanisms in steels are discussed with a schematic illustration of austenite decomposition to ferrite or martensite as shown in Figure 2.3 [3]. Let us assume that the austenite fcc lattice is represented by the square motif shown in the upper left part of Figure 2.3 bounded by a rectangle a–b–c–d. Various substitutional atoms such as silicon, manganese, chromium, and molybdenum are schematically described by different symbols. Initial arrangements of some atoms are denoted by numbers 1 to 6. During the decomposition of austenite to ferrite or martensite, a crystal structure change takes place at the interface between austenite and the product phase (represented by line e–f). The schematic illustration of reconstructive transformation is shown in the bottom of the figure, and the bcc lattice of ferrite is represented by a diamond motif. This crystal structure change from fcc to bcc occurs at the e–f interface and is accompanied by somewhat random hopping of atoms across the interface. Because of this hopping of the atoms across the interface, the original atomic arrangements (implied by the change in the position of 1–6 numbered atoms) are lost. As a result, the transformation involves the reconstruction of an austenite lattice into a ferrite lattice, which leads to no macroscopic shape change of the crystal and mixing or separation of atoms on either side of the austenite and ferrite that would lead to a change in the composition of the phase. However, there is a distinct change in volume. Based on the above facts, the rate transformation is expected to be controlled by long-range diffusion of substitutional atoms in both the ferrite and austenite lattices. In practice, the transformations in steels are complicated by the presence of carbon, an interstitial element, which is not shown in the Figure 2.3. The growth rate of ferrite (which has low solubility of carbon) is controlled by diffusion of both carbon in austenite and substitutional atoms in ferrite and austenite. Under reconstructive transformation, diffusion of all atoms occurs during nucleation and growth and is usually sluggish below 600°C [4].

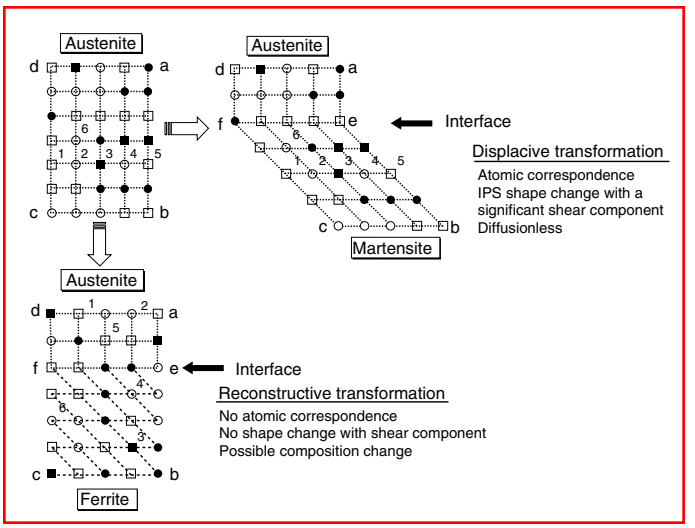

FIGURE 2.3 Schematic illustration of crystal structure change due to reconstructive and displacive transformations. (Adapted from H.K.D.H. Bhadeshia, *Worked Examples in the Geometry of Crystals*, The Institute of Materials, London, 1987.)

The schematic illustration of martensite formation is shown in the upper right side of Figure 2.3, and the bct lattice is represented by a diamond motif. The main difference in this case, compared to the fcc to bcc transformation, is that the crystal structure change from fcc to bct lattice is brought about by coordinated atom movement at the interface e–f, or in other words, a shear deformation of the original fcc lattice. As a result, the original atomic correspondences within the parent phase are maintained in the product phase. For example, the row of atoms 1–6 is just displaced laterally parallel to interface e–f, and the atomic sequence remains the same. This mode of transformation involving a shear deformation is called invariant plane strain (IPS). IPS leads to a macroscopic shape change, as indicated in the schematic illustration. This macroscopic change (from a–b–c–d to a–e–b–c–f–d) manifests itself as a surface relief on the polished surface of the sample after the decomposition of austenite to martensite. For more crystallographic details, the reader is referred to the literature [5–7]. The displacive transformation is also associated with a large strain energy. Therefore, to sustain this reaction, the chemical thermodynamic driving force must be large, and as a result, the martensite transformation occurs only at low temperatures where the magnitude of chemical free energy increases above the strain energy requirement. The large strain energy also induces the lenticular or plate-shaped region of martensite to minimize the strain energy. This mode of transformation also implies that both interstitial and substitutional atoms are trapped within the martensite and that there is no change in composition between the austenite and martensite phases (i.e., it is a diffusionless mode of transformation). As a result, the growth rate of martensite is usually athermal. The Widmanstätten and bainitic ferrite transformations occur at higher temperatures than the martensite transformation. They exhibit displacive transformation for a crystal structure change and varying degrees of diffusion of interstitial carbon during nucleation and growth.

In the following sections, the steel microstructure evolution during cooling (austenite decomposition) and heating (tempering and austenite formation) will be described based on reconstructive and displacive transformation mechanisms.

2.3 MICROSTRUCTURE EVOLUTION DURING AUSTENITE DECOMPOSITION

There have been numerous reviews of austenite decomposition over the past five decades [8–10]. The ferrite morphologies, which form during austenite decomposition, were originally classified by Dubé [11,12]. A change in morphology from one to another was found to occur as the austenite decomposition temperature was lowered. The common ferrite morphologies are grain boundary allotriomorphic ferrite, idiomorphic ferrite, Widmanstätten ferrite, and intragranular ferrite [13,14]. Other microstructures that form at lower transformation temperatures are pearlite, bainite, and martensite. The evolution of each one of the above microstructure is discussed below.

2.3.1 Allotriomorphic Ferrite

Decomposition of austenite to allotriomorphic ferrite occurs over a wide range of temperatures below the austenite to austenite + ferrite phase boundary (see Figure 2.1). This section is not intended to be a comprehensive review of this subject, but rather a short summary of extensive literature. The reader can consult the classic reviews by Aaronson and other researchers for details [10,13].

Allotriomorphic ferrite usually nucleates along the austenite–austenite grain boundary. It first grows laterally along the boundary and then can proceed perpendicularly into the austenite grain. The nucleation and growth involve a reconstructive mode of crystal structure change that leads to an absence of any macroscopic shape change, and only a volume change

is observed. During nucleation, the allotriomorphic ferrite crystals exhibit a preferred orientation relationship with one of the austenite grains (γ_1). The orientation relationship is usually of the Kurdjumov–Sachs (KS) type:

$$\{1\ 1\ 1\}_\gamma // \{1\ 1\ 0\}_\alpha \quad \text{and} \quad \langle 1\ \bar{1}\ 0\rangle_\gamma // \langle 1\ \bar{1}\ 1\rangle_\alpha.$$

The KS relationship indicates that the close-packed planes of austenite and ferrite are parallel to each other and that the close-packed directions of austenite and ferrite are parallel to each other. On some occasions, the ferrite may deviate slightly from having close-packed parallel directions, as shown by the Nishiyama–Wasserman (NW) orientation relationship:

$$\{1\ 1\ 1\}_\gamma // \{1\ 1\ 0\}_\alpha \quad \text{and} \quad \langle 1\ 1\ \bar{2}\rangle_\gamma // \langle 1\ \bar{1}\ 0\rangle_\alpha.$$

The KS or NW orientations allow for the existence of a semicoherent boundary between austenite and ferrite and thereby minimize the surface energy required to nucleate the ferrite at the austenite boundary. A small free energy is sufficient to satisfy the KS and NW orientations with one of the austenite grains for the nucleation of a ferrite, and then the ferrite can grow into the adjacent austenite grain (γ_2) with no specific orientation relationship. On the latter side of the interface, which shows the random orientation, a disordered boundary will exist and rapidly grow into the austenite. An example of such ferrite growth in an Fe–C–Si–Mn steel is shown in Figure 2.4. The optical micrograph (Figure 2.4a) shows the allotriomorphic ferrite grains along the prior austenite grain boundary (marked by arrow). The remaining microstructure is bainitic ferrite. A transmission electron microscopy image of this sample (see Figure 2.4b) shows an allotriomorphic ferrite grain situated along the boundary (marked as B) of two austenite grains (γ_1 and γ_2). Electron diffraction analysis of the above structure indicated that the allotriomorphic ferrite had a KS orientation relationship with a γ_1 grain and that there was no special orientation relationship with γ_2. Further detailed observation also showed small steps in the interface along the protuberances on the γ_1 side of the allotriomorphic ferrite. However, the interface on the γ_2 side showed disordered boundary with no specific structure [15]. The rate of growth on the γ_2 side is more rapid than that on the γ_1 side. This apparent difference in growth rate was shown by classic *in situ* transmission electron microscopy experiments by Purdy [16]. The observed semicoherent boundary on only one side of the austenite grain also plays a critical role in the development of secondary Widmanstätten ferrite, which is described in the following section.

2.3.2 Widmanstätten Ferrite

Widmanstätten ferrite describes a ferrite morphology in the form of side plates or laths and grows into austenite grains with a KS orientation relationship. The lath ferrite, which forms from the austenite grain boundary, is referred to as primary Widmanstätten ferrite. The ferrite that nucleates on the preexisting allotriomorphic ferrite is referred to as secondary Widmanstätten ferrite [14]. Nucleation of secondary Widmanstätten ferrite occurs mostly on the semicoherent interphase boundary between the ferrite and the austenite. A typical microstructure of secondary Widmanstätten ferrite in a steel weld is shown in Figure 2.5a. A schematic illustration of such a microstructure evolution is shown in Figure 2.5b. As the steel cools from high temperature, the allotriomorphic ferrite forms with a KS–NW relationship with austenite grain γ_1 and has a semicoherent interface boundary. With further cooling, secondary Widmanstätten ferrite nucleates on the γ_1 side of the allotriomorphic ferrite and grows into the austenite grain. This nucleation and growth process leads to apparent saw-tooth morphology.

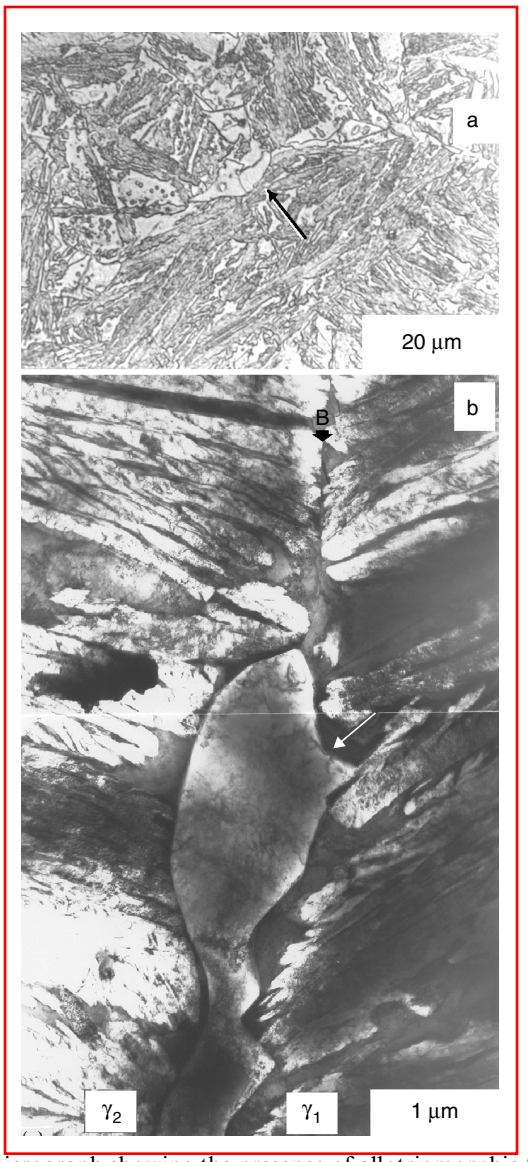

FIGURE 2.4 (a) Optical micrograph showing the presence of allotriomorphic ferrite (marked by arrow) and bainite microstructure in an Fe–C–Si–Mn steel. (b) Transmission electron micrograph showing the presence of allotriomorphic ferrite along an austenite grain boundary (γ_1 and γ_2) marked by b. The orientation relationship between allotriomorphic ferrite and the γ_1 grain was close to a KS–NW orientation relationship and was in a random orientation relationship with the γ_2 grain.

Two growth mechanisms of Widmanstätten ferrite have been proposed. In the first mechanism, the growth is attributed to lateral movement of semicoherent interfaces by small steps (ledges) in the interface [17,18]. In the second mechanism, the Widmanstätten ferrite may grow through a displacive transformation mechanism [19]. Many experimental results are in agreement with the second mechanism. Thin, wedge-shaped Widmanstätten ferrite is produced due to cooperative, back-to-back growth of two ferrite crystallographic variants. The Widmanstätten ferrite plates grow into untransformed austenite by extension along their length. Since Widmanstätten ferrite forms at temperatures well below that for allotriomorphic ferrite, growth occurs by a paraequilibrium (PE) mode (i.e., the ratio of the

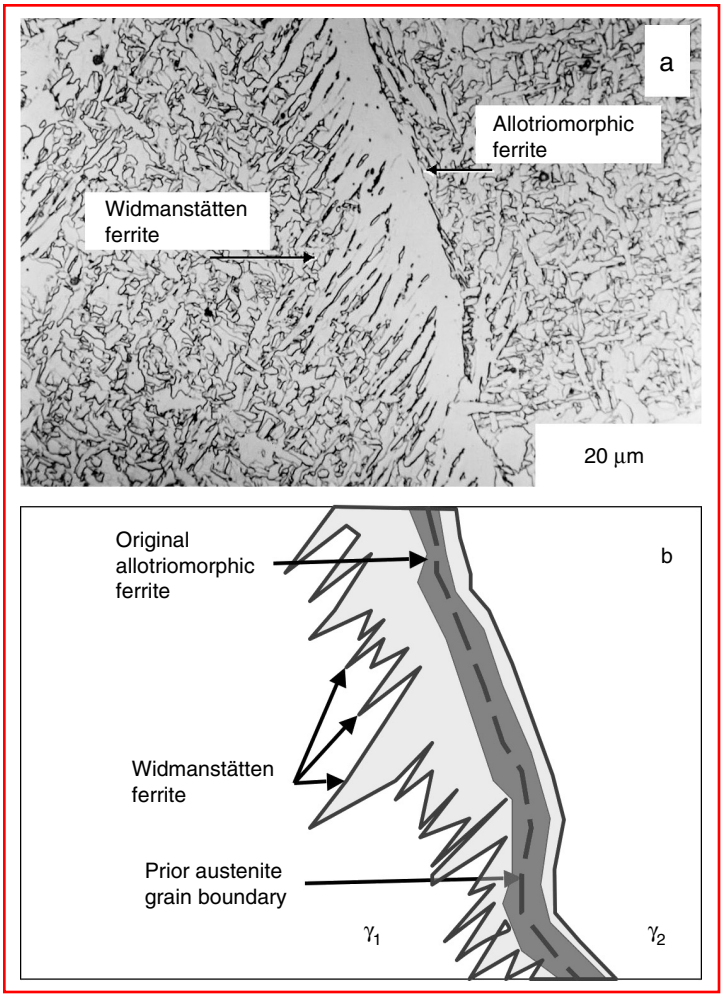

FIGURE 2.5 (a) Optical micrograph showing secondary Widmanstätten ferrite microstructure in an Fe–C–Mn steel weld obtained through continuous cooling. The growth of these plates occurs on only one side of the allotriomorphic ferrite. (b) Schematic illustration showing possible mechanism for the formation of Widmanstätten ferrite microstructure on only one side of the original allotriomorphic ferrite.

iron concentration to the substitutional atom concentration is frozen in both the parent and the product phases). The rate of growth is controlled only by carbon diffusion in the austenite ahead of the plate. It is possible to estimate the growth rate of Widmanstätten ferrite with diffusion-controlled growth models of Bhadeshia et al. [20] and Trivedi [21,22] by considering only the carbon diffusion.

2.3.3 Bainite

The growth of bainitic ferrite has been discussed in the literature based on either reconstructive or displacive transformation mechanisms. In the reconstructive definition, the growth of bainite is the product of diffusional, noncooperative, competitive ledgewise growth of ferrite and cementite into austenite during eutectoid decomposition with cementite appearing in a nonlamellar form [23]. In this definition, the transformation kinetics is related to the rate of

ledge movement at the interface and is controlled by carbon diffusion. In the displacive definition, a subunit of ferrite forms from the austenite with complete supersaturation of carbon through a displacive transformation involving IPS deformation. Carbon diffusion to austenite occurs through a post-transformation event. The overall transformation kinetics is then related to the nucleation of this ferrite subunit. The bainitic subunits are expected to show surface relief, no substitutional partitioning, an incomplete reaction phenomenon, and a KS–NW orientation relationship [24]. They are also expected to show compliance with an externally applied elastic stress on the austenite similar to martensite [25]. The reader can consult the recent discussions by Hillert [26] for current research in bainite transformation mechanisms. In this section, the bainitic transformation mechanisms are discussed from the displacive mode of transformation point of view [4].

The bainite microstructure consists of aggregates of ferrite plates separated by thin films of austenite, martensite, or cementite. These aggregates of plates are called sheaves [4]. A typical bainitic sheaf in an Fe–Cr–C steel is shown in Figure 2.6a. This microstructure was attained by austenitization followed by isothermal transformation below the bainitic start temperature B_s [25]. The small ferrite plates that make up the sheaves are often referred to as subunits, and often they are related to each other through a specific crystallographic orientation. These subunits are normally plate-shaped and under certain conditions may exhibit a lath structure. The presence of subunits within the sheaf can also be seen by transmission electron microscopy. Transmission electron microstructures of an Fe–C–Si–Mn steel (see Figure 2.6b) and an Fe–Cr–C steel (see Figure 2.6c) show the subunit ferrite plates within a

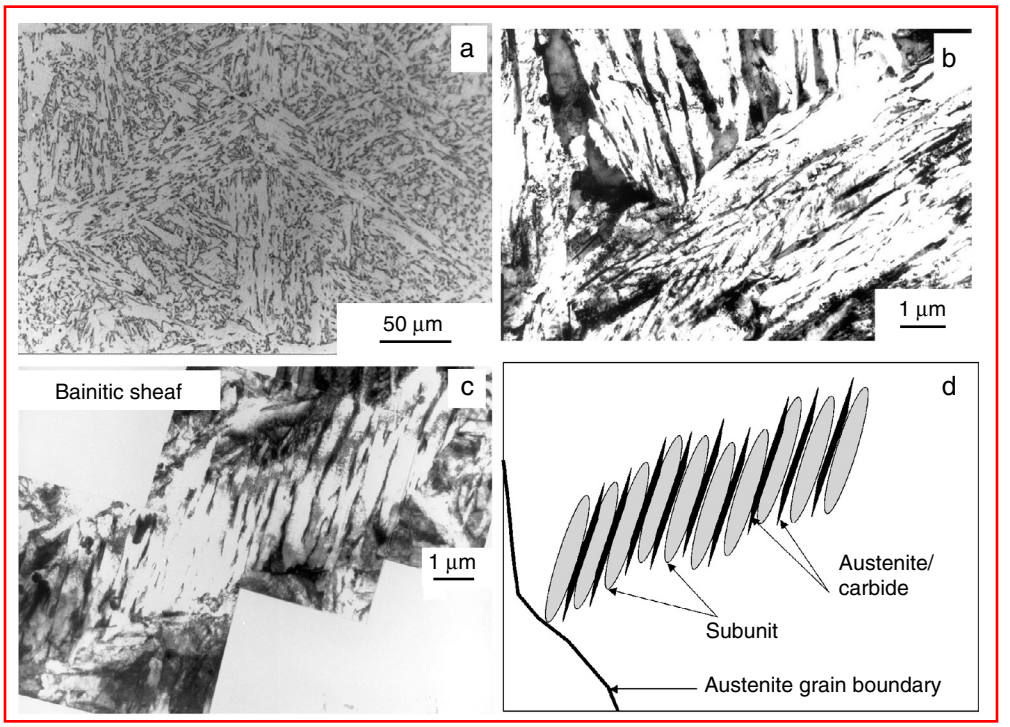

FIGURE 2.6 (a) Optical micrograph from an Fe–Cr–C steel showing a bainitic sheaf structure. (b) Transmission electron micrograph from an Fe–C–Si–Mn steel showing many sheaves of bainitic ferrite. (c) Another transmission electron micrograph of a bainitic sheaf structure from an Fe–Cr–C steel. (d) Schematic illustration of the growth mechanism by subunit nucleation and growth. (Adapted from H.K.D.H. Bhadeshia, *Bainite in Steels*, 2nd ed., The Institute of Materials, London, 2001.)

bainitic sheaf. The first ferrite subunit that nucleates on the austenite–austenite grain boundary grows to a particular size, and successive plates form to produce the microstructure shown in Figure 2.6d. The plates are separated by untransformed austenite, which can transform to martensite on cooling to low temperature. In certain conditions, this austenite can decompose into cementite, giving rise to a classical ferrite + cementite mixture of bainitic microstructure.

The bainitic steels can occur in two different forms, upper bainite and lower bainite. The microstructures shown in Figure 2.6 are examples of the upper bainite. The upper bainite forms at temperatures higher than the martensite start (M_s) temperature. Because of the IPS that accompanies the bainitic transformation, a large number of dislocations are observed within the austenite and the ferrite. These dislocations limit the growth of each subunit to a certain size.

Due to the displacive mode of transformation, the substitutional and interstitial atoms are configurationally frozen and there is no redistribution of these elements between austenite and bainitic ferrite during transformation. However, after the bainite reaches a certain size, the carbon mobility is sufficient to redistribute to austenite while substitutional atoms remain frozen in place. This carbon partitioning from the bainite to austenite enriches the austenite with the progress of bainitic transformation. The successive nucleation of subunits from this carbon-enriched austenite continues to occur. The successive spatial alignment of nucleated subunits occurs due to an autocatalytic mechanism that leads to a typical sheaf structure. When the carbon enrichment of austenite increases above a critical level, the displacive mode of bainite formation cannot be sustained (the free energy of ferrite is equal to that of austenite) and the reaction stops (i.e., an incomplete reaction). This residual austenite may remain untransformed in the form of films between the ferrite subunits or may transform to martensite on cooling, depending upon the carbon concentration. In certain steels containing strong carbide formers such as chromium, this austenite film may decompose to a mixture of ferrite and carbide.

In certain steels, most of the carbides are present within the bainitic than in between bainite subunits and are referred to collectively as lower bainite. Typically, lower bainite forms in high-carbon steels, below the temperature at which upper bainite forms and above M_s. Although, the lower bainite microstructure is similar to that of tempered martensite, the main difference is the occurrence of only one crystallographic variant* of the carbide in lower bainite. When these carbides are cementite, the major axis of the cementite is aligned at ~60° to the long axis of the ferrite plates. These cementite plates appear to form on $\{1\ 1\ 2\}_\alpha$ ferrite planes. In certain steels, lower bainitic ferrite has ε-carbides rather than cementite. It is noteworthy that both upper and lower bainites form from austenite through a displacive transformation. The only difference is that, in the case of upper bainite, the carbon from the bainitic subunit partitions into austenite before the carbide precipitates within the subunit. In the case of lower bainite, carbide precipitation occurs within the ferrite before all the carbon partitions completely from the ferrite. This competition between carbon escape from supersaturated ferrite plate and precipitation of carbide within the ferrite plates is schematically shown in Figure 2.7 [4].

2.3.4 Pearlite

A typical pearlite microstructure has many colonies of a lamellar mixture of ferrite and cementite (see Figure 2.8a). Under an optical microscope, each colony of pearlite (schematically shown in Figure 2.8b) may appear to be made up of many alternating crystals of ferrite and cementite; however, they are mostly interpenetrating single crystals of ferrite and cementite in three dimensions. The ferrite and cementite within the pearlite colony show preferred

* In contrast, tempered martensite shows many crystallographic variants of carbides.

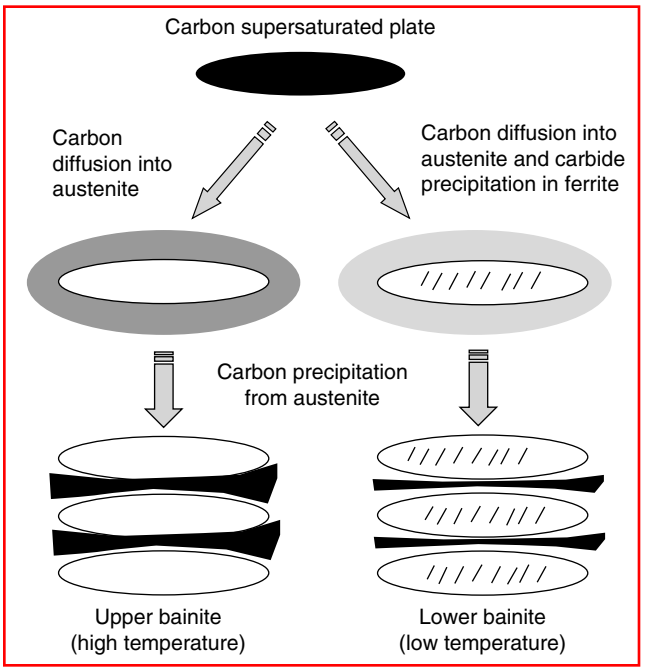

FIGURE 2.7 Schematic illustration of upper and lower bainite formation mechanism. The dark regions between the plates represent carbides that form in the residual austenite. The dark lines represent carbides that form within the ferrite plates. (Adapted from H.K.D.H. Bhadeshia, *Bainite in Steels*, 2nd ed., The Institute of Materials, London, 2001.)

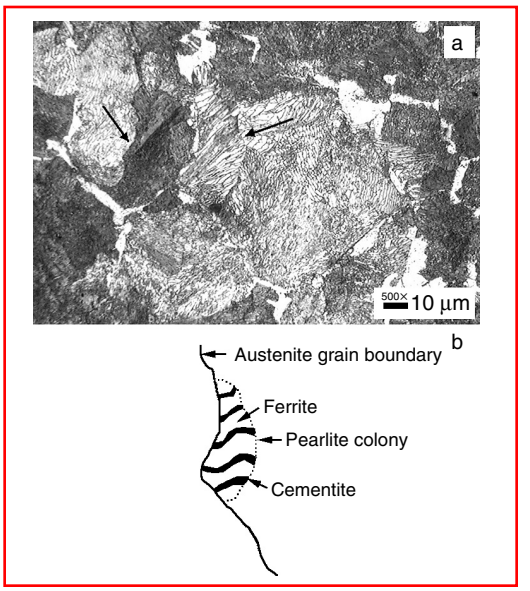

FIGURE 2.8 (a) A typical optical microstructure of a pearlite in an Fe–C–Mn steel. Several distinct colonies are marked with arrows. (b) Schematic illustration of pearlite colony growth.

crystallographic relationships. The most common orientation relationships are Pitsch–Petch relationship [14]:

$$(0\,0\,1)_{\text{cementite}}//(\bar{5}\,2\,\bar{1})_{\text{ferrite}};\ (0\,1\,0)_{\text{cementite}}\ 2-3^{\circ}\ \text{from}\ [1\,1\,\bar{3}]_{\text{ferrite}};\ (1\,0\,0)_{\text{cementite}}\ 2-3^{\circ}\ \text{from}\ [1\,3\,1]_{\text{ferrite}},$$

and the Bagaryatski relationship,

$$[1\,0\,0]_{\text{cementite}}//[0\,1\,\bar{1}]_{\text{ferrite}};\ [0\,1\,0]_{\text{cementite}}//[\bar{1}\,1\,1]_{\text{ferrite}};\ (0\,0\,1)_{\text{cementite}}//(2\,1\,1)_{\text{ferrite}}.$$

The pearlite grows into austenite by cooperative growth of ferrite and cementite. Neither the ferrite nor the pearlite shows any preferred crystallographic orientation with the austenite into which they are growing. The colony interface with austenite is an incoherent high-energy interface. As a result, the pearlite that nucleates on preexisting allotriomorphic ferrite always chooses the ferrite side (high-energy interface) that has no crystallographic relationship with an austenite grain. In contrast, Widmanstätten ferrite and bainite always nucleate on low-energy interfaces (see Section 2.3.2 and Section 2.3.3). There is a well-known relationship between pearlite colonies and transformation conditions. The spacing of lamellae decreases with a decrease in the transformation temperature. It is possible to determine the lamellar spacing by equating the increase in interfacial energy to a decrease in energy due to transformation. The pearlite transformation occurs very close to thermodynamic equilibrium (i.e., partitioning of alloying elements occurs under local equilibrium), and often occurs at higher temperatures and exhibit sluggish growth rates in comparison to bainite. Therefore, it is possible to use state-of-the-art computational thermodynamic and kinetic tools to predict the growth rate of pearlite.

2.3.5 Martensite

Martensite forms from austenite through a displacive transformation. This section briefly outlines the morphology, nucleation, and growth of martensite and the crystallographic aspects of the martensite transformation. This section is not a comprehensive review of this subject; rather, it is a short summary of extensive existing literature [7].

The martensite transformation occurs athermally below M_s, i.e., the extent of transformation is proportional to undercooling below the M_s and does not depend on the time spent below the M_s. The transformation from austenite to martensite proceeds as the temperature is reduced below M_s until the martensite finish temperature (M_f) is reached, at which point 100% martensite is expected. However, if the M_f temperature is below room temperature, then some austenite may be retained if only cooled to room temperature. The martensite transformation is also sensitive to external and internal stresses. The martensite plates are related to austenite through a KS orientation relationship and show very preferred habit planes. The habit plane of martensite in low-carbon steel is parallel to $\{1\,1\,1\}_{\text{austenite}}$ and in high-carbon steel it is parallel to $\{2\,2\,5\}_{\text{austenite}}$. Because the martensite transformation occurs through a shear mechanism and without diffusion, the morphology of martensite is mostly lath-, lenticular-, or plate-like.

Experimental evidence has shown that the martensite formation (bct crystal structure) from austenite (fcc crystal structure) is accompanied by IPS. However, the bct structure cannot be obtained crystallographically by just one IPS. This anomaly, schematically illustrated in Figure 2.9, was elucidated by Bowles and Mackenzie [5] and Wechsler et al. [6]. If an austenite crystal structure is represented by a shape bounded by ABCD in (I), on applying a shear deformation (IPS deformation), the observed martensite shape is attained as shown in II. However, this leads to the wrong crystal structure. Nevertheless, another homogeneous shear (III) can be applied that leads to correct the crystal structure (bct). However, because the

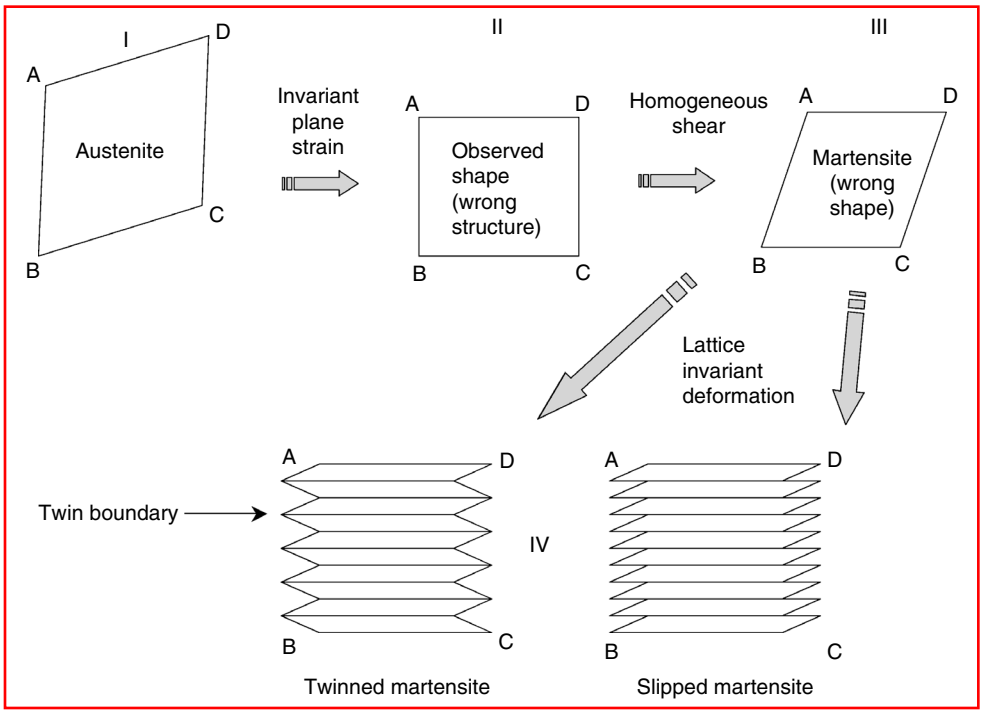

FIGURE 2.9 Schematic illustration of the phenomenological theory of martensite formation (bcc or bct structure) from austenite (fcc structure), showing the intermediate stages before the fcc structure changes to a bct structure through invariant plane strain, homogeneous shear, and lattice-invariant deformation. The model agrees with the experimentally observed orientation relationship as well as with the macroscopic shape of the martensite plate.

shape attained in (III) does not match the observed shape change during martensite transformation, the shape attained after (III) needs to be reset to the shape at (II) by slip and twin lattice invariant deformations. Therefore, in the next step, an inhomogeneous lattice invariant deformation produces a slipped or twinned martensite that matches the observed shape. In summary, the change in crystal structure from austenite to martensite is achieved through two IPSs and an inhomogeneous lattice invariant strain. Because this is a phenomenological theory, it does not predict the sequences of these deformations. Rather, it defines a method by which the austenite crystal can be transformed to a martensite crystal. Another important feature of martensite transformation in carbon containing steels is that the tetragonal distortion of bct structure ($a = b \neq c$) increases with carbon content, given by the following relation [14]:

$$\frac{c}{a} = 1 + 0.045 \times (\text{wt\% C}).$$

An increase in tetragonality also leads to the hardening of martensite. Martensite that forms in low-carbon steel (<0.5 wt% C) shows mainly dislocations, whereas martensite that forms from high-carbon steels shows twins. A typical example of dislocated martensite formed from 0.05 wt% C steel is shown in Figure 2.10. The martensite was attained even with the presence of a low concentration of carbon by rapid quench conditions attained through resistance spot welding. Transmission electron microscopy shows lath martensite with a high dislocation density.

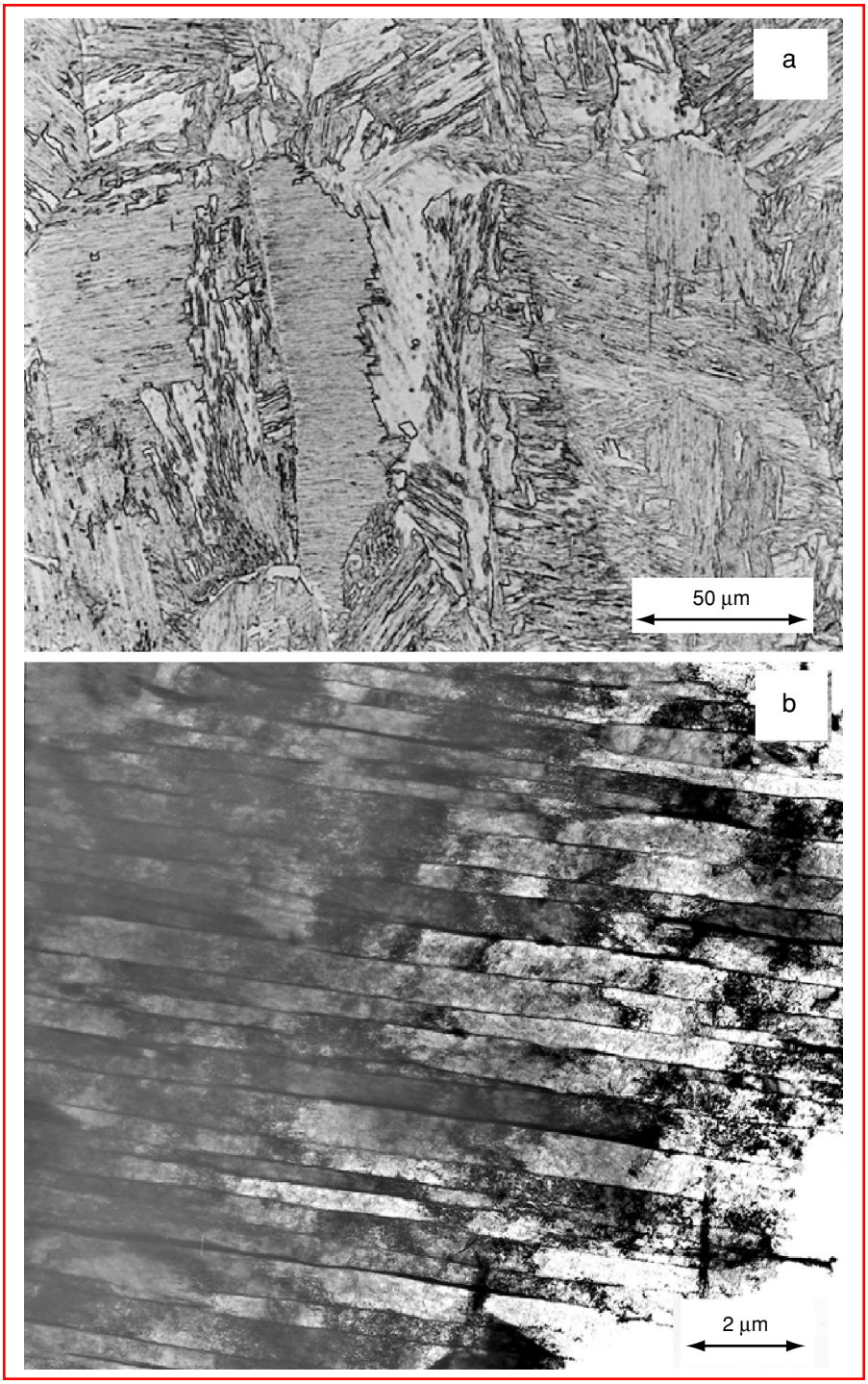

FIGURE 2.10 (a) Optical microstructure of lath martensite observed in a low-carbon steel obtained by rapid cooling in a weld. (b) Transmission electron micrograph of the same microstructure exhibiting parallel and long lath martensite plates with high dislocation density.

The kinetics of martensite is often discussed in terms of nucleation and growth that are related to the thermodynamic free energy of austenite and martensite, defect density, and glissile interfaces between austenite and martensite. The M_s temperature is closely linked to thermodynamic parameter T_0 (i.e., the temperature at which the Gibbs free energy of austenite equals that of the martensite with the same composition). However, a certain amount of undercooling is needed before martensite forms from austenite. This undercooling is defined by the driving force of austenite to martensite $\left(\Delta G^{\gamma \rightarrow \alpha'}\right)$ and by the amount of strain energy (1250 J/mol) that needs to be accounted for because of the growth of martensite. It has been shown that the strain energy needed for martensite formation is independent of the carbon concentration. It is now possible to use thermodynamic models to calculate the M_s temperature* by using similar principles for any multicomponent steel [27]. The next step is to describe the nucleation rate of martensite in austenite. Application of homogeneous nucleation theory principles clearly shows that martensite nucleation cannot be described based on pure atomic vibrations due to thermal energy. As a result, heterogeneous nucleation theories have been developed based on the presence of preexisting embryos of martensite [7]. These embryos are dislocation loops in certain crystallographic orientations and are hypothesized to grow by nucleation of new loops. Recently, Olson showed that the first step in the creation of these dislocation loops is the formation of stacking faults in the closely packed planes of austenite [7]. Once the nuclei of martensite is established, the next step is the growth of these crystals. Because the growth of the martensite is modeled as the glide of parallel dislocations, the rate of growth is rapid. Research has shown three types of martensite growth exist: athermal, burst, and isothermal transformations [7,14]. In athermal growth, martensite formation is only a function of undercooling below the M_s temperature and not the time spent at each temperature. This transformation starts exactly at M_s temperature. This mode of transformation also exhibits a strong dependence on thermal cooling conditions. If the quenching of austenite to a low temperature was interrupted and aged at a temperature in between the M_s and M_f temperatures, then further martensite formation would not occur until further undercooling is instituted. This austenite stabilization is related to the carbon segregation to nucleation sites for martensite. Burst transformation involves the formation of a certain fraction of martensite (ranging from a few percent to 50%) from austenite below M_s temperature, instead of a gradual increase as in the case of athermal growth. The time interval for a burst of martensite transformation is about 1 μs. Burst transformation is attributed to an extreme form of autocatalysis (i.e., the formation of one martensite plate triggers the formation of another). Isothermal transformation involves an increase in the martensite fraction with holding time at a given temperature. This mode of transformation is also related to autocatalytic events. The isothermal cooling transformation diagrams (or time temperature transformation [TTT] diagrams) for isothermal martensite formation show a typical C-curve behavior, indicating that both thermal and athermal characters are present. Athermal or burst martensite formation is observed in steels; isothermal martensite formation is observed only in iron alloys that do not contain carbon.

2.4 MICROSTRUCTURE EVOLUTION DURING REHEATING

The previous section focused on microstructure evolution due to austenite decomposition that occurs during cooling from the austenitization temperature. In most heat treatments, microstructure evolution during reheating is also important. For example, the tempering of martensite to impart toughness is achieved by reheating the martensite to a high temperature.

* Software to calculate M_s temperature can be downloaded freely from www.msm.cam.ac.uk/map.

There is a need to understand the various phase transformations that occur during tempering to achieve an optimum combination of strength and toughness. Austenite formation itself is also important. For example, in the case of induction heat treatment, the depth of hardening is related to the depth of austenite formation. In this section, various phase transformations that occur during tempering and austenite formation are highlighted.

2.4.1 Tempered Martensite

In principle, various physical processes that lead to tempering of martensite start in as soon as martensite is heated to about room temperature [7]. These physical processes are associated with different temperature ranges. The transformation mechanisms in these stages are predominantly reconstructive modes with short- or long-range transport of atoms. However, in certain cases, decomposition may be possible by just the movement of carbon atoms with only a small distortion of the martensite lattice through displacive transformation [28,29].

2.4.1.1 Carbon Segregation and Aging of Martensite

During aging of martensite in some alloys, a coherent spinodal decomposition (i.e., modulated martensite structure with high- and low-carbon regions) may occur up to 100°C [30]. This spinodal decomposition may also lead to formation of transition carbides such as Fe_4C and $Fe_{16}C_2$. The carbon atoms may segregate to dislocations or may diffuse to interlath-retained austenite. Ohmori and Tamura have postulated that carbon segregation to defects such as dislocations may be the overwhelming factor for the observation of carbon-rich and carbon-depleted regions in the martensite [31]. The evidence for carbon clustering or spinodal decomposition has been obtained indirectly through electron diffraction or atom probe field ion microscopy [28,32].

2.4.1.2 First Stage of Tempering

In the first stage of tempering (100 to 200°C), ε-carbide forms from martensite. The composition of this carbide is close to $Fe_{2.4}C$. In the case of alloyed steels, the iron atoms may be replaced by other elements. The ε-carbide has a close-packed hexagonal structure and occurs as narrow laths or rods on cube planes of the martensite with Jack's orientation relationship [7]:

$$(1\ 0\ 1)_{\alpha'}//\left(1\ 0\ \bar{1}\ 1\right)_{\varepsilon};\ \ (0\ 1\ 1)_{\alpha'}//(0\ 0\ 0\ 1)_{\varepsilon};\ \ [1\ 1\ \bar{1}]_{\alpha'}//[1\ \bar{2}\ 1\ 0]_{\varepsilon}.$$

The nucleation of this transition carbide is related to the modulated structure that formed during the low-temperature aging step or even the carbon clustering along the dislocations. There is some evidence that the growth of this carbide may show some displacive characteristics instead of a reconstructive transformation mechanism [33]. After the precipitation of ε-carbide in stage I, the martensite is still supersaturated with carbon to certain extent and would undergo further decomposition on heating to higher temperatures.

2.4.1.3 Second Stage of Tempering

In the temperature range of 200 to 350°C, the retained austenite in the steel decomposes into ferrite and cementite. This decomposition was detected successfully by x-ray diffraction and dilatometric and specific volume measurements [7]. The kinetics of this decomposition are related to carbon diffusion in austenite. The untransformed austenite may undergo transformation on application of strain and thus affect the toughness of the steel. However, the fraction of retailed austenite is usually low in steels containing less than 0.2 wt% C. The

formation of stable carbides that is typical to third stage of tempering may overlap in the second stage of tempering.

2.4.1.4 Third Stage of Tempering

In the temperature range of 250 to 750°C, cementite precipitates within the martensite. The composition of the cementite is Fe_3C. In alloyed steels, it is referred as M_3C, where M corresponds to substitutional alloying additions (e.g., Cr, Mn) in addition to Fe. Cementite has an orthorhombic crystal structure and usually occurs as Widmanstätten plates. An example of tempered martensite in 300-M steel is shown in Figure 2.11a. The orientation relationship between ferrite and cementite is of the Bagaryatski type:

$$[1\ 0\ 0]_{\text{cementite}}//[0\ 1\ \bar{1}]_{\text{ferrite}};\quad [0\ 1\ 0]_{\text{cementite}}//[\bar{1}\ 1\ 1]_{\text{ferrite}};\quad (0\ 0\ 1)_{\text{cementite}}//(2\ 1\ 1)_{\text{ferrite}}.$$

The habit planes of cementite can be parallel to either $\{0\ 1\ 1\}_\alpha$ or $\{1\ 1\ 2\}_\alpha$ of ferrite. The nucleation of cementite may occur at ε-carbide and may grow by dissolution of the ε-carbide. In high-carbon steels, the cementite precipitates along the twin boundaries of martensite. Other sites for nucleation of cementite are the prior austenite grain boundaries or interlath boundaries. With the formation of cementite, most of the carbon in martensite is removed from solid solution. As a result, the tetragonality of bct structure is lost. Early stages of cementite growth occur only by carbon diffusion with no significant partitioning of substitutional alloying elements [32,33]. However, with extended tempering, redistribution of alloying elements also occurs between ferrite and cementite [32]. In addition, the plate-like cementite particles may coarsen and spheroidize with extended tempering. At this stage, the recovery and recrystallization of martensite laths may also be initiated. In high-carbon martensite, higher order carbides such as M_5C_2 (χ-carbide) can also form. It has been shown that higher order carbides are actually polytypes of the basic trigonal prism basis of cementite structure [34].

2.4.1.5 Fourth Stage of Tempering

Tempering at higher temperatures (>700°C) leads to the precipitation of more equilibrium alloy carbides such as M_7C_3 and $M_{23}C_6$. In steels containing Cr, Mo, V, and Ti, these carbides are associated with hardening of the steel that is called secondary hardening. The precipitation of these carbides also leads to the dissolution of cementite. An example of alloy carbide formation by tempering at 600°C in 300-M steel is shown in Figure 2.11b. At this

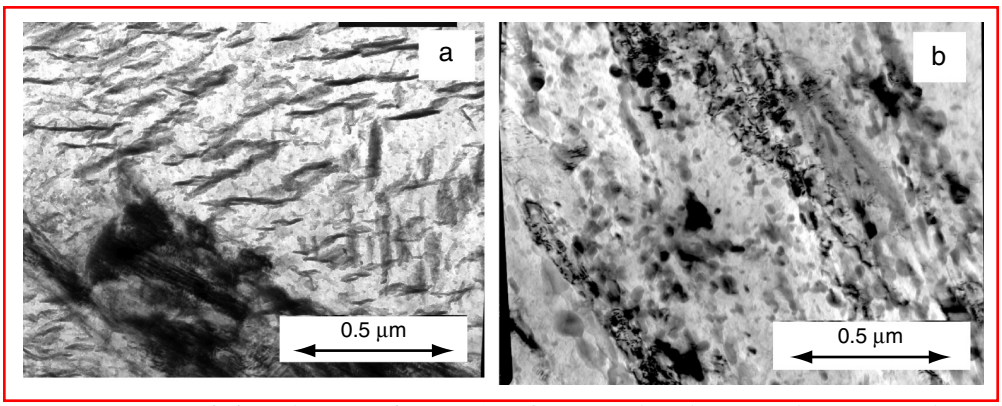

FIGURE 2.11 Transmission electron micrographs of quenched and tempered 300-M steel samples (a) after tempering at 300°C for 2 min, showing cementite plates in a martensite lath and (b) after tempering at 600°C for 1 min, showing alloy carbides.

stage, the recrystallization of martensite lath is more complete, and there is a tendency for the formation of equiaxed grains and extensive grain growth.

2.4.2 Austenite Formation

The early work on austenite formation by Robert and Mehl [35] focused on the nucleation of austenite from a ferrite–pearlite mixture. Various researchers have since shown the complexity of austenite formation from a two-phase mixture of ferrite and cementite and have made attempts at modeling austenite formation as a function of composition and microstructure [36–41]. On heating steel, with a spheroidized ferrite + cementite mixture, the austenite phase nucleates at the ferrite–cementite boundary. With further heating, the austenite phase consumes the cementite and then grows into ferrite through diffusion-controlled growth. In a pearlitic microstructure, the austenite may nucleate in the cementite and grow into the colony by dissolving both ferrite and cementite. A typical micrograph of austenite growth into a pearlite colony is shown in Figure 2.12a. A schematic illustration of the growth is shown in Figure 2.12b. Recent work has shown that it is possible to model the above phenomenon with computational tools [42]. It is possible to construct TTT diagrams for the austenite growth for any steel to evaluate the effect of the initial microstructure. These diagrams do not show a C-curve behavior because both the driving force for austenite formation and the diffusivity increase with temperature. This results in monotonic acceleration of austenite formation as the temperature increases. The rate of austenite formation also increases with the presence of residual austenite in the microstructure, as demonstrated by Yang and Bhadeshia, who studied the austenite growth kinetics in a bainitic microstructure [43,44]. The microstructure contained residual austenite films, and there was no requirement for nucleation of austenite and the austenite films grew with an increase in the temperature. After the completion of austenite formation, continued heating leads to grain growth of austenite. The grain growth is also affected by the presence of fine carbonitride precipitates. With the presence of these precipitates the grain boundaries are pinned and therefore, grain growth characteristics are sluggish. However, on heating above the dissolution temperature of these precipitates, the austenite grain may coarsen at an accelerated rate [45,46]. Most of the austenite formation from ferrite occurs by a diffusion-controlled reconstructive transformation mechanism. However, at rapid rates, the transformation of ferrite to austenite may occur by interface controlled or by displacive transformation [47].

2.5 SUMMARY OF STEEL MICROSTRUCTURE EVOLUTION

An overview of all microstructure evolution through reconstructive or displacive transformation mechanisms during heating and cooling of steel can be classified as shown in Figure 2.13 [4]. Reconstructive transformation involves substitutional diffusion. The reconstruction of a parent lattice into a product lattice occurs through a noncoordinated motion of atoms across the interface. The growth mostly occurs by nucleation and growth of product phases. Reconstructive transformations are slow below 600°C. The formation of allotriomorphic ferrite, idiomorphic ferrite, massive ferrite, pearlite, carbide, and austenite all belong to the category of reconstructive transformation. Displacive transformation involves coordinated atom, causing a change from a parent crystal to a product crystal. This change is achieved by IPS deformation with a large shear component, leading to a plate or lath shape. During this transformation, the substitutional atoms do not diffuse. However, displacive transformations occurring at high temperatures (above M_s) may involve varying amounts of interstitial carbon diffusion during nucleation and growth. In the case of Widmanstätten ferrite formation, both nucleation and growth involve carbon diffusion. In contrast, in bainitic ferrite formation,

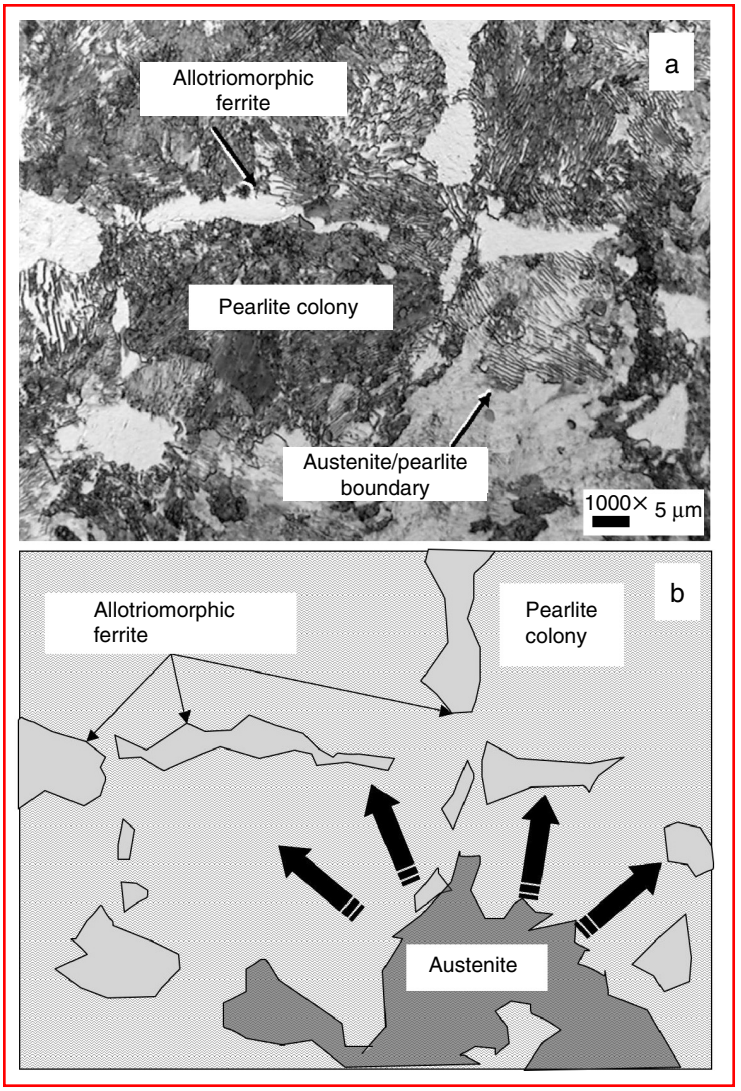

FIGURE 2.12 (a) Optical micrograph of a steel sample with ferrite + pearlite microstructure heated to an intercritical temperature for a short time, showing the formation of austenite in the pearlite colony. (b) Schematic illustration of the austenite growth mechanism that dissolves the pearlite colonies and eventually the allotriomorphic ferrite to attain an equilibrium austenite fraction.

carbon diffusion occurs only during nucleation. In the case of martensite, the carbon diffusion does not occur during nucleation and growth. Recently, attempts have been made to use theoretical formulations to describe this varying carbon supersaturation during displacive transformation within a coupled diffusional-displacive transformation framework [48–50].

2.6 PREDICTION OF MICROSTRUCTURE EVOLUTION DURING HEAT TREATMENT

The final properties of heat-treated parts depend on the microstructure that evolves during the heat-treating process. The microstructure evolution is in turn controlled by the complex

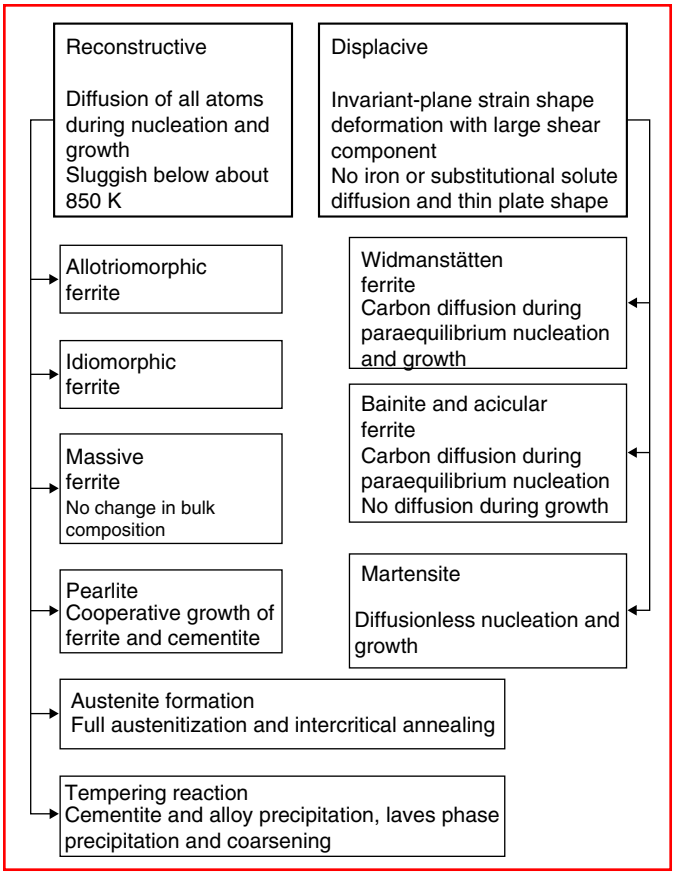

FIGURE 2.13 Classification of steel microstructure evolution during heating and cooling based on the mechanism of transformation. (Adapted from H.K.D.H. Bhadeshia, *Bainite in Steels*, 2nd ed., the Institute of Materials, London, 2001.)

thermal cycles and the composition of the alloy. Over a period of many decades, heat-treatment processes have been developed through extensive experimentation and characterization of particular alloy compositions and final properties. This methodology, in conjunction with an extensive experimental database, often achieves the required properties. However, this approach has the following limitations: (1) it is rigid and cannot be changed easily to meet the ever-increasing demand for optimization of cost and quality and to meet the requirements of strict codes and standards and (2) it cannot be extended to newly developed steels. In this regard, tools that can predict the evolution of microstructure as a function of composition and heat-treatment history will be useful. These predictive tools should be capable of addressing the effect of alloy composition on the stability of various phases. In addition, the effect of time–temperature histories on the growth and dissolution of these phases must be addressed. For example, given the phase diagram information for a steel, these tools must be capable of predicting the continuous heating and cooling transformation diagrams as a function of steel composition (see Figure 2.14). The figure on the left-hand side shows an iron-rich corner of the Fe–C phase diagram showing the phase stability at different temperature. The schematic figure in the middle shows the initiation of austenite formation from ferrite as a function of heating curves. The schematic figure in the right shows the initiation of ferrite formation from austenite as a function of different cooling rate. With the

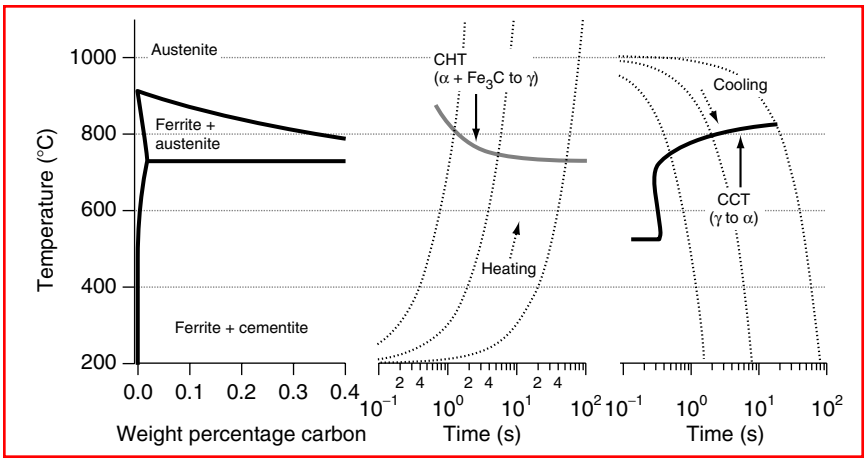

FIGURE 2.14 Schematic illustration, showing the importance of continuous heating transformation (CHT) and continuous cooling transformation (CCT) diagrams with reference to an Fe–C metastable binary diagram.

framework of microstructural evolution presented in the earlier sections and state-of-the-art computational and kinetic models presented in the following sections, it is possible to predict microstructural evolution during heat treatment of steels as a function of composition and thermal history.

2.6.1 Calculation of Multicomponent Multiphase Diagrams

The stability of a phase is governed by its free energy, which is a function of temperature and its constitution. A generic description of free energy of a solid-solution phase, ϕ, G^{ϕ}, is given by the following equation [51]:

$$G^{\phi} = G^{\phi}_{o} + G^{\phi}_{\text{ideal}-\text{mix}} + G^{\phi}_{\text{excess}-\text{mix}}, \tag{2.1}$$

where G^{ϕ}_{o} is the free energy contribution from pure components in that phase, $G^{\phi}_{\text{ideal}-\text{mix}}$ is the contribution from ideal mixing, and $G^{\phi}_{\text{excess}-\text{mix}}$ is the contribution due to nonideal interactions between the components.

Many thermodynamic models describe various phases (see Ref. [15]). With the description of this G^{ϕ} for all phases that can form in a given alloy, it is possible to estimate equilibrium fractions of each phase and their constitution at a given temperature. This estimation is performed by minimization of the free-energy curves of the various phases. This procedure also allows for determination of the tie line, which is schematically shown in Figure 2.15. The tie line is represented by a common tangent and is mathematically represented by the following equation:

$$\mu^{\alpha}_{A} = \mu^{\beta}_{A}; \;\; \mu^{\alpha}_{B} = \mu^{\beta}_{B}, \tag{2.2}$$

where μ^{ϕ}_{i} is the chemical potential of element i in the ϕ-phase. The chemical potentials are obtained from the free-energy expressions given in Equation 2.1 with the following equation:

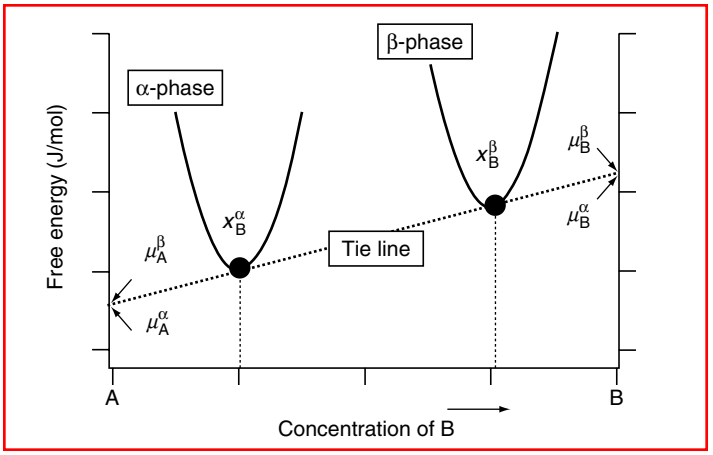

FIGURE 2.15 Schematic illustration of the methodology used to calculate phase stability in a binary alloy: free energy of an α-phase and a β-phase and the common-tangent construction for the description of the tie line and chemical potential of elements A and B.

$$\mu_A^\phi = G^\phi - x_B^\phi \frac{\partial G^\phi}{\partial x_B^\phi}; \quad \mu_B^\phi = G^\phi + \left(1 - x_B^\phi\right) \frac{\partial G^\phi}{\partial x_B^\phi}. \tag{2.3}$$

Equation 2.2 and Equation 2.3 can be extended to multicomponent systems by invoking the equality of the chemical potentials of all the components. The following equation determines the governing equilibrium between α- and γ- phases in the Fe–Cr–Ni–C alloy system:

$$\mu_C^\gamma = \mu_C^\alpha; \quad \mu_{Fe}^\gamma = \mu_{Fe}^\alpha; \quad \mu_{Cr}^\gamma = \mu_{Cr}^\alpha; \quad \mu_{Ni}^\gamma = \mu_{Ni}^\alpha. \tag{2.4}$$

Using the relations in Equation 2.4 and mathematical methods, a phase equilibria between the γ- and α-phases as a function of Cr, Ni, and C concentrations can be calculated. This methodology has proven to be useful for describing the phase stability in multicomponent alloys such as aluminum alloys, stainless steels, low-alloy steels, and Nibase alloys [52–57]. For example, a simple Fe–C binary diagram is compared with an (Fe,Cr,Mo)–C quasibinary phase diagram in Figure 2.16. The diagram shows that a simple ferrite + austenite + cementite phase equilibrium is modified to ferrite + austenite + cementite + $M_{23}C_6$ + M_6C + M_3C_2 + MC due to the addition of Cr and Mo to the Fe–C systems. ThermoCalc software was used to construct these diagrams with solid solution database [58].

2.6.2 Calculation of Diffusion-Controlled Growth

Although the phase stability calculation allows the estimation of the equilibrium microstructure at a particular temperature, microstructure control in most heat-treatment processes relies on the kinetics of product-phase formation from the parent phase. For example, in dual phase low-alloy steels, it is important to understand the kinetics of austenite formation to control the mixture of ferrite and martensite. In addition to the kinetics of transformation, there is a need to understand the equilibration of the nonequilibrium microstructure that is formed during processing. Both phenomena can be described by diffusion-controlled growth models by coupling thermodynamic models with diffusion-controlled growth calculations. The methodology is presented below.

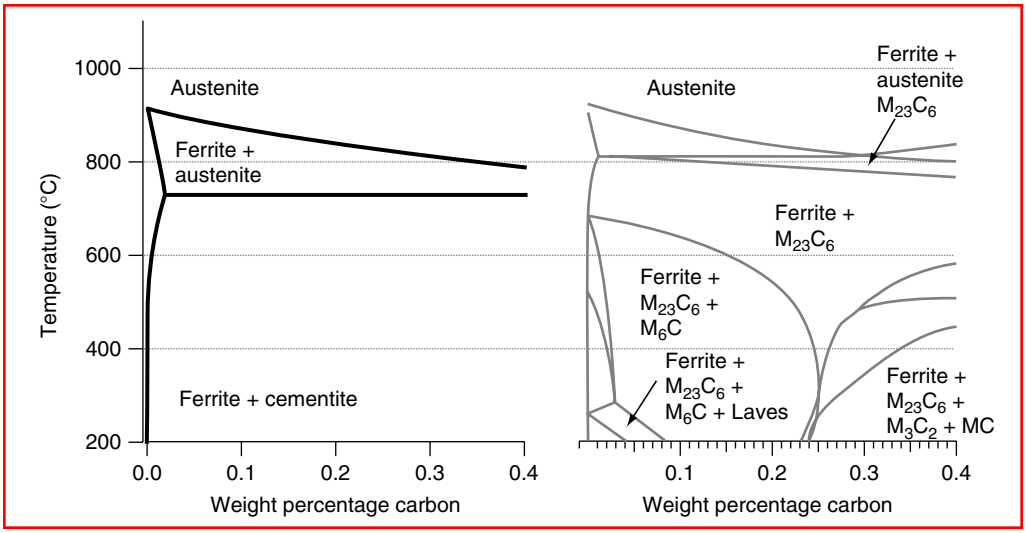

FIGURE 2.16 Comparison of a calculated Fe–C binary-phase diagram with an Fe–Cr–Mo–C quasi-binary diagram, showing the complex stability between ferrite, austenite, and other carbides.

The formation of a product phase with a different composition from the parent phase involves diffusion of partitioning elements. If local equilibrium exists between the parent and product phases at the interface, the interfacial concentrations can be given by the tie lines drawn in the phase diagram. Given this condition, it is possible to describe the movement of this interface as a function of temperature and time by solving Fick's second law and by maintaining a mass balance at the interface. The governing equation for α-phase formation in γ-phase in one-dimensional geometry is given in the following example [59,60]:

$$\left(C_{\mathrm{I}}^{\mathrm{m},\alpha} - C_{\mathrm{I}}^{\mathrm{m},\gamma}\right)(\mathrm{d}l/\mathrm{d}t) = D_{\gamma}^{\mathrm{m}}\left(\mathrm{d}C_{\gamma}^{\mathrm{m}}/\mathrm{d}x\right) - D_{\alpha}^{\mathrm{m}}\left(\mathrm{d}C_{\alpha}^{\mathrm{m}}/\mathrm{d}x\right). \tag{2.5}$$

In the above equation, $(\mathrm{d}l/\mathrm{d}t)$ is the rate of interface movement or velocity. The terms $C_{\mathrm{I}}^{\mathrm{m},\alpha}$ and $C_{\mathrm{I}}^{\mathrm{m},\gamma}$ are the interface concentrations of element m in the α- and γ-phases. The terms D_{α}^{m} and D_{γ}^{m} are the diffusivities of element m in α- and γ-phases. The terms $(\mathrm{d}C_{\gamma}^{\mathrm{m}}/\mathrm{d}x)$ and $\left(\mathrm{d}C_{\alpha}^{\mathrm{m}}/\mathrm{d}x\right)$ are the concentration gradients* of element m in α- and γ-phases at the interface. The conditions at the interface are schematically shown in Figure 2.17. In a multicomponent alloy, Equation 2.5 must be satisfied for all elements, and a unique velocity of the interface is obtained. This restriction leads to the selection of the interface compositions as determined by the tie lines that may shift with time and may not pass through the nominal alloy composition. Therefore, these calculations must adjust local equilibrium conditions while solving the diffusion equations and require close coupling with thermodynamic models. This is the methodology implemented in the DicTra software [61] and other published works.

An example calculation is presented below. The final microstructure of a stainless steel weld often contains ferrite and austenite at room temperature. This microstructure is far from equilibrium. However, given a high-temperature heat treatment, equilibration of this microstructure will occur. During this heat treatment, the ferrite may grow or dissolve, depending upon the alloy composition, the initial state, and the heat treatment temperature. Examples are shown in Figure 2.18. In case A, the initial austenite composition was Fe–15%Cr–20%Ni

* Ideally, the chemical potential gradient needs to be used instead of concentration gradient.

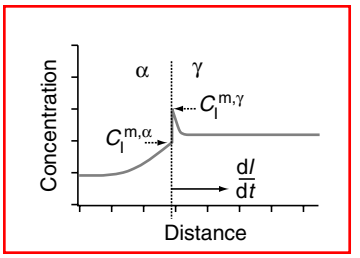

FIGURE 2.17 Schematic illustration of interface concentrations and diffusion in both α- and β- phases to describe diffusion-controlled transformations.

(wt%), and the initial ferrite composition was Fe–20%Cr–10%Ni (wt%). The initial volume percentage of ferrite was 9%. The calculations predicted rapid dissolution of ferrite if this weld was aged at 1300°C. In case B, the initial austenite composition was Fe–21%Cr–11%Ni (wt%), and the initial ferrite composition was Fe–30%Cr–4.5%Ni (wt%). The initial volume percentage of ferrite was again set to 9%. The calculations predicted that the volume percentage of ferrite would increase from 9 to 25% if the weld was aged at 1300°C. In addition, the calculations showed different stages where the kinetics of this transformation were controlled by either solute diffusion in ferrite or solute diffusion in austenite. This condition is due to the large differences in the diffusivity of Cr and Ni in the ferrite and austenite phases. The above methodology has been applied to continuous cooling and heating conditions. Such calculations allow for the design of postweld heat treatment of stainless steel welds.

However, the local equilibrium assumption used in the above model leads to some paradoxes for simulating growth below ~600°C. At temperatures below 600°C, the diffusion profile of substitutional atoms (see Figure 2.17) may be extremely steep, with a width that is smaller than interatomic distances. Hultgren and other authors have addressed this issue [62–65]. It is hypothesized that under these conditions, the concentration ratio of substitutional atoms to iron atoms will remain configurationally frozen and that interface growth will be controlled purely by carbon (interstitial) diffusion. The carbon concentration at the interface will now be determined by a phase-boundary calculation similar to the Fe–C phase diagram, with a constraint that the C activity will be modified by the configurationally frozen substitutional atoms. This mode of transformation is called PE transformation. PE appears to correlate well with the accelerated ferrite growth observed under large undercooling in most heat treatment and welding conditions. In steels, PE growth rates are always higher than

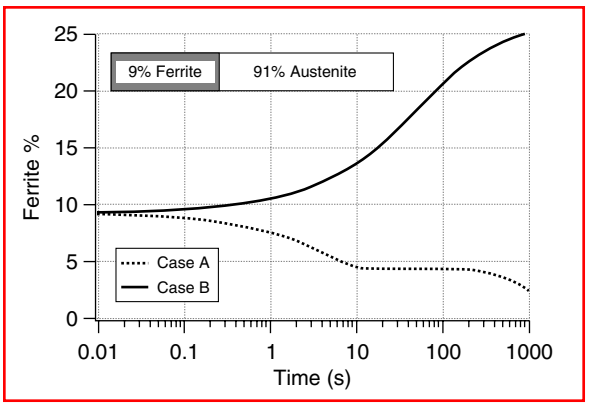

FIGURE 2.18 Variation of ferrite percentage while aging at 1573 K for two initial conditions: (A) corresponds to Fe–15Cr–20Ni (wt%) austenite and Fe–20Cr–10Ni (wt%) ferrite; (B) corresponds to Fe–21Cr–11Ni (wt%) austenite. (The ferrite composition was Fe–30Cr–4.5Ni [wt%] ferrite.)

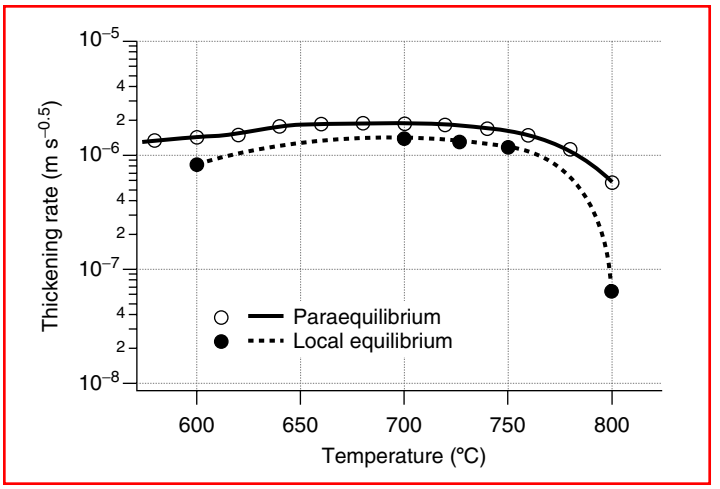

FIGURE 2.19 Calculated parabolic thickening rate of ferrite growth into austenite in an Fe–0.1C–2.25Cr–1Mo steel under (●) local equilibrium and (○) paraequilibrium.

growth rates calculated by local equilibrium models. This discrepancy is demonstrated by a comparison of the parabolic thickening rates of ferrite into austenite in an Fe–Cr–Mo–C steel at different temperatures (see Figure 2.19). It is now possible to use models to predict TTT and continuous cooling transformation (CCT) diagrams with commercial software that are available on the Internet and from the commercial organizations [66–68]. Typical TTT and CCT diagrams calculated with the JMatPro software are shown in Figure 2.20a and Figure 2.20b, respectively. A TTT and CCT diagram for 0.1% transformation to ferrite calculated by using an Internet tool is shown in Figure 2.20c. The methods of calculation for each tool are different and are constantly refined. As a result, these results must be used as guidance rather than as accurate predictions. However, with the advent of new models [69] and detailed thermodynamic and diffusion data, an accurate description of transformation in steels should be possible. The final goal of these predictive approaches is to couple these microstructure models with thermal and structural models to describe the overall response of steel structures to heat treatment as envisioned by Kirkaldy [70] (see Figure 2.21). In this integrated model, it would be possible to describe transient thermal fluctuations in a steel part during heat treatment in a furnace and during quenching or cooling. In addition, during such thermal responses, it should be possible to describe the thermal stress evolution based on the constitutive relations of different phases. By coupling all the above parameters with a microstructure model that describes the transformation kinetics as a function of temperature, time, and stress, it is possible to evaluate the properties of steel parts subjected to different heat treatments as a function of steel composition.

2.7 SUMMARY

In this chapter, phase transformations in alloys are categorized in terms of different thermodynamic, microstructural, and mechanistic bases. The predominant transformation mechanisms in steels (i.e., reconstructive and displacive mechanisms) are explained. The important microstructures observed during steel heat treatment, including allotriomorphic ferrite, Widmanstätten ferrite, bainite, pearlite, martensite, and carbide formation during tempering and austenite formation during reheating, are described based on this framework. Finally, computational thermodynamic and kinetic methodologies that are available to predict the microstructure evolution in steels are highlighted.

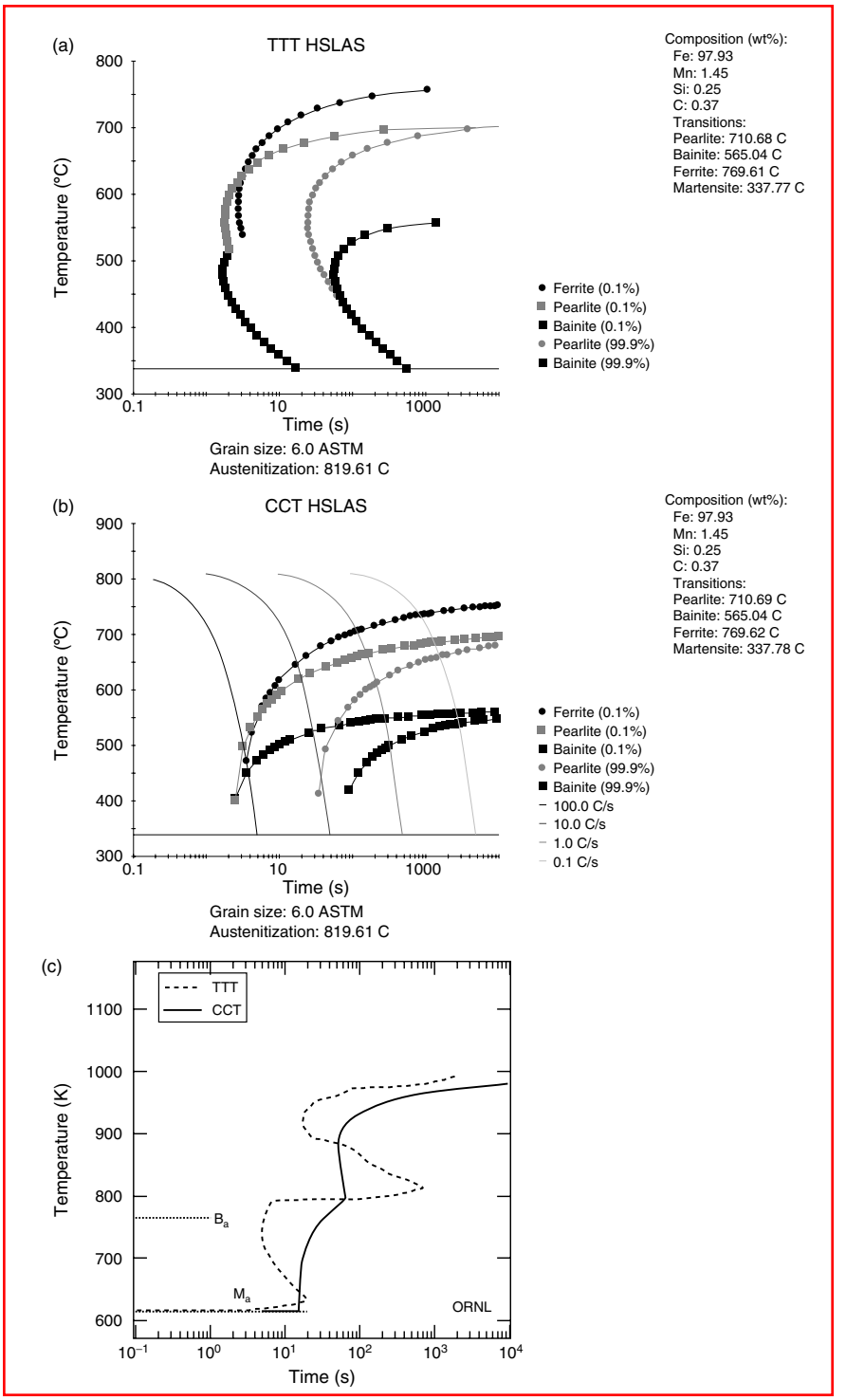

FIGURE 2.20 Calculated (a) time temperature transformation (TTT) diagram and (b) continuous cooling transformation (CCT) diagram for a steel using JMatPro® software for an Fe–0.37C–0.25Si–1.45Mn steel. (c) TTT and CCT transformation diagram is calculated using the tool found on the Internet at http://engm01.ms.ornl.gov.

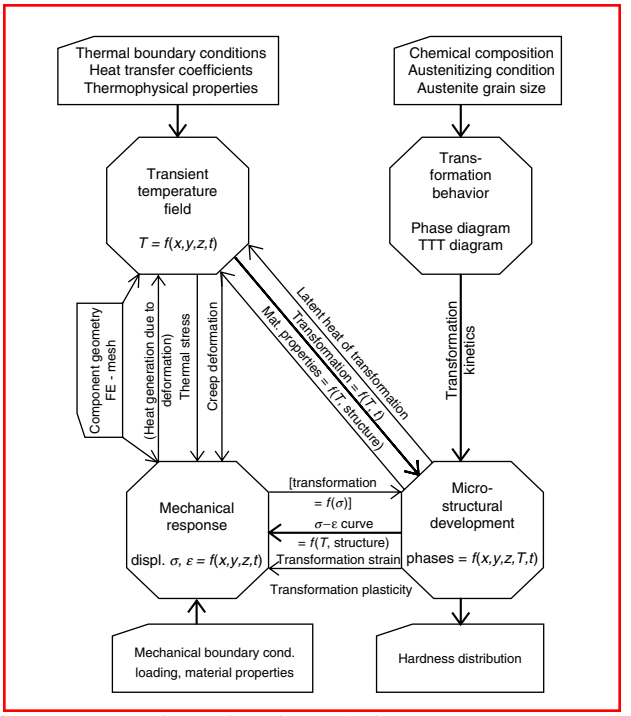

FIGURE 2.21 Modeling phase transformations in steels, in response to thermomechanical conditions. (Adapted from J.S. Kirklady, *Scand. J. Metall.*, 20, 1991.)

2.8 ACKNOWLEDGMENTS

Part of the results presented in this paper is based on the research sponsored by the Division of Materials Sciences and Engineering and Assistant Secretary for Energy Efficiency and Renewable Energy, Office of Industrial Technologies, Advanced Industrial Materials Program, U.S. Department of Energy, under contract DE-AC05-00OR22725 with UT-Battelle, LLC. The author also wishes to thank Prof. H.K.D.H. Bhadeshia, Dr. J.M. Vitek, and Dr. S.A. David for help and guidance in the research related to different topics discussed in this chapter. Finally, the author would like to thank Drs. M.K. Miller and Dr. J.M. Vitek of ORNL for helpful suggestions and review of the manuscript.

REFERENCES

1. J. Agren, *Scr. Mater.*, **46**, 2002, 893–8.
2. J.W. Christian, *The Theory of Transformations in Metals and Alloys*, 2nd ed., Part 1, Pergamon Press, Oxford, 1981, p. 9.
3. H.K.D.H. Bhadeshia, *Worked Examples in the Geometry of Crystals*, The Institute of Materials, London, 1987.
4. H.K.D.H. Bhadeshia, *Bainite in Steels*, 2nd ed., The Institute of Materials, London, 2001.
5. J.S. Bowles and J.K. Mackenzie, *Acta Metall.*, **2**, 1954, 129.
6. M.S. Wechsler, D.S. Lieberman, and T.A. Read, *Trans. AIMME*, **197**, 1953, 1503.
7. *Martensite—A Tribute to Morris Cohen*, G.B. Olson and W.S. Owen, Eds., ASM International, Materials Park, OH, 1992.
8. C. Zener, *Trans. AIMME*, **167**, 1946, 550–95.
9. A. Hultgren, *Trans. ASM*, **39**, 1947, 915–1005.
10. H.I. Aaronson, *Decomposition of Austenite by Diffusional Processes*, Interscience, New York, 1962.

11. C.A. Dubé, Ph.D. Thesis, Carnegie Institute of Technology, Pittsburgh, PA, 1948.
12. C.A. Dubé, H.I. Aaronson, and R.F. Mehl, *Rev. de Met*., **55**, 1958, 201.
13. W.T. Reynolds, Jr., M. Enomoto, and H.I. Aaronson, The Proeutectoid Reaction, in The Proceedings of an International Conference on Phase Transformations in Ferrous Alloys, A.R. Marder and J.I. Goldstein, Eds., 1988.
14. R.W.K. Honeycombe and H.K.D.H. Bhadeshia, *Steels, Microstructure, and Properties*, 2nd ed., Edward Arnold, London, 1995.
15. S.S. Babu and H.K.D.H. Bhadeshia, *Mater. Sci. Eng*., **A141**, 1990, 209.
16. G.R. Purdy, *Acta Metall*., **26**, 1978, 477–86.
17. H.I. Aaronson, *Metall. Trans. A*, **24A**, 1993, 241–76.
18. G. Spanos, W.T. Reynolds, Jr., and R.A. Vandermeer, *Metall. Trans. A*, **22A**, 1991, 1367–80.
19. H.K.D.H. Bhadeshia, *Acta Metall*., **29**, 1981, 1117.
20. H.K.D.H. Bhadeshia, L.-E. Svensson, and B. Gretoft, *Acta Metall*., **33**, 1985, 1271–83.
21. R. Trivedi, *Metall. Trans*., **1**, 1970, 921.
22. R. Trivedi, *Acta Metall*., **18**, 1970, 287.
23. H.I. Aaronson, W.T. Reynolds, Jr., G.J. Shiflet, and G. Spanos, *Metall. Trans. A*, **21A**, 1990, 134–80.
24. H.K.D.H. Bhadeshia and J.W. Christain, *Metall. Trans. A*, **21A**, 1990, 767–97.
25. S.S. Babu and H.K.D.H. Bhadeshia, *Mater. Sci. Eng*., **A156**, 1992, 1–9.
26. M. Hillert, *Scr. Mater*., **47**, 2002, 137–8.
27. H.K.D.H. Bhadeshia, *Met. Sci*., **16**, 1982, 159–65.
28. K.A. Taylor, L. Chang, G.B. Olson, G.D.W. Smith, M. Cohen, and J.B. Vander Sande, *Metall. Trans. A*, **20A**, 1989, 2749–65.
29. B.P.J. Sandvik, *Metall. Trans. A*, **13A**, 1982, 789–800.
30. K.A. Taylor, L. Chang, G.B. Olson, G.D.W. Smith, M. Cohen, and J.B. Vander Sande, *Metall. Trans. A*, **20A**, 1989, 2717–37.
31. Y. Ohmori and I. Tamura, *Metall. Trans. A*, **23A**, 1992, 2147–58.
32. S.S. Babu, K. Hono, and T. Sakurai, *Metall. Trans. A*, **25A**, 1994, 499–508.
33. R.C. Thomson and M.K. Miller, *Acta Mater*., **46**, 1998, 2203–13.
34. S. Nakagura, T. Suzuki, and M. Kusunoki, *Trans. Jpn. Inst. Met*., **22**, 1981, 699.
35. G.A. Robert and R.F. Mehl, *ASM Trans*., **31**, 1943, 613–50.
36. R.R. Judd and H.W. Paxton, *Trans. AIME*, **242**, 1968, 206–15.
37. G. Molinder, *Acta Metall*., **4**, 1956, 565–71.
38. M. Hillert, K. Nilsson, and L.E. Trondahl, *JISI*, **209**, 1971, 49–66.
39. T. Akbay, R.C. Reed, and C. Atkinson, *Acta Metall. Mater*., **42**, 1994, 1469–80.
40. C. Garcia De Andres, F.G. Caballero, C. Capdevilla, and H.K.D.H. Bhadeshia, *Scr. Mater*., **39**, 1998, 791–6.
41. F.G. Caballero, C. Capdevilla, and C. Garcia De Andres, *Mater. Sci. Tech*., **17**, 2000, 1114–8.
42. A. Jacot and M. Rappaz, *Acta Mater*., **47**, 1999, 1645–51.
43. J.R. Yang, C.Y. Huang, *Mater. Chem. Phys*., **35**, 1993, 168–75.
44. J.R. Yang and H.K.D.H. Bhadeshia, *Mater. Sci. Eng. A*, **131**, 1991, 99–113.
45. M. Chapa, S.F. Medina, V. Lopez, and B. Fernandez, *ISIJ Int*., **42**, 2002, 1288–96.
46. T. Gladman, *Heat Treat. Met*., **21**, 1994, 11–4.
47. W.J. Kaluba, R. Taillard, and J. Foct, *Acta Mater*., **46**, 1998, 5917–27.
48. G.B. Olson, H.K.D.H. Bhadeshia, and M. Cohen, *Acta Metall*., **37**, 1989, 381–9.
49. G.B. Olson, H.K.D.H. Bhadeshia, and M. Cohen, *Metall. Trans. A*, **21A**, 1990, 805–9.
50. S.A. Mujahid and H.K.D.H. Bhadeshia, *J. Phys. D*, **34**, 2001, 2573–80.
51. N. Saunders and A.P. Miodownik, *CALPHAD-Calculation of Phase Diagrams—A Comprehensive Guide*, Pergamon, Elsevier Science, Amsterdam, 1998.
52. S.S. Babu, S.A. David, J.M. Vitek, and M.K. Miller, *Metall. Mater. Trans. A*, **27A**, 1996, 763–74.
53. S.S. Babu, S.A. David, and M.K. Miller, *Appl. Surf. Sci*., **94/95**, 1996, 280–87.
54. S.A. David, J.M. Vitek, S.S. Babu, L. Boatner, and R.W. Reed, *Sci. Tech. Weld. Join*., **2**, 1996, 79–88.
55. P. Hofer, M.K. Miller, S.S. Babu, S.A. David, and H. Cerjak, *Metall. Mater. Trans. A*, **31A**, 2000, 975–984.

56. M.K. Miller, S.S. Babu, and M.G. Burke, *Mater. Sci. Eng*., **A270**, 1999, 14–8.
57. S.S. Babu, S.A. David, J.M. Vitek, and R.W. Reed, *Sci. Tech. Weld. Join*., **6**, 2001, 31–40.
58. B. Sundman, B. Jansson, and J.O. Andersson, *CALPHAD*, **9**, 1985, 153–90.
59. J.M. Vitek, S.A. Vitek, and S.A. David, *Metall. Mater. Trans. A*, **26A**, 1995, 2007–25.
60. H.K.D.H. Bhadeshia, *Prog. Mater. Sci*., **29**, 1985, 321–86.
61. J. Ågren, *ISIJ Int*., **32**, 1992, 292–6.
62. A. Hultgren, *Jerkontorets Ann*., **135**, 1951, 403.
63. J.B. Gilmour, G.R. Purdy, and J.S. Kirkaldy, *Metall. Trans*., **3**, 1972, 3213–22.
64. G. Ghosh and G.B. Olson, *Acta Mater*., **50**, 2002, 2009–19.
65. E. Kozeschnik, *J. Phase Equilibria*, **21**, 2000, 336–41.
66. http://www.msm.cam.ac.uk/map
67. http://engm01.ms.ornl.gov, Modeling Microstructure Development in Welds, Internet online computational tool, Oak Ridge National Laboratory, Oak Ridge, Tenn.
68. JMatPro, http://www.thermotech.co.uk
69. J. Odqvist and M. Hillert, *Acta Mater*., **50**, 2002, 3211–25.
70. J.S. Kirkaldy, *Scand. J. Metall*., **20**, 1991, 50–61.

3 Fundamental Concepts in Steel Heat Treatment

Alexey V. Sverdlin and Arnold R. Ness

CONTENTS

3.1 Introduction 122
3.2 Crystal Structure and Phases 122
3.2.1 Crystal Structure of Pure Iron 122
3.2.2 Iron–Carbon Equilibrium Diagram 123
3.2.2.1 Metastable Fe–Fe_3C Equilibrium Diagram 123
3.2.2.2 Stable Fe–C Equilibrium Diagram 124
3.2.3 Effect of Carbon 125
3.2.4 Critical (Transformation) Temperatures 127
3.3 Structural Transformations in Steel 128
3.3.1 Austenite–Pearlite Transformation 128
3.3.2 Structure of Pearlite 129
3.3.3 Transformation of Austenite in Hypo- and Hypereutectoid Steels 130
3.3.4 Martensite Transformation 131
3.3.5 Morphology of Ferrous Martensites 133
3.3.6 Bainite Transformation 134
3.3.7 Morphology of the Bainite Transformation 135
3.3.8 Tempering 135
3.4 Kinetics of Austenite Transformation 137
3.4.1 Isothermal Transformation Diagrams 137
3.4.2 Continuous-Cooling Transformation Diagrams 138
3.4.2.1 Transformations That Take Place under Continuous Cooling of Eutectoid Steels 139
3.4.2.2 Transformations of Austenite on Cooling in the Martensite Range 141
3.4.3 Derivation of the Continuous-Cooling Transformation Diagram from the Isothermal Transformation Diagram 142
3.4.4 Continuous-Cooling Transformation Diagram as a Function of the Bar Diameter 143
3.4.5 Definition of Hardenability 145
3.5 Grain Size 146
3.5.1 Structure of Grain Boundaries 146
3.5.1.1 Structural Models 147
3.5.2 Determination of Grain Size 149
3.5.3 Austenite Grain Size Effect and Grain Size Control 150
3.5.4 Grain Size Refinement 152
3.6 Strengthening Mechanism in Steel 153

3.6.1 Solid Solution Strengthening 153
3.6.2 Grain Size Refinement 154
3.6.3 Dispersion Strengthening 154
3.6.4 Work Hardening (Dislocation Strengthening) 158
3.6.5 Thermal Treatment of Steels 159
3.6.5.1 Annealing 159
3.6.5.2 Quenching (Strengthening Treatment) 162
3.6.5.3 Tempering 163
References 163
Further Reading 163

3.1 INTRODUCTION

The purpose of heat treatment is to cause desired changes in the metallurgical structure and thus in the properties of metal parts. Heat treatment can affect the properties of most metals and alloys, but ferrous alloys, principally steels, undergo the most dramatic increases in properties, and therefore structural changes in iron–carbon alloys are considered in this chapter. In general, the most stable steel structures are produced when a steel is heated to the high-temperature austenitic state (to be defined later) and slowly cooled under near-equilibrium conditions. This type of treatment, often referred to as annealing or normalizing, produces a structure that has a low level of residual stresses locked within the part, and the structures can be predicted from an equilibrium diagram. However, the properties that interest heat treaters the most are those exhibiting high strength and hardness, usually accompanied by high levels of residual stresses. These are metastable structures produced by nonequilibrium cooling or quenching from the austenitic state.

Most of this chapter discusses equilibrium and nonequilibrium structures, their properties, and the tools that we have at our disposal to predict different types of phase formations and their properties. It is essential that heat treaters have a clear understanding of the structures that can be produced in steel under different treatment conditions that they can apply in their equipment.

3.2 CRYSTAL STRUCTURE AND PHASES

3.2.1 Crystal Structure of Pure Iron

Iron in the solid state is known in two allotropic states. (Allotropy is the phenomenon of an element having different crystal lattices depending on the particular temperature and pressure.) Starting from low temperatures and up to 910°C (1670°F), iron possesses a body-centered cubic (bcc) lattice and is called α-iron (α-Fe). At 910°C α-iron crystals turn into γ-iron crystals possessing a face-centered cubic (fcc) lattice. The γ crystals retain stability up to temperature of 1400°C (2500°F). Above this temperature they again acquire a bcc lattice and are usually called δ crystals. The δ crystals differ from α crystals only in the temperature region of their existence. Iron has the following lattice constants: 0.286 nm for bcc lattices (α-Fe, δ-Fe) and 0.364 nm for fcc lattices (γ-Fe).

At low temperatures, α-Fe exhibits a strongly ferromagnetic character. When it is heated to about 770°C (1418°F), ferromagnetism vanishes. In accordance with the latest findings, this is because the lattice loses its ferromagnetic spin ordering. The state of iron above 770°C is called β-Fe. The lattice of paramagnetic β crystals is identical to the lattice of α crystals.

The points at which one allotropic form of iron transforms to another are conventionally symbolized by the letter A with subscripts indicating the ordinal number of the transformation. The subscripts 0 and 1 signify transformations that are absent in pure iron but are observed in carbon alloys of iron. The subscript 2 denotes a magnetic transformation of the α-phase, while the subscripts 3 and 4 stand for transformation of α to γ and γ to δ.

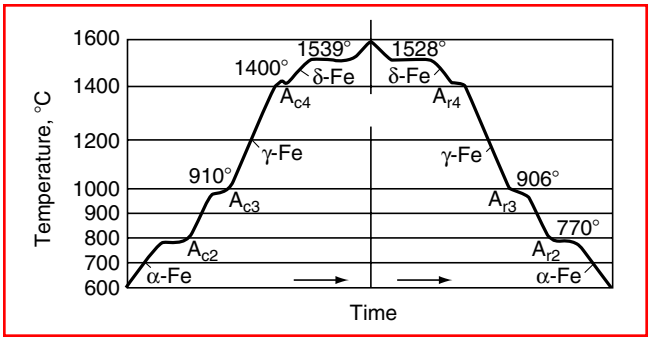

FIGURE 3.1 Heating and cooling curves for pure iron.

In going from one form to another, iron is capable of undercooling. This causes a difference in the position of transformation points on heating and cooling. The difference depends on the cooling rate (Figure 3.1) and is termed hysteresis. The letters "c" and "r" indicate whether the transformation is due to heating or cooling.

A change in the density of α-Fe as it transforms to γ-Fe results in an abrupt change in the volume of the material. Sometimes this gives rise to stresses that exceed the elastic limit and lead to failure. The density of γ-Fe is about 4% higher than that of α-Fe.

3.2.2 Iron–Carbon Equilibrium Diagram

The structure of iron–carbon alloys can contain either pure carbon (graphite) or a chemical compound (cementite) as the carbon-enriched component. Cementite is present even in relatively slowly cooled alloys: a long holding at elevated temperatures is required to decompose cementite to iron and graphite. For this reason the iron–carbon diagram is usually treated as the iron–iron carbide diagram. The former is stable, whereas the latter is metastable.

The iron–carbon diagram is shown in Figure 3.2. Dashed lines stand for the stable Fe–C diagram, and solid lines denote the metastable Fe–Fe_3C diagram.

3.2.2.1 Metastable Fe–Fe_3C Equilibrium Diagram

As shown in Figure 3.2, the lattices of allotropic forms of iron (δ, γ, and α) serve as sites of formation of δ, γ, and α solid solutions of carbon in iron (the same symbols are adopted for the designation of solid solutions).

When carbon-depleted alloys crystallize, crystals of the δ solid solution precipitate at the liquidus AB and solidus AH. The δ solid solution has a bcc lattice. At the maximum carbon temperature of 1490°C (2714°F), the δ solution contains 0.1% C (point H). At 1490°C a peritectic reaction takes place between the saturated δ solution and the liquid containing 0.5% C (point B). As a result, the γ solid solution of carbon in γ-Fe is formed. It contains 0.18% C (point I).

If the carbon content is higher than 0.5%, the γ solid solution crystallizes directly from the liquid (at the liquidus BC and solidus IE). At 1130°C (2066°F) the limiting solubility of carbon in γ-Fe is close to 2.0% C (point E). Decreasing the temperature from 1130°C (2066°F) leads to lowering the carbon solubility in γ-iron at the line ES. At 723°C (1333°F) the solubility is 0.8% C (point S). The line ES corresponds to precipitation of iron carbide from the γ solution.

As the carbon content is raised, the temperature at which the γ lattice transforms to the α lattice lowers, and the transformation takes place over the temperature interval corresponding to the curves GS and GP.

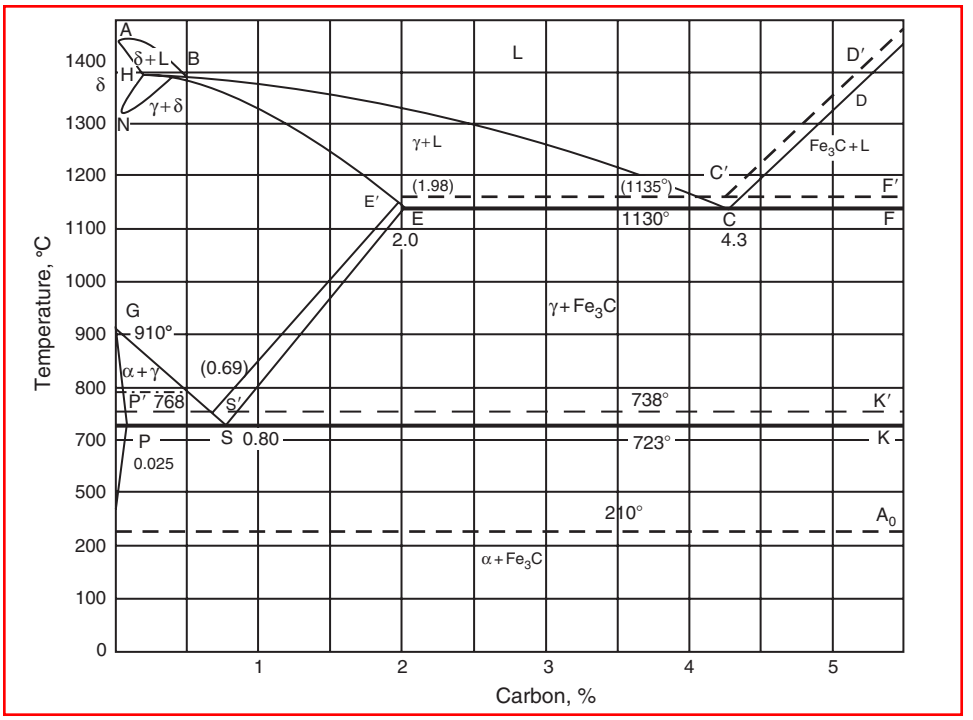

FIGURE 3.2 Iron–carbon diagram.

The α-phase precipitation curve GS intersects the iron carbide precipitation curve ES. The point S is a eutectoid point with the coordinates 723°C (1333°F) and 0.80% C. At this point a saturated α solution and Fe_3C precipitate simultaneously form the eutectoid concentration γ solution.

The lattice of the α solid solution is identical to the lattice of the δ solid solution. At the eutectoid temperature of 723°C (1333°F) the α solid solution contains 0.02% C (point P). Further cooling leads to lowering of the carbon solubility in α-Fe, and at room temperature it equals a small fraction of a percent (point D).

When the carbon content is 2.0–4.3%, crystallization starts with precipitation of the γ solution at the line BC. An increase in the carbon content to over 4.3% causes precipitation of iron carbide at the line CD.

Precipitation of the surplus primary phase in all alloys containing over 2.0% C is followed by a eutectic crystallization of the γ solution and iron carbide at point C, whose coordinates are 1130°C (2066°F) and 4.3% C.

The line A_o is associated with a magnetic transformation, that is, a transition from the ferromagnetic to the paramagnetic state.

Table 3.1 describes structural components of the iron–carbon system.

3.2.2.2 Stable Fe–C Equilibrium Diagram

Given very low rates of cooling, carbon (graphite) can crystallize directly from the liquid. In this case, a eutectic mixture of austenite and graphite is formed instead of the eutectic of austenite and cementite. As is seen in Figure 3.2, the dashed lines symbolizing the iron–graphite system are at higher temperatures than the lines of the iron–cementite system. This testifies to the greater stability and closeness to a full equilibrium of the iron–graphite system.

TABLE 3.1
Components of the Iron–Carbon System

Phase or Mixture of Phases	Name
Solid solution of carbon in α (δ) iron	Ferrite
Solid solution of carbon in γ-iron	Austenite
Iron carbide (Fe_3C)	Cementite
Eutectoid mixture of carbon solid solution in γ-iron with iron carbide	Ledeburite
Eutectoid mixture of carbon solid solution in α-iron with iron carbide	Pearlite

The conclusion is also supported by the fact that heating of high-carbon alloys with a large amount of cementite leads to its decomposition: $Fe_3C \rightarrow 3Fe + C$.

At intermediate rates of cooling, part of the alloy can crystallize according to the graphite system and the other part according to the cementite system.

Phase equilibrium lines in the diagrams of both the systems can be displaced depending on particular cooling rates. A most pronounced displacement can be observed for the lines of precipitation of the carbon solid solution in γ-Fe (austenite). For this reason the diagram holds completely true only with respect to the alloys that are subjected to a relatively slow cooling rate.

3.2.3 Effect of Carbon

A maximum solubility of carbon in α-Fe is observed at 721°C (1330°F) and is equal to 0.018% C. Subject to quenching, carbon can remain in the α solid solution, but soon precipitation of phases commences, by an aging mechanism.

In the α solid solution, carbon can form either (1) a homogeneous solution, a statically uniform interstitial distribution (a rare case), or (2) an inhomogeneous solution, with the formation of clusters at places where the crystal lattice structure is disturbed (grain boundaries, dislocations). The latter is the most probable state of the solid solution. The clusters thus formed represent an obstacle to movement of dislocations during plastic deformation and are responsible for an inhomogeneous development of the deformation at the onset of plastic flow.

To analyze the influence of the carbon content on iron–carbon alloys, every structural component should be characterized. Slowly cooled alloys comprise ferrite and cementite or ferrite and graphite. Ferrite is plastic. In the annealed state, ferrite has large elongation (about 40%), is soft (Brinell hardness is 65–130 depending on the crystal dimension), and is strongly ferromagnetic up to 770°C (1418°F). At 723°C (133°F), 0.22% C dissolves in ferrite, but at room temperature only thousandths of a percent of carbon is left in the solution.

Cementite is brittle and exhibits great hardness (the Brinell hardness is about 800); it is weakly magnetic up to 210°C (410°F), is a poor conductor of electricity and heat, and has a complicated rhombic lattice. Usually a distinction is made between primary cementite, which crystallizes from the liquid at the line CD; secondary cementite, which precipitates from the γ solution at the line ES; and tertiary cementite, which precipitates from the α solution at the line PQ.

Graphite is soft. It is a poor conductor of current but transfers heat well. Graphite does not melt even at temperatures of 3000–3500°C (5430–6330°F). It possesses a hexagonal lattice with the axis relation

$$\frac{c}{a} > 2.$$

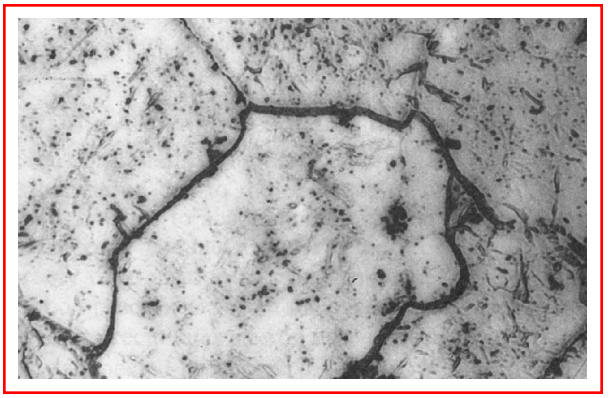

FIGURE 3.3 Steel microstructure of ferrite and tertiary cementite at grain boundaries, 500×.

Austenite is soft (but is harder than ferrite) and ductile. Elongation of austenite is 40–50%. It has lower conductivity of heat and electricity than ferrite, and is paramagnetic. Austenite possesses an fcc lattice.

The structure of the steel containing 0–0.02% C comprises ferrite and tertiary cementite (Figure 3.3). A further increase in the carbon content leads to the appearance of a new structural component—a eutectoid of ferrite and cementite (pearlite). Pearlite appears first as separate inclusions between ferrite grains and then, at 0.8% C, occupies the entire volume. Pearlite represents a two-phase mixture, which usually has a lamellar structure (Figure 3.4).

As the carbon content of steel is raised to over 0.8%, secondary cementite is formed along with pearlite. The secondary cementite is shaped as needles (Figure 3.5). The amount of cementite increases as the carbon content is increased. At 2% C it occupies 18% of the field of vision of the microscope. A eutectic mixture appears when the carbon content exceeds 2%. In rapidly cooled steels, not all the surplus phase (ferrite or cementite) has time to precipitate before a eutectoid is formed.

Alloys with 3.6% C contain ledeburite (a eutectic mixture of carbon solid solution in γ-Fe and iron carbide). An electron microscopic image of the carbides is shown in Figure 3.6. The alloys would be more properly classified with hypoeutectic white cast irons.

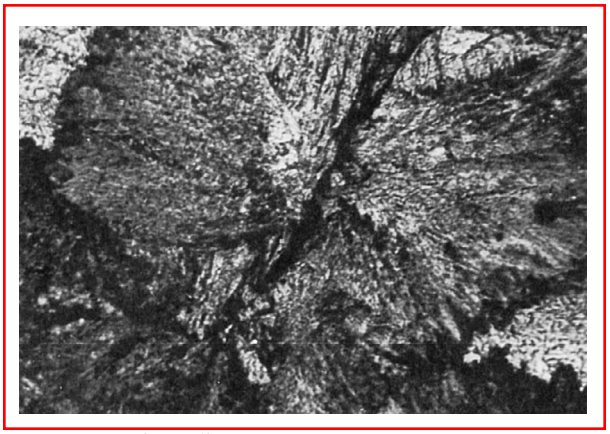

FIGURE 3.4 Steel microstructure of pearlite, 500×.

FIGURE 3.5 Steel microstructure of secondary cementite (needles) and pearlite, 500×.

3.2.4 Critical (Transformation) Temperatures

Carbon has a pronounced effect on transformations of iron in the solid state. The positions of the lines GS and NI in the iron–carbon equilibrium diagram show that an increase in the carbon content leads to lowering of the point A_3 and raising of the point A_4 with respect to their counterparts depicted in Figure 3.2 for pure carbon. So carbon extends the temperature range of the δ-phase.

When a eutectoid (pearlite) is formed, heating and cooling curves exhibit a stop, which is designated as the point A_1 (A_{c1} on heating and A_{r1} on cooling). This phenomenon takes place at 0.9% C (point S in the Fe–C diagram). Precipitation of ferrite in hypoeutectoid steels (on crossing the line GOS) shows up in heating and cooling curves as an inflection symbolized as the point A_3. The point corresponds to the $\gamma \rightarrow \alpha$ transformation in pure iron. Precipitation of cementite (crossing of the line ES), which precedes the eutectoid precipitation, is seen in the cooling curve as a weak inflection designated as the point A_{cm} ($A_{c,cm}$ on heating and $A_{r,cm}$ on cooling). Addition of carbon has little influence on the magnetic transformation temperature (point A_2). Therefore, the line MO corresponds to the magnetic transformation in alloys with a low-carbon content. In alloys containing greater amounts of carbon, this transformation occurs at the line GOS, which corresponds to the onset of ferrite precipitation. If the carbon content is higher than the one corresponding to point S, then the magnetic transformation coincides with the temperature A_1.

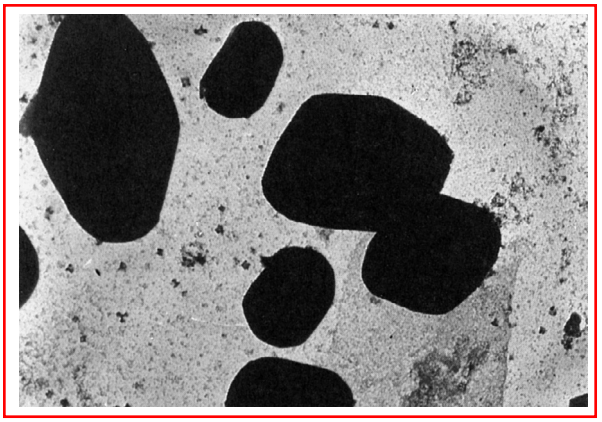

FIGURE 3.6 Steel microstructure of electron microscopic image of iron carbides, 3000×.

Cementite undergoes a magnetic transformation. Whatever the carbon content, the transformation takes place at a temperature of 210–220°C (410–430°F). It occurs without a marked hysteresis, as does the magnetic transformation of pure iron at point A_2.

3.3 STRUCTURAL TRANSFORMATIONS IN STEEL

When a steel part is hardened, it is heated to a high temperature in order to convert the entire structure to the austenite phase. As discussed earlier, austenite is a single-phase structure of iron and carbon stable at high temperatures. If the steel were cooled slowly, the austenite would transform to pearlite, which is the equilibrium phase at room temperature. A pearlitic structure is an annealed structure and is relatively soft with low physical properties. If the steel is cooled very rapidly, a very hard and strong structure called martensite forms that is a metastable phase of carbon dissolved in iron. It may be tempered to produce lower hardness structures that are less brittle. Intermediate cooling rates will produce other structures referred to as bainites, although this type of structure is only produced in quantity in an alloy steel. Eutectoid carbon steels produce predominantly martensite or pearlite, depending on the cooling rate.

3.3.1 Austenite–Pearlite Transformation

Transformation of the fcc lattice of austenite to the bcc lattice of ferrite is hampered due to the presence of dissolved carbon in austenite. The austenite lattice has enough space to accommodate carbon atoms at the centers of unit cells. The bcc lattice of ferrite has no such space. For this reason the solubility of carbon is lowered considerably on transition from austenite to ferrite. During the $\beta \rightarrow \alpha$ transformation, almost all carbon precipitates from the austenite lattice. In accordance with the metastable Fe–Fe_3C diagram, it precipitates as iron carbide (cementite). This transformation can be described by three interconnected processes:

1. Transformation of the γ-Fe lattice to the α-Fe lattice
2. Precipitation of carbon as the carbide Fe_3C (cementite)
3. Coagulation of the carbides

At the temperature of point A_1 processes 1 and 2 proceed almost simultaneously, with the formation of a lamellar mixture of ferrite and cementite.

Atoms of dissolved carbon are distributed randomly in the lattice. For this reason cementite nucleates in carbon-rich regions and ferrite in carbon-depleted regions that have little if any carbon. Such a redistribution of carbon is realized through diffusion and depends on temperature and time.

When hypoeutectoid steels containing less than 0.8% C are subjected to slow cooling, the transformation starts with the formation of ferrite at grain boundaries. The boundaries act as ferrite crystallization centers. Carbon is forced inside the crystallite. As ferrite precipitates, a concentration necessary for the ferrite formation is achieved in central volumes.

When hypereutectoid steels (carbon content less than 0.8%) are subjected to slow cooling, on crossing the line ES cementite starts precipitating at grain boundaries. Here the grain boundaries also serve as crystallization sites.

The carbon diffusion rate in the lattices of γ- and α-Fe decreases rapidly as the temperature is lowered, since the diffusion coefficient depends on temperature as

$$D = D_0^{-Q/RT}.$$

Presenting an appropriate cooling rate, undercooling can be enhanced to such an extent that formation of pearlite becomes impossible.

In the range of low temperatures, the transformation mechanism and the character of the formed structure depend solely on the temperature at which the transformation takes place. Considering the degree of undercooling, three transformation temperature ranges are distinguished: (1) the pearlite range, (2) the intermediate range, and (3) the martensite range. A continuous transition from one transformation mechanism to another can take place over these temperature ranges. The processes strongly depend on the content of alloying elements, especially of carbon, in steel. They can commence by a more rapid mechanism and end by a slower one.

In the pearlite range, the transformation is characterized by the simultaneous formation of a mixture of ferrite and carbide. Free ferrite or carbides can precipitate at the austenite grain boundaries. Here the formation and growth of both phases are controlled by diffusion processes (diffusion crystallization). Diffusion of iron and other alloying elements also plays a significant part. The structure fineness is enhanced as the temperature is lowered, until a longer time is required for diffusion crystallization of ferrite and carbides.

3.3.2 Structure of Pearlite

A mechanical mixture of ferrite and carbide plates is formed on transformation in the pearlite range. The rate at which nuclei of pearlite crystallization are formed depends on supersaturation of austenite with carbide, which increases as the temperature is lowered. The rate also depends on the diffusion rate, which decreases with temperature. The growth of pearlite islets depends in the main on the diffusion rate of carbon and iron atoms. The other decisive factors are the degree of supersaturation and the free energy advantage during the ferrite formation. Pearlite islets grow not only through the formation of new plates but also by way of further growth of old plates in all directions. Carbide plates grow faster than ferrite plates. The process can start, however, with the formation of ferrite nuclei. Multiple alternations of nucleation of ferrite and cementite plates and branching of the plates of both phases lead to the formation of plane-parallel and fan-shaped pearlite plates.

Pearlite nuclei appear predominantly in the lattice regions with crystal structure defects: grain boundaries, insoluble carbides, or nonmetal inclusions such as sulfides. A very significant characteristic of pearlite is the plate-to-plate spacing. Strength properties of steel improve with a decrease in that spacing.

The formation rate of cementite and ferrite crystallization centers in the pearlite range accelerates as the temperature is lowered. The plate-to-plate spacing decreases, and the fineness of the structure increases. In the eutectoid steel, the pearlite transformation takes place on cooling to 600–700°C (1100–1300°F). In this case, the plate-to-plate spacing equals 0.5–1 μm. Precipitation of austenite over the temperature interval of 650–600°C (1200–1100°F) provides the plate-to-plate distance of 0.4–0.2 μm. In this case, the eutectoid is finer pearlite. When austenite precipitates over the temperature interval of 600–500°C (1100–930°F), an extremely fine eutectoid mixture is formed, where the plate-to-plate spacing equals ~0.1 μm.

An important characteristic that influences the properties of steel is the dimension of the pearlite colony. A decrease in the colony dimension is accompanied by a growth of the impact strength and decrease of brittleness. The critical brittleness temperature depends on the pearlite morphology as

$$T_{cr} = f\left(\frac{1}{\sqrt{d}}\right)$$

where d is the pearlite colony dimension. Thus a relatively high strength pearlite is formed in the case of the breaking of ferrite and cementite plates, forming a high density of dislocations inside the ferrite.

A better fracture strength of pearlite is achieved through spheroidization of cementite particles. The spheroidization can be facilitated by deformation of pearlite, subsequent heating, and holding at a temperature near A_{c1}. Another method providing relatively high strength and ductility of pearlite consists in deformation during pearlite transformation. This leads to the formation of a polygonal structure and spheroidization of cementite.

The yield stress of the ferrite–pearlite mixture depends on the properties of ferrite and pearlite in an additive manner:

$$\sigma_0^2 = f_\alpha \sigma_\alpha + (1 - f_\alpha)\sigma_p,$$

where f_α is the volume fraction of ferrite, σ_α is the yield stress of pearlite, and σ_p is the yield stress of pearlite.

3.3.3 Transformation of Austenite in Hypo- and Hypereutectoid Steels

The transformation of austenite in eutectoid composition steels was considered above. In hypo- and hypereutectoid steels, the pearlite transformation should be preceded by precipitation of excess phases—ferrite and secondary cementite (see the Fe–C equilibrium diagram in Figure 3.2).

The relative amount of the structurally free excess phase depends on the degree of austenite undercooling. The amount of excess ferrite or cementite decreases with an increase in the cooling rate. Given a sufficient degree of undercooling, the formation of an excess phase as an independent structural component can be avoided.

When a hypoeutectoid steel containing a small amount of eutectoid austenite is subjected to slow cooling, eutectoid ferrite grows on the grains of excess ferrite and eutectoid cementite is left as structurally free interlayers at grain boundaries. In a hypereutectoid steel, the eutectoid can also be subject to structural degeneration. Cementite, which is formed as a result of the eutectoid precipitation under a very low cooling below the point A_1 (above ~700°C or 1300°F), is deposited on secondary cementite. Areas of structurally free ferrite are found alongside.

This eutectoid transformation, which is accompanied by separation of the phases, is referred to as abnormal. In normal eutectoid transformation, ferrite and cementite grow cooperatively in the form of colonies with a regular alternation of the two phases. In the case of abnormal transformation, a coarse mixture of ferrite and cementite does not have a characteristic eutectoid structure. During a eutectoid transformation the mechanism can change from abnormal to normal. Therefore, with a rapid cooling and a correspondingly great undercooling of austenite, the abnormal transformation can be suppressed altogether.

Consider the forms and structure of excess ferrite in hypoeutectoid steels. The ferrite is found in two forms: compact equiaxial grains and oriented Widmannstatten plates (Figure 3.7). Compact precipitates of hypoeutectoid ferrite appear predominantly at austenite grain boundaries, whereas Widmannstatten plates are formed inside grains. The Widmannstatten ferrite is observed only in steels with less than 0.4% C and rather coarse grains of austenite. As the dimensions of austenite grains decrease, the share of ferrite in the form equiaxial grains grows. The Widmannstatten ferrite is formed over the temperature interval from A_3 (50°C or 90°F) to 600 to 550°C (1112–1022°F). With an increase in the carbon content of steel, the share of the Widmannstatten ferrite in the structure lowers.

It is assumed that the Widmannstatten ferrite is formed owing to a shear $\gamma \rightarrow \alpha$ rearrangement of the lattice, which is accompanied by an ordered interrelated movement of atoms. Equiaxial grains of ferrite grow by a normal diffusive rearrangement of the lattice with a disordered transition of atoms across the γ/α boundary.

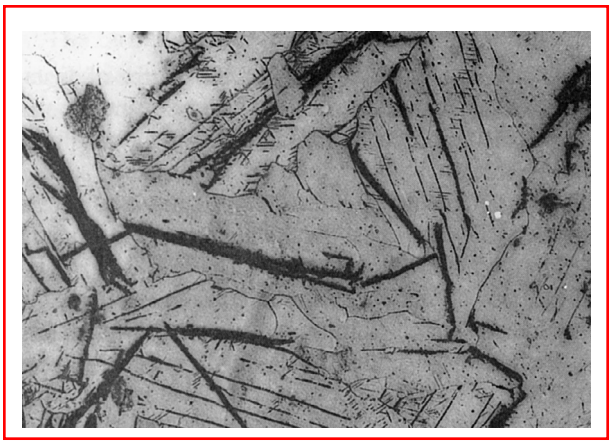

FIGURE 3.7 Structure of excess ferrite in hypereutectoid steel, 500×.

One of the methods used to strengthen steels consists in providing a structure with hypoeutectoid ferrite containing dispersed carbide precipitates. To produce such a structure, the steel should be heated until special carbides dissolve in austenite and then cooled rapidly so as to preclude the usual precipitation of carbide directly from austenite before hypoeutectoid ferrite starts forming.

3.3.4 Martensite Transformation

The martensite transformation takes place on quick cooling of the high-temperature phase, a process that is referred to as quenching. The most characteristic features of the martensite transformation in carbon steels are as follows:

1. The martensite transformation is realized on rapid cooling of steel from a temperature above A_1 in, for example, water. In this case, diffusive precipitation of austenite to a mixture of two phases (ferrite and carbide) is suppressed. The concentration of carbon in martensite corresponds to that in austenite. The main difference between the martensite transformation and the pearlite transformation is that the former is diffusionless.
2. Transformation of austenite to martensite starts from the martensite start temperature (M_s). Whereas the pearlite start temperature lowers with an increase in the cooling rate, the martensite start temperature depends little if at all on the cooling rate. Martensite is formed over a certain temperature interval. The particular temperature is determined by the carbon content of the steel (Figure 3.8).
3. Termination of cooling over the temperature interval M_s–M_f suspends formation of martensite. This feature distinguishes the martensite transformation from the pearlite

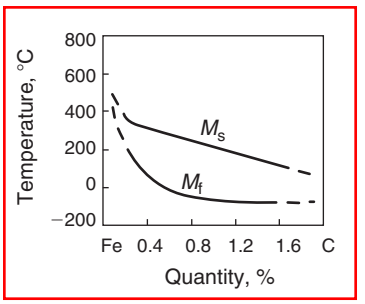

FIGURE 3.8 Martensite start M_s and finish M_f temperatures versus carbon content.

transformation. In the latter case, transformation continues to the end at a constant temperature below the point A_1, and the final result is a complete disappearance of austenite given a sufficient isothermal holding time. With the martensite transformation, a certain amount of retained austenite is left.

4. As distinct from the pearlite transformation, the martensite transformation has no incubation period. A certain amount of martensite is formed instantaneously below the temperature M_s.
5. On cooling below M_s, the amount of martensite increases rapidly owing to the quick formation of new plates. The initially formed plates do not grow with time. This feature also distinguishes the martensite transformation from its pearlite counterpart; in the latter case new colonies nucleate and old colonies continue growing.
6. The martensite lattice is regularly oriented relative to the austenite lattice. A certain orientation relationship exists between the lattices. With the pearlite transformation, lattices of the phases comprising the eutectoid mixture exhibit a random orientation with respect to the starting austenite grain.

The temperature M_s characterizes an alloy of a certain composition that has been subjected to a particular pretreatment. In a given steel, the martensite transformation starts at the same temperature whatever the cooling rate. That temperature depends on the alloy composition and decreases greatly as the carbon content of the steel is raised (see Figure 3.8). Part of the carbon enters carbides, which coexist with austenite. The carbides dissolve in austenite if the quenching temperature is elevated. Consequently, the carbon concentration of austenite increases and the M_s point lowers.

The martensite formation is characterized by a shear mechanism of the austenite lattice rearrangement. The martensitic (shear) mechanism of phase transformation is distinguished by an ordered interrelated movement of atoms to distances shorter than the interatomic spacing, and the atoms do not exchange places. An atom in the initial phase preserves its neighbors in the martensite phase. This is the main feature specific to a shear rearrangement of the lattice.

This character of the lattice rearrangement provides coherence of the boundary between the old and new phases. Coherence, or an elastic conjugation of lattices at the boundary between martensite and the initial phase, ensures a very fast movement of the boundary toward the matrix even at low temperatures. The atoms move cooperatively to distances shorter than the interatomic spacing; hence the growth of the martensite crystal.

As the martensite crystal grows, an elastic strain accumulates at the coherence boundary. On reaching the yield stress, coherence is disturbed. Atoms become disordered at the boundary between the martensite crystal and the starting matrix. Slipping movement of the boundary is rendered impossible. Hence, growth of the crystal by the martensitic mechanism is terminated, and subsequently the crystal can grow by diffusion only. But the martensite transformation takes place at low temperatures, where the diffusion rate is very small. Therefore, after coherence is broken, little if any growth of the martensite crystal is observed.

The polymorphous transformation of solid solutions by the martensitic mechanism is characterized by the absence of diffusive redistribution of the components. We consider the conditions necessary for the martensitic mechanism by which the high-temperature phase transforms to the low-temperature phase in the following discussion. The martensite transformation is impossible at a small undercooling. This is explained by the fact that in the case of a disordered rearrangement of the lattice, elastic deformation is determined by changes in the volume only, whereas with the martensite transformation, it additionally depends on coherence of the lattices of the initial and martensite crystals. As the degree of undercooling is increased, the disordered rearrangement rate of the lattice increases, achieves a maximum,

and then drops. When γ-Fe is undercooled to 911 to 750°C (1670–1380°F), the normal γ → α transformation is realized, while below 750°C (1380°F) the martensite γ → α transformation takes place. To realize the martensitic mechanism of polymorphous transformation in iron, samples should be strongly overheated in the γ range and then cooled very quickly to suppress development of the normal transformation.

3.3.5 Morphology of Ferrous Martensites

Consider the crystallogeometry of the rearrangement of the fcc lattice of austenite to the bcc tetragonal lattice of martensite, which is similar to the bcc lattice of α-Fe.

The austenite lattice transforms into the martensite lattice through the Bain deformation. The deformation consists in compression of the tetragonal cell of austenite along the *c*-axis and a simultaneous increase in dimensions along the *a*-axis. The degree of the tetragonal distortion of the martensite lattice, *c*/*a*, grows directly as the carbon concentration of martensite. The martensite lattice retains tetragonality at room temperature.

The orientation relationship of the initial and martensite phases has been established. Three basic orientation relationships are known for austenite and martensite lattices in iron alloys: those due to Kurdyumov and Zacks, Nishiyama, and Treninger and Trojano.

The Kurdyumov–Zacks relationship: (1 1 1)A ‖(1 0 1)M; [1 1 1 0]A‖[1 1 1]M.

The Nishiyama relationship: (1 1 1)A ‖(1 0 1)M; [1 2 1]A‖[1 0 1]M.

The Treninger–Trojano relationship is intermediate between the first two relationships.

Several hypotheses are available as to the character of martensite nucleation. Most of them suggest a heterogeneous nucleation at special defect sites in the starting matrix. It was shown experimentally that the sites do not include grain and subgrain boundaries, as these are not places of preferable nucleation of martensite. They might be stacking fault arising in the γ-phase during splitting of dislocations. According to other hypotheses, the sites include special configuration dislocation pile-ups or separate dislocations, which are the sources of fields of internal stresses. This decreases the work on critical nucleus formation.

By morphology, martensite can be divided into two basic types: plate and massive martensite. They are different in shape, mutual arrangement of crystals, substructure, and habit plane. Plate (needle) martensite is found most frequently in high-carbon steels and carbon-free iron alloys. Martensite crystals are shaped as thin lenticular plates (Figure 3.9). Neighboring plates are not parallel to one another.

FIGURE 3.9 Martensite plates and retained austenite (dark) in quenched steel, 1000×.

Plates that appear first pass throughout the unit, dividing it into separate parts. But they cannot cross the matrix grain boundary. Therefore, the plate dimension is limited by the dimension of the austenite grain. New martensite plates are formed in austenite sections. Here the plate dimension is limited to the dimension of the section (see Figure 3.9). If the austenite grain is small, martensite plates are so fine that the needle structure of martensite cannot be seen in it microsection specimens. Such martensite is called structureless martensite, and it is most desirable.

Massive (lath) martensite can be observed in low- and medium-carbon steels. Crystals of this type of martensite are shaped as interconnected plates having approximately the same orientation. The habit plane of laths is close to the {1 1 1}A plane. Plates of massive martensite are separated with low-angle boundaries. An electron microscopic image of massive martensite is given in Figure 3.10. As is seen, a package of plates is the main structural component. Several martensite packages can be formed in an austenite grain.

3.3.6 Bainite Transformation

The bainite transformation is intermediate between pearlite and martensite transformations. The kinetics of this transformation and the structures formed exhibit features of both diffusive pearlite transformation and diffusionless martensite transformation.

A mixture of the α-phase (ferrite) and carbide is formed as a result of the bainite transformation. The mixture is called bainite. The bainite transformation mechanism involves $\gamma \rightarrow \alpha$ rearrangement of the lattice, redistribution of carbon, and precipitation of carbide.

Most researchers are of the opinion that ferrite precipitates from austenite by the martensitic mechanism. This is attested to by the presence of retained austenite in alloyed steels, a similarity in the structure of lower bainite and martensite, and the resemblance of upper bainite to low-carbon martensite.

Closeness of the bainite transformation to its pearlite and martensite counterparts can be explained as follows. The diffusive movement of atoms of the basic component, iron, is almost completely suppressed over the bainite transformation range. Then the $\gamma \rightarrow \alpha$ formation of ferrite is difficult because pearlite precipitation is suppressed. However, carbon diffusion is rather active and causes precipitation of carbides.

Over the intermediate range the γ-phase crystals are formed through coherent growth similarly to martensite plates. But the α-phase plates are formed slowly rather than instantaneously. This is due to the fact that over the intermediate temperature range the α-phase can

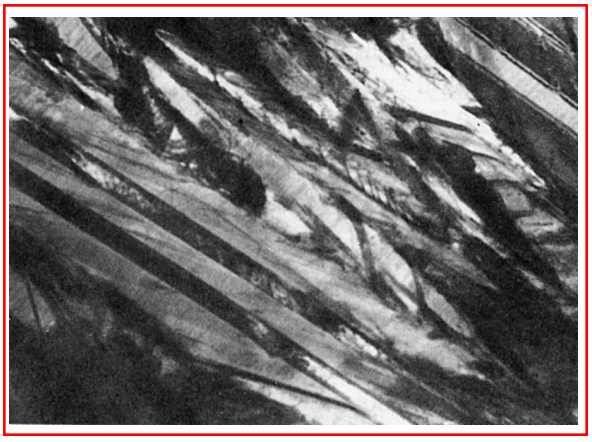

FIGURE 3.10 Electron microscopic image of lath martensite, 20,000×.

precipitate only from the carbon-depleted γ-phase. Thus the growth rate of the α-phase crystals depends on the carbon diffusive removal rate. In this case, the martensite start point M_s in austenite rises and the martensite $\gamma \rightarrow \alpha$ transformation takes place at temperatures above the temperature M_s typical of the steel with a given composition.

At the instant of martensite transformation the carbon concentration remains unchanged. Only the crystal lattice is altered and a supersaturated α solution is formed. Carbide precipitates after $\gamma \rightarrow \alpha$ transformation.

3.3.7 Morphology of the Bainite Transformation

A distinction is drawn between upper and lower bainite, which are formed in the upper and lower parts of the intermediate temperature range. The conventional boundary between the bainites is close to 350°C (660°F). Upper bainite has a feathery structure, whereas lower bainite exhibits an acicular morphology, which is close to that of martensite. The difference in the structures of upper and lower bainites is attributed to a different mobility of carbon in the upper and lower parts of the bainite temperature range.

An electron microscopic analysis showed that the α-phase substructure of upper bainite resembles the substructure of massive martensite in low-carbon steels, while the α-phase structure of lower bainite approximates the structure of martensite in high-carbon steels. In upper bainite, carbide particles can precipitate both at lath boundaries and inside laths. This fact suggests that here carbides precipitate directly from austenite. In lower bainite, carbide is found inside the α-phase. This means that carbide is formed during precipitation of a supersaturated solid solution of carbon in the α-phase. Both upper and lower bainites exhibit a high density of dislocations inside the α-phase.

Cementite is the carbide phase in upper bainite, and ε-carbide in lower bainite. As the holding time is increased, ε-carbide turns into cementite. The austenite grain dimensions have no effect on the martensite transformation kinetics.

3.3.8 Tempering

The main processes that take place during tempering are precipitation and recrystallization of martensite. Quenched steel has a metastable structure. If subjected to heating, the structure becomes closer to equilibrium. The character of the processes that occur during tempering is determined by three major features of quenched steel: strong supersaturation of the martensite solid solution, high density of crystal lattice defects (dislocations, low- and large-angle boundaries, twin interlayers), and the presence of retained austenite.

The main process taking place during tempering of steels is precipitation of martensite accompanied by formation of carbides. Depending on the temperature and duration of tempering, the martensite precipitation may involve three stages: preprecipitation, precipitation of intermediate metastable carbides, and precipitation and coagulation of cementite. Retained austenite can precipitate simultaneously.

Owing to a high density of dislocations in martensite, its substructure is similar to the substructure of a work-hardened (deformed) metal. Hence, polygonization and recrystallization can develop during tempering.

When carbon steels are tempered, supersaturation of the γ' solution in austenite increases with an increase in the carbon content of steel. This leads to lowering of the temperature M_s and transition from massive martensite to plate martensite. The amount of retained austenite also increases.

Carbon segregation represents the first structural changes that take place during tempering of carbon steels. The segregated carbon can nucleate heterogeneously at lattice defects or

homogeneously in the matrix. The heterogeneous nucleation of the segregated carbon occurs either during quenching or immediately after it.

Flat homogeneous clusters of carbon atoms that are not connected with lattice defects are formed at tempering temperatures below 100°C (212°F). Their formation is due to considerable displacements of iron atoms and the appearance of elastic distortions. As the tempering temperature is increased, the clusters become larger and their composition is close to Fe_4C. This process depends on carbon diffusion. Metastable ε-carbide (Fe_2C) is formed above 100°C (212°F). It possesses a hexagonal lattice and appears directly from carbon clusters when the carbon concentration is increased. Metastable ε-carbide can also precipitate directly from the α solution. At low temperatures ε-carbide precipitates as very fine (10–100 nm) plates or rods (Figure 3.11). With an increase in tempering temperature or time, ε-carbide particles become coarser. This carbide precipitates in steels containing a minimum of 0.2% C.

In steels having a high M_s temperature, i.e., in all structural steels, partial precipitation of martensite accompanied by deposition of excess carbide is accomplished during quench cooling in the martensite range. Then self-tempering of these steels occurs during their quenching.

Cementite, Fe_3C, is formed at a temperature above 250°C (482°F). Two mechanisms of cementite nucleation have been known. First, it precipitates directly from a supersaturated α solid solution. Cementite particles grow at the expense of the dissolution of less stable carbides. Second, cementite appears as a result of transformation of the intermediate carbide lattice to the Fe_3C lattice.

The final stage of the carbide formation during tempering is coagulation and spheroidization of carbide. These processes develop intensively starting from 350 to 400°C (660–750°F). Above 600°C (1112°F), all cementite particles have a spherical shape and undergo coagulation only.

A considerable part of the tempering process is devoted to the precipitation of retained austenite accompanied by deposition of carbides. Precipitation occurs over the temperature interval 200–300°C (400–570°F). During tempering, retained austenite transforms into lower bainite.

A decrease in the carbon concentration of the α-phase during carbide formation causes changes in the phase structure. Martensite precipitation can conventionally be divided into two stages. The first stage of precipitation is realized below 150°C (300°F). At these temperatures, the mobility of carbon atoms is sufficient for the formation of carbide plates. However, it is insufficient for the carbide plates to grow by diffusion of carbon from the areas of unprecipitated martensite with a high-carbon concentration. This results in a nonuniform

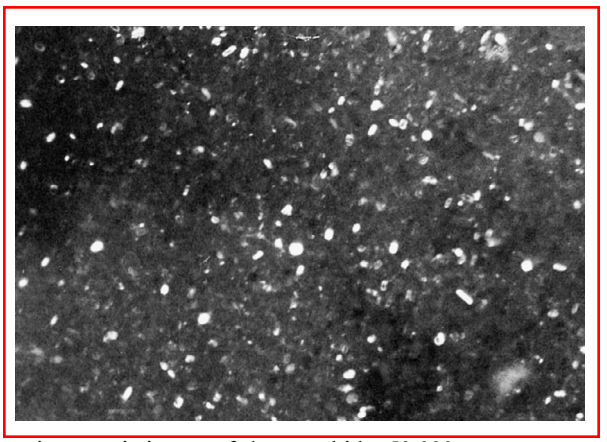

FIGURE 3.11 Electron microscopic image of the ε-carbide, 50,000×.

content of carbon in different areas of the martensite and consequently inhomogeneity of martensite with respect to its tetragonality. In areas with precipitated carbide, tetragonality is lower than in unprecipitated areas. Two solid solutions with different carbon concentrations coexist. For this reason the precipitation is referred to as a two-phase precipitation. The two-phase precipitation of martensite results from the deposition of new carbide particles in areas containing martensite with the initial carbon concentration. Carbide particles do not grow at this stage.

At the second stage of martensite precipitation (150–300°C; 300–570°F) the α solution is depleted of carbon owing to diffusive growth of carbide particles. But the process proceeds very slowly. Therefore, the precipitation kinetics are characterized by a rapid depletion of the α solution in carbon (the timespan decreases as the annealing temperature is increased). Subsequently, depletion of the solid solution in carbon stops. At 300°C (570°F) about 0.1% C is left in the α solution. Above this temperature no difference between the lattice of the α solution and that of the α-Fe is detected. Below 300°C the degree of tetragonality ($c/a > 1$) is still measurable. Above 400°C (750°F) the α solution becomes completely free of excess carbon and transformation of martensite to ferrite is finished.

As mentioned earlier, plates (needles) of quenched martensite have a high density of dislocations, which is comparable to the density of the deformed material. However, recrystallization centers and their development to recrystallized grains have not been observed. This is because carbide particles pin dislocations and large-angle boundaries. It is only above 600°C (1112°F), when the density of the particles decreases owing to their coagulation, that recrystallization growth of grains takes place at the expense of migration of large-angle boundaries. Therewith the morphological features of lath martensite vanish. These processes are hampered in high-carbon steels in comparison with low-carbon alloys, because the density of carbides is greater in high-carbon steels. The acicular structure is retained up to the tempering temperature of about 650°C.

The structural changes that occur during tempering cause alteration of steel properties. They depend on the tempering temperature and time. Hardness lessens as the tempering temperature is raised.

3.4 KINETICS OF AUSTENITE TRANSFORMATION

3.4.1 Isothermal Transformation Diagrams

To understand the kinetics of transformations to austenite, it is important to follow the process at a constant temperature. To this end, a diagram was constructed that characterizes the isothermal process of austenite precipitation. In this diagram, the transformation time is the abscissa on the logarithmic scale and the temperature is plotted on the ordinate (see Figure 3.12). From this diagram, the incubation period (left-hand curve) can be determined and also the time required for completion of the process (right-hand curve). The instant an alloy passes the points A_3 and A_1 during quenching is usually taken as the zero time reference. The time required to achieve the temperature of the quenching medium is often neglected. The start and finish of the transformation are difficult to determine from the transformation curve behavior at the initial and final sections of the curve. Therefore, the lines of the isothermal transformation (IT) diagram usually correspond to a certain final volume that underwent transformation, e.g., 3 and 97% for the transformation start and finish, respectively. The volume value is usually not shown in the diagram.

In addition to the above-mentioned curves, the diagram often contains intermediate curves that correspond to certain values of the transformed volume, e.g., 10, 50, or 90%. A decrease in the transformation rate causes displacement of the transformation start and

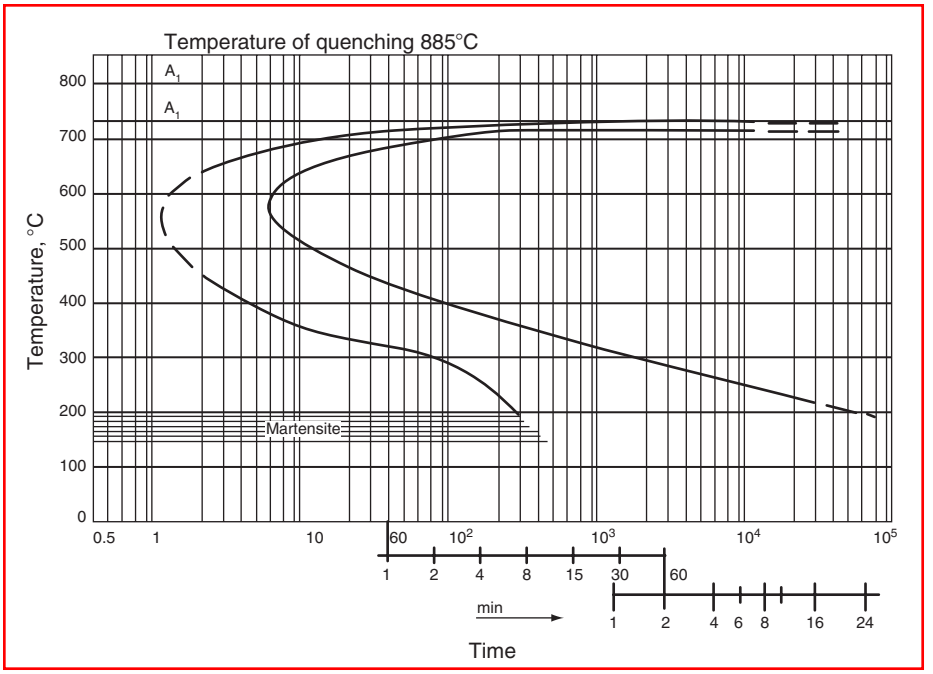

FIGURE 3.12 Isothermal transformation diagram.

finish curves to the right, i.e., toward greater duration. This phenomenon can be observed if the quenching heating temperature rises as a result of a decrease in the number of foreign inclusions, enlargement of austenite grains, etc.

An increase in the transformation rate leads to displacement of the IT curves to the left. This phenomenon can be accounted for by a decrease in the quenching heating temperature, the presence of carbides or foreign inclusions, and refinement of the austenite grain. For a given steel the temperature that corresponds to a maximum transformation rate (the so-called nose of the sigmoid curve) does not, as a rule, change significantly.

3.4.2 Continuous-Cooling Transformation Diagrams

Continuous-cooling transformation (CCT) diagrams consider the transformation kinetics of a eutectoid steel. The major transformation that takes place during annealing cooling of steel is a eutectoid precipitation of austenite into a mixture of ferrite and carbide. The eutectoid transformation kinetics are given by IT diagrams of austenite (Figure 3.13) at a temperature of 727°C (1340°F). The structure obtained after tempering below 300°C (572°F) is called tempered martensite. An acicular structure is observed after tempering at 300–450°C (572–842°F). Tempering over the temperature interval of 450–600°C (842–1112°F) exhibits a pronounced dot structure. The structure obtained after tempering below 300°C (572°F) is called tempered martensite. Austenite is in a thermodynamically stable equilibrium with the ferrite–cementite mixture. Stability of undercooled austenite is defined by a period of time during which the appearance of precipitation products in the diagram cannot be registered by conventional methods (see Figure 3.13). It is equal to the distance from the *y*-axis to the left-hand curve. The degree of austenite undercooling is the main factor that determines the steel microstructure. The necessary degree of undercooling is provided by either continuous cooling or isothermal treatment. The diagram in Figure 3.13 shows the entire range of structures formed in a eutectoid steel depending on particular undercooling conditions.

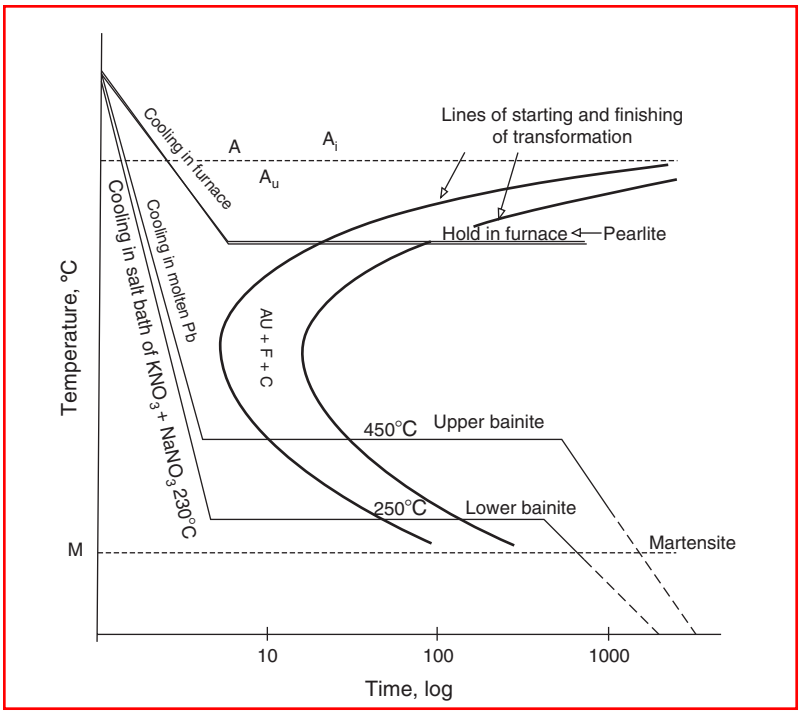

FIGURE 3.13 Isothermal transformation diagram for a eutectoid composition steel. A, stable austenite; A_u, undercooled austenite; F, ferrite; C, carbide.

3.4.2.1 Transformations That Take Place under Continuous Cooling of Eutectoid Steels

As mentioned above, in hypoeutectoid steels the formation of pearlite is preceded by precipitation of hypoeutectoid ferrite. With a decrease in the transformation temperature and a rise in the degree of undercooling, precipitation of hypoeutectoid ferrite is suppressed. The amount of pearlite increases and the carbon content becomes less than that in pearlite of the eutectoid steel. In the region of the maximum transformation rate, the two curves merge. Thus, a purely pearlitic structure is formed in steel with 0.4% C (Figure 3.14). In steels containing greater amounts of carbon, the precipitation of ferrite cannot be suppressed even if the carbon content decreases. Ferrite precipitation precedes the formation of pearlite

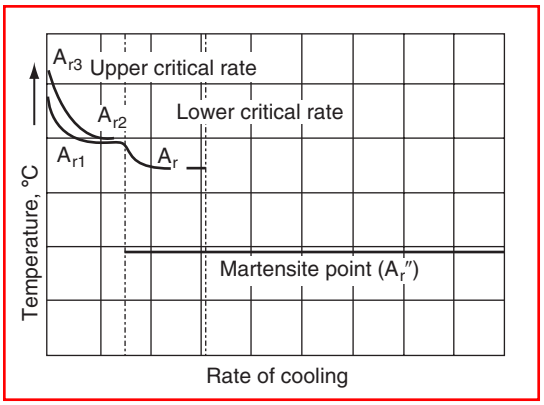

FIGURE 3.14 Schematic diagram showing changes in location of the critical points depending on the particular cooling rate.

even at a maximum transformation rate, but the amount of ferrite will be less than that was formed at smaller undercooling.

These propositions are valid for the precipitation of cementite in hypereutectoid steels, but it can be suppressed even at relatively small undercooling. In this case, the carbon content of pearlite becomes higher than that in the eutectoid steel.

As a result of suppression of the hypoeutectoid ferrite precipitation under continuous cooling from the region of the γ solid solution, the point A_{r3} lowers much faster than the point A_{r1} as the cooling rate is increased. Given a certain cooling rate, both points merge into one point A'_2 (see Figure 3.14), which corresponds to the formation of a fine plate structure of the pearlite type free of ferrite.

Under continuous cooling the transformation process can also be pictured as diagrams in temperature–time coordinates (Figure 3.15). Hence the behavior of cooling curves should be analyzed to obtain characteristics of the transformation processes. In this diagram, the ferrite and pearlite start lines are shifted toward longer periods of time compared to the IT diagram of Figure 3.13. This is due to an increase in the temperature interval necessary for preparing the transformation processes in the austenite lattice. As a result, only part of the incubation period, which is required for the IT to start, is effective. In this case, the incubation period is the mean of the effective lengths of time corresponding to different periods of time in the given range. This proposition can be used to calculate the behavior of the transformation start line in the pearlite range from the IT diagram. The reverse calculation is also possible.

Similar to the pearlite range, in the bainite temperature range, the precipitation of undercooled austenite starts after a certain incubation period. Resemblance of the bainite and pearlite transformation kinetics consists not only in the presence of an incubation period but also in the character of the volume increase during isothermal soaking: the fraction of the transformed volume of austenite increases first with acceleration and then with deceleration. At the same time, as in the case of the martensite transformation, retained austenite does not disappear completely during the bainite transformation. Every point in the bainite finish curve corresponds to a certain amount of retained austenite. Similar to the pearlite transformation, the bainite transformation can take place both during isothermal soaking and under continuous cooling (see Figure 3.15). Austenite that has not been transformed over the bainite range turns partially into martensite

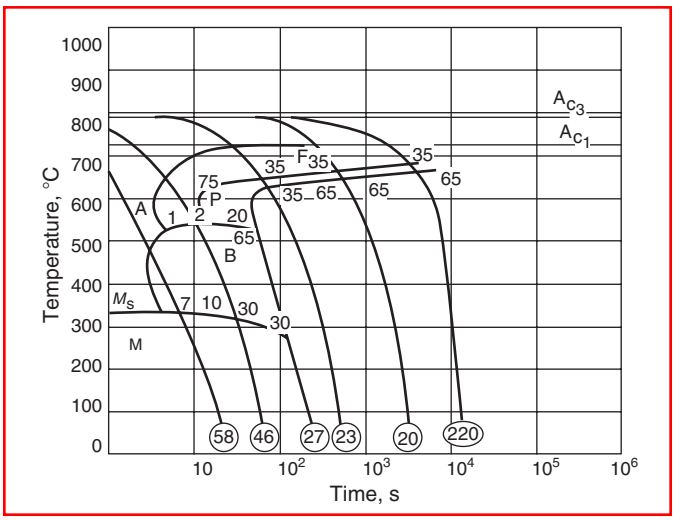

FIGURE 3.15 Continuous-cooling transformation (CCT) diagram. A, austenite range; F, ferrite range; P, pearlite range; B, bainite range; M, martensite range. Shown in circles is hardness HV or RC. Numerals at the curves denote the relative amounts of structural components.

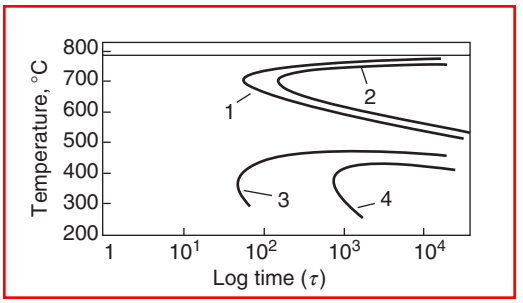

FIGURE 3.16 Diagram of isothermal precipitation of austenite in steel with 0.43% C and 3% C. Curve 1, pearlite formation start; curve 2, pearlite formation finish; curve 3, bainite formation start; curve 4, bainite formation finish.

when the steel is cooled to room temperature. Because after the bainite transformation austenite is inhomogeneous with respect to the carbon content, martensite is formed predominantly in carbon-enriched regions.

In the case of high-alloy steels, isothermal curves can be separated by a temperature interval in which undercooled austenite is highly stable. In this interval, pearlite precipitation does not take place for many hours, while undercooling is insufficiently great for the bainite transformation (Figure 3.16). In carbon steels, the bainite transformation proceeds concurrently with the pearlite transformation. Products of the pearlite transformation dominate at higher temperatures, and those of the bainite transformation at lower temperatures.

3.4.2.2 Transformations of Austenite on Cooling in the Martensite Range

The martensite component in the steel structure appears when the cooling rate achieves a certain value. The minimum cooling rate at which the martensite component is formed is called the lower critical rate of cooling. The rate at which transformations by the pearlite and bainite mechanisms are suppressed completely is referred to as the upper critical rate of cooling (quenching). If the conditions of austenite formation (austenitization temperature and the holding time at this temperature) and the cooling conditions (cooling rate should exceed the upper critical rate) are constant, the location of the martensite point M_s depends only on the content of carbon and alloying elements in the steel.

If the cooling rate is high, the formation rate of separate needles of martensite is also high, and transformation of austenite to martensite commences on reaching M_s. It continues on subsequent cooling to lower temperatures. As the temperature of the quenching medium is lowered, the amount of formed martensite rises first rapidly and then slowly. With an increase in the quenching heating temperature (austenitization temperature), the transformation also shifts toward lower temperatures (Figure 3.17) as more of the alloying elements are taken into solution. A certain amount of martensite may be formed during isothermal holding, but it is not high in carbon steels. Retained austenite is stabilized during isothermal holding. As a result, more martensite is formed during subsequent cooling. Formation of martensite stops at the point M_f.

Figure 3.18 shows a relationship between some factors that influence the stabilization of martensite. As is seen, if continuous cooling is stopped at the temperature T_{h1} and a holding time is allowed at this temperature, the formation of martensite starts after passing through a certain temperature interval rather than immediately when cooling is resumed. Subject to cooling below the point M'_s, further formation of martensite takes place. If holding is realized at a lower temperature, T_{h2}, the effect of stabilization is enhanced, because further formation of martensite commences at the temperature M_{s2} after passing through a greater temperature

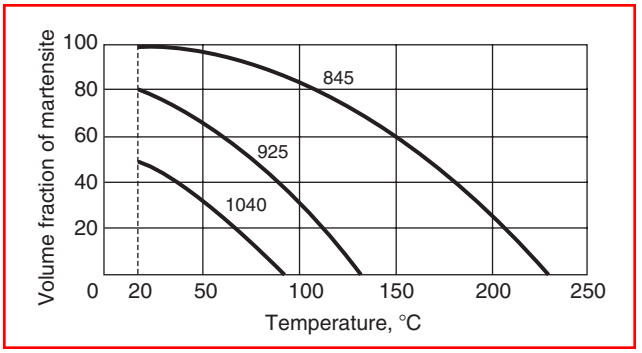

FIGURE 3.17 Curves showing variation of the relative amount of martensite as a function of the transformation in steel with 1.1% C and 2.8% Cr for different homogenization temperatures.

interval (curve 3, Figure 3.18). The effect of stabilization increases with the amount of martensite in the structure or, the amount of martensite being equal, with temperature. Joining of the points M'_s determined after holding at different temperatures yields a curve that intersects the curve that corresponds to the relative amount of martensite formed under continuous cooling. The point of intersection of the curves, σ_s, means that stabilization of austenite is impossible at a higher temperature.

3.4.3 Derivation of the Continuous-Cooling Transformation Diagram from the Isothermal Transformation Diagram

When solving practical problems involved in thermal treatment of steel, it is often necessary to know how the continuous cooling rate affects the structure formed as a result of austenite transformation. To this end, attempts were made to establish the relationship between the transformation kinetics of austenite under isothermal conditions (IT diagram) and under continuous cooling (CCT diagram). The attempts started from the concept of additivity of the transformation processes at different temperatures. It was assumed that holding of undercooled austenite at a preset temperature is part of the incubation period. It was found, however, that calculated and experimental data coincide satisfactorily only if the pearlite transformation is continuous.

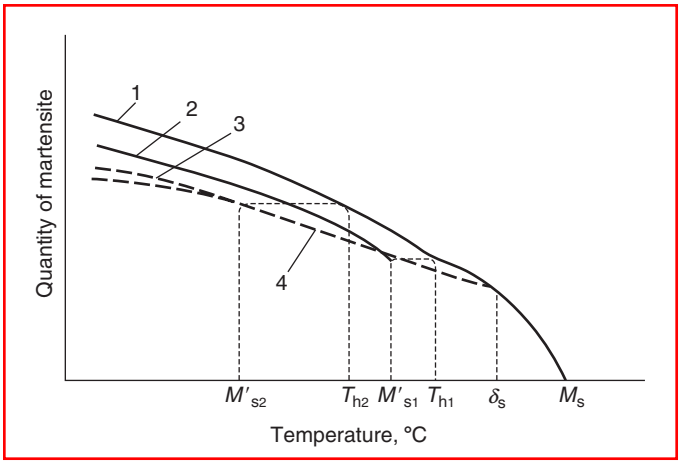

FIGURE 3.18 Curves showing the relative amount of martensite as a function of the austenite stabilization temperature. 1, Under continuous cooling; 2, after isothermal holding at T_{h1}; 3, after isothermal holding at T_h; 4, M'_s curve, τ_s is the limiting stabilization temperature.

If the pearlite transformation is preceded by precipitation of eutectoid pearlite or the pearlite and bainite transformations occur concurrently, calculated data are at a discrepancy with the experimental data. It was found that the discrepancy is due to the following factors:

1. Holding of austenite during the time accounting for fractions of the incubation period causes acceleration of the subsequent intermediate transformation at the expense of preparatory processes.
2. Precipitation of hypoeutectoid ferrite alters the austenite composition. This delays the subsequent intermediate transformation.
3. Partial transformation of austenite over the intermediate range decreases the rate of the said transformation at lower temperatures and facilitates an increase in retained austenite. This is due to a redistribution of carbon and enrichment of the nontransformed part of austenite in carbon.
4. A change in the cooling rate over the martensite range affects stabilization of austenite in different ways.

For this reason, special methods of constructing thermokinetic transformation diagrams of austenite subject to continuous cooling were elaborated for noneutectoid steels (see Figure 3.15). From these diagrams it is possible to determine the critical rate of quenching cooling or continuous cooling that is necessary to complete a particular stage of austenite precipitation.

3.4.4 Continuous-Cooling Transformation Diagram as a Function of the Bar Diameter

When steel is subjected to martensitic hardening, it should be cooled from the quenching temperature so that on undercooling to a temperature below the M_s point austenite has no time to precipitate and form a ferrite–carbide mixture. To achieve this, the cooling rate should be less than the critical value. The critical cooling rate is the minimum rate at which austenite does not precipitate to a ferrite–carbide mixture. Of course, the cooling rate of steel products is nonuniform over their cross section. It can be higher than the critical rate on the surface and lower than the critical rate at the center.

The critical cooling rate at different points of a product can be directly determined from an IT diagram (Figure 3.19). In the first approximation, it is given by the slope of the tangent to the C curve that denotes the austenite precipitation onset. This method gives a value that is

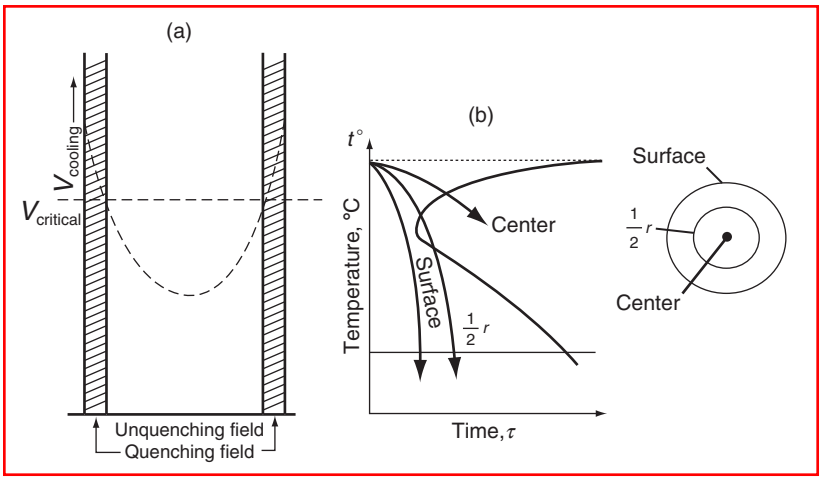

FIGURE 3.19 Diagram showing distribution of the cooling rate over the cross section of a sample and the corresponding IT curve.

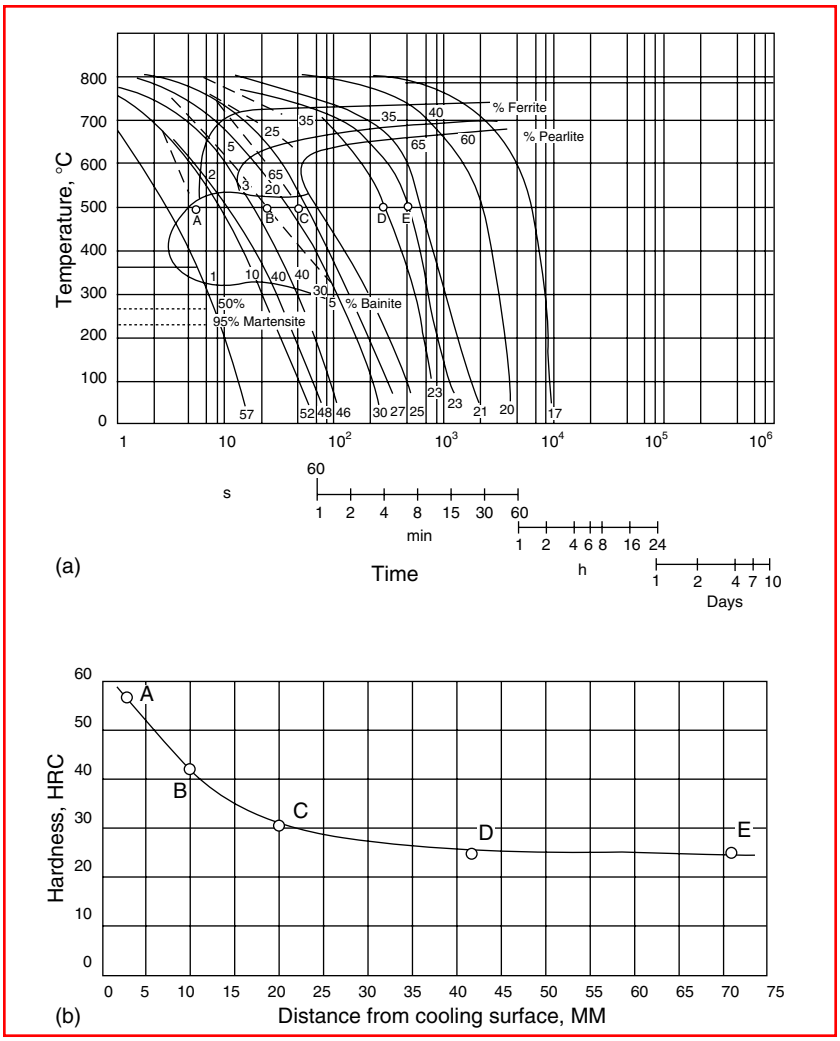

FIGURE 3.20 (a) Time–transformation temperature diagram for continuous cooling of steel containing 0.38% C compared with (b) the process of the sample's cooling during face quenching. Numerals at the bottom of the curves denote hardness (RC) after cooling to room temperature.

about 1.5 times the true critical rate. The cooling rate can be determined more accurately if one uses thermokinetic diagrams (Figure 3.20). Intercepts of the cooling curves with the lines of the thermokinetic diagrams show the start and finish temperatures of the corresponding transformation.

From the transformation diagram it is possible to determine, for example, the rate that will provide 50% martensite in the structure or the rates at which the entire transformation occurs in the pearlite range, i.e., hardening is excluded altogether. Because the data on the critical hardening rate depend on cooling time and should be associated with a particular temperature (at which direct measurements of the hardening rate are practically impossible), it is appropriate to specify the cooling time for a specific temperature interval, for example, from the point A_3 to 500°C (932°F). Point A_3 in the diagram is the time reference. Then it is possible to straightforwardly determine the critical cooling time K: K_m for fully martensitic hardening; K_f for initial appearance of ferrite; K_p for full transformation in the pearlite range. Since the cooling time (see Figure 3.20) and the progress of the subsequent cooling of the

sample during end-face hardening are known, the outcome of hardening can be determined from the transformation diagram. It should be remembered that a transformation diagram is valid only for particular conditions of melting and homogenization. Deviations in the composition or grain dimensions cause changes in the trend of thermodynamic curves. This is explained by the fact that an increase in the homogenization temperature and time and, consequently, enlargement of the grains enhance the stability of austenite. Conversely, refinement of grains lowers the critical cooling rate, because stability of austenite decreases with an increase in the extent of grain boundaries.

3.4.5 Definition of Hardenability

The depth of the hardened zone is termed hardenability. This is one of the most important characteristics of steel. Since the cooling rate is nonuniform along the cross section of a sample (see Figure 3.19), austenite can pass into martensite in surface layers only, while at the center of the sample austenite undergoes the pearlite transformation. In the first place, hardenability depends on the critical cooling rate. An examination of the temperature curves (see Figure 3.20) plotted for different areas of the sample shows that the cooling rate of the core of a large-diameter product is lower than the critical value and therefore the core is not martensitically hardened. Martensite is present in the surface layer only.

After hardening treatment, a bulky part with a large cross section may exhibit the entire range of structures: a smooth transition from martensite near the surface through troostite–martensite and troostite to pearlite at the center.

The geometry of samples can influence the character of the cooling curves. However, given the same surface-to-volume ratio, the curves coincide in general. The greatest changes in the cooling rate are incurred by the diameter of samples.

Considering what has been said above, to achieve a through hardening of bulky products or full martensitic hardening to the core of a product, one has to provide the critical hardening rate along the entire cross section of the product. IT and CCT diagrams can be used to determine this rate. The diagrams were plotted for different grades of steel, taking into account the progress of cooling in different sections and in different hardening media.

Note that hardenability depends on the steel composition, specifically on the carbon content. Hardenability of each grade of steel is presented as a hardenability band (Figure 3.21). These diagrams have been plotted for almost all existing grades of steel. They show how to achieve hardening of a product made of a particular steel.

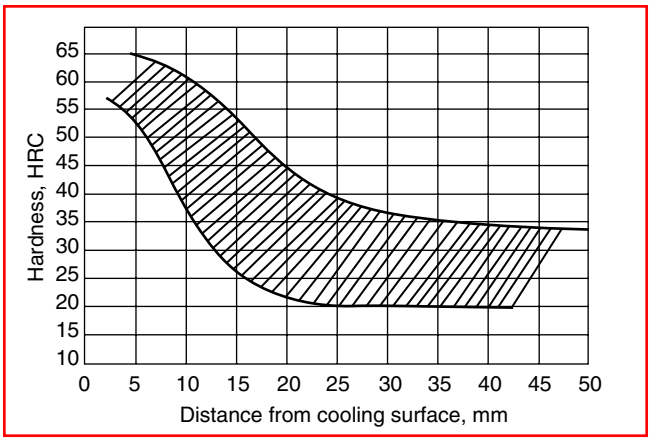

FIGURE 3.21 Steel hardenability band.

Hardenability of steel is also characterized by transformation time–temperature curves (IT curves). The more the curve is shifted to the right along the abscissa axis, the greater is the hardenability of the steel. This is explained by the fact that the rightward shift of the IT curve is due to better stability of austenite.

An improvement in the stability of undercooled austenite and hence an increase in the critical hardening rate lead to a greater depth of hardening. Then hardenability depends on all the factors that improve the stability of undercooled austenite. For example, the stability of austenite can be raised by alloying steel with chromium and tungsten. These elements lower the austenite precipitation rate and can make a steel an air-hardening one. Steel with a usual (commercial) content of impurities is hardened to a strength ten times that of a pure iron–carbon alloy.

Elevation of the hardening temperature favors an increase in the hardening depth thanks to the homogenization of austenite and enlargement of austenite grains. Refinement of grains impairs hardenability as grain boundaries affect the stability of austenite.

The hardening depth also depends on the hardening medium used. The greater the intensity of cooling, the greater the depth of hardening. Besides, the hardening depth depends on the cross-sectional diameter of the products. The critical diameter is that of the greatest cross section that lends itself to through hardening in a given hardening medium. The critical diameter is different for different hardening media and characterizes the hardenability provided by a particular method only.

Hardenability has an effect on the mechanical properties of steel. In the case of through hardening, the properties do not differ along the cross section of a product. Otherwise they decrease from the surface to the center. Let us analyze the influence of hardenability on the properties of steels that were tempered after hardening. A high temperature favors equalization of hardness along the cross section. However, the structure of weakly hardenable steels remains inhomogeneous; a grain structure will appear on the surface, where martensite is formed during quenching, while a lamellar structure will remain at the center. A grain structure will be present along the entire cross section of a through-hardening steel. This determines the character of changes in the properties of steels with different hardenability. The properties that are independent of the cementite form (yield stress, specific elongation, impact strength) will differ. A decrease in σ_s and a_k is observed at the center of nonthrough-hardening steels, while in a through-hardening steel these quantities remain unchanged along the cross section.

The properties of tempered steels (fracture stress, yield stress, impact strength, reduction of area) are impaired if ferrite precipitates during quenching. The mechanical properties of a product depend on its cross-sectional area. To obtain the best mechanical properties in the tempered state, a grain structure should be provided along the entire cross section; i.e., through hardenability should be ensured in the quenched state.

3.5 GRAIN SIZE

3.5.1 Structure of Grain Boundaries

When analyzing any processes or properties associated with grain boundaries, it is necessary to know the structure of the material. The overwhelming majority of structural materials are polycrystalline. They comprise a set of grains separated by boundaries. The grain boundary is one of the basic structural elements in polycrystalline materials.

The grain boundary represents an interface between two differently oriented crystals. This is the region of crystal imperfection. It is capable of moving and adsorbing impurities. The boundary has a high diffusive permeability.

In polycrystalline materials, the boundaries determine the kinetics of many processes. For example, movement of grain boundaries controls the process of recrystallization. A high

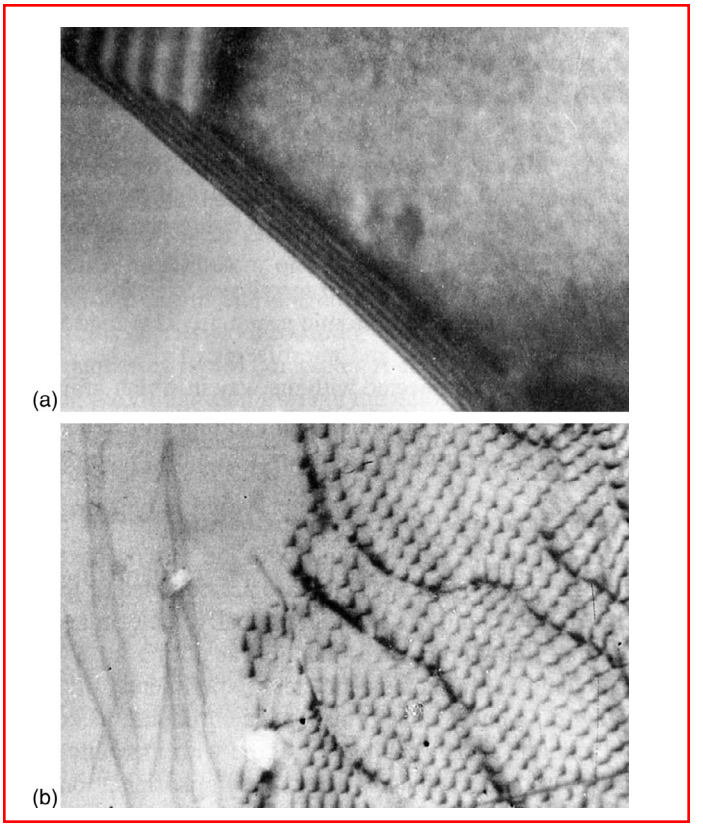

FIGURE 3.22 Electron microscopic image of (a) low-angle boundary and (b) large-angle boundary, 50,000×.

diffusive permeability of grain boundaries determines the kinetics of diffusion-dependent processes at moderate temperatures. Grain boundaries adsorb impurities. Embrittlement of metal material is connected with enrichment of grain boundaries in impurities.

Grain boundaries may conventionally be divided into two large groups: low-angle and large-angle boundaries. Low-angle boundaries (or subgrain boundaries with an angle of less than 10°) represent networks or walls of dislocations. The structure of large-angle boundaries is much more complicated. Figure 3.22 shows both types of grain boundaries.

The progress in understanding the structure of grain boundaries is connected with elaboration of the models describing the observed microscopic properties of the boundaries.

3.5.1.1 Structural Models

The pioneering structural model is the model of an amorphous boundary. It allows an explanation of the value of the surface tension Γ_3 and the grain boundary slip. In terms of this model, it was assumed that the usual boundary with a large angle has random regions of incontingency similar to a liquid. The width of the regions does not exceed three atomic diameters. In later models, amorphous portions of the boundaries were added with crystalline portions. According to Mott and coworkers [1,2], Γ_3 represents portions of good and poor contingency. In the opinion of Smoluchowski [3,4], even when the boundary angle exceeds 15°, dislocations combine themselves into groups and form incontingency regions separated by undistorted areas. If the misorientation angle is greater than 35°, then Γ_3 is a solid region of incontingency. Geisler and Hill [5] and Hargreaves [6] described the grain boundary in

terms of the model of a transition lattice. According to this model, a certain system in the arrangement of atoms exists in Γ_3. The arrangement corresponds to a minimum energy possible under given conditions.

At certain mutual orientations of neighboring grains (special orientations), a superlattice, which is common for both grains, may appear. The superlattice sites will be atoms that are common to the crystal lattices of both grains. The boundaries lying in close-packed planes of such superlattices will be most favorable with respect to energy. If the misorientation angle is small, the coincidence is upset.

Coinciding atoms are present in the boundary plane for some discrete values of the grain misorientation angles. Boundaries that meet the conditions required for the coinciding atoms to appear are called partial contingency (or special) boundaries.

Direct experimental studies of Γ_3 are scarce. Microscopy studies and transmission electron microscopy have shown that the transition zone occupies two to three interatomic spacings. The zone is saturated with defects like grain boundary dislocations, steps, and microfacets.

Particular grain boundary characteristics are closely connected with the way in which grain boundaries are formed. A grain structure, and correspondingly Γ_3, can be formed as a result of crystallization from the liquid state, phase transformations in the solid state, or recrystallization annealing of a deformed material during deformation.

Only conjectures can be made as to the formation of grain boundaries during crystallization. Under real conditions of crystallizations the growth of crystals often exhibits an oriented rather than chaotic character. Correspondingly, the spectrum of boundaries in a cast material should differ from the random distribution.

In the case of recrystallization in the solid state, i.e., polymorphous transformations of metals and alloys, the new phase has certain orientation relationships with the initial phase. Obviously, when transformations within a single grain of the matrix phase are completed, the formed boundaries should have strictly defined and crystallographically determined misorientations rather than random orientations. Many boundaries that appear during a polymorphous transformation are close to special boundaries of coincident sites. Experimental studies into misorientations of the crystals formed during phase transformations in chromium–nickel steel and titanium alloy showed that misorientations at real boundaries agree with theoretical ones (what is meant here is the calculation of crystallographically determined misorientations for the fcc–hcp and hcp–fcc, hcp–bcc and bcc–hcp, and fcc–bcc transformations). Then the crystallogeometry of the boundaries resulting from polymorphous transformations is controlled by orientation relationships of the phases formed.

In the case of recrystallization processes, the grain structure depends on the stage of recrystallization at which annealing was stopped. During primary recrystallization the formation of the structure starts with the appearance of nuclei, that is, dislocation-free portions of the matrix. They are surrounded by large-angle Γ_3. The proposed models of nucleation assume that nuclei of new grains are formed near the initial Γ_3 owing to a rearrangement of intergrain lattice dislocations. However, it has been established recently that new grains with large-angle boundaries can be formed without participation of intergrain dislocations but rather during splitting of initial boundaries. This process can be accounted for in the following way. After plastic deformation the grain boundaries are in a nonequilibrium state owing to the trapping of lattice dislocations. During annealing the grain boundary structure regains the equilibrium state at the expense of splitting of the boundaries. Splitting of the boundaries during recrystallization is caused by lowering of the total energy of the grain system because high-energy boundaries are replaced by low-energy ones. Here mutual misorientations depend on misorientation of the nuclei in the deformed matrix.

At subsequent states of recrystallization the grains become coarser owing to migration of the boundaries. One would expect that the average statistical trend of the process should be

toward formation of low-energy special boundaries. However, the available experimental data are contradictory. This fact suggests that in addition to the tendency to a thermodynamic equilibrium, kinetic factors (different mobility of the boundaries, their pinning by impurities and precipitates) play an important role in the process of structure formation during annealing. It was found, for example, that at the stage of collecting recrystallization, random boundaries dominate in iron and molybdenum alloys. However, in ultrapure aluminum the fraction of these boundaries decreases with an increase in the recrystallization temperature and time. In contrast, in commercially pure aluminum the fraction of special boundaries decreases.

The state of grain boundaries in a material depends not only on their misorientation but also on the content of lattice defects. For this reason the boundaries of recrystallization nuclei are not in equilibrium; they are formed in the regions of the deformed matrix with an excess density of dislocations of like sign. Rearrangement of the dislocations within the nucleus boundaries is not complete. A nonequilibrium state of the boundaries is also preserved during their migration through the deformed matrix as the matrix absorbs lattice dislocations. Then the boundaries are nonequilibrium in ultrafine grain materials formed at the early stage of recrystallization. The degree of boundary nonequilibrium decreases at later stages of recrystallization during collecting growth of the grains.

Grain boundaries of the deformation origin can be divided into two groups: grain boundaries formed at a low-tempered (<0.3–$0.4T_{melt}$) deformation and those formed under deformation at high temperatures.

At low temperatures new boundaries are formed at relatively large degrees of deformation. First they represent broken boundaries, which appear nonuniformly in separate grains of a polycrystal. A continuous network is formed in the areas adjacent to the initial boundaries. It is only under large deformations that a network of these boundaries covers the whole volume. On the average, two out of three boundaries are large-angle ones. In this case, the fraction of special boundaries is small.

When subject to deformation at high temperatures, the formation of grain boundaries is due to development of recrystallization processes directly during deformation. This phenomenon is called a dynamic recrystallization. The grains formed during a dynamic recrystallization are large-angle ones. Data on crystallogeometrical parameters of these boundaries are very scarce.

From the above discussion it appears that, depending on their origin, grain boundaries have different structures and therefore possess different properties. The properties of polycrystalline materials are largely determined by the extent of these structural components, which is controlled by the grain size.

3.5.2 Determination of Grain Size

The size of the grain that is formed under a given treatment is determined from microsections after their etching. For carbon and alloyed steels the following reagent is used: 1–5 ml $HNO_3 + 100$ ml ethyl or methyl alcohol. Austenitic steel is etched in a copper sulfate chloride solution containing 10 g copper sulfate, 50 ml hydrochloric acid, and 50 ml water. When carbon low-alloy steels are etched, the reagents turn pearlite dark and make visible the ferrite grain boundaries, the martensite structure, and tempering products. The etching rate rises with the amount of nitric acid. The etching time is from several seconds to a minute. Etching of austenitic steel reveals the austenite structure and the austenite grain boundaries.

Carburization is also used to establish the austenite grain boundaries. In this case, samples are heated to 930°C (1700°F) in a carburizing medium (e.g., a mixture of 40% $BaCO_3$ and 60% charcoal), cooled, and etched.

In addition, an oxidation method is used according to which microsections are heated in vacuum to a temperature 20–30°C (35–55°F) higher than the quenching temperature and are soaked for 3 h. Subsequently air is fed to the furnace for 30–60 s, and the samples are cooled in water. Before quenching it is recommended to heat samples in a borax melt at 930–950°C (1700–1750°F) for 30–40 s and then cool them in water. After these treatments microsections are polished and etched in a 15% solution of hydrochloric acid in ethyl alcohol. Grain boundaries are seen as the oxide network.

Apart from this, use is made of the method of etching austenite grain boundaries, the method of the network of ferrite (for steels with a carbon content of up to 0.6%) or cementite (for hypereutectoid steels), and the method of the pearlite network for steels that are closer in composition to eutectoid steels.

The grain size is determined by comparing the observed microstructure at a 100× magnification with standard scales (the scales are elaborated so that at a magnification of 100× the grain number N corresponds to the formula $n = 8 \times 2^n$, with n the number of grains per 1 mm^2 of the microsection area) or by counting the number of grains per unit area of the microsection, or by calculating the mean nominal diameter of the grains or their number per cubic millimeter.

The number of grains (at least 50) is counted on the focusing screen of the microscope or from a photomicrograph within the area bounded by a circle 79.8 mm in diameter. At 100× magnification this value corresponds to a microsection area of 0.5 mm^2. The total number of grains is calculated from the formula $m_{100} = m + 0.5m_1$, where m is the number of grains inside the circle and m_1 is the number of grains intersected by the circle. The number of grains per mm^2 of the microsection is $M - 2m_{100}$. If a magnification other than 100 power is used, $M = 2(g/100)^2 m_g$ (g the magnification power used and m_g the number of grains counted at this magnification power). The mean number of grains (M_{mean}) is calculated using three characteristic areas.

The mean area (S_{mean}) and diameter (d_{mean}) of the grains are calculated using the formula

$$S_{mean} = 1/M_{mean} \quad \text{and} \quad d_{mean} = 1(M_{mean})^{1/2}.$$

The values of equiaxial grains are characterized by the mean nominal diameter, which is determined on the focusing screen of the microscope or from a photomicrograph. For this purpose several arbitrary straight lines are drawn so that every line intersects at least ten grains. The number of intersections on the length of all the lines is counted. Finally, the mean diameter of the grains is calculated.

Statistical methods are used, and bar charts are plotted to obtain quantitative characteristics of the structure, particularly grain dimensions. The mean diameter of grains is calculated using the distribution curve.

It is possible to calculate the mean area of grains (S_{mean}) from the formula used to determine d_{mean} if one assumes that the grain is spherical in shape ($x = \pi D^2/4$): $S_{mean} = k^2\ \varepsilon(\pi D^2/4)\ m/\varepsilon m$. Then the number of grains (N) per mm^2 is found from the formula $N = 1/S_{mean}$.

3.5.3 Austenite Grain Size Effect and Grain Size Control

The austenite grain boundary structure that is produced on heating above the critical points is important because the austenite transformation products formed during cooling (martensite, pearlite, etc.) appear inside austenite crystals. A coarse austenite grain determines a coarse plate structure of martensite during quenching or a coarse cellular network of ferrite (cementite) precipitates at the boundary of the initial austenite grains during annealing or normalization. The pearlite structure is also the coarser, the larger the pearlite grain.

As is known, a coarse-grain structure of steel (ferrite–pearlite, martensite, etc.) is characterized by lower mechanical properties. For this reason a fine-grain structure of steel is preferable in practice. Then the primary task is to produce fine-grain austenite. Since austenite appears during heating of a ferrite–carbide mixture, growth centers of the austenite phase are very numerous, and initially austenite grains are extremely small, on the order of 10–20 μm. But with an increase in the heating temperature or holding time in the austenite range, the grains begin to grow intensively.

Two types of steels exist: hereditarily coarse-grained steels and hereditarily fine-grained steels. This difference is due to the grain growth kinetics with an increase in temperature. In hereditarily coarse-grained steels a grain gradually and rather uniformly becomes larger as the temperature is raised above A_{c3}. In hereditarily fine-grained steels, fine grains are preserved up to about 950°C (1750°F). On transition through the coarsening temperature, separate grains start growing intensively and variations in grain size arise. Near 1100–1200°C (2000–2200°F), grains of hereditarily fine-grained steels may be even larger than those of hereditarily coarse-grained steels.

Such differences in the growth of grains in steels are explained by the differences in number and state of disperse nonmetal inclusions such as, above else, aluminum nitrides, certain carbides, and oxides. These articles retard movement of grain boundaries until temperatures are reached at which the particles dissolve in austenite. The barrier effect of the particles diminishes nonuniformly, which leads to variations in grain size.

A standard test can be used to distinguish between the steel classes. If a noticeable growth of austenite grains is not observed for 8 h after carburization at 925°C (1700°F), the steel is assumed to be a hereditarily fine-grained one. Extrapure steels, those produced with a minimum amount of foreign impurities, nitrogen and oxygen, are distinguished by a rapid growth of grains above the critical point A_{c3}.

In the case of the usual commercial steels, a grain 20–25 μm in size corresponds to standard heating for quenching, normalization, or annealing. As the temperature is elevated to 1200–1250°C (2200–2250°F), the grain size reaches 0.1 mm, and in large forgings and welds, grains of several millimeters in size occur. In ingots and castings, grains can be as large as several centimeters.

If a steel is heavily alloyed with elements that stabilize austenite, the austenite structure is fixed during cooling to or below room temperature and the steel grain is equal to the initial austenite grain. If austenite passes to pearlite, then, for example, for a hypereutectoid steel one should take into account the size of the pearlite colony, which is characterized by the same crystallographic orientation of ferrite and cementite plates. A pearlite colony usually differs in size from an austenite grain. Several pearlite colonies are formed in every grain. So an austenite grain is broken into several grains. This is also true of the ferrite–pearlite structure of a hypoeutectoid steel. But in the latter case a network of excess ferrite is formed at grain boundaries. This suggests a connection between a grain of a thermally treated steel and the initial austenite grain.

When steel undergoes quenching, a large number of martensite crystals appear in every austenite grain. They are connected with the initial austenite grain by certain orientation relationships. For this reason a correlation is easily seen between the initial austenite grain and grains of the quenched steel. Refinement of the initial grain under heating above A_{c3} results in refinement of grains in the quenched steel. Then it is possible to correct a coarse-grained structure by heating to the austenite state.

However, correction of a coarse-grained austenite or bainite structure may be complicated by structural inheritance. When crystallographically ordered structures of bainite or martensite are heated, austenite can also be formed, under certain conditions, in a crystallographically ordered way. Therefore, under heating above A_{c3} the austenite grain is equal in size to a coarse

grain of steel. In this case, refinement of the crystal structure as a result of phase recrystallization during the $\alpha \rightarrow \gamma$ transformation does not take place. After the $\alpha \rightarrow \gamma$ transformation the structure of the initial austenite is restored. Both the grain size and its crystallographic orientation are reestablished. However, the restored austenite is structurally unstable. If the temperature or holding time is increased, the austenite structure changes. But the grain is refined rather than becoming larger as is normally the case. The degree of grain refinement is different, but the structure changes completely above a certain temperature in the range of the stable γ-phase. The austenite structure is altered within the temperature interval where phase transformations do not occur. Therefore, this phenomenon is attributed to a spontaneous recrystallization of austenite. It is caused by the $\gamma \rightarrow \alpha \rightarrow \gamma$ transformation hardening.

The primary recrystallization of austenite, which is due to the transformation hardening, is followed, with a further increase in temperature, by collective recrystallization. The grain becomes still coarser. Note once again the unusual character of this two-stage process, which includes first a reestablishment of the initial austenite grain and then a refinement of the grain with temperature.

Plastic deformation inhibits the structural inheritance. This is due to the appearance of globular austenite in deformed steel that is subjected to either rapid or slow heating. Besides, deformation intensifies the austenite recrystallization in the α state.

If a hypoeutectoid steel undergoes sufficiently slow heating, austenite is often formed as same-oriented sections. As the temperature is raised, excess ferrite dissolves in these sections. When ferrite dissolves completely, newly formed grains of austenite fully duplicate the initial austenite grains. With an increase in the heating rate, sections of austenite with a different orientation appear. If isothermally heated these sections grow larger and absorb the restored austenite and excess ferrite. The greater the number of such sections formed at a faster rate of heating, the finer the austenite grain.

Formation of these sections cannot be explained in terms of the austenite recrystallization because their growth stops as soon as the excess ferrite dissolves completely. They appear in a somewhat overheated and therefore nonequilibrium ferrite–austenite structure. Note an anomalous dependence of the point A_{c3} on the heating rate. Increasing the heating rate of the steel allows completion of austenitization at lower temperature.

3.5.4 Grain Size Refinement

Tchernov [7] was the first to show that it was possible to refine a coarse-grained structure in 1868. Since that time the procedure has been widely used for treatment of steel products. The grain refinement, which takes place on heating steels above the temperature A_{c3}, is related to a transition to the austenite state through nucleation of numerous centers of the austenite phase. Development of these centers leads to formation of a relatively fine-grained structure. Above A_{c3}, the cross-sectional size of the grain is 10–30 μm. Initially the grain size is independent of the grain of the starting structure; it can be very fine irrespective of whether the starting structure of the steel was fine or coarse. A fine-grained structure of the restored austenite provides a fine-grained structure of cooled steel whatever structural components are formed—pearlite, bainite, or martensite. This is due to the fact that all the transformation products nucleate within each separate grain of austenite.

Excess phases (ferrite in hypoeutectoid steels and cementite in hypereutectoid steels) precipitate at boundaries of small austenite grains, and the pearlite transformation is accompanied by the appearance of smaller pearlite colonies. Fine austenite grains determine the formation of fine-needle martensite. This underlies the grain refinement effect that is associated with hearing above A_{c3}. Heating the steel above A_{c3} during full annealing, normalization, or quenching is followed by recrystallization. Given an initially coarse-grained structure,

recrystallization results in refinement of grains at a heating temperature corresponding to A_{c3}. If the heating temperature is much higher than A_{c3}, the grain is enlarged again, and the expected correction of the structure during the $\gamma \rightarrow \alpha$ transformation does not take place. Refinement of crystallites is especially pronounced when transformation to the austenite state starts in many centers inside the initial structure. The formed centers should have a random orientation, which is not connected with the orientation of the α-phase in the initial structure. Normally such centers are sufficiently great in number that the grain size does not exceed 15–30 μm.

Breaking of an austenite grain into pearlite colonies, each of which can be considered an independent grain, also represents refinement of steel during pearlite precipitation of austenite.

3.6 STRENGTHENING MECHANISM IN STEEL

3.6.1 Solid Solution Strengthening

Solid solution strengthening is a phenomenon that occurs when the number of impurity atoms in the lattice of the basic element is so small that they are incapable of forming both stable and metastable precipitation phases under any thermal treatment conditions. Nevertheless the impurity atoms favor improvement of mechanical properties. This can be accounted for by the following. The presence of impurity atoms in the matrix lattice leads to distortion of the lattice because of the difference in size between the atomic radii of the impurity and the basic component. This in turn leads to the appearance of elastic deformation fields, which retard movement of dislocations in slip planes under the action of applied stresses. In addition, the impurity atoms can inhibit movement of dislocations by forming impurity atmospheres around them. Both of the above factors play a leading role in solid solution strengthening.

Consider the influence of carbon, which is statistically uniformly distributed in the lattice of the α-iron, on the structure and properties of α-iron. Solubility of carbon in α-iron is much lower than in the γ-iron. It forms interstitial solid solutions with both irons. However, whereas the γ-iron lattice has sufficiently large pores for implantation of carbon atoms, the cubic lattice of the α-iron suffers, upon introduction of carbon atoms, a tetragonal distortion similar to the one of the martensite lattice, except that in the former case the distortion is much smaller. In addition, implantation of carbon atoms causes the entire lattice of the α-iron to expand somewhat. For example, at a carbon content of 0.015% the lattice constant increases at room temperature by $0.025c$.

From the above discussion it is evident that carbon affects the properties of the α-phase. Indeed, a dependence of the yield stress on the carbon concentration in the solid α solution was detected. The yield stress rises most dramatically with an increase in the carbon concentration from 10^{-7} to 10^{-4}–10^{-3}%. The influence that carbon exerts on plastic deformation resistance of the α-phase is due to both its strong interaction with dislocations and pinning of the dislocations and elastic deformations arising as a result of the tetragonal distortion of the α-phase lattice after implantation of carbon atoms.

What is more, the presence of carbon in lattices of different structural components formed during thermal treatment of steel also leads to changes in their mechanical characteristics. For example, the location of implanted carbon atoms predominantly in one of the sublattices of interstitial sites during the martensite formation brings about additional tetragonal distortions of the martensite crystal lattice. This enhances plastic deformation resistance owing to the interaction between the stress fields around carbon atoms and those at dislocations.

The flow stress grows linearly or in proportion to the square root of the percent carbon with an increase in the carbon content. This is accompanied by impairment of the plastic characteristics of the steel and lowering of the fracture stress. For example, if the carbon content is raised from 0.25% to 0.4% in a steel with 5% Cr, after quenching and low tempering

the tensile strength increases from 1600 to 2000 MPa, the fracture stress of samples with a purpose-produced crack decreases from 1300 to1000 MPa, and the impact strength drops from 0.3 to 0.04 J m^2.

The influence of carbon dissolved in the α-phase on the mechanical properties of steel is also observed in the case of the ferrite–pearlite transformation. The factors responsible for this phenomenon were analyzed above. Both in the homogeneous α-phase and the ferrite–pearlite mixture, the yield stress rises most sharply when the carbon concentration of ferrite is raised from 10^{-7} to 10^{-4}–10^{-3}%.

A direct examination of the crystal structure of the α-phase formed over the temperature interval of 250–300°C (482–572°F) during the intermediate (bainite) transformation also revealed a tetragonal structure with the c/a axis ratio equal to 1.006 and 1.008 at carbon contents of 1 and 1.2%, respectively. This attests to dissolution of part of the carbon in the α-phase and suggests that the solid solution strengthening of the phase is one of the factors providing the high strength properties of intermediate transformation products.

3.6.2 Grain Size Refinement

In Section 3.5.4 the possibility of refining steel grains by phase recrystallization under heating to a temperature above A_{c3} was considered. Although austenite passes to other phases during cooling, its grain size represents an important characteristic of steel. This is due to the fact that all structural components are formed within each separate crystal. The smaller the austenite grains, the finer the network of excess ferrite at their boundaries and the smaller the pearlite colonies and martensite crystals. Therefore, a fine grain corresponds to a fine-crystal fracture of steel and vice versa at the temperatures where austenite has already precipitated. Impact strength is especially sensitive to the austenite grain size, and it decreases with grain enlargement. A decrease in the dimensions of pearlite colonies inside the initial austenite grain favors a rise in impact strength also.

Although the grain size has a considerable effect on impact strength, its influence is small if any on the statistical characteristics of mechanical properties such as hardness, fracture stress, yield stress, and specific elongation. Only the actual grain size affects steel properties, the inherited size has no effect. However, the technological process of heat treatment is determined by the inherited grain. For example, a hereditarily fine-grained steel may be deformed at a higher temperature with the assurance that the coarse-grained structure will not occur.

3.6.3 Dispersion Strengthening

In the majority of metal alloys, precipitation of supersaturated solid solutions formed during quenching is followed by precipitation of disperse particles enriched in atoms of the alloying components. It was found that the strength (hardness) of the alloys increases with the precipitation of these particles. The increment in the value of these characteristics increases as the dispersion and volume fraction of the particles increase. This phenomenon has been referred to as dispersion strengthening.

Precipitation of supersaturated solid solutions occurs during heating (aging) of quenched alloys. The study of precipitation processes is ultimately aimed at elaboration of the most efficient methods for strengthening aging materials. In a general case, strengthening results from an increase in resistance to the movement of dislocations in a crystal when obstacles (barriers) of any type are formed. In aging alloys, dislocations meet regions (ordered atomic clusters [ГП zones] or different-structure precipitate particles) that retard their movement. The character of interaction between moving dislocations and precipitates of the second phase can be different depending on the phase morphology and structure.

The total effect of aging on the strength properties of alloys is determined by (1) the strength of the precipitates formed, (2) the volume fraction of precipitates, (3) the degree of precipitate dispersion, (4) morphology, structure, and type of binding with the matrix, and (4) test temperature.

When a solid solution of carbon in α-iron is cooled below point A_1, carbon should precipitate as cementite with lowering of the carbon solubility and a decrease in temperature. This process is realized under sufficiently slow cooling, which is accompanied by diffusion processes, leading to the formation of cementite.

In the case of abrupt cooling, e.g., water quenching, carbon has no time to precipitate. A supersaturated α solid solution appears. At room temperature the retained amount of carbon can correspond to its maximum solubility of 0.018%. During subsequent storage at room temperature (natural aging) carbon tends to precipitate from the solid solution. Carbon-enriched regions appear predominantly in defective sections of the matrix. Precipitation of carbon from a supersaturated solid solution during natural aging results in improvement of its strength characteristics and hardness. However, plastic characteristics—reduction of area, specific elongation, and impact strength—are impaired (see Figure 3.23). A clearly pronounced yield stress appears after a long natural aging. Hardness may increase by 50% over that of the as-quenched state. The phenomenon of dispersion strengthening is observed.

As the heating temperature is increased (artificial aging), dispersion strengthening accelerates. At 50°C (122°F) the precipitation rate of carbon from the α-iron increases to such an extent that in several hours of aging it reaches the value obtained after several days of natural aging (Figure 3.24). This is due to intensification of diffusion processes with an increase in temperature. As the temperature is elevated further, precipitation of the supersaturated α solid solution proceeds still faster.

The total process of carbon precipitation from the supersaturated solid solution in α-iron comprises several consecutive processes. Mechanical characteristics and hardness are not sensitive to structural changes that take place during the aging of alloys. Sharp changes in properties indicate alterations in the structural state of the steel.

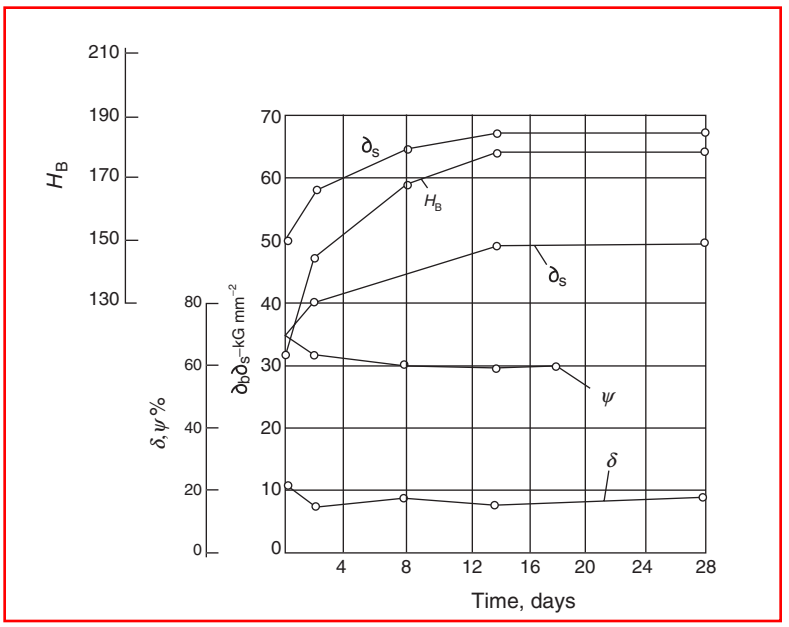

FIGURE 3.23 Curves showing strengthening of fcc crystals.

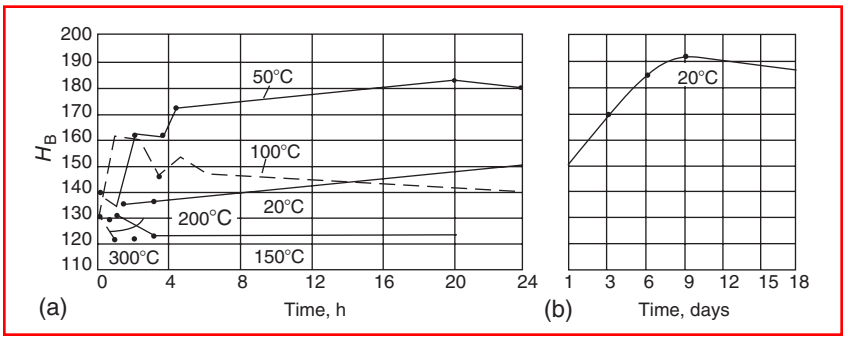

FIGURE 3.24 The aging temperature dependence of hardness of carbon steel.

A maximum change in mechanical properties during precipitation is achieved only if excess crystals in a highly disperse state precipitate. Subsequent coagulation of the crystals leads to degradation of the properties (Figure 3.24 and Figure 3.25).

As the temperature is raised above 100°C (212°F), carbides begin to homogeneously precipitate directly from the solid solution. The precipitating phase has the carbide lattice below 200°C and the cementite lattice above 300°C (572°F). A transition from one phase to the other is realized over the temperature interval of 200–300°C (392–572°F). The onset of transition from atomic clusters near dislocations to precipitation of the ε-carbide remains to be ascertained. The temperature and time during which the ε-carbide crystals precipitate from the inhomogeneous solid solution depend on the degree of the solution supersaturation and concentration of vacancies.

Coagulation of the ε-carbide crystals lowers the increment in hardness, fracture stress, and yield stress as the effect of breaking the slip dislocations diminishes. Above 200°C (392°F),

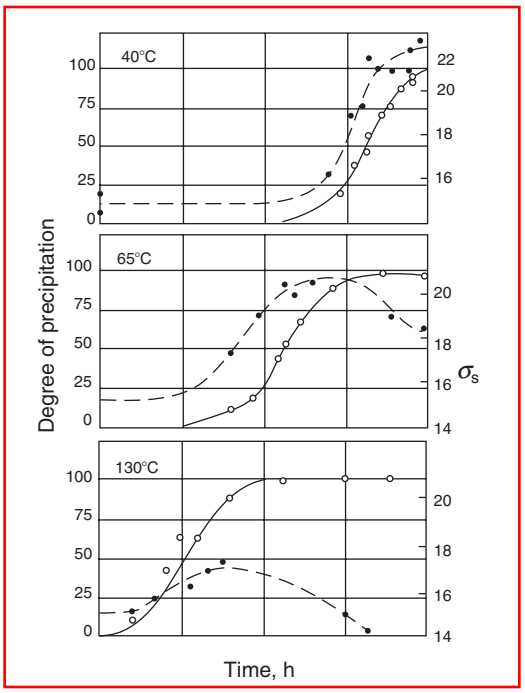

FIGURE 3.25 Variation of the yield stress as a result of carbon precipitation from the α-iron lattice at different temperatures.

where precipitation of the particles is detected even by metallographic methods, hardness stops increasing.

If a naturally aged sample of steel is heated at a temperature of 100–200°C (212–392°F), a decrease in hardness can be observed. This is due to the phenomenon of recovery where the phase nuclei that were formed at room temperature dissolve on heating to higher temperatures.

The influence of different solubilities of carbon in α-iron on the properties of the alloy (dispersion strengthening) during low-temperature aging is pronounced in steels with a very low content of carbon. In steels containing over 0.4% C, the effects considered above are obscured by the influence of cementite particles formed during the pearlite transformation. Besides, nucleation of the precipitating phase can be inhibited owing to migration of carbon to the cementite–ferrite interfaces. As a result, the amount of carbon concentrated at lattice defects decreases.

Cold plastic deformation greatly accelerates precipitation of a supersaturated solid solution. This is due both to an increase in the density of dislocations, which are preferable sites of heterogeneous nucleation of precipitates, and to an increase in the concentration of vacancies, which facilitates the diffusion of carbon to clusters. The phenomenon has also been observed in other aging alloys. Mechanical properties change during aging after cold deformation in the same way as after quenching. That is, the yield stress, the fracture stress, and hardness are altered. With an increase in aging time, specific elongation and reduction of area decrease and the tendency to brittle fracture is enhanced. The rate of change is greater than in a quenched alloy. What is more, the character of the changes is different. Whereas in the case of aging after quenching, hardness reaches a maximum and then drops, after cold deformation hardness does not decrease with the aging time (Figure 3.26). As the aging temperature is raised, the maximum hardness of a quenched alloy lowers, while after cold deformation hardness is independent of the aging temperature. This is explained by the fact that a considerable amount of carbon is concentrated near dislocations. Few if any clusters nucleate in the matrix homogeneously. Consequently, clusters cannot grow at the expense of other clusters, i.e., they cannot coagulate.

As the solubility of carbon in γ-iron is also susceptible to changes, one can also expect the effect of dispersion strengthening. However, the γ-phase is not fixed during quenching but undergoes martensite transformation. For this reason an additional amount of carbon transferred to the solid solution at the line ES will just enhance the precipitation of martensite and retained austenite during tempering of steel. Still, an increase in hardness as a result of carbide precipitation is observed in purely austenitic steels.

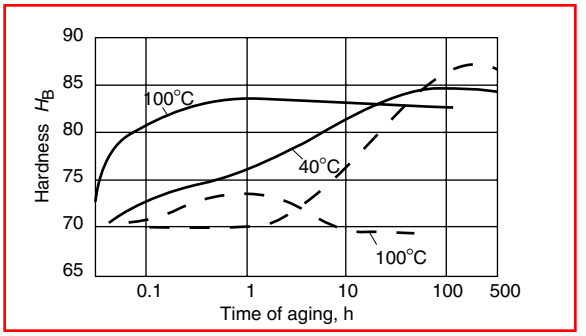

FIGURE 3.26 Aging after quenching from 720°C (1328°F) (- - - -) and after 10% cold deformation (—) of cast steel.

3.6.4 Work Hardening (Dislocation Strengthening)

An important method used to strengthen steels is deformation strengthening. Strengthening achieved with crystal deformation can be judged from the shape of stress–strain curves. The actual shape of these curves largely depends on the crystal lattice type of the metal, its purity, and thermal treatment.

In the case of cubic lattice metals, strengthening curves are parabolic, whereas for hexagonal lattice metals a nearly linear dependence is observed between the stress and the strain. This fact suggests that plastic deformation strengthening is determined mainly by the interaction of dislocations and is associated with the structural changes that impede the movement of dislocations. Metals with a hexagonal lattice are less prone to deformation strengthening than cubic lattice metals because the hexagonal lattice has fewer easy slip systems. In cubic lattice metals, the slip proceeds in several intersecting planes and directions.

Examinations of fcc crystals showed that their strengthening curve is complicated (Figure 3.27). Three stages can be distinguished in this curve.

Stage I is characterized by easy slip. It depends on the orientation of the crystal relative to external forces and on the presence of impurities. This stage is characterized by a linear dependence of strain stresses on the strain at a small work-hardening rate. Dislocations slip in primary systems.

The work-hardening rate is much greater at stage II than at stage I. Dislocations move in intersecting slip planes and, on colliding, form additional obstacles to their movement. This state is most extensive in the stress–strain curve. The ratio between the work-hardening rate and the shear modulus (or any other elastic constant) is almost independent of the applied stress and temperature. It depends little on the crystal orientation and presence of impurities. For most fcc metals the ratio between the work-hardening rate and the shear modulus is about 4×10^3.

A cellular structure is formed at stage II. Cells 1–3 mm in diameter are practically free of dislocations (Figure 3.28). Groups of like dislocations represent subboundaries of the cells. During their movement, dislocations overcome stress fields of different groups. The formation of obstacles that inhibit propagation of the shear in slip planes and cause a high degree of strengthening at stage II leads to a nonuniform distribution of the strain over the crystal volume.

At stage III, changes are possible in the distribution of dislocations. They can either get around obstacles that retard their movement at stage II or interact with dislocations. As a result, the work-hardening rate lowers compared to that observed at stage II. At this stage a

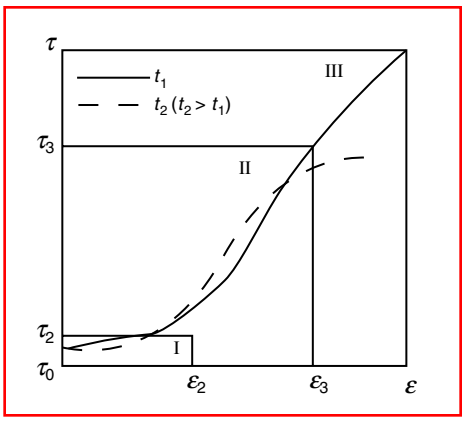

FIGURE 3.27 Curves showing strength of fcc crystals.

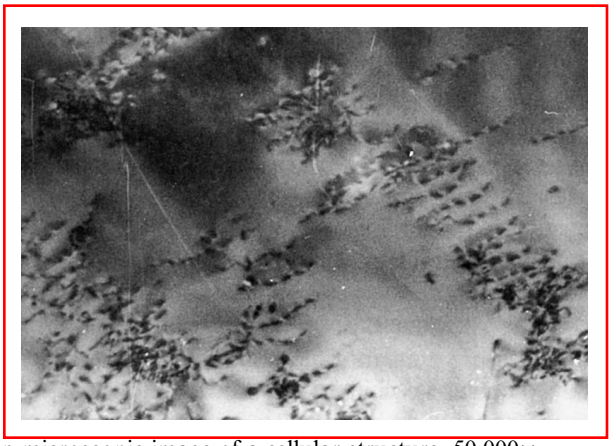

FIGURE 3.28 Electron microscopic image of a cellular structure, 50,000×.

partial relaxation of stresses may occur owing to the appearance of the secondary slip system. The diminishment of distortion may have the result that deformation continues in the primary system, which gets rid of a certain number of dislocations passing to the system. A characteristic feature of deformation at stage III is the development of a cross-slip representing the main mechanism by which dislocations bypass the obstacles formed at stage II.

3.6.5 Thermal Treatment of Steels

There are three basic types of thermal treatment of steels: annealing, quenching, and tempering.

3.6.5.1 Annealing

Annealing has the following forms: (a) diffusion annealing; (b) softening; (c) phase-recrystallization annealing or full annealing (normalization, high-temperature or coarse-grain annealing, pearlitization); and (d) stress relief annealing and recrystallization annealing.

3.6.5.1.1 Diffusion Annealing

The goal of diffusion annealing is to eliminate, insofar as possible, inhomogeneities of the chemical composition, in particular liquation inhomogeneities, which appear during crystallization of alloys. This annealing is usually carried out in the range of the γ solid solution at a temperature of 1100–1300°C (2012–2372°F). Diffusion annealing can be used primarily to smooth out a difference in the content of alloying elements, the difference being due to the intercrystal liquation. This shows up as smearing of dendrites with an increase in temperature and heating time. Differences in microhardness are eliminated simultaneously. The overall hardness of the alloy decreases because liquation regions possessing high hardness are removed. Some average hardness is obtained. The success of diffusion annealing largely depends on the steel purity and liquation. This type of annealing is usually used to improve properties of medium-purity steels.

3.6.5.1.2 Softening

Softening is used to produce the structure of globular pearlite. This structure is very soft and readily lends itself to deformation during drawing, cold rolling, etc. Steels with a low-carbon content become too soft after this annealing treatment. The globular pearlite structure is favorable in steels with a carbon concentration of more than 0.5%. Another goal of softening is to produce a uniform fine structure with finely dispersed carbon after quenching.

The simplest method of softening consists in holding for many hours at a temperature slightly above A_{c1}. In this case, martensite that is left from the previous treatment is removed and the work hardening caused by deformation (e.g., forging) is eliminated.

Carbide plates of pearlite fully coagulate only after a long annealing time. As fine-plate pearlite transforms more easily to globular pearlite, it is recommended that normalization (see Section 3.6.5.1.3) be carried out before softening treatment. Cooling after softening can be done in air starting from 600°C (1112°F).

Refinement of the structure subjected to softening is achieved only above the point A_1. In practical applications, this type of annealing represents an intermediate treatment, and therefore no strict requirements are imposed on the mechanical properties of annealed materials.

3.6.5.1.3 Phase Recrystallization Annealing (Normalization, High-Temperature Annealing or Coarse-Grain Annealing, Pearlitization)

A twofold $\gamma \rightarrow \alpha$ transformation, which takes place during phase recrystallization annealing, leads to the appearance of a fine-grained uniform structure differing completely from the initial structure. Refinement of the grain during normalization results in the disappearance of the Widmannstatten and coarse-grained cast structures, which have poor mechanical properties. Inhomogeneity of the structure in the deformed state is eliminated.

The closer the annealing temperature is to A_{c3} and the shorter the holding time at this temperature, the finer the grain. The mechanisms of this phenomenon are analyzed in detail in Section 3.5.3. Refinement of the grain structure is also facilitated if the heating rate to the annealing temperature and the cooling rate from this temperature are increased.

In the case of normalization, cooling is done in air. Here it is important to allow for different rates of cooling along the cross section of large-diameter products. The arising thermal stresses are removed by stress relief annealing or high-temperature tempering. To obtain a fine-grained structure, rapid cooling is realized only over the transformation temperature interval.

The normalization heating temperature should not be much higher than the transformation point; otherwise the grain may be too coarse (overheating). An excessively long holding time will have the same result.

The optimal heating temperature is determined by the carbon content. For steels with a carbon concentration of up to 0.9%, it is 20–30°C higher than A_{c3}. For eutectoid steels, heating between A_{c1} and A_{cm} suffices. In the case of low- and medium-carbon steels, the best results are obtained if ferrite and plate pearlite are formed during subsequent heat treatment.

3.6.5.1.4 Stress Relief Annealing and Recrystallization Annealing

Dislocation pile-ups and crystal lattice distortions arising in cold-deformed metals may result in the appearance of macroscopic stresses (stresses of the first kind). Usually these stresses are very high. Changes in properties that occur under cold deformation can be rectified during subsequent heating. The greater the degree of deformation, the lower the heating temperature. Depending on the temperature and time of annealing, various structural changes take place in a cold-deformed material. The changes are divided into recovery and recrystallization processes.

Recovery is a totality of any spontaneous processes of variation in the density and distribution of defects before the onset of recrystallization. If recovery proceeds without the formation and migration of subgrain boundaries inside the recrystallized grains, it is called restoring. If subgrain boundaries are formed and migrate inside the crystallites, recovery is referred to as polygonization.

Restoring does not include an incubation period. Properties start changing right at the beginning of annealing. Restoring is accompanied by a redistribution of point defects whose

concentration decreases subsequently from excess concentration to the equilibrium concentration. Simultaneously, dislocations are redistributed and unlike-sign dislocations are annihilated. The total density of dislocations decreases during restoring. Restoring is realized at a temperature below $0.3T_{melt}$.

The main process that takes place during polygonization is the redistribution of dislocations accompanied by formation of walls. A dislocation wall does not have long-range stress fields, and therefore the wall formation process is energetically favorable. A wall composed of like-sign dislocations represents a low-angle boundary separating neighboring subgrains with a small misorientation of the lattices. As the annealing time and temperature are increased, the subgrains tend to become coarser. They may be as large as ~10 μm. However, the subgrains grow within the old-deformed grains.

In iron, polygonization starts at 200°C (392°F) (block boundaries appear in the structure). Clearly delineated boundaries of the blocks are retained up to 850°C (1562°F) and persist even after long holding at this temperature.

Starting from a certain annealing temperature, the structure changes drastically. New rather equilibrium grains are observed along with extended deformed grains. They differ from the grains of the deformed matrix by having a more perfect internal structure. While the density of dislocations in a strongly deformed matrix is $10^{11}-10^{12}\,cm^{-2}$, after recrystallization it lowers to $10^{6}-10^{8}\,cm^{-2}$. As distinct from the polygonized structure, recrystallized grains are separated from the matrix with large-angle boundaries.

The formation and growth of grains with a more perfect structure that are surrounded by large-angle boundaries at the expense of initially deformed grains of the same phase is called primary recrystallization. Recrystallization begins with an incubation period. The recrystallization rate first increases from zero to a maximum and then decreases owing to an ever rising number of new grains in contact with one another.

Inclusions of insoluble impurities (carbides, nitrides) lower the tendency to growth of recrystallized grains. This is especially important in the case of ferritic steels, which are prone to grain growth. Another phase may precipitate during recrystallization in alloys that were subjected to a strong cold deformation.

Sometimes the intensive growth of individual crystals can be observed after a strong deformation and long holding (for several days) at temperatures close to the melting point. This phenomenon is called secondary or collective recrystallization.

The carbon content of steel affects the polygonization and recrystallization kinetics. With an increase in the carbon content, polygonization slows down or shifts toward higher temperatures. Given a large initial grain size, recrystallization commences the earlier, the greater the degree of deformation. At a given degree of deformation, higher the recrystallization temperature, the coarser the initial grain. After recrystallization an initially coarse-grained structure gives a larger grain than a fine-grained structure does. In iron–carbon alloys, coarse grains are formed until the appearance of new grains associated with a polymorphous transformation.

Under critical conditions of recrystallization the grain size decreases with an increase in the carbon content. This is due to lowering of the point A_3 and narrowing of the recrystallization temperature range. Besides, the number of γ-phase crystals formed between A_{c1} and A_{c3} increases. They impede the growth of the α-phase grains at temperatures above A_{c1}. Carbides also retard growth of the grains.

As recrystallization proceeds, strengthening lowers. A fine-grained material possesses an improved long-time strength at lower temperature, while a coarse-grained material exhibits this property at higher temperatures. A required size can be obtained by a proper choice of the deformation and recrystallization conditions. In the case of steels, where no transformations take place (pure ferritic or austenitic steels) this combination of technological operations is the only opportunity to influence the grain size.

3.6.5.2 Quenching (Strengthening Treatment)

Quenching refers to cooling from the temperature range of the solid solution at such a rate that transformations in the primary and bainite ranges are suppressed and martensite is formed. In this state, steels are characterized by the greatest hardness. A distinction is made between (a) normal quenching, which is used mainly for treatment of medium- and high-carbon steels and (b) quenching after a thermochemical treatment (carburization, high-temperature cyaniding), which is used for low-carbon steels.

3.6.5.2.1 Normal Quenching

To provide a required cooling rate during quenching, various cooling media and methods are employed. Water, oil, or air can serve as the cooling medium. Many alloyed steels, which are characterized by a high stability of austenite, are subjected to step quenching. With this method of quenching, the temperature drop is less than in the case of direct cooling to room temperature and consequently quenching stresses are less.

A certain amount of austenite is retained during quenching even in steels with a relatively small content of carbon. For this reason it is impossible to impart the maximum hardness to a product. Since austenite is stable at room temperature and passes to martensite at lower temperatures, steels undergo a subzero treatment. Under this treatment quenching is continued and steels with a high content of retained austenite are immersed in liquid air or quenching mixtures whose temperature is below room temperature.

For surface quenching (if it is necessary to harden only the surface layer to a preset depth), special quenching heating regimes are used. The surface of the product is fully heated, while the core is cold and remains unquenched on subsequent rapid cooling. The selection of steel for surface quenching must be governed by the sensitivity of the metal to quick heating and cooling. For this reason the carbon concentration is limited to 0.7%. Otherwise cracks are formed.

Among the main quenching defects are excessive holding and overheating. They show up as enlargement of martensite needles and coarse-grain fracture. This leads to a high brittleness of quenched products and the formation of cracks. Cracks often form at the boundaries of initial austenite grains. A low quenching temperature or too short a holding time at the given temperature causes incomplete quenching. In this case, a quenched metal is insufficiently hard.

3.6.5.2.2 Thermochemical Treatment

Carburization is associated with surface saturation of steel with carbon and nitrogen. These elements quickly dissolve in iron by the interstitial method and are capable of rapid diffusion to a considerable depth. Products made of low-carbon (up to 0.25%) steels are subject to carburization. Carburization is carried out at 900–950°C (1650–1750°F) and sometimes 1000–1050°C (1800–1900°F). Gas carburization is used mostly, under which steel is heated in the atmosphere generated from natural gas (containing predominantly CH_4) or from liquid hydrocarbons (kerosene, gasoline, etc.). Carburization is aimed at enrichment of the surface layer in carbon. The required strengthening of the surface layer is achieved by quenching, which is performed after carburization. The specific volume of the quenched carburized layer is greater than the specific volume of the core, and therefore considerable compression stresses arise in the layer. This enhances the fatigue strength of products.

Cyaniding is the saturation of the surface of products with carbon and nitrogen in a cyanide-containing salt bath. The carbon–nitrogen ratio in the diffusion layer is controlled by changing the medium's composition and the processing temperature. Advantages of cyaniding over carburization consist in a shorter process time and improved wear and corrosion resistance (owing to the presence of nitrogen in the surface layer).

3.6.5.3 Tempering

The main purpose of tempering is to provide a disperse structure at a preset degree of cooling. In the case of low-carbon steels, quenching serves as tempering; even if not subjected to high-temperature tempering, the steel has a high viscosity and a relatively great strength.

When certain steels are quenched in oil, a structure is formed even during transformation in the bainite range that is more disperse than the one formed after cooling in air. But the most disperse distribution of carbides and the most favorable properties are obtained after martensite tempering. The structure dispersion has the greatest effect on the yield stress. An improvement of the fracture stress and yield stress and an increase in the fracture stress–yield stress ratio may be taken as a measure of the tempering efficiency. The tempering efficiency depends on the cross-sectional area and on the content of carbon and alloying elements in the steels.

Although to achieve a thorough quenching the critical quenching rate has to be exceeded over the entire cross section, full tempering does not require this procedure. For example, in a quenched steel that has martensite in the surface zone and pearlite in the core, the hardness of the core sometimes may be higher than that of the surface zone after tempering. This is especially the case during a short tempering when precipitation of carbides from martensite proceeds faster than the coagulation of pearlite plates.

Tempering of hypoeutectoid steels, which do not contain free ferrite, provides a uniform improved structure. In the presence of ferrite precipitates, the fracture stress–yield stress ratio decreases and the impact strength is smaller than in the surface zone. Therefore, in selecting the content of carbon and alloying elements and particular conditions of austenitization and cooling, the size of the product to be tempered must be considered. For tempering to yield adequate properties, it often suffices to suppress the formation of ferrite during continuous cooling. Only when a very high fracture stress is required an abrupt cooling is used for tempering. In this case, susceptibility to full tempering can be improved by raising the quenching temperature and thus enlarging the austenitic grain size.

REFERENCES

1. N.F. Mott, *Imperfections in Nearly Perfect Crystals*, John Wiley & Sons, New York, 1952, p. 173.
2. N.F. Mott and F.R.N. Nabarro, *Proc. Phys. Soc. 52*:8 (1940).
3. R. Smoluchowski, *Physica 15*:179 (1949).
4. R. Smoluchowski, *Phase Transformations in Solids*, John Wiley & Sons, New York, 1952, p. 173.
5. A.H. Geisler and J.K. Hill, *Acta Cryst. 11*:238 (1948).
6. M.E. Hargreaves, *Acta Cryst. 4*:301 (1951).
7. D.K. Tchernov, *Metals Science*, Metallurizdat, Moscow, 1950 (in Russian).

FURTHER READING

M.V. Belous, V.T. Cherepin, and M.A. Vasiliev, *Transformations During Tempering of Steel*, Metallurgiya, Moscow, 1973 (in Russian).

M.L. Bernshtein and A.G.M. Richshtadt (Eds.), *Physical Metallurgy and Thermal Treatment of Steels—Handbook*, 3rd ed., Vols. 1–3, Metallurgiya, Moscow, 1983 (in Russian).

M.E. Blanter, *Phase Transformations During Thermal Treatment of Steel*, Metallurgiya, Moscow, 1962 (in Russian).

M.E. Blanter, *Physical Metallurgy and Thermal Treatment*, Mashinostroyeniye, Moscow, 1963 (in Russian).

V.A. Delle, *Structural Alloy Steel*, Metallurgiya, Moscow, 1959 (in Russian).

M.I. Goldshtein, S.V. Grachev, and Yu.G. Veksler, *Special Steels*, Metallurgiya, Moscow, 1985 (in Russian).

E. Gudreman, *Special Steels*, Vols. 1 and 2, Metallurgiya, Moscow, 1959 (in Russian).
A.P. Gulyaev, *Physical Metallurgy*, Metallurgiya, Moscow, 1976 (in Russian).
A.P. Gulyaev, *Pure Steel*, Metallurgiya, Moscow, 1975 (in Russian).
H.K. Hardy and T.J. Heal, *Prog. Met. Phys. 5*:143 (1954).
G.A. Kaschenko, *Fundamentals of Physical Metallurgy*, Metallurgiya, Moscow, 1964 (in Russian).
G.V. Kurdyumov, L.M. Utevski, and R.I. Entin, *Transformations in Iron and Steel*, Nauka, Moscow, 1977 (in Russian).
V.S. Meskin, *Fundamentals of Steel Alloying*, Metallurgiya, Moscow, 1964 (in Russian).
N.F. Mott, *Proc. Phys. Soc. B 64*:729 (1951).
N.F. Mott, *Phil. Mag. 8*(1):568 (1956).
I.I. Novikov, *Theory of Thermal Treatment of Metals*, Metallurgiya, Moscow, 1986 (in Russian).
A.A. Popov, *Phase Transformations in Metal Alloys*, Metallurgiya, Moscow, 1963 (in Russian).
M.I. Vinograd and G.P. Gromova, *Inclusions in Alloy Steels and Alloys*, Metallurgiya, Moscow, 1972 (in Russian).
R. Zimmerman and K. Gunter, *Metallurgy and Materials Science—Handbook*, Metallurgiya, Moscow, 1982 (in Russian).

4 Effects of Alloying Elements on the Heat Treatment of Steel

Alexey V. Sverdlin and Arnold R. Ness

CONTENTS

4.1 Effects of Alloying Elements on Heat Treatment Processing of Iron–Carbon Alloys 166
4.1.1 γ- and α-Phase Regions 166
4.1.2 Eutectoid Composition and Temperature 169
4.1.3 Distribution of Alloying Elements 171
4.1.4 Alloy Carbides 172
4.2 Effect of Alloying Elements on Austenite Transformations 174
4.2.1 Influence of Alloying on Ferrite and Pearlite Interaction 175
4.2.2 Effect on Martensite Transformation 177
4.2.3 Retained Austenite 179
4.2.4 Effect on Bainite Transformation 181
4.2.5 Transformation Diagrams for Alloy Steels 183
4.3 Hardening Capacity and Hardenability of Alloy Steel 185
4.3.1 Hardness and Carbon Content 185
4.3.2 Microstructure Criterion for Hardening Capacity 187
4.3.3 Effect of Grain Size and Chemical Composition 189
4.3.4 Boron Hardening Mechanism 193
4.3.5 Austenitizing Conditions Affecting Hardenability 195
4.4 Tempering of Alloy Steels 196
4.4.1 Structural Changes on Tempering 196
4.4.2 Effect of Alloying Elements 197
4.4.3 Transformations of Retained Austenite (Secondary Tempering) 198
4.4.4 Time–Temperature Relationships in Tempering 199
4.4.5 Estimation of Hardness after Tempering 199
4.4.6 Effect of Tempering on Mechanical Properties 200
4.4.7 Embrittlement during Tempering 201
4.5 Heat Treatment of Special Category Steels 201
4.5.1 High-Strength Steels 201
4.5.2 Boron Steels 202
4.5.3 Ultrahigh-Strength Steels 202
4.5.4 Martensitic Stainless Steels 204
4.5.5 Precipitation-Hardening Steels 205
4.5.5.1 Structural Steels 205
4.5.5.2 Spring Steels 206
4.5.5.3 Tool Steels 207
4.5.5.4 Heat-Resistant Alloys 208
4.5.6 Transformation-Induced Plasticity Steels 208

4.5.7 Tool Steels 209
4.5.7.1 Carbon Tool Steels 209
4.5.7.2 Alloy Tool Steels 209
4.5.7.3 Die Steels 210
4.5.7.4 High-Speed Steels 210
Further Reading 211

4.1 EFFECTS OF ALLOYING ELEMENTS ON HEAT TREATMENT PROCESSING OF IRON–CARBON ALLOYS

A steel that contains, in addition to iron and up to 2% carbon, specially introduced chemical elements not found in a usual carbon steel is called an alloy steel. Chemical elements purposely added into steel are termed alloying elements. Steels may contain various numbers of alloying elements, and accordingly they are classified as ternary steels, which have, along with Fe and C, one specially introduced alloying element; quaternary steels, which contain two additional alloying elements, and so on. Alloying elements impart a wide variety of microstructures to steel after heat treatment that gives scope for a wide range of properties.

The following elements, arranged in descending order of their application in practice, are usually used for alloying of steel: Cr, Ni, Mn, Si, W, Mo, V, Co, Ti, Al, Cu, Nb, Zr, B, N, and Be. The alloying elements interact with iron, carbon, and other elements in the steel, resulting in changes in the mechanical, chemical, and physical properties of the steel. Improvement of the properties of steel in accordance with its designated purpose is the main goal of alloying. The level to which the properties of steel are changed by alloying depends on the amount of alloying elements introduced and the character of their interaction with the main elements of the steel, i.e., Fe and C. That is why an analysis of the influence of alloying elements on the properties of steel should begin with consideration of the relationship between particular alloying elements, and Fe and C. What should be considered is the effect of alloying elements on the critical points of iron and steel, and also the distribution of the alloying elements in the steel.

4.1.1 γ- and α-Phase Regions

The position of the critical points A_3 and A_4 and the location of the eutectoid temperature A_1 are of great significance because they determine the lowest temperature to which a steel should be heated for quenching, annealing, or normalization as well as the temperatures of the maxima in the cure showing the precipitation rate of undercooled austenite. The processes that take place at the critical temperatures in steels are associated with the $Fe_\gamma \cap Fe_\alpha$ transformations and dissociation of carbides.

Different alloying elements have different effects on the position of the critical points A_3 and A_4. The alloying elements are accordingly divided into two large groups, each in turn broken down into two subgroups.

Addition of the elements from the first group is followed by lowering of the critical point A_3 and a simultaneous rise of the point A_4. This effect is shown schematically in Figure 4.1 and is most vividly pictured in Fe–Mn and Fe–Ni equilibriums. It is seen that with an increase in the content of the alloying element, the γ-phase region broadens considerably, and starting from a certain concentration the alloys are found in the state of the γ-solid solution until they melt. This shift of the critical points is brought about by such elements as Ni, Co, Mn, Pt, Pd, Rh, and Ir (Ni group).

The other subgroup of the first group includes elements that in general have a limited solubility in iron. Given a certain concentration of these elements in iron alloys, chemical compounds are formed and eutectic or eutectoid transformations are observed. In other

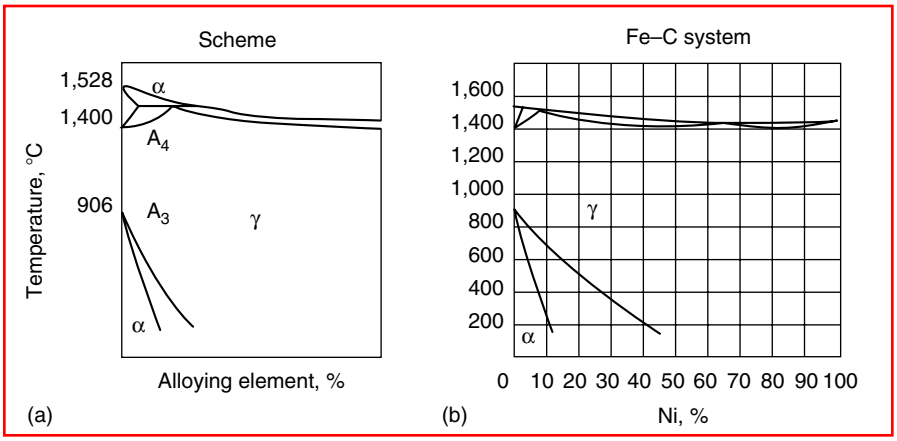

FIGURE 4.1 Scheme (a) and equilibrium diagram (b) for Fe and alloying elements with extended γ-phase range and unlimited solubility.

words, heterogeneous regions appear in diagrams of the iron-alloying elements system. The heterogeneous regions limit the γ-phase occurrence range. This type of phase diagram of alloys is exemplified in Figure 4.2. As is seen, with an increase in the concentration of the alloying element in the alloy, the critical point A_3 lowers and A_4 rises. As a result, the range of γ-solid solutions widens. But then, owing to the formation of heterogeneous regions, the γ-phase narrows and, finally, vanishes. Equilibrium diagrams of this type (exhibiting first a wide range of the γ-phase and then a narrowing of the phase caused by the appearance of heterogeneous regions) are found for N, C, Cu, Zn, Au, Re, etc.

As distinct from the elements of the first group, elements entering the second group elevate the point A_3 and lower the point A_4 as their content in the alloy is raised. This leads initially to narrowing and then to a complete closing of the region of the γ-solid solution as shown schematically in Figure 4.3. This shift of the critical points of alloys is induced by such elements as Cr, Mo, W, Si, T, Al, and Be (Cr group). These elements can be placed in the first subgroup of the second group of alloying elements. The second subgroup includes elements

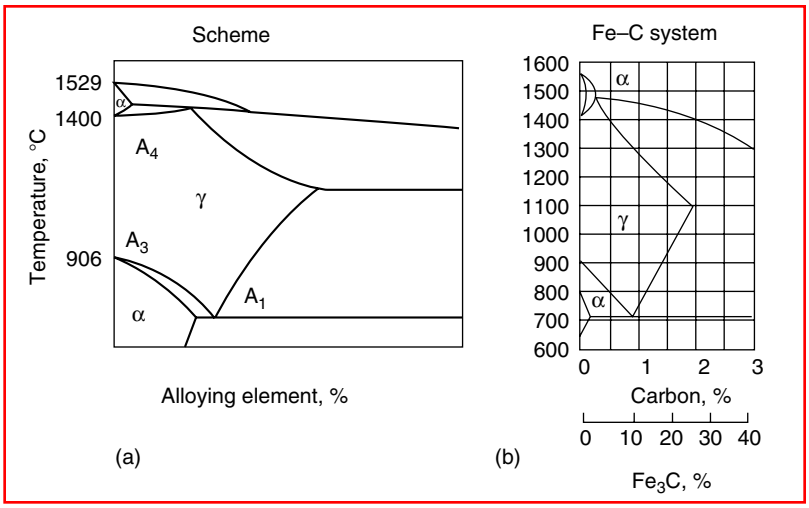

FIGURE 4.2 Scheme (a) and equilibrium diagram (b) for Fe and alloying elements with extended γ-phase range and limited solubility.

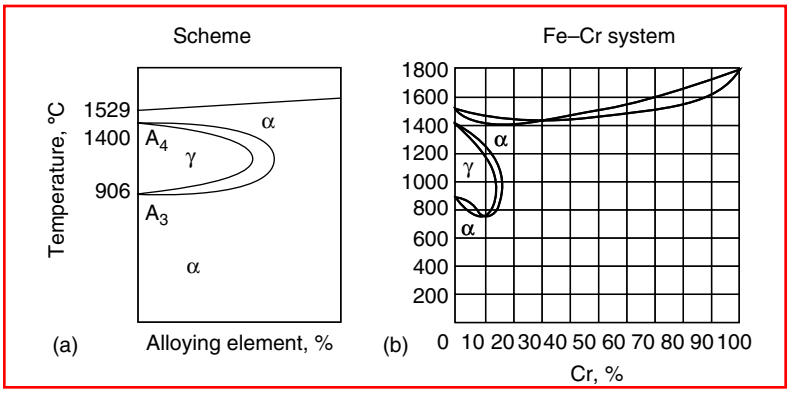

FIGURE 4.3 Scheme (a) and equilibrium diagram (b) for Fe and alloying elements with closed γ-phase range.

whose introduction causes the appearance of other phases in the equilibrium diagrams before the γ-phase range is closed. It follows from Figure 4.4 that in this case the narrow range of the γ-phase is limited by adjacent heterogeneous regions. Equilibrium diagrams of this type (with a narrow range of the γ-phase and its limitation by an adjacent heterogeneous region) are due to Zr, Ta, Nb, Ce, etc.

The above-described division of alloying elements into two large groups can be applied to ternary and more complex systems. The first basic ternary diagram is obtained when iron is alloyed with two elements, each leading to broadening of the γ-phase range in binary iron alloys. Such alloys can be exemplified by Fe–Co–Ni, Fe–Co–Mn, and Fe–Ni–Mn.

The second basic diagram covers iron alloys with two elements, which close the γ-phase range. An example of these alloys is the Fe–Cr–Mo system, but it includes, along with regions of solid solutions, intermetallic compounds that are formed at high concentrations.

The third basic type of equilibrium diagram applies to a ternary system where one of the elements widens the γ-phase range and the other element closes it. An example is the Fe–Cr–Ni system, which is important in technical terms. Thus even ternary systems may include purely ferritic (α-phase) and purely austenitic (γ-phase) alloys as well as alloys possessing a multi-phase structure.

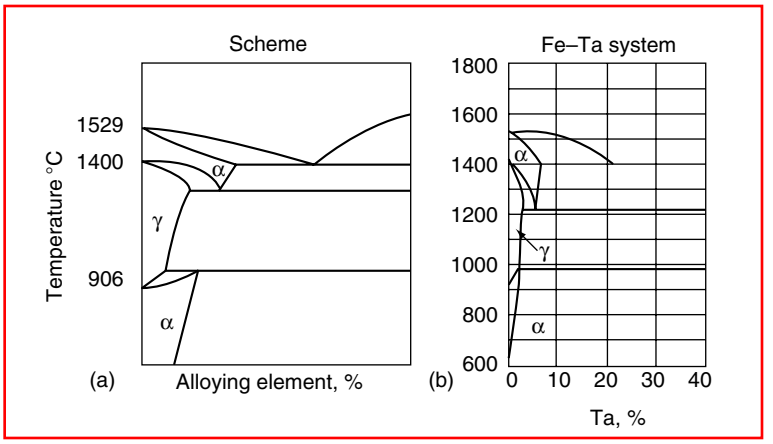

FIGURE 4.4 Scheme (a) and equilibrium diagram (b) for Fe and alloying elements with narrow γ-phase range limited by adjacent heterogeneous region.

4.1.2 Eutectoid Composition and Temperature

The aforementioned division of alloying elements into groups according to their influence on allotropic transformations in alloys of the iron-alloying element system allows one to predict to some extent the effect of the elements on the critical points of carbon steel. For example, considering the diagram lines that correspond to the transition of Fe from one allotropic form to another, it can be expected that the elements extending the γ-phase range (Ni group) will lower the $\alpha \rightarrow \gamma$ iron transition point A_{c3}, while the elements narrowing the γ-phase range (Cr group) will elevate that point.

A similar effect of the elements is observed, to a certain extent, in the pearlite transformation A_{c1} as in this case, too, an allotropic change of iron takes place: Fe_α transforms to Fe_γ. Figure 4.5 illustrates the influence of the most important alloying elements on the position of the critical point A_{c1}. As is seen, the elements narrowing the γ-phase range do raise the critical point A_{c1}, while the elements broadening the γ-phase range lower it.

It should be noted that in the case of Cr group elements one observes a known relationship between the limiting concentration necessary to close the γ-phase range in iron-alloying element alloys and the degree of elevation of the point A_{c1}. The lower the concentration of the element at which the γ-phase range is closed, the more abrupt the rise of the critical point A_{c1}.

If a steel simultaneously contains two or more alloying elements that influence its critical points in the same direction, the critical points usually lower or elevate to a greater extent than would be the case if only one of the elements exerted its influence. But here the result cannot be presented by a simple dependence. If a carbon steel contains alloying elements that have an opposite effect on the position of the critical points during heating, the influence of the elements shows up differently depending on their quantitative ratio. Table 4.1 gives values of the critical points during heating and cooling for some multialloy steels. As is seen, rather high A_{c1} and A_{c3} points are characteristic of chromium–silicon and chromium–silicon–molybdenum steels of the heat-resistant type, high-chromium steels of the stainless type, chromium–molybdenum–vanadium steels, and others. The data of Table 4.1 are also interesting in that they show a simultaneous effect of the most significant alloying elements on the critical points A_{r3} and A_{r1} under constant-rate cooling. In particular, a very sharp lowering of these points in multialloy steels is caused by molybdenum. Molybdenum is responsible for a drastic drop of the critical points under cooling in steels that contain chromium and nickel at the same time. This last fact is especially important for structural steel.

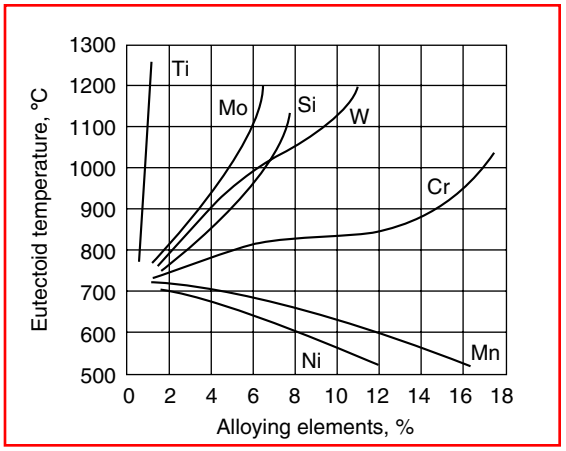

FIGURE 4.5 Effect of alloying elements on the eutectoid transformation temperature A_{c1}.

TABLE 4.1
Position of Critical Points during Heating and Cooling of Some Multialloy Steels

	Chemical Composition[a] (%)								Critical Points[b] (°C)			
									Heating		Cooling	
No.	C	Mn	Si	Cr	Ni	Mo	V	W	A_{c1}	A_{c3}	A_{r3}	A_{r1}
1	0.20	—	2.25	1.50	—	—	—	—	820	860	800	715
2	1.10	—	1.55	4.83	—	0.51	—	—	845	880	865	760
3	0.06	—	—	5.33	—	0.57	—	—	830	880	820	750
4	0.36	—	—	0.96	—	0.20	—	—	770	810	745	680
5	0.45	—	—	1.00	—	0.35	0.26	—	775	790	700	650
6	0.30	—	—	4.82	—	2.20	0.42	—	885	920	745	710
7	0.34	—	—	4.72	—	1.65	—	0.93	780	820	310	225
8	0.25	1.26	—	—	—	0.41	—	—	745	840	750	690
9	0.22	1.15	—	—	—	1.18	—	—	750	840	540	430
10	0.35	—	—	—	2.73	0.39	—	0.19	710	765	495	400
11	0.36	—	—	—	2.87	0.39	—	—	715	760	515	400
12	0.29	—	—	0.64	3.44	—	—	—	715	770	600	525
13	0.60	—	—	0.75	1.40	0.22	—	—	730	765	540	630
14	0.28	—	—	0.86	1.97	0.35	—	—	740	785	490	390
15	0.15	—	—	11.27	0.13	—	—	—	810	860	770	715
16	0.12	—	—	12.19	—	0.58	—	—	830	870	700	—
17[c]	0.13	—	—	13.15	—	—	—	—	890	900	810	785

[a] The content of Mn and Si is standard if not specified otherwise. Residual Cr and Ni are also present in all steels.
[b] The critical points were determined by the dilatometric method; the cooling rate ~2°C/s (~4°F/s).
[c] No. 17 also has 0.25% Al.

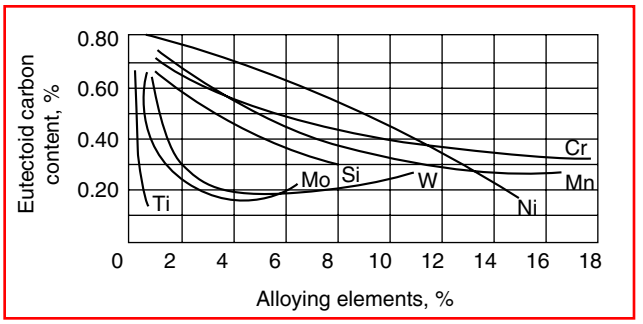

FIGURE 4.6 Effect of alloying elements on the concentration of carbon in eutectoid.

The effect of alloying elements manifests itself in a shift of the critical points with respect not only to temperature but also concentration. Figure 4.6 illustrates how the content of alloying elements in steel affects the carbon concentration at the eutectoid point. As can be seen from the figure, all the alloying elements shift the eutectoid point to the left, i.e., toward lowering of the carbon concentration, and consequently decrease the carbon content of alloy pearlite. In analogy to the shift of the eutectoid point to the left, the addition of most alloying elements in steel is followed by a leftward displacement of the point E in the Fe–C equilibrium diagram, which determines the solubility limit of carbon in austenite. The point E is shifted most by Cr, Si, W, Mo, V, and Ti, which are arranged here in ascending order of their influence. All these elements narrow the γ-phase range in alloys of the iron-alloying element system.

If a carbon steel contains a certain amount of an alloying elements, point E is displaced to the left to such an extent that even at a carbon concentration of several tenths of a percent the steel structure may have ledeburite, which is present in pure iron–carbon steels only when the carbon content is over 1.7%.

It is of interest to note that the more strongly an element shifts the points E and S, the lower the element concentration at which it closes the γ-phase range in the iron-alloying element diagram. Therefore a leftward shift of the points E and S can be considered as the tendency of a specific alloying element to narrow the γ-phase (austenite) range.

Therefore the introduction of alloying elements into a carbon steel is accompanied by a shift of the equilibrium critical points with respect to both temperature and carbon concentration. The greater the shift, the larger the amount of the elements introduced.

4.1.3 Distribution of Alloying Elements

In commercial alloy steels, which are multicomponent systems, alloying elements can be found (1) in the free state; (2) as intermetallic compounds with iron or with each other; (3) as oxides, sulfides, and other nonmetal inclusions; (4) in the carbide phase as a solution in cementite or in the form of independent compounds with carbon (special carbides); or (5) as a solution in iron.

As to the character of their distribution in steel, alloying elements may be divided into two groups:

1. Elements that do not form carbides in steel, such as Ni, Si, Co, Al, Cu, and N
2. Elements that form stable carbides in steel, such as Cr, Mn, Mo, W, V, Ti, Zr, and Nb

The law determining the manner in which elements of the first group are distributed in steel is very simple. These elements do not form chemical compounds with iron and carbon, and consequently the only possible form in which they can be present in steel is in solid

solutions with iron. The only exceptions are Cu and N. Copper dissolves in α-iron at normal temperatures in amounts of up to 1.0%. If the Cu content exceeds 7%, iron will contain copper in the free state as metal inclusions. Similar behavior is typical of the alloying elements that do not dissolve in solid iron at all (e.g., Pb or Ag). Nitrogen also has a limited solubility in ferrite. When the N content is higher than 0.015%, nitrogen is found in steel in the form of chemical compounds with iron or some alloying elements (V, Al, Ti, Cr). These chemical compounds are called nitrides.

Most alloying elements can form intermetallic compounds with iron and with each other. But these compounds are formed only at concentrations of the alloying elements, which are not used in the usual commercial steels. Therefore it can be assumed that the common quantity-produced steels do not have intermetallic compounds of alloying elements with iron or with each other. Intermetallic compounds are formed in high-alloy steels, a fact that is of great significance for these steels.

Alloying elements, whose affinity for oxygen is greater than that of iron, are capable of forming oxides and other nonmetal compounds. When added at the very end of the steel melting process, such elements (e.g., Al, Si, V, Ti) deoxidize steel by taking oxygen from iron. The deoxidizing reaction yields Al_2O_3, TiO_2, V_2O_5, and other oxides. Owing to the fact that alloying elements that are deoxidizers are introduced at the final stages of the steel melting process, the majority of oxides have no time to coagulate or to pass to slag, and as a result they are retained in the solid steel as fine nonmetal inclusions. In addition to a great affinity for oxygen, some alloying elements have a greater affinity for sulfur than iron does, and upon introduction into steel, they form sulfides.

Compared to noncarbide-forming elements, alloying elements that form stable carbides in steel exhibit a much more complicated distribution. They can be found in the form of chemical compounds with carbon and iron or be present in the solid solution. The distribution of these elements depends on the carbon content of steel and the concurrent presence of other carbide-forming elements. If a steel contains a relatively small amount of carbon and a great quantity of an alloying element, then obviously carbon will be bound to carbides before the carbide-forming elements are completely used. For this reason excess carbide-forming elements will be found in the solid solution. If a steel has a large amount of carbon and little of the alloying elements, the latter will be present in steel mainly as carbides. Carbide formation is treated in detail in the next section.

Note in conclusion that most alloying elements, except C, N, O, B, and metalloids standing far from iron in the periodic table, dissolve in great amount in iron. The elements standing to the left of iron in the periodic table are distributed between iron (base) and carbides; those to the right of iron (Co, Ni, Cu, etc.) form solutions with iron only and do not enter into carbides. Thus one can state that alloying elements dissolve predominantly into basic phases (ferrite, austenite, cementite) of iron–carbon alloys or form special carbides.

4.1.4 Alloy Carbides

Carbides are formed in steels only by iron and metals that stand to the left of iron in the periodic table: Mn, Cr, W, V, Zr, Nb, Ti. Here the elements are arranged in accordance with their affinity for carbon. The elements at the left end of the row form relatively unstable carbides that dissociate readily on heating. In contrast, the elements at the right end of the row form extremely stable carbides that dissociate at temperatures much higher than the critical points of steel.

Similar to iron, the above-mentioned carbide-forming elements refer to the elements of transition groups but possess a less perfect d-electron band. The further left a carbide-forming element stands in the periodic table, the less perfect is its d-band.

There is reason to believe that during carbide formation carbon donates its valence electrons to fill the d-electron band of the metal atom, while valence electrons of the metal form a metal bond, which determines the metallic properties of carbides. At the same time numerous experiments show that the more to the left an element stands in the periodic table, the less perfect is its d-electron band and the more stable is the carbide. From these facts, it is possible to formulate the general principles of carbide formation in steels: only metals whose d-electron band is filled less than that of iron are carbide-forming elements. Their activity as carbide-forming elements is greater and the stability of the carbide phases formed is the higher, the less perfect is the d-band of the metal atom. This principle allows specifying conditions of carbide formation in steels in the presence of several carbide-forming elements, the sequence of dissolution of various carbides in austenite, and other factors that are important for the theory of alloying, manufacturing practice, and application of alloy steels. The formation activity and stability of carbides in alloy steels will increase in going from Mn and Cr to Mo, W, V, Ti, and other elements whose d-bands are less perfect than those of Mn and Cr. This means that if a steel contains, e.g., both chromium and vanadium, one should expect vanadium carbides to form first (under equilibrium conditions).

If the atomic radius of carbon is taken equal to 0.079 nm, it is easy to calculate that for all carbide-forming elements except Fe, Mn, and Cr, the ratio of atomic radii of carbon and metal is less than 0.59. It is known that if the ratio of atomic radii of a transition group metal and a metalloid with a small atomic radius (C, N, H) is less than 0.59, special types of compounds called interstitial phases can be formed.

The carbon/metal ratio of most carbide-forming alloying elements is lower than 0.59, and therefore the elements and carbon are capable of forming interstitial phases. It was found that the following carbide compounds may be formed in steels:

Carbides of Group I	Carbides of Group II
Fe_3C	Mo_2C
Mn_3C	W_2C, WC
$Cr_{23}C_6$, Cr_7C_3	VC
Fe_3Mo_3C	TiC
Fe_3W_3C	NbC
	TaC, Ta_2C
	ZrC

However, the above carbides are not found in steels in pure form. Carbides of all alloying elements contain iron in solution, and if other alloying elements are present, they include these elements too. Thus, in a chromium–manganese steel the carbide $(Cr, Mn, Fe)_{23}C_6$, which contains iron and manganese in the solution, is formed instead of the pure chromium carbide $Cr_{23}C_6$.

Owing to the fact that carbides with the same chemical formula mutually dissolve, in the presence of titanium and niobium, for example, rather than two kinds of carbides forming, a single carbide will be formed that includes titanium and niobium on equal terms. For this reason possible variants of carbide formation are fewer, and actually we have only six kinds of carbides in steels:

Carbides of Group I	Carbides of Group II
M_3C	MC
$M_{23}C_6$	M_2C
M_7C_3	
M_6C	

where M denotes a sum of carbide-forming (metal) elements.

The carbides placed in group I possess a complicated crystal structure; an example is cementite. A specific structural feature of the carbides of group II as interstitial phases is a simple crystal lattice. They usually crystallize with a great carbon deficiency.

It is worth noting that interstitial phases dissolve poorly in austenite and may not pass into solid solution even at high temperatures. This distinguishes interstitial phases from the carbides of group I, which readily dissolve in austenite on heating. All carbide phases have a high melting temperature and high hardness. Interstitial phases surpass the carbides of group I in this respect.

4.2 EFFECT OF ALLOYING ELEMENTS ON AUSTENITE TRANSFORMATIONS

The overwhelming majority of alloy steels are used after heating to the austenite stage, quenching, and subsequent annealing. During quenching and annealing, austenite transforms with three types of transformations possible: pearlite transformation (often called diffusive transformation, precipitation to the ferrite–carbide mixture, or stage I transformation), intermediate transformation (bainite or stage II transformation), and martensite transformation (stage III transformation). The precipitation stability of undercooled austenite is characterized by the diagrams of isothermal and thermokinetic austenite transformation.

The isothermal diagrams characterize the precipitation kinetics of austenite at constant temperature of undercooling. Such diagrams are useful for comparative evaluation of different steels and also for clarifying the influence of alloying and other factors (heating temperature, grain size, plastic deformation, and so on) on the precipitation kinetics of undercooled austenite.

Thermokinetic diagrams characterize the precipitation kinetics of austenite under continuous cooling. These diagrams are less illustrative but have great practical importance, because when subjected to thermal treatment, austenite precipitates under continuous temperature variation rather than under isothermal conditions. Under continuous cooling, transformations occur at a lower temperature and take a longer time than in the isothermal case. Alloying elements have considerable influence on the kinetics and mechanism of all three types of transformations of undercooled austenite: pearlite, bainite, and martensite transformations. However, these elements influence austenite precipitation in different ways.

Alloying elements that dissolve only in ferrite and cementite without the formation of special carbides exert just a quantitative effect on the transformation processes (Figure 4.7). Cobalt speeds up a transformation but the majority of elements, including Ni, Si, Cu, Al, etc., slow it down.

Carbide-forming elements produce both quantitative and qualitative changes in the kinetics of isothermal transformations. Thus, the alloying elements forming group I carbides influence the austenite precipitation rate differently at different temperatures:

At 1300–930°F (700–500°C) (pearlite formation), they slow the transformation.
At 930–750°F (500–400°C), they dramatically slow the transformation.
At 750–570°F (400–300°C) (bainite formation), they speed up the transformation.

Thus, steels alloyed with carbide-forming elements (Cr, Mo, Mn, W, V, etc.) have two maxima of the austenite isothermal precipitation rate separated by a region of relative

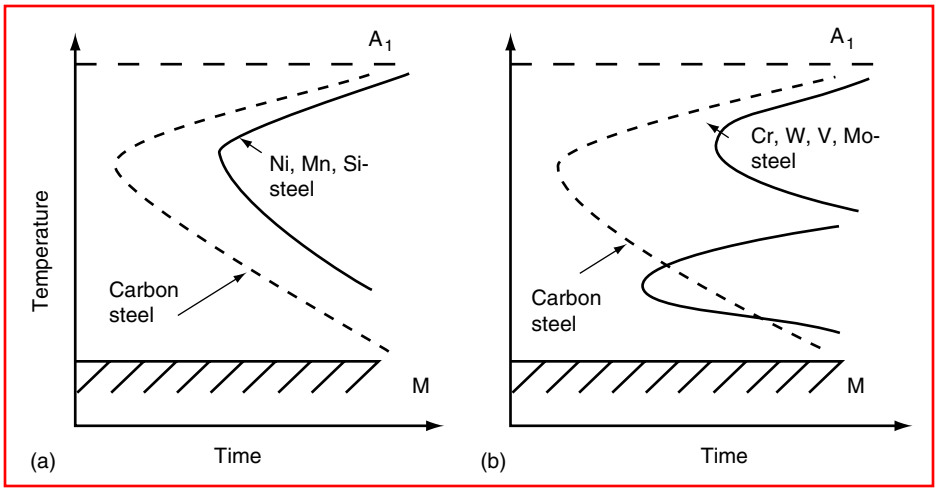

FIGURE 4.7 Diagrams of isothermal austenite precipitation. (a) Carbon steel and steel alloyed with noncarbide-forming elements; (b) carbon steel and steel alloyed with carbide-forming elements.

stability of undercooled austenite (Figure 4.7). The isothermal precipitation of austenite has two clearly defined intervals of transformation: (1) to a lamellar structure (pearlite transformation) and (2) to a needle-like structure (bainite transformation). At temperatures lower than those indicated above and given greater degrees of undercooling as in the $\gamma \rightarrow \alpha$ transformation start temperature, the martensite transformation develops in alloy steels. As a result, a supersaturated α-iron-based solid solution is formed.

The remainder of this section considers in more detail the influence of alloying elements on the mechanism and kinetics of austenite precipitation for all three types of transformations.

4.2.1 Influence of Alloying on Ferrite and Pearlite Interaction

The most important practical feature of alloying elements is their capacity to decrease the austenite precipitation rate in the region of the pearlite transformation, which shows up as a rightward shift of the line in the isothermal austenite precipitation diagram. This favors a deeper hardening and undercooling of austenite up to the range of martensite transformation under slow cooling such as air cooling.

In alloy steels, the pearlite transformation consists of a polymorphous $\gamma \rightarrow \alpha$ transformation and diffusion redistribution of carbon and alloying elements. As a result, special carbides and a ferrite–cement mixture (pearlite) are formed. Particular alloying elements and their amounts in the initial γ-solid solution determine the rates of the individual steps of pearlite transformation and consequently its kinetics as a whole.

The polymorphous $\gamma \rightarrow \alpha$ transformation in iron under small undercooling of austenite (near the temperature of stage I) proceeds by means of disordered displacement of atoms, as distinct from the martensite transformation (under greater undercooling), which proceeds through ordered shear. As mentioned above, all alloying elements dissolved in austenite, except Co, slow the pearlite transformation and shift the top section of the isothermal austenite precipitation curve to the right.

The nature of the increase in stability of undercooled austenite under the influence of alloying elements is rather complicated. Whereas in carbon steels the pearlite transformation is associated with the $\gamma \rightarrow \alpha$ rearrangement of the lattice and diffusion redistribution of carbon,

in alloy steels these processes can be supplemented with the formation of special carbides and diffusion redistribution of alloying elements dissolved differently in ferrite and carbide.

Not only do austenite-dissolving elements have small diffusion coefficients of their own which are sometimes several orders of magnitude smaller than that of carbon, but also some of them (e.g., Mo, W) slow the diffusion of carbon in the γ lattice. Besides, some of the elements (e.g., Cr, Ni) retard the $\gamma \rightarrow \alpha$ rearrangement, which is part of the pearlite transformation. Depending on the steel composition and degree of undercooling, the decisive role may belong to one of the above-mentioned factors.

The formation of carbides during pearlite transformation in steel results from a redistribution of carbon and alloying elements between the phases that are formed: ferrite and carbides. In the presence of dissolved strong carbide-forming elements (Nb, V, Cr, etc.), special carbides are formed in undercooled austenite before the $\gamma \rightarrow \alpha$ transformation begins, in excess ferrite (in eutectoid and hypereutectoid steels this stage is absent) and in eutectoid ferrite (pearlite). Every stage yields special carbides whose type depends on the austenite composition.

If a steel contains carbide-forming elements (V, Nb, Ti, Zr) that pass into solid solution during austenitization, then a carbide of one type, MeC (VC, NbC, TiC, ZrC), is formed at all the stages.

The scheme of austenite precipitation and the carbide formation process during pearlite transformation in steels with V, Nb, Ti, and Zr are as follows:

$$\gamma \rightarrow \mathrm{MeC_A} + \gamma'$$

$$\alpha_{se} + \gamma_e$$

$$\mathrm{MeC_f} + \alpha_{ee}\mathrm{Fe_3C} + \alpha_{se} \rightarrow \mathrm{MeC_e} + a_{ee}$$

Here γ is the initial undercooled austenite; $\mathrm{MeC_A}$ is the carbide precipitated in austenite; γ' is austenite after carbide precipitation; α_{se} is excess ferrite supersaturated with a carbide-forming element and carbon; α_{ee} is equilibrium excess ferrite; $\mathrm{MeC_f}$ is the carbide precipitated in excess ferrite; γ_e is austenite of eutectoid composition; $\mathrm{Fe_3C}$ is the eutectoid cementite (pearlite); α_{se} is the supersaturated eutectoid ferrite (pearlite); α_{ee} is the equilibrium eutectoid ferrite; $\mathrm{MeC_e}$ is the carbide precipitated in the eutectoid ferrite.

The formation of carbide ($\mathrm{MeC_A}$) in undercooled austenite before the $\gamma \rightarrow \alpha$ transformation starts is due to the fact that solubility of the carbide-forming element and carbon in austenite decreases with decreasing temperature. As is seen from the scheme, after the polymorphous $\gamma \rightarrow \alpha$ transformation the ferrite (both excess and eutectoid) is first supersaturated with the carbide-forming element and carbon, then a carbide is formed from ferrite, and subsequently the state of ferrite approximates the equilibrium condition. This process lasts for a few seconds.

In steels containing other carbide-forming alloying elements (Cr, Mo, W), the carbide formation process is much more complicated. Depending on their content in austenite, these elements can form several types of carbides: alloy cementite $(Fe, Cr)_3C$ and special carbides $(Fe, Cr)_7C_3$ and $(Fe, Cr)_{23}C_6$ in Cr steels and carbides $(Fe, Mo)_{23}C_6$, MoC, Mo_2C, and $(Fe, Mo)_6C$ in steels with Mo (W forms analogous carbides).

Noncarbide-forming elements (Ni, Co, Si, etc.) do not participate directly in carbide formation. As a rule their amount in cementite equals their average concentration in steel. These elements can indirectly influence the thermodynamic activity of other elements, i.e., the process of their redistribution during carbide formation. As mentioned above, the process of

carbide formation is limited by the mobility of the carbide-forming elements. With a decrease in temperature their diffusion mobility diminishes and special carbides are not formed below 400–500°C (750–930°F). At lower temperatures the intermediate (bainite) transformation takes place, and at higher undercooling rates martensite (diffusionless) transformation occurs.

4.2.2 Effect on Martensite Transformation

As in carbon steels, the martensite transformation in alloy steels takes place under rapid cooling from temperatures higher than the equilibrium temperature of the $\gamma \rightarrow \alpha$ transformation (A_1). At the martensite transformation temperature both the diffusion movement of metal atoms of iron and alloying elements and that of metalloid atoms of carbon and nitrogen are suppressed. For this reason the martensite transformation in steels proceeds by a diffusionless mechanism.

The martensite transformation can take place in carbon-containing alloy steels, noncarbon-containing alloy steels, and binary iron-alloying element alloys. The martensite transformation usually leads to formation of a supersaturated α-iron-based solid solution. In carbon-containing steels, the solid solution is supersaturated mainly with carbon, and in noncarbon-containing alloy steels, with alloying elements. The content of carbon and alloying elements in martensite is the same as that in the initial austenite.

The transformation of austenite into martensite during cooling starts at a certain temperature called M_s. This temperature is independent of the cooling rate over a very wide range of cooling rates.

The martensite transformation kinetics of most carbon and structural and tool alloy steels is athermal in character. The athermal martensite transformation is characterized by a smooth increase in the amount of martensite as the temperature is lowered continuously in the martensite interval M_s–M_f, where M_f is the martensite finish temperature. As a rule, this transformation takes place in steels with the martensite point M_s higher than room temperature.

A version of athermal martensite transformation is explosive martensite transformation, where a certain quantity of martensite is formed instantly at or a little below the temperature M_s. This transformation is observed in alloys with the martensite point below room temperature.

The position of the martensite point also determines the microstructure and substructure of the martensitic-quenched steel. At temperatures M_s below room temperature, lamellar (plate) martensite is formed in quenched iron–carbon and alloy steels. Crystals of this martensite are shaped as fine lenticular plates. In steels with the martensite point M_s higher than room temperature, lath martensite is formed during quenching. Crystals of this martensite have the form of approximately equally oriented thin plates, which are combined into more or less equiaxial packets. The substructures of needle and lath martensite are qualitatively different.

From what has been said above, it might be assumed that the martensite transformation kinetics, the morphological type of martensite, the substructure of martensitic-quenched steels, and other phenomena are connected to a great extent with the martensite-start temperature M_s. Thus the influence of the elements on martensite transformation is determined primarily by their influence on the position of the martensite point M_s. Of practical importance is also the martensite finish temperature M_f.

Experiments concerned with the influence of alloying elements on the position of the martensite point show that Co and Al elevate the martensite start temperature, Si has little if any effect, and all the other elements decrease M_s (Figure 4.8).

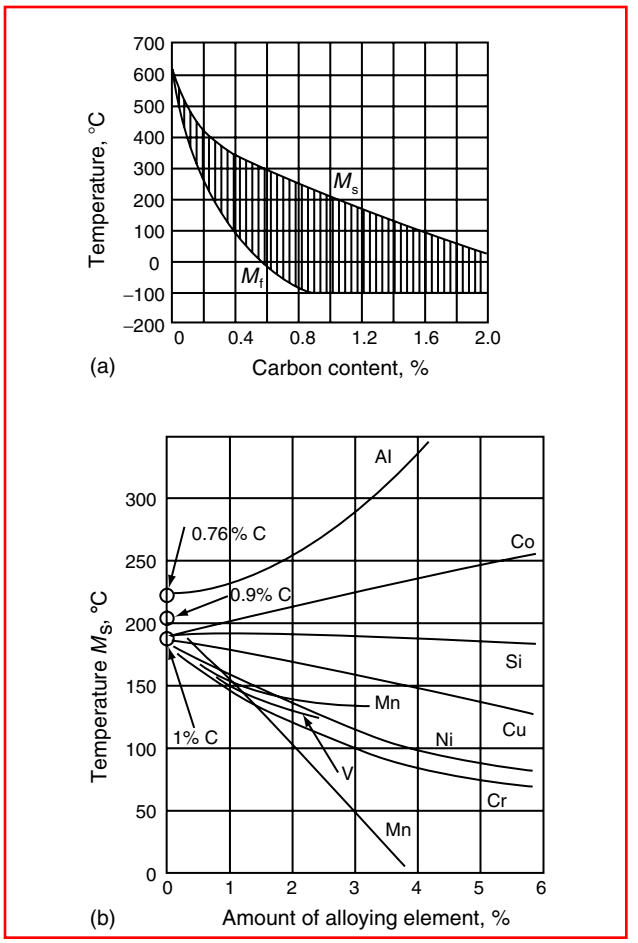

FIGURE 4.8 The influence of the content of (a) carbon and (b) alloying elements at 1% C on the martensite point position.

The quantitative influence of alloying elements is approximately as follows (per 1 wt% of the alloying element):

Element	Mn	Cr	Ni	V	Si	Mo	Cu	Co	Al
Shift of point M_s (°C)	−45	−35	−26	−30	0	−25	−7	+12	+18 (°C)
	−81	−63	−47	−54	0	−45	−13	+22	+32 (°C)

These data are given for carbon steels containing 0.9–1.0% C. For a wider range of C content, the quantitative influence of the elements can be different. In particular, it was established that the smaller the C content, the weaker is the influence of the alloying elements on the position of point M_s. The martensite start temperature of medium-carbon alloy steels can be estimated using empirical formula

$$M_H(^\circ C) = 520 - 320(\%\ C) - 50(\%\ Mn) - 30(\%\ Cr) - 20[\%(Ni + Mo)] - 5[\%(Cu + Si)],$$

where % C, % Mn, etc. are the contents of the corresponding elements in weight percent.

The results of calculations by this formula for steels containing 0.2–0.8% C are in good agreement with the experimental data. However, for multialloy steels this formula does not always yield reliable data because if a steel contains several alloying elements it is impossible to determine their combined effect on the martensite point by simple summation. Thus, for example, Mn lowers the point M_s to a greater extent than Ni, but in a steel with a high Cr content its effect is weaker than that of Ni.

The martensite point M_s is affected mostly by C dissolved in austenite (Figure 4.8). The transformation finish temperature M_f intensively decreases too, as the C content is increased up to 1% [to 100°C (212°F)] and remains constant at higher amounts of carbon.

The reason carbon and alloying elements influence the position of the martensite point is mainly a change in the relative thermodynamic stability of γ- and α-phases of iron, because the martensite transformation itself is a $\gamma \rightarrow \alpha$ transformation.

4.2.3 Retained Austenite

A characteristic feature of the martensite transformation in steels, whatever its character (athermal, explosive, or fully isothermal), is that transformation of austenite to martensite is never complete. Figure 4.9 shows the amount of martensite formed when the temperature is decreased continuously in the martensite range M_s–M_f (martensite curve) for the athermal type of martensite transformation. The transformation starts at the point M_s, and the amount of martensite increases with decrease in temperature. The end of the transformation corresponds to the temperature M_f. At this temperature a certain amount of austenite is still left (retained austenite, A, %). Cooling below M_s does not lead to further transformation or lower the amount of retained austenite.

Investigations show that martensite curves of different steels, both carbon and steels and steels alloyed with different elements and in different amounts, exhibit approximately the same behavior. Then, if the martensite finish temperature is below room temperature, the amount of retained austenite should, in a general case, be higher, the lower the martensite point M_s. Strictly speaking, the amount of retained austenite depends on the martensite temperature range, i.e., on the M_s–M_f temperature difference; it increases as the range narrows. But the martensite range itself depends on the position of the martensite point M_s: the range narrows as the point M_s lowers.

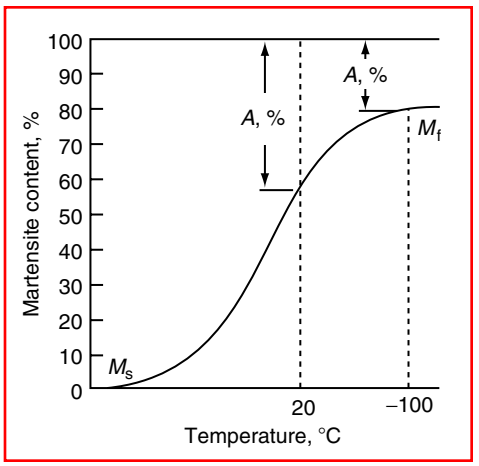

FIGURE 4.9 Martensite curve.

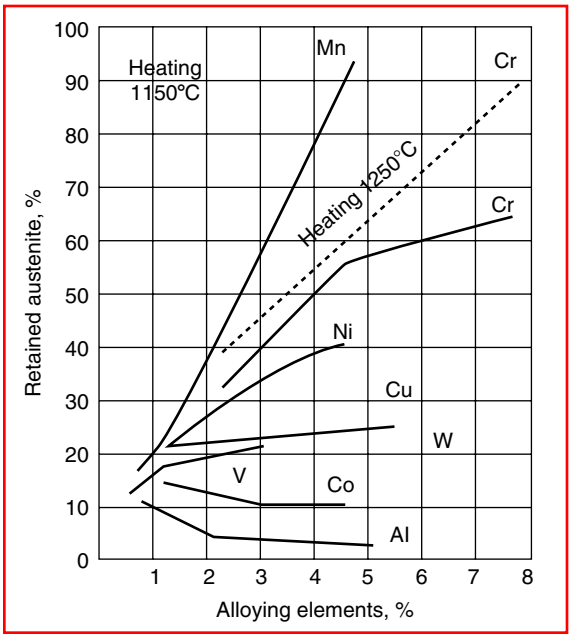

FIGURE 4.10 The influence of alloying elements on the amount of retained austenite in quenched steel (1% C).

Thus the influence of alloying elements on the amount of retained austenite formed during the quenching of steels should qualitatively and, to a great extent, quantitatively correspond to their influence on the position of the martensite start point M_s. Available experimental data show that alloying elements that lower and raise the martensite start point increase and decrease the amount of retained austenite, respectively (Figure 4.10). Besides, a certain sequence in the arrangement of the elements is observed from the point of view of their quantitative influence. In particular, the largest amount of retained austenite in accordance with their influence on the position of the martensite point is due to Mn, Cr, Ni, etc. As illustrated in Figure 4.11, the influence of these elements on the martensite range follows the same sequence.

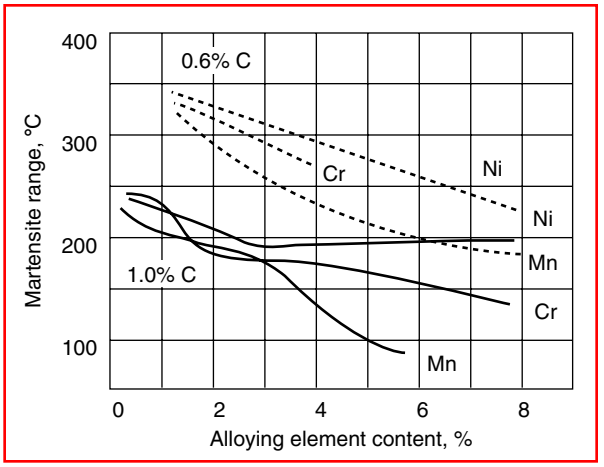

FIGURE 4.11 The influence of alloying elements on the martensite range.

In alloy steels, the martensite point M_s lowers most and the martensite range narrows under the influence of carbon. Therefore the influence of carbon on the amount of retained austenite is much stronger than that of alloying elements. An increase in the C content of chromium–nickel steel from 0.4 to 0.6% increases the amount of retained austenite to ~8.5% after quenching; an increase in the Ni content of the same steel from 1 to 4% brings the amount of retained austenite to ~6% only. The fact that carbon promotes the greatest retention of austenite during quenching is especially unfavorable for low-alloy tool steels.

In multiple alloy steels a given element favors the formation of a greater amount of retained austenite than the law of summation suggests. However, in multiple alloy steels too, the relationship between lowering of the martensite point under the influence of a given element and an increase in the amount of retained austenite caused by the same element persists in the main.

In addition to the content of carbon and alloying elements, other factors can influence the amount of retained austenite formed during quenching of steel. The most important of these is the rate of cooling below the martensite point M_s and the quenching temperature.

The steel cooling rate has no influence on the position of the martensite point, but it affects the martensite transformation process in a certain way. A little below the point M_s, slower cooling enhances the transformation of austenite to martensite. The ability of austenite to isothermally formate martensite at temperatures a little lower than the point M_s is realized here. At temperatures close to the martensite finish temperature M_f but within the interval M_s–M_f, when a rather significant amount of martensite has been formed already, acceleration of cooling favors a more complete transformation. Here a phenomenon called the stabilization of austenite comes into play. Holding in the region of the martensite finish temperature makes retained austenite less prone to subsequent transformation. With slow cooling the austenite stabilizing processes have time to near completion and the transformation proceeds more slowly. Austenite stabilization is associated with stress relaxation. The longer the holding time, the greater the stress relaxation and the greater the degree of the metal cooling needed to accumulate stresses required for the martensite transformation to continue.

The quenching temperature can influence largely, either directly or indirectly, the amount of retained austenite. Its direct effect can be connected with thermal stresses facilitating the transformation of austenite. An indirect effect of the quenching temperature is associated with enrichment of intercrystallite boundaries of austenite in carbon and alloying elements and, primarily, with the transfer of carbides, ferrite, and other phases to the solution. If a steel is heated to a temperature falling within the interval between the critical point A_{c1} and the temperature of full dissolution of ferrite or carbides, the heating temperature will determine the content of carbon and alloying elements in austenite. If carbides dissolve above A_{c1}, then the amount of retained austenite will increase with quenching temperature. If the quenching temperature is elevated above A_{c1} and excess ferrite dissolves (with resulting decrease in the austenite concentration), then the martensite point will occupy the lowest position when a steel is quenched from temperatures slightly higher than the point A_{c1}. Correspondingly, the amount of retained austenite must be the largest at these temperatures and must subsequently decrease until the temperature of full ferrite dissolution is reached.

4.2.4 Effect on Bainite Transformation

The bainite transformation (stage II transformation) takes place in carbon steels under the precipitation curve of undercooled austenite (C curve) in the interval of approximately 500–250°C (930–480°F). This is called the intermediate transformation. It occurs in between the pearlite and martensite transformations. The kinetics of this transformation and the structures produced are similar to those observed during the diffusion pearlite or diffusionless

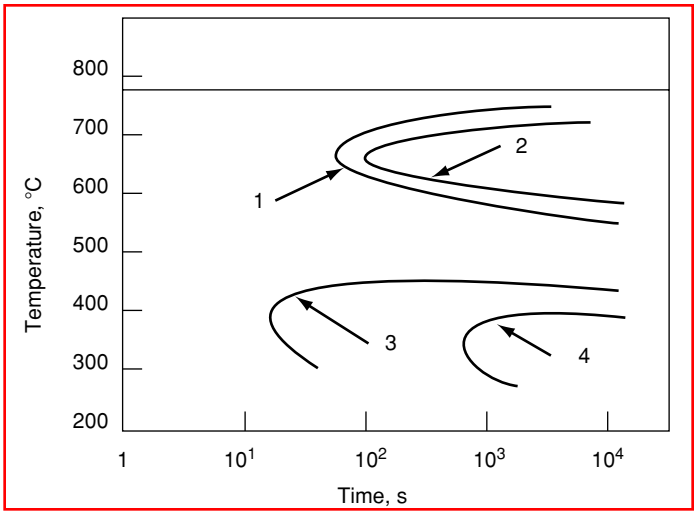

FIGURE 4.12 The austenite precipitation diagram of alloy steels with separate C curves of pearlite and bainite transformations. 1, Start of pearlite formation; 2, finish of pearlite formation; 3, start of bainite formation; 4, finish of bainite formation.

martensite transformation. A mixture of the α-phase (ferrite) and carbide is formed as a result of the bainite transformation, the mixture referred to as bainite.

The kinetics of the intermediate transformation is characterized by a number of peculiarities, such as an incubation period; in the bainite temperature range, precipitation of undercooled austenite begins with a certain time delay. The temperature of the maximum transformation rate (minimum incubation period) depends mainly on the chemical position of the steel.

For alloy steels, C curves of pearlite and bainite transformations can be separated by a temperature interval of a highly stable undercooled austenite where pearlite does not precipitate for many hours, while undercooling is insufficient for the bainite transformation (Figure 4.12).

Alloying elements affect the kinetics of the intermediate transformation, although to a lesser degree than in the case of the pearlite transformation. In some alloy steels, the isothermal transformation is retarded over the entire range of the intermediate transformation, whereas in other steels it is inhibited only at temperatures in the upper part of that range. In steels alloyed with 2% Si or Cr, the transformation of austenite stops even at the lowest temperatures of the intermediate transformation. When steel is alloyed with Ni or Mn, the transformation is retarded only at high temperatures of the intermediate transformation, whereas at lower temperatures austenite transforms almost completely.

Many alloying elements produce a marked effect of the duration of the incubation period, the temperature of minimum stability of austenite, and the maximum transformation rate in the intermediate range. Figure 4.13 shows the influence of some alloying elements on these parameters for high-carbon steels with 1.0% C. As is seen, Mn and Cr strongly influence the kinetics of the intermediate transformation, increasing the duration of the incubation period and lowering the temperature of minimum stability of austenite and the maximum transformation rate. At the same time, alloying with Mo and W, which markedly delays the pearlite transformation, does not have a pronounced effect on the kinetics of the intermediate transformation.

The intermediate transformation in alloy steels consists of a diffusion redistribution of carbon in austenite, diffusionless $\gamma \rightarrow \alpha$ transformation, and formation of carbides, namely

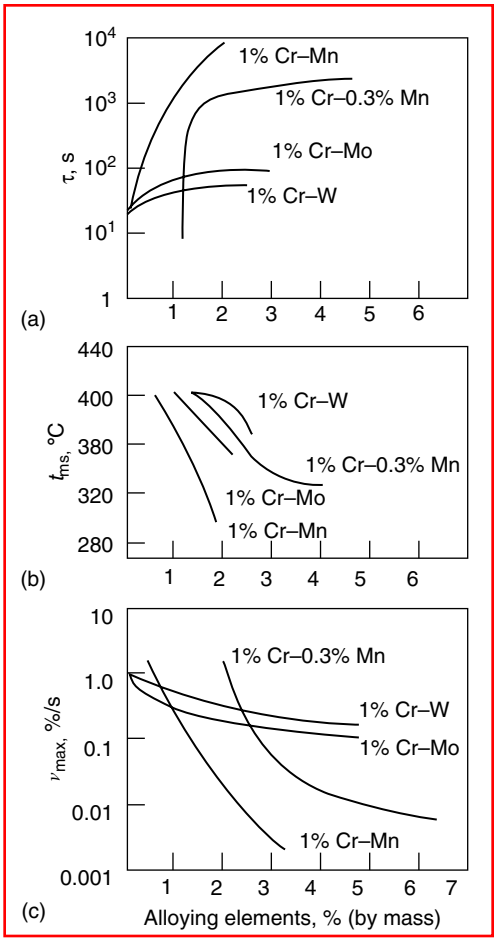

FIGURE 4.13 The influence of Cr, Mo, W, and Mn (a) on the bainite period τ at a minimum stability of austenite; (b) on the temperature of minimum stability t_{ms}, and (c) on the maximum transformation rate v_{max} in the intermediate range.

ε-carbide (a type of Fe carbide) and cementite. Owing to the low diffusion mobility of metallic alloying elements, which are substitutional impurities, special carbides are not formed during the intermediate transformation. The content of alloying elements in the ε-carbide and cementite of bainite is the same as in the initial austenite. Alloying elements do not undergo redistribution during the bainite transformation.

4.2.5 Transformation Diagrams for Alloy Steels

The kinetics of austenite transformation, i.e., the form of the precipitation diagram, depends on a variety of factors, primarily on the chemical composition of austenite. Depending on the alloying of a steel, it is possible to distinguish six basic versions of the diagram of isothermal precipitation of austenite (see Figure 4.14). In carbon steels and some low-alloy steels containing basically noncarbide-forming elements such as Ni, Si, and Cu, the isothermal precipitation is characterized by C-shaped curves with one maximum (Figure 4.14a). The pearlite and intermediate stages are not separated. When these steels are subjected to continuous cooling, three types of structures—martensite, martensite and a ferrite–carbide mixture, and only a ferrite–carbide mixture—can be formed depending on the cooling rate.

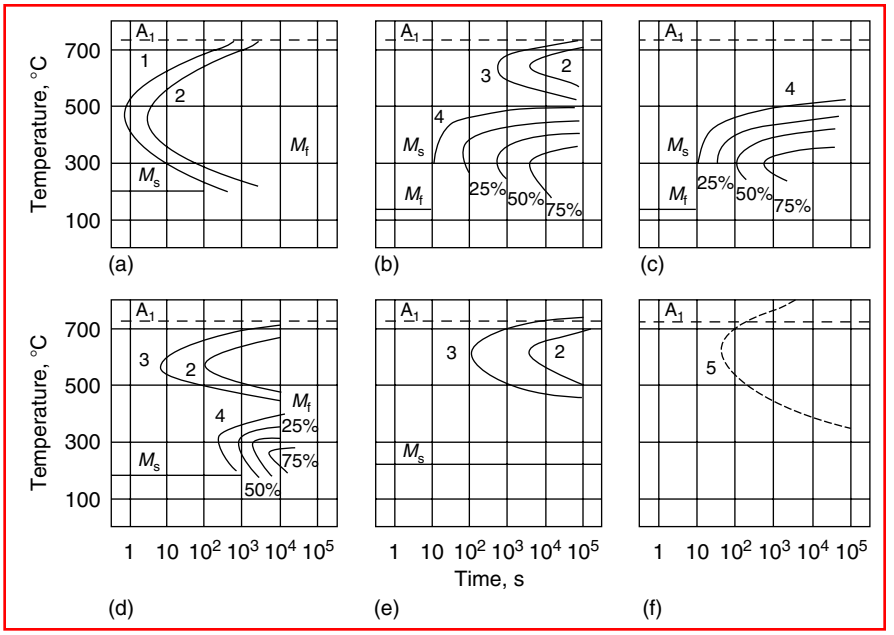

FIGURE 4.14 Basic versions of precipitation diagrams of undercooled austenite. (a) Carbon and low-alloy steels containing no carbide-forming elements; (b) alloy steels (up to 0.4–0.35% C) containing carbide-forming elements; (c) steels alloyed with Cr, Ni, Mo, and W and having a low content of carbon (up to 0.2–0.25% C); (d) alloy steels containing carbide-forming elements (over 0.4–0.5% C); (e) high-alloy steels with a high content of Cr; (f) high-alloy austenitic steels. 1, Transformation start; 2, transformation finish; 3, start of formation of a ferrite–carbon mixture; 4, start of formation of the intermediate transformation products; 5, start of carbide precipitation.

In the case of alloy steels containing carbide-forming elements such as Cr, MO, W, and V (Figure 4.14b and d), the precipitation diagrams have two clearly separated ranges of pearlite and intermediate transformations. Each of the ranges is characterized by its own C-shaped curves. When the carbon content of structural steels is up to 0.4–0.5%, the stage I transformation is shifted to the right relative to the stage II transformation (Figure 4.14b); if the carbon content is higher, stage I is found to the left of stage II (Figure 4.14d).

Chromium–nickel–molybdenum and chromium–nickel–tungsten steels containing 0.15–0.25% carbon (Figure 4.14c) are characterized by a rather high stability of undercooled austenite in the pearlite range and a low stability of undercooled austenite in the bainite range. As a consequence, stage I is absent from the austenite precipitation diagram.

In high-alloy chromium steels, the intermediate transformation may be strongly inhibited and shifted to the martensite temperature range. For this reason the austenite precipitation diagrams have only pearlite transformation and no intermediate transformation (Figure 4.14e).

In steels of the austenitic class (high-alloy steels), the martensite start temperature is below room temperature and stages I and II precipitation practically do not take place owing to a high content of Cr, Ni, Mn, and C (Figure 4.14f). Thanks to the high content of carbon in the austenite of these steels, excess special carbides may be formed on undercooling.

It is worth noting that the aforementioned distinction of the diagrams is conventional to a certain measure as they do not cover a great variety of isothermal and thermokinetic precipitation diagrams of supersaturate austenite.

4.3 HARDENING CAPACITY AND HARDENABILITY OF ALLOY STEEL

As noted in Section 4.2, at great rates of cooling when the cooling curves do not touch the region of isothermal transformation even at inflection points where austenite is least stable, the latter is undercooled to the martensite range (below the point M_s) and steels is fully martensitically hardened. Martensitic transformation of austenite results in a supersaturated solid solution of carbon in α-Fe; the higher the carbon content of the austenite, the more supersaturated the solution. Compared with other austenitic transformation products (pearlite and upper and lower bainite), martensite possesses the greatest hardness and gives very hard steels.

The ability of a steel to increase in hardness during quenching is called its hardenability or hardening capacity. The hardening capacity is characterized by the maximum hardness that can be obtained on the surface of a given steel product by quenching. To achieve maximum hardness it is necessary to observe basic conditions: the rate of cooling should be equal to or higher than the critical rate at which quenching gives martensite alone (inevitability with some retained austenite, of course, but without bainite); all carbon at the quenching temperature should be in the solid solution in austenite (the quenching temperature should be above the critical points A_{c1} and A_{c3} by 30–50°C (80–120°F) for hypereutectoid and hypoeutectoid steels, respectively).

Alongside the notion of hardening capacity, broad use is made in practice of the notion of hardenability, though these two characteristics depend on different factors and are achieved in different ways. The hardening capacity of a steel is determined by the factors affecting the hardness of martensite, while its hardenability is determined by those affecting the quantity of the martensite obtained and the hardness penetration depth. Upon quenching, steel can feature high hardening capacity and low hardenability at the same time. Such a steel would correspond to the schematic curve 1 in Figure 4.15. If for a workpiece of the same diameter D cooled under the same conditions, the distribution of hardness over the cross section is characterized by curve 2; such a steel possesses medium or poor hardening capacity but good hardenability. Finally, steel that corresponds to curve 3 would possess high hardening capacity and high hardenability.

4.3.1 Hardness and Carbon Content

The hardening capacity of a steel whose general characteristic could be maximum hardness depends mainly on the carbon content and, to a lesser extent, on the amount of alloying elements and austenite grain size. Increasing the carbon content of martensite increases its

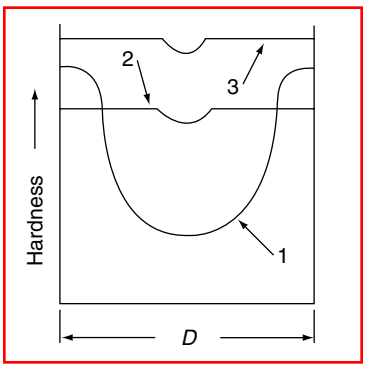

FIGURE 4.15 Distribution of hardness over the cross section of workpiece for three steels differing in hardenability and hardening capacity.

hardness (Figure 4.7). Note that the hardness of a quenched steel and the hardness of martensite crystals are not the same thing because quenched steel contains retained austenite. The hardness of a steel quenched from austenite temperatures passes its maximum at a carbon concentration of 0.8–0.9% C and then decreases due to an increase in the volume fraction of soft retained austenite (Figure 4.16). For the above carbon content of steel, the martensite point M_s drops significantly, which leads to an increase in the proportion of retained austenite in quenched steel. Steel with 1.9% C quenched from a temperature higher than A_{st} has the same hardness as quenched steel with 0.1% C. If hypereutectoid steels are quenched from a temperature of $A_{c1} + (20–30^\circ C)$ (70–90°F), as is common practice, all hypereutectoid steels would have practically the same austenite composition at the same quenching temperature and level of hardness (Figure 4.16, curve b).

Another important feature of the dependence of steel hardness on carbon content is that an increase in the carbon content to ~0.6% results in a most dramatic rise in the maximum hardness; then the curve becomes less steep. This is probably associated with the very nature of high martensite hardness in steel.

The martensite transformation of austenite results in a supersaturated solid solution of carbon in α-Fe. An increase in the carbon content of martensite weakens, rather than strengthens, the interatomic bonds. This is due to an increase in the distance between iron atoms brought about by implanted carbon atoms. Carbon nevertheless increases the hardness of martensite, which is explained primarily by the fact that carbon atoms implanted into the α-Fe lattice impede the slip of dislocations in martensite (the so-called solid-solution strengthening mechanism).

During quenching or during the aging of quenched steel, carbon atoms in martensite crystals surround dislocations (atmospheres around dislocations), thus pinning them. This leads to a general increase in plastic deformation resistance despite the fact that carbon weakens interatomic bonding in the martensite lattice. In steels with a high martensite start point M_s such as carbon steels containing less than 0.5% C [$M_s > 300^\circ C$ (570°F)], quench cooling over the martensite range is characterized by the most favorable conditions for partial precipitation of martensite with the release of disperse carbide particles. Moreover, in all steels hardened at normal rates, carbon has time to segregate as the steel cools above the point M_s. The carbon segregates of austenite are inherited by martensite, and since the latter is already supersaturated with carbon, these segregates become nucleation sites of carbide particles. This is in agreement with the fact that at very high cooling rates the hardness of

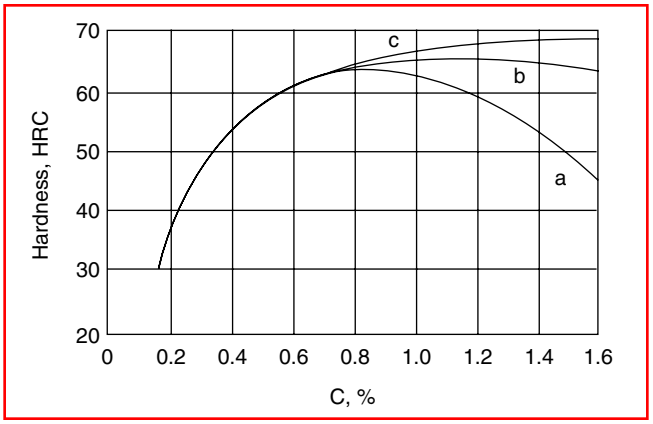

FIGURE 4.16 Hardness of carbon and alloy steels depending on the carbon content and quenching temperature. (a) Quenching above A_{c3}; (b) quenching above A_{c1} (770°C); (c) microhardness of martensite.

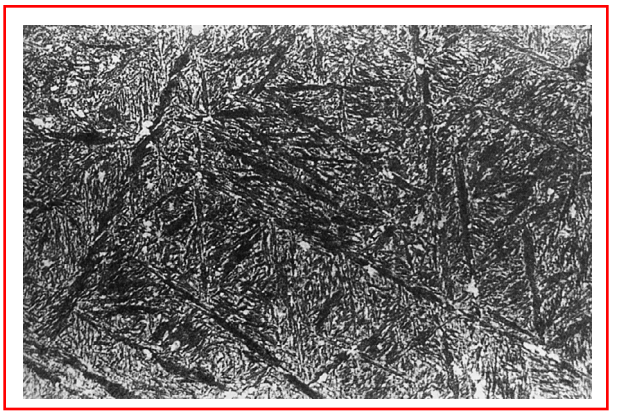

FIGURE 4.17 Microstructure of plate martensite. Light shading = retained austenite 50,000×.

martensite crystals is two thirds of that obtained at normal cooling rates. High hardness of martensite may also be due to the fact that carbon makes a noticeable contribution to covalent bonding whose main property is high plastic deformation resistance.

Owing to the above strengthening mechanisms, carbon has such a strong strengthening effect on martensite that the hardness of a quenched steel does not depend on the concentration of alloying elements dissolved in the martensite by the substitutional mechanism, but is determined by the concentration of carbon.

To conclude, extreme strengthening of steels during martensitic hardening is due to the formation of a carbon-supersaturated α-solution, an increase in the density of dislocations during the martensite transformation, the formation of carbon atom atmospheres around dislocations, and precipitation of disperse carbide particles from the α-solution.

4.3.2 Microstructure Criterion for Hardening Capacity

Studies of the structure of hardened carbon steels and carbon-free iron-based alloys revealed two main morphological types of martensite: plate and lath. These two types of martensite differ in the shape and arrangement of crystals, substructure, and habit plane.

Plate martensite (which is also called needle type, low temperature, and twinned) is a well-known classical type of martensite that is most pronounced in quenched high-carbon iron alloys with a high concentration of the second element—for instance, Fe–Ni alloys with a Ni content higher than 28%. Martensite crystals are shaped as thin lenticular plates. Such a shape corresponds to the minimum energy of elastic distortions when martensite is formed in the austenite matrix; it is similar to the shape of mechanical twins (Figure 4.17).

Neighboring plates of martensite are commonly not parallel to each other and form frame-like ensembles. Plates that are formed first (near the point M_s) extend through the entire length of the austenite grain, dividing it into sections. A martensite plate cannot, however, cross the boundary of the matrix phase; therefore the maximum size of the martensite plate is limited by the size of the austenite grains. As the temperature is lowered, new martensite plates are formed in the austenite sections, the size of the plates limited by the size of the matrix sections. In the course of transformation the austenite grain splits into still smaller sections, in which smaller and smaller martensite plates are formed. In the case of a small austenite grain caused by, for instance, a small overheating of steel above A_{c3}, the martensite plates are so small that the needle-type pattern cannot be observed in the microsection and the martensite is usually called structureless. It is this type of martensite that is most desirable. After quenching, martensite retains some austenite between its plates at room temperature (Figure 4.18).

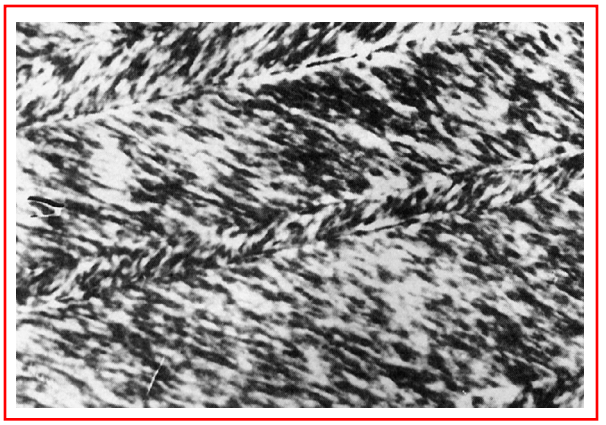

FIGURE 4.18 Microstructure of lath martensite. 50,000×.

Lath martensite (which is also called massive, high-temperature, or nontwinned) is a widespread morphological type that can be observed in quenched low-carbon and medium-carbon steels, the majority of structural alloy steels, and comparatively low-alloy noncarbon-containing iron alloys—for instance, Fe–Ni alloys with a Ni concentration of less than 28%. Crystals of lath martensite are shaped like thin plates of about the same orientation, adjacent to each other and forming more or less equiaxial laths.

The plate width within the lath is about the same everywhere, ranging from several micrometers to fractions of a micrometer (commonly 0.1–0.2 μm); i.e., it can reach or even exceed the resolution limit of a light microscope. Inside the martensite laths there are interlayers of retained austenite 20–50 nm thick. One austenite grain can contain several martensite laths.

The formation of lath martensite has all the main features specific to the martensite transformation, including the formation of a relief on a polished surface. Transmission electron microscopy reveals a rather complicated fine structure of martensite crystals with many dislocations and twins in many iron alloys.

The substructure of the plate martensite shows an average zone of elevated etchability, also called a midrib, even under a light microscope. Electron microscopy has shown that the midrib is an area with a dense arrangement of parallel fine twin interlayers. The twinning plane in martensite of iron-based alloys is commonly $\{1\,1\,2\}_M$. Depending on the composition of the alloy and martensite formation conditions, the thickness of the twinned interlayers may form several tenths of a nanometer to several tens of nanometers. On both sides of the central twinned zone there are peripheral areas of martensite plates that contain dislocations of relatively low density (10^9–10^{10} cm^{-2}).

The substructure of lath martensite is qualitatively different from the substructure of plate martensite in that there is no zone of fine twin interlayers. It is a complex dislocation structure characterized by high-density dislocation pileups with densities on the order of 10^{11}–10^{12} cm^{-2}, i.e., the same as in a metal subjected to strong cold deformation. The laths of lath martensite often consist of elongated slightly misoriented subgrains. Twin interlayers can occur in lath martensite, but their density is much lower than in the midrib in plate martensite, while many of the laths do not contain twins at all.

The substructure of retained austenite differs from that of the initial austenite by a higher density of imperfections occurring under local plastic deformation due to martensite crystals. Flat dislocation pileups, dislocation tangles, and stacking faults may be observed in austenite around martensite crystals.

At present it is believed that the decisive role in the formation of plate martensite belongs to accommodating (complementary) twinning deformation, whereas for the lath type this role is played by slip. As temperature is decreased, resistance to slip increases at a higher rate than that of resistance to twinning; therefore, the martensite transformation at low and high temperatures results in twinned and lath martensite, respectively. In alloys a decrease in temperature causes the morphology of martensite to change from the plate to lath type. The composition of iron-based alloys has a substantial effect on the martensite morphology. Shown below is the effect of some alloy compositions on the formation of plate and lath martensite; the numerals show the second component content in percent.

System	Fe–C	Fe–N	Fe–Ni	Fe–C_2
Lath type, M	≤0.6	≤0.7	≤29	≤10
Plate, M	0.6–2.0	0.7–2.5	29–34	—

Chromium–nickel, manganese, chromium–manganese, and other steel alloys with low-energy stacking faults contain hexagonal ε-martensite with plates in parallel to planes $\{1\,1\,1\}\gamma \parallel \{0\,1\,1\}\varepsilon$ (Figure 4.19). Some alloy steels have a mixture of ε- and α-martensites.

In conclusion it should be noted that the structure of a metal or alloy that has undergone martensite transformation features many more imperfections than after a disordered rearrangement of its crystal lattice: the more the developed grain boundaries and subboundaries, the greater the density of dislocations and twin interlayers.

4.3.3 Effect of Grain Size and Chemical Composition

As noted in Section 4.3.1, the hardening capacity of a steel, i.e., its ability to undergo martensitic hardening, depends mainly on its carbon content and to a lesser extent on its content of alloying elements and the size of austenite grains. At the same time these two factors—grain size and chemical composition of the steel (or austenite, to be more exact)—can produce a substantial effect on hardenability, i.e., the depth to which the martensite zone can penetrate. It is reasonable, therefore, to consider the effects of grain size and chemical composition of austenite on hardening capacity and hardenability separately.

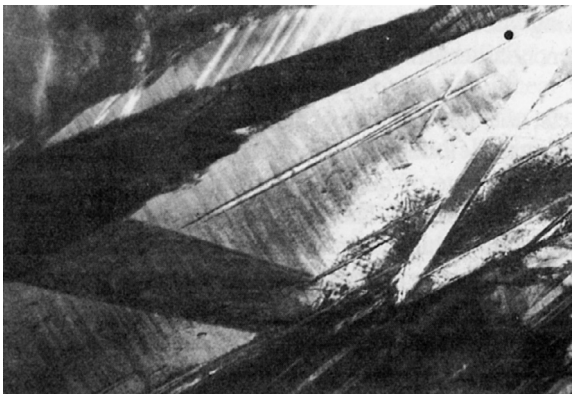

FIGURE 4.19 Microstructure of ε-martensite. 50,000×.

In the case of austenite–martensite transformation, martensite plates develop inside the austenite grain, extending from one side to the other. If the steel is considerably overheated above the critical point A_{c3}, then coarse grains of austenite are formed; this results in larger martensite plates than normal. In quenched steel the volume fraction of retained austenite is higher if its structure is dominated by large martensite plates. Although the hardness of martensite is practically independent of the plate size, an increase in the total soft austenite content of quenched steel leads to a decrease in its maximum hardness, i.e., impairs its hardening capacity. Moreover, the plastic properties of steel, particularly its toughness, also deteriorate with the coarsening of the structure. It is therefore advisable to obtain a fine-needle structure after quenching if a set of good mechanical properties is needed; this may be achieved with a fine-grain austenite structure, which is produced at small overheating of steel at temperatures higher than A_{c3}.

Alloying elements can have direct or indirect effects on the hardening capacity of steel. Indirect effects are associated primarily with hardenability. Since the majority of the elements tend to shift the isothermal austenite precipitation curves to the right and hence decrease the critical rate of cooling, it is easier to obtain maximum hardness for an alloy steel than for an ordinary carbon steel. Specifically, the presence of alloying elements facilitates the achievement of maximum hardness by cooling the steel in more lenient media (in oil, for instance) when the mass of the workpiece to be hardened is comparatively large.

A second indirect effect is related to the carbide-forming elements. If hardening is to be applied to an alloy steel containing elements that form stable carbides by heating below the carbide dissolution point, then the carbon content of the major martensite mass will be lower than the total carbon content of the steel. As a result, the maximum achievable hardness for this carbon content will not be attained because the hardening capacity of the steel will deteriorate.

It should be noted that high-carbon steel, such as tool grade steel, features high hardness even if it is quenched from a temperature somewhat lower than the carbide dissolution point, despite the fact that part of the carbon stays outside the solution. The martensite hardness also decreases. This decrease is small and is due mainly to the fact that hardness versus carbon curves for carbon steels and alloy steels are rather smooth at carbon concentrations higher than 0.6% (Figure 4.16); it is compensated for by a considerably lower amount of retained austenite and the high hardness of the carbides themselves.

The situation is different for structural steels containing less than 0.4% C. The maximum hardness curve is so steep (Figure 4.16) that even a small decrease in the concentration of carbon in martensite in an alloy steel due to incomplete dissolution of special carbides would lead to a considerable reduction in the hardness of the martensite. The steepness of the curve over the range of 0.1–0.4% C shows that from the viewpoint of hardening capacity it is essential to heed even the smallest fluctuations in the carbon content, specifically fluctuations within the quality limits, up to individual ingots. Therefore the carbon content limits for specific structural steels should be as narrow as possible, although this may encounter some technological difficulties.

The indirect effect of alloying components on hardenability is not great. It is therefore possible to construct a general curve for the dependence of maximum hardness on the carbon content for carbon and alloy steels (Figure 4.16). This is understandable because martensite of an alloy steel is a combined solid solution in which atoms of the alloying elements replace iron atoms in the lattice, while carbon atoms are implanted into this lattice. Carbon atoms introduced into the α-Fe lattice impede the slip of dislocations in martensite and thereby increase its hardness.

A certain increase in the hardness of martensite due to alloying elements can be expected only because of the strengthening of α-Fe during quenching. The possibility of quench

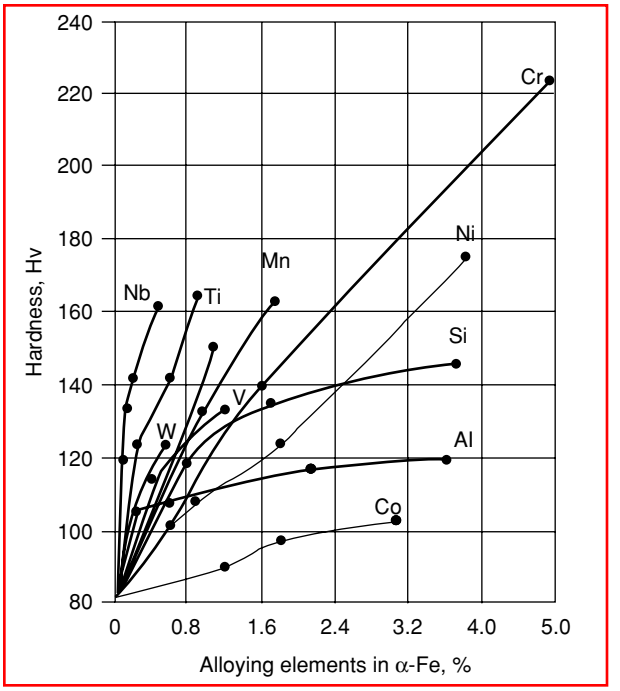

FIGURE 4.20 Effect of dissolved alloying elements on hardness of ferrite after quenching from 1200°C in water.

strengthening an alloyed ferrite has been studied in detail. From Figure 4.20, one can judge roughly how different elements increase the hardness of ferrite with ~0.01% C upon quenching from 1200°C in water. Alloying elements causing substantial strengthening of ferrite should also increase the hardness of martensite in a quenched steel, though this increase in hardness should be comparatively low.

During the quenching of steel products, the rate of cooling is the greatest for the surface, decreasing steadily toward the center of the section. Evidently, the depth of the hardened zone (hardenability) will be determined by the critical rate of quenching; thus, hardenability will increase with a decrease in the critical rate of quenching. This rate, in turn, depends on the resistance of austenite to precipitation at temperatures higher than the martensite point M_s. The farther to the right the lines in the isothermal austenite precipitation diagram, the lower the critical rate of quenching and the higher the hardenability of the steel products. Thus, the factors that affect the stability of undercooled austenite will affect the hardenability as well.

The main factors that produce a decisive effect on the hardenability of steel are (1) the chemical composition of the steel (composition of austenite, to be more exact); (2) austenite grain size; and (3) the homogeneity of austenite. Under otherwise equal conditions, coarse austenite grains improve the hardening capacity of steel. This circumstance is connected with the extent of grain boundaries; the extent is less, the coarser the grain. Since nucleation centers are formed primarily along the austenite grain boundaries during austenite precipitation above the point M_s, it is always easier to undercool austenite with coarse grains, thereby increasing hardenability.

To estimate hardenability, in practice, use is made of the quantity called the critical diameter. The critical diameter (D_{cr}) is the maximum diameter of a bar permitting through hardening for a given cooling medium. To avoid putting hardenability in dependence on the

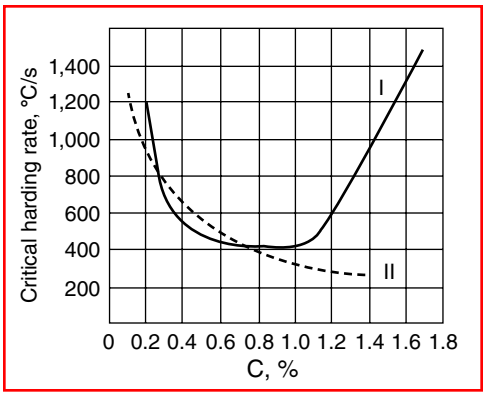

FIGURE 4.21 Curves showing the effect of carbon on the critical rates of quenching. I, low-heating temperatures; II, high-heating temperatures.

method of cooling and type of coolant, use is made of still another notion, the ideal critical diameter (D_∞), which is the diameter of a maximum section allowing through hardening in an ideal cooling liquid that is absorbing heat at an infinitely great rate. It was established that the grain size and quantity D^2_∞ have an approximately linear inverse dependence on one another.

The chemical composition of a steel has the strongest impact on its hardenability. This is due primarily to the fact that carbon and alloying elements affect the critical rate of quenching.

Figure 4.21 shows the effect of carbon on the critical rate of quenching for carbon steel. It can be seen that the minimum rate of quenching is observed in steels that are close to eutectoid with respect to carbon content (curve I). A decrease in the carbon content of steel below 0.4% leads to a sharp increase in the critical rate to the extent that at a certain minimum carbon content martensitic hardening becomes virtually impossible. An increase in the critical rate of hypereutectoid steel with an increase in the carbon content is explained by the presence of cementite nuclei facilitating the austenite precipitation. Hence, the trend of curve I is related to the incomplete hardening of hypereutectoid steels. If completely hardened (sufficient holding at a temperature higher than A_{st}), an increase in the carbon content leads to a continuous decrease in the critical rate of quenching (curve II), with a resulting rise in hardenability.

The effect of alloying elements on hardenability can be estimated by the degree of increase or decrease in stability of undercooled austenite in the pearlite and intermediate ranges. With the exception of cobalt, all alloying elements dissolved in austenite impede its precipitation, decrease the critical rate of quenching, and improve hardenability. To this end, broad use is made of such additives such as Mn, Ni, Cr, and Mo. Particularly effect is complex alloying whereby a combination of elements enhances their individual useful effects on hardenability. Figure 4.22 shows the effect of third-element alloying on the hardenability of an iron–nickel steel. It can be seen that Mn, Cr, and Mo additives improve hardenability to a considerable extent.

The improving effect of alloying on hardenability is used in two ways. First, alloying ensures through hardening across sections inaccessible for carbon steels. Second, in the case of small-section products, replacing carbon steel with an alloy steel permits less radical cooling regimes. Small-diameter carbon steel products can be hardened by quenching in water. This, however, may result in impermissible residual stresses, deformations, and cracks, particularly in products of a complicated shape. If an alloy steel is used, quenching in water can be replaced with softer hardening in emulsion, oil, or even air.

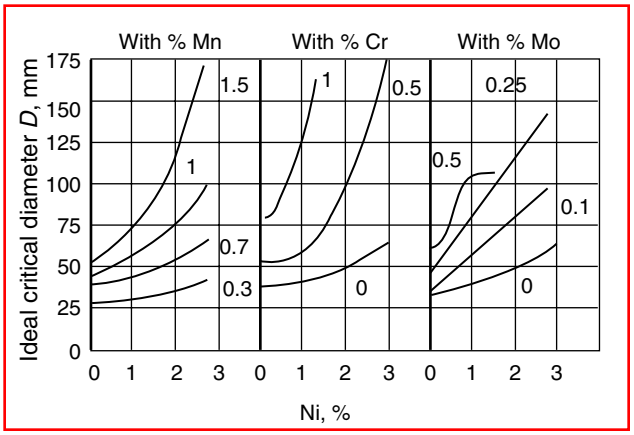

FIGURE 4.22 The effect of manganese, chromium, and molybdenum on the hardenability of steels with different nickel contents.

4.3.4 Boron Hardening Mechanism

It has long been observed that small additions of certain elements, e.g., titanium, aluminum, vanadium, zirconium, and boron, can considerably improve the hardening properties of steel. The most effective in this respect is boron. Hardenability of carbon and low-alloy steels increases considerably upon introduction of boron in amounts of thousandths of a percent. A further increase in the boron content does not produce any further improvement in hardenability. The improving effect of boron is noticeable only where steel has been preliminarily well deoxidized and denitrified, because boron has good affinity for oxygen and nitrogen. Therefore, before introducing boron into steel it is necessary to add aluminum, titanium, or zirconium. Figure 4.23 shows hardenability curves for a low-carbon steel without boron, with boron added, with boron and vanadium, and with boron, vanadium, and titanium. It can be seen that the extent of the martensite range for all the steels with boron added is greater than that in steels without boron; however, it is practically the same for steels with several additives. At the same time, the extent of the half-martensite structure range is much greater if the steel contains other additives along with boron.

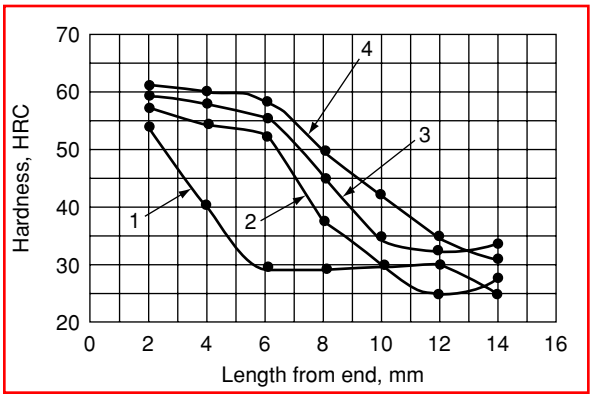

FIGURE 4.23 Curves of hardenability for steels with 0.44–0.43% C and various small amounts of additives. 1, Without boron; 2, with an addition of boron; 3, with boron and vanadium added; 4, with boron, vanadium, and titanium added.

The effect of boron on hardenability decreases with an increase in the carbon content. If the carbon content exceeds 0.9%, boron does not have any measurable effect on hardenability. Boron alloying for the purpose of improving hardenability is therefore useful only for low-carbon steels of various applications. It does not have any effect on the hardenability of tool steels or on high-carbon carburized layers. The above relationship between the carbon content and the effect of boron on the hardenability of steel is due to the fact that the two elements have the same effect on austenite precipitation. Boron increases the length of the austenite precipitation incubation period, thereby decreasing the critical temperature of quenching. Like carbon, boron facilitates the enlargement of austenite grains under heating. These two factors have a positive effect on the hardenability of steel. Therefore, in high-carbon steels the effect of small doses of boron is practically negligible.

It should be also noted that the positive effect of boron on hardenability is full only if the quenching temperature is sufficiently high [850–900°C (1560–1650°F)]. Various suggestions have been put forward with respect to the mechanism by which boron affects the hardenability of steel. Quite probably, this is a very special mechanism because boron can produce its effect at very low concentrations above, above which no further effect on hardenability is observed. Some researchers believe that boron increases hardenability just because it facilitates the increase in the size of austenite grains under heating. Although boron does tend to increase the grain size, it produces the same hardenability-improving effect in steels with small grains. Others explain the fact that boron increases the stability of austenite and consequently improves hardenability by the fact that it increases the coefficient of surface tension at the austenite–new-phase nucleus interface. Therefore more energy is required for the formation of a nucleus of a critical size capable of growth. Because of this stability of austenite increases. An increase in hardenability following the addition of small doses of boron is more frequently explained by the fact that this element is surface-active in austenite. There is experimental evidence that boron is segregated at the boundaries of austenite grains and dissolves in insignificant amounts in this layer. Since boron forms an interstitial solid solution with iron, interaction between its atoms and iron atoms must, evidently, be the same as in carbon, which leads to a decrease in the difference in free energy between the γ- and α-phases. This impedes the formation of new-phase nuclei of critical size, which are formed primarily at the austenite grain boundaries. The resistance of austenite to precipitation improves, thereby increasing the hardenability of the steel. The cessation of the boron effect on hardenability with increasing boron content is due to its low limiting solubility in γ-iron at a given temperature [about 0.003% at 1000°C (1832°F)]. As soon as the boron solubility limit at the grain interface is achieved, any further increase in its total content leads to the formation of iron–boron compounds such as Fe_2B within austenite grain boundaries and to the distribution of boron over the bulk of the grain. As centers of crystallization, chemical compound particles cause an earlier onset of austenite precipitation, which results in lower hardenability. At the same time, an earlier onset of austenite precipitation at grain boundaries is compensated for by a delay in the formation of critical new-phase nuclei in the bulk of the grain caused by boron due to an increase in its content up to the solubility limit for austenite. Therefore, alloying with boron in amounts exceeding thousandths of a percent does not have any effect on hardenability and even may impair it.

Based on this viewpoint, one can explain some other specific effects of boron on the hardenability of steel that were noted above. Thus, boron increases the duration of the austenite precipitation incubation period only, the duration determined by the formation of critical nuclei at grain boundaries but not affecting the length of austenite precipitation. From this viewpoint it is also clear that boron, like carbon, facilitates enlargement of austenite grains under heating. An increase in the quenching temperature first improves hardenability owing to an increase in the concentration of boron at the austenite grain boundaries to its

solubility limit at these boundaries. A further increase in the quenching temperature and enrichment of the grain boundaries in boron can lead to the formation of boron–iron compounds. The hardenability of the steel will not increase further and may even decrease. Finally, the reduction of the boron effect by carbon can be explained by the fact that boron and carbon have virtually the same effect on hardenability. In high-carbon steels, the effect of boron becomes practically negligible owing to its poor solubility in iron.

4.3.5 Austenitizing Conditions Affecting Hardenability

The austenite condition prior to quenching (chemical composition, grain size, homogeneity of austenite) has the decisive effect on the hardening capacity and, especially, hardenability of steel. Other factors are secondary or derive from the basic three. These factors, in turn, are determined by the carbon content, type, and amount of alloying elements at the time of quenching, the quenching temperature (austenitizing temperature), and the holding time at a given temperature.

Austenitizing of a heated alloy steel consists of a polymorphous $\alpha \rightarrow \gamma$ transformation, the dissolution of cementite, special carbides, nitrides, and intermetallics in austenite, and recrystallization of the austenite grains.

To improve the hardening capacity and hardenability of steel, the austenitizing conditions should be such as to ensure that a maximum amount of carbon passes from the ferrite–carbide mixture to the solution and, at the same time, no marked growth of grains occurs as a result of overheating, as this would lead to a high brittleness and the formation of quenching cracks. The quenching temperature should be maintained as constant as possible, and the holding time should be just enough to ensure uniform heating of the workpiece and dissolution of carbides. For their complete dissolution in austenite, coarse-plate and coarse-grain carbides need more time than thin-plate and fine-grain ones. Steels alloyed with elements forming special carbides should be heated to a temperature considerably exceeding A_{c3}. Small carbides available in the structure impede enlargement of grains and the nuclei of the new phase facilitate transformation of austenite in the pearlite range and increase the critical rate of quenching, thus decreasing the hardenability of the steel. As the quenching temperature and time are increased, the critical rate of quenching decreases and, accordingly, hardenability rises, because carbides and other inclusions playing the role of new-phase nuclei dissolve most.

The degree of austenite homogeneity and dispersion of local carbon pileups (which can act as nuclei during transformation in the pearlite range) can have a strong effect on hardenability and hardening capacity. When the quenching temperature is increased, carbides dissolve together with other minute, sometimes hardly measurable, quantities of inclusions such as nitrides and sulfides, which can also serve as nuclei during transformation.

Finally, when the quenching temperature and holding time are increased, enlargement of austenite grains has its effect on the process of transformation. Since the pearlite transformation begins at grain boundaries, an increase in the austenite grain size causes a decrease in the critical rate of quenching and hardenability improves.

Nearly all of the alloying elements impede the growth of austenite grains. The exception is manganese, which adds to the growth of grains. The strongest growth retardants are V, Ti, Al, Zr, W, Mo, and Cr; Ni and Si produce a weaker retarding effect. The main cause of this retarding effect is believed to be the formation of low-soluble carbides, nitrides, and other phases, which may serve as barriers for the growth of austenite grains. Such active carbide-forming elements as Ti, Zr, and V impede growth more strongly than Cr, W, and Mo do, because the carbides of the former elements are more stable and less soluble in austenite. Experimental studies on the solubility of V, Nb, Ti, and Al carbides and nitrides in austenite

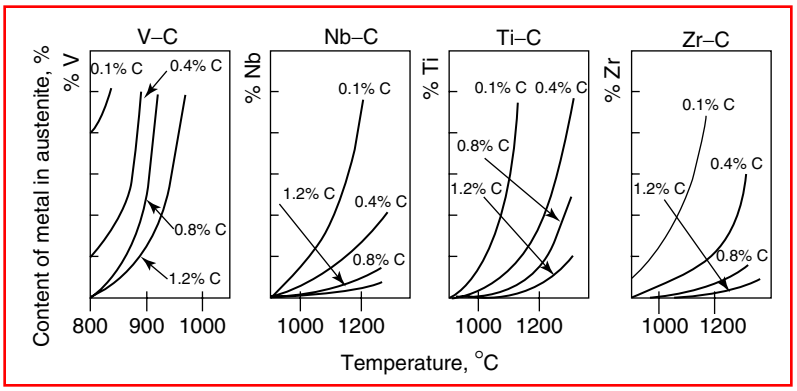

FIGURE 4.24 Solubility of carbides in austenite at various temperatures depending on the carbon content (shown as % C on the curves) for (a) vanadium; (b) niobium; (c) titanium; (d) zirconium.

show that the carbides of these elements (Ti in particular) are more soluble than nitrides. Titanium nitrides are virtually insoluble in austenite no matter what the temperature is. Niobium and aluminum nitrides also have poor solubility in austenite. Carbon has a great effect on the solubility of carbides. Figure 4.24 shows relevant data on V, Nb, Ti, and Zr carbides. An increase in the temperature of carbide solubility in austenite with a rise in the carbon content is due to the greater activity of carbon at its higher concentrations in a solid solution and higher thermodynamic activity. It should be noted that C, N, and Al are not bound to carbides or nitrides, but found in the solid solution of austenite facilitate the growth of austenite grains. The elements B, Mn, and Si also favor the growth of grains. Therefore, addition of these elements into steel improves its hardenability.

Different heats of steels of the same quality may considerably differ in their tendency toward the growth of austenite grains because they contain different amounts of low-soluble disperse particles of carbides, nitrides, and other phases, which are barriers to the growth of austenite grains. The distribution and size of these particles depend both on steelmaking conditions and preliminary heat treatment. Thus, the tendency of steel to grain size growth under heating depends on, in addition to its composition, the metallurgical quality and process, i.e., its history preceding the thermal treatment.

Liquidation also has a considerable effect on hardenability. In order to obtain homogeneous austenite in steel exhibiting liquation, it is necessary to keep the steel at the quenching temperature for a sufficiently long time. This refers to cat steel where liquation is the highest and also to forged and rolled steels. Longer quenching times increase hardenability owing to the elimination of residual liquation and fluctuation in homogeneity of austenite.

Note in conclusion that hardening capacity and hardenability are not important by themselves in practical applications. They are important if they can improve overall properties of steels in accordance with practical needs.

4.4 TEMPERING OF ALLOY STEELS

4.4.1 Structural Changes on Tempering

Structural changes on tempering were considered in detail in Chapter 3. Therefore, this section briefly considers only the most characteristics effects.

Tempering is a thermal martensitic treatment of quenched steels. The basic process that takes place during tempering is martensite precipitation. The first structural change during

tempering is carbon segregation at dislocations. The second stage of tempering is precipitation of intermediate ε-carbide with a hexagonal lattice, which forms under heating above 100°C (212°F). During the third stage, cementite precipitates above ~250°C (~480°F). At the final stage of tempering above 350°C (660°F), cementite particles coagulate and spheroidize.

Consider the changes that take place in martensite and austenite structures at different stages of tempering. During the first stage, beginning at 80°C (175°F) and up to 170°C (330°F), the c parameter of the martensite lattice decreases. The ratio c/a becomes close to unity. Tetragonal martensite transforming to a cubic form is called tempered martensite. The decrease of tetragonality is connected with precipitation of carbon from the solution.

Heating of steels over 200°C (390°F) and up to 300°C (570°F) activates transformation of retained austenite to a heterogeneous mixture composed of a supersaturated α-solution and the Fe_3C carbide. This means that retained austenite transforms to tempered martensite,

$$Fe_\gamma(C) \rightarrow Fe_\alpha(C) + Fe_3C$$

By the end of transformation (~300°C; 570°F), the retained austenite contains about 0.15–0.20% C.

Heating above 300°C (570°F) leads to a further precipitation of carbon and the relaxation of internal stresses arising from previous transformations. Complete precipitation of carbon was found to occur at 400°C (750°F). A further increase in temperature leads only to coagulation of ferrite and cementite particles.

During tempering, cementite acquires a globular form when a ferrite–cementite mixture is formed from martensite. The different form of cementite in the ferrite–cementite mixture determines the difference in properties.

4.4.2 Effect of Alloying Elements

The influence of alloying elements on transformations during tempering depends on whether they dissolve in ferrite and cementite or form special carbides. The diffusion mobility of atoms of alloying elements dissolved in α-Fe by the substitutional method is many orders of magnitude lower than the diffusion mobility of carbon atoms dissolved by the interstitial method. So at a temperature below 400°C (750°F) no diffusion redistribution of alloying elements in the matrix takes place. First the ε-carbide and then cementite precipitate from the α-solid solution. The concentration of alloying elements in them is the same as in martensite. Atoms of alloying elements in the ε-carbide and cementite lattice formed below 400°C (750°F) partly replace iron atoms. Complex carbides such as $(Fe, Cr)_3C$ and $(Fe, V)_3C$ are formed.

The first stage of transformations in martensite (formation of tempered martensite) at a temperature below 150°C (300°F) is affected little by alloying elements. At this stage of tempering, nucleation of carbide particles depends basically on supersaturation of the α-solution with carbon.

The second stage of martensite precipitation is strongly influenced by a number of alloying elements. They retard the growth of carbide particles, and consequently supersaturation of the α-solution with carbon is preserved. Thus the state of tempered martensite is retained up to temperatures of 450–500°C (840–930°F). Additions of Cr, W, Mo, V, Co, and Si bring about this effect.

A delay in martensite precipitation can be explained by two factors. First, one of the alloying elements lowers the rate of carbon diffusion in the α-solution. Second, the other elements can increase the strength of interatomic bonds in the α-solution lattice. This will prevent the atoms from crossing the α-solution carbide interface. Both factors impede precipitation of martensite.

Alloying elements affect carbide transformation under tempering under 450°C (840°F) when their diffusion movement becomes possible. In this case special carbides are formed. With an increase in the tempering temperature, intermediate metastable carbides stabilize. For example, when molybdenum and tungsten steels are tempered, Me_2C (Mo_2C and W_2C) is formed first, then $Me_{23}C_6$ appears, and finally Me_6C emerges. The sequence of their formation can be written as

$$Fe_3C \rightarrow Me_2C + Me_{23}C_6 \rightarrow Me_6C$$

Alloying elements affect the coagulation rate of carbide particles. Nickel accelerates the coagulation rate while chromium, molybdenum, vanadium, and other elements slow it down. Owing to the low diffusion rate of alloying elements, the coagulation of special carbides proceeds slowly. Even alloyed cementite (Fe, Cr)C_3 coagulates much more slower than Fe_3C in a carbon steel.

Additions of alloying elements slow down recrystallization and polygonization. Atoms of these elements form impurity atmospheres near dislocations and prevent their movement during polygonization. Disperse particles of special carbides retard movement of large-angle boundaries during polygonization.

4.4.3 Transformations of Retained Austenite (Secondary Tempering)

Alloying elements have the greatest influence on the martensite transformation temperature. This affects the amount of retained austenite in alloy steel. Some elements (e.g., cobalt) raise the point M_s, thus decreasing the amount of retained austenite. Others (e.g., silicon) have no influence on M_s. However, the majority of elements decrease the martensite point and increase the amount of retained austenite in quenched steel. Up to 60% of retained austenite is left in high-carbon steels during quenching and 10–15% in a large number of structural alloy steels.

During tempering of carbon and low-alloy steels, retained austenite transforms over the temperature interval of 230–280°C (440–540°F) or at lower temperatures if the holding time is extended. Alloying elements, especially Cr and Si, inhibit that transformation, shifting it to higher temperatures and longer tempering time. The transformation kinetics of retained austenite during tempering is similar to those of undercooled austenite. Steels with two clearly distinguished transformation ranges (pearlite and bainite) also exhibit two regions of fast transformation of retained austenite during tempering that are separated by a zone of high stability of retained austenite.

When alloy steels are tempered at 500–600°C (930–1110°F), in many cases the transformation of retained austenite is not complete. The retained austenite that did not precipitate at these tempering temperatures transforms during cooling from those temperatures (secondary quenching). The phenomenon is most pronounced in high-speed and high-chromium steels. The secondary martensite transformation during cooling after tempering is caused by the depletion of austenite in carbon and alloy elements in the course of tempering. As a result, the temperature of retained austenite M_s during cooling is increased.

Secondary quenching (double tempering) is also observed in structural steels. It takes place if the primary quenching is accompanied by a partial intermediate transformation leading to an increase in the carbon content of austenite. During tempering at 500–550°C (930–1020°F), retained austenite with a high content of carbon yields carbides intensively, and the martensite transformation temperature M_s increases. As a result, the secondary martensite transformation takes place during cooling after tempering.

In high-alloy steels, for example high-speed steels, even a very long tempering at high temperatures does not completely eliminate the retained austenite. To obtain a full

transformation, it is necessary to perform double tempering. Double tempering favors additional precipitation of special carbides and decreases the degree of austenite alloying. This causes another increase in the transformation temperature M_s. Sometimes multiple tempering is required to realize the most complete transformation of retained austenite.

4.4.4 Time–Temperature Relationships in Tempering

The kinetics of structural transformations during tempering is described by temperature–time curves similar to the curves shown in Figure 4.25. After quenching from 900°C (1650°F), steels with 0.7% C, 1% Cr, and 3% Ni contain 30% of retained austenite. When plotting the curve and diagram, the nontransformed austenite (30%) was taken to be 100%. It is found that at 600°C (1110°F) 5% of primary austenite transforms in 7 min and 5% of retained austenite transforms in 30 s. However, after 10–15% of the retained austenite is transformed, the transformation rate of retained austenite becomes smaller than that of the initial austenite. The transformation of retained austenite is not complete. It is inhibited on reaching 45% at 500°C (930°F) and 60% at 550°C (1020°F). The retained austenite that does not precipitate immediately at these tempering temperatures transforms during cooling after tempering. The transformation rate of retained austenite in the intermediate range is much higher than that of the initial austenite; 25% of initial austenite transforms at 300°C (570°F) in 75 min and the same amount of retained austenite in 15 s; 75% of the initial austenite transforms in 220 min and 75% of the retained austenite in 9.5 min. In a typical structural steel (0.37% C, 1% Cr, 1% Mn, 1% Si), 5% of the initial austenite transforms in 19 min at 600°C (1110°F) or in 5 min at 400°C (750°F); 5% of retained austenite at the same temperature transforms in a few seconds.

Another specific feature of retained austenite transformation of this steel in the intermediate range is the lowering of the transformation limit. For example, at 350°C (660°F), 70% of the initial austenite and only 40% of retained austenite transform. This difference decreases with increasing temperatures.

4.4.5 Estimation of Hardness after Tempering

Hardness decreases noticeably when alloy steels and addition-free steels are subjected to tempering at 500–600°C (930–1110°F). This decrease is due to the precipitation of martensite and coagulation of cementite. However, when the tempering temperature is higher, the

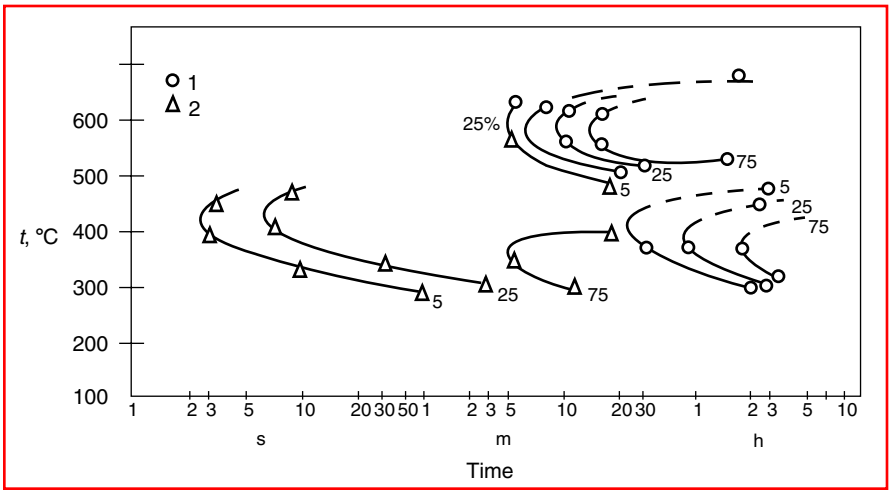

FIGURE 4.25 Time–temperature transformation curves.

hardness of steels with additions of titanium, molybdenum, vanadium, or tungsten increases. This phenomenon is called secondary hardening.

Secondary hardening is caused by the formation of clusters of atoms of alloying elements and carbon (a maximum hardness often corresponds to the clusters) and the replacement of relatively coarse particles of cementite by much more disperse precipitates of special carbides (TiC, VC, Mo_2C, W_2C). When these particles coagulate, hardness decreases. Particles of Me_6C are rather coarse and do not add to strengthening.

The chromium additive causes a small secondary hardening. This is connected with a rapid coagulation of the Cr_7C_3 carbide at 550°C (1020°F) as opposed to Mo_2C and especially W_2C. During secondary hardening an increase in the yield stress is accompanied by an increase in toughness owing to dissolution of coarse cementite particles.

4.4.6 Effect of Tempering on Mechanical Properties

The manner in which structural changes that take place during tempering affect the properties of steels depends on the particular tempering conditions. The general tendency of changes in mechanical properties of carbon steels during tempering is that as the tempering temperature is elevated, the strength parameters σ_B and $\sigma_{0.2}$ (fracture stress and yield stress) decrease, while the elasticity parameters δ and ψ (percent elongation and percent reduction of area) are improved. However, these properties change nonmonotonically, and the variation depends on the tempering temperature intervals.

Low-temperature tempering (120–250°C; 250–480°F) is used for treatment of high-strength structural and tool steels. Medium-temperature tempering (350–450°C; 660–840°F) is applied mainly to spring steels to achieve high elasticity. High-temperature tempering (450–650°C; 840–1200°F) is widely used for products made of structural steels combining a relatively high strength with resistance to dynamic loads.

Alloying of high-strength steels preserves high-strength characteristics up to 400°C (750°F). In steels containing additions of chromium, nickel, tungsten, and aluminum it is possible to obtain a very favorable combination of strength (σ_B, $\sigma_{0.2}$), ductility (δ, ψ), and impact strength under low-temperature tempering (160–200°C; 320–390°F). In low-carbon martensitic steels containing chromium, manganese, nickel, and molybdenum, the tensile strength remains unchanged up to 400–500°C (750–930°F). In steels with secondary hardening (e.g., in steels with 0.26% C, 5% Cr, 1% Mo, 1.2% V, and 1.4% Si), strength and impact strength increase under high-temperature tempering.

These data suggest that mechanical properties of every type of steel exhibit certain specific features that vary with the tempering temperature. These features are determined by the influence of alloying elements on the kinetics of phase transformations: change of the martensite point M_s, stabilization of retained austenite, and carbide formation.

The influence of structural evolution on properties during tempering can be most fully understood through the example of a maraging (martensite-aging) alloy containing 0.02–0.03% C and also Co, Mo, Ti, and Al. Alloying with cobalt increases the temperature M_s and provides 100% martensite after cooling. Tensile strength reaches 1000–1100 MPa. The subsequent tempering (aging) at temperatures of 450–500°C (840–930°F) results in considerable strengthening. Thus, σ_B can reach 1900–2100 MPa, $\sigma_{0.2} = 1800$–2000 MPa, and $\delta = 8$–10%. Such high-strength properties are due to the segregation of impurity atoms during aging (initial stages) and then to Ni_3Ti, Ni_3Mo, Fe_2Mo, etc. phases coherently bound with the matrix. The size of particles is approximately 100 nm. Coagulation of the precipitates with an increase in temperature leads to lowering of the strength characteristics and increasing of the ductility.

4.4.7 Embrittlement during Tempering

When carbon and alloy steels are tempered over the temperature interval of 250–400°C (480–750°F), a dramatic drop in impact strength is observed. If the steel is subjected to a higher temperature tempering and then tempering is repeated at 250–400°C, the brittle state is not recovered. Therefore this phenomenon has been called irreversible tempering brittleness. Such tempering brittleness is typical of almost all carbon steels and alloys. High-temperature mechanical treatment and refinement of grains weaken this type of brittleness. In high-purity steels it does not occur at all. The embrittlement may be caused by nonuniform precipitation of martensite at the second stage of tempering. This structure has a lower resistance to dynamic loads. This effect is enhanced when the initial grain boundaries of austenite get saturated with impurities under quenching heating. The alloying elements, which retard the second stage of martensite precipitation, shift the interval of irreversible brittleness toward higher temperatures.

Another drop in impact strength is found at tempering temperatures of 450–600°C (840–1110°F). A very significant feature of embrittlement is its reversibility under high-temperature tempering. If a steel that has undergone tempering embrittlement is heated to a temperature above 600°C (1110°F) and then cooled rapidly, its impact strength is restored. Therefore such brittleness is termed reversible.

In the state of reversible tempering embrittlement, steel possesses a structure that consists of ferrite and carbide. When subjected to impact tests, fracture occurs mainly along the boundaries of the initial austenite grains.

Embrittlement over a certain temperature interval is typical not only of martensitically hardened steels. It also shows up, although to a lesser degree, in steels with the bainite structure and is least pronounced in steels with the pearlite structure. Additions of chromium, nickel, and manganese facilitate tempering embrittlement. Small additions of molybdenum (not more than 0.2–0.3%) weaken tempering embrittlement. The presence of Sb, P, Sn, and As in industrial steels makes these steels most susceptible to tempering embrittlement.

4.5 HEAT TREATMENT OF SPECIAL CATEGORY STEELS

4.5.1 High-Strength Steels

Low-alloy steels are most often used as construction materials. The combination of high strength and ductility with high resistance to destruction is of particular importance for steels. The mechanical properties of such steels can be improved after hot rolling or normalization and after quenching with tempering. Alloying makes it possible to perfect the properties of steels without using quenching with tempering because

1. Properties of ferrite are changed when alloying elements are dissolved in it (solid-solution strengthening).
2. Disperse strengthening phases precipitate in the process of cooling after hot rolling or normalization.
3. Steel grains and microstructure components become finer, and changes occur in the morphology and location of structural components.

The overall content of alloying elements in low-alloy steels does not exceed 2.5%. In accordance with carbon content and principles of strengthening they can be divided into three groups:

1. Low-carbon steels (0.11–0.22% C) used in the hot-rolled or normalized states. Thermal treatment of such steels (quenching and tempering) only slightly improves their strength characteristics.

2. Low-carbon steels (0.05–0.18% C) strengthened by disperse precipitation of carbides and carbonitrides are used in the normalized or hot-rolled states.
3. Medium-carbon steels (0.25–0.50% C). The required level of properties is achieved in such steels by quenching and high tempering.

The main alloying element in these steels is manganese. Additional alloying of manganese steels with Mo, Nb, and V results in formation of needle ferrite. Owing to their needle structure, these steels combine high strength, high viscosity, and cold resistance. Therefore, the steels with 0.05% C, 2% Mn, 0.4% Mo, 0.01–0.02% Nb, or 0.07% V exhibit the following strength characteristics: $\sigma_B = 650$–750 MPa, $\sigma_{0.2} = 630$ MPa, $\delta = 33\%$. These steels are more often used in the normalized state and seldom in the hot-rolled state.

Low-alloy steels with improved strength characteristics include steels containing mainly manganese and silicon. Tensile strength σ_B in these steels is more than 600 MPa and can be as high as 1800 MPa. Their ductility and viscosity depend on their carbon content and on the types of treatment. High-strength low-alloy steels with $\sigma_B = 1800$ MPa are used in the hot-rolled or cold-worked state. However, in this case, they are characterized by low impact strength. In the normalized state their strength decreases to 800 MPa, and after quenching and tempering to 600 MPa, the impact strength increasing simultaneously.

4.5.2 Boron Steels

Alloying of austenitic steels with rather high amounts of boron results in disperse hardening. The maximum hardness of such steels is attained upon quenching from 1230°C (2250°F) and tempering at 800°C (1470°F). The strength and yield limits the increase simultaneously. At the same time the viscosity of such steels decreases more than in the usual austenite steels. The precipitation of borides, because of the high temperature of disperse hardening (800°C; 1470°F), has a beneficial effect on the properties of refractory alloys (chromium, chromium–nickel, chromium–nickel–cobalt alloys).

At test temperatures up to 700°C (1290°F) but still below the temperature of boride precipitation, the refractory characteristics of steels appreciably improve even at a very low-boron content.

In low-carbon steels with 16–30% Cr and 6.5–30% Ni, the effect of disperse hardening associated with the presence of boron was not observed. But boron binds the elements stabilizing austenite, thus favoring the formation of martensite. Carbon steels with 0.2–0.3% C, on the other hand, are hardened considerably owing to the formation of boride–carbide precipitates.

Addition of boron to cemented steels improves their hardenability and increases the strength of the core. Boron somewhat accelerates carburizing, but its influence on the case lessens with increasing carbon content. The greatest effect of boron was observed in steels with 0.7–0.8% C.

The influence of boron is enhanced as the quenching temperature is raised. However, the sensitivity of steel to overheating also increases. Therefore, boron steels usually contain small quantities of titanium and vanadium, which have a favorable effect on the structure of steels when they are heated to high temperatures.

4.5.3 Ultrahigh-Strength Steels

Low-carbon steels with a martensite structure have been developed recently that, upon cooling in air, undergo subsequent dispersion hardening at 400–500°C (750–930°F). The tensile strength of such steels is in the range 2200–2500 MPa. As a rule, they are alloyed with 12–18% Ni, up to 10% Cr, 3–5% Mo, and 0.6–1.0% Ti. These martensite-aging steels are distinguished

by having a low temperature of brittle fracture, very low sensitivity to cracks, and high-strength characteristics.

The strengthening of martensite-aging alloys is a result of three processes: strengthening of substitutional solid solution in the course of alloying, strengthening brought about by the martensite $\gamma \rightarrow \alpha$ transformation, and strengthening connected with different stages of the solid solution precipitation accompanied by formation of segregates and disperse particles of metastable and stable phases, the main contribution made by the second and third processes. As a consequence of the martensite $\gamma \rightarrow \alpha$ transformation (during cooling in air), a fine substructure with a high density of dislocations is formed. The particles of intermetallics 50–100 Å in size are found at the stage of maximum strengthening. These particles are coherently connected with the matrix.

The high resistance of martensite-aging alloys to brittle fracture is determined by the high viscosity of the matrix—the low-carbon martensite alloyed with Ni and Co, which enhance the mobility of dislocations. In addition, a high density of dislocations in martensite is responsible for high dispersion and homogeneous distribution of phases precipitated during aging.

Alloying with Mo suppresses the precipitation of particles of strengthening phases at the grain boundaries and prevents intergrain brittle fracture. Alloying with Co increases the martensite start temperature M_s and ensures a 100% martensite structure. At the same time, alloying with cobalt reduces the solubility of molybdenum and fosters dispersion hardening.

At low-carbon content and moderate cooling rates, the martensite structure in martensite-aging alloys is obtained through relatively high degrees of alloying. At 10–18% Ni, the point M_s lowers so significantly that the γ transformation can be realized only according to the martensite mechanism.

Compared with the high-strength manganese steels considered in Section 4.5.1, the martensite-aging steels are distinguished by a greater degree of alloying of the γ-solid solution. This promotes almost complete transformation of austenite to martensite. A wide range of alloying elements ensures a stronger solid-solution strengthening and increases the volume fraction of disperse particles precipitated during phase aging. The above-mentioned three factors are responsible for considerable enhancement of strength characteristics of low-alloy steels.

The high-strength state of alloys can be obtained by using various external means to affect their structure. The most advantageous of these is low-temperature thermomechanical treatment (LTMT), which consists of deformation of the undercooled austenite in the region of high stability and subsequent quenching. Undercooling of austenite is used to achieve deformation below the temperature of its recrystallization. Such treatment allows the attainment of advanced mechanical properties. The results gained at LTMT can be achieved by such factors as the composition of the steel, the temperature of austenitization, the rate of cooling to the deformation temperature, the temperature of deformation and holding time at this temperature, the degree and rate of deformation, the rate of cooling to room temperature, and final tempering conditions. The most important are the composition of steel, the temperature, and the degree of steel deformation.

Deformation of the undercooled austenite should be completed prior to the beginning of the bainite transformation. In conformity with this, the steels undergoing LTMT should contain austenite-stabilizing elements. LTMT strengthening is usually employed for high-alloy steels with 1–7% Cr, 1–5% Ni, $\leq$0.5% V, $\leq$2.5% Mo, and $\leq$2% Si and sometimes with other additions as well. The strengthening of steels in LTMT depends on their carbon content. The strengthening effect of carbon is more pronounced in LTMT than in conventional quenching.

With an increasing amount of deformation the yield stress of steel increases continuously. When the thickness of a billet decreases by 1% in LTMT, by rolling, the tensile strength is increased by 7 ± 2 MPa.

A decrease in deformation temperature results in a more intensive strengthening of steel in LTMT. The strength characteristics of steel after a small (up to 30%) deformation are lower and less sensitive to changes in the deformation temperature than at high degrees of compression.

At deformations of up to 20–30%, LTMT leads to a sharp drop in ductility; with a rise in the degree of compression above this value, the ductility begins to increase. There is a critical degree of deformation in LTMT above which the ductility of steel is sufficient. As the temperature of deformation increases, the ductility also increases.

In LTMT, the steel should be tempered as after the usual quenching. It is the opinion of the majority of researchers that the strengthening effect of LTMT is retained up to 350–400°C (660–750°F). If steel is alloyed with Mo, V, or W, the strengthening effect of LTMT persists up to 500°C (930°F). The tensile strength of steel alloyed with tungsten is 2600 MPa after quenching at 350°C (660°F) and 2450 MPa after quenching at 500°C (930°F). The rate of cooling after deformation affects the properties of steel undergoing LTMT only if nonmartensitic structures are formed at insufficiently strong cooling.

The study of the fine structure of alloys subjected to low-temperature thermal treatment has allowed us to explain the appearance of superhigh strength properties at rather satisfactory degrees of ductility by two structural factors: considerable reduction of size of martensite crystals and changes in their morphology. This can be attributed to the emergence of a cellular structure during deformation of undercooled austenite. The sites of dislocation pileups in austenite remain the sites where dislocations accumulate in martensite after the transformation. Upon LTMT deformation, the fragmentation of austenite crystals results in the fragmentation of the martensite structure. Individual fragments measuring fractions of a micrometer mutually disoriented through 10–15° are joined with each other by dense dislocation pileups. These fragments, in turn, consist of 100–200 Å fragments disoriented relative to each other through angles greater than 1°.

Thus, one of the possible mechanisms of strengthening in LTMT is connected with the creation of a high density of structural imperfections in austenite as a result of deformation and the inheritance by martensite of the dislocation structure of the work-hardened austenite. This mechanism provides the most comprehensive explanation for the high strength of martensite obtained with LTMT.

4.5.4 Martensitic Stainless Steels

Pure iron and low-alloy steels are not resistant to corrosion in the atmosphere, water, or many other media. The resistance of steel to corrosion can be enhanced by alloying it with various elements. High strength of such steels is achieved primarily by quenching to obtain the martensite structure and through its subsequent aging.

In martensitic stainless steels, the amount of martensite necessary for strengthening is formed after high-temperature heating and subsequent cooling to room temperature at a relatively small content of alloying components. The majority of alloying additions improve the resistance of martensite by lowering the point M_s. The possibilities for anticorrosion alloying of martensitic steels are limited.

In austenitic–martensitic steels (transition class), quenching does not lead to the complete transformation of austenite to martensite because of the low position of the point M_s. Consequently, no considerable increase in strength occurs. The degree of the $\gamma \rightarrow \alpha$ transformation in these steels can be increased by means of (1) deep freezing treatment to

temperatures below M_g; (2) plastic deformation below M_s; and (3) heating in the region of the most intensive precipitation of alloyed carbides from austenite (700–750°C; 1290–1380°F); when the matrix is depleted in alloying elements, the resistance of austenite decreases.

The austenitic–martensitic steels admit a high degree of alloying and therefore afford more possibilities for achieving total corrosion resistance and high strength. Such alloying elements as copper, tungsten, nickel, molybdenum, silicon, and chromium lower the martensite point at direct $\gamma \rightarrow \alpha$ transformation. The intensity of the influence of one or another element depends on their combination.

Cold plastic deformation initiates the martensite transformation. The less stable the austenite and the lower the deformation temperature, the quicker the transformation. The strength of austenitic–martensitic and martensitic stainless steels increases with decreasing deformation temperature.

If after treatment these steels contain 70–90% martensite, their yield stress can amount to 700–1000 MPa and their tensile strength to 1100–1400 MPa. Further improvement of strength is achieved by aging the martensite. This enhancement of strength is attributed to segregation of the Guinier–Preston regions type.

The effect of martensitic aging is observed when steels are alloyed with titanium, beryllium, aluminum, manganese, zirconium, niobium, copper, or certain other elements. Depending on the alloying elements, intermetallic phases of the types A_3B (Ni_3Ti, Ni_3Al, Ni_3Mn, Ni_3Be), A_2B [$Fe_2Mo(Fe, Ni, Co)_2$], or AB (NiTi, NiAl, NiMn) precipitate during aging.

Greater strength values can be achieved if the deformation of steel upon quenching proceeds below the temperature M_{c1} under rather high compression. On the one hand, this accelerates the martensite transformation, and on the other hand, aging takes place in the martensite strengthened by deformation (sometimes also in the presence of the deformation-strengthened austenite). After complete thermal treatment, steels have the following characteristics: $\sigma_{0.2} = 830–1200$ MPa, $\sigma_B = 1200–1300$ MPa.

The conditions of quenching are set with allowance for complete dissolution of carbides subject to the absence of excessive grain growth. Deep freezing treatment after quenching ensures a more complete transformation of austenite to martensite. The amount of martensite can be as high as 70–90%.

The conditions of aging should provide the required set of mechanical properties and corrosion resistance. The maximum strength values are attained as a result of aging in the temperature range 450–500°C (840–930°F). At the same time, the best corrosion resistance is attained at the lower aging temperature range of 350–280°C (660–540°F) (high total corrosion resistance is obtained at the stage preceding precipitation of strengthening phases).

4.5.5 Precipitation-Hardening Steels

As is known, steels are classified into structural, spring, tool, and heat-resistant alloy steels in conformity with their application. This section considers the behavior of precipitation-hardening alloys in each of these groups.

4.5.5.1 Structural Steels

Low-carbon manganese steels (0.1–0.2% C) containing 1.3–1.7% Mn, 0.10–0.20% V, about 0.1% Ti, and ~0.05% Al can be classified as steels strengthened with disperse precipitates. Such compositions favor the formation of disperse precipitates. Such compositions favor the formation of disperse precipitates of vanadium and titanium carbonitrides or aluminum nitrides. These disperse precipitates can improve not only the strength of the steel but also, owing to grain refinement, its viscosity and cold resistance. A number of industrial alloys with

carbonitride strengthening have been developed. Usually, these steels are used in the normalized state. Their properties are determined by the degree of dissolution of strengthening phases in the process of heating.

Another group of low-alloy precipitation-hardening steels includes low-pearlite steels, which contain up to 0.1% C and up to 2% Mn as well as vanadium (~0.1%), niobium (~0.06%), and sometimes molybdenum (~0.15–0.3%). Aluminum (up to 0.05%) can also be present in these steels. The properties of the steels under consideration are formed in the process of rolling during precipitation of disperse particles of the strengthening phase and grain refinement. The conditions of rolling should ensure maximum dissolution of components that subsequently cause the formation of disperse particles. These particles strengthen ferrite, which leads to grain refinement. The rolling temperature of low-pearlite steels depends on their composition and the strength and viscosity requirements. A high-heating temperature (~1200°C; 2190°F) ensures more complete dissolution of vanadium and niobium. This contributes to the strengthening effect during precipitation of phases containing these elements. However, owing to the grain growth, the strength of these alloys is lower than in the case of heating at 1050–1100°C (1920–2010°F).

The temperature at the end of rolling of low-pearlite steels is usually reduced to 700–800°C (1300–1475°F). This is due to (1) a decrease in the austenite grain size; (2) an increase in the degree of dispersion of the strengthening phase and, hence, enhancement of the hardening effect; and (3) displacement of the $\gamma \rightarrow \alpha$ transformation to the region of lower temperatures, which results in a finer ferrite grain.

4.5.5.2 Spring Steels

Alloys based on Fe–Ni, Fe–Ni–Cr, Co–Ni–Cr, Ni–Cr, and other systems, predominantly with titanium and aluminum or niobium additions, are used for spring steels strengthened by precipitation hardening. The particles of strengthening phases in these alloys precipitate during aging (tempering). Additional improvement of the strength properties of these alloys can be achieved through plastic deformation between quenching and aging. In this case the precipitation of the supersaturated solid solution may proceed according to a discontinuous mechanism. If the discontinuous precipitation cells completely occupy each grain (which is possible for a very fine grain structure), a very strong strengthening of alloys takes place. In the process of aging, additional refinement of the initial grain occurs during discontinuous precipitation.

Strengthening is observed in alloyed martensite-aging steels under developing of disperse particles of precipitating phases. A large number of steels differing in composition and properties are used in the industry. In addition to 0.4–0.8% C, they contain at least two of such alloying elements as Si, Cr, V, Mo, Mn, more rarely Ni and W. Isothermal quenching with subsequent tempering is advantageous for these steels, especially for those containing silicon. The maximum elastic limit in alloyed steels is attained with tempering at 300–350°C (570–660°F). These tempering conditions correspond to the conditions of a sufficiently complete precipitation of austenite accompanied by preservation of a high density of dislocations, since disperse particles of carbides hammer the redistribution and annihilation of dislocations. In addition, the carbide particles increase the resistance to low-plastic deformation.

For carbon steels, the amount of carbides can be increased and the martensite point can be lowered owing to the higher carbon content. This brings about a significant improvement of the strength characteristics of such steels, the highest properties achieved when strong carbide-forming elements (e.g., vanadium) enter into their composition.

Martensite-aging alloys containing nickel and titanium possess the best set of properties. Such alloys are quenched from 870 to 1150°C (1600–2100°F) depending on their titanium

content; the greater the titanium content, the higher the quenching temperature. The finer the grain, the higher the properties of these steels. Fine grain can be attained either by multiple $\gamma \rightarrow \alpha$ transformations or through deformation and recrystallization processes. To reduce the quantity of austenite retained upon quenching, a deep freezing treatment (−70°C; −94°F) is employed. Then comes aging at 450°C (840°F) for 6 h, during which NiTi or Ni_3Ti phases precipitate.

Austenitic steels are also strengthened as a result of precipitation hardening. They may contain chromium, nickel, titanium, or molybdenum. Upon quenching, these alloys have the structure of the γ-solid solution with chromium, titanium, and titanium carbonitride inclusions. The properties of aged alloys depend on the quenching temperature, which determines the degree of supersaturation of the solid solution, and on the cooling rate, which should be as high as possible. Aging may proceed by the discontinuous or continuous mechanism.

4.5.5.3 Tool Steels

Tool steels strengthened by precipitation-hardening tempering on the basis of the initial martensite structure are used to manufacture dies for cold deformation of steels. As a result of tempering, the hardness and strength characteristics of steels are enhanced when strengthening phases (carbides) precipitate from martensite. The retained austenite, a phase with low hardness, transforms to martensite. These processes increase the yield stress under compression but reduce viscosity.

Precipitation-hardening strengthening is also characteristic of heat-resistant steels. The structure of these steels represents a martensite matrix with particles of the strengthening phases—carbides or intermetallics—precipitating during tempering.

The main principles of heat treatment of precipitation-hardening tool steels are now considered in great detail. The basic operations of heat treatment are annealing, quenching, and tempering.

The annealing heating temperature is chosen a little higher than A_1. It is 760–780°C (1400–1435°F) for carbon steels, 780–810°C (1435–1490°F) for alloy steels, and 830–870°C (1525–1600°F) for high-alloy chromium steels, with 2–3 h as the holding time .

Quenching of tool steels is aimed at obtaining martensite with a high concentration of carbon and alloying components with retained fine-grain structure. That is why quenching is carried out at temperatures corresponding to complete dissolution of the basic carbides in austenite. These temperatures, however, should not be conducive to austenite grain growth. Usually, the quenching temperature corresponds to the temperature of heating; it is a little higher than A_1 for steels in which the main carbide phase is cementite; up to 1000–1060°C (1832–1940°F) for steels with a chromium-based carbide phase of types Me_7C_3 and $Me_{23}C_6$, and 1080–1100°C (1975–2010°F) for steels with greater carbide content of the type $Me_{23}C_6$.

At tempering, the assigned level of properties is achieved by changing the structure of the quenched steel. Heating a quenched steel during tempering to 150–200°C (300–390°F) causes the precipitation of small ε-carbide plates from martensite and reduces the carbon concentration. Such tempering only slightly impairs the steel's hardness but significantly improves its strength and viscosity. Heating to 250–280°C (480–535°F) during tempering noticeably decreases the carbon concentration in martensite and enhances the strength and viscosity characteristics of the steel. This tempering permits almost complete removal of the retained austenite.

An appreciable increase in the hardness of steels results from the precipitation of a large number of small carbide particles (intermetallics of alloying elements of the types Me_2C, $Me_{23}C_6$, MeC, and Me_7Me_6) from martensite.

4.5.5.4 Heat-Resistant Alloys

A vast group of heat-resistant alloys consists of austenitic steels strengthened with carbides and intermetallics. To increase heat resistance, elements that strengthen the solid solution and induce precipitation hardening are introduced into iron–nickel-based alloys. These elements include Cr, Mo, W, Nb, V, Ti, and Al. To acquire high heat resistance, the alloys undergo double quenching. The purpose of the first quenching is to obtain grains of a certain size and to transform the excess γ'-phase [intermetallic phases γ'-Ni_3(Al, Ti, B)] to a solid solution. Quenching is followed by cooling in air. The γ'-phase partially precipitates in this process. The aim of the second quenching (1050°C; 1920°F) with subsequent aging is to obtain disperse precipitates of the γ'-phase 200–500 Å in diameter. As a result of these quenching procedures, the strengthened alloy contains a certain number of larger precipitates along with fine inclusions. This structure ensures high strength and the necessary margin of ductility.

4.5.6 Transformation-Induced Plasticity Steels

There are numerous examples for improving the plasticity of load-bearing samples under the influence of phase transformations of the diffusion and shear types. The term transformation-induced plasticity was proposed to denote an improvement of plasticity under martensite transformation. High plasticity of steels below the critical point was called subcritical superplasticity by A.P. Gulyaev.

The Transformation-induced plasticity (TRIP) effect appears under the action of high stresses that exceed the yield stress of austenite. In the segment where localization of flow sets in, martensite deformation occurs. This segment is stronger than austenite, and because of this the flow extends to the neighboring segments of the sample. Thus, the quasiequilibrium flow in TRIP steels is due to high deformation strengthening. The index of the flow stress rate sensitivity remains low.

TRIP is observed at fixed test temperatures. In the case of isothermal transformations, the volume that undergoes such a transformation reaches a certain level and does not increase further. Therefore, the greatest overall effects of plasticity improvement are observed at cyclic temperature changes that lead to multiple occurrences of the phase transformation.

TRIP is found when the temperature of the sample is changed (within limits exceeding the temperature range of the phase transformation), with a constant load. The load applied is usually lower than the yield stress of any of the phases involved in the transformation.

In each temperature-changing cycle, the value of deformation is in tenths of a percent. With a large number of cycles it may amount to several hundred percent. The deformation value in one cycle is directly proportional to the applied stress. An increase in the applied stress above a certain limit disrupts the linear dependence of deformation (per cycle) on stress. This is caused by transition from the plastic deformation to the usual deformation at comparatively high stresses. As the volumetric effect of phase transformation increases, the deformation value per cycle increases.

TRIP can be observed in metals with any grain size, among them coarse-grain metals, and at any temperature, including low temperatures. For example, after 150 temperature-changing cycles in the range of 204–648°C (400–1200°F), a sample of Fe–15.4% Ni alloy with an initial grain size of 150 μm became 160% longer, with no neck formed, owing to the reversible martensite transformation under load.

The deformation mechanisms typical of TRIP have not been clearly established because of difficulties in using direct structural methods during phase transformation when the structure of a sample changes constantly. Among the proposed hypotheses the following may be quoted:

1. Accelerated transfer of dislocations owing to an excess of vacancies formed during volumetric changes

2. Weakening of bonding forces between atoms at the interface at the moment of transformation
3. Changes in the form associated with realization of particular orientations of the formed martensite
4. Summation over the phase and applied stress, which determines the plastic deformation of the weaker phase (ferrite in the case of $\alpha \rightarrow \gamma$ transformation)
5. Formation of ultrafine grain in the course of phase transformation

4.5.7 Tool Steels

Tool steels can be classified into four groups according to their application: (1) steels for cutting tools used in mild conditions; (2) steels for cutting tools used in severe conditions; (3) measuring tools; and (4) die steels.

Steels for cutting tools must have high hardness exceeding $60R_c$. Therefore, such tool steels contain a minimum of 0.6% C. The main requirement imposed on steels used in severe conditions (high-speed steels) is stable hardness under long heating. All tool steels fall into four categories: (1) carbon tool steels, (2) alloy tool steels, (3) die steels, and (4) high-speed steels.

4.5.7.1 Carbon Tool Steels

Carbon tool steels contain 0.60–0.74% C, 0.25–0.35% Mn, and 0.30% Si. The quenching temperature of these steels is chosen in conformity with the Fe–C equilibrium diagram. The tetrahedral structure of martensite and internal stresses in quenched steels bring about considerable brittleness. That is why tempering after quenching is an obligatory operation. The tempering temperature is determined by the required working hardness of the tools. Usually it ranges between 180 and 240°C (350 and 465°F).

Of great importance in terms of machinability is the structure of annealed steels. Steels with the structure of lamellar pearlite are difficult to machine. Therefore, with the help of annealing at a temperature slightly above A_{c1}, easily worked steels with the structure of globular pearlite are obtained. As a rule, carbon steels are quenched in water. Because of this, tools made of such steels have a soft unannealed core and are less brittle than tools made of through-hardened steels.

4.5.7.2 Alloy Tool Steels

Compared with carbon steels, alloy tool steels possess greater hardenability and wear resistance. This is achieved by the introduction of small quantities of alloying elements, predominantly chromium. For chromium steels, it is imperative that quenching be accompanied by subsequent tempering. If it is necessary to preserve hardness at the level of the quenched state, the tempering temperature should not exceed 150–170°C (300–340°F).

In all cases where quenching should be accompanied by minimum deformation during the pearlite → martensite transformation (pearlite is the initial structure in this process), low-deformation tool steels are used. Such steels can be obtained by alloying with elements that increase the amount of retained austenite in the quenched state, namely, chromium and manganese. These steels contain about 12% Cr and ~1.5% C. The formation of a large amount of carbides $(Cr,Fe)_7C_3$ significantly improves their wear resistance.

These high-chromium steels belong to the ledeburitic class. In the cast state, the initial carbides form the eutectic ledeburite. In forging, the eutectic breaks down and the structure of the steels consists of sorbite-forming pearlite with inclusions of excess carbides. When heated for quenching, the carbides dissolve in austenite. The highest hardness of the steel is achieved upon quenching at ~1050°C (~1920°F).

To obtain high hardness, the steel is quenched in oil. The retained austenite precipitates in the process of cold treatment and tempering. Owing to the greater stability of martensite compared to other steels, the tempering temperature is increased to 200–220°C (390–430°F).

4.5.7.3 Die Steels

Dies operating in the cold state need high-hardness steels. The steel to be used in hot pressing should have low sensitivity to local heating. Different grades of steels—from carbon to complex alloy steels—are used in the production of dies. Carbon steel is used for dies operating under mild conditions and alloy steel for dies operating under severe conditions. Carbon steel contains 0.6–1% C. Alloy steel includes 0.3–0.7% C, Cr, Si, and sometimes Ni.

Dies made of alloy steels are usually quenched from ~850°C (1560°F) in oil with subsequent tempering at 500–550°C (930–1020°F). Hardness of the steel amounts to 350–400H_B. Dies for cold pressing are quenched in the temperature range of 860–1050°C (1580–1920°F) (depending on the steel grade) in oil with subsequent tempering at 200–300°C (390–570°F). Depending on the tempering temperature and the steel grade, the steel hardness is within $R_c = 56–62$.

4.5.7.4 High-Speed Steels

High-speed steels must not only possess high hardness in the hot state, but also be able to retain it during long heating (red hardness). To preserve hardness during heating, it is necessary to hamper the process of carbide coagulation. For this purpose, special carbides should be formed. Such carbides can be produced if the steel is alloyed with 3% Cr. The special carbide Cr_7C_3 coagulates at high temperatures to a lesser degree than cementite. Noticeable precipitation and coagulation of special Cr, Mo, W, and V carbides occur at temperatures over 500°C (930°F).

All high-speed steels are rated in the ledeburite class and in the cast state have the structure of white hypoeutectic cast iron. As a result of forging, the structure of the high-speed steel changes and the eutectic is broken down into individual carbides. In the annealed state, three types of carbides are observed: coarse primary carbides, smaller secondary carbides, and fine-grain carbides entering into the composition of upper bainite. Ferrite, which is found in upper bainite, also contains some alloying impurities.

Heating of the high-speed steel to the point A_{c1} (800–850°C; 1470–1560°F) is not accompanied by structural changes. Above this point, the eutectoid transforms to austenite, the secondary carbides dissolve in the austenite, and it is saturated with carbon and alloying elements.

Solubility of carbides depends on how long the steel is held at the quenching temperature. With an increase in the holding time, there is more complete dissolution of carbides in austenite.

Carbon and alloying elements contained in austenite lower the martensite point and increase the content of retained austenite. At quenching temperatures above 1000°C (1832°F) the martensite point decreases to 0°C (32°F) or lower. This peculiarity is taken advantage of in the heat treatment of tools made of high-speed steels.

In the process of steel tempering, the following structural changes take place. Heating to 100–200°C (212–390°F) causes a small compression, since the tetragonal martensite transforms to the cubic modification. At 300–400°C (570–750°F), hardness deteriorates owing to a decrease in the work hardening of retained austenite. At 500–600°C (930–1110°F), finely disperse carbides precipitate from austenite. Cooling the steel from these temperatures brings about the secondary formation of martensite: depleted austenite transforms to martensite in larger quantities.

The higher the tempering temperature or the longer the tempering time, the greater the amount of retained austenite transformed to martensite. Complete transformation of austenite can be attained by multiple tempering. The microstructure of the quenched and tempered steel should consist of finely dispersed martensite and carbides.

The quenching temperature of high-speed steel should be as high as possible, but at the same time it should not allow intensive grain growth (1260–1280°C; 2300–2340°F). During quenching the steel may be cooled comparatively slowly owing to a low-critical rate of quenching (in air or oil). Tempering is an obligatory operation and is usually realized at 560–580°C (1040–1075°F) for 3 h. To obtain still better properties, two- or threefold tempering is used, with the holding time at each stage at least for 1 h.

FURTHER READING

Belous, M.V., Cherepin, V.T., and Vasiliev, M.A., *Transformations During Tempering of Steel*, Metallurgiya, Moscow, 1973.

Bernshtein, M.L. and Richshtadt, A.G. (Eds.), *Physical Metallurgy and Thermal Treatment of Steels, Handbook*, Vols. I, II, and III, 3rd issue, Metallurgiya, Moscow, 1983.

Blanter, M.E., *Phase Transformations during Thermal Treatment of Steel*, Metallurgiya, Moscow, 1962.

Blanter, M.E., *Physical Metallurgy and Thermal Treatment*, Mashinostroyeniye, Moscow, 1963.

Delle, V.A., *Structural Alloy Steel*, Metallurgiya, Moscow, 1959.

Goldshtein, M.I., Grachev, S. V., and Veksler, Yu. G., *Special Steels*, Metallurgiya, Moscow, 1985.

Gudreman, E., *Special Steels*, Vols. I and II, Metallurgiya, Moscow, 1959.

Gulyaev, A.P., *Physical Metallurgy*, Metallurgiya, Moscow, 1976.

Gulyaev, A.P., *Pure Steel*, Metallurgiya, Moscow, 1975.

Kaschenko, G.A., *Fundamentals of Physical Metallurgy*, Metallurgiya, Moscow, 1964.

Kurdyumov, G.V., Utevski, L.M., and Entin, R.I., *Transformations in Iron and Steel*, Nauka, Moscow, 1977.

Meskin, V.S., *Fundamentals of Steel Alloying*, Metallurgiya, Moscow, 1964.

Novikov, I.I., *Theory of Thermal Treatment of Metals*, Metallurgiya, Moscow, 1986.

Popov, A.V., *Phase Transformations of Metal Alloys*, Metallurgiya, Moscow, 1963.

Vinograd, M.I. and Gromova, G.P., *Inclusions in Alloy Steels and Alloys*, Metallurgiya, Moscow, 1972.

Zimmerman, R. and Gunter, K., *Metallurgy and Materials Science Handbook*, Metallurgiya, Moscow, 1982.

5 Hardenability

Božidar Liščić

CONTENTS

5.1 Definition of Hardenability 213
5.2 Factors Influencing Depth of Hardening 215
5.3 Determination of Hardenability 217
5.3.1 Grossmann's Hardenability Concept 217
5.3.1.1 Hardenability in High-Carbon Steels 220
5.3.2 Jominy End-Quench Hardenability Test 228
5.3.2.1 Hardenability Test Methods for Shallow-Hardening Steels 230
5.3.2.2 Hardenability Test Methods for Air-Hardening Steels 233
5.3.3 Hardenability Bands 237
5.4 Calculation of Jominy Curves from Chemical Composition 240
5.4.1 Hyperbolic Secant Method for Predicting Jominy Hardenability 243
5.4.2 Computer Calculation of Jominy Hardenability 247
5.5 Application of Hardenability Concept for Prediction of Hardness after Quenching 249
5.5.1 Lamont Method 253
5.5.2 Steel Selection Based on Hardenability 256
5.5.3 Computer-Aided Steel Selection Based on Hardenability 257
5.6 Hardenability in Heat Treatment Practice 264
5.6.1 Hardenability of Carburized Steels 264
5.6.2 Hardenability of Surface Layers When Short-Time Heating Methods Are Used 266
5.6.3 Effect of Delayed Quenching on the Hardness Distribution 267
5.6.4 A Computer-Aided Method to Predict the Hardness Distribution after Quenching Based on Jominy Hardenability Curves 268
5.6.4.1 Selection of Optimum Quenching Conditions 273
References 275

5.1 DEFINITION OF HARDENABILITY

Hardenability, in general, is defined as the ability of a ferrous material to acquire hardness after austenitization and quenching. This general definition comprises two subdefinitions: the ability to reach a certain hardness level (German: Aufhärtbarkeit) and the hardness distribution within a cross section (German: Einhärtbarkeit).

The ability to reach a certain hardness level is associated with the highest attainable hardness. It depends first of all on the carbon content of the material and more specifically on the amount of carbon dissolved in the austenite after the austenitizing treatment, because only this amount of carbon takes part in the austenite-to-martensite transformation and has relevant influence on the hardness of martensite. Figure 5.1 shows the approximate relationship between the hardness of the structure and its carbon content for different percentages of martensite [1].

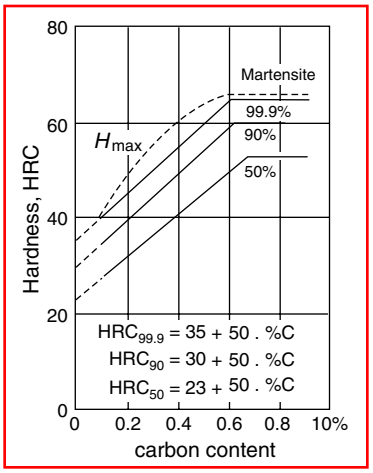

FIGURE 5.1 Approximate relationship between hardness in HRC and carbon content for different percentages of martensite. (From G. Spur (Ed.), *Handbuch der Fertigungstechnik*, Band 4/2, *Wärmebehandeln*, Carl Hanser, Munich, 1987, p. 1012.)

The hardness distribution within a cross section is associated with the change of hardness from the surface of a specified cross section toward the core after quenching under specified conditions. It depends on carbon content and the amount of alloying elements dissolved in the austenite during the austenitizing treatment. It may also be influenced by the austenite grain size. Figure 5.2 shows the hardness distributions within the cross sections of bars of 100 mm diameter after quenching three different kinds of steel [2].

In spite of quenching the W1 steel in water (i.e., the more severe quenching) and the other two grades in oil, the W1 steel has the lowest hardenability because it does not contain alloying elements. The highest hardenability in this case is that of the D2 steel, which has the greatest amount of alloying elements.

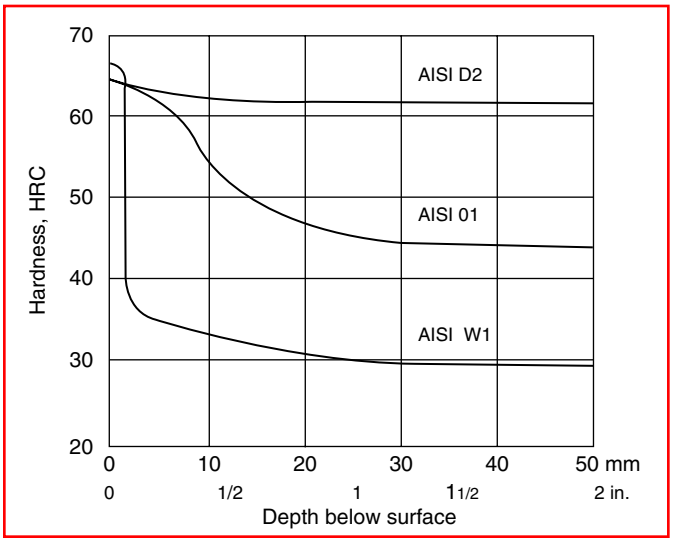

FIGURE 5.2 Hardness distributions within cross sections of bars of 100 mm diameter for three different kinds of steel, after quenching. Steel W1 was water-quenched; the rest were oil-quenched. (From K.E. Thelning, *Steel and Its Heat Treatment*, 2nd ed., Butterworths, London, 1984, p. 145.)

When a steel has high hardenability it achieves a high hardness throughout the entire heavy section (as D2 in Figure 5.2) even when it is quenched in a milder quenchant (oil). When a steel has low hardenability its hardness decreases rapidly below the surface (as W1 in Figure 5.2), even when it is quenched in the more severe quenchant (water).

According to their ability to reach a certain hardness level, shallow-hardening high-carbon steels may reach higher maximum hardness than alloyed steels of high hardenability while at the same time achieving much lower hardness values across a cross section. This can be best compared by using Jominy hardenability curves (see Section 5.3.2). Hardenability is an inherent property of the material itself, whereas hardness distribution after quenching (depth or hardening) is a state that depends on other factors as well.

5.2 FACTORS INFLUENCING DEPTH OF HARDENING

Depth of hardening is usually defined as the distance below the surface at which a certain hardness level (e.g., 50 HRC) has been attained after quenching. Sometimes it is defined as the distance below the surface within which the martensite content has reached a certain minimum percentage.

As a consequence of the austenite-to-martensite transformation, the depth of hardening depends on the following factors:

1. Shape and size of the cross section
2. Hardenability of the material
3. Quenching conditions

Quenching conditions include not only the specific quenchant with its inherent chemical and physical properties, but also important process parameters such as bath temperature and agitation rate.

The cross-sectional shape has a remarkable influence on heat extraction during quenching and consequently on the resulting hardening depth. Bars of rectangular cross sections always achieve less depth of hardening than round bars of the same cross-sectional size. Figure 5.3 is a diagram that can be used to convert square and rectangular cross sections to equivalent circular cross sections. For example, a 38-mm square and a 25 $\times$ 100-mm rectangular cross section are each equivalent to a 40-mm diameter circular cross section; a 60 $\times$ 100-mm rectangular cross section is equivalent to an 80-mm diameter circle [2].

The influence of cross-sectional size when quenching the same grade of steel under the same quenching conditions is shown in Figure 5.4A. Steeper hardness decreases from surface to core and substantially lower core hardness values result from quenching a larger cross section.

Figure 5.4B shows the influence of hardenability and quenching conditions by comparing an unalloyed (shallow-hardening) steel to an alloyed steel of high hardenability when each is quenched in (a) water or (b) oil. The critical cooling rate (ν_{crit}) of the unalloyed steel is higher than the critical cooling rate of the alloyed steel. Only those points on the cross section that have been cooled at a higher cooling rate than ν_{crit} could transform to martensite and attain high hardness. With unalloyed steel this can be achieved up to some depth only by quenching in water (curve a); oil quenching (curve b) provides essentially no hardness increase. With alloyed steel, quenching in water (because of the high cooling rate of water) produces a cooling rate greater than ν_{crit} even in the core, resulting in through-hardening. Oil quenching (curve b) provides, in this case, cooling rates higher than ν_{crit} within quite a large depth of hardening. Only the core region remains unchanged.

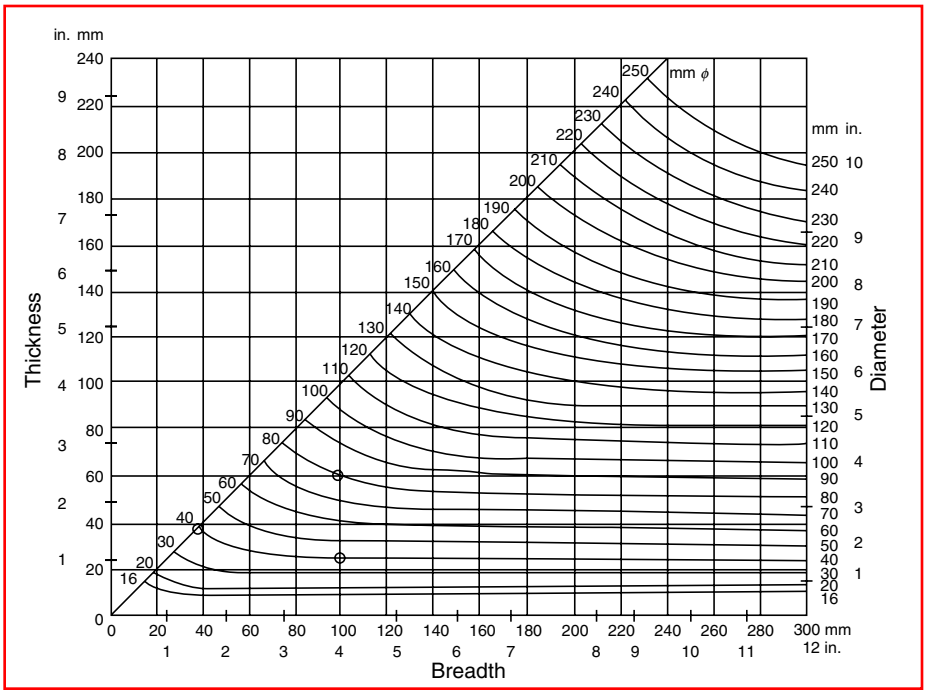

FIGURE 5.3 Correlation between rectangular cross sections and their equivalent round sections, according to ISO. (From K.E. Thelning, *Steel and Its Heat Treatment*, 2nd ed., Butterworths, London, 1984, p. 145.)

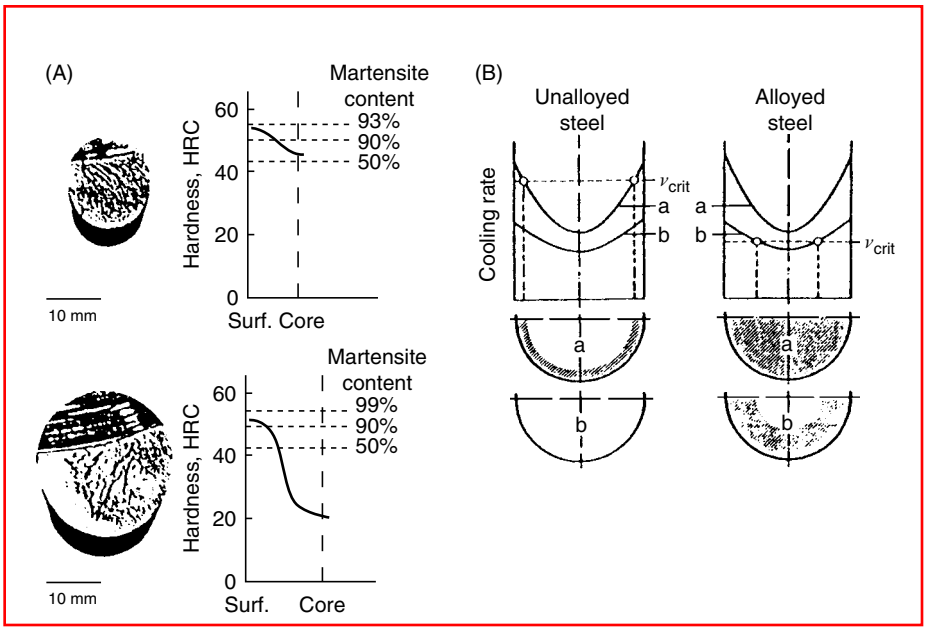

FIGURE 5.4 Influence of (A) cross-sectional size and (B) hardenability and quenching conditions on the depth of hardening. (a) Water quenching; (b) oil quenching, ν_{crit}, critical cooling rate. (From G. Spur (Ed.), *Handbuch der Fertigungstechnik*, Band 4/2, *Wärmebehandeln*, Carl Hanser, Munich, 1987, p. 1012.)

5.3 DETERMINATION OF HARDENABILITY

5.3.1 GROSSMANN'S HARDENABILITY CONCEPT

Grossmann's method of testing hardenability [3] uses a number of cylindrical steel bars of different diameters hardened in a given quenching medium. After sectioning each bar at midlength and examining it metallographically, the bar that has 50% martensite at its center is selected, and the diameter of this bar is designated as the critical diameter (D_{crit}). The hardness value corresponding to 50% martensite will be determined exactly at the center of the bar of D_{crit}. Other bars with diameters smaller than D_{crit} have more than 50% martensite in the center of the cross section and correspondingly higher hardness, while bars having diameters larger than D_{crit} attain 50% martensite only up to a certain depth as shown in Figure 5.5. The critical diameter D_{crit} is valid for the quenching medium in which the bars have been quenched. If one varies the quenching medium, a different critical diameter will be obtained for the same steel.

To identify a quenching medium and its condition, Grossmann introduced the quenching intensity (severity) factor H. The H values for oil, water, and brine under various rates of agitation are given in Table 5.1[4]. From this table, the large influence of the agitation rate on the quenching intensity is evident.

To determine the hardenability of a steel independently of the quenching medium, Grossmann introduced the ideal critical diameter D_I, which is defined as the diameter of a given steel that would produce 50% martensite at the center when quenched in a bath of quenching intensity $H = \infty$. Here, $H = \infty$ indicates a hypothetical quenching intensity that reduces the surface temperature of the heated steel to the bath temperature in zero time. Grossmann and his coworkers also constructed a chart, shown in Figure 5.6, that allows the conversion of any value of critical diameter D_{crit} for a given H value to the corresponding value for the ideal critical diameter (D_I) of the steel in question [2].

For example, after quenching in still water ($H = 1.0$), a round bar constructed of steel A has a critical diameter (D_{crit}) of 28 mm according to Figure 5.6. This corresponds to an ideal critical diameter (D_I) of 48 mm. Another round bar, constructed of steel B, after quenching in oil ($H = 0.4$), has a critical diameter (D_{crit}) of 20 mm. Converting this value, using Figure 5.6, provides an ideal critical diameter (D_I) of 52 mm. Thus, steel B has a higher hardenability than steel A. This indicates that D_I is a measure of steel hardenability that is independent of the quenching medium.

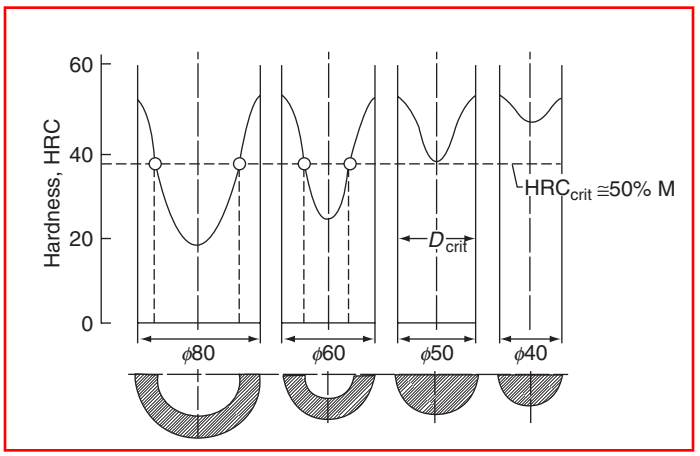

FIGURE 5.5 Determination of the critical diameter D_{crit} according to Grossmann. (From G. Spur (Ed.), *Handbuch der Fertigungstechnik*, Band 4/2, *Wärmebehandeln*, Carl Hanser, Munich, 1987, p. 1012.)

TABLE 5.1
Grossmann Quenching Intensity Factor *H*

Method of Quenching	H Value (in.$^{-1}$)		
	Oil	Water	Brine
No agitation	0.25–0.30	1.0	2.0
Mild agitation	0.30–0.35	1.0–1.1	2.0–2.2
Moderate agitation	0.35–0.40	1.2–1.3	
Good agitation	0.40–0.50	1.4–1.5	
Strong agitation	0.50–0.80	1.6–2.0	
Violent agitation	0.80–1.10	4.0	5.0

Source: *Metals Handbook*, 8th ed., Vol. 2, American Society for Metals, Cleveland, OH, 1964, p. 18.

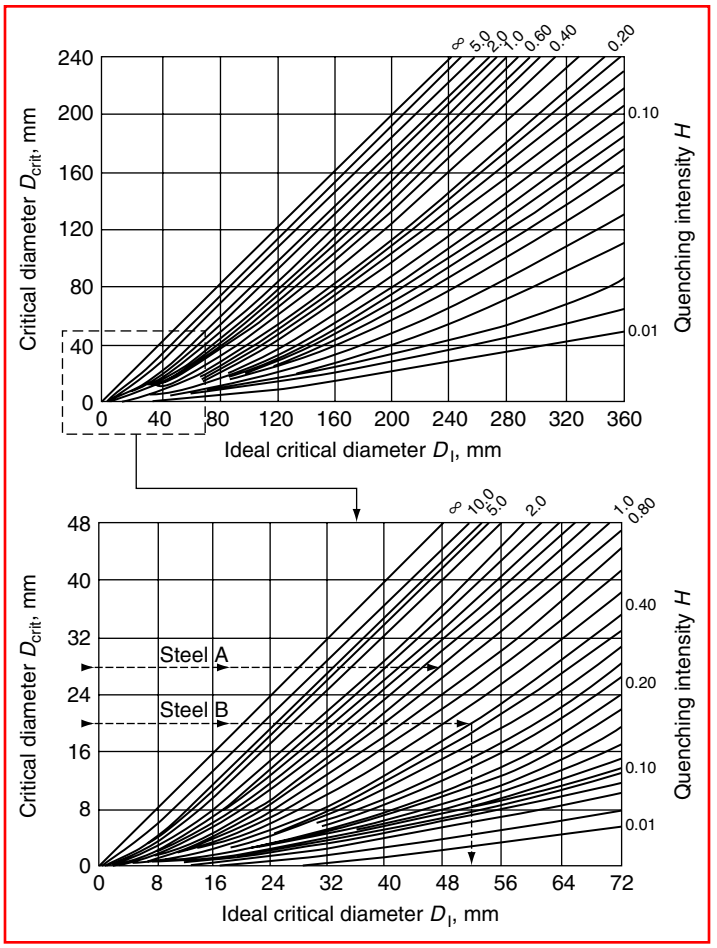

FIGURE 5.6 The chart for converting the values of the critical diameter D_{crit} into the ideal critical diameter D_I, or vice versa, for any given quenching intensity H, according to Grossmann and coworkers. (From K.E. Thelning, *Steel and Its Heat Treatment*, 2nd ed., Butterworths, London, 1984, p. 145.)

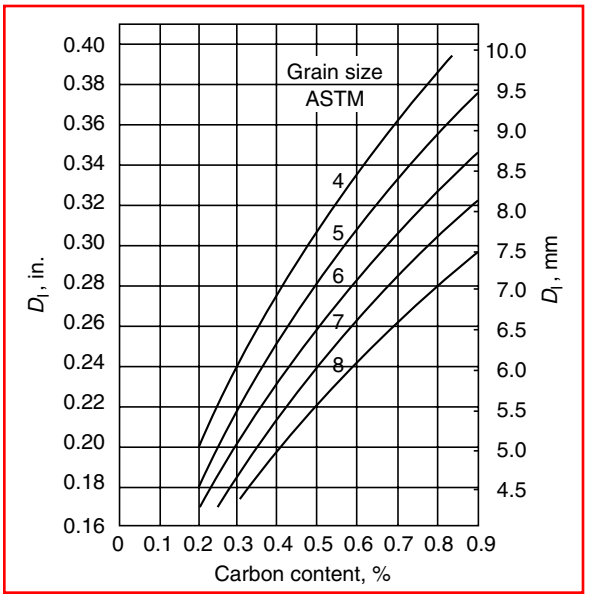

FIGURE 5.7 The ideal critical diameter (D_I) as a function of the carbon content and austenite grain size for plain carbon steels, according to Grossmann. (From K.E. Thelning, *Steel and its Heat Treatment*, 2nd ed., Butterworths, London, 1984, p. 145.)

If D_I is known for a particular steel, Figure 5.6 will provide the critical diameter of that steel for various quenching media. For low- and medium-alloy steels, hardenability as determined by D_I may be calculated from the chemical composition after accounting for austenite grain size. First, the basic hardenability of the steel as a function of carbon content and austenite grain size is calculated from Figure 5.7 according to the weight percent of each element present. For example: if a steel has an austenite grain size of American Society for Testing and Materials (ASTM) 7 and the chemical composition C 0.25%, Si 0.3%, Mn 0.7%, Cr 1.1%, Mo 0.2%, then the basic value of hardenability from Figure 5.7 (in inches) is $D_I = 0.17$. The total hardenability of this steel is

$$D_I = 0.17 \times 1.2 \times 3.3 \times 3.4 \times 1.6 = 3.7\,\text{in.} \tag{5.1}$$

For these calculations, it is presumed that the total amount of each element is in solution at the austenitizing temperature. Therefore the diagram in Figure 5.8 is applicable for carbon contents above 0.8% C only if all of the carbides are in solution during austenitizing. This is not the case, because conventional hardening temperatures for these steels are below the temperatures necessary for complete dissolution of the carbides. Therefore, decreases in the basic hardenability are to be expected for steels containing more than 0.8% C, compared to values in the diagram. Later investigations by other authors produced similar diagrams that account for this decrease in the basic hardenability that is to be expected for steels with more than 0.8% C, compared to the values shown in Figure 5.8 [6]. Although values of D_I calculated as above are only approximate, they are useful for comparing the hardenability of two different grades of steel.

The most serious objection to Grossmann's hardenability concept is the belief that the actual quenching intensity during the entire quenching process can be described by a single H value. It is well known that the heat transfer coefficient at the interface between the metal

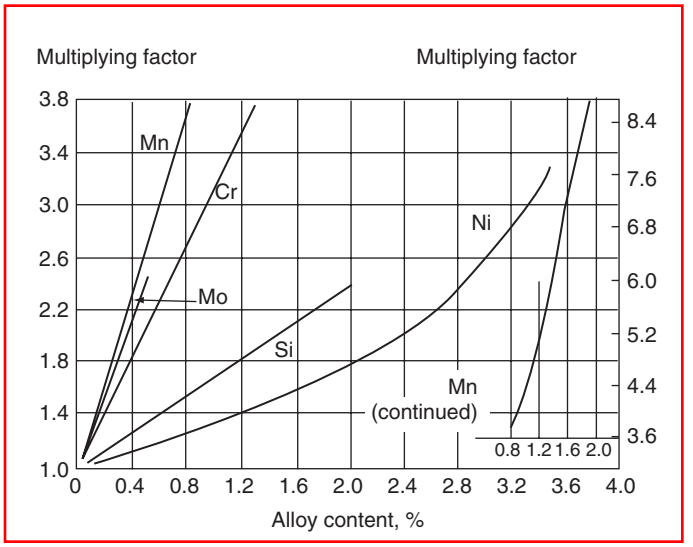

FIGURE 5.8 Multiplying factors for different alloying elements when calculating hardenability as D_I value, according to AISI. (From K.E. Thelning, *Steel and Its Heat Treatment*, 2nd ed., Butterworths, London, 1984, p. 145.)

surface and the surrounding quenchant changes dramatically during different stages of the quenching process for a vaporizable fluid.

Another difficulty is the determination of the H value for a cross-sectional size other than the one experimentally measured. In fact, H values depend on cross-sectional size [7]. Figure 5.9 shows the influence of steel temperature and diameter on H values for an 18Cr8Ni round bar quenched in water from 845°C [7]. It is evident that the H value determined in this way passed through a maximum with respect to terminal temperatures. It is also evident that H values at the centers of round bars decreased with increasing diameter.

Values of the quenching intensity factor H do not account for specific quenchant and quenching characteristics such as composition, oil viscosity, or the temperature of the quenching bath. Table of H values do not specify the agitation rate of the quenchant either uniformly or precisely; that is, the uniformity throughout the quench tank with respect to mass flow or fluid turbulence is unknown. Therefore, it may be assumed that the tabulated H values available in the literature are determined under the same quenching conditions. This assumption, unfortunately, is rarely justified.

In view of these objections, Siebert et al. [8] state: "It is evident that there cannot be a single H-value for a given quenching bath, and the size of the part should be taken into account when assigning an H-value to any given quenching bath."

5.3.1.1 Hardenability in High-Carbon Steels

The hardenability effect of carbon and alloying elements in high-carbon steels and the case regions of carburized steels differ from those in low- and medium-carbon steels and are influenced significantly by the austenitizing temperature and prior microstructure (normalized or spheroidize-annealed). Using Grossmann's method for characterizing hardenability in terms of the ideal critical diameter D_I, multiplying factors for the hardenability effects of Mn, Si, Cr, Ni, Mo, and Al were successfully derived [9] for carbon levels ranging from 0.75 to 1.10% C in single-alloy and multiple-alloy steels quenched at different austenitizing temperatures from 800 to 930°C. These austenitizing temperatures encompass the hardening temperatures of hypereutectoid tool steels, 1.10% C bearing steels, and the case regions of

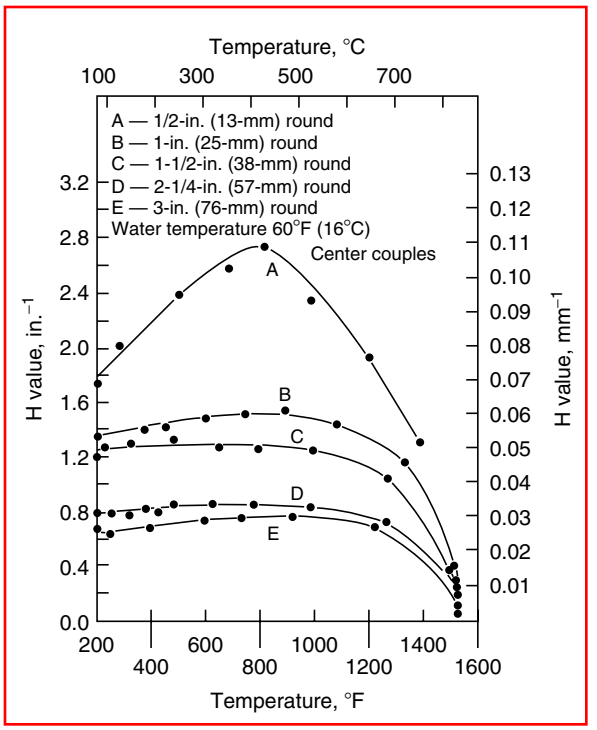

FIGURE 5.9 Change of the *H* value with temperature and size of the round bar. Calculated from cooling curves measured at the center of bars made of 18Cr8Ni steel quenched in water from 845°C, according to Carney and Janulionis. (From D.J. Carney and A.D. Janulionis, *Trans. ASM 43*:480–496, 1951.)

carburized steels. All of these steels, when quenched, normally contain an excess of undissolved carbides, which means that the quantity of carbon and alloying elements in solution could vary with the prior microstructure and the austenitizing conditions. The hardenability of these steels is influenced by the carbide size, shape, and distribution in the prior microstructure and by austenitizing temperature and time. Grain size exhibits a lesser effect because hardenability does not vary greatly from ASTM 6 to 9 when excess carbides are present.

As a rule, homogenous high-carbon alloy steels are usually spheroidize-annealed for machining prior to hardening. Carburizing steel grades are either normalized, i.e., air-cooled, or quenched in oil directly from the carburizing temperature before reheating for hardening. So different case microstructures (from martensite to lamellar pearlite) may be present, all of which transform to austenite rather easily during reheating for hardening. During quenching, however, the undissolved carbides will nucleate pearlite prematurely and act to reduce hardenability.

In spheroidize-annealed steel, the carbides are present as large spheroids, which are much more difficult to dissolve when the steel is heated for hardening. Therefore the amount of alloy and carbon dissolved is less when one starts with a spheroidized rather than a normalized or quenched microstructure. Nevertheless, it has been demonstrated that a spheroidized prior microstructure actually yields higher hardenability than a prior normalized microstructure, at least for austenitizing temperatures up to approximately 855°C. This effect occurs because larger carbides are not as efficient nuclei for early pearlite formation upon cooling as fine and lamellar carbides and the nuclei are present in lower numbers. With either prior microstructure, if strict control is maintained over austenitizing temperature and time, the solution of carbon and alloy can be reproduced with sufficient consistency to permit the

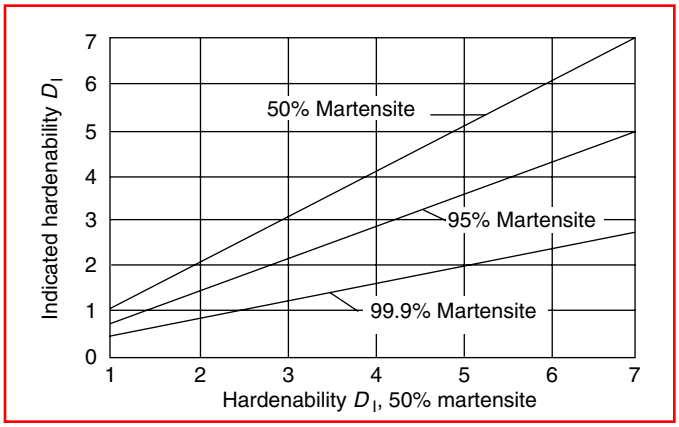

FIGURE 5.10 Average relationships among hardenability values (expressed as D_I) in terms of 50, 95, and 99.9% martensite microstructures. (From *Metals Handbook*, ASM International, Cleveland, OH, 1948, p. 499.)

derivation of multiplying factors. For all calculations, it was important to establish whether pearlite or bainite would limit hardenability because the effects of some elements on these reactions and on hardenability differ widely.

The multiplying factors were calculated according to a structure criterion of D_I to 90% martensite plus retained austenite (or 10% of nonmartensitic transformation) and with reference to a base composition containing 1.0% C and 0.25% of each of the elements Mn, Si, Cr, and Ni, with 0% Mo to ensure that the first transformation product would not be bainite. The 50% martensite hardenability criterion (usually used when calculating D_I) was selected by Grossmann because this structure in medium-carbon steels corresponds to an inflection in the hardness distribution curve. The 50% martensite structure also results in marked contrast in etching between the hardened and unhardened areas and in the fracture appearance of these areas in a simple fracture test. For many applications, however, it may be necessary to through-harden to a higher level of martensite to obtain optimum properties of tempered martensite in the core.

In these instances, D_1 values based on 90, 95, or 99.9% martensite must be used in determining the hardenability requirements. These D_1 values can be either experimentally determined or estimated from the calculated 50% martensite values using the relationships shown in Figure 5.10, which were developed for medium-carbon low-alloy steels [10]. A curve for converting the D_1 value for the normalized structure to the D_I value of the spheroidize-annealed structure as shown in Figure 5.11 is also available. New multiplying factors for D_1 values were obtained from the measured Jominy curves using the conversion curve modified by Carney shown in Figure 5.12.

The measured D_I values were plotted against the percent content of various elements in the steel. These curves were then used to adjust the D_I value of the steels whose residual content did not conform to the base composition. Once the D_I value of each analysis was adjusted for residuals, the final step was to derive the multiplying factors for each element from the quotient of the steels D_I^* and that of the base as follows:

$$f_{Mn} = \frac{D_I^* \text{ at } x\% \text{ Mn}}{D_I} \tag{5.2}$$

where D_I is the initial reference value.

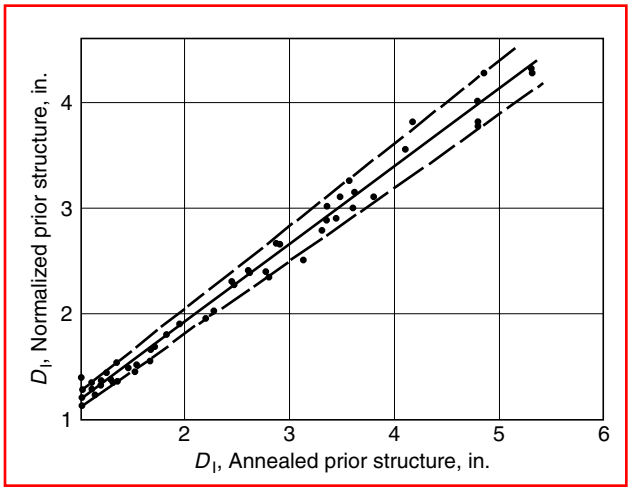

FIGURE 5.11 Correlation between hardenability based on normalized and spheroidize-annealed prior structures in alloyed 1.0% C steels. (From C.F. Jatczak, *Metall. Trans. 4*:2267–2277, 1973.)

Excellent agreement was obtained between the case hardenability results of carburized steels assessed at 1.0% carbon level and the basic hardenability of the 1.0% C steels when quenched from the normalized prior structure. It was thus confirmed that all multiplying factors obtained with prior normalized 1.0% C steels could be used to calculate the hardenability of all carburizing grades that are reheated for hardening following carburizing.

Jatczak and Girardi [11] determined the difference in multiplying factors for prior normalized and prior spheroidize-annealed structures as shown in Figure 5.13 and Figure 5.14. The influence of austenitizing temperature on the specific hardenability effect is evident. The multiplying factors shown in Figure 5.15 through Figure 5.18 were principally determined in compositions where only single-alloy additions were made and that were generally pearlitic in initial transformation behavior. Consequently, these multiplying factors may be applied to

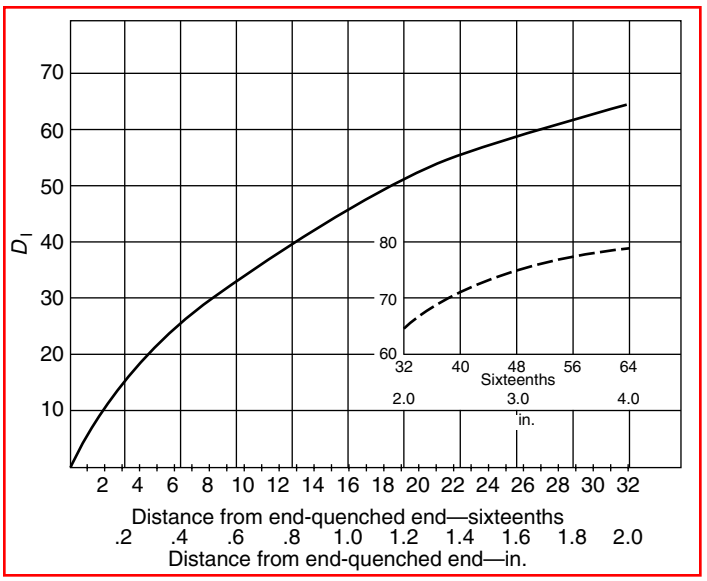

FIGURE 5.12 Relationship between Jominy distance and D_I. (From C.F. Jatczak, *Metall. Trans. 4*:2267–2277, 1973.)

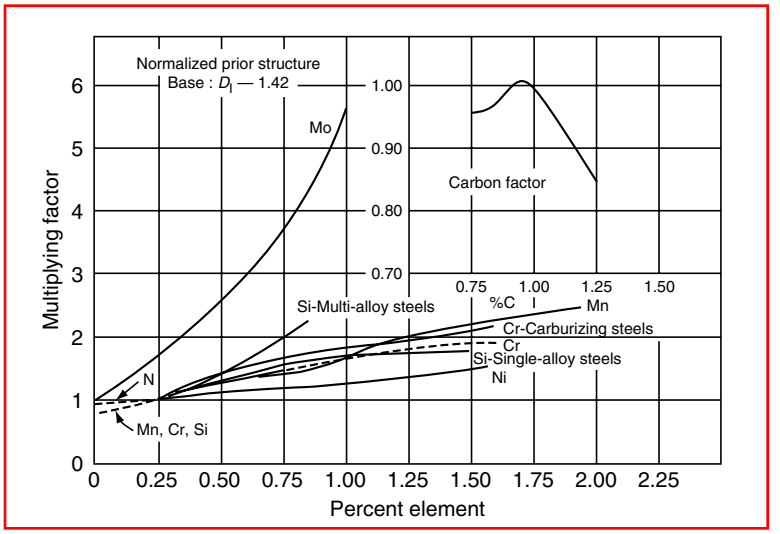

FIGURE 5.13 Multiplying factors for calculation hardenability of high-carbon steels of prior normalized structure. (From C.F. Jatczak and D.J. Girardi, *Multiplying Factors for the Calculation of Hardenability of Hypereutectoid Steels Hardened from* 1700°F, Climax Molybdenum Company, Ann Arbor, MI, 1958.)

the calculation of hardenability of all single-alloy high-carbon compositions and to those multialloyed compositions that remain pearlitic when quenched from these austenitizing conditions. This involves all analyses containing less than 0.15% Mo and less than 2% total of Ni plus Mn and also less than 2% Mn, Cr, or Ni when they are present individually. Of course, all of the factors given in Figure 5.15 through Figure 5.18 also apply to the calculation of case hardenability of similar carburizing steels that are rehardened from these temperatures following air cooling or integral quenching.

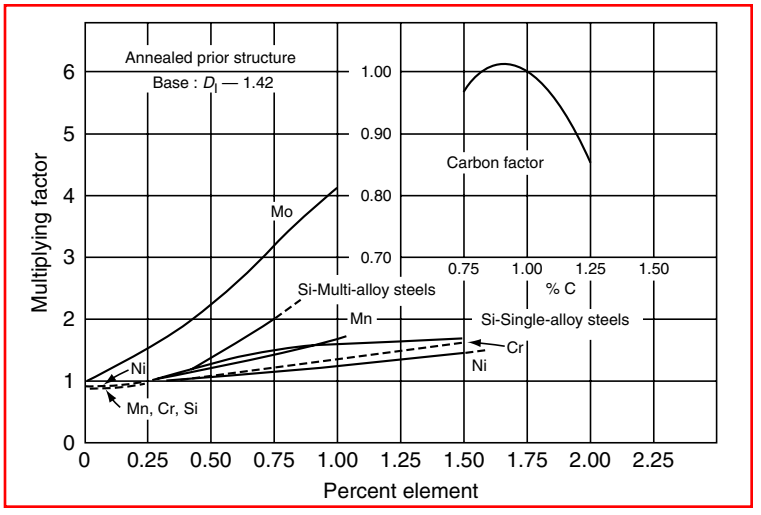

FIGURE 5.14 Multiplying factors for calculation of hardenability of high-carbon steels of prior spheroidize-annealed structure. (From C.F. Jatczak and D.J. Girardi, *Multiplying Factors for the Calculation of Hardenability of Hypereutectoid Steels Hardened from* 1700°F, Climax Molybdenum Company, Ann Arbor, MI, 1958.)

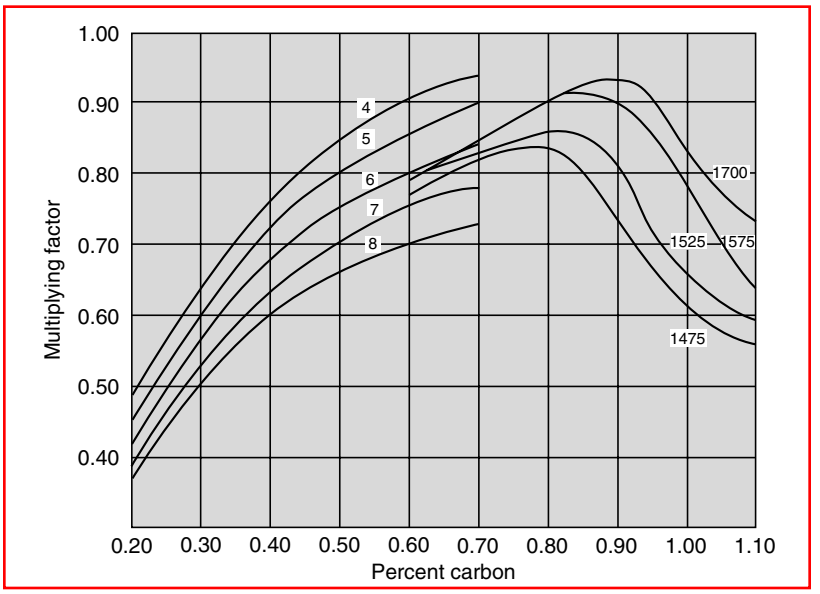

FIGURE 5.15 Multiplying factors for carbon at each austenitizing condition. Data plotted on the left-hand side are data from Kramer for medium-carbon steels with grain size variation from ASTM 4 to ASTM 8. (From C.F. Jatczak, *Metall. Trans. 4*:2267–2277, 1973.)

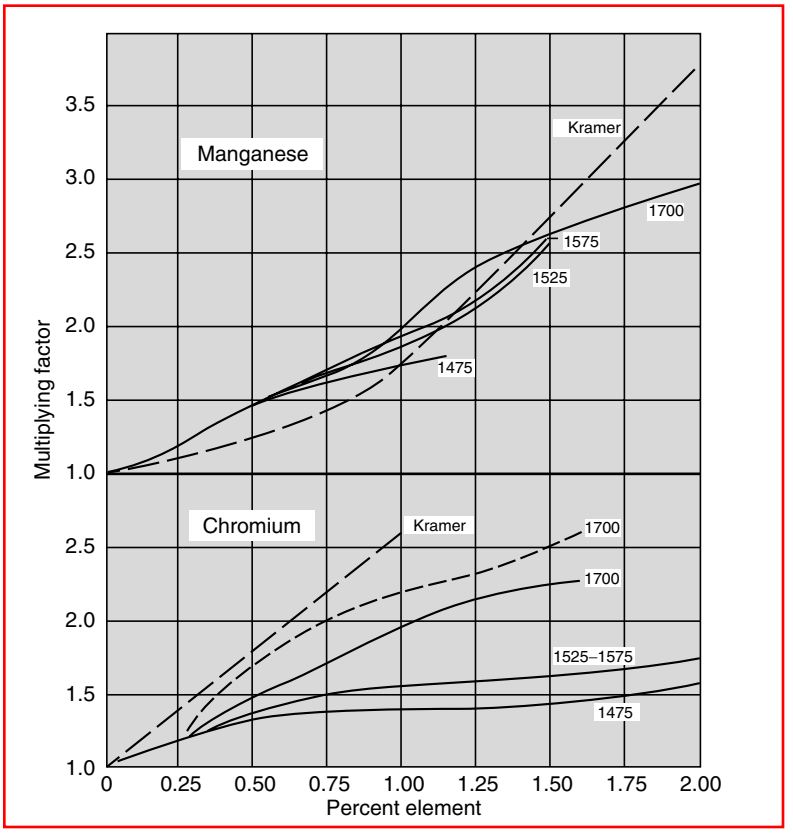

FIGURE 5.16 Effect of austenitizing temperature on multiplying factors for Mn and Cr at high-carbon levels (Kramer data for medium-carbon steels). (From C.F. Jatczak, *Metall. Trans. 4*:2267–2277, 1973.)

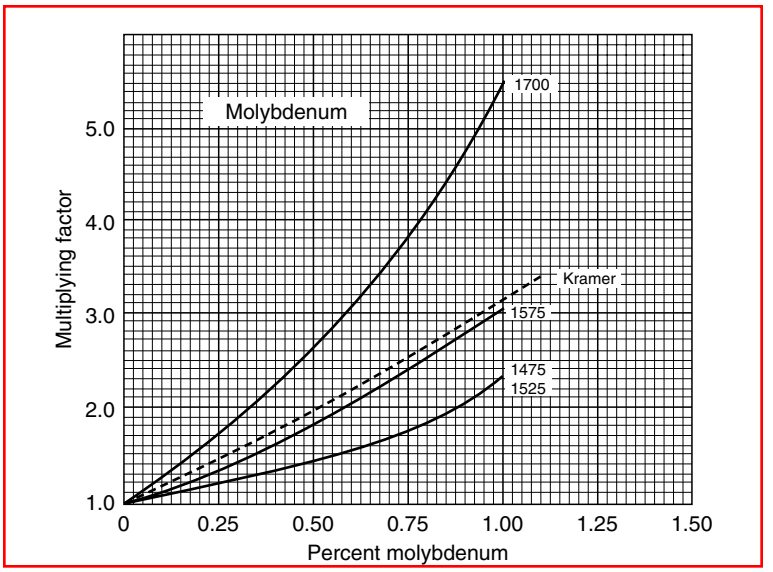

FIGURE 5.17 Effect of austenitizing temperature on multiplying factors for Mo at high carbon levels. (From C.F. Jatczak, *Metall. Trans. 4*:2267–2277, 1973.)

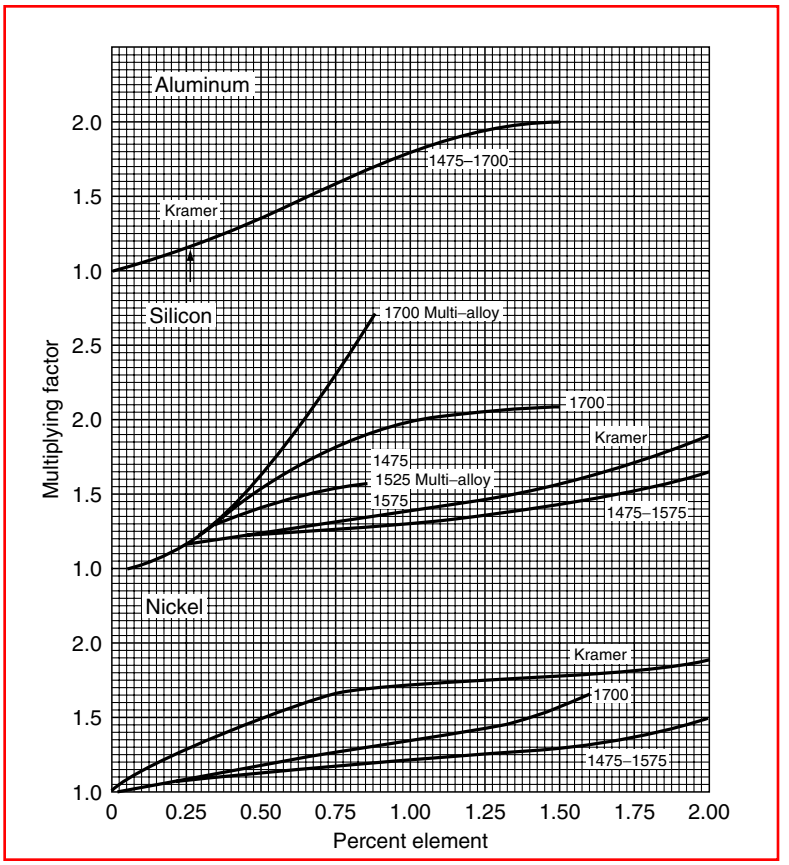

FIGURE 5.18 Effect of austenitizing temperature on multiplying factors for Si, Ni, and Al at high-carbon levels. (Arrow on Al curve denotes maximum percentage studies by Kramer.) (From C.F. Jatczak, *Metall. Trans. 4*:2267–2277, 1973.)

For steels containing more Mo, Ni, Mn, or Cr than the above percentages, the measured hardenability will always be higher than calculated with the single-alloy multiplying factors because these steels are bainitic rather than pearlitic and also because synergistic hardenability effects have been found to occur between certain elements when present together. The latter effect was specifically noted between Ni and Mn, especially in steels made bainitic by the addition of 0.15% or more Mo and that also contained more than 1.0% Ni.

The presence of synergistic effects precluded the use of individual multiplying factors for Mn and Ni, as the independence of alloying element effects is implicit in the Grossmann multiplying factor approach. This difficulty, however, was successfully surmounted by computing combined Ni and Mn factors as shown in Figure 5.19.

The factors from Figure 5.15 through Figure 5.18 can also be used for high-carbon steels that are spheroidize-annealed prior to hardening. However, the calculated D_I value must be converted to the annealed D_I value at the abscissa on Figure 5.11. The accuracy of hardenability prediction using the new factors has been found to be within $\pm 10\%$ at D_I values as high as 660 mm (26.0 in.).

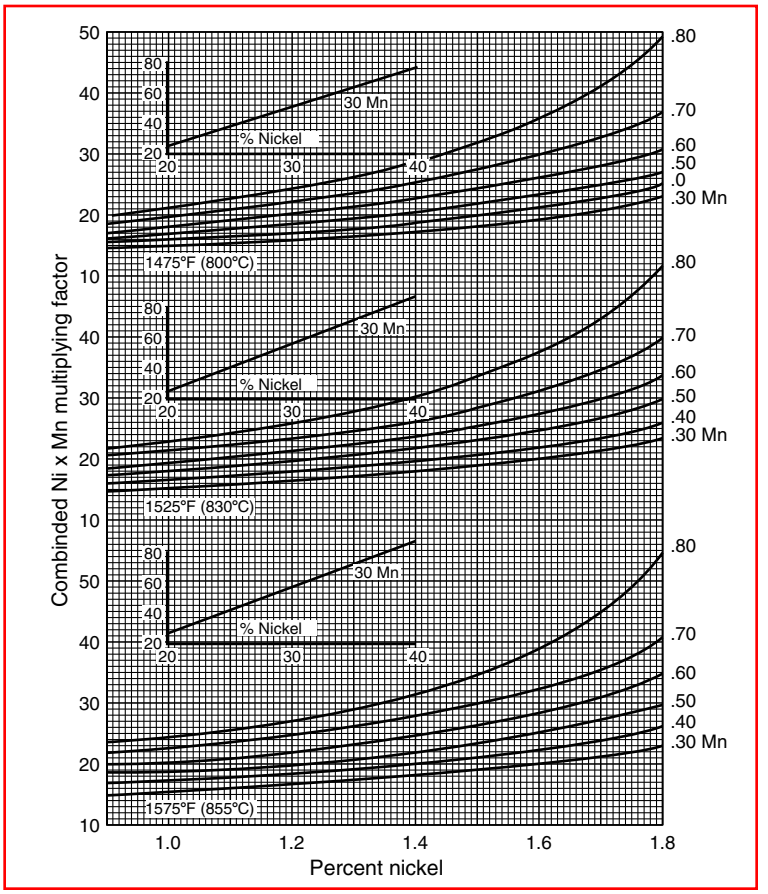

FIGURE 5.19 Combined multiplying factor for Ni and Mn in bainitic high-carbon steels quenched from 800 to 855°C, to be used in place of individual factors when composition contains more than 1.0% Ni and 0.15% Mo. (From C.F. Jatczak, *Metall. Trans. 4*:2267–2277, 1973.)

5.3.2 Jominy End-Quench Hardenability Test

The end-quench hardenability test developed by Jominy and Boegehold [12] is commonly referred to as the Jominy test. It is used worldwide, described in many national standards, and available as an international standard [13]. This test has the following significant advantages:

1. It characterizes the hardenability of a steel from a single specimen, allowing a wide range of cooling rates during a single test.
2. It is reasonably reproducible.

The steel test specimen (25 mm diameter $\times$ 100 mm) is heated to the appropriate austenitizing temperature and soaked for 30 min. It is then quickly transferred to the supporting fixture (Jominy apparatus) and quenched from the lower end by spraying with a jet of water under specified conditions as illustrated in Figure 5.20. The cooling rate is the highest at the end where the water jet impinges on the specimen and decreases from the quenched end, producing a variety of microstructures and hardnesses as a function of distance from the quenched end. After quenching, two parallel flats, approximately 0.45 mm below surface, are ground on opposite sides of the specimen and hardness values (usually HRC) are measured at 1/16 in. intervals from the quenched end and plotted as the Jominy hardenability curve (see Figure 5.21). When the distance is measured in millimeters, the hardness values are taken at every 2 mm from the quenched end for at least a total distance of 20 or 40 mm, depending on the steepness of the hardenability curve, and then every 10 mm. On the upper margin of the Jominy hardenability diagram, approximate cooling rates at 700°C may be plotted at several distances from the quenched end.

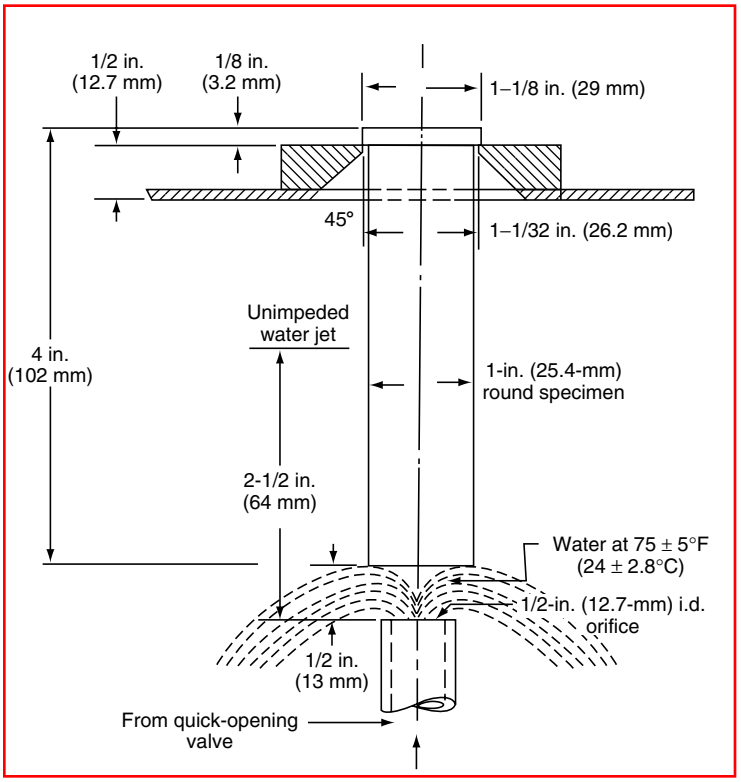

FIGURE 5.20 Jominy specimen and its quenching conditions for end-quench hardenability test.

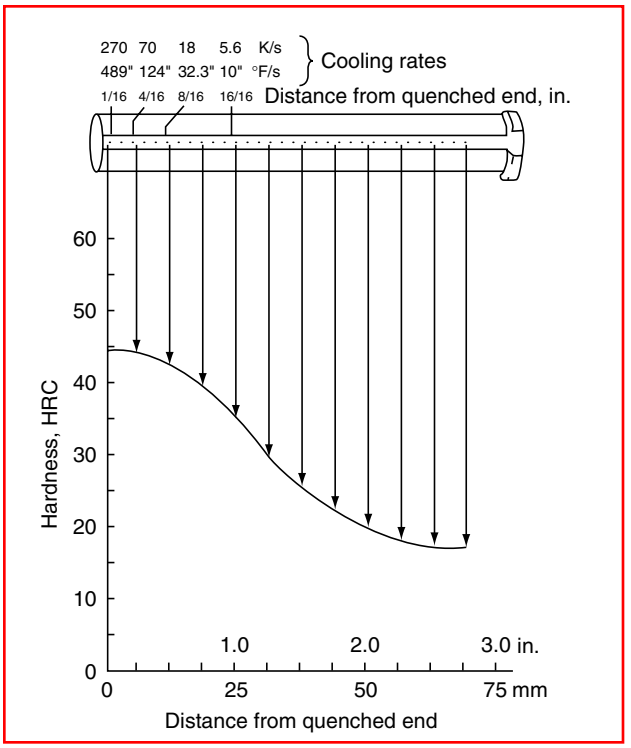

FIGURE 5.21 Measuring hardness on the Jominy specimen and plotting the Jominy hardenability curve. (From G. Krauss, *Steels Heat Treatment and Processing Principles*, ASM International, Metals Park, OH, 1990.)

Figure 5.22 shows Jominy hardenability curves for different unalloyed and low-alloyed grades of steel. This figure illustrates the influence of carbon content on the ability to reach a certain hardness level and the influence of alloying elements on the hardness distribution expressed as hardness values along the length of the Jominy specimen. For example, DIN Ck45, an unalloyed steel, has a carbon content of 0.45% C and exhibits a higher maximum hardness (see the value at 0 distance from the quenched end) than DIN 30CrMoV9 steel,

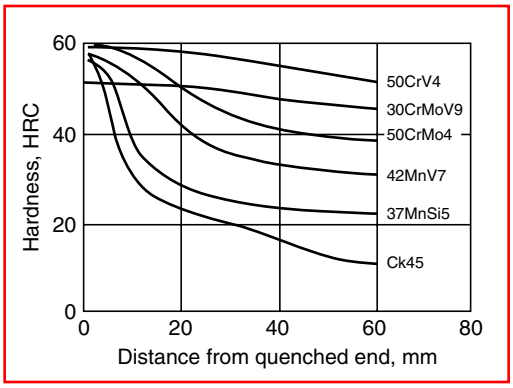

FIGURE 5.22 Jominy hardenability curves (average values) for selected grades of steel (designations according to German DIN standard). (From G. Spur (Ed.), *Handbuch der Fertigungstechnik*, Band 4/2, *Wärmebehandeln*, Carl Hanser, Munich, 1987, p. 1012.)

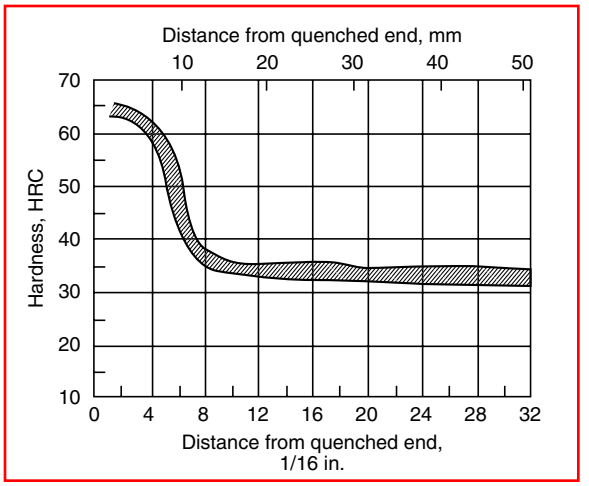

FIGURE 5.23 Reproductibility of the end-quench hardenability test. Hardenability range (hatched area between curves) based on tests by nine laboratories on a single heat of SAE 4068 steel. (From C.A. Siebert, D.V. Doane, and D.H. Breen, *The Hardenability of Steels*, ASM International, Cleveland, OH, 1997.)

which has only 0.30% C. However, the latter steel is alloyed with Cr, Mo, and V and shows a higher hardenability by exhibiting higher hardness values along the length of the specimen.

The Jominy end-quench test is used mostly for low-alloy steels for carburizing (core hardenability) and for structural steels, which are typically through-hardened in oils and tempered. The Jominy end-quench test is suitable for all steels except those of very low or very high hardenability, i.e., $D_1 < 1.0$ in. or $D_1 > 6.0$ in. [8]. The standard Jominy end-quench test cannot be used for highly alloyed air-hardened steels. These steels harden not only by heat extraction through the quenched end but also by heat extraction by the surrounding air. This effect increases with increasing distance from the quenched end.

The reproducibility of the standard Jominy end-quench test was extensively investigated, and deviations from the standard procedure were determined. Figure 5.23 shows the results of an end-quench hardenability test performed by nine laboratories on a single heat of SAE 4068 steel [8]. Generally, quite good reproducibility was achieved, although the maximum difference may be 8–12 HRC up to a distance of 10 mm from the quenched end depending on the slope of the curve. Several authors who have investigated the effect of deviations from the standard test procedure have concluded that the most important factors to be closely controlled are austenitization temperature and time, grinding of the flats of the test bar, prevention of grinding burns, and accuracy of the measured distance from the quenched end. Other variables such as water temperature, orifice diameter, free water-jet height, and transfer time from the furnace to the quenching fixture are not as critical.

5.3.2.1 Hardenability Test Methods for Shallow-Hardening Steels

If the hardenability of shallow-hardening steels is measured by the Jominy end-quench test, the critical part of the Jominy curve is from the quenched end to a distance of about 1/2 in. Because of the high critical cooling rates required for shallow-hardening steels, the hardness decreases rapidly for every incremental increase in Jominy distance. Therefore the standard Jominy specimen with hardness readings taken at every 1/16 in. (1.59 mm) cannot describe precisely the hardness trend (or hardenability). To overcome this difficulty it may be helpful

to (1) modify the hardness survey when using standard Jominy specimens or (2) use special L specimens.

5.3.2.1.1 Hardness Survey Modification for Shallow-Hardening Steels

The essential elements of this procedure, described in ASTM A255, are as follows:

1. The procedure in preparing the specimen before making hardness measurements is the same as for standard Jominy specimens.
2. An anvil that provides a means of very accurately measuring the distance from the quenched end is essential.
3. Hardness values are obtained from 1/16 to 1/2 in. (1.59–12.7 mm) from the quenched end at intervals of 1/32 in. (0.79 mm). Beyond 1/2 in., hardness values are obtained at 5/8, 3/4, 7/8, and 1 in. (15.88, 19.05, 22.23, and 25.4 mm) from the quenched end. For readings within the first 1/2 in. from the quenched end, two hardness traverses are made, both with readings 1/16 in. apart: one starting at 1/16 in. and completed at 1/2 in. from the quenched end, and the other starting at 3/32 in. (2.38 mm) and completed at 15/32 in. (11.91 mm) from the quenched end.
4. Only two flats 180° apart need be ground if the mechanical fixture has a grooved bed that will accommodate the indentations of the flat surveyed first. The second hardness traverse is made after turning the bar over. If the fixture does not have such a grooved bed, two pairs of flats should be ground, the flats of each pair being 180° apart. The two hardness surveys are made on adjacent flats.
5. For plotting test results, the standard form for plotting hardenability curves should be used.

5.3.2.1.2 The Use of Special L Specimens

To increase the cooling rate within the critical region when testing shallow-hardening steels, an L specimen, as shown in Figure 5.24, may be used. The test procedure is standard except that the stream of water rises to a free height of 100 ± 5 mm (instead of the 63.55 mm with a standard specimen) above the orifice, without the specimen in position.

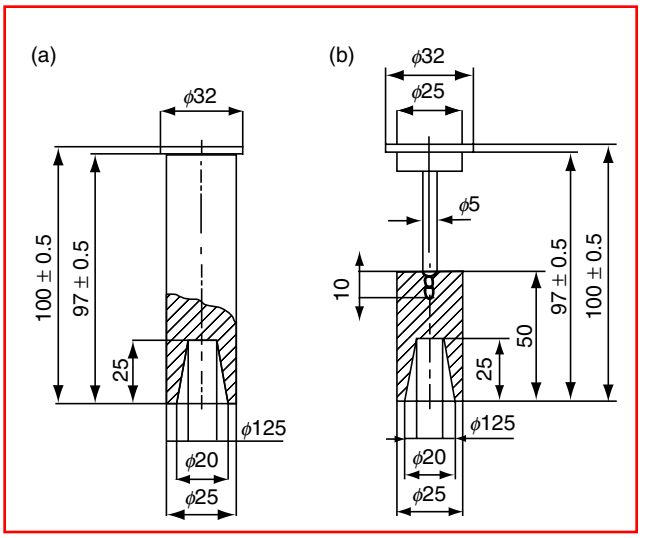

FIGURE 5.24 L specimens for Jominy hardenability testing of shallow-hardening steels. All dimensions in millimeters.

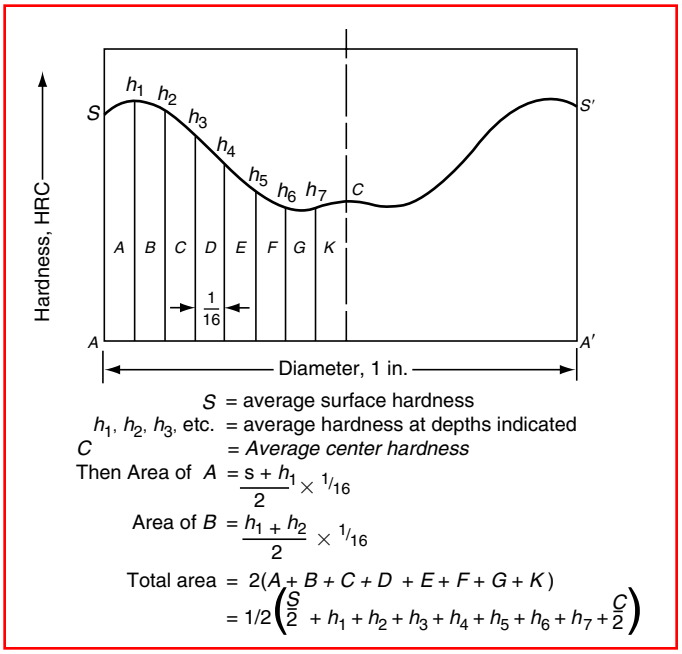

FIGURE 5.25 Estimation of area according to SAC method. (From *Metals Handbook*, 9th ed., Vol. 1, ASM International, Metals Park, OH, 1978, pp. 473–474.) [15]

5.3.2.1.3 The SAC Hardenability Test

The SAC hardenability test is another hardenability test for shallow-hardening steels, other than carbon tool steels, that will not through-harden in sizes larger than 25.4 mm (1 in.) in diameter. The acronym SAC denotes surface area center and is illustrated in Figure 5.25. The specimen is 25.4 mm (1 in.) in diameter and 140 mm (5.5 in.) long. After normalizing at the specified temperature of 1 h and cooling in air, it is austenitized by being held at temperature for 30 min and quenched in water at $24 \pm 5^{\circ}C$, where it is allowed to remain until the temperature is uniform throughout the specimen.

After the specimen has been quenched, a cylinder 25.4 mm (1 in.) in length is cut from its middle. The cut faces of the cylinder are carefully ground parallel to remove any burning or tempering that might result from cutting and to ensure parallel flat surfaces for hardness measuring.

First HRC hardness is measured at four points at 90° to each other on the surface. The average of these readings then becomes the surface reading. Next, a series of HRC readings are taken on the cross section in steps of 1/16 in. (1.59 mm) from the surface to the center of the specimen. From these readings, a quantitative value can be computed and designated by a code known as the SAC number.

The SAC code consists of a set of three two-digit numbers indicating (1) the surface hardness, (2) the total Rockwell (HRC)-inch area, and (3) the center hardness. For instance, SAC 60-54-43 indicates a surface hardness of 60 HRC, a total Rockwell-inch area of 54, and a center hardness of 43 HRC. The computation of the total Rockwell-inch area is shown in Figure 5.25.

5.3.2.1.4 Hot Brine Hardenability Test

For steels of very low hardenability, another test has been developed [15] that involves quenching several specimens 2.5 mm (0.1 in.) thick and 25 mm (1.0 in.) square in hot brine at controlled temperatures (and controlled quench severity), and determining the hardness and percent martensite of each specimen. The brine temperature for 90% martensite structure expressed as an equivalent diameter of a water-quenched cylinder is used as the hardenability

criterion. Although somewhat complex, this is a precise and reproducible method for experimentally determining the hardenability of shallow-hardening steels. By testing several steels using this method, a linear regression equation has been derived for estimating hardenability from chemical composition and grain size that expresses the relative contribution of carbon and alloying elements by additive terms instead of multiplicative factors.

5.3.2.2 Hardenability Test Methods for Air-Hardening Steels

When a standard Jominy specimen is used, the cooling rate at a distance of 80 mm from the quenched end (essentially the opposite end of the specimen) is approximately 0.7 K/s. The hardenability of all steel grades with a critical cooling rate greater than 0.7 K/s can be determined by the standard Jominy end-quench hardenability test as a sufficient decrease in hardness will be obtained from increasing amounts of nonmartensite transformation products (bainite, pearlite, ferrite). However, for steels with a critical cooling rate lower than 0.7 K/s there will be no substantial change in the hardness curve because martensite will be obtained at every distance along the Jominy specimen. This is the case with air-hardening steels. To cope with this situation and enable the use of the Jominy test for air-hardening steels, the mass of the upper part of the Jominy specimen should be increased [16] by using a stainless steel cap as shown in Figure 5.26. In this way, cooling rates of the upper part of the specimen are decreased below the critical cooling rate of the steel itself.

The complete device consists of the conical cap with a hole through which the specimen can be fixed with the cap. When austenitizing, a leg is installed on the lower end of the specimen as shown in Figure 5.26 to equalize heating so that the same austenitizing conditions exist along the entire test specimen. The total heating time is 40 min plus 20 min holding time at the austenitizing temperature. Before quenching the specimen according to the standard Jominy test procedure (together with the cap), the leg should be removed. Figure 5.27 illustrates cooling rates when quenching a standard Jominy specimen and a modified specimen with added cap. This diagram illustrates the relationship between the cooling times from the austenitizing temperature to 500°C and the distance from the quenched end of the specimen for different austenitizing temperatures.

Figure 5.27 shows that at an austenitizing temperature of 800°C up to a distance of 20 mm from the quenched end, the cooling time curves for the standard specimen and the modified

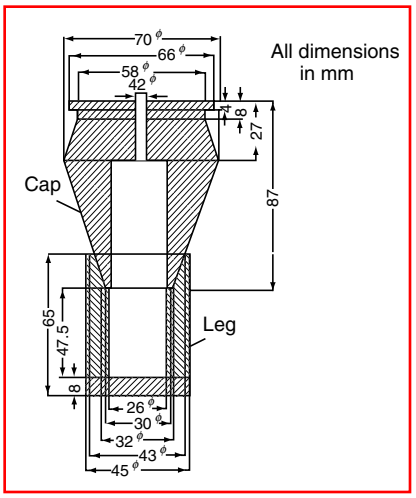

FIGURE 5.26 Modification of the standard Jominy test by the addition of a cap to the specimen for testing the hardenability of air-hardening steels. (From A. Rose and L. Rademacher, *Stahl Eisen 76*(23):1570–1573, 1956 [in German].)

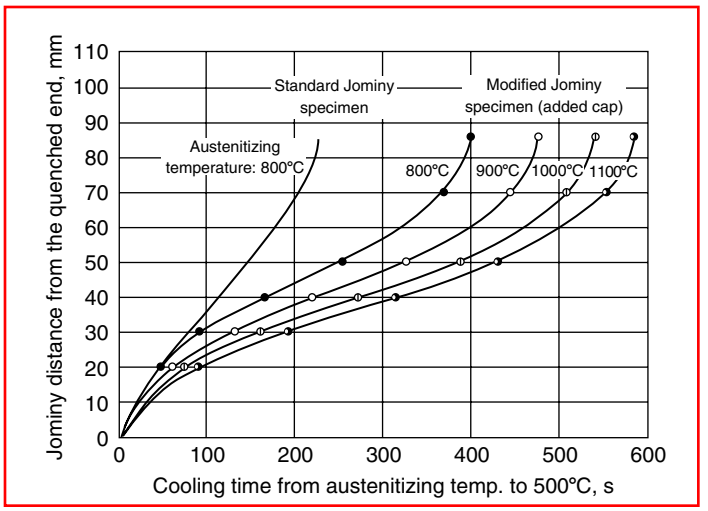

FIGURE 5.27 Cooling times between austenitizing temperature and 500°C for the standard Jominy specimen and for a specimen modified by adding a cap. (From A. Rose and L. Rademacher, *Stahl Eisen 76*(23):1570–1573, 1956 [in German].)

specimen have the same path and thus the same cooling rate. At distances beyond approximately 20 mm, the cooling time curve for the modified specimen exhibits increasingly slower cooling rates relative to the standard specimen. By adding the cap, the cooling time is nearly doubled, or the cooling rate is approximately half that exhibited by the unmodified test piece.

Figure 5.28 shows two Jominy hardenability curves, one obtained with the standard specimen and the other with the modified specimen, for the hot-working tool steel DIN 45CrMoV67 (0.43% C, 1.3% Cr, 0.7% Mo, 0.23% V). Up to 20 mm from the quenched end, both curves are nearly equivalent. At greater distances, the retarded cooling exhibited by the modified specimen causes the decrease in hardness to start at 23 mm from the quenched end, while the decrease in hardness for the standard specimen begins at approximately 45 mm.

The full advantage of the test with modified specimens for an air-hardening steel can be seen only if a quenched Jominy specimen is tempered at a temperature that will result in a secondary hardening effect. Figure 5.29 illustrates this for the tool steel DIN 45CrVMoW58

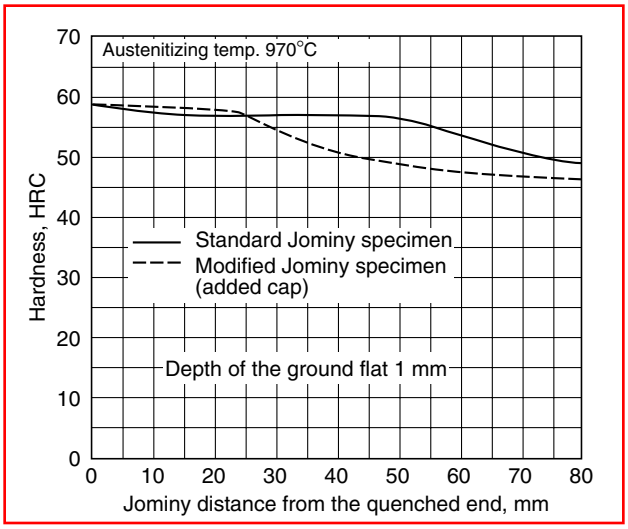

FIGURE 5.28 Jominy hardenability curves of grade DIN 45CrMoV67 steel for a standard specimen and for a specimen modified by adding a cap. (From A. Rose and L. Rademacher, *Stahl Eisen 76*(23):1570–1573, 1956 [in German].)

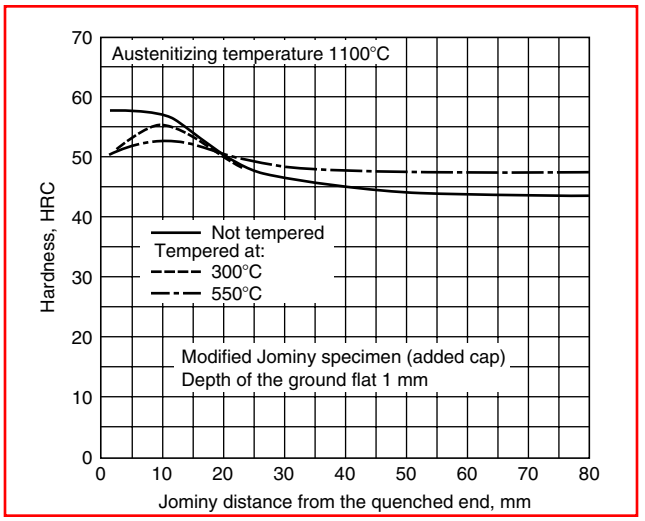

FIGURE 5.29 Jominy hardenability curves of grade DIN 45CrVMoW58 steel after quenching (solid curve) and after quenching and tempering (dashed curves) for a specimen modified by adding a cap. (From A. Rose and L. Rademacher, *Stahl Eisen 76*(23):1570–1573, 1956 [in German].)

(0.39% C, 1.5% Cr, 0.5% Mo, 0.7% V, 0.55% W). After tempering at 300°C, the hardness near the quenched end decreases. Within this region martensitic structure is predominant. At about 25 mm from the quenched end the hardness curve after tempering becomes equal to the hardness curve after quenching. After tempering to 550°C, however, the hardness is even more decreased up to a distance of 17 mm from the quenched end, and for greater distances a hardness increase up to about 4 HRC units can be seen as a result of the secondary hardening effect. This increase in hardness can be detected only when the modified Jominy test is conducted.

Another approach for measuring and recording the hardenability of air-hardening steels is the Timken Bearing Company Air hardenability Test [17]. This is a modification of the air-hardenability testing procedure devised by Post et al. [18].

Two partially threaded test bars of the dimensions shown in Figure 5.30 are screwed into a cylindrical bar 6 in. in diameter by 15 in. long, leaving 4 in. of each test bar exposed. The total setup is heated to the desired hardening temperature for 4 h. The actual time at temperature is 45 min for the embedded bar sections and 3 h for the sections extending outside the large cylinder. The test bar is then cooled in still air. The large cylindrical bar restricts the cooling of the exposed section of each test bar, producing numerous cooling conditions along the bar length.

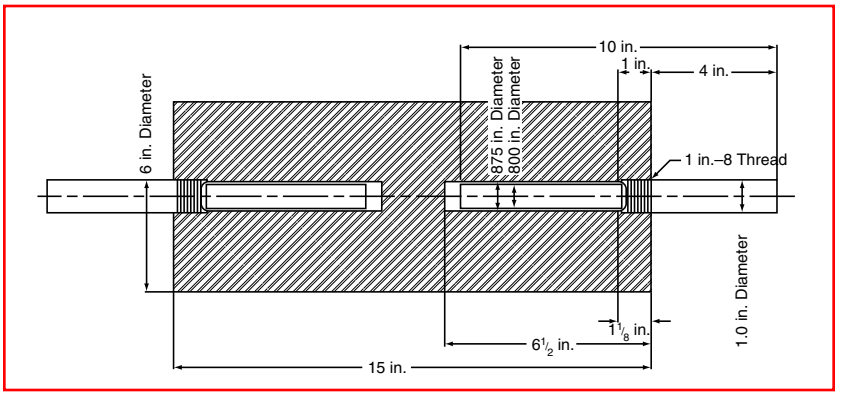

FIGURE 5.30 Timken Roller Bearing Company air hardenability test setup. Two test specimens with short threaded sections as illustrated are fixed in a large cylindrical bar. (From C.F. Jatczak, *Trans. ASM 58*:195–209, 1965.)

The various positions along the air-hardenability bar, from the exposed end to the opposite end (each test bar is 10 in. long), cover cooling rates ranging from 1.2 to 0.2°F/s. The hardenability curves for six high-temperature structural and hot-work die steels are shown in Figure 5.31. The actual cooling rates corresponding to each bar position are shown. Each bar position is equated in this figure to other section sizes and shapes producing equivalent cooling rates and hardnesses at the section centers when quenched in air. To prevent confusion, equivalent cooling rates produced in other media such as oil are not plotted in this chart. However, position 20 on the air-hardenability bar corresponds to the center of a 13-in. diameter bar cooled in still oil and even larger cylindrical bars cooled in water.

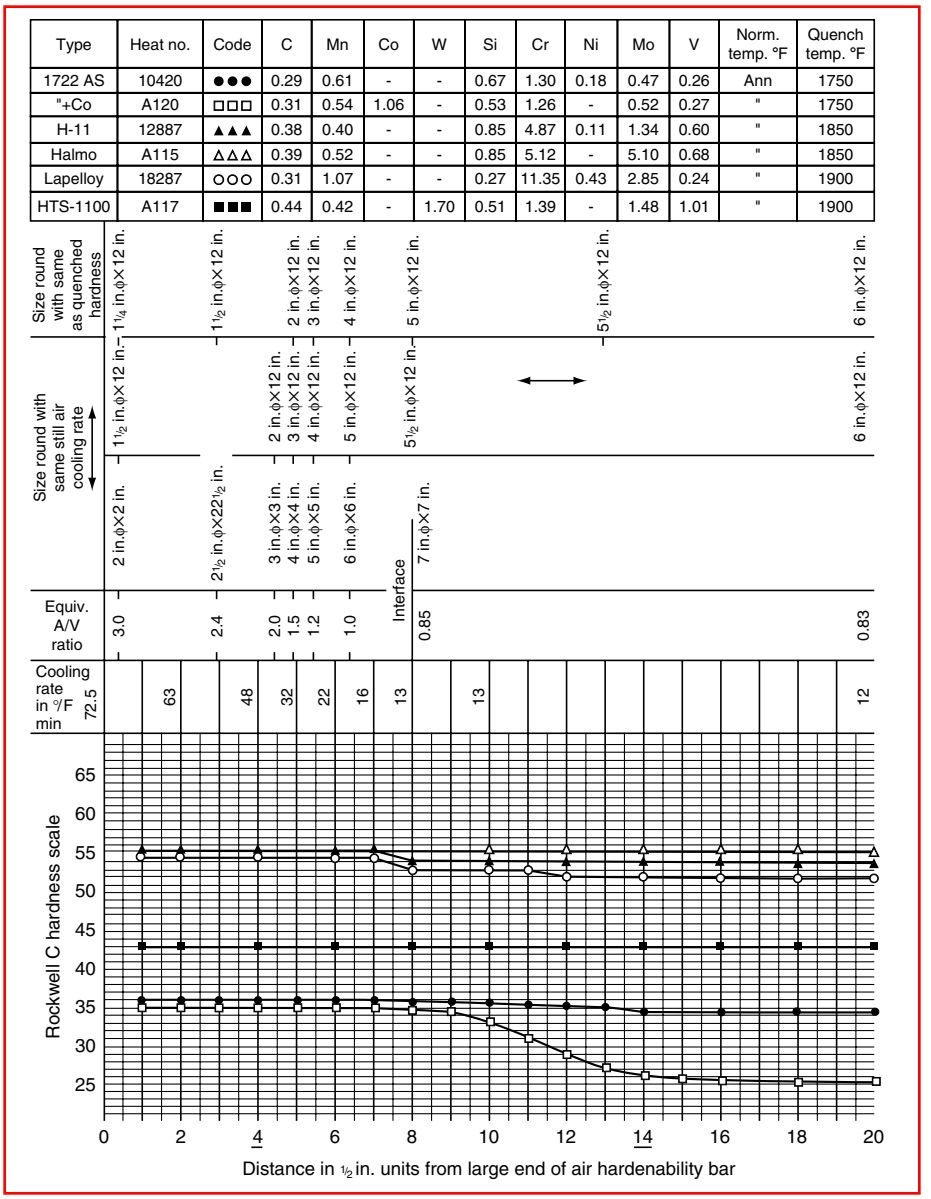

FIGURE 5.31 Chemistry and air-hardenability test results for various Cr–Mo–V steels. (From C.F. Jatczak, *Trans. ASM 58*:195–209, 1965.)

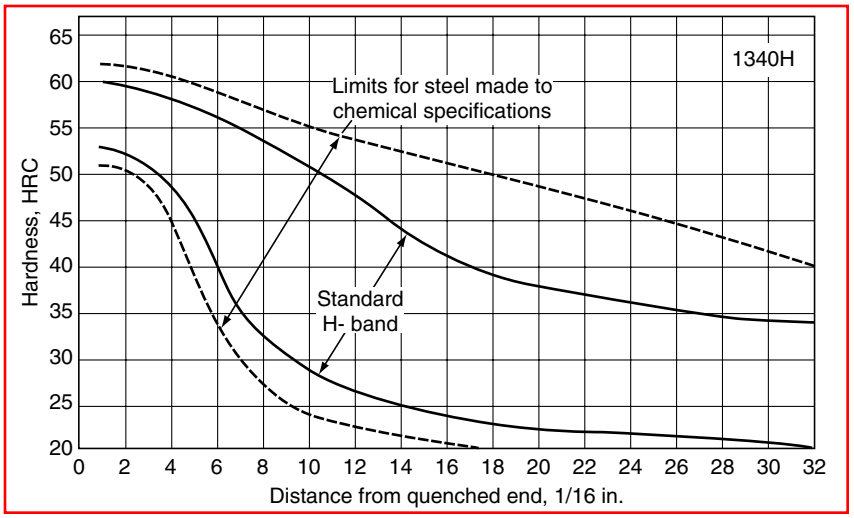

FIGURE 5.32 Hardenability band for SAE 1340H steel.

5.3.3 Hardenability Bands

Because of differences in chemical composition between different heats of the same grade of steel, so-called hardenability bands have been developed using the Jominy end-quench test. According to American designation, the hardenability band for each steel grade is marked by the letter H following the composition code. Figure 5.32 shows such a hardenability band for 1340H steel. The upper curve of the band represents the maximum hardness values, corresponding to the upper composition limits of the main elements, and the lower curve represents the minimum hardness values, corresponding to the lower limit of the composition ranges.

Hardenability bands are useful for both the steel supplier and the customer. Today the majority of steels are purchased according to hardenability bands. Suppliers guarantee that 93 or 95% of all mill heats made to chemical specification will also be within the hardenability band. The H bands were derived from end-quench data from a large number of heats of a specified composition range by excluding the upper and lower 3.5% of the data points. Steels may be purchased either to specified composition ranges or to hardenability limits defined by H bands. In the latter case, the suffix H is added to the conventional grade designation, for example 4140H, and a wider composition range is allowed. The difference in hardenability between an H steel and the same steel made to chemical specifications is illustrated in Figure 5.32. These differences are not the same for all grades.

High-volume production of hardened critical parts should have close tolerance of the depth of hardening. The customer may require, at additional cost, only those heats of a steel grade that satisfy, for example, the upper third of the hardenability band. As shown in Figure 5.33, the SAE recommended specifications are: means-different ways of specifications

- A minimum and a maximum hardness value at any desired Jominy distance. For example,

$$J_{30-56} = 10/16 \text{ in. (A–A, Figure 5.33)} \tag{5.3}$$

If thin sections are to be hardened and high hardness values are expected, the selected Jominy distance should be closer to the quenched end. For thick sections, greater Jominy distances are important.

- The minimum and maximum distance from the quenched end where a desired hardness value occurs. For example,

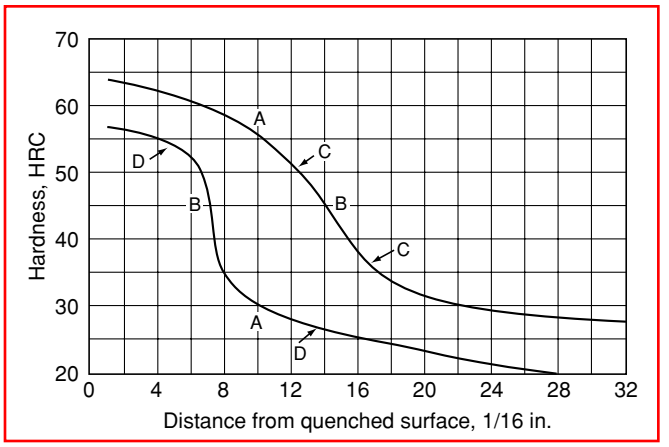

FIGURE 5.33 Different ways of specifying hardenability limits according to SAE.

$$J_{45} = 7/16 - 14/16 \text{ in. (B–B, Figure 5.33)} \tag{5.4}$$

- Two maximum hardness values at two desired Jominy distances. For example,

$$J_{52} = 12/16 \text{ in. (max)}; \quad J_{38} = 16/16 \text{ in. (max)} \tag{5.5}$$

- Two minimum hardness values at two desired Jominy distances. For example,

$$J_{52} = 6/16 \text{ in. (min)}; \quad J_{28} = 12/16 \text{ in. (min)} \tag{5.6}$$

Minimum hardenability is significant for thick sections to be hardened; maximum hardenability is usually related to thin sections because of their tendency to distort or crack, especially when made from higher carbon steels.

If a structure–volume fraction diagram (see Figure 5.34) for the same steel is available, the effective depth of hardening, which is defined by a given martensite content, may be determined from the maximum and minimum hardenability curves of the band. The structure—volume fraction diagram can also be used for the preparation of the transformation diagram when limits of the hardenability of a steel are determined. If the structure—volume fraction diagram is not available, the limit values of hardness or the effective depth of hardening can be estimated form the hardenability band using the diagram shown in Figure 5.35. Hardness depends on the carbon content of steel and the percentage of martensite after quenching. Figure 5.36. shows the hardenability band of the steel DIN 37MnSi5; the carbon content may vary from a minimum of 0.31% to a maximum of 0.39%.

The tolerance in the depth of hardening up to 50% martensite between a heat having maximum hardenability and a heat with minimum hardenability can be determined from the following examples. For $C_{min} = 0.31\%$ and 50% martensite, a hardness of 38 HRC can be determined from Figure 5.35. This hardness corresponds to the lower curve of the hardenability band and found at a distance of 4 mm from the quenched end. For $C_{max} = 0.39\%$ and 50% martensite, a hardness of 42 HRC can be determined from Figure 5.35. This hardness corresponds to the upper curve of the hardenability band and is found at 20 mm from the quenched end.

In this example, the Jominy hardenability (measured up to 50% martensite) for this steel varies between 4 and 20 mm. Using conversion charts, differences in the depth of hardening for any given diameter of round bars quenched under the same conditions can be determined.

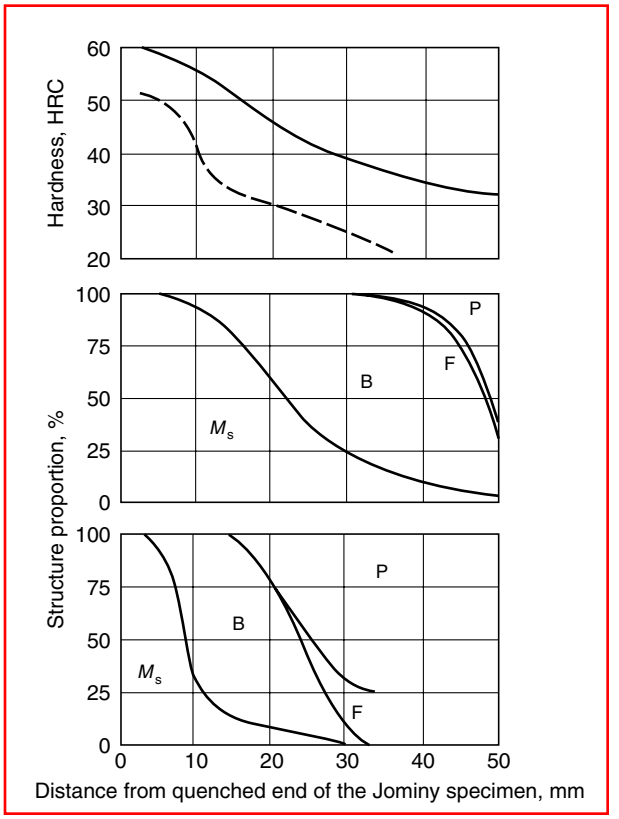

FIGURE 5.34 Hardenability band and structure–volume fraction diagram of SAE 5140 steel. F = ferrite, P = pearlite, B = bainite, M_s = martensite. (From B. Liščić, H.M. Tensi, and W. Luty, *Theory and Technology of Quenching*, Springer-Verlag, Berlin, 1992.)

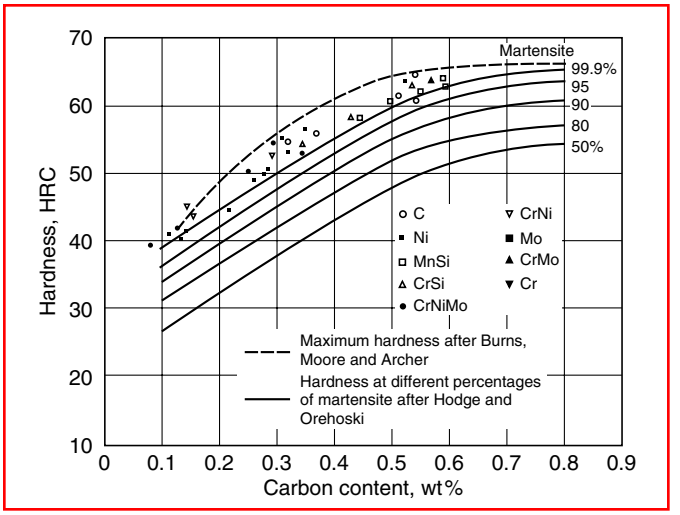

FIGURE 5.35 Achievable hardness depending on the carbon content and percentage of martensite in the structure. (From B. Liščić, H.M. Tensi, and W. Luty, *Theory and Technology of Quenching*, Springer-Verlag, Berlin, 1992.)

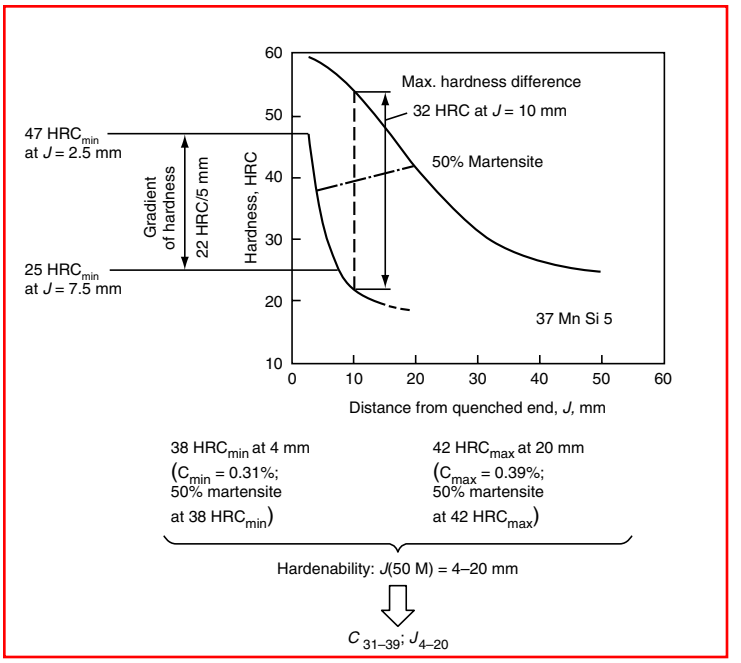

FIGURE 5.36 Hardenability band of DIN 37MnSi5 steel and the way technologically important information can be obtained. (From B. Liščić, H.M. Tensi, and W. Luty, *Theory and Technology of Quenching*, Springer-Verlag, Berlin, 1992.)

Effective depth of hardening is not the only information that can be derived from the hardenability band. Characteristic features of every hardenability band provide information on the material-dependent spread of hardenability designated the maximum hardness difference as shown in Figure 5.36. The hardness difference at the same distance from the quenched end, i.e., at the same cooling rate, can be taken as a measure of material-dependent deviations. Another important technological point that can be derived from the hardenability band is the hardness gradient. In Figure 5.36, this is illustrated by the minimum hardenability curve for the steel in question where there is a high gradient of hardness (22 HRC for only 5 mm difference in the Jominy distance). High hardness gradients indicate high sensitivity to cooling rate variation.

5.4 CALCULATION OF JOMINY CURVES FROM CHEMICAL COMPOSITION

The first calculations of Jominy curves based on the chemical composition of steels were performed in the United States in 1943 [21,22]. Later, Just [23], using regression analysis of fictitious Jominy curves from SAE hardenability bands and Jominy curves of actual heats from the USS *Atlas* (USA) and *MPI-Atlas* (Germany), derived expressions for calculating the hardness at different distances (E) from the quenched end of the Jominy specimen. It was found that the influence of carbon depends on other alloying elements and also on the cooling rate, i.e., with distance from the quenched end (Jominy distance).

Carbon starts at a Jominy distance of 0 with a multiplying factor of 50, while other alloying elements have the factor 0 at this distance. This implies that the hardness at a Jominy distance of 0 is governed solely by the carbon content. The influence of other alloying elements generally increases from 0 to values of their respective factors up to a Jominy distance of about 10 mm. Beyond this distance, their influence is essentially constant. Near the quenched end the

influence of carbon prevails, while the influence of other alloying elements remains essentially constant beyond a Jominy distance of about 10 mm. This led Just to propose a single expression for the whole test specimen, except for distances shorter than 6 mm:

$$J_{6-80} = 95\sqrt{\mathrm{C}} - 0.00276E^2\sqrt{\mathrm{C}} + 20\mathrm{Cr} + 38\mathrm{Mo} + 14\mathrm{Mn} + 5.5\mathrm{Ni} + 6.1\mathrm{Si} + 39\mathrm{V} + 96\mathrm{P} - 0.81K - 12.28\sqrt{\mathrm{E}} + 0.898E - 13\mathrm{HRC} \tag{5.7}$$

where J is the Jominy hardness (HRC), E the Jominy distance (mm), K the ASTM grain size, and the element symbols represent weight percentage of each.

In Equation 5.7, all alloying elements are adjusted to weight percent, and it is valid within the following limits of alloying elements: $\mathrm{C} < 0.6\%$; $\mathrm{Cr} < 2\%$; $\mathrm{Mn} < 2\%$; $\mathrm{Ni} < 4\%$; $\mathrm{Mo} < 0.5\%$; $\mathrm{V} < 0.2\%$. Calculation of hardness at the quenched end (Jominy distance 0), using the equation for the maximum attainable hardness with 100% martensite, is

$$H_{\max} = 60\sqrt{\mathrm{C}} + 20\,\mathrm{HRC}, \quad \mathrm{C} < 0.6\% \tag{5.8}$$

Although Equation 5.7 was derived for use up to a distance of 80 mm from the quenched end of the Jominy specimen, other authors argue that beyond a Jominy distance of 65 mm the continuous decrease in cooling rate at the Jominy test cannot be ensured even for low-alloy steels because of the cooling effect of surrounding air. Therefore, newer calculation methods rarely go beyond a Jominy distance of 40 mm.

Just [23] found that a better fit for existing mutual correlations can be achieved by formulas that are valid for groups of similar steels. He also found that multiplying hardenability factors for Cr, Mn, and Ni have lower values for case-hardening steels than for structural steels for hardening and tempering. Therefore, separate formulas for case-hardening steels were derived:

$$J_{6-40}(\text{case-hardening steels}) = 74\sqrt{\mathrm{C}} + 14\mathrm{Cr} + 5.4\mathrm{Ni} + 29\mathrm{Mo} + 16\mathrm{Mn} - 16.8\sqrt{E} + 1.386E + 7\mathrm{HRC} \tag{5.9}$$

and for steels for hardening and tempering,

$$J_{6-40}(\text{steels for hardening and tempering}) = 102\sqrt{\mathrm{C}} + 22\mathrm{Cr} + 21\mathrm{Mn} + 7\mathrm{Ni} + 33\mathrm{Mo} - 15.47\sqrt{E} + 1.102E - 16\mathrm{HRC} \tag{5.10}$$

In Europe, five German steel producers in a VDEh working group jointly developed formulas that adequately define the hardenability from different production heats [24]. The goal was to replace various existing formulas that were used individually.

Data for some case-hardening steels and some low-alloy structural steels for hardening and tempering have been compiled, and guidelines for the calculation and evaluation of formulas for additional families of steel have been established. This work accounts for influential factors from the steel melting process and for possible deviations in the Jominy test itself. Multiple linear regression methods using measured hardness values for Jominy tests and actual chemical compositions were also included in the analyses. The number of Jominy curves of a family of steel grades necessary to establish usable formulas should be at least equal to the square of the total number of chemical elements used for the calculation. Approximately 200 curves were suggested. To obtain usable equations, all Jominy curves for steel grades that had similar transformation characteristics (i.e., similar continuous cooling transformation [CCT] diagram)

TABLE 5.2
Regression Coefficients for the Calculation of Jominy Hardness Values for Structural Steels for Hardening and Tempering Alloyed with about 1% Cr

Jominy Distance (mm)	Regression Coefficients										
	Constant	C	Si	Mn	S	Cr	Mo	Ni	Al	Cu	N
1.5	29.96	57.91	2.29	3.77						−2.65	83.33
3	26.75	58.66	3.76	2.16		2.86				−2.59	59.87
5	15.24	64.04	10.86		−41.85	12.29					−115.50
7	−7.82	81.10	19.27	4.87	−73.79	21.02				4.56	−176.82
9	−27.29	94.70	22.01	10.24	−37.76	24.82			38.31	8.58	−144.07
11	−39.34	100.78	21.25	14.70		25.39		6.66	52.63	7.97	
13	−42.61	95.85	20.54	16.06		26.46	30.41		54.91	9.0	
15	−42.49	88.69	20.82	17.75		25.33	38.97		47.16	8.89	
20	−41.72	78.34	17.57	20.18		23.85	26.95	7.51		9.96	
25	−41.94	72.29	18.62	20.73	−65.81	24.08	35.99	7.69		9.64	
30	−44.63	72.74	19.12	21.42	−81.41	24.39	27.57	10.75		9.71	

Source: R. Caspari, H. Gulden, K. Krieger, D. Lepper, A. Lübben, H. Rohloff, P. Schüler, V. Schüler, and H.J. Wieland, *Härterei Tech. Mitt. 47*(3):183–188, 1992.

when hardened were used. Therefore, precise equations for the calculation of Jominy hardness values were derived only for steel grades of similar composition [24].

The regression coefficients for a set of equations to calculate the hardness values at different Jominy distances from 1.5 to 30 mm from the quenched end are provided in Table 5.2. The chemistry of the steels used for this study is summarized in Table 5.3. The regression coefficients in Table 5.2 do not have the same meaning as the hardenability factors in Equation 5.7, Equation 5.9, and Equation 5.10; therefore, there is no restriction on the calculation of Jominy hardness values at less than 6 mm from the quenched end. Because the regression coefficients used in this method of calculation are not hardenability factors, care should be taken when deriving structural properties from them.

The precision of the calculation was determined by comparing the measured and calculated hardness values and establishing the residual scatter, which is shown in Figure 5.37. The

TABLE 5.3
Limiting Values of Chemical Composition of Structural Steels for Hardening and Tempering Alloyed with about 1% Cr[a]

	Content (%)										
	C	Si	Mn	P	S	Cr	Mo	Ni	Al	Cu	N
Min.	0.22	0.02	0.59	0.005	0.003	0.80	0.01	0.01	0.012	0.02	0.006
Max.	0.47	0.36	0.97	0.037	0.038	1.24	0.09	0.28	0.062	0.32	0.015
Mean	0.35	0.22	0.76	0.013	0.023	1.04	0.04	0.13	0.031	0.16	0.009
s	0.06	0.07	0.07	0.005	0.008	0.10	0.02	0.05	0.007	0.05	0.002

[a]Used in calculations with regression coefficients of Table 5.2.

Source: R. Caspari, H. Gulden, K. Krieger, D. Lepper, A. Lübben, H. Rohloff, P. Schüler, V. Schüler, and H.J. Wieland, *Härterei Tech. Mitt. 47*(3):183–188, 1992.

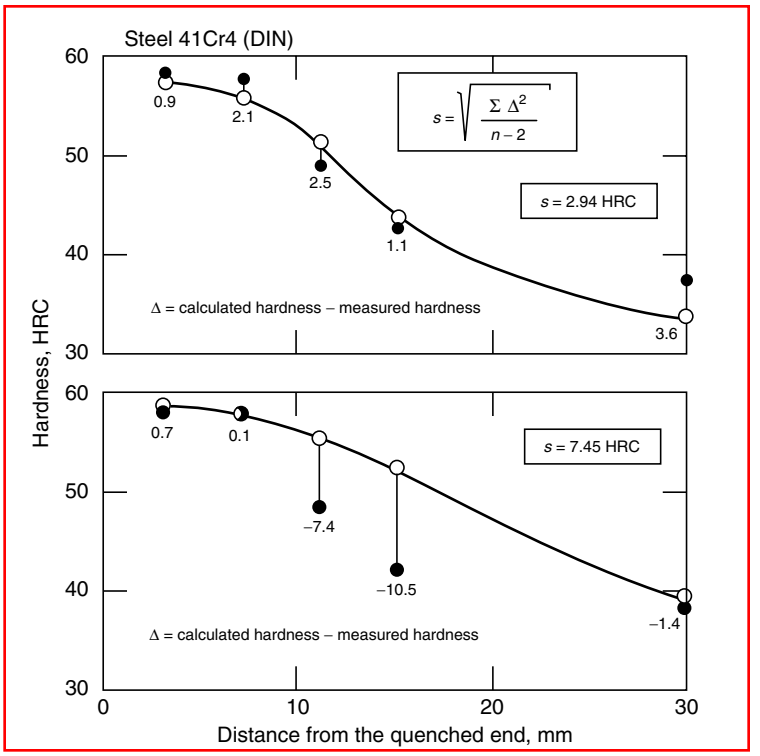

FIGURE 5.37 Comparison between measured (○) and calculated (●) hardness values for a melt with adequate consistency (top) and with inadequate consistency (bottom). (From R. Caspari, H. Gulden, K. Krieger, D. Lepper, A. Lübben, H. Rohloff, P. Schüler, V. Schüler, and H.J. Wieland, *Härterei Tech. Mitt. 47*(3):183–188, 1992.)

upper curve for a heat of DIN 41Cr4 steel, having a residual scatter of $s = 2.94$ HRC, shows an adequate consistency, while the lower curve for another heat of the same steel, with a residual scatter of $s = 7.45$ HRC, shows inadequate consistency. Such checks were repeated for every Jominy distance and for every heat of the respective steel family. During this process it was found that the residual scatter depends on the distance from the quenched end and that calculated Jominy curves do not show the same precision (compared to measured curves) at all Jominy distances. For different steel grades with different transformation characteristics, the residual scatter varies with Jominy distance, as shown in Figure 5.38. In spite of the residual scatter of the calculated results, it was concluded "that properly calibrated predictors offer a strong advantage over testing in routine applications" [25].

When judging the precision of a calculation of Jominy hardness values, hardenability predictors are expected to accurately predict (± 1 HRC) the observed hardness values from the chemical composition. However, experimental reproducibility of a hardness value at a fixed Jominy distance near the inflection point of the curve can be 8–12 HRC (see Figure 5.23 for J_{10}mm). Therefore it was concluded "that a properly calibrated hardenability formula will always anticipate the results of a purchaser's check test at every hardness point better than an actual Jominy test" [25].

5.4.1 Hyperbolic Secant Method for Predicting Jominy Hardenability

Another method for predicting Jominy end-quench hardenability from composition is based on the four-parameter hyperbolic secant curve-fitting technique [26]. In this method, it is

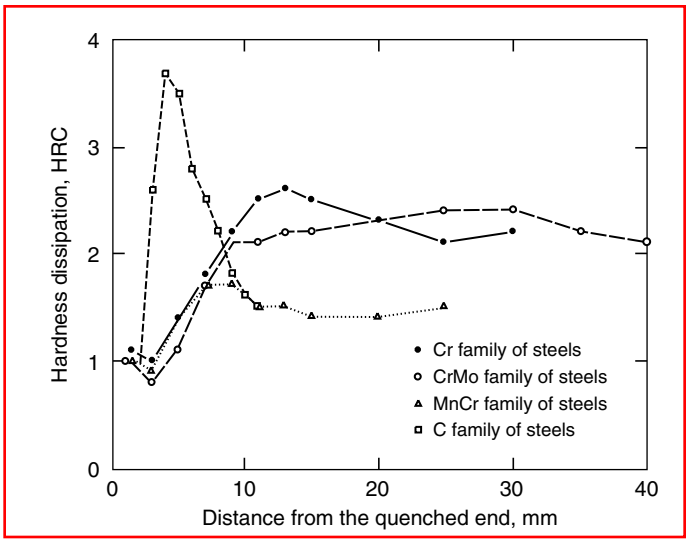

FIGURE 5.38 Residual scatter between measured and calculated hardness values versus distance to the quenched end, for different steel grade families. (From R. Caspari, H. Gulden, K. Krieger, D. Lepper, A. Lübben, H. Rohloff, P. Schüler, V. Schüler, and H.J. Wieland, *Härterei Tech. Mitt. 47*(3):183–188, 1992.)

assumed that the Jominy curve shape can be characterized by a four-parameter hyperbolic secant (sech) function (SECH).

The SECH curve-fitting technique utilizes the equation

$$\mathrm{DH}_x = A + B\{\mathrm{sech}[C(x-1)^D] - 1\} \tag{5.11}$$

or alternatively

$$\mathrm{DH}_x = (A - B) + B\{\mathrm{sech}[C(x-1)^D]\} \tag{5.12}$$

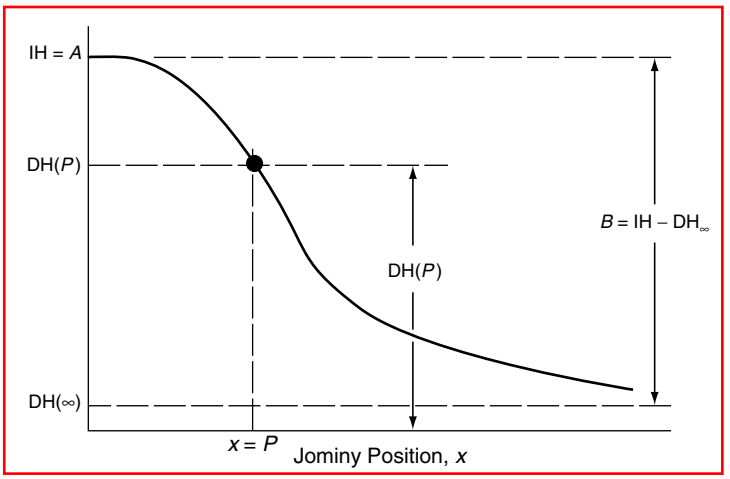

FIGURE 5.39 Schematic showing the relationships between the hyperbolic secant coefficients A and B and Jominy curve characteristics. (From W.E. Jominy and A.L. Boegehold, *Trans. ASM 26*:574, 1938.)

where the hyperbolic secant function for any y value is

$$\operatorname{sech}_y = \frac{2}{e^y + e^{-y}} \tag{5.13}$$

where x is the Jominy distance from the quenched end, in 1/16 in., DH_x the hardness at the Jominy distance x, and A, B, C, D are the four parameters, which can be set such that DH_x conforms closely to an experimental end-quench hardenability curve. The relationship between parameters A and B and a hypothetical Jominy curve is illustrated in Figure 5.39.

The parameter A denotes the upper asymptotic or initial hardness (IH) at the quenched end. The parameter B corresponds to the difference between the upper and lower asymptotic hardness values, respectively (DH_∞). This means that for a constant value of A, increasing the value of B will decrease the lower asymptotic hardness, as shown in Figure 5.40a.

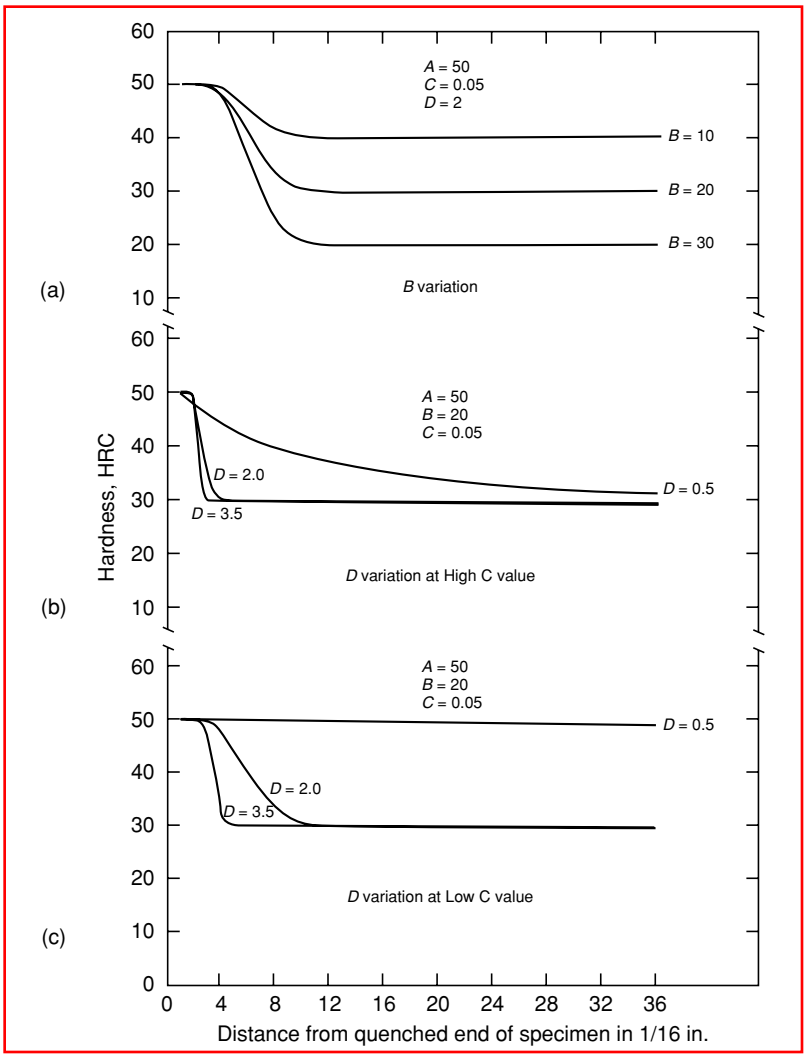

FIGURE 5.40 Effect of SECH parameter variation on Jominy curve shape. (From W.E. Jominy and A.L. Boegehold, *Trans. ASM 26*:574, 1938.)

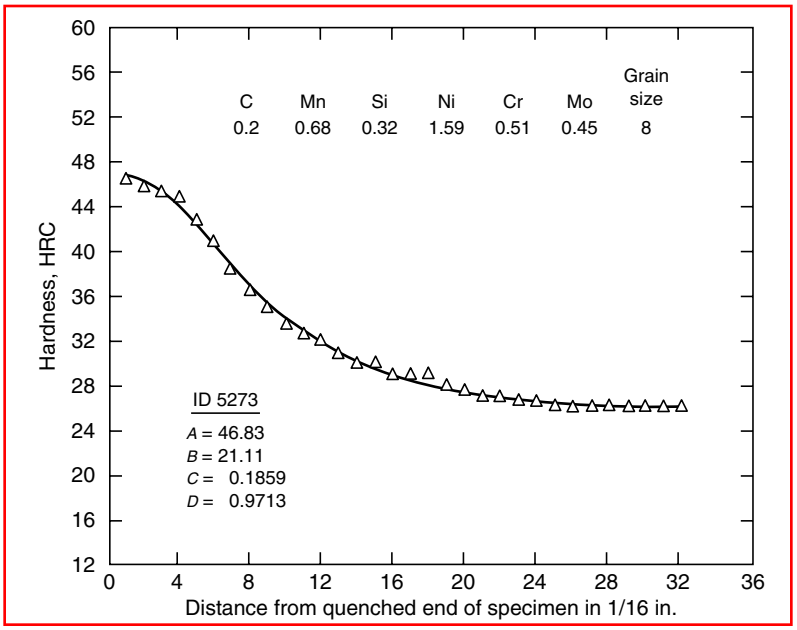

FIGURE 5.41 Experimental end-quench hardenability data and best-fit hyperbolic secant function. (From W.E. Jominy and A.L. Boegehold, *Trans. ASM 26*:574, 1938.)

The parameters C and D control the position of, and the slope at, the inflection point in the calculated Jominy curve. If the A, B, and C parameters are constant, lowering the value of parameter D will cause the inflection point to occur at greater Jominy distances, as shown in Figure 5.40b and Figure 5.40c. A similar result will be obtained if parameters A, B, and D are kept constant, and parameter C is shown by comparing Figure 5.40b and Figure 5.40c. In fact, it may be appropriate to set C and D to a constant value characteristic of a grade of steels and describe the effects of compositional variations within the grade by establishing correlations with the other three parameters.

It should be noted that some Jominy curves cannot be well described by a general expression such as Equation 5.11 or Equation 5.12. For example, if a significant amount of carbide precipitation were to occur in the bainite or pearlite cooling regime, a ''hump'' in the Jominy curve might be observed that could not be calculated.

To calculate the values of the four SECH parameters for each experimentally obtained Jominy curve, the minimum requirement is a data set from which the predictive equations will be developed. This data set should contain compositions of each steel grade (or heat), with associated values of Jominy hardness at different end-quench distances, as determined by the experiment. Other metallurgical or processing variables such as grain size or austenitizing temperature can also be included. The data set must be carefully selected; the best predictions will be obtained when the regression data set is both very large and homogeneously distributed over the range of factors for which hardenability predictions will be desired.

A linear–nonlinear regression analysis program using least squares was used to calculate separate values of the four parameters for each experimental Jominy curve in the regression data set by minimizing the differences between the empirical and analytical hardness curves, i.e., obtaining the best fit.

Figure 5.41 provides experimental end-quench hardenability data and best fit hyperbolic secant function for one steel in a data set that contained 40 carburizing steel compositions. Excellent fits were obtained for all 40 cases in the regression data set. Once the four

TABLE 5.4
Multiple Regression Coefficients for Backward-Elimination Regression Analysis

Dependent Variable (SECH Parameter)

A		B		C		D	
Ind. Var.	**Coeff.**	**Ind. Var.**	**Coeff.**	**Ind. Var.**	**Coeff.**	**Ind. Var.**	**Coeff.**
C*C*C	481.27031	Cr*Mo	−28.17764	Cr*Mo	−0.79950	Cr*Mo	1.19695
(Constant)	41.44362	Mn*Si	−61.55499	Mn*Si	−1.04208	Mn*Si	1.97624
		GS	−1.71674	Ni*Ni*Ni	−0.04871	Ni*Ni*Ni	0.09267
		Ni*Ni*Ni	−1.35352	C*C*C*	−14.85249	C*C*C	33.57479
		(Constant)	60.23736	33.57479	0.92535	(Constant)	−0.26580

parameters A, B, C, and D have been obtained for each heat as described above, four separate equations with these parameters as dependent variables are constructed using multiple regression analysis by means of a statistical analysis computer package.

Table 5.4 provides multiple regression coefficients obtained with the backward elimination regression analysis of the above-mentioned 40 cases. In this elimination process, 31 variables were arbitrarily defined for possible selection as independent variables in the multiple regression analysis. The list of these variables consisted of all seven single-element and grain size terms, the seven squares and seven cubes of the single element and grain size terms, and all 10 possible two-way element interaction terms that did not include carbon or grain size.

Based on the multiple regression coefficients from Table 5.4, the following four equations for SECH parameters were developed for the regression data set of 40 carburizing steels:

$$A = 481\mathrm{C}^3 + 41.4 \tag{5.14}$$

$$B = -28.7\mathrm{CrMo} - 61.6\mathrm{MnSi} - 1.72\mathrm{GS} - 1.35\mathrm{Ni}^3 + 60.2 \tag{5.15}$$

$$C = -0.8\mathrm{CrMo} - 1.04\mathrm{MnSi} - 0.05\mathrm{Ni}^3 - 14.9\mathrm{C}^3 + 0.93 \tag{5.16}$$

$$D = 1.2\mathrm{CrMo} + 1.98\mathrm{MnSi} + 0.09\mathrm{Ni}^3 + 33.6\mathrm{C}^3 - 0.27 \tag{5.17}$$

where an element name denotes percentage of that element in the steel and GS denotes grain size. Equation 5.14 through Equation 5.17 are valid for steel compositions in the range of 0.15–0.25% C, 0.45–1.1% Mn, 0.22–0.35% Si, 0–1.86% Ni, 0–1.03% Cr, and 0–0.76% Mo, with ASTM grain sizes (GS) between 5 and 9.

After the four parameters are calculated, they are substituted into Equation 5.11 or Equation 5.12 to calculate distance hardness (DH) at each Jominy distance x of interest. To validate this method, the Jominy curves were predicted for an independently determined data set of 24 heats, and this prediction was compared with those obtained by other two methods (AMAX [27] and Just [28] prediction methods). The SECH predictions were not as accurate as distance hardness predictions based on the two methods developed earlier because of the limited size and sparsely populated sections (not homogeneously distributed) of the initial data set.

5.4.2 Computer Calculation of Jominy Hardenability

The application of computer technology has greatly enhanced the precision of these calculations. Commercial software is available for the calculation of Jominy hardness. For example,

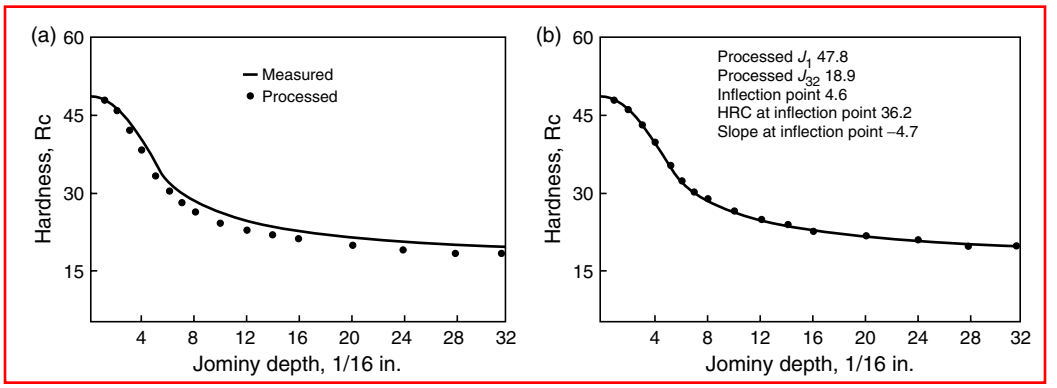

FIGURE 5.42 Outputs from Minitech Predictor data processing program for best fit to measured Jominy data. (a) Initial trial; (b) final trial. (From J.S. Kirkaldy and S.E. Feldman, *J. Heat. Treat.* 7:57–64, 1989.)

the Minitech Predictor [25] is based on the initial generation of an inflection point on the Jominy curve. Figure 5.42 shows a typical output of the Minitech Predictor operating in the data processing mode. Input values are Jominy hardness values, chemical composition, and estimated grain size.

The Minitech program generates a predicted Jominy curve (J_n) and a predicted inflection point distance from quenched end x' and displays a comparison of the predicted and experimentally obtained curves as shown in Figure 5.42a. A weighting pattern J_n is accessed that specifies a weight of 1.5 for all distances from $n = 1$ to $n = 2x'$ and a weight of 0.75 for $n > 2x'$ to $n = 32$ mm (or any limit of the data). Using an effective carbon content and grain size as adjustable parameters, the theoretical curve is then iterated about J'_n and x' to minimize the weighted root mean square deviation of the calculated curve from the experimental curve. The final best-fit calculated curve is plotted along with the main processed data as shown in Figure 5.42b.

Jominy distance (mm)	Hardness (HV)
1.5	460
5.0	370
9.0	270

HV is the Vickers pyramid hardness.

Calculated Jominy hardness curves are used to replace Jominy testing by equivalent predictions for those steel grades (e.g., very shallow-hardening steels) that it is difficult or impossible to test. Although the accurate prediction of hardenability is important, it is more important for the steel manufacturer to be able to refine the calculations during the steelmaking process. For example, the steel user indicates the desired Jominy curve by specifying three points within H band for SAE 862OH as shown in Figure 5.43 [29].

Using these data, the steel mill will first compare the customer's specification against two main criteria:

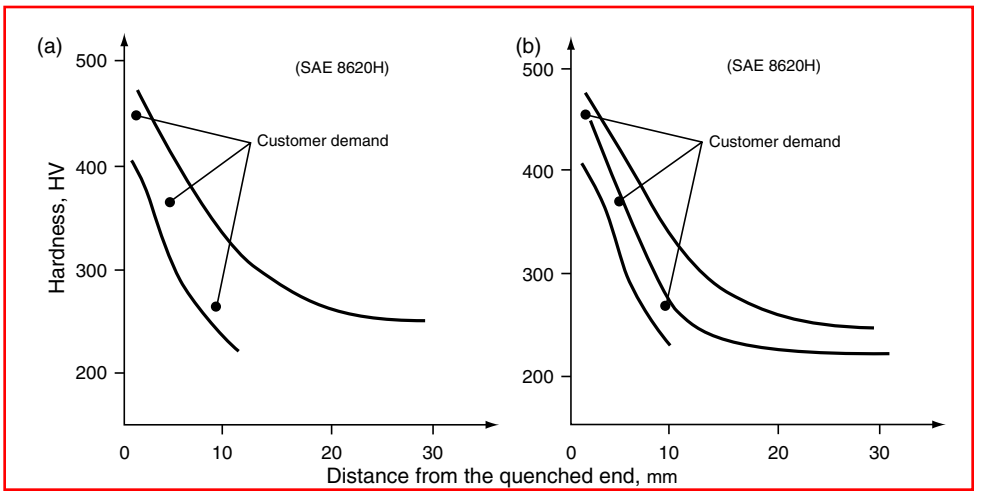

FIGURE 5.43 (a) Customer's specification of hardenability within an H band for SAE 8620H. (b) Jominy curve for finished heat. (From T. Lund, *Carburizing Steels: Hardenability Prediction and Hardenability Control in Steel-Making*, SKF Steel, Technical Report 3, 1984.)

1. That the hardenability desired is within limits for the steel grade in question
2. That the specified points fall on a Jominy curve permissible within the analysis range for SAE 862OH, i.e., the specified points must provide a physically possible Jominy curve

When the actual heat of steel is ready for production, the computer program will automatically select the values for alloy additions and initiate the required control procedures. The samples taken during melting and refining are used to compute the necessary chemical adjustments. The computer program is linked directly to the ferroalloy selection and dispensing system. By successive adjustments, the heat is refined to a chemical composition that meets the required hardenability specification within the chemical composition limits for the steel grade in question.

The use of calculated Jominy curves for steel manufacturing process control is illustrated in the following example. Quality control analysis found that the steel heat should have a manganese value of 0.85%. During subsequent alloying, the analysis found 0.88% Mn. This overrun in Mn was automatically compensated for by the computer program, which adjusted hardenability by decreasing the final chromium content slightly. The resulting heat had the measured Jominy curve shown in Figure 5.43b. In this case, the produced steel does not deviate from the required specification by more than ± 10 HV at any Jominy distance below 19 mm.

5.5 APPLICATION OF HARDENABILITY CONCEPT FOR PREDICTION OF HARDNESS AFTER QUENCHING

Jominy curves are the preferred methods for the characterization of steel. They are used to compare the hardenability of different heats of the same steel grade as a quality control method in steel production and to compare the hardenability of different steel grades when selecting steel for a certain application. In the latter case, Jominy curves are used to predict the depth of hardening, i.e., to predict the expected hardness distribution obtained after hardening parts of different cross-sectional dimensions after quenching under various conditions. Such predictions are generally based on the assumption that rates of cooling prevailing

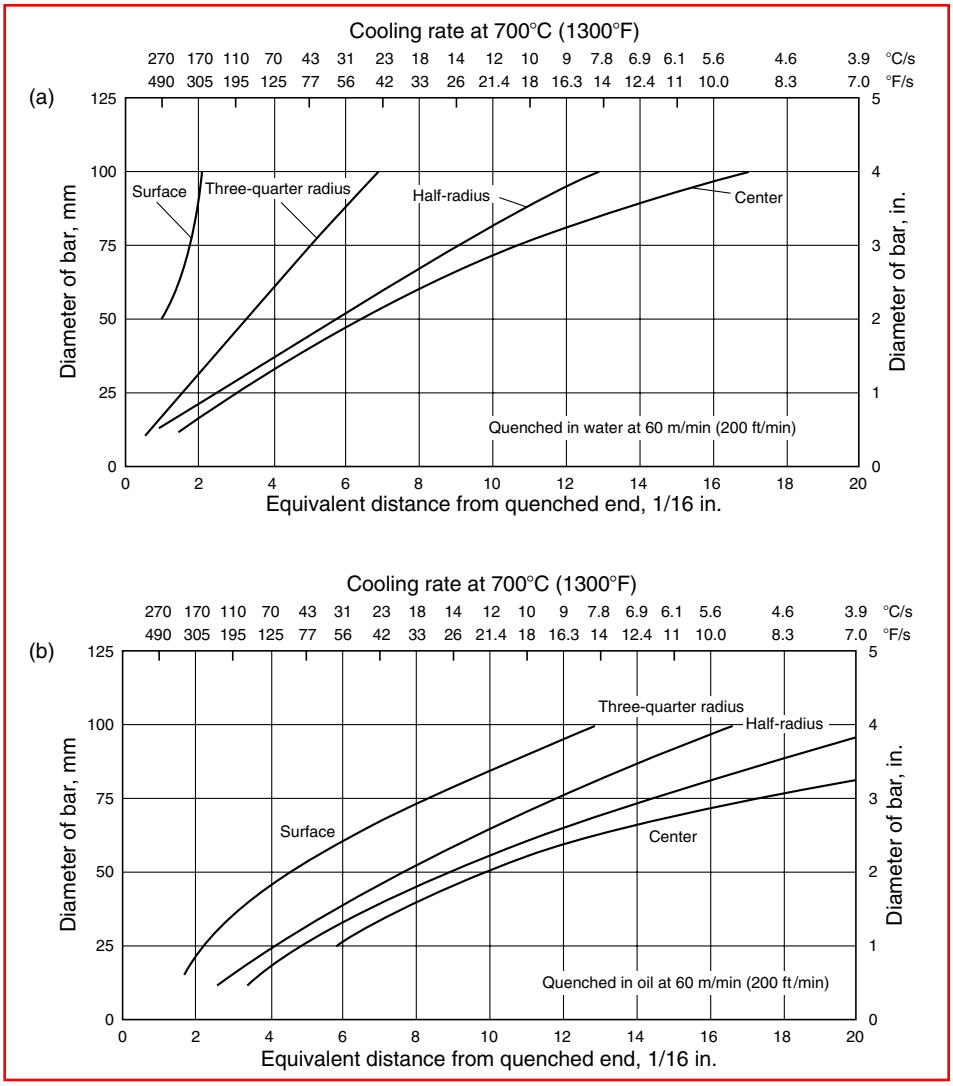

FIGURE 5.44 Correlation of equivalent cooling rates at different distances from the quenched end of the Jominy specimen and at different locations on the cross section of round bars of different diameters, quenched in (a) water agitated at 1 m/s and in (b) oil agitated at 1 m/s. (From *Metals Handbook*, 9th ed., Vol. 1, ASM International, Metals Park, OH, 1978, p. 492.)

at different distance from the quenched end of the Jominy specimen may be compared with the cooling rates prevailing at different locations on the cross sections of bars of different diameters. If the cooling rates are equal, it is assumed that equivalent microstructure and hardness can be expected after quenching.

The diagrams shown in Figure 5.44 have been developed for this purpose. These diagrams provide a correlation of equivalent cooling rates at different distances from the quenched end of the Jominy specimen and at different locations (center, half-radius, three-quarter radius, surface) on the cross section of round bars of different diameters. They are valid for the specified quenching conditions only. Figure 5.44a is valid only for quenching in water at an agitation rate of 1 m/s, and the diagram in Figure 5.44b is valid only for quenching in oil at an agitation rate of 1 m/s.

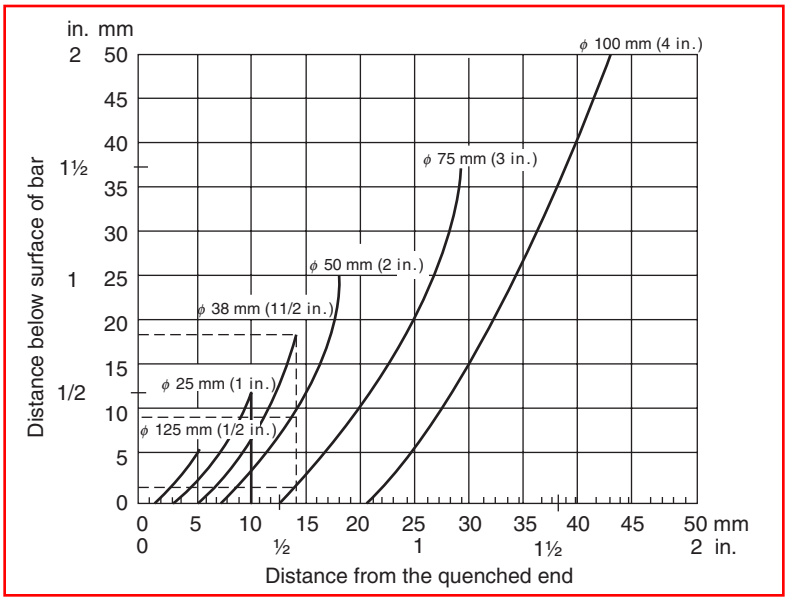

FIGURE 5.45 Relationship between cooling rates at different Jominy distances and cooling rates at different points below the surface of round bars of different diameters quenched in moderately agitated oil. (From K.E. Thelning, *Steel and Its Heat Treatment*, 2nd ed., Butterworths, London, 1984, p. 145.)

Another diagram showing the relation between cooling rates at different Jominy distances and cooling rates at different distances below the surface of round bars of different diameters, taken from the ASTM standard, is shown in Figure 5.45. From this diagram, the same cooling rate found at a Jominy distance of 14 mm prevails at a point 2 mm below the surface of a 75-mm diameter bar, at 10 mm below the surface of 50-mm diameter bar, and at the center of a 38-mm diameter bar when all the bars are quenched in moderately agitated oil. Using this diagram, it is possible to construct the hardness distribution curve across the section after hardening. This type of diagram is also valid for only the specified quenching conditions.

To correlate the hardness at different Jominy distances and the hardness at the center of round bars of different diameters that are quenched in various quenchants under different quenching conditions, the critical diameter (D_{crit}), the ideal critical diameter (D_I), and Grossmann's quenching intensity factor H must be used. The theoretical background of this approach is provided by Grossmann et al. [5], who calculated the half-temperature time (the time necessary to cool to the temperature halfway between the austenitizing temperature and the temperature of the quenchant). To correlate D_{crit} and H, Asimow et al. [31], in collaboration with Jominy, defined the half-temperature time characteristics for the Jominy specimen also. These half-temperature times were used to establish the relationship between the Jominy distance and ideal critical diameter D_I, as shown in Figure 5.46. If the microstructure of this steel is determined as a function of Jominy distance, the ideal critical diameter can be determined directly from the curve at that distance where 50% martensite is observed as shown in Figure 5.46. The same principle holds for D_{crit} when different quenching conditions characterized by the quenching intensity factor H are involved. Figure 5.47 shows the relationship between the diameter of round bars (D_{crit} and D_I) and the distance from the quenched end of the Jominy specimen for the same hardness (of 50% martensite) at the center of the cross section after quenching under various conditions [31].

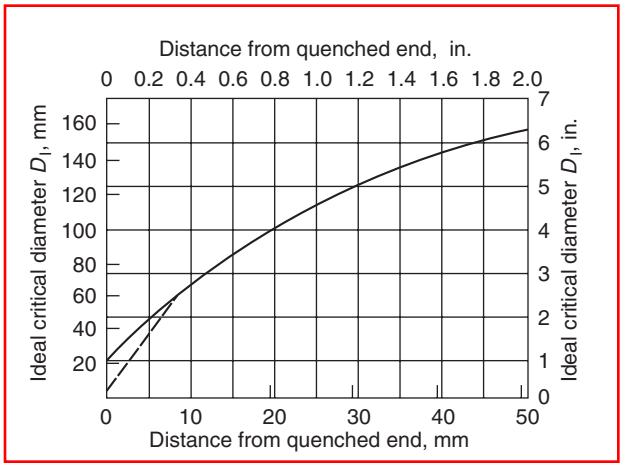

FIGURE 5.46 Relationship between the distance from the quenched end of the Jominy specimen and the ideal critical diameter. (From M. Asimov, W.F. Craig, and M.A. Grossmann, *SAE Trans.* *49*(1):283–292, 1941.)

The application of the Figure 5.47 diagram can be explained for the two steel grades shown in Figure 5.48. The hardness at 50% martensite for the unalloyed steel grade Ck45 (0.45% C) is 45 HRC, while for the low-alloy grade 50CrMo4 steel (0.5% C) the hardness is 48 HRC. The lower part of the diagram depicts two H curves taken from the diagram in Figure 5.47. One is for vigorously agitated brine ($H = 5.0$), and the other for moderately agitated oil ($H = 0.4$). From both diagrams in Figure 5.48, it is seen that quenching the grade 50CrMo4 steel in vigorously agitated brine provides a hardness of 48 HRC in the center of the cross section of a round bar of 110-mm diameter. Quenching the same steel in moderately agitated oil provides this hardness at the core of round bars of only 70-mm diameter. The unalloyed grade Ck45 steel, having lower hardenability when quenched in vigorously agitated brine, provides a hardness of 45 HRC in the center of a 30-mm diameter bar. Quenching in moderately agitated oil provides this hardness in the center of a round bar of only 10 mm diameter.

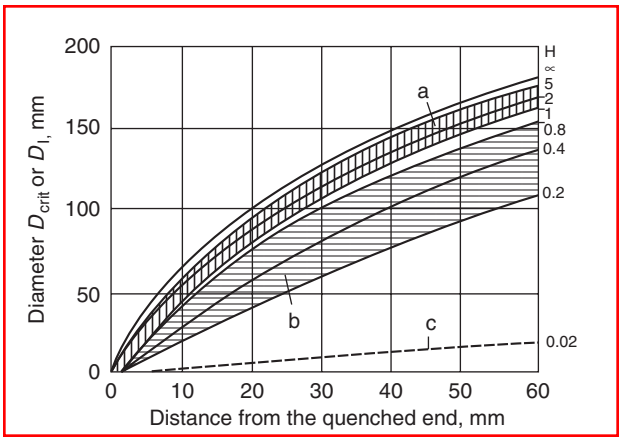

FIGURE 5.47 Relationship between the round bar diameter and the distance from the quenched end of the Jominy specimen, giving the hardness in the center of the cross section after quenching under different quenching conditions, a, water; b, oil; c, air. (From M. Asimov, W.F. Craig, and M.A. Grossmann, *SAE Trans.* *49*(1):283–292, 1941.)

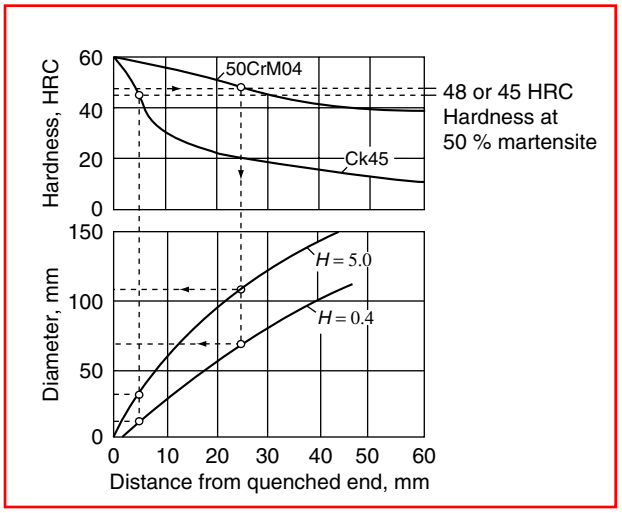

FIGURE 5.48 Determining the critical diameter of round bars (i.e., the hardness of 50% martensite at the center) from the Jominy hardenability curves of two steel grades quenched in vigorously agitated brine ($H = 5.0$) and in moderately agitated oil ($H = 0.4$). (Steel grade designation according to DIN.) (From G. Spur (Ed.), *Handbuch der Fertigungstechnik*, Band 4/2, *Wärmebehandeln*, Carl Hanser, Munich, 1987, p. 1012.)

5.5.1 Lamont Method

The diagram shown in Figure 5.47 permits the prediction of hardness only at the center of round bars. Lamont [32] developed diagrams relating the cooling rate at a given Jominy distance to that at a given fractional depth in a bar of given radius that has been subjected to a given Grossmann quenching intensity (H) factor. Analytical expressions have been developed for the Lamont transformation of the data to the appropriate Jominy distance J:

$$J = J(D, r/R, H) \tag{5.18}$$

where D is the diameter of the bar, r/R the fractional position in the bar ($r/R = 0$ at the center; $r/R = 1$ at the surface), and H the Grossmann quenching intensity factor. These expressions [33] are valid for any value of H from 0.2 to 10 and for bar diameters up to 200 mm (8 in.).

Lamont developed diagrams for the following points and fractional depths on the cross section of round bars: $r/R = 0$ (center), $r/R = 0.1$, $r/R = 0.2, \ldots,$ $r/R = 0.5$ (half-radius), $r/R = 0.6, \ldots, r/R = 1.0$ (surface). Each of these diagrams is always used in connection with Jominy hardenability curve for the relevant steel. Figure 5.49 through Figure 5.51 show the Lamont diagram for $r/R = 0$ (center of the cross section), $r/R = 0.5$, and $r/R = 0.8$, respectively.

The Lamont method can be used for four purposes:

1. To determine the maximum diameter of the bar that will achieve a particular hardness at a specified location on the cross section when quenched under specified conditions. For example, if the Jominy hardenability curve of the relevant steel grade shows a hardness of 55 HRC at a Jominy distance of 10 mm, then the maximum diameter of the bar that will achieve this hardness at half-radius when quenched in oil with $H = 0.35$ will be 28 mm. This result is obtained by using the diagram in Figure 5.50 for $r/R = 0.5$ and taking the vertical line at a Jominy distance of 10 mm to the intersection with the curve for $H = 0.35$, giving the value of 28 mm on the ordinate.

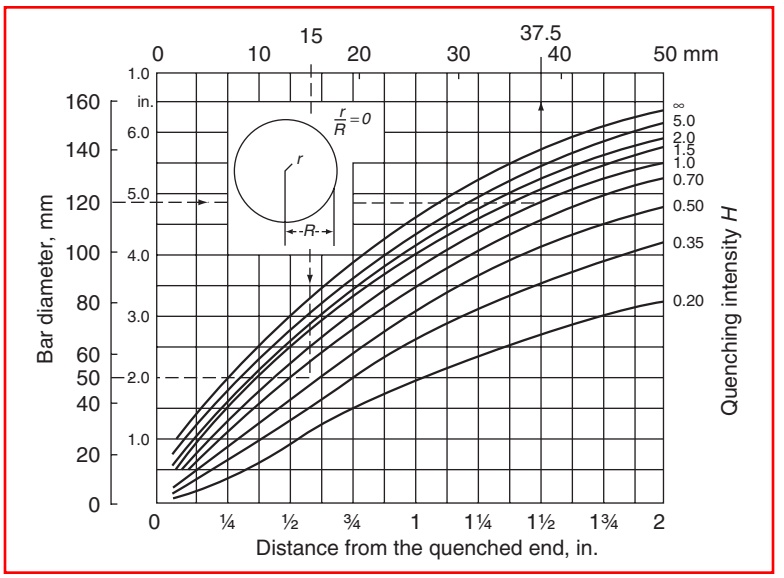

FIGURE 5.49 Relation between distance from the quenched end of Jominy specimen and bar diameter for the ratio $r/R = 0$, i.e., the center of the cross section, for different quenching intensities. (From J.L. Lamont, *Iron Age 152*:64–70, 1943.)

2. To determine the hardness at a specified location when the diameter of the bar, the quenching intensity H, and the steel grade are known. For example, if a 120-mm diameter bar is quenched in still water ($H = 1.0$), the hardness at the center ($r/R = 0$) will be determined at a distance of 37.5 mm from the quenched end on the Jominy curve of the relevant steel grade (see Figure 5.49).

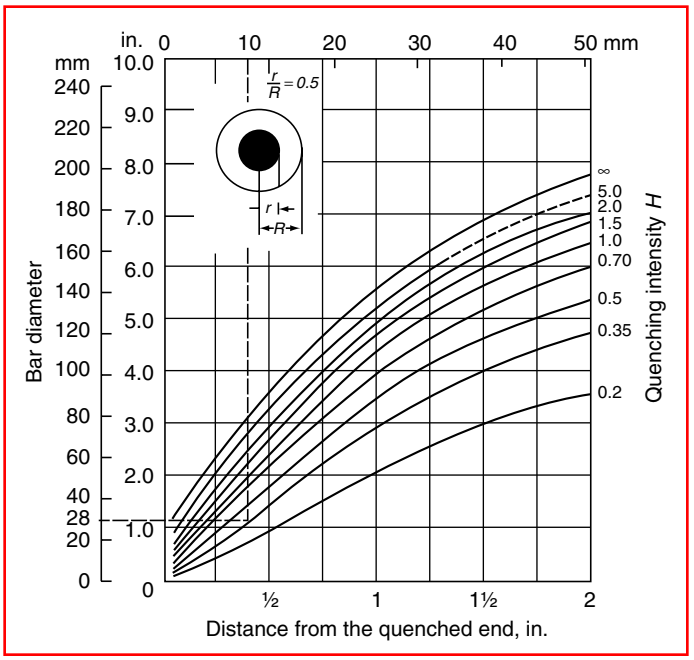

FIGURE 5.50 Relation between distance from the quenched end of Jominy specimen and bar diameter for the ratio $r/R = 0.5$, i.e., 50% from the center, for different quenching intensities. (From J.L. Lamont, *Iron Age 152*:64–70, 1943.)

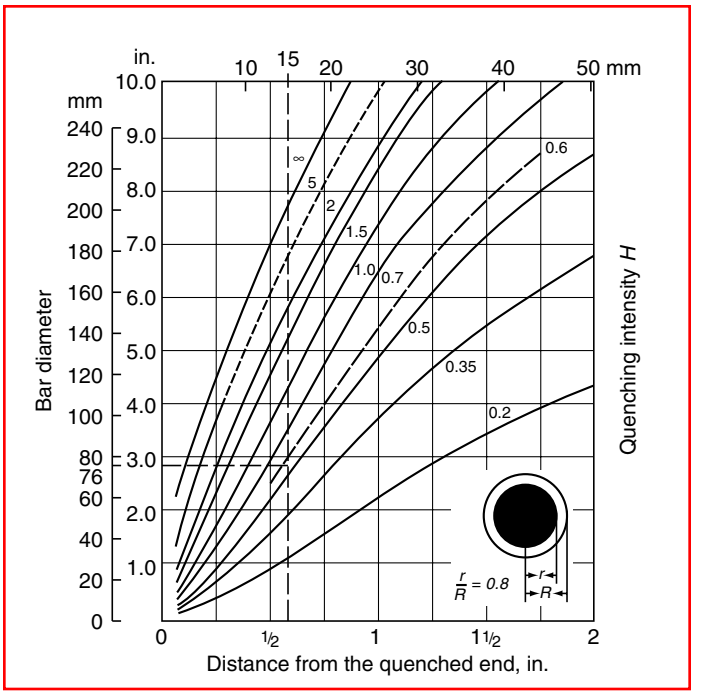

FIGURE 5.51 Relation between distance from the quenched end of Jominy specimen and bar diameter for the ratio $r/R = 0.8$, i.e., 80% from the center, for different quenching intensities. (From J.L. Lamont, *Iron Age 152*:64–70, 1943.)

3. To select adequate quenching conditions when the steel grade, the bar diameter, and the location on the cross section where a particular hardness should be attained are known. For example, a hardness of 50 HRC, which corresponds to the distance of 15 mm from the quenched end on the Jominy curve of the relevant steel grade, should be attained at the center of a 50-mm diameter bar. The appropriate H factor can be found by using Figure 5.49. In this case, the horizontal line for a 50-mm diameter and the vertical line for a 15-mm Jominy distance intersect at the point that corresponds to $H = 0.5$. This indicates that the quenching should be done in oil with good agitation.

If the required hardness should be attained only up to a certain depth below the surface, the fractional depth on the cross section must be first established to select the appropriate transformation diagram. For example, if 50 HRC hardness, which corresponds to a distance of 15 mm from the quenched end on the Jominy curve of the relevant steel grade, should be attained at 7.6 mm below the surface of a 76-mm diameter bar, then

$$\frac{r}{R} = \frac{38 - 7.6}{38} = 0.8 \tag{5.19}$$

This calculation indicates that the diagram for $r/R = 0.8$ (Figure 5.51) should be used. In this case, the horizontal line for 76 mm diameter intersects the vertical line for 15-mm Jominy distance on the interpolated curve $H = 0.6$. This indicates that quenching should be performed in oil with strong agitation (see Table 5.1).

4. To predict the hardness along the radius of round bars of different diameters when the bar diameter and steel grade and its Jominy curve and quenching intensity H are

known. For this calculation, diagrams for every ratio r/R from the center to the surface should be used. The following procedure should be repeated with every diagram. At the point where the horizontal line (indicating the bar diameter in question) intersects the relevant H curve, the vertical line gives the corresponding distance from the quenched end on the Jominy curve from which the corresponding hardness can be read and plotted at the corresponding fractional depth. Because some simplifying assumptions are made when using Lamont diagrams, hardness predictions are approximate. Experience has shown that for small cross sections and for the surface of large-diameter bars, the actual hardness is usually higher than predicted.

5.5.2 Steel Selection Based on Hardenability

The selection of a steel grade (and heat) for a part to be heat-treated depends on the hardenability that will yield the required hardness at the specified point of the cross section after quenching under known conditions. Because Jominy hardenability curves and hardenability bands are used as the basis of the selection, the method described here is confined to those steel grades with known hardenability bands or Jominy curves. This is true first of all for structural steels for hardening and tempering and also for steels for case hardening (to determine core hardenability).

If the diameter of a shaft and the bending fatigue stresses it must be able to undergo are known, engineering analysis will yield the minimum hardness at a particular point on the cross section that must be achieved by hardening and tempering. Engineering analysis may show that distortion minimization requires a less severe quenchant, e.g., oil. Adequate toughness after tempering (because the part may also be subject to impact loading) may require a tempering temperature of, e.g., 500°C.

The steps in the steel selection process are as follows:

Step 1. Determine the necessary minimum hardness after quenching that will satisfy the required hardness after tempering. This is done by using a diagram such as the one shown in Figure 5.52. For example, if a hardness of 35 HRC is required after hardening and then tempering at 500°C at the critical cross-sectional diameter, the minimum hardness after quenching must be 45 HRC.

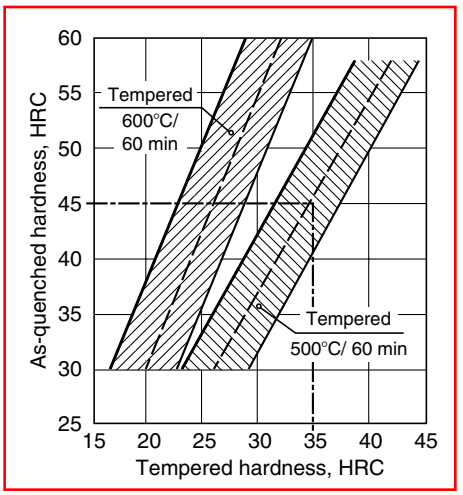

FIGURE 5.52 Correlation between the hardness after tempering and the hardness after quenching for structural steels (according to DIN 17200).

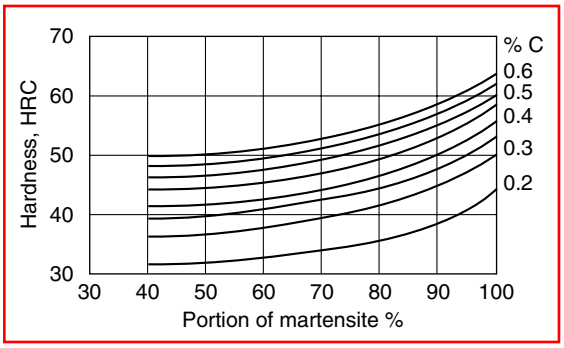

FIGURE 5.53 Correlation between as-quenched hardness, carbon content, and percent martensite (according to Hodge and Orehovski). (From *Metals Handbook*, 9th ed., Vol. 1, ASM International, Metals Park, OH, 1978, pp. 473–474, p. 481.)

Alternatively, if the carbon content of the steel and the percentage of as-quenched martensite at the critical point of the cross section is known, then by using a diagram that correlates hardness with percent carbon content and as-quenched martensite content (see Figure 5.53), the as-quenched hardness may then be determined. If 80% martensite is desired at a critical position of the cross section and the steel has 0.37% C, a hardness of 45 HRC can be expected. Figure 5.53 can also be used to determine the necessary carbon content of the steel when a particular percentage of martensite and a particular hardness after quenching are required.

Step 2. Determine whether a certain steel grade (or heat) will provide the required as-quenched hardness at a critical point of the cross section. For example, assume that a shaft is 45 mm in diameter and that the critical point on the cross section (which was determined from engineering analysis of resultant stresses) is three fourths of the radius. To determine if a particular steel grade, e.g., AISI 4140H, will satisfy the requirement of 45 HRC at $(3/4)R$ after oil quenching, the diagram shown in Figure 5.54a should be used. This diagram correlates cooling rates along the Jominy end-quench specimen and at four characteristic locations (critical points) on the cross section of a round bar when quenched in oil at 1 m/s agitation rate (see the introduction to Section 5.5 and Figure 5.44). Figure 5.54a shows that at $(3/4)R$ the shaft having a diameter of 45 mm will exhibit the hardness that corresponds to the hardness at a distance of 6.5/16 in. (13/32 in.) from the quenched end of the Jominy specimen.

Step 3. Determine whether the steel grade represented by its hardenability band (or a certain heat represented by its Jominy hardenability curve) at the specified distance from the quenched end exhibits the required hardness. As indicated in Figure 5.54b, the minimum hardenability curve for AISI 4140H will give a hardness of 49 HRC. This means that AISI 4140H has, in every case, enough hardenability for use in the shaft example above.

This graphical method for steel selection based on hardenability, published in 1952 by Weinmann and coworkers, can be used as an approximation. Its limitation is that the diagram shown in Figure 5.54a provides no information on the quality of the quenching oil and its temperature. Such diagrams should actually be prepared experimentally for the exact conditions that will be encountered in the quenching bath in the workshop; the approximation will be valid only for that bath.

5.5.3 Computer-Aided Steel Selection Based on Hardenability

As in other fields, computer technology has made it possible to improve the steel selection process, making it quicker, more intuitive, and even more precise. One example, using a

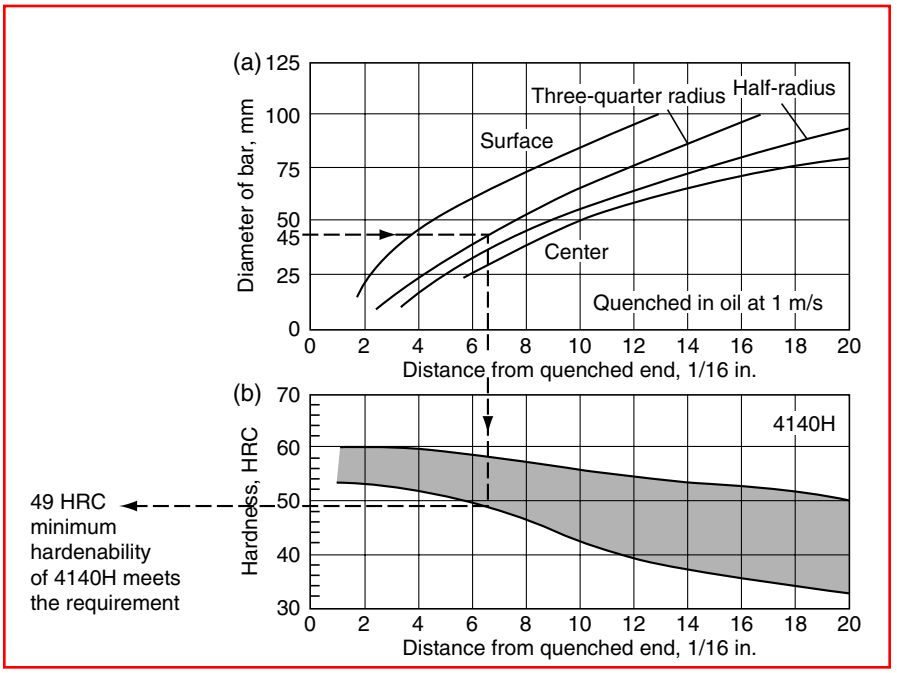

FIGURE 5.54 Selecting a steel of adequate hardenability. (a) equivalent cooling rates (and hardness after quenching) for characteristic points on a round bar's cross section and along the Jominy end-quench specimen. (b) Hardenability band of AISI 4140H steel. (From *Metals Handbook*, 9th ed., Vol. 1, ASM International, Metals Park, OH, 1978, pp. 473–474, p. 493.)

software package developed at the University of Zagreb [35], is based on a computer file of experimentally determined hardenability bands of steels used in the heat-treating shop. The method is valid for round bars of 20–90-mm diameters. The formulas used for calculation of equidistant locations on the Jominy curve, described in Ref. [23], were established through regression analysis for this range of diameters.

The essential feature of this method is the calculation of points on the optimum Jominy hardenability curve for the calculated steel. Calculations are based on the required as-quenched hardness on the surface of the bar and at one of the critical points of its cross section [$(3/4)R$, $(1/2)R$, $(1/4)R$, or center]. The input data for the computer-aided selection process are the following:

- Diameter of the bar (D mm)
- Surface hardness HRC
- Hardness at a critical point HRC
- Quenching intensity factor I (I equals the Grossmann quenching intensity factor H as given in Table 5.1)
- Minimum percentage of martensite required at the critical point

The first step is to calculate the equidistant locations from the quenched end on the Jominy curve (or Jominy hardenability band). These equidistant locations are the points on the Jominy curve that yield the required as-quenched hardness. The calculations are performed as follows [23]:

On the surface:

$$E_s = \frac{D^{0.718}}{5.11I^{1.28}} \tag{5.20}$$

At $(3/4)R$:

$$E_{3/4R} = \frac{D^{1.05}}{8.62I^{0.668}} \tag{5.21}$$

At $(1/2)R$:

$$E_{1/2R} = \frac{D^{1.16}}{9.45I^{0.51}} \tag{5.22}$$

At $(1/4)R$:

$$E_{1/4R} = \frac{D^{1.14}}{7.7I^{0.44}} \tag{5.23}$$

At the center:

$$E_c = \frac{D^{1.18}}{8.29I^{0.44}} \tag{5.24}$$

[*Note*: The calculated E values are in millimeters.]

After calculating the equidistant locations for the surface of the bar (E_s) and for one of the critical points (E_{crit}), using the hardenability band of the relevant steel, the hardness values achievable with the Jominy curve of the lowest hardenability (H_{low}) and the hardness values achievable with the Jominy curve of the highest hardenability (H_{high}) for both E_s and E_{crit} locations are then determined as shown in Figure 5.55.

The degree of hardening S is defined as the ratio of the measured hardness after quenching (at a specified point of the cross section) to the maximum hardness that can be achieved with the steel in question:

$$S = \frac{H}{H_{max}} \tag{5.25}$$

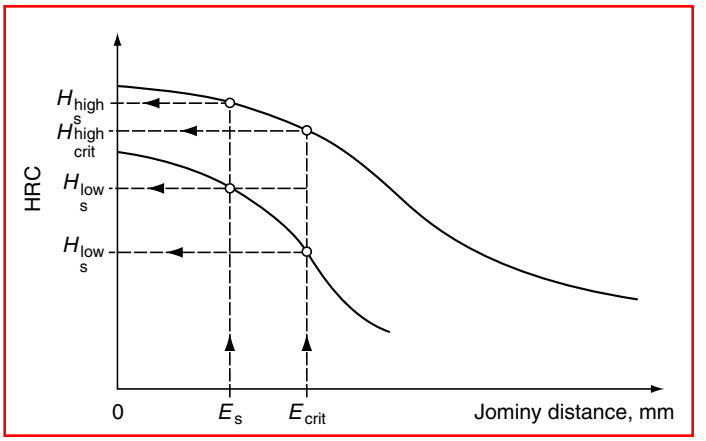

FIGURE 5.55 Determination of minimum and maximum hardness for equidistant location E_s and E_{crit} from a relevant hardenability band. (After T. Filetin, *Strojarstvo* 24(2):75–81, 1982 [in Croatian].)

TABLE 5.5
Correlation between Degree of Hardening *S* and Percentage of Martensite in As-Quenched Structure

Percent Martensite	Degree of Hardening *S*
50–60	0.70–0.74
60–70	0.74–0.76
70–80	0.76–0.78
80–85	0.78–0.81
85–90	0.81–0.86
90–95	0.86–0.91
95–97	0.91–0.95
97–100	0.95–1.00

Source: T. Filetin and J. Galinec, Software programme for steel selection based on hardenability, Faculty of Mechanical Engineering, University of Zagreb, 1994.

It can be easily calculated for the equidistant location E_{crit} on the upper and lower curves of the hardenability band, taking the value for H_{max} from the relevant Jominy curve at distance 0 from the quenched end ($J = 0$). In this way, two distinct values of the degree of hardening, S_{upper} and S_{lower}, are calculated. Each corresponds to a certain percentage of martensite in the as-quenched structure as shown in Table 5.5.

It is also possible to determine whether the required percentage of martensite can be achieved by either Jominy curve of the hardenability band. Instead of providing the percentage of martensite in the as-quenched structure as input data, the value of S (degree of hardening) may be given. For statically stressed parts, $S < 0.7$; for less dynamically stressed parts, $0.7 < S < 0.86$; and for highly dynamically stressed parts, $0.86 < S < 1.0$. In this way, a direct comparison of the required S value with values calculated for both Jominy curves at the E_{crit} location can be performed. There are three possibilities in this comparison:

1. The value of S required is even lower than the S value calculated for the lower curve of the hardenability band (S_{lower}). In this case all heats of this steel will satisfy the requirement. The steel actually has higher hardenability than required.
2. The value of S required is even higher than the S value calculated for the upper curve of the hardenability band (S_{upper}). In this case, none of the heats of this steel can satisfy the requirement. This steel must not be selected because its hardenability is too low for the case in question.
3. The value of required degree of hardening (S) is somewhere between the values for the degree of hardening achievable with the upper and lower curves of the hardenability band (S_{upper} and S_{lower}, respectively).

In the third case, the position of the S required, designated as X, is calculated according to the formula:

$$X = \frac{S - S_{lower}}{S_{upper} - S_{lower}}$$

where X is the distance from the lower curve of the hardenability band on the ordinate E_{crit} to the actual position of S required, which should be on the optimum Jominy curve. This calculation divides the hardenability band into three zones:

The lower third, $X \leq 0.33$
The middle third, $0.33 < X \leq 0.66$
The upper third, $0.66 < X$

All heats of a steel grade where the Jominy curves pass through the zone in which the required S point is situated can be selected as heats of adequate hardenability. This zone is indicated in a graphical presentation of the method. Once the distance X is known, the optimum Jominy hardenability curve can be drawn. The only requirement is that for every distance from the quenched end the same calculated ratio (X) that indicates the same position of the Jominy curve relative to the lower and upper hardenability curves of the hardenability band is maintained.

The following example illustrates the use of this method in selecting a steel grade for hardening and tempering.

A 40-mm diameter shaft after hardening and tempering should exhibit a surface hardness of $H_s = 28$ HRC and a core hardness of $H_c = 26$ HRC. The part is exposed to high dynamic stresses. Quenching should be performed in agitated oil.

The first step is to enter the input data and select the critical point on the cross section (in this case the core) as shown in Figure 5.56. Next, the required percentage of martensite at the critical point after quenching (in this case 95%, because of high dynamic stresses) and the quenching intensity I (in this case 0.5, corresponding to the Grossmann value H) are selected. The computer program repeats the above-described calculations for every steel grade for which the hardenability band is stored in the file and presents the results on the screen as shown in Figure 5.57. This is a list of all stored steel grades regarding suitability for the application being calculated. Acceptable steel grades, suitable from the upper, middle, or lower third of the hardenability band, and unacceptable steel grades with excessively high hardenability are determined.

Selection of steel in hardened and tempered condition

Diameter, mm (0–90):40

Critical point on the cross-section:	<1> 3/4R
	<2> 1/2R
	<3> 1/4R
Core	<4> Core
Required value:	<1> Hardness, HRC (20–50)
	<2> Tensile strength, N/mm^2 (750–1650)

Hardness, HRC

– On the surface:	28 H_s
– At the critical point:	26 H_c

FIGURE 5.56 Input data for computer program. (From T. Filetin and J. Galinec, Software programme for steel selection based on hardenability, Faculty of Mechanical Engineering, University of Zagreb, 1994.)

Results of steel selection

JUS	AISI	
Č4181		Not suitable
Č4730	4130	Not suitable
Č4731	E4132	Suitable heats from upper third of band
Č4781		Suitable heats from upper third of band
Č4732	4140	Suitable heats from middle third of band
Č4782		Suitable heats from middle third of band
Č4733	4150	Suitable heats from middle third of band
Č4738		Too high hardenability
Č4734		Too high hardenability

FIGURE 5.57 List of computer results. (From T. Filetin and J. Galinec, Software programme for steel selection based on hardenability, Faculty of Mechanical Engineering, University of Zagreb, 1994.)

For each suitable steel grade, a graphical presentation as shown in Figure 5.58 can be obtained. This gives the optimum Jominy hardenability curve for the case required and indicates the desired zone of the hardenability band.

In addition, the necessary tempering temperature can be calculated according to the formula:

$$T_{\text{temp}} = 917 \sqrt[6]{\frac{\ln = \frac{H_{\text{crit}}^{-8}}{H_{\text{temp}}^{-8}}}{S}} \tag{5.26}$$

where T_{temp} is the absolute tempering temperature (K) (valid for $400^\circ\text{C} < T_{\text{temp}} < 660^\circ\text{C}$), H_{crit} the hardness after quenching at the critical point HRC (taken from the optimum Jominy curve at the distance for the critical point), H_{temp} the required hardness after tempering at the critical point HRC, and S the degree of hardening (ratio between hardness on the optimum Jominy curve at the distance E_{crit} and at the distance $E = 0$).

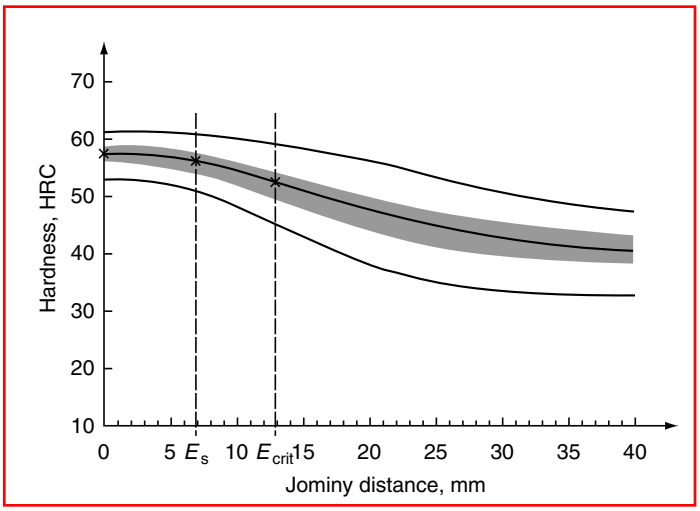

FIGURE 5.58 Graphical presentation of the optimum Jominy hardenability curve. (From T. Filetin and J. Galinec, Software programme for steel selection based on hardenability, Faculty of Mechanical Engineering, University of Zagreb, 1994.)

Tensile strength (R_m, N/mm^2) is also calculated at the relevant points using the formula:

$$R_m = 0.426H^2 + 586.5 \ [\text{N/mm}^2] \tag{5.27}$$

where H is the corresponding hardness value in HRC. Knowing the tensile strength (R_m), other mechanical properties are calculated according to the formulas:

Yield strength:

$$R_{p\,0.2} = (0.8 + 0.1S)R_m + 170\text{S} - 200 \ [\text{N/mm}^2] \tag{5.28}$$

Elongation:

$$A_5 = 0.46 - (0.0004 - 0.00012S)R_m \ [\%] \tag{5.29}$$

Contraction:

$$Z = 0.96 - (0.00062 - 0.00029S)R_m \ [\%] \tag{5.30}$$

Bending fatigue strength:

$$R_d = (0.25 + 0.45Z)R_m \ [\text{N/mm}^2] \tag{5.31}$$

Impact energy (toughness):

$$\text{KU} = [460 - (0.59 - 0.29S)R_m](0.7) \ [\text{J}] \tag{5.32}$$

For every steel grade (and required zone of the hardenability band) that has been found suitable, the mechanical properties for the surface and for the critical cross section point can be calculated. The computer output is shown in Figure 5.59.

Compared to the previous steel selection processes, these computer-aided calculations have the following advantages:

(AISI 4140)

Heats from the middle third of the band

Calculated tempering temperature: 643°C

Mechanical properties	Surface	Critical point
Yield strength: $R_{p0.2}$, N/mm^2	793	735
Tensile strength: R_m, N/mm^2	920	874
Bending fatigue strength: R_d, N/mm^2	499	474
Elongation: A_5, %	20	21
Contraction: Z, %	65	65
Impact engergy: KU, J	125	123

FIGURE 5.59 Computer display of calculated mechanical properties. (From T. Filetin and J. Galinec, Software programme for steel selection based on hardenability, Faculty of Mechanical Engineering, University of Zagreb, 1994.)

1. Whereas the previously described graphical method is valid for only one specified quenching condition for which the relevant diagram has been plotted, the computer-aided method allows great flexibility in choosing concrete quenching conditions.
2. Selection of the optimum hardenability to satisfy the requirements is much more precise.
3. Calculations of the exact tempering temperature and all mechanical properties after tempering at the critical point that give much more information and facilitate the steel selection are possible.

5.6 HARDENABILITY IN HEAT TREATMENT PRACTICE

5.6.1 Hardenability of Carburized Steels

Carburized parts are primarily used in applications where there are high surface stresses. Failures generally originate in the surface layers where the service stresses are most severe. Therefore, high case strength and high endurance limits are critical factors. High case hardness improves the fatigue durability. Historically, it was thought that core hardenability was required for the selection of carburizing steels and heat treatment of carburized parts and that core hardenability would ensure adequate case hardenability. Equal additions of carbon, however, do not have the same effect on the hardenability of all steel compositions; therefore the historical view of core hardenability may not be correct. In fact, hardenability of both case and core is essential for proper selection of the optimum steel grade and the heat treatment of carburized parts.

It is now also known that the method of quenching after carburizing, i.e., direct quenching or reheat and quench, influences case hardenability. The case hardenability of carburized steel is determined by using the Jominy end-quench test.

Standard Jominy specimens are carburized in a carburizing medium with a high C potential for sufficient time to obtain a carburized layer of the desired depth. In addition to the Jominy specimens, two bars of the same steel and heat, the same surface finish, and the same dimensions (25 mm diameter) are also carburized under identical conditions. These bars are used to plot the carbon gradient curve shown in Figure 5.60a, which is produced by chemical analysis of chips obtained from machining of the carburized layer at different layer thicknesses. In this way, as shown in Figure 5.60a, the following carbon contents were found as a function of case depth:

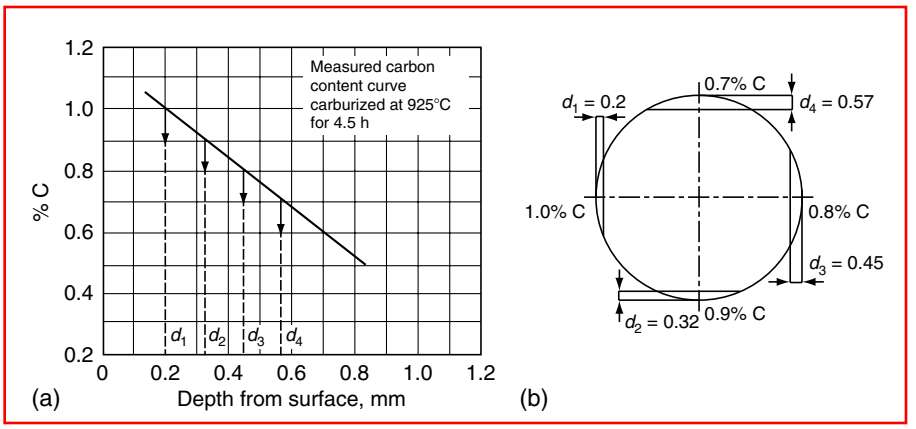

FIGURE 5.60 (a) Measured carbon gradient curve after gas carburizing at 925°C for 4.5 h. (b) Grinding of the carburized Jominy specimen. (From T. Filetin and B. Liščič, *Strojarstvo 18*(4):197–200, 1976 [in Croatian].)

1.0% C at 0.2 mm depth (distance from the surface of the bar)—d_1
0.9% C at 0.32 mm depth—d_2
0.8% C at 0.45 mm depth—d_3
0.7% C at 0.57 mm depth—d_4

One of the carburized Jominy specimens should be end-quenched in the standard way using the Jominy apparatus directly from the carburizing temperature (direct quenching), and the other should be first cooled to room temperature and then reheated and quenched from a temperature that is usually much lower than the carburizing temperature (reheat and quench).

After quenching, all Jominy specimens should be ground on four sides of the perimeter to the depths, d_1, d_2, d_3, and d_4, as shown in Figure 5.60b. Hardness is measured in the standard way on each of the ground surfaces, and the corresponding Jominy curves are plotted. Figure 5.61a

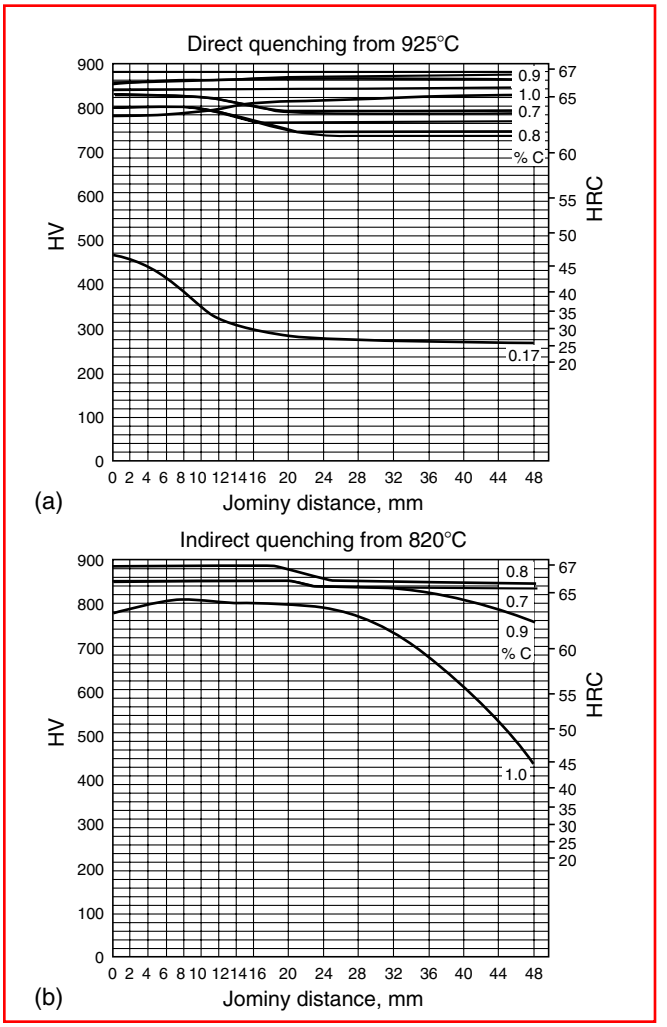

FIGURE 5.61 Jominy case hardenability curves of carburized DIN 16MnCr5 steel (a) after direct quenching from 925°C and (b) after reheating followed by quenching from 820°C. (From T. Filetin and B. Liščič, *Strojarstvo 18*(4):197–200, 1976 [in Croatian].)

provides an example of Jominy hardenability curves for the carburizing steel grade DIN 16MnCr5 (0.17% C, 0.25% Si, 1.04% Mn, 1.39% Cr). The carbon contents in the case were 1.0, 0.9, 0.8, and 0.7% C, and the core carbon content was 0.17% C after direct quenching from the carburizing temperature, 925°C. Figure 5.61b provides Jominy curves for the same carburized case after indirect quenching (reheated to 820°C). From both diagrams of Figure 5.61 the following conclusions can be drawn:

1. The hardenability of the core is substantially different from the hardenability within the carburized case.
2. The best hardenability of the carburized case is found for this steel grade at 0.9% C with direct quenching and at 0.8% C with indirect quenching (reheat and quench).

Consequently, the carburizing process should be controlled so that after carburizing a surface carbon content of 0.9% is obtained for direct quenching and one of 0.8% for indirect quenching.

5.6.2 Hardenability of Surface Layers When Short-Time Heating Methods Are Used

When short-time (zero time) heating processes for surface hardening are used, e.g., flame hardening, induction hardening, or laser hardening, the same metallurgical reactions occur as in conventional hardening except that the heating processes cycle must be much shorter than that of conventional hardening. Heating time for these proceses vary by one to three orders of magnitude; approximately 100 s for flame hardening, 10 s or less for induction hardening, and 1 s or less for laser hardening. This means that the heating rates are very high. Problems associated with these high heating rates are twofold.

1. The transformation from the bcc lattice of the α-iron to the fcc lattice of the γ-iron does not occur between normal temperatures Ac_1 and Ac_3 as in conventional hardening because the high heating rate produces nonequilibrium systems. The Ac_1 and Ac_3 temperatures are displaced to higher temperatures as shown in Figure 5.62. Although an austenitizing temperature may be sufficiently high to form austenite under slow heating conditions (conventional hardening), the same temperature level may not be sufficient to even initiate austenization under high heating rates [37]. Therefore, substantially higher austenitizing temperatures are used with flame, induction, and laser hardening (especially the latter) than for conventional hardening of the same steel.
2. For quench hardening, the austenitization must dissolve and uniformly distribute the carbon of the carbides in the steel. This is a time-dependent diffusion process (sometimes called homogenization), even at the high temperatures used in short-time heating methods. At very high heating rates, there is insufficient time for diffusion of carbon atoms from positions of higher concentrations near carbides to the positions of lower concentrations (areas that originated from practically carbon-free ferrite). This diffusion depends on the path length of carbon atoms and therefore is dependent on the distribution of carbon in the starting structure. Coarse pearlitic structures, spheroidized structures, and (particularly) nodular cast iron with a high content of free ferrite are undesirable in this regard. Tempered martensite, having small and finely dispersed carbides, provides the shortest paths for carbon diffusion and is therefore most desirable.

Figure 5.62a illustrates a time temperature transformation diagram for continuous heating at different heating rates when austenitizing an unalloyed steel with 0.7% C with a starting structure of ferrite and lamellar pearlite. Figure 5.62b shows a similar diagram for

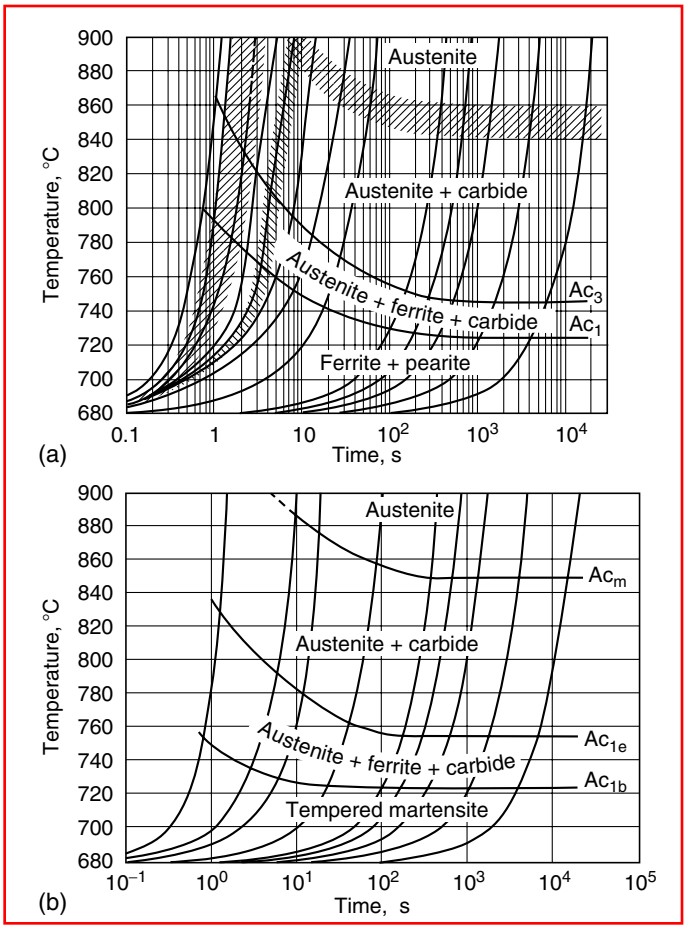

FIGURE 5.62 Time temperature transformation diagram for continuing heating with different heating rates, when austenitizing an unalloyed steel with 0.7% C. (a) Starting structure, ferrite and lamellar pearlite; (b) starting structure, tempered martensite. (From A. Rose, The austenitizing process when rapid heating methods are involved, Der Peddinghaus Erfahrungsaustausch, Gevelsberg, 1957, pp. 13–19 [in German].)

a starting structure of tempered martensite. A comparison of the two diagrams illustrates the influence of starting structure on the austenitizing process. Whereas for the ferrite–pearlite starting structure at maximum heating rate the upper transformation temperature Ac_3 is 865°C, for the starting microstructure of tempered martensite, the Ac_3 temperature is 835°C. This means that the austenite from a starting structure of tempered martensite has a better hardenability than the austenite of a pearlite–ferrite starting structure. The practical consequence of this is that prior to surface hardening by any short-time heating process, if the steel is in the hardened and tempered condition, maximum hardened case depths are possible. If the annealed material has a coarse lamellar structure, or even worse, globular carbides, minimum hardening depths are to be expected.

5.6.3 Effect of Delayed Quenching on the Hardness Distribution

Delayed quenching processes have been known for a long time. Delayed quenching means that austenitized parts are first cooled slowly and then after a specified time they are quenched at a much faster cooling rate. Delayed quenching is actually a quenching process in which a discontinuous change in cooling rate occurs. In some circumstances, depending on steel

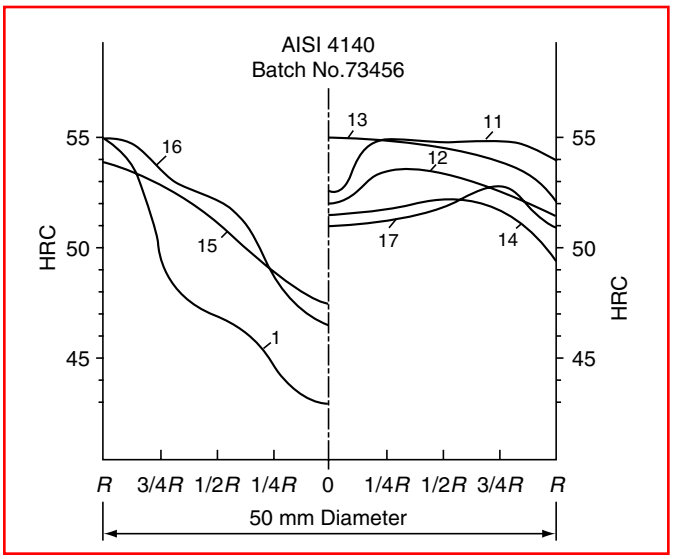

FIGURE 5.63 Measured hardness distribution on the cross section of 50 mm diameter × 200 mm bars made of AISI 4140 steel quenched according to conditions given in Table 5.6. (From B. Liščić, S. Svaic, and T. Filetin, Workshop designed system for quenching intensity evaluation and calculation of heat transfer data. *ASM Quenching and Distortion Control*, Proceedings of First International Confererence On Quenching and Control of Distortion, Chicago, IL, 22–25 Sept. 1992, pp. 17–26.)

hardenability and section size, the hardness distribution in the cross section after delayed quenching does not have a normal trend (normally the hardness decreases continuously from the surface toward the core) but instead exhibits an inverse trend (the hardness increases from the surface toward the core). This inverse hardness distribution is a consequence of the discontinuous change in the cooling rate and related to the incubation period (at different points in the cross section) before changing the cooling rate. This process has been explained theoretically by Shimizu and Tamura [40,41] in Figure 5.63.

In every experiment, the delay in quenching was measured as the time from immersion to the moment when maximum heat flux density on the surface (t_{qmax}) occurred. As shown in Figure 5.63 and Table 5.6 for AISI 4140 steel with a section 50 mm in diameter, when the delay in quenching (due to high concentration of the PAG polymer solution and corresponding thick film around the heated parts) was more than 15 s ($t_{qmax} > 15$ s), a completely inverse or inverse to normal hardness distribution was obtained. In experiments where t_{qmax} was less than 15 s, a normal hardness distribution resulted.

Besides the inherent hardenability of a steel, delayed quenching may substantially increase the depth of hardening and may compensate for lower hardenability of the steel [39]. Interestingly, none of the available software programs for predicting as-quenched hardness simulates the inverse hardness distribution because they do not account for the length of the incubation period before the discontinuous change in cooling rate at different points in the cross section.

5.6.4 A Computer-Aided Method to Predict the Hardness Distribution after Quenching Based on Jominy Hardenability Curves

The objective here is to describe one method of computer-aided calculation of hardness distribution. This method, developed at the University of Zagreb [44], is based on the Jominy

TABLE 5.6
Time from Immersion (t_{qmax}) until Maximum Heat Flux Density under Various Quenching Conditions for AISI 4140 Bars (50 mm Diameter × 200 mm)[a]

Figure 63 Curve No.	Quenching Conditions	t_{qmax} (s)
1	Mineral oil at 20°C, without agitation	14
11	Polymer solution (PAG) 5%; 40°C; 0.8 m/s	16
12	Polymer solution (PAG) 15%; 40°C; 0.8 m/s	33
13	Polymer solution (PAG) 25%; 40°C; 0.8 m/s	70
14	Polymer solution (PAG) 20%; 35°C; 1 m/s	30
15	Polymer solution (PAG) 10%; 35°C; 1 m/s	12
16	Polymer solution (PAG) 5%; 35°C; 1 m/s	13
17	Polymer solution (PAG) 20%; 35°C; 1 m/s	47

[a]See Figure 63.

Source: B. Liščić, S. Svaic, and T. Filetin, Workshop designed system for quenching intensity evaluation and calculation of heat transfer data. *ASM Quenching and Distortion Control*, Proceedings of First International Confererence On Quenching and Control of Distortion, Chicago, IL, 22–25 Sept. 1992, pp. 17–26.

hardenability curves. Jominy hardenability data for steel grades of interest are stored in a databank. In this method, calculations are valid for cylindrical bars 20–90 mm in diameter. Figure 5.64 shows the flow diagram of the program, and Figure 5.65 is a schematic of the step-by-step procedure:

Step 1. Specify the steel grade and quenching conditions.

Step 2. Harden a test specimen (50 mm diameter × 200 mm) of the same steel grade by quenching it under specific conditions.

Step 3. Measure the hardness (HRC) on the specimen's cross section in the middle of the length.

Step 4. Store in the file the hardness values for five characteristic points on the specimen's cross section (surface, $(3/4)R$, $(1/2)R$, $(1/4)R$, and center). If the databank already contains the hardness values for steel and quenching conditions obtained by previous measurements, then eliminate steps 2 and 3 and retrieve these values from the file.

Step 5. From the stored Jominy hardenability data, determine the equidistant points on the Jominy curve (E_s, $E_{3/4R}$, $E_{1/2R}$, $E_{1/4R}$, E_c) that have the same hardness values as those measured at the characteristic points on the specimen's cross section.

Step 6. Calculate the hypothetical quenching intensity I at each of the mentioned characteristic points by the following regression equations, based on the specimen's diameter D_{spec} and on known E values:

$$I_s = \left[\frac{D_{spec}^{0.718}}{5.11E_s}\right]^{0.78} \tag{5.33}$$

$$I_{3/4R} = \left[\frac{D_{spec}^{1.05}}{8.62E_{3/4R}}\right]^{1.495} \tag{5.34}$$

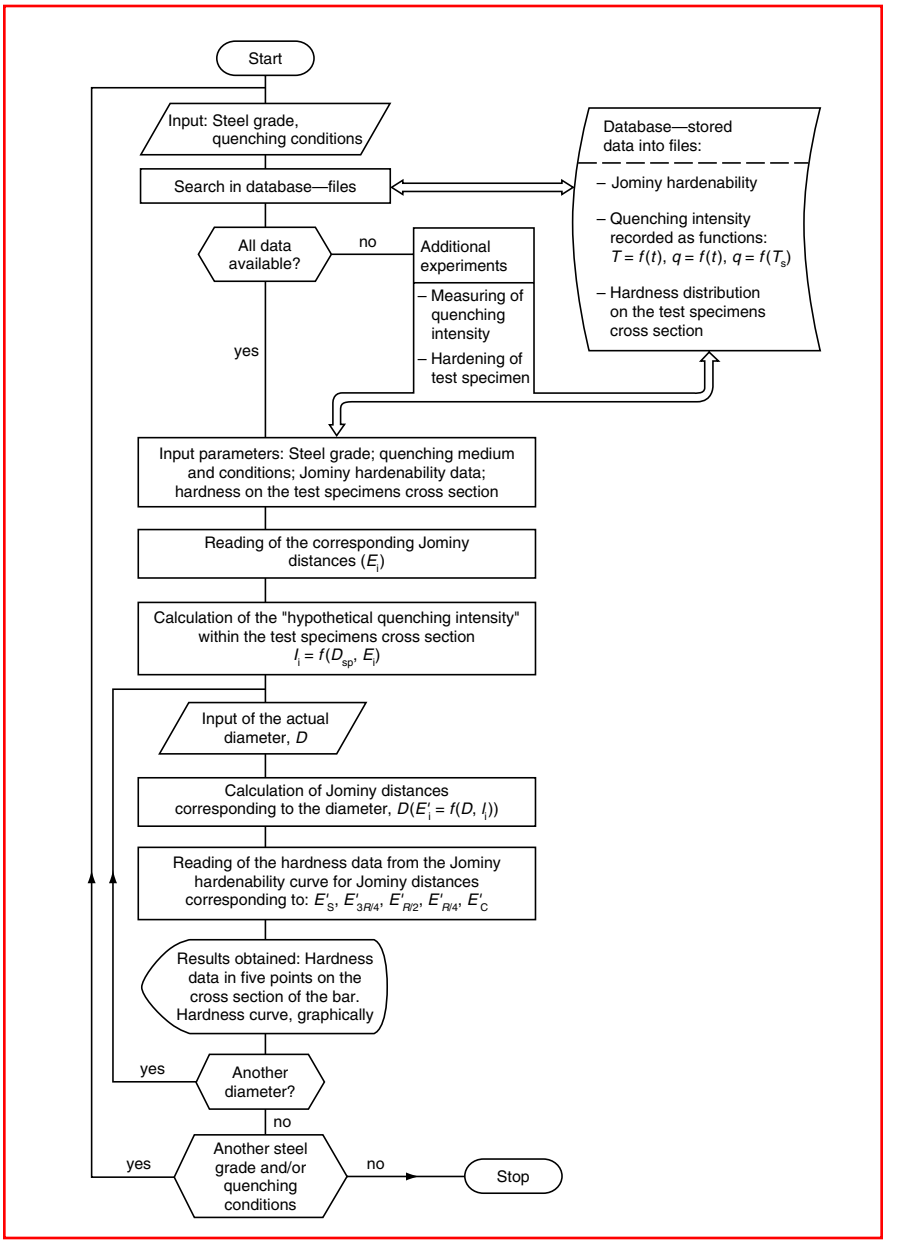

FIGURE 5.64 Flowchart of computer-aided prediction of hardness distribution on cross section of quenched round bars. (From B. Liščić, H.M. Tensi, and W. Luty, *Theory and Technology of Quenching*, Springer-Verlag, Berlin, 1992.)

$$I_{1/2R} = \left[\frac{D_{\text{spec}}^{1.16}}{9.45E_{1/2R}}\right]^{1.495} \tag{5.35}$$

$$I_{1/4R} = \left[\frac{D_{\text{spec}}^{1.14}}{7.7E_{1/4R}}\right]^{2.27} \tag{5.36}$$

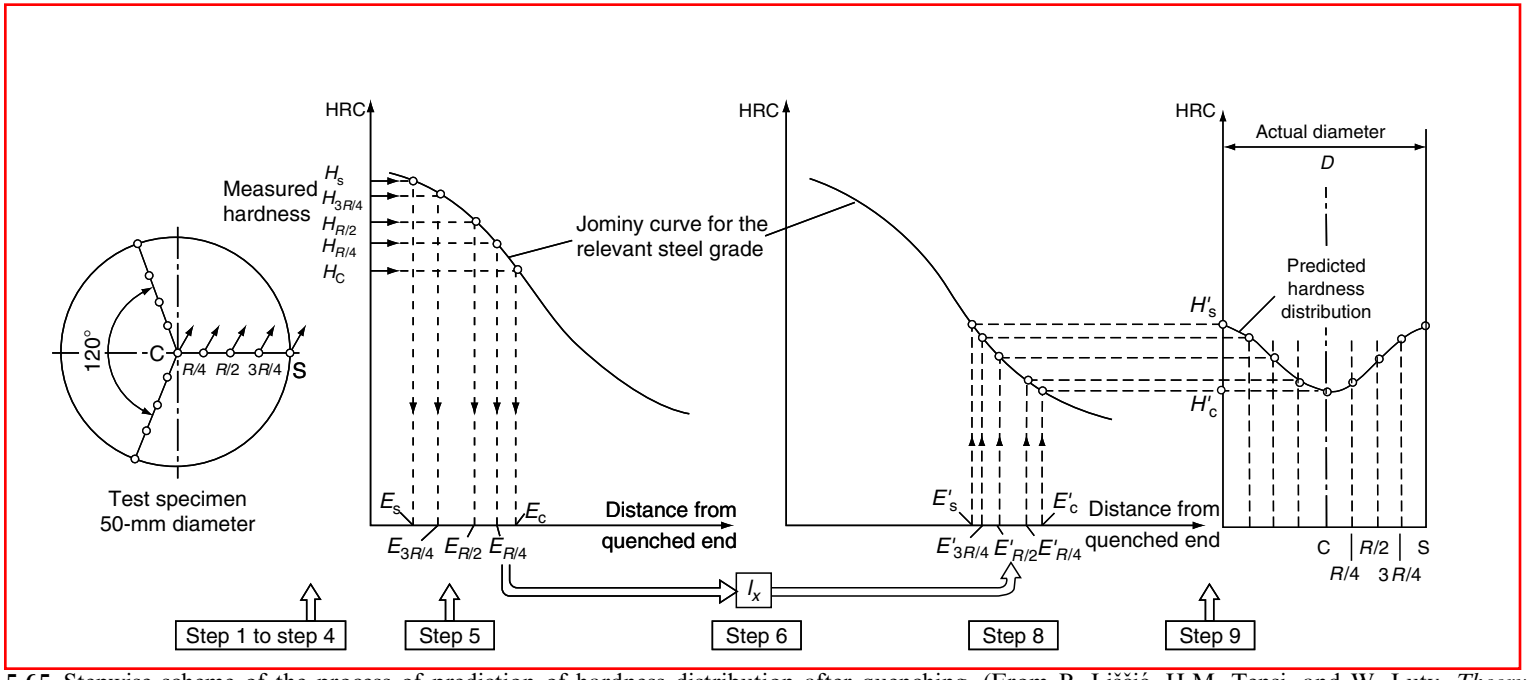

FIGURE 5.65 Stepwise scheme of the process of prediction of hardness distribution after quenching. (From B. Liščić, H.M. Tensi, and W. Luty, *Theory and Technology of Quenching*, Springer-Verlag, Berlin, 1992.)

$$I_c = \left[\frac{D_{spec}^{1.18}}{8.29E_c}\right]^{2.27} \tag{5.37}$$

Equation 5.33 through Equation 5.37 combine the equidistant points on the Jominy curve, the specimen's diameter, and the quenching intensity and were derived from the regression analysis of a series of Crafts–Lamont diagrams [22]. This analysis is based on Just's relationships [42] for the surface and the center of a cylinder:

$$E_i = A\frac{D^{B_1}}{I^{B_2}} \tag{5.38}$$

where E_i is the corresponding equidistant point on the Jominy curve, A, B_1, B_2 the regression coefficients, D the bar diameter, and I the quenching intensity (H according to Grossmann)

Step 7. Enter the actual bar diameter D for which the predicted hardness distribution is desired.

Step 8. Calculate the equidistant Jominy distances E'_s, $E'_{3/4R}$, $E'_{1/2R}$, $E'_{1/4R}$, E'_c that correspond to the actual bar diameter D and the previously calculated hypothetical quenching intensities $I_s - I_c$ using the formulas:

$$E'_s = \frac{D^{0.718}}{5.11I^{1.28}} \tag{5.39}$$

$$E'_{3/4R} = \frac{D^{1.05}}{8.62I^{0.668}} \tag{5.40}$$

$$E'_{1/2R} = \frac{D^{1.16}}{9.45I^{0.51}} \tag{5.41}$$

$$E'_{1/4R} = \frac{D^{1.14}}{7.7I^{0.44}} \tag{5.42}$$

$$E'_c = \frac{D^{1.18}}{8.29I^{0.44}} \tag{5.43}$$

Step 9. Read the hardness values H'_s, $H'_{3/4R}$, $H'_{1/2R}$, $H'_{1/4R}$, and H'_c from the relevant Jominy curve associated with the calculated Jominy distances and plot the hardness distribution curve over the cross section of the chosen actual diameter D.

Figure 5.66 provides an example of computer-aided prediction of hardness distribution for 30-and 70-mm diameter bars made of AISI 4140 steel quenched in a mineral oil at 20°C without agitation. Experimental validation using three different steel grades, four different bar diameters, and four different quenching conditions was performed, and a comparison to predicted results is shown in Figure 5.67. In some cases, the precision of the hardness distribution prediction was determined using the Gerber–Wyss method [43]. From examples 2, 3, 5, and 6 of Figure 5.67 it can be seen that the computer-aided prediction provides a better fit to the experimentally obtained results than the Gerber–Wyss method.

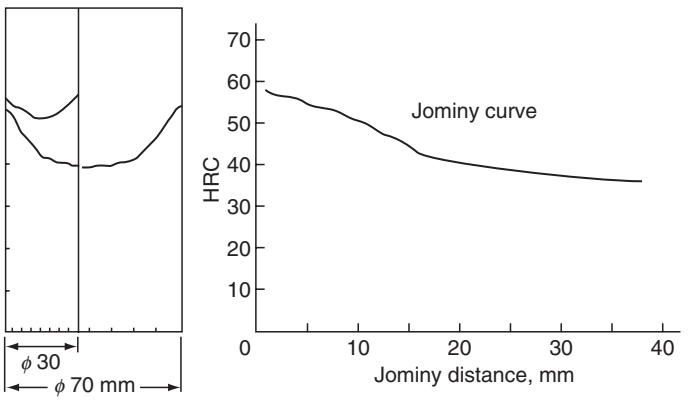

Prediction of hardness distribution

Input data:

Steel grade: Č. 4732 (SAE 4140H) ; B. NO. 43111
Quenching conditions: oil-UTO-2;20 °C; Om/s

Diameter for hardening, mm: 30

Results of computer aided prediction:
****

Calculated hardness:

Diameter = 30mm

Surface, hrc ..... = 55.3
3/4 Radius ..... = 54.3
1/2 Radius ..... = 53
1/4 Radius ..... = 51.5
Center ..... = 51.1

Graphic presentation (yes = 1, no = 0)
Another diameter (yes = 1, no = 0)

Diameter for hardening, mm: 70

Diameter = 70

Surface, hrc ..... = 53.1
3/4 Radius ..... = 46.4
1/2 Radius ..... = 40.7
1/4 Radius ..... = 39.6
Center ..... = 39

Graphic presentation (yes = 1, no = 0)
Another diameter (yes = 1, no = 0)

FIGURE 5.66 An example of computer-aided prediction of hardness distribution for quenched round bars of 30 and 70 mm diameter, steel grade SAE 4140H. (From B. Liščić, H.M. Tensi, and W. Luty, *Theory and Technology of Quenching*, Springer-Verlag, Berlin, 1992.)

5.6.4.1 Selection of Optimum Quenching Conditions

The use of above relationship and stored data permits the selection of optimum quenching condition when a certain hardness value is required at a specified point on a bar cross section of known diameter and steel grade. Figure 5.68 illustrates an example where an as-quenched

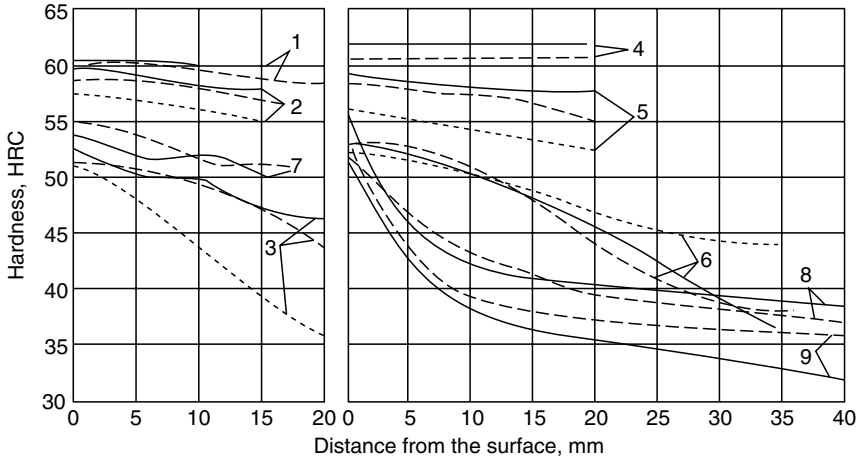

FIGURE 5.67 Comparison of the hardness distribution on round bar cross sections of different diameters and different steel grades, measured after experiments and obtained by computer-aided prediction as well as by prediction according to the Gerber–Wyss method. (From B. Liščić, H.M. Tensi, and W. Luty, *Theory and Technology of Quenching*, Springer-Verlag, Berlin, 1992.)

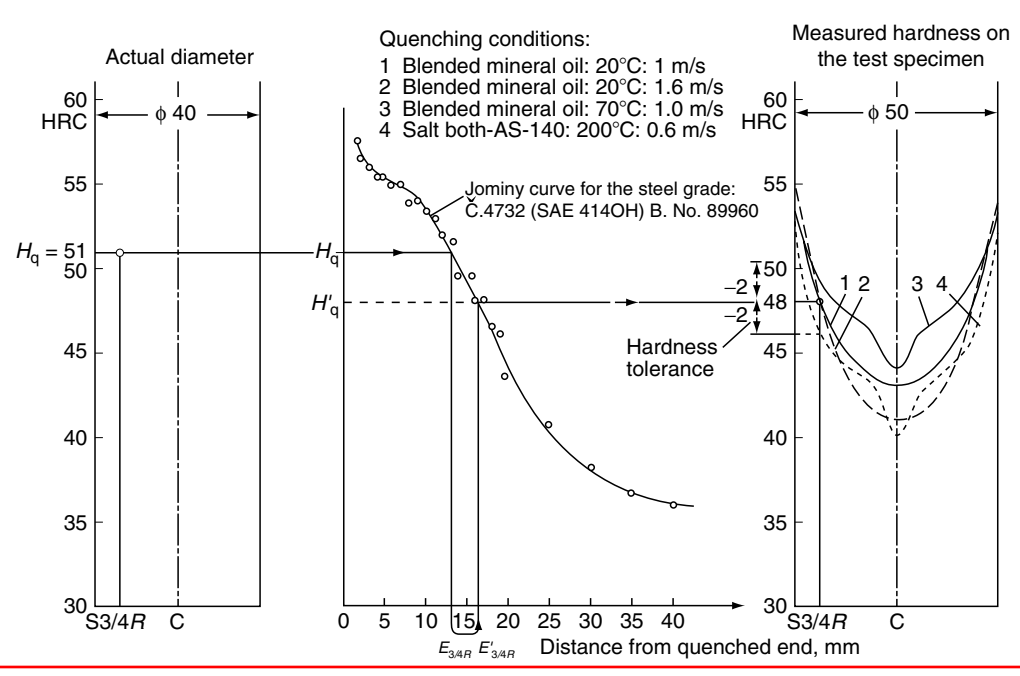

FIGURE 5.68 An example of computer-aided selection of quenching conditions (From B. Liščić, H.M. Tensi, and W. Luty, *Theory and Technology of Quenching*, Springer-Verlag, Berlin, 1992.)

hardness of 51 HRC (H_q) at $(3/4)R$ of a 40-mm diameter bar made of SAE 4140H steel is required. Using the stored hardenability curve for this steel, the equivalent Jominy distance $E_{3/4R}$ yielding the same hardness can be found. Using $E_{3/4R}$ and the actual diameter D, hypothetical quenching intensity factor $I_{3/4R}$ can be calculated according to Equation 5.34. That equation also applies to the test specimen of 50-mm diameter and can be written as

$$I_{3/4R} = \left[\frac{7.05}{E_{3/4R}}\right]^{1.495} \tag{5.44}$$

By substituting the calculated value of $I_{3/4R}$ and $D = 50$ mm, the equivalent Jominy distance $E_{3/4R}$ corresponding to $(3/4)R$ of the specimen's cross section, can be calculated:

$$E'_{3/4R} = \frac{10.85}{0.668} I_{3/4R} \tag{5.45}$$

For calculated $E'_{3/4R}$, the hardness of 48 HRC can be read off from the Jominy curve as shown in Figure 5.68. This means that the same quenching condition needed to produce a hardness value $H_q = 51$ HRC at $(3/4)R$ of a 40-mm diameter bar will yield a hardness H_s' of 48 HRC at $(3/4)R$ of the 50-mm diameter standard specimen.

The next step is to search all stored hardness distribution curves of test specimens made of the same steel grade for the specific quenching condition by which the nearest hardness H_q' has been obtained (tolerance is ± 2 HRC). As shown in Figure 5.68, the required hardness may be obtained by quenching in four different conditions, but the best-suited are conditions 1 and 2.

The special advantage of computer-aided calculations, particularly the specific method described, is that users can establish their own databanks dealing with steel grades of interest and take into account (by using hardened test specimens) the actual quenching conditions that prevail in a batch of parts using their own quenching facilities.

REFERENCES

1. G. Spur (Ed.), *Handbuch der Fertigungstechnik*, Band 4/2, *Wärmebehandeln*, Carl Hanser, Munich, 1987, p. 1012.
2. K.E. Thelning, *Steel and Its Heat Treatment*, 2nd ed., Butterworths, London, 1984, p. 145.
3. M.A. Grossmann, M. Asimov, and S.F. Urban, *Hardenability of Alloy Steels*, ASM International, Cleveland, OH, 1939.
4. *Metals Handbook*, 8th ed., Vol. 2, American Society for Metals, Cleveland, OH, 1964, p. 18.
5. M.A. Grossmann, M. Asimov, and S.F. Urban, Hardenability its relation to quenching and some quantitative data, *Hardenability of Alloy Steels*, ASM International, Cleveland, OH, 1939.
6. A. Moser and A. Legat, Determining hardenability from composition, *Härterei Tech. Mitt. 24*(2):100–105 (1969) (in German).
7. D.J. Carney and A.D. Janulionis, An examination of the quenching constant *H*, *Trans. ASM 43*:480–496 (1951).
8. C.A. Siebert, D.V. Doane, and D.H. Breen, *The Hardenability of Steels*, ASM International, Cleveland, OH, 1997.
9. C.F. Jatczak, Hardenability in high carbon steel, *Metall. Trans. 4*:2267–2277 (1973).
10. *Metals Handbook*, ASM International, Cleveland, OH, 1948, p. 499.
11. C.F. Jatczak and D.J. Girardi, *Multiplying Factors for the Calculation of Hardenability of Hypereutectoid Steels Hardened from 1700°F*, Climax Molybdenum Company, Ann Arbor, MI, 1958.
12. W.E. Jominy and A.L. Boegehold, *Trans. ASM 26*:574 (1938).

13. These procedures are described in ASTM A 255, SAE J 406, and ISO/R 642 (1967).
14. *Metals Handbook*, 9th ed., Vol. 1, ASM International, Metals Park, OH, 1978, pp. 473–474.
15. R.A. Grange, Estimating the hardenability of carbon steels, *Metall. Trans. 4*:2231 (1973).
16. A. Rose and L. Rademacher, Weiterentwicklung des Stirnabschreckversuches zur Prüfung der Härbarkeit von tiefer einhartenden Stählen, *Stahl Eisen 76*(23):1570–1573 (1956) (in German).
17. C.F. Jatczak, Effect of microstructure and cooling rate on secondary hardening of Cr–Mo–V steels, *Trans. ASM 58*:195–209 (1965).
18. C.B. Post, M.C. Fetzer, and W.H. Fenstermacher, Air hardenability of steel, *Trans. ASM 35*:85 (1945).
19. G. Krauss, *Steels Heat Treatment and Processing Principles*, ASM International, Metals Park, OH, 1990.
20. B. Liščić, H.M. Tensi, and W. Luty, *Theory and Technology of Quenching*, Springer-Verlag, Berlin, 1992.
21. J. Field, Calculation of Jominy end-quench curve from analysis, *Met. Prog. 1943*:402.
22. W. Crafts and J.I. Lamont, *Hardenability and Steel Selection*, Pitman, London, 1949.
23. E. Just, Formel der Härtbarkeit, *Härterei Tech. Mitt. 23*(2):85–100 (1968).
24. R. Caspari, H. Gulden, K. Krieger, D. Lepper, A. Lübben, H. Rohloff, P. Schüler, V. Schüler, and H.J. Wieland, Errechnung der Härtbarkeit im Stirnabschreckversuch bei Einsatz und Vergütungsstählen, *Härterei Tech. Mitt. 47*(3):183–188 (1992).
25. J.S. Kirkaldy and S.E. Feldman, Optimization of steel hardenability control, *J. Heat. Treat. 7*:57–64 (1989).
26. J.M. Tartaglia, G.T. Eldis, and J.J. Geissler, Hyperbolic secant method for predicting Jominy hardenability; an example using 0.2 C–Ni–Cr–Mo steels, *J. Heat. Treat. 4*(4):352–364 (1986).
27. J.M. Tartgalia and G.T. Eldis, *Metall. Trans. 15A*(6):1173–1183 (1984).
28. E. Just, *Met. Prog. 96*(5):87–88 (1969).
29. T. Lund, *Carburizing Steels: Hardenability Prediction and Hardenability Control in Steel-Making*, SKF Steel, Technical Report 3, 1984.
30. *Metals Handbook*, 9th ed., Vol. 1, ASM International, Metals Park, OH, 1978, p. 492.
31. M. Asimov, W.F. Craig, and M.A. Grossmann, Correlation between Jominy test and quenched round bars, *SAE Trans. 49*(1):283–292 (1941).
32. J.L. Lamont, How to estimate hardening depth in bars, *Iron Age 152*:64–70 (1943).
33. D.V. Doane and J.S. Kirkaldy (Eds.), *Hardenability Concepts with Applications to Steel*, Proceedings of a Symposium, Chicago, Oct. 24–26, 1977, The Metallurgical Society of AIME, 1978.
34. T. Filetin, A method of selecting hardenable steels based on hardenability, *Strojarstvo 24*(2): 75–81 (1982) (in Croatian).
35. T. Filetin and J. Galinec, Software programme for steel selection based on hardenability, Faculty of Mechanical Engineering, University of Zagreb, 1994.
36. T. Filetin and B. Liščić, Determining hardenability of carburizing steels, *Strojarstvo 18*(4):197–200 (1976) (in Croatian).
37. *ASM Handbook,* 9th ed., Vol. 4, *Heat Treating*, ASM International, Metals Park, OH, 1991, p. 287.
38. A. Rose, The austenitizing process when rapid heating methods are involved, Der Peddinghaus Erfahrungsaustausch, Gevelsberg, 1957, pp. 13–19 (in German).
39. B. Liščić, S. Svaic, and T. Filetin, Workshop designed system for quenching intensity evaluation and calculation of heat transfer data. *ASM Quenching and Distortion Control*, Proceedings of First International Confererence On Quenching and Control of Distortion, Chicago, IL, 22–25 Sept. 1992, pp. 17–26.
40. N. Shimizu and I. Tamura, Effect of discontinuous change in cooling rate during continuous cooling on pearlitic transformation behavior of steel, *Trans. ISIJ 17*:469–476 (1977).
41. N. Shimizu and I. Tamura, An examination of the relation between quench-hardening behavior of steel and cooling curve in oil, *Trans. ISIJ 18*:445–450 (1978).
42. E. Just, Hardening and tempering—influencing steel by hardening, *VDI Ber. 256*:125–140 (1976) (in German).
43. W. Gerber and U. Wyss, Hardenability and ability for hardening and tempering of steels, *Von Roll Mitt. 7*(2/3):13–49 (1948) (in German).
44. B. Liščić and T. Filetin, Computer-aided evaluation of quenching intensity and prediction of hardness distribution, *J. Heat. Treat. 5*(2):115–124 (1988).

6 Steel Heat Treatment

Božidar Liščić

CONTENTS

6.1 Fundamentals of Heat Treatment 278
6.1.1 Heat Transfer 278
6.1.2 Lattice Defects 285
6.1.3 Application of TTT (IT) and CCT Diagrams 287
6.1.3.1 Isothermal Transformation Diagram 287
6.1.3.2 Continuous Cooling Transformation Diagram 288
6.1.3.3 Heat Treatment Processes for Which an IT or CCT Diagram May Be Used 292
6.1.3.4 Using the CCT Diagram to Predict Structural Constituents and Hardness upon Quenching Real Workpieces 293
6.1.3.5 Special Cases and Limitations in the Use of CCT Diagrams 298
6.1.4 Oxidation 301
6.1.4.1 Scaling of Steel 304
6.1.5 Decarburization 306
6.1.5.1 The Effect of Alloying Elements on Decarburization 308
6.1.5.2 Definitions and Measurement of Decarburization 309
6.1.6 Residual Stresses, Dimensional Changes, and Distortion 312
6.1.6.1 Thermal Stresses in the Case of Ideal Linear-Elastic Deformation Behavior 314
6.1.6.2 Transformational Stresses 315
6.1.6.3 Residual Stresses when Quenching Cylinders with Real Elastic–Plastic Deformation Behavior 317
6.1.6.4 Dimensional Changes and Distortion during Hardening and Tempering 324
6.2 Annealing Processes 330
6.2.1 Stress-Relief Annealing 330
6.2.2 Normalizing 334
6.2.3 Isothermal Annealing 339
6.2.4 Soft Annealing (Spheroidizing Annealing) 344
6.2.5 Recrystallization Annealing 349
6.2.5.1 Grain Recovery 351
6.2.5.2 Polygonization 351
6.2.5.3 Recrystallization and Grain Growth 352
6.3 Hardening by Formation of Martensite 355
6.3.1 Austenitizing 355
6.3.1.1 Metallurgical Aspects of Austenitizing 355
6.3.1.2 Technological Aspects of Austenitizing 364

6.3.2 Quenching Intensity Measurement and Evaluation Based on Heat Flux Density 374
6.3.3 Retained Austenite and Cryogenic Treatment 384
6.3.3.1 Transforming the Retained Austenite 387
6.4 Hardening and Tempering of Structural Steels 390
6.4.1 Mechanical Properties Required 390
6.4.2 Technology of the Hardening and Tempering Process 397
6.4.3 Computer-Aided Determination of Process Parameters 402
6.5 Austempering 407
References 413

6.1 FUNDAMENTALS OF HEAT TREATMENT

6.1.1 Heat Transfer

Heat treatment operations require a direct or an indirect supply of energy into the treated workpieces and its subsequent removal to effect the heating and the cooling, respectively, of these pieces. Because this chapter deals only with heat treatment operations involving the whole volume of treated workpieces, let us consider only the relevant heat transfer problems, not taking into account other heating methods connected to surface heat treatment operations. As an example, Figure 6.1 shows the temperature distribution on the cross section of a plate during heating (Figure 6.1a) and during cooling (Figure 6.1b).

In heat treatment operations, when heating or cooling the treated workpieces, nonstationary temperature fields develop in which the temperature distribution changes with time. Through the surface F of the plate of thickness s (Figure 6.1), the heat flux Q is supplied (during heating) or extracted (during cooling):

$$Q = \frac{\mathrm{d}Q}{\mathrm{d}t} = -\lambda F \frac{\mathrm{d}T}{\mathrm{d}x}, \quad x = 0, \ldots, s/2 \tag{6.1}$$

where T is temperature (K); t is time (s); λ is heat conductivity (W/(m K)); F is surface area (m^2); and $\mathrm{d}T/\mathrm{d}x$ is the temperature gradient (K/m).

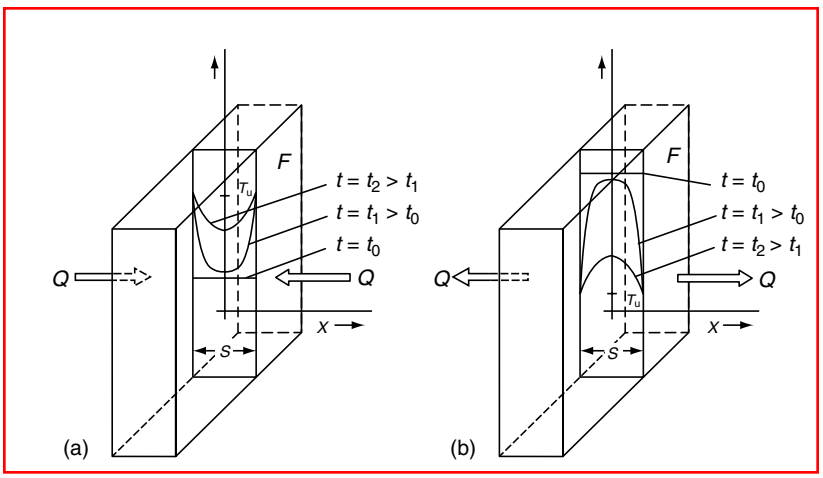

FIGURE 6.1 Temperature distribution on the cross section of a plate (a) during heating and (b) during cooling. t_0, Beginning of temperature change; T_u, surrounding temperature; Q, heat flux; s, thickness of the plate. (From G. Spur and T. Stöferle (Eds.), *Handbuch der Fertigungstechnik, Vol. 4/2, Wärmebehandeln*, Carl Hanser, Munich, 1987.)

From the other side, based on the first law of thermodynamics,

$$dQ = \rho\, dx\, FC_p\, z dT \tag{6.2}$$

where ρ is the density of the workpiece (kg/m^3) and C_p the specific heat capacity of the workpiece at constant pressure (J/(kg K)).

From Equation 6.1 it follows that

$$\frac{d}{dx}\left(\frac{dQ}{dt}\right) = -\lambda F \frac{d^2T}{dx^2} = \frac{d}{dt}\left(\frac{dQ}{dx}\right) \tag{6.3}$$

From Equation 6.2 it follows that

$$\frac{d}{dt}\left(\frac{dQ}{dx}\right) = -\rho F C_p \frac{dT}{dt} \tag{6.4}$$

and for the one-dimensional heat flux, the time-dependent temperature distribution inside the workpiece is

$$\frac{dT}{dt} = \frac{\lambda}{\rho C_p}\frac{d^2T}{dx^2} = a\frac{d^2T}{dx^2} \tag{6.5}$$

where $a = \lambda/\rho C_p$ (m^2/s) is the temperature diffusivity.

In the case of three-dimensional heat flux, Equation 6.5 reads

$$\frac{dT}{dt} = a\left(\frac{d^2T}{dx^2} + \frac{d^2T}{dy^2} + \frac{d^2T}{dz^2}\right) = a\nabla T \tag{6.6}$$

where

$$\nabla = \frac{d^2}{dx^2} + \frac{d^2}{dy^2} + \frac{d^2}{dz^2}$$

is the Laplace operator.

Equation 6.5 and Equation 6.6 are the temperature conduction equations in which the temperature diffusivity represents the amount of the time-dependent temperature change of a workpiece because of nonstationary heat conduction.

A heat flux dQ flowing through a surface of area F is, according to Fourier's heat conduction law, proportional to the temperature gradient at the relevant position:

$$dQ = -\lambda \frac{dT}{dx} F\, dt \tag{6.7}$$

or, expressed as heat flux density per unit time (s) and unit surface (m^2),

$$q = -\lambda \frac{dT}{dx} = -\lambda\, \text{grad}\, T\ [\text{W/m}^2] \tag{6.8}$$

Equation 6.8 clearly shows that the temperature gradient is the driving force of the heat flux. The heat conductivity (λ), as a proportional factor in this heat conduction equation, represents the influence of the material's properties on the heat transport. Table 6.1 gives approximate values for heat conductivity λ (in W/(m K)) for selected materials.

In the above equations, the heat conductivity λ is assumed to be a constant value, but in reality it depends on temperature. Figure 6.2 shows the temperature dependence of heat

TABLE 6.1
Approximate Values for Heat Conductivity λ, W/(m K)

Metals		Stiff inorganic materials	
Copper	350	Chamotte	0.5–1.2
Aluminum	170–230	Brick	0.8
Brass	80–115	Concrete	0.8–1.4
Gray iron	58	Mineral wool	0.05–0.1
Steel	40		
Liquids		Gases	
Water	0.6–0.7	Air (20–2000°C)	0.026–0.11
Oil	0.1–0.2	H_2 (20–2000°C)	0.18–0.75

Source: From G. Spur and T. Stöferle (Eds.), *Handbuch der Fertigungstechnik, Vol. 4/2, Wärmebehandeln*, Carl Hanser, Munich, 1987.

conductivity for groups of steel. As can be seen, the biggest differences in heat conductivity among different steel grades are at room temperature. Whereas for unalloyed steels the heat conductivity decreases with increasing temperature, for high-alloy steels it slightly increases with increasing temperature. At about 900°C (1652°F), the value of λ is almost the same for all steel grades. The specific heat capacity C_p depends also on temperature.

The transport of thermal energy through a solid body, described by the heat conduction equation (Equation 6.8), extends naturally beyond the body surface; i.e., heat transfer takes place between the body and its environment. This heat transfer is expressed as the amount of heat exchanged between the surface of the body and its environment per unit surface area and per unit time. According to Newton's law of cooling, the amount of heat exchanged between a body and its environment depends on the difference between the body surface temperature and the temperature of its environment. The relevant heat flux density is

$$q = \frac{\mathrm{d}Q}{\mathrm{d}F\mathrm{d}t} = \alpha\,(T_\mathrm{K} - T_\mathrm{U}) \quad \text{for } T_\mathrm{K} > T_\mathrm{U} \tag{6.9}$$

where T_K is the body surface temperature, T_U is the temperature of the environment, and α is the heat transfer coefficient, W/(m^2 K).

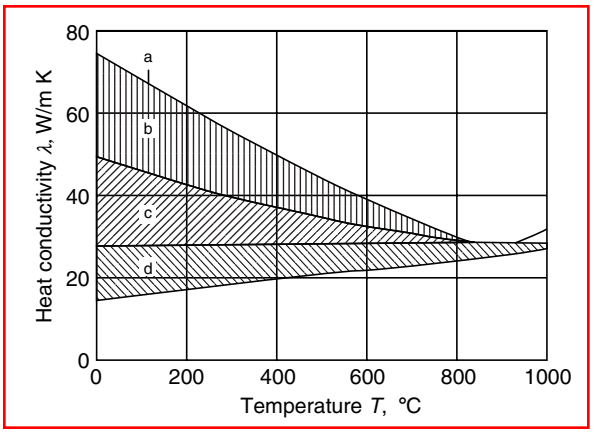

FIGURE 6.2 Temperature dependence of the heat conductivity λ for selected steel groups. (a) Pure iron; (b) unalloyed steels; (c) low-alloy steels; (d) high-alloy steels. (From G. Spur and T. Stöferle (Eds.), *Handbuch der Fertigungstechnik, Vol. 4/2, Wärmebehandeln*, Carl Hanser, Munich, 1987.)

The actual conditions of the heat transfer in each case are represented by the relevant heat transfer coefficient α, which depends on

1. The shape and cross-sectional size of the body
2. The position of the body (standing or lying)
3. The surface condition of the body
4. The physical properties of the body's material
5. The physical properties of the surrounding fluid (density, specific heat capacity, dynamic viscosity)
6. The agitation (flow) rate of the surrounding fluid

During every heating or cooling process, the temperature difference between the body surface and its environment becomes smaller with time, i.e., the exchanged heat quantity becomes smaller. The heat transfer coefficient α is therefore not a constant but varies with the body surface temperature.

Gases, liquids, and vacuums are the environments in which heat transfer occurs during heat treatment operations. Heat can be transferred by three different heat transfer mechanisms: heat conduction, heat convection, and heat radiation.

Heat conduction (in fluids) is the heat transfer that occurs in a nonagitated liquid or gaseous medium between directly adjoining particles owing to a temperature gradient.

Heat convection is directly connected to the movement (flow or agitation) of the heat-carrying fluid, because it is realized through movement of the fluid particles from one place to another. Therefore heat convection is possible only in liquids and gases. The amount of heat transferred by heat convection in a gas also depends on the number of particles in the gas. Because this number depends on gas pressure, heat convection is proportional to gas pressure.

If the only cause of particle movement is the difference in density caused by the temperature difference, the movement is called free or natural convection. When the movement of particles of the fluid is caused by an outside force, the movement is called forced convection. Generally, free and forced convections take place simultaneously. The amount of free convection contributing to the heat transfer depends on the temperature gradient within the fluid, and the contribution of the forced convection depends on the flow velocity, i.e., on the agitation rate.

When an air stream passes toward a cylinder, the convective heat transfer coefficient α_K can be calculated, according to Eckstein [2], by using the formula

$$\alpha_K = (4.64 + 3.49 \times 10^{-3}\Delta T)\frac{v^{0.61}}{D^{0.39}} \ [\mathrm{W/(m^2\,K)}] \tag{6.10}$$

where D is the diameter (m); ΔT is the temperature difference between air and cylinder surface; and v is the air velocity (m/s).

The third heat transfer mechanism is heat radiation. Solid bodies, liquids, and gases can all transfer heat in the form of radiation. This kind of heat transfer does not depend on any heat transfer carrier; therefore, it can take place in vacuum also. Heat radiation is in the form of electromagnetic waves whose length is in the range of 0.3–500 μm. When radiation strikes the surface of a body, part of it will be absorbed, part of it will be reflected, and the rest may pass through the body. Every body emits radiation corresponding to its temperature. The body that, at a certain temperature, emits or absorbs the largest amount of radiation is called a blackbody. All other bodies emit or absorb less radiation than the blackbody. The ratio of the radiation of a body to that of a blackbody is called the emission-relation coefficient ε.

The total heat flux density emitted by radiation from a body can be calculated according to the Stefan–Boltzmann law

$$q = \varepsilon\sigma T^4 \tag{6.11}$$

where ε is the emission-relation coefficient, $\varepsilon < 1.0$; σ is the Stefan–Boltzmann constant, $\sigma = 5.67 \times 10^{-8}$ W/(m^2 K^4); and T is the absolute temperature (K).

If two bodies mutually exchange radiant heat, then not only is the warmer body emitting heat to the colder one, but the colder body is also emitting heat to the warmer body, so that the transferred heat consists of the difference of the amounts of heat absorbed by the two bodies. The total heat transferred by radiation from one body having a surface area F_1 to another solid body of any surface area can be calculated according to

$$Q = \varepsilon_{1,2}\sigma F_1(T_1^4 - T_2^4) \tag{6.12}$$

where $\varepsilon_{1,2}$ is the emission-relation coefficient, which depends on the emission-relation coefficients of both bodies, their surface relation, and their mutual position in space; T_1 is absolute temperature of the emitting body; and T_2 is absolute temperature of the absorbing body.

In industrial furnaces, heat is transferred substantially by simultaneous heat convection and heat radiation. The heat transferred by heat conduction (in fluids) is negligible compared to the heat transferred by convection and radiation. When calculating the total heat transferred by both mechanisms, it is appropriate to express the heat transferred by radiation with a formula similar to Newton's law

$$q = \alpha_\varepsilon(T_1 - T_2) \tag{6.13}$$

The heat transfer coefficient for radiation α_ε can be calculated by combining Equation 6.12 and Equation 6.13:

$$\alpha_\varepsilon = \varepsilon_{1,2}\sigma\frac{T_1^4 - T_2^4}{T_1 - T_2} \tag{6.14}$$

The total heat transfer coefficient is then

$$\alpha = \alpha_k + \alpha_\varepsilon \tag{6.15}$$

where α_k is the heat transfer coefficient for convection.

Table 6.2 gives, according to Eckstein [2], the average values of the heat transfer coefficient for cooling or quenching in liquid or gaseous media. This complex heat transfer coefficient depends in each case on many specific factors, discussed earlier, but also depends strongly on the surface temperature of the workpiece. It is a temperature-dependent and location-dependent value that changes during heat transfer as the body surface temperature equalizes to the environment's temperature. According to Eckstein [2], the complex heat transfer coefficient can increase 30 to 50 times between 50 and 1500°C (122 and 2732°F). At temperatures below 300°C (572°C), heat transfer by convection is predominant. With increasing temperature, heat transfer by radiation becomes more important, and at about 800°C (1472°F) it reaches 80% of the total heat transfer.

Especially in operations that employ immersion quenching in liquids, where two-phase heat transfer takes place with high heat flux densities under nonstationary conditions, the heat transfer coefficient value changes very much. Therefore nowadays when heat transfer calculations are carried out by computer a temperature-dependent function of the heat transfer coefficient instead of an average value should be used. One practical way to obtain this function in each actual case is to measure the surface temperature of an adequately instrumented probe (cylinder or plate of adequate dimensions) placed appropriately in the quenching tank and, from the measured surface temperature vs. time history, calculate the corresponding heat flux density and heat transfer coefficient vs. temperature functions.

TABLE 6.2
Average Values of the Heat Transfer Coefficient α When Cooling or Quenching in Liquid or Gaseous Media

Medium	α [W/(m^2 K)]
Furnace	15
Still air	30
Moving air	40
Compressed air	70
Air–water mixture	520
Hardening oil	580
Liquid lead	1200
Water	3500

Source: From H.J. Eckstein (Ed.), *Technologie der Wärmebehandlung von Stahl*, 2nd ed., VEB Deutscher Verlag für Grundstoffindustrie, Leipzig, 1987.

Figure 6.3 shows, as an example, the heat transfer coefficient vs. surface temperature for quenching a stainless steel cylinder of 50-mm diameter × 200 mm in still oil of 20°C (68°F) [3]. If there is no adequate thermocouple to measure the surface temperature of the probe, the temperature can be measured near the surface and, by using the inverse heat conduction method and an adequate mathematical procedure finite element method (FEM), the surface temperature of the probe can be calculated.

To explain the dependence between the heat transfer conditions and the temperature fields in solid bodies, let us consider the heating of a plate of thickness s (see Figure 6.4). At the beginning of heating ($t = 0$), the plate has a temperature $T_K = 0$ and is suddenly transferred in standing position into a furnace, where the environmental temperature is T_U. Equal amounts of heat are transferred from both sides of the plate. Because boundary conditions of the third

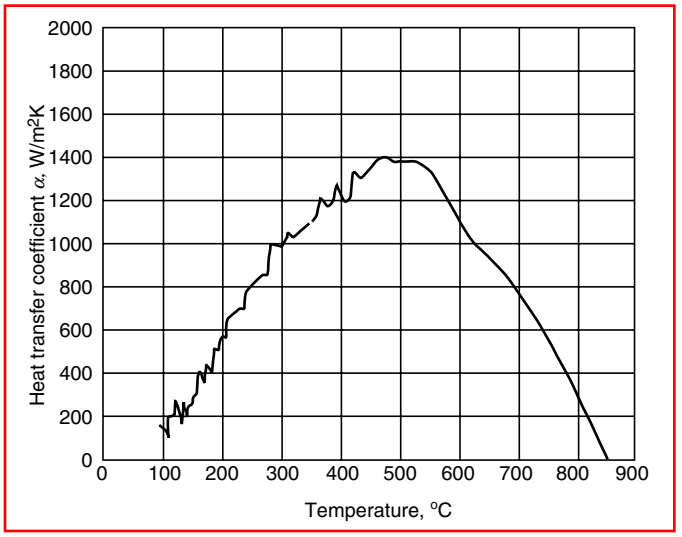

FIGURE 6.3 Heat transfer coefficient vs. surface temperature when quenching a stainless steel cylinder of 50-mm diameter × 200 mm in still oil of 20°C, calculated from the measured surface temperature–time history. (From B. Liščić, S. Švaić, and T. Filetin, Workshop designed system for quenching intensity evaluation and calculation of heat transfer data, *Proceedings of the First International Conference on Quenching and Control of Distortion*, Chicago, IL, September 1992, pp. 17–26.)

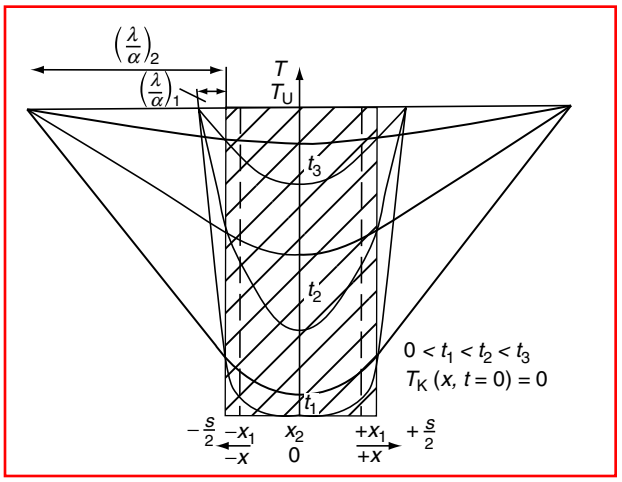

FIGURE 6.4 Change of the temperature distribution with time when heating a plate of thickness s, depending on different heat transfer conditions expressed by the ratio λ/α. (From H.J. Eckstein (Ed.), *Technologie der Wärmebehandlung von Stahl*, 2nd ed., VEB Deutscher Verlag für Grundstoffindustrie, Leipzig, 1987.)

kind exist, the ratio between the heat conductivity and the heat transfer coefficient (λ/α) gives a point at temperature T_U outside the plate. The straight line connecting this point and the relevant surface temperature is the tangent on the temperature distribution curve at the body surface. As time progresses, both the surface temperature and the temperature in the middle of the plate increase. The temperature gradient inside the body is different for different λ/α ratios and changes over time. If the heat conductivity λ of the body's material is small or the heat transfer between the environment and the body surface is large, the ratio λ/α is small and heat accumulates in the surface region because the amount of heat transferred is greater than the amount transported by conduction into the body's interior. The smaller the ratio λ/α, the faster the surface temperature equalizes to the temperature of the environment. The relevant changes of temperature at points x_1 and x_2 and the value and the change in the temperature gradient over time are also greater. This can be seen in Figure 6.5 when comparing the curves for $(\lambda/\alpha)_1$ small to $(\lambda/\alpha)_2$ big. If the heat conductivity λ is big or the heat transfer coefficient α is small, i.e.,

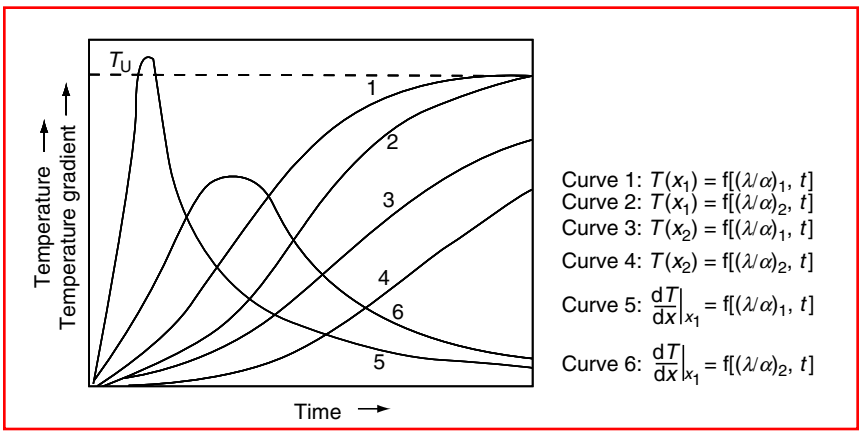

FIGURE 6.5 Change of the plate temperatures at points x_1 and x_2 and temperature gradients at point x_1 in the cross section of the plate shown in Figure 6.4 when different heat transfer conditions $(\lambda/\alpha)_1$ and $(\lambda/\alpha)_2$, respectively, exist. (From H.J. Eckstein (Ed.), *Technologie der Wärmebehandlung von Stahl*, 2nd ed., VEB Deutscher Verlag für Grundstoffindustrie, Leipzig, 1987.)

the heat is transported from the surface to the core of the body faster than it is transferred from the environment to the body's surface, the λ/α ratio becomes big, and the temperature in the interior of the body increases relatively faster than the surface temperature.

Other factors that should be taken into account when analyzing such heat transfer problems are the shape and cross-sectional size of the body. As to the influence of different shapes of workpieces it should be borne in mind that at constant heat transfer conditions and constant thermal properties of the material and equal temperature of the environment, the temperature change with time depends on the surface-to-volume ratio of the body. The greater the ratio is, the greater is the temperature change over time.

6.1.2 Lattice Defects

Generally the lattice of a metal crystal contains imperfections, i.e., aberrations from a perfect atomic arrangement. These imperfections may be divided, from the geometrical standpoint, into the following categories:

Zero-dimensional or point imperfections
One-dimensional or linear
Two-dimensional or superficial
Three-dimensional or spatial

The most important lattice defects that occur in metals are shown schematically in Figure 6.6. Figure 6.6a shows a plane consisting of equal regular atoms *a* of which the spatial lattice is built, with four different types of lattice point defects. At position *b* one atom is missing; this defect is called a vacancy. Atom *c* occupies a place between the regular places in the lattice and it is called an interlattice atom; in this case *c* is the same kind of atom as the regular atoms. In position *d*, a strange atom (of an alloying element) with a larger diameter has taken the place of a regular atom; therefore it is called a substitutional atom. A practical example of this is a manganese atom dissolved in iron. In position *e*, a strange atom with a much smaller diameter than the regular atoms of the lattice is inserted between regular atoms in a position that is not occupied by regular atoms. It is called an interstitial atom. A practical example of this is a carbon atom dissolved in iron. Both substitutional and interstitial atoms cause local deformations and microstresses of the crystal lattice.

Figure 6.6b shows at *f* a linear lattice defect. A row of atoms in the outlined atomic plane terminates at this point. If we imagine the outlined atomic plane as a section through a crystal that stretches perpendicular to the plane shown, then the row of atoms terminating at *f* becomes a half-plane of atoms that has been inserted between regular planes of atoms and ends inside the crystal. The boundary line of the inserted half-plane of atoms that stretches through the greater lattice region, perpendicular to the plane shown, is a linear lattice defect called an edge dislocation. Every edge dislocation is connected with characteristic deformations and microstresses of the lattice.

The lattice defects *g* and *h* are superficial defects. The line *g–g* represents schematically a low-angle grain boundary that consists of edge dislocations arranged regularly one under the other. The inserted half-plane of each edge dislocation terminates at the associated atom shown in black. The dashed area is a section through a low-angle grain boundary between neighboring parts of the crystal lattice that are inclined at a low angle to each other. The line *h–h* represents a twinning boundary. It is characterized by the fact that the atoms on both sides of the boundary are symmetrically distributed, and therefore neighboring parts of the crystal lattice are completely equal, looking like twins in a mirror.

Figure 6.6c shows at *i* a superficial imperfection (in the outlined plane) where a group of atoms is missing. This zone of missing atoms could have developed by way of an accumulation of vacancies. It can be stretched to other planes of atoms perpendicular to the outlined one. The imperfection *k* is a more or less irregular distribution of atoms between two neighboring parts of

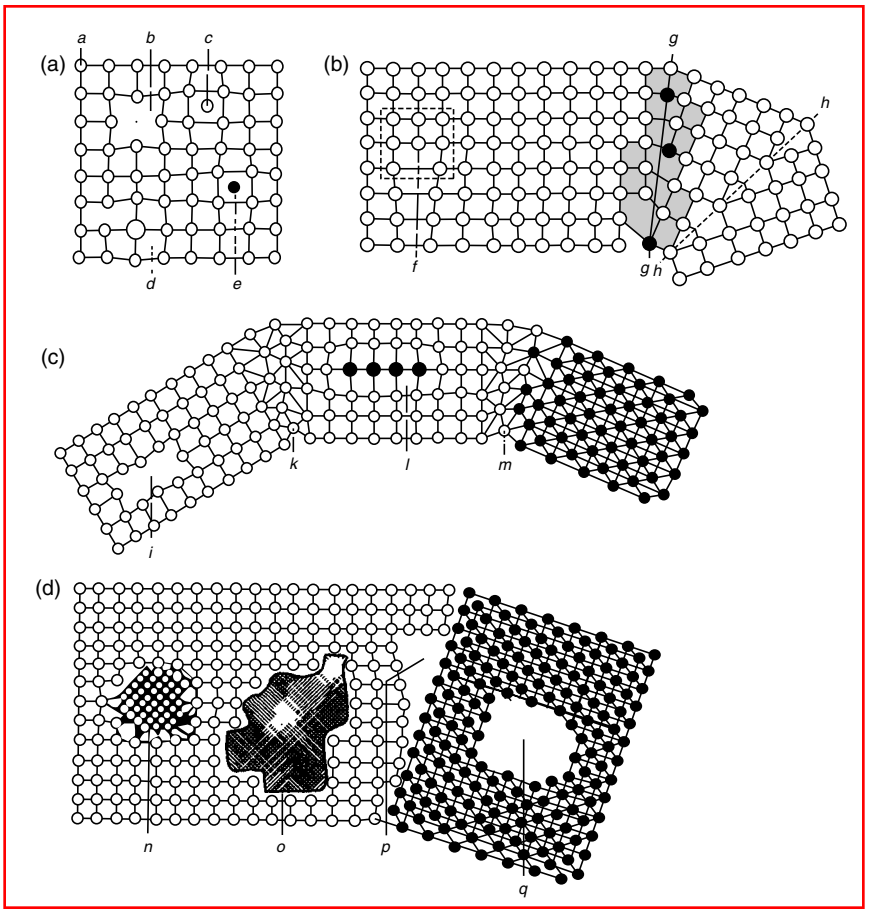

FIGURE 6.6 Lattice defects. (a) Lattice point defects; (b) linear and superficial lattice defects; (c) superficial lattice defects; (d) spatial lattice defects. *a*, Regular lattice atom; *b*, vacancy; *c*, interlattice atom; *d*, substitutional atom; *e*, interstitial atom; *f*, edge dislocation; *g*, low-angle grain boundary; *h*, twinning boundary; *i*, vacancy zone; *k*, high-angle grain boundary; *l*, strange atoms zone; *m*, phase boundary; *n*, precipitate; *o*, inclusion; *p*, microcrack; *q*, micropore. (From G. Spur and T. Stöferle (Eds.), *Handbuch der Fertigungstechnik, Vol. 4/2, Wärmebehandeln*, Carl Hanser, Munich, 1987.)

the crystal lattice with big differences in orientation, which interrupts the continuity of the lattice. It is called a high-angle grain boundary, or simply a grain boundary. The superficial imperfection at *l* is a section through a zone of strange atoms that stretches in two dimensions perpendicular to the plane shown. The boundary plane *m* between two different lattices is called a phase boundary, which is also a two-dimensional lattice defect.

Figure 6.6d shows schematically the characteristic three-dimensional lattice defects. In many metal alloys, within the lattice of grains under specific thermodynamic conditions, new lattice regions with changed structure are formed. Such a lattice defect shown at *n* is called a precipitate. The spatial imperfection at *o* is called an inclusion. Such inclusions, which develop unfailingly during the production of alloys, are nonmetallic or intermetallic compounds. Like precipitates, inclusions have their own structure and phase and are separated by a phase boundary from the surrounding lattice. Microcrack is denoted by *p*, a spatial imperfection that is created by three edge dislocations that came to a phase boundary and formed a hollow among the three half-planes of the lattice. The hollow stretches perpendicular or at a slope to the plane shown. At *q* a sphere-like hollow inside the crystal's lattice is

shown; this is called a micropore. Such defects can originate from the accumulation of either vacancies or gases.

Of all the lattice defects discussed above, vacancies and edge dislocations are especially important in the heat treatment of metals. Vacancies enable neighboring atoms or substitutional atoms of alloying elements to change their positions and thus enable diffusion processes. The diffusion of interstitial atoms (e.g., a carburizing process) is possible without vacancies. Dislocations can move, increase in number, and accumulate. By lowering the share force (as a consequence of the intermittent movement of the atoms), compared to the case of a perfect iron crystal (whisker), dislocations facilitate the plastic deformation of the material.

6.1.3 Application of TTT (IT) and CCT Diagrams

Time–temperature–transformation diagrams for isothermal transformation (IT diagrams) and for continuous cooling transformation (CCT diagrams) are used to predict the microstructure and hardness after a heat treatment process or to specify the heat treatment process that will yield the desired microstructure and hardness. The use of the either type of diagram requires that the user be acquainted with its specific features, possibilities, and limitations.

6.1.3.1 Isothermal Transformation Diagram

Figure 6.7 shows an IT diagram of the low-alloy steel DIN 50CrV4. The regions of transformation of the structural phases ferrite (F), pearlite (P), and bainite (B) as positioned in the time–temperature diagram (the abscissa of which is always in logarithmic scale) are valid only under conditions of fast quenching from the austenitizing temperature to the chosen transformation temperature and subsequent holding at that temperature. This is the way

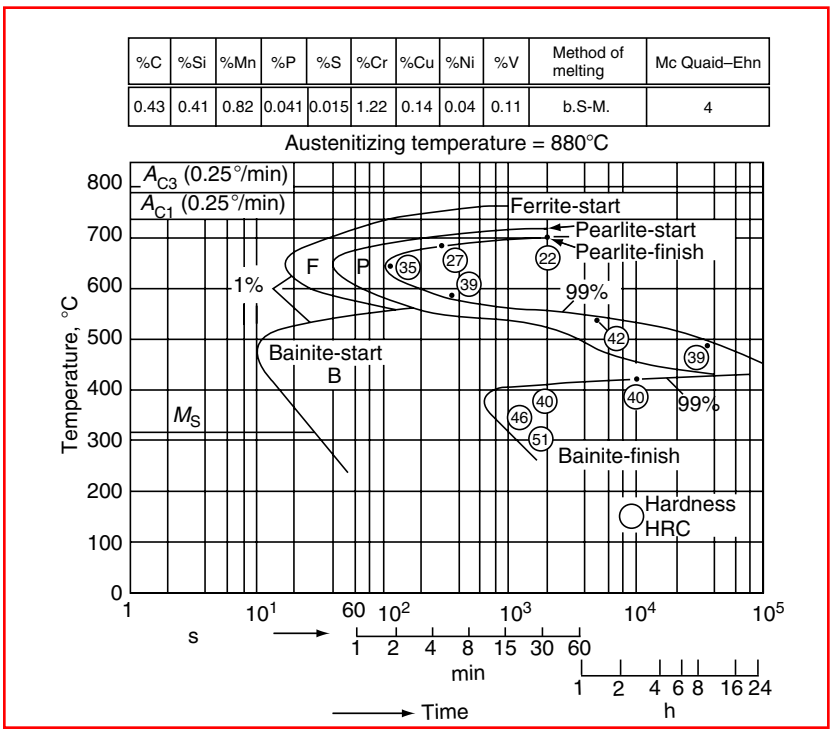

FIGURE 6.7 Isothermal transformation (IT) diagram of DIN 50CrV4 steel. (From A. Rose and W. Strassburg, *Archiv. Eisenhüttenwes. 24*(11/12):505–514, 1953 [in German].)

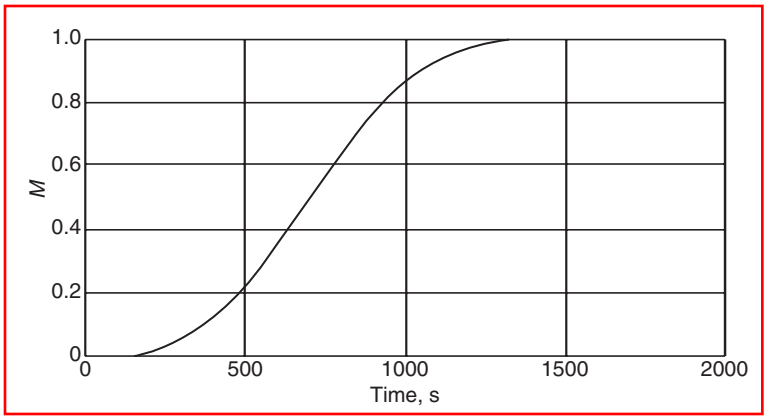

FIGURE 6.8 Relation between the amount of transformed structure (M) and time in IT diagrams, according to Equation 6.16. (From H.P. Hougardy, *Härterei-Tech. Mitt. 33*(2):63–70, 1978 [in German].)

the diagram itself was developed. Therefore the IT diagram may be read only along the isotherms. The beginning and end of transformation of ferrite, pearlite, and bainite in isothermal processes take place according to the function

$$M = 1 - \exp(-bt^n) \tag{6.16}$$

where M is the fraction of phase transformed; t is time (s); and $b = 2 \times 10^{-9}$ and $n = 3$.

Because, as shown in Figure 6.8, this function starts and ends very flat, the actual beginning and end of transformation are difficult to determine exactly. Therefore, an agreement is reached, according to which the curve marking the beginning of transformation denotes 1% of relevant phase originated, and the curve marking the end of transformation denotes 99% of the austenite transformed.

Only the formation of martensite takes place without diffusion, instantly, depending only on the temperature below the M_s point. Hougardy [5] gave the following formula (valid for structural steels for hardening and tempering) for this transformation:

$$M_a = 1 - 0.929 \exp[-0.976 \times 10^{-2}(M_s - T)^{1.07}] \tag{6.17}$$

where M_a is the amount of martensite, M_s is the martensite start temperature, and T is a temperature below M_s.

Some IT diagrams, when read along the isotherms, enable the user to determine the percentages of phases transformed and the hardness achieved. Figure 6.9, for example, shows that when the DIN 41Cr4 steel (austenitized at 840°C (1544°F) with 5-min holding time) is fast quenched to 650°C (1200°F) and held at this temperature, after 12 s ferrite starts to form. After 30 s the formation of pearlite begins. After 160 s the transformation is completed with 5 vol% of ferrite and 95 vol% of pearlite formed. The hardness achieved is about 20 HRC. If a specimen of this steel is quenched to 300°C (572°F), instantly, 50% (v/v) of martensite will be formed.

The accuracy of an IT diagram with respect to the position of isotherms can generally be taken as ±10°C (50°F), and with respect to the time ordinates, as ±10%.

6.1.3.2 Continuous Cooling Transformation Diagram

Figure 6.10 shows the CCT diagram of the same heat (as Figure 6.7) of the low-alloy DIN 50CrV4 steel.

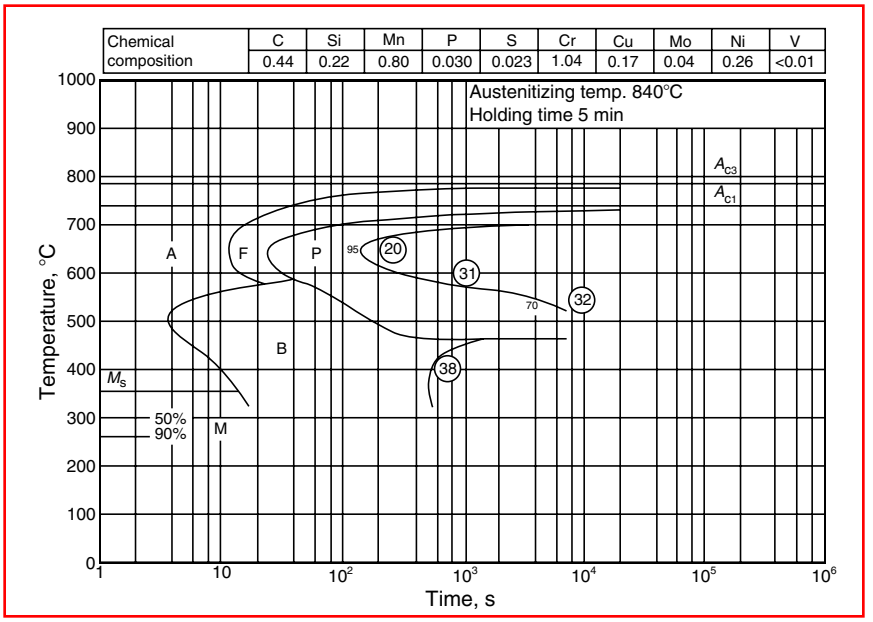

FIGURE 6.9 Isothermal transformation (IT) diagram of DIN 41Cr4 steel. (From H.P. Hougardy, *Härterei-Tech. Mitt. 33*(2):63–70, 1978 [in German].)

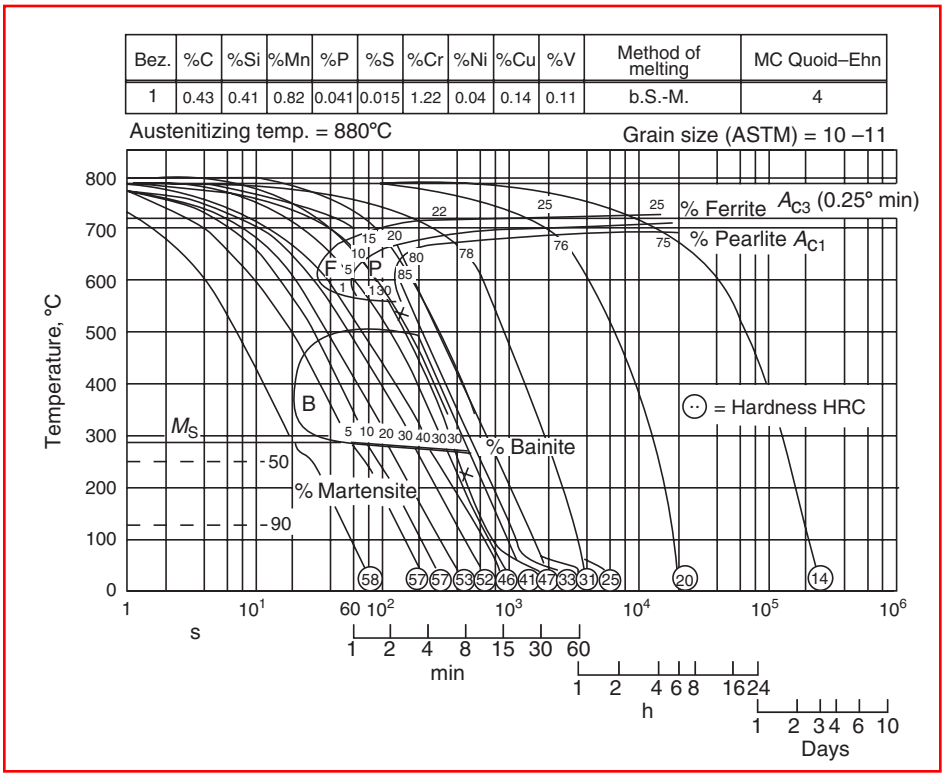

FIGURE 6.10 Continuous cooling transformation (CCT) diagram of DIN 50CrV4 steel. (From A. Rose and W. Strassburg, *Archiv. Eisenhüttenwes. 24*(11/12):505–514, 1953 [in German].)

When comparing the curves for the start of transformation in CCT and IT diagrams for the same heat and steel grade (Figure 6.7 and Figure 6.10), we found that in the CCT diagram the curves are slightly shifted to longer times and lower temperatures. For example, in the IT diagram of Figure 6.7, the shortest time to start the transformation of ferrite is 16 s at 650°C (1200°F) and the corresponding time for bainite is 9 s at 480°C (900°F). In the CCT diagram of Figure 6.10, however, the shortest transformation start time for ferrite is 32 s at 620°C (1150°F) and the corresponding time for bainite is 20 s at 380°C (716°F). This indicates that in CCT processes the transformation starts later than in IT processes. The basis of this phenomenon is related to the incubation time and can be found in a hypothesis of Scheil [6].

It should also be noted that with higher austenitizing temperature the curves denoting the start of transformation of a particular phase can be shifted to longer times. Figure 6.11 shows the CCT diagram of DIN 16MnCr5 steel after austenitizing at 870°C (1600°F) (a), and after austenitizing at 1050°C (1922°F) (b). In the latter case, the regions of ferrite and pearlite are shifted to longer times. It is necessary, therefore, when using a CCT diagram, to ascertain that the austenitizing temperature used to develop the CCT diagram corresponds to the austenitizing temperature of the parts treated.

A CCT diagram is developed in the following way. Many small specimens (e.g., 4-mm diameter $\times$ 2 mm for high cooling rates, and 4.5-mm diameter $\times$ 15 mm for medium and low cooling rates) are austenitized and cooled within a dilatometer with different cooling rates. Start and finish of transformation of relevant phases with each cooling curve are recorded and these points are connected to obtain the regions of transformation for the relevant phases (see Figure 6.10). Therefore, a CCT diagram can be read only in the way in which it was developed, i.e., along the cooling curves. As can be seen from Figure 6.10, a single-phase structure occurs only in cases of very high cooling rates (martensite) and very slow cooling rate (pearlite). In all other cooling regimes a mixture of more structural phases results. How much of each phase such a mixture contains can be read in percentage from the numbers along the cooling curve (usually marked in CCT diagrams of German origin). The numbers at the end of each cooling curve denote the relevant hardness after quenching (usually in HRC (two-digit numbers) or in HV (three-digit numbers)). For example, as shown in Figure 6.10 for grade DIN 50CrV4 steel, if cooling proceeds at the rate marked with $\times$, a mixture of 10% ferrite, 30% pearlite, 30% bainite, and (the rest) 30% martensite will result at room temperature, and the hardness after quenching will be 47 HRC. It should be noted that the part of the area (region) of a phase that the cooling curve intersects is by no means a measure of the amount of transformed phase.

Sometimes a CCT diagram can be supplemented with a diagram showing portions of each structural phase and hardness after quenching; see the lower part of Figure 6.12. The abscissa of this diagram denoting time enables the cooling time to 500°C (932°F) to be determined for every cooling curve. To determine the portions of structural phases and hardness after quenching, one should follow the relevant cooling curve until its intersection with the 500°C (932°F) isotherm and from this point down along the vertical line read the phase portions and hardness after quenching. For example, for cooling curve C, which intersects the 500°C (932°F) isotherm at 135 s, the readings are 4% ferrite, 7% pearlite, 78% bainite, and 11% martensite and a hardness of 34 HRC.

It should be noted that every CCT diagram is exactly valid only for the heat of a steel that was used for its construction. The influence of different heats (having slightly different compositions) of the same grade of steel on the position of transformation curves in the relevant CCT diagram, as an example, is shown in Figure 6.13.

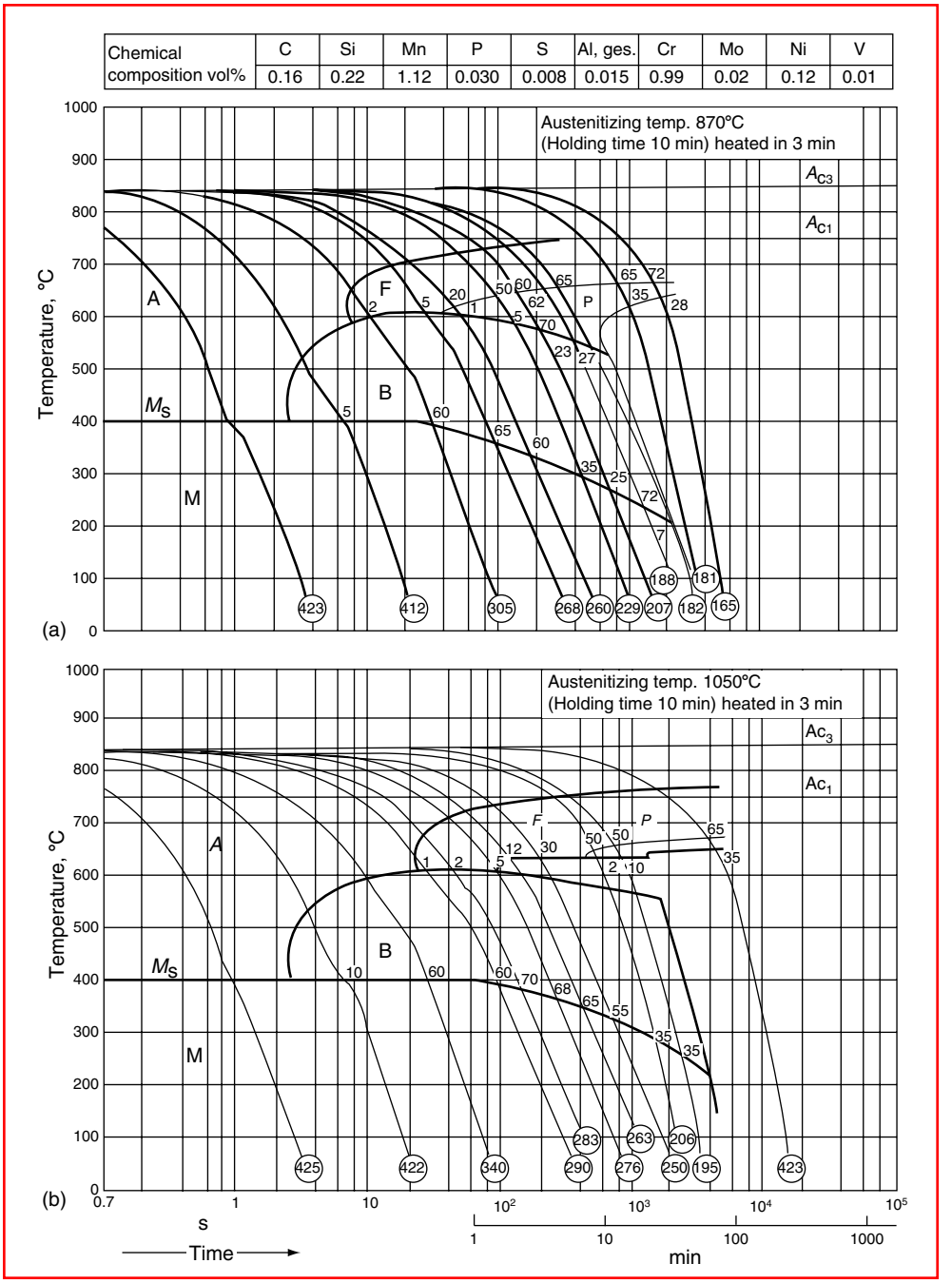

FIGURE 6.11 CCT diagrams of DIN 16MnCr5 steel (a) when austenitizing temperature is 870°C and (b) when austenitizing temperature is 1050°C. (From F. Wever and A. Rose (Eds.), *Atals zur Wärmebehandlung der Stähle*, Vols. I and II, Verlag Stahleisen, Düsseldorf, 1954/56/58.)

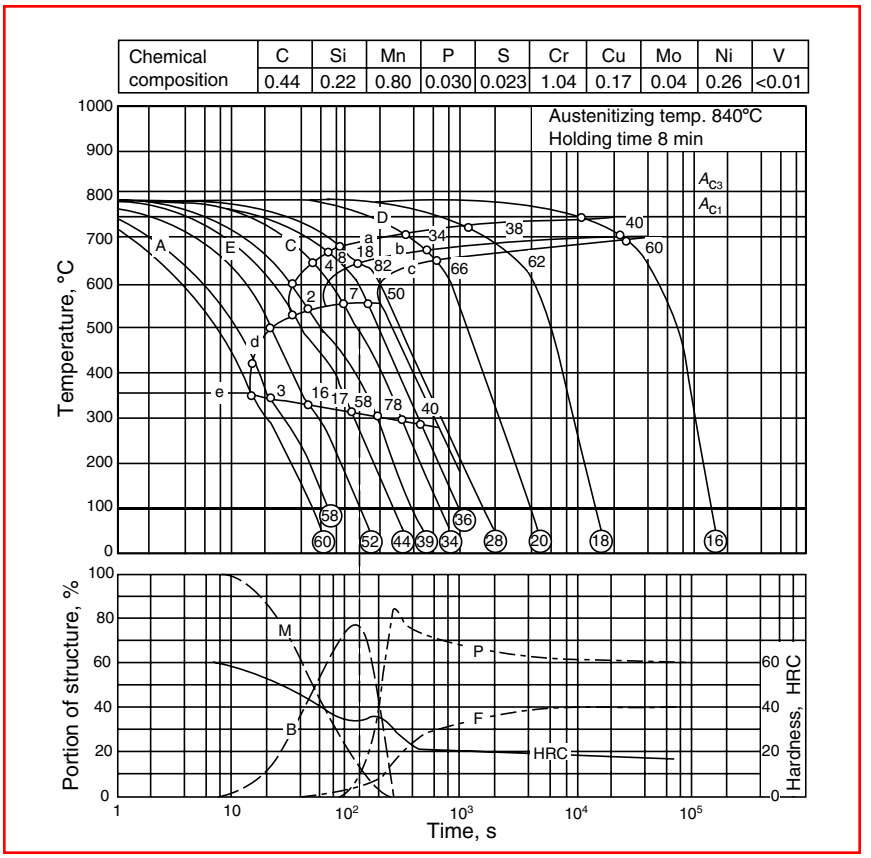

FIGURE 6.12 CCT diagram of 41Cr4 steel (top) with the diagram at bottom showing portions of each structural phase and hardness after quenching depending on the cooling time to 500°C. (From H.P. Hougardy, *Härterei-Tech. Mitt. 33*(2):63–70, 1978 [in German].)

As for IT diagrams, the accuracy of a CCT diagram, according to Hougardy [5], with respect to the position of isotherms is ±10°C (50°F) and with respect to time ordinates ±10% of the relevant time.

6.1.3.3 Heat Treatment Processes for Which an IT or CCT Diagram May Be Used

Taking into account what was explained above about how IT and CCT diagrams can be read, Figure 6.14 shows the isothermal heat treatment processes for which only IT diagrams may be used. The first is isothermal annealing to obtain a coarse ferritic–pearlitic structure, for better machinability (Figure 6.14a). In this case, the IT diagram gives the crucial information, the optimum temperature at which annealing should take place to achieve the full transformation in the shortest possible time.

The second process is isothermal transformation to bainite, i.e., the austempering process (Figure 6.14b). In this case, the IT diagram is used first of all to ascertain that the steel in question is applicable for this process, i.e., has enough hardenability (which means that its start of transformation curves are not too close to the ordinate). If this condition is fulfilled, the diagram enables the heat treater to select the appropriate temperature according to the hardness desired and read the minimum time needed at this temperature to achieve the full transformation to bainite.

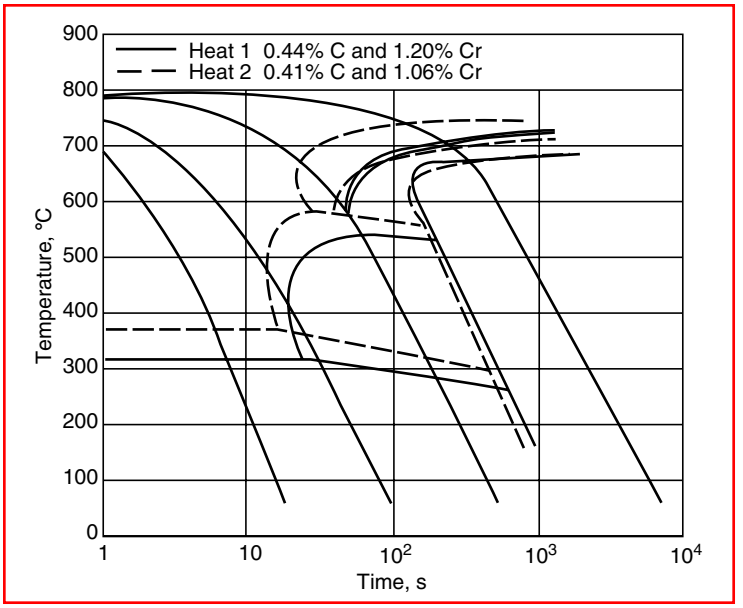

FIGURE 6.13 Influence of the difference in composition between two heats of DIN 41Cr4 steel on the position of transformation curves in the relevant CCT diagram. (From H.P. Hougardy, *Härterei-Tech. Mitt. 33*(2):63–70, 1978 [in German].)

The third process is the martempering process (Figure 6.14c), an interrupted quenching in a hot bath to obtain the martensite structure with minimum stress and distortion. The applicability of a steel for the martempering process may be checked in the same way as above. In this case the diagram gives information about the necessary temperature of the hot bath and the maximum time the parts can be immersed in it (in order to obtain only martensite) before they are taken out to be cooled in air.

Figure 6.15 shows, as an example, the only three cases of continuous cooling for which only a CCT diagram may be used. The first case (Figure 6.15a) is direct quenching to obtain full martensitic structure. In this case the diagram enables the user to determine the critical cooling rate for the steel in question. The second case (Figure 6.15b) is a continuous slow cooling process, e.g., cooling in air after normalizing annealing. In this case the diagram enables the user to select the cooling rate required to yield the desired hardness of the ferritic–pearlitic structure at room temperature. The percentage of ferrite and pearlite can be read as described above if the diagram allows it. The third case (Figure 6.15c) represents any continuous cooling regime that results in more than two structural phases. In any of these cases the diagram enables the user to determine the portion of each phase and the hardness after quenching.

6.1.3.4 Using the CCT Diagram to Predict Structural Constituents and Hardness upon Quenching Real Workpieces

Each CCT diagram describes only those transformations of the structure that occur along the cooling curves of specimens used for its construction. This means that a CCT diagram is valid only for the cooling conditions under which it was constructed. The cooling law for the specimens of small diameter and small volume that were used in constructing the CCT diagram can, according to Rose and Strassburg [4], be described by the exponential function

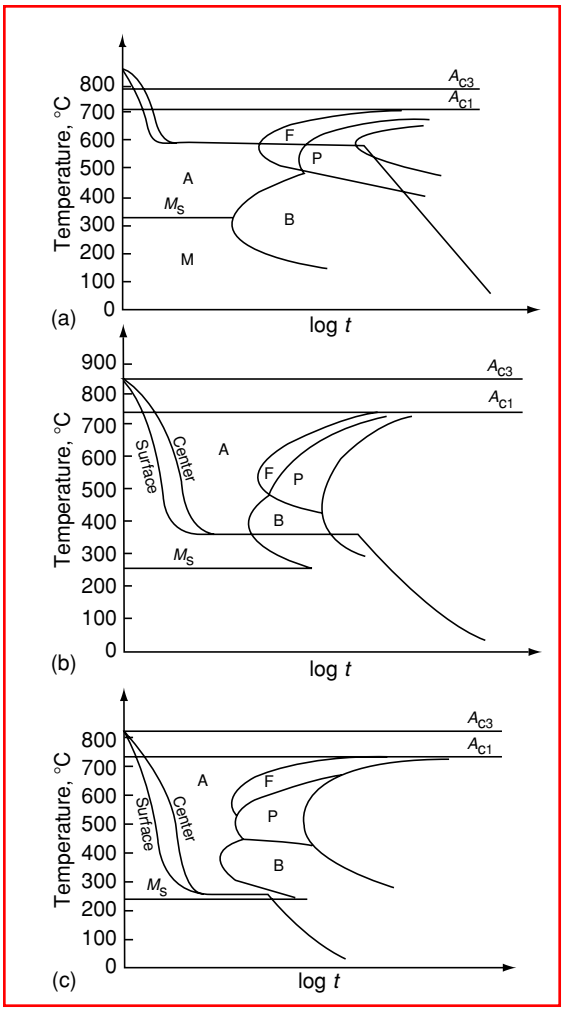

FIGURE 6.14 Isothermal heat treatment processes for which only IT diagrams may be used. (a) Isothermal annealing; (b) austempering; (c) martempering.

$$T = T_0 e^{-\alpha t} \tag{6.18}$$

where T_0 is the austenitizing temperature, α the heat transfer coefficient, and t the time.

The exactness of the predictions of structural constituents (phases) and hardness values upon quenching depends on the extent to which the cooling law at different points in the cross section of real workpieces corresponds to the cooling curves of specimens drawn in the CCT diagram. Experimental work [4] using round bars of 50-mm diameter × 300 mm with thermocouples placed 1, 5, 10, 15, and 25 mm below the surface showed that the cooling curves in different points of a round bar's cross section correspond in form to the cooling curves in CCT diagrams to the extent that the structural transformation, i.e., the resulting structural constituents and hardness values, can be compared. Figure 6.16 shows how a hardness distribution can be predicted by using this correspondence.

If the temperature–timescales of the measured cooling curves and the CCT diagram are the same (as in Figure 6.16a and Figure 6.16b), then by using a transparent sheet of paper the

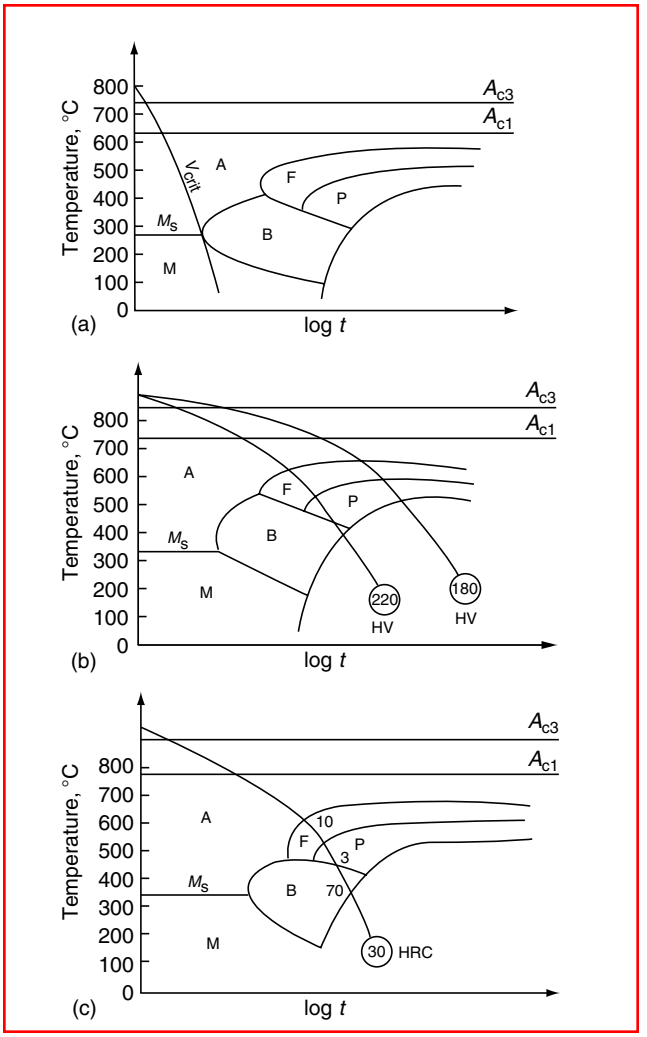

FIGURE 6.15 Heat treatment processes with continuous cooling for which only CCT diagrams may be used. (a) Direct quenching to obtain full martensitic structure; (b) slow cooling to obtain a ferrite–pearlite structure of required hardness; (c) continuous cooling regime where a mixed structure is obtained.

measured cooling curves on CCT diagrams of different steel grades can be superimposed, and in this way steel grade can be selected that will develop the required structure and hardness at the desired point of the cross section. The accuracy of such prediction from a CCT diagram decreases as the radius of the workpiece's cross section increases. According to Peter and Hassdenteufel [8], sufficiently exact predictions are possible using CCT diagrams for round bars up to 100 mm in diameter when quenching in oil and up to 150 mm in diameter when quenching in water.

It appears that the main problem in the practical use of CCT diagrams for prediction of structural constituents and hardness upon quenching is to establish exactly the cooling curve for the specified point on the workpiece's cross section. This can be done either by calculation (if symmetrical parts and one-dimensional heat flow are involved and the boundary conditions are known) or experimentally (for asymmetric parts) by measuring the

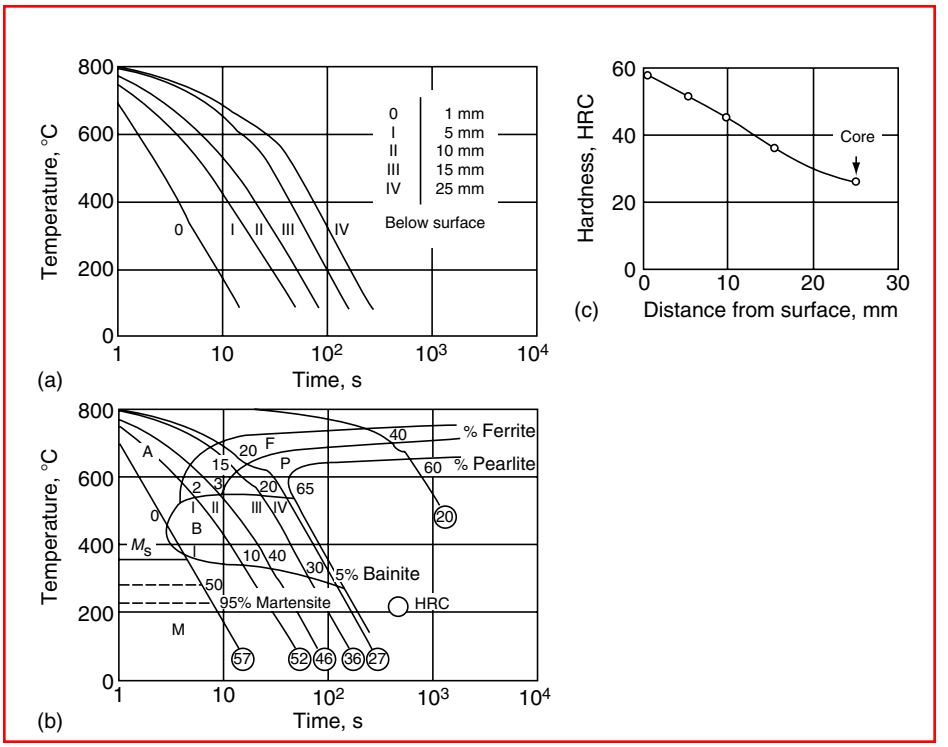

FIGURE 6.16 Prediction of hardness distribution on a round bar cross section. (a) Cooling curves measured at different points below surface, as indicated. (b) CCT diagram of the relevant steel with superimposed cooling curves from (a). (c) Hardness distribution on the bars' cross section upon quenching, obtained by reading the hardness values from (b).

temperature–time history with a thermoelement. The correspondence between cooling curves of real workpieces and cooling curves drawn on CCT diagrams also enables the reverse, to draw conclusions about the cooling history (curve) at a specified point of the cross section of a workpiece of any shape and size based on metallographic analysis of the structure and measured hardness upon quenching.

When CCT diagrams (of American origin) are used, the manner of predicting structural constituents and hardness is slightly different. For example, in Figure 6.17, instead of dilatometric cooling curves, cooling curves taken at different distances from the quenched end of the Jominy test specimen are superimposed.

If one follows one of these cooling curves, e.g., the one for 19.1 mm (3/4 in.) from the quenched end (the heavier line in the diagram), one can read that after 25 s of cooling, the Jominy specimen made of AISI 3140 steel at this distance from the quenched end starts to develop ferrite, after 30 s, pearlite; and after 45 s bainite. After 90 s of cooling 50% of the austenite is already transformed. After 140 s, when the temperature at this point has fallen to 315°C (599°F), formation of martensite begins.

The corresponding Jominy curve at the bottom of Figure 6.17a shows that this cooling curve (at this Jominy distance) with the steel in question will yield a hardness of 48 HRC. To correlate this hardness to different points of the round bars' cross sections of different diameters, an auxiliary diagram (valid in this case only for quenching in moderately agitated oil) such as that shown in Figure 6.17b should be used. From this diagram one can see that the same hardness of 48 HRC can be met, after quenching in moderately agitated oil, 9 mm below the surface of a round bar of 75-mm diameter.

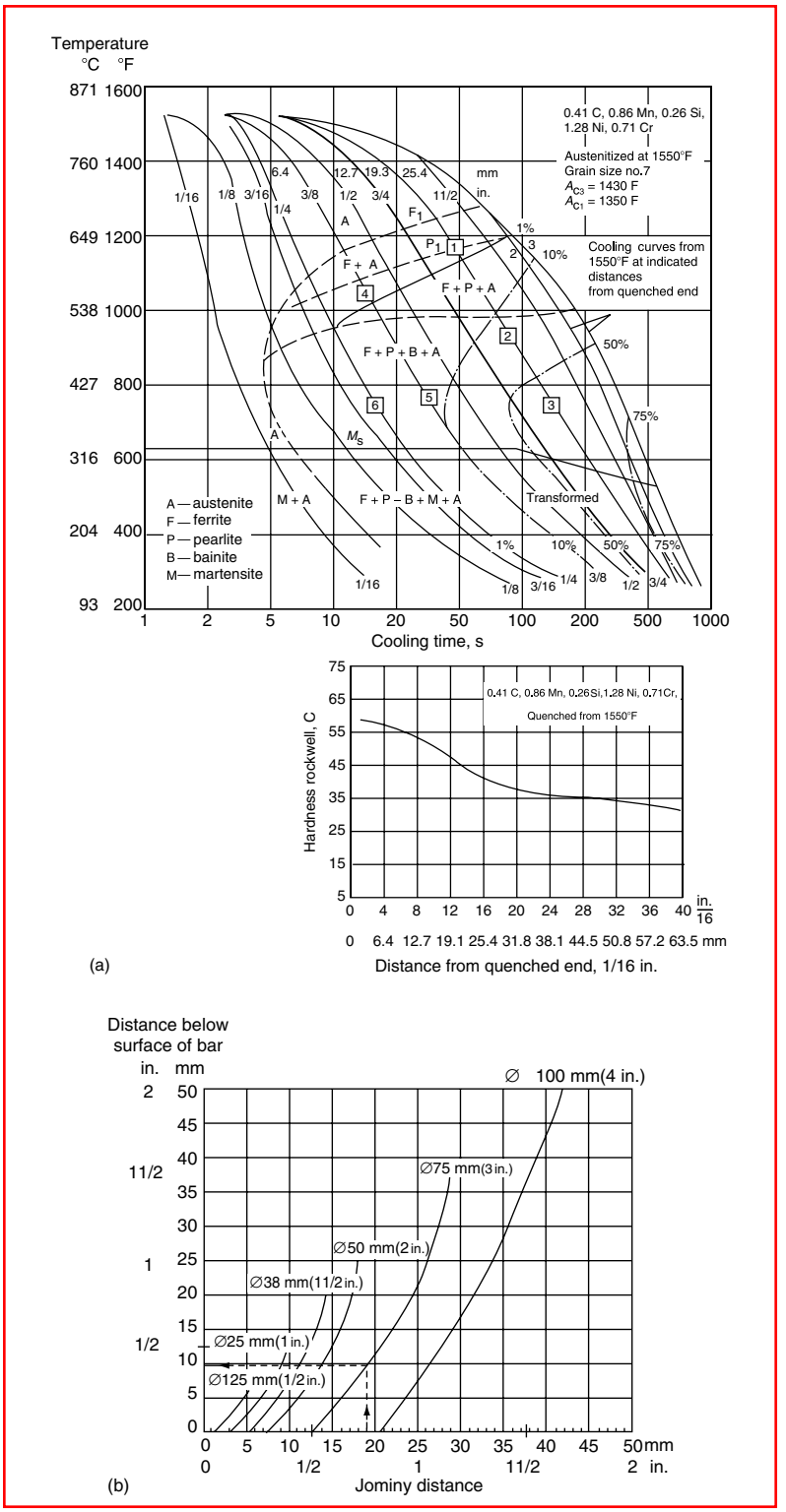

FIGURE 6.17 (a) CCT diagram and Jominy hardenability curve for AISI 3410. (From *Met. Prog.*, October 1963, p. 134.) (b) Chart showing relationship between rate of cooling at different Jominy distances and rate of cooling in moderately agitated oil of round bars of 12.5–100-mm diameter. (From K.E. Thelning, *Steel and Its Heat Treatment*, 2nd ed., Butterworths, London, 1984.)

There also exist CCT diagrams of another type, developed by Atkins [9]; an example is given in Figure 6.18. These diagrams were developed by cooling and quenching round bars of different diameters in air, oil, and water, recording their cooling curves in the center of the bar, and later simulating these cooling curves in a dilatometric test in order to identify the transformation temperatures, microstructures, and hardness. These diagrams therefore refer only to the center of a bar. Instead of a timescale on the abscissa, these diagrams have three parallel scales, denoting bar diameters cooled in air, quenched in oil, and quenched in water. A scale of cooling rates (usually at 700°C (1292°F)) in °C/min is added.

These diagrams are to be read only along vertical lines (from top to bottom), denoting different cooling rates. For example, to determine the microstructure developed and resulting hardness in the center of a 10-mm bar of the steel in question when cooling it in air, one takes the vertical line at 10-mm diameter on the scale for air cool (see Figure 6.18), starts in the austenite region and proceeds downward. Transformation in this case (unalloyed steel grade with 0.38% C) starts at 700°C (1292°F) with the formation of ferrite, continuing to nearly 50% transformation at 640°C (1184°F) when pearlite begins to form. At 580°C (1076°F), a trace of bainite is indicated before transformation is complete.

If oil quenching of a 10-mm bar is now considered, the 10-mm position should be located on the oil-quenched bar diameter scale in Figure 6.18. Again starting in the top region and following the vertical line down, it is seen that in this case bainite is the first phase to form from austenite at 560°C (1040°F). At 330°C (626°F), after about 40% transformation, the remaining austenite transforms to martensite until the reaction is complete at 150°C (300°F). Similarly, the center of a water-quenched 10-mm diameter bar will transform to martensite starting at 360°C (680°F) and finishing at 150°C (300°F).

Relevant hardness values after quenching (and in some cases after tempering to different specified temperatures) can be read following the same vertical line further down into the hardness after transformation diagram.

An examination of the left-hand side of the upper diagram in Figure 6.18 for the steel in question shows that martensite will form on air cooling with bars up to 0.18 mm in diameter, on oil quenching up to 8 mm in diameter, and on water quenching up to 13 mm in diameter.

A special feature of this type of CCT diagram is that the hardenability of the steel can be assessed at a glance. Figure 6.19a is a CCT diagram for a very low hardenability steel previously rolled and austenitized at 950°C (1242°F). It shows early transformation to ferrite and pearlite (even with oil and water quenching of smallest diameters). Figure 6.19b shows a similar diagram for a high-hardenability steel previously rolled, softened at 600°C (1112°F), and austenitized at 830°C (1526°F). In this case the austenite changed predominately to martensite and bainite over a wide range of bar diameters and quenching rates. Diagrams of this type representing 172 steel grades have been published in the British Steel Corporation (BSC) atlas [9].

6.1.3.5 Special Cases and Limitations in the Use of CCT Diagrams

When dealing with carburized steels, one should be aware that, because of the big difference in carbon content between the core (≈0.2%) and the case (≈0.8%), the CCT diagram for the case will be totally different from the one for the core of the same steel, as shown in Figure 6.20 and Figure 6.21. The increased carbon content in the case increased the hardenability and caused the pearlite and bainite regions to be shifted to much longer times. The ferrite region disappeared, and the M_s point was lowered. Cooling at the same rate results in different portions of structural constituents and substantially different hardness values.

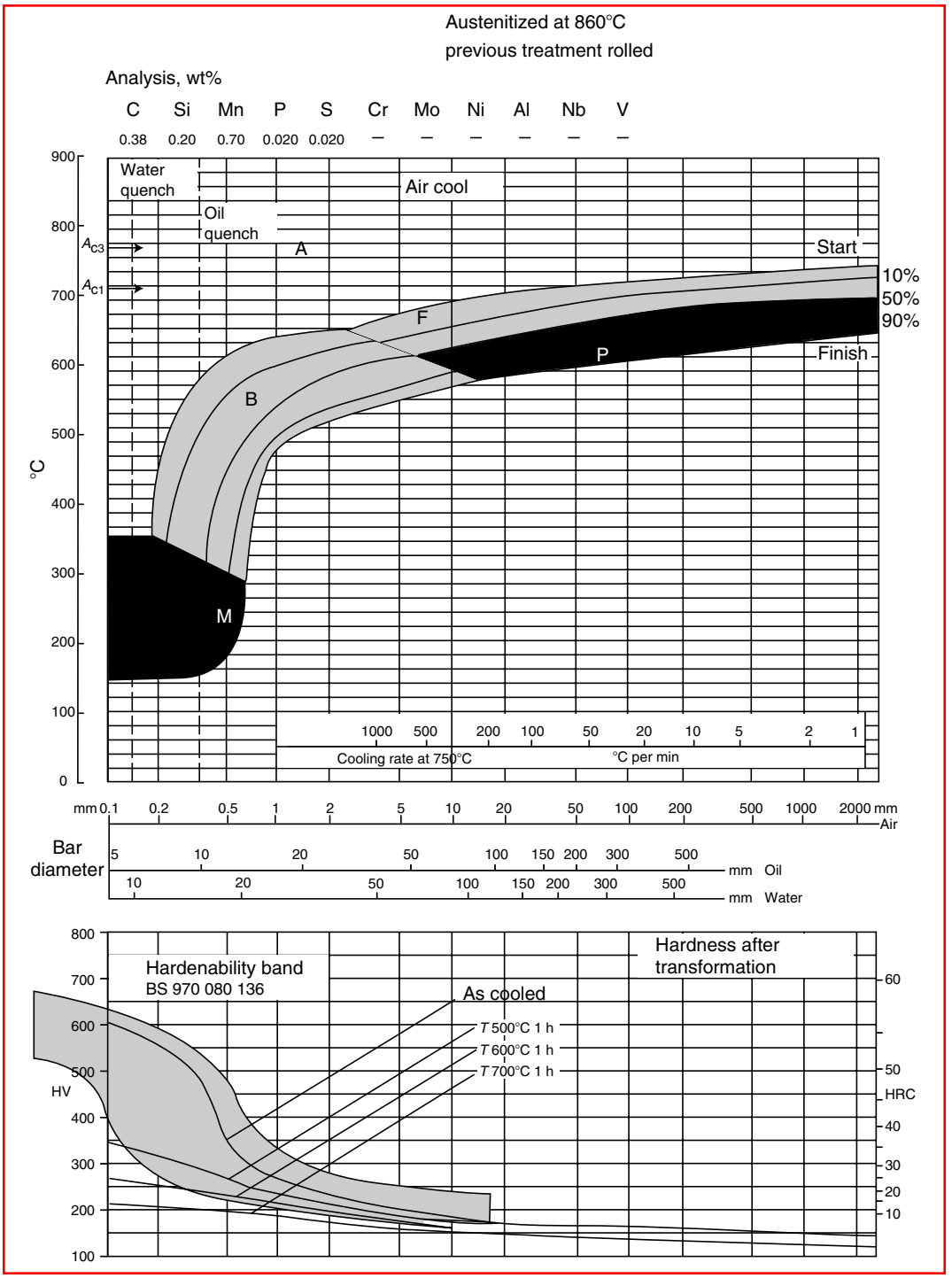

FIGURE 6.18 CCT diagram for rolled steel austenitized at 860°C. (From M. Atkins, *Atlas of Continuous Transformation Diagrams for Engineering Steels*, British Steel Corporation, BSC Billet, Bar and Rod Product, Sheffield, U.K., 1977.)

Another limitation in the use of CCT diagrams concerns cooling regimes with discontinuous change in cooling rate, as for example a delayed quenching in air followed by water or oil quenching. The left-hand part of Figure 6.22a shows the start of transformation as in the conventional CCT diagram for the steel in question. The right-hand part (Figure 6.22b) of this diagram holds for air cooling to approximately A_{c1}, followed by water quenching (a delayed quenching process). It shows a significant displacement of the ferrite and bainite regions to longer times. Such a cooling mode enhances hardenability and results in higher hardnesses than expected from the conventional CCT diagram for the same steel. The effect of discontinuous change in cooling rate is based on nucleation and on incubation time before the change in cooling rate occurs and is theoretically explained by Shimizu and Tamura [11].

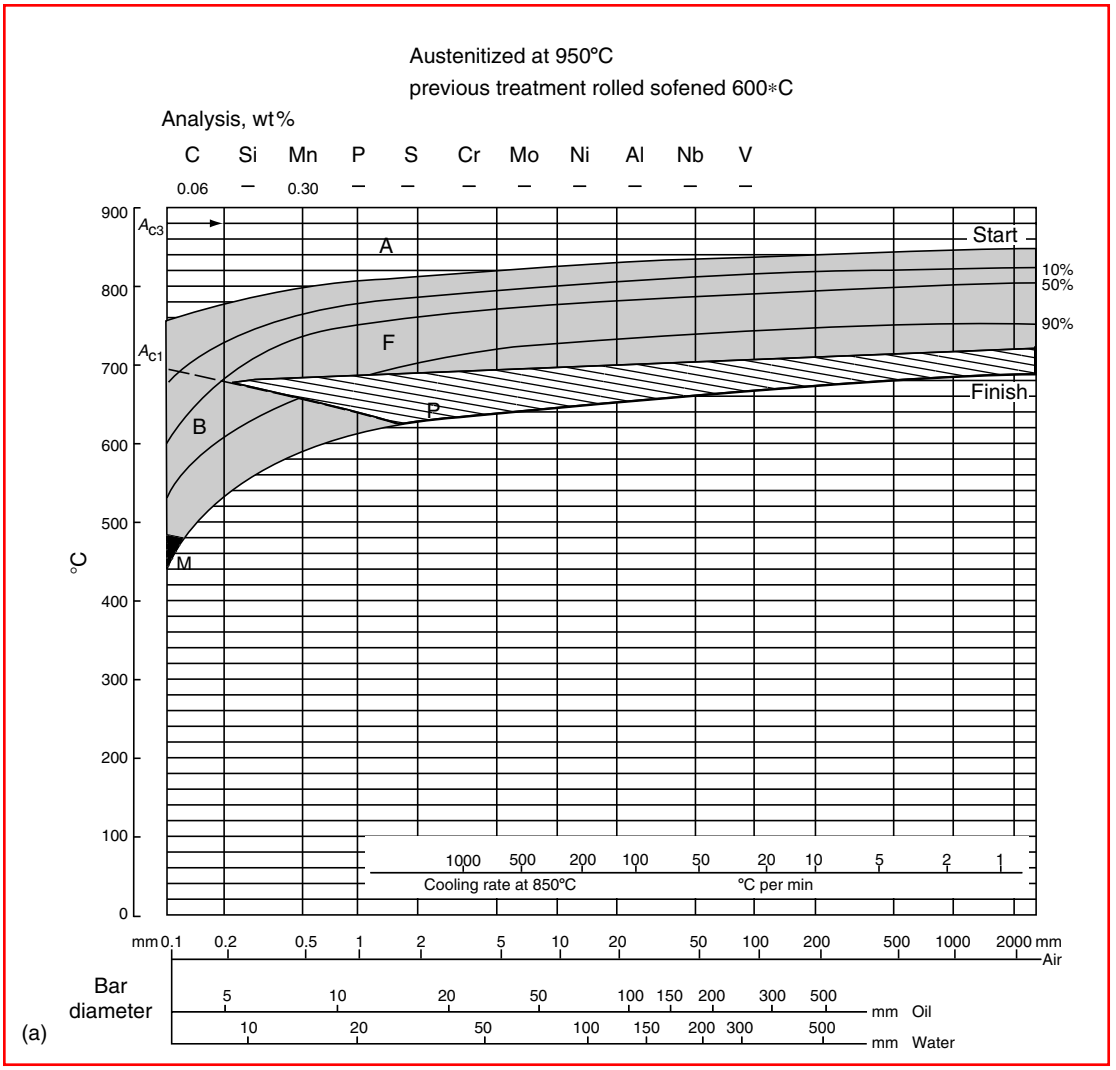

FIGURE 6.19 Examples of (a) a low-hardenability and (b) a high-hardenability steel as depicted in CCT diagrams. (According to M. Atkins, *Atlas of Continuous Transformation Diagrams for Engineering Steels*, British Steel Corporation, BSC Billet, Bar and Rod Product, Sheffield, U.K., 1977.)

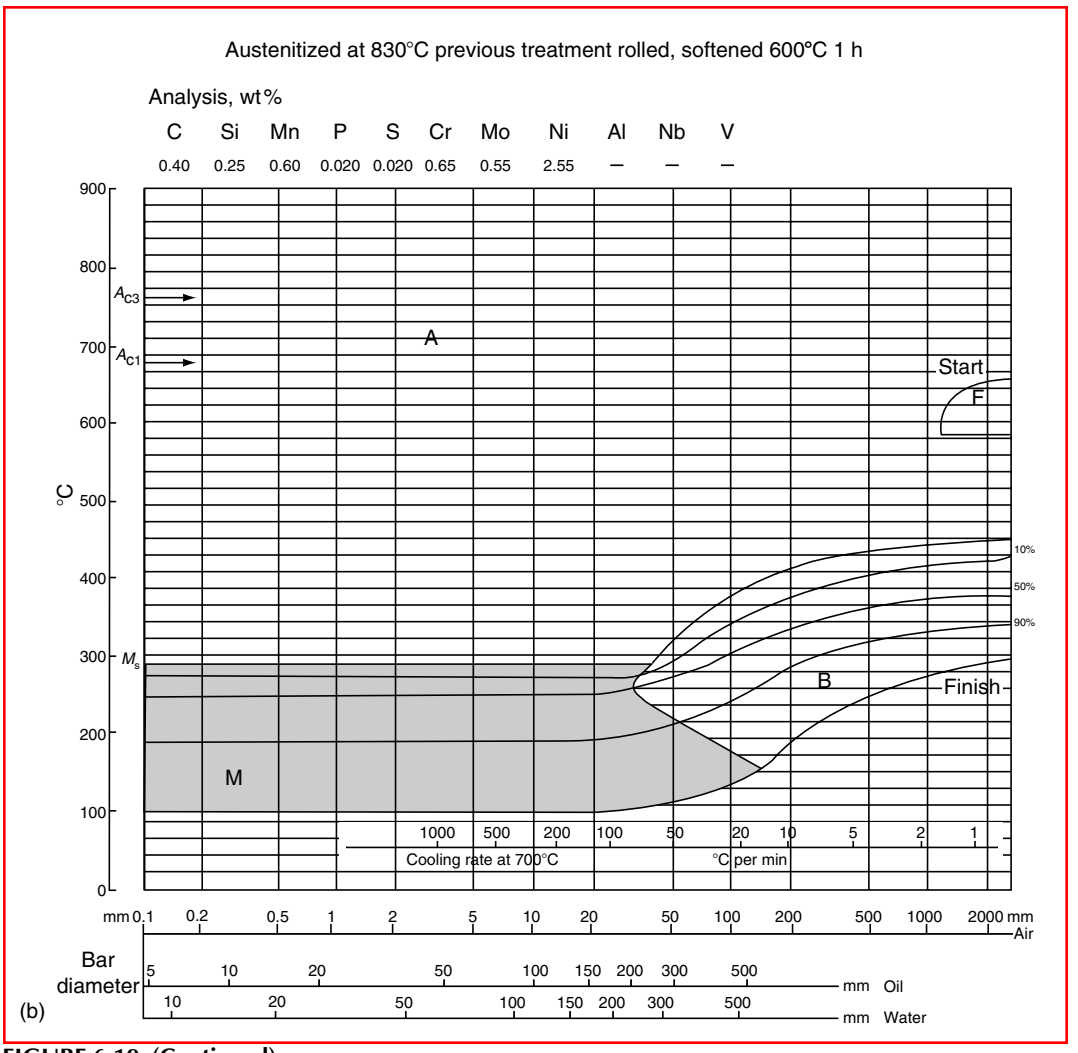

FIGURE 6.19 (Continued)

6.1.4 Oxidation

Oxidation takes place as an undesirable accompanying phenomenon during every heat treatment of metals in a noninert atmosphere. Chemical reactions that occur during the oxidation of a metal are generally expressed by the formula

$$\frac{2x}{y}\mathrm{Me} + \mathrm{O_2} \rightleftharpoons \frac{2}{y}\mathrm{Me}_x\mathrm{O}_y \tag{6.19}$$

where x and y denote integer numbers.

The oxidation process proceeds at a set temperature spontaneously from left to right (according to formula 6.19). During this process the free enthalpy of the reaction products (G_R) becomes smaller than the enthalpy of the original materials (G_A), i.e., the difference can be expressed as

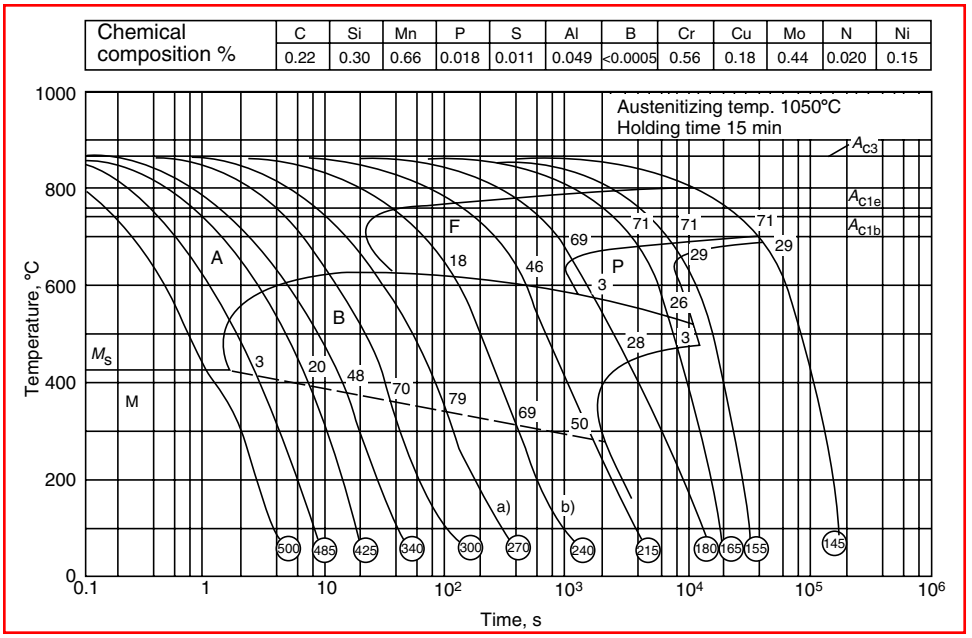

FIGURE 6.20 The CCT diagram for the core (0.22% C) of DIN 20MoCr5 steel. (From H.J. Eckstein (Ed.), *Technologie der Wärmebehandlung von Stahl*, 2nd ed., VEB Deutscher Verlag für Grundstoffindustrie, Leipzig, 1987.)

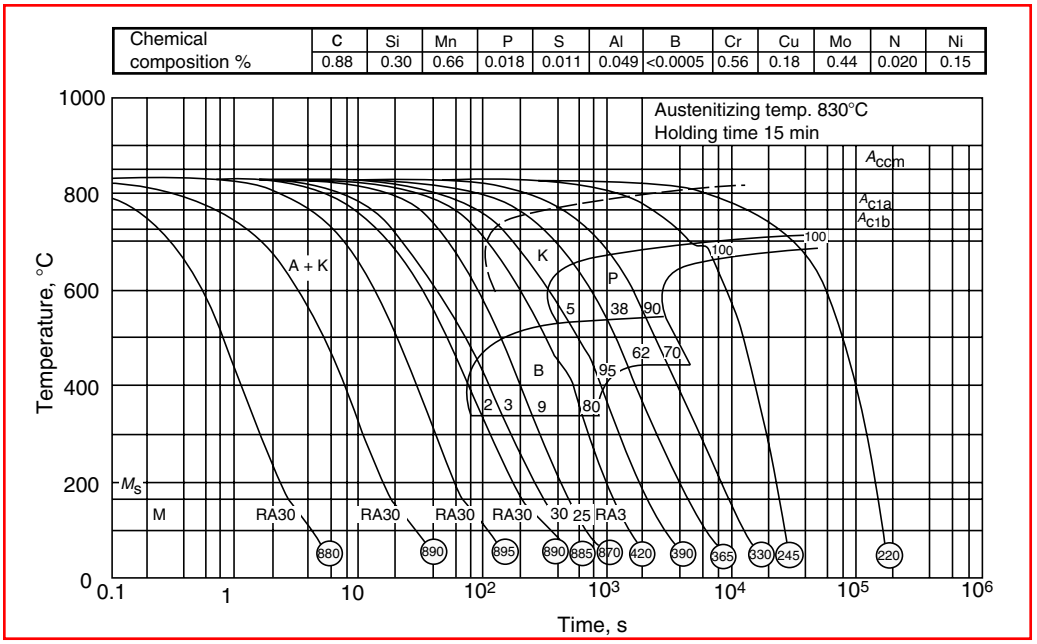

FIGURE 6.21 The CCT diagram for the case (0.88% C) of DIN 20MoCr5 steel. (From H.J. Eckstein (Ed.), *Technologie der Wärmebehandlung von Stahl*, 2nd ed., VEB Deutscher Verlag für Grundstoffindustrie, Leipzig, 1987.)

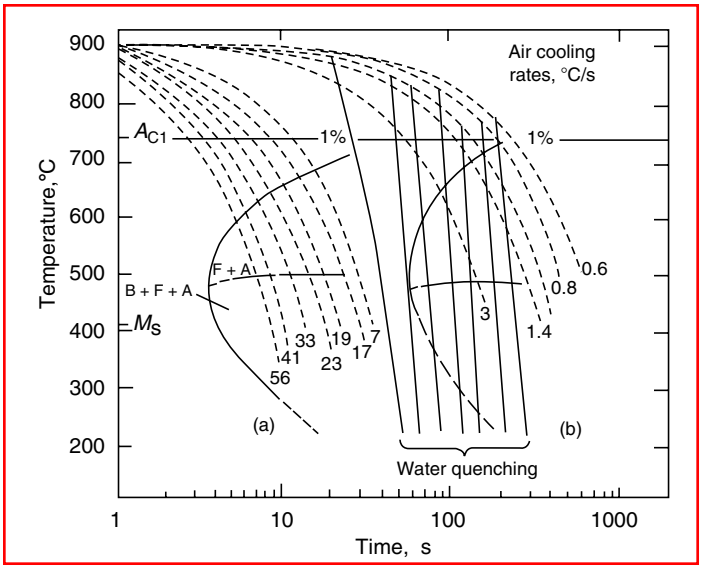

FIGURE 6.22 Cooling curves and CCT diagrams for a steel containing 0.20% C, 0.78% Mn, 0.60% Cr, 0.52% Ni, and 0.16% Mo after austenitizing at 900°C. (a) Conventional CCT diagram and (b) various air cooling rates to approximately A_{c1} followed by water quenching. (From E.A. Loria, *Met. Technol.*, 1977, pp. 490–492.)

$$\Delta G_0 = G_R - G_A \quad \text{for } G_A > G_R \tag{6.20}$$

If $\Delta G_0 > 0$, reaction 6.19 will take place from right to left, i.e., the metal oxide will be reduced.

When the oxygen pressure (p_{O_2}) equals 1 bar, ΔG_0 is called the free standard creating enthalpy. Figure 6.23 shows the temperature dependence of the free standard creating enthalpy (ΔG_0) for oxidation reactions of some metals.

If (p_{O_2}) at temperature T differs from 1 bar, then the characteristic change of the free creating enthalpy may be calculated as follows:

$$\Delta G = \Delta G_0 - RT \ln p_{O_2} \tag{6.21}$$

where R is the universal gas constant and T is absolute temperature.

As can be seen from Figure 6.23 for all of the metals represented except silver, the values of ΔG_0 are negative with an increasing trend at higher temperatures. In the case of silver, $\Delta G_0 = 0$ at 190°C (324°F). At this temperature, equilibrium exists between Ag, O_2, and Ag_2O, i.e., the disintegration pressure of Ag_2O has reached the oxygen pressure of 1 bar that was taken as the basis. At higher temperatures the disintegration pressure of Ag_2O becomes higher and the metal oxide (Ag_2O) will be disintegrated.

From Figure 6.23 it can be concluded that the chosen metals, with the exception of silver, within the shown temperature range would form oxides. Because the oxidation takes place on the surface, the oxide layer that is formed separates the two reaction partners, i.e., the metal and the oxygen. This oxide layer, which is material-specific, becomes thicker with time. There are several formulas expressing the dependence of the oxide layer thickness on time. For higher temperatures a parabolic law is usually used:

$$y = \sqrt{A_1 t} \tag{6.22}$$

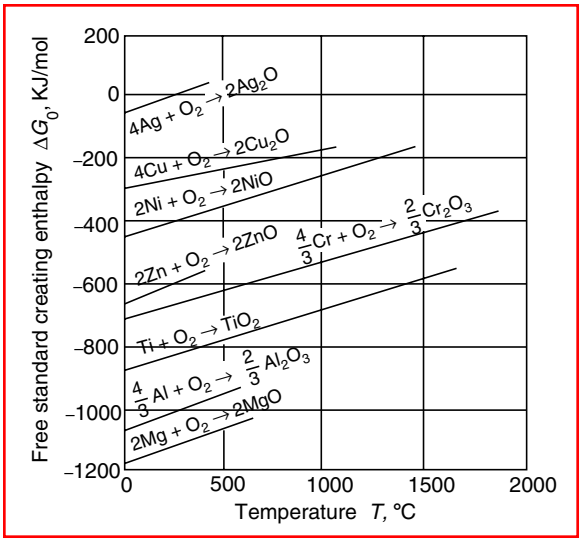

FIGURE 6.23 Temperature dependence of the free standard creating enthalpy of some oxidation reactions between 0°C and the melting point of the relevant metal. (From G. Spur and T. Stöferle (Eds.), *Handbuch der Fertigungstechnik, Vol. 4/2, Wärmebehandeln*, Carl Hanser, Munich, 1987.)

where y is the oxide layer thickness, A_1 is a material-specific constant, and t is time. This parabolic law is valid for oxidation processes when the rate of oxidation depends on the diffusion of metal ions and oxygen ions through the oxide layer.

When the oxide layer is porous, i.e., permeable for the gas, and therefore the metal and oxygen are not separated, build-up of the layer follows a linear law:

$$y = A_2 t \tag{6.23}$$

where A_2 is another material-specific constant.

An oxide layer of a pure metal is constituted of uniform chemical compound if a single valency is involved, e.g., FeO. If more valencies are involved, the oxide layer consists of sublayers with oxygen valencies increasing from the inside to the outside, e.g., FeO, Fe_3O_4, and Fe_2O_3, as shown in Figure 6.24. In Figure 6.24a, an oxide layer of pure iron, created during a 5-h annealing at 1000°C (1832°F), is shown. Relevant processes during development and build-up of the layer are schematically shown in Figure 6.24b.

6.1.4.1 Scaling of Steel

When metallic parts are heated above 560°C (1040°F) (this is the temperature at which the creation of wüstite or FeO begins), after creation of the first part of the layer in the starting phase, the reaction follows by diffusion of Fe^{2+} ions from the steel toward the outside and the diffusion of oxygen ions at the scale–metal interface toward the inside. As time passes, the linear law of oxidation valid for the starting phase changes to a parabolic law.

The growth of the oxide layer (scale) depends very much on the chemical composition of the steel. Different alloying elements, having different diffusion abilities, have different influences on the oxidation process and the build-up of scale. The chemical composition of the original material on the surface is subject to changes.

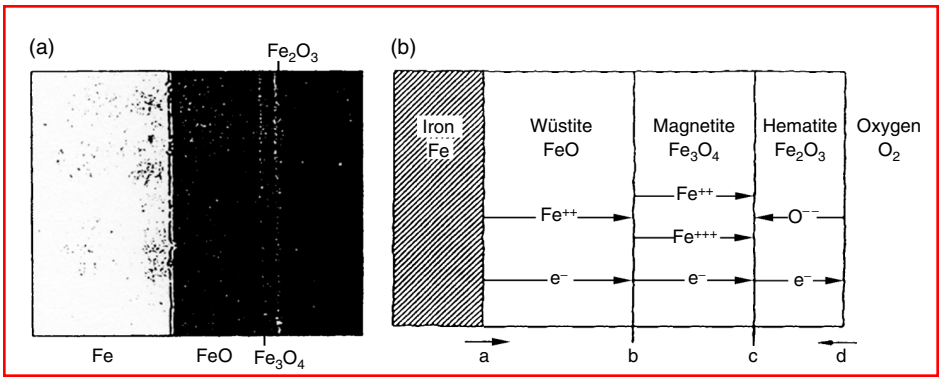

FIGURE 6.24 Oxidation of pure iron. (a) Oxide layer and (b) processes during the build-up of the oxide layer; *a*, transition of $Fe^{2+} + 2e^-$ from the metal into FeO; *b*, creation of FeO; *c*, creation of Fe_3O_4 and Fe_2O_3; *d*, input of oxygen. (From. G. Spur and T. Stöferle (Eds.), *Handbuch der Fertigungstechnik, Vol. 4/2, Wärmebehandeln*, Carl Hanser, Munich, 1987.)

According to their affinity for oxygen, the alloying elements in steel can be divided into three groups with respect to their influence on the scaling process [2]:

Group I contains those elements whose oxygen affinity is less than the affinity of the richest oxide compound wüstite (FeO), e.g., Ni and Co. After saturation of the basic metal with oxygen, the outer oxidation of iron begins with the creation of wüstite. The alloying elements become richer at the scale–metal interface.

Group II contains those elements whose oxygen affinity is greater than that of iron (Cr, Si, V, Al). After saturation of the basic metal with oxygen, inner oxidation begins. Because of the creation of internal oxides of alloying elements, a diffusion barrier builds up against the diffusion of metal and oxygen ions, hampering the development of scale.

Group III contains those elements whose oxygen affinity is similar to that of wüstite (Mo, W). No inner oxidation takes place. The alloying elements become richer in the basic metal at the scale–metal interface.

Figure 6.25 shows the influence of Cr additions to a steel on the depth of scale (mm/year) at temperatures of 600, 700, and 800°C (1112, 1292, and 1472°F). A particularly high oxidation resistance of steels may be achieved by Cr additions of 6–30% by mass.

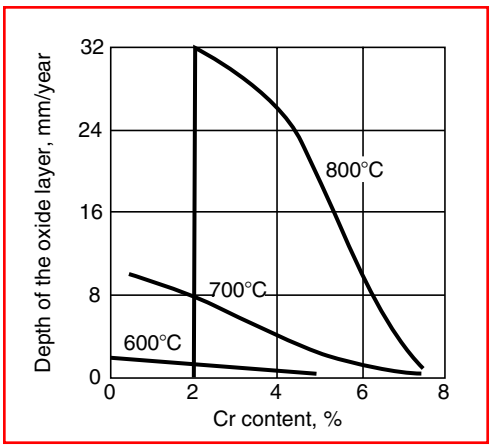

FIGURE 6.25 Influence of Cr on the oxidization of a steel at temperatures of 600, 700, and 800°C. (From ISI, *Decarburization*, ISI Publication 133, Gresham Press, Old Woking, Surrey, England, 1970.)

6.1.5 Decarburization

Under conditions that cause the oxidation of iron, the oxidation of carbon is also to be expected. Decarburization of a metal is based on the oxidation at the surface of carbon that is dissolved in the metal lattice. It should be noted that, depending on the carbon potential of the surrounding atmosphere, decarburization can take place independently of scaling. However, in heat treatment processes iron and carbon usually oxidize simultaneously. During the oxidation of carbon, gaseous products (CO and CO_2) develop. In the case of a scale layer, substantial decarburization is possible only when the gaseous products can escape, i.e., when the equilibrium pressures of the carbon oxides are high enough to break the scale layer or when the scale is porous.

The carbon consumed on the surface has to be replaced by diffusion from the inside. Hence the process of decarburization consists of three steps:

1. Oxygen transport within the gas to the metal surface
2. Carbon exchange at the gas–metal interface
3. Diffusion of carbon within the metal

Generally the diffusion of carbon within the metal is the most important factor in controlling the rate of decarburization, which after a short starting period follows a parabolic time law. When a mild steel is heated below 910°C (1670°F), a surface layer of ferrite is formed that acts as a barrier to carbon transport owing to the very low solubility of carbon in ferrite. Above 910°C (1670°F) the steel remains austenitic throughout, and decarburization becomes severe. The model used to represent decarburization in the fully austenitic condition is shown in Figure 6.26. The steel surface is continually oxidized to form a scale, while the carbon is oxidized to form the gases CO and CO_2. The scale is assumed to be permeable to these gases, which escape to the atmosphere.

The carbon content at a scale–metal interface is assumed to be in equilibrium with the oxygen potential of the scale, which at that position corresponds to the equilibrium between iron and wüstite. The carbon concentration profile in the metal varies from the low surface concentration to the original carbon content within the metal, as shown in Figure 6.26. In using this model, distances are measured from the original metal surface; the instantaneous scale–metal interface lies at the position $x = X$ at time t. This means that scaling has consumed a thickness X of metal during time t.

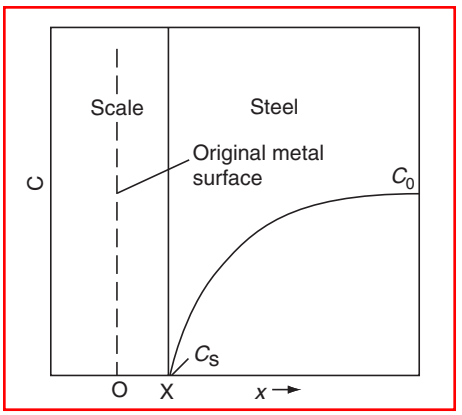

FIGURE 6.26 Model for decarburization in fully austenitic condition. (From ISI, *Decarburization*, ISI Publication 133, Gresham Press, Old Woking, Surrey, England, 1970.)

To calculate the depth of decarburization, the distribution of carbon in the metal is calculated by solving Fick's second law for the relevant boundary condition:

$$\frac{\delta C}{\delta t} = D\frac{\delta^2 C}{\delta x^2} \quad \text{for } x > X \tag{6.24}$$

$$C = C_0, \quad x > 0; \quad t = 0 \tag{6.25}$$

$$C = C_s, \quad x = X; \quad t > 0 \tag{6.26}$$

Equation 6.25 indicates that initially the carbon concentration was uniform throughout the specimen; Equation 6.26 indicates that the carbon concentration at the metal–scale interface is constant (in equilibrium with the scale). It is assumed that decarburization does not extend to the center of the specimen and that the diffusion coefficient of carbon in austenite is independent of composition; enhanced diffusion down grain boundaries is neglected. Under these conditions the solution at a constant temperature (for which the diffusion coefficient is valid) reads

$$\frac{C_0 - C}{C_0 - C_s} = \frac{\text{erfc}\,(x/2\sqrt{2}Dt)}{\text{erfc}\,(k_c/2D)^{1/2}} \tag{6.27}$$

where C_0 is the original carbon content of the metal, C_s is the carbon concentration at the metal–scale interface, D is the carbon diffusion coefficient, t is time, erfc = 1 − erf (here erf is the error function), and k_c is the corrosion constant of the metal ($k_c = X^2/2t$).

Equation 6.27 provides the carbon content within the metal for $x > X$ as a function of time and position.

The value of k_c for the relevant steel in the relevant atmosphere is expressed as

$$k_c = 0.571 \exp(-43{,}238/RT)\ \text{cm}^2/\text{s} \tag{6.28}$$

Although the variation of the diffusion coefficient of carbon in austenite was ignored in solving Equation 6.24, it was found that the best agreement between calculated and measured carbon profiles was obtained when values relating to very low carbon content were used. Therefore, in this calculation, a diffusion coefficient for zero carbon content was used, which reads

$$D_{(C=0)} = 0.246 \exp(-34{,}900/RT)\ \text{cm}^2/\text{s} \tag{6.29}$$

A comparison of measured decarburization depths with values calculated using these data showed that with 12 measurements of isothermal treatments between 1,050 and 1,250°C (1922 and 2282°F) for time between 900 and 10,800 s, the mean prediction was 97% of the measured value [12]. It was found that the inner limit of the decarburized zone is placed, by metallographic examination, at the position where the carbon content is 92.5% of the original carbon content.

To ascertain the effect of scaling rate on decarburization, it may seem logical to try to reduce decarburization by reducing the oxidizing potential of the atmosphere. This is a fallacy, as the carbon concentration at the metal–scale interface is constant in equilibrium with iron oxide as long as scale is present. However, the scaling rate can be affected by changing the atmosphere, and this will affect the observed depth of decarburization.

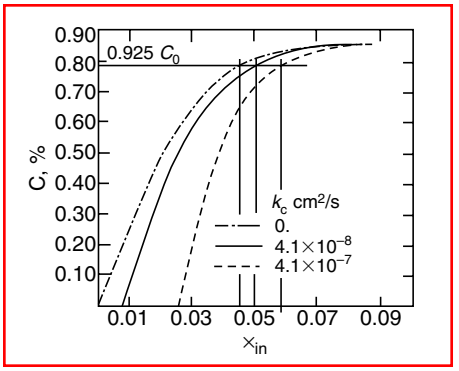

FIGURE 6.27 Effect of scaling rate on decarburization of an 0.85% C steel after 1.5 h at 1050°C. The position where the carbon profile cuts the *x*-axis indicates the position of the scale–metal interface for the three k_c values. (From ISI, *Decarburization*, ISI Publication 133, Gresham Press, Old Woking, Surrey, England, 1970.)

To illustrate this, carbon profiles have been calculated and plotted in Figure 6.27 for a 0.85% C steel heated for 1.5 h at 1050°C (1922°C). The carbon profiles are plotted relative to the original metal surface, while the point at which a carbon profile cuts the *x*-axis indicates the position of the scale–metal interface for the related conditions. The curves refer to k_c values of 0, 4.1×10^{-8}, and 4.1×10^{-7} cm^2/s. The depth of decarburization is determined by the position at which $C = 0.925C_0$ (see the horizontal line drawn in Figure 6.27). From Figure 6.27 it appears that with increased values of k_c the scale–metal interface on the *x*-axis shifts progressively toward the inside of the metal, while the depth of decarburization (which is the horizontal distance between the intersection of a carbon profile curve with the horizontal $0.925C_0$ line and its intersection with the *x*-axis) is found to decrease as k_c increases. These results are shown in Table 6.3. This reveals an interesting situation where, by reducing the oxidation rate, the depth of decarburization is increased yet less metal is wasted.

When scaling and decarburization take place simultaneously, decarburization is prevented during the starting phase of scaling. It takes place substantially only after the equilibrium pressures of CO and CO_2 increase at increased temperatures and the adhesion strength of the scale (because of its increased thickness) diminishes or the scale becomes porous.

6.1.5.1 The Effect of Alloying Elements on Decarburization

Alloying elements may affect decarburization due to their effect on

TABLE 6.3
Effect of Scaling Rate on Decarburization

	Total Depth of Metal Affected		Depth of Decarburized Layer	
Scaling Rate k (cm^2/s)	cm	in.	cm	in.
0	0.119	0.047	0.119	0.047
4.1×10^{-8}	0.130	0.051	0.109	0.043
4.1×10^{-7}	0.150	0.059	0.084	0.033

Source: From ISI, *Decarburization*, ISI Publication 133, Gresham Press, Old Woking, Surrey, England, 1970.

1. The ferrite–austenite transformation temperature
2. The activity of carbon in solution
3. The diffusion coefficient of carbon in solution
4. The scaling characteristics of iron

Although this subject is a complex one, even when considered only qualitatively, the following statement is generally valid. Decarburization increases with (1) increased rate of carbon diffusion, (2) increased carbon activity, and (3) increased ferrite–austenite transformation temperature.

A complication arises due to the fact that during scaling alloying elements tend to concentrate either in the scale or in the metal at the scale–metal interface. In special cases, when strong carbide-forming elements are involved, decarburization may also be influenced by the rate of dissolution of carbides in the matrix. When the alloying elements are less valuable than iron, the possibility of oxidation arises; an external oxide layer may also be formed under circumstances that are normally protective to iron. If either type of oxide formation occurs, the concentration of the alloying element in solution is reduced at the metal surface, and so the effect on carbon behavior will be altered correspondingly.

When an external scale is formed, the effect of the alloying element on the scaling rate must also be considered. If the scaling rate is increasing, then, in the absence of other factors, the observed depth of decarburization will be reduced.

Although quantitative predictions are not possible, it is instructive to predict what the effects of a few common alloying elements may be:

Nickel will concentrate at the scale–metal interface and, although the scaling rate may not be greatly affected, the solubility of carbon in the surface layers may be reduced, thus restricting carbon diffusion outward and reducing the depth of decarburization.

Manganese is taken into the scale in solid solution in the wüstite and magnetite layers. Scaling rates are hardly affected, and any effect on decarburization will be restricted to its effects on carbon activity and the diffusion coefficient. Since manganese is denuded in the surface layers of the metal, however, the effect may be only slight.

Silicon also concentrates in the scale and forms fayalite, which reduces the scaling rate. This should lead to deeper observed decarburization. Silicon also increases the activity of carbon and therefore increases the tendency of carbon to diffuse out to the scale–metal interface. Thus the general effect expected of silicon is to increase decarburization.

Chromium concentrates in the scale, forming spinel, depending on its concentration. In general, scaling rates are reduced. The formation of stable carbides introduces the possibility of a slow carbide decomposition step into the mechanism. At the usual reheating temperatures and times, however, the chromium carbides may dissolve completely. In this case the effect of chromium would be to reduce the activity of carbon in solution, thus tending to reduce the rate of migration to the surface. There are therefore two conflicting factors. The lower scaling rate would tend to increase the observed decarburization, whereas the reduction of carbon activity would tend to reduce it. The later factor may be expected to predominate and reduce decarburization.

6.1.5.2 Definitions and Measurement of Decarburization

The strength of a steel depends on the presence of carbides in its structure; therefore, loss of carbon from the surface softens and weakens the surface layers. In such a case the wear resistance is obviously decreased, and in many circumstances there can be a serious drop in fatigue resistance.

To avoid the real risk of failure or inferior performance of engineering components, it is essential to minimize decarburization at all stages in the processing of steel. This requires inspection and the laying down of specifications for decarburization in various components and semiproducts. The decarburization limits in such specifications must be related to the function of the component and must enable checking by the use of agreed-upon preferably standardized measuring techniques.

There are several different definitions of decarburization. A rigorous definition is that the depth of decarburization is the thickness of the layer in which the carbon content is less than that of the core, i.e., the distance from the surface to a boundary at which the carbon content of the core is reached. This boundary corresponds to the asymptote of the graph of carbon content vs. distance from the surface and is therefore somewhat diffuse and difficult to locate with precision. Thus the depth of decarburization according to this definition is difficult to measure reproducibly. A functional definition is that the depth of decarburization is the thickness of the layer in which loss of carbon has a significant effect on properties that affect the functioning of the final component. The limit of this layer can be expressed as a carbon content or a hardness level. Finally, a practical definition of the depth of decarburization is that it is the thickness of the layer in which the structure differs significantly from that of the core. This definition is suitable when a metallographic examination is undertaken.

There is a distinction between complete decarburization and partial decarburization. Complete decarburization leaves the surface layer entirely ferritic, which can be clearly distinguished under the microscope. The depth of complete decarburization is the thickness of the ferrite layer, i.e., the distance from the surface to the first particle of a second phase. In the zone of partial decarburization, the carbon content increases progressively from the ferrite layer to the core and approaches the core composition asymptotically.

The total thickness of the decarburization layer, i.e., the distance from the surface to the inner boundary of the core, is the total depth of decarburization—the sum of the depths of complete and partial decarburization. It should be noted also that the depth of decarburization may vary around the circumference of a component.

A number of methods for measuring decarburization are available. The requirements that such techniques have to meet are:

1. Ability to measure a clearly defined depth of decarburization, e.g., compatibility with the functional definition of the depth of decarburization
2. Reproducibility of measurement
3. Ease and convenience of measurement

Optical metallography is the most useful and convenient method. A cross section of the component or sample around the periphery is examined, and the depth of decarburization is measured from the surface to the practical boundaries of complete and partial decarburization. This method is suitable for ferrite–pearlite structures only.

For the metallographic examination of high-speed steels, a method has been established that depends on color staining by means of etching in alcoholic nitric acid (Nital). A polished cross section of annealed high-speed steel is etched in 4% Nital. During the first 30 s in the etchant the specimen surface progresses through a gray color to a purplish-blue, which changes suddenly after about 60 s to a blue-green. Where the functional definition of decarburization calls for the development of the full hardness in the surface layers, the practical boundary is the start of the general core structure, i.e., the edge of the blue-green zone.

The arrest-quench method consists of austenitizing a very thin specimen in a neutral atmosphere or salt bath and quenching it in a hot bath held at an appropriate temperature. This is the M_s temperature corresponding to the carbon content at which it is desired to place the boundary. The specimen is held at that temperature for about 5 s and is then

water-quenched. During this short arrest the decarburized zone, which has an M_s temperature above the temperature of the bath, will partly transform to martensite; the core will remain austenitic. As soon as martensite has formed in the decarburized zone, martensite needles will begin to temper slightly. Thus, after water quenching the core will consist of fresh light-etching martensite, while the decarburized zone will contain dark-etching tempered martensite needles. A very sharp contrast is achieved at the boundary between the decarburized zone and the core, and the boundary can be located with considerable accuracy at any desired carbon content below the original carbon content of the core.

Figure 6.28 shows specimens taken from the same hot-rolled rod that have been arrest quenched at different temperatures to place the decarburization boundary at different carbon contents. The micrographs are placed on a graph of carbon content vs. depth of decarburization, and the carbon profile has been drawn through the microstructures. This technique is compatible with the functional definition of the depth of decarburization based on a particular carbon content and gives very reproducible results.

Microhardness measurement is a fairly convenient method for quantitatively accurate determinations of a functional decarburization limit by determining the variations of hardness with distance from the surface of the test piece. As this involves polishing a cross section, it is invariably preceded by a metallographic scan that facilitates the location of the best area for the hardness survey.

A graph of hardness vs. distance from the surface is plotted, and the deviation from the core hardness can be detected. Chemical analysis of successive surface layers is the classical referee method for measuring decarburization. The sample has to be large enough to permit accurate chemical analysis, and yet each surface layer must be fairly thin in order to give an adequate number of points on a graph of carbon content vs. distance from the surface. The graph of carbon content against distance can be used to indicate the first deviation from the core composition or to locate any decarburization boundary. Complete decarburization is not very easy to locate on this graph, because the carbon content of ferrite is too low for very accurate chemical analysis.

Chemical analysis can be replaced by the carbon determination with a vacuum spectrograph. This has several advantages, particularly in speed and convenience and also because

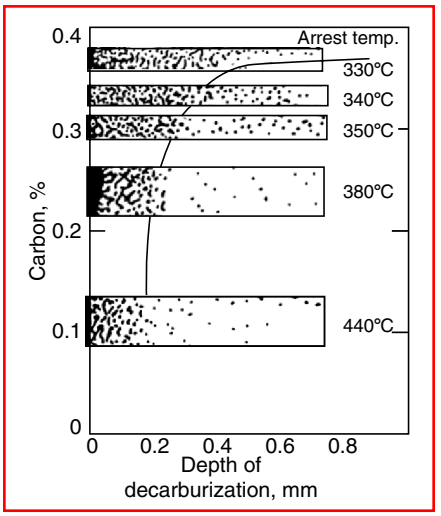

FIGURE 6.28 Depth of decarburization to various carbon contents, established by the arrest-quench method. (From ISI, *Decarburization*, ISI Publication 133, Gresham Press, Old Woking, Surrey, England, 1970.)

the sample size required is much smaller than for other methods. The only limitation is the need to place the spark accurately on a flat area parallel to the original surface and at least 15 mm in diameter. Successive layers have to be exposed by grinding, because the maximum depth measured in one exposure is limited to about 500 μm.

6.1.6 Residual Stresses, Dimensional Changes, and Distortion

Residual stresses are stresses in a body that is not externally loaded by forces and moments. They are in mechanical equilibrium within the body, and consequently the resultant force and the resultant moment produced by residual stresses must be zero. Residual stresses are classified, according to the area within which they are constant in magnitude and direction (i.e., in which they are homogeneous), into three categories:

- Residual stresses of the first kind are those homogeneous across large areas of the material, i.e., across several grains. Internal forces resulting from these stresses are in equilibrium with respect to any cross section, and mechanical moments resulting from these stresses are in equilibrium with respect to any axis. Any intervention in the equilibrium of forces and moments of a volume element containing such residual stresses will change the element's macroscopic dimensions.
- Residual stresses of the second kind are those homogeneous across microscopically small areas (one grain or subgrain region) and are in equilibrium across a sufficient number of grains. Macroscopic changes in the dimensions of a volume element possessing these stresses may become apparent only if distinct disturbances of this equilibrium occur.
- Residual stresses of the third kind are those inhomogeneous across microscopically small areas (within several atomic distances of single grains) and are in equilibrium across subgrain regions. No macroscopic changes of the dimensions of the stressed material will result when such equilibria are disturbed.

Residual stresses of the first kind are called macroresidual stresses, and those of the second and third kinds are called microresidual stresses.

Typical residual stresses of the third kind are stresses connected with dislocations and other lattice defects. An example of residual stresses of the second kind are stresses within grains of a material consisting of two structural phases with different expansion coefficients.

In practice, only residual stresses of the first kind are considered, and they are characterized by the technological processes by which they originate. The main groups of residual stresses are:

Casting residual stresses
Forming residual stresses
Working-out residual stresses
Heat treatment residual stresses
Joining residual stresses
Coating residual stresses

In every stressed workpiece all three kinds of residual stresses are present.

Figure 6.29 is a schematic presentation of all three kinds of residual stresses and their superposition in a two-phase material after quenching. (RS I–III denote residual stresses of the first to third kinds, respectively.)

Estimation of residual stresses in a workpiece is very important because they represent a preloading of the material. There is always a linear superposition of internal (residual) and external stresses, and the resulting stress affects the strength of the material and its deformation behavior.

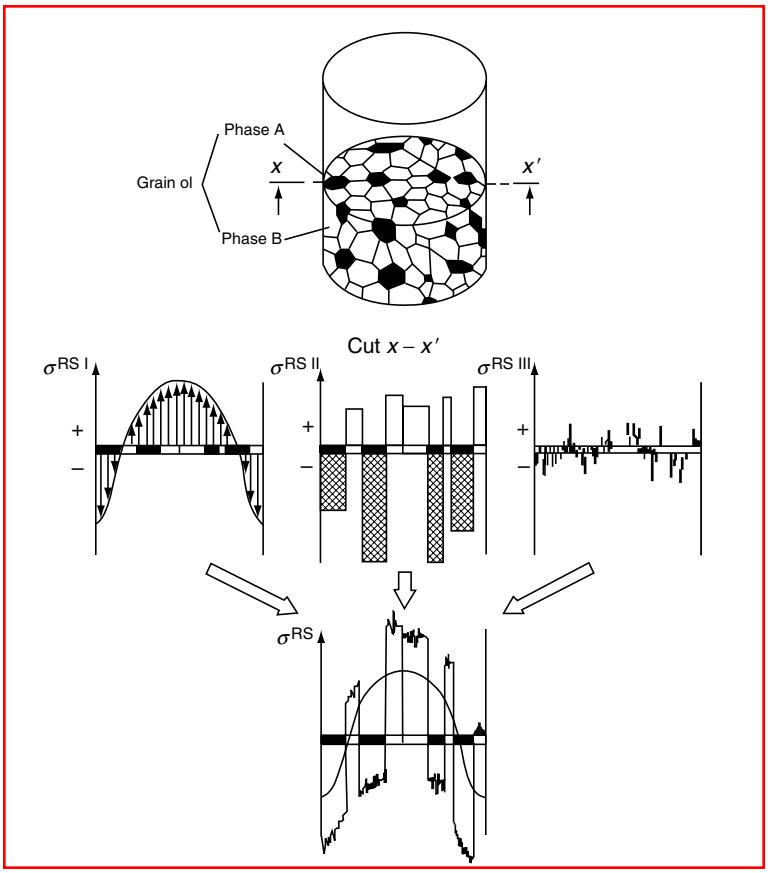

FIGURE 6.29 All three kinds of residual stresses in a two-phase material after quenching and their superposition (shown schematically). (From B. Liščić, H.M. Tensi, and W. Luty (Eds.), *Theory and Technology of Quenching*, Springer-Verlag, New York, 1992.)

In the case of a dynamic loading on a component, the residual stresses act as a constant preloading. Tensile stresses decrease the fatigue strength, and compression stresses increase it. The fatigue strength of a component depends not only on the resulting stresses on the surface but also on the distribution of stresses across the section. Figure 6.30 shows schematically two cases with the same external stress (straight line *c*) and some fatigue strength (straight line *a*). The only difference is in the distribution of residual stresses (curve *b*). In case I, a high residual stress (compressive) on the surface rapidly decreases below the surface, while in case II the residual stress, although smaller at the surface, decreases more slowly below the surface. The component can withstand the applied load only when the curve $c + b$ representing the sum of the external and residual stresses does not intersect the fatigue strength (straight line *a*). In case I, in spite of higher compressive residual stresses at the surface, at a distance below the surface the sum of external and residual stresses is higher than the fatigue strength, and a crack can be expected to form at this point. In case II, although the compressive residual stress is lower at the surface, its distribution below the surface is more favorable and the sum of external and residual stresses does not intersect the fatigue strength curve at any point.

There is a further point to consider when dealing with resulting stresses. This is their multiaxis nature. In practice, the estimation of the sum of external and residual stresses is complicated by the difficulty of determining the direction of the stresses at the critical point of the workpiece.

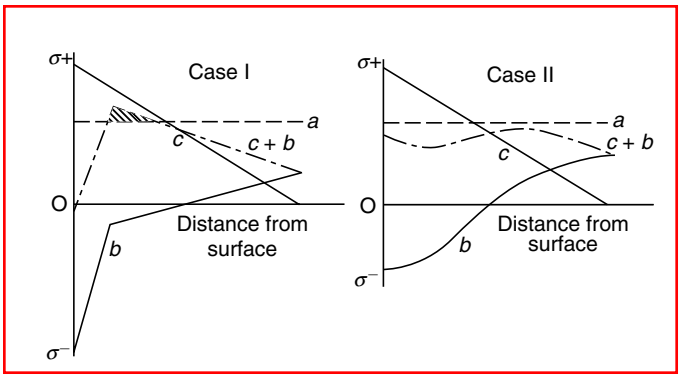

FIGURE 6.30 Schematic presentation of superposition of the external load and residual stresses at a fatigue test. (From H.J. Eckstein (Ed.), *Technologie der Wärmebehandlung von Stahl*, 2nd ed., VEB Deutscher Verlag für Grundstoffindustrie, Leipzig, 1987.)

6.1.6.1 Thermal Stresses in the Case of Ideal Linear-Elastic Deformation Behavior

When a metallic body is heated or cooled, as soon as a temperature difference between the surface and the core is established, residual stresses of the first kind occur. In heat treatment, quenching processes usually produce the biggest temperature gradients across the section and hence the greatest residual stresses. Let us therefore discuss thermal stresses due to local and temporal differences in shrinking during quenching of ideal linear-elastic cylinders in which no plastic deformation can arise.

Transformation-free cooling of cylinders is accomplished by the development of a sequence of inhomogeneous temperature distributions, which, as a consequence of the thermal shrinking behavior, in turn cause locally and temporally different thermal strains and hence shrinking stresses. It is assumed that linear-elastic cylinders can elastically accommodate these stresses at all temperatures. At the beginning of quenching, the surface of such a cylinder contracts more rapidly than its core. As a result, the surface zones of the cylinder are subject to tensile stresses in the longitudinal and tangential directions, while radially compressive stresses are created, as shown in Figure 6.31. In order to establish equilibrium, these stresses are counterbalanced by longitudinal, tangential, and radial compressive stresses within the core of the cylinder.

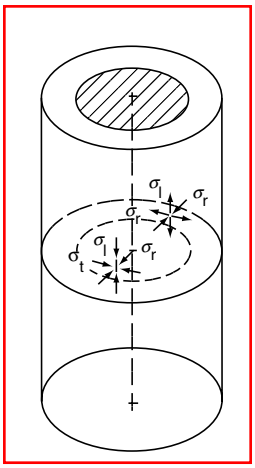

FIGURE 6.31 Thermal stresses in the surface zone and core of an ideal linear-elastic cylinder during rapid cooling (quenching). (From B. Liščić, H.M. Tensi, and W. Luty (Eds.), *Theory and Technology of Quenching*, Springer-Verlag, New York, 1992.)

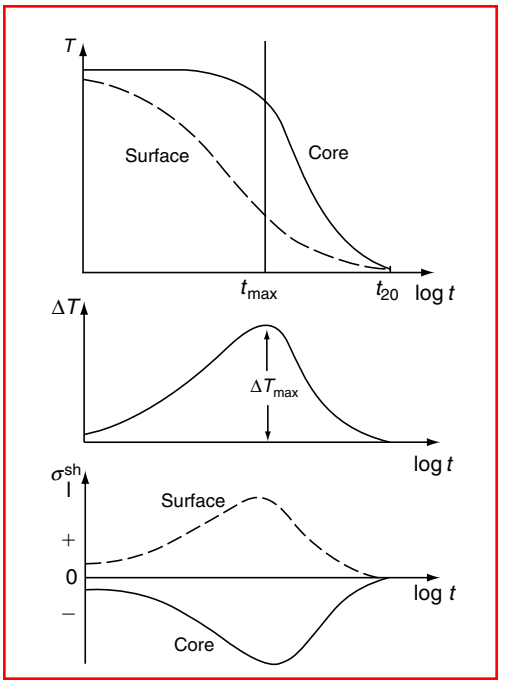

FIGURE 6.32 Top to bottom: time–temperature history, temperature difference between surface and core, and development of longitudinal stresses during transformation-free quenching of an ideal linear-elastic cylinder. (From B. Liščić, H.M. Tensi, and W. Luty (Eds.), *Theory and Technology of Quenching*, Springer-Verlag, New York, 1992.)

Figure 6.32 shows the temperature–time history at the very surface and at the core of the cylinder, the temperature difference between surface and core, and the development of longitudinal stresses during quenching of an ideal linear-elastic cylinder. The largest temperature difference ΔT_{max} is attained at $t = t_{max}$, where the slopes of temperature–time curves are identical for the core and the surface. Obviously, the surface reaches its maximum thermal stress before $t = t_{max}$; the core, however, reaches its maximum later than $t = t_{max}$.

The magnitude of the developed longitudinal stresses depends on cylinder diameter, as shown in Figure 6.33 for cylinder diameters of 30, 50, and 100 mm, when the cylinders were quenched from 800°C (1472°F) in water at 20°C (68°F). Because the maximum temperature difference between surface and core occurs later for the larger diameter cylinders, the maximum stresses also occur later for larger diameters. The longitudinal surface stress maximum always occurs at $t < t_{max}$, whereas those of the core occurs later than t_{max}. At $t < t_{max}$, steep temperature gradients are present near the cylinder surface (see Figure 6.32), which cause high tensile stresses. In contrast, at $t > t_{max}$, relatively steep core temperature gradients are established, which cause large compressive stresses in the core. Upon reaching the temperature balance at 20°C (68°F) ($t = t_{20}$), the ideal linear-elastic cylinders are free of residual stresses.

6.1.6.2 Transformational Stresses

Let us consider the development of pure transformational stresses in a material whose coefficient of thermal expansion is zero. Furthermore, assume that if in the course of quenching the martensite start temperature M_s is passed, complete martensitic transformation occurs, with corresponding volume increase.

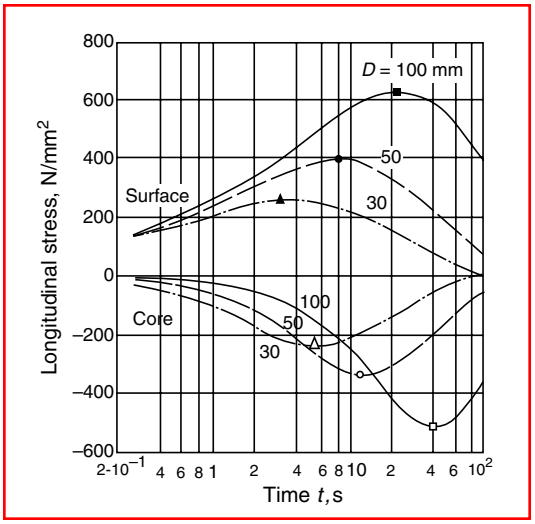

FIGURE 6.33 Dependence of longitudinal stresses at surface and core of ideal linear-elastic cylinders on their diameters, when quenched in water from 800 to 20°C. Calculated for unalloyed steel with medium carbon content. (From B. Liščić, H.M. Tensi, and W. Luty (Eds.), *Theory and Technology of Quenching*, Springer-Verlag, New York, 1992.)

The temperature–time curves for the surface and core of a cylinder of such a material are shown in Figure 6.34. After passing the M_s temperature at time $t = t_1$, as a consequence of transformation-induced volume increase, compressive transformational stresses develop at the surface. These stresses within the surface zone must be compensated for by tensile transformational stresses within the core of the cylinder. The magnitudes of both stresses increase in the course of further surface cooling.

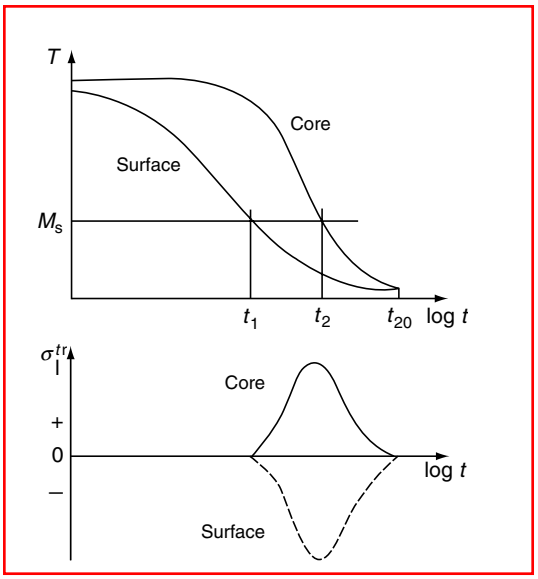

FIGURE 6.34 Temperature–time history and development of longitudinal transformation stresses, when quenching an ideal linear-elastic cylinder that transforms only to martensite. (From B. Liščić, H.M. Tensi, and W. Luty (Eds.), *Theory and Technology of Quenching*, Springer-Verlag, New York, 1992.)

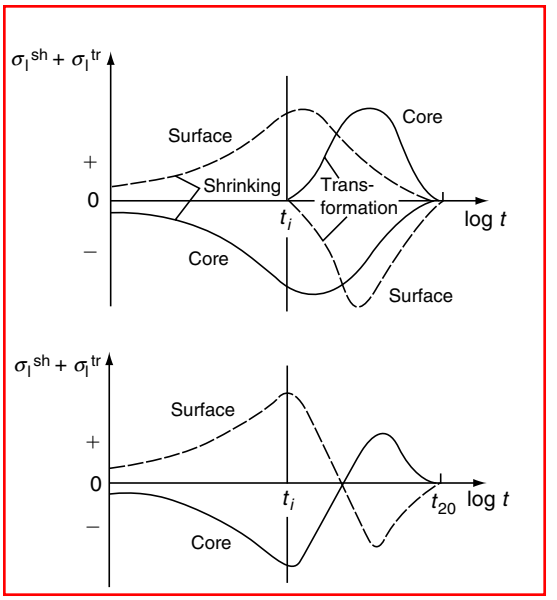

FIGURE 6.35 Combined thermal (shrinking) and transformation stresses during quenching of an ideal linear-elastic cylinder that transforms from austenite to martensite. (From B. Liščić, H.M. Tensi, and W. Luty (Eds.), *Theory and Technology of Quenching*, Springer-Verlag, New York, 1992.)

When the core temperature reaches M_s at time $t = t_2$, a transformation-induced volume increase occurs in the core, which leads to a reduction of the tensile stresses present there. The surface compressive stresses are correspondingly reduced. After reaching temperature equalization at $t = t_{20}$, the same amounts of martensite are present across the whole cylinder, so that finally a residual stress-free state is established. If, however, different amounts of martensite are formed within distinct areas, also under the idealized assumptions made here, some transformational residual stresses will remain.

In addition to the longitudinal stresses, tangential and radial residual stresses are caused by structural transformation. Within the surface zone, tangential compressive and radial tensile stresses are to be expected, while in the core all components should be tensile stresses.

When thermal (shrinking) and transformational stresses act simultaneously during quenching of an ideal linear-elastic cylinder that transforms from austenite to martensite, superposition of the two types of stresses occurs as shown in Figure 6.35. The upper graph shows the time dependence of the longitudinal components of thermal and transformational stresses at surface and core. The lower graph shows the time dependence of the total stress after the formal superposition of the two. The initiation of martensitic transformation immediately reduces the absolute stress value within both core and surface.

Further increasing martensitic transformation causes a stress inversion in both regions. Provided that the transformation occurs uniformly across the whole cylinder, at $t = t_{20}$ the tensile core stresses and the compressive surface stresses approach zero. Hence when temperature equalization is achieved in an ideal linear-elastic cylinder no residual stresses remain.

6.1.6.3 Residual Stresses When Quenching Cylinders with Real Elastic–Plastic Deformation Behavior

In real practice there is no ideal linear-elastic deformation behavior as assumed above. The yield strength (R_y) of metallic materials, which limits the elastic deformation range, is strongly temperature-dependent and decreases with increasing temperature.

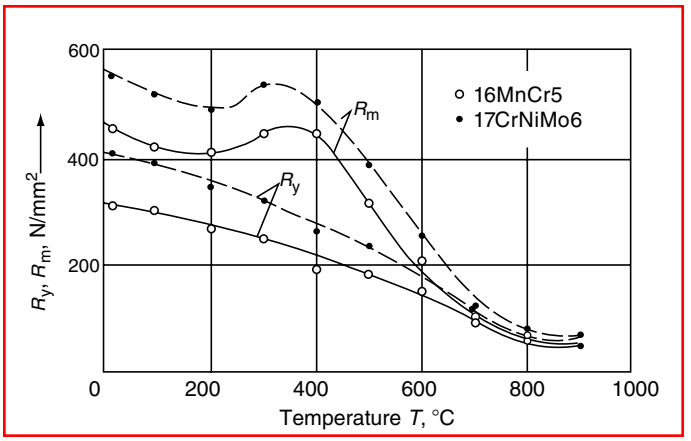

FIGURE 6.36 Yield strength (R_y) and tensile strength (R_m) of the steels DIN 16MnCr5 and DIN 17CrNiMo6 as a function of temperature. (From B. Liščić, H.M. Tensi, and W. Luty (Eds.), *Theory and Technology of Quenching*, Springer-Verlag, New York, 1992.)

At any temperature, plastic deformations will develop when stresses surpass the corresponding yield strength. The ultimate tensile strength, which limits the uniaxial loading capacity of the material, is also temperature-dependent as shown in Figure 6.36 for two low-alloy steels. During quenching of a cylinder, biaxial longitudinal and tangential stresses develop in its surface zone, whereas triaxial longitudinal, tangential, and radial stresses develop in the cylinder core. Plastic deformations can occur only if the local equivalent stresses equal or exceed the yield strength of the material at the corresponding temperature.

Equivalent stresses can be calculated according to various hypotheses. Assuming the validity of the van Mises criterion, the equivalent stress of a triaxial stress state, given by the principal stresses σ_1, σ_2, σ_3, is

$$\sigma_{eq} = \frac{1}{\sqrt{2}}[(\sigma_1 - \sigma_2)^2 + (\sigma_2 - \sigma_3)^2 + (\sigma_3 - \sigma_1)^2]^{1/2} \tag{6.30}$$

During quenching of a cylinder in its surface zone, $\sigma_1 = \sigma_l$ and $\sigma_2 = \sigma_t$, while in its core $\sigma_1 = \sigma_l$, $\sigma_2 = \sigma_t$, and $\sigma_3 = \sigma_r$.

The condition for the onset of plastic deformation will be fulfilled when $\sigma_{eq} = R_y$. The local shrinking and transformational stress components and consequently the equivalent stress (σ_{eq}) depend on temperature, cooling conditions, geometry, and the mechanical and thermal properties of the material, and the yield strength (R_y) depends on temperature and the structure of the material.

The temperature dependence of the yield strength is obviously of particular importance for the stresses that result upon quenching. Figure 6.37 shows the temperature–time history and development of yield strength for surface and core of a cylinder during quenching. Figure 6.37a depicts the case of transformation-free cooling, and Figure 6.37b is valid for cooling with martensitic transformation. To determine the occurrence of plastic deformations at any instant, the local yield strength must be compared with the local equivalent stress. Because plastic deformations never occur homogeneously over the whole cross section of the cylinder, residual stresses always remain after temperature equalizations. Plastic deformations can be caused by either thermal (shrinking) stresses or transformational stresses or by a combination of the two.

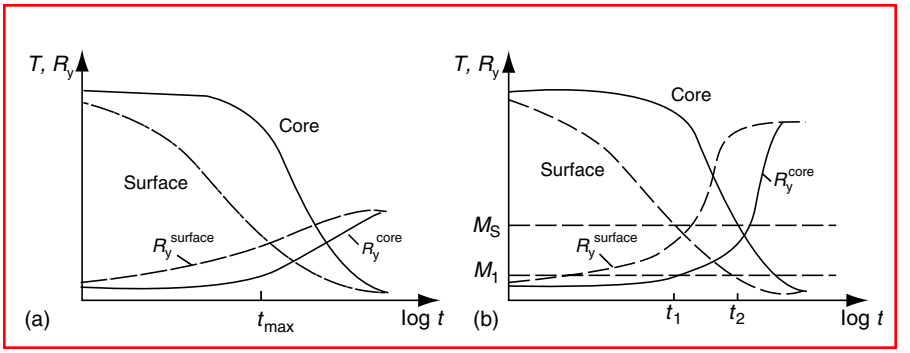

FIGURE 6.37 Temperature–time history and development of yield strength for surface and core during quenching of a cylinder (a) without and (b) with martensitic transformation. (From B. Liščić, H.M. Tensi, and W. Luty (Eds.), *Theory and Technology of Quenching*, Springer-Verlag, New York, 1992.)

6.1.6.3.1 Thermal (Shrinking) Residual Stresses

Figure 6.38 shows the cooling curves for the surface and core of a cylinder during quenching without martensitic transformation and the temperature- (and time-) dependent yield strengths, which at the same temperature are assumed to be identical for tensile and compressive loading. At the start of quenching, the surface temperature decreases faster than the core temperature (Figure 6.38a). As a result, longitudinal tensile stresses develop at the surface and compressive stresses develop at the core. If they were elastically accommodated,

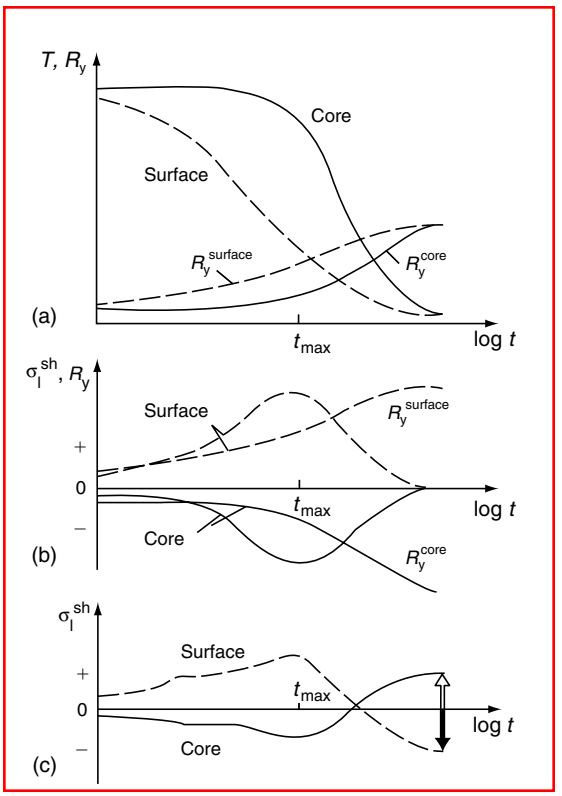

FIGURE 6.38 Longitudinal thermal (shrinking) residual stresses when quenching a cylinder. (From B. Liščić, H.M. Tensi, and W. Luty (Eds.), *Theory and Technology of Quenching*, Springer-Verlag, New York, 1992.)

their development would be as shown in Figure 6.38b. However, because of the temperature dependence of the yield strengths for surface and core, neither the surface nor the core can withstand these stresses without plastic deformation, and so the surface zone is plastically extended and the core is plastically compressed. After the time $t = t_{max}$, the temperature of the core decreases faster than that of the surface, leading to a reduction of the magnitudes of shrinking stresses in both regions. However, the stress values of core and surface reach zero at different instants, as they can no longer coexist at the same time in a stress-free state because of plastic extension at the surface and plastic compression in the core. Upon further cooling, this extension and compression cause compressive and tensile stresses, respectively, which are opposed by those due to the temperature differences still existing between core and surface. These latter stresses ultimately vanish after reaching the temperature equalization at the end of quenching, and hence thermal (shrinking) residual stresses remain that are compressive at the surface and tensile in the core, as depicted in Figure 6.38c.

6.1.6.3.2 Transformational Residual Stresses

Figure 6.39 shows cooling curves for surface and core when quenching a cylinder that, upon cooling below the M_s temperature, transforms completely to martensite. For simplicity, it is assumed that no thermal (shrinking) stresses occur. Figure 6.39b shows the yield strengths for surface and core, showing their strong increase with the onset of martensitic transformation.

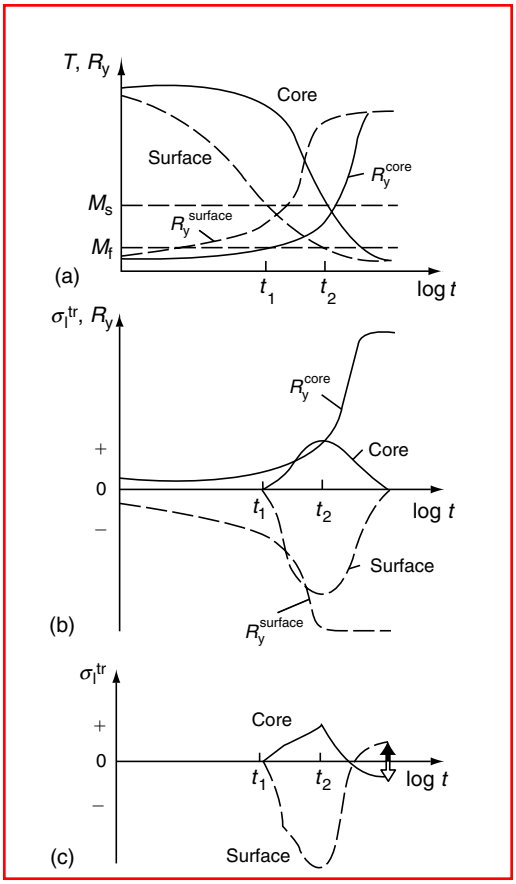

FIGURE 6.39 Longitudinal transformation residual stresses when quenching a cylinder. (From B. Liščić, H.M. Tensi, and W. Luty (Eds.), *Theory and Technology of Quenching*, Springer-Verlag, New York, 1992.)

The surface of the cylinder starts to transform to martensite at $t = t_1$. At that time the volume expansion of the surface zone is impeded by the core not yet transformed. As a result, compressive transformational stresses are established at the surface that are compensated for by tensile stresses at the core. From Figure 6.39b it can be concluded that both areas plastically deform. In the course of further cooling, the tensile stressed core reaches M_s at $t = t_2$. The immediate volume increase reduces both the tensile stresses of the core and the compressive stresses of the surface. Due to the differently sized and opposing plastic deformations generated, the stresses at surface and core pass zero values at different time. Upon further cooling the still existing volume incompatibilities between surface and core create transformational stresses of opposite sign to those that are produced by the plastic deformations. After reaching temperature equalization, compressive residual stresses remain in the core and tensile residual stresses remain at the surface, as shown in Figure 6.39c.

It should be noted also that transformation-induced plastic deformations that occur under local tensile or compressive stresses may enhance the local strains.

6.1.6.3.3 Hardening Residual Stresses

When austenitized steel cylinders are quenched to room temperature, both thermal (shrinking) and transformational stresses develop, causing hardening residual stresses, which cannot be described by simply superimposing the shrinking and transformational stresses. Of fundamental importance is the fact that any local martensitic transformation coupled with a volume increase always shifts the existing stress (irrespective of its sign) to more negative values. As a reaction, for reasons of equilibrium, the unaffected material zones react with positive stress changes. Structural transformations that occur in tensile-stressed material regions are therefore inevitable to reduce the stresses, while transformations that take place in compressively stressed zones always enhance the (negative) values of the stresses. Consequently, because the thermal (shrinking) stresses of core and surface change sign in the course of cooling during the time interval $t_{c,0}-t_{s,0}$ as depicted in Figure 6.40a, the positions of the initiation time of transformation at the surface ($t_{s,i}$) and in the core ($t_{c,i}$) relative to this time interval are of key importance for the hardening residual stresses that will remain at the end of quenching.

The average time that passes before the quenching stresses invert is

$$t_0 = (1/2)(t_{s,0} + t_{c,0}) \tag{6.31}$$

Because for full-hardening steel cylinders the time for surface transformation ($t_{s,i}$) always occurs earlier than the time for core transformation ($t_{c,i}$), it is appropriate to distinguish between the following cases:

$t_0 < t_{s,i} < t_{c,i}$ (Figure 6.40b)

$t_0 \approx t_{s,i} < t_{c,i}$ (Figure 6.40c)

$t_{s,i} < t_{c,i} \approx t_0$ (Figure 6.40d)

$t_{s,i} < t_{c,i} < t_0$ (Figure 6.40e)

Figure 6.40 shows schematically the development of longitudinal stresses as a function of time and remaining longitudinal residual stress distributions across the section of cylinder

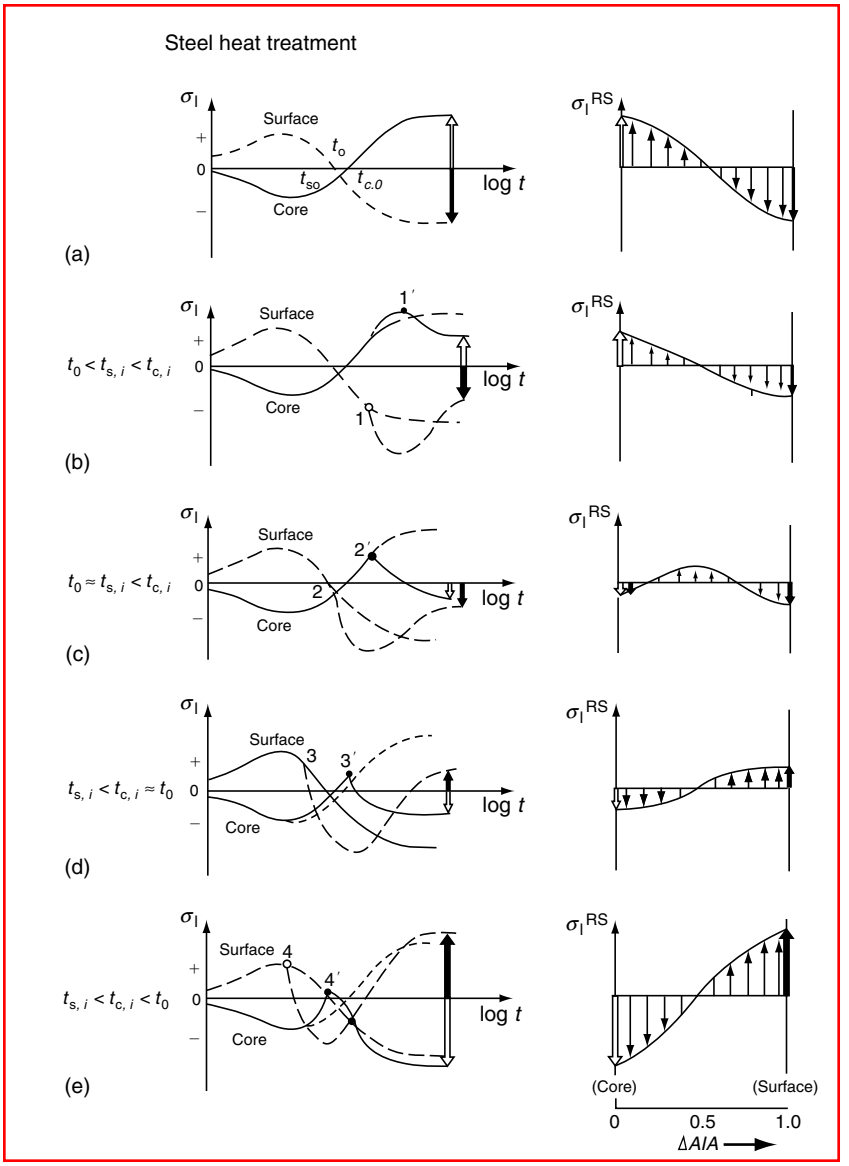

FIGURE 6.40 Different possibilities of generation and development of hardening residual stresses (b–e) compared to pure thermal (shrinking) residual stresses (a), when quenching a cylinder with real elastic–plastic deformation behavior. (From B. Liščić, H.M. Tensi, and W. Luty (Eds.), *Theory and Technology of Quenching*, Springer-Verlag, New York, 1992.)

specimens with real elastic–plastic deformation behavior after complete temperature equalization at the end of the quenching process.

Figure 6.40a shows a transformation-free quenching, and Figure 6.40b–Figure 6.40e demonstrate the combined effects of thermal (shrinking) and transformational processes. The numbers 1–4 depict the initiation of transformation at the surface, while 1′–4′ represent that of the core. Figure 6.40b illustrates the case when both surface and core transform after t_0. At the end of this cooling process, compressive stresses at the surface and tensile stresses in the core remain.

Figure 6.40c illustrates the stress development in the case when the surface transforms slightly before t_0 and the core transforms later. At the end of this cooling process, both core

and surface remain under compressive residual stresses, while the regions in between are subjected to tensile residual stresses.

Figure 6.40d illustrates the case when the surface transforms before t_0 and the core at about t_0. At the end of this cooling process, tensile surface residual stresses and compressive core residual stresses remain.

Figure 6.40e illustrates the case when both surface and core transform before t_0. In this case the start of transformation at the surface caused a rapid reduction of the tensile stresses. For reasons of equilibrium, the longitudinal stresses at the core must also change during further cooling. Martensitic transformation in the core takes place when tensile stresses are acting there. This again causes stress inversions in the surface zone and in the core. At the end of this cooling process, tensile stresses at the surface and compressive stresses in the core remain.

When full hardening of equal-sized cylinders with different M_s temperatures is compared with respect to residual stress distributions, one finds that cylinders made of steels with low M_s temperatures show tensile surface residual stresses, whereas cylinders made of steel with high M_s temperatures give compressive surface residual stresses, as schematically illustrated in Figure 6.41.

Because the high-temperature yield strength usually increases with decreasing M_s temperature, the largest tensile shrinking stresses develop at the surface of the steel with $M_{s,3}$ and the smallest at the surface of the steel with $M_{s,1}$. The martensitic transformation, however, begins earliest for the steel with the highest and latest for the steel with the lowest M_s temperature.

When high shrinking stresses and high M_s values act together, no secondary stress inversion occurs during further cooling, and ultimately compressive residual stresses remain within the surface zone.

On the basis of the preceding discussion, the whole range of expected hardening residual stress distributions in quenched steel cylinders can be divided into three main groups, as

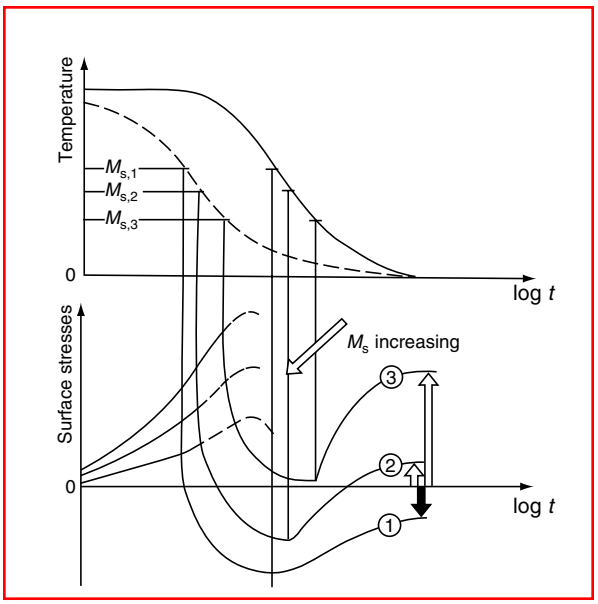

FIGURE 6.41 Influence of different M_s temperatures on the development of surface residual stresses. (From B. Liščić, H.M. Tensi, and W. Luty (Eds.), *Theory and Technology of Quenching*, Springer-Verlag, New York, 1992.)

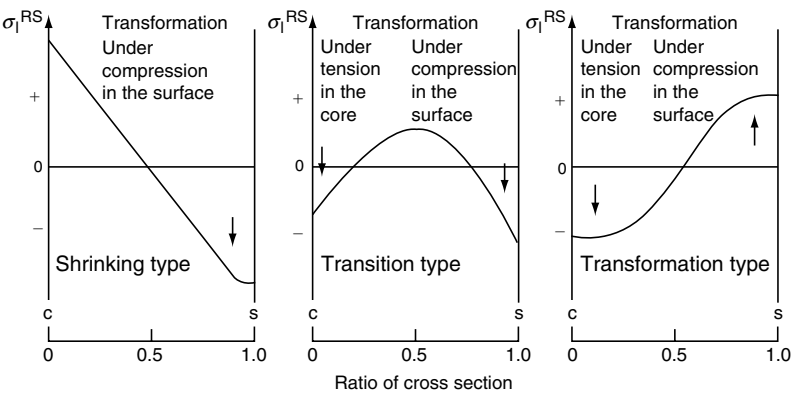

Steel	Quenching process	Cylinder diameters in mm for residual stresses of		
		Shrinking type	Transition type	Transformation type
Ck 45	850°C→20°C H_2O	100···30	15	5
	850°C→60°C oil	50	30	10

FIGURE 6.42 Basic types of hardening residual stresses. (From B. Liščić, H.M. Tensi, and W. Luty (Eds.), *Theory and Technology of Quenching*, Springer-Verlag, New York, 1992.)

schematically illustrated in Figure 6.42. The arrows indicate how local transformations under existing stress states will affect the residual stress distribution.

It should be emphasized that the residual stress distributions that are created during quenching of cylinders with different diameters but made of the same steel can be shifted from the transformation type to the shrinking type with increasing cylinder diameter as well as with the higher quenching intensity, i.e., higher cooling rates. Some cylinder diameter and quenchants are specified for the unalloyed steel DIN Ck45 where the basic residual stress types occur.

The above statements and specifically the principle that local stresses are shifted to more negative values due to transformation-induced volume increase also hold for all nonmartensitic transformations that are accompanied by volume changes. In the individual case, the effect of volume changes on the final residual stress state depends on when the transformations start at the core and surface relative to time t_0.

6.1.6.4 Dimensional Changes and Distortion during Hardening and Tempering

As a consequence of thermal (shrinking) stresses and transformational stresses, changes occur in both the shape and size of workpieces during hardening and tempering. Because there are many factors that influence dimensional changes and distortion, the most difficult problem in practice is to predict the amount of dimensional changes and distortion. It is likely that computer modeling of the quenching process, which can account for the influence of all relevant factors, will in the future enable more precise prediction. Let us therefore discuss only some basic mechanisms of dimensional changes and distortion during hardening and tempering.

6.1.6.4.1 Influence of Thermal (Shrinking) Stresses

Because of thermal (shrinking) stresses during quenching, generally all bodies whose shape is different from a sphere tend by deformation to assume a spherical shape, which offers the

least resistance during deformation. This means, at the practical level, that bodies that have the shape of a cube will assume spherically distorted sides, bodies with the shape of a prism will become thicker and shorter, and plates will shrink in area and become thicker. These deformations are greater with greater temperature differences between the surface and the core, i.e., with higher quenching intensity (which also corresponds to bigger differences between the austenitizing temperature and the temperature of the quenchant); with greater cross-sectional size of the workpiece; and with smaller heat conductivity and smaller high-temperature strength of the material.

The effect of thermal (shrinking) stresses can be studied in a low-carbon steel or an austenitic steel, in which the martensitic transformation can be disregarded. Figure 6.43 shows, according to Frehser and Lowitzer [15], the effect of different quenching intensities on dimensional changes and distortion of plates made of low-carbon steel (0.10% C) after quenching in water, oil, molten salt bath, and air. In Figure 6.43a the plate is solid, and in Figure 6.43b the plate has an inner square hole of 100×100 mm. The outer full lines denote the original size of each plate. To illustrate the dimensional changes more clearly, they have been drawn to a larger scale (see the 0.4-mm scale). From this figure it is evident that the more drastic the quench, the greater are the dimensional changes and distortion.

Figure 6.44 shows that a greater difference between the austenitizing temperature and the temperature of the quenchant causes greater dimensional changes and distortion. Figure 6.45 shows the effect of the high-temperature strength of the material. The steel having the greatest high-temperature strength (18/8 steel) exhibits the highest dimensional stability.

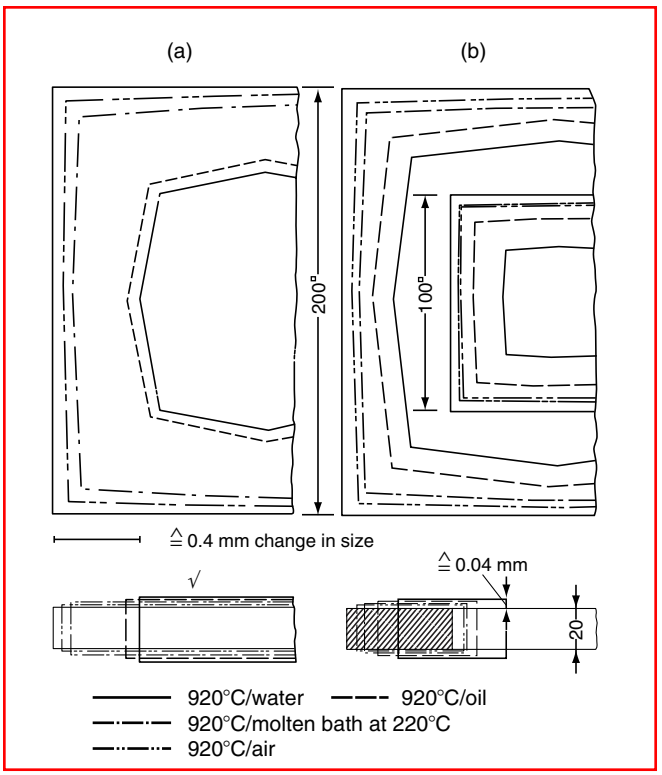

FIGURE 6.43 Dimensional changes and distortion of plates made from low-carbon steel (0.10% C) after cooling in water, oil, molten salt bath, and air. (From K.E. Thelning, *Steel and Its Heat Treatment*, 2nd ed., Butterworths, London, 1984.)

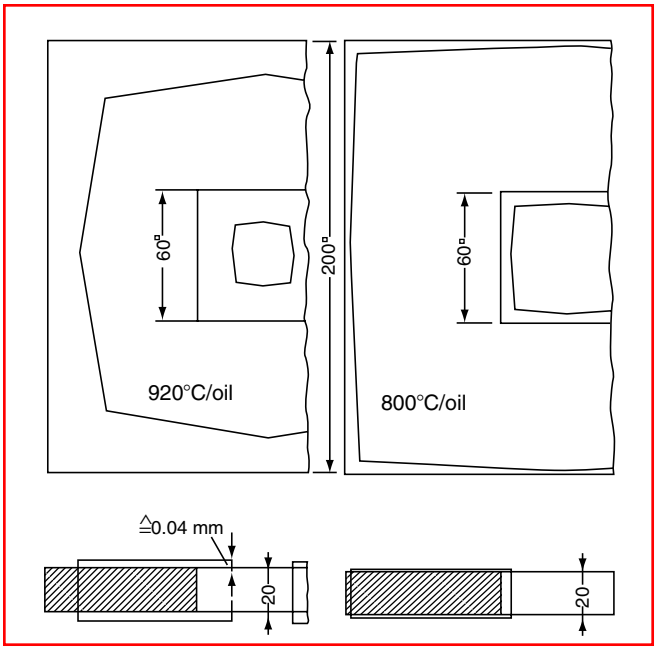

FIGURE 6.44 Effect of difference between the austenitizing temperature and the temperature of the quenchant on dimensional changes after quenching plates of low-carbon steel in oil. (From K.E. Thelning, *Steel and Its Heat Treatment*, 2nd ed., Butterworths, London, 1984.)

6.1.6.4.2 Influence of Transformation Stresses

During heating and cooling, steels pass through various structural transformations accompanied by volume changes. These changes are usually studied by using a dilatometer and are registered as changes in length of the specimen, as shown, for example, in Figure 6.46 for eutectoid steel. During heating a continuous increase in length occurs up to A_{c1}, where the steel shrinks as it transforms to austenite. After the austenite formation is completed, the length increases again. However, the expansion coefficient for austenite is not the same as the expansion coefficient for ferrite.

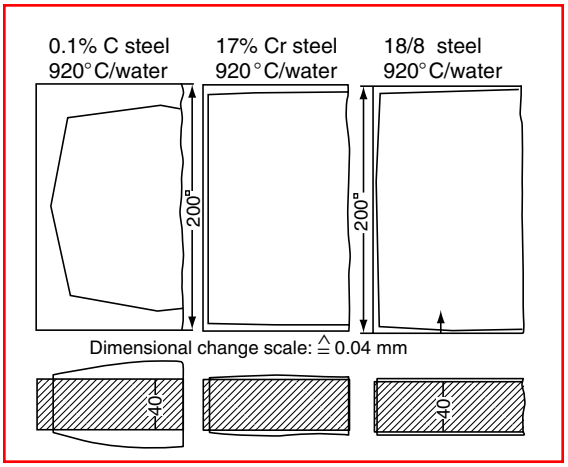

FIGURE 6.45 Dimensional changes and distortion after quenching steel plates of different composition from 920°C in water. (From K.E. Thelning, *Steel and Its Heat Treatment*, 2nd ed., Butterworths, London, 1984.)

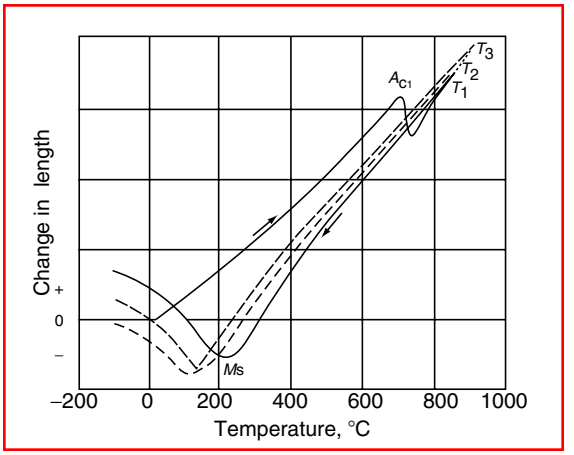

FIGURE 6.46 Dilatometer curves showing change in length during heating and rapid cooling of a eutectoid (0.8% C) steel. (From K.E. Thelning, *Steel and Its Heat Treatment*, 2nd ed., Butterworths, London, 1984.)

On cooling, thermal contraction takes place, and when martensite starts to form at the M_s temperature, the volume increases and the length of the specimen therefore increases. After cooling to room temperature, most martensitic steels contain some retained austenite, the amount of which increases with increased carbon content, with higher austenitizing temperature, and with the amount of some alloying elements dissolved during austenitization. The larger the quantity of retained austenite contained in the steel after hardening, the smaller the increase in volume and in length of the specimen.

Various structural constituents have different densities and hence different values of specific volume, as shown in Table 6.4. The amount of carbon dissolved in austenite, in martensite, or in different carbides has a relatively strong effect on the specific volume as the formulas for calculating specific volume in this table indicate. When calculating the changes in volume that take place during the transformations of different structural phases, the carbon content must be taken into account, as shown in Table 6.5.

TABLE 6.4
Specific Volume of Phases Present in Carbon Tool Steels

Phase or Phase Mixture	Range of Carbon (%)	Calculated Specific Volume at 20°C (cm^3/g)
Austenite	0–2	$0.1212 + 0.0033 \times (\%C)$
Martensite	0–2	$0.1271 + 0.0025 \times (\%C)$
Ferrite	0–0.02	0.1271
Cementite	6.7 ± 0.2	0.130 ± 0.001
ε-Carbide	8.5 ± 0.7	0.140 ± 0.002
Graphite	100	0.451
Ferrite + cementite	0–2	$0.271 + 0.0005 \times (\%C)$
Low carbon content martensite ε-carbide	0.25–2	$0.1277 + 0.0015 \times (\%C - 0.25)$
Ferrite + ε-carbide	0–2	$0.1271 + 0.0015 \times (\%C)$

Source: From K.E. Thelning, *Steel and its Heat Treatment*, 2nd ed., Butterworths, London, 1984.

TABLE 6.5
Changes in Volume during Transformation to Different Phases

Transformation	Change in Volume (%)
Spheroidized pearlite → austenite	$-4.64 + 2.21 \times (\%C)$
Austenite → martensite	$4.64 - 0.53 \times (\%C)$
Spheroidized pearlite → martensite	$1.68 \times (\%C)$
Austenite → lower bainite	$4.64 - 1.43 \times (\%C)$
Spheroidized pearlite → lower bainite	$0.78 \times (\%C)$
Austenite → upper bainite	$4.64 - 2.21 \times (\%C)$
Spheroidized pearlite → upper bainite	0

Source: K.E. Thelning, *Steel and Its Heat Treatment*, 2nd ed., Butterworths, London, 1984.

Taking as a basis the proportions of martensite and austenite, together with the amount of carbon dissolved therein, and using the data from Table 6.5, one can calculate the changes in volume that occur during hardening. If the steel contains undissolved cementite, this volume has to be deducted during the calculation. The following equation should be used:

$$\frac{\Delta V}{V} = \frac{100 - V_c - V_a}{100} \times 1.68C + \frac{V_a}{100}(-4.64 + 2.21C) \tag{6.32}$$

where $\Delta V/V$ is the change in volume in %, V_c is the amount of undissolved cementite in vol%, V_a is the amount of austenite in vol%, $100 - V_c - V_a$ is the amount of martensite in vol%, and C is the carbon dissolved in austenite and martensite, respectively, in % by weight.

The increase in volume during martensitic transformation depends not only on the carbon content but also on the kind and amount of alloying elements in the steel. Consequently, different groups of steels undergo different changes in volume during hardening. The unalloyed water-hardening steels experience the greatest volume changes, followed by low-alloy oil-hardening steels, while the high-alloy ledeburitic Cr alloy steels show the least volume increase during hardening, as shown in Figure 6.47. The austenitizing temperature, as mentioned earlier, has an influence on the amount of retained austenite after hardening. Because the retained austenite producing volume contraction (compared to the original volume) counteracts the volume increase caused by martensitic transformation, the austenitizing temperature may influence the volume changes during hardening.

It should also be noted that engineering steels are not isotropic materials (because of the rolling process they have undergone), which means that the linear change occurring during hardening will not be the same in the direction of rolling as in the direction perpendicular to it.

6.1.6.4.3 Dimensional Changes during Tempering

During tempering, relaxation as well as structural transformations occur, which change the volume of the hardened steel and its state of stress. Martensite decomposes to form ferrite and cementite, which implies that there is a continuous decrease in volume. The continuous decomposition of martensite during tempering causes at the same time a continuous reduction in the state of stress. Figure 6.48 is a schematic presentation of the effect of changes of structural constituents on the volume changes during tempering of a hardened steel. The dashed curves represent increases in volume during different tempering stages. The retained austenite, which in carbon steels and low-alloy steels is transformed to bainite in the second stage of tempering at about 300°C (572°F), results in an increase in volume.

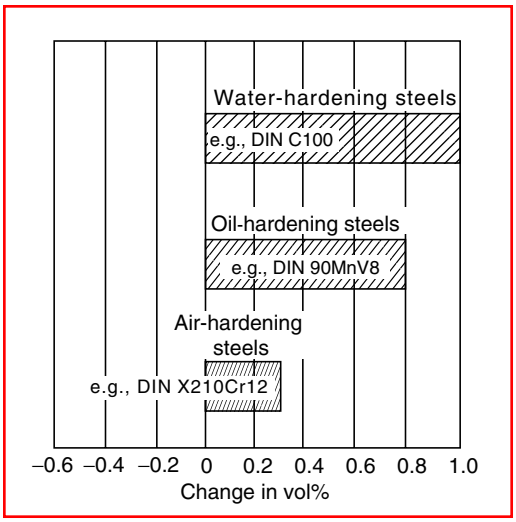

FIGURE 6.47 Volume changes of different steels during hardening when martensite is formed across the whole section. (From H.J. Eckstein (Ed.), *Technologie der Wärmebehandlung von Stahl*, 2nd ed., VEB Deutscher Verlag für Grundstoffindustrie, Leipzig, 1987.)

When high-alloy tool steels are tempered at 500–600°C (932–1112°F), very finely distributed carbides are precipitated. This gives rise to a stress condition that results in increased hardness and greater volume. Simultaneously with the precipitation of carbides the alloy content of the matrix is reduced, which implies that the M_s point of the retained austenite will be raised to higher temperatures. During cooldown from the tempering, the retained austenite will transform to martensite, which also results in an increase in volume.

Figure 6.49 shows changes in length for different steels as a function of tempering temperature. For low-alloy steels (105WCr6, see curve 1 of Figure 6.49), one can easily recognize the particular tempering stages. At low tempering temperatures (first tempering stage), a volume contraction takes place as a consequence of ε-carbide precipitation. At higher tempering temperatures (second tempering stage), transformation of the retained

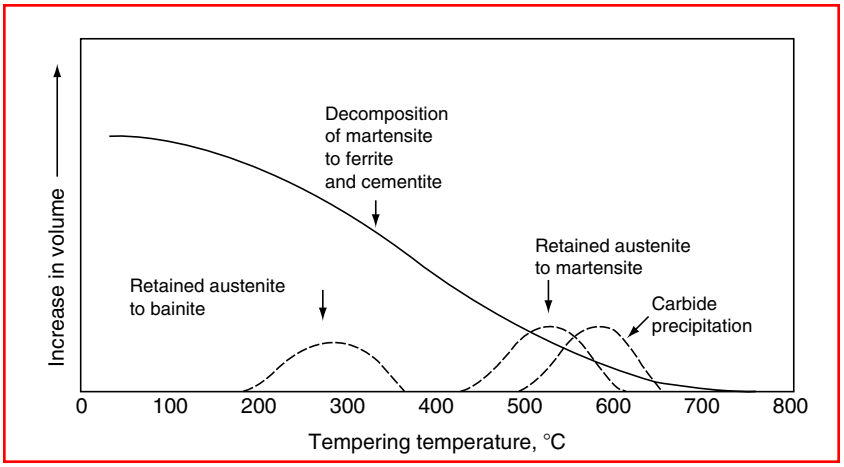

FIGURE 6.48 Schematic presentation of the effect of changes of structural constituents on volume changes during tempering of hardened steel. (From K.E. Thelning, *Steel and Its Heat Treatment*, 2nd ed., Butterworths, London, 1984.)

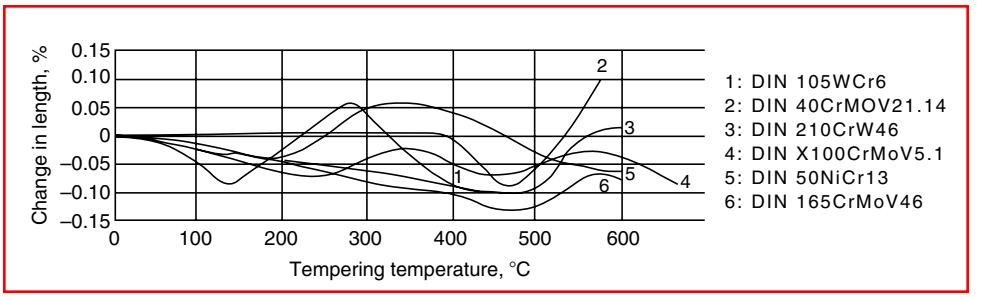

FIGURE 6.49 Change in length of different steels during tempering as a function of tempering temperature. (Designation of steels according to DIN.) (From H.J. Eckstein (Ed.), *Technologie der Wärmebehandlung von Stahl*, 2nd ed., VEB Deutscher Verlag für Grundstoffindustrie, Leipzig, 1987.)

austenite again causes a certain volume increase, and in the third tempering stage the progressive decomposition of martensite leads to the volume decrease.

For high-alloy tool steels (e.g., 210CrW46, curve 3 of Figure 6.49), a stabilization of austenite is evident, so that the effect of the volume increase (due to austenite–bainite or austenite–martensite transformation) takes place only at higher temperatures. In most cases, as can be seen from Figure 6.49, a reduction in length, i.e., a volume decrease, can be found after tempering.

It should be noted that the changes in length shown in Figure 6.49 represent only the order of magnitude of the expected changes, because the actual value depends in each case on the specific heat treatment conditions. The austenitizing temperature, which determines the amount of carbon dissolved and the amount of retained austenite, has a strong influence on expected volume changes.

6.2 ANNEALING PROCESSES

6.2.1 Stress-Relief Annealing

Stress-relief annealing is an annealing process below the transformation temperature A_{c1}, with subsequent slow cooling, the aim of which is to reduce the internal residual stresses in a workpiece without intentionally changing its structure and mechanical properties.

Residual stresses in a workpiece may be caused by

1. Thermal factors (e.g., thermal stresses caused by temperature gradients within the workpiece during heating or cooling)
2. Mechanical factors (e.g., cold-working)
3. Metallurgical factors (e.g., transformation of the microstructure)

In processes that involve heat, residual stresses are usually caused by the simultaneous existence of thermal and transformational stresses (e.g., during the solidification of liquid metals, hot forming, hardening, or welding). Thermal stresses are always directly proportional to the existing temperature gradient, which further depends on the cross-sectional size and on the heating or cooling rate.

In workpieces made of steel, for the above reasons, local residual stresses may amount to between about 10 N/mm^2 and values close to the yield strength at room temperature. The consequences of residual stresses may include

1. Dimensional changes and warpage of the workpiece
2. Formation of macroscopic and microscopic cracks
3. Asymmetric rotation of shafts
4. Impairment of the fatigue strength of engineering components

Residual stresses in a workpiece can be reduced only by a plastic deformation in the microstructure. This requires that the yield strength of the material be lowered below the value of the residual stresses. The more the yield strength is lowered, the greater the plastic deformation and correspondingly the greater the possibility or reducing the residual stresses. The yield strength and the ultimate tensile strength of the steel both decrease with increasing temperature, as shown in Figure 6.50 for a low-carbon unalloyed steel. Because of this, stress-relief annealing means a through-heating process at a correspondingly high temperature. For plain carbon and low-alloy steels this temperature is usually between 450 and 650°C (842 and 1200°F), whereas for hot-working tool steels and high-speed steels it is between 600 and 750°C (1112 and 1382°F). This treatment will not cause any phase changes, but recrystallization may take place. Tools and machine components that are to be subjected to stress-relief annealing should be left with a machining allowance sufficient to compensate for any warping resulting from stress relief.

When dealing with hardened and tempered steel, the temperature of stress-relief annealing should be about 25°C (77°F) below that used for tempering. If the tempering temperature was quite low, after stress-relief annealing quite a high level of residual stresses will remain. In some other cases, for instance with a gray iron, the maximum temperature of the stress-relief annealing should be limited because of possible strength loss. Therefore gray iron must not be stress-relief annealed above 550°C (1022°F).

In the heat treatment of metals, quenching or rapid cooling is the cause of the greatest residual stresses. A high level of residual stress is generally to be expected with workpieces that have a large cross section, are quenched at a high cooling rate, and are made of a steel of low hardenability. In such a case high-temperature gradients will arise on the one side, and on the other side structural transformations will occur at different points of the cross section at different temperatures and different times. In contrast to heat treatment processes with continuous cooling, processes with IT (e.g., austempering) result in a low level of residual stresses.

To activate plastic deformations, the local residual stresses must be above the yield strength of the material. Because of this fact, steels that have a high yield strength at elevated temperatures can withstand higher levels of residual stress than those that have a low yield strength at elevated temperatures.

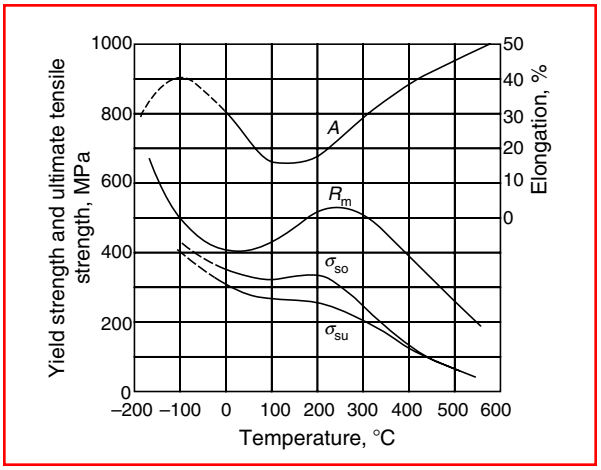

FIGURE 6.50 Change in some mechanical properties of low-carbon unalloyed steel with increasing temperature, according to Christen. A, Elongation; R_m, ultimate tensile strength; σ_{so}, upper yield strength; σ_{su}, lower yield strength. (From H.J. Eckstein (Ed.), *Technologie der Wärmebehandlung von Stahl*, 2nd ed., VEB Deutscher Verlag für Grundstoffindustrie, Leipzig, 1987.)

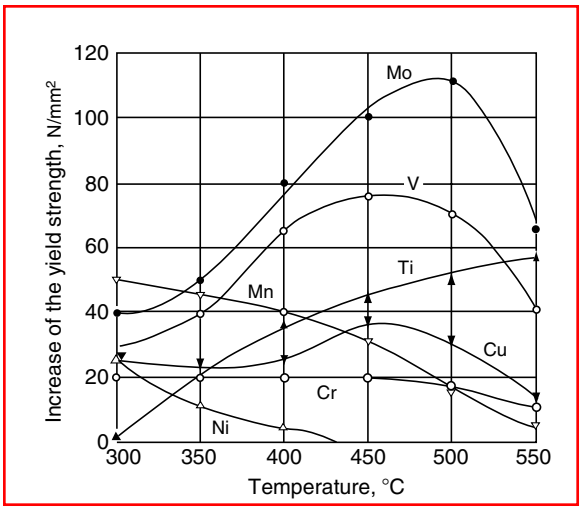

FIGURE 6.51 Increase in yield strength at elevated temperatures when 0.5% of each alloying element indicated is added to an unalloyed steel. (From G. Spur and T. Stöferle (Eds.), *Handbuch der Fertigungstechnik, Vol. 4/2, Wärmebehandeln*, Carl Hanser, Munich, 1987.)

The level of yield strength at elevated temperatures depends on the alloying elements in the steel. Figure 6.51 shows the increase in yield strength at temperatures of 300–550°C (572–1022°F) when 0.5% of each element was added to an unalloyed steel. It can be seen from this diagram that additions of Mo and V are most effective in increasing the yield strength at elevated temperatures.

To reduce residual stresses in a workpiece by stress-relief annealing, a temperature must be reached above the temperature corresponding to the yield strength that is adequate to the maximum of the residual stresses present. In other words, every level of residual stress in a workpiece corresponds to a yield strength that in turn depends on temperature. In addition to temperature, soaking time also has an influence on the effect of stress-relief annealing, i.e., on the reduction of residual stresses, as shown in Figure 6.52.

The relation between temperature and soaking time during stress-relief annealing can be described by Hollomon's parameter:

$$P = T(C + \log t) \tag{6.33}$$

where P is Hollomon's parameter (heat treatment processes with the same Hollomon parameter value have the same effect), C is the Hollomon–Jaffe constant, T is temperature (K), and t is time (h).

The Hollomon–Jaffe constant can be calculated as

$$C = 21.3 - (5.8 \times \%\ \text{carbon}) \tag{6.34}$$

Figure 6.53 shows (according to Larson–Miller method) calculated values of the yield strength at elevated temperatures (for 0.2% strain) for three grades of alloyed structural steels for hardening and tempering (designations according to DIN). Using this diagram, the abscissa of which represents the actual Hollomon parameter P, knowing the temperature and time of the stress-relief annealing, one can read off the level of residual stresses that will remain in the workpiece after this annealing process, i.e., the level up to which the residual stresses will be reduced by this stress-relief annealing. If, for instance, for DIN 24CrMoV5.5 steel, a

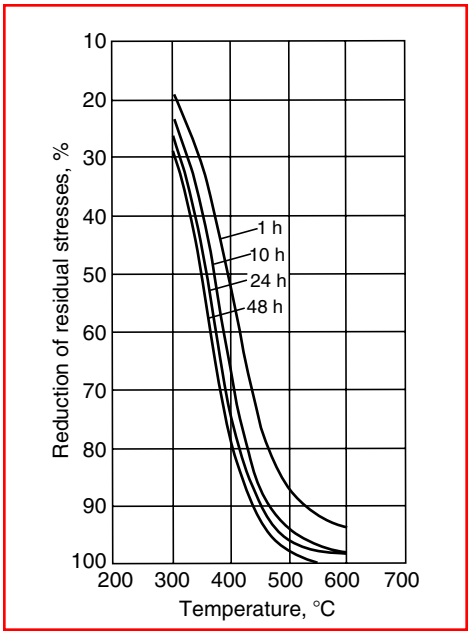

FIGURE 6.52 Effect of soaking time (at different temperatures) of stress-relief annealing on the reduction of residual stresses for hardening and tempering steels. (From G. Spur and T. Stöferle (Eds.), *Handbuch der Fertigungstechnik, Vol. 4/2, Wärmebehandeln*, Carl Hanser, Munich, 1987.)

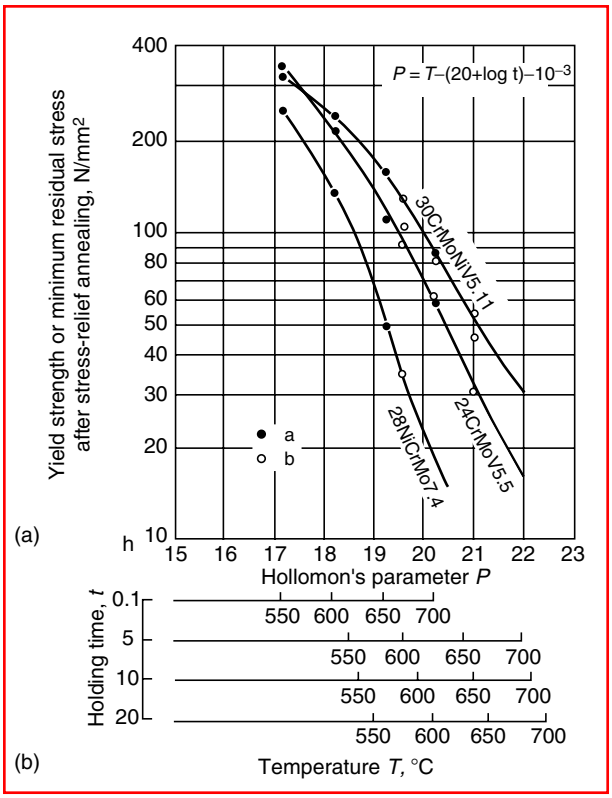

FIGURE 6.53 Yield strength at elevated temperatures (for 0.2% strain) calculated according to the Larson–Miller method for three grades of alloyed structural steels for hardening and tempering (designations according to DIN). (a) Calculated values and (b) experimentally obtained values. (From G. Spur and T. Stöferle (Eds.), *Handbuch der Fertigungstechnik, Vol. 4/2, Wärmebehandeln*, Carl Hanser, Munich, 1987.)

temperature of 600°C (1112°F) and a soaking time of 10 h are chosen for stress-relief annealing, the residual stresses will, after this annealing, be reduced to a maximum of 70 N/mm^2. Higher temperatures and longer times of annealing may reduce residual stresses to lower levels, as can be seen from Figure 6.53.

As in all heat treatment processes where Hollomon's parameter is involved, selection of a higher temperature may dramatically shorten the soaking time and contribute substantially to the economy of the annealing process.

Dealing with structural steels for hardening and tempering, the stress-relief process and the tempering process can be performed simultaneously as one operation, because Hollomon's parameter is also applicable to tempering. In such a case the stress-relief diagram may be used in combination with the tempering diagram to optimize both the hardness and the level of reduced residual stresses.

The residual stress level after stress-relief annealing will be maintained only if the cool-down from the annealing temperature is controlled and slow enough that no new internal stresses arise. New stresses that may be induced during cooling depend on the cooling rate, on the cross-sectional size of the workpiece, and on the composition of the steel. Figure 6.54 shows the effect of cooling rate and cross-sectional diameter of forgings made of a CrMoNiV steel on the level of tangential residual stresses after stress-relief annealing.

A general conclusion about stress-relief annealing is the following: In the temperature range 450–650°C (842–1200°F), the yield strength of unalloyed and low-alloyed steels is lowered so much that a great deal of residual stress may be reduced by plastic deformation. The influence of the steel composition on the level of residual stresses after annealing can be considerable. While unalloyed and low-alloy steels with Ni, Mn, and Cr after stress-relief annealing above 500°C (932°F) may get the residual stresses reduced to a low level, steels alloyed with Mo or Mo + V will retain a much higher level of the residual stresses after stress-relief annealing at the same temperature because of their much higher yield strength at elevated temperature.

6.2.2 Normalizing

Normalizing or normalizing annealing is a heat treatment process consisting of austenitizing at temperatures of 30–80°C (86–176°F) above the A_{c3} transformation temperature (for

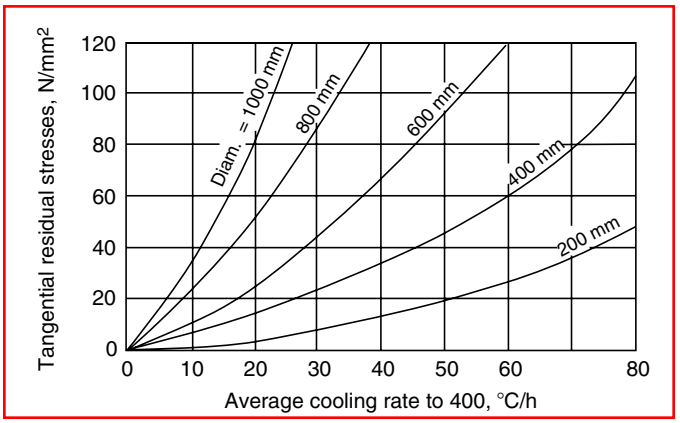

FIGURE 6.54 Tangential residual stresses in a CrMoNiV alloy steel depending on the cooling rate and cross-section diameter. (From G. Spur and T. Stöferle (Eds.), *Handbuch der Fertigungstechnik, Vol. 4/2, Wärmebehandeln*, Carl Hanser, Munich, 1987.)

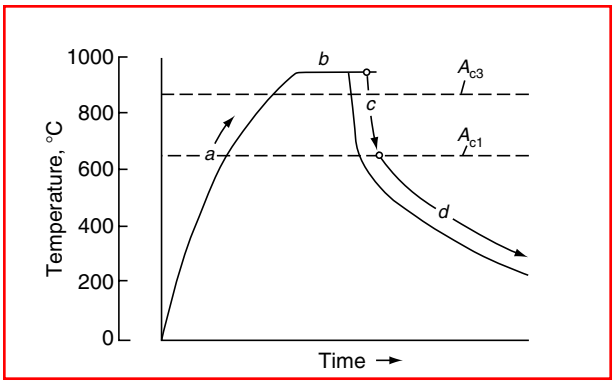

FIGURE 6.55 Time–temperature regime of normalizing. *a*, Heating; *b*, holding at austenitizing temperature; *c*, air cooling; *d*, air or furnace cooling. (From G. Spur and T. Stöferle (Eds.), *Handbuch der Fertigungstechnik, Vol. 4/2, Wärmebehandeln*, Carl Hanser, Munich, 1987.)

hypoeutectoid steels) followed by slow cooling (usually in air), the aim of which is to obtain a fine-grained, uniformly distributed, ferrite–pearlite structure.

Normalizing is applied mainly to unalloyed and low-alloy hypoeutectoid steels. For hypereutectoid steels normalizing is performed only in special cases, and for these steels the austenitizing temperature is 30–80°C (86–176°F) above the A_{c1} transformation temperature.

Figure 6.55 shows the thermal cycle of a normalizing process, and Figure 6.56 shows the range of austenitizing temperatures for normalizing unalloyed steels depending on their carbon content. The parameters of a normalizing process are the heating rate, the austenitizing temperature, the holding time at austenitizing temperature, and the cooling rate.

Normalizing treatment refines the grain of a steel that has become coarse-grained as a result of heating to a high temperature, e.g., for forging or welding. Figure 6.57 shows the effect of grain refining by normalizing a carbon steel of 0.5% C. Such grain refinement and

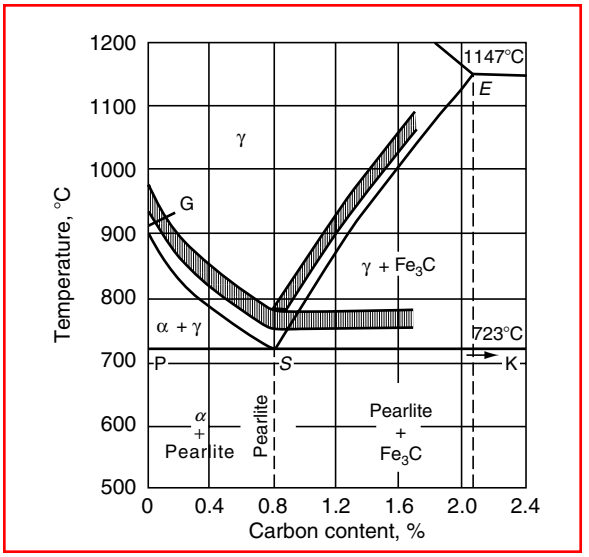

FIGURE 6.56 Range of austenitizing temperatures for normalizing unalloyed steels depending on their carbon content. (Temperature range above the line *S–E* is used for dissolution of secondary carbides.) α, ferrite; γ, austenite; Fe_3C, cementite. (From G. Spur and T. Stöferle (Eds.), *Handbuch der Fertigungstechnik, Vol. 4/2, Wärmebehandeln*, Carl Hanser, Munich, 1987.)

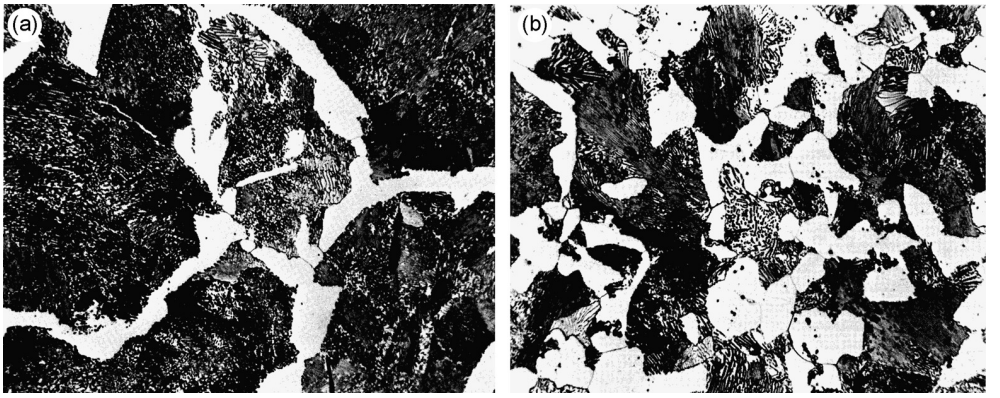

FIGURE 6.57 Effect of grain refining by normalizing a carbon steel of 0.5% C. (a) As-rolled or forged, grain size ASTM 3 and (b) normalized, grain size ASTM 6. Magnification 500×. (From K.E. Thelning, *Steel and Its Heat Treatment*, 2nd ed., Butterworths, London, 1984.)

homogenization of the structure by normalizing is usually performed either to improve the mechanical properties of the workpiece or (previous to hardening) to obtain better and more uniform results after hardening. In some cases, normalizing is applied for better machinability of low-carbon steels.

A special need for normalizing exists with steel castings because, due to slow cooling after casting, a coarse-grained structure develops that usually contains needlelike ferrite (Widmannstätten's structure), as shown in Figure 6.58. A normalizing treatment at 780–950°C (1436–1742°F) (depending on chemical composition) removes this undesirable structure of unalloyed and alloyed steel castings having 0.3–0.6% C.

After hot rolling, the structure of steel is usually oriented in the rolling direction, as shown in Figure 6.59. In such a case, of course, mechanical properties differ between the rolling direction and the direction perpendicular to it. To remove the oriented structure and obtain the same mechanical properties in all directions, a normalizing annealing has to be performed.

After forging at high temperatures, especially with workpieces that vary widely in cross-sectional size, because of the different rates of cooling from the forging temperature, a heterogeneous structure is obtained that can be made uniform by normalizing.

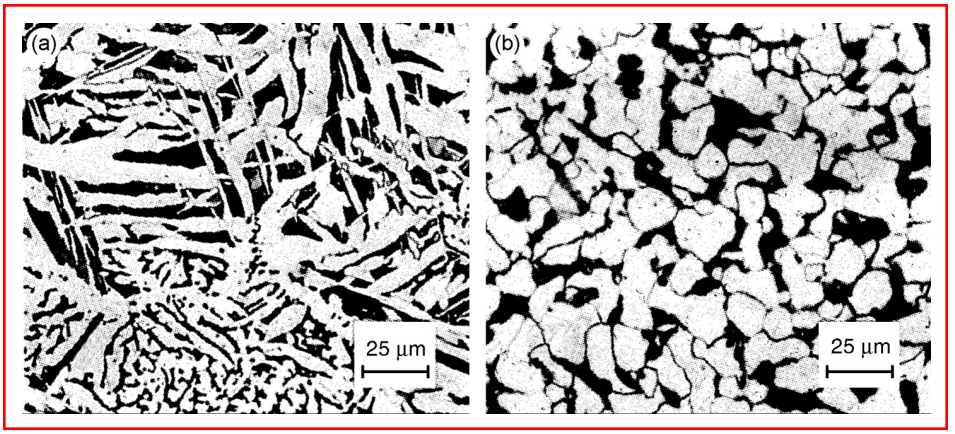

FIGURE 6.58 Structure of a steel casting (a) before normalizing and (b) after normalizing. (From H.J. Eckstein (Ed.), *Technologie der Wärmebehandlung von Stahl*, 2nd ed., VEB Deutscher Verlag für Grundstoffindustrie, Leipzig, 1987.)

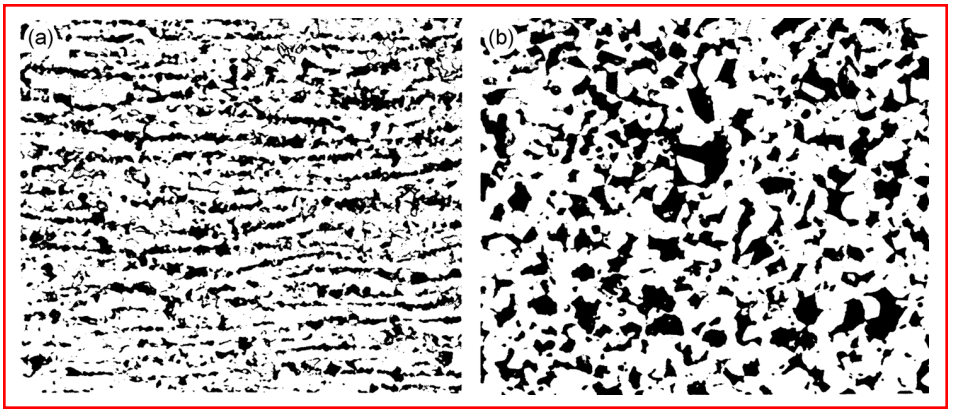

FIGURE 6.59 Structure of DIN 20MnCr5 steel (a) after hot rolling and (b) after normalizing at 880°C. Magnification 100×. (From G. Spur and T. Stöferle (Eds.), *Handbuch der Fertigungstechnik, Vol. 4/2, Wärmebehandeln*, Carl Hanser, Munich, 1987.)

From the metallurgical aspect the grain refinement and the uniform distribution of the newly formed ferrite–pearlite structure during normalizing treatment can be explained with the following mechanism. At normalizing, the steel is subjected first to a $\alpha \rightarrow \gamma$ (ferrite–pearlite to austenite) transformation, and after the holding time at austenitizing temperature, to a recurring $\gamma \rightarrow \alpha$ (austenite to ferrite–pearlite) transformation. The effect of normalizing depends on both austenitization and cooling from the austenitizing temperature.

During austenitizing a far-reaching dissolution of carbides is aimed at, but this process competes with the growth of austenite grains after complete carbide dissolution, which is not desirable. Besides the carbide dissolution, the degree of homogenization within the austenite matrix is important for obtaining a new arrangement of ferrite and pearlite constituents in the structure after normalizing. Both dissolution and homogenizing are time- and temperature-dependent diffusion processes that are slower when the diffusion paths are longer (higher local differences in carbon concentration) and the diffusion rates are smaller (e.g., increasing amounts of alloying elements). Therefore, especially with alloyed steels, lower austenitizing temperatures and longer holding times for normalizing give advantages taking into account the austenite grain growth. As shown in Figure 6.60, high austenitizing temperatures result in a coarse-grained austenite structure, which yields a coarse structure after normalizing.

Holding time at austenitizing temperature may be calculated using the empirical formula

$$t = 60 + D \tag{6.35}$$

where t is the holding time (min) and D is the maximum diameter of the workpiece (mm).

When normalizing hypoeutectoid steels (i.e., steels with less than 0.8% C), during cooling from the austenitizing temperature, first a preeutectoid precipitation of ferrite takes place. With a lower cooling rate, the precipitation of ferrite increases along the austenite grain boundaries. For the desired uniform distribution of ferrite and pearlite after normalizing, however, a possibly simultaneous formation of ferrite and pearlite is necessary. Steels having carbon contents between 0.35 and 0.55% C especially tend to develop nonuniform ferrite distributions as shown in Figure 6.61. The structure in this figure indicates overly slow cooling in the temperature range of preeutectoid ferrite precipitation between A_{r3} and A_{r1}. On the other hand, if the cooling through this temperature region takes place too fast, with steels having carbon contents between 0.2 and 0.5%, formation of an undesirable needlelike ferrite (oriented at austenite grain boundaries), the so-called Widmannstätten's structure, may result as shown in Figure 6.62. Formation of pearlite follows only after complete

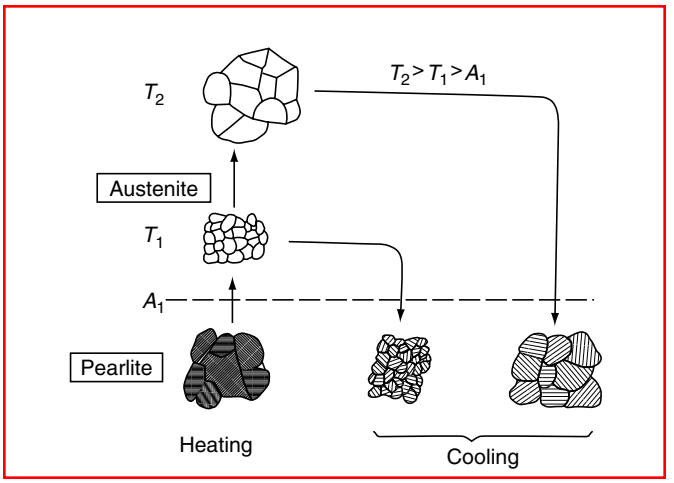

FIGURE 6.60 Schematic presentation of the influence of austenitizing temperature on the grain size of the structure of a eutectoid steel after normalizing. (From H.J. Eckstein (Ed.), *Technologie der Wärmebehandlung von Stahl*, 2nd ed., VEB Deutscher Verlag für Grundstoffindustrie, Leipzig, 1987.)

precipitation of ferrite by transformation of the remaining austenite structure at temperature A_{r1}. It starts first at the boundaries of ferrite and austenite and spreads to the interior of the austenite grains. The greater the number of the pearlitic regions formed, the more mutually hindered the pearlite grains are in their growth, and consequently the finer the grains of the normalized structure. The influence of alloying elements on the austenite to ferrite and pearlite transformation may be read off from the relevant CCT diagram.

Care should be taken to ensure that the cooling rate within the workpiece is in a range corresponding to the transformation behavior of the steel in question that results in a pure ferrite–pearlite structure. If, for round bars of different diameters cooled in air, the cooling curves in the core have been experimentally measured and recorded, then by using the appropriate CCT diagram for the steel grade in question, it is possible to predict the structure and hardness after normalizing. To superimpose the recorded cooling curves onto the CCT diagram, the time–temperature scales must be equal to those of the CCT diagram.

Figure 6.63 shows, for example, that the unalloyed steel DIN Ck45 will attain the desired ferrite–pearlite structure in the core of all investigated bars of different diameters cooled in

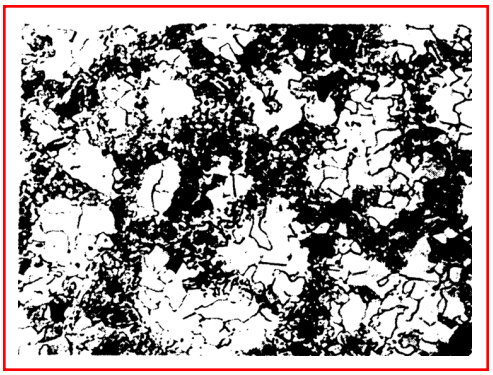

FIGURE 6.61 Nonuniform distribution of ferrite and pearlite as a consequence of unfavorable temperature control during normalizing of unalloyed DIN C35 steel. Magnification 100×. (From G. Spur and T. Stöferle (Eds.), *Handbuch der Fertigungstechnik, Vol. 4/2, Wärmebehandeln*, Carl Hanser, Munich, 1987.)

FIGURE 6.62 Formation of needlelike ferrite at grain boundaries after normalizing of the unalloyed steel DIN C35, because of too fast a cooling rate. Magnification 500×. (From G. Spur and T. Stöferle (Eds.), *Handbuch der Fertigungstechnik, Vol. 4/2, Wärmebehandeln*, Carl Hanser, Munich, 1987.)

air. On the other hand, as shown in Figure 6.64, the alloyed steel DIN 55NiCrMoV6 cooled in the same way in air will transform to martensite and bainite. In this case, to obtain a desired structure and hardness after normalizing, a much slower cooling of about 10°C/h (50°F/h), i.e., furnace cooling, has to be applied from the austenitizing temperature to the temperature at which the formation of pearlite is finished (≈600°C (≈1100°F)).

6.2.3 Isothermal Annealing

Hypoeutectoid low-carbon steels for carburizing as well as medium-carbon structural steels for hardening and tempering are often isothermally annealed, for best machinability, because

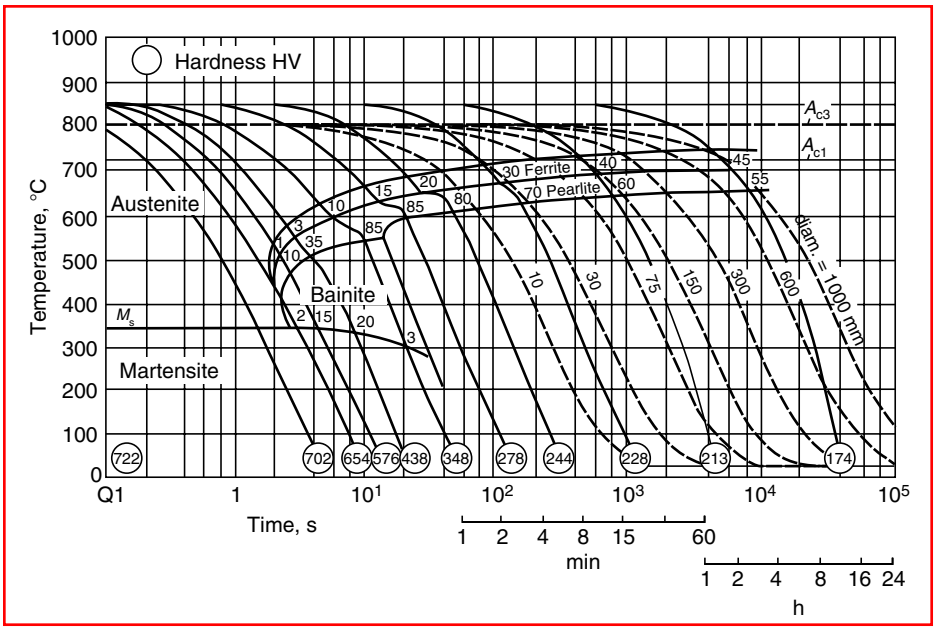

FIGURE 6.63 CCT diagram of the unalloyed steel DIN Ck45 (austenitizing temperature 850°C), with superimposed cooling curves measured in the core of round bars of different diameters cooled in air. (From G. Spur and T. Stöferle (Eds.), *Handbuch der Fertigungstechnik, Vol. 4/2, Wärmebehandeln*, Carl Hanser, Munich, 1987.)

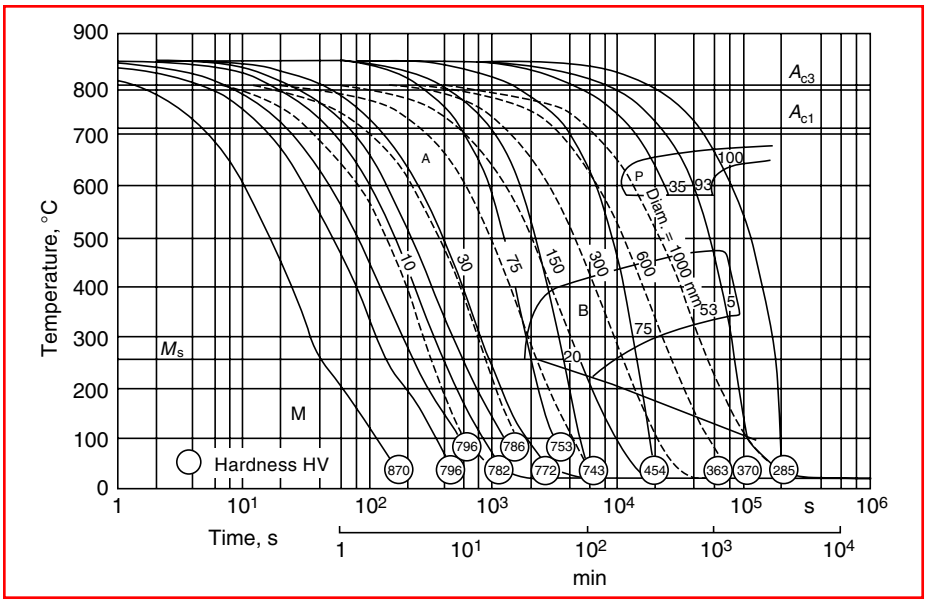

FIGURE 6.64 CCT diagram of the alloyed steel DIN 55NiCrMoV6 (austenitizing temperature 950°C), with superimposed cooling curves measured in the core of round bars of different diameters cooled in air. (From G. Spur and T. Stöferle (Eds.), *Handbuch der Fertigungstechnik, Vol. 4/2, Wärmebehandeln*, Carl Hanser, Munich, 1987.)

a well-differentiated, nontextured ferrite–pearlite structure is the optimum structure for machinability of these steels. If low-carbon steels are soft annealed, they give long shavings when turned and a bad surface appearance (sometimes called "smearing" or "tearing") because of the accumulation of the material on the tool's cutting edge. On the other hand, nonannealed workpieces, having harder structural constituents like bainite, result in heavy wear of the cutting edge when machined.

An isothermally annealed structure should have the following characteristics:

1. High proportion of ferrite
2. Uniformly distributed pearlite grains
3. Fine lamellar pearlite grains
4. Short pearlite lamellae
5. Coarse ferrite grains

Figure 6.65 shows the structure of a thin-wall die forging made of low-alloy steel for carburizing (DIN 16MnCr5) after a normalizing anneal (Figure 6.65a) and after an isothermal annealing process (Figure 6.65b). The desired ferrite–pearlite structure originates during an isothermal annealing, the principle of which is explained by Figure 6.66. This figure shows an IT diagram of a low-alloy steel for carburizing (DIN 15CrNi6) with superimposed cooling curves for different cooling rates at continuous cooling. The slowest cooling rate of 3 K/min relates to a furnace cooling, and the fastest cooling rate of 3000 K/min relates to a quenching process. From the diagram in Figure 6.66 it can be clearly seen that bainite formation can be avoided only by very slow continuous cooling, but with such a slow cooling a textured (elongated ferrite) structure results (hatched area in Figure 6.66). There is only one way to avoid both the formation of bainite and the formation of a textured structure (see the open arrow in Figure 6.66), and this is the isothermal annealing process, which consists of

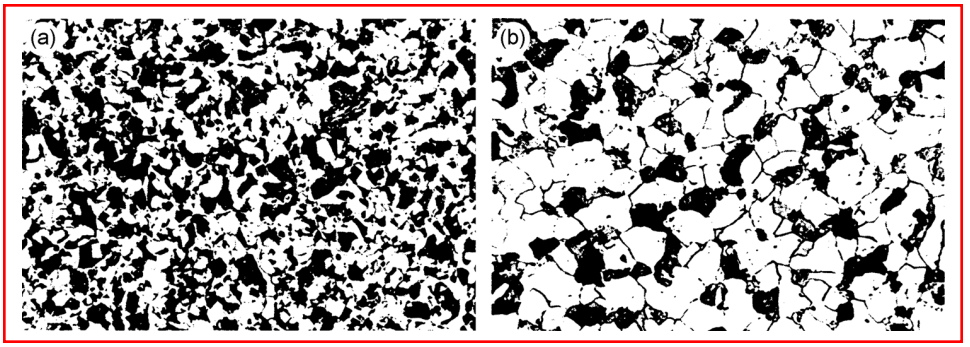

FIGURE 6.65 Structure of a forging made of low-carbon steel for carburizing (DIN 16MnCr5) (a) after normalizing and (b) after isothermal annealing. Magnification 200×. (From G. Spur and T. Stöferle (Eds.), *Handbuch der Fertigungstechnik, Vol. 4/2, Wärmebehandeln*, Carl Hanser, Munich, 1987.)

austenitizing followed by a fast cooling to the temperature range of pearlite formation (usually about 650°C (1200°F)), holding at this temperature until the complete transformation of pearlite, and cooling to room temperature at an arbitrary cooling rate. The temperature–time diagram of an isothermal annealing is given in Figure 6.67. The metallurgical mechanism of a good isothermally annealed structure depends on the austenitizing conditions as well as on the temperature and time of the isothermal transformation and on cooling from the austenitizing temperature to the isothermal transformation temperature.

The austenitizing temperature and time should be high enough to completely dissolve all carbides, to homogenize the austenite matrix, to stabilize the austenite structure, and achieve a coarse-grained ferrite–pearlite structure after cooling. The undesired textured structure originates by preeutectoid ferrite precipitation along stretched phases acting as germs, for instance manganese sulfides, carbon segregations, or aluminum nitride precipitations. These phases have been stretched as a consequence of a preliminary hot-forming process.

To avoid the textured structure the steel has to contain as little sulfur, nitrogen, and aluminum as possible, and during austenitizing a complete dissolution of nitride precipitations and carbides should be achieved. Therefore the austenitizing temperature is adequately high, i.e., about 100°C (212°F) above A_{c3}, and the holding times are usually about 2 h.

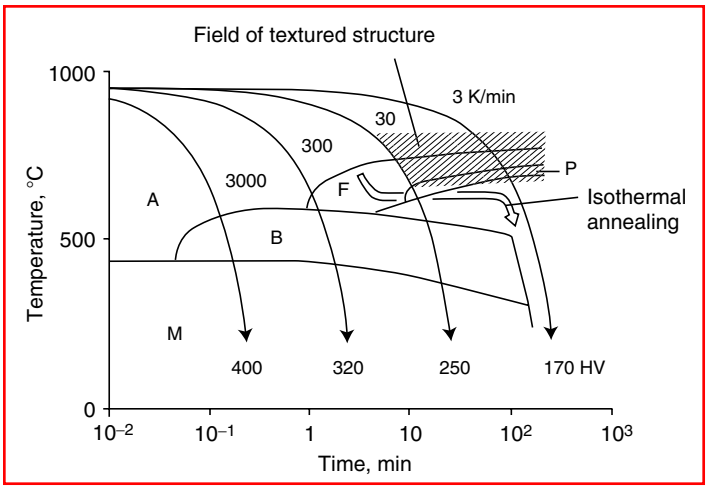

FIGURE 6.66 The principle of isothermal annealing. TTT diagram of the low-alloy steel for carburizing DIN 15CrNi6. (From J. Wünning, *Härterei-Tech. Mitt. 32*:43–49, 1977, pp. 43–49 [in German].)

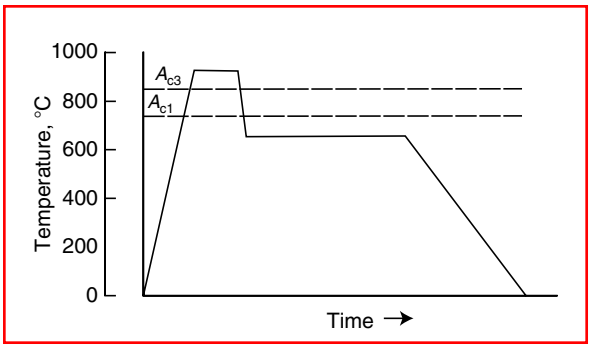

FIGURE 6.67 Temperature–time cycle of isothermal annealing. (From G. Spur and T. Stöferle (Eds.), *Handbuch der Fertigungstechnik, Vol. 4/2, Wärmebehandeln*, Carl Hanser, Munich, 1987.)

Another very important condition to avoid a textured structure is to realize a minimum cooling rate between the austenitizing temperature (≈950°C (≈1750°F)) and the isothermal transformation temperature (≈650°C (1200°F)). Thus, about 300°C (572°F) decrease should pass through at a minimum cooling rate of 20–40 K/min. This means that the whole batch of treated workpieces should be cooled from about 950°C (1750°F) to about 650°C (1200°F) in less than 10 min. During this cooling process an undercooling below the chosen isothermal transformation temperature must be avoided to prevent the formation of bainite.

The physical mechanism that accounts for the manner and magnitude of ferrite precipitation is the carbon diffusion during cooling from the austenitizing temperature. To achieve a good structure after isothermal annealing, all measures that reduce the carbon diffusion rate or restrict the diffusion time for carbon atoms during cooling are useful.

Figure 6.68 shows three structures after isothermal annealing of the low-alloy steel DIN 16MnCr5. It can be seen that cooling too slowly from the austenitizing temperature to the transformation temperature results in an undesirable textured structure of ferrite and pearlite, and if during this cooling process an undercooling takes place (i.e., the transformation temperature has been chosen too low) before the pearlite formation, then bainite will be present in the structure, which is not allowed.

Big companies usually have internal standards to estimate the allowable degree of texturing of the isothermally annealed structures, with respect to machinability, as shown in Figure 6.69. The transformation temperature and the necessary transformation time for the steel in question may be determined by means of the appropriate IT diagram. Figure 6.70 shows such a diagram for the steel DIN 17CrNiMo6. As can be seen, the lower the transformation temperature chosen,

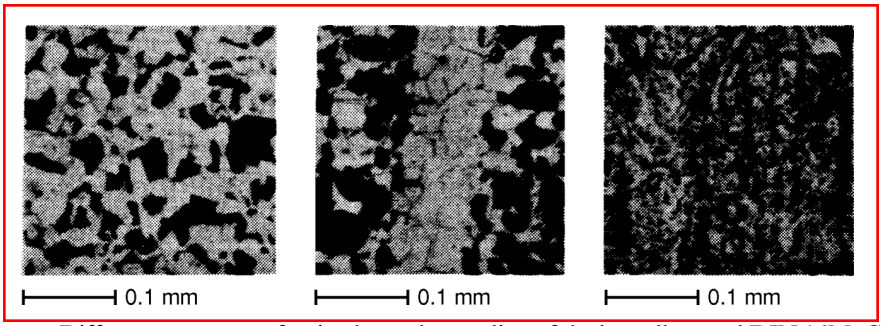

FIGURE 6.68 Different structures after isothermal annealing of the low-alloy steel DIN 16MnCr5 (left). Well-distributed ferrite–pearlite; correct annealing (center). Textured ferrite–pearlite structure; too slow cooling from the austenitizing to the transformation temperature (right). Ferrite – pearlite + bainite; undercooling before pearlite transformation. (From J. Wünning, *Härterei-Tech. Mitt. 32*:43–49, 1977, pp. 43–49 [in German].)

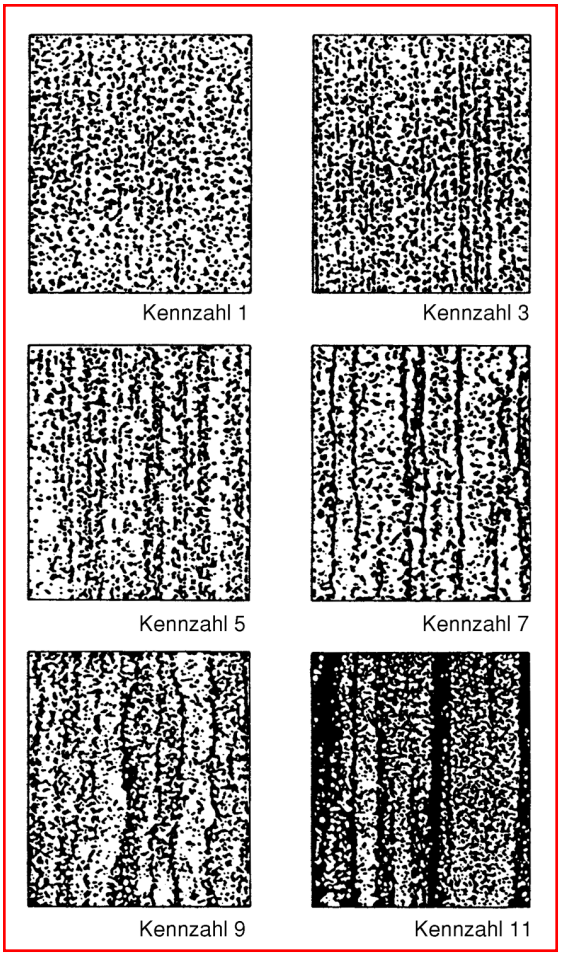

FIGURE 6.69 Internal standard of the German company Edelstahlwerke Buderus A.G.-Wetzlar for estimation of the allowable degree of texturing of the structure after isothermal annealing. Magnification 100×. (From G. Spur and T. Stöferle (Eds.), *Handbuch der Fertigungstechnik, Vol. 4/2, Wärmebehandeln*, Carl Hanser, Munich, 1987.)

the sooner the transformation starts, up to a temperature (the so-called pearlite nose) at which the shortest time to start the transformation is achieved. Below this temperature, longer times are again necessary to start the transformation. In the range of the pearlite nose temperature, fine lamellar pearlite will be formed, and the time to complete pearlite transformation is the shortest.

For unalloyed steels, the pearlite nose temperatures are between 550 and 580°C (1022 and 1076°F), while for alloyed steels they are between 640 and 680°C (1184 and 1256°F). The optimum isothermal annealing temperature is 10–20°C (50–68°F) above the pearlite nose temperature.

The necessary transformation time depends on the alloying elements in the steel. In the practice of isothermal annealing the holding time at the transformation temperature includes an adequate reserve because of compositional tolerances in different steel heats. Usually for low-alloy steels for carburizing and structural steels for hardening and tempering the transformation times are below 2 h.

From the technical standpoint, when a batch of workpieces has to be isothermally annealed, the biggest problem is to realize sufficiently fast cooling from the austenitizing

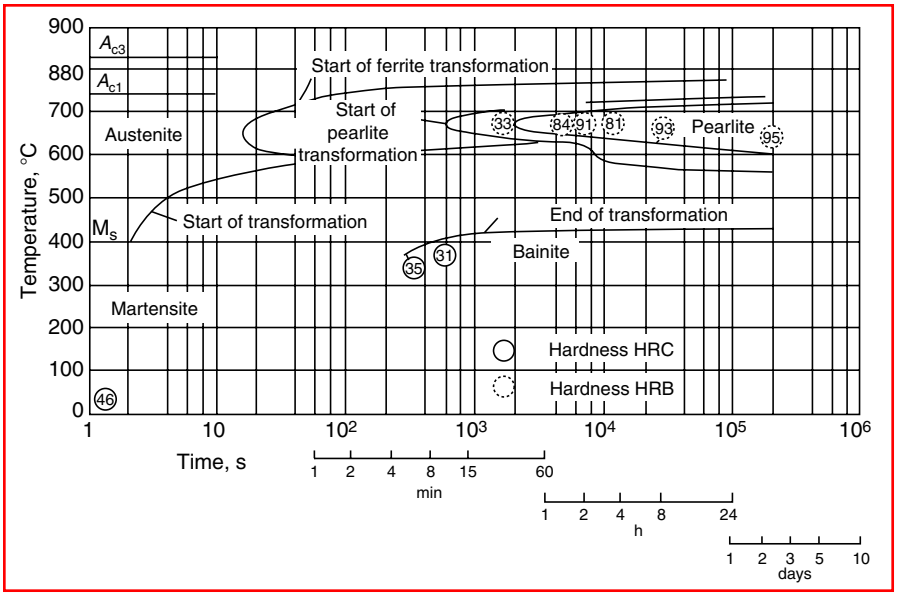

FIGURE 6.70 Isothermal transformation (IT) diagram of the steel DIN 17CrNiMo6. Austenitizing temperature 870°C. (From G. Spur and T. Stöferle (Eds.), *Handbuch der Fertigungstechnik, Vol. 4/2, Wärmebehandeln*, Carl Hanser, Munich, 1987.)

temperature to the chosen transformation temperature without any undercooling. This cooling process depends on several factors, and the main factors include the workpiece cross-sectional size, the loading arrangement, the temperature difference between the austenitizing temperature and the temperature of the cooling medium, and the heat transfer coefficient between the workpieces' surface and the ambient.

6.2.4 Soft Annealing (Spheroidizing Annealing)

Soft or spheroidizing annealing is an annealing process at temperatures close below or close above the A_{c1} temperature, with subsequent slow cooling. The microstructure of steel before soft annealing is either ferrite–pearlite (hypoeutectoid steels), pearlite (eutectoid steels), or cementite–pearlite (hypereutectoid steels). Sometimes a previously hardened structure exists before soft annealing. The aim of soft annealing is to produce a soft structure by changing all hard constituents like pearlite, bainite, and martensite (especially in steels with carbon contents above 0.5% and in tool steels) into a structure of spheroidized carbides in a ferritic matrix.

Figure 6.71 shows the structure with spheroidized carbides (a) after soft annealing of a medium-carbon low-alloy steel and (b) after soft annealing of a high-speed steel. Such a soft structure is required for good machinability of steels having more than 0.6% C and for all cold-working processes that include plastic deformation. Whereas for cold-working processes the strength and hardness of the material should be as low as possible, for good machinability medium strength or hardness values are required. Therefore, for instance, when ball bearing steels are soft annealed, a hardness tolerance is usually specified. In the production sequence, soft annealing is usually performed with a semiproduct (after rolling or forging), and the sequence of operations is hot working, soft annealing, cold forming, hardening, and tempering.

The required degree of spheroidization (i.e., 80–90% of globular cementite or carbides) is sometimes specified. To evaluate the structure after soft annealing, there are sometimes internal standards, for a particular steel grade, showing the percentage of achieved globular

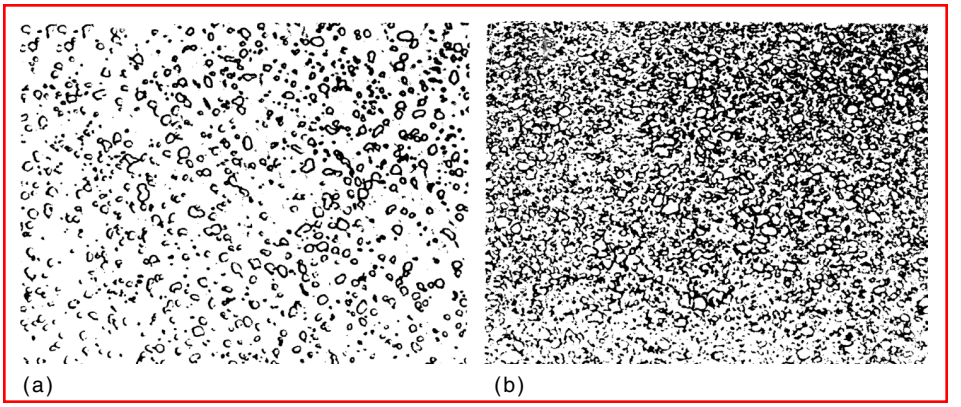

FIGURE 6.71 Structures of (a) a medium-carbon low-alloy steel DIN 50CrMoV4 after soft annealing at 720–740°C and (b) a high-speed steel annealed at 820°C. Magnification 500×. (From G. Spur and T. Stöferle (Eds.), *Handbuch der Fertigungstechnik, Vol. 4/2, Wärmebehandeln*, Carl Hanser, Munich, 1987.)

cementite, as shown in Figure 6.72 for the ball bearing steel DIN 100Cr6. The degree of spheroidization is expressed in this case as percentage of remaining lamellar pearlite.

The physical mechanism of soft annealing is based on the coagulation of cementite particles within the ferrite matrix, for which the diffusion of carbon is decisive. Globular cementite within the ferritic matrix is the structure having the lowest energy content of all structures in the iron–carbon system. The carbon diffusion depends on temperature, time, and the kind and amount of alloying elements in the steel. The solubility of carbon in ferrite, which is very low at room temperature (0.02% C), increases considerably up to the A_{c1} temperature. At temperatures close to A_{c1}, the diffusion of carbon, iron, and alloying atoms is so great that it is possible to change the structure in the direction of minimizing its energy content.

The degree of coagulation as well as the size of carbides after soft annealing is dependent also on the starting structure before annealing. If the starting structure is pearlite, the spheroidization of carbides takes place by the coagulation of the cementite lamellae. This process can be formally divided into two stages. At first the cementite lamellae assume a knucklebone shape, as shown in Figure 6.73. As annealing continues, the lamellae form globules at their ends and, by means of boundary surface energy, split up into spheroids, hence the name spheroidizing. During the second stage, some cementite (carbide) globules grow at the cost of fine carbide particles, which disappear. In both stages, the rate of this process is controlled by diffusion. The thicker the cementite lamellae, the more energy necessary for this process. A fine lamellar pearlite structure may more easily be transformed to a globular form.

In establishing the process parameters for a soft (spheroidizing) annealing, a distinction should be drawn among hypoeutectoid carbon steels, hypereutectoid carbon steels, and alloyed steels. In any case the value of the relevant A_{c1} temperature must be known. It can be taken from the relevant IT or CCT diagram or calculated according to the formula

$$A_{c1} = 739 - 22(\%\ \mathrm{C}) + 2(\%\ \mathrm{Si}) - 7(\%\ \mathrm{Mn}) + 14(\%\ \mathrm{Cr}) + 13(\%\ \mathrm{Mo}) + 13(\%\ \mathrm{Ni}) + 20(\%\ \mathrm{V}),\ [^{\circ}\mathrm{C}] \tag{6.36}$$

The temperature range for soft annealing of unalloyed carbon steels may be taken from the iron–carbon diagram as shown in Figure 6.74. The holding time at the selected temperature is approximately 1 min/mm of the workpiece cross section.

For alloyed steels, the soft annealing temperature may be calculated according to the empirical formula

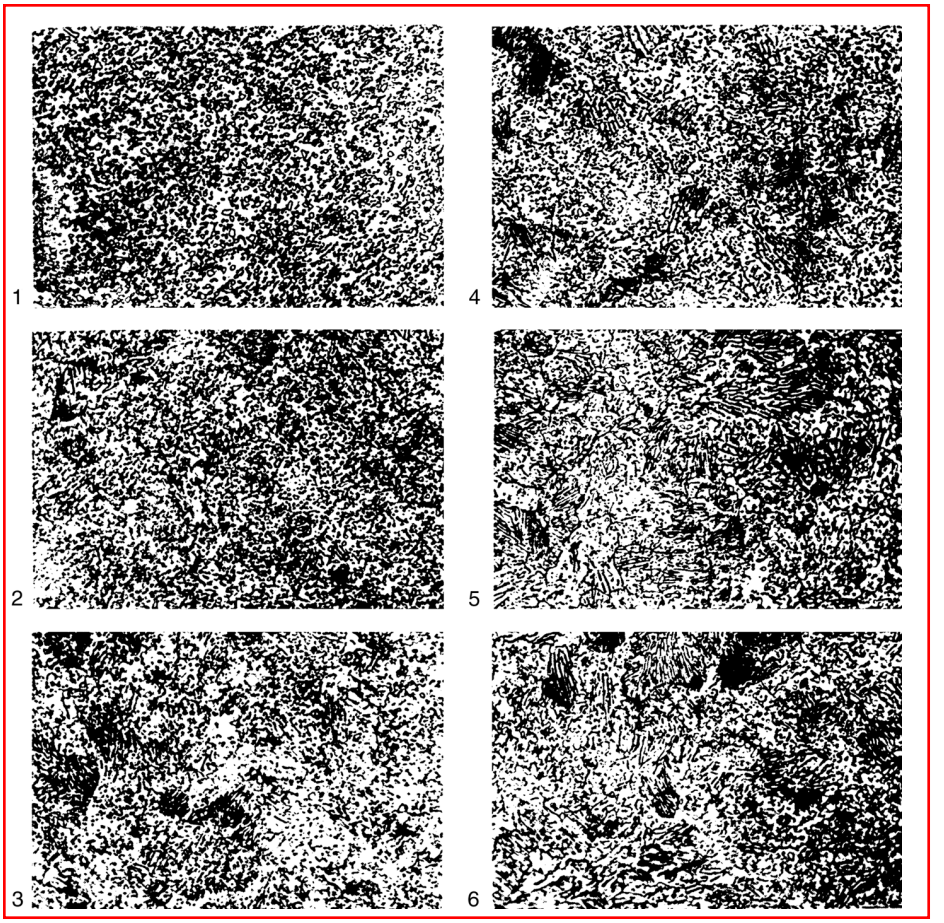

FIGURE 6.72 Internal standard of the German company Edelstahlwerke Buderus A.G.-Wetzlar for evaluation of the degree of spheroidization after soft annealing of grade DIN 100Cr6 steel. Magnification 500×. Amount of lamellar pearlite remaining 1, 0%; 2, 8%; 3, 20%; 4, 35%; 5, 60%; 6, 80%. (From G. Spur and T. Stöferle (Eds.), *Handbuch der Fertigungstechnik, Vol. 4/2, Wärmebehandeln*, Carl Hanser, Munich, 1987.)

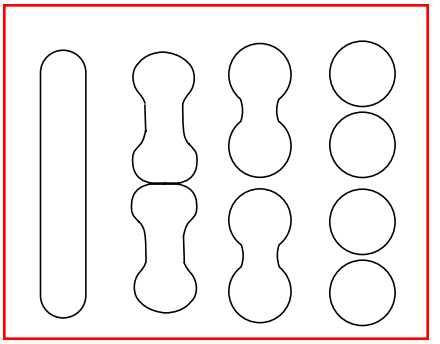

FIGURE 6.73 Schematic presentation of the process of transforming cementite lamella to spheroids during soft annealing. (From K.E. Thelning, *Steel and Its Heat Treatment*, 2nd ed., Butterworths, London, 1984.)

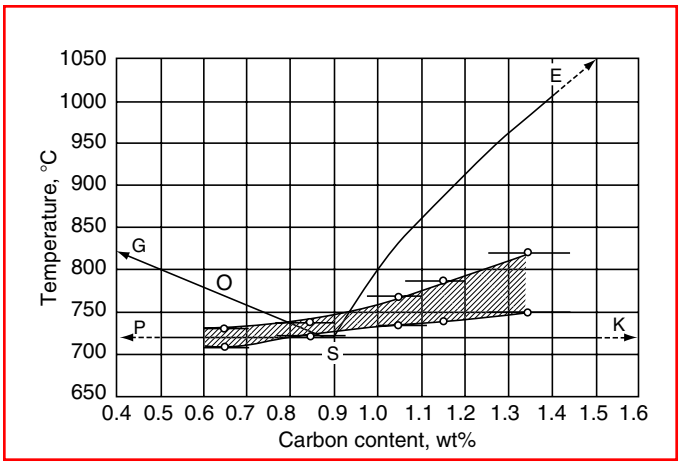

FIGURE 6.74 Temperature range for soft annealing of unalloyed steels having carbon contents of 0.6–1.35% C. (From G. Spur and T. Stöferle (Eds.), *Handbuch der Fertigungstechnik, Vol. 4/2, Wärmebehandeln*, Carl Hanser, Munich, 1987.)

$$T = 705 + 20(\%\ \text{Si} - \%\ \text{Mn} + \%\ \text{Cr} - \%\ \text{Mo} - \%\ \text{Ni} + \%\ \text{W}) + 100(\%\ \text{V})\ [^\circ\text{C}] \quad (6.37)$$

This formula is valid only up to the following values of the alloying elements: 0.9% C; 1.8% Si; 1.1% Mn; 1.8% Cr; 0.5% Mo; 5% Ni; 0.5% W; and 0.25% V. If the steel has higher amounts of alloying elements, only these indicated maximum values are to be taken into account.

Figure 6.75 shows possible temperature–time regimes for soft annealing. The swinging regime (Figure 6.75c) is used to accelerate the transformation of cementite lamellae to globular form. Increasing the temperature above A_{c1} facilitates the dissolution of cementite lamellae. At subsequent cooling below A_{c1} this dissolution process is interrupted and the parts broken off (which has less resistance to boundary surface energy) coagulate more easily and quickly.

On the basis of the investigations of Köstler, a degree of spheroidization e has been established that gives the amount of globular cementite compared to the total amount of

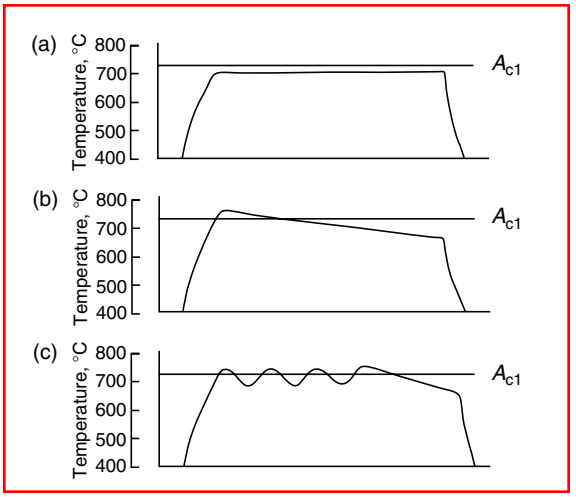

FIGURE 6.75 Temperature–time regimes at soft annealing. (a) Annealing at 20°C below A_{c1}, for unalloyed steels and for alloyed steels with bainitic or martensitic starting structure; (b) annealing at 10°C above A_{c1} (start) and decreasing temperature to 30°C below A_{c1} for alloyed steels; (c) swinging annealing ±5°C around A_{c1} for hypereutectoid steels. (From G. Spur and T. Stöferle (Eds.), *Handbuch der Fertigungstechnik, Vol. 4/2, Wärmebehandeln*, Carl Hanser, Munich, 1987.)

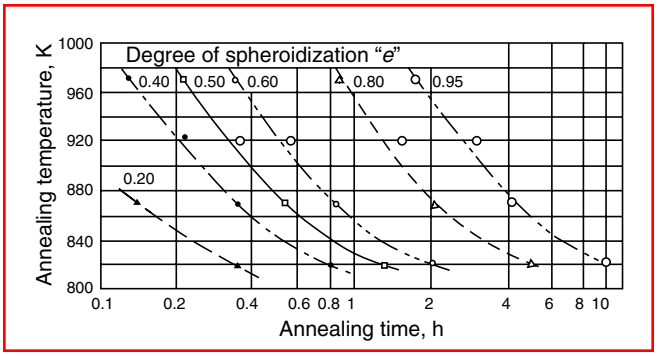

FIGURE 6.76 Time–temperature diagram for soft annealing of the unalloyed steel DIN C35 (previously deformed 50%), to achieve the required degree of spheroidization. (After Köstler; see H.J. Eckstein (Ed.), *Technologie der Wärmebehandlung von Stahl*, 2nd ed., VEB Deutscher Verlag für Grundstoffindustrie, Leipzig, 1987.)

cementite in a steel after soft annealing. $e = 1$ means that 100% of the globular cementite (i.e., no lamellar cementite) has remained. Because the degree of spheroidization depends on the time and temperature of the soft annealing process, diagrams may be established that correlate the degree of spheroidization with the time and temperature of soft annealing. Figure 6.76 shows such a diagram for the unalloyed steel DIN C35.

The degree of spheroidization, especially above 80% ($e = 0.8$), has considerable influence on ultimate tensile strength, yield strength, and elongation, as shown in Figure 6.77 for the unalloyed eutectoid steel DIN C75. The hardness after soft annealing depends on the time and temperature of spheroidization, as shown in Figure 6.78 for an unalloyed steel with 0.89% C.

The machinability of steels with more than 0.6% C can be increased by soft annealing as shown in Figure 6.79, from which it can be seen that decreasing tensile strength and increasing the degree of spheroidization allows a higher turning speed (v_{60}) in m/min.

The cooling after soft annealing should generally be slow. Depending on the steel grade, the cooling should be performed as follows:

For carbon and low-alloy steels up to 650°C (1200°F), with a cooling rate of 20–25 K/h (furnace cooling)

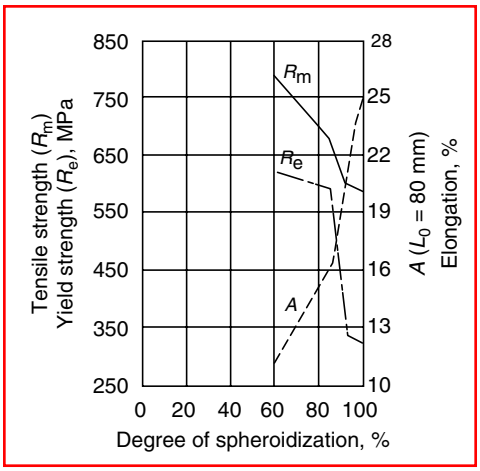

FIGURE 6.77 Change of ultimate tensile strength, yield strength, and elongation with increasing spheroidization of an unalloyed eutectoid steel, DIN C75. (From H.J. Eckstein (Ed.), *Technologie der Wärmebehandlung von Stahl*, 2nd ed., VEB Deutscher Verlag für Grundstoffindustrie, Leipzig, 1987.)

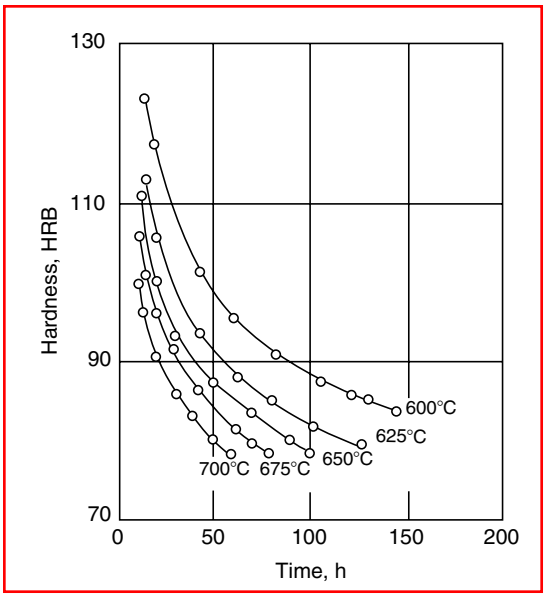

FIGURE 6.78 Hardness of an unalloyed steel with 0.89% C after soft annealing, depending on the spheroidization time and temperature. (From H.J. Eckstein (Ed.), *Technologie der Wärmebehandlung von Stahl*, 2nd ed., VEB Deutscher Verlag für Grundstoffindustrie, Leipzig, 1987.)

For medium-alloy steels up to 630°C (1166°F), with a cooling rate of 15–20 K/h (furnace cooling)
For high-alloy steels up to 600°C (1112°F), with a cooling rate of 10–15 K/h (furnace cooling)
Further cooling below the temperatures indicated is usually performed in air

6.2.5 Recrystallization Annealing

Recrystallization annealing is an annealing process at temperatures above the recrystallization temperature of the cold-worked material, without phase transformation, that aims at regeneration of properties and changes in the structure that exists after a cold-forming process

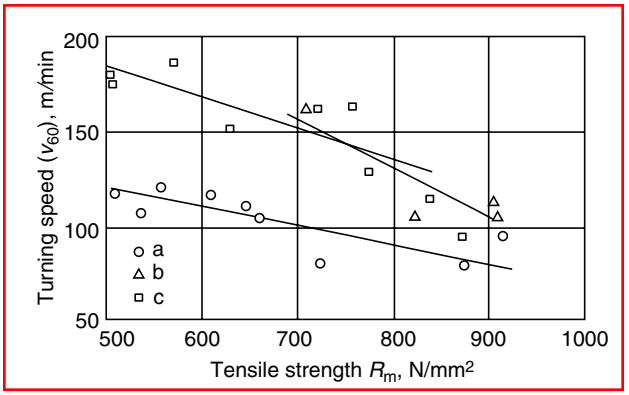

FIGURE 6.79 Influence of the ultimate tensile strength and degree of spheroidization on machinability of steels for carburizing and structural steels for hardening and tempering, expressed as 1 h turning speed (v_{60}) in m/min. (a) Spheroidization degree less than 30%; (b) spheroidization degree between 40 and 60%; (c) spheroidization degree greater than 70%. (From G. Spur and T. Stöferle (Eds.), *Handbuch der Fertigungstechnik, Vol. 4/2, Wärmebehandeln*, Carl Hanser, Munich, 1987.)

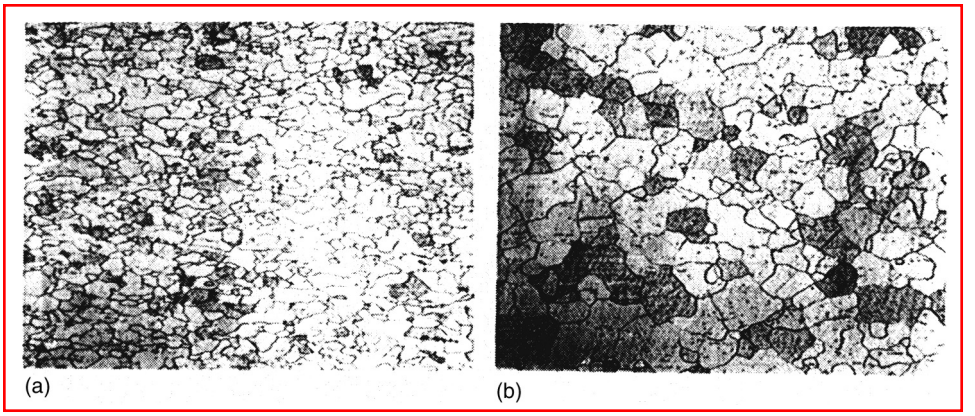

FIGURE 6.80 Low-carbon steel with 0.05% C (a) after cold working with 20% reduction (hardness 135 HV) and (b) after subsequent recrystallization annealing at 750°C (hardness 75 HV). Magnification 200×. (From K.E. Thelning, *Steel and Its Heat Treatment*, 2nd ed., Butterworths, London, 1984.)

such as cold rolling, deep drawing, or wire drawing. Materials that are to be subjected to a cold-forming process and subsequent recrystallization annealing must possess good cold-forming ability. These materials include soft unalloyed steels, microalloyed steels for deep drawing, microalloyed high-strength steels, unalloyed and alloyed carbon steels, stainless steels, and soft magnetic steels.

The prerequisite to recrystallization on annealing is that the degree of deformation during cold working has been large enough to produce the required number of defects in the crystals to initiate nucleation, which is then followed by grain growth. Figure 6.80 shows the microstructure of a low-carbon steel (a) after cold working and (b) after subsequent recrystallization annealing. During cold working of metallic materials, by far the greatest amount of the energy applied for deformation is transformed into heat, but a relatively small part (less than 5%) of it remains accumulated in the material due to the formation of crystal lattice defects. It is a known fact that every cold-working process (i.e., plastic deformation of the material) increases the dislocation density by some orders of magnitude. Because every dislocation is a crystal defect associated with internal stresses, the increase in the dislocation density causes the accumulation of internal stresses (i.e., of internal energy) and thereby increases the free enthalpy. Such a thermodynamically unstable material condition tends, at increased temperatures, to decrease the free enthalpy by rearranging and demolishing lattice defects. The greater the plastic deformation in a cold-forming process, the greater the strengthening of the material, which is characterized by an increase in tensile strength and yield strength and a decrease in elongation as shown in Figure 6.81. The material becomes harder and more

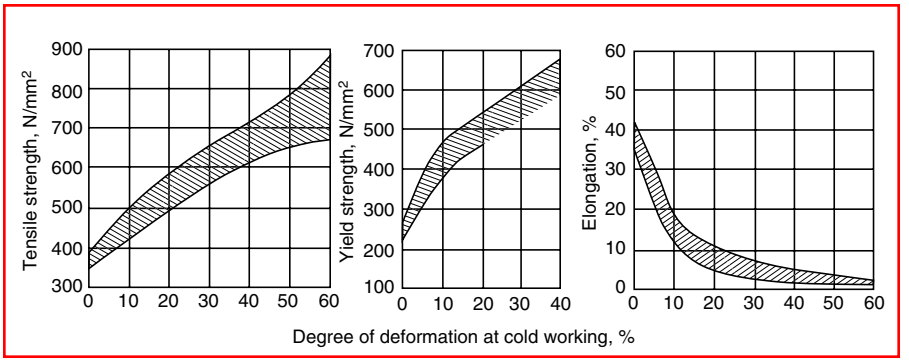

FIGURE 6.81 Strengthening of a low-carbon steel by the cold-rolling process. (From G. Spur and T. Stöferle (Eds.), *Handbuch der Fertigungstechnik, Vol. 4/2, Wärmebehandeln*, Carl Hanser, Munich, 1987.)

brittle, so that in some cases a further step in the forming process cannot be applied without a recrystallization annealing. Also the anisotropy of the material, i.e., the dependence of mechanical properties on the direction of the cold-forming process, can be annulated by recrystallization annealing, by bringing the oriented grains that are deformed in one direction back to the original globular form.

Thermic activation, i.e., increasing the temperature at recrystallization annealing, can be used to reestablish the original structure (before cold working) with the original density of dislocations, which results in decreased hardness and strength and increased ductility and formability. The recrystallization annealing process includes the following phenomena: grain recovery, polygonization, recrystallization, and grain growth.

6.2.5.1 Grain Recovery

Grain recovery is a process of tempering a cold-worked metallic structure at low temperatures (150–350°C (300–662°F)) without causing any discernible changes in the microstructure. It results only in decreasing the internal stresses without substantially decreasing the strength of the material. However, during this process characteristic changes occur in the electrical resistance and its temperature coefficient of the cold-worked material. The activation energy needed for grain recovery depends on the degree of cold working. The higher the degree (i.e., the greater the deformation), the less the activation energy required. The temperature of grain recovery correlates with the recrystallization temperature of the same material according to the formula

$$T_{GR} = T_R - 300\ [^\circ C] \tag{6.38}$$

6.2.5.2 Polygonization

Polygonization of a cold-worked structure is the creation of a new polygonal arrangement of edge dislocations in the metallic crystal lattice that takes place at temperatures close above the grain recovery temperature. As shown in Figure 6.82, in such a case the applied thermal energy is sufficient to rearrange the edge dislocations. In this case the originally bent sliding planes take a polygonal shape, forming segments within a grain called subgrains. The angles between subgrains are very small (about 1°). As a consequence of a substantial energy discharge by discharge of internal stresses, material strength is decreased. Polygonization takes place primarily in heavily cold-worked structures, especially in ferritic matrices, below the recrystallization temperature.

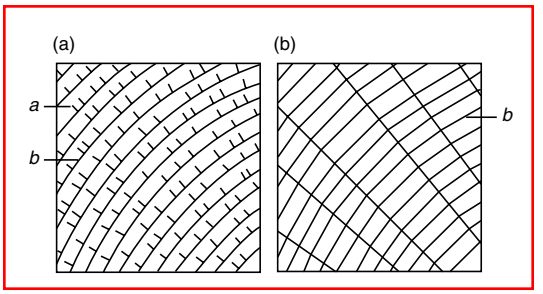

FIGURE 6.82 Schematic presentation of polygonization. Arrangement of edge dislocations and sliding planes (a) before polygonization and (b) after polygonization. *a*, Edge dislocations; *b*, sliding planes. (From G. Spur and T. Stöferle (Eds.), *Handbuch der Fertigungstechnik, Vol. 4/2, Wärmebehandeln*, Carl Hanser, Munich, 1987.)

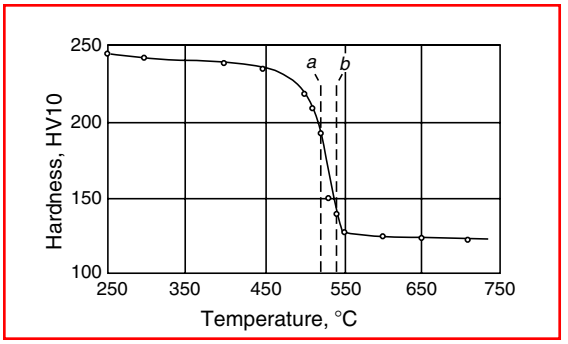

FIGURE 6.83 Decrease in hardness during recrystallization of a steel having 0.03% C, 0.54% Si, and 0.20% Mn that was cold rolled (805 deformation), as a function of annealing temperature. (Heating rate 20°C/h.) *a*, Begin formation of new grains; *b*, end formation of new grains. (From G. Spur and T. Stöferle (Eds.), *Handbuch der Fertigungstechnik, Vol. 4/2, Wärmebehandeln*, Carl Hanser, Munich, 1987.)

6.2.5.3 Recrystallization and Grain Growth

The process of recrystallization begins when the recrystallization temperature is overstepped. The recrystallization temperature of a material is the temperature at which the formation of new grains begins within a cold-worked microstructure, as shown in Figure 6.83. From this figure one can conclude that for the steel in question the recrystallization temperature is 520°C (968°F). During recrystallization, as can be seen from Figure 6.83, hardness and strength decrease substantially while ductility increases. In practice, the recrystallization temperature T_R is often considered the temperature of a cold-worked material at which recrystallization is completed after 1 h of annealing. There is a correlation between the recrystallization temperature (T_R) and the melting temperature (T_M) of the material, which reads

$$T_R = 0.4T_M \tag{6.39}$$

Figure 6.84 shows that this correlation holds for practically all pure metals if both temperatures T_R and T_M are taken in deg. K. The recrystallization temperature can be

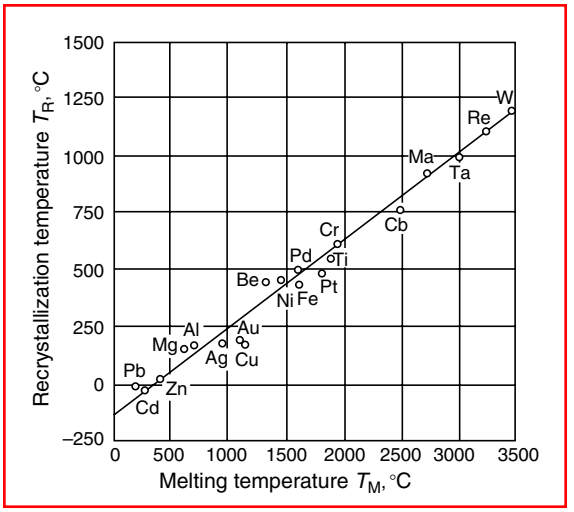

FIGURE 6.84 Correlation between the recrystallization temperature and the melting temperature for pure metals. (From G. Spur and T. Stöferle (Eds.), *Handbuch der Fertigungstechnik, Vol. 4/2, Wärmebehandeln*, Carl Hanser, Munich, 1987.)

influenced by the degree of deformation during cold working, the heating rate, and the starting microstructure.

In contrast to the grain recovery process (which follows a parabolic law), the recrystallization process begins only after an incubation period (because of nucleation), starting slowly, reaching a maximum rate, and finishing slowly. The nuclei from which new grains grow are situated preferably at the grain boundaries of compressed cold-worked grains. New grains grow from these nuclei until they meet up with other grains. Recrystallization brings about the formation and movement of large-angle grain boundaries.

Figure 6.85 is a schematic presentation of new grain formation and growth during the recrystallization process as a function of annealing time. As time passes, the new grains, starting from nuclei, grow unhindered within the cold-worked grains. Simultaneously, new nuclei are formed. At the movement of large-angle grain boundaries, new grains consume the previously deformed grains. The recrystallization process is locally finished when new neighboring grains collide with each other. The size, form, and orientation of the new structure, as well as the condition of the lattice defects in it, differ substantially from those of the previous structure. The recrystallization process itself can be hindered by precipitations, dispersions, and a second phase.

The most important technological parameters of recrystallization annealing that influence the rate of recrystallization and the material properties after recrystallization are:

1. Material-dependent parameters—the chemical composition and the starting structure (including the degree of deformation)
2. Process-dependent parameters—annealing temperature, annealing time, and heating and cooling rates

The course of a recrystallization process can be presented in an isothermal time–temperature–recrystallization diagram as shown in Figure 6.86. As can be seen from this diagram, the higher the temperature of recrystallization annealing, the shorter the necessary annealing time. The lower the degree of deformation at cold working, the higher the required

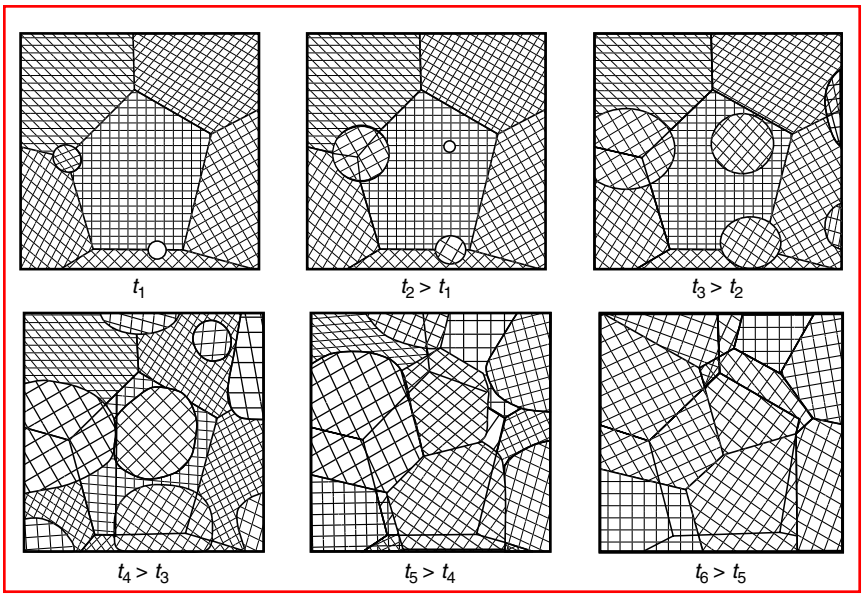

FIGURE 6.85 Schematic presentation of new grain formation and growth during the recrystallization process as a function of annealing time t. (From G. Spur and T. Stöferle (Eds.), *Handbuch der Fertigungstechnik, Vol. 4/2, Wärmebehandeln*, Carl Hanser, Munich, 1987.)

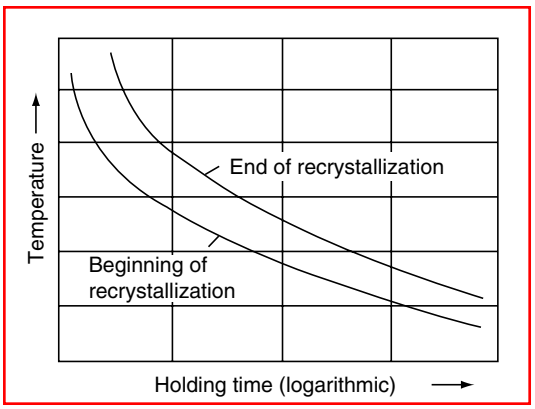

FIGURE 6.86 An isothermal time–temperature–recrystallization diagram. (From H.J. Eckstein (Ed.), *Technologie der Wärmebehandlung von Stahl*, 2nd ed., VEB Deutscher Verlag für Grundstoffindustrie, Leipzig, 1987.)

recrystallization temperature, as shown in Figure 6.87. The higher the heating rate, the higher the recrystallization temperature. It can be concluded from Figure 6.86 that with substantially longer annealing times, a full recrystallization can be achieved at relatively low temperatures.

The degree of deformation at cold working has a very important influence on the size of newly formed grains during recrystallization. If the cold working is carried out with a very low degree of deformation but without sufficient strengthening of the material to enable the process of recrystallization, a decrease in stresses can still be achieved by movement of the deformed grain boundaries. In this case grains with low dislocation density grow (because there are only a few nuclei) and a coarse-grained structure develops as shown in Figure 6.88. Consequently, there is a critical degree of deformation at cold working that at subsequent recrystallization annealing leads to sudden grain growth, as shown in Figure 6.89 for a low-carbon steel. With an increase in the carbon content of the steel, this critical degree of deformation shifts from about 8 to 20% of deformation at cold working.

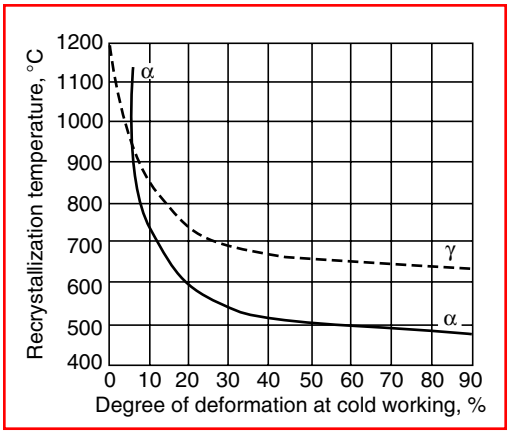

FIGURE 6.87 Recrystallization temperature of α- and γ-iron as a function of the degree of deformation at cold working. (From G. Spur and T. Stöferle (Eds.), *Handbuch der Fertigungstechnik, Vol. 4/2, Wärmebehandeln*, Carl Hanser, Munich, 1987.)

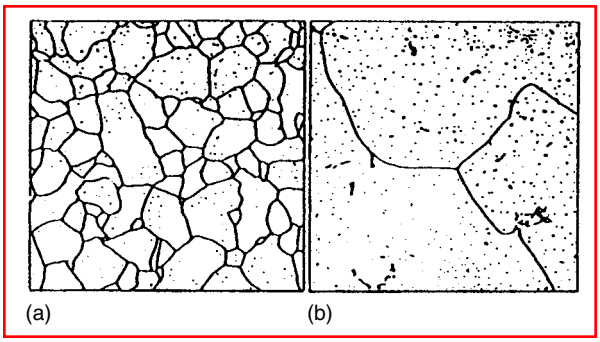

FIGURE 6.88 Development of coarse-grained structure during recrystallization of soft iron. (a) Microstructure before cold working and (b) microstructure after cold working with very low degree of deformation (10%) and subsequent recrystallization annealing at 700°C. Magnification 500×. (From G. Spur and T. Stöferle (Eds.), *Handbuch der Fertigungstechnik, Vol. 4/2, Wärmebehandeln*, Carl Hanser, Munich, 1987.)

6.3 HARDENING BY FORMATION OF MARTENSITE

6.3.1 Austenitizing

Austenitizing is the first operation in many of the most important heat treatment processes (hardening, carburizing, normalizing) on which the properties of heat-treated parts depend. Let us assume the bulk heat treatment of real batches of workpieces and consider the metallurgical and technological aspects of austenitizing.

6.3.1.1 Metallurgical Aspects of Austenitizing

The way austenite is formed when a certain steel is heated depends very much on the steel's starting microstructure. Let us take as an example an unalloyed eutectoid steel with 0.8% C and follow the process of its austenitization using the schemes shown in Figure 6.90. At room temperature the cementite (Fe_3C) plates of the pearlite are in direct contact with ferrite (α-Fe, see Figure 6.90a). The carbon atoms from cementite have a tendency to diffuse into the ferrite lattice. The higher the temperature, the greater this tendency is. Upon heating, on reaching the A_{c1} temperature (723°C (1333°F)), the transformation of ferrite into austenite (γ-Fe)

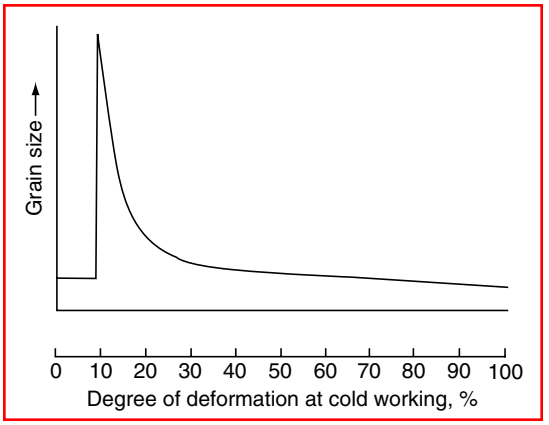

FIGURE 6.89 Grain growth in the range of the critical degree of deformation (at 10%) for a steel with 0.06% C. Recrystallization temperature, 700°C. (From G. Spur and T. Stöferle (Eds.), *Handbuch der Fertigungstechnik, Vol. 4/2, Wärmebehandeln*, Carl Hanser, Munich, 1987.)

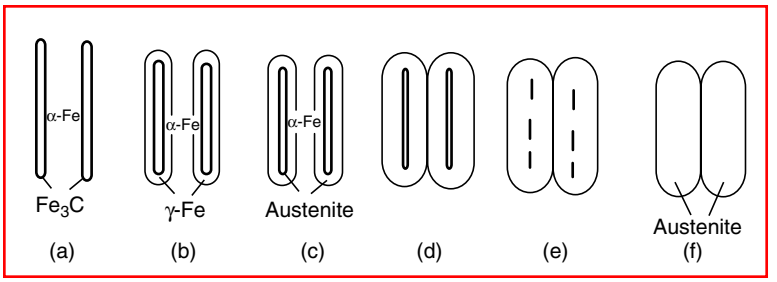

FIGURE 6.90 Transformation of a pearlitic structure to austenite when heating an unalloyed eutectoid steel of 0.8% C.

starts immediately adjacent to the cementite plates (see Figure 6.90b). After that the cementite plates start to dissolve within the newly formed austenite, becoming thinner and thinner (Figure 6.90c and Figure 6.90d). So two processes take place at the same time: the formation of austenite grains from ferrite and the dissolution of cementite plates in the austenite lattice. Experiments have shown that the process of ferrite-to-austenite transformation ends before all the cementite has been dissolved. This means that after all the ferrite has transformed into austenite, small particles of cementite will remain within the austenite grains (Figure 6.90e). Figure 6.91 shows the formation of austenite in a microstructure of eutectoid steel. Areas of

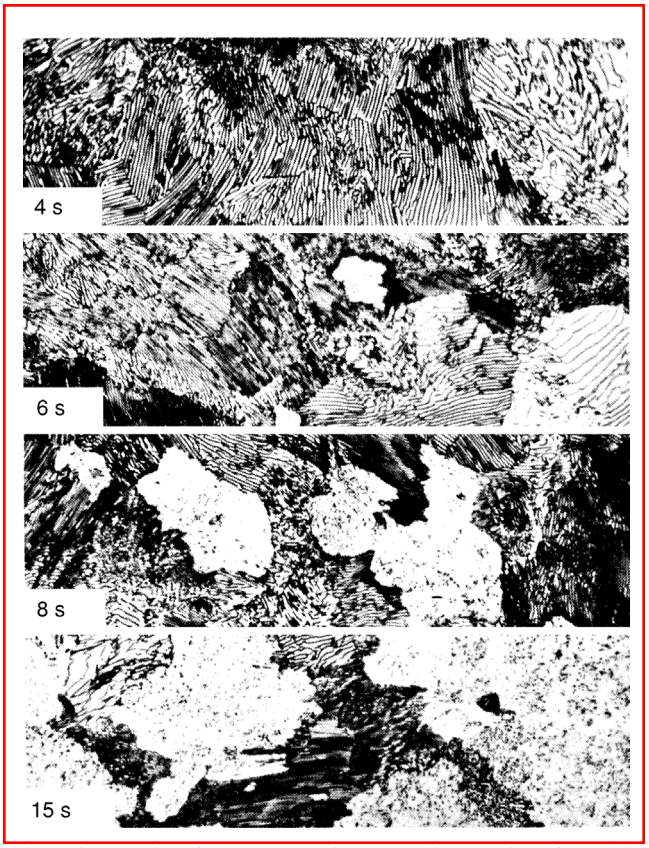

FIGURE 6.91 Formation of austenite (light patches) from pearlite as a function of time. (From G. Krauss, *Steels: Heat Treatment and Processing Principles*, ASM International, Materials Park, OH, 1990.)

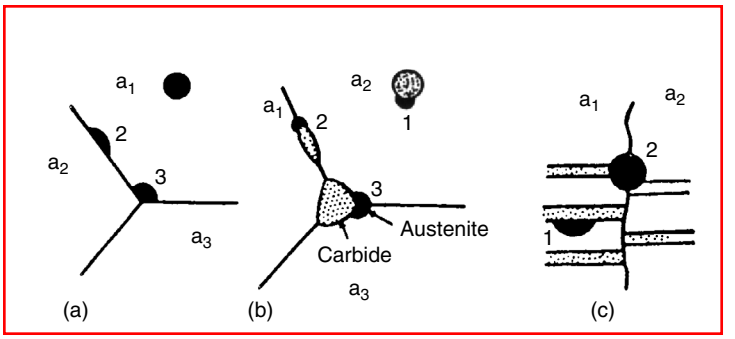

FIGURE 6.92 Nucleation sites for austenite formation in microstructures of (a) ferrite; (b) spheroidite; (c) pearlite. (From G. Krauss, *Steels: Heat Treatment and Processing Principles*, ASM International, Materials Park, OH, 1990.)

austenite formation are visible as white patches within the lamellar pearlitic structure. Some of the cementite persists in the form of spheroidized particles (the small dark spots in the white areas). They dissolve only with longer holding times at temperature. Once these cementite particles completely dissolve, the structure consists of only one phase—austenite (see Figure 6.90f). In this state, however, there are still differences in carbon concentration among particular austenite grains. In spots where cementite plates were previously to be found, the carbon concentration is high, while in other spots far from cementite plates it is low.

Equalizing of the carbon concentration proceeds gradually by diffusion, resulting in a homogeneous austenite structure at the end of this process. The holding time at austenitizing temperature necessary for this process is called the homogenization time. During pearlite–austenite transformation, several austenite grains are formed from one pearlite grain, i.e., the newly formed austenite is fine-grained.

Nucleation sites for austenite formation depend on the starting microstructure as shown in Figure 6.92. In ferrite the nucleation sites are situated primarily at grain boundaries. In spheroidized structures nucleation starts on carbide particles, whereas in pearlitic structures it starts primarily at the intersection of pearlite colonies but also at cementite lamellae.

6.3.1.1.1 Kinetics of Transformation during Austenitizing

Figure 6.93 shows the volume percent of austenite formed from pearlite in eutectoid steel as a function of time at a constant austenitizing temperature. From the beginning of austenitization

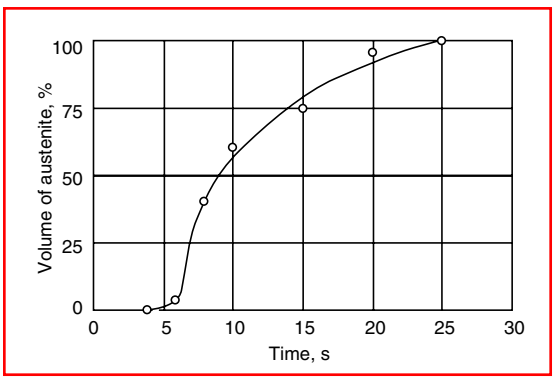

FIGURE 6.93 Volume percent austenite formed from pearlite in eutectoid steel as a function of time at a constant austenitizing temperature. (From G. Krauss, *Steels: Heat Treatment and Processing Principles*, ASM International, Materials Park, OH, 1990.)

a certain incubation time is necessary to form the first nuclei, and then the process proceeds at a more rapid rate as more nuclei develop and grow. At higher temperatures the diffusion rate increases and austenite forms more rapidly, as shown in Figure 6.94.

The duration of austenitizing process depends on the austenitizing temperature and the steel composition. The influence of time at austenitization can best be explained by the diagrammatic illustrations shown in Figure 6.95. From Figure 6.95a and Figure 6.95b, which apply to eutectoid carbon steel of 0.8% C, one can see that if an austenitizing temperature of 730°C (1346°F) is maintained (after a rapid heating to this temperature), the transformation will start in about 30 s. If instead an austenitizing temperature of 750°C (1382°F) is chosen, the transformation will begin in 10 s, and if a temperature of 810°C (1490°F) is selected, in about 1 s. The transformation of pearlite to austenite and cementite is in this case completed in about 6 s. If the steel is to be fully austenitic (all carbides dissolved, hatched area), it must be held at this temperature for about 2 h (7×10^3 s).

Figure 6.95c and Figure 6.95d apply to a hypoeutectoid plain carbon steel of 0.45% C. They show that in this case at an austenitizing temperature of 810°C (1490°F) the transformation from pearlite to austenite starts in about 1 s. In about 5 s the pearlite has been transformed and the structure consists of ferrite, austenite, and cementite. About 1 min later the carbon has diffused to the ferrite, which has thereby been transformed to austenite. Residual particles of cementite remain, however, and it takes about 5 h at this temperature to dissolve them completely.

Figure 6.95e and Figure 6.95f apply to a hypereutectoid steel containing 1.2% C. If this steel is austenitized at 810°C (1490°F), the pearlite starts to transform in about 2 s, and in about 5 s the structure consists only of austenite and cementite. It is not possible for the cementite to be completely dissolved at this temperature. To achieve complete solution of the cementite, the temperature must be increased above A_{cm}, in this case to at least 860°C (1580°F).

The holding time at austenitizing (hardening) temperature depends on the desired degree of carbide dissolution and acceptable grain size, taking into account that the grain growth increases with higher austenitizing temperatures and longer holding times. Since the amount of carbide is different for different types of steel, the holding time (from the metallurgical point of view) depends on the grade of steel. However, carbide dissolution and the holding time are dependent not only on the austenitizing temperature but also the rate of heating to

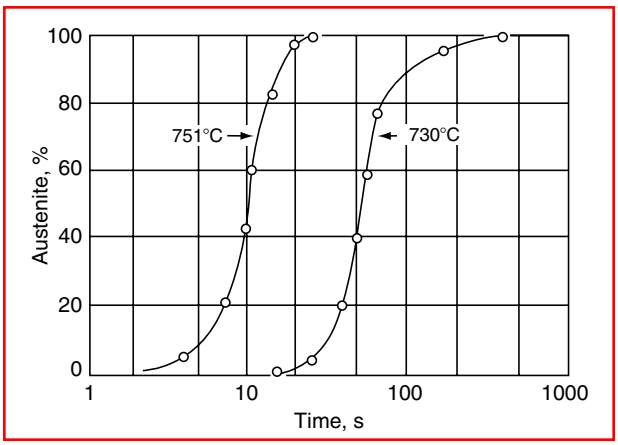

FIGURE 6.94 Effect of austenitizing temperature on the rate of austenite formation from pearlite in a eutectoid steel. (From G. Krauss, *Steels: Heat Treatment and Processing Principles*, ASM International, Materials Park, OH, 1990.)

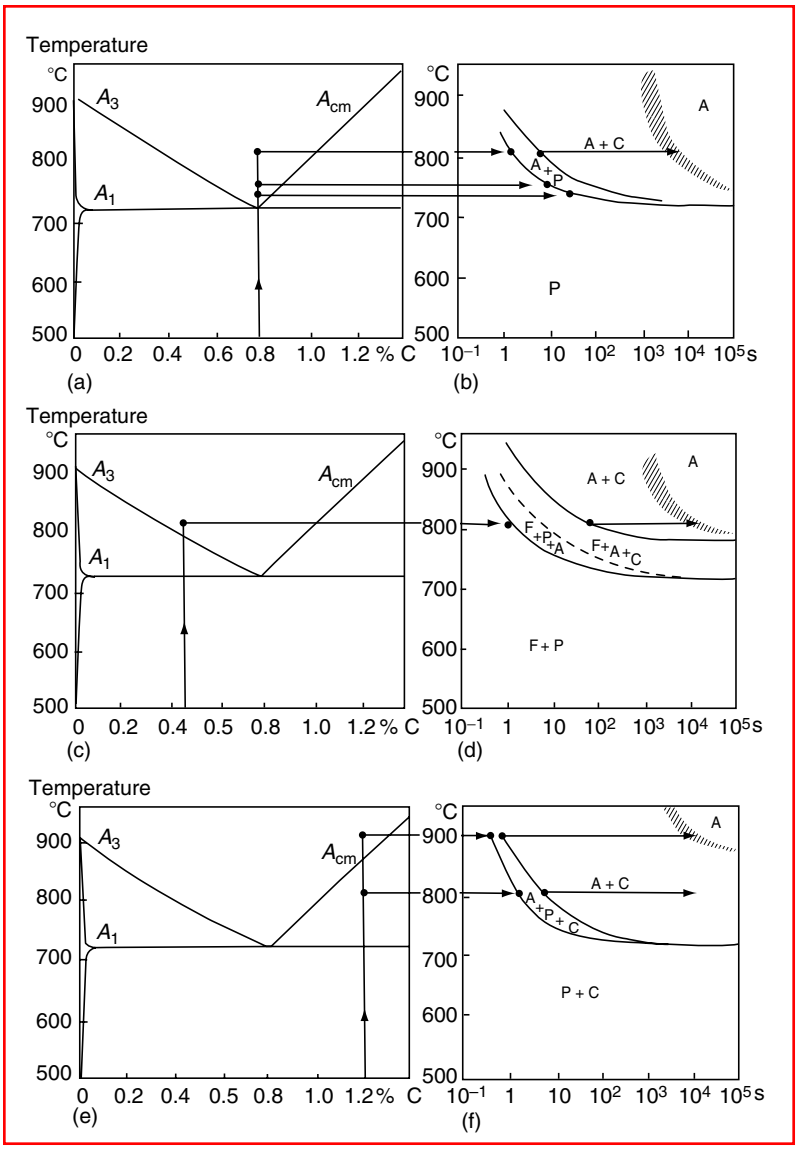

FIGURE 6.95 Structural transformations during austenitizing steels containing (a, b) 0.8% C; (c, d) 0.45% C; (e, f) 1.2% C. A, austenite; C, cementite; F, ferrite; P, pearlite. (From K.E. Thelning, *Steel and Its Heat Treatment*, 2nd ed., Butterworths, London, 1984.)

this temperature. Varying the rate of heating to this temperature will have an effect on the rate of transformation and dissolution of the constituents.

The influence of the role of heating (and correspondingly of the holding time) on carbide dissolution, grain growth, and hardness after hardening for various grades of steel has been studied in detail and published in Refs. [18,19]. These time–temperature–austenitizing diagrams (*Zeit-Temperatur-Austenitisierung Schaubilder* in German) have been produced either as isothermal diagrams (the steel specimens were heated rapidly at the rate of 130°C/s (266°F/s) to the temperature in question and held there for a certain predetermined time) or as continuous heating diagrams (the steel specimens were heated continuously at different heating rates).

Consequently, isothermal diagrams may be read only along the isotherms, and the continuous heating diagrams may be read only along the heating rate lines.

Figure 6.96 shows an isothermal type of time–temperature–austenitizing diagram of grade DIN 50CrV4 steel. From this type of diagram one can read off, for instance, that if the steel is held at 830°C (1526°F), after about 1 s, pearlite and ferrite will be transformed to austenite, but more than 1000 s is necessary to completely dissolve the carbides to achieve a homogeneous austenite.

In practice, the continuous heating diagrams are much more important because every austenitizing process is carried out at a specified heating rate. Figure 6.97 shows a time–temperature–austenitizing diagram of the continuous heating type for grade DIN Ck45 steel. The continuous heating was carried out at various constant rates ranging from 0.05 to 2400°C/s (32.09 to 4352°F). If the heating rate was extremely slow (e.g., 0.22°C/s (32.4°F/s)) to about 775°C (1427°F), on crossing the A_{c3} temperature after about 1 h all pearlite and ferrite would have been transformed to inhomogeneous austenite. At a heating rate

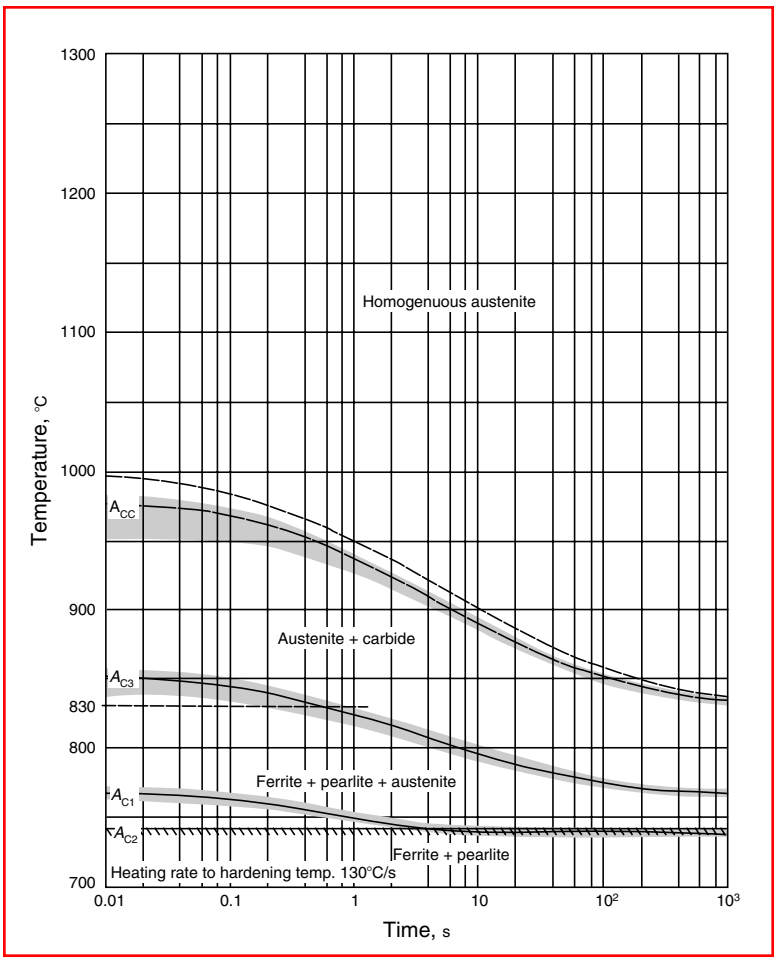

FIGURE 6.96 Isothermal time–temperature–austenitizing diagram of the steel grade DIN 50CrV4 (0.47% C, 0.27% Si, 0.90% Mn, 1.10% Cr). (From J. Orlich and H.J. Pietrzenivk (Eds.), *Atlas zur Wärmebehandlung der Stähle*, Vol. 4, *Zeit-Temperatur-Austenitisierung-Schaubilder*, Part 2, Verlag Stahleisen, Düsseldorf, 1976 [in German].)

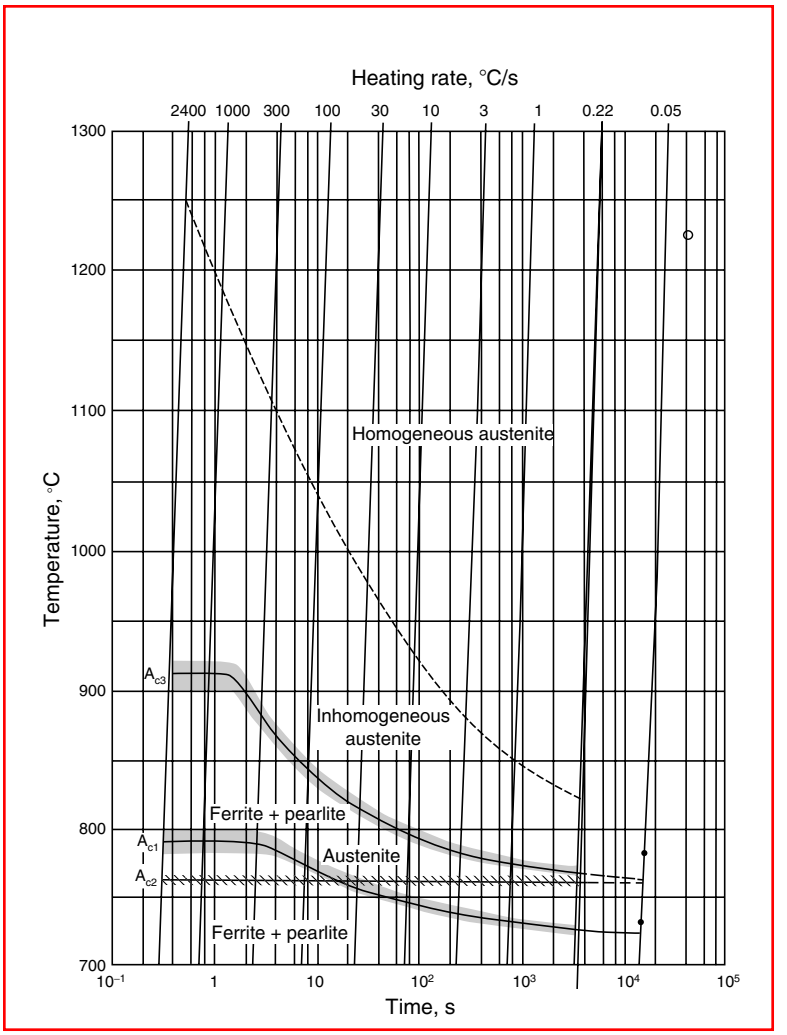

FIGURE 6.97 Time–temperature–austenitizing diagram for continuous heating of the steel grade DIN Ck45 (0.49% C, 0.26% Si, 0.74% Mn). (From J. Orlich, A. Rose, and P. Wiest (Eds.), *Atlas zur Wärmebehandlung der Stähle*, Vol. 3, *Zeit-Temperatur-Austenitisierung-Schaubilder*, Verlag Stahleisen, Düsseldorf, 1973 [in German].)

of 10°C/s (50°F/s) the pearlite and ferrite would have been transformed to inhomogeneous austenite after crossing the A_{c3} temperature at about 800°C (1472°F) after only 80 s.

A remarkable feature of such diagrams is that they show precisely the increase of A_{c1} and A_{c3} transformation temperatures with increasing heating rates. This is especially important when short-time heating processes like induction hardening or laser beam hardening, with heating rates ranging to about 1000°C/s (1832°F/s), are applied for surface hardening. In such a case this diagram should be consulted to determine the required austenitizing temperature, which is much higher than in conventional hardening of the same grade of steel. For the steel in question, for example, the conventional hardening temperature would be in the range of 830–850°C (1526–1562°F), but for induction or laser beam hardening processes the hardening temperatures required are between 950 and 1000°C (1742 and 1832°F). When heating at a rate of 1000°C/s (1832°F/s) to the austenitizing temperature of 1000°C (1832°F), only 1 s is necessary, and the above-mentioned short heating time processes operate in approximately this time range. As Figure 6.97 shows, much higher temperatures are necessary to achieve the

homogeneous austenite structure. In such a case one is, of course, concerned with the grain growth.

Figure 6.98 shows the grain growth (according to American Society for Testing and Materials [ASTM]) when grade DIN Ck45 steel is continuously heated at different heating rates to different austenitizing temperatures. Figure 6.99 shows the achievable Vickers hardness after hardening for grade DIN Ck45 steel austenitized at various heating rates to various temperatures. It shows, for example, that maximum hardness would be achieved upon austenitizing the steel at 850°C (1562°F) for about 900 s (or heating at a heating rate of 1°C/s (33.8°F/s)), which corresponds to the field of homogeneous austenite (see Figure 6.97).

The hardness after quenching, which depends on the amount of carbide dissolution, is also dependent on the initial structure of the steel. This is illustrated in Figure 6.100. Figure 6.100a shows that a structure of spheroidized cementite (after soft annealing) of the hypoeutectoid DIN Cf53 carbon steel will attain the maximum hardness of 770 HV when heated at a rate of 1°C/s (33.8°F/s) to 875°C (1609°F) (holding time 855 s or 14 min). The hardened and

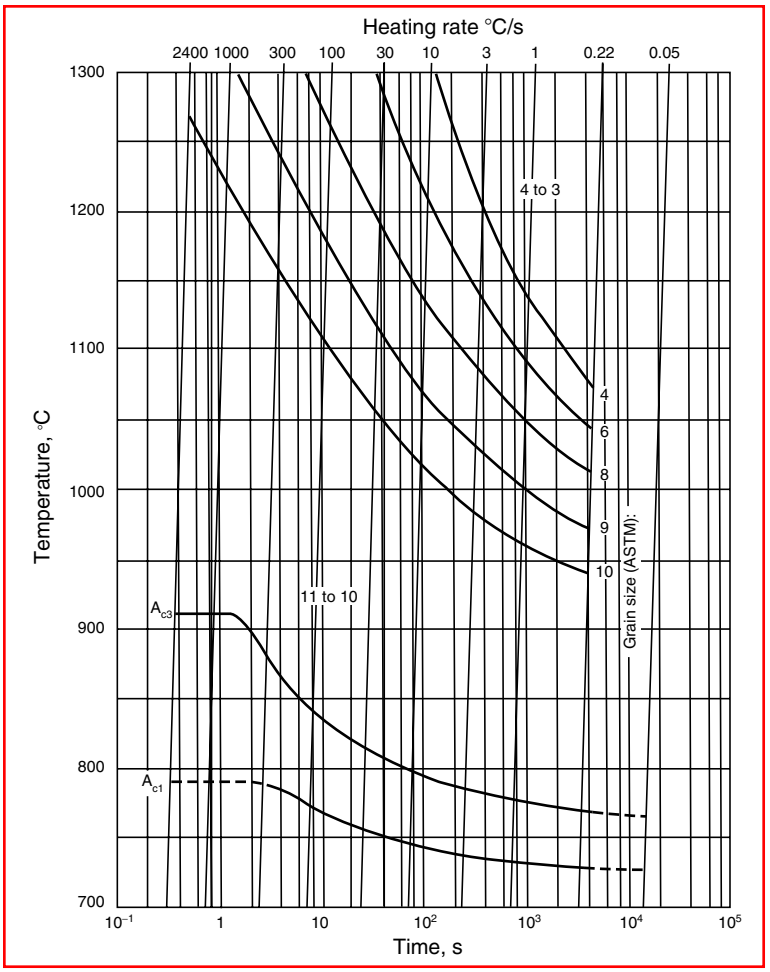

FIGURE 6.98 Time–temperature–austenitizing diagram for continuous heating showing the grain growth of steel grade DIN Ck45. (From J. Orlich, A. Rose, and P. Wiest (Eds.), *Atlas zur Wärmebehandlung der Stähle*, Vol. 3, *Zeit-Temperatur-Austenitisierung-Schaubilder*, Verlag Stahleisen, Düsseldorf, 1973 [in German].)

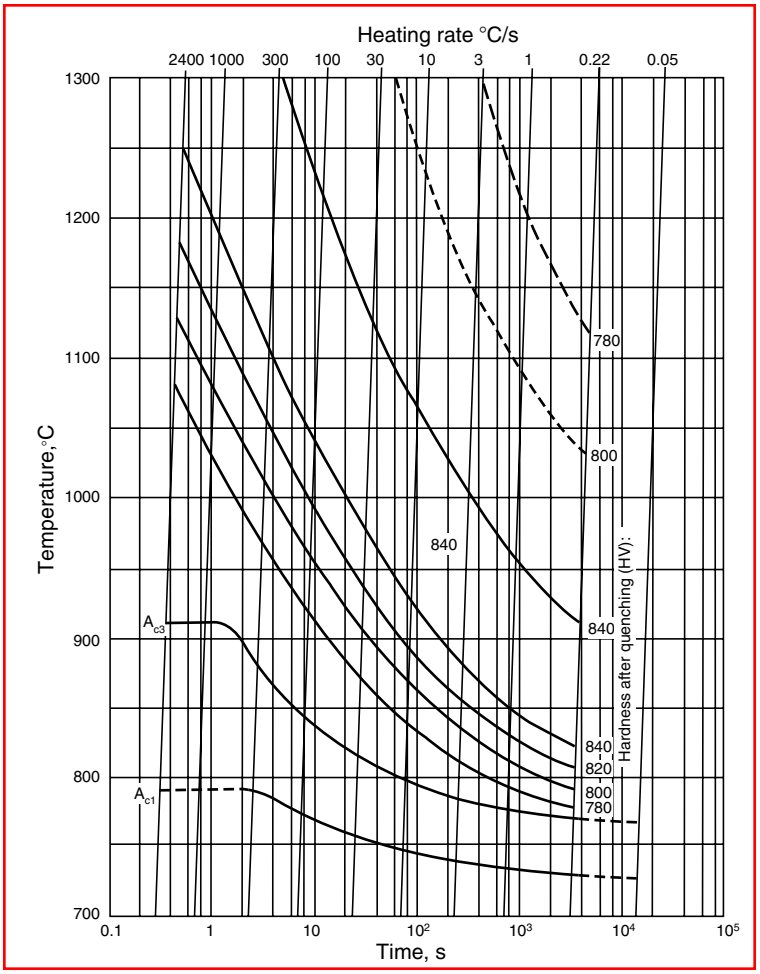

FIGURE 6.99 Time–temperature–austenitizing diagram for continuous heating showing the achievable hardness after hardening steel grade DIN Ck45. (From J. Orlich, A. Rose, and P. Wiest (Eds.), *Atlas zur Wärmebehandlung der Stähle*, Vol. 3, *Zeit-Temperatur-Austenitisierung-Schaubilder*, Verlag Stahleisen, Düsseldorf, 1973 [in German].)

tempered structure (tempered martensite) of the same steel, as shown in Figure 6.100b, will attain the maximum hardness of 770 HV, however, if heated to 875°C (1609°F) at the rate of 1000°C/s (1832°F/s) (holding time less than 1 s). For this reason, when short-time heating processes are used, the best results are achieved with hardened and tempered initial structures.

For eutectoid and hypereutectoid steel grades, which after quenching develop substantial amounts of retained austenite, the attainment of maximum hardness after quenching is more complicated. Figure 6.101 shows the hardness after quenching for the ball bearing hypereutectoid grade DIN 100Cr6 steel (1.0% C, 0.22% Si, 0.24% Mn, and 1.52% Cr). The maximum hardness of 900 HV after quenching is attained on heating to a very narrow temperature range, and furthermore this temperature range is displaced toward higher temperatures as the heating rate is increased. If this steel is quenched from temperatures that exceed the optimum range, the resulting hardness is reduced owing the presence of an increasing amount of retained austenite.

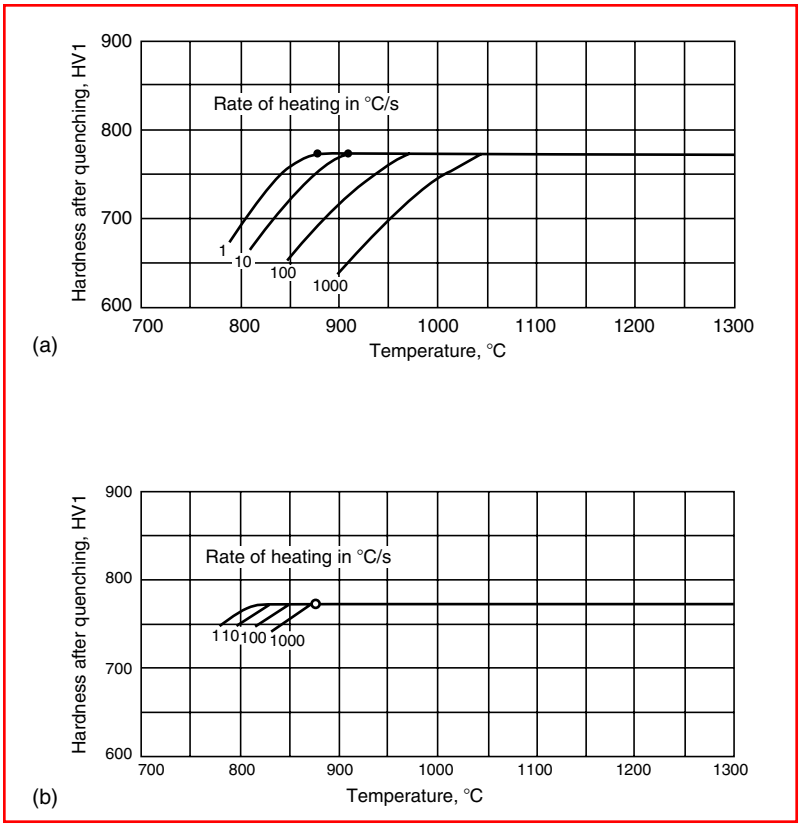

FIGURE 6.100 Hardness after quenching as a function of the rate of heating and austenitizing temperature for grade DIN Cf53 steel (hypoeutectoid carbon steel) (a) for soft-annealed condition and (b) for hardened and tempered condition. (From K.E. Thelning, *Steel and Its Heat Treatment*, 2nd ed., Butterworths, London, 1984.)

For plain carbon and low-alloy structural steels, which contain easily dissolved carbides, a holding time of 5–15 min after they have reached the hardening temperature is quite enough to make certain that there has been sufficient carbide dissolution. For medium-alloy structural steels this holding time is about 15–25 min. For low-alloy tool steels, it is between 10 and 30 min; and for high-alloy Cr steels, between 10 min and 1 h.

6.3.1.2 Technological Aspects of Austenitizing

In heating metallic objects to their austenitizing (hardening) temperature, there are two kinds of heating rates to be distinguished: those that are technically possible and those that are technologically allowed.

The technically possible heating rate is the heating rate the heating equipment could realize in actual use. It depends on

1. The installed heating capacity of the equipment
2. The heat transfer medium (gas, liquid, vacuum)
3. The temperature difference between the heat source and the surface of the heated objects (workpieces put in a hot or cold furnace)
4. The mass and shape of the workpiece (the ratio between its volume and superficial area)
5. The number of workpieces in a batch and their loading arrangement

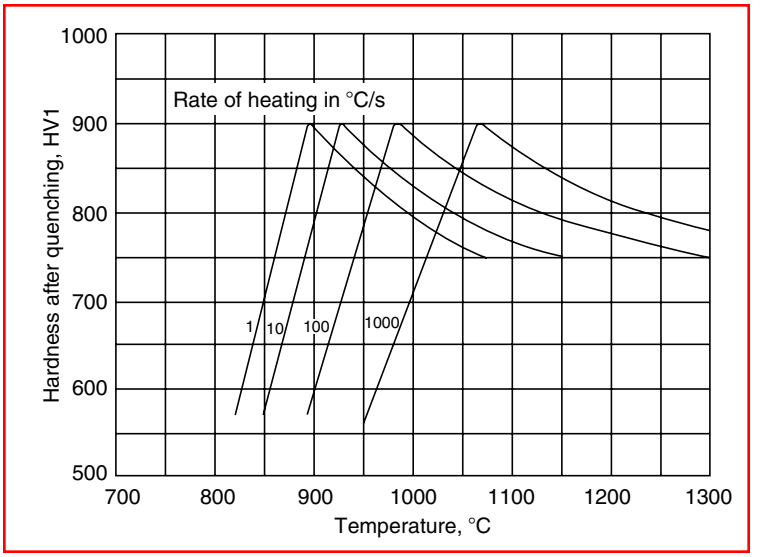

FIGURE 6.101 Hardness after quenching as a function of the rate of heating and austenitizing temperature for grade DIN 100Cr6 steel initially soft annealed. (From K.E. Thelning, *Steel and Its Heat Treatment*, 2nd ed., Butterworths, London, 1984.)

The technologically allowed heating rate is the maximum heating rate that can be applied in actual circumstances, taking into account the fact that thermal stresses that develop within the workpiece must not exceed the critical value because this could cause warping or cracking, since sections having different dimensions heat up at different speeds and large temperature gradients can arise between the surface and the core of the workpiece. This heating rate depends on

1. The mass and shape of the workpiece (the ratio between its volume and superficial area)
2. The chemical composition of the material
3. The initial microstructure

When workpieces of heavy sections or of complicated shapes are heated, temperatures between 250 and 600°C (482 and 1112°F) are particularly dangerous, because in this temperature range the steel does not have enough plasticity to compensate for thermal stresses. If the heating of an object is asymmetrical, the object will warp. If thermal stresses are developed that overstep the strength of the material (which is substantially lower at higher temperatures), cracks will result.

If the heating rate is too high through the transformation temperature range (between A_{c1} and A_{c3}), warping may occur because of volume change of the structure lattice. The tendency of a steel to crack during heating depends on its chemical composition. Carbon content has the decisive influence. The higher the carbon content, the greater the sensitivity to cracking. The complex influence of carbon and other alloying elements is expressed by the following empirical formula termed the *C* equivalent (C_{ekv}):

$$C_{ekv} = \frac{C + Mn}{5} + \frac{Cr}{4} + \frac{Mo}{3} + \frac{Ni}{10} + \frac{V}{5} + \frac{Si - 0.5}{5} + \frac{Ti}{5} + \frac{W}{10} + \frac{Al}{10} \tag{6.40}$$

where the element symbols represent wt% content. This formula is valid up to the following maximum values of alloying elements.

C $\leq$ 0.9%	V $\leq$ 0.25%
Mn $\leq$ 1.1%	Si $\leq$ 1.8%
Cr $\leq$ 1.8%	Ti $\leq$ 0.5%
Mo $\leq$ 0.5%	W $\leq$ 2.0%
Ni $\leq$ 5.0%	Al $\leq$ 2.0%

The values of the alloying elements actually present are put into the formula in wt%. If the amount of an alloying element exceeds the limit given above, then the indicated maximum value should be put into the formula.

The higher the calculated C_{ekv} value, the greater the sensitivity of the steel to cracking. For instance,

$C_{ekv} \leq 0.4$: The steel is not sensitive to cracking (it may be heated quite rapidly).
$C_{ekv} = 0.4$–0.7: The steel is medium sensitive to cracking.
$C_{ekv} \geq 0.7$: The steel is very sensitive to cracking (when heating up a preheating operation should be included).

The initial microstructure also has some influence on the technologically allowed heating rate. A steel with a homogeneous microstructure of low hardness may be heated more rapidly than a steel of high hardness with inhomogeneous microstructure.

The thermal gradients and consequently the thermal stresses developed when heating to austenitizing temperature can usually be diminished by preheating the workpiece to temperature lying close below the transformation temperature A_{c1} and holding it there until temperature equalizes throughout the cross section.

The theoretical time–temperature diagram of the austenitizing process is shown in Figure 6.102. Practically, however, there is no such strict distinction between the heating and soaking

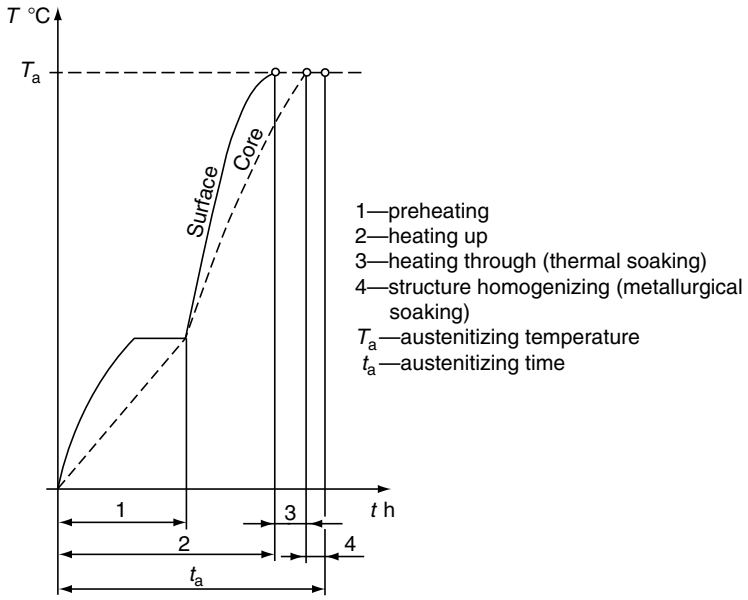

FIGURE 6.102 Austenitizing process (theoretically).

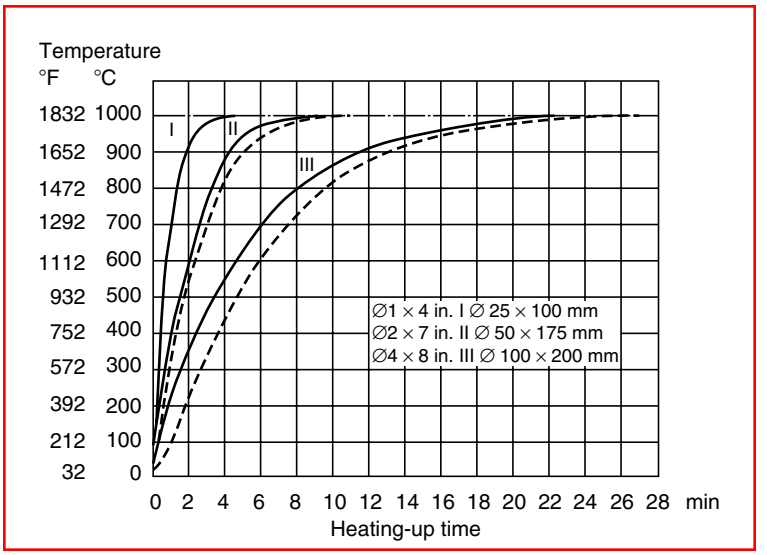

FIGURE 6.103 Time–temperature curves for steel bars of different diameters heated in a salt bath at 1000°C. Full line, measured temperature at surface; dashed line, measured temperature at center. (From K.E. Thelning, *Steel and Its Heat Treatment*, 2nd ed., Butterworths, London, 1984.)

times. Contrary to the generally widespread belief that the surface of the steel reaches the preset temperature considerably earlier than the center, the closer the temperature of the steel approaches the preset temperature, the smaller the temperature difference between surface and core, as shown in Figure 6.103. It can therefore be assumed that when the surface has reached the preset temperature, part of the soaking time (depending on the cross-sectional size) has already been accomplished. Certainly, one has to be aware of the corner effect—corners, sharp edges, and thin sections reach the preset temperature much earlier than the core of the workpiece.

The most important parameters of every austenitizing process are:

1. The austenitizing temperature
2. The heat-up and soak time at austenitizing temperature

For each grade of steel there is an optimum austenitizing (hardening) temperature range. This temperature range is chosen so as to give maximum hardness after quenching and maintain a fine-grained microstructure. It can be determined experimentally as shown in Figure 6.104 and Figure 6.105. From Figure 6.104 it is clear that the lowest possible hardening temperature for the steel in question is 850°C (1562°F). A lower hardening temperature would result in the formation of bainite and even pearlite with inadequate hardness.

When the hardening temperature is increased (see Figure 6.105), the grain size and the amount of retained austenite increase. At 920 and 970°C (1688 and 1778°F) the retained austenite may be discerned as light angular areas. On the basis of these experiments, the optimum hardening temperature range for the steel in question has been fixed at 850–880°C (1562–1616°F). The optimum hardening temperature range for unalloyed steels can be determined from the iron–carbon equilibrium diagram according to the carbon content of the steel. This range is 30–50°C (86–122°F) above the A_{c3} temperature for hypoeutectoid steels and 30–50°C (86–122°F) above A_{c1} for hypereutectoid steels, as shown in Figure 6.106. Because the curve *S*–*E* in this diagram denotes also the maximum solubility of carbon

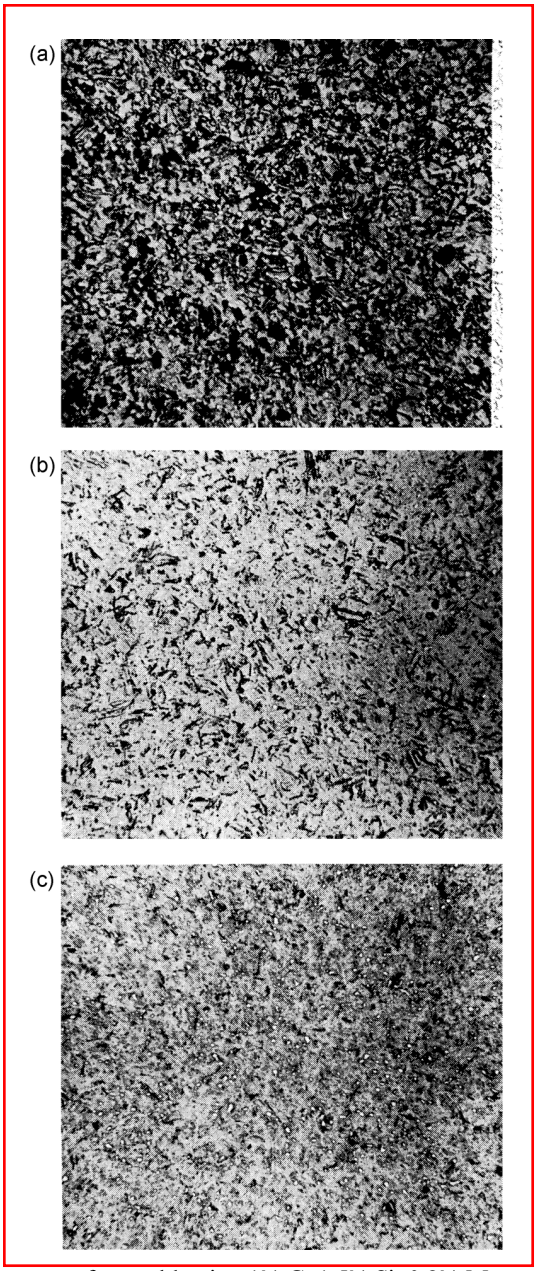

FIGURE 6.104 Microstructures of a steel having 1% C, 1.5% Si, 0.8% Mn, and 1% Cr, hardened from hardening temperatures between 800 and 850°C. Dimensions of test pieces: 30-mm diameter × 100 mm. Magnification 400×. (a) Hardening temperature 800°C, hardness 55 HRC; (b) hardening temperature 825°C, hardness 61.5 HRC; (c) hardening temperature 850°C, hardness 66 HRC. (From K.E. Thelning, *Steel and Its Heat Treatment*, 2nd ed., Butterworths, London, 1984.)

in austenite, it is clear that the higher the austenitizing (hardening) temperature, the more carbon can be dissolved in austenite. For alloyed steels the optimum austenitizing (hardening) temperature range depends on the chemical composition, because different alloying elements shift the A_1 temperature to either higher or lower temperatures. For

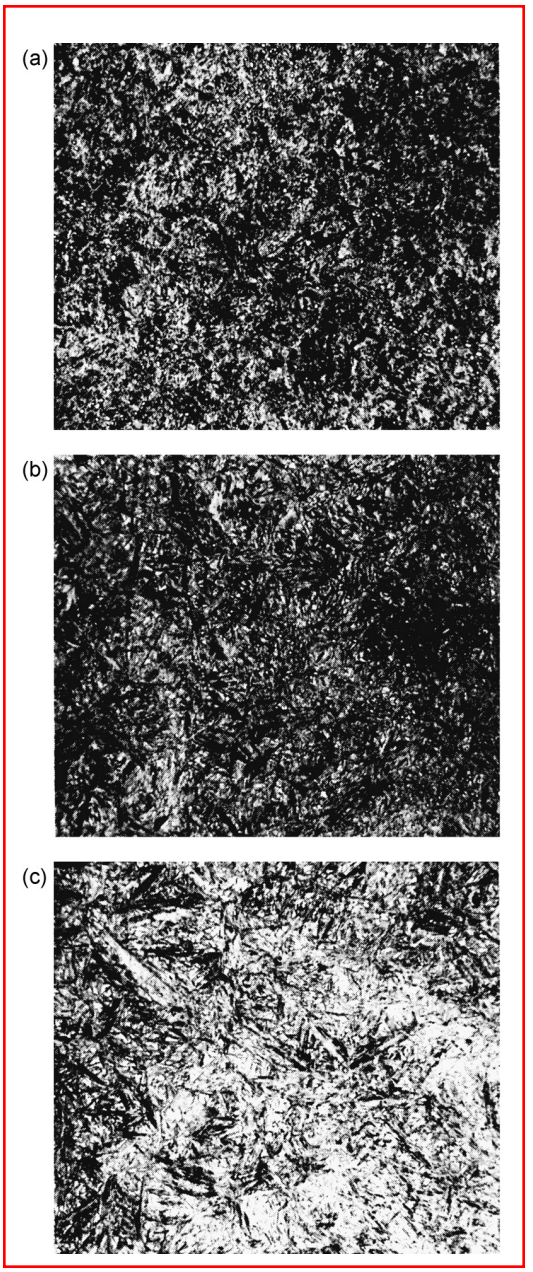

FIGURE 6.105 Microstructures of steel having 1% C, 1.5% Si, 0.8% Mn, and 1% Cr, hardened from hardening temperatures between 870 and 970°C. Dimensions of test pieces: 30-mm diameter × 100 mm. Magnification 400×. (a) Hardening temperature 870°C, hardness 62.5 HRC, retained austenite 12%; (b) hardening temperature 920°C, hardness 62 HRC, retained austenite 20%.; (c) hardening temperature 970°C, hardness 61 HRC, retained austenite 28%. (From K.E. Thelning, *Steel and Its Heat Treatment*, 2nd ed., Butterworths, London, 1984.)

these steels, therefore, data from the literature on the optimum hardening temperature range have to be consulted.

It should also be mentioned that increasing the austenitizing temperature causes the following effects.

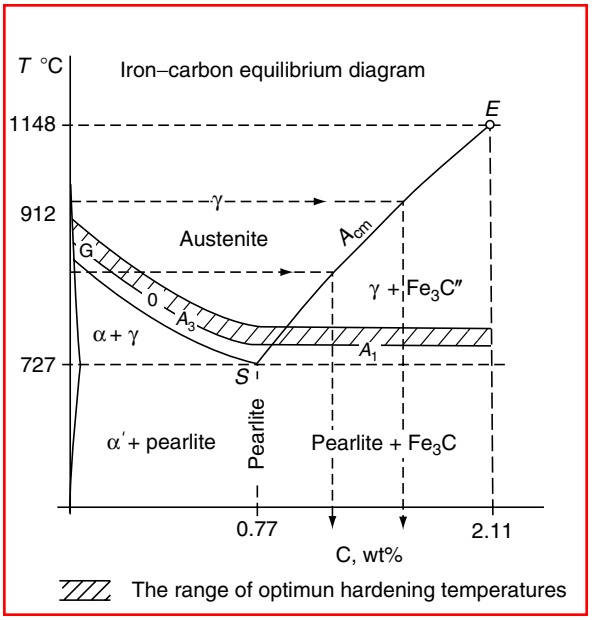

FIGURE 6.106 Optimum hardening temperature range for unalloyed steels, depending on the carbon content.

1. It increases the hardenability of the steel because of the greater amount of carbide going into solution and the increased grain size.
2. It lowers the martensite start temperature (M_s). Owing to the more complete carbide dissolution, the austenite becomes more stable and starts to transform upon quenching at lower temperature.
3. It increases the incubation time, i.e., the time until the isothermal transformation to pearlite or bainite starts. This is expressed as a shift in the start of transformation curves in an IT diagram to later times.
4. It increases the amount of retained austenite after quenching due to stabilization of the austenite, which at higher temperatures is more saturated with carbon from dissolved carbides.

Heat-up and soak time at austenitizing temperature is a very important parameter for bulk heat treatment because it not only determines the furnace productivity and economy (consumption of energy) but may also affect the properties of the treated workpieces. Until recently there was no reliable, objective method for accurately predicting heat-up and soak times for heat treatment cycles that took into account all workpiece characteristics, variations in furnace design, and load arrangement. Current determinations of heat-up and soak time are based on either a very conservative and general rule (e.g., 1 h/in. of cross section) or some empirical method, the results of which [20] differ substantially.

By heat-up and soak time we mean the time it takes for the heated workpiece to go from starting (room) temperature to the preset temperature in its core. The main factors that influence heat-up and soak time are diagrammed in Figure 6.107.

On the basis of experiments with 26 specimens (cylinders, round plates, and rings of various dimensions) made of unalloyed and low-alloy structural steels, Jost et al. [20] found from core temperature measurements that the heat-up and soak time depends substantially on the geometry of the heated workpiece and its mass. They found the heat-up and soak time to be directly proportional to the mass/surface area (m/A, kg/m^2) ratio, as shown in Figure 6.108. By regression analysis for their conditions (the specimens were heated in an electrically heated chamber furnace of 8 kW capacity and 240 × 240 × 400 mm working space, to the hardening

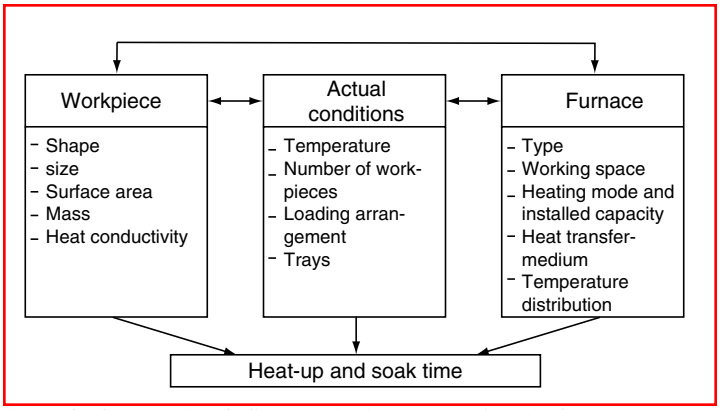

FIGURE 6.107 The main factors that influence the heat-up and soak time. (From S. Jost, H. Langer, D. Pietsch, and P. Uhlig, *Fertigungstech. Betr. 26*(5):298–301, 1976 [in German].)

temperature, 870°C (1598°F)), they found that the heat-up and soak time (t) can be calculated using the equation

$$t = 0.42(m/A) - 3.7 \tag{6.41}$$

The regression coefficients 0.42 and 3.7 are, of course, valid for their experimental conditions only. Comparison with their experimentally obtained results (see the points in Figure 6.108) showed a standard deviation of $s^2 = 1.4$ min^2, or $s = \pm 1.2$ min, indicating that this way of predicting heat-up and soak time in specific circumstances may be quite precise.

The Jost et al. [20] approach may be used generally for prediction of heat-up and soak times according to the general expression

$$t = a(m/A) + b \tag{6.42}$$

provided that for a given situation the straight line of regression and relevant values of the regression coefficients a and b are fixed by means of some preliminary experiments. It should be stressed, however, that the described results of this investigation are valid for single workpieces only.

In another investigation [21], a method enabling heat treaters to accurately determine the heat-up and soak times for different loads treated in batch-type indirect fired furnaces was

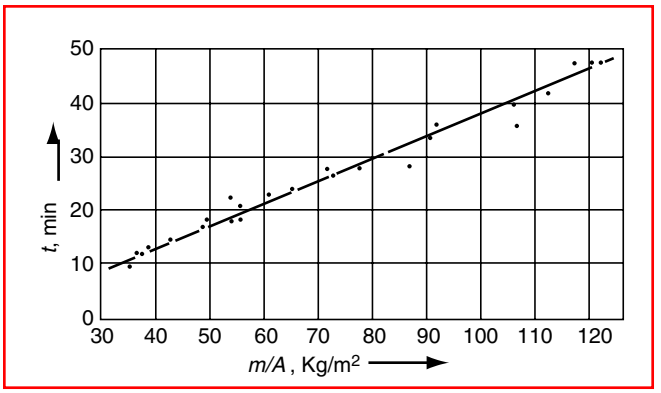

FIGURE 6.108 Dependence of the heat-up and soak time on the mass/surface area ratio, (m/A). (From S. Jost, H. Langer, D. Pietsch, and P. Uhlig, *Fertigungstech. Betr. 26*(5):298–301, 1976 [in German].)

developed. To develop the method, a statistical and experimental investigation of load temperature conditions was performed. A computer-aided mathematical model of heat and mass transfer throughout the furnace and load was developed. The computer model accurately predicts the suitable heat-up and soak times for various types of furnace loads, load arrangements, workpiece shapes, and thermal properties. The treated loads were divided into several groups in terms of workpiece allocation and aerodynamic patterns of the furnace atmosphere, as shown in Figure 6.109.

The experiments with six different loads were conducted in indirectly fired batch furnaces, the working space of which was of length 915–1680 mm, width 610–1420 mm, and height 610–1270 mm. The furnaces were equipped with four burners firing into the trident burner tubes located on the side walls, with a circulating fan located on top of the furnace as shown in Figure 6.110. The thermocouples were located in different parts of the load (measuring always the surface temperature of the workpieces)—on the top and bottom, in the core, at the corners, and on the surfaces facing radiant tubes—to determine temperature variations across the load.

As can be seen from Figure 6.110, the heat and mass transfer in the furnace and load are very complicated and are characterized by nonlinear three-dimensional radiation and convection and by nonlinear heat conduction within the workpieces. In this case, the mathematical

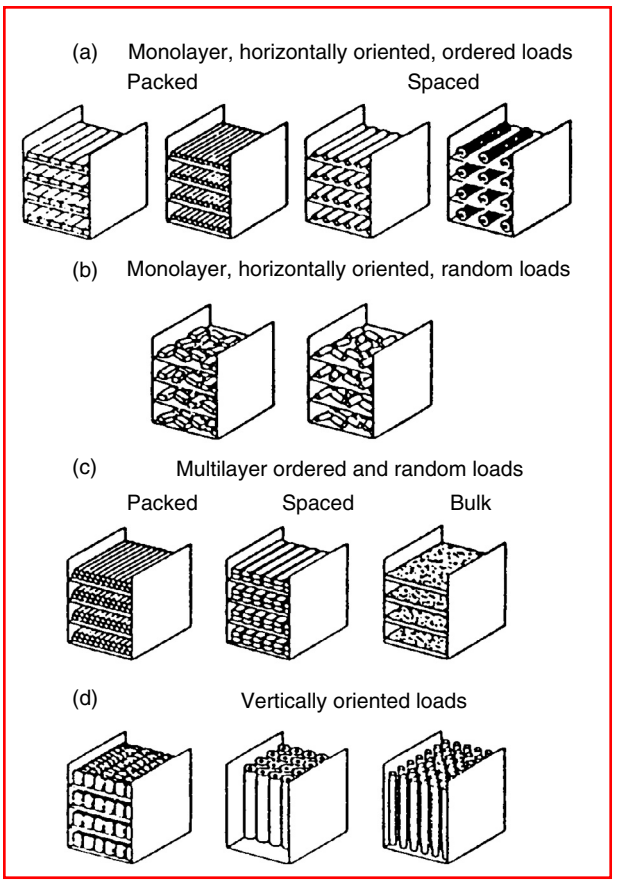

FIGURE 6.109 Load characterization. (a) Monolayer, horizontally oriented, ordered loads; (b) monolayer, horizontally oriented, random loads; (c) multilayer ordered and random loads. (d) Vertically oriented loads. (From M.A. Aronov, J.F. Wallace, and M.A. Ordillas, System for prediction of heat-up and soak times for bulk heat treatment processes, *Proceedings of the International Heat Treatment Conference on Equipment and Processes*, April, 18–20, 1994, Schaumburg, IL, pp. 55–61.)

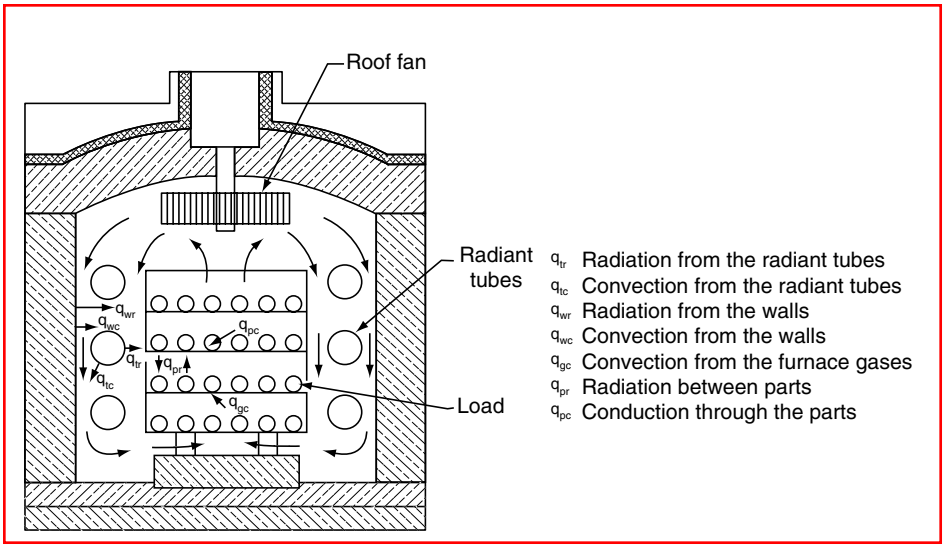

FIGURE 6.110 Heat transfer in the used furnace and load. (From M.A. Aronov, J.F. Wallace, and M.A. Ordillas, System for prediction of heat-up and soak times for bulk heat treatment processes, *Proceedings of the International Heat Treatment Conference on Equipment and Processes*, April, 18–20, 1994, Schaumburg, IL, pp. 55–61.)

model to describe the heat and mass exchange is a system of integral and differential nonlinear equations. The input parameters to the computer program were as follows:

Geometrical data of the furnace and load: Furnace working space dimensions, radiant tube diameter and layout in the furnace, dimensions of the baskets, number of trays in the basket, workpiece characteristic size
Type of load (according to load characterization, see Figure 6.109)
Type of steel (carbon, alloyed, high-alloy)
Load thermal properties
Load and furnace emissivities
Temperature conditions (initial furnace and load temperature)
Fan characteristic curve parameters
Composition of protective atmosphere

As an example, maximum and minimum steel part temperatures for a test (heating of shafts) together with the calculated data are shown in Figure 6.111. The experimental data show that the temperature curve of the load thermocouple usually reaches the set furnace temperature well within the soak time requirements. The experimentally determined soak time is seen to be considerably shorter than the soak time defined by the heat treater. It was found that the discrepancy between soak times determined from the test data and calculations does not exceed 8%, which is acceptable for workshop practice.

The developed computer model was used for simulation of temperature conditions for different load configurations, and a generalized formula and set of graphs were developed. The generalized equation for the soak time determination is

$$t_s = t_{sb}k \tag{6.43}$$

where t_s is the calculated soak time, min; t_{sb} is soak time for baseline temperature conditions, min; and k is a correction factor for the type of steel.

The basic soak time (t_{sb}) is obtained from graphs derived from the computer simulation. Such a graph for packed loads is shown in Figure 6.112. Other load shapes and configurations

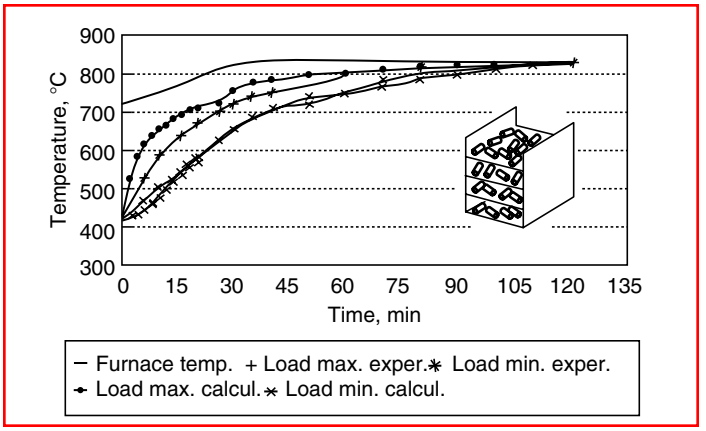

FIGURE 6.111 Computer simulation for heating of shafts. (From M.A. Aronov, J.F. Wallace, and M.A. Ordillas, System for prediction of heat-up and soak times for bulk heat treatment processes, *Proceedings of the International Heat Treatment Conference on Equipment and Processes*, April, 18–20, 1994, Schaumburg, IL, pp. 55–61.)

require different graphs. The correction factor k depends on the type of steel. The generalized equation (Equation 6.43) for the heat-up and soak time determination was set into a user-friendly computer package that incorporates charts for the calculation. This resulted in a straightforward way of determining the soak time without the use of charts while allowing for a quick and accurate soak time calculation.

6.3.2 Quenching Intensity Measurement and Evaluation Based on Heat Flux Density

In designing the method for practical measurement, recording, and evaluation of the quenching and cooling intensity in workshop conditions, in contrast to the Grossmann H value concept, which expresses quenching intensity by a single number, the main idea of Liščić was to express the quenching intensity by continuous change of relevant thermodynamic functions during the whole quenching process. Instead of recording only one cooling curve (as in laboratory-designed tests) in the center of a small (usually 1/2 in.) cylindrical specimen, the

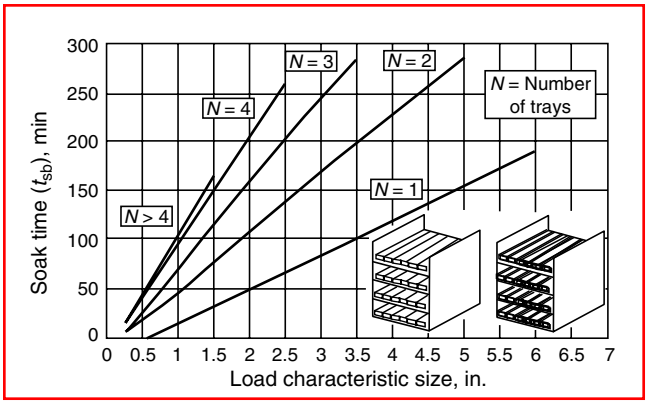

FIGURE 6.112 Thermal soak time for a packed load. (From M.A. Aronov, J.F. Wallace, and M.A. Ordillas, System for prediction of heat-up and soak times for bulk heat treatment processes, *Proceedings of the International Heat Treatment Conference on Equipment and Processes*, April, 18–20, 1994, Schaumburg, IL, pp. 55–61.)

heat flux density at the surface of a standard-size probe becomes the main feature in measuring, recording, and evaluating the quenching intensity.

The first substantial difference between using the small laboratory specimen and using the probe applied in the method described below is that when quenching, for example, in an oil quenching bath, because of its small mass and small heat capacity the former will cool down in 15–30 s, whereas the latter will take 500–600 s to cool to the bath temperature, allowing the entire quenching process of real components to be followed.

This workshop-designed method is applicable to

1. All kinds of quenchants (water and brine, oils, polymer solutions, salt baths, fluid beds, circulated gases)
2. A variety of quenching conditions (different bath temperatures, different agitation rates, different fluid pressures)
3. All quenching techniques (direct immersion quenching, interrupted quenching, martempering, austempering, spray quenching)

The method is sufficiently sensitive to reflect changes in each of the important quenching parameters (specific character of the quenchant, its temperature, and mode and degree of agitation).

This method

- Enables a real comparison of the quenching intensity among different quenchants, different quenching conditions, and different quenching techniques
- Provides an unambiguous conclusion as to which of two quenchants will give a greater depth of hardening (in the case of the same workpiece and same steel grade) and enables the exact calculation of cooling curves for an arbitrary point on a round bar cross section of a specified diameter, to predict the resulting microstructure and hardness (an exception is the case of delayed quenching, where the cooling rate is discontinuously changed; for an explanation see Ref. [23])
- Furnishes information about thermal stresses and possible superposition of structural transformation stresses that will occur during a quenching process
- Provides the basis for automatic control of the quenching intensity during the quenching process

The method itself, known in the literature as the temperature gradient method, is based on the known physical rule that the heat flux at the surface of a body is directly proportional to the temperature gradient at the surface multiplied by the thermal conductivity of the body material:

$$q = \lambda \frac{\delta T}{\delta x} \tag{6.44}$$

where q is the heat flux density (W/m^2) (i.e., quantity of heat transferred through a surface unit perpendicular to the surface per unit time); λ is thermal conductivity of the body material (W/(m K)), and $\delta T/\delta x$ is the temperature gradient at the probe surface perpendicular to the surface (K/m).

The essential feature of the method is a cylindrical probe [32] of 50-mm diameter $\times$ 200 mm, instrumented with three thermocouples placed along the same radius at the half-length cross section as shown in Figure 6.113. As can be seen, the thermocouple at the surface reproducibly measures the real surface temperature of the probe (T_n), which is important to register all the phenomena that are taking place on the surface during quenching. The intermediate thermocouple (T_i) measures the temperature at a point 1.5 mm below the surface. The readings of T_n and T_i enable the heat treater to easily calculate the temperature gradient near the surface of the probe at each moment of cooling. The central thermocouple

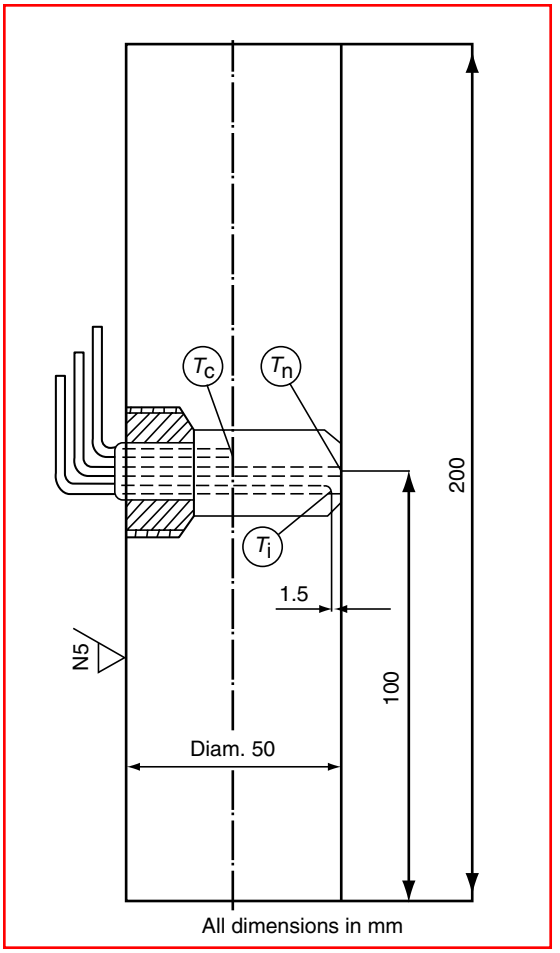

FIGURE 6.113 The Liščić-NANMAC probe (made by the NANMAC Corp., Framingham Center, MA) for measurement of the temperature gradient on the surface.

(T_c), placed at the center of the cross section, indicates how long it takes to extract heat from the core and provides at every moment the temperature difference between the surface and the core, which is essential for the calculation of thermal stresses.

Specific features of probe are the following:

1. The response time of the surface thermocouple is 10^{-5} s; the fastest transient temperature changes can be recorded.
2. The intermediate thermocouple can be positioned with an accuracy of ± 0.025 mm.
3. The surface condition of the probe can be maintained by polishing the sensing tip before each measurement (self-renewable thermocouple).
4. The body of the probe, made of an austenitic stainless steel, does not change in structure during the heating and quenching process, nor does it evolve or absorb heat because of structural transformation.
5. The size of the probe and its mass ensure sufficient heat capacity and symmetrical radial heat flow in the cross-sectional plane where the thermocouples are located.
6. The heat transfer coefficient during the boiling stage, which, according to Kobasko [22], depends on bar diameter, becomes independent of diameter for diameters greater than 50 mm.

When a test of the quenching intensity is performed, the probe is heated to 850°C (1562°F) in a suitable furnace and transferred quickly to the quenching bath and immersed. The probe is connected to the temperature acquisition unit and a PC. Adequate software enables the storage of the temperature–time data for all three thermocouples and the calculation and graphical display of relevant functions. The software package consists of three modules:

Module I. TEMP-GRAD (temperature gradient method)
Module II. HEAT-TRANSF (calculation of heat transfer coefficient and cooling curves)
Module III. CCT-DIAGR (prediction of microstructure and hardness after quenching)

As an example let us compare two different quenching cases:

Case A. Quenching in a mineral oil bath at 20°C (68°F) without agitation (Figure 6.114a through Figure 6.114f)
Case B. Quenching in a 25% polyalkalene glycol (PAG) polymer solution at 40°C (104°F) and 0.8 m/s agitation rate (Figure 6.115a through Figure 6.115f)

By comparing Figure 6.114b and Figure 6.115b it is clear that case B involves delayed quenching with a discontinuous change in cooling rate, because in case A the time when maximum heat flux density occurs (t_{qmax}) is 15 s whereas in case B it is 72 s.

In case A (oil quenching), by 20 s after immersion (see Figure 6.114e) the extracted amount of heat was already 34 MJ/m^2, and by 50 s, it was 50 MJ/m^2, whereas in case B (high concentration polymer solution quenching; see Figure 6.115e) by 20 s, the extracted heat was only 5 MJ/m^2 and by 50 s this value was only 20 MJ/m^2. However, immediately after that in the period between 50 and 100 s, in case A the extracted amount of heat increased from 50 to only 55 MJ/m^2, whereas in case B it increased from 20 to 86 MJ/m^2. Both of the calculated integral ($\int q\,dt$) curves, designated with the open square symbols in Figure 6.114e and Figure 6.115e, have been calculated as the area below the heat flux density vs. time curves, designated similarly in Figure 6.114b and Figure 6.115b. That is, they represent the heat extracted only through the surface region between the point 1.5 mm below the surface and the surface itself.

Comparing the time required to decrease the heat flux density from its maximum to a low value of, e.g., 100 kW/m^2 (see Figure 6.114b and Figure 6.115b), one can see that in case A 45 s is necessary, whereas in case B only 28 s is necessary. This analysis certifies that case B (quenching in PAG polymer solution of high concentration) is a quenching process with delayed burst of the thick polymer film.

Discontinuous change in cooling rate is inherent to this quenching regime. In this respect it is interesting to analyze the cooling rate vs. surface temperature diagrams of Figure 6.114f and Figure 6.115f. While in oil quenching (case A), the cooling rate at the surface of the probe (○) has a higher maximum than the cooling rates at 1.5 mm below the surface (□) and at the center (Δ), in case B the maximum cooling rate at 1.5 mm below surface (during a certain short period between 350 and 300°C (662 and 572°F) surface temperature) is higher than the maximum cooling rate at the surface itself. This can also be seen in Figure 6.115a, which shows that the slope of the cooling curve T_i between 500 and 300°C (932 and 842°F) is greater than the slope of the cooling curve for the very surface (T_n). This is another experimental proof that in delayed quenching cooling rates below the workpiece surface can be higher than at the surface itself.

Another analysis, with respect to thermal stresses during quenching (on which the residual stresses and possible distortion depend), is possible by comparing Figure 6.114d and Figure 6.115d. This comparison shows that quenching in a PAG polymer solution of high

concentration (case B), compared to oil quenching (case A), resulted in 27% lower maximum temperature difference (read thermal stress) between the center and surface of the probe (○) or 36% lower maximum temperature difference between the center and the point 1.5 mm below the surface, (Δ), contributing to lower distortion than in oil quenching. Whereas with oil quenching the maximum temperature difference between the center and the point 1.5 mm below the surface (Δ) is higher than the maximum temperature difference between the point

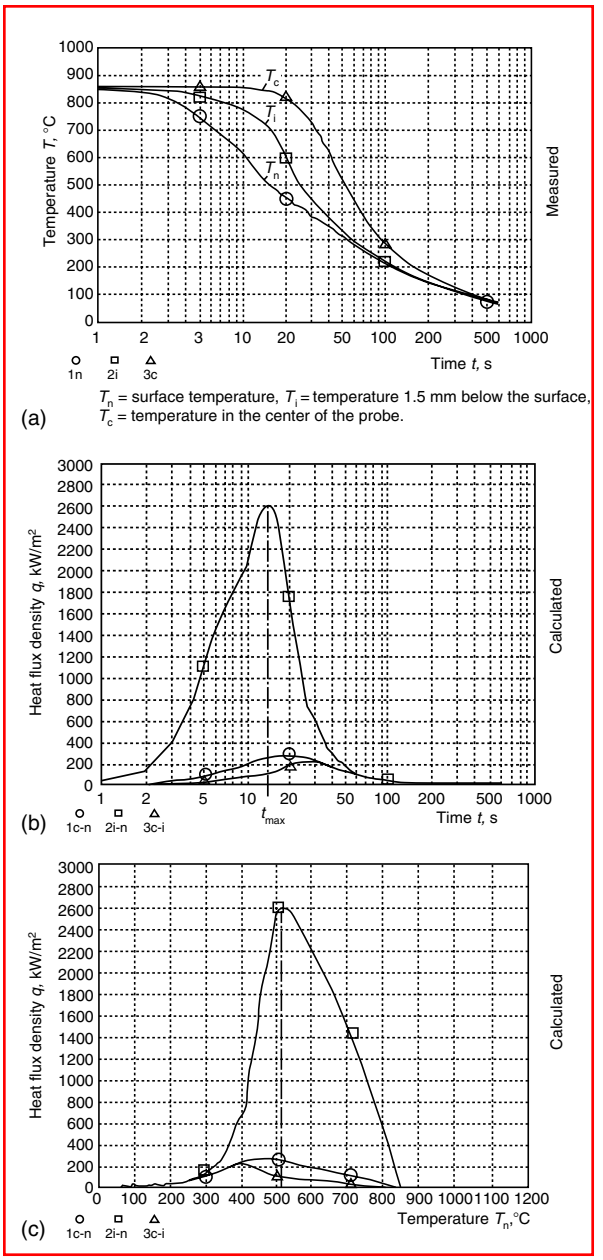

FIGURE 6.114 Graphical display from Module I, TEMP-GRAD, when quenching the Liščić-NANMAC probe in a 20°C mineral oil bath without agitation. (a) Measured and recorded temperature vs. time, $T=f(t)$; (b) calculated heat flux density vs. time, $q=f(t)$; (c) calculated heat flux density vs. surface temperature, $q=f(T_n)$.

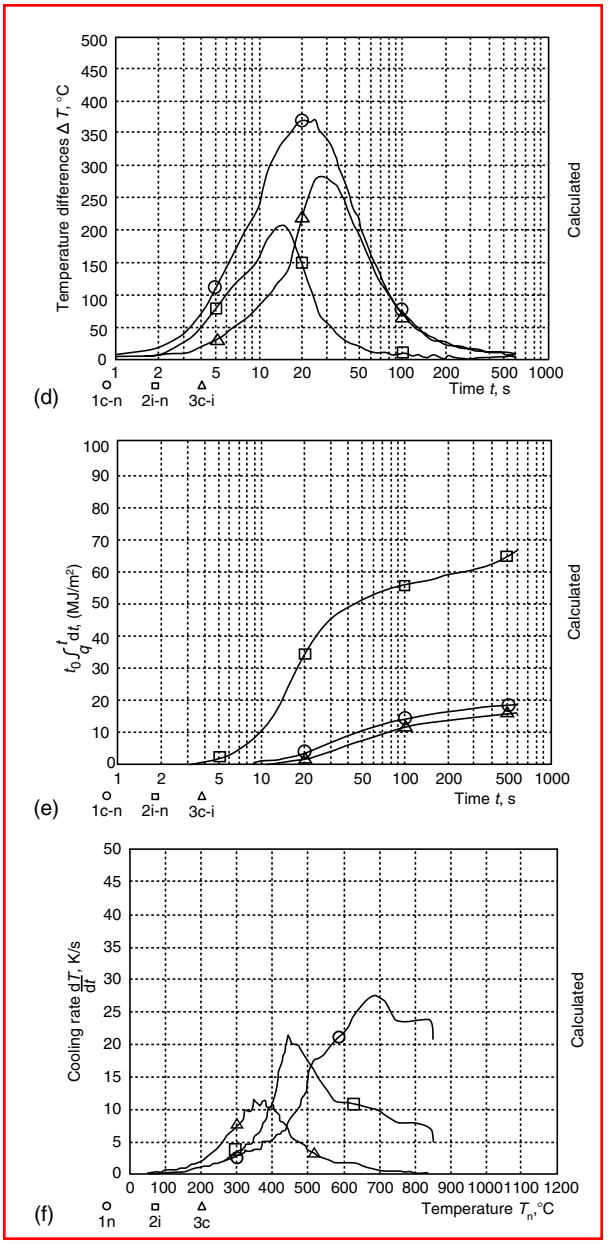

FIGURE 6.114 (Continued) (d) Calculated temperature differences vs. time, $\Delta T = f(t)$. (e) Calculated integral $\int q\, dt$ = heat extracted vs. time. (f) Calculated cooling rates vs. surface temperature $dT/dt = f(T_n)$.

1.5 mm below the surface and the surface itself. (□), In the case of delayed quenching (case B), the maximum temperature difference between the point 1.5 mm below the surface and the surface itself (□ in Figure 6.115d) is slightly higher than the maximum temperature defference between the center and the point 1.5 mm below the surface (Δ), which is reached about 20 s later. This also shows an abrupt heat extraction when the polymer film bursts.

On the other hand, Figure 6.114d shows that in oil quenching the maximum temperature difference between the center and surface (○) occurs 20 s after immersion, when the surface temperature is 450°C (842°F) (see Figure 6.114a), i.e., above the temperature of the M_s point. In

PAG polymer solution quenching (Figure 6.115d), the maximum temperature difference between the center and the surface (○) occurs much later, when the surface temperature has already fallen to 360°C (680°F) (see Figure 6.115a). In this respect, dealing with steels that have a high M_s temperature, water-based polymer solutions always run a higher risk of overlapping thermal stresses with those created due to austenite-to-martensite transformation.

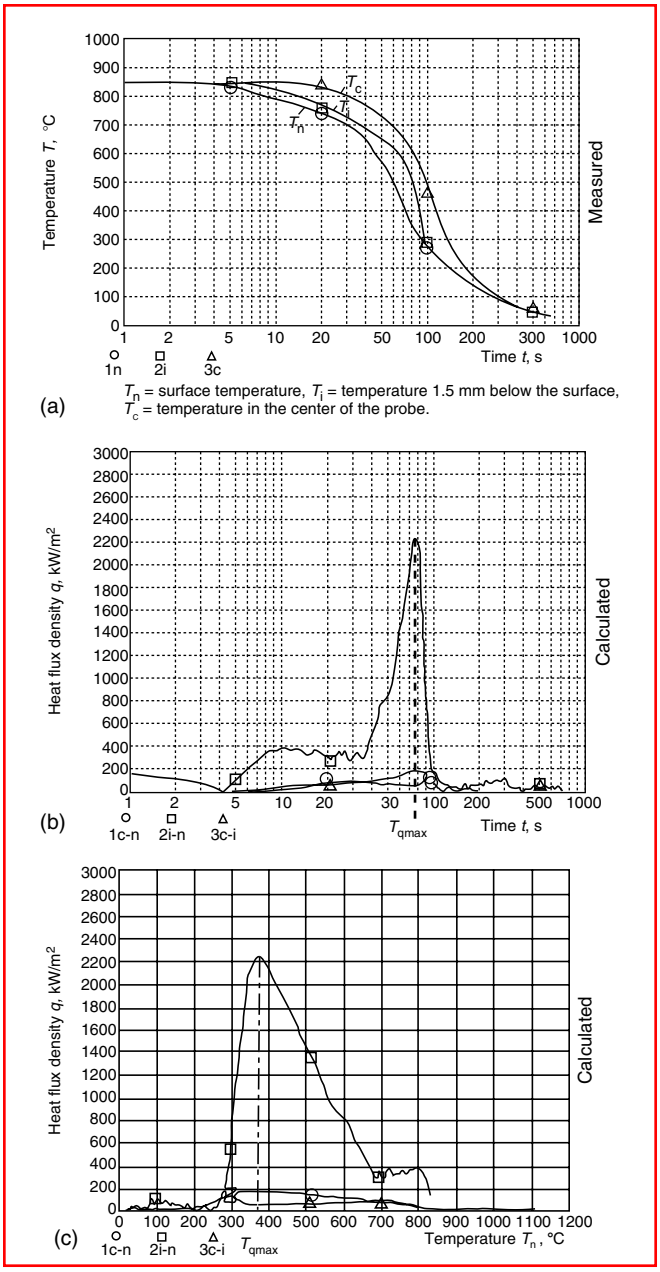

FIGURE 6.115 Graphical display from Module I, TEMP-GRAD, when quenching the Liščić-NANMAC probe in a PAG polymer solution of 25% concentration, 40°C bath temperature, and 0.8 m/s agitation rate. (a) Measured and recorded temperature vs. time data, $T = f(t)$. (b) Calculated heat flux density vs. time, $q = f(t)$. (c) Calculated heat flux density vs. surface temperature, $q = f(T_n)$.

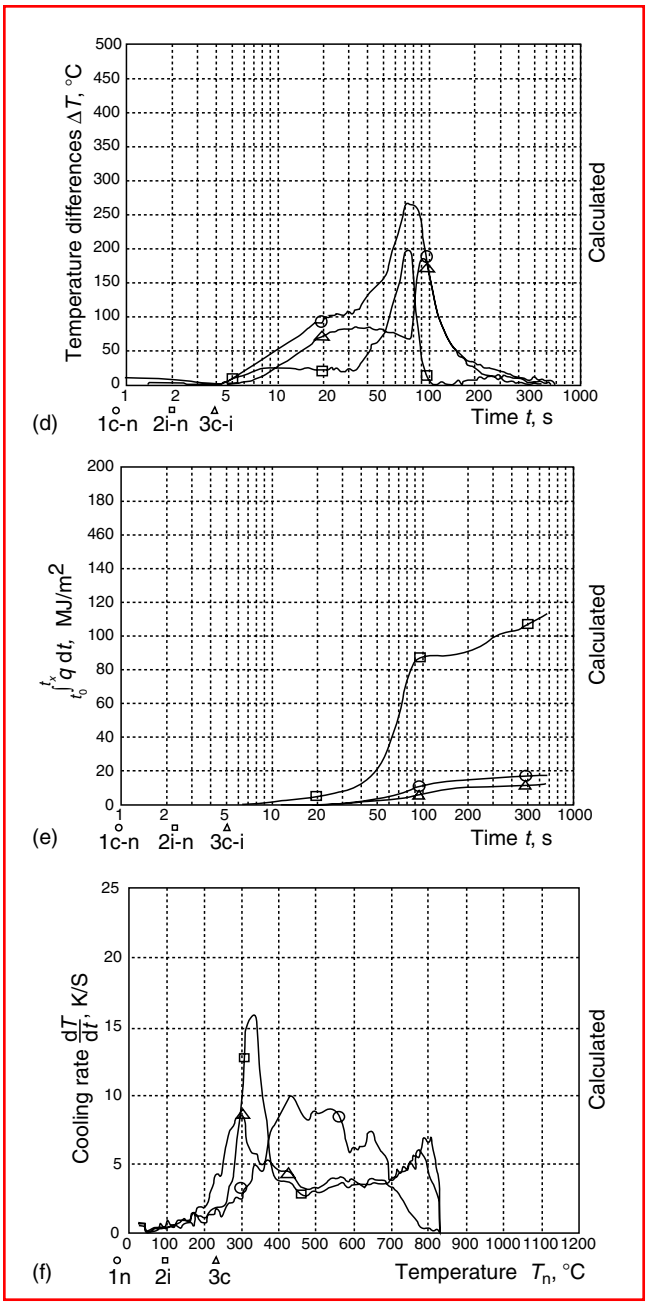

FIGURE 6.115 (Continued) (d) Calculated temperature differences vs. time, $\Delta T = f(t)$. (e) Calculated integral $\int q\,dt$ = heat extracted vs. time. (f) Calculated cooling rates vs. surface temperature, $dT/dt = f(T_n)$.

The probability of crack formation can be seen at a glance by comparing the surface temperature of the probe at the moment the maximum heat flux density occurs (T_{qmax}). As seen in Figure 6.114c, T_{qmax} is 515°C (959°F) for oil quenching (case A), while for water-based polymer solution (case B), T_{qmax} is 380°C (716°F) (see Figure 6.115c). The lower the value of T_{qmax}, the higher is the risk of crack formation, especially with steel grades having high M_s temperature.

When direct immersion quenching is involved with continuous cooling (not delayed quenching with discontinuous cooling), the depth of hardening, when comparing two quenching processes, is determined as follows: The larger the values of q_{max} and $\int q\,dt$ and the shorter the time $t_{qmax,}$, the greater will be the depth of hardening.

Module II of the software package, HEAT-TRANSF, makes it possible (based on the input of measured surface temperatures and calculated heat flux density on the very surface) to calculate (by a numerically solved method of control volumes) and graphically present

1. The heat transfer coefficient between the probe's surface and the surrounding fluid vs. time, $\alpha = f(t)$ (Figure 6.116a)
2. The heat transfer coefficient between the probe's surface and the surrounding fluid vs. surface temperature, $\alpha = f(T_n)$ (Figure 6.116b)

Using the calculated values of α, the software program enables the calculation of cooling curves at any arbitrary point of the round bar cross section of different diameters, as shown in Figure 6.117a and Figure 6.117b.

The Module III of the software package, CCT-DIAGR, is used to predict the resulting microstructure and hardness after quenching of round bar cross sections of different diameters. This module contains an open data file of CCT diagrams in which users can store up to 100 CCT diagrams of their own choice. The program enables the user to superimpose every calculated cooling curve on the CCT diagram of the steel in question. From the superimposed cooling curves shown on the computer screen, the user can read off the percentage of structural phases transformed and the hardness value at the selected point after hardening as shown by Figure 6.118.

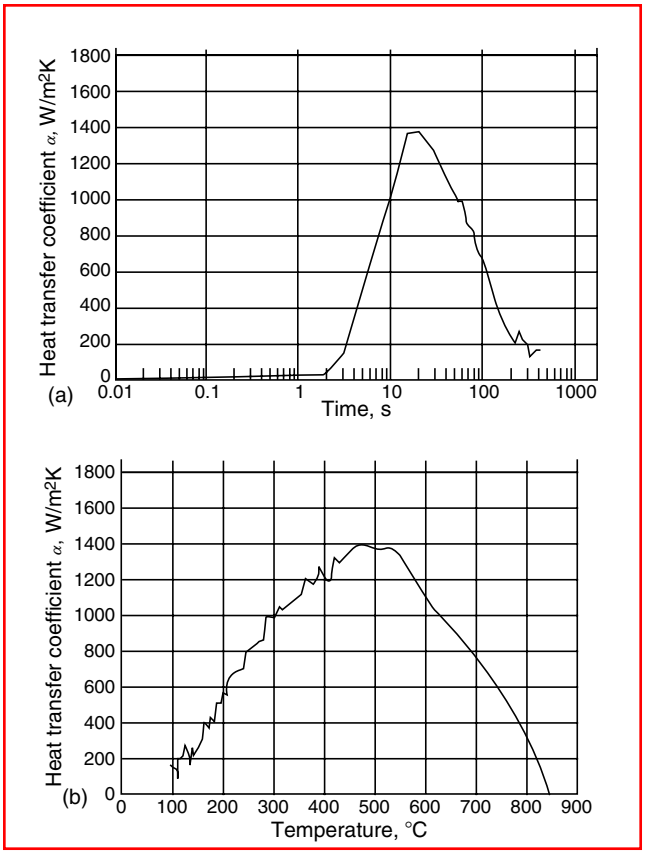

FIGURE 6.116 Heat transfer coefficient (a) vs. time and (b) vs. surface temperature when quenching the Liščić-NANMAC probe (50-mm diameter × 200 mm) in a 20°C mineral oil bath without agitation.

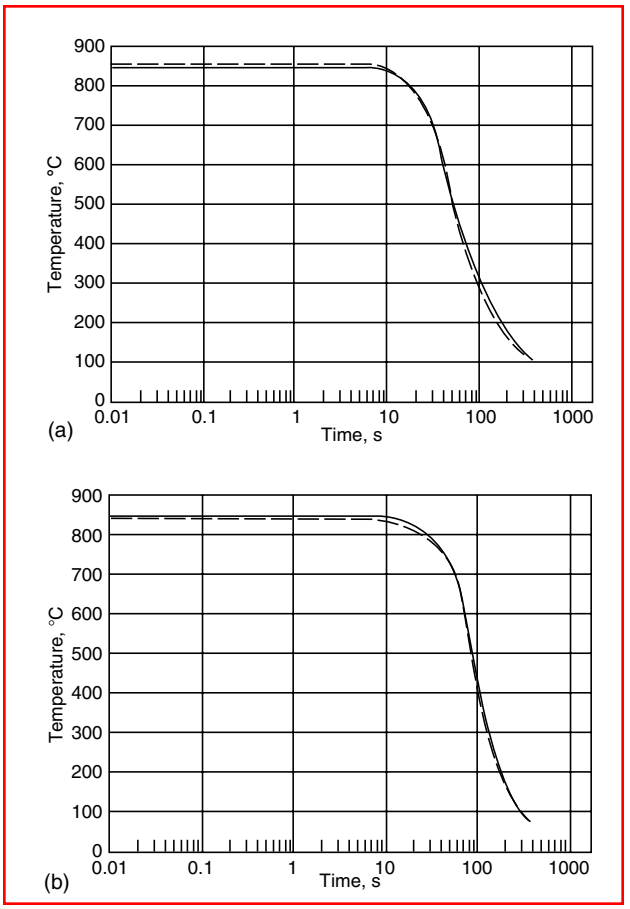

FIGURE 6.117 Comparison of measured (- - -) and calculated (—) cooling curves for the center of a 50-mm diameter bar quenched in (a) mineral oil at 20°C, without agitation and (b) 25% PAG polymer solution, 40°C bath temperature, and 0.8 m/s agitation rate.

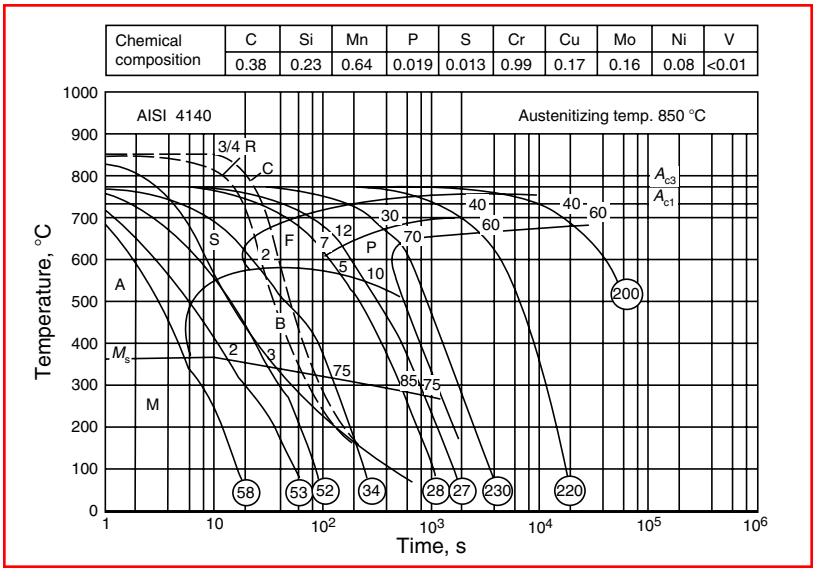

FIGURE 6.118 CCT diagram of AISI 4140 steel with superimposed calculated cooling curves for surface (S), three-quarter radius (3/4R) and center (C) of a round bar of 50-mm diameter.

If for a round bar cross section of the chosen diameter the cooling curves are calculated at three or five characteristic points (surface, (3/4)R, (1/2)R, (1/4)R, center), using the HEAT-TRANSF module, the CCT-DIAGR module enables the user to read off the hardness values after quenching at those points and to obtain the hardness distribution curve displayed graphically on the computer screen. In the case of delayed quenching with discontinuous change of cooling rate, the prediction of structural transformations and hardness values after quenching from an ordinary CCT diagram is not correct because the incubation time consumed (at any point of the cross section) before the cooling rate abruptly changes has not been taken into account.

For a detailed explanation see Shimizu and Tamura [11].

6.3.3 Retained Austenite and Cryogenic Treatment

The martensite start (M_s) and martensite finish (M_f) temperatures for unalloyed steels depend on their carbon content, as shown in Figure 6.119. As can be seen from this diagram, when steels of more than 0.65% C are quenched the austenite-to-martensite transformation does not end at room temperature (20°C (68°F)) but at some lower temperature, even at temperatures much lower than 0°C (32°F). Consequently, after these steels are quenched to room temperature, a portion of austenite will remain untransformed; this is referred to as retained austenite. The greater the amount of carbon in the steel, the greater the amount of retained austenite after quenching, as shown in Figure 6.120c.

Retained austenite, which is a softer constituent of the structure, decreases the steel's hardness after quenching. If present in amounts of more than 10%, a substantial decrease in the hardness of the quenched steel may result (see curve *a* of Figure 6.120a).

When quenching hypereutectoid steels from the usual hardening temperature (Figure 6.120b) i.e., from the $\gamma + Fe_3C$ region, the same hardness will result independently of carbon content (curve *b* in Figure 6.120a), because the hardness of martensite depends only on the carbon dissolved in austenite (γ), which further depends (according to the solubility limit, line *S–E*) on the hardening temperature. The structure of hardened hypereutectoid steels therefore consists of martensite + Fe_3C + retained austenite.

When quenching hypereutectoid steels from the region of pure austenite (γ), i.e., from above the A_{cm} temperature (which is not usual), the structure after hardening consists only of martensite and retained austenite, and the hardness decreases with carbon content as shown

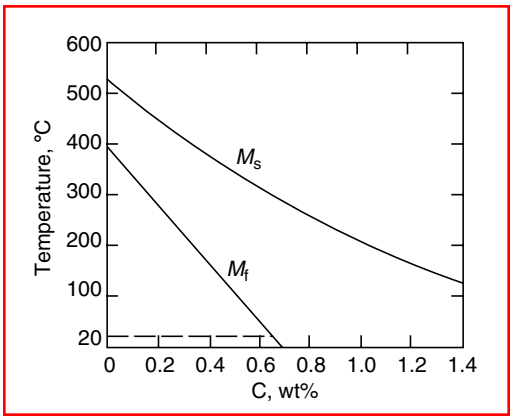

FIGURE 6.119 Martensite start (M_s) and martensite finish (M_f) temperatures vs. carbon content in unalloyed steels.

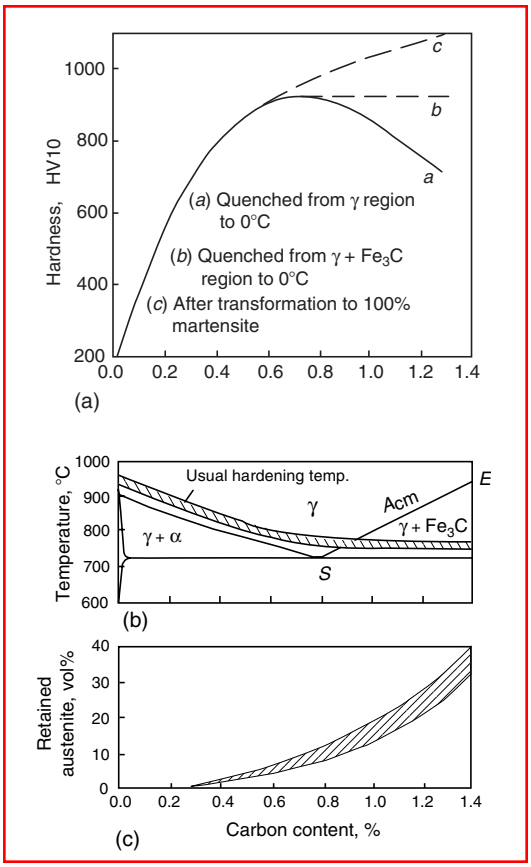

FIGURE 6.120 (a) Hardness of carbon (unalloyed) steels depending on carbon content and austenitizing temperature; (b) the range of usual hardening temperatures; (c) volume percent of retained austenite. (From H.J. Eckstein (Ed.), *Technologie der Wärmebehandlung von Stahl*, 2nd ed., VEB Deutscher Verlag für Grundstoffindustrie, Leipzig, 1987.)

by curve *a* of Figure 6.120a. If the retained austenite is transformed (e.g., by subsequent cryogenic treatment) to 100% martensite, the hardness would follow curve *c* in Figure 6.120a.

When after hardening the steel is kept at room temperature for some time or is heated to the temperature range corresponding to the first tempering stage, the retained austenite is stabilized, which implies that it has become more difficult to transform when subjected to cryogenic treatment. The stabilization of retained austenite is assumed to be due to the dissolution, at the arrest temperature, of the martensite nuclei formed during cooling from the austenitizing temperature.

When martempering is performed, i.e., the quenching process is interrupted somewhere around the M_s temperature, a similar stabilization of retained austenite occurs. When the cooling to room temperature is then continued, the same effect, in principle, results as that obtained by the subzero cryogenic treatment with respect to the transformation of retained austenite to martensite.

The initial amount of retained austenite (after quenching) is dependent to a very large extent on the austenitizing (hardening) temperature. The higher the hardening temperature, the greater the amount of retained austenite, but greater amounts of retained austenite may also be transformed to martensite by subzero cryogenic treatment for the same stabilizing temperature and same stabilizing time as shown in Figure 6.121. The stabilizing effect

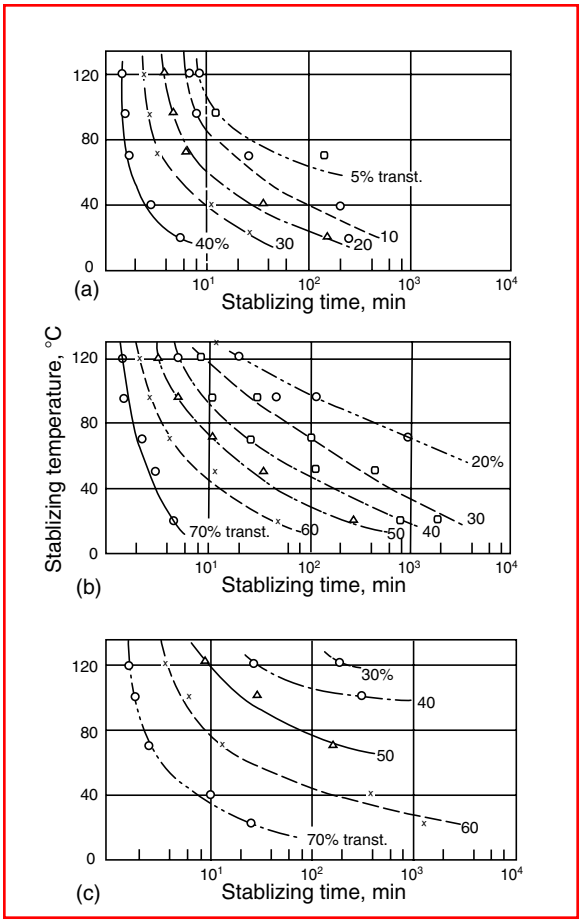

FIGURE 6.121 Influence of stabilizing temperature and time on the amount of retained austenite that transforms on being subzero treated at −180°C for the ball bearing steel AISI 52100. (a) Austenitizing temperature 780°C; 9.4% retained austenite after quenching; (b) austenitizing temperature 840°C; 18% retained austenite after quenching; (c) austenitizing temperature 900°C; 27% retained austenite after quenching. (From K.E. Thelning, *Steel and Its Heat Treatment*, 2nd ed., Butterworths, London, 1984.)

increases as the stabilizing temperature and time increase. After quenching from, say, 840°C (1544°F) (Figure 6.121b), there is 18% retained austenite. If the subzero treatment is carried out within 5 min after the temperature of the steel has reached 20°C (68°F), about 70% of the retained austenite will be transformed. If 40 min is allowed to pass before the subzero treatment, 60% will be transformed, and after 50 h holding at 20°C (68°F) only 30% of the retained austenite will respond to the subzero cryogenic treatment.

If the steel is held after quenching at a higher temperature, e.g., at 120°C (248°F), for only 10 min before subzero treatment, only 30% of the retained austenite will be transformed. In order to transform the greatest possible amount of retained austenite, the subzero cryogenic treatment should be performed immediately after quenching before tempering.

The question of whether the retained austenite in the structure is always detrimental or whether in some cases it can be advantageous has still not been answered unambiguously. When dealing with carburized and case-hardened components, because of the high carbon content in the case, the problem of retained austenite is always a real one, especially with steels containing nickel. The higher alloy nickel steels, such as types AISI 4620, 4820, and

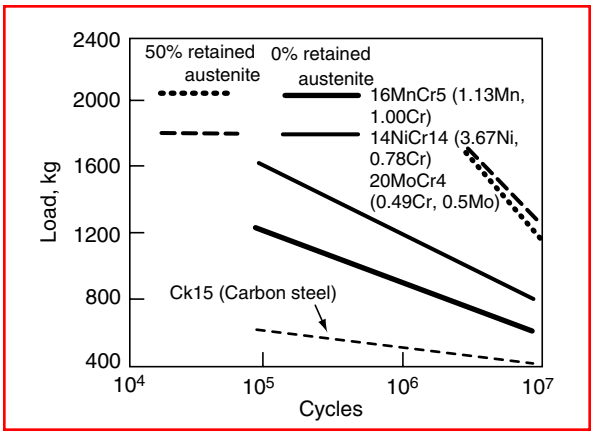

FIGURE 6.122 Improvement of contact fatigue of carburized and case-hardened steels containing 50% retained austenite, according to C. Razim. (From J. Parrish, *Adv. Mater. Process. 3*:25–28, 1994.)

9310, are particularly likely to have retained austenite in their microstructures after heat treatment because nickel acts as an austenite stabilizer.

Tests performed by M. Shea (cited in Ref. [24]), showed marked improvement in tensile bending strain values when retained austenite was present in the 20–30% range for AISI 8620 and 4620 steels and up to 40% for AISI 3310 steel. This report indicated that the transformation of retained austenite in the range of more than 20% allows more plastic strain to be accommodated before crack initiation because the austenite deforms and subsequently transforms to martensite.

The graph in Figure 6.122, taken from work done by C. Razim, shows where large quantities of retained austenite (in the range of 50%) improve contact fatigue of carburized and case-hardened steels. In another publication [24], several grades of carburized and case-hardened steels were compared (both before and after subzero treatment), and a clear improvement in bend ductility is reported for those having retained austenite.

As a result of the above-mentioned investigations, when dealing with carburized and case-hardened gears, an amount of 10–20%, and in some instances up to 25%, of retained austenite is not objectionable for most applications and may be beneficial. On the other hand, retained austenite can be detrimental, causing premature wear of sliding on the components' surface or of sliding and rolling of gear teeth, because it is a softer constituent of the microstructure. The presence of retained austenite in cases of carburized and case-hardened components that are to be subsequently ground is definitely detrimental because under certain grinding conditions it causes severe grinding burns and cracking. The susceptibility of carburized and case-hardened components to cracking during grinding becomes greater, the greater the amount of retained austenite, this amount further depending on the steel grade and carburizing temperature as shown in Figure 6.123.

6.3.3.1 Transforming the Retained Austenite

When steels are tempered, retained austenite decomposes to bainite during the second tempering stage (230–280°C (446–536°F)). For high-alloy chromium steels, hot-work steels, and high-speed steels, the range of decomposition of retained austenite is shifted toward higher temperatures. The product of decomposition, i.e., whether it is bainite or martensite, depends on the tempering temperature and time. Bainite formation occurs isothermally, i.e., at

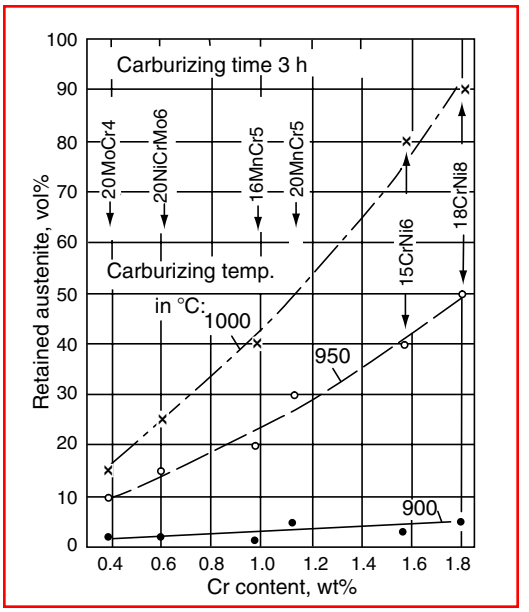

FIGURE 6.123 Influence of the Cr content of low-alloy steels for carburizing on the amount of retained austenite at carburizing. The amount of retained austenite was determined metallographically 0.05 mm below the specimen's surface. (From H.J. Eckstein (Ed.), *Technologie der Wärmebehandlung von Stahl*, 2nd ed., VEB Deutscher Verlag für Grundstoffindustrie, Leipzig, 1987.)

constant temperature during the tempering process, whereas martensite forms as the steel is cooling down from the tempering temperature.

Subzero cryogenic treatment may be applied to transform the retained austenite to martensite, substantially lowering its amount, sometimes to as little as about 1 vol%, which cannot be detected metallographically but only by x-ray diffraction.

Decreasing the amount of retained austenite achieves

1. Increase in hardness and consequently in wear resistance
2. More dimensional stability in the finished part (smaller change in dimensions due to structural volume change in use)
3. Less susceptibility to the development of cracks at grinding

Figure 6.124 shows a heat treatment cycle that includes subzero treatment. The most important parameters of the treatment are (1) the temperature below 0°C (32°F) that should

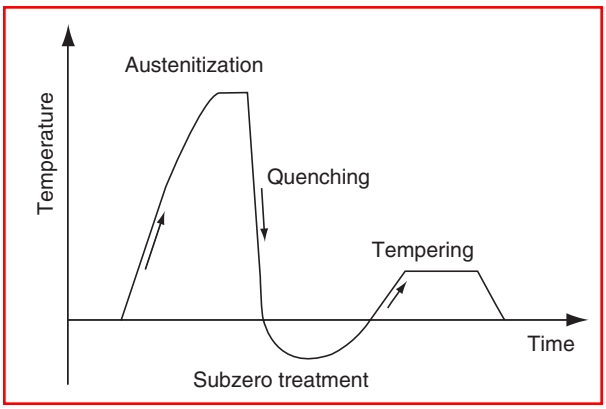

FIGURE 6.124 A heat treatment cycle including subzero treatment.

be attained and (2) the cooling capacity of the equipment. In some cases, temperatures of −80 to −100°C (−112 to −148°F) are sufficient, but for other steels, especially high-alloy ones, lower temperatures of −140°C (−280°F) or even −180°C (−292°F) are necessary. Holding time at low temperature is unimportant, because the transformation of retained austenite to martensite does not depend on time, but only on the temperature to which the metal has been cooled. Only that portion of the retained austenite will be transformed to martensite that corresponds to the cooling temperature realized. Further transformation will take place only if the temperature is lowered further.

There are four methods using different types of equipment for the subzero treatment:

1. Evaporation of dry ice (CO_2 in the solid state). This method is capable of reaching at most −75°C (−103°F) or −78°C (−108°F) and is used for small quantities and small mass of parts.
2. Circulating air that has been cooled in a heat exchanger. This low-temperature cascade system (Figure 6.125) cools the parts put in a basket with air circulated by a fan. The air flows from top to bottom, extracting the heat of the parts, exiting through a grate at the bottom of the basket and flowing further through the heat exchanger, which is cooled by two or four compressors. Such metal-treating freezers have been built with a capacity to cool a mass of 270–680 kg of parts to −85°C (−121°F) in about 2 h.
3. Evaporation of liquid nitrogen. For subzero treatment of relatively small quantities of parts down to −180°C (−292°F), equipment such as that shown in Figure 6.126 is used. The parts to be cooled are put in the working space 1, and the liquid nitrogen is in the container 4. Because of heat coming through the walls, the pressure in the container 4 increases. Using this pressure, when the valve 6 is opened, liquid nitrogen is injected into the working space, where it evaporates instantly. A fan 7 circulates the evaporated nitrogen through the working space, taking the heat out of parts and lowering their temperature. The amount of the injected liquid nitrogen and consequently the temperature of cooling can be controlled by adjusting the valve 6. The overpressure that develops in the working space because of constant nitrogen evaporation is let out through the exhaust valve 8. A temperature of −180°C (−292°F) can be reached in less than 10 min.
4. In a container connected to a cryogenerator. This method enables subzero treatment of large quantities of parts to as low as −190°C (−310°F). The cryogenerator powered

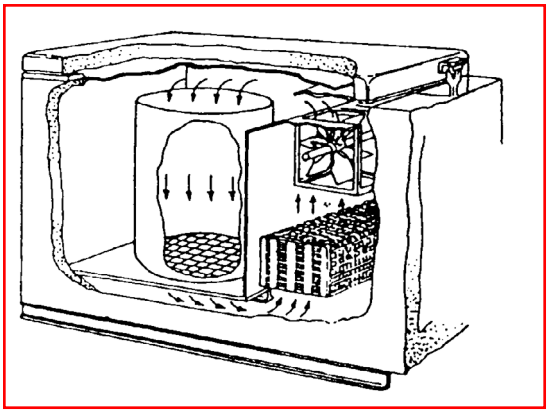

FIGURE 6.125 Low-temperature cascade system for subzero cooling by circulating air that has been cooled in a heat exchanger.

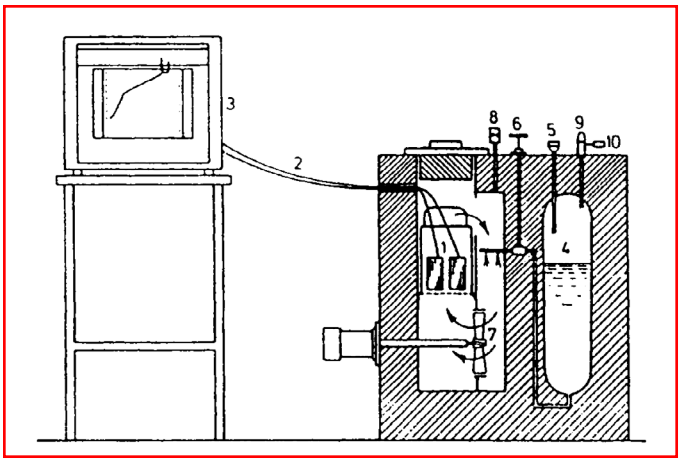

FIGURE 6.126 Subzero treatment equipment with evaporation of liquid nitrogen.

by an electric motor works on the principle of the Stirling cycle. By continuous circulation of air the working space with parts is gradually cooled to desired temperature. Figure 6.127 shows the cooling curve from room temperature to −180°C (−292°F) and the natural reheating curve from −180 to 0°C (−292 to 32°F) for the empty container of 100 dm^3, connected to a cryogenerator. It can be seen that after 1 h of cooling a temperature of −120°C (−184°F) has already been reached, but an additional 1.5 h is necessary to reach −180°C (−292°F). The natural reheating from −180 to 0°C (−292 to 32°F), as shown, takes much longer (about 20 h).

6.4 HARDENING AND TEMPERING OF STRUCTURAL STEELS

6.4.1 Mechanical Properties Required

A combined heat treatment process consisting of hardening plus tempering (to temperatures between 450 and 680°C (842 and 1256°F)) applied to structural steels (in German called *Vergütung*) is performed to achieve maximum toughness at a specified strength level. Toughness is a very important mechanical property, especially for components that must be able to

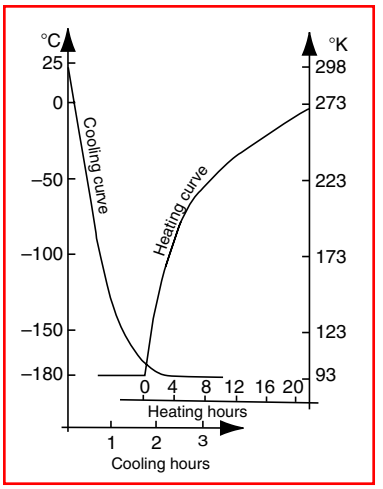

FIGURE 6.127 Cooling curve and natural heating back curve of an empty container connected to a cryogenerator.

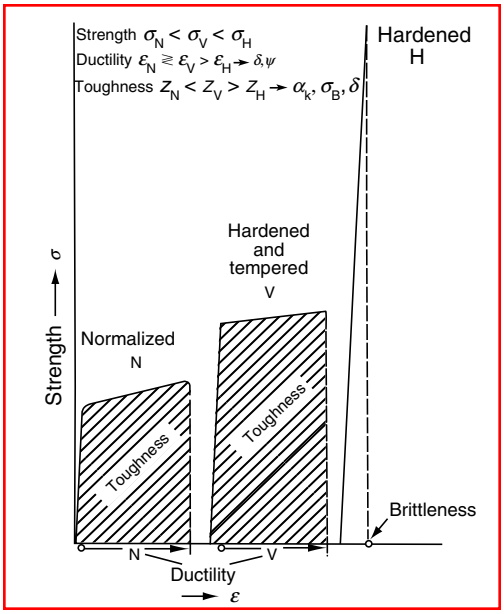

FIGURE 6.128 Schematic presentation of ductility, toughness, and brittleness. (From E. Just, *VDI-Ber. 256*:125–140, 1976 [in German].)

withstand dynamic loading or impact. The aim of hardening and tempering structural steels will be better understood if one has a clear notion of the difference between toughness and ductility.

Ductility is the property denoting the deformability of a material and is measured in a tensile test as elongation (A in %) and reduction of area (Z in %). It is a one-dimensional property. Toughness of a material, however, is a two-dimensional property because it is an integral (or product) of strength and ductility, as schematically shown in Figure 6.128. Steels of the same ductility but different strength levels can differ in toughness. As Figure 6.128 shows, a normalized steel (N) having the same ductility as a hardened and tempered steel (V) will have lower toughness because of its lower strength level. Toughness is measured in separate tests as impact toughness (a_k, J/cm^2) or as fracture toughness (K_{IC}, N/mm$^{3/2}$). The lower the ductility of a material, the more brittle it is. Total brittleness accordingly denotes zero ductility of the material.

The aim of the hardening and tempering process can also be explained by means of the stress–strain diagram schematically shown in Figure 6.129. As hardened, a steel has high yield strength but low ductility, and a small area below the stress–strain curve (curve 2) indicates low toughness. As-hardened and tempered (curve 3) steel has higher yield strength than in its normalized condition but also much higher ductility than in its hardened condition. The greatest area below the stress–strain curve indicates a substantial increase in toughness compared to either normalized or hardened conditions.

For a certain steel grade, the relation between mechanical properties and the tempering temperature can be read off from a diagram as shown in Figure 6.130 for the steel DIN 20CrNiMo2 (0.15% C, 0.20% Si, 0.88% Mn, 0.53% Cr, 0.50% Mo, 0.86% Ni). It can be clearly seen from the lower part of this diagram how the impact toughness increases when the steel is tempered to a temperature above 550°C (1022°F). Such diagrams enable precise optimization of the strength level and toughness by selection of the proper tempering temperature.

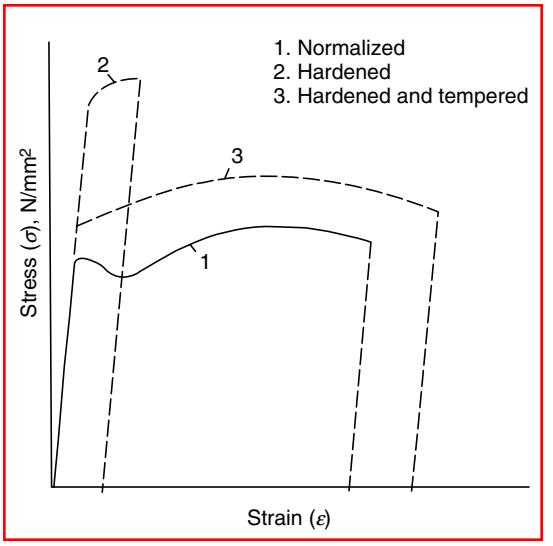

FIGURE 6.129 Stress–strain diagram of a steel after different heat treatments. 1, Normalized; 2, hardened; 3, hardened and tempered.

The properties of a hardened and tempered steel correlate to a high degree with the microstructure after hardening and tempering. Maximum toughness values are obtained when tempering a structure that after quenching consists of fine-grained martensite (having a grain size of ASTM ≥ 6) (see Figure 6.131). How different microstructures after different heat treatment processes influence the impact toughness of 3.5% Ni steel at low temperatures

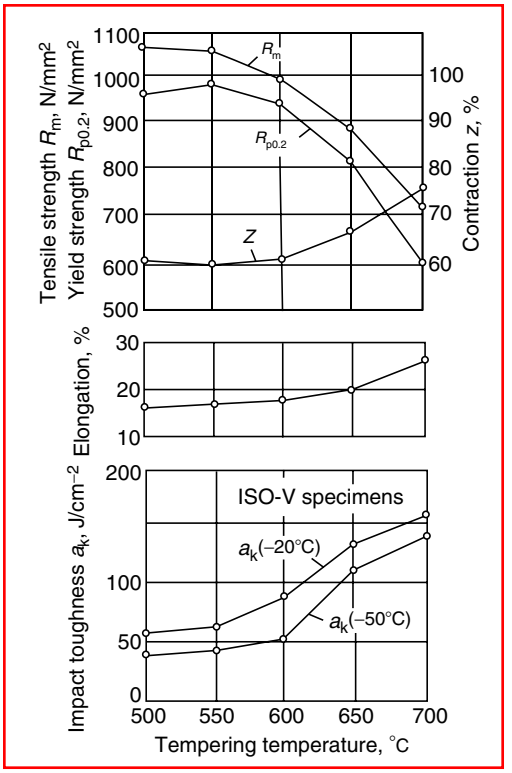

FIGURE 6.130 Hardening and tempering diagram of DIN 20CrNiMo2 steel. Hardening temperature 950°C; quenched in water. Specimen from a plate of 25-mm thickness; testing direction longitudinal. (From G. Spur and T. Stöferle (Eds.), *Handbuch der Fertigungstechnik, Vol. 4/2, Wärmebehandeln*, Carl Hanser, Munich, 1987.)

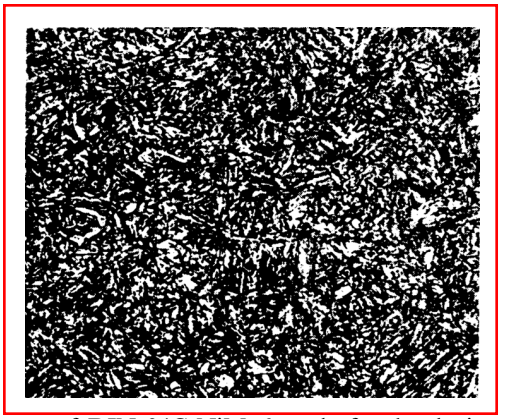

FIGURE 6.131 Microstructure of DIN 34CrNiMo6 steel after hardening and tempering. Tempered fine-grained martensite. Magnification 500×. (From G. Spur and T. Stöferle (Eds.), *Handbuch der Fertigungstechnik, Vol. 4/2, Wärmebehandeln*, Carl Hanser, Munich, 1987.)

is shown in Figure 6.132. The maximum toughness is achieved after tempering water-quenched specimens (tempered martensite). When testing the impact toughness at low temperatures, the so-called transition temperature (the temperature at which a substantial drop in impact toughness begins) is of special interest. The lower the transition temperature, the higher the toughness. Certainly, when hardening workpieces of big cross section, not only martensite is obtained, but also other constituents such as bainite, pearlite, and even pre-eutectoid ferrite, depending on the decrease in cooling rate at quenching, below the surface toward the core of the workpiece. So after tempering, besides tempered martensite, other structural constituents having lower toughness are present.

Figure 6.133 shows the relationships among transition temperature, yield strength, and microstructure. For high strength values especially, the superiority of fine-grained martensite structure with respect to toughness is evident.

From a series of tests with hardened and tempered steels with about 0.4% C, Figure 6.134 shows a general relation between the structural constituents and the properties characterizing ductility (elongation and reduction of area) and impact toughness, respectively, for different levels of yield strength. It is clear that tempered martensite always gives the best ductility and toughness.

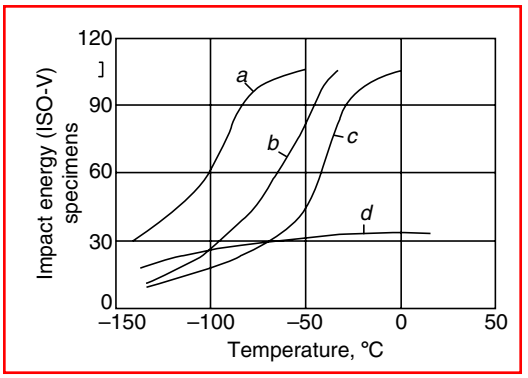

FIGURE 6.132 Influence of different microstructure and respective heat treatments on the impact toughness at low temperatures (ISO notch specimens) of a 3.5% Ni alloyed steel. *a*, Hardened by quenching in water and tempered; *b*, normalized and tempered; *c*, normalized only; *d*, hardened by quenching in water only. (From G. Spur and T. Stöferle (Eds.), *Handbuch der Fertigungstechnik, Vol. 4/2, Wärmebehandeln*, Carl Hanser, Munich, 1987.)

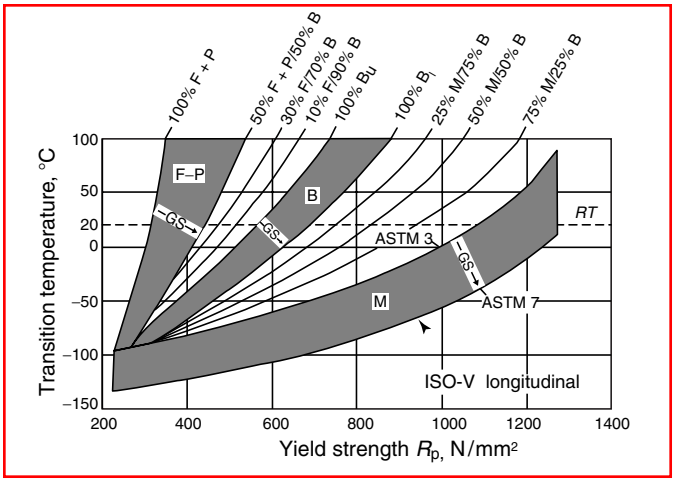

FIGURE 6.133 Transition temperature as a function of yield strength and microstructure. F, Ferrite; P, pearlite; B, bainite; B_u, upper bainite; B_l, lower bainite; M, martensite; GS, grain size (ASTM). (From G. Spur and T. Stöferle (Eds.), *Handbuch der Fertigungstechnik, Vol. 4/2, Wärmebehandeln*, Carl Hanser, Munich, 1987.)

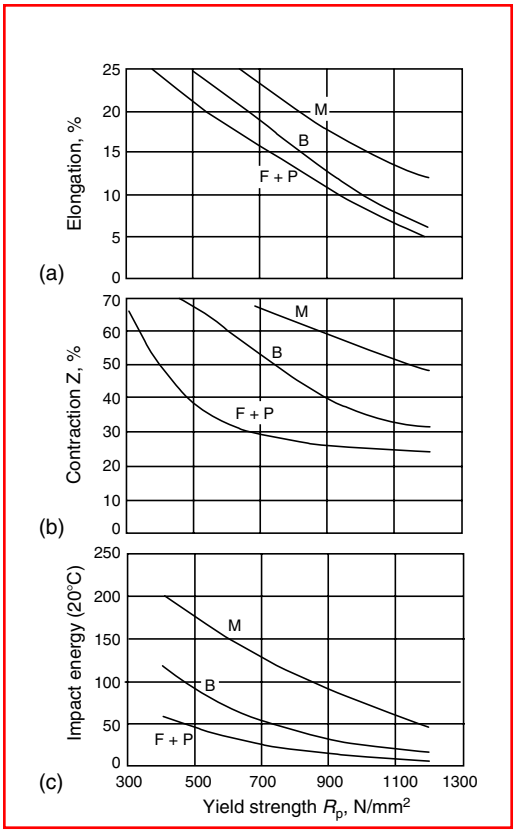

FIGURE 6.134 (a) Elongation; (b) reduction of area; and (c) impact toughness of hardened and tempered steels having about 0.4% C, as a function of structure constituents and yield strength. F, Ferrite; P, pearlite; B, bainite; M, martensite. Grain size: ASTM 6–7. Impact toughness: ISO notch specimens. Testing direction: longitudinal. (From G. Spur and T. Stöferle (Eds.), *Handbuch der Fertigungstechnik, Vol. 4/2, Wärmebehandeln*, Carl Hanser, Munich, 1987.)

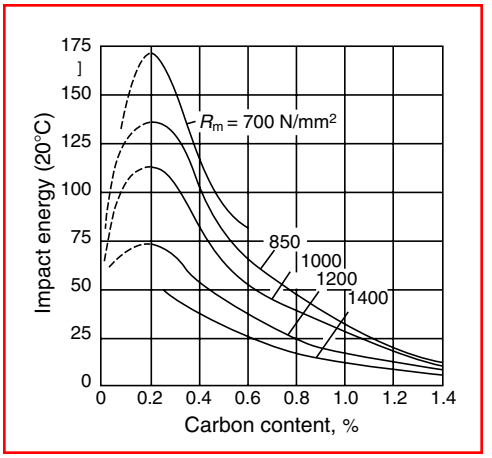

FIGURE 6.135 Impact toughness as a function of tensile strength and carbon content for the structure of tempered martensite. Grain size: ASTM 6–7. (From G. Spur and T. Stöferle (Eds.), *Handbuch der Fertigungstechnik, Vol. 4/2, Wärmebehandeln*, Carl Hanser, Munich, 1987.)

When comparing the impact toughness of tempered martensite at different strength levels (different hardness levels), one can perceive the influence of carbon content. As shown in Figure 6.135, of steels for hardening and tempering, those with 0.2–0.3% C have the best impact toughness. When testing the impact toughness of a steel, one should be aware that toughness is usually higher in the longitudinal direction (rolling direction) than in the transverse direction. That is because some phases or nonmetallic inclusions that are present in every steel (carbides, oxides, and sulfides) are stretched during rolling in the longitudinal direction. In this way a textured structure originates that has lower impact toughness in the transverse direction than in the longitudinal direction. As a measure of this effect, the factor of isotropy (the ratio of transverse impact toughness to longitudinal impact toughness) is sometimes used.

The great influence of the microstructure after hardening (before tempering) on the impact toughness of a steel is evident from Figure 6.136. Appearance of preeutectoid

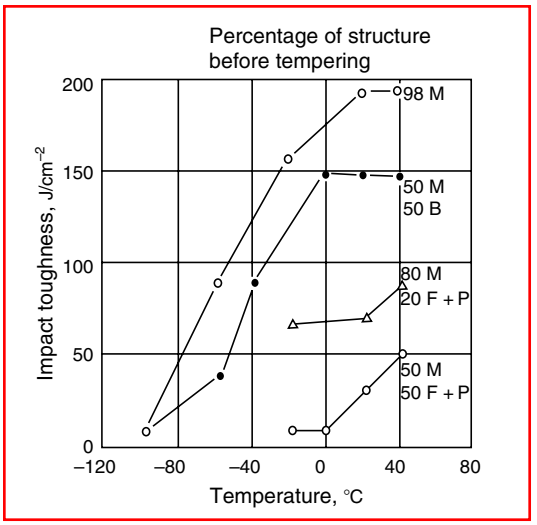

FIGURE 6.136 Influence of the microstructure after hardening (before tempering) on the impact toughness of DIN 16MnCr5 steel. (From H.J. Spies, G. Münch, and A. Prewitz, *Neue Hütte* 8(22):443–445, 1977 [in German].)

ferrite or ferrite and pearlite in the structure results in a substantial decrease in the impact toughness.

When selecting a structural steel for hardening and tempering, in order to better adapt the mechanical properties to the requirements of the treated parts, the expected microstructure must be considered. To be able to reproducibly influence mechanical properties, one should know the relationships among the heat treatment regime, microstructure, and resulting mechanical properties.

Unalloyed steels for hardening and tempering, because of their low hardenability, exhibit a high degree of section sensitivity with respect to hardness distribution after hardening as shown in Figure 6.137. After quenching a bar specimen of 30-mm diameter of the steel in question in conventional quenching oil, a hardness of only 40 HRC was achieved at the surface. When specimens of the same diameter were quenched in fast quenching oil, the hardness was 45 HRC; when quenched in 10% aqua-quench solution the hardness was 56 HRC; and when quenched in water containing 5% Na_2CO_3, it was 58 HRC (see Figure 6.138).

This example leads to two important conclusions:

1. By using different quenchants and quenching conditions, different hardness distributions can be obtained with the same steel grade and same cross-sectional size.
2. With an unalloyed steel (shallow-hardener), even when the most severe quenchant is used, for large cross-sectional sizes, the depth of hardening will be small and the core will remain unhardened.

Because of the second conclusion, when selecting a structural steel grade for hardening and tempering, its hardenability must always be adapted to the workpiece's cross-sectional size and the required strength level. Figure 6.139 shows the preferred fields for the application of some common steel grades for hardening and tempering according to the actual bar diameter and the strength level required. This recommendation is based on the assumption that a minimum impact toughness of about 50 J/cm^2 at room temperature will be achieved. As can be seen from Figure 6.139, for bigger cross-sectional sizes (bigger diameters) and

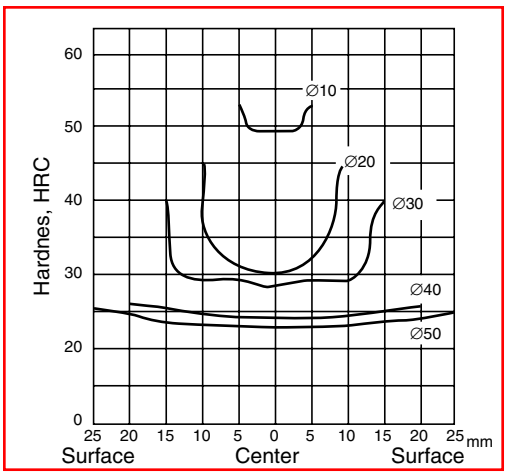

FIGURE 6.137 Hardness distribution (measured) on the cross section of bars of different diameters made of unalloyed steel (0.52% C, 0.24% Si, 0.90% Mn, 0.06% Cr) quenched in conventional hardening oil from 860°C. (From K.E. Thelning, *Steel and Its Heat Treatment*, 2nd ed., Butterworths, London, 1984.)

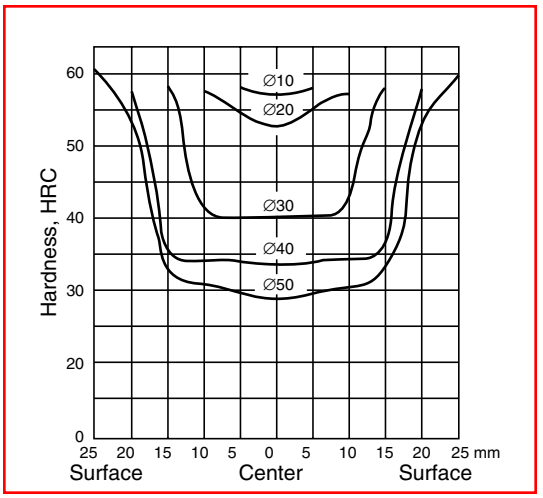

FIGURE 6.138 Hardness distribution (measured) on the cross section of bars of 10–50-mm diameters made of unalloyed steel (0.52% C, 0.24% Si, 0.90% Mn, 0.06% Cr) quenched from 860°C in water containing 5% Na_2CO_3. (From K.E. Thelning, *Steel and Its Heat Treatment*, 2nd ed., Butterworths, London, 1984.)

higher strength levels, steels of higher hardenability (i.e., with more alloying elements) are required.

6.4.2 Technology of the Hardening and Tempering Process

Hardening, which is the first operation of the hardening and tempering process, will yield a martensitic structure (provided a correct austenitization and quenching with a cooling rate greater than the critical rate for the steel in question have been realized), the hardness of which depends on the dissolved carbon content, according to the empirical formula

$$H_{100\%\ \text{mart}} \approx 60\sqrt{C} + 20 \tag{6.45}$$

where C is the carbon content in wt%.

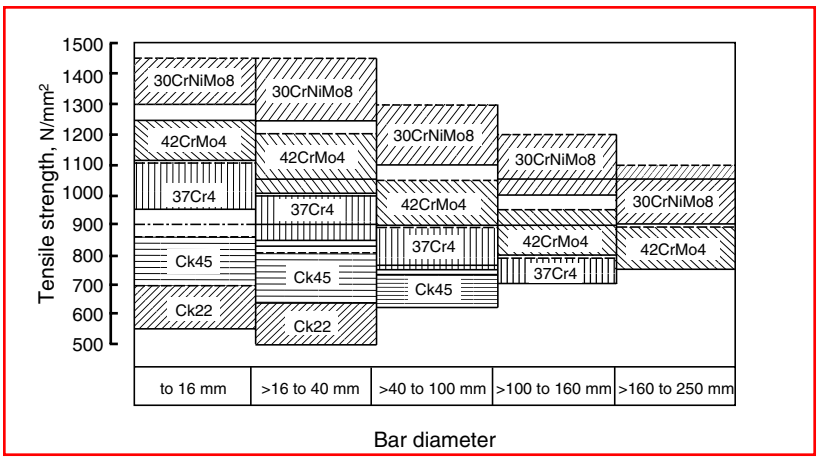

FIGURE 6.139 Applicability of steel grades for hardening and tempering according to required strength level and bar diameter. Steel designations according to DIN. (From German standard DIN 17200.)

The required critical cooling rate for unalloyed steels is about 250°C/s (482°F/s). Alloyed steels have lower critical cooling rates or a higher hardenability, which means that the same quenching conditions yield a greater depth of hardening.

As a measure of hardenability, the ideal critical diameter D_1 (see Chapter 5) can be applied. The actual depth of hardening, however, is influenced by, in addition to the alloying elements, the austenitizing temperature (especially for steels containing carbides difficult to dissolve) and quenching conditions. Consequently, two steels having the same D_1 value may give different depths of hardening.

For a designer, therefore, information based only on the percentage of martensite does not seem practical, because even for the same D_1 values the designer might get different depths of hardening. Besides, microstructures having the same amount of martensite do not always give the same hardness. The hardness of martensite depends on dissolved carbon content and may be calculated for 50% martensite according to the empirical formula

$$H_{50\%\ \text{mart}} \approx 44\sqrt{C} + 14 \quad \text{for } C < 0.7\% \tag{6.46}$$

More practical information for the designer, about expected depth of hardening, may be obtained for round bars from the correlation among the applied radius of the bar (R in mm), quenching intensity according to the Grossmann H factor (see Chapter 5), and the equivalent distance (E in mm) on the relevant Jominy curve. According to Just [25], this correlation for the surface of round bars reads

$$E_{\text{surf}} = \frac{R^{1/2}}{(3/4)H^{3/4}} - 3\ [\text{mm}] \quad \text{for } R < 50\ \text{mm};\ E < 30\ \text{mm} \tag{6.47}$$

and for the core of round bars:

$$E_{\text{core}} = \frac{R}{2H^{1/4}}\ [\text{mm}] \tag{6.48}$$

After calculating the equivalent Jominy distance E, one can read off the hardness from the relevant Jominy curve. Figure 6.140 shows this correlation as a diagram (for radii from 0 to 50 mm and H values from 0.3 to 2) for convenient use.

As already explained, the properties of hardened and tempered parts depend first of all on how well the hardening operation has been performed. The higher the percentage of martensite at a specified point of the cross section after hardening, the better will be the properties after subsequent tempering. To check the quality of hardening achieved, the degree of hardening (S) can be used. It is the ratio between the achieved (measured) hardness and the maximum hardness attainable with the steel in question:

$$S = \frac{H}{H_{\max}} = \frac{H}{60\sqrt{C} + 20} \tag{6.49}$$

where H is the actual hardness measured at a specified point of the cross section, in HRC, and $H_{\max}$ is the maximum attainable hardness in HRC. The degree of hardening is valid, of course, for the point of the cross section where the hardness was measured.

For highly stressed parts that are to be hardened and tempered to high strength levels, the required degree of hardening is $S > 0.95$, whereas for less stressed components values of $S > 0.7$ (corresponding to about 50% martensite) are satisfactory.

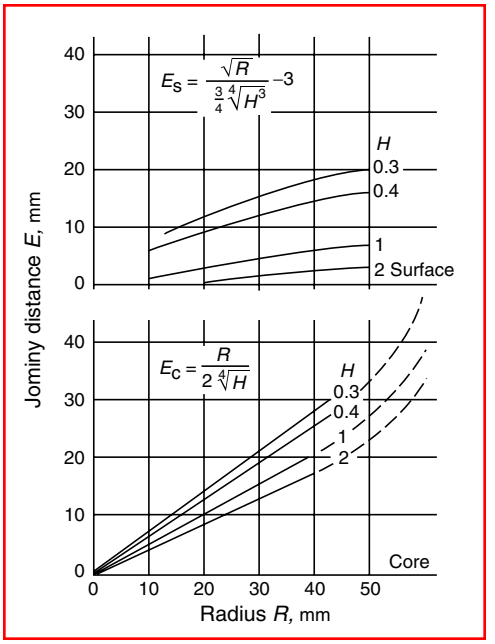

FIGURE 6.140 Correlation among radius of round bars (quenched by immersion), quenching intensity H and equivalent Jominy distance for the surface and core of the bars. (From E. Just, *VDI-Ber. 256*:125–140, 1976 [in German].)

When hardening and tempering structural steels, the value of hardness after hardening and tempering is usually specified. The required degree of hardening can also be expressed as a function of the hardness after hardening and tempering (H_t):

$$S \geq \frac{1}{1 + 8e^{-H_t/8}} \tag{6.50}$$

Figure 6.141 shows the minimum values of the required degree of hardening as a function of hardness after hardening and tempering, limiting the allowed area.

By specifying the required degree of hardening, one can avoid the risk of an incorrect hardening and tempering. It is known that too low a value of hardness after hardening (not enough martensite) can be covered up by tempering intentionally at a lower temperature. Although in such a case the final hardness after hardening and tempering may correspond to the required value, the toughness and other mechanical properties important for dynamically stressed parts will be insufficient because of an inadequate microstructure. Such a risk can be avoided by specifying the minimum degree of hardness for the critical point of the cross section, which can easily be checked after hardening.

In selecting sufficiently severe quenchants to obtain a high percentage of martensite and great depth of hardening, one has to be aware of the risk of cracking. Hardening cracks are dependent on:

1. The shape of the workpiece (big differences in the size of the cross section, edges, and corners favor the formation of cracks)
2. The heat treatment process (high austenitizing temperatures and severe quenching conditions favor the formation of cracks)
3. The steel grade itself (the lower the M_s temperature of the steel, the greater the risk of cracking)

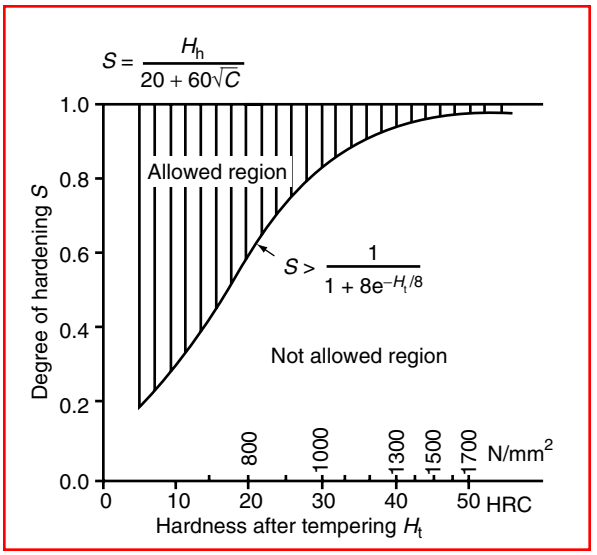

FIGURE 6.141 Minimum values of the degree of hardening required as a function of hardness after hardening and tempering. (From E. Just, *VDI-Ber. 256*:125–140, 1976 [in German].)

The M_s temperature can be calculated using the formula

$$M_s = 548 - 440\,C - 14Si - 26Mn - 11Cr - 9Mo - 14Ni + 2V\ [^\circ C] \qquad (6.51)$$

where contents of alloying elements are in wt%.

The carbon content, as is known, has the greatest influence on the M_s temperature and on the risk of cracking. Tempering, which is the second important operation, decreases high hardnesses more than low hardnesses, as can be seen in Figure 6.142. This figure shows the Jominy curve of the steel DIN 28Cr4 (0.24–0.31% C, 0.15–0.36% Si, 0.62–0.78% Mn, 0.75–1.07% Cr) in hardened condition and after tempering the Jominy specimen to 500 and 600°C (932 and 1112°F). It can be seen that high hardness near the quenched end of the specimen has

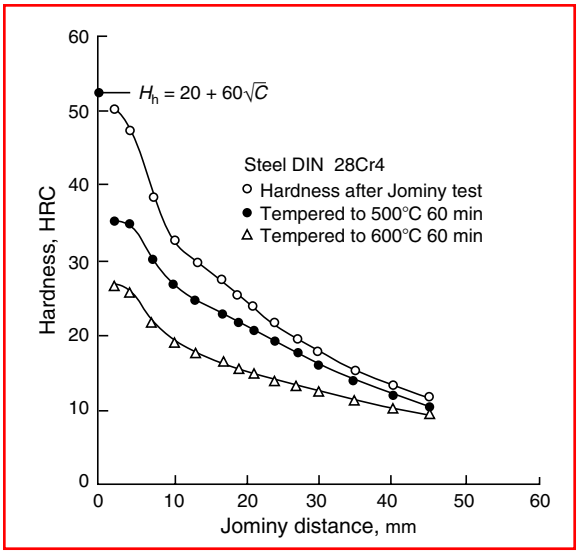

FIGURE 6.142 Influence of tempering temperature on level of hardness at various Jominy distances. (From E. Just, *VDI-Ber. 256*:125–140, 1976 [in German].)

been decreased much more by tempering than low hardness values at greater distances from the quenched end. With respect to the cross section of hardened real components, this effect means that tempering more or less equalizes the hardness differences between surface and core. It is known that the hardness after tempering is a linear function of tempering temperature (in the range from about 320 to 720°C (608 to 1328°F)) and a logarithmic function of tempering time, according to the following formula [25], which is valid for a 100% martensite structure:

$$H_t = 102 - 5.7 \times 10^{-3}[T_t(12 + \log t)] \text{ [HRC]} \tag{6.52}$$

where T_t is the tempering temperature (K) and t is tempering time (s).

Tempering temperature and tempering time are consequently interchangeable with respect to resulting hardness; however, very short or very long tempering times do not yield optimum toughness. To obtain the optimum toughness for chromium steels, the tempering times should be between 1 and 5 h.

There is a firm relationship between the hardness after tempering and the hardness after hardening. Spies et al. [26] have, by using multiple linear regression, quantified the influence of hardness after hardening, chemical composition, and tempering temperature on hardness after tempering and developed the formula

$$\begin{aligned} \text{HB} = {} & 2.84H_h + 75(\%\ \text{C}) - 0.78(\%\ \text{Si}) + 14.24(\%\ \text{Mn}) + 14.77(\%\ \text{Cr}) \\ & + 128.22(\%\ \text{Mo}) - 54.0(\%\ \text{V}) - 0.55T_t + 435.66 \end{aligned} \tag{6.53}$$

where HB is hardness after hardening and tempering (Brinell), H_h is hardness after hardening (HRC), and T_t is tempering temperature (°C).

Equation 6.53 is valid for the following ranges:

H_h	20–65 HRC
C	0.20–0.54%
Si	0.17–1.40%
Mn	0.50–1.90%
Cr	0.03–1.20%
T_t	500–650°C (932–1202°F)

According to the German standard DIN 17021, an average relation between the hardness after hardening (H_h) and the hardness after hardening and tempering (H_t) reads

$$H_h = (T_t/167 - 1.2)H_t - 17 \text{ [HRC]} \tag{6.54}$$

where T_t is tempering temperature (°C); and H_t is hardness after hardening and tempering (HRC). This formula is valid for 490°C (914°F) < T_t < 610°C (1130°F) and for tempering time of 1 h. Because, as already mentioned, high hardnesses decrease at tempering much more than low hardnesses, the prediction is more precise if the degree of hardening (S) is accounted for.

$$H_h = 8 + (H_t - 8)\exp[S(T_t/917)^6] \text{ [HRC]} \tag{6.55}$$

where S is the degree of hardening, $S <$ and T_t is tempering temperature (K).

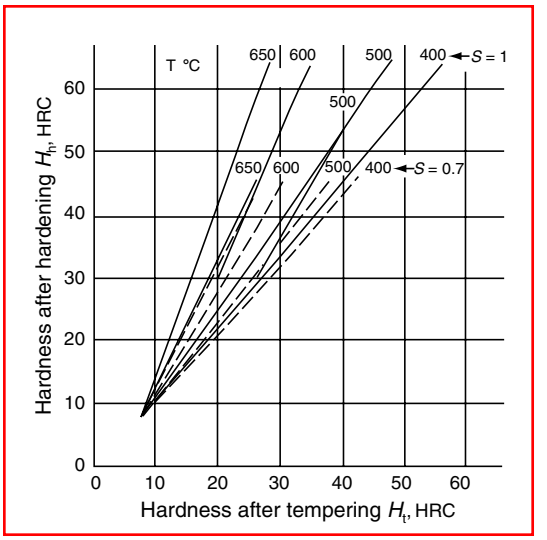

FIGURE 6.143 Relationship among hardness after hardening, degree of hardening, tempering temperature, and hardness after tempering. (From E. Just, *VDI-Ber. 256*:125–140, 1976 [in German].)

Figure 6.143 shows a diagram from which it is possible to predict at a glance the hardness required after hardening for a desired hardness after tempering, taking into account the actual tempering temperature and the necessary degree of hardening.

It is also possible to calculate the necessary tempering temperature for a specified hardness after hardening and tempering when chemical composition and the degree of hardening are known:

$$T_t = 647[S(60\sqrt{c} + 20)/H_t - 0.9]^{1/4} - 3.45SH_t + (537 - 561S)(\%\text{g C}) + 505\text{S}(\%\text{g V}) + 219\text{S}(\%\text{ Mo}) + 75\text{S}(\%\text{ Cr}) + 66S(\%\text{ Si}) - 51(\text{C}) \quad (6.56)$$

where H_t is hardness after hardening and tempering [HRC]; S is the degree of hardening, $S \leq 1.0$; and alloying elements are given in wt%. This formula is valid for a tempering time of 2 h.

There are also diagrams for practically every steel grade from which the tempering temperature may be determined if the ultimate tensile strength or yield strength required after hardening and tempering is known. Figure 6.144a and Figure 6.144b show such diagrams for the unalloyed steel DIN Ck45 after quenching in water (25-, 50-, and 100-mm-bar diameter) and in oil (25- and 50-mm-bar diameter), respectively.

6.4.3 Computer-Aided Determination of Process Parameters

Increasingly, modern heat treatment equipment incorporates microprocessors for automatic control of temperature–time cycles, protective or reactive atmosphere, material handling, and, to some extent, quenching operations. On the other hand, determination of the process parameters necessary to achieve the heat-treated properties required is normally based on empirical results.

For routine often-repeated heat treatment processes (e.g., carburizing, hardening, and tempering), computer programs can be written to establish treatment parameters provided that adequate data are available on workpiece geometry, material properties desired after heat treatment, steel grade used, and the actual heat treatment equipment itself. The aims of such an approach are to optimize the heat treatment operation by saving time and energy and to maintain close tolerances on the material properties imparted. The basic prerequisite is the

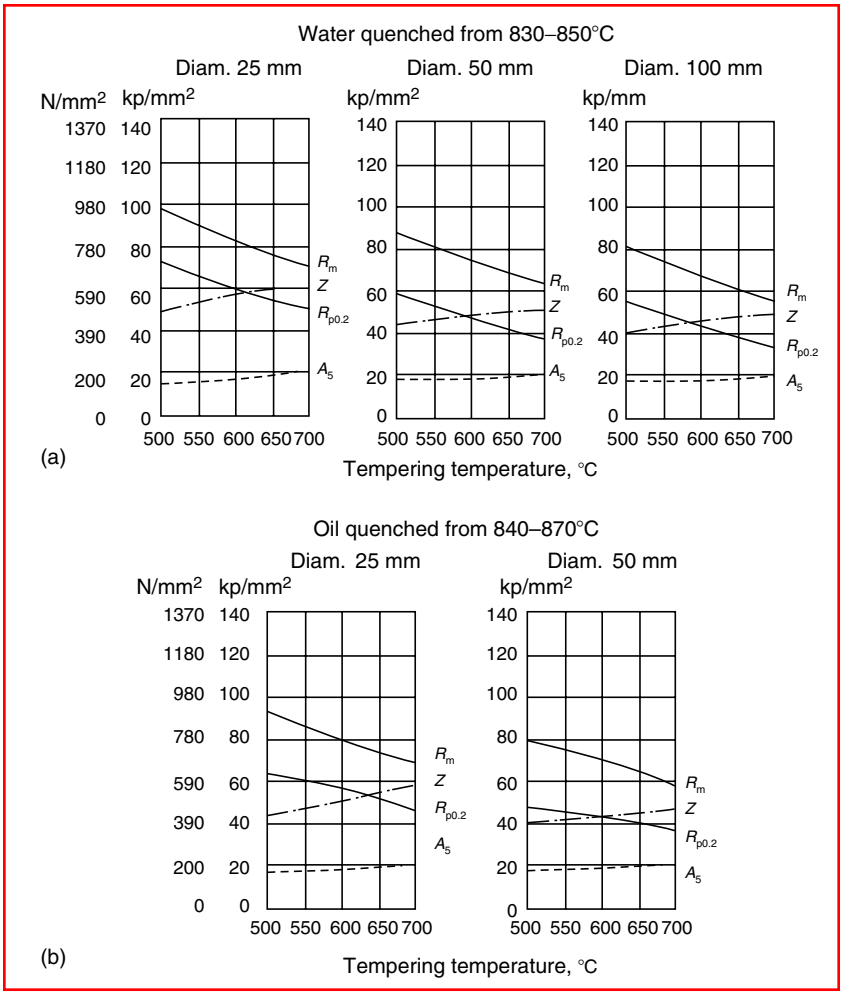

FIGURE 6.144 Tempering diagrams for the unalloyed steel DIN C45 when quenched (a) from 830 to 850°C in water, for bar diameters 25, 50, and 100 mm and (b) from 840 to 870°C in oil, for bar diameters 25 and 50 min. (From K.E. Thelning, *Steel and Its Heat Treatment*, 2nd ed., Butterworths, London, 1984.)

availability of satisfactory mathematical models that enable the presentation and prediction of relevant metallurgical and physical phenomena.

As described by Liščić and Filetin [27], the process of hardening and tempering has been divided into operations of austenitization (A), quenching (Q), and tempering (T) as shown in Figure 6.145. Within the austenitization operation, the phases are (1) preheating, (2) heating to austenitization temperature with workpiece equalization at that temperature, and (3) homogenization of the structure. Within tempering, the phases are (5) heating to the tempering temperature and temperature equalization, (6) soaking at tempering temperature, and (7) cooling down from the tempering temperature.

Computer-aided determination of process parameters has a greater number of advantages compared with earlier methods:

1. Planning of the process and preparation of the technological documentation are incomparably faster and simpler.

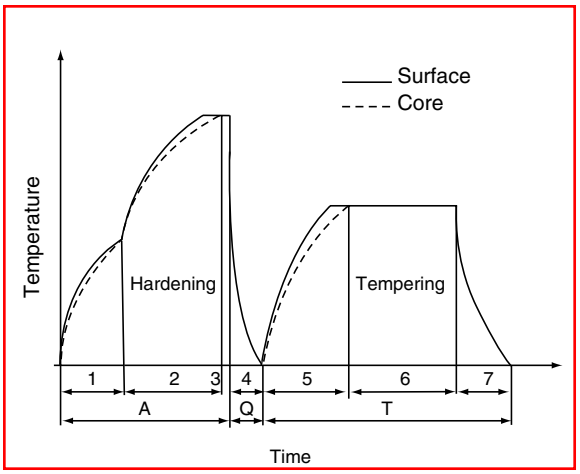

FIGURE 6.145 Operations and phases in the process of hardening and tempering.

2. Since the computer program takes into account the influences of all relevant factors, provided that all necessary input data are used, the resulting parameters and time–temperature profiles can be determined more precisely.
3. The professional level of the technological documentation is always high and consistent, irrespective of the ability and experience of an individual technologist.
4. It is possible (by using appropriate subprograms and inserting the data for alternative equipment) to examine the potential energy savings or economy of using some other equipment for the same process.
5. If modern heat treatment equipment with microprocessor control is available, the resulting treatment parameters can be distributed directly (online) to all units where the process will be performed and controlled automatically.

The general scheme of computer-aided planning of the hardening and tempering process is shown in Figure 6.146. Use of a computer for this purpose requires

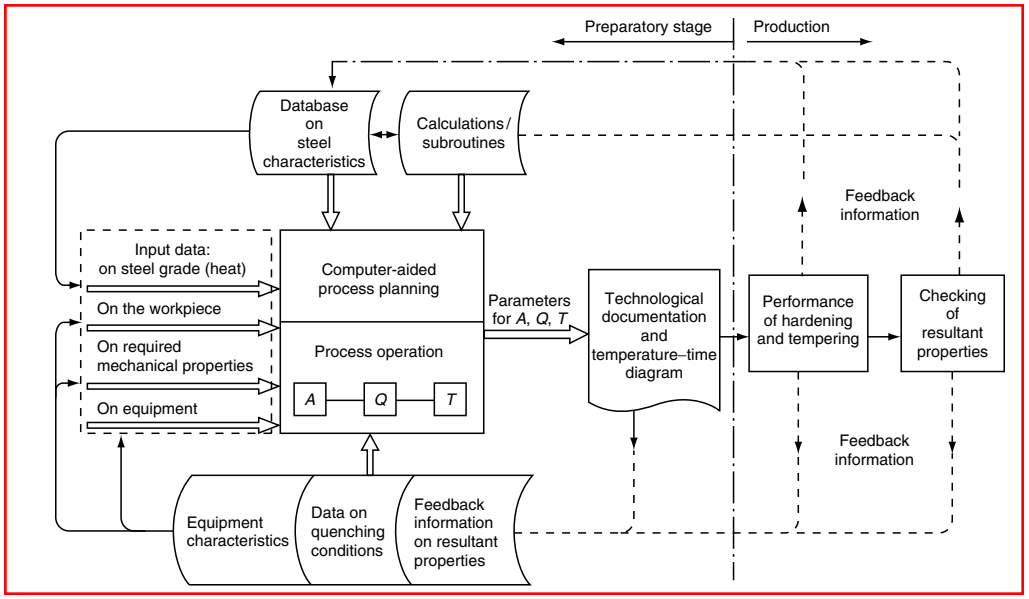

FIGURE 6.146 Scheme of computer-aided planning of the hardening and tempering process. (From B. Liščić and T. Filetin, *Heat Treat. Met. 3*:62–66, 1987.)

1. A database on characteristics of the steel grades treated
2. A database on the equipment employed (especially data on quenching severities available)
3. Subprograms stored in the computer memory for the necessary calculation of parameters

The input data in a particular case are:

1. Data on the steel grade in question
2. Data on the workpiece (shape, critical cross section, surface condition, number of pieces in a batch)
3. Data on mechanical properties required, after hardening and tempering, at a specified point of the cross section (hardness or ultimate tensile strength, yield strength, ductility, impact toughness, minimum grade of hardening or minimum percentage of martensite after quenching)
4. Data on the equipment used for all operations and phases of the process (preheating, austenitization, quenching, tempering)

The database on steels contains the following information for every specified steel grade or heat: chemical composition; carbon equivalent; austenitizing temperature; time for homogenization of the structure; M_s temperature; Jominy hardenability curve; holding time at tempering temperature; and susceptibility to temper brittleness.

To determine the parameters of the hardening and tempering process, the following relationships must be known and stored in the computer memory in the form of adequate mathematical equations:

1. The effect of shape and cross-sectional size of the workpiece on the time necessary for heating and austenitization under the specific heat transfer conditions of the equipment employed. For the case of a 40-mm bolt made of grade BS 708A37 (En 19B) steel (see Figure 6.147), because of the high value of the carbon equivalent (0.82), a preheating stage at 450°C (842°F) was necessary. For calculation of preheating time, as well as the time for heating to austenitizing temperature and temperature equalization, formula 6.42 was used (see Section 6.3.1) whereby the regression coefficients a and b were experimentally determined for the equipment used.
2. The influence of steel grade, cross-sectional size, and actual quenching conditions on the depth of hardening. This is necessary for selection of optimum quenching conditions (quenching medium, temperature, and agitation rate) to satisfy the required degree of hardening. The method by which this selection was performed is described in Chapter 5 (see Section 5.6.4).
3. The relationship between hardness after tempering and tempering temperature for the steel in question.

The necessary tempering temperature (T_t) was calculated by means of the formula

$$T_t = 917\left[\frac{\ln (H_h - 8)/(H_t - 8)}{S}\right]^{1/6} - 273\ [^\circ\mathrm{C}] \tag{6.57}$$

where H_h is hardness after hardening, HRC; H_t is required hardness after tempering, HRC; and S is degree of hardening. This equation is valid for tempering temperatures between 390 and 660°C (734 and 1220°F).

The time necessary for heating up to the tempering temperature and for temperature equalization through the cross section was calculated in the same manner as for austenitization, taking into account the data for the specific tempering furnace. The holding time at tempering temperature was taken from the database for the steel grade in question.

Technological documentation for the process:
hardening and tempering

Workpiece: bolt | Dimensions, mm: 40 dia. x 120 | Steel grade: BS 708A37

Requirements:

Hardening grade = .84 | $R = 900$ N/mm^2 | Point on cross section: 1/4R

Technological parameters

Operation	Equipment and/or media	Temperature (°C)	Time (min)
Preheating	Chamber furnace air atmosphere	450	62
Austenitization	Chamber furnace air atmosphere	840	47
Quenching	Oil-agitation 1 m/s	20	10
Tempering	Pit furnace-circulating air	627	152
Cooling after tempering	In air	20	140

Total time = 411 min

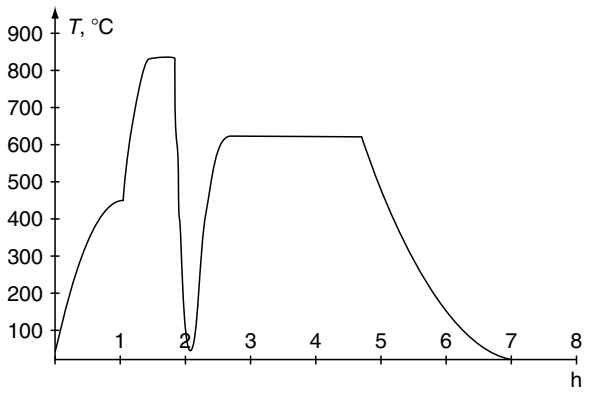

FIGURE 6.147 An example of the computer-generated parameters and time–temperature cycle for hardening and tempering a 40-mm diameter bolt made of BS 708A37 (En 19B) steel. (From B. Liščić and T. Filetin, *Heat Treat. Met. 3*:62–66, 1987.)

Cooling from the tempering temperature is carried out in air or inert gas in all cases where the steel is not prone to temper brittleness. If it is susceptible, faster cooling in oil or in air blast in necessary.

By using the described subprograms, the input data are processed by means of stored equations into the following output data or process parameters:

1. Temperature and time of preheating
2. Temperature and time for austenitization
3. Quenching conditions (quenching medium, its temperature, its agitation rate; time required for complete cooling of the workpiece)

TABLE 6.6
Comparison of Required and Measured Hardness at the Center of Cylinders Made of Steel Grade BS 708A37 (En 19B), after Hardening and Tempering under Computer-Calculated Conditions

Dimensions (mm)		Required Values				Measured Values	
Diameter	Length	Hardening Grade (*S*)	Ultimate Tensile Strength[a] (N/mm^2)	Hardness after Tempering (HRC)	Tempering Temperature (°C)	Ultimate Tensile Strength (N/mm^2)	Hardness after Tempering (HRC)
30	120	0.95	1240	38	519	1210	37.3
50	200	0.84	1000	31	583	1050	32.6
80	320	0.65	850	24.5	621	900	27.7

[a]Calculated from the hardness (DIN 50150).
Source: From B. Liščić and T. Filetin, *Heat Treat. Met.* 3:62–66 (1987).

4. Temperature and time for tempering
5. Mode of cooling from tempering temperature to room temperature

Figure 6.147 shows an example of computer-generated documentation for hardening and tempering a 40-mm diameter bolt made of BS 708A37 (En 19B) steel.

Table 6.6 compares the required hardness (ultimate tensile strength) for the center of bars of 30-, 50-, and 80-mm diameters made of grade BS 708A37 steel with the measured hardness after hardening and tempering under computer-calculated conditions.

6.5 AUSTEMPERING

The austempering process (see Figure 6.148) consists of austenitization, quenching into a hot bath maintained between 260 and 450°C (500 and 842°F), holding at this temperature until the transformation of austenite to bainite is complete, and cooling to room temperature at

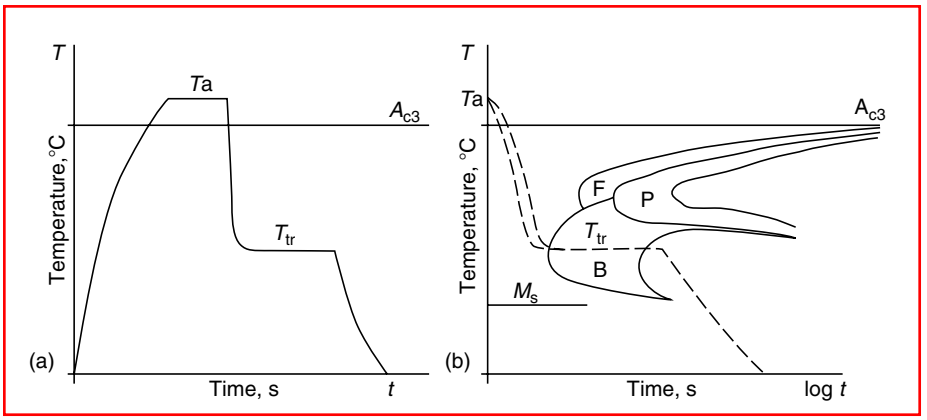

FIGURE 6.148 Scheme of an austempering process (a) in time–temperature diagram and (b) in isothermal transformation (IT) diagram.

will. Compared with the process of hardening and tempering, there are the following substantial differences:

1. At austempering there is no austenite-to-martensite transformation, but the final structure (bainite) is obtained gradually during the isothermal transformation of austenite to bainite.
2. After austempering there is no tempering.
3. While hardening and tempering is a two-operation process, austempering is performed in one cycle only, which is an advantage for the automation of the process

Dealing with austempering one should use the IT diagram of the steel in question to optimize the process parameters, among them first of all the transformation temperature (T_{tr}) and holding time at this temperature.

Austempering of steel offers two primary potential advantages:

1. Reduced distortion and less possibility of cracking
2. Increased ductility and toughness, especially in the range of high strength (hardness) values between 50 and 55 HRC

Reduced distortion and less possibility of cracking are the result of lower thermal stresses, as well as lower transformational stresses compared to conventional hardening. Although at austempering there are also temperature differences between the surface and core of the workpiece, during quenching, these differences are substantially smaller, as shown in Figure 6.149, because the difference between the austenitizing temperature and the temperature of the quenching bath is much smaller (for 200–400°C (392–752°F)) than in conventional hardening. Smaller temperature gradients across the section mean smaller thermal stresses. On the other hand, at austempering there is no momentary austenite-to-martensite transformation, connected with the volume increase, taking place at different moments at different points of the cross section. Instead there is a gradual transformation from austenite to bainite, which takes place almost simultaneously in thin and thick cross sections. Both effects contribute to much lower risk of cracking and distortion, thereby minimizing the production of scraped parts and additional cost for straightening or grinding to repair the distortion.

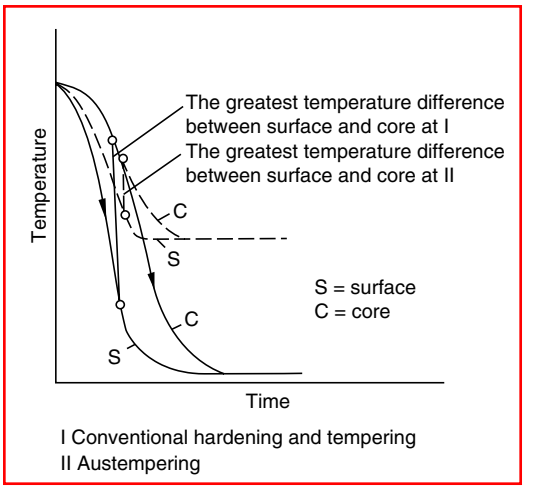

FIGURE 6.149 Temperature differences between surface and core of the workpiece in conventional hardening and in austempering. (From K.H. Illgner, *Fachber. Hüttenpraxis Metallweiterverarb. 17*(4):281–288, 1979 [in German].)

Increased ductility and toughness as well as increased bendability and fatigue life are the strongest reasons to apply austempering instead of hardening and tempering. Figure 6.150 shows the relation of impact toughness and Brinell hardness (HB) of a Cr–Mn–Si steel after conventional hardening and tempering and after austempering, as a function of tempering temperature and austempering temperature, respectively. The most important difference is that a good combination of hardness and toughness after conventional hardening and tempering is possible only at high tempering temperatures, which means low hardness, whereas at austempering a good combination of hardness and impact toughness may be achieved at high hardness values.

Another comparison of impact toughness of a carbon steel after hardening and tempering and after austempering, as a function of hardness, is shown in Figure 6.151. It is evident that austempering yields much better impact toughness, especially at high hardness, around 50 HRC. It is necessary to emphasize that high toughness after austempering is possible only under conditions of complete transformation of austenite to bainite. Table 6.7 shows a comparison of some mechanical properties of austempered and of hardened and tempered bars made of AISI 1090 steel. In spite of having a little higher tensile strength and hardness, austempered specimens have had remarkably higher elongation, reduction of area, and fatigue life.

Figure 6.152 shows the fatigue diagram of DIN 30SiMnCr4 steel after conventional hardening and tempering and after austempering. The increase in fatigue resistance values is especially remarkable for notched specimens.

Regarding bendability, Figure 6.153, from an early work of Davenport [30], shows the results of bending a carbon steel wire austempered and hardened and tempered to 50 HRC.

When selecting a steel for austempering, IT diagrams should be consulted. The suitability of a steel for austempering is limited first of all with minimum incubation time (the distance of the transformation start curve from the ordinate). Another limitation may be the very long transformation time. Figure 6.154 shows the transformation characteristics of four AISI grades of steel in relation to their suitability for austempering. The AISI 1080 steel has only limited suitability for austempering (i.e., may be used only for very thin cross sections)

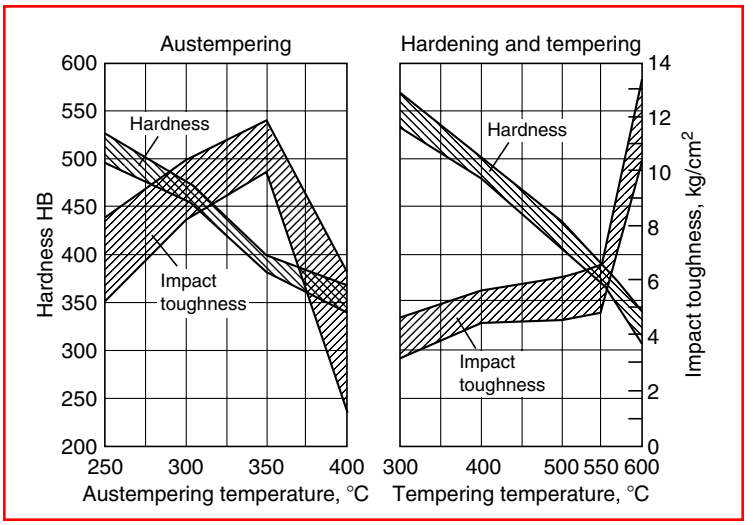

FIGURE 6.150 Impact toughness and hardness (HB) of five heats of a Cr–Mn–Si steel after conventional hardening and tempering and after austempering, as a function of tempering temperature and austempering temperature, respectively. (From F.W. Eysell, *Z. TZ Prakt. Metallbearb. 66*:94–99, 1972 [in German].)

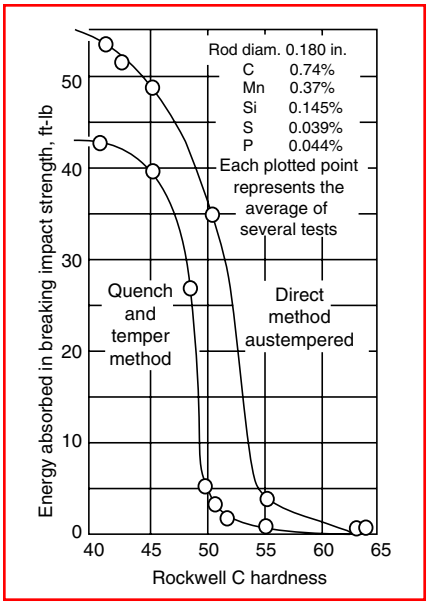

FIGURE 6.151 Comparison of impact toughness of a carbon steel after conventional hardening and tempering and after austempering, as a function of hardness. (From G. Krauss, *Steels: Heat Treatment and Processing Principles*, ASM International, Materials Park, OH, 1990.)

because the pearlite reaction starts too soon near 540°C (1004°F). The AISI 5140 steel is well suited to austempering. It is impossible to austemper the AISI 1034 steel because of the extremely fast pearlite reaction at 540–595°C (1004–1103°F). The AISI 9261 steel is not suited to austempering because the reaction to form bainite is too slow (too long a transformation time) at 260–400°C (500–752°F).

The austempering process is limited to sections that can be cooled at a sufficient rate to prevent transformation to pearlite during quenching to the austempering bath temperature. Maximum section thickness is therefore important in determining whether or not a part can be successfully austempered. For eutectoid or hypereutectoid carbon steels like AISI 1080, a section thickness of about 5 mm is the maximum that can be austempered to a fully bainitic structure. Unalloyed steels of lower carbon content are restricted to a proportionately lesser thickness (except those containing boron). With increasing alloy content, heavier sections can be austempered, in some alloy steels up to 25 mm cross section. When some pearlite is permissible in the microstructure, even carbon steels can be austempered to sections significantly thicker than 5 mm. Table 6.8 lists section sizes and hardness values of austempered parts made of various steels.

Process parameters for the austempering process are:

1. Austenitizing temperature and time
2. Quenching intensity when cooling from the austenitizing temperature to the austempering bath temperature
3. Temperature of transformation, i.e., the austempering bath temperature
4. Holding time at austempering temperature

The austenitizing temperature and time (as in any hardening process) are responsible for carbide dissolution and homogenizing of the structure, which has a substantial influence on the impact toughness of treated parts.

TABLE 6.7
Comparison of Some Mechanical Properties of Austempered and of Hardened and Tempered Bars Made of AISI 1090 Steel

Property[a]	Austempered at 400°C (750°F)[b]	Quenched and Tempered[c]
Tensile strength, MPa (ksi)	1,415 (205)	1,380 (200)
Yield strength, MPa (ksi)	1,020 (148)	895 (130)
Elongation, %	11.5	6.0
Reduction of area, %	30	10.2
Hardness, HB	415	388
Fatigue cycles[d]	105,000[e]	58,600[f]

[a] Average values.
[b] Six tests.
[c] Two tests.
[d] Fatigue specimens 21 mm (0.812 in.) in diameter.
[e] Seven tests: range 69,050–137,000.
[f] Eight tests: range 43,120–95,220.
Source: From *ASM Handbook*, 9th ed., Vol. 4, *Heat Treating*, ASM International, Materials Park, OH, 1991, p. 155.

Quenching must be severe enough to avoid any pearlite formation on cooling from the austenitizing temperature to the temperature of the austempering bath. Molten nitrite–nitrate salts are used as quenching media for austempering. To increase the quenching severity, agitation and sometimes the addition of some percentage of water is used. When adding water to a hot salt bath, care must be taken to prevent spattering. The higher the temperature of the salt bath, the less water should be added. Because of evaporation, the amount of water added must be controlled.

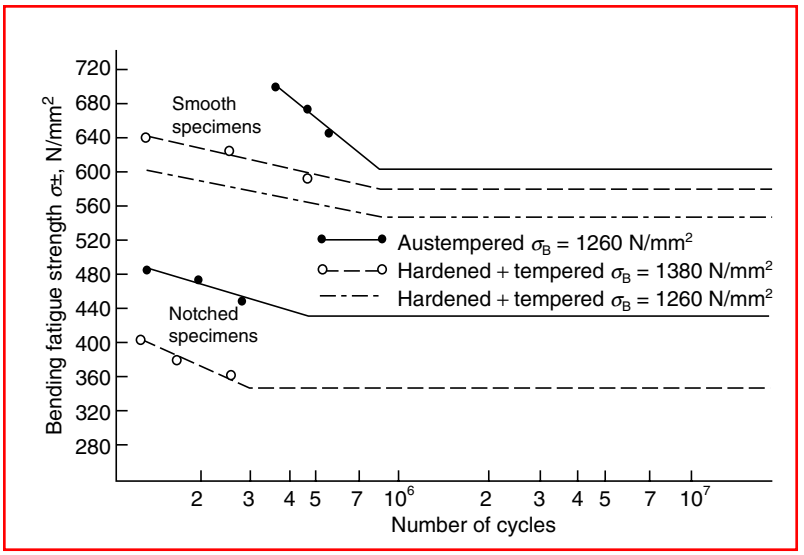

FIGURE 6.152 Fatigue of DIN 30SiMnCr4 steel after conventional hardening and tempering and after austempering. (From F.W. Eysell, *Z. TZ Prakt. Metallbearb. 66*:94–99, 1972 [in German].)

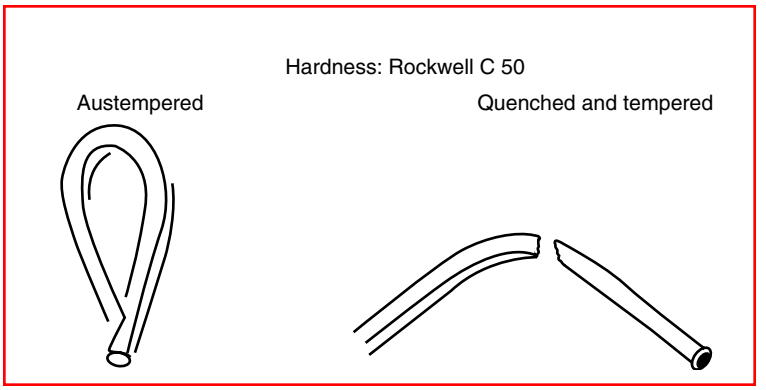

FIGURE 6.153 Carbon steel wire (0.78% C, 0.58% Mn) of 4.6-mm diameter, (left) austempered and (right) hardened and tempered to 50 HRC and bent under comparable conditions. (From E.S. Davenport, *Steel*, March *29*, 1937.)

Transformation temperature, i.e., austempering bath temperature, is one of the two most important parameters as it directly influences the strength (hardness) level of the treated parts. The higher the austempering temperature, the lower the strength (hardness) of the austempered parts. The bainitic region can be divided according to austempering temperature into upper and lower bainite regions, the boundary between them at about 350°C (662°F). The structure of upper bainite in steels (consisting of parallel plates of carbides and ferrite) is softer and tougher, whereas the structure of lower bainite (needlelike, with small carbides under 60° within the needles) is harder and more brittle.

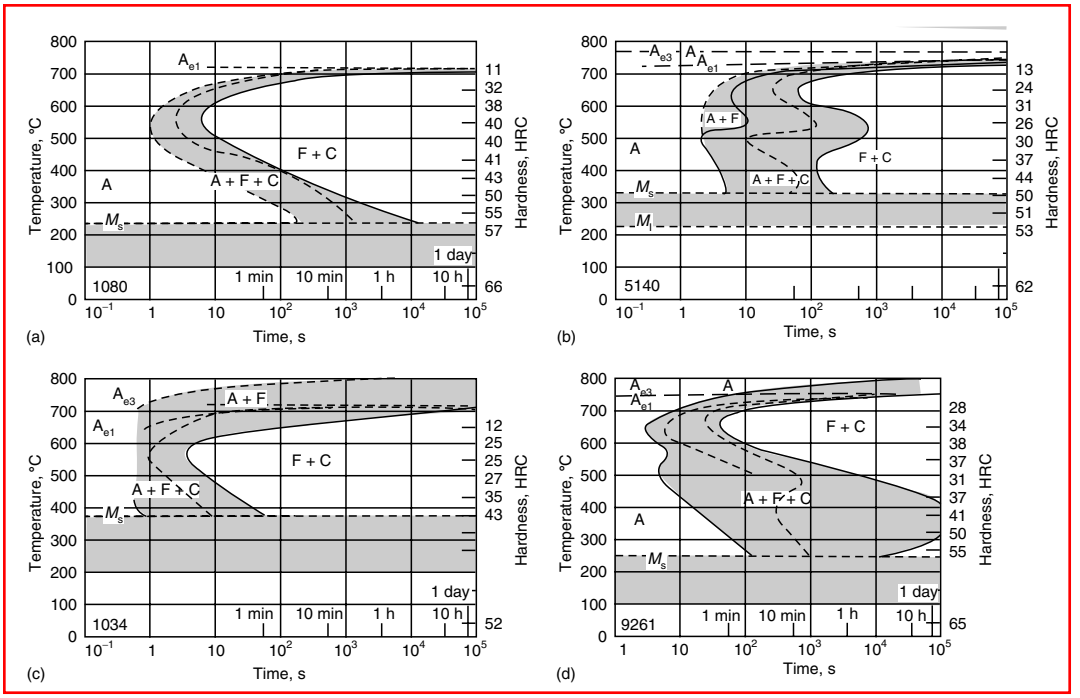

FIGURE 6.154 Transformation characteristics of steel of AISI grades (a) 1080; (b) 5140; (c) 1034; and (d) 9261 in relation to their suitability for austempering (see text). (From *ASM Handbook*, 9th ed., Vol. 4, *Heat Treating*, ASM International, Materials Park, OH, 1991.)

TABLE 6.8
Section Sizes and Hardness Values of Austempered Parts of Various Steel Grades

	Section Size		Salt Temperature		M_s Temperature[a]		
Steel	nm	in.	°C	°F	°C	°F	Hardness (HRC)
1050	3[b]	0.125[b]	345	655	320	610	41–47
1065	5[c]	0.187[c]	—[d]	—[d]	275	525	53–56
1066	7[c]	0.281[c]	—[d]	—[d]	260	500	53–66
1084	6[c]	0.218[c]	—[d]	—[d]	200	395	55–58
1086	13[c]	0.516[c]	—[d]	—[d]	215	420	55–58
1090	5[c]	0.187[c]	—[d]	—[d]	—	—	57–60
1090[e]	20[c]	0.820[c]	315[f]	600[f]	—	—	44.5 (avg.)
1095	4[c]	0.148[c]	—[d]	—[d]	210[g]	410[g]	57–60
1350	16[c]	0.625[c]	—[d]	—[d]	235	450	53–56
4063	16[c]	0.625[c]	—[d]	—[d]	245	475	53–56
4150	13[c]	0.500[c]	—[d]	—[d]	285	545	52 max
4365	25[c]	1.000	—[d]	—[d]	210	410	54 max
5140	3[b]	0.125[b]	345	655	330	630	43–48
5160[e]	26[c]	1.035[c]	315[f]	600[f]	255	490	46.7 (avg.)
8750	3[b]	0.125[b]	315	600	285	545	47–48
50100	8[c]	0.312[c]	—[d]	—[d]	—	—	57–60

[a] Calculated.
[b] Sheet thickness.
[c] Diameter of section.
[d] Salt temperature adjusted to give maximum hardness and 100% bainite.
[e] Modified austempering; microstructure contained pearlite as well as bainite.
[f] Salt with water additions.
[g] Experimental value.

Source: From *ASM Handbook*, 9th ed., Vol. 4, *Heat Treating*, ASM International, Materials Park, OH, 1991, p. 155.

Because not only the strength (hardness) level but also the impact toughness varies with austempering temperature, the temperature of the austempering bath must be kept within close tolerance ($\pm 6°C$ ($\pm 43°F$)).

The holding time at austempering temperature should be sufficient to allow complete transformation. Therefore the IT diagram of the steel grade in question should be consulted. Allowing parts to remain in the bath for longer than the required time will increase the cost of treatment but it is not harmful to the mechanical properties of austempered parts.

REFERENCES

1. G. Spur and T. Stöferle (Eds.), *Handbuch der Fertigungstechnik, Vol. 4/2, Wärmebehandeln*, Carl Hanser, Munich, 1987.
2. H.J. Eckstein (Ed.), *Technologie der Wärmebehandlung von Stahl*, 2nd ed., VEB Deutscher Verlag für Grundstoffindustrie, Leipzig, 1987.
3. B. Liščić, S. Švaić, and T. Filetin, Workshop designed system for quenching intensity evaluation and calculation of heat transfer data, *Proceedings of the First International Conference on Quenching and Control of Distortion*, Chicago, IL, September 1992, pp. 17–26.

4. A. Rose and W. Strassburg, Anwendung des Zeit-Temperatur-Umwandlungs-Schaubildes für kontinuierliche Abkühlung auf Fragen der Wärmebehandlung, *Archiv. Eisenhüttenwes. 24*(11/12):505–514 (1953) (in German).
5. H.P. Hougardy, Die Darstellung des Umwandlungsverhaltens von Stählen in den ZTU-Schaubildern, *Härterei-Tech. Mitt. 33*(2):63–70 (1978) (in German).
6. E.Scheil, *Arch. Eisenhüttenwes. 8*:565–567 (1934/1935) (in German).
7. F. Wever and A. Rose (Eds.), *Atals zur Wärmebehandlung der Stähle*, Vols. I and II, Verlag Stahleisen, Düsseldorf, 1954/56/58.
8. W. Peter and H. Hassdenteufel, Aussagefähigkeit der Stirnabschreckprüfung und der Zeit-Temperatur-Umwandlungsschaubildes für das Ergebnis der Härtung von Rundstäben, *Stahl Eisen 87*(8):455–457 (1967) (in German).
9. M. Atkins, *Atlas of Continuous Transformation Diagrams for Engineering Steels*, British Steel Corporation, BSC Billet, Bar and Rod Product, Sheffield, U.K., 1977.
10. E.A. Loria, Transformation behaviour on air cooling steel in A_3–A_1 temperature range, *Met. Technol*., 490–492 (1977).
11. N. Shimizu and I. Tamura, Effect of discontinuous change in cooling rate during continuous cooling on pearlitic transformation behaviour of steel, *Trans. ISIJ 17*:469–476 (1977).
12. ISI, *Decarburization*, ISI Publication 133, Gresham Press, Old Woking, Surrey, England, 1970.
13. B. Liščić, H.M. Tensi, and W. Luty (Eds.), *Theory and Technology of Quenching*, Springer-Verlag, New York, 1992.
14. K.E. Thelning, *Steel and Its Heat Treatment*, 2nd ed., Butterworths, London, 1984.
15. J. Frehser and O. Lowitzer, The process of dimensional change during the heat treatment of tool steels, *Stahl Eisen. 77*(18):1221–1233 (1957) (in German).
16. J. Wünning, Verfahrenstechnik des Isothermglühens, *Härterei-Tech. Mitt. 32*:43–49 (1977) (in German).
17. G. Krauss, *Steels: Heat Treatment and Processing Principles*, ASM International, Materials Park, OH, 1990.
18. J. Orlich, A. Rose, and P. Wiest (Eds.), *Atlas zur Wärmebehandlung der Stähle*, Vol. 3, *Zeit-Temperatur-Austenitisierung-Schaubilder* Verlag Stahleisen, Düsseldorf, 1973 (in German).
19. J. Orlich and H.J. Pietrzenivk (Eds.), *Atlas zur Wärmebehandlung der Stähle*, Vol. 4, *Zeit-Temperatur-Austenitisierung-Schaubilder* Part 2, Verlag Stahleisen, Düsseldorf, 1976 (in German).
20. S. Jost, H. Langer, D. Pietsch, and P. Uhlig, Rechnerische Ermittlung der Erwärmdauer bei der Wärmebehandlung von Stahl, *Fertigungstech. Betr. 26*(5):298–301 (1976) (in German).
21. M.A. Aronov, J.F. Wallace, and M.A. Ordillas, System for prediction of heat-up and soak times for bulk heat treatment processes, *Proceedings of the International Heat Treatment Conference on Equipment and Processes*, April 18–20, 1994, Schaumburg, IL, pp. 55–61.
22. N.I. Kobasko, Teplovie procesi pri zakalke stali, *Mettaloved. Termiceskaja Obrab. Metalov. 3*:2–6 (1968).
23. B. Liščić and G.E. Totten, Controllable delayed quenching, *Proceedings of the International Conference on Equipment and Processes*, April 18–20, 1994, Schaumburg, IL, pp. 253–262.
24. J. Parrish, Retained austenite: new look at an old debate, *Adv. Mater. Process. 3*:25–28 (1994).
25. E. Just, Vergüten-Werkstoffbeeinflussung durch Härten und Anlassen, *VDI-Ber. 256*:125–140 (1976) (in German).
26. H.J. Spies, G. Münch, and A. Prewitz, Möglichkeiten der Optimierung der Auswahl vergütbarer Baustähle durch Berechnung der Härt-und Vergütbarkeit, *Neue Hütte 8*(22):443–445 (1977) (in German).
27. B. Liščić and T. Filetin, Computer-aided determination of the process parameters for hardening and tempering structural steels, *Heat Treat. Met. 3*:62–66 (1987).
28. K.H. Illgner, Qualitäts-und Kostenvorteile mit Zwischenstufenvergütungsanlagen im Vergleich zu normalen Vergütungsanlagen, *Fachber. Hüttenpraxis Metallweiterverarb. 17*(4):281–288 (1979) (in German).
29. F.W. Eysell, Die Zwischenstufenvergütung und ihre betriebliche Anwendung, *Z. TZ Prakt. Metallbearb. 66*:94–99 (1972) (in German).
30. E.S. Davenport, Heat treatment of steel by direct transformation from austenite, *Steel*, *29*: (1937).
31. *ASM Handbook*, 9th ed., Vol. 4, *Heat Treating*, ASM International, Materials Park, OH, 1991.
32. U.S. Patent 2,829,185, regarding surface temperature measurement.
33. *Met. Prog*., October 1963, p. 134.

7 Heat Treatment with Gaseous Atmospheres

Johann Grosch

CONTENTS

7.1 General Introduction 415
7.2 Fundamentals in Common 417
7.3 Carburizing 422
7.3.1 Introduction 422
7.3.2 Carburizing and Decarburizing with Gases 422
7.3.2.1 Gas Equilibria 423
7.3.2.2 Kinetics of Carburizing 426
7.3.2.3 Control of Carburizing 428
7.3.2.4 Carbonitriding 431
7.3.3 Hardenability and Microstructures 432
7.4 Reactions with Hydrogen and with Oxygen 440
7.5 Nitriding and Nitrocarburizing 446
7.5.1 Introduction 446
7.5.2 Structural Data and Microstructures 448
7.5.2.1 Structural Data 448
7.5.2.2 Microstructures of Nitrided Iron 450
7.5.2.3 Microstructures of Nitrided and Nitrocarburized Steels 452
7.5.2.4 Microstructural Specialties 456
7.5.3 Nitriding and Nitrocarburizing Processes 457
7.5.3.1 Nitriding 457
7.5.3.2 Nitrocarburizing 460
7.5.3.3 Processing Effects on the Nitriding and Nitrocarburizing Results 461
7.6 Properties of Carburized and Nitrided or Nitrocarburized Components 463
References 469

7.1 GENERAL INTRODUCTION

Heat treatment of components is to date mostly accomplished in gaseous atmospheres, the more so if plasma and vacuum are regarded as special cases of gaseous atmospheres. In comparison, heat treatment in solid or liquid media is negligible in numbers. Heat treatment in gaseous atmospheres falls into two categories: processes with the aim of avoiding a mass transfer between the gaseous atmosphere and the material, and processes with the aim of achieving just such a transfer. Mass transfer occurs when there is a difference in the potential between the constituents of a gaseous atmosphere and those of the microstructure of a component. The direction of such a mass transfer is determined by the potential difference, which leaves two fundamental possibilities with regard to the component. One is the intake

of elements of the gaseous atmosphere into the component and the other is the emission of elements of the component into the gaseous atmosphere. This kind of heat treatment falls under heat treatment with gas, which is the subject of this chapter. The deposition of constituents of a gaseous atmosphere onto the surface of a component (coating), which is not connected with the described mass transfer mechanism, is therefore excluded from the subject of heat treatment with gas.

Consequently, a protective gas is a gaseous atmosphere that is free from a potential difference with respect to those elements of both gas and steel that have the ability to transfer mass. A central matter of concern with all the homogeneity treatments (annealing, austenitizing, tempering) is to prevent oxidation. Gas compositions suitable for reducing oxidation may have a potential difference against carbon; furthermore, a reduction of oxide layers makes it always possible for carbon to get into the gas. Protective gases with a reducing effect must hence be adjusted to the carbon content of the steel to prevent decarburization. Inert gases such as rare gas or pure nitrogen as well as high-quality vacua do not contain any reactant constituents and thus prevent a mass transfer. In processes without a mass transfer, the gaseous atmosphere as a protective gas is an important and basic requirement of heat treatment but not used as a parameter to attain or alter certain properties of the component. Processes like these are therefore referred to as heat treatment in gas.

Transport of matter and heat conduction can formally be calculated by applying the same rules. The heat conduction in steel, however, is of a much higher order than the transport of matter, which as a diffusion process causes a uniformly directed flow of atoms. Heat treatments with gases are therefore always isothermal processes. As a rule, the rather slow process of diffusion determines the time needed for the technical processing of a heat treatment with mass transfer. This in turn determines essential processing conditions.

During a technically and economically justifiable treatment time, only the atoms that are interstitially soluted in iron are absorbed in adequate quantity and sufficiently deep to meet the given requirements. Therefore elements used in heat treating are carbon, nitrogen, oxygen, and hydrogen. With these interstitally soluted atoms too, the exchange is limited to the case, with the exception of thin sheets and hydrogen as the smallest element that diffuses most easily, where it is possible to influence the bulk material. Heat treatment with gases is therefore mostly a surface phenomenon. The corresponding thermochemical surface hardening processes with gases are carburizing and decarburizing, nitriding and denitriding, and soaking as well as the combined processes carbonitriding and nitrocarburizing. Treatments with oxygen as the reactant cause almost always an oxide layer (controlled oxidizing, blueing) or lead to a reduction of oxide layers. Boriding with gaseous boron sources is seldom done in practice because the predominant medium, diborane B_2F_6, is highly toxic and the boron halides BBr_3, BF_3, or BCl_3 are also seldom used due to their corrosive effect in humid condition. Plasma-assisted boriding with trimethyl borate $B(OCH_3)_3$ is still on the laboratory scale.

A focus of the industrial heat treating of steel with gases is above all carburizing, surface heat treatment in the austenite phase field, nitrocarburizing and, to a lesser extent, nitriding, surface heat treatment in the ferrite phase field. Consequently, these heat treating processes will be dealt with in detail as to the fundamental principles of introducing carbon, nitrogen, or a mixture of both into the case of a steel, as to the characteristics of the heat treated microstuctures and the properties of carburized or nitrocarburized components. Oxidation, reduction, and the effect and composition of protective gases are often connected with decarburizing processes. Hence this topic will be dealt with following the discussion on carburizing. Some conditions of a desired oxidation will also be treated in connection with oxynitriding. A discussion of the fundamental principles of reactions in and with gaseous atmospheres and of diffusion in solid metals the above-mentioned processes have in common will precede the main chapters.

7.2 FUNDAMENTALS IN COMMON [1–5]

The absorption of material from a gaseous atmosphere occurs in several steps [6,7]:

Processes in the gaseous atmosphere: Formation of transportable gas molecules and transfer of these molecules through the gas phase onto the surface of the metal with subsequent physical adsorption of the gas molecules

Processes in the interface: Dissociation of the gas molecules and chemisorption of the gas atoms, penetration of the atoms through the surface of the metal with transition of the atoms from the state of chemisorption to the interstitially solute state in the solid solution

Diffusion of the atoms from the surface into the core of the material

These steps are based on the premise that there is a potential difference between gas and steel. By analogy, the described steps are also valid for the emission of material, the atoms emitted from the solid solution recombine into molecules at the surface of the material and penetrate into the gaseous atmosphere.

Independent of the composition of the initial gases, the gaseous atmospheres used in heat-treating at processing temperatures consist of the elementary molecules carbon monoxide CO, carbon dioxide CO_2, hydrogen H_2, water vapor H_2O, oxygen O_2, ammonia NH_3, and sometimes also methane CH_4, all of which are able to react with one another and with the catalyzing surface of the component (and the furnace wall), thus releasing or absorbing carbon, oxygen, nitrogen, and hydrogen. Reactions among the constituents of the gas are described as homogeneous reactions; reactions between elements of the gas and elements of the component surface are described as heterogeneous reactions. The heterogeneous reactions that take place in the interface between gaseous atmosphere and component surface are chemophysical processes and responsible for the mass transfer. The reactions, i.e., the transition from an initial state to a final state, are accompanied by a change in the energy u, which is determined by the first law of thermodynamics

$$\mathrm{d}u = q + w \tag{7.1}$$

where q is the amount of heat added during the change of states and w the work done by the system. In many cases it suffices to just consider the work against the surrounding pressure (volume work):

$$w = -P * \mathrm{d}v \tag{7.2}$$

Thus Equation 7.1 can be rewritten

$$\mathrm{d}u = q - P * \mathrm{d}v \tag{7.3}$$

Combined with the entropy derived from the second law of thermodynamics

$$\mathrm{d}s = \frac{\mathrm{d}q_{\mathrm{rev}}}{T} \tag{7.4}$$

follows the basic equation for reversible thermodynamic processes, at constant pressure and constant temperature:

$$\mathrm{d}u = T * \mathrm{d}s - p * \mathrm{d}v \tag{7.5}$$

This relationship allows the derivation of thermodynamic potentials, one of which is the free enthalpy, or Gibbs' free energy

$$g = u + p * v - T * s \tag{7.6}$$

which is subsequently needed.

In a closed system the gas reactions approach a dynamic equilibrium state, which is determined by pressure, temperature, gas composition, and material composition. In this dynamic equilibrium state, the Gibbs' free energy is at its minimum and reactions and reverse reactions, on average, take the same amount of time, i.e., the total of locally absorbed and emitted particles equals zero, thus causing the net flow to cease. The rate of a chemical reaction is in proportion to the active masses of the involved elements, which for gaseous material are described by their partial pressures p_A (volume of constituent A $\times$ total pressure in the system). From the fact that reaction and reverse reaction take the same amount of time, it follows for a general reaction

$$a\mathrm{A} + b\mathrm{B} = c\mathrm{C} + d\mathrm{D} \tag{7.7}$$

(a through d are the stoichiometric factors of the reaction components A through D) that the equilibrium constant K_p of the process is

$$K_p = \frac{p_C^c * p_D^d}{p_A^a * p_B^b} \tag{7.8}$$

where, by agreement, the reaction products C and D are placed over the reactants A and B. Thus, the gas composition is replaced by the equilibrium constant K_p, which is independent of pressure.

The Gibbs' free energy for standard state is thus

$$\mathrm{d}g^0 = -R * T * \ln \mathrm{d}g^0 \frac{p_C^c p_D^d}{p_A^a p_B^b} = -RT \ln K_p \tag{7.9}$$

Values of the Gibbs' free energy for standard state reactions have been studied for many reactions and can be found in special tables [8,9].

The values of the partial pressures of the gaseous atmospheres discussed here vary between 10^{-17} and 10^{-25} bar at treatment temperature and are thus for reasons of convenience often replaced by the activity a_i of the gases by relating the partial pressure p to a standard state pressure. It is most usual to choose as standard state the partial pressure $p_0 = 1$ of the pure component in the same phase at the same temperature, which for carbon, for instance, is the steam pressure p_0^C of graphite (i.e., the activity of the graphite-saturated austenite is by definition $a_{\mathrm{Carbon}} = 1$ [10]).

Equation 7.9 can thus be rewritten as

$$\mathrm{d}g^0 = -R * T * \ln \frac{a_C * a_D}{a_A * a_B} \tag{7.10}$$

These deductions are only valid for reactions where substance is neither added to nor emitted from the system. On changing the amount of substance, the constituents must be taken into consideration by means of their chemical potential, which as partial Gibbs' free energy

$$\mu_i = \left(\frac{\partial g}{\mathrm{d}n_i}\right)_{T,p,j} = \left(\frac{\partial e}{\mathrm{d}n_i}\right)_{S,V,j} \tag{7.11}$$

is defined with $\mathrm{d}n_i$ moles of the substance i. In this case it is necessary to complete Equation 7.5

$$\mathrm{d}u = T * \mathrm{d}s - p * \mathrm{d}v + \Sigma\mu_i * \mathrm{d}n_i \tag{7.12}$$

The mass transfer within the interface is technically described by the mass transfer coefficient β, which determines how fast the particles move, with the mass transfer equation

$$\vec{m} = \beta(a_{\text{gas}} - a_{\text{surface}}) \tag{7.13}$$

and is therefore also called effective reaction rate constant. The direction of the mass transfer is determined by the activity gradient between gaseous atmosphere and the surface of the steel. The reaction rate constant indicates the total of mass transfer in the interface and comprises as a global value the effects of material, the microgeometrical state of the surface, flow conditions, pressure, and temperature on the mass transfer. The individual physicochemical reactions that occur in the interface cannot be described by the mass transfer coefficient.

Single-phase systems are homogeneous when at thermodynamic equilibrium, differences in the distribution of the involved atoms such as those caused during production are equalized by matter flowing from regions of higher concentration toward regions of lower concentration. The cause of this flux, which is called diffusion, is the difference in the chemical potential μ_c of the diffusing substance. The partial molar Gibbs' free energy, according to Equation 7.11, can be rewritten

$$\mu_c = \frac{\mathrm{d}g}{\mathrm{d}c} \tag{7.14}$$

where c is the concentration of the diffusing substance.

The potential difference is equalized by the flux

$$\vec{m} = -\frac{D^*}{RT} c \frac{\partial \mu_c}{\partial c} \operatorname{grad} c \tag{7.15}$$

where m is the number of atoms c that penetrate the area F in the time t, R is the general gas constant (8.314 J/mol K), and D^* the diffusion coefficient (or diffusivity).

In multiphase systems with different chemical potentials it is likely that potential jumps occur at the phase boundaries; in this case it may happen that the flux is opposed to the concentration gradient (uphill diffusion). On carbide formation, for instance, carbon diffuses from the saturated austenite into carbide with a higher concentration of carbon which, however, has a lower chemical potential in the carbide.

In dilute solutions, i.e., when the amount of the diffusing material is small, it is possible to use, with adequate precision, the more easily accessible concentration gradient as a driving force. This approach is valid for the thermochemical surface treatment and leads to Fick's first law of diffusion [11]

$$\frac{\partial c}{\partial t} = -D\frac{\partial c}{\partial x} \tag{7.16}$$

according to which the variation in time of the concentration depends on the concentration gradient $\partial c/\partial x$ parallel to the x-axis. The effective diffusion coefficient D has the unit area/time and is usually expressed in cm^2/s. Fick's first law is valid when there is change in time of the concentration gradient and thus none of the flux. Frequently, diffusion causes a change in the concentration gradient and thus becomes dependent on time and location. This is covered by Fick's second law [11]:

$$\frac{\partial c}{\partial t} = -\frac{\partial}{\partial x} D \frac{\partial c}{\partial x} \quad \text{with } D = f(c) \tag{7.17}$$

or, if D is independent of concentration and consequently of location,

$$\frac{\partial c}{\partial t} = -D \frac{\partial^2 c}{\partial x^2} \quad \text{with } D \neq f(c) \tag{7.18}$$

In the case of a semiinfinite system, that is when the diffusion flow does not reach the end of the specimen as is the case in thermochemical surface treatment, Fick's second law as given in Equation 7.18, the van Orstrand–Dewey solution [12–14] applies

$$c(x,t) - c_0 = (c_s - c_0)\left(1 - \text{erf}\left[\frac{x}{2\sqrt{Dt}}\right]\right) \tag{7.19}$$

where $c(x,t)$ is the concentration c at a distance x from the surface of a steel with the initial concentration c_0 following a diffusion time t, and c_s is the surface concentration of the diffusing element (erf is the Gaussian error function). According to this relation, the depth of penetration increases in proportion to the root of the diffusion time, which leads to the empirical rule that to get double the depth of penetration it is necessary to quadruple the diffusion time.

Fick's second law can also be resolved when substance is emitted, i.e., when c_s is smaller than c_0, in the form

$$c(x,t) - c_s = (c_0 - c_s)\ \text{erf}\left(\frac{x}{2\sqrt{Dt}}\right) \tag{7.20}$$

The diffusion coefficient is given by the empirical relationship

$$D = D_0 \exp\left(-\frac{Q}{RT}\right) \tag{7.21}$$

with the element-dependent constant D_0 and the activation energy Q of the diffusion. From Equation 7.16 and Equation 7.19 it follows that the diffusion time which is needed for a specific depth of penetration can only be reduced by higher temperatures T and an increase in the concentration gradient $\partial c/\partial x$. The activation energy Q is dependent on the mechanisms of solid-state diffusion. The diffusion of the gases nitrogen, oxygen, hydrogen, and of carbon, which are located interstitially mainly on octahedral voids in the lattice, occurs primarily by the interstitial mechanism that is the cause of the already mentioned rather fast diffusion of the above elements, which can still occur at room temperature and even lower temperatures.

The diffusion coefficients D_H, D_C, D_N, and D_O have been thoroughly studied for α-iron. Figure 7.1 [15] offers a comparison of the magnitudes between hydrogen, carbon, oxygen, and nitrogen and of substituted atoms. Figure 7.2 [4] shows a detailed plot of the diffusion

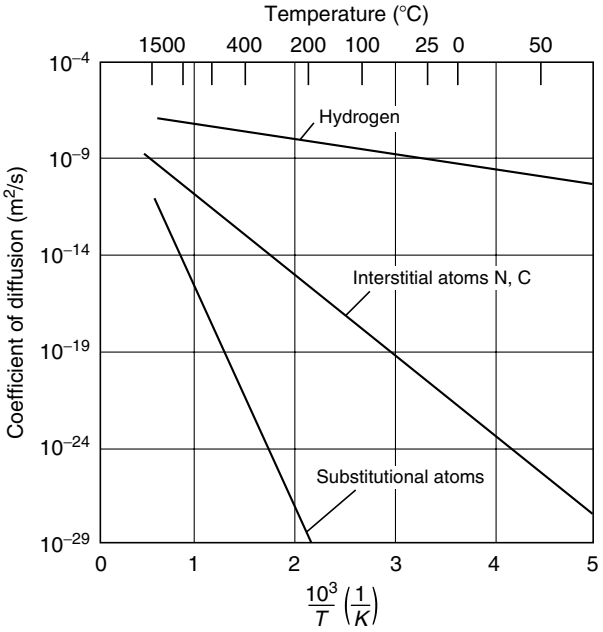

FIGURE 7.1 Diffusion coefficients of hydrogen and of interstitial and substitional elements in α-iron. (From E. Hornbogen, *Werkstoffe*, 2nd ed., Springer-Verlag, Berlin, 1979.)

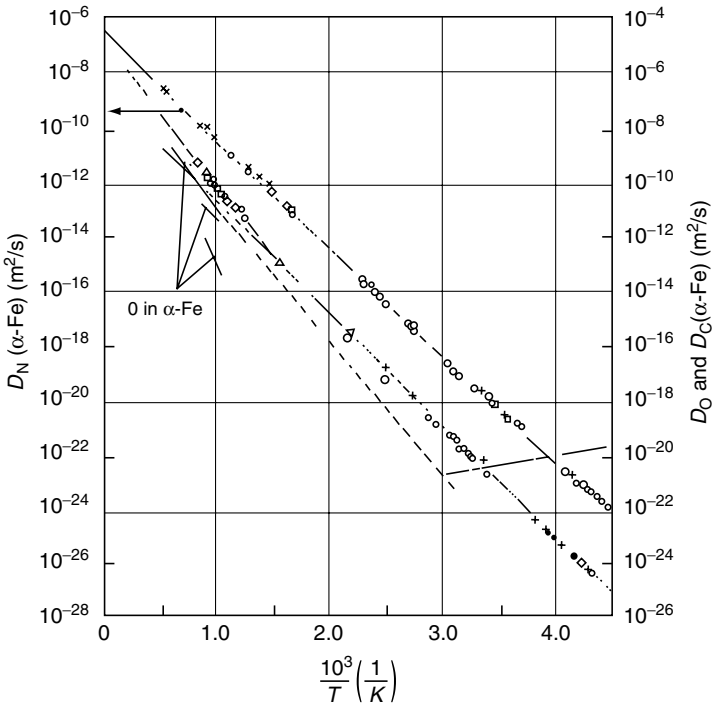

FIGURE 7.2 Diffusion coefficients of C, N, and O in α-iron. (From Th. Heumann, *Diffusion in Metallen*, Springer-Verlag, Berlin, 1992.)

coefficients of carbon, oxygen, and nitrogen. The diffusion coefficients in γ-iron are approximately lowered by the second power of 10, and details on this will be dealt with in Section 7.3 on carburizing. It ought to be noted that the diffusion proceeds faster alongside grain boundaries than in the matrix [3,4]. The directed exchange of matter requires a difference in potential or activity that is established and maintained by the gas composition. With processes near equilibrium it is possible to relate them to their final state and to describe them by specifically derived and easily obtainable values such as the carbon potential, and to control them accordingly. With processes far from equilibrium, where it is not possible to ascertain how great the differences in potential or activity are, it has proved helpful to use process characteristics that allow to maintain a required gas composition, provided that the processing conditions are fixed.

7.3 CARBURIZING

7.3.1 Introduction

Carburizing produces a hard and compared with their dimensions often shallow surface on relatively soft components when the surface microstructure of steels with a (core) carbon content of usually 0.15–0.25% is carburized to carbon contents in the range of 0.7–0.9 (1.0)% C and transformed to martensite. This treatment leads to the formation of a hardness gradient and to a distribution of residual stresses with compressive stresses in the surface microstructure due to the changes in volume during the martensitic transformation. The combined effect of these two parameters causes the main properties of the components, i.e., fatigue strength, rolling contact fatigue strength, and toughness to reach the highest values possible in one part. Carburizing thus comprises the processing steps carbon diffusion, with the result of a carbon gradient, and quenching with the hardness gradient and the distribution of residual stresses as results, where it is possible to establish equal carbon gradients in differently alloyed steels while the respective hardness gradients can differ because of the alloy dependence of the hardenability. The following chapters deal with the fundamentals of carburizing (carbon diffusion), the hardenability as a criterion for the selection of suitable carburizing steels, and the microstructures resulting from hardening. The properties of carburized components will be described in Section 7.6.

7.3.2 Carburizing and Decarburizing with Gases

Carburizing is achieved by heating the steel at temperatures in the homogeneous austenite phase field in an environment of appropriate carbon sources. The carburizing time depends on the desired diffusion depth. The processes in use are classified according to their carbon sources in pack carburizing (solid compounds), salt bath carburizing (liquid carbon sources), and gas and plasma carburizing (gaseous carbon sources), the process of which is subsequently described. Pack carburizing, too, produces a gas atmosphere, which means that the phenomena described for gas carburizing are, in essence, also true for pack carburizing. The processes in the gas phase and in the interface can be described for the present as states of equilibrium [16–23], the enforced transition to a nonequilibrium leads to carburizing or decarburizing. This approach is valid since during the carburizing process the diffusion in the steel is considerably slower than the preceding steps described in Chapter 4. Carburizing procedures for which this condition is no longer valid [24,25] as well as

plasma carburizing [26–29] will not be covered in this context. (See Chapter 18 for plasma caburizing.)

7.3.2.1 Gas Equilibria

Gaseous carbon sources in wide use are hydrocarbon gases such as methane or propane [19–21], alcohols and alcohol derivatives (above all methanol [30]), and other organic carbon compounds [31]. These carbon sources decompose at carburizing temperature to the constituents carbon monoxide (CO) and hydrogen (H_2) with small amounts of carbon dioxide (CO_2), water vapor (H_2O), oxygen (O_2), and methane (CH_4). In general, certain constant proportions of carbon monoxide and hydrogen diluted with nitrogen N_2 are used as a carrier gas, which can be produced separately in a gas generator or in the furnace directly. Such a carrier gas has a carburizing or decarburizing effect due to the reactions

$$2CO = C(\gamma) + CO_2 \text{ (Boudouard reaction)} \tag{7.22}$$

$$CO + H_2 = C(\gamma) + H_2O \text{ (heterogeneous water gas rection)} \tag{7.23}$$

$$CO = C(\gamma) + 1/2O_2 \tag{7.24}$$

$$CH_4 = C(\gamma) + 2H_2 \tag{7.25}$$

and the homogeneous water gas equilibrium

$$CO_2 + H_2 = CO + H_2O \tag{7.26}$$

with which the reaction product carbon dioxide is decomposed again. This means that after a sufficiently long carburizing time, an equilibrium between carburization and decarburization is established whose carbon content is described as carbon potential (C-potential C_p) [32] can be measured by shim stock analysis [33]. (It is customary to define the carbon potential, in mass percent, as the carbon content of pure iron within the homogeneous austenite phase field at a given temperature that is in equilibrium with the furnace atmosphere.) Figure 7.3 [16,18] shows the equilibrium between carburization and decarburization for the Boudouard reaction in presence of pure carbon dependent on pressure and temperature. The equilibrium can be described by the equilibrium constant

$$\log k_B = \log \frac{p_{CO}^2}{p_{CO_2} p_C^0} = \log \frac{p_{CO}^2}{p_{CO_2}} \tag{7.27}$$

with the concentration of the gas constituents as the respective partial pressures and the carbon concentration as vapor pressure p_C^0 of pure carbon (is equal to unity). The equilibrium curve shown in Figure 7.4 at $p_{abs} = 0.2$ bar is equivalent to an amount of 20% carbon monoxide in the carrier gas.

In the carburizing of steel, the influence of the carbon content and the alloy composition of the steel on the carbon concentration must be considered by means of the activity of carbon a_C [25], which is defined as the ratio of the vapor pressure p_C of carbon in the given condition to the vapor pressure p_C^0 of pure carbon

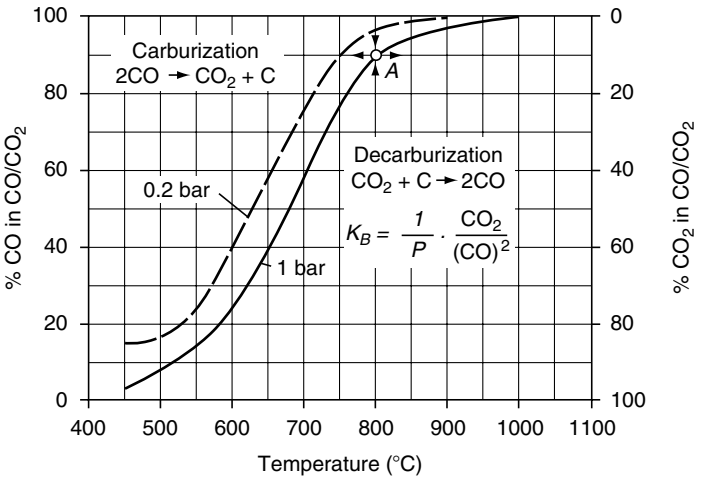

FIGURE 7.3 Boudouard reaction in equilibrium with pure carbon. (From F.E. Harris, *Met. Prog.* 84 (1945); Th. Schmidt, *Härterei Techn. Mitt. Sonderheft Gasaufkohlung* 11, 1952.)

$$a_C = \frac{p_C}{p_0} \tag{7.28}$$

The activity of carbon for plain carbon steels can be calculated [19,23] according to

$$\log a_C = \frac{10{,}500}{4.575T} - \frac{3.95 - 0.69C}{4.575} + \frac{C}{0.785C + 21.5} \tag{7.29}$$

or, less complicated but sufficiently precise, as follows:

$$\log a_C = \frac{2300}{T} - 2.21 + 0.15C + \log C \tag{7.30}$$

and is shown in Figure 7.4 [34] in the form of isoactivity plots [22,34].

The influence of the alloying elements on the activity of carbon is described by the ratio of the C-potential C_p of the carburizing atmosphere (carbon content of pure iron at equilibrium) to the carbon content C_L of the alloyed steel at equilibrium [19,21,35,36]

$$\log(C_p/C_L) = 0.055(\%\,Si) + 0.014(\%Ni) - 0.013(\%Mn) - 0.040(\%Cr) - 0.013(\%Mo) \text{ (Ref. [35])} \tag{7.31}$$

$$\log(C_p/C_L) = 0.062(\%Si) + 0.014(\%Ni) - 0.016(\%Mn) - 0.057(\%Cr) - 0.015(\%Mo) - 0.102(\%V) - 0.014(\%Al) - 0.006(\%Cu) \text{ (Ref. [19])} \tag{7.32}$$

$$\log(C_p/C_L) = 0.075(\%Si) + 0.02(\%Ni) - 0.04(\%Cr) - 0.01(\%Mn) - 0.01(\%Mo) \text{ (Ref. [36])} \tag{7.33}$$

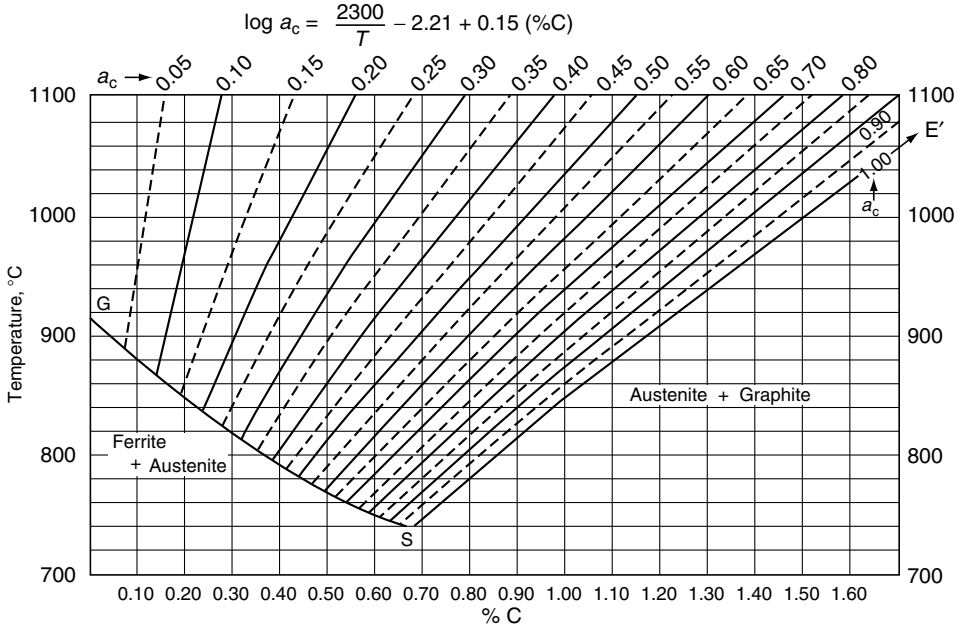

FIGURE 7.4 Isoactivity of carbon in the austenite phase field. (From E. Schürmann, Th. Schmidt, H. Wagener, *Gießerei, Beiheft 16*:91, 1964.)

On calculating the value of a required carbon potential of a carburizing atmosphere, the influence of the alloying elements on the activity of carbon is taken into account by means of the alloy factor $f = C_L/C_p$ for a specific steel [37]. Ni-alloyed steels have alloy factors smaller than 1, Cr-alloyed, Cr-Mn-alloyed, and Cr-Mo-alloyed steels have alloy factors higher than 1, which is why on carburizing these steels in a carburizing atmosphere with a C-potential of 1%, the case carbon content of Ni-alloyed steels is smaller than 1% whereas the case carbon content of the other steels is higher than 1%.

The equilibrium constant of the Boudouard reaction in the carburizing process of steel [19,20,22]

$$\log K_B = \log \frac{p_{CO}^2}{p_{CO_2} a_C} - \frac{8817}{T} + 9.071 \tag{7.34}$$

thus contains the activity of carbon, which can be derived from

$$\log a_C = \log \frac{p_{CO}^2}{p_{CO_2}} - \frac{8817}{T} - 9.071 \tag{7.35}$$

The carburizing equilibria of the Boudouard reaction in the homogeneous austenite phase field are shown in Figure 7.5 [19].

The equilibrium constants of the reactions 7.23 through 7.25 are

$$\log K_{H_2} = \log \frac{p_{H_2} p_{CO}}{p_{H_2O} a_C} - \frac{7100}{T} + 7.496 \tag{7.36}$$

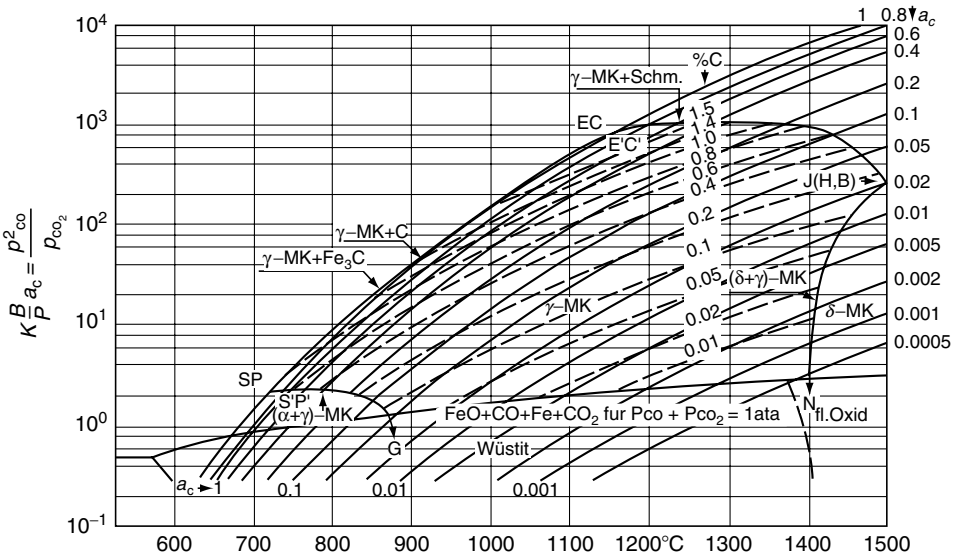

FIGURE 7.5 Boudouard reaction in equilibrium with steel. (From F. Neumann, B. Person, *Härterei Techn. Mitt. 23*:296, 1968.)

$$\log K_{O_2} = \log \frac{p_{CO}}{p_{O_2} a_C} - \frac{9927}{T} + 4.545 \tag{7.37}$$

$$\log K_{CH_4} = \log \frac{p_{CH_4}}{p_{H_2} a_C} - \frac{4791}{T} + 5.789 \tag{7.38}$$

By analogy, it is possible to derive the corresponding relations valid for the activities from Equation 7.35.

Given a certain composition and volume of gas, the described processes cease eventually, having established an equilibrium with the corresponding carbon potential. With the reactions

$$CH_4 + CO_2 \rightarrow 2CO + 2H_2 \tag{7.39}$$

$$CH_4 + H_2O \rightarrow CO + 3H_2 \tag{7.40}$$

methane decomposes the reaction products carbon dioxide and water vapor of the heterogeneous carburizing reactions 7.22 and 7.23, thus regenerating the carburizing atmosphere. Compared with the carburizing reactions 7.22 through 7.24, in particular with the heterogeneous water gas reaction, the reactions with methane are sluggish, which makes it necessary to add large quantities of methane (or propane, which decomposes to methane at carburizing temperature) to maintain the carburizing processes.

7.3.2.2 Kinetics of Carburizing

In the carburizing process, a carrier gas of a composition as constant as possible is enriched with a carburizing agent (for instance propane) to establish and maintain, by means of further

additions of the carburizing agent, a desired carbon potential which exceeds the carbon content of the steel to be carburized. In this nonequilibrium condition [38], the activity of carbon in the carburizing atmosphere $a_{c(gas)}$ is higher than the activity of carbon in the steel $a_{c(steel)}$. The difference in the activities leads to the desired carbon transfer into the steel, the flux m (number of atoms M that penetrate the area F in unit time) proportional to the difference in activities [22]

$$\vec{m} = \frac{M}{F}\mathrm{d}t = -\beta(a_{C(gas)} - a_{C(steel)}) \tag{7.41}$$

The carbon transfer coefficient β is in particular dependent on the composition of the carburizing atmosphere and the carburizing temperature, as given in Figure 7.6 [20] with values for $\beta = 1.25 \times 10^{-5}$ cm/s for endothermic gas consisting of methane–propane up to $\beta = 2.5 \times 10^{-5}$ cm/s for undiluted decomposed alcohols. The surface rate constant is ascertained by means of thin iron foils (thickness of about 0.05 mm or thin iron wires) [20,39], the quantitative connections are however not yet sufficiently known in detail. Figure 7.7 [40] shows the influence of the carbon transfer coefficient on carburizing time.

By combining Equation 7.16—Fick's first law—and Equation 7.41, a formula for the effect of time on the growth of the carbon diffusion depth can be derived [23,41,42]

$$x = At = \frac{0.79\sqrt{Dt}}{0.24 + \dfrac{C_{At} - C_0}{C_p - C_0}} - 0.7\frac{D}{\beta} \tag{7.42}$$

where the limiting carbon content C_{At} determines the depth At of carbon diffusion. For a limiting carbon content of 0.3% the depth $At_{0.3\%C}$ can be assessed [42] as

$$At_{0.3\%C} = k\sqrt{t} - \frac{D}{\beta}\ \text{[mm]} \tag{7.43}$$

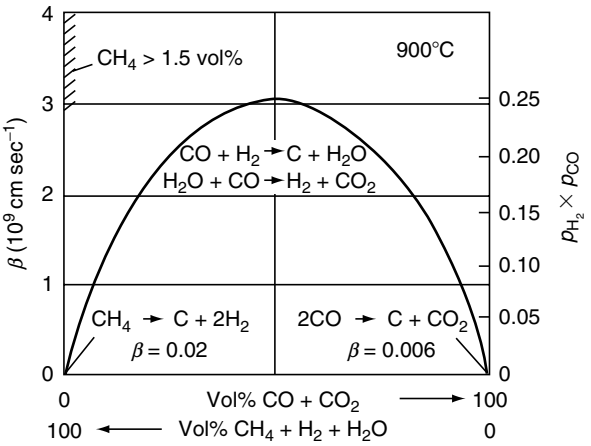

FIGURE 7.6 Carbon transfer coefficient β versus gas composition. (From F. Neumann, U. Wyss, *Härterei Techn. Mitt. 25*:253, 1970.)

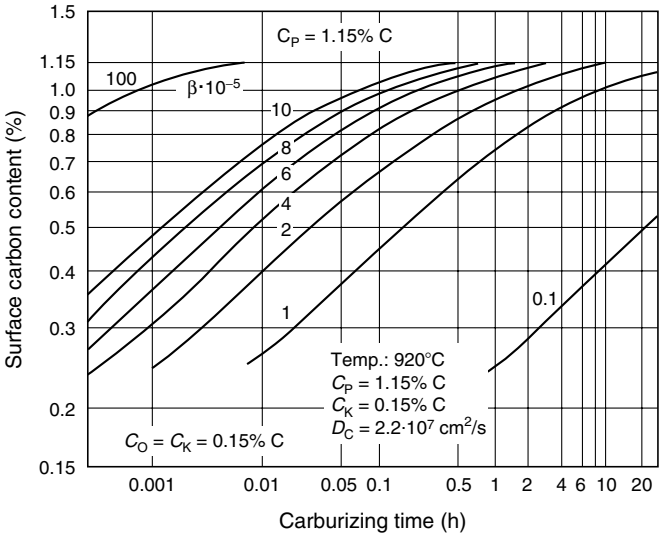

FIGURE 7.7 Effect of carbon transition coefficient on carburizing time. (From K. Rimmer, *Härterei Techn. Mitt. 30*:152, 1975.)

where the proportional value k depends on temperature, carbon potential, and the surface reaction rate constant. The $\sqrt{t}$-rule, as described in Chapter 4, stating that to double the carburizing depth it is necessary to quadruple the carburizing time, is valid for $k = 0.5$ and of sufficient accuracy with carburizing depths of about 1 mm and more [38,42,43]. The formal meaning of the compensating factor D/β is that the point of intersection of carbon diagram and C-potential is shifted from the surface into the gas atmosphere [38,42,43].

Effective decarburizing reactions are [6,44]

$$2C(\alpha,\gamma) + O_2 \rightarrow CO_2 \tag{7.44}$$

$$C(\alpha,\gamma) + 2H_2 \rightarrow CH_4 \tag{7.45}$$

$$C(\alpha,\gamma) + H_2O \rightarrow CO + H_2 \tag{7.46}$$

where molecules from the gaseous atmosphere react with the carbon to form new molecules at the surface of the steel that in turn are emitted in the gaseous atmosphere. Reaction 7.46, occurring in several steps, is used for controlled decarburization, i.e., components such as electric sheets are annealed in moist hydrogen. Taking considerably more time, reaction 7.45, which is also involved, is of minor importance, whereas reaction 7.44 tends to have a slightly deleterious effect when using oxygen containing protective gases or annealing in air.

7.3.2.3 Control of Carburizing

The carbon gradient as the major aim of the carburizing process is determined by the carburizing depth At and the case carbon content C_S and can be controlled at a given temperature by the carburizing time according to Equation 7.43 and by the carbon potential. In industrial carburizing, the carbon potential is controlled by either using [37] Equation 7.22,

monitoring of carbon dioxide content; Equation 7.23, ascertaining of water vapor content; or Equation 7.24, monitoring of content. The partial pressure of CO_2 in the gaseous atmosphere is continually measured by infrared absorption, which is based on the different attenuation of an infrared beam by the content of CO_2 of the gas. The interrelationship between CO_2 content, C-potential, and temperature

$$\log p_{CO_2} = \frac{6552}{T} - 6.841 - 0.15C + \log\left[\frac{p^{CO^2}}{C}(0.785C + 21.5)\right] \tag{7.47}$$

contains the CO content, which is generally held constant by means of an adequate carrier gas composition to avoid undesirable influences. The measuring accuracy, then, is about 0.005–0.01 relative to the C-potential. Figure 7.8 shows an evaluation of Equation 7.47 for a carrier gas generated of propane and propane as the enriching gas [45].

The partial pressure of oxygen, which is about 10^{-17}–10^{-24} bar within the furnace, is measured by means of an oxygen probe [46] whose measuring element consists of a zirconia electrolytic solid that projects into the interior of the furnace in form of a tube. The electric potential or electromotive force E of such an electrolytic solid is according to Nernst's law

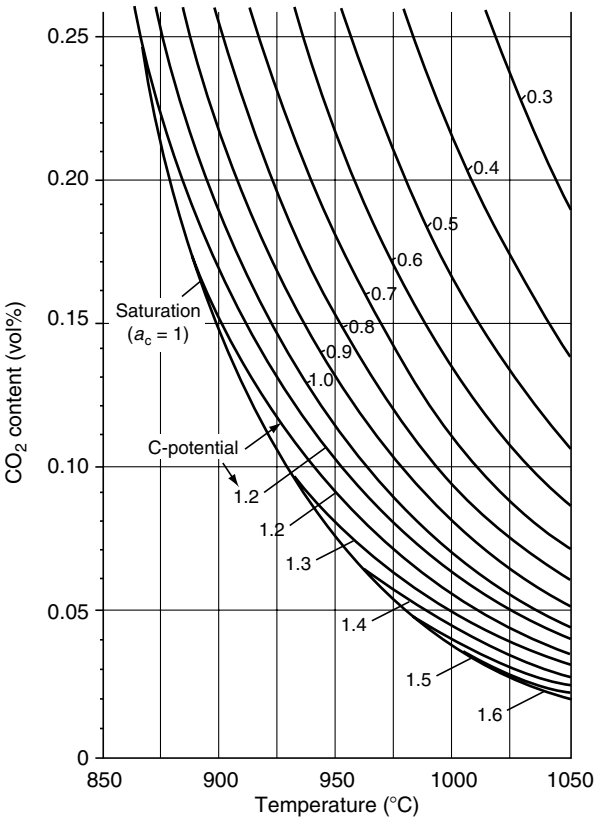

FIGURE 7.8 Carbon potential control by monitoring the carbon dioxide content (endo gas enriched with propane, 23.7 Vol% CO). (From D. Liedtke, Messen und Regeln beim Aufkohlen, *Einsatzhärten*, (J. Grosch, Ed.), expert-Verlag, Renningen, 1994, p. 16.)

$$E = \frac{RT}{4F} \ln \frac{p_{O_2}}{p^0_{O_2}} \tag{7.48}$$

or, with $R = 8.344$ J/mol·grad and $F = 96.5727$ J/mV·mol (Faraday constant)

$$E = 0.0216T \ln \frac{p_{O_2}}{p^0_{O_2}} = 0.0497T \log \frac{p_{O_2}}{p^0_{O_2}} \text{ [mV]} \tag{7.49}$$

The partial pressure $p^0_{O_2}$ is the partial pressure of the reference gas on the inside wall of the tube, usually surrounding air ($= 0.21$ bar). By means of Equation 7.39 and Equation 7.48 and air as the reference gas, it is possible to combine the measured electric potential, which is about 1 V, with the C-potential [22]

$$E = 0.09992T(\log p_{CO} - 1.995 - 0.15C - \log C) - 816 \tag{7.50}$$

or, rewritten [45]

$$E = 807 - \frac{T}{100}\left[36.86 + 1.5C + 4.3 \ln\left(\frac{0.457C}{p_{CO}(0.785C + 21.5)}\right)\right] \tag{7.51}$$

The interrelationship between the electric potential of the probe, temperature, and C-potential according to Equation 7.51 is illustrated in Figure 7.9 [45] for an atmosphere consisting of endothermic gas as a carrier gas and propane as enriching gas. The linear progression facilitates a high resolution that allows the C-potential to be measured with an accuracy smaller than 0.005.

Methane (CH_4) reacts rather slowly according to Equation 7.25 but forms rapidly at carburizing temperature on cracking of the previously mentioned carburizing gases; this is the reason why in actual practice carburizing atmospheres contain more CH_4 than would correspond the state of equilibrium, thus making the content of methane, which can also be measured by infrared analysis, an unsuitable means of controlling carburizing potential. Dew point analysis for measuring the water vapor content according to Equation 7.23 has lost its importance by the development of, above all, the oxygen probe. Thus, the C-potential is always determined indirectly, and direct procedures such as measurement of the electric potential of carbon [47] have so far not proved safe enough in processing.

With the development in computer technique, the van Orstrand–Dewey solution (Equation 7.19, Section 7.2) for carbon could be applied for carbon controlling online [43,48–53]. It suffices to calculate the diffusion coefficient D^γ_C step by step with appropriate formulae that have been derived from test results [54,55] by regression analysis

$$D^\gamma_C = 0.47 \exp\left[-1.6C - \frac{37{,}000 - 6{,}600C}{RT}\right] \text{ (Ref. [54])} \tag{7.52}$$

or

$$D^\gamma_C = 0.78 \exp\left[-\frac{18{,}900}{t} + \left(\frac{4{,}300}{T} - 2.63\right)C^{1.5}\right] \text{ (Ref. [56])} \tag{7.53}$$

The exact and continuous quantitative determination of the C-potential as a controlling factor and the online calculation of the carbon profile have facilitated computer-controlled

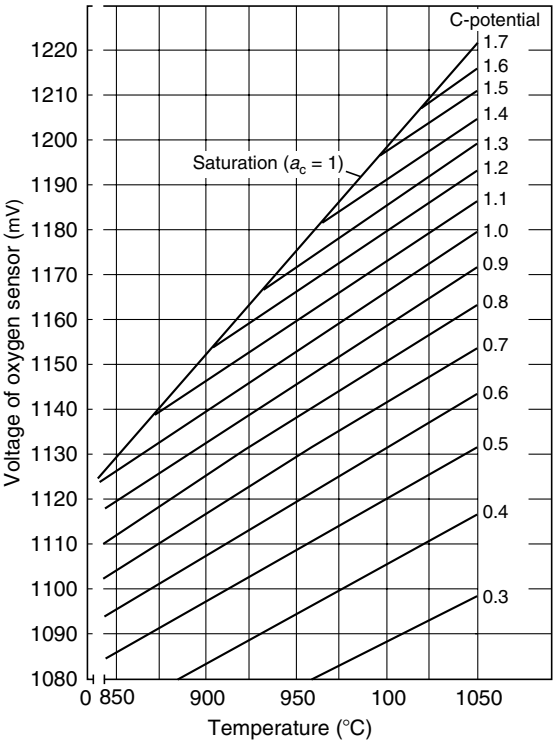

FIGURE 7.9 Carbon potential control by means of the oxygen sensor (endo gas enriched with propane). (From D. Liedtke, Messen und Regeln beim Aufkohlen, *Einsatzhärten*, (J. Grosch, Ed.), expert-Verlag, Renningen, 1994, p. 16.)

carburizing, that is state of the art in heat treatment technique [57–59]. In particular with establishing deeper carbon diffusion depths this technique is frequently applied in a two-stage process (boost–diffuse method of carburizing). In the first stage a C-potential is established, which can be held by means of computer control, just below saturation, avoiding the formation of carbides or soot. The steep carbon concentration gradient, according to Equation 7.16, causes a rapid carbon diffusion. In the second stage, the C-potential is adjusted to the desired surface carbon content and the initial carbon gradient is equalized by some of the carbon diffusing deeper into the component and some of it diffusing into the gaseous atmosphere until the appropriate carbon gradient is reached [59,60]. The overall carburizing time is shortened considerably. At higher carburizing temperatures Equation 7.21 offers a second way to accelerate the carbon diffusion (a carbon diffusion depth of 1 mm is reached at 930°C/1706°F in 6 h, at 1050°C/1922°F in 2 h ($C_p = 1.0$) [61], which has not been used until now because grain sizes of convenient carburizing steels (i.e., DIN EN 10084) remain stable up to 950°C/1742°F only. Recent developments of carburizing steels allow carburizing temperatures up to 1050°C/1922°F without grain growth [62] (and plasma furnaces handle high temperatures much better than atmosphere furnaces [63].

7.3.2.4 Carbonitriding

In carbonitriding, ammonia NH_3 is introduced into the carburizing atmosphere. NH_3 decomposes at carburizing temperature and releases nitrogen with the ability to be absorbed

by the steels. The simultaneous and competing diffusion of carbon and nitrogen leads to some particularities [64,65] that are technically used. Solute nitrogen that occupies an interstitial position in the austenite lattice causes the GSE curve of the homogeneous austenite phase field (see Figure 7.4) to shift to lower temperatures and reduces the carbon content of the eutectoid composition. Nitrogen stabilizes the austenite, thus reducing the diffusion-controlled transformation of the austenite to ferrite and pearlite and lowering the martensite start temperature M_s. Martensite is also stabilized by soluted nitrogen. The essential advantage of carbonitriding lies in the better hardenability (stabilized austenite) because this also allows to better control hardness profiles in steels that are not intended to be carburized as well as in sintered iron and to use milder quenchants with less distortion. Moreover, C–N-martensite has a better tempering behavior. Whereas carburizing temperatures generally exceed 900°C/1652°F, carbonitriding is performed at lower temperatures in the range of 815–900°C/1499–1652°F because at temperatures of more than 900°C/1652°F ammonia decomposes too fast and the nitrogen potential [65] becomes too high, thus causing increased contents of retained austenite and even pores. Consequently, carbonitriding is usually applied with producing case depths of less than 0.5 mm, which can be better accomplished in carbonitriding than in carburizing.

7.3.3 Hardenability and Microstructures

After having been carburized, the components are subjected to a hardening process in which they are quenched in oil (whose temperature is usually held at 60°C/140°F), for economic reasons sometimes from their carburizing temperature (generally 930°C/1076°F) or more often from a lower temperature (830–850°C/1526–1562°F) that is adapted to the temperature of their case carbon content (direct quenching). Reheating is a heat treatment in which a component is slowly cooled from its carburizing temperature to a temperature below Ac3, most often to room temperature, and subsequently austenitized at hardening temperature, corresponding to the established case carbon content. Reheating is a suitable heat treatment for large or single components but otherwise not in wide use. Double quenching from austenitizing temperatures that are adapted to the carbon content of case and core, respectively, is seldom used in commercial practice, with the ensuing distortions caused by two subsequent martensitic transformations only tolerable with simple geometries. The carbon gradient (Figure 7.10 [66]) becomes the desired hardness gradient (Figure 7.11 [66]), which is determined according to DIN 50190, Part 1, by means of HV1 and

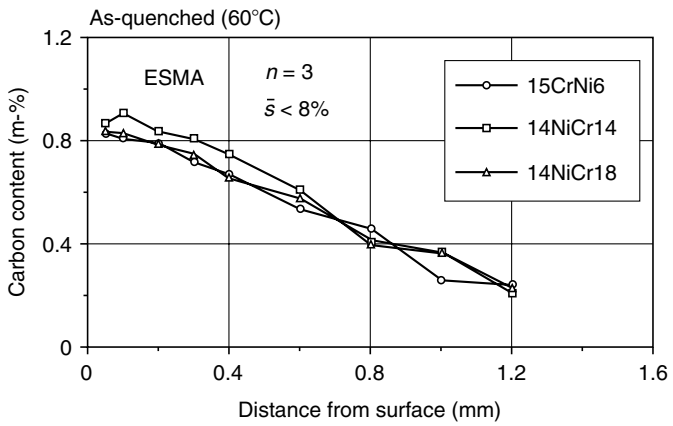

FIGURE 7.10 Carbon gradients of alloyed steels, computer-controlled carburized. (From O. Schwarz, J. Grosch, C. Genzel, W. Reimers, *Härterei Techn. Mitt. 49*:134, 1994.)

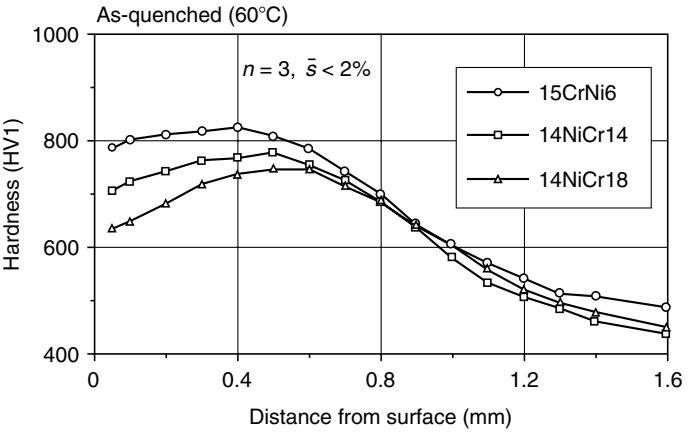

FIGURE 7.11 Hardness gradients of carburized microstructures with carbon gradients according to Figure 7.10. (From O. Schwarz, J. Grosch, C. Genzel, W. Reimers, *Härterei Techn. Mitt. 49*:134, 1994.)

contains the case (hardening) depth that is determined by the limiting hardness of 550 HV1. The carbon gradients in Figure 7.10 verify that it is possible to establish the same gradients as to case carbon content and case depth for differently alloyed carburizing steels when drawing upon the discussed knowledge on carburizing and taking in consideration the influence of the alloy on the carbon absorption by controlling the C-potential. The corresponding hardness gradients contain the hardenability [67], which has an obvious influence on the hardness of case and core, causing the case hardness values to drop and the core hardness values to rise with rising alloying contents. The better hardenability of alloyed microstructures is comprehensible, maximum hardness is however generally attributed to the carbon content (which is equal in the above discussion). The influence of the alloy on the hardness of the case is an indirect one since an increase in the alloying content (and in the carbon content) causes a drop in the martensite start temperature M_s [68,69], thus causing a drop in the martensite formation because the martensite finish temperature M_f is lower than the quench temperature (usually 60°C/140°F). The austenite that has not transformed to martensite is called retained austenite, its microstructure is soft and thus responsible for a drop in the hardness. The amount of retained austenite still existing on quenching (Figure 7.12 [66]) can be reduced by

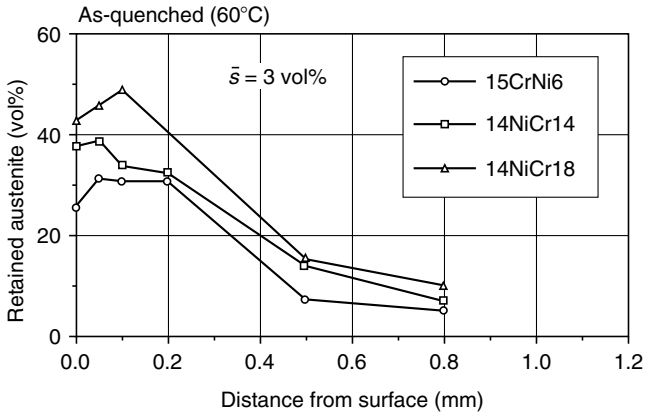

FIGURE 7.12 Amount of retained austenite, as-quenched conditions. (From O. Schwarz, J. Grosch, C. Genzel, W. Reimers, *Härterei Techn. Mitt. 49*:134, 1994.)

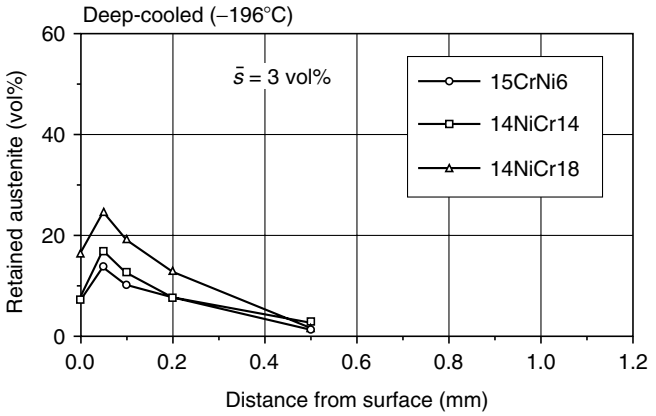

FIGURE 7.13 Amount of retained austenite, deep-cooled conditions. (From O. Schwarz, J. Grosch, C. Genzel, W. Reimers, *Härterei Techn. Mitt. 49*:134, 1994.)

deep cooling, which causes further amounts of austenite to transform into martensite (Figure 7.13 [66]). The case hardness of deep cooled microstructures does not differ within the measuring accuracy (Figure 7.14 [66]). Hence, the hardenability of the case [70] is primarily determined by the content of soluted carbon, the maximum case hardness is determined by the amount of retained austenite in the case microstructure, which depends on the carbon content and the alloying elements. In contrast, the hardenability of the core is markedly dependent on the alloy (Figure 7.15 [71]) and serves as a criterion for the selection of suitable alloy steels, the preferred alloying elements are chromium, manganese, molybdenum, and nickel [72], to a lesser extent also boron [71].

The case microstructure thus consists of (plate) martensite and retained austenite. The influence of the carbon content on the formation of the case microstructure is clearly visible in Figure 7.16 [66] (0.7% C, 25% retained austenite) and Figure 7.17 [66] (1.0% C, 40% retained austenite). Reliable values for the content of retained austenite can be obtained by x-ray

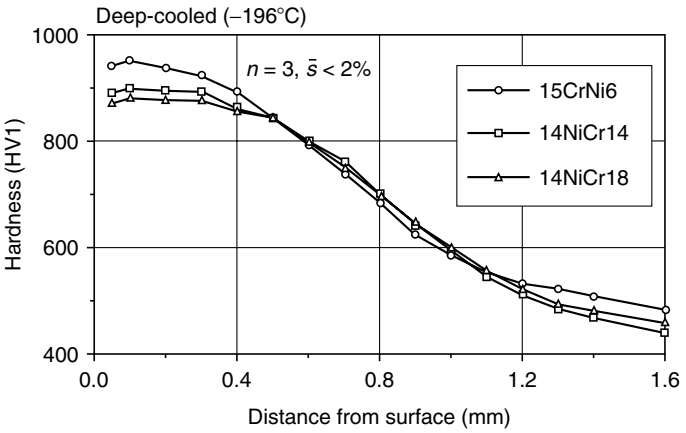

FIGURE 7.14 Hardness gradients, deep-cooled conditions. (From O. Schwarz, J. Grosch, C. Genzel, W. Reimers, *Härterei Techn. Mitt. 49*:134, 1994.)

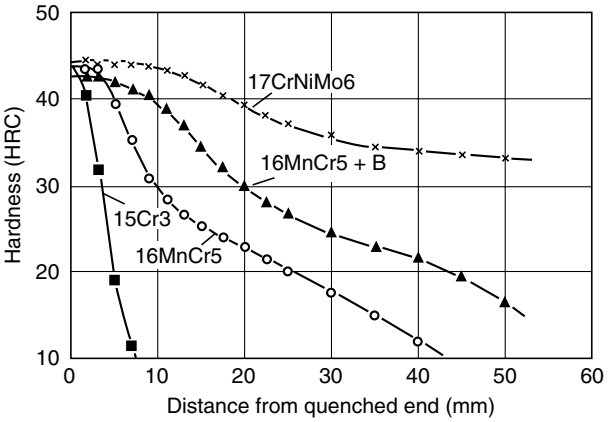

FIGURE 7.15 Jominy test results for some carburizing steels. (From H. Dietrich, W. Schmidt, *Thyssen Techn. Berichte 10*:105, 1984.)

analysis only. The core microstructure consists of (lath) martensite (Figure 7.18 [66]) or, given larger components, of bainite or ferrite and pearlite. The diffusionless, martensitic transformation can only occur within the austenite grains. At low martensite start temperatures, i.e., when the carbon contents of the case microstructure are high, single martensite plates form successively within the austenite grain with $\{225\}_A$ and $\{259\}_A$ habit planes [73–77], originating from nuclei on the austenite grain boundaries [78]. The possible variants of the habit planes lead to the development of nonparallel, irregularly distributed martensite plates that, starting from grain diameter size, successively become smaller until they take up as much space in the austenite grain as is possible. The irregularly distributed single plates are clearly visible in the scanning electron micrograph (SEM) (Figure 7.19), single needles that seem jagged, obtained from cross sections of the plates together with retained austenite, are shown in the light micrograph (Figure 7.16 and Figure 7.17). This martensite morphology is called plate martensite, and is characteristic of the carburized case microstructure. With carbon

FIGURE 7.16 Plate martensite and retained austenite in the case (14NiCr18, 0.7% C, 20% retained austenite). (From O. Schwarz, J. Grosch, C. Genzel, W. Reimers, *Härterei Techn. Mitt. 49*:134, 1994.)

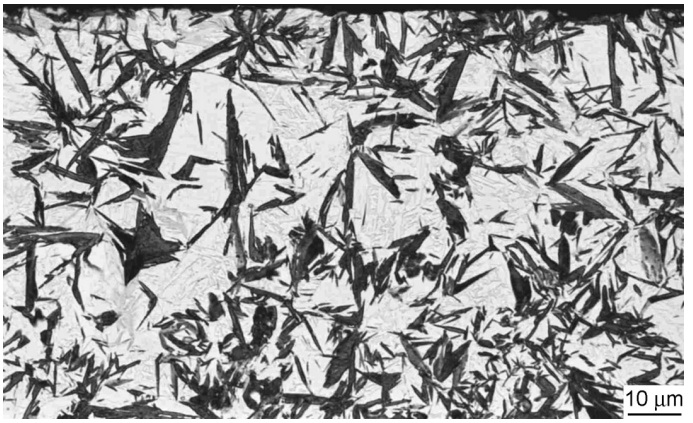

FIGURE 7.17 Plate martensite and retained austenite in the case (14NiCr18, 1.0% C, 60% retained austenite). (From O. Schwarz, J. Grosch, C. Genzel, W. Reimers, *Härterei Techn. Mitt. 49*:134, 1994.)

contents of up to 0.4% carbon in supersaturated solution, martensite consists of plates that are arranged in packets of different orientations within the former austenite grain boundaries (Figure 7.18). The single plates have a thickness of about 0.1–0.5 µm, and their largest diameters are in the range of 1–5 µm. The single plates are clearly visible in SEM magnification (Figure 7.20), as is their arrangement in layered packets. Light micrographs allow often just to discern cross sections of the plates. From studies using the transmission electron microscope it follows that the dislocation density of the single plates is high, in the size range of 10^{11}–10^{12} dislocations per square centimeter [75].

It is possible to make the austenite grain boundaries visible in the carburized microstructure as the prior austenite grain size (Figure 7.21), they can usually only be etched separate from the matrix microstructure. The prior austenite grain size is a further characteristic of carburized microstructures, fine-grained microstructures having a better behavior under all loading conditions. Martensitic transformations within large grains may cause microcracks in

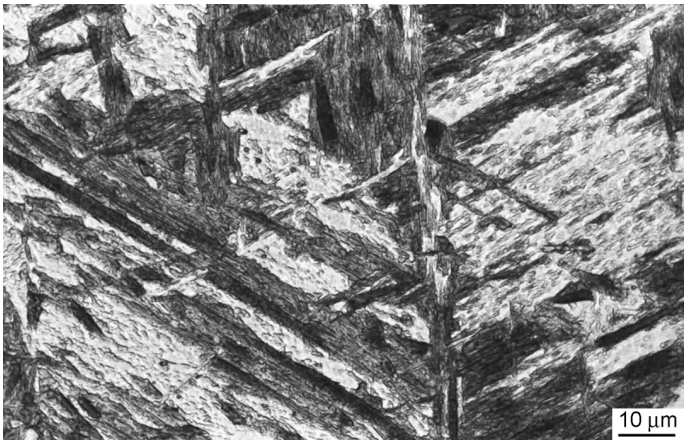

FIGURE 7.18 Lath martensite in the core microstructure (14NiCr18, 0.15% C). (From O. Schwarz, J. Grosch, C. Genzel, W. Reimers, *Härterei Techn. Mitt. 49*:134, 1994.)

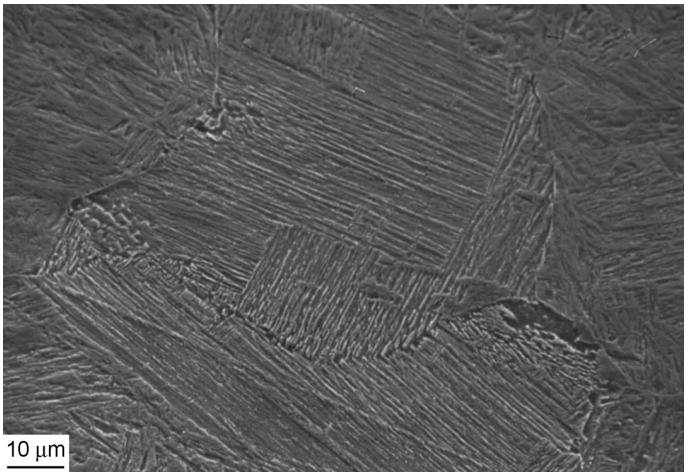

FIGURE 7.19 Lath martensite, SEM micrograph (16MnCr5).

martensite plates (Figure 7.22) if a rapidly growing martensite plate (in the size range of 10^{-7} s [75,76]) in the plate martensite impinges on an already existing plate, thus converting its kinetic energy into an impact that causes the plate to crack. Low transformation temperatures contribute to the development of microcracks [79,80].

In direct hardening, it is necessary to use steels whose austenite grain sizes do not grow much during carburizing. Suitable fine-grained steels are alloyed with aluminum and nitrogen and subjected to a thermomechanical treatment in which a fine grain develops that is stabilized by aluminum nitride precipitation on grain boundaries [81–84]. The ratio of aluminum to nitrogen ought to be about 3 to 5. The absorption of carbon into the case microstructure and the martensitic transformation lead to an increase in volume with respect to the initial microstructure. In combination with the cooling and the tranformation process,

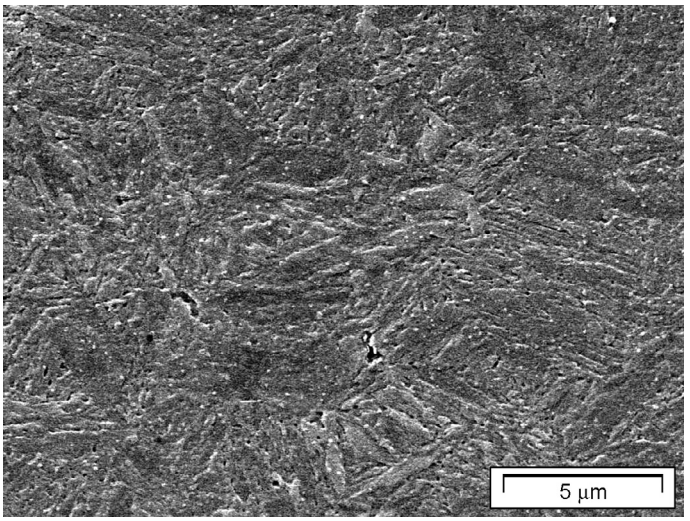

FIGURE 7.20 Plate martensite, SEM micrograph (16MnCr5).

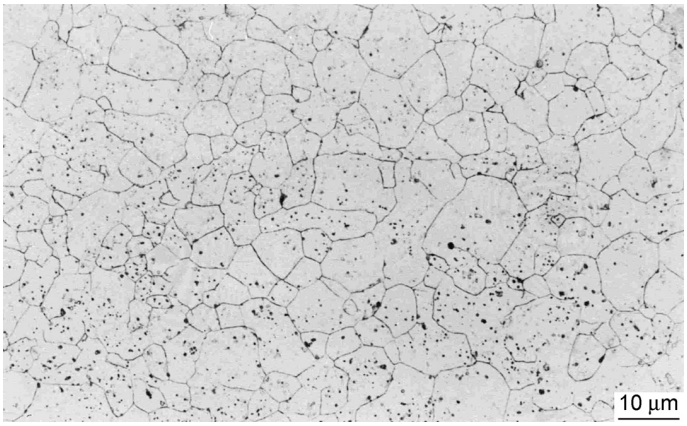

FIGURE 7.21 Austenite grain boundaries in carburized steel (15CrNi6).

residual stresses develop in the carburized microstructure, with compressive residual stresses in the case that turn into tensile residual stresses when reaching the case depth (Figure 7.23 [66]).

Carburized microstructures are almost always tempered to transform the unstable and brittle as-quenched martensite into the more stable tempered martensite. This leads to an increase in ductility and thus minimizes the occurrence of delayed fracture [86]. The transformation of retained austenite tends to decrease distortion. With common carburizing steels the tempering temperatures are limited to 180–200°C/365–392°F to ensure that the usually required surface hardness of more than 60HRC is still maintained, and for economic reasons the tempering time is almost always no more than 2 h. With high-alloyed steels such as the M50-NiL/AMS 6278 [87,88] a change in tempering conditions may become necessary. In tempering, carbon diffuses from the supersaturated martensite lattice in several temperature-dependent stages and segregates at lattice defects or forms carbides with the iron atoms of the matrix [85,89–93]. In the temperature range between 100°C (212°F) and 200°C (392°F), i.e., in the temperature range of conventional tempering of carburized microstructures, transition carbides are precipitated from the martensite in steels with a carbon content higher than 0.2%

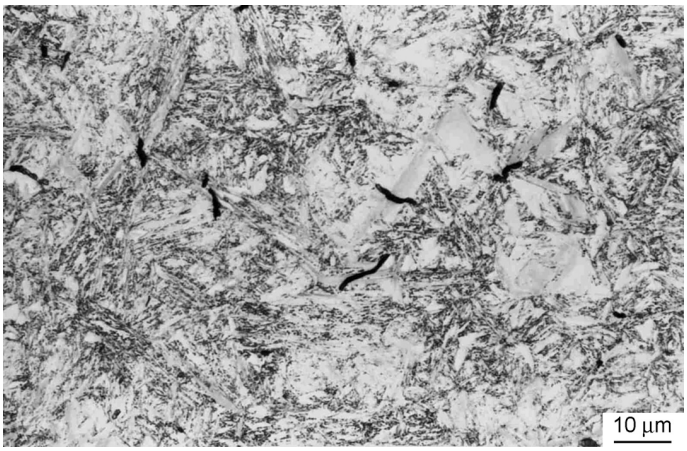

FIGURE 7.22 Microcracks in the plate martensite (16MnCr5).

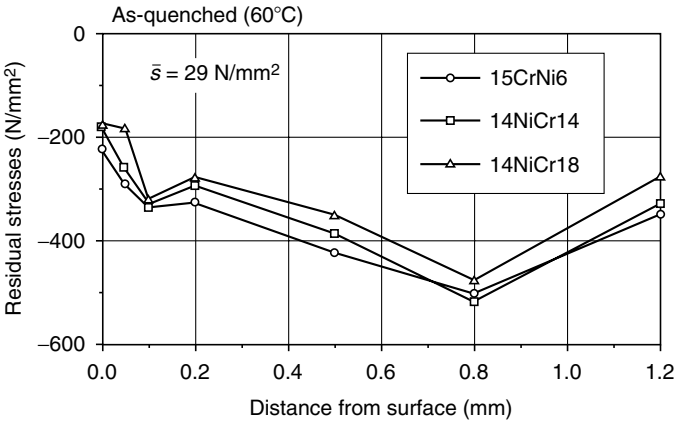

FIGURE 7.23 Residual stresses in the carburized case. (From O. Schwarz, J. Grosch, C. Genzel, W. Reimers, *Härterei Techn. Mitt. 49*:134, 1994.)

(stated are hexagonal ε-carbides Fe_2C and, particularly with higher carbon contents, orthorhombic η-carbides $Fe_{2,4}C$ and monoclinic γ-carbides $Fe_{2,5}C$) [91–97]. As a supersaturated α′-solid solution, the martensite contains up to 0.2% carbon segregated at lattice defects. The tetragonality and ensuing hardness of the martensite decrease [98]. With carbon contents lower than 0.2%, ε-carbide precipitation is highly improbable for energy-related reasons. Under the tempering conditions that are common practice in carburizing, only a small amount of retained austenite is transformed, the complete transformation of retained austenite would take 2 h of tempering at 300°C/572°F [99] or more than 50 h of tempering at 180°C/356°F [100] since the effects of tempering time and tempering temperature are interchangeable [101,102]. It is also possible to decrease the content of retained austenite by means of deep cooling, however only at the expenses of mechanical properties, in particular at the expense of fatigue resistance [65]. The transformations that occur in a microstructure subjected to 2 h of tempering at 180°C/365°F cannot be resolved in the optical microscope.

Impurity atoms, phosphorus in particular, may segregate at the austenite grain boundaries during carbon diffusion. In the diffusionless transformation, this state of segregation is inherited from the martensite and can lead to its embrittlement if retained austenite is transformed in tempering and cementite is precipitated at the former austenite grain boundaries that are segregated with phosphorus [103–108]. This one-step-temper-embrittlement occurs at temperatures around 300°C (572°F) and is only effective in rapid loading. In the common tempering practice, temper embrittlement of carburized components is hence very unlikely. Tempering causes a shift in the hardness gradient toward lower values and deeper case depth (Figure 7.24), the residual stresses become smaller (Figure 7.25).

In all the oxygen-containing carburizing atmospheres, oxygen reacts with the elements of the case microstructure, with chromium, manganese, and silicon oxidizing under carburizing conditions, with the reduction of iron, molybdenum, and nickel [109]. As a consequence, surface oxidation occurs and is most prominent alongside the grain boundaries where diffusion is faster [109–111]. The silicon content of the carburizing steels seems to be a measure of the surface oxidation depth, whereas the mangenese content controls the intensity of the intergranular oxidation [111]. The intergranular surface oxidation (Figure 7.26) is a characteristic of carburized microstructures [110,111] that can be avoided only by oxygen-free carburizing atmospheres as generally used in low-pressure carburizing or in plasma carburizing [26–29]. Carbide formation in carburized microstructures occurs when the C-potential is

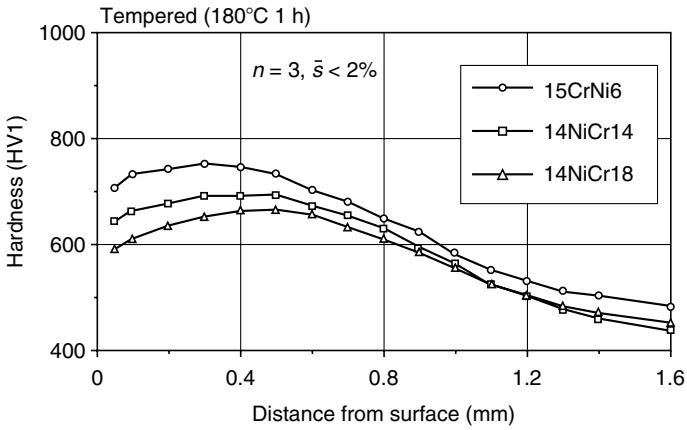

FIGURE 7.24 Effect of tempering on hardness gradients. (From O. Schwarz, J. Grosch, C. Genzel, W. Reimers, *Härterei Techn. Mitt. 49*:134, 1994.)

in the two-phase austenite/cementite field or when a microstructure, carburized in the homogeneous austenite phase field, in a subsequent heat treatment has stayed in the two-phase field for sufficiently long time. It should be taken into consideration that the carbon content of the eutectoid composition and the *S–E* line in the Fe–C diagram shift toward lower values by alloying elements, particularly by chromium [112]. With a C-potential near the cementite point in a two-stage carburization, ledges carburized by two planes are especially vulnerable (Figure 7.27). Carbides are almost always unwelcome, the more so if precipitated on grain boundaries (Figure 7.28). Nonmetal inclusions in steel such as sulfides or oxides remain unchanged by carburizing (appearing as dark areas in Figure 7.29).

7.4 REACTIONS WITH HYDROGEN AND WITH OXYGEN

Atomic hydrogen with the ability to diffuse into steel develops in electrochemical processes [113], welding [114] and heat treatments such as carburizing [115]. Hydrogen in steel can

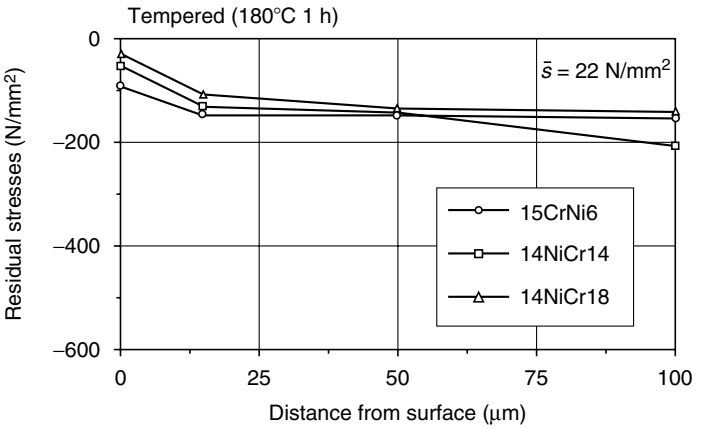

FIGURE 7.25 Effect of tempering on residual stresses. (From O. Schwarz, J. Grosch, C. Genzel, W. Reimers, *Härterei Techn. Mitt. 49*:134, 1994.)

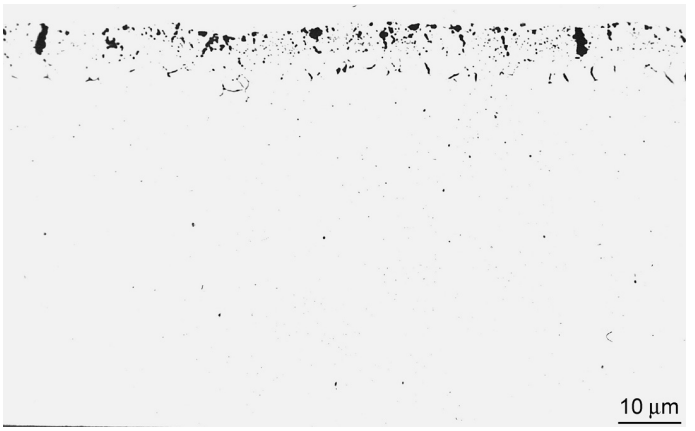

FIGURE 7.26 Surface intergranular oxidation (15CrNi6).

recombine to molecular hydrogen or cause failure by coupling with lattice defects, imperfections, and microcracks, with the hydrogen-induced embrittlement of high-strength steels as the most severe failure [116]. The partial pressure of hydrogen $p_{H_2} = 5.3 \times 10^{-7}$ in an atmosphere of 1 bar is very low, therefore it ought be possible for hydrogen as a highly diffusable element in interstitial position to effuse into the air making effusion annealing (soaking) unnecessary. Hydrogen, however, besides being interstitially soluted is also attached to lattice defects [117–119] such as vacancies, dislocations, and grain boundaries, to elements of the microstructure [120] such as precipitations and inclusions as well as to imperfections [121] such as pores and microcracks. These linkage conditions are zones of increased absorption of hydrogen (hydrogen traps) during intake and act as hydrogen sources in degassing, and therefore solubility and diffusion coefficient are dependent on morphology at temperatures below about 400°C (752°F) [122,123]. Carburizing steels [123] for instance are cited with diffusion coefficients of $D_H = 3.4 \times 10^{-7}$ cm^2/s for the core microstructure (0.2% carbon) and $D_H = 0.9 \times 10^{-7}$ cm^2/s for the case microstructure (0.8% carbon). Moreover, the combined hydrogen means that the maximum degassing rate [6]

$$f = \frac{c_t - c_0}{c_s - c_0} \tag{7.54}$$

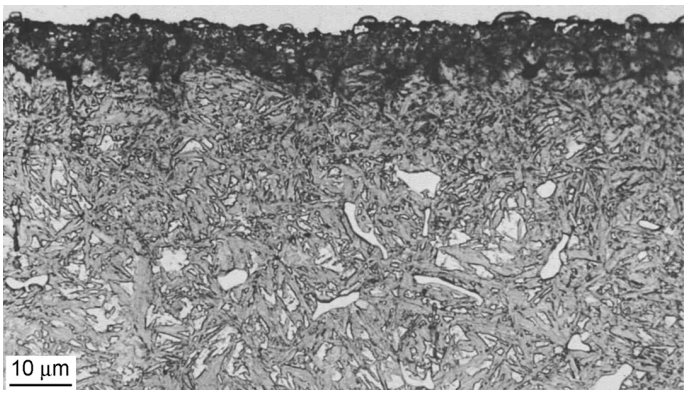

FIGURE 7.27 Globular carbides in the case microstructure (15CrNi6).

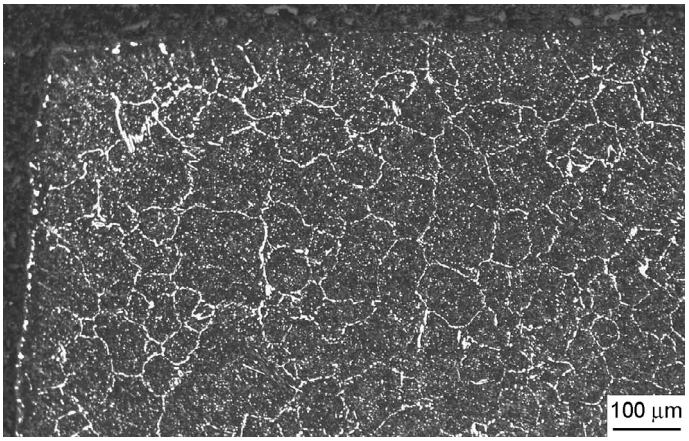

FIGURE 7.28 Carbides on grain boundaries in the carburized case (15CrNi6).

is dependent on degassing time and temperature (Figure 7.29 [124]). In Equation 7.54 c_0 is the initial hydrogen concentration and c_t the concentration after the degassing time t in a component, c_s is the concentration at the surface. At room temperature, normalized steel has a content of H = 0.05–0.1 µgH/gFe [114], which may rise up to 16 µgH/gFe [125] in deformed microstructures that have a high lattice defect density. As oxide layers impede the diffusion of hydrogen into the atmosphere, degassing is usually carried out in an oxygen-reducing atmosphere.

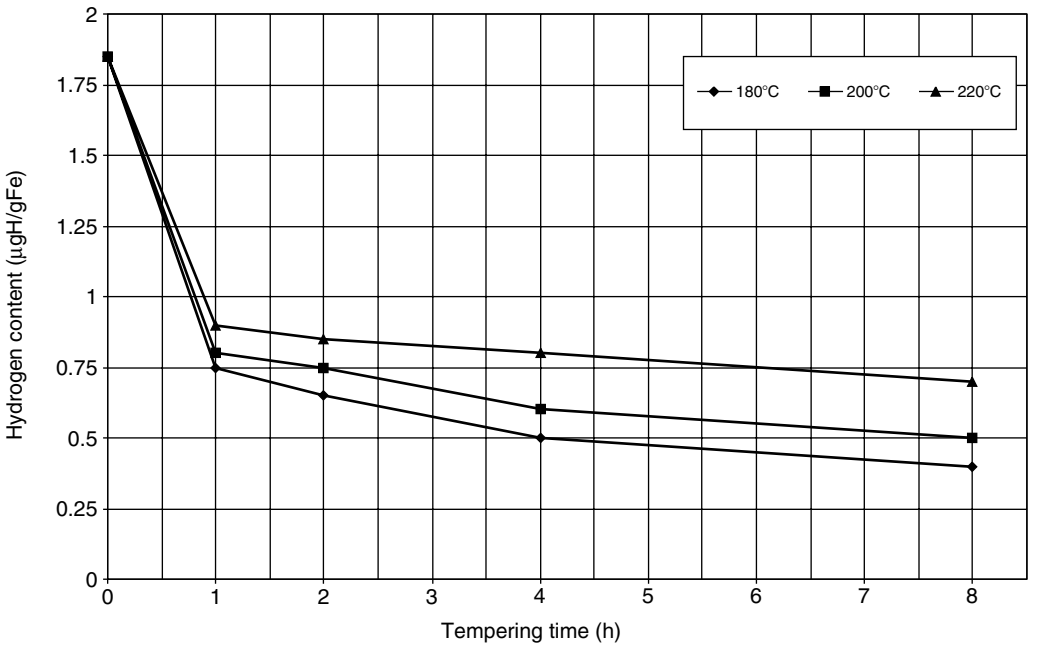

FIGURE 7.29 Effusion of hydrogen during tempering in air. (From H. Streng, *Zähigkeitsoptimierung einsatzgehärteter Gefüge*. Diss. TU Berlin, 1986.)

Iron is produced from iron oxide (and iron sulfide) ores by energy supply and therefore oxidizes in every atmosphere in which the oxygen partial pressure is higher than the oxygen partial pressure of iron oxide [32]. Figure 7.30 shows the dependence of the oxygen partial pressures of iron and its oxides on temperature [126–128]. Oxygen partial pressures above the Fe curve stimulate oxidation. The iron oxides are reduced on falling below their respective partial pressure. It follows that iron and steel with similar behavior oxidize in air ($p_{O_2} = 0.2$ bar). In technical terms, the surface of a steel is referred to as bright when the oxide layer, which inevitably forms in air, is only about 20-nm thick and thus not visible to the eye. Tarnished surfaces that are equivalent to oxide layers between roughly 50 nm (straw color) and roughly 70 nm (blue color) are regarded as technically clean. Layers of more than about 1 μm are discernible in the light microscope and develop up to about 5 μm during blueing, turning black. Oxide layers starting from about 10-μm thickness that form at temperatures exceeding 500°C (932°F) are no longer dense and scale off because of the different volumes of oxide and substrate.

Thick oxide layers may adversely affect the properties of a component whereas thin oxide layers obstruct the mass transfer and must therefore be reduced, in particular prior to carburizing or nitriding. It has been pointed out earlier that oxidation can be avoided either by lowering the (overall) pressure in the furnace (vacuum processing) or by displacing the air in the furnace by a protective gas. The partial pressure of wüstite $Fe_{0.947}O$ is according to [128] 1.07×10^{-19} bar at a temperature of e.g., 800°C (1472°F), i.e., to avoid oxidation caused by air ($p_{O_2} = 0.21$ bar) it would be necessary to decrease the pressure within the furnace to less than 10^{-18} bar. In vacuum furnaces, however, considerably smaller vacuum values in the

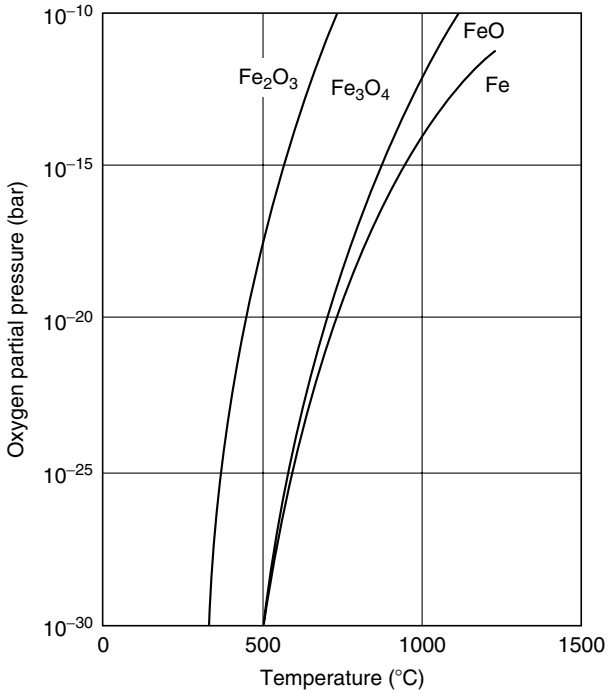

FIGURE 7.30 Oxygen partial pressure of iron and iron oxides. (From R. Hoffmann, *Härterei Techn. Mitt. 39*:61, 99, 1984; F.D. Richardson, J.H. Jeffes, *J. Iron Steel Inst. 171*:165, 1952; I. Barin, O. Knacke, *Thermodynamical Properties of Inorganic Substances*, Springer-Verlag, Berlin, 1973.)

range of 10^{-5} bar suffice to attain bright surfaces. During heating and evacuating, some of the trapped hydrogen will escape and react with the low-oxygen contents in the vacuum according to

$$2H_2 + O_2 \leftrightarrow 2H_2O \tag{7.55}$$

to generate water vapor, whose oxygen partial pressure is considerably lower than that of free oxygen. The reduced oxygen partial pressure may result in the reduction of iron oxides. Oxygen molecules that have not transformed to water vapor react with the steel to form invisible oxide layers. This phenomenon becomes clear by studying how the leakage rate of the vacuum furnace affects the growth of the oxide layer [126]. Figure 7.31 [126] shows the relationship between the maximum thickness of the layer (and the decarburizing depth of the case related to 1% carbon in the steel) and the leakage rate of a vacuum furnace with the parameters final pressure, furnace volume, and treatment time. With leakage rates smaller than 10^{-2} mbar·l/s, which can be obtained without much technical difficulty, the penetrating oxygen is of virtually no importance to the thickness of the oxide layer (and to the decarburizing depth). It follows that in industrial vacuum furnaces oxidation is avoided by gas reactions and thus the vacuum (heat) treatment can be designated as heat treatment with gases.

Pure nitrogen is inert with respect to steel and thus an economical protective gas. In a nitrogen atmosphere with an oxygen partial pressure of zero, iron oxide is reduced until the oxygen partial pressure of the atmosphere, which has developed from the emitted oxygen, reaches the same level as the oxygen partial pressure of the oxide. The oxygen partial pressures of the iron oxides (Figure 7.30) are minimal, and the nitrogen atmosphere scarcely reduces. Industrial nitrogen contains moreover small amounts of oxygen that are equivalent to an oxygen partial pressure in the size range of 10^{-5} bar and even purified nitrogen still contains oxygen equivalent to a partial pressure of about 10^{-6} bar [129]. Therefore, at least 2 Vol% hydrogen are generally added to a nitrogen atmosphere to ensure that according to

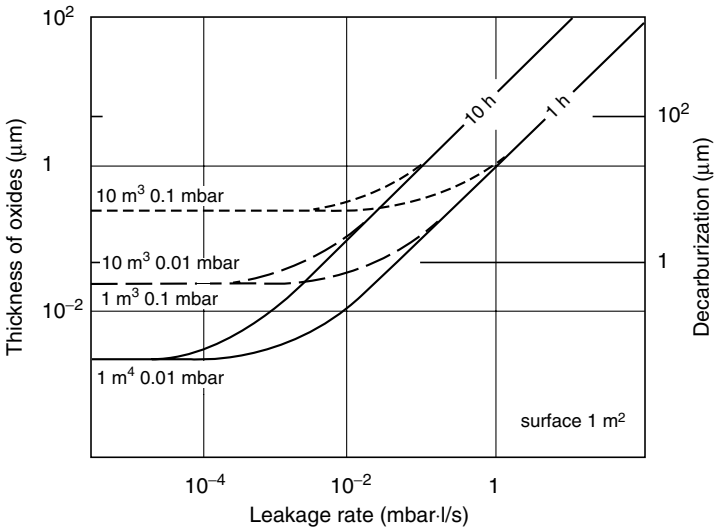

FIGURE 7.31 Leakage rate of a vacuum furnace and decarburization rate. (From R. Hoffmann, *Härterei Techn. Mitt. 39*:61, 99, 1984.)

Equation 7.56 water vapor is generated via the transformation of the total of the existing or developing oxygen that with leaking furnaces diffuses into the furnace from the ambient air. The oxygen partial pressure of such an atmosphere can be calculated according to

$$p_{O_2} = \frac{k_p p_{H_2O}}{p_{H_2}} \tag{7.56}$$

with the equilibrium constant k_p listed in Ref. [128]. Atmospheres consisting of nitrogen, hydrogen, and water vapor can easily be assessed because the ratio of H_2O to H_2 of their respective partial pressures is independent of temperature. Figure 7.32 [126] shows the interrelationship between the ratio of partial pressures, oxygen potential, and temperature, and also plots of the phase fields of iron and iron oxides. From these it is possible to ascertain gas compositions with neutral, reducing, or oxidizing effects. The HN gases, or mono gases, composed of nitrogen and hydrogen, are generated from ammonia decomposing completely,

$$2NH_3 \rightarrow 3H_2 + N_2 \tag{7.57}$$

or from a purified and dried generator gas. According to Equation 7.45 these gases have a decarburizing effect, with a rather sluggish reaction [44] that is only effective at treatment temperatures of about 500°C (932°F) and more. HN gases are therefore mainly used in the heat treatment of steels with a low carbon content or at temperatures below 500°C (932°F) such as for tempering. Pure hydrogen atmospheres have excellent heat conduction properties and are utilized as a protective gas, for instance in bell-type annealing furnaces. Thereby to avoid explosive mixture of oxygen and hydrogen, it is necessary to control the oxygen content by means of the oxygen sensor. In controlled oxidizing or blueing, annealing is accomplished in an atmosphere of saturated water vapor (99.9%), the reaction according to Equation 7.56 proceeding from H_2O, thereby forming a black oxide layer of about 1–5 μm thickness whose

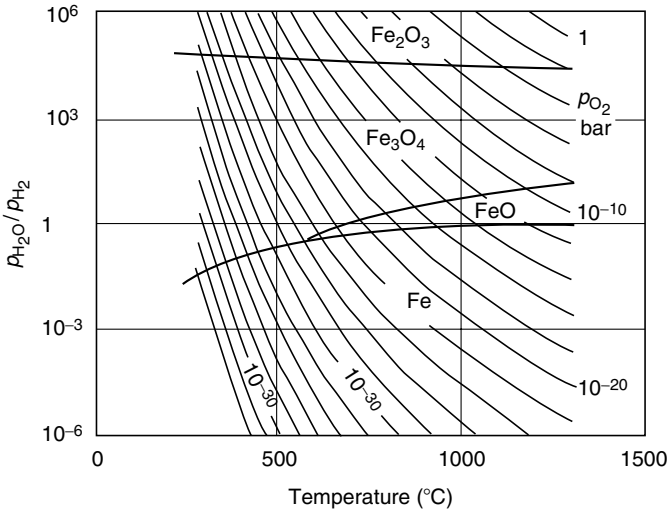

FIGURE 7.32 Partial pressure relation p_{H_2O}/p_{H_2} versus temperature. (From R. Hoffmann, *Härterei Techn. Mitt. 39*:61, 99, 1984.)

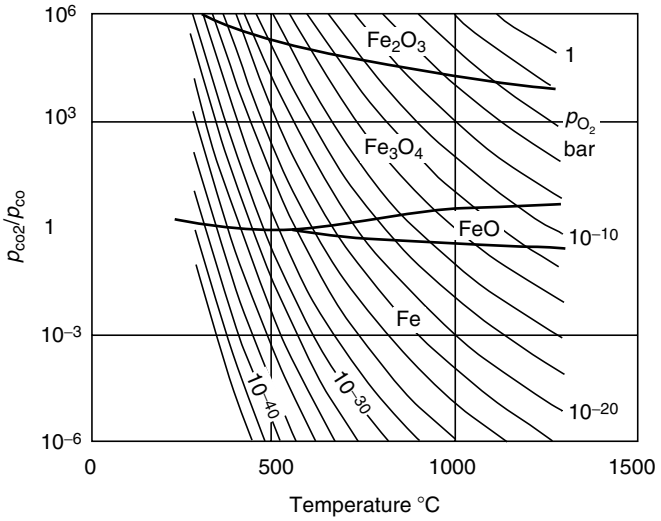

FIGURE 7.33 Partial pressure relation p_{CO_2}/p_{CO} versus temperature. (From R. Hoffmann, *Härterei Techn. Mitt. 39*:61, 99, 1984.)

corrosion resistance is better than that of iron. This procedure is mainly applied for protecting tools against corrosion from handling.

Decarburization is avoided by using gases composed of CO_2 and CO, H_2 and H_2O diluted with N_2 (referred to as CCHN gases or exo gases) as protective gases, with their C-potentials adjusted to the carbon content of the steel according to the interrelationships as discussed in Section 7.3.2. At thermodynamic equilibrium, which is established at higher temperatures according to the homogeneous water gas reaction 7.26, there is a correspondence among the oxygen partial pressures calculated from the ratio of H_2O/H_2 and that of CO_2/CO, and also with the free oxygen. This means that in addition to the interrelationship of the H_2O/H_2 ratio as shown in Figure 7.32, the corresponding interrelationship of the CO_2/CO ratio as shown in Figure 7.33 [126] has to be taken into consideration. As a rule, CCHN gases are generated as generator gases by the combustion of hydrocarbons such as methane (natural gas) or propane with air, the ratio of combustion gas to air determining the quantitative composition, and thus the C-potential.

7.5 NITRIDING AND NITROCARBURIZING

7.5.1 Introduction

The industrial application of nitriding started with studies by Machlet [130] and Fry [131,132], who introduced the classical gas nitriding in ammonia atmospheres at the temperature range of α-iron. This gas nitriding process as recommended by Machlet and Fry is still applied to date as a treatment that causes minimal distortion in components consisting primarily of nitriding steels that have to endure abrasion, rolling fatigue, and fatigue. Depending on the desired nitriding hardness depth, a treatment time of up to 120 h is necessary. Based on studies by Kinzel and Egan [133], nitriding in cyanide-containing molten salts has subsequently been developed [134–136]. In this procedure both carbon and nitrogen are introduced into the case, and the process is termed salt bath or liquid nitrocarburizing. Nitrocarburized

microstructures also develop in gaseous atmospheres when ammonia is blended with a carbon-emitting gas [137–144]. Gas nitrocarburizing is widely applied, with the use of additional gases such as endo gas, exo gas, carbon dioxide, methylamine, and methanol resulting in several processing variants. This chapter describes gas nitriding and gas nitrocarburizing.

At standard pressure, solid and liquid iron dissolve only a small amount of nitrogen, α-iron up to an optimum of 0.005 wt% at 810°C (1490°F) on the transition to γ-iron, which at this temperature has also its maximum solubility of 0.035 wt% for nitrogen (Figure 7.34 [145]), a binary phase diagram of no interest. According to Sieverts, solubility can be improved by increasing the partial pressure of nitrogen in proportion to the square root of the partial pressure of nitrogen, $\sqrt{p_{N_2}}$. The main constituent of nitriding atmospheres is ammonia, NH_3, which on decomposing causes the partial pressures of nitrogen to increase considerably, thus responsible for the formation of different solid phases at equilibrium [146,147] that vary in their respective pressure–temperature–concentration diagrams according to their nitrogen content and can be projected on a joint temperature–concentration surface plane in a Fe–N phase diagram (Figure 7.35 [146–148]) that is consequently not at equilibrium at $p = 1$ bar. In technical application, processing is done mainly in the phase field α-iron, which at 590°C (1094°F) dissolves a maximum of 0.115 wt% nitrogen. The low solubility of nitrogen in α-iron together with the necessity of producing high partial pressures for nitriding has so far made it almost impossible to use nitrogen potentials that lead to a nitrogen absorption only in the α-iron. The aim of the generous nitrogen supply is the formation of both nitrides and a microstructure that consists of a compound layer of nitrides and an adjoining diffusion zone. The nitriding atmospheres are at a nonequilibrium in this process, making a quantitative treatment such as in carburizing impossible. In actual practice, a processing characteristic indicating the nitriding power or nitriding potential [149–153], or sensors [154–155] are therefore used, allowing to adjust the gas composition to the desired microstructure, i.e., characteristic and sensor signals are calibrated with regard to the nitriding

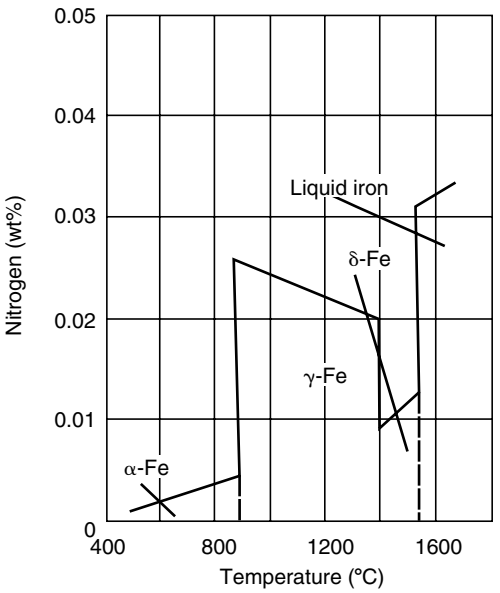

FIGURE 7.34 Solubility of nitrogen in steel at 1 bar. (From F. Leitner, E. Plöckinger, *Edelstahlerzeugung*, Springer-Verlag, Berlin, 1964, p. 259.)

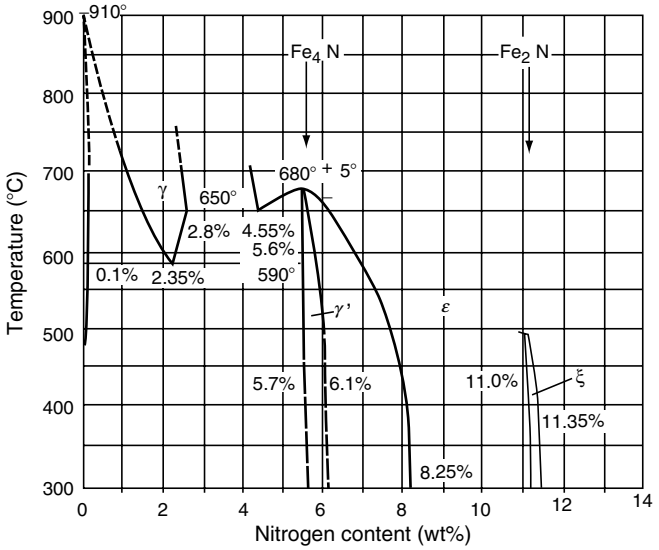

FIGURE 7.35 Binary Fe–N phase diagram. (From M. Hansen, K. Anderko, *Constitution of Binary Alloys*, McGraw Hill, New York, 1958.)

microstructures. Hence, the following discussion starts with describing nitriding and nitrocarburizing microstructures and subsequently deals with the processing.

7.5.2 Structural Data and Microstructures

7.5.2.1 Structural Data

Nitrogen has a (homopolar) atom diameter of 0.142 nm and is soluted in iron in interstitial position in octahedral voids of the cubic lattice, which has a maximum diameter of 0.038 nm in body-centered cubic α-iron and a maximum diameter of 0.104 nm in face-centered cubic γ-iron. Nitriding of pure iron at temperatures of up to 590°C (1094°F) with an increasing nitrogen content according to Figure 7.35 leads to the formation of the following phases:

1. Body-centered cubic α-iron, which dissolves 0.001 wt% nitrogen at room temperature and 0.115 wt% nitrogen at 590°C (1094°F)
2. Face-centered cubic γ′-nitride, Fe_4N, which dissolves 5.7–6.1 wt% nitrogen (stoichiometric 5.88 wt%)
3. Hexaedral ε-nitride, $Fe_{2-3}N$, which exists in the range of 8–11 wt% nitrogen
4. Orthorhombic ζ-nitride, Fe_2N, forms at temperatures below about 500°C (932°F) and nitrogen contents exceeding 11 wt%, i.e., at formation conditions that are not used in technical practice

At temperature above 590°C (1094°F), γ-iron is formed according to the binary Fe–N phase diagram (Figure 7.35), and it dissolves a maximum of 2.8 wt% nitrogen at 650°C (1202°F). At 590°C (1094°F) and 2.35 wt% nitrogen, an eutectoid microstructure designated as braunite is produced that consists of α-iron and γ′-nitride. Nitrogen has a stabilizing effect on austenite, which therefore transforms slowly. Martensite formed on a Fe–N basis is moreover rather soft, the technical nitriding processes are therefore usually limited to the ferrite field. The structural data discussed above are valid only if pure iron is nitrided, that is to say they are valid only as an exception because generally the carbon present in the steel,

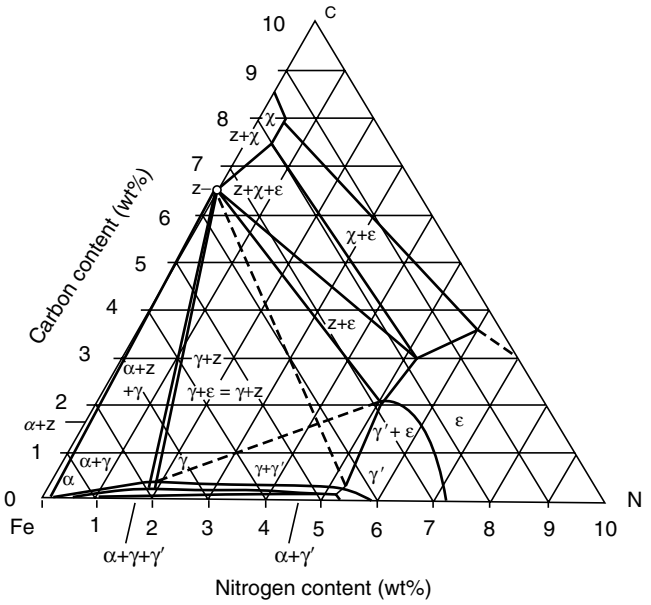

FIGURE 7.36 Ternary Fe–C–N phase diagram at 575°C. (From G. Langenscheidt, Beitrag zum System Eisen-Stickstoff-Kohlenstoff. Diss. BA Clausthal, 1964.)

and in nitrocarburizing also present in the nitriding medium, is incorporated into the case microstructure during the process and competes with the nitrogen. The nitrides absorb carbon, causing the range at which the carbonitrides Fe_x–N_y– C_z exist to broaden relative to the binary system Fe–N, which can be inferred from the ternary system Fe–C–N (Figure 7.36 [156] and Figure 7.37 [157]). Moreover, there is the possibility of θ-carbide (cementite) formation. In nitriding or nitrocarburizing alloyed steels, it should also be taken into account that nitrogen and carbon are prone to form nitrides or carbonitrides with alloying

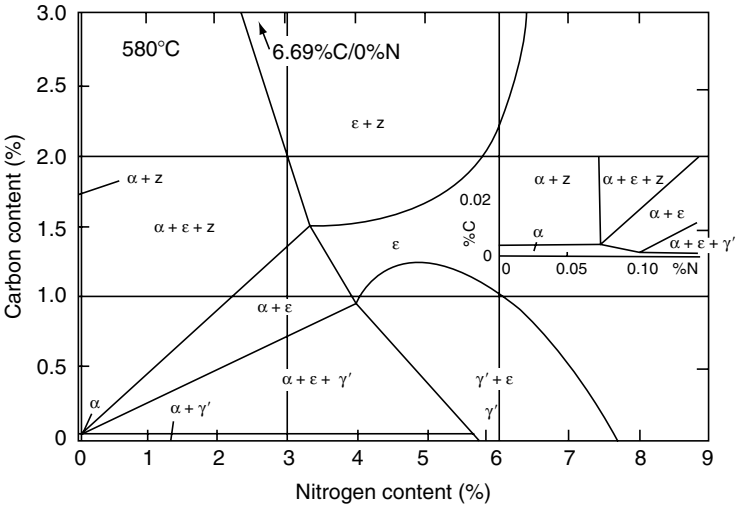

FIGURE 7.37 Part of ternary Fe–C–N phase diagram at 580°C. (From U. Huchel, J. Kunze, *Härterei Techn. Mitt. 46*:351, 1991.)

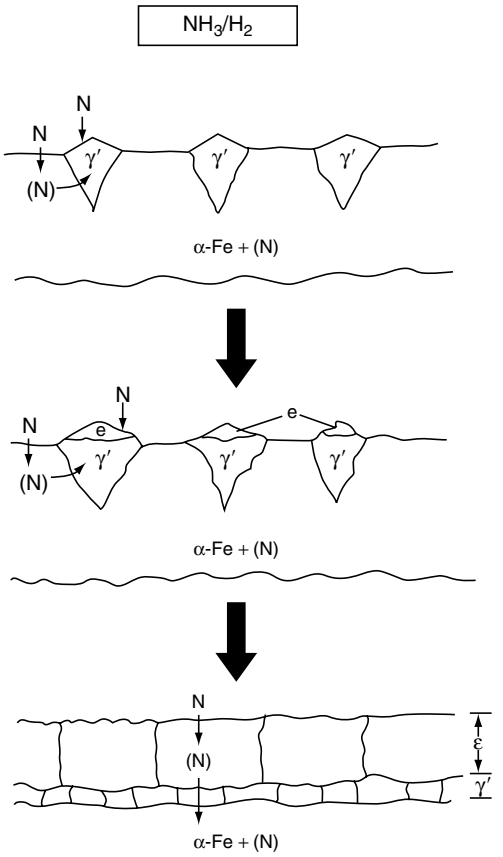

FIGURE 7.38 Scheme of nucleation of γ′- and ε-nitrides on iron. (From M.A.J. Somers, E.J. Mittemeijer, *Härterei Techn. Mitt. 47*:5, 1992.)

elements such as aluminum, chromium, and vanadium, whose composition can only be given in the general term M_x–N_y or M_x–N_y–C_z, where M stands for metal. Present knowledge allows only to apply the van Orstrand–Dewey solution (Equation 7.19) of the diffusion equation for nitrogen in the α-iron [158]. The diffusion coefficients (as listed in Ref. [153]) are: in α-iron, $D_N^{\alpha} = 6.6 \times 10^{-3} \exp(-77{,}820/RT)$; in γ′-nitride, $D_N^{\gamma} \approx (1/25) D_N^{\alpha}$; and in ε-nitride, $D_N^{\varepsilon} \approx (1/60) D_N^{\alpha}$.

Nitrides develop by γ′-nucleation at the interface between nitriding atmosphere and the substrate, and subsequent nucleation of ε-nitrides at the interface between the atmosphere and the already formed γ′-nitrides (Figure 7.38 [159]) until the build-up of a complete layer of γ′-nitride toward the substrate and of ε-nitride toward the surface, which is called the compound layer. This compound layer allows controlled processing because of its defined concentration gradients, nitrogen diffusion is however considerably slower in the compound layer than in the ferrite.

7.5.2.2 Microstructures of Nitrided Iron

The described microstructural formation is found in nitrided pure iron (Figure 7.39), the sequence of nitride layers is clearly visible in SEM micrographs (Figure 7.40). The ε-nitride layer shows pores that, according to pressure theory [159], form when nitrogen atoms in the ε-nitride layer recombine to nitrogen molecules, thus creating high pressures. A consistent

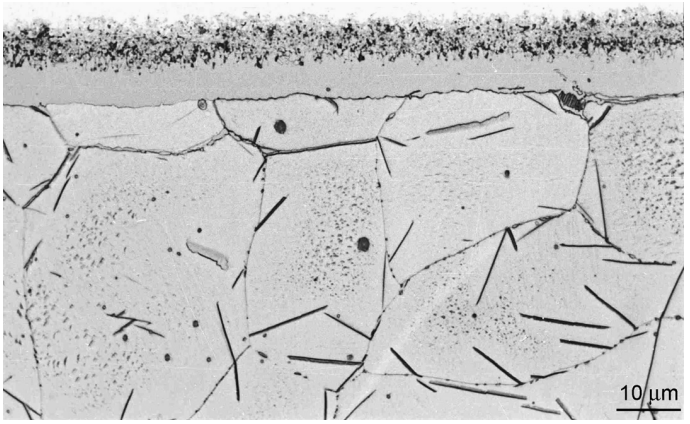

FIGURE 7.39 Pure iron nitrided, etched with Nital.

theory on the causes of porosity has however not been offered yet [160]. Carbon changes the morphology of the compound layer, causing part of the ε-nitride and γ′-nitride to arrange side-by-side. The carbon may originate in the steel or in the nitriding atmosphere (Figure 7.41, nitrocarburized pure iron), in comparison with nitrided pure iron (Figure 7.42). The samples in Figure 7.41 and Figure 7.42 are etched with Murakami solution, which has a stronger effect on carbon-containing microstructure areas, hence making them appear dark. The hardness of the compound layer is in the range of 570 HV0.02 and not significantly affected by the described morphological differences. Beneath the compound layer, nitrogen is soluted in α-iron (diffusion zone) at nitriding temperature and segregates during cooling in correspondence with the decreasing of solubility in α-iron as coarse-shaped hexaedral body-centered α″-nitrides, Fe_8N (Figure 7.39). In quenched microstructures, nitrogen remains in supersaturated solution, and subsequent aging leads to more uniformly dispersed finer α″-nitrides (Figure 7.43, aged 20 min at 325°C/617°F). A considerable increase in the hardness of the diffusion zone is only achieved by the amount of supersaturated soluted

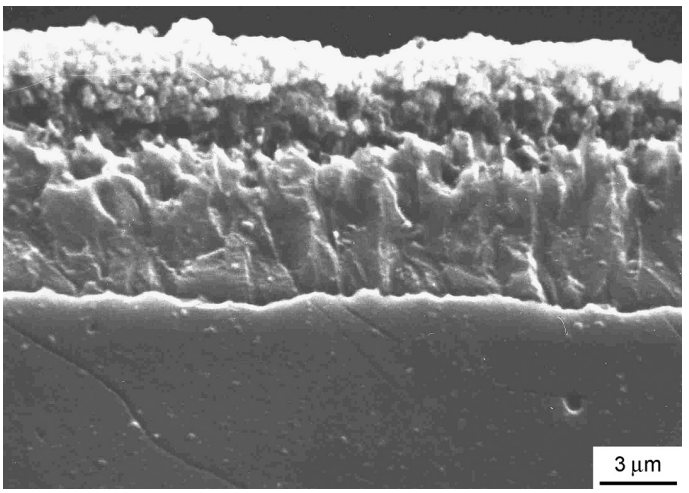

FIGURE 7.40 Pure iron nitrided, SEM micrograph.

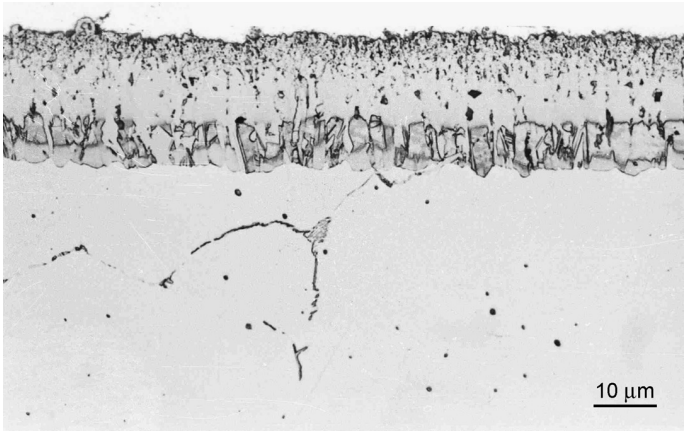

FIGURE 7.41 Pure iron nitrocarburized, etched with Murakami.

nitrogen (solid solution strengthening) and is decreased again to the values characteristic of the slowly cooled diffusion zone by aging.

7.5.2.3 Microstructures of Nitrided and Nitrocarburized Steels

With steels, there are no major changes in the described microstructures, some specific characteristics however are altered by the existing carbon content and by nitride-forming alloying elements. With respect to the conditions at which those nitrides form, it should be noted that the temperatures and concentrations of the phase limits in Figure 7.35 through Figure 7.37 are shifted by alloying elements. Given equal nitriding conditions as to nitrogen supply and nitriding time, the compound layer of plain carbon steels is always thicker than that of steels alloyed with nitride-forming elements (Figure 7.44 [161]) because nitrides or carbonitrides formed with alloying elements contain more nitrogen than nitrides or carbonitrides formed with iron. The thickness of the compound layer, which is equivalent to the area of increased nitrogen content, is further dependent on the nitriding time (Figure 7.45), the

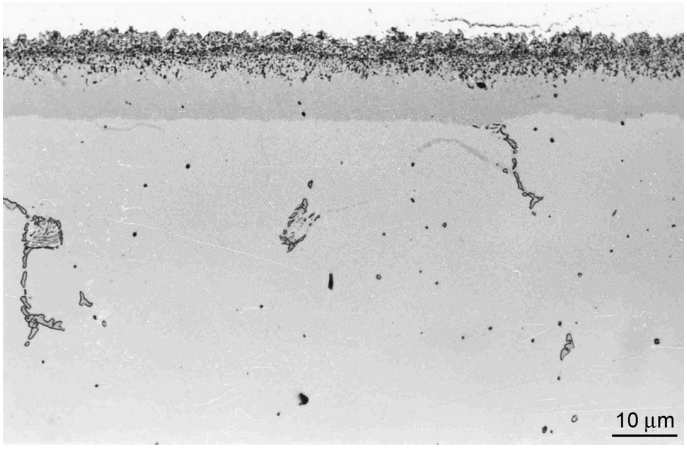

FIGURE 7.42 Pure iron nitrided, etched with Murakami.

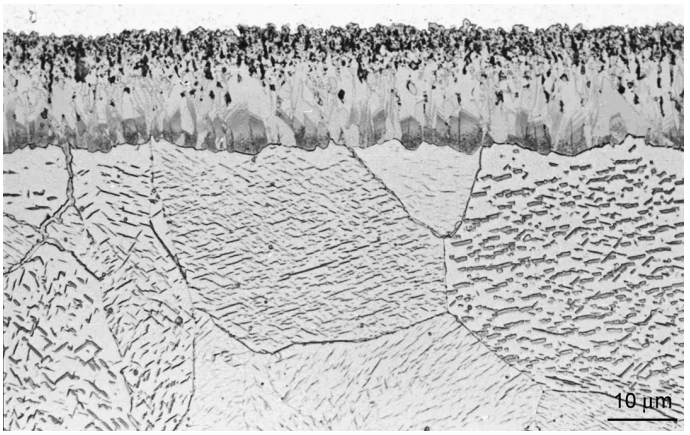

FIGURE 7.43 Pure iron, nitrided, quenched and aged (325°C, 20 min).

nitriding temperature (at set nitriding time, Figure 7.46) and, most markedly, on its preliminary treatment (Figure 7.47, differently processed). The share of the porosity fringe is lower with alloy steels than with plain carbon steels, the nitriding process however has little influence on the formation of the compound layer (Figure 7.44) as well as on the overall microstructure morphology, on condition that the respective nitriding conditions are equal. The compound layer contains carbon, which is located as carbon enrichment in the form of a carbon hill at the inner interface between compound layer and diffusion zone and can be made visible by means of an adequate etching technique (Figure 7.42, Murakami solution) as well as by analytical methods (Figure 7.48). Within the diffusion zone of alloy steels, the total of the diffusing nitrogen is tied up in nitrides or carbonitrides that do not resolve under the

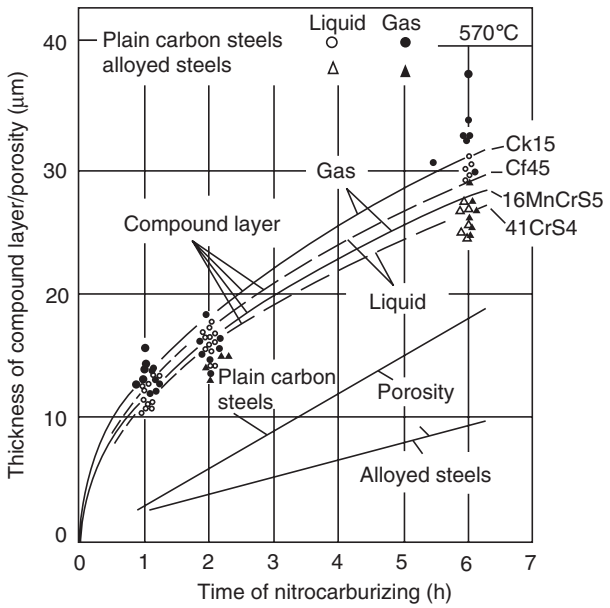

FIGURE 7.44 Thickness of compound layer versus treatment time. (From D. Liedtke, J. Grosch, *Proceedings of the 5th International Congress on Heat Treatment*, Budapest, 1986, pp. 8–16.)

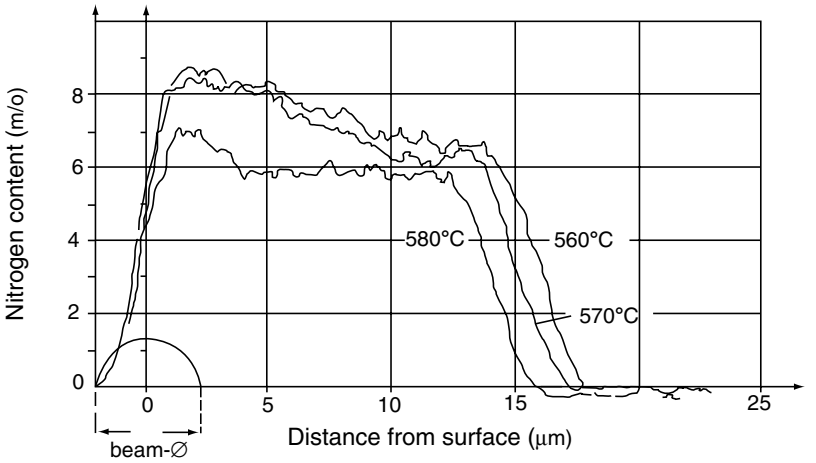

FIGURE 7.45 Influence of treatment temperature on thickness of compound layers (Ck15—gas nitrocarburized at 570°C for 3 h).

light microscope. The formation of a supersaturated α-iron occurs only with plain carbon steels, by slow cooling from nitriding temperatures or by aging of the quenched microstructure (Figure 7.43) is possible for this α-iron to segregate iron nitrides.

The compound layers of plain carbon steels, which form iron nitrides or iron carbonitrides, reach a hardness of 500 to 800 HV0.02, that of alloy steels in which the iron in the nitrides or the carbonitrides is replaced by alloying elements, reach about 900–1000 HV0.02. Nitriding steels that are alloyed with aluminum or molybdenum can have a hardness of up to 1200 HV0.02. Denoting the carbon atoms (soluted or precipitated as nitrides or carbonitrides), the hardness of the diffusion zone must be related to the hardness of the material prior to its heat treatment. The initial hardness is dependent on material proper, above all on its carbon content, and on its microstructure, the higher hardness of quench and temper microstructures is only maintained if at nitriding temperatures the material has good

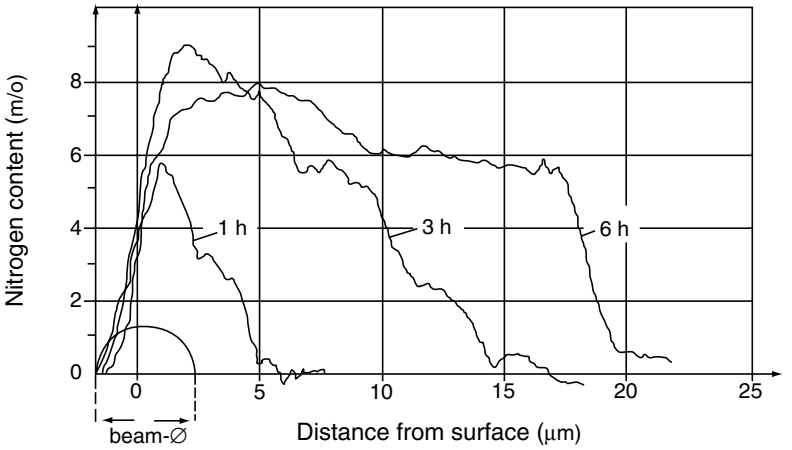

FIGURE 7.46 Influence of treatment time on thickness of compound layers (Ck15—gas nitrocarburized at 570°C for 3 h).

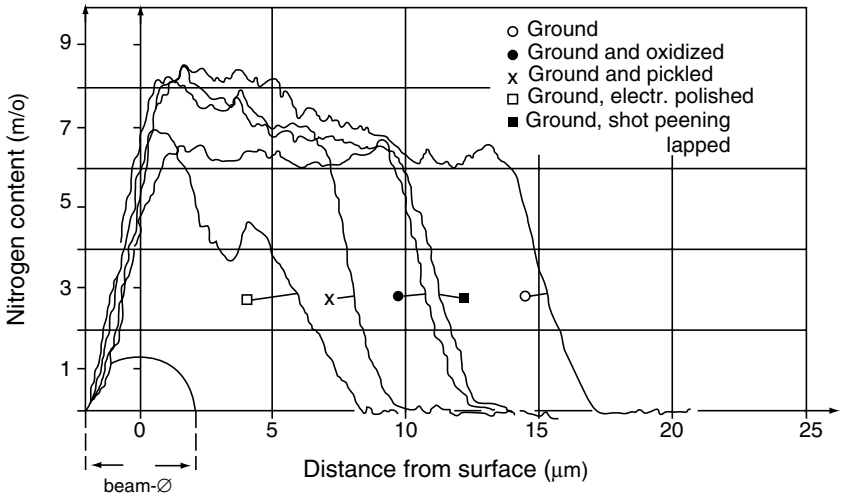

FIGURE 7.47 Influence of pretreatment preparation on thickness of compound layers (Ck15—gas nitrocarburized at 570°C for 3 h).

tempering properties. Figure 7.49 shows a result typical of a gas nitrocarburized quench and temper steel. The nitrides of nitriding steels contain more nitrogen, accounting for the formation of harder compound layers and more shallow nitriding case depths (Figure 7.50) at equal nitrogen supply.

Cr- and Cr–Ni-alloyed stainless steels are comparatively soft and thus have a rather poor wear resistance. In recent years nitriding processes were developed that led to a higher hardness of the case and thus to a better wear resistance of these steels without diminishing their corrosion resistance. The processes can be distinguished by their nitriding temperatures. At the low-temperature nitriding processes [162–164] nitriding is carried out at temperatures between 250 and 450°C, preferably in plasma, and a layer of usually 6–20 µm thickness is produced in which around 8–12 wt% nitrogen are soluted. The metastable tetragonal

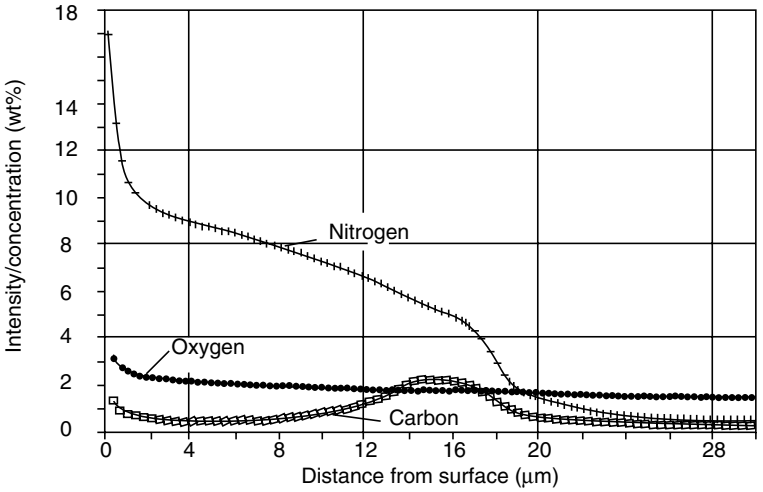

FIGURE 7.48 Gradients of nitrogen, carbon, and oxygen in the compound layer (C15, gas nitrocarburized).

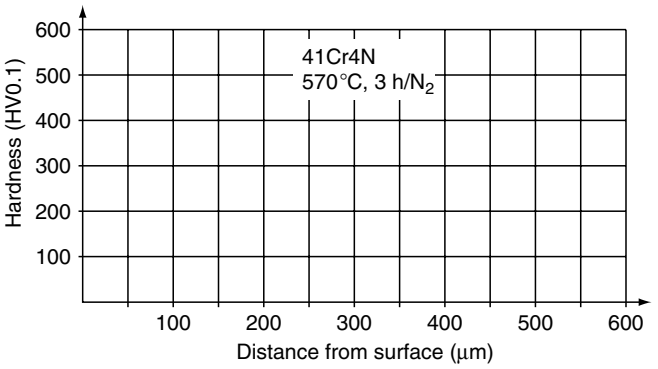

FIGURE 7.49 Hardness gradient of gas nitrocarburized steel 42CrS4 (hardness of compound layer 928 HV0.015, surface hardness 352 HV10, core hardness 189 HV0.1).

face-centered solid solution is markedly expanded and is designated as S-phase.* The corrosion resistance of the stainless steel remains unchanged, or enhanced by the soluted nitrogen as long as no Cr-nitrides are precipitated. The high hardness of the S-phase in the range of 1400–1600HV changes abruptly to the core hardness, i.e., the layer enhances the wear resistance at abrasive and adhesive loading with high relative rates and low pressure directed to the surface. At the high-temperature nitriding processes [165–167] of Cr- and Cr–Ni-alloyed stainless steels, the temperatures range between 1050 and 1150°C. At these temperatures molecular nitrogen is dissociated, nitrogen diffuses into the case at pressures applied between 0.2 and 3 bar, with usually 0.3–0.9 wt% homogeneous soluted nitrogen and depths up to 2.5 mm. Cr- or Cr–Mo-alloyed martensitic stainless steels are diffusionless transformed, Cr–Ni-alloyed stainless steels are cooled down in such a way that Cr-nitride precipitation does not occur and nitrogen remains soluted. In both cases a hardness profile is established, the hardness increase is more marked in the Cr–Ni-alloyed steels (at an overall lower level).

7.5.2.4 Microstructural Specialites

On slow cooling, nitriding and nitrocarburizing at temperatures above 590°C the eutectoid transformation of austenite to ferrite and γ′-nitride leads to a special microstructure

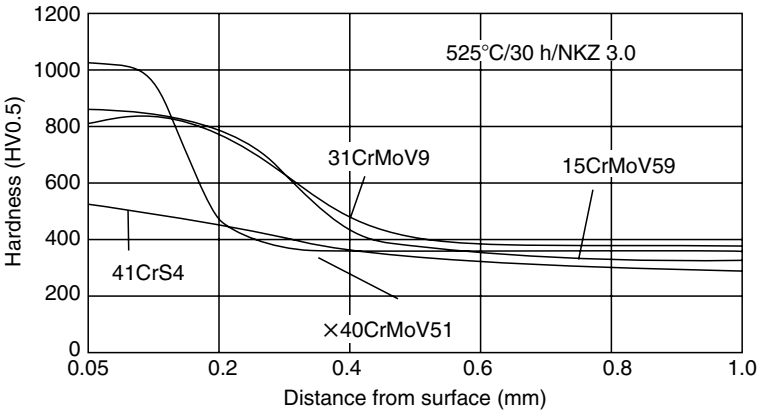

FIGURE 7.50 Hardness gradients of nitrided steels.

*An S-phase in stainless steels can also be obtained by lower temperature carburizing.

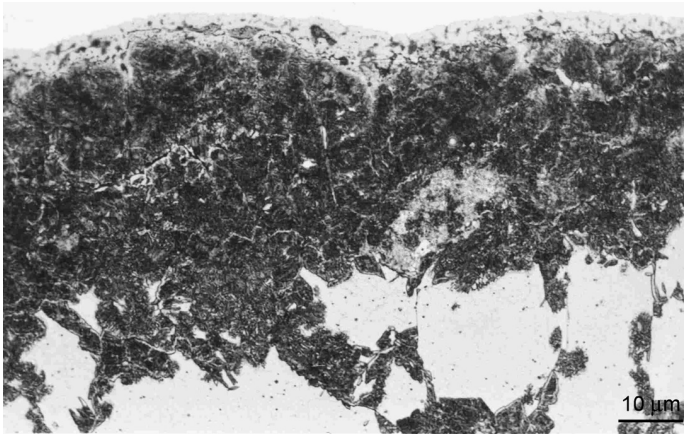

FIGURE 7.51 Braunite (St 37, nitrided at 640°C for 16 h).

(Figure 7.51), which is sometimes called Braunite [132]. In quenched microstructures the austenite beneath the compound layer is retained (Figure 7.52). Carbides in the initial microstructure absorb nitrogen and are transformed to carbonitrides. With larger carbides and carbides with alloying elements, the nitriding time necessary to completely dissolve the carbides in the compound layer is often not long enough, thus explaining the existence of left-over carbides in the compound layer (Figure 7.53). The nitrogen absorption in the carbides is plainly visible by their changed etchability. Nonmetallic inclusions do not respond to nitrogen and remain existent; examples are graphite in globular cast iron (Figure 7.54) and manganese sulfides in machining steels (Figure 7.55).

7.5.3 Nitriding and Nitrocarburizing Processes

7.5.3.1 Nitriding

A nitriding atmosphere consists always of ammonia, NH_3, sometimes diluted with additional gases such as nitrogen, N_2, and hydrogen, H_2. At the usual nitriding temperatures of 500–570°C (932–1058°F), ammonia is in instable thermodynamic state and dissociates according to

$$2NH_3 \rightarrow 2N_{(ad)} + 6H_{(ad)} \rightarrow N_2 + 3H_2 \tag{7.58}$$

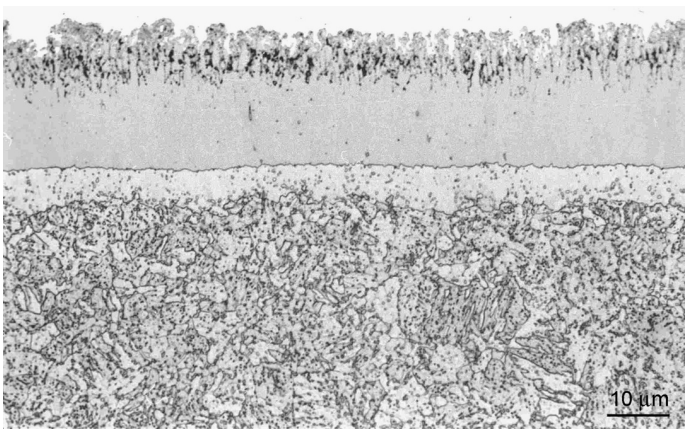

FIGURE 7.52 N austenite (Ck35, nitrocarburized at 630°C for 40 min and quenched in water).

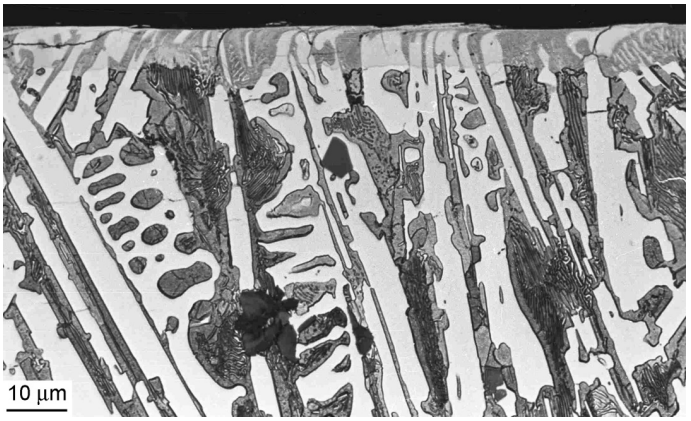

FIGURE 7.53 Carbides in the nitrocarburized case of chill-cast iron.

This reaction, valid for thermal equilibrium, leads to degrees of dissociation higher than 99% and thus to the formation of a protective gas without any nitriding effect, as mentioned in Chapter 10 (Equation 7.57). Despite the beneficial, catalytic effect of the surfaces of the workpieces and the furnace wall, the dissociation of ammonia in the furnace is a very sluggish process, probably because the mean residence time of the gas in the furnace is too short for reaching an equilibrium by recombining to molecular nitrogen [152,168]. Technically used ammonia-based nitriding atmospheres contain therefore rarely less than 20%, frequently up to 50% ammonia, hence their degree of dissociation is far from equilibrium. The remaining ammonia content is decisive for the effect of nitriding, during which nitrogen diffuses into the steel according to the reaction

$$NH_3 \rightarrow N_{(\alpha)} + (3/2)H_2 \tag{7.59}$$

that occurs within the boundary layer. The nitrogen activity, which is the driving force in the mass transfer, can be calculated according to

$$a_N = K_N \frac{p_{NH_3}}{p_H^{3/2}} \tag{7.60}$$

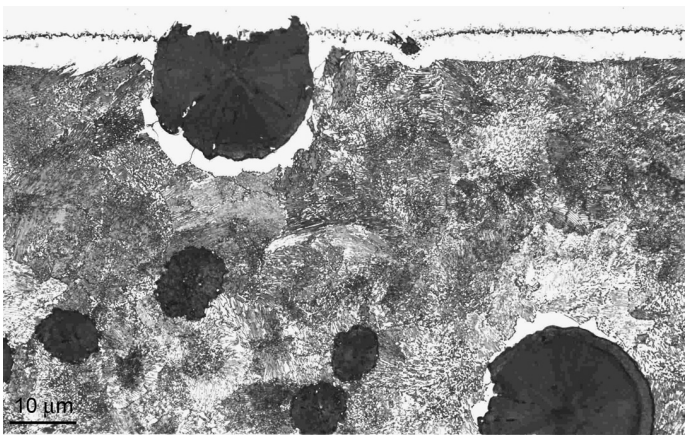

FIGURE 7.54 Graphite spheroides in the compound layer (GGG 70).

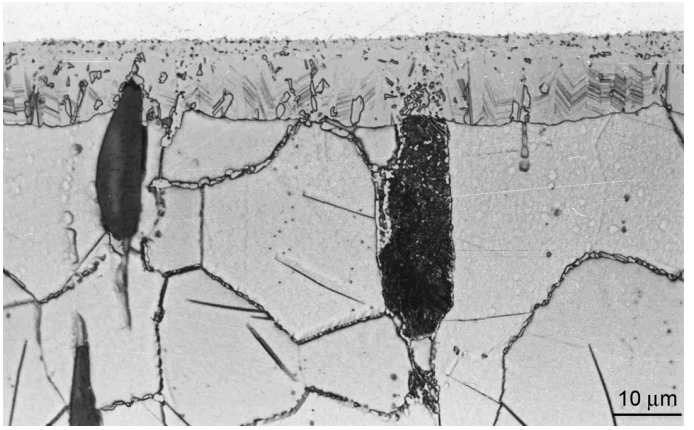

FIGURE 7.55 MnS in the compound layer (9SMnPb28K).

As the nitrogen transfer is comparatively low, the release of hydrogen from the ammonia molecules determines the rate of the process [168]. Therefore, as mentioned earlier, nitriding times are rather long, up to 120 h [169].

The nitriding effect of a nitriding atmosphere is defined by its degree of dissociation and can be used for controlling the nitriding process, with high degrees of dissociation always indicating a near-equilibrium state where the nitriding effect is low. In processing, it is common practice to use a constant degree of dissociation but sometimes a two-stage procedure involving variations of temperature and of dissociation degree is applied (Floe process [170,171]. However, the measured ammonia content is not equivalent to the actual degree of dissociation. In ammonia dissociation according to Equation 7.58, two molecules of ammonia dissociate to one molecule of nitrogen and three molecules of hydrogen. This increase in volume dilutes the ammonia content, as do additional gases, and must be taken into account in ascertaining the actual degree of dissociation. The nitriding effect can be determined more easily by means of the nitriding characteristic NK (nitriding power or nitriding potential) [149–152]

$$\mathrm{NK} = \frac{p_{\mathrm{NH_3}}}{p_{\mathrm{H}}^{3/2}} \tag{7.61}$$

that, following Equation 7.62, is to date generally used for describing the nitridability of an ammonia atmosphere. The hydrogen partial pressure originates from the dissociation of ammonia and can be altered and controlled by additional gases. According to the Lehrer diagram (Figure 7.56 [172]), the microstructure morphologies that can be obtained in a compound layer are determined by both nitriding characteristic and temperature. The validity of the diagram has, in essence, been corroborated in practice, the phase boundaries are valid for pure iron with respect to quantity, and with steels are dependent on their alloy content. From Figure 7.56 it is discernible that at nitriding temperatures of more than 500°C (932°F) a nitriding characteristic of $\mathrm{NK} = 5$ entails the formation of ε-nitride only, the necessary nitriding atmosphere would have to be composed of about 65 Vol% NH_3 and 25 Vol% H_2 at a standard pressure of 1 bar. The reaction

$$\mathrm{N_2} \leftrightharpoons 2\mathrm{N_{(ad)}} \tag{7.62}$$

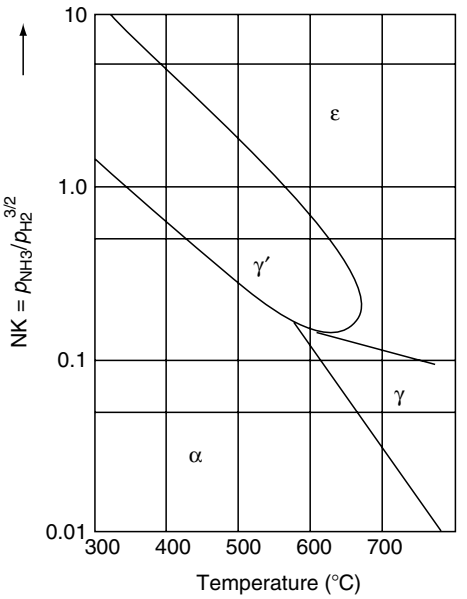

FIGURE 7.56 Lehrer diagram. (From E. Lehrer, *Z. Elektrochemie 36*:3832, 1930.)

that occurs at the surface of the steel is also able to transfer nitrogen, its reaction rate is however too slow to be of actual influence. The reverse reaction, from atomic to molecular nitrogen, is considerably faster and causes an increase in volume, which could account for the formation of pores [151].

7.5.3.2 Nitrocarburizing

In nitrocarburizing, an ammonia atmosphere is blended with carbon- and-oxygen-containing gases that are usually based on carbon dioxide or allow carbon dioxide to be generated [139–144]. In accordance with the homogeneous water gas reaction as discussed in Section 7.2.1, carbon dioxide reacts under near-equilibrium conditions with the hydrogen generated according to the reaction

$$CO_2 + H_2 \rightarrow H_2O + CO \tag{7.26}$$

Given a constant ammonia partial pressure, this leads to a drop in the hydrogen partial pressure and a rise in the nitriding characteristic NK. A state of near-equilibrium is also maintained in the reaction of ammonia with carbon monoxide from Equation 7.22 or from an additional gas

$$NH_3 + CO \rightarrow HCN + H_2O \tag{7.63}$$

where hydrogen cyanide (HCN) is generated [149,151]. In addition to reaction 7.61, nitrogen transition is furthermore promoted by the reaction

$$HCN \rightarrow N(\alpha) + C(\alpha) + (1/2)H_2 \tag{7.64}$$

in which carbon too diffuses into the steel. Carbon, moreover, diffuses into the steel via the Boudouard reaction and the heterogeneous water gas reaction (Equation 7.22 and Equation 7.23, Section 7.3.2.2). Following Equation 7.61, the carburizing effect of a nitrocarburizing atmosphere is described by the carburizing characteristic CK

$$\mathrm{CK} = \frac{p_{\mathrm{CO}}}{p_{\mathrm{CO_2}}} \tag{7.65}$$

The interrelationship between nitriding characteristic NK, carburizing characteristic CK, and the nitrocarburized microstructures is shown in Figure 7.57 [157]. This diagram has been corroborated in practice, as to quantity it is valid for the test conditions established by Langenscheidt [156]. More recent results are given in Refs. [144,157,173,174]. The addition of gases that release CO_2 at nitriding temperature to the original nitriding atmosphere consisting of NH_3 thus enhances the nitriding effect of a nitrocarburizing atmosphere because of the increased nitriding characteristic and the transformation of nitrogen from the decomposition of HCN. In such atmospheres, at the usual nitrocarburizing temperature of about 570°C (1058°F) for ferrous materials, processing times of 2–4 h are enough to lead to the formation of nitrocarburized microstructures, consisting of a compound layer and a diffusion zone, whose properties are such as to greatly enhance the component behavior under many loading conditions. Above all the economic advantage of a considerably shorter processing time and an easier solution to the problem of waste management than in salt bath nitrocarburizing have made gas nitrocarburizing as the most often used process with ferrous materials to date. The advantage of nitriding with ammonia atmospheres lies above all in achieving deep nitriding depths, up to 1 mm, to meet the requirements of specific loading conditions [169].

7.5.3.3 Processing Effects on the Nitriding and Nitrocarburizing Results

By means of Figure 7.57 it is possible to assess the gas composition that has to be established and maintained for a specific microstructure at a given temperature. The thickness of the

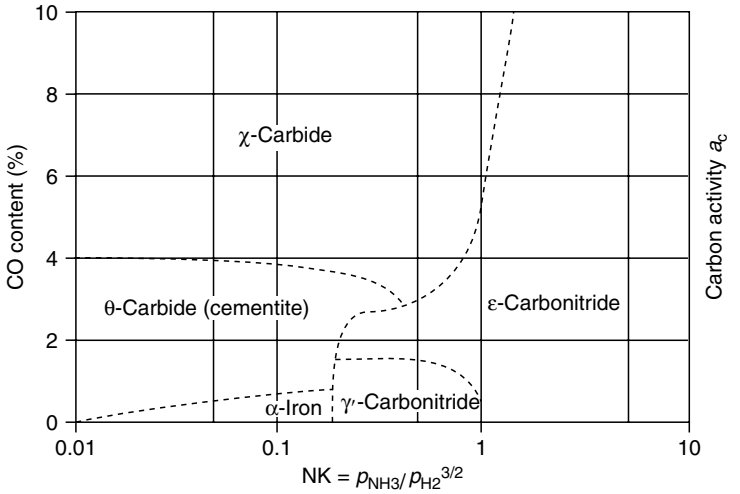

FIGURE 7.57 Influence of the gas composition on nitride formation in the compound layer. (From U. Huchel, J. Kunze, *Härterei Techn. Mitt. 46*:351, 1991.)

compound layer and the nitriding hardness depth are dependent on treatment time and temperature, on pretreatment (see Figure 7.45 through Figure 7.47), and on the material. The rate at which the layer grows corresponds roughly with the square root of the treatment time (Figure 7.48), if processing conditions are such as to guarantee that in nitriding with 100% ammonia the rate of the gas exchange reaches a value that is at least five times higher than that of the furnace volume [175]. Nitrogen-diluted atmospheres have a less distinct nitriding effect, thus requiring increased rates of gas exchange. At an equal rate of gas exchange, additional gases yielding oxygen and carbon accelerate the growth of the compound layer considerably [176] by absorbing hydrogen and thus causing a rise in the nitriding characteristic because of the diminished hydrogen partial pressure. The content of ε-nitride in the compound layer can be controlled via the level of carbon dioxide (Figure 7.58 [177]).

To control the nitriding and the nitrocarburizing process, it is common practice to determine the degree of dissociation and then calculate the nitriding characteristic NK. Values to be measured are the volume percent of ammonia or hydrogen in the atmosphere. A more recent development is the utilization of nitriding sensors, which are either designed following a magnetoinductive measuring principle [154] or as a solid-state electrolyte [152,155]. Nitriding and nitrocarburizing cause the electric and magnetic properties of the material to change. These changes are measured by special sensors [154] that are introduced into the furnace atmosphere and calibrated according to the nitriding result, with the material and the surface of the components as the parameters. This measuring technique also allows to seperately determine microstructural features such as thickness of compound layer or case depth. The oxygen partial pressure can be used as an indirect measurement of the nitriding characteristic NK [152,155] if water vapor or oxygen or carbon dioxide is present in the nitriding atmosphere or is added in small amounts to make this measuring technique work. From the signal of the oxygen sensor it is possible to infer the oxygen partial pressure and thus the degree of dissociation and the nitriding characteristic NK.

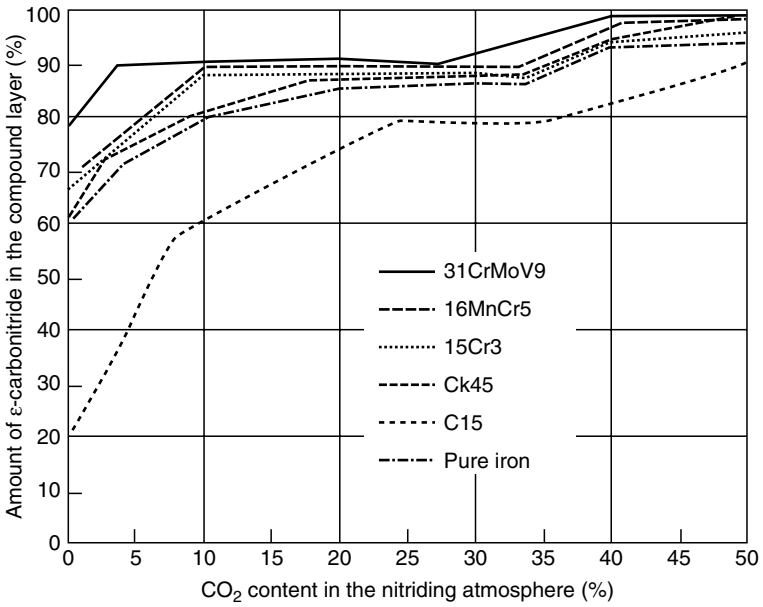

FIGURE 7.58 Influence of CO_2 content on the amount of ε-nitride in the compound layer. (From E. Lehrer, *Z. Elektrochemie 36*:3832, 1930.)

Prior to gas nitriding and gas nitrocarburizing, the surfaces must be thoroughly cleaned because adherent layers and impurities such as oils, forging scales, and preservatives are not entirely susceptible to the treatment at the comparatively low nitriding temperature, inhibiting adsorption and diffusion and diminishing the nitrogen transfer. The thickness of the compound layer and the case depth are therefore shallower than the expected from their nitriding time, or soft zones may develop. As cleaning systems containing halogenated hydrocarbons are not allowed any more for environmental reasons, or only permitted on expensive conditions, thorough cleaning is accomplished by use of hydrous cleaners [174,178] that sometimes are enforced by ultrasonics. Layers still existing on cleaning are frequently further reduced by special preoxidation at about 350°C (662°F) [179].

Oxidizing, frequently carried out in the form of a water vapor treatment at a temperature of at least 450°C (842°F) following nitriding [180–183], leads to the development on the compound layer of iron oxides FeO, α-Fe_2O_4, or Fe_3O_4, depending on processing modes. These oxide layers, above all the seemingly black magnetite layer Fe_3O_4, have a very beneficial effect on corrosion resistance. Magnetite adheres better on nitride layers than on iron because oxide layer and substrate reach a tighter fit (Pilling–Bedworth relationship) by the intermediate nitride layer.

7.6 PROPERTIES OF CARBURIZED AND NITRIDED OR NITROCARBURIZED COMPONENTS

The properties of a component [184] can be modified according to its loading requirements by means of heat treatment, the parameters and possibilities of which must be focussed on this aim. Hence, this chapter deals with the essential properties that can be improved by carburizing and nitriding or nitrocarburizing. The properties of a component have their origin in the interrelationship between the microstructure properties within the component and the loading conditions the component has to endure.

One common characteristic of carburized and nitrided or nitrocarburized microstructures is the hardness gradient with its parameters case hardness, hardness difference between case and core, and case depth. The heat treatment of the surface results moreover in a specific residual stress distribution with compressive residual stresses in the case that turn into tensile residual stresses reaching the case depth. Heavily loaded engineering components demand surface and substrate properties such as resistance to applied loads, to adhesive and abrasive wear, to rolling contact fatigue and to corrosion, all of which must of course be provided in one component. Most of the applied loads result in maximum stresses at the surface of the component or in an area near the surface. Corrosion and wear, as per definition, affect the component surfaces. Nearly all components are therefore stressed by a combined loading, wear, and corrosion system with a maximum effect at or near the surface. Frequently, the required material properties contradict each other as can be observed for instance in the demand for a material that combines high hardness, enhanced abrasive wear resistance, with ductility, enhanced toughness necessary to withstand single impact loads. Surface hardening leads to a distribution of properties that fits the loading demands of most components excellently. In contrast nontreated components, surface hardened components have therefore always much higher fatigue and rolling contact fatigue strength as well as a better wear resistance in all those tribological systems in which a high case hardness is beneficial. A composite with a hard case and a soft core is tougher than a through-hardened component (as to case behavior) but more brittle than a nonhardened microstructure (as to core behavior). A better corrosion resistance can only develop in nitrided or nitrocarburized components as their microstructures have a higher (more positive) corrosion potential.

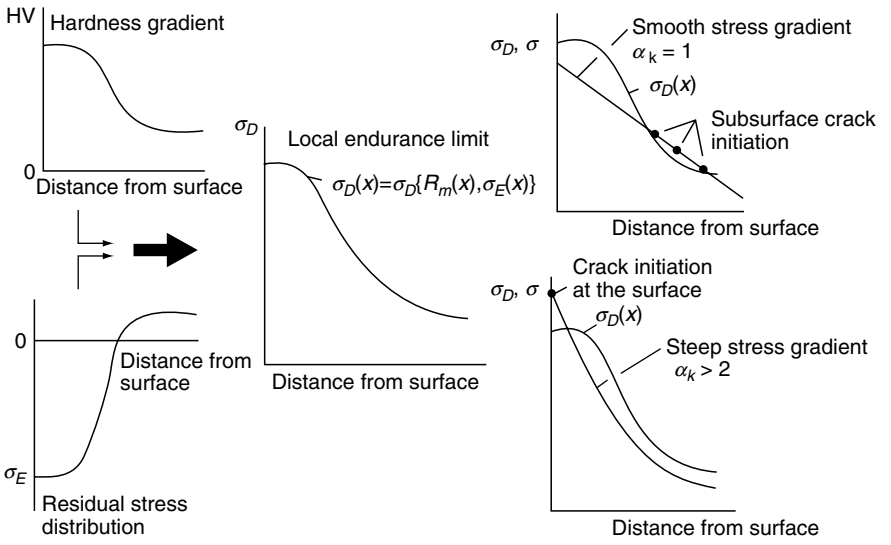

FIGURE 7.59 Local endurance limit of surface hardened specimens. (From K.H. Kloos, *Härterei-Techn. Mitt. 44*:157, 1989.)

The fatigue strength of case-hardened components is improved due to the combined effect of higher case hardness and residual compressive stresses (Figure 7.59 [185]), which results in a local endurance limit [185,186]. This has proved valid with carburized [187] and nitrocarburized [188] specimens. In carburizing, the highest values of fatigue resistance are obtained with case depths in the range of 10–20% of the component size (Figure 7.60 [189]). Given the

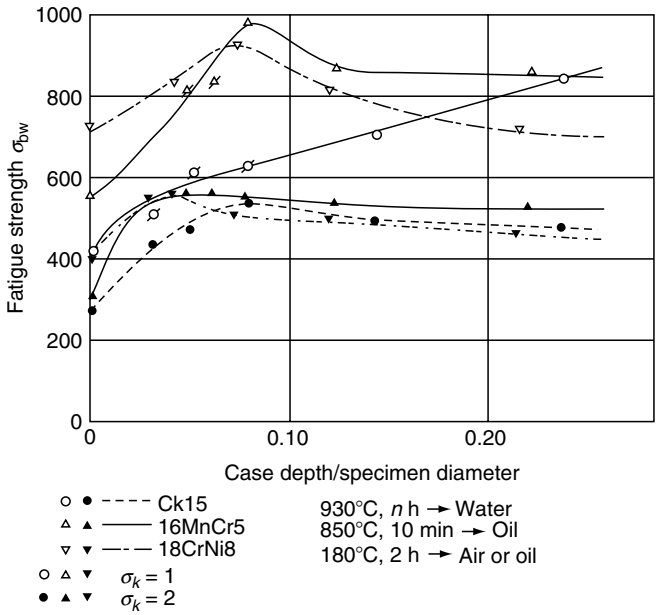

FIGURE 7.60 Influence of case depth on bending fatigue strength of carburized specimens. (From H. Wiegand, G. Tolasch, *Härterei Techn. Mitt. 22*:213, 230, 1967.)

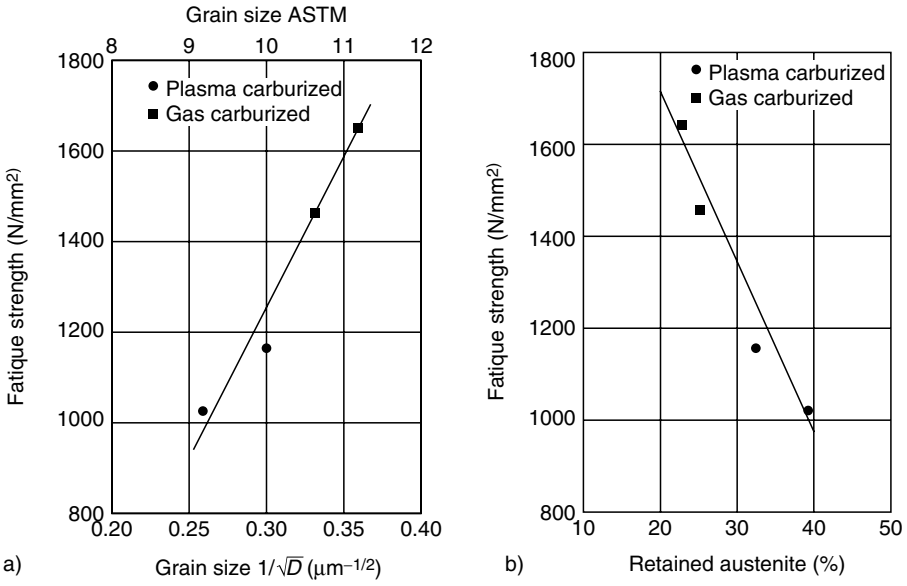

FIGURE 7.61 Effect of grain size and retained austenite content on bending fatigue of carburized steels. (From J.L. Pacheo, G. Krauss, *Härterei Techn. Mitt. 45*:77, 1990.)

same percentage of case depths, fine-grained microstructures [190,191] and a content of retained austenite as low as possible to yield the best results [191], Figure 7.61 [191]. However, the content of retained austenite must not be reduced by deep cooling because deep cooling causes high tensile residual stresses to build up in the retained austenite at the surface [66], which may initiate local cracks. Reheated microstructures have always a better fatigue resistance than as-quenched microstructures [192], where the detrimental effect of phosphorus segregation at the austenite grain boundaries is more distinct [103–107,192,193]. Nitriding and nitrocarburizing lead also to a substantial increase in fatigue resistance, caused by the above-discussed mechanisms (Figure 7.62 [194]), the best effect can be expected starting from about 10% case depth relative to the component size [186]. At equal nitriding conditions,

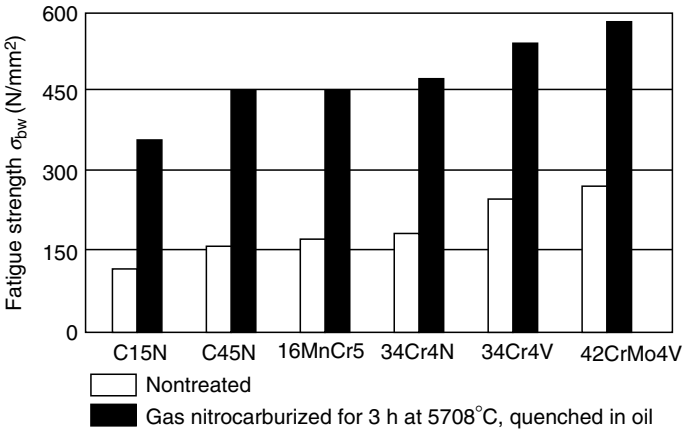

FIGURE 7.62 Bending fatigue strength of nitrocarburized steels. (From R. Chatterjee-Fischer, *Härterei Techn. Mitt. 38*:35, 1983.)

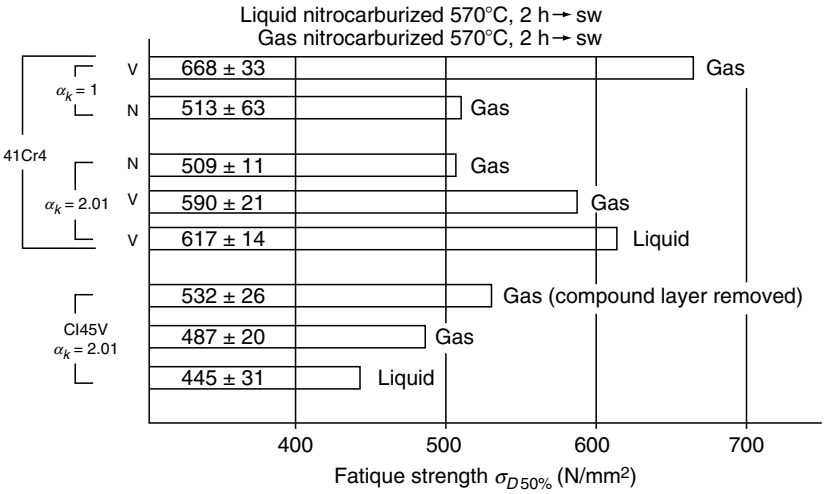

FIGURE 7.63 Bending fatigue strength of nitrocarburized steels.

fatigue resistance is better in microstructures with a high core strength (Figure 7.63), and the nitrocarburizing process has no significant influence.

The case hardness of carburized and nitrided or nitrocarburized microstructures causes a better resistance to abrasive wear. To obtain maximum hardness, carburized microstructures ought to have carbon contents of about 0.7%. The case depth can be determined corresponding to the maximum value of tolerable wear depths. An additional effect of the compound layer is to increase the resistance to adhesive wear, which is best achieved with the formation

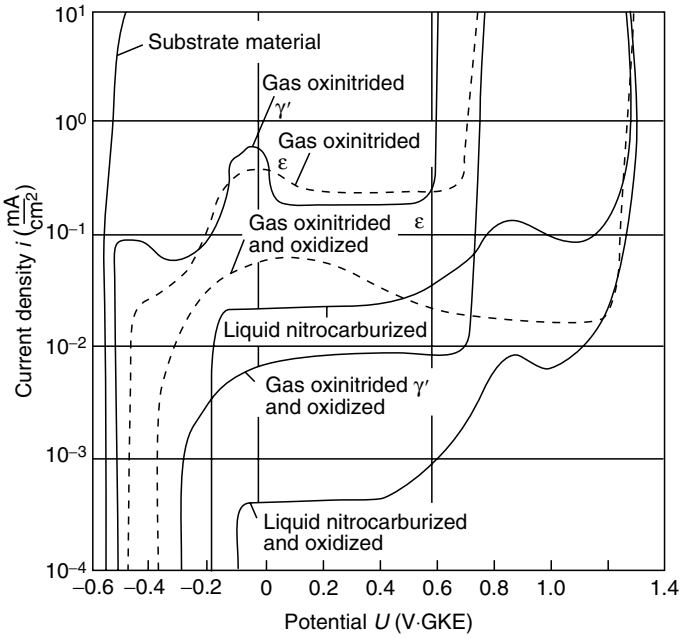

FIGURE 7.64 Current-potential curves of nitrocarburized and oxinitrocarburized steels. (From U. Ebersbach, S. Friedrich, T. Nghia, H.-J. Spies, *Härterei Techn. Mitt. 46*:339, 1991.)

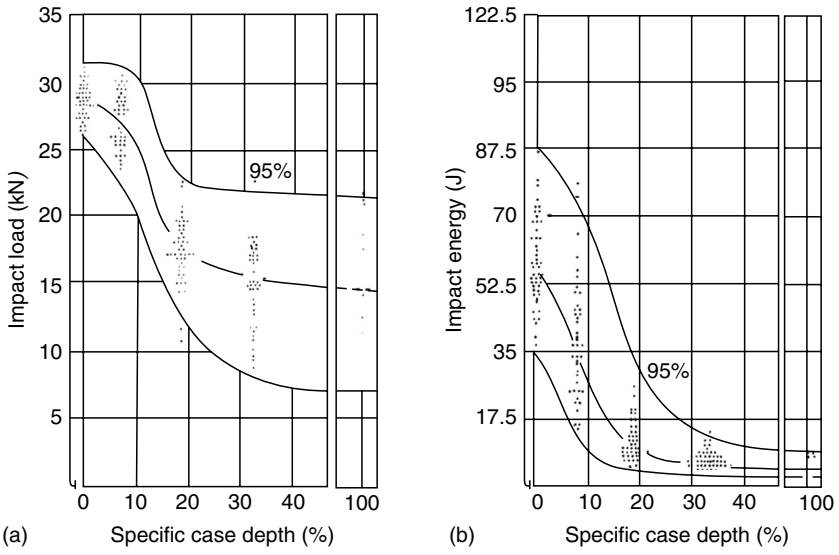

FIGURE 7.65 Influence of case depth on toughness of carburized specimens (gas carburizing 900°C, *n* h; oil; 180°C, 1 h. Data points: mean value of 6 specimens). (From D. Wicke, J. Grosch, *Härterei Techn. Mitt. 32*:223, 1977.)

of ε-nitride [195] and a small band of porosity. Nitride precipitations and a high strength, which can be obtained by a quench and temper process, have an overall beneficial effect on the wear resistance of the diffusion zone.

With the exception of stainless steels, nitrided microstructures have a higher chemical potential than nonnitrided steels and thus a better corrosion resistance [195,196] that can be

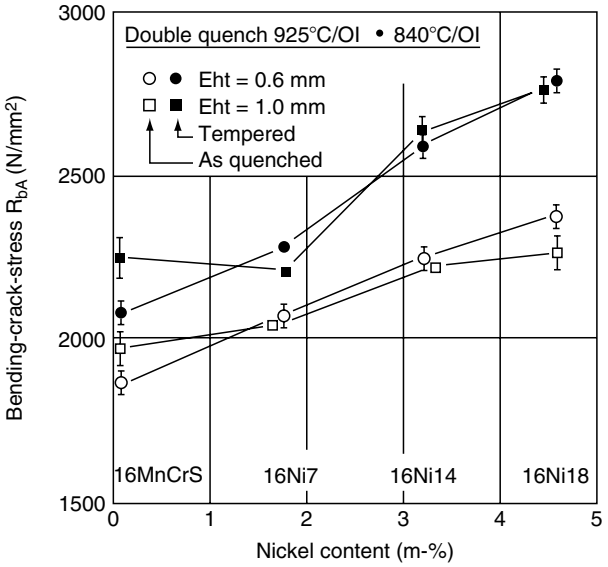

FIGURE 7.66 Effect of nickel content on bending-crack-stress of carburized specimens. (From B. Thoden, J. Grosch, *Härterei Techn. Mitt. 45*:7, 1990.)

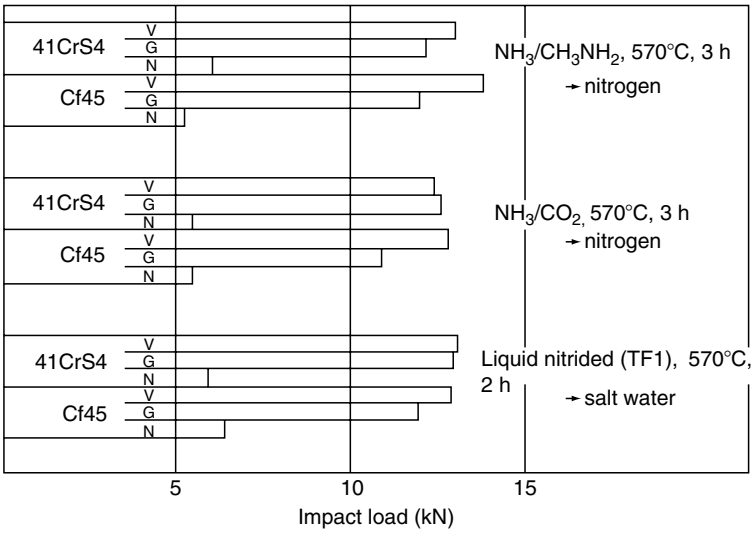

FIGURE 7.67 Influence of core strength on toughness of nitrocarburized specimens. (From J. Grosch, D. Liedtke, *Nitrieren und Nitrocarburieren* (E.J. Mittemeijer, J. Grosch, Eds.), AWT, Wiesbaden, 1991, p. 365.)

further improved by additional, passivating oxide layers [180–183], which has been verified by means of potential–current diagrams (Figure 7.64 [183]). Porosity always accelerates the corrosive effect.

The toughness of carburized components decreases with increasing relative case depth, which describes the amount of brittle case microstructure in the composite. On reaching about 30% relative case depth, the toughness has diminished to the value of the through-hardened microstructure (Figure 7.65) [197]. At equal relative case depth, toughness can be improved by using nickel alloyed carburizing steels (Figure 7.66) [198] with tempered microstructures always tougher than nontempered ones. In nitrocarburized microstructures, the influence of the core is predominant, microstructures consisiting of ferrite and pearlite ought

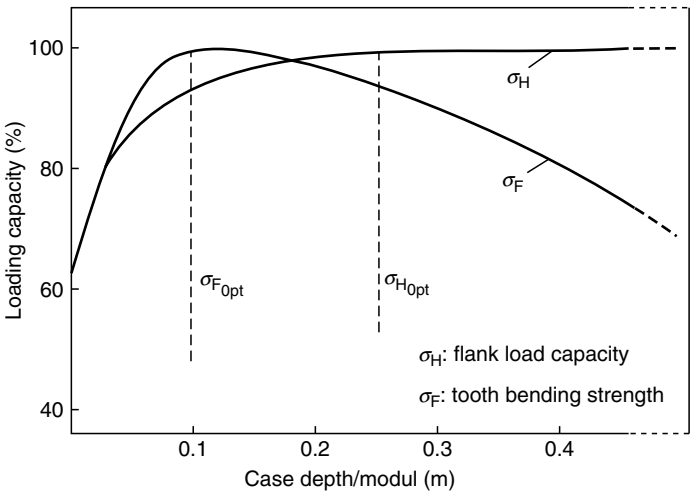

FIGURE 7.68 Gear tooth bending endurance strength and pitting endurance strength, influence of case depth, carburized steels. (From J. Sauter, I. Schmidt, U. Schulz, *Härterei Techn. Mitt. 45*:98, 1990.)

to be avoided, Figure 7.67 [199]. The different nitrocarburizing processes have obviously no effect.

As for rolling contact fatigue, the acting stress according to Mises' criterion reaches its highest value beneath the surface at low-friction coefficients, with increasing friction the maximum value shifts toward the surface [200]. Depending on the applied load, either case depth or surface condition (surface intergranular oxidation, porosity) must be fixed [201]. A high nitriding case depth, which can be produced in the gas nitriding of nitriding steels, is advantageous for gears, but their case depth should however not exceed $0.2 \times$ modulus to avoid nitriding of the tooth tips that would entail embrittlement [202]. The maximum values that can be reached for the flank load capacity of carburized gears can be reached with case depths in the size range of $0.25 \times$ modulus (Figure 7.68 [203]). The optimum case depth for the tooth bending fatigue strength, which is also shown in Figure 7.68 illustrates that in determining the heat treatment parameters it is necessary to weigh optimal tooth bending fatigue strength against optimal flank load capacity.

REFERENCES

1. P.G. Shewmon, Metallurgical thermodynamics, in *Physical Metallurgy* (R.W. Cahn, Ed.), 2nd ed., North-Holland, Amsterdam, 1970, p. 281.
2. M.G. Frohberg, *Thermodynamik für Metallurgen und Werkstofftechniker*, VEB Deutscher Verlag für Grundstoffindustrie, Leipzig, 1980.
3. E. Fromm, *Thermodynamik*, Springer-Verlag, Berlin, 1970.
4. Th. Heumann, *Diffusion in Metallen*, Springer-Verlag, Berlin, 1992.
5. P.G. Shewmon, *Diffusion in Solids*, 2nd ed., McGraw-Hill, New York, 1989.
6. G. Hörz, Kinetik und Mechanismen, in *Gase und Kohlenstoff in Metallen* (E. Fromm, E. Gebhardt, Eds.), Springer-Verlag, Berlin, 1975, p. 84.
7. E. Doehlemeier, *Z. Elektrochemie 42*:561 (1936).
8. JANAF, *Thermochemical Tables*, 2nd ed., 1971.
9. J.F. Elliott, M. Gleiser, *Thermochemistry for Steelmaking*, Addison-Wesley, Reading, 1960.
10. C. Wagner, *Z. anorg. Chemie 199*:321 (1931).
11. A. Fick, *Poggendorf Annalen 94*:59 (1885).
12. C.E. van Orstrand, F.P. Dewey, *U.S. Geological Survey Paper 956*, 1915 (cited according to W. Seith, *Ber. Naturforsch. Ges. Bd. 31*, Heft 1/2, Freiburg 1931).
13. A. Slattenscheck, *Härterei Techn. Mitt. 1*:85 (1942).
14. J.I. Goldstein, A.E. Moren, *Metall. Trans. 9A*:1515 (1978).
15. E. Hornbogen, *Werkstoffe*, 2nd ed., Springer-Verlag, Berlin, 1979.
16. F.E. Harris, *Met. Prog*. 84 (1945).
17. R.W. Gurry, *Trans. AIME 188*:671 (1950).
18. Th. Schmidt, *Härterei Techn. Mitt. Sonderheft Gasaufkohlung* 11 (1952).
19. F. Neumann, B. Person, *Härterei Techn. Mitt. 23*:296 (1968).
20. F. Neumann, U. Wyss, *Härterei Techn. Mitt. 25*:253 (1970).
21. F.J. Harvey, *Metall. Trans. 9A*:1507 (1978).
22. U. Wyss, *Härterei Techn. Mitt. 45*:44 (1990).
23. C.A. Stickels, Heat treating, in *Metals Handbook*, Vol. 4, ASM International, Materials Park, OH, 1991, p. 313.
24. W. Göhring, C.H. Luiten, *Härterei Techn. Mitt. 43*:236 (1988).
25. H.J. Grabke, E.M. Müller, H.V. Speck, G. Konczos, *Steels Res. 56*:275 (1985).
26. W. Rembges, *Härterei Techn. Mitt. 49*:112 (1994).
27. F. Hoffmann, S. Dorn, P. Mayr, *Härterei Techn. Mitt. 49*:103 (1994).
28. M.H. Jacobs, T.J. Law, F. Ribet, *Surf. Eng. 1*:105 (1985).
29. B. Edenhofer, *Härterei Techn. Mitt. 45:*154 (1990).
30. U. Wyss, *Härterei Techn. Mitt. 17:*160 (1962).

31. H.V. Speck, H.J. Grabke, E.M. Müller, *Härterei Techn. Mitt. 40*:92 (1985).
32. F. Neumann, *Härterei Techn. Mitt. 33*:192 (1978).
33. H. Klümper-Westkamp, P. Reimche, K.L. Feiste, M. Bernhard, F.-W. Bach, *Härterei Techn. Mitt. 57*:364 (2002).
34. E. Schürmann, Th. Schmidt, H. Wagener, *Gießerei, Beiheft 16*:91 (1964).
35. S. Gunnarson, *Härterei Techn. Mitt. 22*:292 (1967).
36. K.H. Sauer, M. Lucas, H.J. Grabke, *Härterei Techn. Mitt. 43*:45 (1988).
37. F. Neumann, *Härterei Techn. Mitt. 44*:262 (1989).
38. H.J. Grabke, *Härterei Techn. Mitt. 45*:110 (1990).
39. K.H. Weissohn, *Härterei Techn. Mitt. 49*:118 (1994).
40. K. Rimmer, *Härterei Techn. Mitt. 30*:152 (1975).
41. F.E. Harris, *Met. Prog. 44*:265 (1943).
42. U. Wyss, *Wärmebehandlung der Bau- und Werkzeugstähle* (H. Benninghoff, Ed.), BAZ Buchverlag, Basel, 1978, p. 237.
43. J. Wüning, *Z. wirtsch. Fertigung 77*:424 (1982).
44. H.J. Grabke, G. Tauber, *Arch. Eisenhüttenwes 46*:215 (175).
45. D. Liedtke, Messen und Regeln beim Aufkohlen, *Einsatzhärten* (J. Grosch, Ed.), expert-Verlag, Renningen, 1994, p. 16.
46. H.J. Grabke, *Härterei Techn. Mitt. 44*:270 (1989).
47. J. Wünning, *Härterei Techn. Mitt. 43*:266 (1988).
48. J.I. Goldstein, A.E. Moren, *Metall. Trans. 9A*:1515 (1978).
49. J. Pavlossoglou, H. Burkhard, *Härterei Techn. Mitt. 31*:209 (1976).
50. H.U. Fritsch, H.W. Bergmann, *Härterei Techn. Mitt. 41*:14 (1986).
51. A.R. Marder, S.M. Perpetpetua, J.A. Kowalik, E.T. Stephenson, *Metall. Trans. 16A*:1160 (1985).
52. C.A. Stickels, *Heat Treatment and Surface Engineering* (G. Krauss, Ed.), ASM, Cleveland, OH, 1988, p. 99.
53. T. Reti, M. Cseh, *Härterei Techn. Mitt. 42*:139 (1987).
54. C. Wells, W. Batz, R.F. Mehl, *Trans. TMS-AIME 188*:553 (1950).
55. R.P. Smith, *Acta metall. 1*:578 (1953).
56. G. Leyens, G. Woelk, J. Wünning, *Arch. Eisenhüttenwes. 47*:385 (1976).
57. B. Thoden, J. Grosch, *Neue Hütte 34*:96 (1989).
58. C.A. Stickels, C.M. Mack, *Carburizing—Processing and Performance* (G. Krauss, Ed.), ASM International, Materials Park, OH, 1989, p. 1.
59. B. Edenhofer, *Progress in Heat Treatment and Surface Engineering* (E.J. Mittemeijer, J. Grosch, Eds.), ASM International, Materials Park, OH, 2000, p. 75.
60. B. Edenhofer, H. Pfau, *Heat Treatment and Surface Engineering* (G. Krauss, Ed.), ASM International, Materials Park, OH, 1988, p. 85.
61. J. Grosch, *Härterei Techn. Mitt. 36*:262 (1981).
62. F. Hippenstiel, R. Kohlmann, W. Bleck, B. Clausen, F. Hoffmann, P. Pouteau, *Härterei Techn. Mitt. 57*:290 (2002).
63. B. Gondesen, H. surm, F. Hoffmann, P. Mayr, *Härterei Techn. Mitt. 54*:21 (1999).
64. R. Chatterjee, O. Schaaber, *Härterei Techn. Mitt. 24*:121, 292 (1969).
65. J. Slycke, T. Ericsson, *J. Heat Treating 2*:3 (1981).
66. O. Schwarz, J. Grosch, C. Genzel, W. Reimers, *Härterei Techn. Mitt. 49*:134 (1994).
67. U. Wyss, *Härterei Techn. Mitt. 43*:27 (1988).
68. J.H. Hollomann, L.D. Jaffe, *Trans. AIME 180*:439 (1949).
69. Jicheng Zhao, *Mat. Sci. Technol. 8*:997 (1992).
70. C.A. Siebert, D.V. Doane, D.H. Breen, *The Hardenability of Steels*, ASM International, Materials Park, OH, 1977, p.100.
71. H. Dietrich, W. Schmidt, *Thyssen Techn. Berichte 10*:105 (1984).
72. A.F. de Retana, D.V. Doane, *Met. Prog. 100*:65 (1971).
73. G. Krauss, *Härterei Techn. Mitt. 41*:56 (1986).
74. G. Krauss, *Steels—Heat Treatment and Processing Principles*, ASM International, Materials Park, OH, 1990, p. 43.

75. O. Vöhringer, *Grundlagen der technischen Wärmebehandlung von Stahl* (J. Grosch, Ed.), Werkstofftechn, Verlagsges, Karlsruhe, 1981, p. 75.
76. H.-J. Eckstein, *Wärmebehandlung von Stahl*, VEB-Verlag, Leipzig, 1971, p. 179.
77. Z. Nishiyama, *Martensitic Transformation*, Academic Press, New York, 1978, p. 236.
78. H.K. D.H. Bhadeshia, *J. Mater. Sci. 17*:383 (1982).
79. A.H. Rauch, W.R. Turtle, *Met. Prog. 69*:73 (1956).
80. R.P. Brobst, G. Krauss, *Metall. Trans. 5*:457 (1974).
81. A. Randak, R. Eberbach, *Härterei Techn. Mitt. 32*:223 (1977).
82. W. Knorr, H.-J. Peters, G. Tacke, *Härterei Techn. Mitt. 36*:129 (1981).
83. P.G. Dressel, R. Kohlmann, K.-J. Kremer, A. Stanz, *Härterei Techn. Mitt. 39*:112 (1984).
84. V. Schüler, B. Huchtemann, E. Wulfmeier, *Härterei Techn. Mitt. 45*:57 (1990).
85. Liu Cheng, C.M. Brakman, B.M. Korevaar, E.J. Mittemeijer, *Metall. Trans. 19A*:2415 (1988).
86. H. Streng, C. Razim, J. Grosch, *Härterei Techn. Mitt. 43*:80 (1988).
87. H.J. Böhmer, H.W. Zoch, H. Schlicht, *Härterei Techn. Mitt. 41*:258 (1986).
88. H.J. Böhmer, H.J. Ebert, W. Trojahn, *Proceedings of the 46th Annual Meeting STLE*, Montreal, Canada, 1991.
89. G. Krauss, *Steels—Heat Treatment and Processing Principles*, ASM International, Materials Park, OH, 1990, p. 205.
90. E. Macherauch, O. Vöhringer, *Härterei-Techn. Mitt. 41*:71 (1986).
91. Liu Cheng, A. Böttger, E.J. Mittemeijer, *Metall. Trans. 22A*:1945 (1991).
92. G.R. Speich, *Trans. TMS-AIME 245*:2553 (1969).
93. D. Dengel, *Härterei-Techn. Mitt. 39*:182 (1984).
94. N. DeChristofaro, R. Kaplow, *Metall. Trans. 8A*:35 (1977).
95. N. DeChristofaro, R. Kaplow, W.S. Owen, *Metall. Trans. 9A*:821 (1978).
96. S. Nagakura, T. Suzuki, M. Kusonoki, *Trans. Jpn. Inst. Met. 22*:699 (1981).
97. S. Nagakura, Y. Hirotsu, M. Kusonoki, T. Suzuki, Y. Nakamura, *Metall. Trans. 14A*:1025 (1983).
98. H. Faber, O. Vöhringer, E. Macherauch, *Härterei Techn. Mitt. 34*:1 (1979).
99. M. Bacher, O. Vöhringer, E. Macherauch, *Härterei Techn. Mitt. 45*:16 (1990).
100. T.A. Balliett, G. Krauss, *Metall. Trans. 7A*:81 (1976).
101. J.H. Hollomon, L.D. Jaffe, *Trans. AIME 162*:223 (1945).
102. R.A. Grange, R.W. Baughman, *Trans. ASM 48*:165 (1956).
103. H.K. Obermeyer, G. Krauss, *J. Heat Treat. 1*:31 (1980).
104. J. Grosch, *VDI Berichte 318*:79 (1978).
105. T. Ando, G. Krauss, *Metall. Trans. 12A*:1283 (1981).
106. S.K. Banerjee, C.J. McMahon Jr., H.C. Feng, *Metall. Trans. 9A*:237 (1978).
107. G. Thomas, *Metall. Trans. 9A*:439 (1978).
108. F. Zia Ephraimi, G. Krauss, *Acta Metall. 32*:1767 (1984).
109. I.S. Koslowski, *Met. Sci. Heat Treat. 25*:157 (1967).
110. R. Chatterjee-Fischer, *Metall. Trans. 9A*:1553 (1978).
111. M. Lohrmann, W. Lerche, *Progress in Heat Treatment and Surface Engineering* (E.J. Mittemeijer, J. Grosch, Eds.), ASM International, Materials Park, OH, 2000, p. 129.
112. K. Bungardt, E. Kunze, H. Brandis, *DEW-Techn. Berichte 5*:1 (1965).
113. J.C. Scully, *The Fundamentals of Corrosion*, 3rd ed., Pergamon Press, Oxford, 1990, p. 90.
114. W. Haumann, *Stahl u. Eisen 107*:585 (1987).
115. H. Streng, J. Grosch, C. Razim, *Heat Treatment and Surface Engineering* (G. Krauss, Ed.), ASM International, Materials Park, OH, 1988, p. 313.
116. H.G. Nelson, Hydrogen embrittlement, in *Treatise on Materials Science and Technology*, Vol. 25 (C.L. Briant, S.K. Banerjee, Eds.), Plenum Press, New York, 1983, p. 275.
117. R.A. Oriani, *Acta Metall. 18*:147 (1970).
118. G.M. Pressouyre, *Acta Metall. 28*:895 (1980).
119. K.B. Kim, S. Pyun, *Arch. Eisenhüttenwes. 53*:397 (1982).
120. G.M. Pressouyre, *Metall. Trans. 14A*:2189 (1983).
121. A.M. Brass, M. Aucouturier, H. Barthelemy, *Mem. Scient. Rev. Metallurgie 78*:601 (1981).

122. H.-J. König, K.W. Lange, *Arch. Eisenhüttenwes. 46*:669 (1975).
123. G. Vibrans, *Arch. Eisenhüttenwes. 32*:667 (1961).
124. H. Streng, *Zähigkeitsoptimierung einsatzgehärteter Gefüge*. Diss. TU Berlin, 1986.
125. E. Riecke, *Arch. Eisenhüttenwes. 44*:647 (1973).
126. R. Hoffmann, *Härterei Techn. Mitt. 39*:61, 99 (1984).
127. F.D. Richardson, J.H. Jeffes, *J. Iron Steel Inst. 171*:165 (1952).
128. I. Barin, O. Knacke, *Thermodynamical Properties of Inorganic Substances*, Springer-Verlag, Berlin, 1973.
129. G. Minkler, *Blech-Rohre-Profile 29*:484 (1982).
130. A.W. Machlet, U.S. Patent 1, 092, 925, April 14, 1914.
131. A. Fry, *Stahl und Eisen 23*:1271 (1923).
132. A. Fry, *Kruppsche Mh. 7*:17 (1926).
130. A. Fry, *Trans. Am. Soc. Steel Treat. 16*:111 (1929).
133. A.B. Kinzel, J.J. Egan, *Trans. Am. Soc. Steel Treat. 16*:175 (1929).
134. C. Albrecht, *TZ prakt. Metallbearb. 52*:252 (1942).
135. J.G. Morrison, *Iron Coal Tr. Rev. 147*:135 (1943).
136. J. Müller, *Härterei Techn. Mitt. 3*:219 (1944).
137. F.K. Naumann, G. Langenscheidt, *Arch. Eisenhüttenwes. 36*:583 (1965).
138. B. Prenosil, *Härterei Techn. Mitt. 20*:41 (1965).
139. C. Dawes, D.F. Trenter, *Met. Forming 40*:58 (1973).
140. C. Luiten, *Z. wirtsch. Fert. 68*:482 (1973).
141. H.J. Grabke, *Scripta Met. 8*:121 (1974).
142. J. Wünning, *Härterei Techn. Mitt. 29*:42 (1974).
143. T. Bell, *Heat Treat. Met. 2*:39 (1975).
144. A. Wells, T. Bell, *Heat Treat. Met. 10*:39 (1983).
145. F. Leitner, E. Plöckinger, *Edelstahlerzeugung*, Springer-Verlag, Berlin, 1964, p. 259.
146. M. Hansen, K. Anderko, *Constitution of Binary Alloys*, McGraw Hill, New York, 1958.
147. H.A. Wriedt, N.A. Gokcen, R.H. Nafziger, *Bull. Alloy Phase Diagrams 8*:355 (1987).
148. E.H. van Voorthuysen, N.C. Chechenin, D.O. Boerma, *Metall. Mater. Trans. 33A*:2593 (2002).
149. J. Slycke, L. Sproge, *Surf. Eng. 5*:125 (1989).
150. F. Hoffmann, R. Hoffmann, E.J. Mittemeijer, *Härterei Techn. Mitt. 47*:365 (1992).
151. J. Slycke, L. Sproge, *Härterei Techn. Mitt. 47*:357 (1992).
152. R. Hoffmann, E.J. Mittemeijer, M.A.J. Somers, *Härterei Techn. Mitt. 49*:177 (1994).
153. M.A.J. Somers, Hong Du, *Progress in Heat Treatment and Surface Engineering* (E.J. Mittemeijer, J. Grosch, Eds.), ASM International, Materials Park, OH, 2000, p. 153.
154. H. Klümper-Westkamp, F. Hoffmann, P. Mayr, B. Edenhofer, *Härterei Techn. Mitt. 46*:367 (1991).
155. H.-J. Berg, H.-J. Spies, S. Böhmer, *Härterei Techn. Mitt. 46*:375 (1991).
156. G. Langenscheidt, Beitrag zum System Eisen-Stickstoff-Kohlenstoff. Diss. BA Clausthal, 1964.
157. U. Huchel, J. Kunze, *Härterei Techn. Mitt. 46*:351 (1991).
158. H.-J. Spies, D. Bergner, *Härterei Techn. Mitt. 47*:346 (1992).
159. M.A.J. Somers, E.J. Mittemeijer, *Härterei Techn. Mitt. 47*:5 (1992).
160. Hoffmann, F. et al., *Nitrieren und Nitrocarburieren* (E.J. Mittemeijer, J. Grosch, Eds.), AWT, 1991, p. 105.
161. D. Liedtke, J. Grosch, *Proceedings of the 5th International Congress on Heat Treatment*, Budapest, 1986, pp. 8–16.
162. Y. Sun, X.-Y. Li, T. Bell, *The Formation and Decomposition of Nitrogen and Carbon fct Austenite in Austenitic Stainless Steel* (T. Bell, K. Akamatsu, Eds.), Maney Publications, London, 2001, p. 263.
163. B. Larisch, H. Zimdars, H.-J. Spies, *Härterei Techn. Mitt. 57*:6 (2002).
164. H.-J. Spies, C. Eckstein, H. Zimdars, *Härterei Techn. Mitt. 57*:409 (2002).
165. H. Berns, S. Siebert, *Härterei Techn. Mitt. 49*:123 (1994).
166. H. Berns, R.L. Juse, B. Edenhofer, J.W. Bouwman, *Heat Treat. Met. 27*:39 (2000).
167. H. Berns, R. Zaugg, *Härterei Techn. Mitt. 57*:377 (2002).

168. H.J. Grabke, *Arch. Eisenhüttenwes. 46*:75 (1975).
169. U. Huber-Gommann, *Heat Treating* (1991).
170. C.F. Floe, *Trans. ASM 32*:134 (1944)
171. C.F. Floe, *Met. Prog. 50*:1212 (1946).
172. E. Lehrer, *Z. Elektrochemie 36*:3832 (1930).
173. J. Slycke, L. Sproge, J. Agren, *Scand. J. Met. 17*:122 (1988).
174. E.J. Mittemeijer, *Härterei Techn. Mitt. 36*:57 (1981).
175. C. Dawes, D.F. Trantner, C.G. Smith, *Met. Techn. 6*:345 (1979).
176. C. Dawes, D.F. Trantner, C.G. Smith, *Heat Treat. Met. 7*:1 (1980).
177. W. Vogel, *Heat Treatment und Surface Engineering* (G. Krauss, Ed.), ASM International, Materials Park, OH, 1988, p. 337.
178. B. Haase, K. Bauckhage, A. Schreiner, *Härterei Techn. Mitt. 47*:67 (1992).
179. P.B. Friehling, M.A.J. Somers, *Progress in Heat Treatment and Surface Engineering* (E.J. Mittemeijer, J. Grosch, Eds.), ASM International, Materials Park, OH, 2000, p. 179.
180. M.A.J. Somers, E.J. Mittemeijer, *Härterei Techn. Mitt. 47*:169 (1992).
181. D.J. Coates, B. Mortimer, A. Hendry, *Corrosion Science 22*:951 (1982).
182. H.-J. Spies, H.-P. Winkler, B. Langenhan, *Härterei Techn. Mitt. 44*:75 (1989).
183. U. Ebersbach, S. Friedrich, T. Nghia, H.-J. Spies, *Härterei Techn. Mitt. 46*:339 (1991).
184. J. Grosch, *Z. wirtschaftl. Fertig. 69*:412 (1974).
185. K.H. Kloos, *Härterei-Techn. Mitt. 44*:157 (1989).
186. P. Starker, H. Wohlfahrt, E. Macherauch, *Arch. Eisenhüttenwes. 51*:439 (1980).
187. T. Kuttner, H. Zieger, *Härterei Techn. Mitt. 47*:367 (1992).
188. H.-J. Spies, T. Kern, D.N. Tan, *Mat.-wiss. u. Werkstofftechn. 25*:191 (1994).
189. H. Wiegand, G. Tolasch, *Härterei Techn. Mitt. 22*:213, 230 (1967).
190. C.A. Apple, G. Krauss, *Metall. Trans. 4*:1195 (1973).
191. J.L. Pacheo, G. Krauss, *Härterei Techn. Mitt. 45*:77 (1990).
192. G. Krauss, *Härterei Techn. Mitt. 49*:157 (1994).
193. R.S. Hyde, G. Krauss, D.K. Matlock, *Metall. Mat. Trans. 25A*:1229 (1994).
194. R. Chatterjee-Fischer, *Härterei Techn. Mitt. 38*:35 (1983).
195. H. Woska, *Härterei Techn. Mitt. 38*:10 (1983).
196. B. De Benedetti, E. Angelini, *Advances in Surface Treatments*, Vol. 5, Pergamon Press, Oxford, 1987, p. 3.
197. D. Wicke, J. Grosch, *Härterei Techn. Mitt. 32*:223 (1977).
198. B. Thoden, J. Grosch, *Härterei Techn. Mitt. 45*:7 (1990).
199. J. Grosch, D. Liedtke, *Nitrieren und Nitrocarburieren* (E.J. Mittemeijer, J. Grosch, Eds.), AWT, Wiesbaden, 1991, p. 365.
200. O. Zwirlein, H. Schlicht, *Z. Werkstofftechn. 11*:1 (1980).
201. H. Stangner, H.-W. Zoch, *Härterei Techn. Mitt. 45*:223 (1990).
202. U. Huber-Gommann, H.-J. Grasemann, G. Schulz, *Z. wirtschaftl. Fertigung 75*:9 (1980).
203. J. Sauter, I. Schmidt, U. Schulz, *Härterei Techn. Mitt. 45*:98 (1990).

8 Nitriding Techniques, Ferritic Nitrocarburizing, and Austenitic Nitrocarburizing Techniques and Methods

David Pye

CONTENTS

8.1 Introduction 476
8.2 Process Technology 478
8.3 Composition of the Case 481
8.4 Composition of the Formed Case 486
8.4.1 Epsilon Phase 487
8.4.2 Gamma Prime Phase 487
8.4.3 Diffusion Layer 487
8.5 Two-Stage Process of Nitriding (Floe Process) 488
8.6 Salt Bath Nitriding 489
8.6.1 Safety in Operating Molten Salt Baths for Nitriding 489
8.6.2 Maintenance of a Nitriding Salt Bath 490
8.6.2.1 Daily Maintenance Routine 490
8.6.2.2 Weekly Maintenance Routine 491
8.7 Pressure Nitriding 491
8.8 Fluidized Bed Nitriding 491
8.9 Dilution Method of Nitriding 492
8.10 Plasma Nitriding 493
8.10.1 Plasma Generation 493
8.11 Post-oxy Nitriding 496
8.12 Glow Discharge Characteristics 498
8.12.1 Townsend Discharged Region 498
8.12.2 Corona Region 498
8.12.3 Subnormal Glow Discharge Region 498
8.12.4 Normal Glow Discharge Region 498
8.12.5 Glow Discharge Region 498
8.12.6 Arc Discharge Region 499
8.13 Process Control of Plasma Nitriding 499
8.13.1 Processor Gas Flow Control 501
8.14 Two-Stage (Floe) Process of Gas Nitriding 502
8.15 Salt Bath Nitriding 503
8.16 Dilution Method of Nitriding or Precision Nitriding 503
8.16.1 Control of Precision Nitriding 504

8.17 Furnace Equipment for Nitriding 505
8.17.1 Salt Baths 506
8.18 Plasma Nitriding 506
8.18.1 Plasma Generation 507
8.18.2 Glow Discharge Characteristics 508
8.18.3 Plasma Control Characteristics 509
8.18.4 Equipment Technology 511
8.18.5 Cold-Wall Technology 511
8.18.6 Power Supply 512
8.18.7 Process Temperature Measurement 512
8.18.8 Process Gas Flow Controls 513
8.18.9 Hot-Wall, Pulsed DC Current 513
8.18.10 Plasma Power Generation 515
8.18.11 Process Temperature Control 515
8.18.12 Temperature Control 516
8.18.13 Process Control 516
8.18.14 Low Capital Investment, High Operational Skills 516
8.18.15 Moderate Capital Investment, Moderate Operator Skills 516
8.18.16 High Capital Investment, Low Operational Skills 516
8.18.17 Metallurgical Considerations and Advantages 517
8.18.18 Metallurgical Structure of the Ion Nitrided Case 518
8.18.19 Metallurgical Results 521
8.18.20 Steel Selection 521
8.18.21 Prenitride Condition 523
8.18.22 Surface Preparation 527
8.18.23 Nitriding Cycles 527
8.18.24 Distortion and Growth 528
8.19 Introduction 529
8.20 Case Formation 530
8.21 Precleaning 531
8.22 Methods of Ferritic Nitrocarburizing 531
8.22.1 Salt Bath Ferritic Nitrocarburizing 531
8.22.2 Gaseous Ferritic Nitrocarburizing 532
8.22.2.1 Safety 533
8.22.3 Plasma-Assisted Ferritic Nitrocarburizing 533
8.22.3.1 Applications 534
8.22.3.2 Steel Selection 534
8.22.4 Process Techniques 535
8.22.5 Case Depth 535
8.22.5.1 How Deep Can the Case Go? 535
8.23 Ferritic Oxycarbonitride 537
References 537

8.1 INTRODUCTION

As was stated in the first edition of this handbook, interest in the subject of nitriding has grown even more as a recognized and proven surface engineering process. Further to this (and particularly during the past 10 years) has become recognized as a very simple process and one without serious problems that can arise, such as the problem of distortion. As all heat treaters,

metallurgists, and engineers are aware distortion can be a very serious problem. The process of nitriding, while not distortion free, is a process that can incur minimal distortion such as that seen on the other surface treatment process techniques, which involve higher process temperatures as well as a quench from a high austenitizing temperature. The processes referred to are carburizing and carbonitriding. Both of these processes are high-temperature operations and require metallurgical phase changes in order to induce carbon, or carbon plus nitrogen into the steel surface.

This chapter should be read in conjunction with the previous edition [see chapter 10]. This chapter reviews the process techniques of both gas nitriding and ion nitriding, ferritic nitrocarburizing (FNC) and austenitic nitrocarburizing (ANC). Further to this the chapter will also discuss the resulting metallurgy, mechanical results, and performance of the diffused case under operational conditions. During the past 6 years, an awareness of the performance benefits has been shown in the surface treatments of:

- FNC
- ANC

Great interest has been demonstrated by engineers and metallurgical process engineers in the methods of the four low-temperature thermochemical treatment procedures such as:

- Gaseous nitriding
- Plasma nitriding (ion)
- Salt bath nitriding
- Fluidized bed nitriding

There have also been developments in the applications arena of the process selection in relation to products and applications. The automotive industry has displayed serious interest in the use of high-strength low-alloy materials that are surface enhanced to reduce material costs as well as giving good performance in particular application. Still, the majority of the work on all of the process methods and process metallurgy is still conducted on ferrous materials (iron-based metals) and a very small amount of research work into nonferrous materials such as aluminum. The application of aluminum in the nitriding process was investigated because aluminum is an excellent nitride former. Another area of development with nonferrous materials is that of investigatory work on the surface treatment of titanium to form a nonbrittle surface layer of titanium nitride. Another area of investigation is in the field of nitriding after the process of boronizing to form flexible, but very hard, surface boron nitrides.

It has been noted that specialized gear manufacturers are making greater use of the nitriding process on what is considered to be high-performance gears. The gear manufacturing industry has been very reluctant to consider the nitride process because of a potential surface spalling or surface fracturing at the contact point on the gear flank. With the advances made in the control of the formation of the surface compound layer, it is now possible to almost eliminate the the concerns raised by the automobile industry. The formation of the compound layer can now be accurately controlled to produce a monophase layer, a dual-phase layer, and no compound layer. This can be accomplished in both gas and plasma nitride systems. This is due mainly to the gas delivery and exhaust gas analysis control by the use of mass flow controllers as well as a greater use of the computer [2].

However, the use of the nitriding process as a competitive surface treatment method compared to carburizing, which is followed by austenitizing, quench, and temper, is still a contentious issue especially in terms of production volumes and process cycle times. There is a new thinking applied now with regard to what is really necessary as far as case depth requirements are concerned. The question asked is whether deep case depths are really required. Considerable thought is given for producing a good core hardness to support the formed nitrided case.

Nitriding cannot be complete in the cycle time consumed for the carburizing process. Even with a shallow case depth and a good core support, the cycle times are still not competitive with the carburizing procedure. However the process techniques of FNC and ANC can compete to some extent when the material selected is low-alloy or even medium-alloy steel.

The use of the low-alloy, surface-enhanced steel by the FNC process is making great inroads into the manufacturing industry. It is used extensively (as previously stated) in the automotive industry, in the forging industry for the surface enhancement of forge dies, and in the die-casting industry for the surface enhancement of the hot-forming dies. Certainly North America is now following the industrial trends of Europe for both manufacturing and process methods, due to the amalgamation of the auto manufacturers in both continents.

The process of nitriding and its derivative processes are seen today as a future surface-enhancement technique for many ferrous and nonferrous metals. Thus Machlet's process and Dr. Fry's process are now perhaps gaining the recognition that they deserve [3]. The process of nitriding is coming of age in this new millennium.

8.2 PROCESS TECHNOLOGY

Each of the four process techniques are used at temperature range described in the tree illustration. Figure 8.1 describes the nitriding process, which is the only low-temperature process that does not require a rapid cooling from an elevated temperature such as is required in some instances of the FNC process. The process technique takes the distinct advantage of utilizing the low-temperature transformation range on the iron–carbon equilibrium diagram, which is the ferrite region. This means that the steel does not undergo any phase change at all (Figure 8.2) [4]. The area on the iron–carbon equilibrium diagram, which is below the Curie line, is known as the A1 line. This is a very focused area that all of the nitriding and FNC processes take place in. The nitriding process requires perhaps the lowest temperature range of all the thermochemical diffusion techniques: 315 (600) to 540°C (1000°F). It should be noted, however, that the higher the nitriding process temperature the greater the potential for the phenomenon of nitride networking (Figure 8.3).

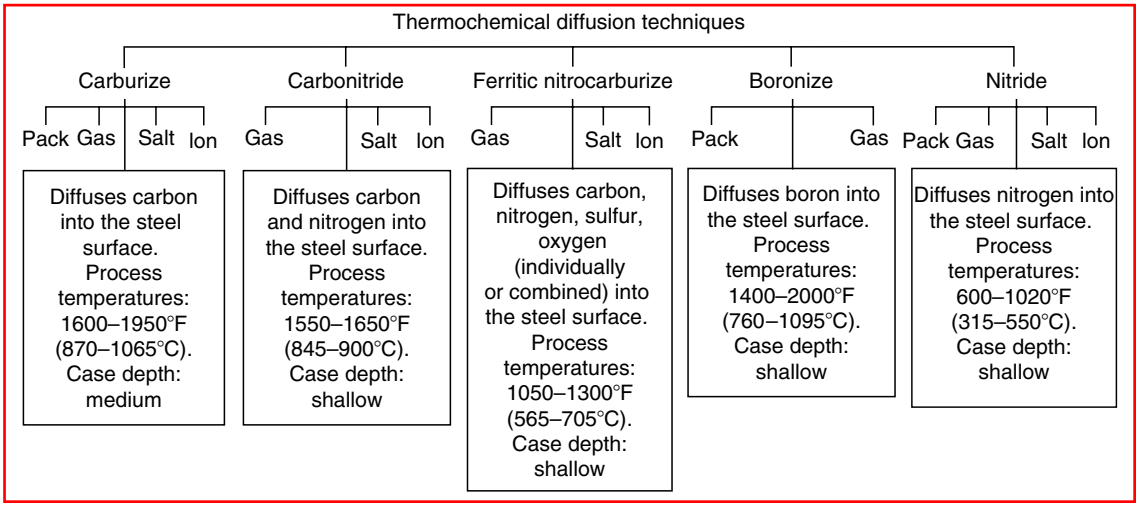

FIGURE 8.1 Comparison of various diffusion surface hardening techniques. (From Pye, D., *Practical Nitriding and Ferritic Nitrocarburizing*, ASM International, Cleveland, OH, 2004.)

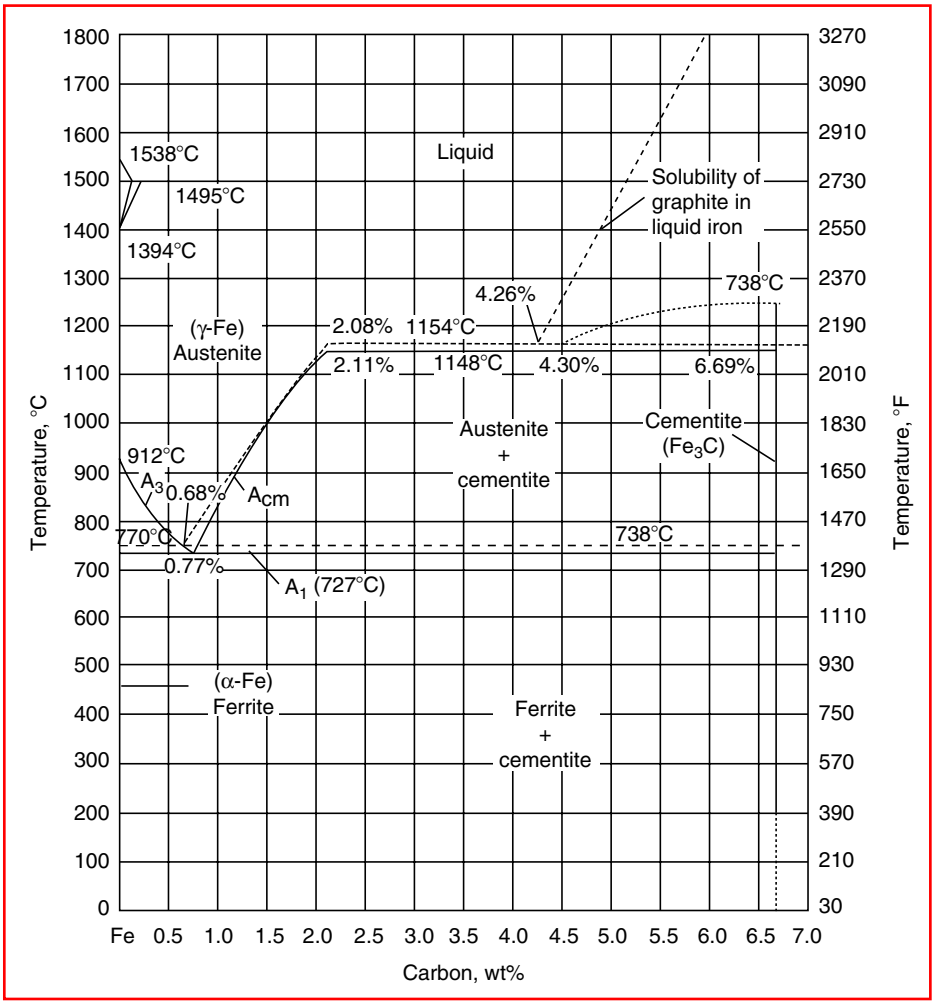

FIGURE 8.2 Iron–carbon equilibrium diagram. (From Totten, G.E. and Howes, G.A.H., *The Steel Heat Treatment Handbook*, Marcel Dekker, New York, 1997.)

This phenomenon occurs with the conventional gas nitriding procedure, which relies on the decomposition of ammonia. However, with the new developments of gas nitriding, which measure and control the exhaust process gases, the problem of precipitation of the nitride networks at corners can now be controlled. The solubility of nitrogen in iron diagram can now play a significant role in accurately determining the area of control necessary to control the formation of the compound layer, and of course the precipitation of networks [5]. In order to take advantage of the diagram and to control the process, the values of the points of the limits of saturation can be determined with a moderate degree of accuracy. What the diagram does not consider is the influence of alloying elements on the critical phase lines of the diagram.

It can be seen that if the Curie temperature of 480°C (882°F) is exceeded in this diagram, then the solubility level of nitrogen will begin to increase, particularly if the process gas dissociation is operating at higher decomposition values. The resulting surface metallurgy in the compound layer will begin to be dominated by the epsilon phase if the weight percentage of nitrogen is greater than 8%. If the temperature selection is high, say in the region of 545°C

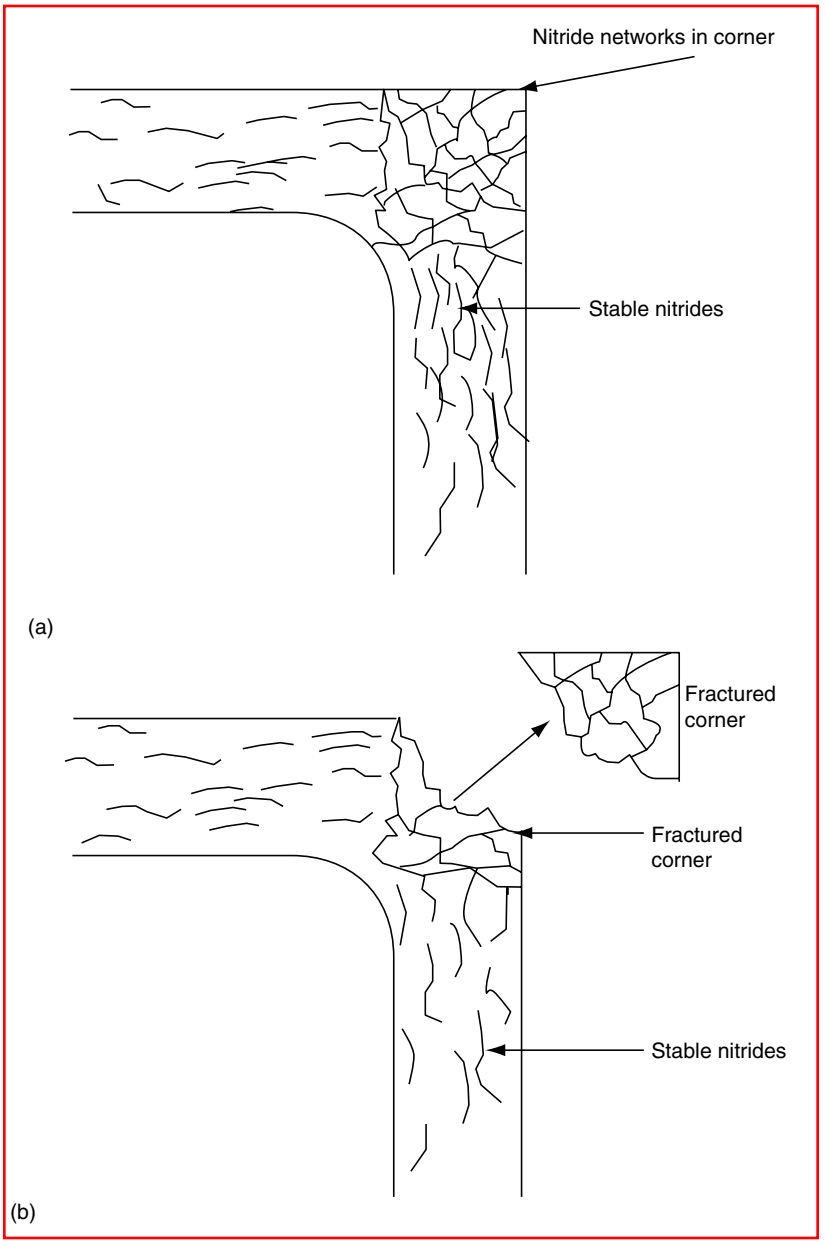

FIGURE 8.3 A schematic illustration of the corner fracturing due to the excessive nitride networks. (Courtesy to Pye D., Practical Nitriding and Ferritic Nitrocarburizing ASM, 2003)

(1000°F), it is advisable to reduce the nitriding potential of the process gas ($2NH_3$). This is accomplished simply by reducing the ammonia flow.

If the nitride network is allowed to form, then particularly at sharp corners on the component, the nitriding case will be extremely brittle and will chip very easily (Figure 8.4) [6]. This means that both temperature control as well as gas flow control are of paramount importance to the success of both the surface metallurgy (compound zone) as well as the diffusion zone. The diffusion zone is the area beneath the formed surface compound zone in which the stable nitrides of the nitride-forming elements are formed (Figure 8.5) [6]. It is also

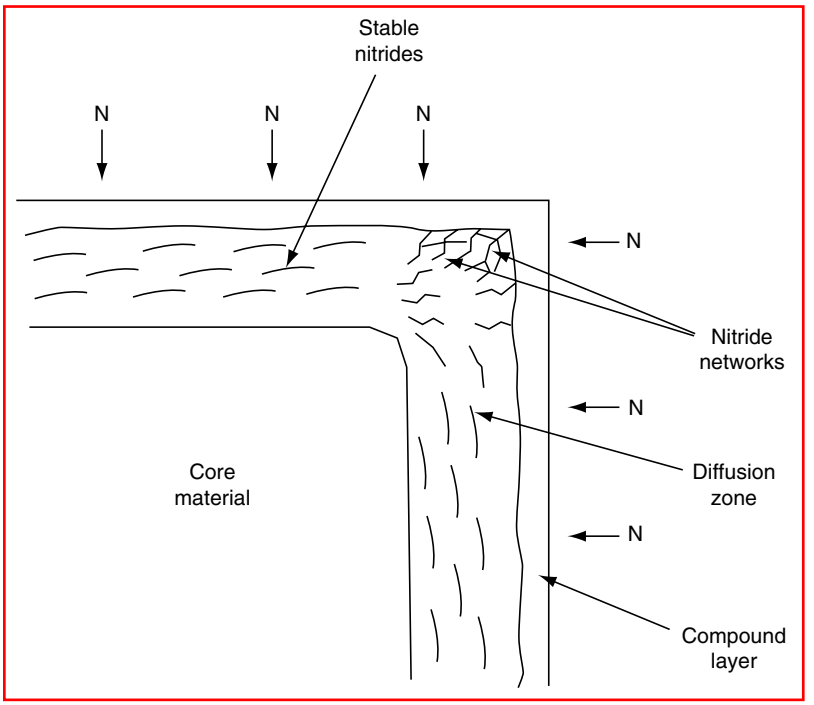

FIGURE 8.4 (a) Illustration of nitride networking. (Courtesy to Pye, D., *Practical Nitriding and Ferritic Nitrocarburizing*, ASM, 2003.)

an important feature of the nitriding process to observe and control the catalytic reaction that takes place at the steel surface interface as a result of the gas decomposition. The mechanics of the nitriding network is simply based on the fact that the higher the process temperature, the greater the volume of ammonia, the greater the risk of the formation of the networks. It also means that the greater is the level of solubility of nitrogen in iron. This is the same principle for a saturated solution of salt and water (Figure 8.6).

It is for this reason that it is most important to maintain and most importantly control a process temperature that is economically achievable and accurately controllable. In addition to the temperature control, the gas flow rates must be equally controllable. This will begin to reduce the potential for the networks formed at sharp corners [7].

There are many commercially accepted methods of controlling the nitriding potential of the nitrogen, as a result of the decomposition of the ammonia process gas. Three of these methods are:

- Volume metric flow control
- Nitrogen gas dilution
- Plasma (ion)

8.3 COMPOSITION OF THE CASE

The case composition of the nitrided steel surface within the formed case is determined by the

- Nitride potential of the steel (composition)
- Process temperature
- Process gas composition

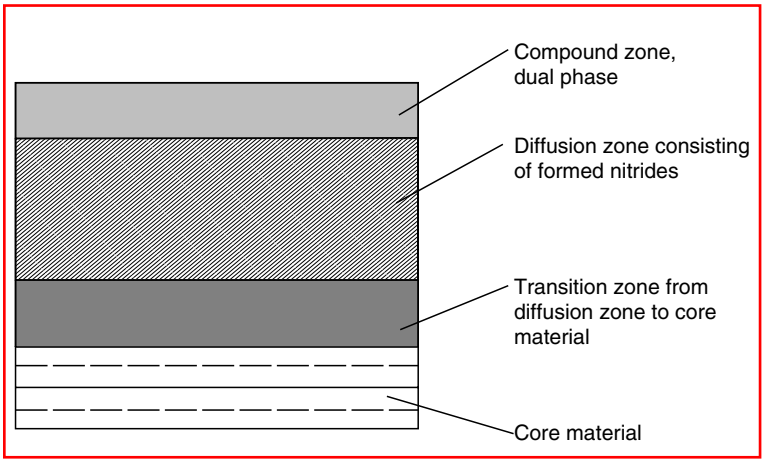

FIGURE 8.5 A typical nitrided structure. (From Totten, G.E. and Howes, G.A.H., *The Steel Heat Treatment Handbook*, Marcel Dekker, New York, 1997.)

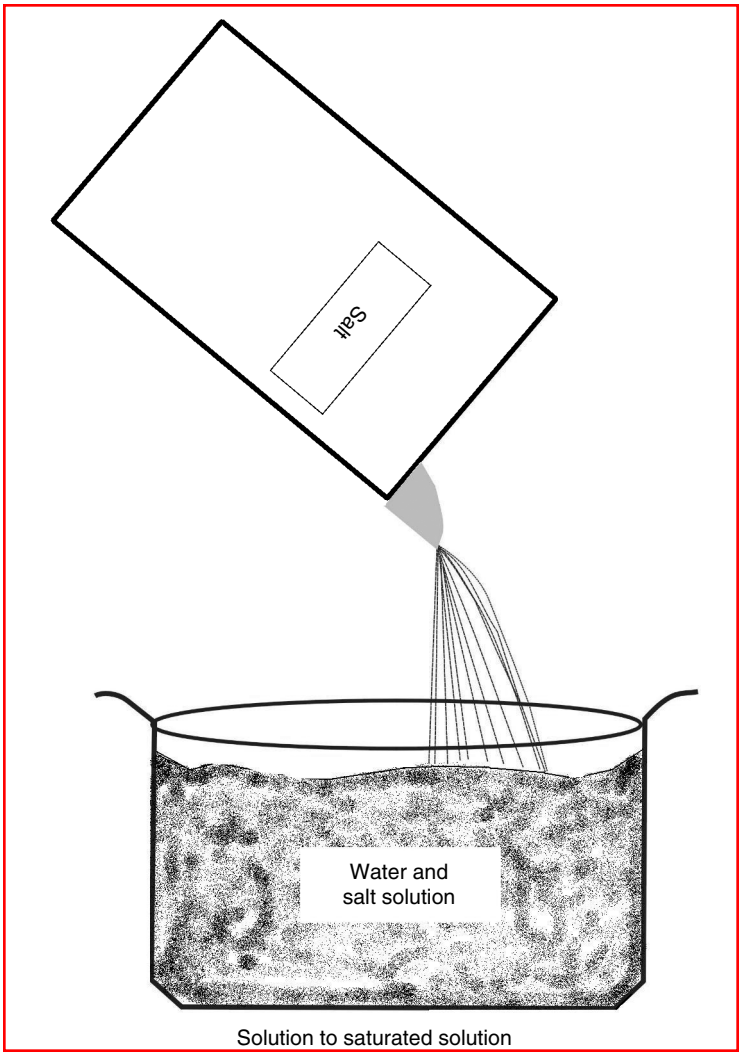

FIGURE 8.6 Solution to saturated solution. (From Pye, D., *Practical Nitriding and Ferritic Nitrocarburizing*, ASM International, Cleveland, OH, 2004.)

- Process gas volume
- Process method

The principle of the nitriding process is based on the long-known affinity of nitrogen for iron at elevated temperatures. Nitrogen has the ability to diffuse interstitially into steel at temperatures below the Ac1 line on both ferritic steel and cementite-type steels. (These steels are known as hypo- and hypereutectoid steels as defined by the traditional iron–carbon equilibrium diagram.) As the steel's temperature is increased toward the Ac1 line, the iron's (steel) crystalline structure will begin to vibrate around their discrete lattice points. The vibration is further seen at the molecular level of the body-centered cubic (bcc) structure. With the vibration at the molecular level, and nitrogen at the atomic level, the nitrogen is small enough to pass through the iron-based lattice structure. The nitrogen will then combine with the iron to form iron nitrides as well as stable nitrides with the alloying elements of the steel chemistry. The diffusion or absorption rate will increase with temperature.

Property of Molecular Nitrogen (N_2)

Atomic weight	14.008
Atomic number	7
Melting point	−210°C
Boiling point	−195.8°C
Liquid density (g/cc)	0.808
Solubility of nitrogen at atmosphere in g/cc all the water at 20°C (100°C = 0.00069)	0.00189
Atomic radius (nm)	0.074

Nitrogen is in the periodic table of nonmetals in Group IVA, along with four other nonmetals. Nitrogen will readily form gases with both hydrogen and oxygen. In addition, nitrogen is diffusible into metals especially at low temperature. Further, it not only will diffuse, but it will also react with metals that it can form nitrides with.

Nitrogen is colorless, odorless, and tasteless, does not support respiration. Although it is not considered to be a poisonous gas, it is however considered to be an almost inert gas. This is not quite true because it will react with oxygen, hydrogen, and certain other metals to form nitrides of those gases and metals.

Nitrogen is generally sourced (in the instance of gas nitriding) by the decomposition of ammonia in the following reaction sequence during the gas nitriding procedure using heat as the method of decomposition and the steel as the catalyst:

$$2NH_3 \leftrightarrow N_2 + 3H_2$$

The structure of the nitrogen atom and its associated bonding mechanism allow nitrogen to bond with iron and certain other elements found in steel. These elements are carbon, sulfur, and other metals that will dissolve readily in iron to form alloys of iron and remain in solution. Steel has the unique property and ability to absorb other elements such as carbon, nitrogen, sulfur, boron, and oxygen into the steel surface in such a manner as to form a new alloy within the steel surface. The group of processes are as follows:

- Surface treatment
- Surface modification
- Surface engineering

The above terms have become the descriptive and collective terms for both chemical and thermochemical treatments. The processes are all diffusion processes and not deposition processes, such as is seen with the thin-film hard-coating processes (Figure 8.7) [8]. The process temperature for the gas nitride procedure is based only on

- An economical diffusion temperature
- A temperature that will not modify the steel's core properties, by decreasing the core hardness value
- A temperature that will not cause a saturated solution of nitrogen in iron at the surface of the treated steel

The steel parts to be treated are placed into a sealed gas tight container that is fitted with a gas inlet port plus a gas exhaust port. The engineering design of this container is very simple (Figure 8.8) [9]. The type of steel recommended for the process container should be of a heat-resisting type such as:

- AISI SS309
- AISI SS310
- AISI SS316
- Inconel
- Inconel 600

It is not recommended to use a mild steel or boilerplate to construct the container. These materials are usually surface contaminated with oxides or decarburization. The container should be completely sealed using a recognized engineering sealing method, taking cognizance of the process operating temperature. The container is then placed in the furnace and the temperature is raised to the appropriate nitriding process temperature. As the temperature of the furnace begins to be distributed within the process container and conducted to the steel through the process gas (ammonia) then the following reactions occur:

$$NH_3 \rightarrow 3H_2 + N \tag{8.1}$$

$$2N \rightarrow N_2 \tag{8.2}$$

$$2H \rightarrow H_2 \tag{8.3}$$

Comparison of the nitriding process

Method	Type of Furnace	Treatment Medium	Temperature	Time (h)	Bonding Layer	Diffusion Layer
Gas nitride	Gas tight	Anhydrous ammonia	950–1060	10–90	$Fe_4 + Fe_{2-3}N$ ($Fe_{2-3}N$)	Nitrides (carbo nitrides)
Fluidized bed	Fluidized bed furnace	Anhydrous ammonia	950–1060	0.1–90	$Fe_4 + Fe_{2-3}N$ ($Fe_{2-3}N$)	Nitrides (carbonitrides)
Pressure nitride	Pressure vessel	Anhydrous ammonia	950–1060	10–90	$Fe_4N + Fe_{2-3}N$ ($Fe_{2-3}N$)	Nitrides (carbo-nitrides)
Powder nitride	Annealing furnace with boxes	Calcium cyanamide and additives	800–1060	3–30	$Fe_{2-3}N$	Carbonitrides
Salt bath nitride	Titanium lined or solid titanium	Cyanide-based salts	950–1060	0.1–4	($Fe_{2-3}N$)	Carbonitrides
Plasma ion nitride	Vacuum-type furnace	Hydrogen + nitrogen + methane	800–1060	0.1–30	$Fe_4N + Fe_{2-3}N$ (free from mixed phases)	Nitrides, carbo-nitrides (free from grain boundary)

FIGURE 8.7 Surface modification diagram (tree type). (From Pye Metallurgical Consulting, *Nitriding Notes*, 1996.)

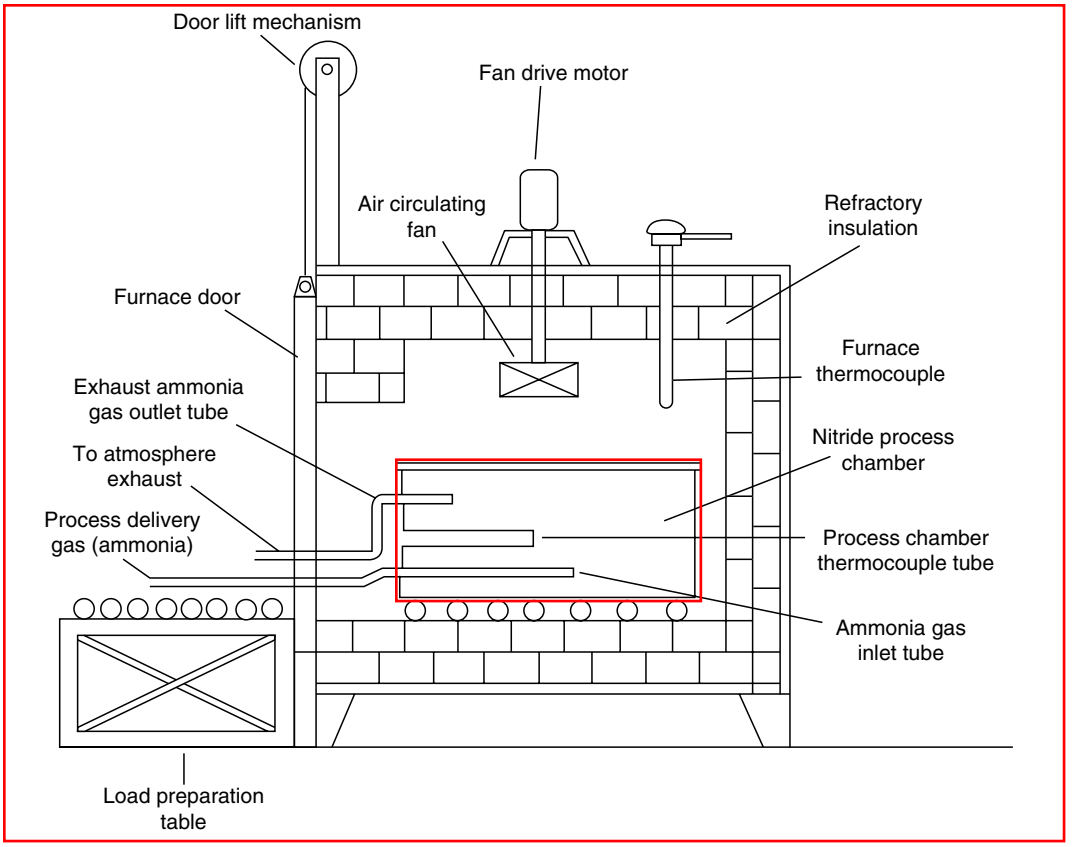

FIGURE 8.8 Simple ammonia gas nitriding furnace. (From Pye, D., *Practical Nitriding and Ferritic Nitrocarburizing*, ASM International, Cleveland, OH, 2004.)

It is known that both atomic nitrogen and hydrogen in reaction 8.1 are unstable and will combine with other like atoms to form molecules as shown in reaction 8.2 and reaction 8.3. When the nitrogen is in the atomic state, diffusion will take place. The diffusion will initiate and take the form of nucleation at the surface of the steel (Figure 8.9) [10].

The formation of compound zone will begin to occur. The composition of the compound layer will depend largely on the composition of the steel, which again will be influenced

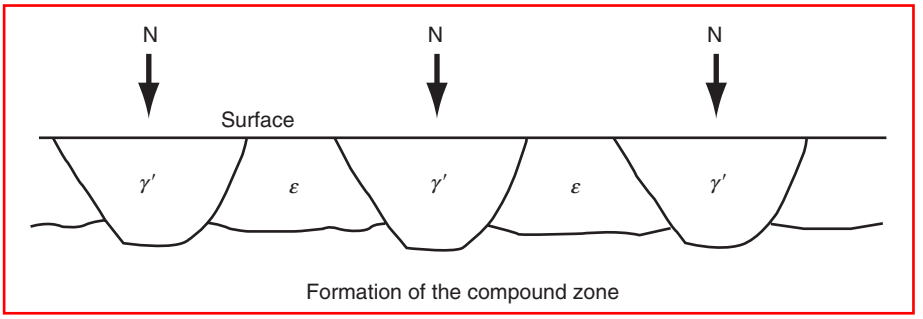

FIGURE 8.9 Formation of the compound zone. (From Pye, D., *Practical Nitriding and Ferritic Nitrocarburizing*, ASM International, Cleveland, OH, 2004.)

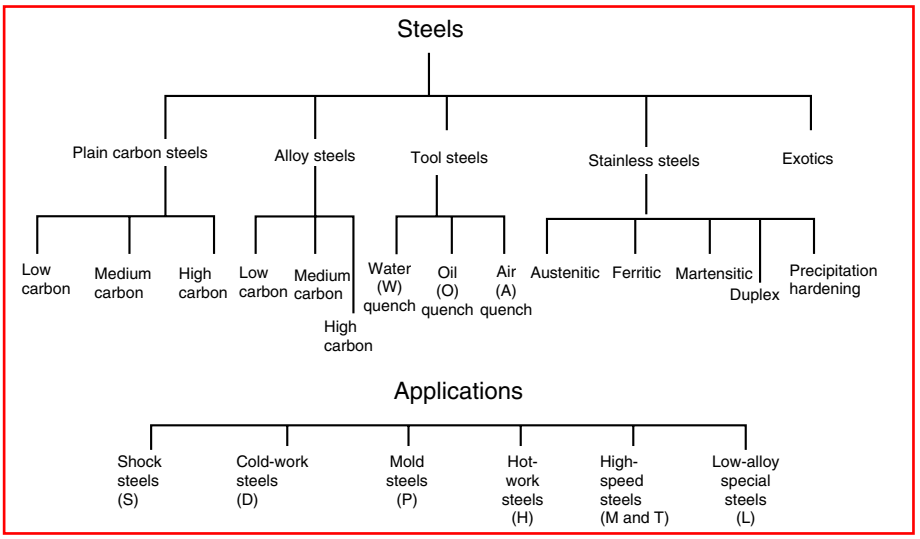

FIGURE 8.10 Steels that can be Nitrided. (From Pye. D. Course notes Pye Metallurgical Consulting.)

strongly by the carbon content of the steel. The carbon content will greatly influence the formation of the epsilon nitride phase (the hard brittle layer). Below this phase, the compound zone will consist of nitrogen, which has diffused into the α-Fe. It can, therefore, be said that the analysis of the steel will also affect the thickness of the compound zone. In other words, plain carbon steels for the same given operating conditions will always produce a thicker compound layer than what will be produced by an alloy steel. Time and temperature will also increase the compound layer thickness. It can be further said that the higher the alloy content of the steel, the shallower or thinner the compound layer will be. The alloy steels with their alloying elements will be more saturated with nitrogen than with a plain carbon steel. Hence the total case that will be shallower on alloy steel will be seen with the plain carbon steels (Figure 8.10) [10].

The question now arises as to the hardness of the nitrided case. We tend to measure the success of heat treatment by the accomplished hardness as far as both case hardening and hardening are concerned. Therefore if we measure the hardness value of plain carbon steel or low-alloy steel after nitriding, we will find a hardness value in the region of 35 Rockwell C scale. By normal standards of accomplished hardness, this will be considered to be low hardness value. However, hardness is relevant. If the wearing surface of another part is in contact with the nitrided surface of a low-alloy steel, and the hardness of that part is of a lower value than the low-alloy nitrided steel, then the nonnitrided part will wear in relation to the low-alloy nitrided steel. What is not often recognized of the nitrided low-alloy steel, although its hardness is of a low value, is that its corrosion resistance is extremely high. Therefore one should not always consider hardness, but also other properties and advantages the nitrided surface of a low-alloy steel will produce.

8.4 COMPOSITION OF THE FORMED CASE

The properties of the compound layer, also known as the white layer, have generated much interest among engineers and metallurgists. The use of the terms compound layer and white layer seems to cause some confusion. It is correct to use both terms for the surface layer. The

term compound means more than one and within the layer there are generally two phases present (unless of course no compound layer is formed). The formed phases within the surface layer are known as:

- The epsilon phase
- The gamma prime phase

When selecting nitriding gas flow ratios and process conditions, and hydrogen, plus the process cycle time, it is necessary to consider the thickness and composition of the compound layer.

The thickness of the compound layer on plain carbon steel will always be of greater thickness than that of the alloy and conventional nitriding steels that contain the strong nitride-forming elements. Once again the thickness of the compound layer will be determined by time, temperature, steel chemistry, and the process gas composition. The thickness of the compound layer is generally seen to be (dependent on steel chemistry and process gas ratios) approximately 10% of the total thickness of the diffused nitrided case. This will of course vary according to the steel treatment. The compound layer is soft and brittle to the point that it can spall and fracture during service, which will cause accelerated wear and premature failure. A simple spot test for the presence of the compound layer (without destroying the component) can be accomplished by using a solution of copper sulfate.

8.4.1 Epsilon Phase

During the gas nitriding process the compound layer is formed and it has been previously stated that the compound layer comprises the two metallurgical phases that are mixed together. Generally each of the two phases is present on the surface. The value of each phase is approximately 50%. The epsilon phase is strongly influenced by the presence of carbon in the steel, and if carbon is present in the gas flow. A compound layer of predominately epsilon phase will create a surface with good wear characteristics, but it will have no impact strength. To create a dominant phase of epsilon in the compound layer it can be accomplished simply by raising the process temperature to 570°C (1060°F) and adding methane to the gas flow.

8.4.2 Gamma Prime Phase

The gamma prime phase is a phase that is present in the compound layer and it will give reasonably good impact strength without surface fracture, provided that the compound layer is not excessively thick. To accomplish this, one would simply maintain a process temperature of 500°C (930°F) and reduce the nitriding potential of the process gas.

Control of the thickness of the compound layer is simply accomplished by process temperature and gas flow manipulation for the process of gas nitriding. The Floe process (two-stage process) is perhaps the simplest method of controlling the thickness of the compound layer. This is done by the manipulation of temperature–time and gas flow. All the dilution processes can control the thickness of the white lead or compound layer. The most effective way of controlling the compound layer is to consider the use of the ion nitride process. The ion nitriding process can be used effectively to create a dual-phase compound layer condition, or a monophase condition or eliminate the compound layer entirely.

8.4.3 Diffusion Layer

As the nitrogen diffuses interstitially into the body of the material it will flow out and combine with the nitride-forming elements in the steel. This means that the diffused

TABLE 8.1
The Harris Formula Factors Based on a Simple Nitriding Steel

Temperature		
°C	°F	Temperature Factor
460	865	0.00221
470	875	0.00233
475	885	0.00259
480	900	0.00289
500	930	0.0030
510	950	0.0033
515	960	0.0035
525	975	0.0037
540	1000	0.0038

The above values are suggested factors only.

nitrogen will be tied up in nitrides and will form nitrides. The diffusion layer is, when examined microscopically, the main body of the nitrided case. The hardness value of the diffusion layer will be determined by the chemistry of the steel treated, and the gas composition in relation to the decomposition of the ammonia and the selected process temperature.

The formation of the total nitrided case is determined (as has been previously stated) by time, temperature, and gas composition. The depth of case is determined by the rate of nitrogen diffusion into the steel surface. Harris of the Massachusetts Institute of Technology concluded that on any given surface treatment procedure, the rate of diffusion is determined by the square root of time, multiplied by a temperature-driven factor. The table above shows the square root of time and the temperature-driven factor (Table 8.1).

It must be pointed out that the above values relate only to alloy nitridable steel. It must not be construed that the table is applicable for all steels. This table is intended only as a guide and not as a reference. On alloying the level of steels increases, and the rate of diffusion of atomic nitrogen into the steel is retarded.

NITRIDING

8.5 TWO-STAGE PROCESS OF NITRIDING (FLOE PROCESS)

The chapter on nitriding in the first edition of this handbook discussed briefly the work of Carl Floe of the Massachusetts Institute of Technology, which was investigated in the early 1940s. His work was recognized as one of the major investigative research programs regarding the formation of the compound layer. His work is still valued today and is used on a daily basis by many companies. It is interesting to note that Floe process has become a very popular method of nitriding. This is because control of the surface metallurgy is far easier than it is with the conventional gas nitriding process. By this is meant that the control of the formation of the compound layer in terms of its thickness and of phase content, is controlled by the higher process temperature and the minimized availability of nitrogen. This process is most popular with the gear manufacturers, but it is not confined to that industry. Once again the reason for its popularity is the better control of the surface metallurgy in terms of the compound layer thickness.

The Floe process is carried out as two distinct events. The first portion of the cycle is completed at a normal nitride process temperature of 495°C (925°F) and is carried out for approximately one third of the total cycle. As the event is concluded, then the temperature is raised approximately to 560°C (1030°F) and the gas dissociation is now run at approximately 75 to 80%. Because now the nitride potential is reduced, which means the nitrogen availability is reduced, the preexisting nitrided case from the first stage of the process will begin to diffuse further into the case and at the same time it will dilute. As a result of this dilution and now with the reduced nitrogen availability, the net result is a thinner compound layer. For applications that require a more precise control of the surface compound layer, the Floe process as well as the precision nitride process are considered. It is important to note that when considering the two-stage process, the tempering temperature of the steel component treated should also be taken into account. The reason is that the process temperature should be kept below the pretempering temperature so as not to affect the core hardness that will support the case. There is of course a very simple way of reducing the thickness of the compound layer to the point that there is no compound layer and that is to simply grind the compound layer off. This would mean having the knowledge of how thick the compound layer is in order to grind it off.

8.6 SALT BATH NITRIDING

The salt bath nitriding can be more likened to the FNC treatment rather than to a pure nitriding treatment. The salt bath treatments employed today are more closely aligned to the FNC process. The control of the salt bath chemistry is of paramount importance and should be tested on a frequent basis in order to ensure a consistent and repeatable surface metallurgy. As with the gaseous process of nitriding and ion nitriding, the case depth is still related to time, temperature, and steel chemistry. The longer the time at temperature, the deeper would be the case depth. With a new bath, it is necessary to age the bath for approximately 24 h to ensure that the bath is settled and aged to the point that surface pitting will not occur. The source of nitrogen for the process comes from the decomposition of cyanide to cyanate. Once the bath has been aged, the processed components would come out of the bath with the traditional matte gray finish. With continual use of the bath, the cyanide level will continue to decrease. Conversely, the cyanate and carbonate levels will increase. If a high cyanate level is experienced, the surface finish of the treated steel will be somewhat darker than the conventional matte gray finish [11].

If it is determined that there is a high cyanate level as a result of a titration, the cyanate can be reduced simply by increasing the temperature of the bath to a temperature of 650 to 700°C (1200 to 1300°F) for approximately 1 h at that temperature. Once the time at the temperature has been completed, it is not advisable to process work through the bath. The bath should be allowed to cool down and then analyzed. Once the titration shows the correct cyanate concentration, then treatment can be carried out. It is recommended that the bath be tested at the commencement of each shift operation and the cyanate level adjusted accordingly. The bath tends to collect sludge at the bottom of the salt bath; therefore, one should desludge the bath periodically. The sludge is created by iron oxide precipitates released into the bath from work support fixtures, holding wires, and of course from the work itself. There will also be some carbonates, some iron oxides, and possibly some cyanide residues mixed in.

8.6.1 SAFETY IN OPERATING MOLTEN SALT BATHS FOR NITRIDING

When operating a molten salt bath of any description it requires a very careful handling by the furnace operator in order to maintain a high degree of safety for both the operator and

the work to be processed [11]. Given below is a simple list of operating procedures and precautions:

- It is essential that all operators ensure good personal hygiene and of course great care when handling any type of heat treatment salts in particular cyanide-based salts.
- Ensure that operators, who are involved with the use of heat treatment salts, are fully aware of the appropriate material data sheets for the salts used. They should also be aware that the salts are extremely poisonous, dangerous, and should be handled with extreme care.
- The operator of the salt bath should wear the appropriate safety clothing and protective equipment such as full arm gloves (not plastic), arm shields, eye protection, safety masks, a fire-resistance apron, plus leggings, and safety shoes.
- It is important that no one mixes cyanide-based salts with nitrate salts, otherwise there is a very serious risk of explosion or fire.
- All work processed through a molten bath should be preheated to remove all traces of surface moisture and to reduce the thermal shock that the work will experience when immersed into a molten bath.
- Store and accurately label all storage drums and containers. Identify the drums as poisonous or toxic. Once again, do not mix cyanide sludge with a nitrate sludge. This leads to a risk of serious explosion or fire.
- It is most important that adequate ventilation be provided around the top of the salt bath and in close proximity to the top of the bath. This will ensure that any fumes that are generated from the molten salt will be exhausted away from the operator.
- Provide a rack for the support of all work fixtures, lifting hooks, desludging tools, and any other tooling required for the operation of the bath.
- Provide a hot water rinse tank in order to ensure not only tooling cleanliness, but also processed work cleanliness after the treatment has been carried out.

8.6.2 Maintenance of a Nitriding Salt Bath

As with any furnace, its maintenance is a necessity. Salt bath furnaces are no exception, and they may even require a greater maintenance schedule than with a normal conventional atmosphere furnace. There are both daily and weekly maintenance routines that the operator of the furnace should perform to ensure optimal performance of the equipment. The following is suggested as routine of both a daily and a weekly maintenance program.

8.6.2.1 Daily Maintenance Routine

- It is necessary that a titration of the bath be conducted on every shift that the furnace is operated on. If the furnace is operated only on a daily basis, then the titration should be conducted every 24 h. The results of the titration should be recorded, and if any trends are observed, they should be noted. The necessary addition of each type of salt required to bring the cyanide–cyanate level to the required concentration level should also be recorded.
- A visual check should be made of the temperature measuring the equipment (the control thermocouple, over temperature thermocouple, controll instrument, and over temperature instrument) that it is completely functional and operational.
- When using an aerated bath, it is necessary that the air pumps and flow meter are operating without any restrictions. If using a compressed airline, ensure that the air is both clean and dry. If the air is wet, moisture will be introduced into the bath and this could have some serious complications such as an explosion.
- Visual observation of the part as it comes out of the salt bath can provide more information. Check the surface color, appearance, and in particular if any surface pitting is occurring.

- On the commencement of each shift, or each day's operation, desludge the bath to remove free iron oxides, carbonates, and other contaminants from the bottom of the bath.

8.6.2.2 Weekly Maintenance Routine

- It is important to check the outside surface of the salt pot. Therefore at the commencement of each operational week, lift out the salt pot and examine the external surface of the pot (especially if gas-fired) for heavy-duty surface oxides (scale). Also check for the size of the salt bath. Remember that the salt bath is carrying a heavy load of molten salts and distortion can occur as a result of the salt mass.
- Regenerate the bath each week by raising the temperature to approximately 600°C (1112°F) and increase the aeration flow into the bath. The iron oxides, carbonates, and other contaminants that are in suspension and in solution will precipitate out of the salt and settle at the bottom of the bath, i.e., ready for desludging.
- Each week ensures that the hot water cleaning the system for washing and rinsing the parts after treatment is drained and cleaned off any salt sludge that may be in the bottom of the cleaning tank. Be aware that the wastewater should not be drained into any city or a municipal drain. If this occurs, serious consequences can arise. The contaminated wastewater will contain residual cyanides and carbonates.

8.7 PRESSURE NITRIDING

As was stated in the previous edition of this handbook, there still remains an interest in pressure nitriding. The same leading German company that was previously mentioned still has a strong investigatory research program on pressure nitriding. Pressure nitriding is becoming as interesting as low-pressure carburizing as a surface treatment method. It is felt that the investigating metallurgists have proposed that the pressure nitriding system takes place at around 2 to 5 bar over pressure. It seems to be the optimum pressure at which to take advantage of pushing the process gas into fine holes without any gaseous stagnation within the hole. Although higher operating pressures will work, the value added to the component is not worth the addition engineering design cost for the furnace.

The procedure is a relatively simple process, in fact the same as gas nitriding. The differing exception will be of course the pressure of the process gas and the chamber pressure. At these process pressures, the retort must be considered to be a pressure vessel, and be manufactured as a pressure vessel with all of the appropriate insurance inspections. As was stated in the previous edition, no advantage is gained by operating at high pressures, higher than 5 bar.

As far as the cost of processing the work with the pressure nitriding technique, it would be more expensive than with conventional gas nitriding. This is because a pressure vessel system is involved and all of the necessary high-pressure gas lines and delivery system are in place to ensure a sound and safe system. What sort of success the pressure nitriding system will enjoy in the future is not known.

8.8 FLUIDIZED BED NITRIDING

The growth of fluidized beds for the nitriding process has grown considerably during the past 10 years. A great deal of investigatory work has been carried out by an Australian company with the purpose of developing a better control system of the decomposed process gas for diffusion into the steel. The investigatory work has been carried out on the tool steels, and in

particular the hot-work group of tool steels, principally for extrusion dies, forging dies, and ejector pins [8].

The principle of nitriding into a fluidized bed as far as gas decomposition is concerned is still the same principle, with the ammonia decomposing into its primary constituents, namely nitrogen and hydrogen. The advantage of the fluidized bed is that process cycle times are reduced simply because of faster temperature recovery and the ability to rapidly change the atmosphere composition when necessary. With the advantages, there are also disadvantages. The principal disadvantage is the volume of the reactive gas required to fluidize the bed is considerably higher than the gas flow that would be required for say, an integral quench furnace. The consumption can increase as much as tenfold [8]. In addition to having the ability to gas nitride in a fluidized bed, one can also accomplish FNC in a fluidized bed simply by a change of gas composition to the appropriate gas mixture. The fluidized bed can also be used for ANC. Claims are also made that the surface finish of the workpiece remains reasonably constant. In other words there is no surface erosion [12], and it is also claimed that the distortion is at an absolute minimum. For example, when measuring pitch diameter on a fluidized bed-nitrided gear, it is claimed that the pitch diameter run out is less than 0.0002 in. per side of all linear growth on measurements over steel balls [13]. The process temperatures and process times are still the same as they would be when using an integral quench furnace, or even a conventional gas furnace [12]. The only process parameter to change will be that of a process gas volumes. Whatever steel can be nitrided in the gaseous system can be nitrided equally so in the fluidized bed furnace.

8.9 DILUTION METHOD OF NITRIDING

It is important to mention, as was mentioned in the previous edition, that Machlet's original patent application reads "for the nitrogenization of irons and cast irons using ammonia diluted with hydrogen." This statement still stands, and has been used to form the basis of the present operating dilution technology that was developed in Europe. The process is designed to reduce the thickness of the compound layer formed at the surface of the steel during the nitriding process. The principle of the process is to either dilute or enrich the available nitrogen for diffusion into the surface of the steel. This is accomplished by precise control methods using a computer in combination with a programmable logic control system. The gas delivery system now relies on precise metering of the process gas flow [14].

The dilution or enrichment is with nitrogen (sourced from ammonia) or hydrogen. This method of nitriding will considerably reduce the thickness of the compound layer. It will also control the phases of the compound layer. In other words, the phase can be dominantly epsilon or gamma prime, depending upon the steel being treated and its application. The control method of this procedure has changed from the traditional dissociation method of measurement of decomposition. It is this change that is making the application of this process most attractive to users. The change in gas decomposition is now with the measurement of the insoluble exhaust gases (nitrogen and hydrogen) that offers a more precise process control than has been accomplished by the traditional control methods.

The method of process control in conjunction with the PC/PLC is seriously competing with the pulsed plasma nitriding control method. The principal advantages of the process are in the following areas:

- Capital investment
- Reliability, because no pulse power generation power pack is necessary
- Controllability of the surface compound layer
- Repeatable surface metallurgy

One can also use the dilution method principle to accomplish the FNC and ANC processes, simply by changing the gas composition and adding a hydrocarbon-based gas. This means that low-alloy steels can be treated quite easily.

The normal precautions are to be applied when using ammonia and hydrogen in terms of fire risk and safety. The furnace should have an effluent stack, which includes an after burner to ignite and burn the effluent gas coming from the process chamber. This is so as not to have raw ammonia as an effluent blowing into the outside surrounding atmosphere.

The resulting formed case will have as good a controlled surface metallurgy as would a formed case by plasma technology. The distinct advantage is of course that the initial capital investment will be considerably less. The growth of this technology is growing each day and is becoming a widely accepted and an almost preferred process.

There are claims that the compound layer is of a much denser nature than that accomplished by plasma processing technology. There will be, of course, the arguments that abound with the superiority of each of the different surface metallurgy by each of the rival process technologies. That debate will continue for many years to come [15].

8.10 PLASMA NITRIDING

Since the writing of this chapter in the previous edition of this handbook, there has been tremendous growth in the use of the process technology and the process has also undergone considerable changes. There is a greater awareness now about the value of plasma processing techniques, which is not confined only to plasma nitriding. Significant changes are seen in the process requirements on engineering drawings, which are required for plasma nitriding technology. It is believed that this awakening has arisen from a greater understanding into what the process involves, and its benefits, ease of control, and its ability to be user-friendly. This growth is beyond that achieved in understanding of the process metallurgy. It is believed that the greater awareness and understanding of plasma nitriding has arisen due to a greater exposure of the process, resulting from the presentation of technical papers and educational courses. Further to this, a greater realization has been made regarding the safety and environmental aspects of using nitrogen and hydrogen as opposed to ammonia [14].

8.10.1 Plasma Generation

The generation of a plasma can be a natural phenomena. For example, the formation of the northern lights is pure plasma. This is the result of atmospheric gases such as hydrogen, nitrogen, argon, oxygen, and other gases present in the upper atmosphere in a low-pressure environment and exposed to the effects of the sun's magnetic rays. This causes the gas to be ionized and as a result of the gas ionization, the gases emit a luminous glow. The gas present in the upper atmosphere will determine the color of the glow. The movement or dancing to affect the northern lights is due to the movement of air at that particular altitude.

Another common display of plasma energy seen during heavy storms is through lightning. Lightning is an intensified flash of energy, or ionized gas into the air, which has become charged with negative ions. The energy buildup is such that the arc will migrate from its charge (cloud activity) to a ground source. This energy is so intense that it can kill animal or person or ignite, for example, a tree.

Other examples of plasma generation are the lumina storm lamps that are sold in the gift shops. The lamp consists of a sealed glass dome that contains air at a partial pressure. Inside the glass dome is an anode connected to a power source. Once the power is turned on, there is electrical discharge between the anode ball inside the dome and inside the glass bowl. The discharge is seen as random discharges over what might appear to be small bolts of lightning

occurring between the discharge of all the glass wall. This is what can be considered as uncontrolled plasma. Another common application of plasma is the fluorescent light tube. This is simply a sealed glass tube that contains a gas at normal atmospheric temperature and pressure. The tube is then connected to a power source and voltage is applied to a sealed tube. The gas within the tube will conduct electricity just as an electrical copper cable conducts electricity. The difference in this instance between the gas and the copper is that the gas will ionize as the gas molecules are excited, which results in a glow. The type of gas present in the tube will determine the color of the glow. Another application, which is commonly seen, is the colored glowing shop window signs that are seen in many store windows, indicating whether the store is open or closed. The colored tubes are also used to identify products.

Plasma technology is used in the field of heat treatment and it is not a new technology. It has been in use since 1932 and was developed by Wehnhelt and Berghaus in Germany. Their partnership led to the formation of a well-known international company. This technology was known as continuous DC power technology. This means that the voltage is switched on and is set at a particular voltage level in relation to pressure within the process chamber and the surface area of the workpiece under treatment, and is continued throughout the process on a continuous basis [14].

In the early 1950s, Claude Jones, Derek Sturges, and Stuart Martin of General Electric in Lynn, Massachusetts, began to work on the commercialization of the plasma nitriding technique in the United States. They were successful with their work and a production unit was developed, which was finally closed in the year 2000 after several years of a very successful process work [8].

In the late 1970s, three scientists at the University of Aachen in Germany began to investigate ways to eliminate the risk of the continued problem of arc discharging. It was their contention that if the continuous power can be interrupted before an arc is discharged, then the risk of arc discharge can be eliminated. The problem of arc discharging is that, should the arc strike a sharp corner of a workpiece, then localized overheating occurs. This is followed by the possibility of burning the steel at the point of contact by the arc. Not only can there be metal loss, but there will be evidence of a localized grain growth as a result of overheating.

The three scientists at Aachen University discovered a method of interrupting the continuous power. This was a birth of the pulsed plasma generation technique. This technology began to be commercialized in the early 1980s and began to be seen in applications where high wear, abrasion resistance, and corrosion resistance are necessary for the success of the performance of the workpiece. It was also seen that by the manipulation of the process gas flows (nitrogen and hydrogen) that one could manipulate the compound layer (white layer or compound layer) surface metallurgy. This was seen as a major breakthrough in the process technique of nitriding. Thus with gas nitriding and salt bath nitriding, the final results are that the surface metallurgy is fixed. In other words the compound layer is of a mixed phase (usually in equal proportions) of epsilon nitride and the gamma prime nitride [16].

The new technology was named pulsed plasma technology. The conventional plasma furnace equipment manufacturers were skeptical about the technology. The users of the conventional plasma nitriding were also skeptical. Due to the belief and persistence of the scientists in Aachen, the technology began to be recognized and accepted by the industry.

The principle of the technology is based on the ability to interrupt the continuous DC power at specific and variable time intervals. The variable time interval can range anywhere from 3 to 2000 μs. Not only can the power be interrupted, but also the voltage power setting is also variable. This enables the user to have the freedom of power requirements in relation to power time on and power time off. It further means that the power time on and power time

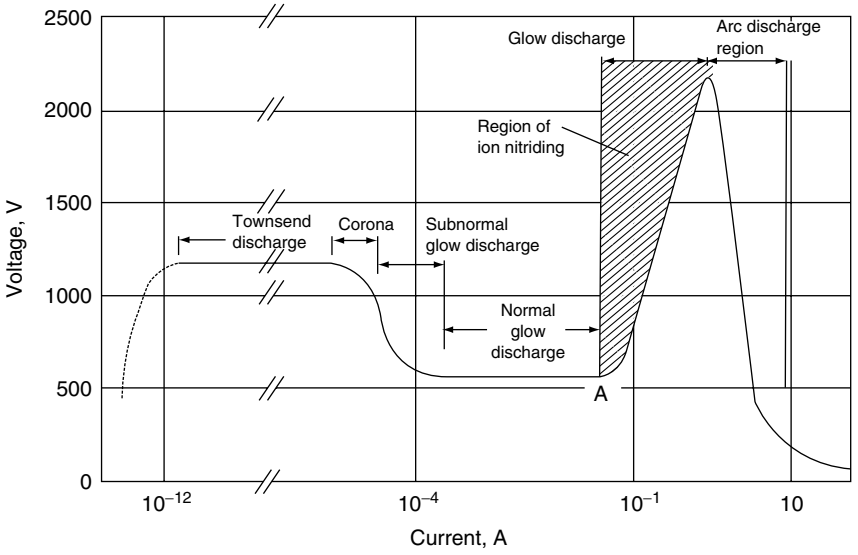

FIGURE 8.11 The Paschen curve. (From Totten, G.E. and Howes, G.A.H., *The Steel Heat Treatment Handbook*, Marcel Dekker, New York, 1997.)

off are also variable. Given now the ability to manipulate the following items, the metallurgy of the surface can now be created to suit the application of the workpiece.

- *Voltage*. The voltage can be set to operate anywhere between the normal glow discharge region on the Pashen curve (Figure 8.11) and the arc discharge region.
- *Pulse time*. The pulse time of both power on and power off can be varied to suit the part geometry (Figure 8.12).
- *Process pressure*. The process pressure can now be manipulated to suit the part geometry. This means that blind holes can be more readily nitrided without the risk of gas

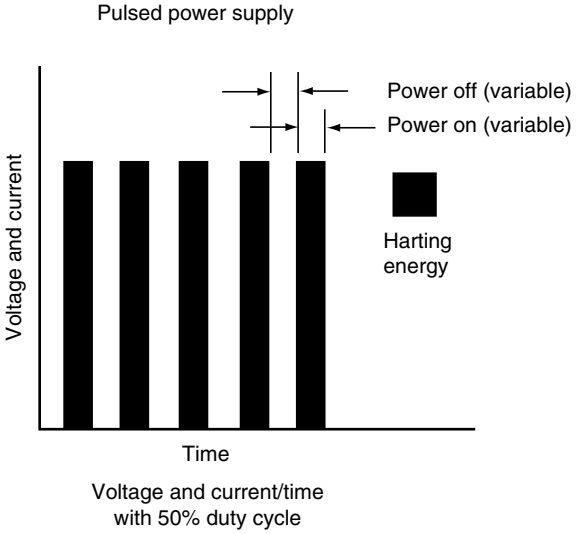

FIGURE 8.12 Variable-pulse duty cycle. (Courtesy of Seco Warwick Corporation, Meadville, PA.)

stagnation as it is sometimes seen in gas nitriding. In addition to this, control of the process pressure can be utilized in order to stop the potential for overheating the sharp corners of the workpiece.

- *Process gas*. The process gases used in the ion nitriding process are nitrogen and hydrogen, and can be significantly reduced in terms of volume in relation to gas nitriding. The gas ratios between nitrogen and hydrogen can be adjusted once again to suit the surface metallurgy necessary for the success of the workpiece in its working environment. The process gases of hydrogen and nitrogen can now be utilized to create the surface metallurgy required. In addition to this, the volumes of the process gas required for the ion nitriding process are significantly reduced in relation to the volumes required during the gas nitriding process.
- *Temperature*. It is now not necessary to use the temperature as the source of decomposition of the process gas (ammonia) during the gas nitriding process. The gas nitriding process relies on two sources for decomposition of the gas: the first the process temperature, and the surface of the steel acting as a catalyst. There is now no need for a catalyst to sustain the decomposition of the process gas. The process gas used is already in a molecular form and is simply decomposed to the atomic form by the use of electricity. Because there is no requirement of a set process temperature as it is with gas nitriding, the user can manipulate the temperature from as low as 315 (600) to 540°C (1000°F). This gives the user a very broad range of temperature selection for the process.
- *Process time*. Because the process gas is prepared in a completely different manner to that of gaseous nitriding (by gas ionization), the net result is shorter process cycle time. The inference is that plasma nitriding is a faster process, and that of the rate of diffusion is faster than it is with gas nitriding. This is not true, simply because of the laws of the physics of diffusion are still the same, be it gas or plasma. Because the process gas for plasma is prepared for diffusion in a completely different manner to that of the gaseous technique the net result is a faster cycle time. Gaseous nitriding relies on the gas decomposition as a result of temperature and surface catalytic reaction. With ion nitriding the gas is converted into nascent nitrogen almost instantaneously, simply by the gas ionization.

It is believed that the future of plasma ion nitriding lies with the pulsed DC technology. This technology offers an almost infinitely variable control of plasma power. Combining this with the previously mentioned features, the process technique can offer the metallurgist and the engineer a very controllable (and most importantly) repeatable surface metallurgy [15].

8.11 POST-OXY NITRIDING

The process of postoxy nitriding has generated a great deal of interest during the past 10 years as a result of the process in normal heat treatment circumstances known as black oxide treatments. In gaseous nitriding techniques, if the processor retort was opened too early at the cool down portion of the cycle, surface discoloration was often seen in the form of random colors on the surface of the workpiece. The end user was usually suspicious of the quality of the nitriding as a result of the formation of the surface colors. In reality, opening of the retort too early had oxidized the surface. Thus, the ingress of air into the process retort will attack the surface of the workpiece. A thin oxide film is formed on the surface of the workpiece.

The black oxide treatment (chemical process) gives surface protection in terms of corrosion resistance and a very pleasant mat black surface finish. The manufacturers of heat-treating salts, and particularly the nitriding salts, were very quick to take advantage of the black surface finish. They accomplished this by treating the surface of the steel by the salt

bath nitride process, which is then followed by polishing the surface of the workpiece. Once this polish has been done, the workpiece is then placed into a molten caustic soda bath (sodium hydroxide). This means that the surface on the polished steel is then oxidized leaving the black finish.

Gaseous nitriding processes then sought to accomplish an oxide finish by purging the process retort after completion of the nitriding process using the nitrogen as the purge gas, followed by the introduction of either oxygen or steam. This formed an oxide layer on the surface of the nitrided steel. The thickness of the oxide layer was dependent on the temperature at which the oxygen-bearing medium was introduced into the process retort and the time that it was held at the temperature at which the oxygen-bearing gas was introduced. The temperature at which the oxygen-bearing gas is introduced into the process retort also determines the color of the surface finish. If the gas is introduced into the retort at 500°C (935°F), the surface color is most likely to be black. If the gas is introduced into the process retort at 370°C (700°F) the finish is likely to be a blue color. However, the thickness of the oxide layer will not be very thick.

The manufacturers of plasma nitriding the equipment were very quick to see an opportunity of improving their process techniques. The advantage of using the plasma system is that the process is operating at partial pressure. The vacuum pumping system is controlling this partial pressure. On completion of the nitriding cycle, one would simply allow the vacuum pumping system to evacuate the process retort. At this point, the choice of oxidizing gas is the choice of the particular equipment manufacturer. Some manufacturers introduce water vapor into the process retort, which could have a long-term detrimental effect on the interior walls of the process retort [15].

The technology of creating a surface oxide on steels has been taken across the field of FNC treatments. Once the FNC process has been completed the immediate surface of the compound layer is deliberately oxidized to form a thin surface oxide layer on the immediate surface of the compound layer. This technique is used extensively on low-alloy steels and is utilized to manufacture cost-effective parts (low-alloy steels), enhanced by the FNC treatment followed by postoxidation treatments. Some of the components that are treated in the automotive industry are:

- Gear shift levers
- Window lift drive gears
- Timing gears
- Windshield wiper arms
- Windshield drive motor housings

The above are a few of the items that are currently ferritic nitrocarburized followed by the postoxidation treatment (Figure 8.13).

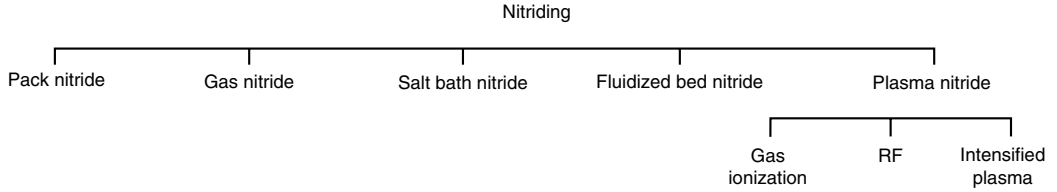

FIGURE 8.13 Methods of Nitriding. (From Pye D. Nitriding course notes, 1998.)

The pulsed plasma ion nitriding technology lends itself to the complete process technique of nitriding followed by postoxidation treatments, or FNC followed by postoxidation techniques. The postoxidation treatment offers the metallurgist and the engineer greater versatility in the equipment usage and process continuity.

8.12 GLOW DISCHARGE CHARACTERISTICS

As was mentioned in the previous section and in the previous edition of this book, it is necessary to understand the glow discharge characteristics. A basic understanding of these characteristics can be seen in the Paschen curve. The curve demonstrates the relationship between voltage and current density. The voltage occupies the vertical axis of the graph and the current density relationship to voltage is shown on the horizontal axis of the graph. The graph indicates the points at which various events take place in the generation of a plasma glow and will assist in determining the process voltage necessary to achieve good glow characteristics in relation to the set-point voltage.

8.12.1 Townsend Discharged Region

If a voltage is applied at partial pressure within this region (which is called the ignition region), the electrical current will cause electrons from the gas atoms within the vacuum chamber to leave the outer shell of the electron circulating around the nucleus of the atom. The released electrons are now accelerated toward the anode, which in this case is the vacuum vessel. Because of the operating partial pressure, the free electron will migrate and accelerate toward another free electron. The distance traveled from one electron to impact with another electron is known as the mean free path. At the point of collision within the partial pressure environment there will be an appropriate release of energy along with ionization of the gas. This is called ignition. If the set-point voltage is increased, then the current density I also increases. Conversely, if the voltage is decreased the current density decreases with the energy output.

8.12.2 Corona Region

In order to achieve good plasma conditions for nitriding a workpiece, it is necessary to increase the process voltage. This means that more electrons can be released by for the gas ionization within this region. This means that the increase in released energy will cause further ionization, thus making the region self-maintained which can be likened to a perpetual chain reaction.

8.12.3 Subnormal Glow Discharge Region

If the current limiting resistance is reduced, then the current density increases and continues to increase, causing a voltage drop between the cathode (the workpiece) and the anode (process retort). The voltage stability at this point cannot be maintained, hence the region is called the transition region.

8.12.4 Normal Glow Discharge Region

It is at this point that a uniform glow will completely cover the surface of the steel inside the process retort that is treated with a uniform glow thickness. This will be seen without variation and with a constant voltage drop.

8.12.5 Glow Discharge Region

Within the glow discharge region, the entire work surface will be completely covered with a uniform glow that will follow the shape and geometrical form of the workpiece. This will look

almost like a glove that is bluish white. This is the region in which ideal conditions exist for plasma nitriding. It is within this region that there will be no arc discharging, which means a damaged surface metallurgy and possibly burning of the surface of the workpiece, if arc discharging occurred.

8.12.6 Arc Discharge Region

This is the region in which a great deal of damage can be done to the work surface. On the process instrumentation a noticeable increase in the voltage drop will occur as the current density increases, in addition to which the power density at the workpiece increases. It will also be seen that there will be a noticeable increase in the work surface temperature, which can result in at least supersaturated solution of nitrogen in iron if the nitrogen potential is left to run adrift. More importantly current density usually results in serious overheating of the workpiece surface, and if this increase in surface temperature is allowed to persist, then serious metallurgical problems will occur. The arc discharge region will usually occur at sharp corners. It can also be in these areas of sharp corners that supersaturation of nitrides will occur. If the process retort is fitted with a sight glass, then it will be seen almost as a lightning storm inside the retort. This is clearly visible.

Control of the power necessary to accomplish good plasma conditions means a very careful control of all aspects of the process:

- Power
- Current density
- Retort and process pressure
- Gas composition (ratios)
- Power on time
- Power off time

It can now be seen that control of the process is somewhat more complex than it would be with gas nitriding. However, it appears that the process will require special control parameters to maintain the surface metallurgy. It does require precise control of the process to manage the complex control aspects. This use requires a very skillful handling. It was with the advent of the pulse technology (as well as the PC/PLC combinations) that the process control parameters could be accurately managed. Once the process technician has set the process parameters, the parameters can be stored in a computer memory, which are permanent until changed. The use of computers in the process means that the repeatability of the process is now assured [17].

8.13 PROCESS CONTROL OF PLASMA NITRIDING

Because of the number of process parameters that have now been identified in the plasma nitriding process, it is now necessary to find suitable method of control for the process. If one considers the number of variables necessary for control, for example the salt bath process, one needs to control only:

- Time
- Temperature
- Salt chemistry control

The same is applicable to the gas nitriding process, with the exception that it is necessary to control the gas flow and gas dissociation.

The plasma nitriding process demands that all of the process parameters be considered in order to ensure good, uniform, and repeatable metallurgy. On that basis it is now necessary to consider control of the following process parameters:

- Time
- Temperature of the workpiece
- Temperature of the process chamber
- Process gas flow (nitrogen, hydrogen, methane, and argon)
- Work surface area
- Support fixturing surface area
- Process power voltage
- Current density
- Power time on
- Power time off
- Process amperage
- Rate of temperature rise
- Process pressure (vacuum level)

This means that the use of a computer and programmable logic controller is taken advantage to control all of the above-mentioned process parameters. The computers that are available today are all of a very high speed and have a large memory, which means the computer is not only able to receive the information generated as a result of processor signals, but also able to store all of the received information. Another feature is the Internet. Access to the computer programs makes it possible for the original furnace manufacturer to observe the equipment and trouble-shoot in case of a problem. But there is a security risk now for the process user. The acquired and stored information can be retrieved to compare the process parameters in relation to the accomplished metallurgy. It can also display both current and historical trends. The computer can also be programmed to identify maintenance schedules [14].

Computers are also able to identify and display the process parameter signals received throughout the process. The received information, however, is only as good as the source of the signal. For example, if the thermocouple has not been calibrated to a standard known thermocouple, or if incorrectly positioned, then the information fed into the computer will be erroneous. It is necessary, therefore, to ensure that the signal generated at their source is accurate, which means regular checking and calibration.

The success of the process will depend largely on the correct interpretation of the generated signal from the thermocouple. The displayed information on the computer screen is a product of the signals received during the process from the various control points within the equipment. If the thermocouple's millivolt is not calibrated, then the displayed information will be out of specification. It is, therefore, prudent to test the millivolt output of the thermocouple on a very frequent basis. Further to this it is also necessary to check the cable lead from the cold junction of the thermocouple to the programmable logic controller. This is done simply by connecting the thermocouple table leads from the PLC and checking the millivolt output at the connection points for the PLC. Once this reading is accurate, then the cable leads should be reconnected to the PLC, and the PLC should then be tested for its ability to receive and interpret the signal correctly.

The next step in ensuring that the signal is generated at the thermocouple point source is to establish the accuracy of the PLC's ability to determine the millivolt signal that is received from the thermocouple. This means checking the accuracy of the PLC.

The information displayed on the computer screen is only as good as the information received from the source of that information. The process parameters of

- Temperature accuracy
- Gas ratios
- Temperature
- Operating pressure
- Power control

are perhaps the most important aspects of the heat treatment procedure.

The placement of the thermocouple into the process retort is also important to ensure that accurate process temperature of the component is received. The ideal position for the control thermocouple is as close to the workpiece as is practically possible to the part under treatment. Usually in plasma nitriding the thermocouple is positioned inside a dummy test coupon far inside the part. This means an almost accurate temperature reading of the components is treated. During plasma nitriding, using the cold-wall, continuous DC method, the thermocouple is fitted into a specially designed ceramic insert. The insert is designed in such a manner that it is inserted into a steel test coupon, which is representative of the same sectional thickness as that of the material treated. This gives an accurate part temperature to the control PC. The process temperature is usually held to better than 5°C (10°F) of set-point temperature of the inserted thermocouple in the dummy test block.

The set-point temperature is most important in the nitriding process, indicating control of temperature generated by the load thermocouple. It is of no consequence if the retort temperature into another area of the retort is 40°C (105°F) over temperature so long as the controlling thermocouple is indicative of the correct temperature.

8.13.1 Processor Gas Flow Control

With gas nitriding, control of the process gas was simply to open the ammonia gas flow main valve and measure the volume of gas flow through a graduated flow meter. When ion nitriding started to develop as a commercially acceptable process, it was recognized that the gas flow control needed to be more accurate. So the gas flow was controlled using micrometer needle valves. As the ion nitriding process began to develop into the pulse technology it was quickly realized that the needle valve was not accurate enough to ensure controllable and repeatable surface metallurgy. A new method has to be found. The answer was found in the mass flow controller. The mass flow controller is a precision manufacturing process gas delivery system, which can deliver the required process gases to the furnace in precise measured volumes. The unit is calibrated for the particular process gas densities and volumes that will be delivered from the gas force to the furnace and controlled by microelectronics. If the user wishes to use a different process gas from the process gas that the mass flow controller is calibrated to, then the gas will be delivered to the furnace in incorrect amounts.

For gas delivery piping from the gas source, it is usually manufactured from the drawn stainless steel tube. The gas piping from the mass flow controller is also made from the drawn stainless steel tube. This is because of the tube cleanliness within the bore. No contamination of the process gas from within the stainless steel tube inner walls is most important to the success of all the ion nitriding processes.

If the gas flow ratios begin to vary during the process cycle, then the current density at the work surface can be affected. Depending upon the surface metallurgy necessary for the successful function of the component, the gas flow can vary from 5 to 100 l/h. This will of course completely depend on the surface area of the workload that is to be treated. If one compares the gas consumption between gas nitriding and ion nitriding, it will be very clear that the gas consumption on ion nitriding is considerably less. The obvious implication of using less process gas on the ion nitride process is that the cost of the process gas is

considerably less. This is because the process gas is used only for the process, and not to use that gas as a sweep gas during the procedure as it is with conventional nitriding methods. The critical aspect of gas nitriding is to prevent the process gas from stagnating, so that the gas flow tends to be on the high side. If time is not critical factor on the cool down cycle, then one can cool down at the completion of the ion nitriding process under vacuum. If the cooling time is critical then the cooling of the load can be accomplished by using recirculated nitrogen from the gas source through an internal heat exchanger.

The quality of the process gas is important to the success of the procedure, and it will be necessary to use clean dry nitrogen with a moisture content not greater than 55 ppm of moisture or oxygen. The cleanliness of the hydrogen process gas should not be greater than 5 ppm of oxygen. Some furnace manufacturers argue that it is acceptable to use ordinary commercial grade nitrogen. The author's experience has shown that while it will work, the risk of surface oxidation is always there. There is also the risk of grain boundary oxidation occurring.

The success of the process metallurgy is dependent on the quality and composition of the process gas. This is most evident with the gas nitriding procedure. It was because of this aspect that the two-stage process (Floe process) was developed in order to reduce the thickness of the formed compound layer on the surface over processed workpiece. The advent of ion nitriding, which now uses two molecular gases as opposed to a gaseous compound, such as ammonia, now opens the door to greater control of the surface metallurgy. This now demands greater control of the individual molecular process gases. The precise and metered amounts of the process gases are of paramount importance for the formation of the surface compound layer. This is the reason why it is necessary to consider the use of the mass flow controller for the ion nitride process as well as for the economics and operating costs of the process.

Using the mass flow controller can be likened to the comparison of the automobile carburetor in relation to the fuel injection system. The mass flow controller is a unique method of precisely controlling gas flow systems for each of the relevant process gases used in the nitriding process. Be careful when ordering a new mass flow controller. The mass flow controllers are calibrated for specific gases, and not for general use. Therefore it is important to have the appropriate MFC. This is particularly true when using methane.

8.14 TWO-STAGE (FLOE) PROCESS OF GAS NITRIDING

As was stated in the previous edition, the Floe process (two-stage process) continues to enjoy good and successful process results. The success of the process is continuous improvement due to the methods of control in terms of

- Temperature control
- Gas flow control, using more accurate delivery systems
- Gas decomposition control
- Improved precleaning methods

Because the process uses the higher temperature for the second stage of the procedure, it is most important that the process temperature does not exceed the previous tempering temperature. If this occurs, then the core hardness is likely to be reduced. This will be followed by premature collapse of the case during the service of the nitrided component.

This process is now using a higher gas dissociation of 75 to 85% during the second stage of the process. This means that the amount of available nitrogen to form the case is reduced, which means that the compound layer thickness will be reduced accordingly. Another reason for the low availability of nitrogen is that nitride networking can be reduced at sharp corners.

The main purpose of the two-stage process is to reduce the thickness of a formed compound zone, and will produce deeper total case depths that can be obtained from a single-stage process. This is because of the higher two-stage process temperature employed. It will also produce a slightly lower surface hardness that can be obtained from a low-temperature single-stage process. If it is necessary for the performance of the treated steel that the compound layer be reduced or even eliminated, it may be more appropriate to use the lower process temperature of the single-stage procedure and grind off the formed compound layer. However, it is necessary to know the thickness of the compound layer before grinding.

8.15 SALT BATH NITRIDING

The traditional method of salt bath nitriding using cyanide-based compounds is perhaps no longer in use today. However the development of low cyanide-based salts has grown tremendously during the past two decades. The uses of the salts are seen in the process of FNC with postoxidation treatments. The oxidation treatment is to accomplish a controlled oxide-formed layer on the surface of the steel. The purpose of this oxide layer is to increase the corrosion resistance of the steel surface. The oxide layer will also produce a very attractive mat black surface finish. Its use is seen in applications where low-alloy steel is used to provide a wear- and corrosion-resistant surface [18]. Such applications can be found for:

- Automotive applications, such as pressure plates, ball joints, gear drives in window lift mechanisms, windshield drive systems, windshield wiper arms, manual gear change levers
- Simple drive shafts
- Simple locking mechanisms
- Diesel engine locomotive cylinder liners

The aerated bath nitriding method is a proprietary process (U.S. patent 3,022,204). This method requires specific amounts of air to be passed through the molten salt. The purpose of the delivery of the air into the salt is to cause agitation of the salt and also the decomposition of the salt from cyanide to cyanate. It is necessary to monitor the composition of the salt by titration on a daily basis. The cyanide contents of the salt should be maintained around 55% with the cyanate content at approximately 35% by volume over the bath. This type of bath would be used to process plain carbon steel with a case depth of up to 0.3 mm (0.012 in.). It should be noted that the case depth is a function of time and temperature.

As a direct result of concerns regarding the environmental influence of the cyanide-bearing salts, the development of cyanide-free salts came into being. The salts are proprietary salts (U.S. patent 4,019,928), which means that after completion of the FNC process, the steel components are quenched into warm oxidizing quench salt, which will neutralize the cyanide and cyanate compounds that are present as a result of carryover from the process salt. A direct result of the quench procedure into the warm salt is a direct reduction of distortion [14].

This process is generating parallel interest as gaseous-based nitriding and FNC process treatments.

8.16 DILUTION METHOD OF NITRIDING OR PRECISION NITRIDING

The control of the compound layer thickness will depend on the following process parameters:

- Process time
- Process temperature selection
- Process gas composition

- Gas dissociation (if gas nitriding)
- Steel composition

Precise control of the above areas will determine the thickness and quality of the compound layer. The dilution method of nitriding and FNC controls the process parameters in a very precise manner. In order to accomplish this and control the process, precisely the use of a combination of PC and programmable logic controller is necessary. In controlling the nitriding potential of the process gas, in relation to the steel treated, one can begin to control the thickness of the formed compound layer.

If the nitriding potential is high (high nitrogen content), then the composition of the compound layer is likely to be that of gamma prime. If the availability of the nitrogen source is diluted with hydrogen then the nitride potential will be low. This means that the composition of the compound layer is likely to be dominant than that of an epsilon layer. This will of course depend on the carbon content of the steel. If it is necessary to form the epsilon layer and the steel does not have sufficient carbon, then carbon can be added in the form of methane. The amount of methane added to the process gas should be very carefully controlled up to a maximum of 2% of the total volume of process gas.

Hydrogen is often used as the dilutant gas during the process. Great care should be taken when using hydrogen as a process gas. Very simple but effective rules apply when using hydrogen and are as follows:

- Ensure that the furnace retort seals are in good condition, undamaged, and well cooled.
- Be sure that oxygen is not present in the retort before raising the process temperature of the retort. If oxygen is present, then a serious explosion or fire risk can occur. It is necessary to purge the process chamber with clean dry nitrogen before starting the procedure, and immediately before opening the chamber. Do not open the chamber until it is purged free and clear of hydrogen by nitrogen and at an inner retort temperature of 150°C (300°F) or below.

These precautions will also be applied to conventional gas nitriding. The reason is that hydrogen could be present as a result of ammonia gas in decomposition during the process.

8.16.1 Control of Precision Nitriding

If the steel treated contains the appropriate alloying elements, then it can be nitrided. It is now the resulting metallurgy that becomes the basis of the philosophy of control. Precision nitriding offers the same (or similar) results as those obtained by the plasma nitride method. The only significant difference in the process is not in the resulting metallurgy, but in the control philosophy. The one major difference between the precision gas nitride and plasma processing technology is that the procedure has almost the same time cycles, as does the gas nitride.

However, significant area of change is in the method of control. The principle advantage of this system as opposed to the plasma system is that there is no requirement necessary for the pulse power pack. This offers to the user a lower capital cost investment, as well as lower maintenance, and spares cost. The user of the plasma system is vulnerable to the point where it is almost mandatory that a pulse power pack generator is kept in stock.

There are many variations on the basic control philosophy, two of which are:

- Control based on the measurement of the exhaust process gas from the process retort. The method of control for this variation on the conventional gas nitride system is the

measurement of the insoluble nitrogen and insoluble hydrogen present in the exhaust gas. Once the measurement has been completed, the additional gases for enrichment or dilution are added from the probe signal to a modulating valve located at the gas flow delivery manifold.

- Another method, which has been developed by a leading European international furnace manufacturer, is a variation of the oxygen probe. This system is based once again on the sensing of the insoluble gases, within the process retort. The retort is now placed in the process chamber and not at the exhaust gas discharge side of the system.

The attractiveness about the precision nitride method is that the furnace design is a relatively simple design, which means that the investments will be kept low. The furnace designs are proven designs, and have simple installation requirements. This technology has a promising future. It seems to be the technology that is giving the process of nitriding a great boost.

8.17 FURNACE EQUIPMENT FOR NITRIDING

The equipment for gas nitriding is of a very simple design and has remained for many years. If one considers a gas nitriding furnace designed today in relation to furnace designed 50 years ago, there will not be a significant degree of a noticeable change. The critical area of furnace design for nitriding procedures is that of temperature uniformity. In addition to this, significant changes have been seen in the transmission and reporting of process data. It is important to note that great faith is often placed in the use of computers for process control technology. It is safe to say that the quality of a reported information displayed on the computer screen is as good as the source and the method of acquiring that process signal. If thermocouples are incorrectly positioned within the process chamber, the information seen on the screen will be incorrect. It is important to ensure that all data reporting points are placed in such a manner as to report accurate information to the computer display screen.

It is most important to have good temperature uniformity within the process chamber in order to ensure good uniform case depth and case metallurgy. The temperature uniformity should not vary more than 5°C (15°F) above or below the set-point temperature. If temperature uniformity varies greater, say 30°C (55°F), considerable variation will occur in the surface metallurgy as well as surface hardness variations. This indicates the difference of forming nitride networks in the case and normal nitride metallurgy. Another concern that arises from nonuniformity of temperature is the fact that the core hardness, surface hardness, and the case depth vary. In order to accomplish temperature uniformity, it is necessary to have a gas circulation fan within the process chamber.

As with any heat treatment process, it is essential that a uniform temperature of the process be maintained. Temperature control can be either single zone or multizone control system. With a single zone control, a single thermocouple may be used in conjunction with an over temperature control thermocouple. If the furnace is a multizone system, a master thermocouple is employed in conjunction with slave thermocouples plus the necessary over temperature thermocouples. This type of system may be set up in such a manner that the master thermocouple will not only control within the master zone but also within each of the remaining zones.

Temperature recording can be accomplished in many ways, such as:

- Conventional time–temperature control instrumentation that will transmit a millivoltage signal to a data-logging instrument or to the controlling PC/PLC.
- Conventional time–temperature controllers that will transmit a millivoltage signal through a microprocess controller and onto the data-logging instrument. This system

will reduce operator involvement, and thus the operator is available for performing other functions.
- It has been during the past 15 years that greater usage of the PC/PLC has occurred.

However as has been stated previously, the use of the system is only as good as the quality of signal it receives. There are many innovative screen displays, which show the occurrence of individual and multiple events during the process. The display screen can also be programmed to indicate the need and frequency of both furnace maintenance and system maintenance.

When selecting the points of insertion of each of the thermocouples, be it for a single zone or multizone system, the thermocouple should be as close to the nitride retort as conveniently possible. In addition to this, provision for a thermocouple to be placed inside of the process retort should be made. This can be accomplished by fitting stainless steel into the process retort with the end of the inside of the retort sealed and gas tight. This will give the operator the facility to measure the internal temperature of the retort and thus close approximation of the work temperature. The tube length of the retort should be controlled to indicate a reasonable temperature average for the whole of the interior of the retort.

Another development of the gas nitriding furnace is the use of vacuum-formed modules for thermal insulation. Today we are seeing greater usage of these thermally efficient lightweight modules [19]. This means:

- Faster production methods of furnace construction
- Cost-effective in terms of construction
- Better thermal efficiencies
- Better economical operating costs
- Less maintenance

8.17.1 Salt Baths

Significant changes that have occurred in the salt bath manufacture, particularly for salt bath nitriding systems, have been in the mechanical handling of the workpieces through the system, event reporting, and the system reporting in terms of time and temperature. Unfortunately, no method has been developed to automatically analyze the salt bath. This means a manual analysis.

The salt pot is constructed either from low-carbon steel with a titanium liner or a highly alloyed stainless steel (Inconel). There have not been any significant changes in the manufacture of salt pot during the past two decades.

Heating systems are still the same, which means directly or indirectly fired electrical or gas firing. The economics of gas or electrical firing will be determined by the geographic location of the operation and the availability of either gas or electricity.

As far as the operation of the bath is concerned it is advisable to try and operate the bath on a continuous 24-h basis. If this is not possible, then the temperature of the bath should be turned down to a temperature that will keep the bath molten.

8.18 PLASMA NITRIDING

The use of plasma nitriding as a process system has received a great deal of success during the past 10 years. Its acceptance by engineers and metallurgists has grown. It is now seen not so much as a new process, but as an accepted process that has a great deal to offer in terms of repeatable and consistent metallurgy. There still seems to be confusion arising as to what its

process name really is. It is known as ion nitriding, glow discharge nitriding, plasma nitriding, and plasma ion nitriding.

The phenomena of plasma are well-known natural phenomena as have been previously described. Two German physicists named Drs. Wehnheldt and Berghaus first developed the use of the plasma phenomena for metallurgical processing in Germany early 1930s. Plasma process technology has matured greatly during the past 15 years. Plasma technology is used on a daily basis for (a) precleaning for surgical instruments, (b) plasma coating technology, and in plasma-assisted surface treatments, such as nitriding, FNC, carbonitriding, and carburizing.

Plasma is a technology that can be used for many process applications, which include the treatments of a metal, plastic, or other surface treatment methods. The use of plasma assistance for thin-film hard coatings has grown considerably during the past 5 years [14].

It was stated in the previous edition that in the early 1950s General Electric in Lynn, Massachusetts had pioneered the use of plasma technology as a means of surface treatment by nitriding. The company is still employing plasma processing as a means of nitriding for surface treatment. It is quite evident that the company believes in the technology of plasma nitriding as a method of precisely producing a desired, repeatable, and consistent metallurgically formed case.

8.18.1 Plasma Generation

When steel is placed in a gas environment at partial atmospheric atmosphere and a voltage is applied to the electrodes, then the gas in the enclosed chamber will begin to glow and emit a light, which will be dependent on the type of gas in the chamber. As previously stated, an example of this is the fluorescent light tube.

The basis of generating a plasma or a glow discharge is that even at atmospheric temperature and pressure, gas molecules are always in a state of movement and are continually colliding with each other. As the collision occurs between two gas molecules, energy is released, resulting in a glow. If we now place the gas in an enclosed vessel with two electrodes, and seal the vessel in such a manner as to make it gas tight, then apply a voltage across the two electrodes, the gas molecules are excited and liberate free electrons from their outer shell. The molecules begin to move in a random manner, colliding with each other. If the gas is at atmospheric pressure, then collision occurs by electrical excitation, there will be a release of very small amount of energy. The energy that is released will be insignificant due to the high probability of collision between the molecules, which means that the mean free path on the molecules is very small. An illustration of this can be seen in Figure 8.14. If the internal pressure of the chamber is reduced to a high-vacuum level, then the probability of molecular collision will be very low because the mean free path of the gas molecule will be very long. The direct result of this is that there will be a large amount of energy released, but cannot be used effectively because of the infrequent molecular collision. Therefore it follows that somewhere between the two extremes of pressure there should be an ideal pressure band in which the phenomenon of plasma can exist. This pressure band has been found to be between 50 and 550 Pa. Therefore process pressure within the process chamber is one of the principal elements of control of the glow discharge, other parameters are voltage, gas composition, and the surface area of the work to be nitrided.

When a nitriding temperature and a high-process operating pressure are used (one that is closer to atmospheric pressure), then the glow will be seen to have incomplete coverage of the surface treated (Figure 8.14). Conversely, if the process pressure is low (that is, at high vacuum), then the area below will appear to be hazy or foggy from the work surface treated.

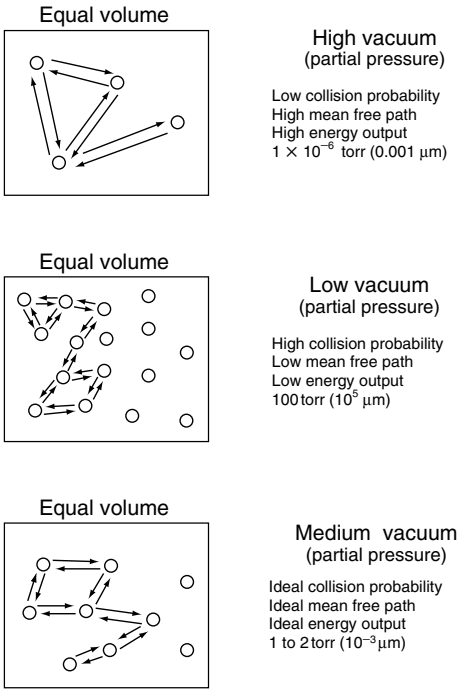

FIGURE 8.14 Probability of molecular collision at various sub-atmospheric pressures. (Courtesy of Seco Warwick.)

8.18.2 Glow Discharge Characteristics

The glow discharge characteristics are previously defined and a relationship between the process voltage and the current density is drawn. The Paschen curve will then define the relationship between voltage and current density. The relationship between voltage and current density can be derived from the Paschen curve to determine the appropriate process voltage for the ion nitride procedure.

A clear understanding of the characteristics of the plasma ignition conditions as well as an understanding of the Paschen curve and its relationship to voltage and current density is necessary to have a clear understanding of the glow discharge characteristics. It is a common misconception that a scientist should operate and control a plasma-generated system. It is necessary to have the understanding how the glow is created, and it is quite simple. The understanding of the glow seam characteristics can be as simple or as complex as one wants to make it [20].

Simply stated, the higher the process voltage in relation to the pressure then greater the risk of reaching the arc discharge region with the potential for the occurrence of arcs. When the arc occurs, it will usually occur on sharp corners (usually, but not limited to corners). This means that there will be a heat-affected zone at and behind the point of the arc occurrence, which will mean the potential for an enlarged grain size and a certain reduction in hardness. Very careful control of the voltage and pressure is, therefore, an essential aspect of the process.

In order to ensure good surface metallurgy with consistent and repeatable results, a careful control of the voltage, amperage, current density, gas composition, and pressure is necessary for the successful and uniform nitriding to take place. It is now necessary to control

the above parameters in a very precise and accurate manner. The control function is now taken over by the integration and use of the PC/PLC combination. This method of control makes the operation of the system much simpler for the process operator to ensure repeatable and controllable results. The operator of the system is free to set up the necessary programs that will produce the formed case in a manner that will best suit the operating conditions of the processed workpiece:

- Dual-phase compound layer
- Single-phase compound layer
- No compound layer

With an understanding of the glow characteristics, the operator can create the necessary case that will enable the component to function in its operating environment and can ensure repeatability due to the memory storage capacity of the computer.

The advent of computers 20 years ago has made the use of computers affordable and their ease of operation has made possible their utility in all walks of life, both at home and at workplaces. The computer has probably had the same significant effect on everyday life as the telephone has. The computer is probably the single most significant contribution to life in the 20th century and the early part of the 21st century. Simply put, if one can operate a computer, then one can operate a plasma system.

8.18.3 Plasma Control Characteristics

When a constant voltage is applied to the workpiece within the partial pressure range in which gaseous ionization will take place, then the electron collision will generate a glow. The glow will surround the workpiece and will also generate energy in the form of heat. The generated heat can be used to assist in the heating of the workpiece. It can be seen that by using different gases, such as nitrogen, hydrogen, methane, and combined gases (N_2, H_2, CH_4), and utilizing the phenomena of the glow discharge (gaseous ionization) many different thermochemical process techniques can be performed. This is possible if the materials of construction for the equipment are designed and built for the appropriate process temperature. The decomposition of ammonia using heat is considered to be the classical nitriding formula, which is as follows:

$$2NH_3 \leftrightarrow N_2 + 3H_2$$

The decomposition on the gas (left to right in the above formula) will liberate both nitrogen and hydrogen as individual gases. Each gas will exist momentarily in its atomic form from which a small proportion of nitrogen atoms are absorbed and diffuse into the steel surface, forming nitrides with the appropriate alloying elements of the steel. The use of ammonia as the process gas and the source for nitrogen dictates the use of fixed gas chemistry, thus resulting in a fixed surface metallurgy [21].

This means that the nature of the formation of the compound zone will always be the same. The composition of the compound layer will be determined by the analysis of the steel.

Using the method of plasma nitriding and combining nitrogen and hydrogen by varying the ratios of the two gases, we can now manipulate the surface metallurgy of the steel. Therefore it can be said that with variable gas chemistry, one can accomplish a variable surface metallurgy. In other words, the appropriate surface metallurgy can be created that will best suit the steel and its application.

The control parameters for gas nitriding is limited to four process areas, which are:

- Process time
- Process temperature
- Gas dissociation
- Work surface area

When one can control the gas dissociation and the nitride potential, by accurately controlling the volume of ammonia that is delivered to the process chamber, then one can reasonably control the thickness of the compound layer.

The process of ion nitriding has many more controllable variables that are necessary to control. When all of the process parameters are managed, then one can manage the process and the results will be more repeatable and consistent. The use of PC/PLC has made the process control both meaningful and accurate (Figure 8.15). The process parameters that are generally controlled are:

- Process time
- Process temperature (process chamber)
- Process temperature (workpiece)
- Process gas flows
- Surface area
- Power voltage
- Power amperage
- Current density
- Rate of temperature rise

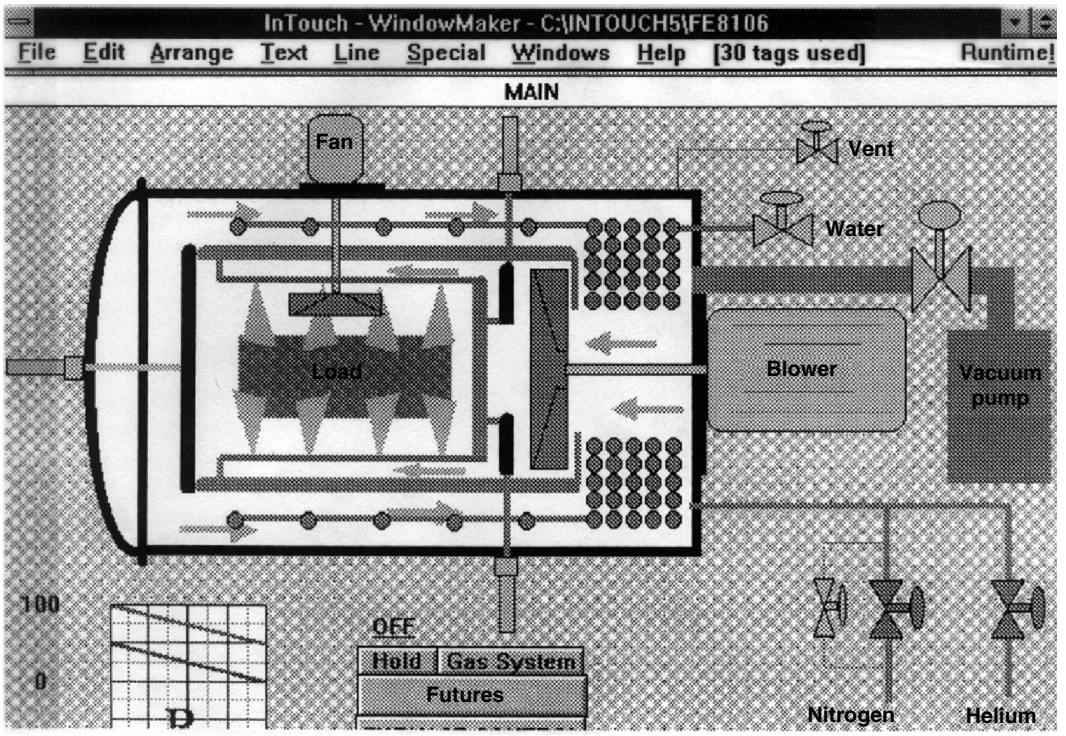

FIGURE 8.15 A typical PC screen configuration for a heat-treatment furnace. (Courtesy of Seco Warwick Corporation, Meadville, PA.)

8.18.4 Equipment Technology

In the ion nitriding process technology there are two distinct process techniques:

- The cold-wall technique (using continuous DC power)
- The hot-wall technique (using pulsed DC power)

8.18.5 Cold-Wall Technology

A typical cold-wall ion nitride furnace is shown in Figure 8.16. The furnace process chamber is made up of two vessels. This means a smaller vessel positioned within a slightly smaller vessel thus making the complete construction of a double wall vessel. The area between the inner vessel and outer vessel will now become a water-cooling jacket to cool the inner process chamber during the process operation. The inner process chamber is usually made from a heat-resisting stainless steel. The outer vessel is usually made from a carbon steel. The two chambers are separated by the bottom shell flange, which will mate with the top shell flange. The bottom shell flange is usually water cooled for a vacuum seal protection. In order to observe the plasma conditions and glow seam, which will surround the workpiece, a water-cooled view port is usually fitted in line with the workload area.

The electrical plasma power feed throughs, which activate the cathode, are fitted through the bottom shell. The power feed through it is of course grounded for operator safety. It is also unusual to fit the process gas supply, thermocouple feed through, and the vacuum pump out port.

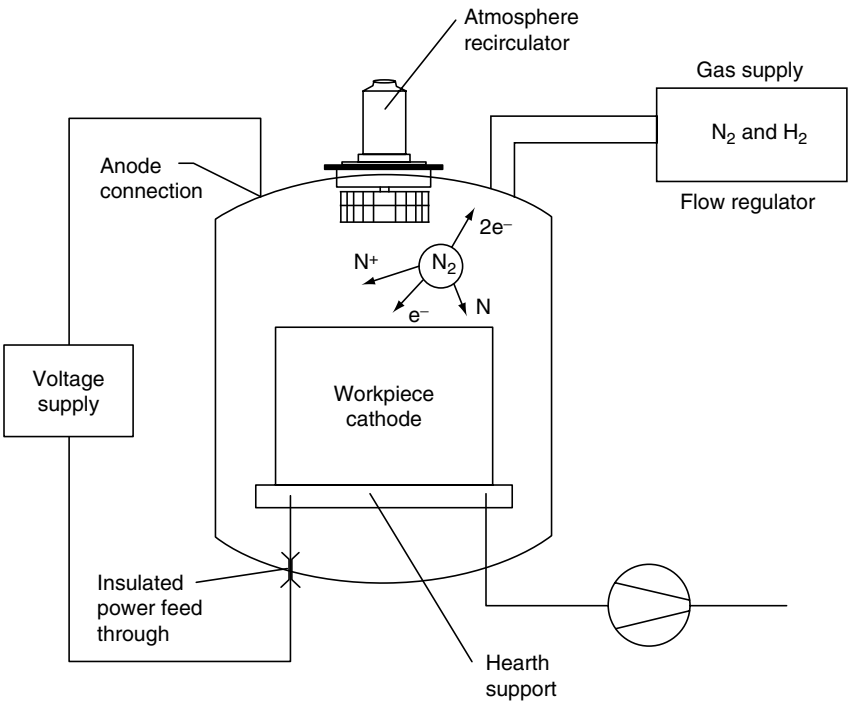

FIGURE 8.16 Schematic of a typical arrangement of a cold-wall, continuous DC plasma nitriding system. (Courtesy of Seco Warwick Corporation, Meadville, PA.)

8.18.6 Power Supply

In order to generate a plasma it is necessary to have a suitable continuous DC power supply that is constructed in such a manner as it did respond to control signals from the process controller. The purpose of the continuous DC generator is to develop a particular voltage that ignite a gas in relation to the Paschen curve. The power supply will allow a continuous voltage flow through the cathode potential located within the process retort. The power to be fed into the cathode will excite the gas electrons and will also create energy in the form of heat at the workpiece. The generated power will be fed to the cathode through the wall of the retort via the power feed through. The usual location for the power feed through is generally located in the place of the retort. The furnace hearth is in contact with the power feed through in order to make the hearth at cathode potential. The power feed through design will allow an uninterrupted passage of power to the cathode and is appropriately insulated from the anode. The correct electrical insulation is necessary from a safety standpoint.

Some of the early power supplies that were initially employed used a continuous DC power to generate the glow discharge. The power supply to the cathode is set up in such a manner so as to create a voltage bias between the anode (vessel wall) and the cathode (furnace hearth) when operating in the lower portion of the glow region (normal glow discharge). Considerable problems to the glow seam stability by this method were particularly noticeable when nitriding complex geometries and blind holes. In order to nitride these types of components, it was necessary to use a higher process voltage as well as higher vacuum levels. This tended to cause serious problems, which were often seen as localized overheating at sharp corners. It was also seen as a high potential for arc discharge. If the arc persisted, then serious metallurgical damage could be caused to the workpiece.

8.18.7 Process Temperature Measurement

A very simple statement is that all metallurgical processing is temperature related. Temperature measurement is, therefore, perhaps the most single process parameter that requires accurate measurement as well as good control and uniform temperature distribution throughout the process chamber. As in the conventional heat treatment procedures, it is a common practice to measure process temperature as close to the workpiece as practically possible. If this can be accomplished, then it will give a good indication of the workpiece temperature. Remember that one naturally assumes that the temperature indicated on the temperature controller is the temperature of the process chamber. This is not necessarily so. All that the thermocouple is indicating through its generated EMF is the temperature at the hot junction of the thermocouple and not, as it is assumed, to be the temperature of the workpiece or the furnace. The ideal position of the thermocouple should be either on the part, or in the part, or in a dummy block that is representative into those of cross-sectional thickness of the part.

The thermocouple is insulated from the cathode by a specially designed ceramic insert that is inserted into the part or the dummy block. Generally there are two thermocouples. One thermocouple will measure the temperature of the thickest part of the block, and the other will measure the thinnest part of the block. The temperature uniformity within the process chamber, from top to bottom and side to side, should not be greater than 5°C (10°F). The EMF that is generated by the thermocouple is transmitted back to the process temperature controller, and it is necessary to use a process computer to record the process parameters.

It is not an issue if the process retort temperature is not uniform. However, it is a problem if the part temperature is not a uniform temperature. Any temperature variation greater than 10°C (16°F) will produce an irregular case depth and nonuniform metallurgy. This will apply

to any nitriding process method. Temperature uniformity in the workpiece is critical to both the metallurgy and the performance of the product.

It has been said on many occasions that the temperature is controlled by the computer; therefore, the temperature displayed on the computer screen must be accurate. Please be aware that the accuracy of the temperature readout shown on the computer screen is only as accurate as the thermocouple, which transmits the EMF signal back to the computer. The assumption is made that the temperature displayed on the computer screen is the temperature within the process chamber on any heat treatment process. Once again it is stated that this is not a correct assumption. All that is displayed on the computer screen is the temperature at the hot junction of the thermocouple, nothing more and nothing less.

8.18.8 Process Gas Flow Controls

The traditional method of controlling the process gas (e.g., ammonia) on the traditional gas nitriding process was originally by flow meters. This idea was utilized in the early experiments on plasma nitriding and in the early equipments. It was found that the flow meter was an inadequate method for process gas flow control.

A more precise method of process gas delivery was needed. Later methods of plasma nitriding equipment then began to make use of the micrometer needle valve gas control system. It was found that this system worked reasonably well, but on a rather limited basis. It was necessary to find a more accurate method of process gas flow control in order to accomplish the precision and repeatability that is required of plasma nitriding.

It is well known that gas ratios and the gas flow relation to the process pressure can adversely affect the current density at the work surface. Therefore it is necessary to deliver and monitor the gas flow as accurately as possible. When ion nitriding, gas flows can be up to (in the total) 100 l/h maximum during the nitriding procedure. It is to be noted that 100 l/h is the maximum flow. More often than not, it is considerably less. The flow rate is dependent on the surface area of a treated workpiece. The ion nitriding process makes very little demand on the gas consumption when compared to conventional methods of gas nitriding. It is safe to say that for every 100 ft^2 of surface area treated by gas nitriding requires approximately 50 ft^3 of ammonia gas per hour. The reason for this is that most of the ammonia gas is used as a sweep gas through the process retort. In other words, large quantities ammonia gas is wasted. However, with the dilution process the gas flow rate is very carefully monitored and controlled in relation to the under treatment steel, the case metallurgy required, and the nitriding potential.

With ion nitriding, the total gas flow requirement is considerably less than 5 ft^3/h. The reason is that only the gas necessary for ionization and diffusion is required. This means that the process is extremely economical as far as process gas costs are concerned. On completion of the process, cooling cycle can be accomplished either by a forced cooling using nitrogen, which would be recirculated through the process chamber or by vacuum cooling, which is of course a very slow method of cooling.

8.18.9 Hot-Wall, Pulsed DC Current

The hot-wall, pulsed DC technology employs a completely different approach to the ion nitriding process. This technology differs from the cold-wall technology so much that the hot-wall technology recognizes that at ambient temperature the power voltage necessary to generate not only plasma but also heat makes the plasma glow seam very dangerous to the metallurgical integrity of the workpiece. It is necessary to generate high voltages in order to generate heat. This requires that the current density is relative to the process voltage. This will be almost at the arc discharge region of the Paschen curve. It is also well known that most

metallurgical damage to the workpiece occurs at ambient temperature owing to the high voltages that are necessary for extended periods of time. This is to generate the process energy, which in turn will heat the work up to the process temperature. A typical hot-wall plasma furnace is shown in Figure 8.17.

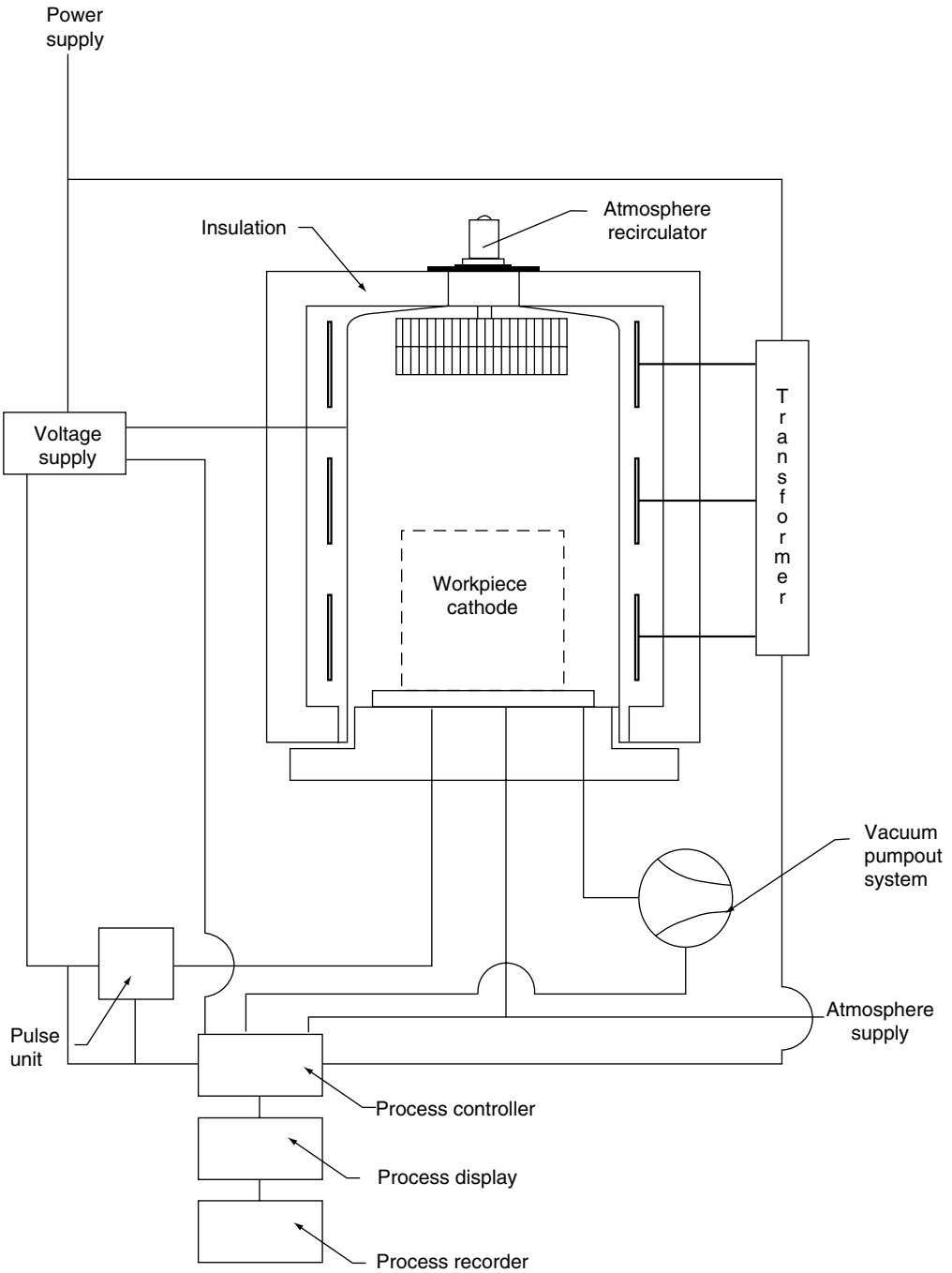

FIGURE 8.17 Hot-wall vacuum plasma nitride furnace. (Courtesy of PlaTeG Gmbh Siegen, Germany.)

8.18.10 Plasma Power Generation

Most steel is sensitive to metallurgical damage, which will be the result of the phenomena of arc discharge. Therefore it was necessary to find a very simple and effective solution. The solution is based on a simple anthology. When one enters a darkened room it is necessary to switch on the light in order to see. When one leaves the room (hopefully), one would switch off the light. This analogy is taken into the field of power generation. The traditional method of plasma power generation is by continuous DC voltage. This new method of power generation is to interrupt power generation by consistent, repeatable, and variable time-based interruptions of the continuous voltage.

The power is now pulsed into the power feed through, thus interrupting the power to generate the plasma. Therefore (and depending on the pulse duration time), there will be almost no possibility for an arc to develop during the process. The interrupted power can be varied upwards from 3 to 2000 μs for power to remain on. Conversely the same will apply for the time that the power will be off. The pulse duration time on and the pulse duration time off can be varied during the program as is seen to be necessary for good and effective control. This makes for a variable but controlled plasma power generation system.

This technology is called pulsed plasma ion nitriding. This method of power generation has been a major breakthrough in the process technology. It disperses all the fears that were previously held by process engineers of an uncontrollable process that was susceptible to arc discharge. This now no longer applies.

8.18.11 Process Temperature Control

A new concept and method of temperature distribution was developed at the same time as the pulse technology. This development was to separate the need to heat from the plasma. In order to overcome this a thermally insulated bell furnace now surrounds a single vessel vacuum process retort. The furnace is designed in such a manner that the heat generation from the heating elements now directly heat the process retort. The air gap between the insulation and the outside wall of the process chamber is used to control the process retort temperature. This means that instead of using valuable recirculating water through a water jacket followed by cooling the water through a heat exchanger, normal shop air is now used as a very effective and inexpensive system of cooling and controlling the wall temperature of the process retort.

The use of pulse technology allows better penetration of plasma into holes and greatly reduces the risk of what is known as hollow cathode. The pulse power can be adjusted to accommodate geometrical section changes in the workpiece treated. With a part that has a complex shape, when using the continuous DC pulse system, thin wall sections of that part will reach temperature in a shorter time than the thicker sections. This means that thermal differences in temperature are introduced to the workpiece, thus causing the potential for stress risers to occur between thick and thin sections. The ability to pulse the power gives the process technician the opportunity to adjust the power to the workpiece so that when the power is off at the thin sections, the residual heat will have the opportunity to dissipate to the thick section, which will be absorbing the heat. Temperature differentials between the sectional differences can usually be kept at a maximum of 5°C (10°F) on either side of the set-point temperature. The frequency of the pulsed power should be such that it is variable enough to allow it to be adjusted in order to accommodate extreme changes in sectional thickness. The pulse plasma system incorporates high-powered transfers to rise switching converter system that operates between 1,000 and 10,000 Hz.

The benefits of this technology simply mean that the process temperature is now derived from an external heating source as opposed to heating, simply by the use of plasma. Only the

voltage necessary to initiate the plasma generation is now required, which means lower process voltages can be used as opposed to the more traditional method of power generation and heating by the use of high process voltage. In simple terms, it means that the risk of arc discharging is dramatically reduced to the point of almost nonexistence.

8.18.12 Temperature Control

When measuring process temperature in the hot-wall, pulsed DC furnace a different method of measurement is used to that of the cold-wall, continuous DC technology. The thermocouple can be at cathode potential and protected by some method of shielding from being nitrided, which will happen if the thermocouple is left exposed at cathode potential. An alternative consideration could be where the thermocouple tip and strategic points of the thermocouple are protected and insulated from cathode potential by a specially designed ceramic insulator. The generated EMF from the thermocouple can now be transmitted to the computer. This information is now displayed on the computer and is recorded.

8.18.13 Process Control

The methods of process control can be wide and varied, as well as simple or complex. The degree of simplicity or complexity will be driven by the investment economics and by the operational skills available to the user.

8.18.14 Low Capital Investment, High Operational Skills

This method of control will take cognizance of a simple pulsed power unit using manual power output control system, with the temperature and pressure controls at a PID loop system which will monitor both pressure and temperature. This type of control requires a high degree of operator skills in terms of having the ability to both recognize the process activities and fluctuations, as well as able to correct them.

8.18.15 Moderate Capital Investment, Moderate Operator Skills

This system operates on the basis of process-generated signals that are transmitted through a microprocess controller. The controller can be either a proprietary unit or a commercially developed unit. The process will usually manage itself with some operator involvement. It will still require manual loading, unloading, and microprocessor programming.

8.18.16 High Capital Investment, Low Operational Skills

The development of the computer to be integrated as a primary process controller has grown tremendously since this chapter was written. The computer is a receiver and interpreter of signals that are generated as a result of process events. The computer still works with a programmable logic controller. The computer can be fitted with a modem control, which enables the manufacturer of the equipment to troubleshoot from a remote location. This also means that the furnace status and programmed events can also be viewed from a remote location. The process information gathered into a memory bank and stored, and can be retrieved and printed at any time. The computer process displays the status of the process at any time during the process sequence. Most operators have a basic computer literacy; therefore, the training of the operator is neither complex nor time-consuming. This means that computer method is user-friendly and all events are visibly displayed for interpretation at a moment's glance.

8.18.17 Metallurgical Considerations and Advantages

There are many arguments against the justification of the equipment investment for ion nitriding in relation to gas nitriding. There are also many arguments against the complexity and handling of the ion nitriding process and many in-depth discussions as to which is the best method of control. While all of these arguments may well have been justifiable in relation to the more traditional methods of ion nitriding, in today's process technology world, they are unfounded. The current state-of-the-art ion nitriding equipment offers to the metallurgist both control and process advantages that would not be previously possible with the early continuous DC plasma generation nitriding techniques. It is possible not only to control but also measure the work surface temperature and heating, as well as control gas composition, gas species activity at the steel surface, process pressure within the retort, and the process time.

Another perceived advantage of the ion nitriding process is that the process does not rely on the decomposition of ammonia by heat as it is with the gas nitriding process. Because the ion nitriding process uses molecular process gases, the decomposition of these gases is accomplished by the electrical ionization technique. Using heat to decompose the ammonia process gas for gas nitriding, it is a time-consuming event. In addition to this, the steel surface will act as the process catalyst in order to aid the diffusion of the nitrogen into the surface of the steel. When using the ion nitriding process, no heat is required to ionize the process gas. The ionization from molecular nitrogen to atomic nitrogen is almost instantaneous, however the laws of physics of diffusion still govern the rate of diffusion into the surface of the steel. However, the net result of the differences of gas preparation is that the floor-to-floor process cycle time is considerably faster with the ion nitriding than with gas nitriding.

The ion nitriding process will also give the operator the ability to control the formation of the surface metallurgy (white layer otherwise known as the compound layer). It can also be made to single phase (epsilon or gamma prime phase), as well as completely eliminated. It will be the engineering design requirements that will determine the choice of surface metallurgy. The result of the process will be determined by the process settings, and in particular process gas ratios.

It can be said that a more appropriate method of eliminating the compound layer will be to grind or lap the compound layer off. While this is true, one needs to know the thickness of the compound layer in order to effectively grind off the layer. Further to this, one needs to be extremely careful with the grinding operation in order that the diffusion zone is not stressed, and that stress patterns are not set up that may lead to crack generation and propagation.

It can be seen that the surface metallurgy can be both controlled and created, in order to suit the process application. Further to this, it has been said that only steels with specific alloying elements in the composition can be nitrided. Because of the ion nitride process and the ability to manipulate the process gases, one can even nitride iron as well as the more complex steels, stainless steels, and some of the refractory materials. This ability to nitride steels as well as irons, and to control the surface metallurgy requires a more versatile process. Further to this, it means that both nitriding and FNC process as well as the postoxidation treatment can be accomplished in the same furnace.

There appears to be some controversy in the basic philosophical thinking regarding the formation of the compound layer. Metallurgists in Europe have a different belief and understanding than the metallurgists in North America. The European philosophy tends to promote the need for the compound layer on many product applications. On the other hand American metallurgists tend to control the formation of the compound layer to suit the application. This means to control the surface metallurgy from no compound layer to a controlled dual-phase compound layer. It is felt by the author that the U.S. metallurgists

make greater use of the ability to create the appropriate surface metallurgy innovation to the European counterparts [14]. The thickness of the compound layer will be determined by:

- Process temperature
- Process gas ratios
- Process time at temperature
- Steel composition

Stainless steels and other more exotic steels have been successfully plasma ion nitrided when little or nothing could be accomplished with more traditional methods of nitriding. However, with the stainless steels (gas or ion nitriding) it is necessary to depassivate the chrome oxide surface layer before nitriding can be effectively commenced. One of the significant advantages of plasma nitriding is that plasma nitriding is able to treat a broader range of steels and irons that could not be successfully treated using the more traditional gas nitriding techniques. A simple but general rule of thumb is that the lower the alloy contents of the steel, the deeper is the formed case, but with low hardness values [22]. The higher the alloy contents of the steel, the shallower the formed case, but higher the surface hardness values. The speed of nucleation and that case development used in the ion nitriding process tends to show that ion nitriding is at least as fast, and in a vast majority of cases, considerably faster than the conventional methods of case formation.

Generally the process of ion nitriding offers a uniform, repeatable, and consistent nitrided case. There appears to be a definite trend to the use of ion nitriding process. This trend has always been apparent in Europe and the Far East, but the awakening is now occurring in North America. The use of plasma generation techniques as a process method is now recognized as a tool for other metallurgical process techniques, particularly in the field of surface treatments, which includes both diffusion and deposition techniques. The metallurgical advantages of plasma processing techniques offer a unique and versatile process method, with repeatable and accurate results. The appropriate metallurgy can be created to suit the component application. As has been previously stated, provided the materials of construction are capable of withstanding the process temperatures, the plasma processing techniques open many doors for surface treatments. The choice of plasma generation technique and process methods (cold-wall, continuous DC method or hot-wall, pulsed DC method) is a matter of personal choice, understanding the process techniques in relation to the advantages offered by each process choice. That choice can be decided either by equipment cost or metallurgical requirements.

8.18.18 Metallurgical Structure of the Ion Nitrided Case

All of the known nitriding techniques are based on nitrogen diffusion into the steel surface, and its reaction with iron- and nitride-forming elements. The conventional gaseous nitriding techniques are based on the decomposition of ammonia to provide the nitrogen source. The decomposition of the ammonia is fixed: one part of nitrogen and three parts of hydrogen. This is a fixed law of chemistry. Even if the ammonia gas is diluted with hydrogen, the decomposition of the ammonia still remains in the same ratios, but now less nitrogen is available for diffusion.

It is usual during plasma nitriding that the source of nitrogen is a molecular nitrogen from a nitrogen storage tank, and the same for hydrogen. If the sources of the nitrogen and the hydrogen are considered as a ratio of one nitrogen to one hydrogen, then the ratio of nitrogen to hydrogen is completely different to that obtained during the gas nitriding process. The method of decomposition of the nitrogen is now accomplished by electrical means. This means that the nitrogen gas molecule is electrically decomposed into atomic nitrogen, and the same is applicable to hydrogen. There is now an opportunity to manipulate the nitrogen to hydrogen in gas ratios in order that a specific surface metallurgy can be created. In addition

to this, there are other process parameters available to enable the technician to create the appropriate surface metallurgy.

In alloying steel, the increased surface hardness gained by nitriding is attributable to the formation and fine dispersion of both coherent and semicoherent nitrides that are formed with the alloying elements of the substrate material. Specific alloys will readily form nitrides, such as vanadium, chromium, titanium, aluminum, molybdenum, tungsten, and silicon. With the exception of aluminum, all of these elements can form carbides as well as nitrides during the nitriding procedure. They will also influence the rate of reaction taking place, and the nucleation of the precipitates taking place at the steel surface during the interaction with the nitrogen process gas. The carbon content of the steel nitrided will also have a direct influence on the ratios of the compound layer phases. Carbon will also affect the rate of nitrogen diffusion. This is in terms of its interaction with the carbide-forming elements and the phase transformation from austenite to martensite at the preharden and temper operation before the nitriding operation. The transverse microhardness profile of the nitrided case will increase as the alloying contents of the steel increase, and conversely with some of the higher alloy concentrations such as chromium, the steel will, to some extent, resist the diffusion of nitrogen.

When considering the use of ion nitriding process, it is accepted that the mixture of nitrogen and hydrogen gases will influence the formation and the composition of the compound zone. When processing highly alloyed steels, such as the martensitic stainless steels, it will be seen that the steel will resist the formation of nitrides at the surface, as well as having an influence on the formation of a compound zone. If it is a requirement of the nitrided case to have little or no compound layer, then this can be accomplished by using a low gas ratio of nitrogen to hydrogen. One also needs to be aware of the solubility of nitrogen in iron. There is a very narrow window in which nitrogen is insoluble in iron (Figure 8.18) and one can very easily step out of that window and create an undesirable surface metallurgy. It would, therefore, follow that with high alloys one needs a low nitrogen to hydrogen ratio, and conversely with low-alloy steels, will require high nitrogen to hydrogen ratio. (The latter part of the statement is made due to the fact that there will be very few alloying elements, if any to work with to form stable nitrides. However, the nitrogen will react with iron to form iron nitrides.) Hydrogen takes a catalytic role in terms of the formation of epsilon compounds

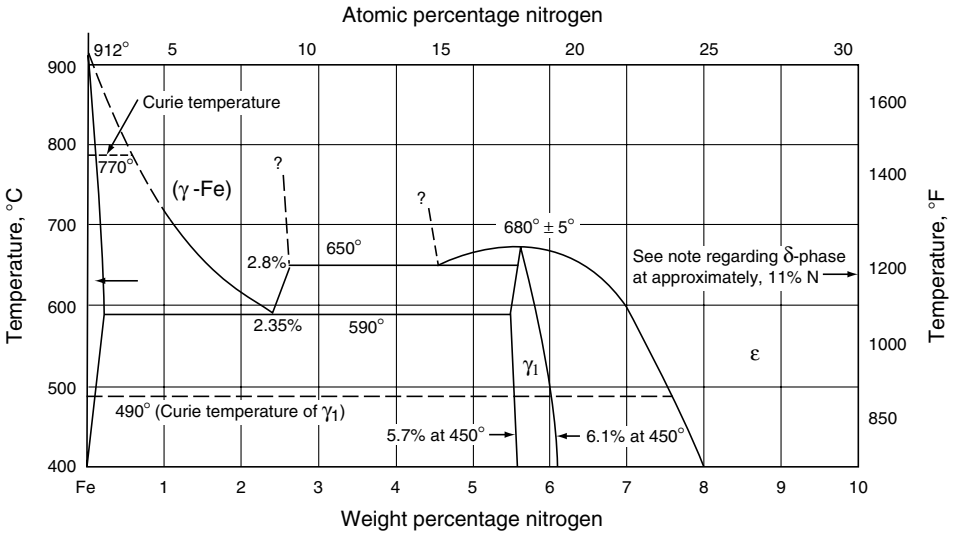

FIGURE 8.18 Iron–nitrogen equilibrium diagram. (From Pye, D., *Practical Nitriding and Ferritic Nitrocarburizing*, ASM International, Cleveland, OH, 2004.)

(Fe_2N and Fe_3N). On the other hand, if the gas compositions are reversed to give higher ratios of nitrogen to hydrogen (3 nitrogen to 1 hydrogen) on pure iron or low-alloy steels, a thick compound layer can be created with hardness values up to 700 VPN. This involves the formation of an Fe_2N phase at the steel surface, which will begin to decompose to Fe_4 (gamma prime) or Fe_2-3N (epsilon). The use of hydrogen in the process is really to act as a catalyst. It has been seen that when nitrogen atmospheres are used during the ion nitriding process the diffusion effect of nitrogen was not as great. The mechanism of the ion nitride process is shown in Figure 8.19.

The ability to create and manipulate the process gases of nitrogen and hydrogen ratios will affect both the formations of the compound zone and the diffusion zone of the total nitrided case [22].

Plasma nitriding offers to the engineer and the metallurgist the following benefits:

- *Environmentally friendly*. This process is a nontoxic process. There are no obnoxious smells or influences onto the environment. It, therefore, has no effluent problems.
- *Operating costs*. This process is a cost-effective method of heat treatment due to the fact that there is reduced operator intervention (other than load–unload and program), reduced flow space, reduced process consumables, and finally reduced energy costs.

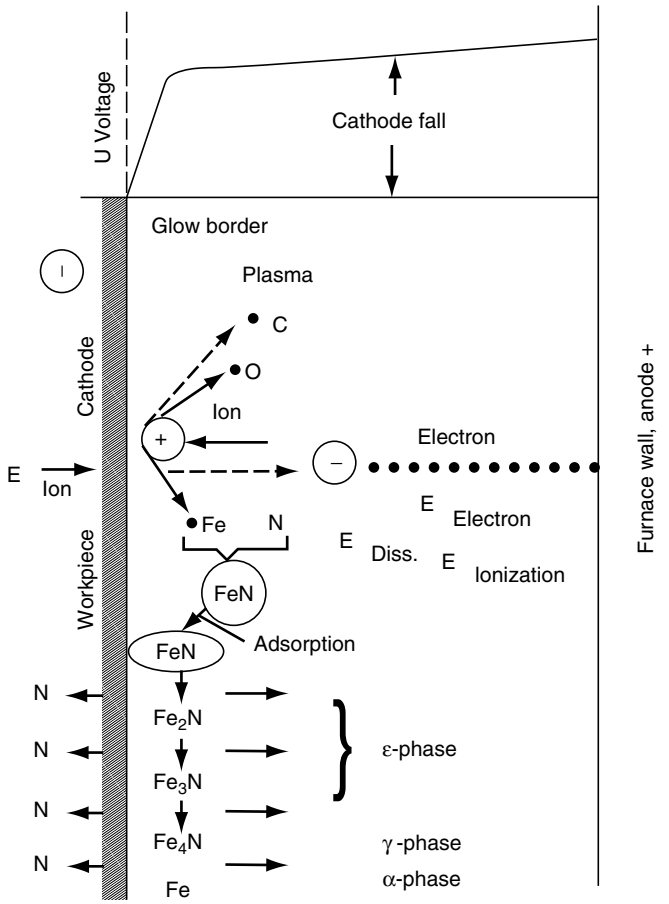

FIGURE 8.19 The ion nitriding mechanism. (From *The ASM Handbook*, Vol. 4, ASM International, Cleveland, OH, 1991.)

Although the equipment is more capital-intensive than the conventional methods of nitriding, it is a more productive system due to the fact that the floor-to-floor process time is considerably shorter than with the traditional methods of nitriding. The lower operating costs and the productivity improvement as well as the improved metallurgy can offset the higher investment.

- *Processor control*. The use of the computer and the accurate delivery of process gas ensure that close tolerance, repeatability, and created metallurgy can be accomplished. The metallurgy of the case can also be created and repeated.
- *Posttreatment-cleaning requirements*. It has been found that it is necessary to clean the work surfaces in a thorough manner. However, this does not mean that it is necessary to use high-tech precleaning equipment. Simple aqueous cleaning systems with the appropriate cleaning additive added to the solution are sufficient. It should be noted that it is necessary to remove any surface residual silicones, chlorides, and sulfides that could be present as a result of previous metal-cutting operations. Further cleaning can be accomplished during the initial part of the process cycle by the procedure known as sputter cleaning. This is a method of surface cleaning by ionic bombardment of gaseous ions onto the work surface. When using this method of surface preparation, the intensity and choice of sputter cleaning gases will determine the intensity of surface cleanliness. Sputter cleaning can be likened to atomic shot blasting, but instead of using air as the carrier and the steel shot as the abrasive material, use is made of the transfer of gas ions from the anode to the cathode at very high speeds. This will cause fine metallic particles to be dislodged.

8.18.19 Metallurgical Results

Because the process is controlled by the combination of PC/PLC, the results can be more accurately controlled and determined during the process cycle. The process now controls more of the process parameters that can be controlled with the more conventional methods of nitriding, thus more repeatable metallurgy. Precise control of the gas flows can also determine the thickness and phases of the compound zone.

What the reader perceives as a panacea of all processes is simply not a true perception. It should be recognized that the ion nitriding process is firstly, a phase of process development, and secondly that it is a niche process in the selection of nitriding methods in relation to components and metallurgical requirements. Salt bath and gas nitriding have their place in the ladder of requirements. In order to make the selection as to the choice of process method, one needs to review the geometrical complexity of the component, the material of manufacture, pre- and postmachining methods, distortion, and the desired surface metallurgical requirements (Figure 8.20 and Figure 8.21).

8.18.20 Steel Selection

The selection of the steel for nitriding must be considered very carefully in relation to:

- What is the product to be manufactured, and how complex is the part geometry?
- What are the operating conditions that the component will operate under? It is the load compressive and to what extent, are their impact load conditions, and to what extent, tensile loads and to what extent, and cyclical loading conditions and to what extent?
- Are there abrasive conditions to be considered?
- To what extent will corrosion be a factor?
- Is thermal cycling necessary to consider?

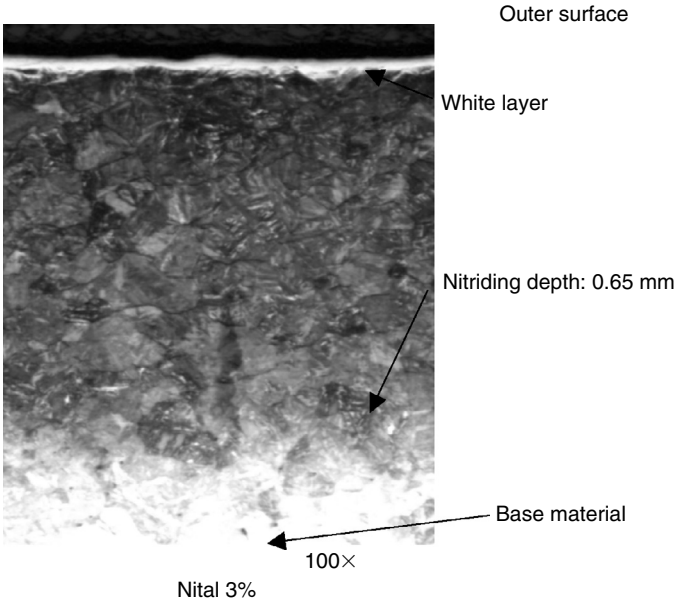

FIGURE 8.20 Photomicrograph showing plasma nitriding. (Courtesy of Nitrion, Munich, Germany.)

- Will there be adequate lubrication delivered to the finished component?
- Will further machining be required after nitriding?

Once the above conditions have been addressed, then considerations can be given to the steel selection. It has been a popular belief, which has been held by many, that only certain steels can be nitrided. This is not true, all steels will nitride including pure iron. The qualification for this statement is based on the following facts:

- Nitrogen is soluble in iron.
- Ammonia will decompose by heat to provide a nitrogen source.
- Nascent nitrogen will diffuse into iron and steel.
- Nitrogen will react to form nitrides of iron and soluble alloys.

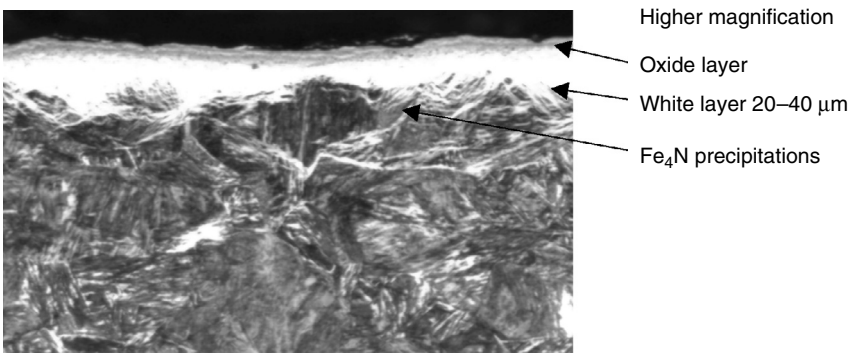

FIGURE 8.21 Photomicrograph showing plasma nitriding. (Courtesy of Nitrion, Munich, Germany.)

The success of any heat treatment procedure is usually determined by the resulting hardness value. That hardness value will be determined by whatever the process method that has been selected. Therefore if nitrogen is soluble in iron and it will react to form iron nitrides, then the newly formed iron nitrides will have a different hardness value to the substrate of iron. This is to say that the surface hardness will be higher than it was originally. Given this, a transformation has taken place, which has resulted in a higher hardness. In addition to this, the corrosion resistance of the surface of the iron has now improved. This also applies to the low-alloy steels. It is a known fact that hardness is relative to the material, which is abrading it [23].

Further to this, it is not often recognized that the corrosion resistance of the steel or iron surface has been greatly improved. This means that the low-alloy material now has a higher degree of corrosion resistance than it had previously.

The concept that was initially held in the formative years of nitriding was that only steels with special alloying elements can be nitrided. While it is true that special steels that contain:

- Aluminum
- Chromium
- Molybdenum
- Vanadium
- Tungsten
- Silicon

will nitride very readily, it is equally true the steels with iron (and this means all steels) will nitride, but will only form iron nitrides, which are fairly soft in comparison to the steels that contain the aforementioned alloying elements. However another consideration to the low-alloy and plain carbon steels is that when they are nitrided, the corrosion resistance will improve dramatically (Table 8.2).

8.18.21 Prenitride Condition

In order for alloyed steel to be successfully nitrided, it is necessary to ensure a core metallurgy of tempered martensite. This applies to the tool steels as well as to the alloy steels. The purpose of the pretreatment is to ensure an adequate core support of the nitrided case as well as to ensure a tempered martensite core. It is essential that the pretreatment procedure be conducted in an atmosphere that can be considered to be oxidizing thus providing good control (over the furnace atmosphere is mandatory). This is necessary to ensure that the steel surface is completely free of surface oxides as well as a decarburized free surface. If the surface is oxidized, it is safe to assume that the surface will also be decarburized. This means that the formed case arising for the nitriding process will not be uniform in its formation. In addition to this, the nitrides will not form in the same manner as they would with a clean oxide and decarburized free surface. The resulting newly formed nitrided surface will exhibit an orange peel effect on the immediate surface, which will exfoliate from the steel surface.

If one considers the molecular shape of the austenite molecule in relation to the tempered martensite molecule, it will be seen that the austenite molecule construction is made up of 14 atoms in a cubic construction, in relation to the martensite molecule being a tetragonal, nine-atom structure (Figure 8.22). The diffusion of the nitrogen atom is much easier with the austenite structure than with the tetragonal structure. It is also known that the hardness of austenite is much lower than that of the martensite structure. Therefore the newly nitrided case will form, but will exhibit a lower surface hardness and will not have an adequate support of the case. This is why, when nitriding a low-alloy or plain carbon steel, the surface hardness will not be very high when compared to high-alloy steel. This is due to the fact that the core

TABLE 8.2
Steels That Have Been Designed and Developed as Nitriding Steels[a]

Alloy Steels	C%	Cr%	Mo%	Si%	Mn%	Ni%	V%
SAE 4132	0.34	1	0.2	—	—	—	—
SAE 4137	0.35	1	0.2	0.25	0.8	—	—
SAE 4142	0.42	1	0.2	—	—	—	—
SAE 4140	0.40	1	0.2	0.25	0.85	—	—
SAE 9840	0.36	1	0.2	—	—	1	—
SAE 4150	0.5	1	0.2	—	—	—	—
28 Ni Cr Mo V 85	0.3	1.3	0.4	—	—	2	0.1
32 Ni Cr Mo 145	0.32	1	0.3	—	—	3.3	—
30 Cr Ni Mo 8	0.3	2	0.4	—	—	2	—
34 Cr Ni Mo 6	0.34	1.5	0.2	—	—	1.5	—
SAE 4337	0.38	0.8	0.4	—	—	1.5	—
SAE 4130	0.26	1	0.2	—	—	—	—

	C%	Si%	Mn%	P%	Cr%	Mo%	Ni%	V%	Al%
Nitralloy	0.20–0.30	0.10–0.35	0.40–0.65	0.05 max	2.90–3.50	0.40–0.70	0.40 max	—	—
Nitralloy M	0.30–0.50	0.10–0.35	0.40–0.80	0.05 max	2.50–3.50	0.70–1.20	0.40 max	0.10–0.30	—
Nitralloy 135	0.25–0.35	0.10–0.35	0.65 max	0.05 max	1.40–1.80	0.10–0.25	0.40 max	—	0.90–1.30
Nitralloy 135M	0.35–0.45	0.10–0.35	0.65 max	0.05 max	1.40–1.80	0.10–0.25	0.40 max	—	0.90–1.30

Cold tool steels	C%	Si%	Mn%	Cr%	Mo%	Ni%	V%	W%
F2	1.45	—	—	0.3	—	—	0.3	3.0

Special-purpose tool steels	C%	Si%	Mn%	Cr%	Mo%	Ni%	V%	W%
H13	0.5	1.0	—	5	1.4	—	1.4	—
	1.2	—	—	0.2	—	—	0.1	1.0
	0.9	—	—	0.2	—	—	0.3	1.0

Dimensionally stable tool steels	C%	Si%	Mn%	Cr%	Mo%	Ni%	V%	W%
D2	1.55	—	—	11.5	0.8	—	1.0	—
D3	2.0	—	—	12.0	—	—	—	—

A2	1.0	—	—	5.0	1.0	—	0.2	—
O1	0.95	—	10.5	—	—	0.1	0.5	
O2	0.9	—	20.4	—	—	0.2	—	
D6	2.1	—	—	11.5	—	—	0.2	0.7
D2	1.65	—	—	11.5	0.6	—	0.1	0.5
S1	0.59	—	—	1.1	—	—	0.2	1.9
Die block steels	C%	Cr%	Mo%	Ni%	V%			
L6		0.55	5	0.5	1.7	0.1		
L6	0.55	0.2	0.3	1.7	0.1			
Hot-work tool steels	C%	Cr%	Mo%	Ni%	V%	W%	Co%	
H12		0.36	5.2	1.4	—	0.4	1.3	
H13	0.4	5	1.3	—	1	—	—	
H11	0.4	5	1.3	—	0.6	—	—	
H21	0.3	2.7	—	—	0.4	8.5	—	
H19	0.4	4.3	0.4	—	2	4.3	4.3	
H10	0.32	2.8	2.8	—	−0.5	0.3	—	
High-speed steel tungsten base	C%	Cr%	Mo%	V%	W%	Co%		
T5	0.75	4	0.6	1.6	18	9.5		
T4	0.8	4	0.7	1.6	18	5		
T1	0.75	4	—	1	18	—		
T15	1.5	5	—	5	12.5	5		
M42	1.08	4	9.5	1.2	1.5	8		
M41	0.92	4	5	1.8	6.5	5		
M3	1.2	4	5	3	6.5	—		
M2	0.87	4	5	1.8	6.5	—		
M2	1.0	4	5	1.8	6.5	—		
M7	1.0	4	8.7	2	1.8	—		
M1	0.83	4	9	1.2	1.8	—		

[a]These are typical alloy steels that will gas or salt bath nitride.

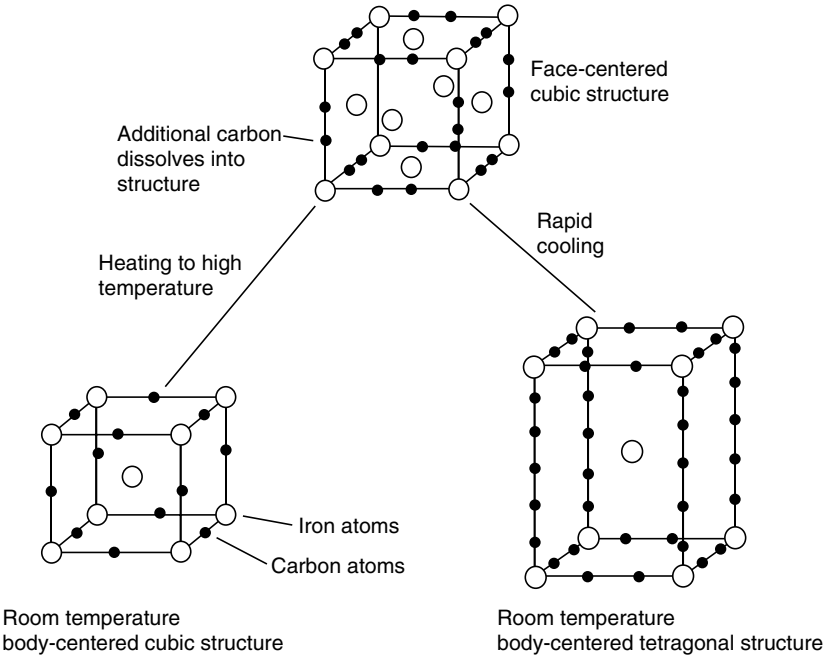

FIGURE 8.22 Crystal lattice changes that take place during high-temperature heat treatment processes such as carburizing. Ferrite is bcc structure; austenite, fcc; martensite, bct. (From Stickes, C.A. and Mack, C.M., *Overview of Carburizing Processes & Modeling, Carburizing: Processing & Performance*, Krauss, G., Ed., ASM International, Cleveland, OH, 1989, pp. 1–9.)

will be a mixture of ferrite and pearlite and will not form any martensite when austenitized and quenched.

Stainless steels will readily nitride because of the presence of high amount of chromium, however the austenitic and ferritic stainless steels will not exhibit a high surface hardness due to the fact that the carbon content is too low to transform the austenite to fresh martensite.

The hardenable groups of stainless steel such as the precipitation hardening stainless steels will nitride very well. It should be noted that the precipitation hardening stainless steels will benefit from the nitriding process, because the nitride procedure will act as a further ''precipitation hardening'' process and will assit with further dimensional stability. One should be aware that the selected nitride temperature should be approximately 27.8°C (50°F) lower than the previous precipitation treatment. All of the precipitation-treatable steels can be successfully nitrided.

The martensitic group of stainless steels will also nitride extremely well to form very high surface hardness values. This is due to the ability of each of the martensitic stainless steels to readily form the phase of martensite, followed by tempering to produce tempered martensite. With the martensitic stainless steels, the nitrided surface hardness values will be relatively high.

If one considers gas nitriding, the hardness values will be around 1000 VPN with a formed compound layer (albeit very thin), which will be formed in two phases, epsilon and gamma prime. The compound layer will have a degree of porosity to it. If the steel is ion nitrided, then the surface hardness can be as high as 1400 VPN with a controlled compound layer created by the process gas ratios. If the compound layer will be formed, then the layer will exhibit a high-density layer on the immediate surface. The ability to manipulate the gas ratios enables the technician to accomplish a great deal in terms of the control of the surface hardness, the formation of the phase composition, and the compound layer density.

8.18.22 Surface Preparation

The surface cleanliness is a mandatory procedure be it for gas, salt, or ion nitriding conditions. The surface should be free of any contamination otherwise it will interfere with the formation of the formed case. The stainless steel groups require the surface to be free of any oxide formation. It is well documented and well known that chromium has an affinity for oxygen and will readily form chromium oxide in an air atmosphere. The chrome oxide is what makes stainless steel corrosion-resistant. Therefore for the diffusion of nitrogen into the surface, it is necessary to depassivate the surface chromium oxide. In other words, the chrome oxide must be reduced to chromium to allow the nitrogen to react with the chromium to now form chromium nitrides.

With gas or salt bath nitriding, this can be accomplished by glass bead blasting, shot blast, or vapor blast. In addition there are chemical methods that can reduce the surface cleaning such as pickling or other means of chemical reduction of the oxide layer. Once passivation is completed, then extreme care should be exercised to ensure the freedom of the handler's fingerprints. Fingerprint contamination will deposit body oil onto the steel surface, which will act as a nitrogen-resistant carbon barrier to the steel, and the diffusion of nitrogen will not take place, which means a soft spot on the surface of the steel.

With ion nitride process, the surface preparation can simply be an aqueous wash followed by sputter cleaning on the ramp up to the allotted process temperature. Sputter cleaning will reduce the surface chrome oxide due to heat, hydrogen (reducing), and the sputtering action of the hydrogen, which will remove any fine particulate matter lodged on the steel surface. The steel will then readily nitride.

Precleaning of the steel is particularly important to the success of any nitride process method, be it gas, salt, or ion. The ion nitride process is somewhat more forgiving than with the gas method due to the presputter cleaning as the work is brought to the appropriate process temperature. There should be no paint, marker ink, or any other marking material on the surface of the steel. This will definitely inhibit the nitride process.

8.18.23 Nitriding Cycles

The gas nitride process is generally (but not in all cases) run as a single-stage procedure at a process temperature around 500°C (925°F). The process temperature selection will be determined by:

- Material composition
- Surface metallurgy requirements
- Required surface hardness

When nitriding stainless steels, it should be noted that the corrosion resistance of the stainless steel will be reduced. If a lower process temperature is selected, then the corrosion resistance of the stainless steel can be protected to some extent. It would be necessary to study the corrosion temperatures of the steel from the steel manufacturer handbook. However, it can be safely assumed that the process temperature will be in the region of 400 (750) to 425°C (800°F). The case depth accomplishment will of course take considerably longer due to the lower process temperatures.

In some cases where it is necessary to have a reduced compound layer thickness, the process selection method will usually consider the two-stage process. This process involves approximately one third of the cycle processed at approximately 500°C (925°F) with a gas dissociation of 30%, followed by the second stage of the process at a higher temperature of 550°C (1025°F) and a dissociation of approximately 15%. This will ensure a reduction in the thickness of the

compound layer. However, there is the danger of nitride networks forming at sharp corners due to the greater solubility of nitrogen in iron at the higher process temperatures.

With the ion nitride process, there is no necessity to go to the higher second-stage temperature due to the fact that the gas ratios are adjusted to reduce and sometimes eliminate the compound layer. As a result, the risk is reduced for the potential to form nitride networks, however nitride networks can still occur if the gas ratios are not controlled. Therefore with the ion nitride process, accurate control is required for the process gas delivery.

Process temperature uniformity control during the process of nitriding is a mandatory process requirement. This is due to the fact that, if there are wide temperature gradients with in the process chamber (be it gas nitride or ion nitride) there will be:

- Varying case depth formation
- Varying compound layer formation
- Various areas of nitride network formations
- Varying surface hardness values

It is, therefore, necessary to have good temperature control to within 5°C (10°F) maximum deviation from the set-point process temperature. This rule applies to all methods of nitriding, be it gas, salt, fluid bed, or ion. Temperature uniformity is mandatory for good and consistent metallurgical results from nitriding. This applies to any heat treatment process and not just to nitriding.

8.18.24 Distortion and Growth

Distortion is a term that is very familiar to all that are involved with thermal processing techniques especially in the field of heat treatment. No matter how careful one is, distortion cannot be avoided. It is important to at least understand the basic causes of the distortion problem. Distortion describes the movement of a metal during its heat treatment process. The distortion will manifest itself in one of two forms, or a combination of both:

- Shape distortion
- Size distortion

Shape distortion can occur as a direct result of one or any combinations of the following:

- Forging
- Rolling
- Casting
- Machining stresses induced due to manufacturing operations
- Grain size
- Variations in homogeneity of the material
- Incomplete phase changes

The only effective way that induced stress can be relieved is by the application of heat, and heat is applied during the nitriding process. If there are any induced stresses, then the stress will manifest itself in the form of twisting, bending, out of round. It is, therefore, most important that the component be appropriately stress relieved before the nitriding process.

Size distortion occurs as a direct result of changing the surface chemistry of steel. The size will change due to a surface volume change. In other words, the thicker the formed case, the greater the growth that will occur.

When a piece of steel is austenitized and cooled at various rates (as can occur due to sectional thickness changes), various structures can result. The structure of the austenite phase has the smallest volume, and the untempered martensite phase has the largest phase. If there are mixed phases, any residual austenite will transform to martensite over time or with the application of heat. This will cause a dimensional change in the steel.

With the diffusion of nitrogen into the steel surface, a volume change will occur, which means a size change in the form of growth. The amount of growth that will take place will be determined by the thickness of the formed case. The thickness of the formed compound layer will also contribute to the amount of growth. With gas nitriding, and considering nitriding steel, the thickness of the compound layer is generally 10% of the total case thickness. Do not be confused by this to mean the effective case. It is the total case. With the ion nitride procedure, the thickness of the compound layer can be controlled by the gas ratios selected for the process, which ultimately means the growth can be controlled more effectively. There will always be a growth, no matter what process method is chosen. The growth will also be uniform in all directions. Another method of ensuring dimensional stability is to subject the steel to a cryogenic treatment followed by a final temper, followed by the final machine and then the nitride procedure. The cryogenic treatment will ensure a complete phase change, which means any residual retained austenite will be transformed to untempered martensite. This means that no further phase transformation will occur and will thus ensure dimensional stability of the part.

FERRITIC NITROCARBURIZING

8.19 INTRODUCTION

FNC is a low-temperature process that is processed in the ferrite region of the iron–carbon equilibrium diagram at a process temperature of approximately 580°C (1075°F). The objective of the process is to form both carbides and nitrides in the immediate surface of the steel. The process is usually applied to low-carbon and low-alloy steels to enhance the surface characteristics in terms of hardness and corrosion resistance. In addition to this, the surface is further enhanced by deliberately oxidizing the surface to produce a corrosion-resistant surface oxide barrier to the steel. The process has gained a great deal of popularity during the past 5 to 10 years (Figure 8.23).

The process is diffusional in nature and introduces both nitrogen and carbon into the steel surface while the steel is in the ferrite phase with respect to the temperature. Nitrogen is soluble in iron at the temperature range of 315°C (600°F) and upward. Carbon is also soluble in iron at a temperature higher than 370°C (700°F). These elements are soluble in a solid solution of iron. Generally the process occurs at a temperature range of 537 (1000) to 600°C (1100°F). The diffused elements will form a surface compound layer in the steel which produces good wear and fatigue properties in the steel surface. Below the compound layer is the diffused nitrogen solid solution in a diffusion layer. In other words, the case formation is very similar to that of nitriding (Figure 8.24).

The process started life as a cyanide-based salt bath process around the late 1940s and components such as high-speed auto components (including gears, cams, crankshafts, valves) were processed. It was used primarily as an antiscuffing treatment. This process was also used on cast iron components for an improvement in antiscuffing resistance. During the 1950s, investigatory work was conducted in the U.K. into gaseous methods of FNC [15].

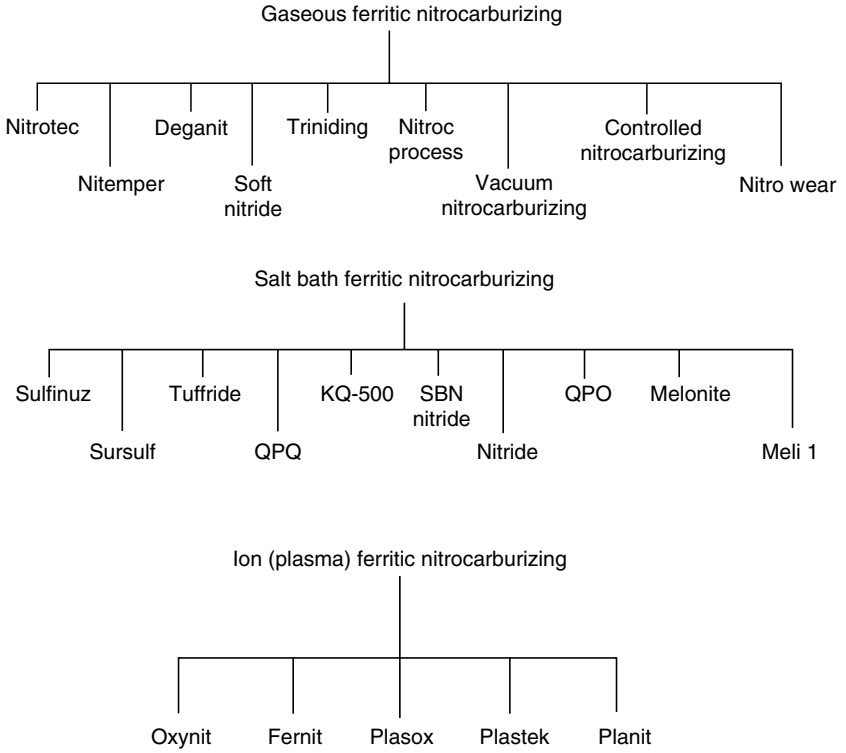

FIGURE 8.23 Various trade names for gases, salt bath, and ion (plasma). Ferritic nitrocarburizing processes. Fluidized bed processes are also available. (From Pye, D., *Practical Nitriding and Ferritic Nitrocarburizing*, ASM International, Cleveland, OH, 2004.)

8.20 CASE FORMATION

The case is formed by the diffusion of both nitrogen and carbon into a solid solution of iron in the previously mentioned temperature range to produce the surface layer of carbonitrides and nitrides. Because there is insufficient carbon in the low-alloy and plain carbon steels, it is necessary to add a hydrocarbon gas to the gas flow control system. The hydrocarbon gas can

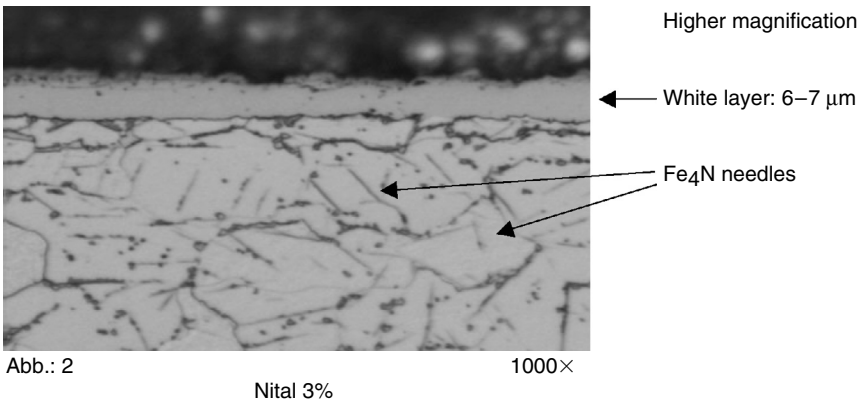

FIGURE 8.24 Photomicrograph showing diffused nitrogen solid solution in a diffusion layer. (Courtesy of Nitrion, Munich, Germany.)

be methane, propane, or acetylene. The choice will depend on gas availability and the ability to control the release of carbon into the process chamber. The surface layer is known (as in the nitriding process) as the compound layer or white layer. The layer is comprised of the same two metallurgical phases as are seen in a nitrided case of both epsilon and gamma prime nitrides. The balance of the two phases is determined by the carbon content of the steel and the presence of nitride-forming elements on the steel surface and is also influenced by the composition of the process atmosphere.

8.21 PRECLEANING

It is necessary to ensure a clean, oxide-free surface. The surface should have no contaminants such as oil or grease surface residuals, or paint markings, or marker pen markings as these will influence the final resulting metallurgy.

Cleaning can be done by washing in an aqueous solution followed by a good rinse and dry, or by the use of ultrasonic cleaning methods and vapor degreasing. If the surface is oxidized, the oxide layer should be removed either by vapor blast, or a fine glass bead blast. It should be noted that the precleaning requirements are as with the nitriding process. It is recommended that the components to be treated are stress relieved at a temperature of 28°C (50°F) above the FNC process temperature.

As with any heat treatment process and in particular any surface treatment process, the steel surface preparation is of paramount importance to the success of the particular process. Any surface contamination can seriously and adversely affect the quality of the formed case, be it for nitriding, carburizing, carbonitriding, or FNC.

8.22 METHODS OF FERRITIC NITROCARBURIZING

There are essentially three methods of FNC, each of these methods will be discussed separately:

- Salt bath FNC
- Gaseous FNC
- Plasma- or ion-assisted FNC

8.22.1 Salt Bath Ferritic Nitrocarburizing

Salt bath FNC was probably the first method that was developed for the technique. The principle of the salt bath procedure is based on the decomposition of cyanide to cyanate at an approximate process temperature of 560°C (1050°F) and the part was held in the bath for approximately 2 to 3 h at this temperature.

Probably the first salt bath process was developed by Imperial Chemical Industries (ICI) in England and was known as the Sulfinuz process. It was followed closely by the Degussia process, developed in Germany and was known as Tufftride [15].

The chemical reaction that takes place is a well-known reaction, which is as follows:

$$4NaCN + 2O_2 \rightarrow 4NaCNO \text{ [14]}$$

This reaction is promoted by the introduction of air into the process salt bath when the salt is molten. The volume of air required to activate the cyanide to cyanate will depend largely on the volume of molten salt in the bath, in relation to the surface area treated, and in relation to the frequency of use of the bath. It will be necessary to analyze the rates of decomposition of the bath by chemical titration.

The steel surface will act as a catalyst and assist in the breaking down of the cyanate. This means that both carbon and nitrogen will be available for diffusion into the surface of the steel, in the following reaction:

$$8NaCNO \rightarrow 2Na_2CO_3 + 4NaCN + CO_2 + (C)Fe + 4(N)Fe \text{ [14]}$$

The surface of the steel treated will begin to form a compound layer rich in carbon and nitrogen. The compound layer will be predominantly epsilon phase nitrides and thickness, which will be dependent on the material treated and the process cycle time.

The first derivative of the basic FNC process will be the ICI process known as a Sulfinuz. This process will form an iron sulfide in the immediate surface of the steel. In addition to this surface porosity will occur, and the net result is that the pores in the surface will hold oil that is supplied as a lubricant.

Because of the toxicity of the cyanide-based salt bath, great concern was expressed regarding the effluent waste product of the salt and its disposal. This led to the development of the low cyanide-based salts. A new salt was developed, which offered extremely low cyanide waste products [11].

In addition to this new salt development, an additional surface treatment was developed which was that of postoxidation. The process rapidly gained recognition as a process which could not only give a high degree of surface hardness to the steel treated, but it could also produce an esthetically pleasing, yet corrosion-resistant surface.

8.22.2 Gaseous Ferritic Nitrocarburizing

Joseph Lucas Ltd., of England applied for a patent for the gaseous process of FNC [15]. The process essentially used a gaseous mixture, which is comprised of:

- Ammonia
- A hydrocarbon gas such as methane or propane
- Endothermically generated gases

The treatment was initially accomplished using partial pressure systems (below atmospheric pressure). The treatment was carried out at an approximate temperature of 570°C (1060°F). The resulting metallurgy produced an epsilon-rich compound layer on the immediate surfaces with presence of porosity. A further development of the process was to purge the process chamber of the process gas with the nitrogen, followed by the controlled introduction of oxygen. The purpose for the introduction of oxygen is to deliberately create a surface oxide layer on the immediate surface of the steel. The oxide layer will act as a corrosion-resistant barrier on top of the diffused-formed case.

There are numerous scientific reports as to the chemistry of the FNC process. T. Bell reported that Prenosil conducted his investigations on the composition, and the structure of the FNC-formed compound layer of pure iron using an atmosphere of 50% ammonia and 50% propane at a process temperature of 580°C (1075°F). He found that the wear characteristics of the iron were considerably improved as well as having a predominantly epsilon phase in the compound layer [14].

Professor Bell reports the gaseous decomposition to be as follows:

$$NH_3 \rightarrow [N]Fe + 3/2H_2$$

This means that the active nitrogen will begin to diffuse into the steel surface and will become saturated with the epsilon phase after the nucleation of the compound zone

$$NH_3 \rightarrow [N]e + 3/2H_2$$

It was then discovered that endothermic gas could be used as a source of carbon plus the addition of ammonia. Professor Bell reports the decomposition reaction to be

$$2CO \rightarrow [c]E + CO_2$$

This reaction will control the atmosphere carbon potential necessary for the formation of the epsilon phase within the compound layer of the formed case.

There have been many variations in the FNC process technique, each one with a slight variation on the other and are:

- Nitroc
- Triniding
- Nitemper
- Deganit
- Controlled nitrocarburizing
- Vacuum nitrocarburizing

8.22.2.1 Safety

Great care must be exercised when using an endothermic atmosphere, ammonia, and propane at temperatures below 760°C (1400°F), because the gases can become exothermic below these temperatures in the presence of oxygen. In other words if using a batch furnace, such as an integral quench furnace, the furnace should be gas tight with no possible potential for gas leaks, particularly around:

- Apertures into the furnace, especially pneumatic cylinders and particularly around the gasket joints (both internal and external).
- All door safety interlocks and flame curtains must be operating satisfactorily.
- All the burn off ports must be fitted and are reliably operating.
- Pilot lights must be functional and operating to ignite any gas burn off that may occur.
- The oil quench medium must be checked on a very regular basis for the presence of water in the oil. If water is present, it can lead to a violent fire or explosion.
- Emergency nitrogen purge system must be provided to both the quench vestibule chamber as well as the heating chamber.

Only if all of these precautions are taken, one can successfully implement the integral quench furnace as the process unit. Please be aware that while the integral quench furnace is an excellent choice of equipment, it can only be used if all of the appropriate safety compliance measures are met.

8.22.3 Plasma-Assisted Ferritic Nitrocarburizing

Plasma-assisted FNC has been accepted by the metallurgical processing industry for a number of years as a proven and reliable process. This process is based on existing technology, which is the gaseous process technique. However in this instance, the process is a partial pressure process and uses both molecular, elemental- and hydrocarbon-based gases. This procedure can also accomplish the postoxidation treatment, which makes it as versatile as the salt bath process. This process is infinitely repeatable and consistent (probably more so)

compared with the gaseous process techniques. Once the concept of plasma processing, and the variability of the process gas mixtures are understood then the complete concept of plasma-assisted FNC is easily understood.

8.22.3.1 Applications

The process is generally used for (but not limited to) low-alloy or plain carbon steels and is used to provide a hardwearing surface without high core hardness. In addition to the FNC process, the steel surface can be postoxidized at the completion of the FNC to produce the deliberately oxidized layer for corrosion resistance. Typical applications for the process would be:

- Simple timing gears
- Wear plates
- Windshield wiper arms
- Windshield drive motor housings
- Clutch plates
- Liners
- Sprocket gears
- Exhaust valves
- Wheel spindles
- Washing machine gear drives
- Rocker arms spacers
- Gear stick levers
- Pump housings
- Hydraulic piston rods

Obviously the above-mentioned components are not all of the components that can be treated using the plasma-assisted FNC process, there are many others that can benefit from the process. It is a question of once again understanding the process, its strengths, and its limitations. Once that is understood then decisions can be made. It is strongly recommended that a feasibility study of heat treat as to the advantages, disadvantages, and the material selection is done.

8.22.3.2 Steel Selection

The steel selection has to be made based on the following operating conditions:

- Operating temperature
- Cyclical loading conditions
- Compressive load conditions
- Corrosive environment
- Wear requirements
- Material cost
- Plant available
- Plant capacity

The steels that are typically used for component manufacture are as follows:

- Plain low carbon steels
- Low-alloy steels

- Low carbon alloy steels
- High strength low-alloy steels

8.22.4 Process Techniques

The process of FNC using the plasma-assisted method is almost the same technique as the plasma nitriding process. The difference is that the steel processed usually does not have sufficient nitride-forming elements, except of course iron. Iron will readily form iron nitrides with nitrogen and this is the basis on which the process operates.

This process is based on the solubility of nitrogen in iron and the solubility of carbon in iron. The compound layer will be formed at the component surface. At the surface layer, nucleation will begin, with the first epsilon phase at low temperatures [24]. The source for the carbon to form the epsilon phase, alongside the gamma prime phase will be methane or propane as an additive gas. The volume of hydrocarbon gas used to promote the epsilon phase will determine the amount of the epsilon phase. Another gas that could be used (if kept at levels of 1% and no greater) is carbon dioxide. If the amount increases to 1.5 to 2.0% by volume, then surface oxides begin to form and grain boundary oxidation takes place.

There is no method of controlling the gas flow for the appropriate phases, as there is with gas nitriding where one would simply measure the ammonia gas dissociation by the water absorption method. With the plasma-assisted FNC, one simply cannot measure the gas decomposition or the free oxygen, or the nitrogen potential of the process gases within the plasma glow chamber. It is, therefore, controlled by gas ratios of:

- Nitrogen
- Hydrogen
- Hydrocarbon gas

A system of plasma photosynthesis and spectrometry was developed at the Moscow State University in 1995 [22]. The author, under controlled experiments, observed the results, and the results were analyzed and found to be accurate as far as both diffused carbon and nitrogen were concerned. The system observed the glow seam around the workpiece and analyzed the nitrogen and carbon potentials. It is not known if the system was ever commercialized outside of the Soviet Union.

As a result of process work by the author and colleagues [22] it has been found that the higher nitrogen potential (ratio of nitrogen to hydrogen) can control the surface iron nitride formation. This provides surface hardness values up to 700 HVN (HVN, Vickers hardness number). If an appropriate hydrocarbon gas is added, then the surface hardness of the formed surface compound layer can exceed 700 HVN.

8.22.5 Case Depth

8.22.5.1 How Deep Can the Case Go?

Do not be mislead by claims of case depths of 0.030 in. in an hour. There are many claims made of case depth accomplishments that will surpass case depths that cannot be achieved by carburizing other than by going up to temperatures around 1037°C (1900°F).

The laws of the physics of diffusion govern the rate of solid-state diffusion of any element into the surface of any steel. In other words, the diffusion of the element cannot go into the steel faster than the laws of physics will allow it go. Many claims are made of very deep

case depths accomplished with very short cycle times at the process temperature (in the region of 580°C or 1075°F). The caveat emptor should be let the buyer beware. The case depth definition is not usually made. Then one should ask, is the definition of the case depth total or effective case? Also what is meant by core hardness? Is core plus 5 Rockwell C points, or is it the actual core hardness itself This can and will make a very significant difference to the case depth.

If the reported case depths are achievable and in the times specified, then the process has a great deal more to offer both the engineer and the metallurgist than has been previously thought. It would make great sense to dispense with the carburize process and go with the ferritic nitrocarburize in terms of:

- Reduction of distortion
- Improved part cleanliness
- Improved productivity and efficiency
- Elimination postoperation cleaning

The following table is an approximate table of values and is given only as a guide. The guide is based on the fact of plasma-assisted FNC. The guide is also based on plain low-carbon steel and low-alloy steel. Once again using the formula of the square root of time multiplied by a temperature-derived factor. The formula is based on the Harris formula and on the use of plain carbon and low-alloy steels. The addition of alloying the elements to steel will influence the rate of diffusion of nitrogen and carbon into the steel. As the alloying contents increase, the rate of diffusion will decrease; therefore, the following table should only be used as a guide for time at process temperature.

13,"8.23 Ferritic

Temperature		Factor
°F	°C	
1050	565	0.0021
1075	579	0.0025
1085	585	0.0027
1100	593	0.0029
1125	607	0.0031
1150	621	0.0033
1175	635	0.0036
1200	649	0.0039
1225	663	0.0042

The rate of nitrogen and carbon diffusions will begin to retard as the alloying content is increased by the addition of chromium, molybdenum, nickel (particularly nickel), aluminum, tungsten, vanadium, and manganese. The higher the alloying content, the slower the rate of nitrogen diffusion, but the higher the resulting surface hardness. The lower the alloy contents of the steel, the faster the rate of nitrogen diffusion, but lower the resulting surface hardness. Nickel is not a nitride-forming element, thus diffusion will be severely retarded. For steel containing all of the above elements (not accounting for the percentage variations) the rate of diffusion can be retarded by as much as 17 to 20% [8].

8.23 FERRITIC OXYCARBONITRIDE

This process is simply an addendum at the end of the FNC procedure. The objective of the deliberate oxidizing procedure after the nitride process or the FNC process is to enhance the surface characteristics of the steel by producing a corrosion-resistant surface. This procedure involves introducing oxygen in a controlled manner into the process chamber. There are many sources of oxygen for the procedure, however the source of the oxygen will need to be carefully considered. Gases that can be used are as follows:

- Steam
- Oxygen
- Nitrous oxide
- Air

These gases are all suitable sources of oxygen for the oxidation process. The oxygen-bearing process gas is introduced into the process chamber only on completion of the FNC procedure. One needs to select the process gas with great care. Generally the vapor of steam could cause problems with the electrical equipment such as power feed through and control systems of the furnace. The preferred gases are either nitrous oxide or oxygen. The nitrous oxide tends to be more user-friendly to valves and control systems rather than oxygen.

The thickness of the oxygen-rich compound zone after treatment will be determined by the time at temperature and the time of cool down. The oxidizing gas will also play a part in the oxide surface quality and finish. There are a number of gases that can be utilized as the oxidizing gas, which include (among others) oxygen and air.

The primary reason for the oxygen treatment after the FNC treatment is to enhance the surface characteristics in terms of corrosion resistance. The procedure is comparable to the black oxide type of treatment and will enhance the cosmetic surface appearance of the component. The surface finish of the steel component will depend on the quality of the surface finish of the component before the treatment just as it does with the salt bath treatments. The higher the polishes of the component before the ferritic nitrocarburize treatment, the better the finish after the oxidizing procedure.

The surface corrosion resistance of the FNC-treated steels has been seen to exceed the 200-h mark by a considerable margin. The resistance to the salt spray corrosion test will be determined by the created oxide layer thickness after the treatment.

The oxidization treatment after the FNC procedure has almost no cost attached to it, other than a portion of the amortization of the original equipment. Generally there is no power consumption, or if there were, it would only be for say 1 h at temperature after the post-FNC treatment. Then of course, there would be the cost of the oxidation process gas, followed by furnace occupancy. The FNC process offers the opportunity for the engineer to enhance the surface characteristics of a low carbon or low-alloy steel.

REFERENCES

1. Pye, D., *Industrial Heating Magazine*, September 1991.
2. Pye, D., private communication with J.U. Dillon, Bayside Motion Group, February 2004.
3. Fry, A., U.S. Patent 1,487,554, March 18, 1924.
4. SSI personal communication, March 2005.
5. Hawkins, D.T., *The Source Book on Nitriding*, ASM International, Cleveland, OH, 1977.

6. Pye, D., *Practical Nitriding and Ferritic Nitrocarburizing*, ASM International, Cleveland, OH, 2004.
7. Clayton, D.B. and Sachs, W., *Heat-treatment 1976*, The Materials Society, U.K.
8. Pye, D., *Practical Nitriding and Ferritic Nitrocarburizing*, ASM International, Cleveland, OH, 2004.
9. Pye Metallurgical Consulting, *Nitriding Notes*, 1996.
10. Totten, G.E. and Howes, M.A.H., Nitriding techniques and methods, *The Steel Heat Treatment Handbook*, Marcel Dekker, New York, 1997.
11. ICI Cassell, *Manual of Heat Treatment and Case Hardening*, 7th ed., ICI, U.K., 1964.
12. Reynoldson, R.W., *Principles of Heat Treatment in Fluidized Beds*, ASM International, Cleveland, OH, 1993.
13. Krauss, G., *Principles of Heat Treatment of Steel*, 5th ed., ASM International, Cleveland, OH, 1988.
14. Totten, G.E. and Howes, G.A.H., *The Steel Heat Treatment Handbook*, Marcel Dekker, New York, 1997.
15. *Anon., Source Book on Nitriding*, ASM International, Cleveland, OH, 1997.
16. Pye Metallurgical Consulting and PlaTeG, personal correspondence, Germany.
17. Pye Metallurgical Consulting, personal correspondence.
18. Degussa Druferrit, personal communication, U.K., 1996.
19. Jones, C.K., Sturges, D.J., and Martin S.W., Glow discharge nitriding in production, *Metals Progress.*, *104*: 62–63 (1973).
20. Pye, D., Pulsed plasma nitriding and control of the compound zone, *Carburizing and Nitriding with Atmospheres*, ASM International, Cleveland, OH, 1995.
21. Thelning, K.-E., *Steel and Its Heat Treatment*, Butterworths, England, 1986.
22. Pye, D., *Carburizing and Nitriding with Atmospheres*, ASM International, Cleveland, OH, 1995.
23. Pye, D., *FWP Journal*, South Africa, April 1978.
24. Pye, D., *The ASM Handbook*, Vol. 4, ASM International, Cleveland, OH, 1994.

9 Quenching and Quenching Technology

Hans M. Tensi, Anton Stich, and George E. Totten

CONTENTS

9.1 Introduction 540
9.2 Metallurgical Transformation Behavior during Quenching 541
9.2.1 Influence of Cooling Rate 541
9.2.2 Influence of Carbon Concentration 544
9.2.3 Influence of Alloying Elements 544
9.2.4 Influence of Stresses 548
9.3 Quenching Processes 549
9.4 Wetting Kinematics 551
9.5 Determination of Cooling Characteristics 553
9.5.1 Acquisition of Cooling Curves with Thermocouples 553
9.5.2 Measurement of Wetting Kinematics 558
9.5.2.1 Conductance Measurement 558
9.5.2.2 Temperature Measurement 559
9.6 Quenching as a Heat Transfer Problem 560
9.6.1 Heat Transfer in a Solid 560
9.6.2 Heat Transfer across the Surface of a Body 562
9.7 Process Variables Affecting Cooling Behavior and Heat Transfer 567
9.7.1 Immersion Quenching 567
9.7.1.1 Bath Temperature 567
9.7.1.2 Effect of Agitation 568
9.7.1.3 Effect of Quenchant Selection 569
9.7.1.4 Surface Oxidation and Roughness Effects 569
9.7.1.5 Effect of Cross-Section Size on Cooling 571
9.7.1.6 Effects of Cooling Edge Geometry 573
9.7.1.7 Effects of Steel Composition 574
9.7.2 Spray Quenching 575
9.7.3 Gas Quenching 578
9.7.4 Intensive Quenching 583
9.8 Property Prediction Methods 589
9.8.1 Potential Limitations to Hardness Prediction 590
9.8.2 Grossmann *H*-Values 591
9.8.3 The QTA Method 594
9.8.4 Correlation between Hardness and Wetting Kinematics 596
9.8.5 Computer-Based Calculation of Hardness Profile 599
List of Symbols 601
References 602

9.1 INTRODUCTION

The outstanding importance of steels in engineering is based on their ability to change mechanical properties over a wide range when subjected to controlled heat treatment. For unalloyed carbon steels, for example, the hardness can be increased by up to 500% just by changing the cooling rate from the austenitizing temperature from extremely slow to extremely fast. However quenching at a rate faster than in still air does not only determine the desired mechanical properties but is an important side effect of quenching is the formation of thermal and transformational stresses that lead to changes in size and shape and thus may result in quenching cracks that damage the workpiece.

Figure 9.1 schematically represents the coupling effects among the three different characteristics of quenching—cooling rate, metallic structure, and internal stresses. The cooling rate influences the phase transformation of the metallic structure, whereas the latent heat due to structural changes affects the cooling rate. All phase transformations of austenite during quenching are accompanied by volume expansion. In addition, steels contract with decreasing temperature. As a consequence, locally and temporally different changes of structure and temperature cause nonuniform volumetric changes in the quenched part that can result in transformational and thermal stresses. These stresses accelerate or hinder the phase transformation and influence the volume expansion. While the phase transformation brings out a defined metallic structure, the volumetric dilatation and thermal and transformational stresses result in deformation and residual stresses. At room temperature, both characteristics influence the material properties.

The coupling effects between temperature distribution during quenching, metallic structure, and stresses require correct cooling rate during heat treatment. This includes sufficient reproducibility and predictability of quenching performance as well as the ability to exactly control quenching intensity by varying the type of quenchant and its physical state. The main objective of the quenching process is to achieve the desired microstructure, hardness, and strength while minimizing residual stresses and distortion.

The most common quenchants in hardening practice are liquids including water, water that contains salt, aqueous polymer solutions, and hardening oils. Inert gases, molten salt, molten metal, and fluidized beds are also used.

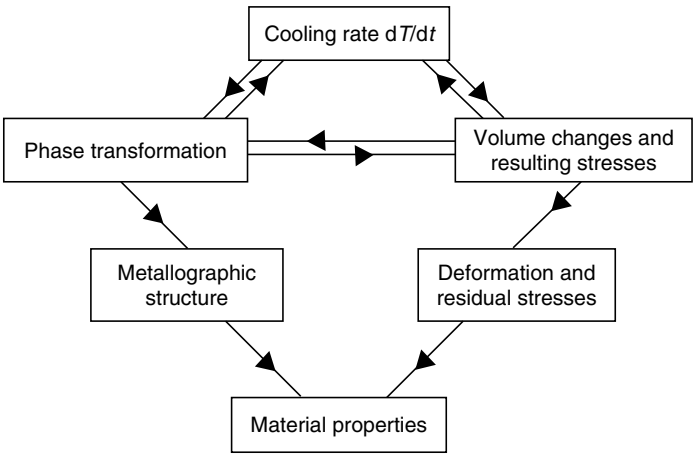

FIGURE 9.1 Coupling effects between cooling rate, phase transformation and stresses, and their influence on the material properties.

Quenching techniques used for liquid media are immersion quenching and spray quenching. Immersion quenching, where the part is submerged into an unagitated or agitated quenchant, is the most widely used. The part may be quenched directly from the austenitizing temperature to room temperature (direct quenching) or to a temperature above the M_S temperature, where it is held for a specified period of time, followed by cooling in a second medium at a slower cooling rate (time quenching or interrupted quenching; see Section 9.3). The quenching intensity can be changed by varying the type of quenchant, its concentration and temperature, and the rate of agitation. Spray quenching refers to spraying the liquid through nozzles onto those areas of the hot workpiece where higher cooling rates are desired. The heat transfer is mainly determined by the impingement density and its local distribution.

9.2 METALLURGICAL TRANSFORMATION BEHAVIOR DURING QUENCHING

9.2.1 Influence of Cooling Rate

The transformation behavior during very slow cooling of an unalloyed steel with 0.45 wt% carbon (1040 steel) from austenitizing temperature (about 850°C [1560°F]) is described by the metastable iron–cementite equilibrium diagram [1–3] (Figure 9.2a). The stable iron–carbon system is not of interest for steels. At 850°C (1560°F) the face-centered cubic γ-iron, called austenite after Sir Robert Austin, is the stable phase. The transformation starts at 785°C (1445°F) (A_3 temperature) with a precipitation of the body-centered cubic α-iron, called ferrite. The transformation into proeutectoid ferrite is finished when the eutectoid temperature of 723°C (1333°F) (A_1 temperature) is reached. The concentration of carbon in the austenite grains increases from the initial concentration of 0.45% at 785°C to 0.8% at 723°C (1333°F), where the concentration of the metastable eutectoid is at equilibrium. At 723°C (1333°F), the austenite transforms into a lamellar-like structure of ferrite and cementite called pearlite* (see Figure 9.3c). At room temperature there is a metastable equilibrium between ferrite and pearlite (Figure 9.3b), which, strictly speaking, does not correspond to the exact thermodynamic equilibrium. Tempering this metallographic structure over a long time (2 or 3 days) at a temperature just below the eutectoid temperature A_1, a temperature where no phase

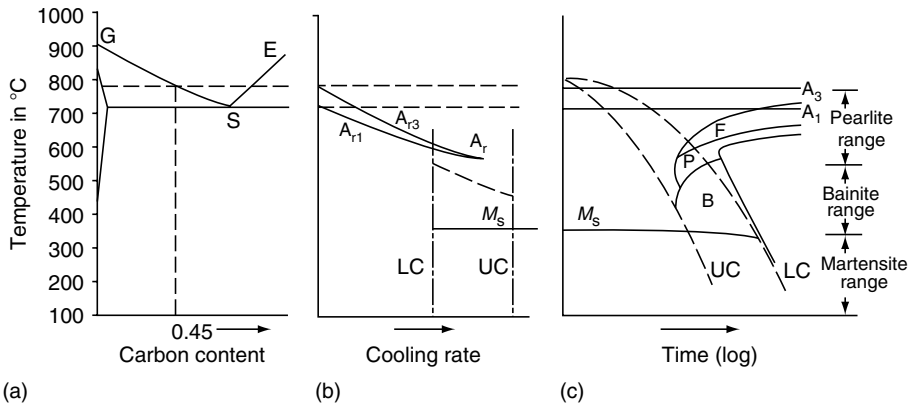

FIGURE 9.2 Influence of cooling rate on the transformation temperatures of austenite. (a) Metastable iron–cementite equilibrium diagram; (b) change of transformation temperatures of a 1040 steel with increasing cooling rate; (c) CCT diagram of a 1040 steel.

*After the pearly appearance of the metallographically prepared surface.

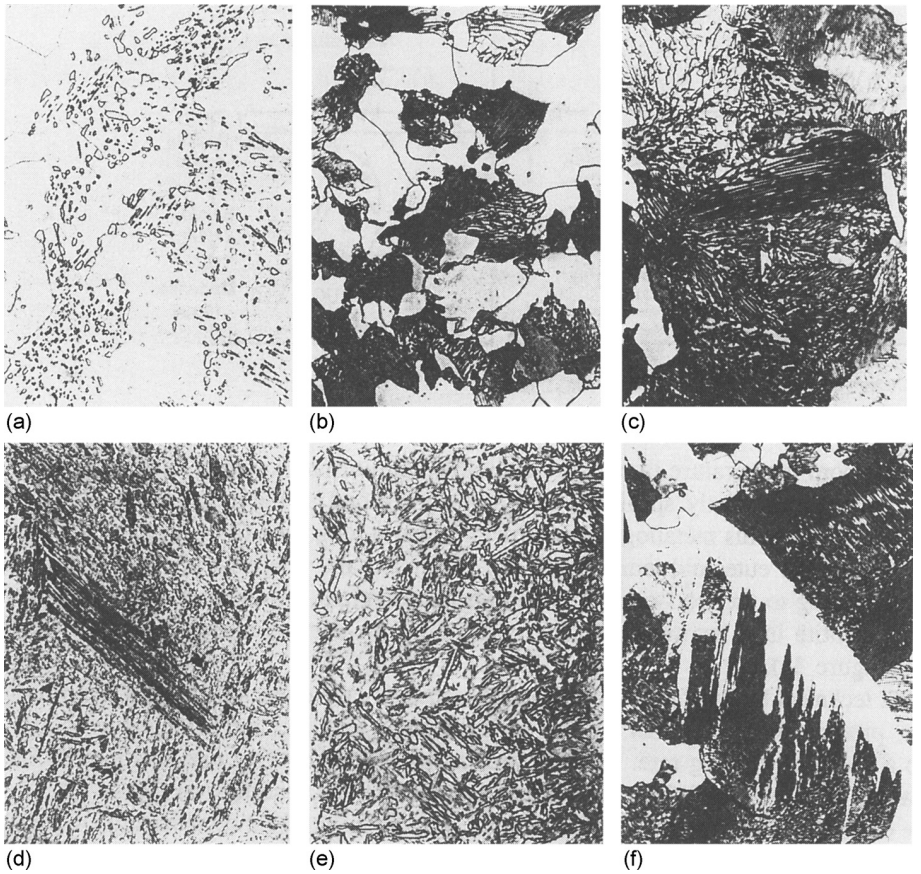

FIGURE 9.3 Microstructures of a 1040 steel obtained with increasing cooling rate from austenitizing temperature (850°C). Magnification 1000×. (a) Globular cementite (gray) in a ferritic matrix (white), after tempering at 680°C over 60 h starting from a ferrite–pearlite microstructure; (b) proeutectoid ferrite (white) and pearlite (dark) in a normalized structure. Heat treatment: 850°C/still air; (c) pearlite–ferrite (white) and carbide (dark) in an arrangement of parallel plates, and small amounts of proeutectoid ferrite (white); (d) bainite. Heat treatment: 850°C/oil; (e) martensite. Heat treatment: 850°C/water; (f) widmannstätten structure. Heat treatment: 1100°C/still air.

transformations occur according to the iron–cementite equilibrium diagram, produces a stable structure of globular cementite in a ferritic matrix by minimizing the surface energy between ferrite and carbide (Figure 9.3a).

Nearly all quench treatments, especially quenching from austenitizing temperature, produce structures that are not in accordance with the thermodynamic equilibrium due to a specified cooling rate. The effect of an increasing cooling rate on the transformation behavior of a 1040 steel from austenitizing temperature is described in Figure 9.2b. The temperature of proeutectoid ferrite precipitation (A_{r3}) and the eutectoid temperature (A_{r1}) decrease with increasing cooling rate; the A_{r3} point decreases faster than the A_{r1} point, so the distance between them decreases until they join in a single curve called the A_r point. Consequently, the volume fraction of proeutectoid ferrite permanently decreases with an increasing cooling rate while the volume fraction of pearlite increases [1]. At the A_r point, ferrite precipitation is suppressed and the structure consists only of pearlite with an average carbon content of 0.45 wt% (deviating from the carbon concentration of the eutectoid

equilibrium of 0.8 wt%). The mechanical behavior of the single pearlite structure (Figure 9.3c) strongly differs from that of the ferritic–pearlitic structure (Figure 9.3b). Ferrite is nearly pure iron with low tensile and yield strengths, R_m and R_p, and high elongation A. Pearlite, which is a mixture of ferrite and cementite, has high strength values and low elongation. Therefore, the strength distribution of ferritic–pearlitic structures is inhomogeneous.

If the cooling rate is further increased and reaches a limit, which is called the lower critical (LC) cooling rate, the diffusion-controlled transformation in the pearlite range is first partly and then completely suppressed. The solid solution of austenite is maintained down to lower temperatures and transforms into bainite and martensite (Figure 9.3d and Figure 9.3e). The microstructures of the bainite range grow partly by a diffusion-controlled process while the microstructures of the martensite range are mainly diffusionless [4]. Similar to the A_{r3} and A_{r1} points, the beginning of bainite transformation, A_b, shifts to lower temperatures with increasing cooling rate. The formation of martensite starts at a temperature called M_s, which does not depend on the cooling rate.

The upper critical (UC) cooling rate is the upper limit of the cooling rate at which plain martensite is formed. Martensitic structures are the objective of most hardening processes, because martensite exhibits the highest tensile and yield strength a steel of a given chemical composition can achieve.

If the same 1040 steel is quenched at a definite cooling rate from an overheated austenitizing temperature, ferrite may be formed inside large grains at crystallographically preferred glide plains in spite of the under-eutectoid carbon concentration (Figure 9.3f). After precipitation of ferrite, the retained austenite transforms into pearlite. This structure, which is practically useless for technical applications, is called the Widmannstätten arrangement.*

The correlation between the cooling rate and the microstructure for a given chemical composition and definite austenitizing conditions is described in the continuous cooling transformation (CCT) diagrams, which can also contain data on hardness [5]. An example for a 1040 steel is shown in Figure 9.2c. For an infinitely slow cooling rate the transformations described by the CCT diagram are identical with that of the equilibrium diagram. The S-shaped curves describe the beginning (B) and the completion (C) of the transformation of austenite into the indicated microstructure. The microstructures that are formed with increasing cooling rate from the austenitizing temperature of a steel are ferrite and pearlite, pearlite, bainite, and martensite with retained austenite. For certain cooling rates these microstructures can occur in combinations. The prediction of the microstructures and microstructural combinations formed during cooling is restricted by the fact that the shape of the cooling curves has an essential influence on the course of phase transformation [6]. Therefore transformation diagrams are valid only for specified temperature–time cycles. In addition, deviation from the specified chemical composition and metallographic structure before austenitizing as well as differences in the austenitizing conditions (temperatures and time) exhibit a very strong influence on the transformation behavior.

An uncomplicated experimental procedure to describe the dependence of phase transformation on cooling rate is given by hardenability curves derived from Joiminy end-quench tests (see chapter 5.3.2). In the end-quench test, the cooling rate continuously decreases with increasing distance from the water-quenched end. The change of hardness as a function of the distance from the quenched end describes the hardenability of a steel. In addition to the hardness values, structural changes along the mantle line can be observed. For a 1040 steel, for example, the hardness reaches from about 850 Vickers hardness (HV) (HRC 66) at the water-quenched end (martensite microstructure) to 200 HV (HRA 56) at the upper end of the sample (ferrite and pearlite microstructure). Deviations in the chemical composition can be taken into account in the form hardenability bands that describe the upper and lower limits of the measured hardness values as shown in Figure 5.23.

*Dr. Widmannstätten investigated the structure of parts of a meteor fell in Czechien in 1808. The friction of air in the atmosphere caused extreme overheating of the alloy; the quenching was done by the marshy ground.

9.2.2 Influence of Carbon Concentration

The hardness of steels increases with the concentration of carbon dissolved in austenite before quenching, as shown in Figure 9.4a. The increase of hardness is caused by the increasing dislocation density and distortion of the body-centered martensite lattice due to the inserted carbon atoms. If the carbon concentration exceeds approximately 0.5 wt%, the hardness increases only slightly [7] because the extremely high distortion of the formed martensite hinders further transformation of austenite; the temperature for completing the martensite formation M_f falls below the room temperature (Figure 9.4b), and increasing amounts of retained austenite remain in the martensite structure with increasing content of dissolved carbon (Figure 9.4c) [8]. Compared to martensite, retained austenite possesses a very low yield strength and hardness and is so unstable that it immediately transforms to martensite or bainite if energy is induced in the structure during the application. The volume expansions that accompany this transformation process cause changes of shape and size and can result in cracks that damage the workpieces. The volume expansion of rollers in bearings during the rolling motion, for example, can burst the ball races. Moreover, with rising carbon content, the toughness of martensite decreases with high local stresses because of the carbon supersaturation. The consequence is that unalloyed steels with carbon concentrations higher than 0.5 wt% are used only after tempering. Tempering reduces the volume fraction of the retained austenite and releases the tension of martensite by reducing the dislocation density and carbon supersaturation by precipitation. In addition, tempering leads to a reduction of quenching stresses.

9.2.3 Influence of Alloying Elements

As described in the previous section, the concentration of carbon dissolved in austenite before quenching has a great effect on hardness and strength. While carbon is placed at interstitial locations in the iron lattice, alloying elements are dissolved at the original lattice sites. The additional warping of the iron lattice due to the alloying elements causes only a slight increase in hardness but strongly affects the mobility of carbon, which results in a drastically reduced transformation rate. This influence can be used to produce steels whose transformation characteristics are adapted to the desired microstructure and to the geometry of the parts to be quenched.

The influence of alloying elements at the beginning and at the end of austenite transformation with regard to transformation time and temperature is graphically described in Figure 9.5 for the alloying element chromium. Figure 9.5a through Figure 9.5c represents CCT diagrams of three different steels with similar carbon content and increasing chromium content [5]. For the unalloyed 1040 steel, the incubation period of beginning austenite transformation is very short. Fully martensitic structures can be achieved only for very fast quenching rates with suppressed transformation in the pearlite and bainite range. The incubation period of the subcooled austenite drastically rises with increasing chromium concentration, as illustrated by Figure 9.5b and Figure 9.5c. In the unalloyed 1040 steel, a low cooling rate, according to a cooling curve that crosses the temperature of 500°C (932°F) at a time of about 300 s, produces a structure consisting only of ferrite and pearlite (Figure 9.5a). After quenching at the same cooling rate, the austenite of the low-alloy 5140 steel transforms to mainly bainite and martensite and small amounts of ferrite and pearlite (Figure 9.5b). After the same cooling, bainite and martensite are formed in the high-alloy DIN 45CrMoV67 steel (Figure 9.5c).

To illustrate the effect of a reduced transformation rate on the hardenability of steels, Figure 9.6 shows the measured hardness distributions over the cylindrical cross-section of a

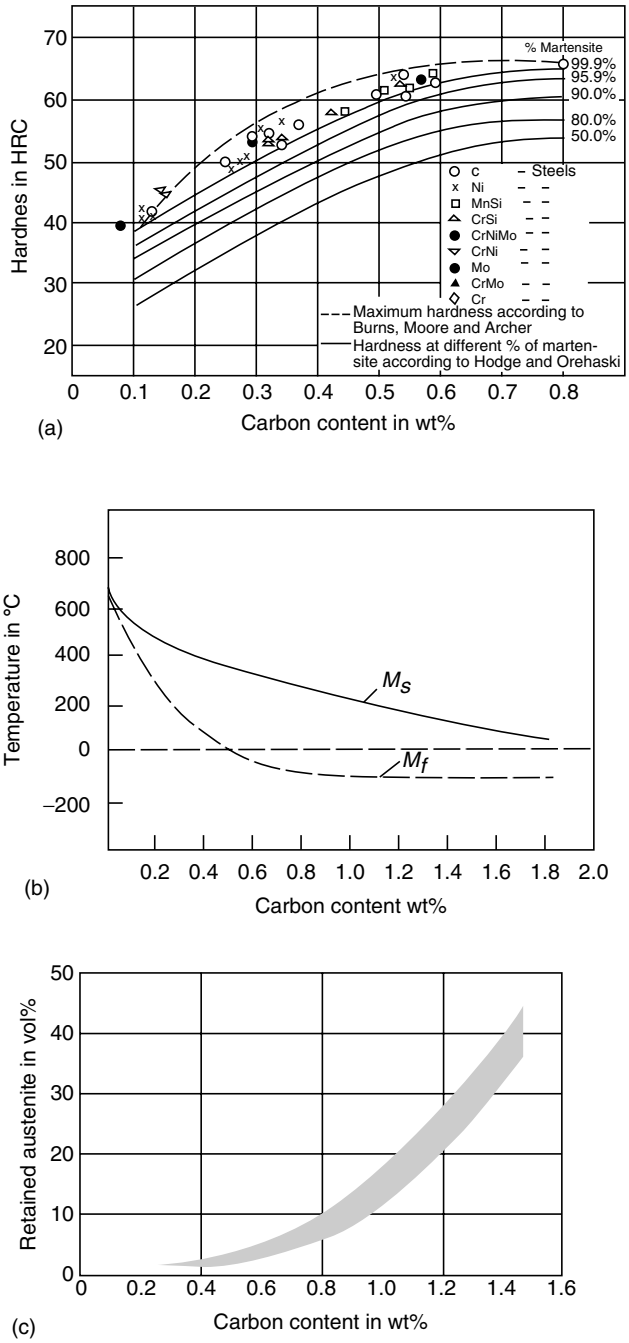

FIGURE 9.4 Effect of carbon concentration on (a) hardness for structures with different martensite content; (b) temperature for starting and completing the martensite formation M_s and M_f; (c) retained austenite.

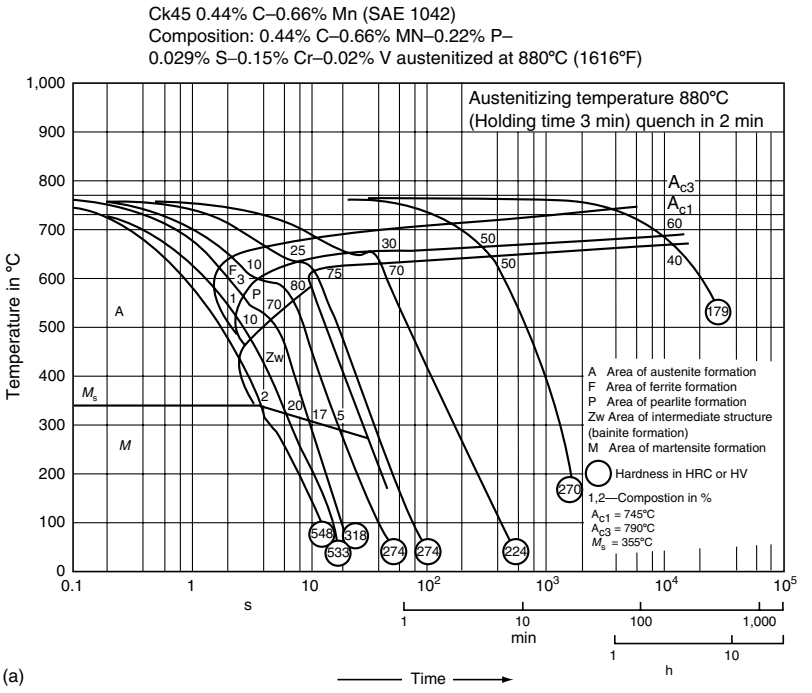

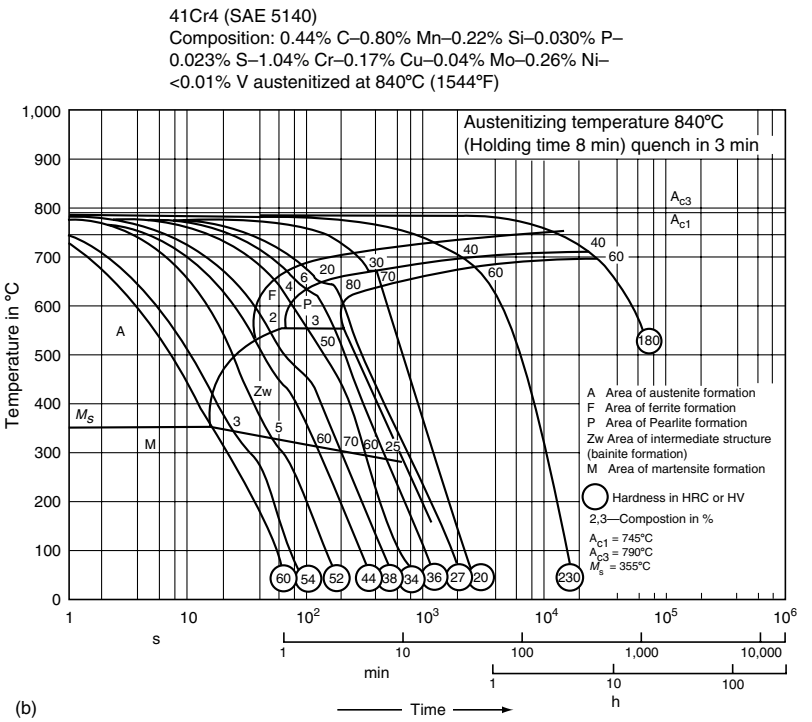

FIGURE 9.5 Influence of allowing elements, here chromium, on the transformation of subcooled austenite described according to CCT diagrams of (a) a 1040 steel with about 0.15 wt% Cr (German grade Ck 45) and (b) a 5140 steel with about 1 wt% Cr (German grade 41 Cr 4), and

Continued

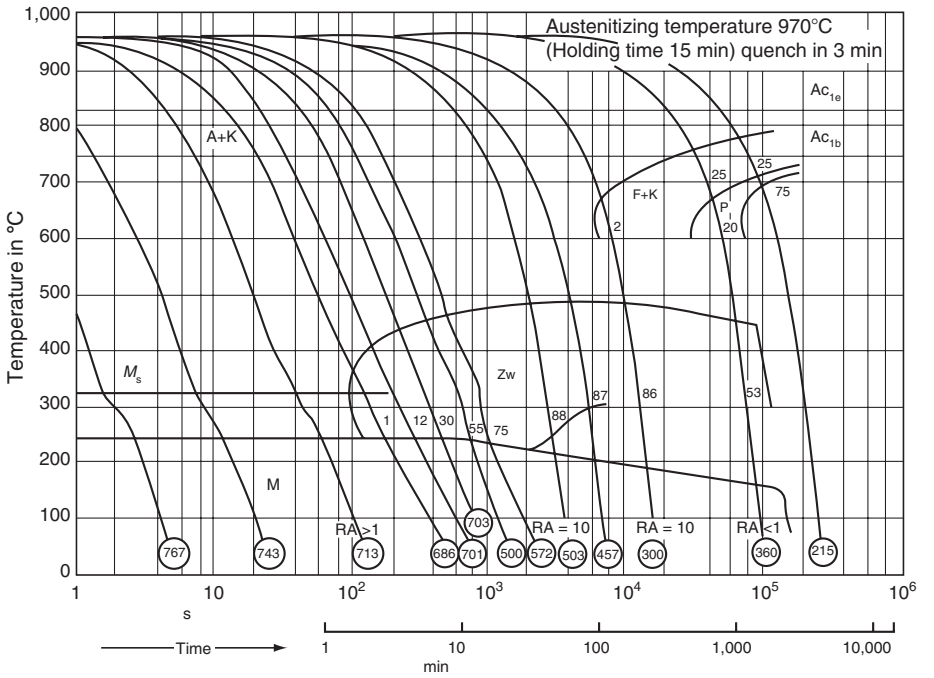

A + K	Area for austenite and carbides
K	Area for carbide formation
P	Area for pearlite formation
Q	Hardness in HV
Zw	Area for intermediate structure (bainite formation)
M	Area for martensite formation
RA	Residual austenite
F	Area for ferrite formation
F + K	Area for nonlamellar eutectoids
Z	Cementite
10Z	10% cementite
1; 2 . . .	(refers to numbers on curves) proportion of structure formed, in percent

Ac_{1b} = 745°C
Ac_{1e} = 830°C
M_s = 325°C

(c)

FIGURE 9.5 (Continued) (c) a steel with about 1.5 wt% Cr and 0.7 wt% Mo (German grade 45CrMoV67).

1040 and a 5140 steel for two sample diameters (15 and 40 mm) after identical quenching in water. With the smaller diameter of 15 mm and the unalloyed 1040 steel, the hardness decreases from about 850 HV (HRC 66) at the surface (martensite microstructure) down to 500 HV (HRC 49) in the core (ferrite, pearlite, bainite, and martensite microstructure). In contrast, the hardness of the 5140 steel is constant over the cylindrical cross-section because the martensitic transformation in the sample volume is due to the longer incubation period of the subcooled austenite. As the cooling rate dramatically decreases with increased section thickness, the cooling rate in the core of the larger diameter is limited by the rate of heat conduction from the interior to the surface. The consequence is that for the 40-mm diameter 1040 steel, austenite transforms only to ferrite and pearlite in the inner regions because of the reduced cooling rate. Compared to the 15-mm diameter, this results in a decreased hardness in the core; hardness values of about 220 HV (HRA 57) nearly correspond to the initial hardness of the steel. Martensitic hardening occurs only in a thin outer shell of the cylindrical sample (Figure 9.6b). The higher carbon concentration of about 1 wt% in the 5140 steel clearly delays the transformation in the pearlite and bainite

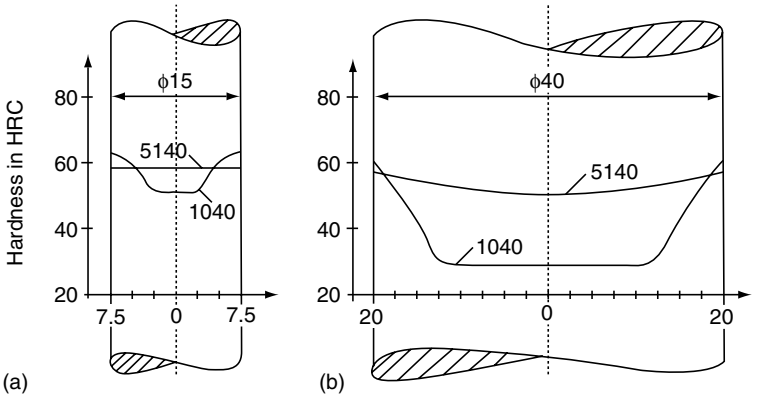

FIGURE 9.6 Influence of alloying elements on hardness distribution over the cross-section of cylindrical samples with a diameter of (a) 15 mm and (b) 40 mm, described for a 1040 steel and a 5140 steel. The samples were quenched in water at 30°C and an agitation rate of 0.3 m/s.

range and results in only a slight decrease in hardness with increasing distance from the cylinder surface.

9.2.4 Influence of Stresses

The internal stresses formed during quenching have a decisive influence on the transformation behavior of austenite as already described in Figure 9.1. Depending on the chemical composition and the cooling rate, austenite can transform in the pearlite, bainite, or martensite range. All these phase transformations are accompanied by volume expansion. The change of length during slow and rapid cooling of unstressed and tensile stressed austenite is shown in Figure 9.7. After cooling austenite at a very slow cooling rate, close to the equilibrium, ferrite and pearlite are formed in the temperature range between A_{r3} and A_{r1} temperatures (continuous line). With fast cooling rates (dashed lines), the diffusion-controlled transformations are suppressed, and below the martensite start temperature, M_s, the unstressed austenite transforms into martensite with an increase in specific volume. If tensile stresses occur within the sample, the martensite start temperature increases from M_s to M_s' and larger changes of length occur [9]. The opposite is true for compressive stresses. This phenomenon is called transformation plasticity.

The volume changes of the ferritic–pearlitic transformation as well as those of the martensitic transformation are due to the transformation of the face-centered cubic austenite crystal lattice into the body-centered cubic ferrite lattice or the tetragonal-deformed martensite lattice. The ferritic and martensitic crystal lattices have a higher specific volume.

According to Kobasko [10], with increasing cooling rate within the martensitic transformation range, the probability of quench crack formation increases to a maximum value and then decreases to zero. This phenomenon can be explained by transformation plasticity and the change of specific volume during phase transformation. The higher the cooling rate, and thus the temperature gradient, the greater the surface layer expansion at the moment of superplasticity. During very fast cooling (“intensive quenching”), the surface layer compresses and tensile stresses occur because of the heated and expanded core. At room temperature, high compressive stresses arise at the surface of the part. In this way martensitic hardening of large parts made of unalloyed steels, e.g., a lorry axis, is possible.

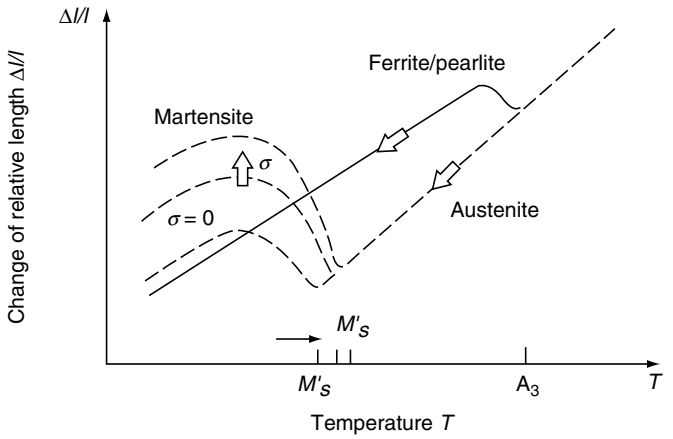

FIGURE 9.7 Effect of tensile stresses on the change of relative length during very fast cooling compared to a slow cooling rate, shown schematically.

9.3 QUENCHING PROCESSES

Previously it was shown that the cooling rate and the shape of the cooling curve influence the course of phase transformations, residual stresses and distortion. In quench hardening, fast cooling rates, depending on the chemical composition of the steel and its section size, are frequently applied to prevent diffusion-controlled transformations in the pearlite range and to obtain a structure consisting mainly of martensite and bainite. However, the reduction of undesirable thermal and transformational stresses due to volume changes usually requires slower cooling rates. Quenching processes therefore require the selection of cooling rates that are fast enough to permit the desired microstructure to form but slow enough to minimize residual stresses and distortion. These considerations have resulted in different quenching methods such as direct quenching, interrupted quenching, spray quenching, and gas and fog quenching. The time–temperature cycles that can be obtained with different quenching methods are shown in Figure 9.8 for the center and surface of the quenched part together with the time–temperature–transformation diagram [5].

Direct quenching, the most common quenching technique, refers to the quenching of the part from the austenitizing temperature directly to room temperature by immersion into a vaporizable liquid quenchant (Figure 9.8a). Petroleum solutions or aqueous polymer solutions are often used for this process.

Interrupted quenching consists of rapidly quenching steel from the austenitizing temperature to a temperature above the M_s temperature, where it is held for a time sufficient to affect the desired transformation and then cooled in air. Interrupted quenching comprises three different quenching techniques—marquenching, austempering, and isothermal annealing—which differ in the temperature at which quenching is interrupted and the time for which the steel is held at this temperature. The quenchants usually used for interrupted quenching are molten salt baths and specialty oils such as martempering oils.

Marquenching consists in rapidly quenching the steel to a temperature just above the M_s temperature, holding it at this temperature to equalize the temperature throughout the workpiece, and then removing it from the bath before transformation into bainite begins (Figure 9.8b). The martensite structure formed during marquenching is the same as after direct quenching; however, residual stresses are minimized owing to the more homogeneous temperature distribution throughout the part and slower cooling rate during martensite formation.

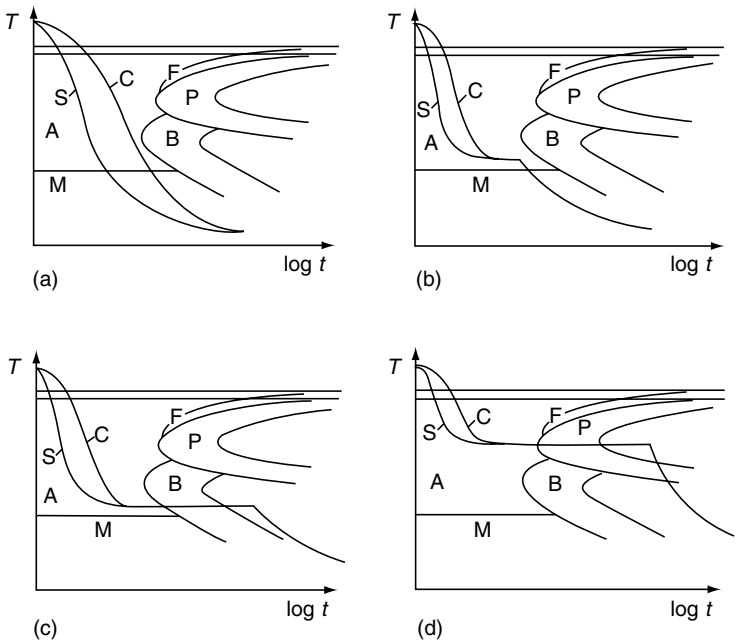

FIGURE 9.8 Cooling curves for the center and the surface of quenched parts for different quenching methods correlated to a time–temperature transformation schematic diagram. (a) Direct quenching; (b) marquenching; (c) austempering; (d) isothermal annealing or pearlitizing.

Austempering is similar to marquenching in that the steel is rapidly quenched from the austenitizing temperature to a temperature above M_s but differs in that the workpiece is held at temperature for sufficient time to allow an isothermal transformation into bainite (Figure 9.8d). Relative to untempered martensite, bainite has better toughness and strength than would be formed by marquenching. Martensite formed during direct quenching and marquenching is often tempered, because tempered martensite exhibits a more homogeneous elemental distribution and improved toughness and strength.

Isothermal annealing, differs from marquenching and austempering in that the bath temperature is sufficiently high that isothermal transformation into pearlite occurs (Figure 9.8d). Pearlite exhibits high toughness and sufficient strength to be the optimal structure for parts such as wires or cables and railroad rails.

Spray quenching with a liquid quenchant, generally water or an aqueous polymer solution, at sufficiently high pressures on the surface of the workpiece produces fast cooling rates because the liquid droplets impact the surface and cause a high rate of heat transfer. The rate of heat extraction can be varied over a wide range by varying the quantity of the sprayed liquid or by spraying a mixture of water and air (fog quenching). Compared to immersion quenching, spray quenching allows better control in cooling the workpiece.

In gas quenching, heat removal is achieved by blowing a stream of gas over the workpiece, sometimes after austenitizing it in a vacuum furnace. Usually, the cooling rate is faster than that obtained in still air but slower than that achieved in oil and is controlled by the type, pressure, and velocity of the cooling gas. Inert gases including helium, argon, and nitrogen are most commonly used.

9.4 WETTING KINEMATICS

During quenching in liquid media with boiling temperatures far below the initial temperature of the body, three stages of heat removal occur. These are referred to as (1) the film boiling or vapor blanket stage, (2) the nucleate boiling stage, and (3) the convection stage.

In the film-boiling stage the surface temperature of the workpiece is sufficiently high to vaporize the quenching liquid and form a stable film around the part. The vapor film has an insulating effect; therefore the cooling rate during film boiling is relatively slow. The temperature above which the stable vapor blanket occurs is called the Leidenfrost temperature after Johann Gottlieb Leidenfrost.

When surface temperature is less than the Leidenfrost temperature, the vapor film collapses and the nucleate boiling begins [11]. In this stage, the liquid in contact with the hot surface evaporates, and immediately the vapor bubbles leave the surface. This causes strong convection, which results in a high rate of heat transfer from the metal to the fluid.

Upon further cooling, the surface temperature becomes less than the boiling point of the liquid, and the surface is permanently wetted by the fluid. The cooling rate is low and determined mainly by the rate of convection and the viscosity of the liquid quenchant.

Some typical examples of the wetting sequences on steel and silver samples quenched in water, oil, and aqueous polymer solutions are depicted in Figure 9.9 through Figure 9.12. Quenching in water and oil usually results in slow wetting with a clearly visible wetting front. Figure 9.9 and Figure 9.10 show two wetting processes that were observed during quenching of a cylindrical CrNi steel specimen in water at 30°C (86°F) and oil at 60°C (140°F) with an agitation rate of 0.3 m/s [12,13]. Wetting begins at the lower edge of the sample and the wetting front, which is the interface between film boiling and nucleate boiling, and then ascends to the top in an almost annular manner. An additional descending wetting front can be observed from the upper edge that is more characteristic of quenching in oil. The time required for completely wetting the sample is about 14 s for the water quench and about 13 s for the oil quench. Thus, the three phases of cooling, with their widely varying heat transfer coefficients, are simultaneously present on the sample surface and the cooling of the part is inherently nonuniform.

When quenching of prismatic cylinders, the wetting front is parabolically shaped as shown in Figure 9.11 [14,15]. The wetting along the cylinder edges accelerates the wetting front of the flanks and reduces the time interval of simultaneous presence of film boiling and nucleate boiling.

The wetting process can be strongly influenced by the addition of additives [12,14–18]. Figure 9.10a and Figure 9.10b show two wetting sequences that were obtained in water with different chemical admixtures. On the surface of the sample, a polymer film forms that provides a uniform breakdown of the vapor blanket and reduces heat transfer in the lower temperature range. When the polymer film has completely redissolved, heat transfer is achieved entirely by convection.

The velocity of the spreading wetting front and the time interval of the simultaneous presence of film boiling and nucleate boiling can be strongly influenced by changing the physical properties of the quenchant and the sample. The items varied are:

1. Type of quenchant as described by its boiling temperature, viscosity, thermal capacity, and surface tension
2. Additives to the quenchant, and their concentration
3. Temperature and agitation rate of the quenchant
4. Thermal characteristics of the body and its transformation behavior

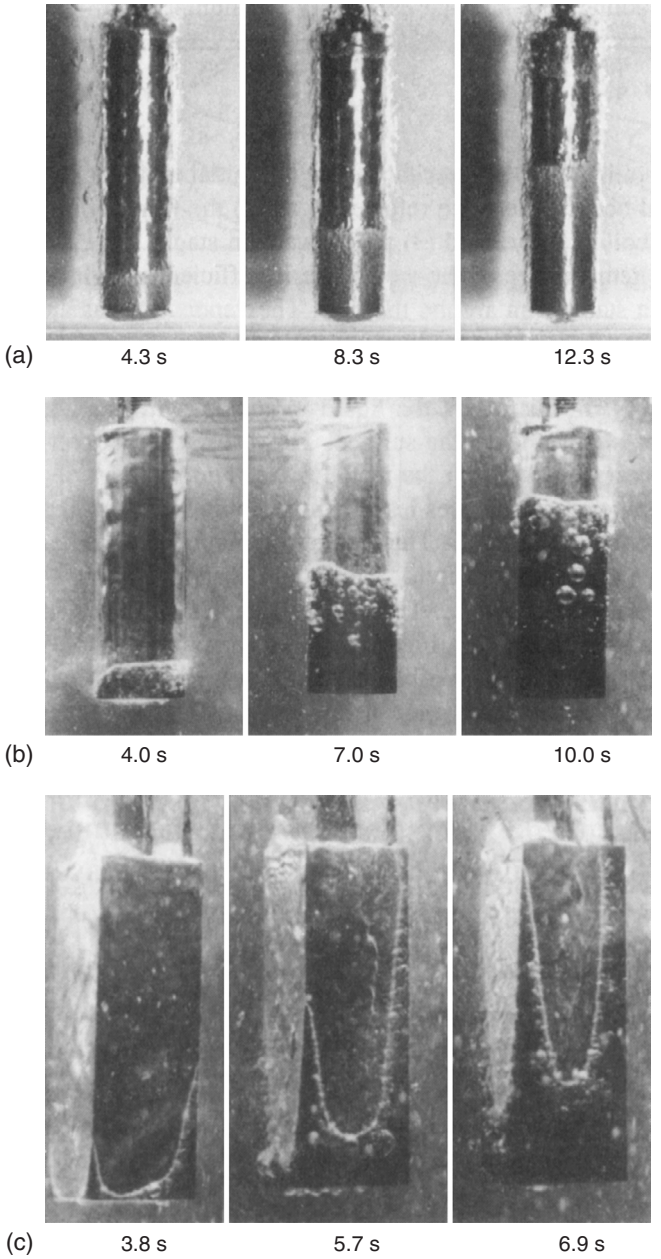

FIGURE 9.9 Wetting process on the surface of CrNi steel specimens quenched from 850°C into water and oil. (a) Cylinder (25-mm diameter × 100 mm) in water at 30°C flowing at 0.3 m/s; (b) cylinder (25-mm diameter × 100 mm) in oil at 60°C flowing at 0.3 m/s; (c) prismatic cylinder (15 × 15 × 45 mm) in water at 60°C without forced convection.

5. Surface roughness of the body and surface layers
6. Geometry and initial temperature distribution of the sample

An overview of the effect that varying these properties has on the wetting kinematics is extensively described in Ref. [19]. The influence of some selected properties on the time when

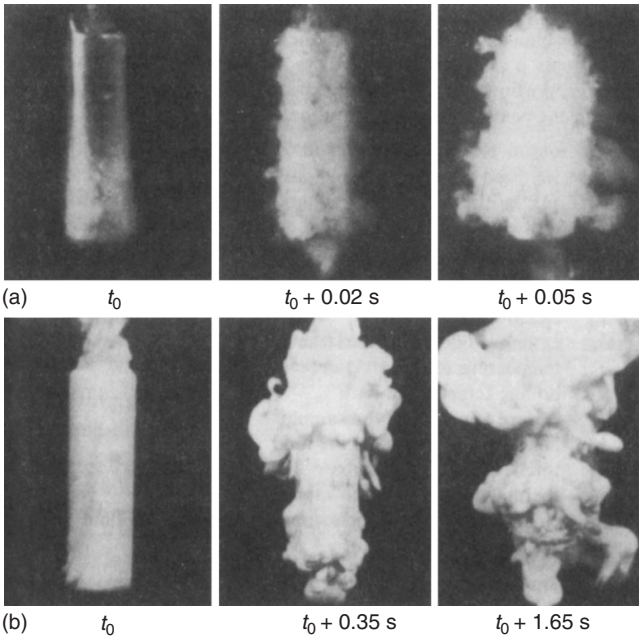

FIGURE 9.10 Wetting process on the surface of cylindrical samples which is quenched in water with different admixtures. (a) CrNi steel cylinder (25-mm diameter × 100 mm) quenched in 5% aqueous polymer solution at 30°C without forced convection and (b) silver cylinder (15-mm diameter × 45 mm) quenched in a 10% aqueous polymer solution with a chemical additive at 25°C without forced convection.

wetting starts t_s, the time when wetting is finished t_f, the time interval of wetting $\Delta t_w = t_f - t_s$, and the heat transfer coefficient α is summarized in Table 9.1.

The great importance of the wetting kinematics for steel hardening can be explained with respect to the wetting process and the corresponding surface hardness along the length of a cylinder of the 1040 steel, which is quenched in water with different agitation rates (Figure 9.11 and Figure 9.12). Agitation increases the wetting speed and reduces the time during which the different cooling phases are simultaneously present. In Figure 9.11 the finishing time of wetting is reduced from 9 to 2.5 s by agitation at 1 m/s. Considering that the heat transfer from the surface to the fluid dramatically increases at the transition from film boiling to nucleate boiling (see Figure 9.22), it becomes apparent that a change of the wetting process has a significant effect on the cooling behavior and hardness distribution. Figure 9.12 compares the hardness profile and the wetting time related to the distance z from the sample bottom for cooling in still and agitated water [20]. The wetting time t_k increases toward the top of the sample in accordance with the migration of the wetting front (see Figure 9.12). With increasing wetting time, a decrease of surface and core hardness becomes apparent for the still-water quench. With water agitated at 1 m/s, the wetting front proceeds to the top in approximately 2 s, resulting in a constant hardness along the cylinder length. Other examples of the effect of wetting kinematics on steel hardening are given in Refs. [12,15,21,22].

9.5 DETERMINATION OF COOLING CHARACTERISTICS

9.5.1 Acquisition of Cooling Curves with Thermocouples

The most common way to describe the complex mechanism of quenching is to use cooling curves. In almost all the heat treatment processes, cooling curves are measured with metal test

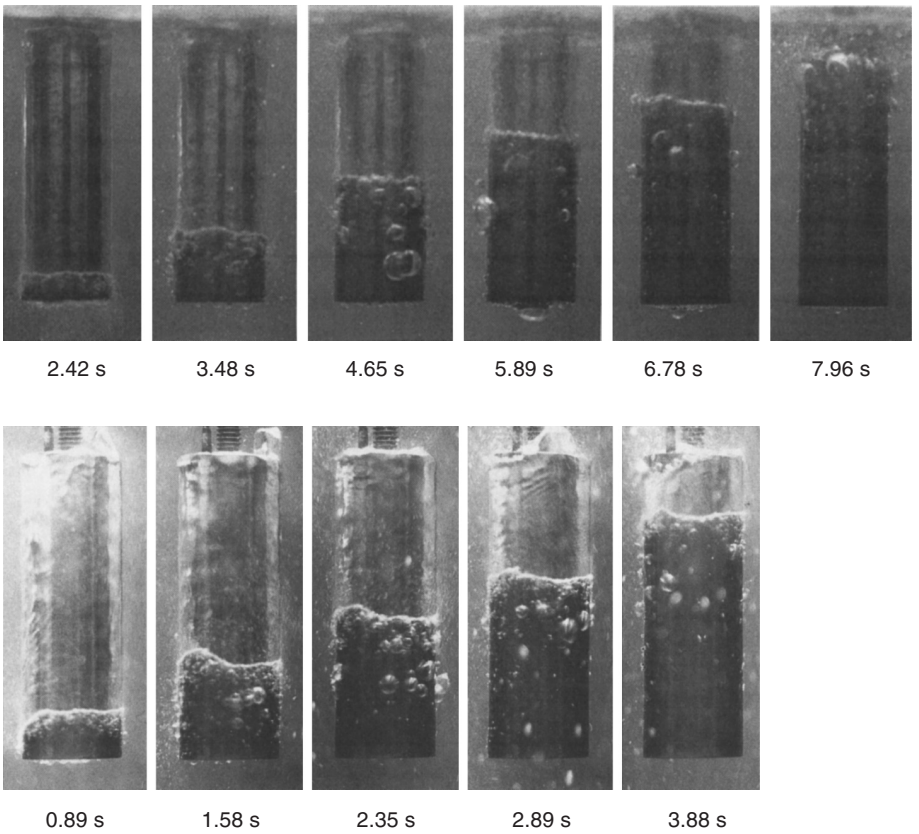

FIGURE 9.11 Wetting process on the surface of a 1040 steel (15-mm diameter × 45 mm) quenched from 850°C in water at 50°C (a) without forced convection and (b) with an agitation rate of 1 m/s.

pieces (probes) instrumented with thermocouples [23]. A thermocouple consists of two metallic wires of different chemical composition that are brought into contact at their ends and usually the wires are welded. When this assembly is connected to a measurement apparatus and the two metal junctions have different temperatures, a voltage can be measured

TABLE 9.1
Influence of Some Physical Properties of the Fluid and the Body on the Characteristics Data of Wetting and the Heat Transfer Coefficient for Immersion Quenching

Properties of the Fluid	t_s, t_f	Δt_w	α
Type of quenchant	↑↓	↑↓	↑↓
Additives to the fluid	↑↓	↑↓	↑↓
Rate of agitation v (↑)	↓	↓	↑
Bath temperature T_b (↑)	↑	↑	↓
Properties of the Sample			
Thermal diffusivity a (↑)	↑	↑	↑
Sample diameter (↑)	↑	↑	
Surface roughness (↑)	↓	↓	↑
Surface oxidation (↑)	↓	↓	↓

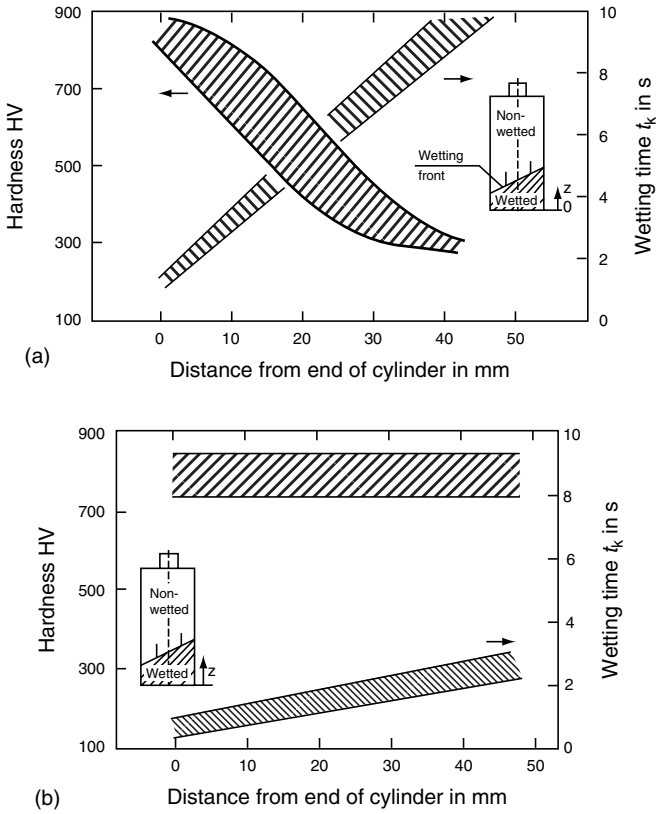

FIGURE 9.12 Wetting time t_b and surface hardness HV 2 along the length of a cylindrical 1040 steel (15-mm diameter × 45 mm) which is quenched in water of 50°C (a) without forced convection and (b) with an agitation rate of 1 m/s.

that is independent of the absolute temperature but dependent on the temperature difference between the two ends of the thermocouple. Therefore, one end, called the cold junction or reference junction, is immersed in melting ice at the constant reference temperature of 0°C (32°F). The temperature at the other end, called the hot or measuring junction, can then be determined. In practice, instead of melting ice, electronic temperature compensation is used.

For many applications, especially very fast cooling processes, it is important to identify the exact response time of the thermocouples. Response time is primarily a function of the thermocouple dimension and its construction, thermal properties of the thermocouple materials, the method of installation, and heat exchange conditions within the surrounding metal.

Commercial thermocouples consist of two thermoelectric wires, insulation material, and a surrounding sheath that protects the thermoelectric couple against high-temperature corrosion and oxidation (Figure 9.13). The most common type of hot junction is the insulated version (Figure 9.13a). Despite the delayed heat conductance due to the electrical insulation of the hot junction, a short response time can be achieved by choosing small diameters down to 0.25 mm. Figure 9.14 compares the response time of two sheathed thermocouples with outside diameters of 0.5 and 1.0 mm [24]. The thermocouples were installed into the test piece as shown in Figure 9.13a. For exactly the same quenching process, the maximum cooling rate and the temperature–time gradient are significantly greater for the smaller dimension. The

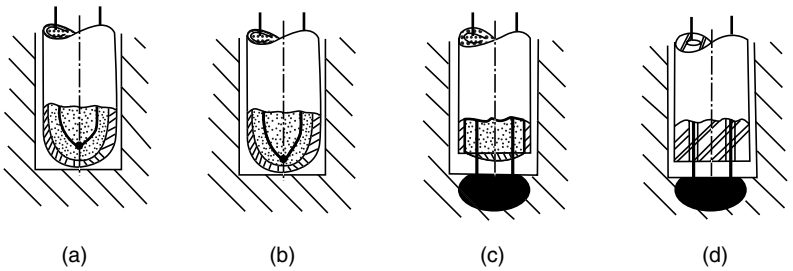

FIGURE 9.13 Construction of different thermocouples. (a) Mantle-sheathed thermocouple with insulated hot junction; (b) mantle-sheathed thermocouple with sheath-welded hot junction; (c) mantle-sheathed thermocouple with open sheath and thermoelectric wires are welded to the sample material; (d) thermocouple in which the thermoelectric wires are welded to the sample material and insulated with a ceramic tube.

response time can also be slightly reduced by welding the hot-junction wires to the metal sheath (Figure 9.13b) provided the samples do not contain an electric charge that can influence the measuring process.

An elegant method to determine the true change of temperature during quenching is shown in Figure 9.13c and Figure 9.13d. In Figure 9.13c, the metal sheath of the thermocouple is opened and the thermoelectric wires are welded to the sample material. The advantage of this assembly is that the response time is minimized and the integral temperature of the crosshatched region is measured. An error in the thermoelectric voltage may be due to the sample volume, which is not known.

Figure 9.13d describes a similar thermocouple assembly where the hot-junction wires are insulated with a ceramic tube. As the thermophysical properties of ceramics and steels differ, this thermocouple construction may produce significant errors in temperature measurement.

When measuring cooling curves, it is important to minimize the amount of material removed from the workpiece when drilling a hole for thermocouple placement. The cooling behavior of a part, especially a part with a small cross-section, changes dramatically with increased hole diameter. Therefore, all investigations concerning the cooling behavior of

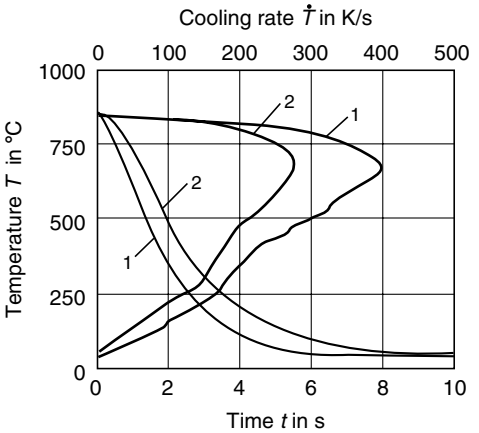

FIGURE 9.14 Response sensitivity of mantle-sheathed thermocouples with different outer diameters. The temperature–time cycles were measured in the center of a cylindrical CrNi steel sample of 8-mm diameter during spraying with water of room temperature: 1, 0.5-mm diameter; 2, 1.0-mm diameter.

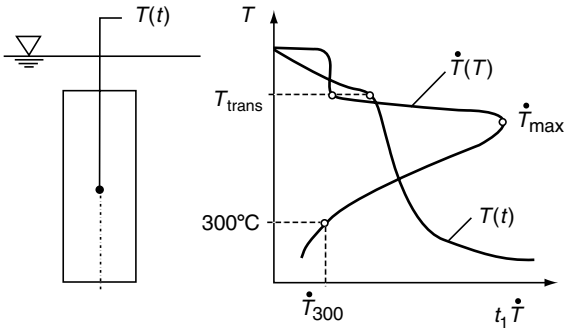

FIGURE 9.15 Determination of cooling characteristics by measuring temperature–time and temperature–cooling rate curves (schematic).

workpieces with respect to temperature measurement require good thermocouple-to-specimen contact and minimal thermocouple diameter and material removal.

Cooling curves are usually obtained by quenching a test probe and measuring the temperature as a function of time at a specified point within the specimen. From the temperature–time curve, a temperature–cooling rate curve can be calculated. The test probes may be cylinders, plates, and spheres. The most common test probe is a cylinder with a length three to four times its diameter and with a thermocouple located at its geometric center (see diagram at left of Figure 9.15) [25,26].

There are various national and international standards for cooling curve analysis. The most common are: ASTM D6200 (based on ISO 9950) for unagitated quenchants and ASTM D6482 and D6549 for agitated quenchants.

Two characteristic parameters that can be obtained from cooling curves are the maximum cooling $\dot{T}_{max}$ and the cooling rate at 300°C (572°F) ($\dot{T}_{300°C}$). When hardening the steel, the maximum cooling rate and the temperature at which it occurs must be sufficiently high to minimize ferrite and pearlite transformation. The cooling rate of 300°C (572°F) can be used to indicate the probability of distortion and cracking because it is near the martensite temperature of most carbon and low-alloy steels.

The main limitation of cooling curve analysis is that relatively little information can be derived about the wetting process. The temperature in the sample center at the transition point from lower to higher cooling velocity (the so-called transition temperature, T_{trans}) only describes the wetting of the corresponding surface point and gives no information about the time when wetting starts (t_s) and the time when wetting is finished (t_f) (Figure 9.16).

Figure 9.16a compares the cooling curves that were measured in the center of a cylindrical CrNi steel sample (25-mm diameter × 100 mm), which is quenched in water and a 10% aqueous polymer solution [27,28]. The bath temperature is 30°C (86°F), and the rate of agitation is 0.3 m/s. Though the sample center cools in almost the same way, the process of wetting differs considerably, as evidenced by the near-surface temperatures measured at three heights of the sample (Figure 9.16b). Quenching in water causes a slow wetting with a total wetting time of about 14 s. Wetting begins at the lower edge of the sample, and the wetting front ascends to the upper edge. This results in high localized temperature differences (continuous lines in Figure 9.16b).

When the sample is quenched in the polymer solution, explosive wetting occurs after 6 s of stable film boiling. The temperature–time curves for the three locations near the same surface are almost congruent (dashed lines in Figure 9.16b). As the wetting process controls the temperature distribution in the quenched part, it directly influences the hardness distribution. Whereas the slowly wetted sample will have a characteristic axial hardness gradient, similar

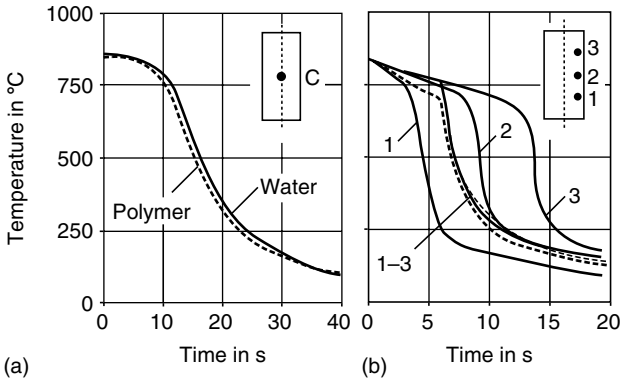

FIGURE 9.16 Comparison of cooling curves measured at different points in a cylindrical CrNi steel sample (25-mm diameter × 100 mm) during slow wetting (water) and during sudden wetting (10% aqueous polymer solution). Points of measurement: (a) center and (b) close to the specimen surface at three heights.

hardness values along a centerline can be expected in the suddenly wetted sample (with the exception of a small range near the ends). This explains why low concentrations of a polymer quenchant may be added to water to eliminate or significantly reduce cracking or distortion.

9.5.2 Measurement of Wetting Kinematics

9.5.2.1 Conductance Measurement

A method better suited for determining the wetting process is to measure the electrical conductance between the sample and the quenchant and between the sample and a counter electrode and measure the temperature change at the specimen center [21,29,30] (Figure 9.17a). When a vapor blanket forms around the entire sample surface, the conductance between the sample and the counter-electrode is low. When the vapor blanket collapses at

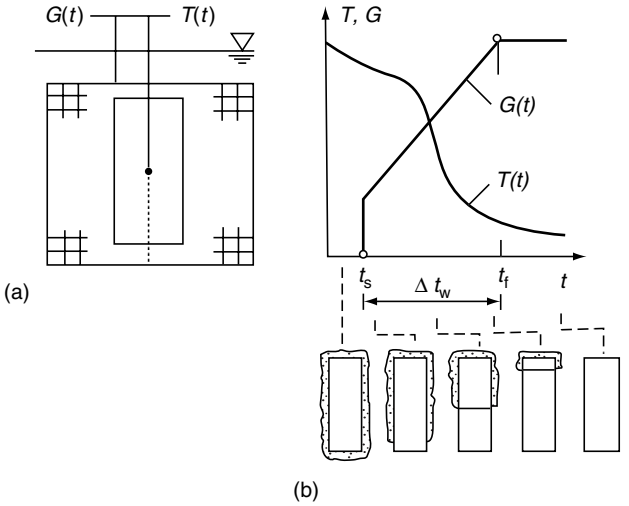

FIGURE 9.17 Determination of the percentage of the wetted surface area. (a) Measuring principle and (b) temperature–time $T(t)$ and conductance–time $G(t)$ curves with corresponding wetting state of the quenched sample (schematic).

an arbitrary position on the sample surface, conductance increases (Figure 9.17b). The increase in conductance is approximately proportional to the wetted portion of the sample surface. Conductance is at its highest value when the surface is completely wetted. (Note that the formation of bubbles after wetting can reduce conductance. This may result in a failure to identify the end of wetting.) The main parameters provided from conductance–time curves are the time when wetting starts (t_s) and the time when wetting is finished (t_f).

In Figure 9.18a, wetting starts at time t_s, and is completed at time t_f (usually for quenching in water, oil, and some aqueous polymer solutions; see Figure 9.9 through Figure 9.11). In Figure 9.18b, the transition from film boiling to nucleate boiling is explosive (see Figure 9.10). In Figure 9.18c, the wetting time is also infinitely short, but bubbles or polymer separations remain on the surface, which reduces conductance. In Figure 9.18d, sudden wetting occurs, but immediately a new vapor blanket forms, then collapses again. This sequence may be repeated several times [13].

9.5.2.2 Temperature Measurement

A second method to ascertain the wetting process is by inserting thermocouples in near-surface positions along the cylindrical sample [31]. Figure 9.19 shows the basic information that can be derived from the near-surface cooling curves when a wetting front migrates from the lower end of the sample to its top. Each temperature cycle defines a period of slow cooling and a subsequent period of fast cooling. The point of transition indicates the transition from

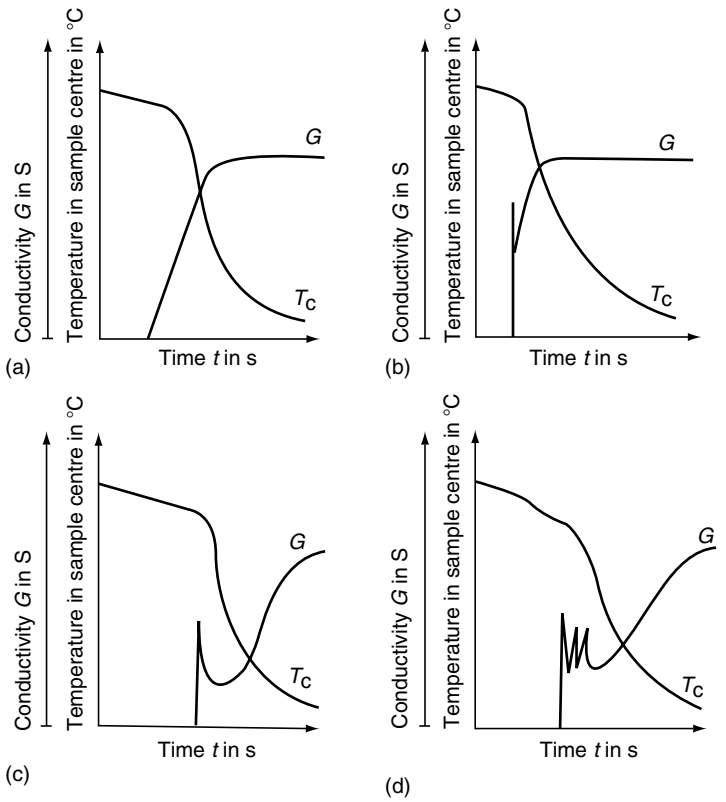

FIGURE 9.18 Schematic temperature–time and conductance–time curves for different wetting processes. (a) Slow wetting; (b) explosive wetting; (c) explosive wetting with large bubbles remaining on the surface; (d) repeatedly explosive wetting with large bubbles remaining on the surface.

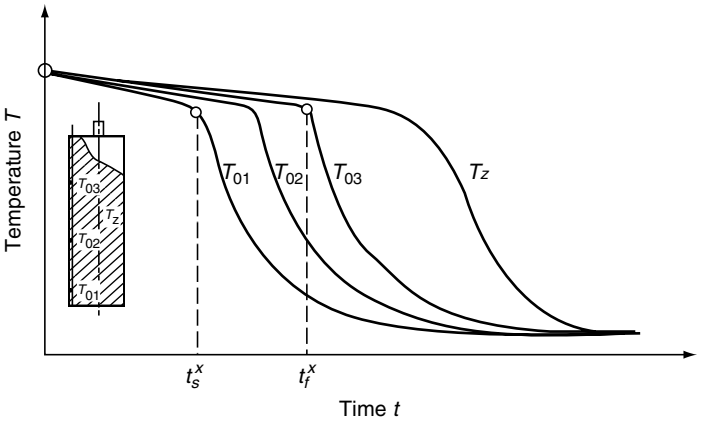

FIGURE 9.19 Determination of wetting kinematics by means of three thermocouples close to the sample surface.

film boiling to nucleate boiling at the thermocouple location. The onset and conclusion of wetting, and thus the velocity of the wetting edge, can be calculated by extrapolating the local transition times to the front ends of the sample. The cooling curves in Figure 9.19 were obtained during quenching of a CrNi steel cylinder (15-mm diameter × 100 mm) in water at 50°C (120°F) without forced convection.

9.6 QUENCHING AS A HEAT TRANSFER PROBLEM

9.6.1 Heat Transfer in a Solid

When a part is heated to a specified temperature, heat is transferred to it by the furnace. Conversely, when the part is quenched, heat is transferred to the surrounding medium. This produces localized temperature gradients where there is conductive heat transfer from the higher temperature region to the lower temperature region. The heat transfer rate per unit area is proportional to the local temperature gradient and can be expressed by Fourier's law of heat transfer,

$$Q = -\lambda A \frac{\delta T}{\delta x} \tag{9.1}$$

where Q is the heat transfer rate in J/s, λ is the thermal conductivity in J/(s m K), A is the unit area in m^2, T is the temperature in K, and x is a local coordinate. The minus sign is inserted because the heat flows from higher to lower temperature areas according to the second law of thermodynamics.

Heat transfer in a solid where temperature changes with time and no heat sources are present within the body is

$$\frac{\partial T}{\partial t} = a\left(\frac{\delta^2 T}{\delta x^2} + \frac{\delta^2 T}{\delta y^2} + \frac{\delta^2 T}{\delta z^2}\right) \tag{9.2}$$

where t is the time in s, a is the thermal diffusivity in m^2/s, and x, y, and z are local coordinates. According to Equation 9.2 the temperature distribution within a body depends

not only on the local temperature gradients but also on the thermal diffusivity, which includes all thermodynamic parameters of the material. The thermal diffusivity a is defined as

$$a = \frac{\lambda}{\rho C_p} \tag{9.3}$$

where ρ is the density in kg/m^3 and C_p is the specific heat capacity under constant pressure in J/(kg K). The larger the value of a, the more quickly heat will diffuse through the material. A high value of a can be achieved by either high thermal conductivity λ or low-heat capacity ρC_p, which means that less of the heat moving through the material is absorbed which will increases the temperature of the material. This fact is illustrated by faster cooling of silver relative to austenitic steels. In the simple form of the Fourier equation (Equation 9.2), thermal diffusivity is assumed to be constant, but in reality λ, ρ, and C_p, and therefore a, are temperature dependant.

The heat capacity ρC_p of steel does not vary considerably with the chemical composition. However, the thermal conductivity (λ) of iron alloys does vary with temperature as illustrated in Figure 9.20 [26]. At room temperature, the value of λ is drastically reduced with increasing carbon content and to a lesser extent with the content of other alloying elements. The decrease of λ is caused by the distortion of the iron lattice due to insertion of foreign atoms. The thermal conductivities of pure iron, plain carbon steel with 0.45% carbon (1045 steel), and an austenitized (CrNi) stainless steel are 75, 55, and 1415 W/(m K), respectively [27]. Above 800°C (1472°F), there is no significant influence of chemical composition on thermal conductivity. Figure 9.20 shows that λ decreases with increasing temperature for pure iron, plain carbon steels, and low-alloy steels. Low-alloy steels exhibit a maximum value that increases with higher amounts of alloying elements and shifts to a higher temperature.

High-alloy steels such as ferritic and austenitic steels exhibit an inverse temperature dependence [32]. In addition to temperature and alloying elements, thermal conductivity is also influenced by internal stresses and structural changes. During transformation from austenite to ferrite, λ increases discontinuously by approximately 7% for pure iron [32]. Every phase transformation is also accompanied by a change of latent heat and specific volume. Because exact information about the influence of temperature, chemical composition, structural changes, and stresses on the thermodynamic data is not available, the

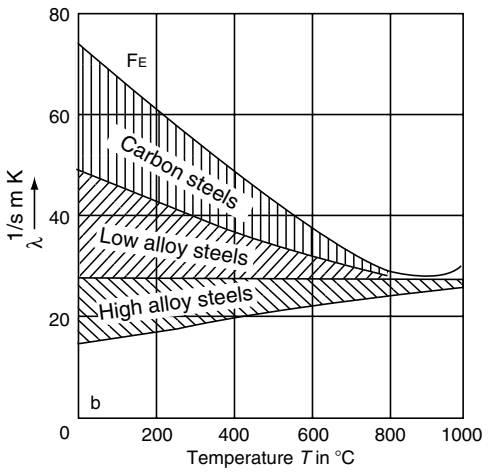

FIGURE 9.20 Influence of temperature and alloying elements on the thermal conductivity of steels.

TABLE 9.2
Approximate Values of Thermal Conductivity λ and Thermal Diffusivity α of Selected Materials at Room Temperature

Material	Thermal Conductivity [J/(s m K)]	Thermal Diffusivity (10^6 m^2/s)
Silver	407	165
Inconel 600	15.0	3.8
Austenitic steel	15.0	3.8
Ferritic steel	19	5.1
1040 steel	55	14.3
Iron	75	21

accuracy of calculations of the temperature distribution during heating or cooling of steels is limited. For examination of the cooling characteristics of quenchants, test probes constructed from silver, nickel-base alloys such as Inconel, and stainless steel (1040 steel) are often used. Thermodynamic data for these materials are compared to those of austenitic and ferritic steels in Table 9.2.

9.6.2 Heat Transfer across the Surface of a Body

Another important problem for the determination of the cooling behavior of steels concerns heat transfer across the surface of the body to the surrounding medium. This is mathematically described in terms of the (interfacial) heat transfer coefficient α:

$$\alpha = \frac{Q}{A(T_1 - T_2)} \tag{9.4}$$

where the units of α are J/(s m^2 K)[8], T_1 is the surface temperature of the body, and T_2 is the temperature of the medium. Determination of the heat transfer coefficient is based on Fourier's law of heat transfer (Equation 9.1), which states that heat flow across the surface of a body is proportional to the temperature gradient at the surface. In practice, the surface temperature of a body can only be determined with high-precision measuring equipment. Therefore α is often calculated from cooling curves that are recorded just beneath the surface of the test piece being measured.

During quenching, the heat transfer coefficient of steel is strongly dependent on the surface temperature and may vary by more than an order of magnitude between the austenitizing and quenchant bath temperatures due to variations in the interfacial film heat transfer such as film boiling and nucleate boiling. The temperature dependence of α during quenching of an austenitic steel in water and oil is shown in Figure 9.21 [12].

Three cooling stages can be present simultaneously on the surface of an immersion-quenched part for a significant period of time. Therefore, the heat transfer coefficient varies not only with temperature but also with surface location. Figure 9.22 shows the wetting state of a cylinder of 1040 steel during quenching in water for a constant cooling time and the corresponding variation of the heat transfer coefficient. Stable film boiling produces a low heat transfer coefficient due to the insulating properties of the surrounding vapor blanket [$\alpha_{FB} \approx 400$ W/(m^2 K)]. Just below the wetting front, nucleate boiling occurs. The heat transfer coefficient α reaches its maximum value of approximately 15,000 W/(m^2 K) and subsequently decreases. When the surface temperature decreases to less than the boiling point of the fluid, heat transfer occurs by convection and conduction, with α reaching even lower values, or

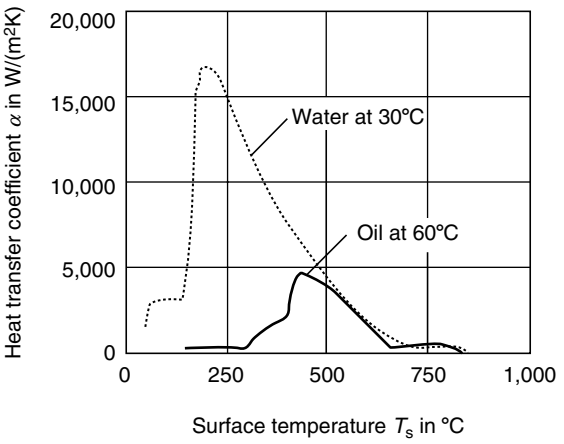

FIGURE 9.21 Heat transfer coefficient versus surface temperature of an austenitic steel cylinder (25-mm diameter × 100 mm) quenched into water at 30°C and into a fast oil at 60°C flowing at 0.3 m/s.

$\alpha_{conv} \approx 1500$ W/(m^2 K). This example demonstrates that heat transfer conditions during quenching can be complicated, especially when considering wetting behavior variation throughout the quenching process.

An example of the influence of wetting kinematics on heat removal during immersion quenching is illustrated in Figure 9.23a, which shows the change of wetting time and Leidenfrost temperature T_L, i.e., the surface temperature of the body at the transition from film boiling to nucleate boiling, along the length of a solid cylindrical CrNi steel test probe during quenching in water. Wetting starts at the lower edge of the cylinder, and the wetting front ascends from the bottom to the top (see also Figure 9.9). This results in an almost linear decrease of Leidenfrost temperature with increasing wetting time. The change in the corresponding heat transfer coefficient α at half-height of the cylindrical sample ($z = 5$ mm) with the migrating wetting front is given in Figure 9.23b. Here, α is plotted as a function of the distance x from the actual position of the wetting edge. In the case of a negative value of x, the surface point at half-height is covered with the vapor film, whereas for positive values of x,

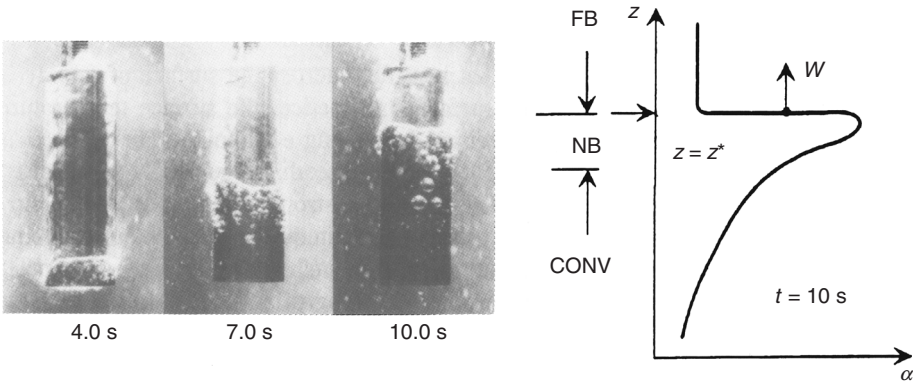

FIGURE 9.22 Wetting state on the surface of a cylindrical sample quenched into water at 30°C and schematic of variation of the corresponding heat transfer coefficient along the length of the cylinder for a given cooling time.

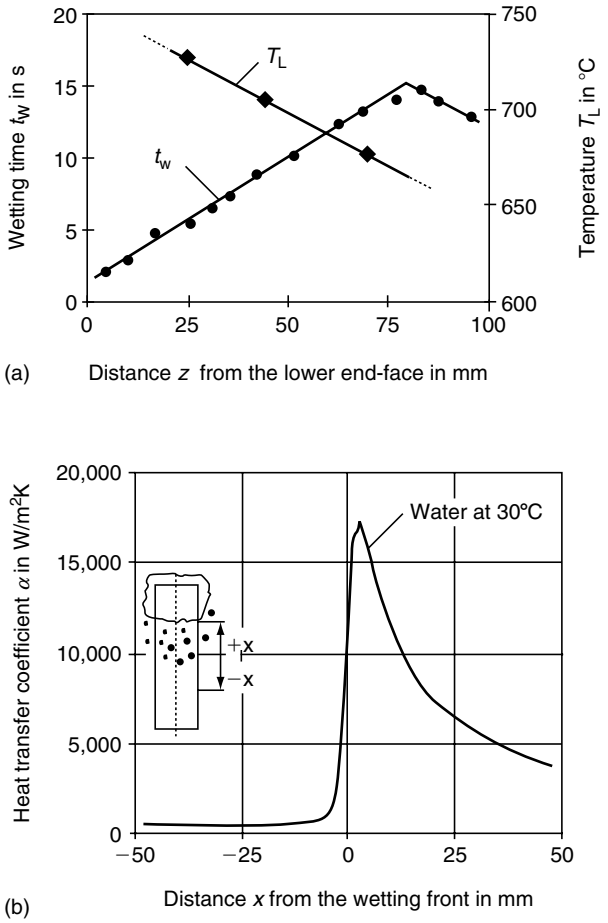

FIGURE 9.23 (a) Wetting time t_w and Leidenfrost temperature T_L along the length of an austenitic steel cylinder (25-mm diameter × 100 mm) quenched into water at 30°C flowing at 0.3 m/s and (b) correspondingly changing heat transfer coefficient at half-height for varying positions of the wetting front.

nucleate boiling and subsequently convective heat transfer occur. When the edge of nucleate boiling passes the considered surface point ($x = 0$), the heat transfer coefficient rapidly increases to its maximum value and then decreases with decreasing surface temperature.

Heat transfer coefficients are required for finite-element or finite-difference heat transfer calculations of temperature distribution during quenching. Calculated cooling curves may be used to determine as-quenched microstructures and mechanical properties such as the hardness and yield strength of steel. The wetting kinematics of the quenching process, expressed by the variable Leidenfrost temperature, must also be incorporated in these calculations. Figure 9.24 compares calculations achieved with different heat transfer coefficients [33,34]. In Figure 9.24a, the heat transfer coefficient was assumed to be equal for all surface locations. This would correspond to a very fast velocity of the wetting front (see Figure 9.10). It is apparent that the lines of constant temperature are parallel along the length of the cylinder and parallel to the cylinder end-face in the region of the lower front-end. However, high axial temperature differences actually occur when the wetting front migrates from the bottom to the top of the cylinder with an infinite wetting speed.

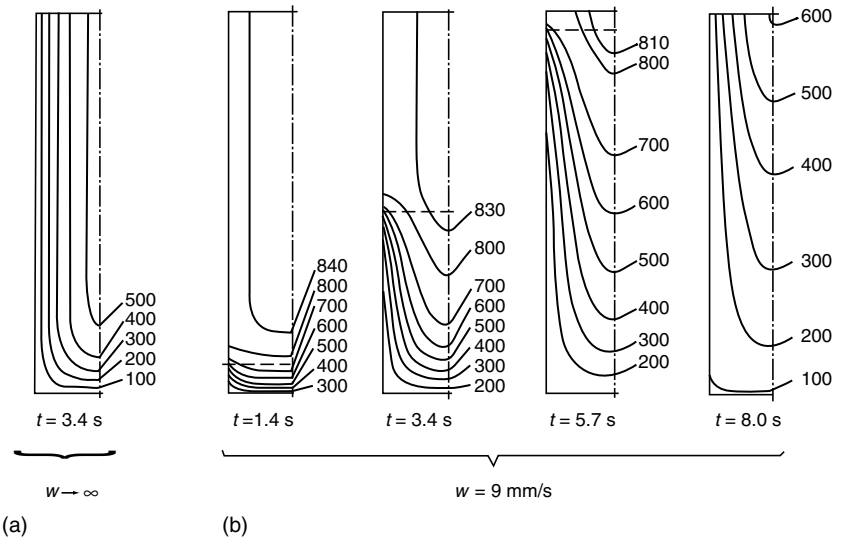

FIGURE 9.24 Calculated temperature distribution in an austenitic steel cylinder (15-mm diameter × 45 mm) during immersion quenching in water with different velocities of the ascending wetting front. (a) Sudden wetting and (b) slow setting with $w = 9$ mm/s.

Figure 9.24b illustrates the calculated temperature distribution during cooling, at four points in time, for a wetting velocity of 9 mm/s. This calculation procedure is identical with the assumption that the heat transfer coefficient α varies with the surface temperature and the distance from the lower front-end. From these figures, it can be seen that the axial temperature difference is greater than 600 K even for the small sample used. As already shown, this wetting process may have a substantial impact on hardening results.

Thermal stresses are dependent on temperature gradients within the sample. Figure 9.25 and Figure 9.26 are for solid austenitics stainless solid steel cylinders (15 mm in diameter × 45 mm). Figure 9.25 shows the distributions of radial and axial heat flux for the relatively slow wetting speed of 9 mm/s. The lines of constant radial and axial heat flux, q_r and q_a, respectively expand in the opposite direction to the ascending wetting front. Distributions

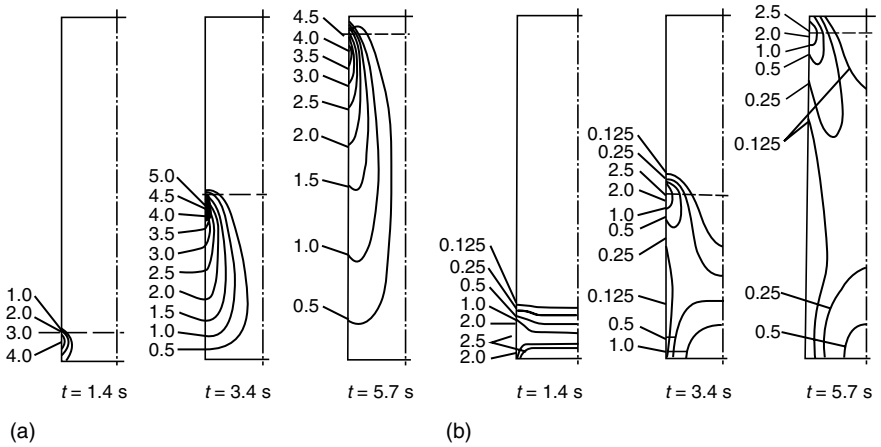

FIGURE 9.25 Calculated distributions of (a) radial and (b) axial heat flux in an austenitic steel cylinder (15-mm diameter × 45 mm) during immersion quenching in water with a wetting velocity of 9 mm/s.

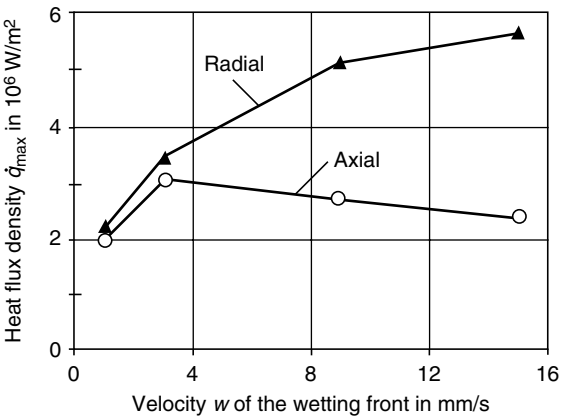

FIGURE 9.26 Influence of the velocity of an ascending wetting front on the maximum values of radial and axial heat flux for an austenitic steel specimen (15-mm diameter × 45 mm) quenched into water at 20°C.

of axial heat flux are determined by relatively high heat removal in the region below the wetting front and by heat removal at the cylinder end. The highest values of radial and axial heat flux occur along the wetting front. With increasing wetting velocity, the maximum value of radial heat flux increases, while the axial heat flux decreases after it has reached a maximum at a wetting velocity of approximately 3 mm/s are shown in Figure 9.26. Therefore, high wetting velocities reduce thermal gradients along the length of the cylinder, which may decrease the distortion and cracking.

In quench hardening, heat removal is often expressed by the Grossmann number or H factor instead of the heat transfer coefficient α. The Grossmann number [35] is defined as

$$H = \alpha/2\lambda \tag{9.5}$$

Thus, the H factor is equal to the interfacial heat transfer coefficient divided by twice the thermal conductivity. When the H factor is multiplied by the diameter of the body D, their product corresponds to the well-known dimensionless BiOT number (Bi):

$$\mathrm{HD} = \mathrm{Bi}\frac{\alpha}{\lambda}R \tag{9.6}$$

The BiOT number is important because all bodies with the same BiOT number exhibit similar heat flow. If thermal conductivity λ is constant, although it is dependent on the chemical composition of the steel, the structural changes during quenching are as shown in Figure 9.20, and the value of H depends only on the heat transfer at the surface and thus on the cooling capacity of the quenchant.

The most significant deficiency of the H factor is the incorrect assumption that cooling occurs at a constant rate (Newtonian cooling) during quenching. The heat transfer coefficient and therefore the H-value vary throughout the three stages of cooling and also with the surface wetting process as shown in Figure 9.21 and Figure 9.22. Even with this limitation, H-values have been widely accepted by heat treaters and are often required as input data in software packages for predicting the hardness distribution of quenched components. Table 9.3 provides some illustrative H-value data along with the corresponding interfacial heat transfer coefficients for selected quenchants [36].

TABLE 9.3
Grossman *H* Factor and Corresponding Heat Transfer Coefficient for Selected Quenchants

Quenchant	Quenchant Temperature (°C)	Quenchant Velocity (m/s)	*H*-Value (in.$^{-1}$)	Heat Transfer Coefficient [W/(m^2 K)]
Air	27	0.0	0.05	35
		5.1	0.08	62
Conventional oil	65	0.51	0.7	3,000
Fast oil	60	0.00	0.5	2,000
		0.25	1.0	4,500
		0.51	1.1	5,000
		0.76	1.5	6,500
Water	32	0.00	1.1	5,000
		0.25	2.1	9,000
		0.51	2.7	12,000
		0.76	2.8	12,000
	55	0.00	0.2	1,000
		0.25	0.6	2,500
		0.51	1.5	6,500
		0.76	2.4	10,500

9.7 PROCESS VARIABLES AFFECTING COOLING BEHAVIOR AND HEAT TRANSFER

Steel hardening requires a wide variation and sufficient reproducibility of heat transfer across the cooling surface to achieve the required cooling rate (which is dependent on the hardenability of the steel and the section size of the sample) and the desired mechanical properties. The influence of the cooling behavior during various quenching processes will now be described.

9.7.1 Immersion Quenching

Heat transfer during immersion quenching is influenced by many factors such as the dimensions and shape of the part that is quenched, the quenchant, and the quenching facility. In the heat treatment shop only a few of these parameters can be realistically varied, including bath temperature, agitation rate, and the quantity and racking arrangement of the parts during the quenching process. Of these, only agitation is readily varied during the quench, because rapid bath temperature changes and variation of the quenchant (and concentration, if an aqueous polymer solution is used) cannot realistically be accomplished during the quenching process itself.

9.7.1.1 Bath Temperature

The principal mechanism of heat transfer for vapor blanket cooling during immersion quenching is illustrated in Figure 9.27. Heat is transported across the surface through the vapor blanket by conduction ($\dot{q}_\lambda$) and radiation ($\dot{q}_g$). Only a fraction of the heat is released to the liquid by convection ($\dot{q}_\alpha$). The remainder ($\dot{q}_v$) vaporizes and stabilizes the fluid into the vapor blanket. The hot vapor flows upward, and at the vapor–liquid interface bubbles pass

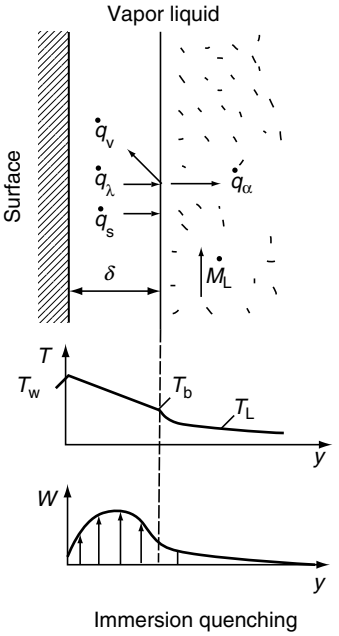

FIGURE 9.27 Mechanism of heat transfer during film boiling and distribution of temperature and flow velocity in the bordering layer (schematic).

from the vapor film into the fluid, especially at the top of the cooling workpiece. A local decrease of the thickness δ of the vapor film immediately increases the heat flow by conduction ($\dot{q}_\lambda$), resulting in additional vaporization of the fluid, thus sustaining the vapor film.

When the surface temperature decreases, the thickness δ of the vapor film is reduced until the fluid contacts the hot metal, which is the start of wetting. Heat is no longer passed through the vapor film, and fluid is evaporated upon direct contact with the sample surface, dramatically increasing the rate of the heat flow. With increasing liquid temperature T_1, the energy required for fluid evaporation is reduced and is proportional to the difference between the boiling point and the liquid temperature. The thickness δ of the vapor film is increased, and film boiling occurs at lower surface temperatures. Figure 9.27 shows that within the vapor film the temperature drops from the surface temperature T_s to the boiling temperature T_b of the fluid and further decreases to the liquid temperature T_1.

The effect of water temperature on cooling curves in the center of an Inconel 600 probe (12.5-mm diameter $\times$ 60 mm) is illustrated in Figure 9.28 [37]. With increasing water temperature the duration of film boiling increases, which is indicated by the delayed transition from low cooling to fast cooling. In addition, the cooling rates of the three different stages of heat transfer are reduced.

9.7.1.2 Effect of Agitation

In addition to bath temperature, the stability of the vapor film is greatly influenced by the velocity profile in the liquid. As illustrated in the lower part of Figure 9.27, the velocity profile is caused by the buoyancy-driven vapor flow and possibly by agitation (forced convection). A high flow velocity increases the heat transfer by convection ($\dot{q}_\alpha$) and reduces δ, therefore reducing the duration of film boiling. With agitation, heat transfer during the three stages of cooling is increased.

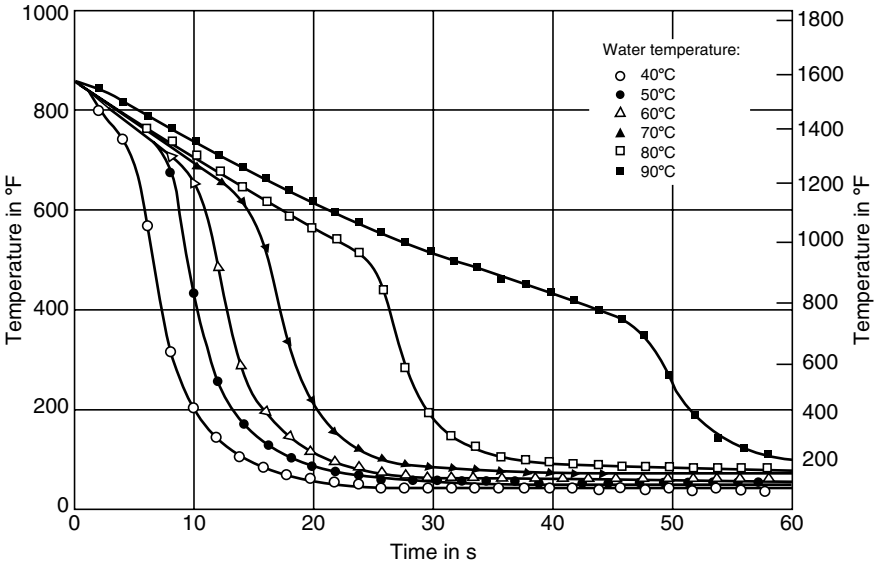

FIGURE 9.28 Effect of bath temperature on cooling curves measured in the center of an Inconel 600 probe (12.5-mm diameter × 60 mm) quenched into water flowing at 0.25 m/s.

Figure 9.29 shows the effect of selected liquid velocities (0, 0.3, and 0.6 m/s) on cooling curves measured in the center of an austenitic stainless steel specimen quenched in 60°C (140°F) water [13]. In the range of stable film boiling, the temperature of the cylinder decreases slowly, almost independently of the liquid flow velocity. As the vapor film collapses, the steel temperature decreases rapidly. Thus, the transition from lower to higher cooling rates may be strongly influenced by the liquid flow velocity and turbulance.

9.7.1.3 Effect of Quenchant Selection

The quenchant also exhibits dramatic effects on cooling behavior. The cooling curves in Figure 9.30a were obtained with a 25-mm diameter probe quenched in water at two temperatures, a 10% aqueous polymer solution, and a fast quenching oil. All quenchants were evaluated at 0.6 m/s. Using the same probe size (cross-section) and flow velocity, different cooling curves were obtained for each quenchant.

The effect of the quenchant and flow velocity becomes even more apparent when the time $t_{A/5}$ from austenitizing temperature (for this example 850°C [1562°F]) to 500°C [932°F] is considered as shown in Figure 9.30b [12,13]). While the values of $t_{A/5}$ strongly differ for the quenchants shown, only a small influence of the flow velocity can be observed in water at 30°C (86°F) and oil at 60°C (140°F) for the cross-section size used (25-mm diameter). The $t_{A/5}$ time can be drastically reduced with increasing slow velocity in water at 60°C (140°F) and the 10% aqueous polymer solution at 30°C (86°F). As expected, the effect of the flow velocity becomes clearer when smaller cross-sections are used.

9.7.1.4 Surface Oxidation and Roughness Effects

The surface roughness of the body and surface layers, such as oxides or organic substances, also strongly influences the cooling process. Chromium-alloy steels are oxidation-resistant due to concentration of chromium oxide at the surface. Oxide layers have greater surface roughness and a lower thermal conductivity.

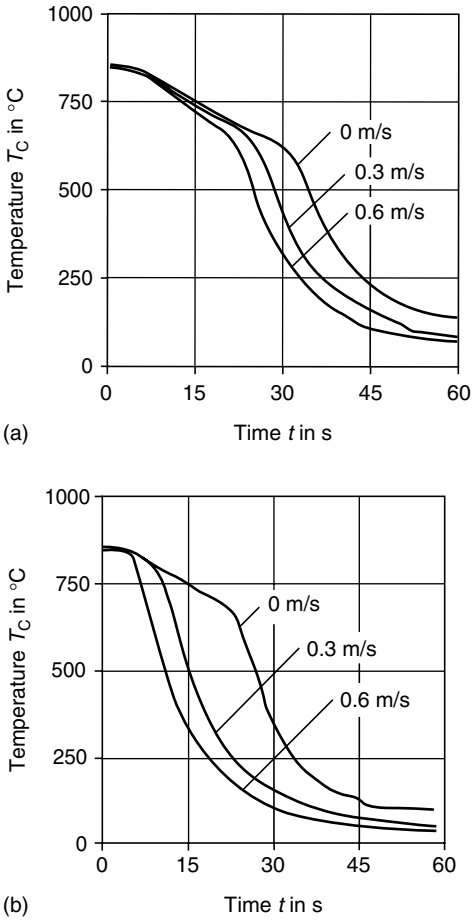

FIGURE 9.29 Effect of quenchant velocity on cooling curves in the center of an austenitic stainless steel specimen (25-mm diameter × 100 mm) quenched (a) into water at 60°C and (b) into a 10% aqueous polymer solution at 30°C.

In Figure 9.31, the time interval of wetting ($t_f - t_s$) of austenitic stainless steel cylinders heated to 850°C (1562°F) in an oxidizing atmosphere after annealing at 820°C (1508°F) for 20 h in air is compared to that of similar cylinders heated to the same temperature in a protective, reducing atmosphere [20]. Water at 20 and 50°C (68 and 122°F) flowing at various flow velocities was used as the quenchant. The wetting time is shorter for the oxidized surface and is further reduced with increasing liquid flow velocity sustained by a decreasing bath temperature as shown in Figure 9.31. When the oxidized specimen was quenched in an aqueous polymer solution, the rough oxide layer facilitated immediate contact between the specimen surface and the liquid. A identical specimen that had been heated in a protective atmosphere was surrounded by a vapor envelope for a much longer time.

A more distinct effect of surface oxidation on wetting behavior is given in Figure 9.32 [13]. In addition to the oxidized and bright surfaces, the austenitic stainless steel specimen was passivated by etching with 1.5 and 3% nitric acid over 10 min in all. There is no observable influence on t_s, the time when wetting starts, but t_f, the time when wetting is finished, decreases and the time interval of wetting $t_f - t_s$ becomes shorter with increasing surface oxidation. In addition, the variance of the t_f values increases significantly.

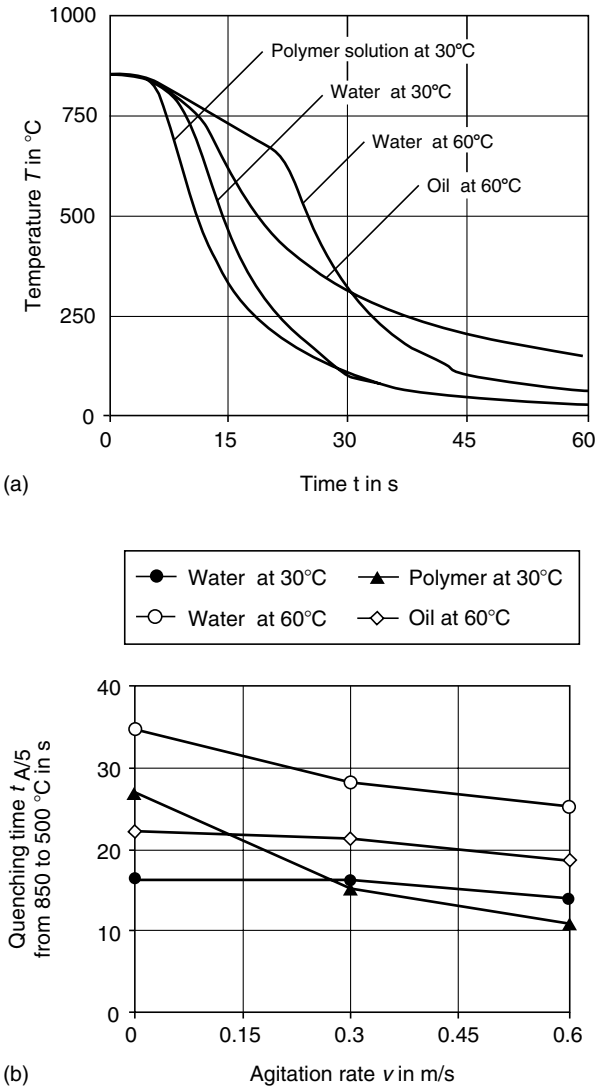

FIGURE 9.30 Influence of quenching media and agitation on the cooling behavior of a cylindrical specimen (25 mm [diameter] × 100 mm [length]). (a) Influence of different quenchants, some with different bath temperature, on cooling curve behavior (agitation velocity of 0.6 m/s) and (b) influence of agitation rate on the cooling time from 850 to 500°C using the same probe with different quenchants at different temperatures.

9.7.1.5 Effect of Cross-Section Size on Cooling

With large cross-sections, the cooling rate in the specimen center is limited by the rate of heat conduction from the interior to the surface. The effect of cross-section size on the center-cooling curves produced when 15-, 25-, and 40-mm diameter probes were quenched in water at 30°C (86°F) flowing at a velocity of 0.3 m/s is illustrated in Figure 9.33a. Cooling is proportionately slower with increasing test probe diameter. Rapid cooling at the center of test probes with large cross-sections is therefore impossible with any quenching method. Full

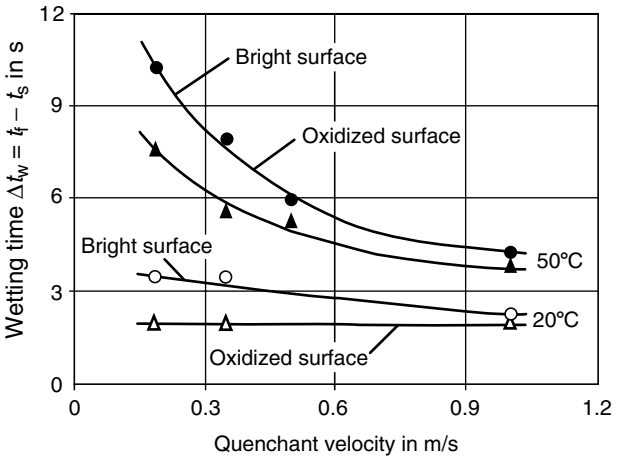

FIGURE 9.31 Influence of surface oxidation on the time interval of wetting ($t_f - t_s$) of an austenitic stainless steel specimen (15-mm diameter × 45 mm) quenched into water at two bath temperatures, 20 and 50°C. Oxidized surface: after annealing 20 h at 820°C in oxidizing atmosphere. Bright surface: after heating in protective atmosphere.

through-hardening of large sections requires a high-hardenability steel because cooling rates are limited by the thermal diffusion of the steel.

Section size also exhibits a dramatic influence on the wetting kinematics as shown in Figure 9.33b. In water at 30°C (86°F), wetting starts immediately upon immersion at the lower cylinder edge and the time t_s remains unaffected with varying size. The velocity of the spreading wetting front is reduced and the time interval of wetting increases with increased section size [12].

The wetting kinematics vary with water temperature. As the water temperature increases, the vapor blanket surrounds the surface for a longer time and the time (t_s) of first contact between the specimen surface and the water increases substantially with increasing diameter.

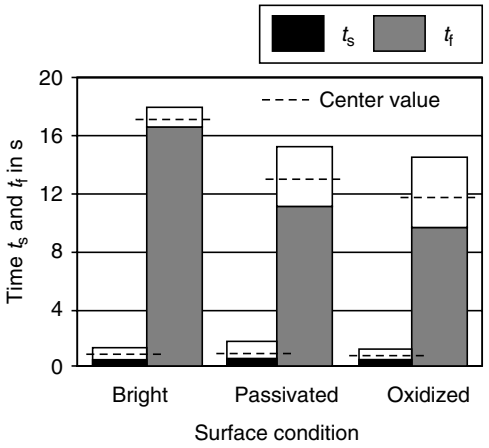

FIGURE 9.32 Influence of surface oxidation on the time when wetting starts (t_s) and the time when wetting is finished (t_f) of an austenitic stainless steel specimen (25-mm diameter × 100 mm) quenched into water at 30°C without forced convection.

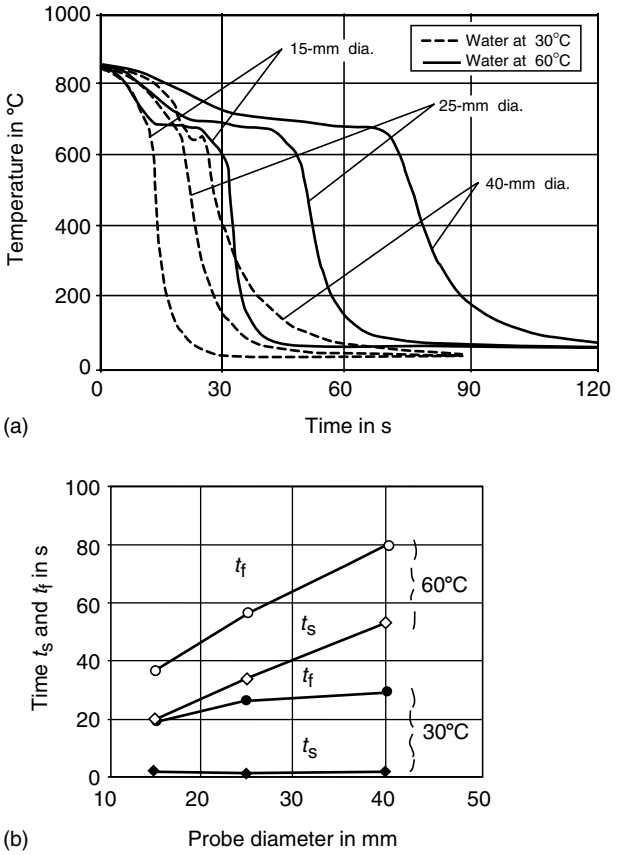

FIGURE 9.33 Influence of sample diameter on cooling behavior and wetting kinematics of a 25-mm diameter × 100 mm CrNi steel specimen quenched into 30 and 60°C water flowing at 0.3 m/s. (a) Cooling curve in the center of the specimen and (b) characteristic values of wetting t_s and t_f.

Practically, this means that water temperature must be carefully controlled to get reproducible hardness results, as increasing wetting times results in decreased cooling rates and soft spots on parts. For example, hardness values of the 1045 steel bars quenched in water at 60°C (140°F) (Figure 9.33b) are less than $R_c = 30$ (HRC 30) and are independent of the section size.

9.7.1.6 Effects of Cooling Edge Geometry

As the initial rupture of the vapor blanket is always related to the decrease of surface temperatures below the wetting temperature (Leidenfrost temperature), wetting behavior is strongly influenced by the radius of the lower edge of a cylindrical steel sample. Figure 9.34 shows the influence of different types of lower-edge geometries on the starting temperature T_s during wetting of austenitic stainless steel test probes in water at different bath temperatures [14,20].

A sharp edge will cause high heat removal rates across the surface and a premature breakdown of the vapor blanket. Increasingly, the lower surface radius from a rounded edge to a radius of 2.5 mm reduces the initial wetting temperature and the influence of bath temperature is diminished due to the greater thickness of the vapor blanket.

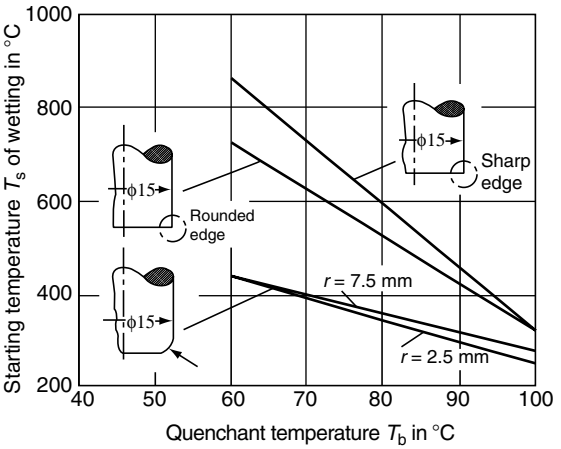

FIGURE 9.34 Influence of quenchant temperature T_b on wetting kinematics, here on the temperature T_s when wetting starts, of a CrNi steel specimen (15-mm diameter × 45 mm) with different kinds of lower edge geometry during quenching in water. Sharp edge according to C1 DIN 6784; rounded edge according to D2 DIN 6784.

9.7.1.7 Effects of Steel Composition

The chemical composition of steel determines the thermodynamic parameters of the material, the transformation behavior of austenite, and oxidation of the surface and therefore influences the wetting and cooling behavior during quenching. The effect of chemical composition on cooling curves and cooling rate curves produced in the center of steel cylinders with 25-mm diameter quenched in water at 60°C (140°F) and 0.3 m/s agitation is illustrated in Figure 9.35a [12]. All samples were austenitized at 850°C (1562°F), except the 20MnCr5 steel, which was austenitized at 870°C (1600°F).

Cooling curves for different alloys were obtained with the same diameter and cooling conditions. High cooling rates for 1045 carbon steel are related directly to its high thermal conductivity.

The minima in the cooling rate curves are caused by the latent heat of transformation of austenite into ferrite–pearlite, bainite, or martensite. The transformation temperature and the amount of latent heat depend on the hardenability of the steel grade and the cooling rate.

Thermodynamic properties of the material also exhibit a marked effect on the wetting kinematics as indicated in Figure 9.35b, which shows the time when wetting starts (t_s) and the time when wetting is finished (t_f) as a function of the thermal conductivity λ at 20°C (68°F). Samples were quenched into different fluids agitated at 0.3 m/s. In 30°C (86°F) water and 60°C (140°F) oil, the start of wetting remains unaffected by effects from the thermal conductivity. However, water at 60°C (140°F) and the 10% aqueous polymer solution at 30°C (86°F) exhibit delayed wetting start time for λ values greater than about 30 W/(m K). The time when wetting is finished increases with increasing thermal conductivity for all fluids.

Surface effects were neglected because the probes were heated and transferred into the quenching bath in a protective, reducing atmosphere. For practical applications, unalloyed steels must be quenched very fast because of their transformation sensitivity and their unfavorable wetting process [12,28].

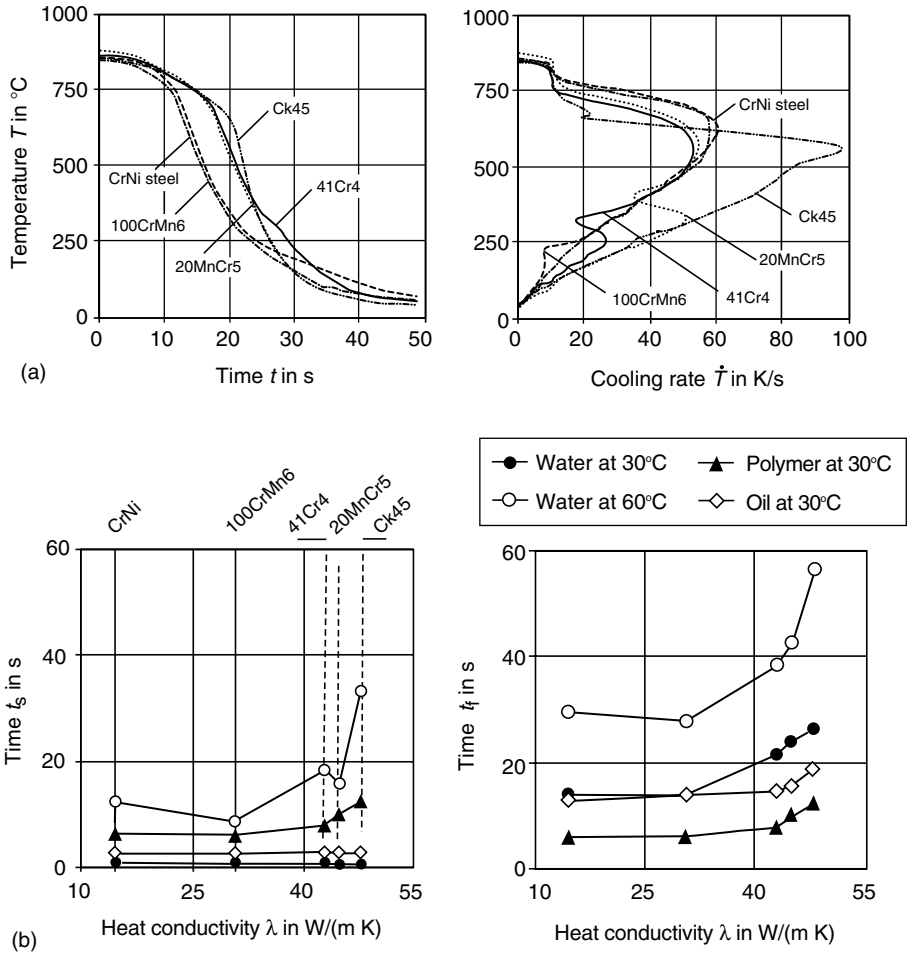

FIGURE 9.35 Influence of the chemical composition of steels on the cooling behavior and wetting kinematics of 25 × 100 mm steel bars quenched into different fluids flowing at 0.3 m/s. (a) Center cooling curves and cooling rate curves for 30°C water and (b) characteristic values of wetting t_s and t_f for water at 30 and 60°C, a 10% aqueous polymer solution at 30°C, and a fast oil at 60°C.

9.7.2 Spray Quenching

For spray quenching, high-pressure streams of liquid are directed through nozzles onto selected parts of the hot surface, thus permitting localized cooling. In addition to localized cooling, the primary advantage of spray quenching compared with immersion quenching is that the degree of heat transfer across the surface can be controlled during the cooling operation by varying the quantity of the sprayed liquid, thus allowing computer-controlled cooling. However, careful adaptation of the quenching nozzles to the geometry of the workpiece is necessary because the cooling operation is extremely sensitive to any variations of the spraying action [38].

As with immersion quenching, a stable vapor film initially forms over the hot surface, reducing heat removal across the surface and resulting in slow cooling. Subsequently, nucleate boiling from the surface allows high heat flux densities.

The initial wetting process and the mechanism of heat transfer from steel to the liquid in the film boiling stage are shown in Figure 9.36. The sprayed liquid may flow upward or

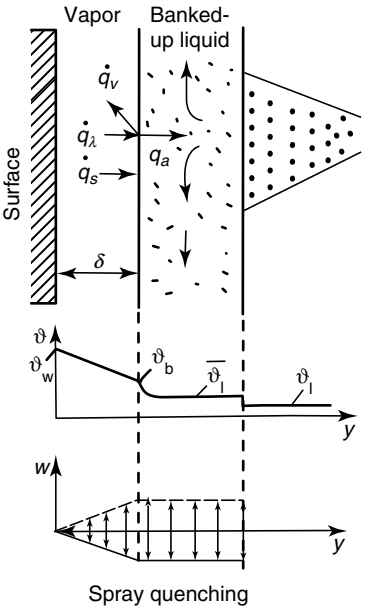

FIGURE 9.36 Heat balance during film boiling in the boundary region of a spray-cooled surface and distribution of temperature and flow velocity.

downward. Vapor flow is also affected by the liquid flow. As heat transfer is defined primarily by the velocity distribution within the liquid, it depends on the amount of sprayed fluid and thus on the impingement density, which is the amount of liquid at the metal surface per unit time per unit area.

Figure 9.37 shows the dependence of the heat transfer coefficient during film boiling on the impingement density for water spray cooling [39–41]. It is evident that the heat transfer

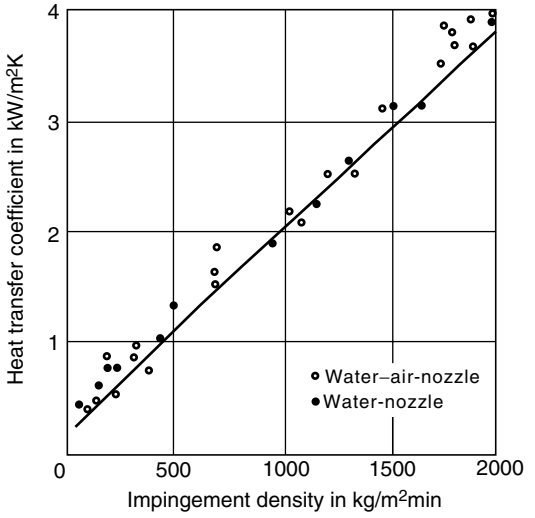

FIGURE 9.37 Effect of the impingement density on the heat transfer coefficient during film boiling for spraying with water.

coefficient values of film bonding (α_{FB}) may be much higher than with immersion quenching (see Figure 9.21) because of the higher density of sprayed water on the cooling surface.

The addition of air to the water spray, as shown in Figure 9.37, influences local distribution of the impingement density but does not increase heat transfer. It should be noted that heat transfer coefficients may also be influenced by the liquid temperature. For water, this influence increases with increasing impingement densities at temperatures above 20°C (68°F) [42].

In Figure 9.38a, the total heat transfer coefficient for water is given as a function of the surface temperature with various impingement densities [43]. Increasing the impingement densities increases heat transfer across the surface and shifts the wetting temperature to higher values. In the range of stable film boiling, the heat transfer coefficient does not depend on the surface temperature; however, significant variation is observed at lower temperatures.

Figure 9.38b indicates that the heat transfer coefficient depends not only on the impingement density but also on heat flow within the specimen and thus on the type of metal. This influence can be described by the coefficient of heat penetration b:

$$b = (\lambda \rho C_p)^{1/2}$$

The maximum heat transfer coefficient increases with increasing values of b. The value of b in Figure 9.38b varies from nickel [$b = 14.3$ kW· s$^{1/2}$/(m K)], brass [$b = 21.3$ kW s$^{1/2}$/(m K)], and aluminum [$b = 23.6$ kW s$^{1/2}$/(m K)] to copper [$b = 35.5$ kW s$^{1/2}$/(m K)].

When a mixture of water and air is sprayed, heat transfer varies with air and water pressure as illustrated in Figure 9.39 [44] where heat flux density is plotted versus surface temperature for three sets of air and water supply conditions (air only, varying air pressure with no water pressure, varying water pressure with maximum air pressure). A control system for water and air pressure provides continual variation of the heat flux across the surface following a predetermined cooling curve [45].

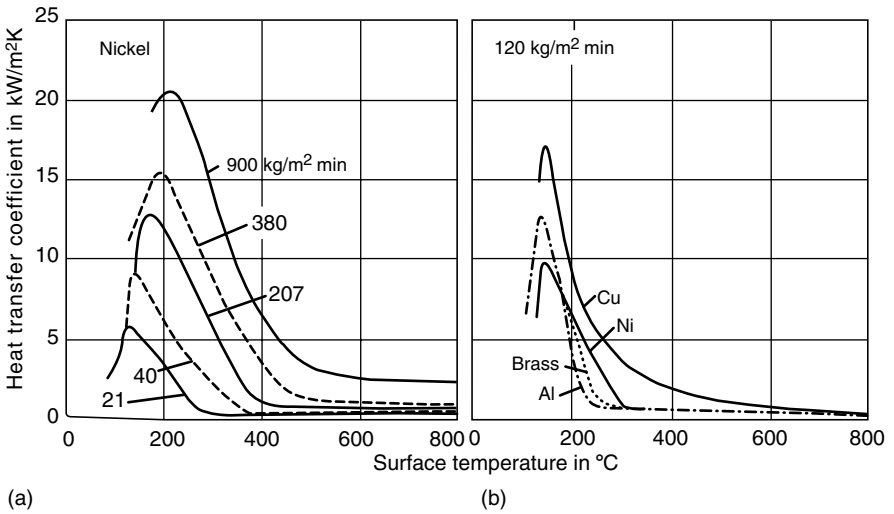

FIGURE 9.38 Heat transfer coefficient as a function of the surface temperature for spray quenching with water. (a) Influence of the impingement density and (b) influence of the chemical composition of the metal.

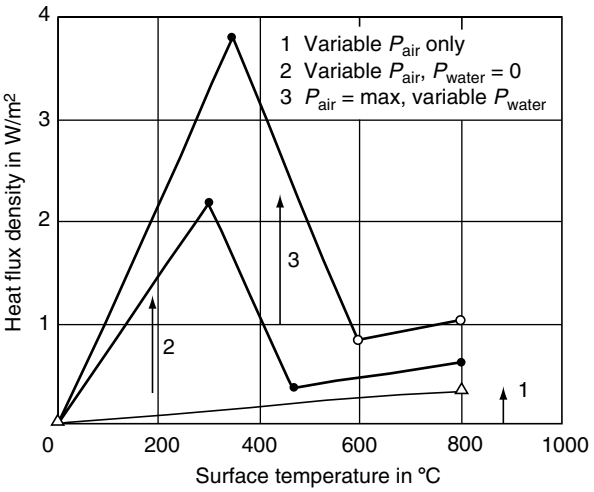

FIGURE 9.39 Heat flux density versus surface temperature for different, but constant, water and air pressures. (Δ) Variable P_{air}, no water; (•) variable P_{air}, $P_{water} = 0$; (○) $P_{air} = \max$, variable P_{water}.

In Figure 9.40a, an isothermal pearlitic transformation of an AISI 1034 steel was obtained by real-time controlled spray quenching. The desired set-point curve (curve 2) is nearly completely reproduced by the regulated spray-quench operation (curve 3). Because the isothermally formed pearlite is very thin, the mechanical properties are higher compared to these in the continuous transformation (curve 1).

A second example, shown in Figure 9.40b, illustrates the effect of surface heat treatment of carbon steel. Induction heating of cylindrical parts was coupled with computer-controlled cooling, providing a fully automated heat treatment process. Here too, the real-time cooling control (irregular curve) allows the extraction of heat according to the desired temperature–time curve (straight-line segments).

9.7.3 Gas Quenching

In gas quenching, the hot workpiece is cooled by blowing gas over the surface. Gas quenching is generally used when cooling rates obtained in still air are too slow to produce the required hardness and oil quenching is undesirable because of residual stresses, cracking distortion, or handling (ecological, toxicological, or safety) problems.

Figure 9.41 compares cooling curves that were obtained during quenching of AISI 4130 steel tubing with an outer diameter of 31.7 mm and a wall thickness of 1.6 mm in still air, gas (the specific gas quenchant was not identified), and oil [37]. It is evident that the cooling rate achieved in gas is lower than that obtained in oil. This example illustrates that the favorable use of gas quenching depends on hardenability of the steel and size of the workpiece.

An advantage of gas quenching compared to liquid quenchants (oil, water, and aqueous polymers) is that quenching with gas proceeds more uniformly, minimizing residual stresses and distortion. Vaporizable liquids such as oils may exhibit an extended film boiling phase, and the beginning of nucleate boiling is variable (see Section 9.4). This nonuniform heat removal from the surface may produce a nonuniform hardness (soft spots) and an unfavorable stress distribution, leading to cracking and distortion.

In addition to potentially improved quench uniformity, gas quenching is a clean process, eliminating the need for the vapor degreasing step often used for oil quenching processes. Potential fire hazards and disposal problems are also eliminated.

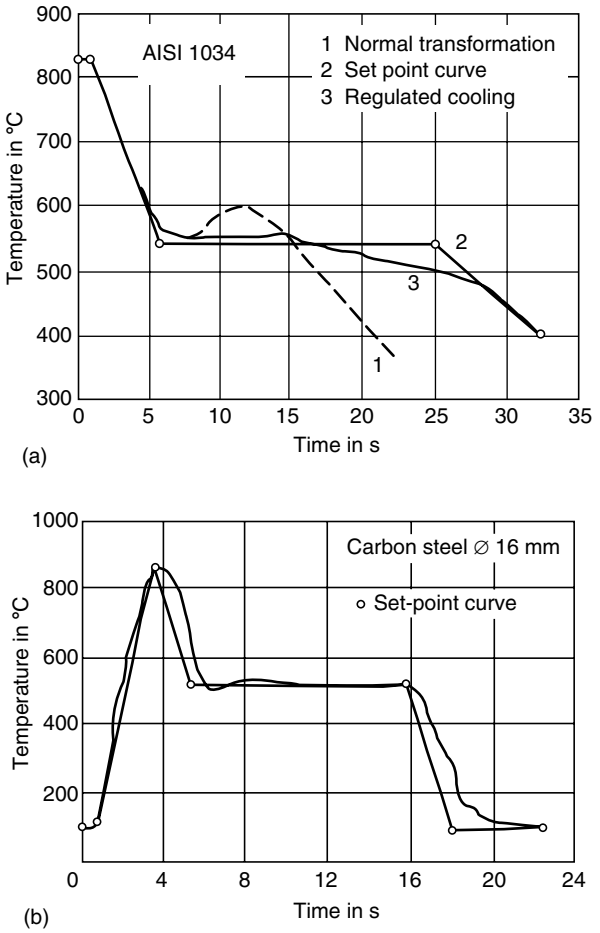

FIGURE 9.40 (a) Isothermal pearlitic transformation of a 16-mm diameter 1034 steel. The real-time controlled spray cooling (curve 3) allows the extraction of heat due to the desired transformation and (b) surface heat treatment of a 16-mm diameter carbon steel. The set-point curve is achieved by coupling the heating and spray-cooling process.

Cooling operation can be precisely controlled by varying the type, pressure, velocity, and temperature of the gas, thus providing uniform heat transfer across the surface and a variety of possible cooling rates. The use of inert gases avoids chemical reactions with the steel surface, eliminating the need for any surface cleaning or finishing treatment after quenching.

Gas quenching is usually used after austenitization in vacuum furnaces. During quenching, gases are blown through nozzles or vanes toward the workload. After absorbing heat from the load, the gas is cooled by passage through water-cooled heat exchangers and then recycled to the nozzles for subsequent reuse.

Cooling rates obtainable for gas quenching are limited by the type, pressure, velocity, and temperature of the cooling gas and by the surface conditions, geometry, and thermal properties of the material [46]. The most common cooling gases used in vacuum furnaces are argon, nitrogen, helium, and, to some extent, hydrogen. The physical properties of these gases are summarized in Table 9.4 [47]. Thermal conductivity, specific heat, density, and dynamic viscosity influence the heat transfer coefficient. Figure 9.42 shows that the largest heat transfer coefficient is achieved with hydrogen, followed by helium, nitrogen, and argon, in

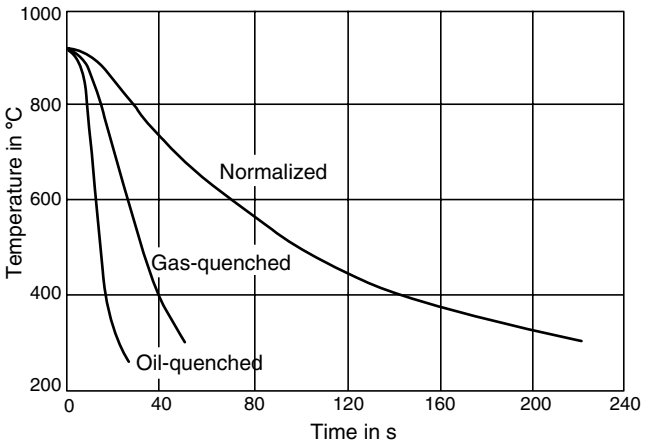

FIGURE 9.41 Cooling curve of a 4130 steel tube 31.7-mm diameter × 1.6 mm quenched into oil, gas, and still air (normalizing).

that order. Heat transfer coefficients are directly proportional to the thermal conductivity and specific heat of these gases.

Hydrogen is explosive and exhibits decarburizing properties above 1000°C (1832°F). Helium is relatively expensive and is therefore used only with a recycling facility. Argon exhibits relatively low cooling rates. Nitrogen is the gas most commonly used in vacuum furnaces today. Both nitrogen and argon pressure are limited to approximately 10^6 Pa because of the high flow-resistance of these gases, which is due to their high density and dynamic viscosity.

Figure 9.42 shows that heat transfer coefficients increase with gas pressure [48]. The heat transfer coefficient was calculated for a solid cylinder that was radially quenched with a velocity of 20 m/s and a temperature of 200°C (392°F). In practice, gas pressures vary between 1 and 10 bar for argon and nitrogen and between 1 and 20 bar for helium and hydrogen. At these gas pressures, heat transfer coefficients are considerably less than those for oil quenchants. However, oil quenching produces less uniform surfaces during heat transfer because of widely varying heat transfer coefficients exhibited by the three different cooling stages. (Increasing the flow velocity of the gas also increases the heat transfer coefficient.)

Figure 9.43 shows the effect of the bar diameter and the type of gas on the center cooling curves of a DIN 1.2080 steel cylinder with a length of 200 mm, which was quenched, after vacuum heat treatment, in nitrogen and hydrogen at a pressure of 5 bar [49]. The cooling rate decreases with increased section size and greater cooling rates will be achieved with hydrogen than with nitrogen under the same quenching conditions. The center cooling curve of the

TABLE 9.4
Physical Properties of Hydrogen, Helium, Nitrogen, and Argon

Property	Hydrogen	Helium	Nitrogen	Argon
Density (kg/m^3)	0.303	−0.601	4.207	6.008
Specific heat (J/(kg K))	14,450	5,200	1,050	520
Heat conductivity (×10^4 W/(m K))	2,256	1,901	326	222
Dynamic viscosity (×10^6 N s/m^2)	10.8	24.4	21.6	28.2

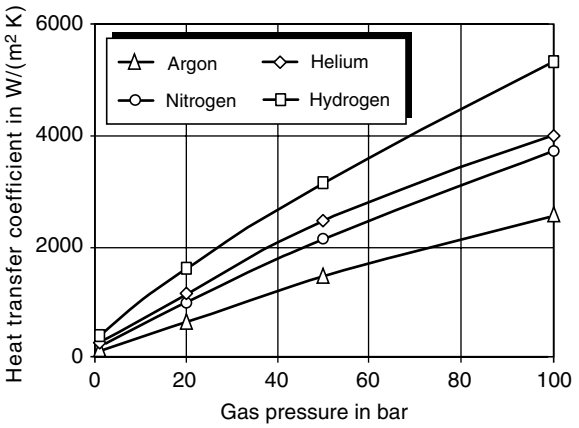

FIGURE 9.42 Heat transfer coefficients of inert gases (hydrogen, helium, nitrogen, and argon) as a function of the gas pressure, calculated for the case of a cylinder with transverse gas flow.

80-mm diameter sample quenched in nitrogen is similar to that obtained in the center of the 120-mm diameter sample quenched in hydrogen. Corresponding hardness values in the core are almost identical: HRC = 63 versus 62. For an 80-mm diameter, the core hardnesses can be improved to HRC = 66 by quenching with hydrogen.

Figure 9.44 compares the cooling curves produced when steel cylinders with a diameter of 20 mm and a length of 500 mm, arranged in a 520-kg net mass workload, were quenched in nitrogen at 6 bar and in hydrogen at 6 and 20 bar [49]. It is evident that cooling times can be decreased by 30% with the use of hydrogen instead of nitrogen at the same gas pressure. Increasing the hydrogen pressure from 6 to 20 bar further increases the cooling rate by about 75% compared to the 6-bar nitrogen quench.

Figure 9.45 compares the hardness values in the core and in the boundary region of a case-hardened DIN 1.7131 steel that was obtained when 20-, 40-, and 60-mm diameter probes were quenched in helium at a pressure of 17.5 bar and in oil [48]. Examination of the 60-mm diameter probe shows that the oil quench can be replaced by the high-pressure helium quench (see Figure 9.45a) and that the surface and core hardnesses are slightly higher for the helium quench.

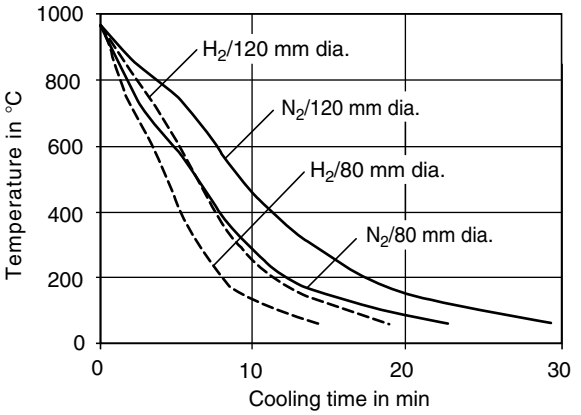

FIGURE 9.43 Cooling curves in the center of a DIN 1.2080 steel with 80- and 120-mm diameter and 200-mm length during cooling in hydrogen and nitrogen at a pressure of 5×10^5 Pa.

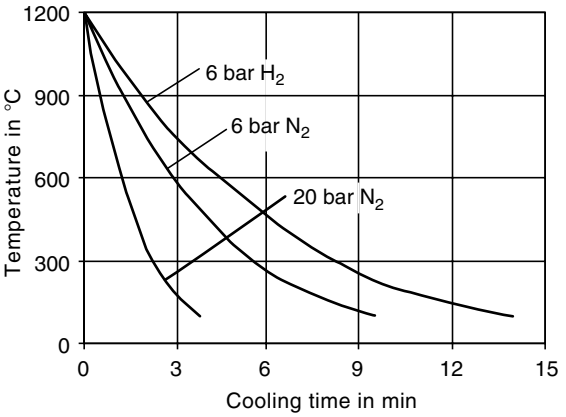

FIGURE 9.44 Influence of the type of gas, hydrogen and nitrogen, and of hydrogen pressure on the cooling curve during quenching of a batch of cylinders (30-mm diameter × 500 mm).

Figure 9.45b illustrates that when the section size is reduced from 40- to 20-mm diameter, core hardness increases and the hardness increase is higher for helium than oil. These results show that the more uniform quenching obtained by gas quenching is advantageous for large sections. Conversely, for smaller diameter sections, oil quenching is preferred because the film boiling stage decreases with decreasing section size and nucleate boiling begins at a higher temperature, resulting in higher heat transfer coefficients at higher temperatures.

A comparison of nitrogen at 5 bar and molten salt for high-speed quenching of steel after vacuum heat treatment has also been reported [46,47]. Cooling curve and hardness results showed that the two processes were nearly identical. An example of an automated gas quenching facility for parts is presented in Figure 9.46 [50–52]. The hot ball-bearing races

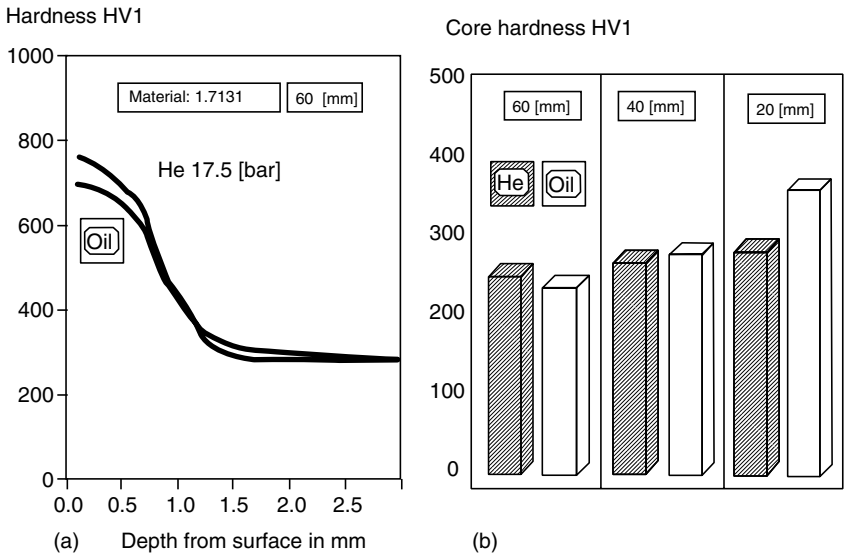

FIGURE 9.45 Hardness of case-hardened DIN 1.7131 steel bars of 20-, 40-, and 60-mm diameter during quenching in oil and in helium at a pressure of 17.5×10^5 Pa. (a) Hardness distribution in the boundary region of the 60-mm steel bar and (b) hardness in the center of the 20-, 40-, and 60-mm bars.

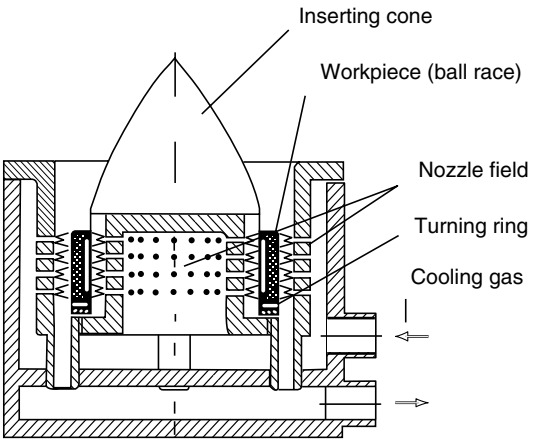

FIGURE 9.46 Gas quenching device with standard nozzle length for bearing shells.

fall with the help of a cone in the quenching device, where they are multidirectionally sprayed with streams of gas. The pieces are turned during the quenching operation to minimize the differences in heat transfer in the region of a single gas stream. The primary advantage of this quenching system is the uniformity of heat transfer across the surface, which cannot be achieved with other quenching methods. In an oil or water quench, heat transfer increases during the transition from film boiling to nucleate boiling. Because the breakdown of the vapor film does not occur simultaneously around the circumference of the ball race, this process results in distortion and high residual stresses.

9.7.4 Intensive Quenching

During quenching from austenitizing temperature, localized temperature differences occur within the workpiece, creating thermal stresses. These are due to the temperature dependence of the specific volume of the microstructures formed in the steel during quenching. The transformation-induced volume changes combined with the transformation plasticity cause additional transformation stresses that interact with the thermal stress state. Both thermal and transformational stresses cause plastic deformations if they are in excess of the yield strength of the material. This may result in quench cracks if the equivalent stresses exceed the tensile strength of the hot steel.

Traditionally, heat treaters have striven to achieve the critical cooling rate necessary to form 100% martensite. (This critical cooling rate is the cooling rate at the initial transition from austenite, pearlite, and bainite.) However, maximizing cooling rates may increase the risk of quench crack formation. Numerous experimental studies have shown that as cooling rates within the martensitic transformation range increase, the probability of quench crack formation first increases to a maximum, then reduces to zero as shown in Figure 9.47 [10]. This was confirmed by calculation of the thermal and transformational quenching processes using finite-element methods and a mathematical model that included the equation of non-stationary heat conduction and equations for thermoelastic–plastic flow with kinematic strengthening under the appropriate boundary conditions. It was found that the tensile residual stresses first increase to a maximum value with increasing cooling rate, then decrease and change to compressive stresses. The probability of quench cracking decreases with increasing cooling rate due to the presence of high compressive stresses at the cooling metal

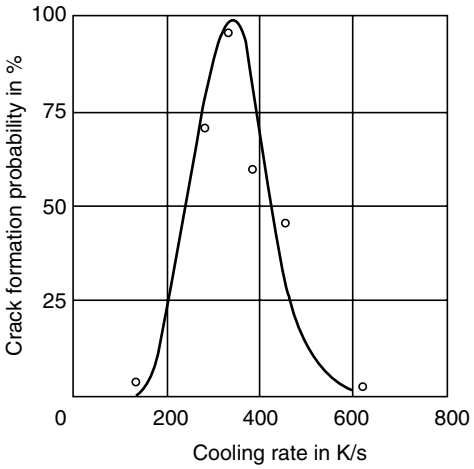

FIGURE 9.47 Probability of crack formation versus cooling rate within the martensite formation range of a 6-mm diameter steel cylinder (41Cr4 according to DIN).

surface. These results were validated by measurement of the surface residual stress of quenched parts.

The development of stresses during rapid cooling of solid steel cylinders is schematically illustrated in Figure 9.48. (Refs. [4,4a] provide an excellent overview on the formation of quench stresses.) The temperature at the surface and core of the solid cylinder and the corresponding stress components will be considered as functions of the cooling time. For simplification, ideal elastic deformation behavior and transformation-free quenching will be assumed.

Initially, the surface temperature decreases faster than the core temperature, as shown in Figure 9.48a. This causes the surface of the cylinder to contract more rapidly than the core, resulting in tensile residual stresses in the longitudinal and tangential directions. These stresses are balanced by compressive stresses in the core of the cylinder, as shown in Figure 9.48b. Maximum thermal stresses develop when the maximum temperature difference between surface and core (T_{max}) is attained at cooling time t_{max}. Maximum surface stresses occur at $t < t_{max}$, and maximum core stresses occur at a later time, $t > t_{max}$. At $t = t_{max}$, the temperature of the core decreases faster than that of the surface, leading to a reduction of the stresses in both regions. If these stresses are elastic, the cylinder is free of residual stresses after it reaches thermal equilibrium.

In reality, metals always exhibit elastic–plastic deformation behavior. The elastic deformation is limited by the yield strength of the material, which increases with decreasing material temperature. In Figure 9.48b, the yield strength of surface (S) and core (C) are plotted (in broken lines) assuming a transformation-free quenching process. As the longitudinal stresses approach the yield strength, plastic deformation begins. The surface is plastically extended, and the core is plastically compressed. Both effects reduce the stresses in the core and surface regions compared to the ideal elastic deformation behavior shown in Figure 9.48c.

At $t > t_{max}$, the temperature difference between the core and surface decreases and the shrinkage stresses in both regions are reduced. As a result of the plastic compression in the core and the plastic extension at the surface, the stresses of the core and surface become zero before the temperature balance is reached. At the end of the cooling process, the plastic deformations of core and surface produce tensile residual stresses at the core and compressive stresses at the surface.

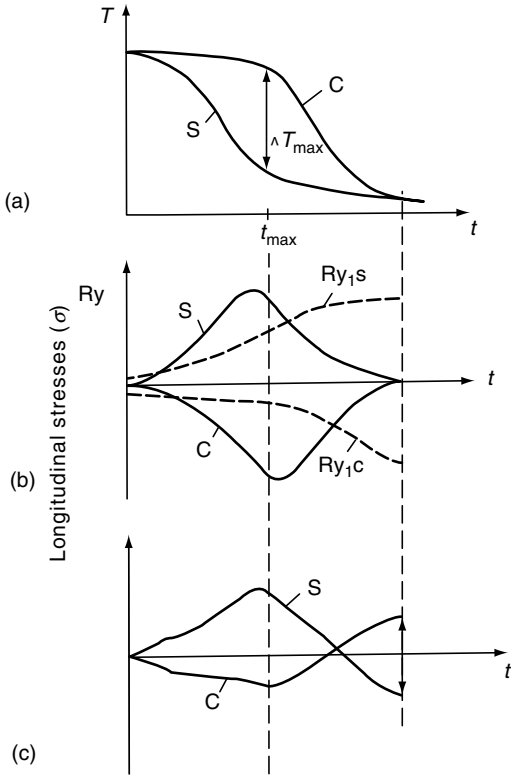

FIGURE 9.48 (a) Development of temperature and (b,c) formation of longitudinal stresses in the core and at the surface of a steel cylinder during transformation free quenching considering; (b) ideal elastic; (c) elastic–plastic deformation behavior (schematic). S, surface; C, core.

If phase transformations occur during quenching, they will result in thermal transformation stresses. For simplicity, it will be assumed that austenite is completely transformed into martensite and that the coefficient of thermal expansion is zero. This condition will produce no thermal stresses. Temperature–time curves for the surface and core of such a material are illustrated in Figure 9.49a. The surface of the cylinder begins transformation at t_1, at or below the martensite start temperature M_s. Volume expansions due to the formation of martensite produce compressive stresses at the surface, which are compensated for by tensile stresses within the core as shown in Figure 9.49b. Both stress components increase until the temperature of the core reaches the martensite start temperature, at time $t = t_2$. The volume increase of the core transformation immediately reduces the tensile stresses at the core and compressive stresses at the surface. Below the martensite finish temperature (M_f) in the core, the same amounts of martensite are formed within the cylinder and no residual stresses will occur if ideal elastic transformation behavior is assumed.

In elastic–plastic deformation, the temperature-dependent yield strength must be considered. Figure 9.49b shows yield strength variation at the surface and core with respect to cooling time. Martensitic formation strongly increases the yield strength at $T < M_s$. As the stresses approach the yield strength, the surface and core are plastically deformed as shown in Figure 9.49c. Upon further cooling, the stress values increase until the core temperature reaches M_s. The corresponding volume increase in the core reduces the stress values of both areas, and at temperature equilibrium, compressive stresses remain in the core and tensile stresses at the surface.

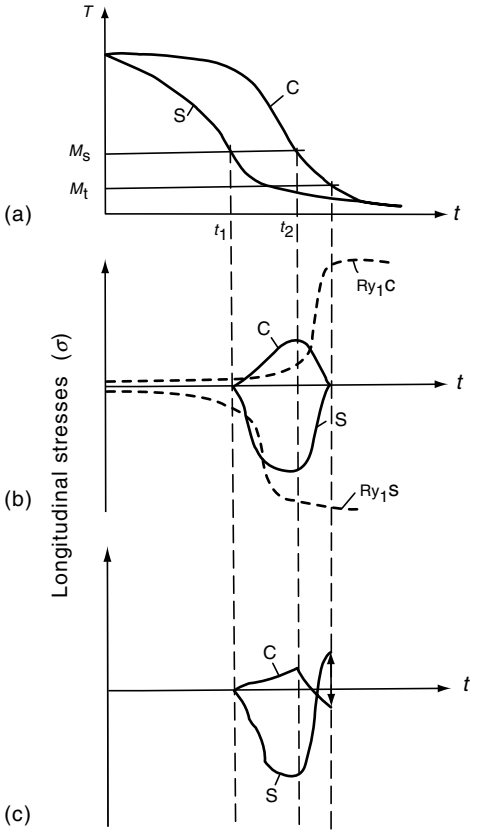

FIGURE 9.49 (a) Development of temperature and (b, c) formation of longitudinal stresses in the core and at the surface of a steel cylinder during (b) ideal elastic and (c) elastic–plastic deformation behavior, considering only austenite–martensite transformation and neglecting thermal expansion (schematic).

During quenching of hardenable steels, thermal and transformational stresses occur simultaneously. Residual stress after cooling is primarily determined by the time when transformation begins at the surface and in the core as expressed by the times t_1 and t_2, respectively, in relation to the time t_0 when the thermal stresses of surface and core change sign as shown in Figure 9.50a. Generally, transformations occurring in compressively stressed material increase the stresses, whereas transformations occurring in tensile-stressed areas reduce stresses. Figure 9.50b and Figure 9.50c illustrate the simultaneous formation of both thermal and transformational stresses. Figure 9.50b illustrates that both surface and core transformation start after time t_0. In this particular case, surface compressive stresses and tensile stresses occur in the core after quenching. Figure 9.50c shows the development of stresses when surface and core begin to transform before t_0. The increase of the specific volume at the surface after transformation initially reduces tensile stresses and causes surface compressive stresses upon further cooling. Tensile stresses occur when martensitic transformation begins in the core. This inverts the stress state in both areas, leading to compressive residual stresses in the core and tensile residual stresses at the surface after thermal equilibrium.

Figure 9.50 shows that the final stress state after quenching depends on the temperature gradient within the sample and on the transformation behavior of the material. However,

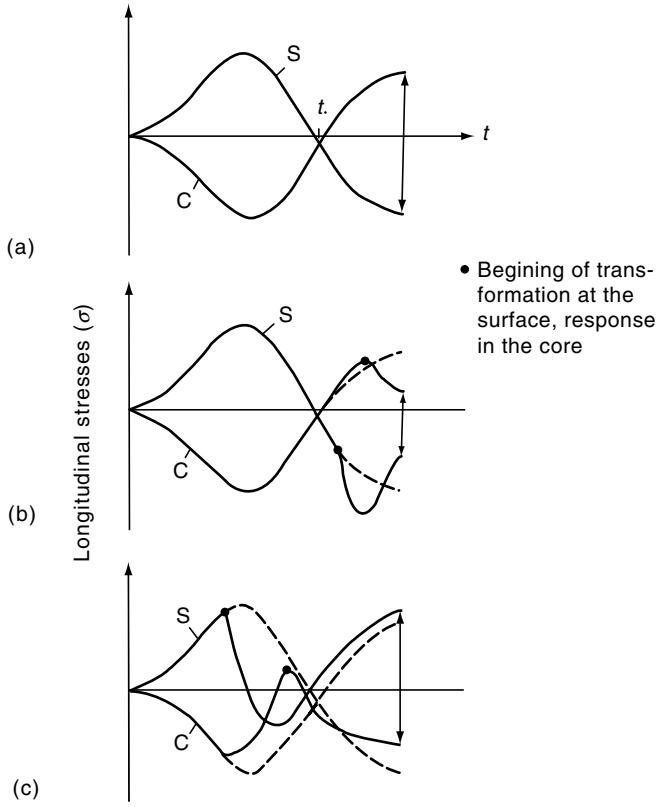

FIGURE 9.50 (a) Development of temperature and (b, c) formation of longitudinal stresses in the core and at the surface of a steel cylinder during transformation free quenching considering thermal expansion and martensite transformation (schematic).

measurements of residual stresses at the surface of quenched cylinders have shown that the M_s temperature strongly influences the sign of the stress values. Increasing M_s temperature decreases yield strength, and the tensile residual stresses change to transformation stresses as shown in Figure 9.51 [9]. Therefore, the effects of transformation plasticity must also be considered. (See Section 9.2.4.)

The development of residual stresses during intensive quenching is caused by transformation plasticity and changes in the specific volume due to the transformation of austenite into martensite. With rapid cooling rates, the surface temperature is cooled immediately to the bath temperature, while the core temperature is nearly unaffected. Rapid cooling causes surface layer contraction and high tensile stresses, which are balanced by stresses in the core. Increasing temperature gradients produce increasing tensile stresses at the beginning of martensite transformation, and increasing M_s temperatures produce surface layer expansions due to transformation plasticity as shown in Figure 9.7. If high M_s temperatures accompany high volume expansion during martensite transformation, surface tensile stresses are significantly reduced, changing to compressive stresses. The amount of surface compression is proportional to the amount of surface martensite formed. These surface compressive stresses dictate whether the martensitic transformation at the core occurs under compression or forces a tensile stress inversion at the surface during further cooling. If the volume increase of the core upon martensite transformation is sufficiently large and if the surface martensite layer is very hard and brittle, destruction of the surface layer may occur due to stress inversion.

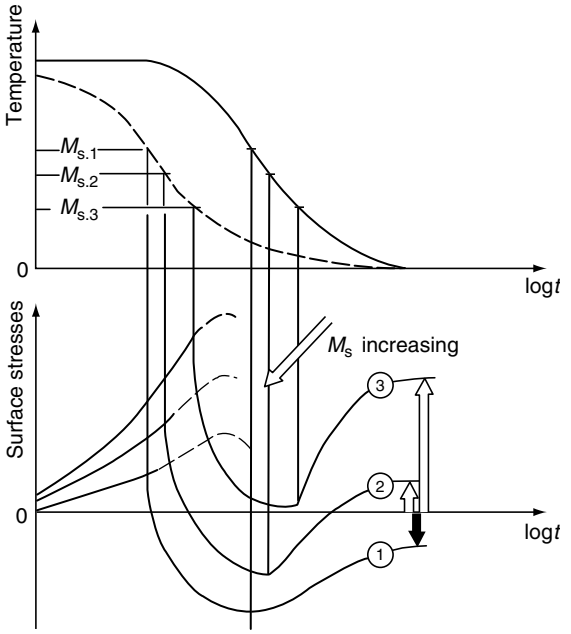

FIGURE 9.51 Effect of martensite start temperature M_s on the formation of longitudinal stresses at the surface of a cylinder (schematic).

Therefore, to ensure surface compressive stresses, martensite formation in the core must be retarded [10].

These results indicate that the intensive quenching process is stopped when surface maximum compressive stresses are formed. The isothermal cooling process is then held at approximately the M_s temperature. This will delay cooling at the core, thus retarding martensite formation, which will produce high surface compressive stresses. The intensive quenching process is completed when an optimal depth of the surface layer is achieved corresponding to maximum compressive stresses.

A second method for minimizing quench crack formation is to ensure material plasticity, which will occur if there is less than about 30% newly formed martensite in the supercooled austenite [10,53]. Initially, intensive quenching occurs until the surface temperature of the part is maintained at such a level that not more than 30% martensite can be formed in the subcooled austenite. Then the intensive quenching process is interrupted and the part is cooled in air until temperature equilibrium is achieved over the cross-section. The newly formed martensite in the surface zone is self-tempered and quench crack formation is hindered because stresses are decreased. Subsequently, intensive cooling to room temperature is applied to transform the rest of the austenite into martensite. The intensification of cooling within the martensite range improves the plastic characteristics of the material and increases its strength properties.

The advantage of intensive quenching methods is that high residual surface compressive stresses are created, reducing the probability of quench crack formation, with a corresponding improvement in hardness and strength values. Microstructures consisting of 100% martensite can be achieved at the surface, and a maximum hardening depth can be obtained for a given steel grade. In this way, an unalloyed carbon steel may be used instead of a more expensive alloy steel. Intensive quenching also produces more uniform mechanical properties

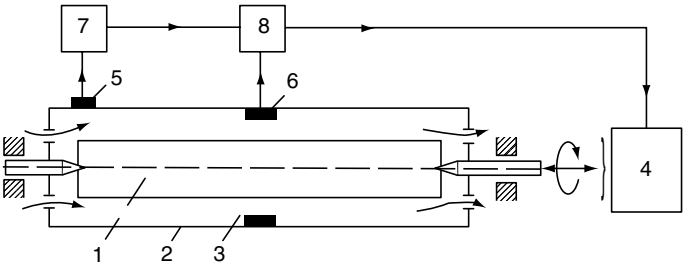

FIGURE 9.52 Quenching chamber for intensive quenching of semiaxes in a pressurized water flow: 1, semiaxis; 2, quenching chamber; 3, water flow; 4, mechanical drive for the semiaxis; 5, sensor for analyzing the process of film boiling and nucleate boiling; 6, sensor for analyzing the portion of formed structures; 7, 8, amplifiers.

and minimal distortion. Furthermore, it has been demonstrated that the service life under cyclic loads may be increased by approximately one order of magnitude [54].

Intensive quenching requires appropriate quenching facilities and quenching media. Quenching media include pressurized water streams, water containing various additives, and liquid nitrogen. Figure 9.52 shows a quenching chamber for the intensive cooling of an automobile semiaxis using pressurized water flow.

The water supply to the chamber and the charging and discharging of the axles are controlled by two sensors. The first sensor (5 in Figure 9.52) analyzes the process of film boiling and nucleate boiling, and the second, 6, describes the transformation of austenite into martensite by the change of the ferromagnetic state of the material. One method of intensive quenching has been used that achieves maximum compressive stresses at the surface when sensor 6 indicates a specific magnetic phase transformation. In this case, sensor 5 is used to minimize the duration of film boiling by regulating the water flow velocity. A second method has also been used, with sensor 5 indicating the beginning and completion of nucleate boiling, while sensor 6 controls the water pressure and determines the end of intensive quenching, so that no more than 30% martensite is formed.

Intensive quenching methods offer many possibilities for the successful cooling of parts with optimized strength properties and improved service life. However, a precondition for the use of this technology is the development of appropriate quenching equipment that enables precise control of the quenching performance. Ref. [4c] provides an overview of intensive quenching probes design.

9.8 PROPERTY PREDICTION METHODS

There are increasing demands on the heat treater to achieve as-quenched properties while simultaneously reducing heat treatment costs. To achieve these goals it is becoming increasingly important that experimentally or mathematically based methods to predetermine the as-quenched strength and hardness properties be applied with sufficient accuracy. Currently, a computer-based selection of steels and optimization of quenching conditions according to the desired service properties are generally possible. Hardenability is one of the most important properties to be predicted because it determines as-quenched microstructure formation. The ability to predict hardenability curves from chemical composition has already been described in Chapter 5, Section 5.4. However, these hardenability curves provide only limited information about the distribution of mechanical properties in the quenched part. It is necessary to correlate steel chemical composition, cooling rates during quenching, metallurgical transformation behavior, and the final physical properties. These correlations are often complex.

This section discusses various methods, ranging from relatively simple to more complicated methods, for determining the as-quenched hardness distribution. Traditionally only hardness values have been effectively predicted. However, with the application of computer technology, additional calculations of residual stresses and distortion are becoming increasingly possible, at least for simple shapes. A detailed overview of published methods for prediction of hardness is given in Ref. [55]. Ref. [46] provides an overview of the current status of predicting mechanical properties such as fatigue.

9.8.1 Potential Limitations to Hardness Prediction

The final hardness of a steel is determined by the amount of different microstructural constituents formed during cooling and by their individual hardnesses. The microstructures that develop with increasing cooling rate from the austenitizing temperature are ferrite–pearlite, bainite, and martensite, probably containing retained austenite. The individual hardnesses of these microstructures depend primarily on the chemical composition of the steel, especially the carbon content, and the cooling rate and formation temperature. For example, in a 1040 plain Carbon steel, austenite fully transforms into martensite with a HV of approximately 850 (HRC 66) at high cooling rates. At low cooling rates, ferrite and pearlite are formed with HV of about 200 (HRA 57). At medium cooling rates, microstructures consisting of ferrite, pearlite, bainite, and martensite are produced. To make hardness prediction more difficult, different microstructural combinations can have the same hardness, so that there is a one-way relationship between microstructural combinations and final hardness [56,57]:

$$[\text{Microstructure and microstructural combinations}] \rightarrow [\text{Final hardness}] \tag{9.7}$$

A two-way relationship exists only between the course of cooling and microstructure formation:

$$[T(t) \text{ curve during cooling}] \leftrightarrow [\text{Microstructure and microstructural combinations}] \tag{9.8}$$

Therefore, accurate prediction of the final hardness from the course of cooling always requires a quantification of the transformation structure:

$$\begin{aligned}[T(t) \text{ curve during cooling}] &\rightarrow [\text{Microstructure and microstructural combinations}] \\ &\rightarrow [\text{Final hardness}]\end{aligned} \tag{9.9}$$

Even with these restrictions, several methods of hardness prediction have been developed that use the simplified, but physically incorrect, assignment of hardness from cooling curves:

$$[T(t) \text{ curve during cooling}] \rightarrow [\text{Final hardness}] \tag{9.10}$$

Cooling curves obtained at different points over the cross-section of real parts are compared to temperature–time relationships obtained from Jominy end-quench tests or CCT diagrams. However, these data describe only those transformations of austenite that occur along the cooling curves of the specimens used for their construction. Therefore, the accuracy of predicted hardness values depend on how well cooling curves in real parts correlate to the cooling of the steel that was used for the construction of the CCT diagrams or Jominy end-quench hardness curves.

An example of insufficient conformity between these data is provided in Figure 9.53, which compares cooling curves that were obtained at different points in solid austenitic

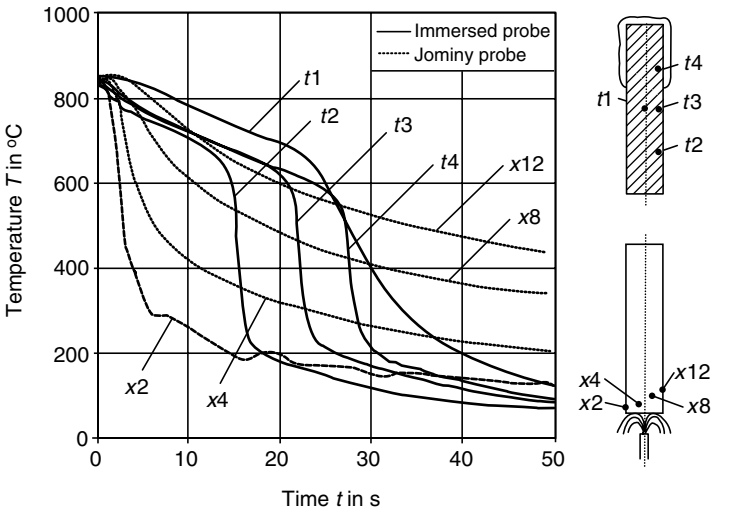

FIGURE 9.53 Cooling curves for the surface of a Jominy probe 2, 4, 8, and 12 mm from the quenched end (dashed lines) and for an identical cylinder quenched in 60°C water flowing at 0.3 m/s for the points 1 mm below the surface at 25-, 50-, and 75-mm height and for the probe center (full lines). Material: austenitic stainless steel. Geometry: 25 × 100 mm. (From J.G. Leidenfrost, *J. Heat Mass Transfer 9*: 1153–1166 (1966), translated by C. Waves.)

stainless steel cylinder that was immersion-quenched in 60°C (140°F) water flowing at 0.3 m/s (solid lines) and spray quenched with 12°C (54°F) water at the lower end-face of a test bar from a Jominy end-quench test (dashed lines) [12]. Cooling curves obtained in the end-quench test have progressively lower cooling rates with increasing distance from the water-quenched end and differ completely from those produced with the immersion-quenched cylinder, which have low cooling rates in the vapor blanket stage and highest cooling rates in the nucleate boiling stage. Therefore, for the same cooling time $t_{g/5}$, from 800 to 500°C (1472 to 932°F), the microstructure formed may be quite different if different temperature–time cycles are applied.

In addition to proper modeling of the cooling process, exact prediction of the material properties also requires that all the metallurgical and thermal boundary condition reference curves and the production quenching process be similar. These are material composition and initial microstructure before austenitizing, the austenitizing conditions (temperature and time), and the chemical properties of the quenchant and its physical state (viscosity, temperature and flow conditions).

9.8.2 Grossmann *H*-Values

A practical method to predict the hardness distribution in a steel cylinder after quenching is based on the Grossmann *H*-value [35]. The *H*-value reflects the ability of a quenchant to remove heat from the surface of a hot workpiece during quenching and is defined by the heat transfer coefficient divided by twice the thermal conductivity (see Equation 9.5). The *H*-value of still water at 18°C (64°F) is usually taken as 1.0. *H*-values of oil, water, and brine with different bath temperatures and flow velocities are provided in Table 9.3 (see Section 9.6.2) [58]. They are commonly determined by recording a cooling curve in the center of a test probe, determining the average cooling rate within a temperature region (e.g., from 700°C to 600°C [1292 to 1112°F]) and comparing it with the cooling rate at standard conditions, i.e., for still

water at 18°C (64°F). A polynomial expression has been published that allows a direct estimation of the *H*-value from the center cooling rate at 700°C (1292°F) [59,60].

When using *H*-values, it is important one has to be aware that *H* is a constant and does not describe the heat transfer conditions at the surface of a workpiece quenched in a vaporizable fluid. It is well known that the heat transfer coefficient α varies substantially with the three different stages of cooling—film boiling, nucleate boiling, and convection—and also varies with the wetting sequence, i.e., with the actual position of the wetting front (see Section 9.6). The thermal conductivity (λ) of steel depends on temperature and possible microstructural changes.

Figure 9.54 compares the temperature–time curve and the temperature–heat flux density curve of an actual cooling process with values calculated using a constant *H*-value [61]. The solid line was obtained at the center of an 8-mm diameter silver cylinder quenched in oil; the dashed line was calculated according to Newton's law of cooling with a constant *H*-value of 0.42 in.$^{-1}$. As Figure 9.54a illustrates, the calculated cooling curve does not show the rapid decrease in temperature that occurs in the nucleate boiling stage and intersects the actual cooling curve at temperature T_H (temperature halfway between austenitizing temperature and bath temperature).

Another limitation of *H*-values is that sample size is not accounted for when the *H*-value is determined from core cooling curves. Cooling curves measured in the core of steel cylinders do not reflect the heat flux at the surface due to the damping effect of thermal conductivity (λ).

Figure 9.55 illustrates that the temperature difference between surface and core increases with increasing bar diameter [9]. For example, after 40 s, when the temperature within the cylinder of smallest cross-section has decreased below 180°C (356°F) and the convection stage begins, the surface temperature of the 100-mm diameter cylinder has only cooled to approximately 380°C (716°F), and the temperature at the core is 700°C (1292°F). This shows that the

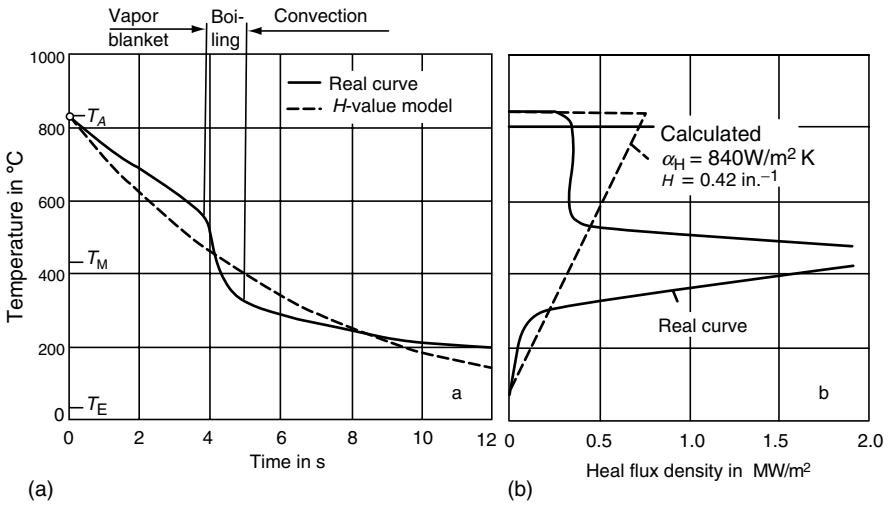

FIGURE 9.54 (a) Temperature–time curves and (b) temperature–heat flux density curves for an 8-mm diameter silver cylinder quenched in oil. The full lines are the real curves, the dashed lines are calculated using an *H*-value of 0.42 in.$^{-1}$. T_A: temperature at start of cooling, T_E: temperature at the end of cooling, T_H: half-temperature. $T_H = (T_A - T_E)/2 + T_E$. (From International Standard ISO/9950, Industrial Quenching Oils—Determination of Cooling Characteristics—Laboratory Test Method.)

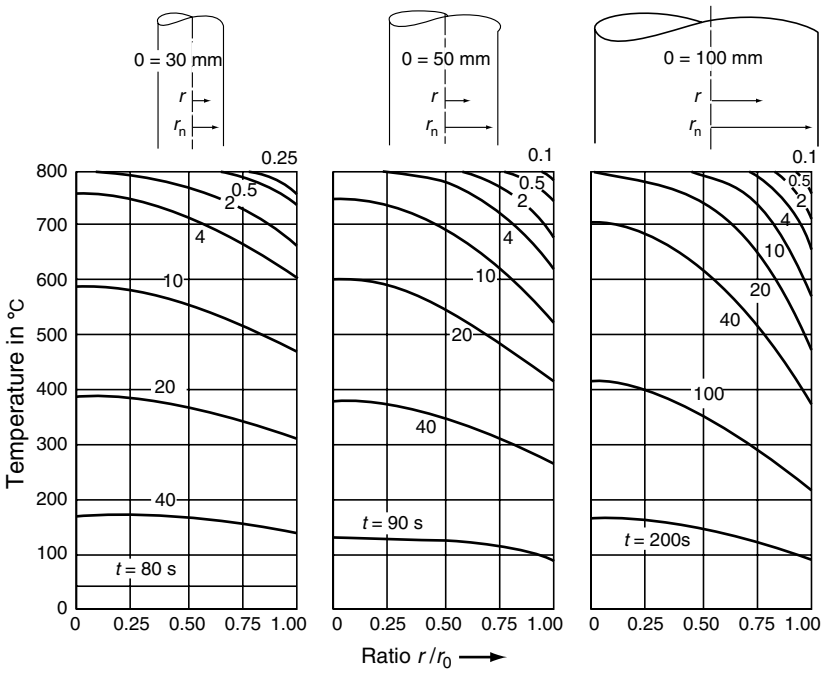

FIGURE 9.55 Calculated temperature distributions at selected times as a function of the radius ratio for 30-, 50-, and 100-mm diameter cylinders (34Cr4 steel) quenched in water at 20°C. (From W. Pitsch and S. Sauthof, Microstructure of steels, in *Steel: A Handbook for Material Research and Engineering*, Vols. 1 and 2, Springer-Verlag, New York, 1991, 1992.)

heat transfer conditions at the surface differ substantially from those at the core. Depending on sample dimensions and the cooling conditions, heat extraction from the surface can occur during the film boiling, nucleate boiling, or convection stage. Therefore, application of *H*-values determined from a relatively small cross-section (a diameter of 12.7 mm is often used) to larger cross-sections is fundamentally erroneous.

For hardness predictions, reference *H*-values are typically taken from a reference table (see Table 9.3), accounting for the particular quenchant bath temperature and agitation. (Another fundamental limitation of this approach is that the reference data do not adequately quantify either flow rates or turbulence.) Temperature–time cycles at different locations over the cross-section are calculated from the solution of the heat transfer equation (Equation 9.2) using the determined *H*-value. The calculation of hardness is based on the supposition that specimens that were made of the same steel grade have followed the same law of cooling if they have the same hardness. That means that if a point of the cross-section of a quenched part has the same hardness as the point shown, e.g., at a given distance from the quenched end of a Jominy specimen made from the steel that is quenched, both points have undergone identical cooling processes. Therefore, a calculated cooling curve at a point on the cross-section of the quenched part is related to an equivalent Jominy distance whose cooling curve shows the identical half-temperature time t_H (time until T_H is reached, as shown in Figure 9.54a). The corresponding hardness of the Jominy hardenability curve yields the hardness at the cross-sectional location in question. Of course, this supposition is not necessarily correct and can be taken only as an approximation, because the shape of the cooling curve obtained in the actual quenching process and that achieved in the end-quench test may differ considerably (see Figure 9.53).

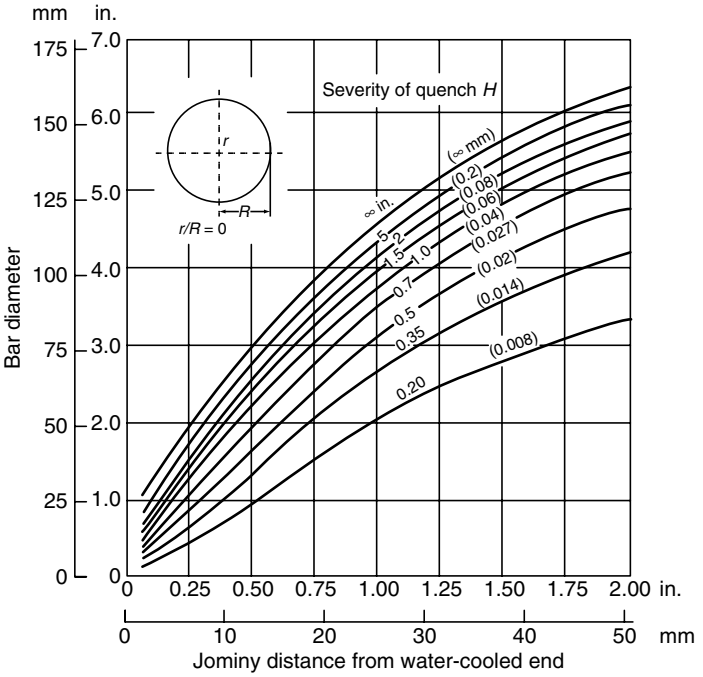

FIGURE 9.56 Lamont diagram for the center of round bars: the relation between bar diameter and distance from the quenched end of a Jominy probe for different *H*-values. (From H.M. Tensi, P. Stitzelberger-Jakob, and A. Stich, A Proposal for Standardization: Industrial Polymer Quenchants—Determination of Cooling Characteristics—Laboratory Test Method, 1992.)

Grossmann et al. [62] or Lamont [63] diagrams interrelate the *H*-value, bar diameter, and hardenability of the steel and have been used to calculate hardness. The Lamont diagram shown in Figure 9.56 is applicable for the center of round bars. Lamont developed these diagrams for different radius ratios in the range $0 \leq r/R \leq 1$, in steps of 0.1. In this diagram, *H*-values are plotted as follows. If a 25-mm bar is quenched in a strongly agitated oil quench, which is assigned an *H*-value of ≈ 0.7 in.$^{-1}$, the value of 6.35 mm of the Jominy hardenability specimen is obtained by reading the diagram across the 25-mm horizontal line to the line of $H = 0.7$ in.$^{-1}$ and then down as shown. This means that the core of the bar will have the indicated hardness at 6.35 mm from the quenched end of the Jominy hardenability specimen made of the steel that is quenched.

9.8.3 The QTA Method

As opposed to the Grossmann approach, the QTA method developed by Wünning et al. [61,64,65] does account for the three stages of cooling—film boiling, nucleate boiling, and convective heat transfer—which are described by the three model parameters *Q*, *T*, and *A*.

Q is the average heat flux density on the surface of the quenched part until it cools to the surface temperature at which the vapor envelope collapses, i.e., the wetting temperature T_L. Because T_L values are generally unavailable (the wetting temperature is influenced by many factors, some of which cannot be exactly quantified), Wünning recommends the use of a constant T_L value of 500°C (932°F). To determine the value of *Q* for each particular quenching process, a standard steel probe with a known hardenability is used.

T is the temperature at which the extrapolated line of the heat flux density in the nucleate boiling stage intersects the zero temperature axis as shown in Figure 9.57. This temperature

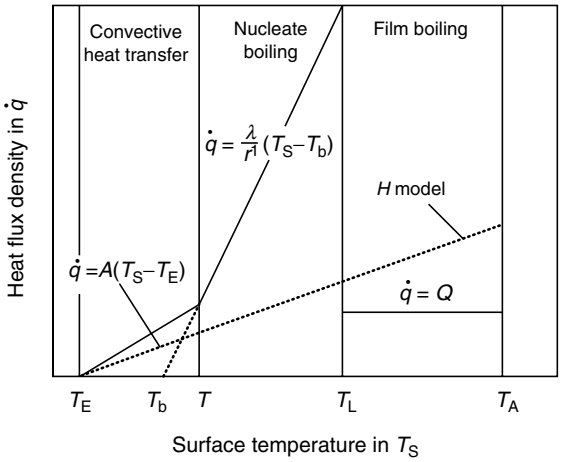

FIGURE 9.57 Parameters of the QTA model.

approximately corresponds to the boiling temperature of the quenchant and therefore does not depend on the cooling conditions ($T \approx T_b$).

A is the average heat transfer coefficient of the convention phase and can be calculated using known heat transfer relationships.

Surface heat transfer described by the QTA model is illustrated in Figure 9.57. During the film boiling stage, the temperature variations are calculated using the heat flux density Q. The parameter Q depends on the properties of the fluid (thermal conductivity, viscosity, etc.), the subcooling and flow conditions, and the geometry of the part. The assumption of constant average heat flux density is valid because the cooling course in the film boiling stage is usually linear. At the wetting temperature T_L (500°C [932°F]), transition from the film boiling to the nucleate boiling occurs.

The heat transfer coefficient increases by up to two orders of magnitude so that the heat extraction from the surface can be calculated using the first boundary condition assuming that the surface temperature drops immediately to temperature T. To dampen this infinitely high heat transfer rate, the temperature T is arbitrarily assigned the distance r' on the sample surface. According to Wünning, r' is 1 mm for quenching in water and 2 mm for quenching in oil.

The transition from nucleate boiling to convective cooling occurs when the heat flux densities become equal. This temperature (T) is approximately the boiling temperature of the quenchant, $T_b = T$.

The value A depends on the agitation rate and on the dimensions of the workpieces. Although A-values can be calculated from the physical conditions of the quenchant and the T-value can be determined from a laboratory test, the Q-value must be measured under workshop conditions. Wünning claims that only one hardness measurement is necessary to define the Q-value of a steel part quenched under known conditions, provided that a calibration curve is available describing the relationship between different Q-values and the resulting as-quenched hardness. The calibration curve is determined using a standard Q-probe made of low-alloy steel (Wünning suggests DIN 46Cr2 steel) with 25–30-mm diameter and a length of 100 mm. Using different quenching conditions, the temperature–time cooling curve at radius ratio $r/R = 0.7$ and the corresponding hardness value are measured. Calculations have shown that for most applications the average cooling curve follows the cooling curve at $r = 0.7R$. The Q-value is then inversely proportional to the

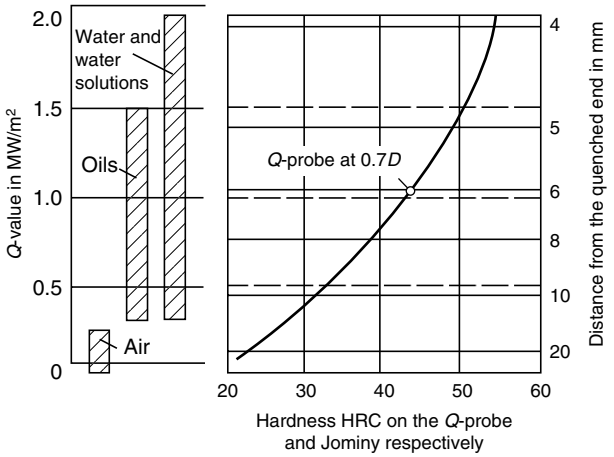

FIGURE 9.58 Calibration curve for the Q-probe, relation between Q value at $0.7R$ and hardness on the Q-probe. The hardness is also related to the distance of the quenched end of the Jominy specimen. (From H.M. Tensi, A. Stich, and G.E. Totten, Fundamentals about quenching by submerging, *Proceedings of the 1st International Conference Equipment and Processes*, 18–20 April, 1994, Schaumburg, IL, published by ASM International.)

cooling time down to 500°C (932°F) ($T = 500$°C) and depends on the thermodynamic properties of the material and the volume–surface relation:

$$Q = \rho C_p \frac{V}{A}\left(T_A - T\frac{500^\circ\text{C}}{t_{500^\circ\text{C}}}\right) \tag{9.11}$$

The Q value for a batch of workpieces under particular quenching conditions can be determined by measuring the hardness at the point $0.7R$ of the Q-probe quenched in exactly the same manner. Figure 9.58 illustrates the calibration curve for the Q-probe and interrelates the Q-values to the appropriate Jominy hardenability curve. If, after quenching, a hardness of 44 HRC is measured at point $0.7R$, Q yields a value of 1.05 MW/m^2 while the same hardness is found at a distance of 6 mm from the water-cooled end of the Jominy sample.

Figure 9.59 validates that the rapid decline of temperature during the nucleate boiling stage can be modeled by calculations based on the QTA model but that cooling to 500°C (932°F) is less accurate relative to the actual cooling curve. A more precise calculation can be obtained using the actual value of wetting temperature. According to Lübben et al. [66], the QTA model is limited by the assumption that Q-values and hardness strongly depend on the boiling temperature of the fluid. The use of a single Q-probe made of a particular steel is not sufficient for establishing the calibration curve because the hardness at point $0.7R$ of the standard Q-probe (steel 46Cr2) is occasionally insensitive to variations of Q, especially for hot oils. However, the QTA model can still produce reasonably accurate calculations of cooling curves at different points of a workpiece taking into account the boiling effects. Thus the results can be used as input data in property prediction methods such as those described next.

9.8.4 Correlation between Hardness and Wetting Kinematics

One limitation of property prediction methods is that correlations between wetting kinematics and metallurgical properties for various still alloys have not been performed. Therefore,

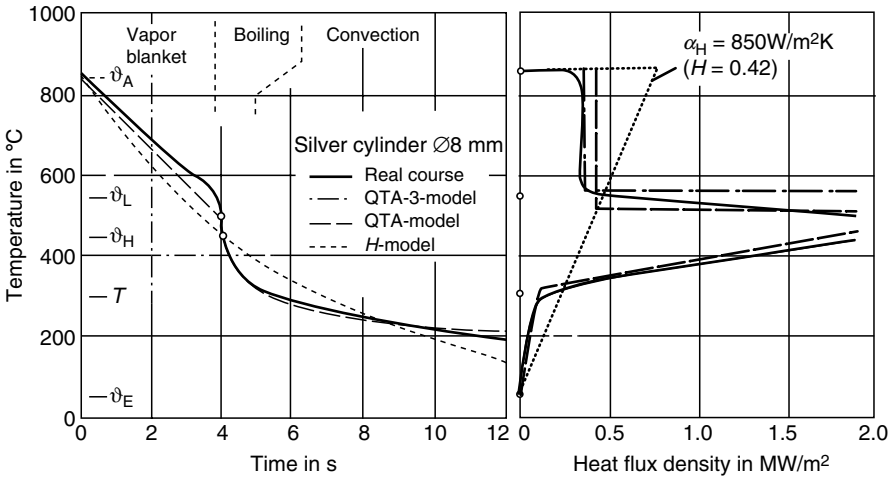

FIGURE 9.59 (a) Temperature–time curves and (b) temperature–heat flux density curves for a 9-mm diameter silver cylinder quenched in oil. Solid lines are the real curves; the dashed lines were calculated using a constant *H*-value, the QTA model, and the QTA-3 model. (From International Standard ISO/DIS 9950, Industrial Quenching Oils—Determination of Cooling Characteristics—Laboratory Test Method.)

correlation diagrams between surface hardness and wetting time have recently been developed for various steels. Figure 9.60 shows that a wetting time of more than 25 s was observed for a 1040 steel quenched in 30°C (86°F) water flowing at 0.3 m/s. The vapor envelope first collapses at the bottom of the cylinder, and the wetting time increases toward the top for solid cylindrical test piece. The hardness values measured along the cylinder length decrease with the progression of the wetting front. From this plot, a correlation between surface hardness and wetting time can be derived that may be used as a calibration curve for hardness prediction. The prediction method itself is based on the fact that the heat extraction on the surface of a quenched part varies with the position of the wetting front but varies only slightly

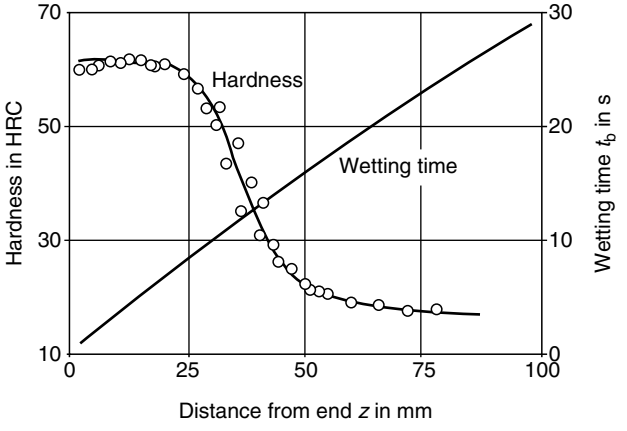

FIGURE 9.60 Surface hardness (HV) and wetting time t_b as a function of the distance from the lower end of a 1040 steel bar of 25-mm diameter and 100-mm length quenched from 850°C in 30°C water flowing at 0.5 m/s.

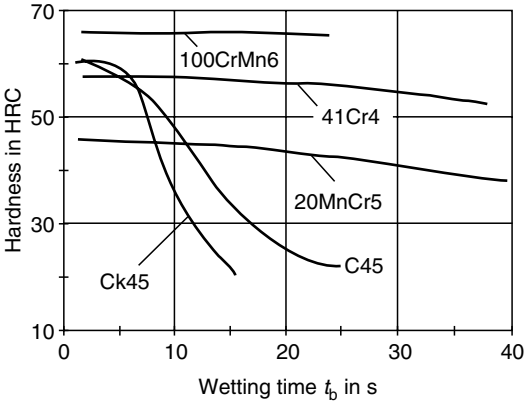

FIGURE 9.61 Calibration curves for selected steels. Relation between surface hardness and wetting time for quenching in water and an initial state of the material defined by the steel composition and the austenitizing conditions. (From J.G. Leidenfrost, *J. Heat Mass Transfer 9*: 1153–1166 (1966), translated by C. Waves.)

with the quenching conditions in identical quenching liquids. Therefore, the same hardness can be expected at points showing the same wetting time [15,22,57,67].

The correlation between surface hardness and wetting time shown in Figure 9.61 was developed from a series of calibration tests in water with five different solid steel cylindrical specimens (100-mm long and 25 mm in diameter) [12]. Hardness increased with carbon concentration and decreased with decreasing concentration of other alloying elements. The higher hardenability of the 1045 steel compared to the 1040 steel (nominally both steels have the same concentration of carbon and alloying elements) depends on deviations in the chemical composition and the higher austenitizing temperature (880°C [1616°F] and 850°C [1562°F], respectively). This result shows that the relationship between surface hardness and wetting time is valid only for the initial state of the material, metallurgically defined by alloy composition and the austenitizing temperature. Similar calibration curves must be developed for other quenchants.

Calibration curves permit reliable prediction of surface hardness obtained with varying wetting conditions such as bath temperature and agitation rate. Two procedures have been developed for obtaining wetting times, one by recording cooling curves at different heights of a cylinder with multiple thermocouples as described previously in Section 9.5.2.2 and the other by measuring the change of conductance between the quenched workpiece and a counter electrode, described previously in Section 9.5.2.1. The hardness at a certain point of the workpiece surface is then derived from the calibration curve and wetting time. Interestingly, no effect on section size was found for the calibration curves when 15-, 25-, and 40-min diameter probes were quenched in water [12]. These calibration curves are used to correlate the critical wetting time with hardness. A 100% martensitic microstructure can be achieved only when the time t_f at the conclusion of wetting is less than the cooling time where martensite is formed.

For hardness determination across the cylinder cross-section, a method is suggested that is based on the Grossmann *H*-value and the Jominy hardenability curve for the steel which is quenched [15,57,67]. However, the *H*-values are not taken from a table but are determined from the Lamont diagram of the surface $r/R = 1$. The equivalent distance from the quenched end of the Jominy sample is determined from the surface hardness of the cylindrical section desired, which is obtained from the calibration and wetting time. Then, from the Lamont

diagram for the surface, the intersection of the horizontal line of the bar diameter and the line of the determined Jominy distance provides the H-value. This H-value is then used to calculate the Jominy distances corresponding to different radius ratios r/R of the quenched sample. From the Jominy hardenability curve, each Jominy distance is assigned to a specific hardness value. If these hardness values are transferred to the immersion-cooled cylinder, the radial hardness profile is determined.

If the three determined phases of cooling vapor blanket, nucleate boiling, and convective heat transfer are simultaneously present on the sample surface, large variations in axial cooling occur, which will produce axial hardness gradients as shown in Figure 9.60. In this case, different hardnesses along the cylinder length produce different H-values for each distance z from the lower cylinder end-face.

9.8.5 Computer-Based Calculation of Hardness Profile

Finite-element modeling has been used to compute the transient temperature fields in a quenched part and to predict microstructure and properties such as hardness or residual stresses. In this method, the temperature and corresponding phase transformation are predicted, and in the second step the corresponding mechanical properties are calculated. These microstructural calculations assume that the transformation of austenite during continuous cooling is predicted by dividing a cooling curve into discrete temperature–time increments and comparing the amount of time at each horizontal step with the transformations that occur at that temperature in the isothermal time–temperature–transformation (TTT) diagram [68–71] (Figure 9.62). The transfer from isothermal to continuous cooling conditions at a certain temperature is determined using the Avrami equation

$$w_{\mathrm{f/p/b}} = 1 - \exp[-b(t/t_0)^n] \tag{9.12}$$

where $w_{\mathrm{f/p/b}}$ is the volume fraction of austenite transformed into ferrite–pearlite or bainite, t is the transformation time, t_0 is the reference time, b is the coefficient of the austenite transformation kinetics, and n is the exponent of the austenite transformation kinetics. The values of b and n depend on the transformation temperature and are fitted for each individual steel grade from the transformation curves plotted in the isothermal TTT diagram.

The microstructural computation sequence is illustrated in Figure 9.63. Austenite transformation begins when the actual time step represents the line for 1% volume fraction transformed. If at temperature T_i the volume fraction of transformed austenite is w_i, then according to Equation 9.11 the fictitious time $t_{i+1,\mathrm{fict.}}$ is calculated where the same volume fraction would transform at temperature T_{i+1}. This time is added to the time interval Δt_{i+1} and then the total transformed volume fraction of austenite w_{i+1} at temperature T_{i+1} is calculated. The new transformed volume fraction is $w_{i+1} - w_i$.

If in a known temperature range the austenite transforms into two microstructures, e.g., into microstructures a and b, then it is assumed that microstructure a ceases to grow when microstructure b has increased to 1%. If correct data are available, an overlapping transformation can likewise be represented.

The athermic transformation of austenite into martensite below the martensite start temperature M_s is described by the equations

$$w_{\mathrm{M}} = 1 - \exp[c(M_s - T)^m] \tag{9.13}$$

or

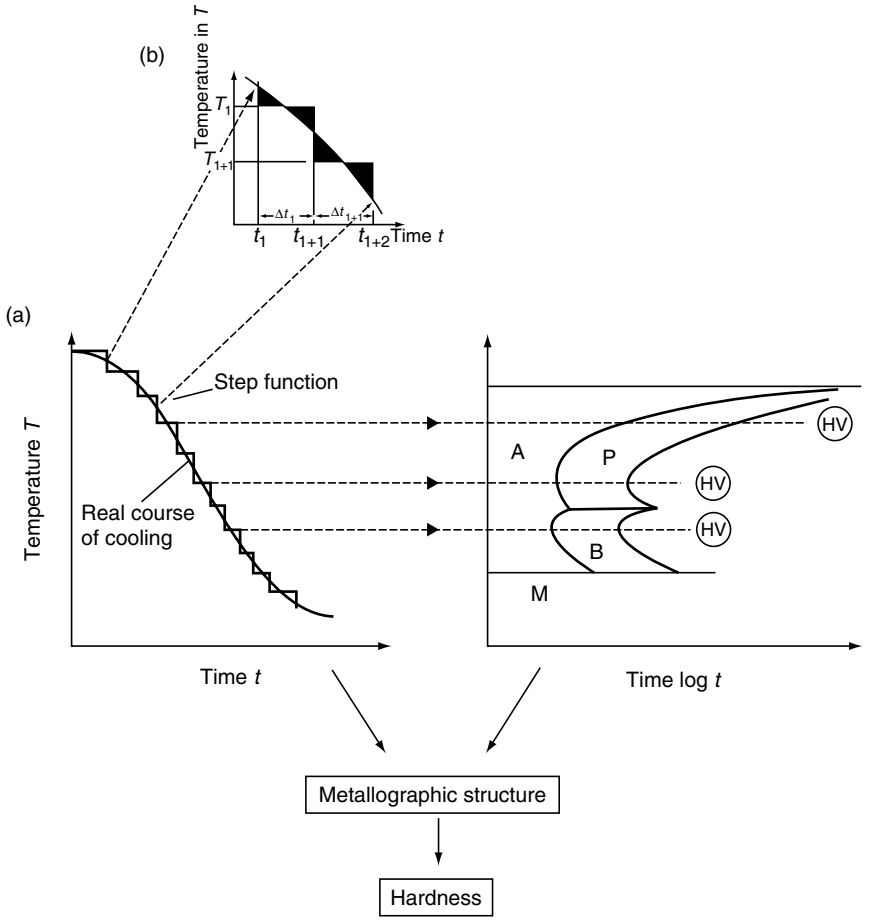

FIGURE 9.62 Prediction of microstructure and mechanical properties by dividing a cooling curve into a step function and comparing the horizontal steps to the transformations in the isothermal TTT diagram (schematic).

$$w_{\mathrm{M}} = 1 - \left(\frac{T - M_{\mathrm{f}}}{M_{\mathrm{s}} - M_{\mathrm{f}}}\right)^{m} \tag{9.14}$$

where w_{M} is the volume fraction of the austenite that transformed into a martensite, M_{s} is the martensite start temperature, T is the transformation temperature, c is the coefficient of austenite transformation, and m is the exponent of austenite transformation.

The final hardness after quenching can be determined by applying an additivity rule provided that the hardness values of the different microstructures formed at the individual temperatures are known [72]:

$$\mathrm{HV} = \Sigma\{\Sigma[\Delta w_k(\mathrm{T}_i)\mathrm{HV}_k(T_i)]\} \tag{9.15}$$

where HV is the final hardness at a defined location, w_k is the volume fraction of microstructure k formed at temperature T_i, and HV_k is the microhardness of microstructure k formed at temperature T_i.

This method can be used to predict the transformation behavior of austenite during continuous cooling and then to calculate the mechanical properties of the final product

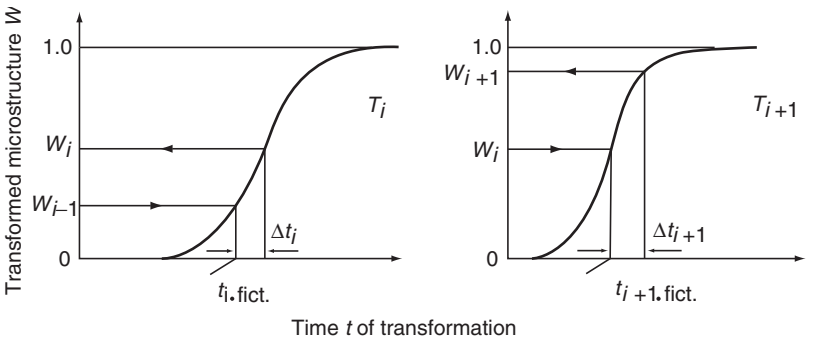

FIGURE 9.63 Sequence of the microstructural computation for iteration steps i and $i+1$. (From H.M. Tensi, A. Stich, H.-J. Spies, and A. Spengler, Grundlagen des Abschreckens durch Tauchkühlen, *Proceedings of ATTT/AWT Tagung Abkühlen/Abschrecken*, 20–21 April, 1994, Strasbourg, France, pp. 43–50.)

based on the predicted microstructure. The effect of latent heat evolution on the temperature–time cycle and the transformation kinetics can be taken into account. But this method is limited by the isothermal TTT diagram, which usually fails to give reliable information on the transformation behavior of an actual quenched part because of deviations in the chemical composition within the standard range, segregations within the workpiece, and variations in the initial microstructures prior to austenitizing. In addition, the effects of transformation plasticity are not quantified. Another limitation is that Equation 9.11 is based only on empirical data for the transformation behavior. Theoretical approaches to nucleation and nuclear growth are more suitable and provide a greater range of application. Finally, it is questionable whether the application of isothermal transformation kinetics of austenite to a continuous cooling curve that is divided into a step function is even permissible.

LIST OF SYMBOLS

A	surface, m^2
A	elongation, %
A	parameter of the QTA model, average heat transfer coefficient of the convection stage, $W/(m^2K)$
A_b	temperature of beginning bainite formation dependent on cooling rate, °C
A_{r1}	temperature of beginning pearlite formation dependent on cooling rate, eutectoid temperature, °C
A_{r3}	temperature of proeutectoid ferrite precipitation dependent on cooling rate, °C
$A_{r'}$	temperature of beginning pearlite transformation and suppression of ferrite precipitation dependent on cooling rate, °C
Bi	BiOT number, dimensionless
G	electrical conductance, S
H	heat transfer equivalent, m^{-1} or $in.^{-1}$
HV	Vickers hardness
M_f	temperature for completing the martensite formation, °C
M_s	temperature at beginning of martensite formation, °C
Q	parameter of the QTA model, average heat flux density of the vapor blanket stage from austenitizing temperature to 500° (932°F), W/m^2

R	probe radius, m
R_m	tensile strength, Pa
R_p	yield strength, Pa
T	temperature, °C
T	parameter of the QTA model, temperature at which the extrapolated line of heat flux density of the nucleate boiling stage intersects the zero temperature axis, °C
T_A	starting temperature in sample (austenitizing temperature), °C
T_E	temperature at the end of cooling, °C
T_H	half-temperature [$= (T_A - T_E)/2 + T_E$], °C
T_b	boiling temperature of the quenchant, °C
T_s	core temperature at which wetting begins, °C
T_s	surface temperature of the probe, °C
T_{trans}	transition temperature, core temperature at the point of transition from lower to higher cooling rate, °C
$\dot{T}_{max}$	highest core cooling rate, K/s
$\dot{T}_{300°C}$	cooling rate at 300°C (572°F), K/s
V	probe volume, m^3
a	thermal conductivity ($=\lambda/\rho C_p$), m^2/s
b	coefficient of heat penetration, W $s^{1/2}$(m K)
C_p	specific heat capacity, J/kg K
$\dot{q}$	heat flux density, W/m^2
$\dot{q}_\lambda$	heat transfer by conduction, W/m^2
$\dot{q}_\varepsilon$	heat transfer by radiation, W/m^2
$\dot{q}_v$	heat transfer by vaporization of the fluid, W/m^2
t	time, s
$t_{A/5}$	time from austenitizing temperature down to 500°C (932°F), s
t_b	wetting time, s
t_s	time at which wetting starts, s
t_f	time at which wetting is finished, s
w	average velocity of the ascending wetting front, mm/s
$w_{f/p/b}$	volume fraction of austenite transformed into ferrite/pearlite or bainite, %
w_M	volume fraction of austenite transformed into martensite, %
α	heat transfer coefficient, W/(m^2 K)
α_{conv}	heat transfer coefficient of the convection stage, W/(m^2 K)
α_{FB}	heat transfer coefficient of the film boiling stage, W/(m^2 K)
α_{NB}	heat transfer coefficient of the nucleate boiling stage, W/(m^2 K)
δ	thickness of film boiling phase, m
λ	heat conductivity, W/(m K)
ρ	density, kg/m^3
Δt_w	time interval of simultaneous presence of film boiling and nucleate boiling ($=t_f - t_s$), s

REFERENCES

1. D. Hortsmann, Das Zustandsschaubild Eisen-Kohlenstoff, in Bericht Nr. 180 des Werkstoffausschusses des Vereins Deutscher Eisenhüttenleute, 6 Aufl., 1985, Verlag Stahleisen m.b.H., Düsseldorf.
2. *Metals Handbook*, Vol. 8, *Metallography, Structures, and Phase Diagrams*, 8th ed., ASM International, Cleveland, OH, 1973.
3. H.P. Hougardy, Description and control of transformation in technical applications, in *Steel: A Handbook for Material Research and Engineering*, Vols. 1 and 2, Springer-Verlag, New York, 1991, 1992.

4. W. Pitsch and S. Sauthof, Microstructure of steels, in *Steel: A Handbook for Material Research and Engineering*, Vols. 1 and 2, Springer-Verlag, New York, 1991, 1992.
4a. G. Totten, M. Howes, and T. Inowe, *Handbook of Residual Stress and Deformation of Steel*, 2002, ASM International, Material Park, OH, pp. 499.
4b. E. El-magd, Modeling and Simulation of Mechanical Behaviour, in *Modeling and Simulation for Material Selection and Mechanical Design*, G.R. Totten, L. Xie and K. Funatani, Eds., 2004, Marcel Dekker, New York, NY, pp. 195–300.
4c. N.I. Kobasko, B.K. Ushakov, and W.S. Morhunink, chapter 17–Design of steel Intensive Quench Processes, in Handbook of Metallurgical Process Design, G.E. Totten, K. Funatani, and L. Xie, Eds., 2004, Marcel Dekker, New York, NY, pp. 733–764.
5. F. Wever, A. Rose, W. Peter, W. Strassburg, and L. Rademacher, *Atlas zur Wärmebehandlung der Stähle*, Max-Planck-Institut für Eisenforschung in Zusammenarbeit mit dem Werkstoffausschuss des Vereins deutscher Eisenhüttenleute, VDI Verlag Stahleisen mbH, Dusseldorf, Germany, Vols. 1–4, 1954–1956.
6. A. Kulmberg, F. Kornteuer, and E. Kaiser, *HTM 42*: 69–74 (1987).
7. U. Wass, Die wichtigsten Gesetzmässigkeiten des Verzugs bei der Wärmebehandlung von Stählen, in *Wärmebehandlung der Bau- und Werkzeugstähle*, W. Benninghoff, Ed., BAZ-Verlag, Basel, 1978.
8. H.-J. Eckstein, *Wärmebehandlung van Stahl*, VEB Deutscher Verlag für Grundstoffindustrie, 1971.
9. E. Macherauch and O. Vöhringer, Residual stresses after cooling, in *Theory and Technology of Quenching*, B. Liscic, H.M. Tensi, and W. Luty, Eds., Springer-Verlag, New York, 1992, pp. 117–181.
9. N.I. Kobasko, Intensive steel quenching methods, in *Theory and Technology of Quenching*, B. Liscic, H.M. Tensi, and W. Luty, Eds., Springer-Verlag, New York, 1992, pp. 366–389.
11. J.G. Leidenfrost, De aqua communis nonnullis qualitatibus tractatus, 1756, *J. Heat Mass Transfer 9*: 1153–1166 (1966), translated by C. Waves.
12. A. Stitch, Wechselwirkung zwischen Bauteil, Wärmeübergang und Fluid beim Abschreckhärten, Doctoral Thesis, Technical University of Munich, Faculty of Mechnical Engineering, Munich, 1994.
13. H.M. Tensi, H.-J. Spies, A. Spengler, and A. Stich, Wechselwirkung zwischen Benetzugskinematik und Stahlhärtung beim Tauchkühlen, DFG Rep., Deutsche Forschungsgemeinschaft, Bonn, Contracts Te 65/35-1, 2 and Sp 367/1-1, 2, 1994.
14. H.M. Tensi, P. Stitzelberger-Jakob, T. Künzel, and A. Stich, Gefügebeeinflussung/Benetzungskinetik, DGF Rep., Deutsche Forschungsgemeinschaft, Bonn, Contract number Te 65/27-1, 2, 1989.
15. P. Stitzelberger-Jakob, Härtevorherbestimmung mit Hilfe des Benetzungsablaufs beim Tauchkühler von Stählen, Doctoral Thesis, Technical University of Munich, Faculty of Mechnical Engineering.
16. H.M. Tensi and A. Stich, Characterization of polymer quenchants, *J. Heat Treat. 5*: 25–29 (1993).
17. E. Steffen, Untersuchung von Abkühlmedien auf Polymerbasis für die Stahlhärtung, Doctoral Thesis, Technical University of Munich, Faculty of Mechnical Engineering, 1986.
18. H.M. Tensi and M. Schwalm, Wirkung von Abschreckflüssigkeiten unter Berücksichtigung spezieller wässriger Kunststofflösungen (Polyäthylenoxide), *HTM 34*: 122–131 (1980).
19. H.M. Tensi, Wetting kinematics, in *Theory and Technology of Quenching*, B. Liscic, H.M. Tensi, and W. Luty, Eds., Springer-Verlag, New York, 1993, pp. 93–116.
20. T. Künzel, Eingluss der Wiederbenetzung auf die allotrope Modifikationsänderung tauchgekühlter Metallkörper, Doctoral Thesis, Technical University of Munich, Faculty of Mechnical Engineering, 1986.
21. H.M. Tensi and P. Stitzelberger-Jakob, Influence of wetting kinematics of quenching and hardening in water based polymers with forced convection, *Proceedings of the 6th International Conference Heat Treatment of Metals*, 28–30 September, 1988, Chicago, published by ASM International.
22. H.M. Tensi, P. Stitzelberger-Jakob, and A. Stich, Steuern und Berechnen der Abkühlung zylinderfömiger Körper und Vorherbestimmung der Härteverteilung, *HTM 45*: 145–153 (1990).
23. L.V. Körtvelyessy, *Thermoelement Praxis*, Vulkan-Verlag, Essen, 1987.
24. H.M. Tensi and A. Stich, Anzeigeträgheit unterschiedlicher Thermoelemente für Temperaturmessungen beim Abschrecken, *HTM 49*: 26–30 (1994).

25. S. Segerberg, Draft International Standard ISO/DIS 9950 (VDC 621.78.084: 621.78.065.2), Industrial Quenching Oils—Determination of Cooling Characteristics—Laboratory Test Method, 1988.
26. H.M. Tensi, P. Stitzelberger-Jakob, and A. Stich, A Proposal for Standardization: Industrial Polymer Quenchants—Determination of Cooling Characteristics—Laboratory Test Method, 1992.
27. H.M. Tensi, A. Stich, and G.E. Totten, Fundamentals about quenching by submerging, *Proceedings of the 1st International Conference Equipment and Processes*, 18–20 April, 1994, Schaumburg, IL, published by ASM International.
28. H.M. Tensi, A. Stich, H.-J. Spies, and A. Spengler, Grundlagen des Abschreckens durch Tauchkühlen, *Proceedings of ATTT/AWT Tagung Abkühlen/Abschrecken*, 20–21 April, 1994, Strasbourg, France, pp. 43–50.
29. H.M. Tensi, G. Welzel, and T. Künzel, Problems of getting characteristics out of quenching experiments useful to control the heat treatment of metallic materials, *Proceedings of the 8th International Conference on Heat Transfer*, August 1986, San Francisco, pp. 3031–3035.
30. H.M. Tensi and P. Stitzelberger-Jakob, Evaluation of apparatus for assessing effect of forced convection on quenching characteristics, *Mater. Sci. Technol. 5*: 718–724 (1989).
31. H.M. Tensi, Methods and standards for laboratory tests of liquid quenchants, in *Theory and Technology of Quenching*, B. Liscic, H.M. Tensi, and W. Luty, Eds., Springer-Verlag, New York, 1992, pp. 208–219.
32. F. Richter, Die wichtigsten physikalischen Eigenschaften von 52 Eisenwrkstoffen, *Stahl-Eisen-Sonderber. 8*: (1973).
33. V.E. Loshkaroev, H.M. Tensi, H. Gese, and A. Stich, Calculation of temperature and heat flux in quenched cylinders for different wetting processes, *Steel Res. 9*: (1994).
34. H.M. Tensi, A. Stich, and V.E. Loshkaroev, Influence of wetting kinematics on temperature and heat flux, *Proceedings of the 1st International Conference on Equipment and Processes*, 18–20 April, 1994, Schaumburg, IL, published by ASM International.
35. M.A. Grossmann and M. Asimow, Hardenability and quenching, *the Iron Age*, April 25, 1940, p. 25 and May 2, 1940, p. 39.
36. C.E. Bates, *J. Heat Treat. 6*: 27–45 (1988).
37. C.E. Bates, G.E. Totten, and R.L. Brennan, Quenching of steel, in *ASM Handbook*, Vol. 4, *Heat Treating*, ASM International, Materials Park, OH, 1991, pp. 67–120.
38. R. Jeschar and E. Specht, Abschreckwirkung durch Aufspritzen von Gas-Wasser-Gemischen, *Proceedings of ATTT-AWT-Tagung Abkühlen/Abschrecken*, Strasbourg, France, 20–21 April, 1994, pp. 161–167.
39. R. Jeschar, U. Reiners, and R. Scholz, Heat transfer during water and water-air spray cooling in the secondary cooling zone of continuous casting plants, *Proceedings of the 69th Conference on Steelmaking*, Washington, 1986, Vol. 69, pp. 511–521.
40. R. Jeschar, U. Reiners, and R. Scholz, Wärmeübergang bei der zweiphasigen Spritzwasserkühlung, *Gaswärme Int. 33*: 299–308 (1984).
41. R. Jeschar, E. Specht, and C. Köhler, Heat transfer during cooling of heated metallic objects with evaporating liquids, in *Theory and Technology of Quenching*, B. Liscic, H.M. Tensi, and W. Luty, Eds., Springer-Verlag, New York, 1992, pp. 73–92.
42. U. Reiners, Wärmeübertragung durch Spritzwasserkühlung heisser Oberflächen im Bereich der stabilen Filmverdampfung, Doctoral Thesis, Technical University of Clausthal, 1987.
43. H.R. Müller and R. Jeschar, Wärmeübergang bei der Spritzwasserkühlung von Nichteisenmetallen, *Metallkunde 74*: 257–264 (1983).
44. G. Didier and F. Moreaux, Automatisation dùn système de refroidissement par pulverization pneumatique, *Rev. Gén. Therm. 256*: 333–339 (1983).
45. P. Archambault and F. Moreaux, Computer controlled spray quenching, in *Theory and Technology of Quenching*, B. Liscic, H.M. Tensi, and W. Luty, Eds., Springer-Verlag, New York, 1992, pp. 360–367.
46. E.J. Radcliffe, Gas quenching in vacuum furnaces—a review of fundamentals, *Ind. Heat.*, November 1987, pp. 34–39.
47. K. Ahlberg, *AGA Gas Handbook*, Almquist & Wiksell, Sweden, 1985.
48. G. Schmitt and P. Heilmann, Die Vorteile der Hochdruckgasabschreckung, *Proceedings of ATTT-AWT-Tagung Abschrecken/Abkühlen*, 20–21 Apr. 1994, Strasbourg, France, pp. 115–125.

49. H. Altena, Hochdruck-Wasserstoff-Abschreckung, *Proceedings of ATTT-AWT-Tagung Abschrecken/Abkühlen*, 20–21 Apr. 1994, Strasbourg, France, pp. 127–136.
50. F. Limque and F. Bless, Härten von Werkzeugstählen in Vakuumöfen mit Hochdruck-Gasabschreckung, *Z. Wirtschaftl. Fertigung 9*: 1–4 (1982).
51. J.W. Bauwmann, Erfahrungen mit der Hochdruckgasabschreckung in Vakuumöfen und desses Weiterentwicklung, *HTM 39*: 1–5 (1984).
52. J. Wünning, Gasabschrecken von Serienbauteilen, *Proceedings of ATTT-AWT-Tagung Abschrecken/Abkühlen*, 20–21 April, 1994, Strasbourg, France, pp. 195–204.
53. J.R. Lyman, High carbon steel microcracking control during hardening, U.S. Patent 4,523,965; Patent 472656 (1983).
54. R. Kern, Intense quenching, *Heat Treat. 9*: 19–23 (1986).
55. B. Liscic, H.M. Tensi, and W. Luty (Eds.), *Theory and Technology of Quenching*, Springer-Verlag, New York, 1992.
56. H.M. Tensi and A. Stich, Possibilities and limits to predict the quench hardening of steels, *Proceedings of the 1st International Conference on Quenching and Distortion Control*, 22–25 September, 1992, Chicago, pp. 27–32.
57. H.M. Tensi, Prediction of hardness profile in workpiece, based on characteristic cooling parameters and material behaviour during cooling—prediction of hardening behaviour from wetting kinematics, in *Theory and Technology of Quenching*, B. Liscic, H.M. Tensi, and W. Luty, Eds. Springer-Verlag, New York, 1992, pp. 390–408.
58. C.E. Bates, *J. Heat Treat. 6*: 27–45 (1988).
59. R.W. Monroe and C.E. Bates, Evaluating quenchants and facilities for hardening steel, *J. Heat Treat. 3*(2): 83–99 (1983).
60. G.E. Totten, C.E. Bates, and N.A. Clinton, *Handbook of Quenchants and Quenching Technology*, ASM International, Materials Park, OH, pp. 94–96.
61. J. Wünning, Berechnung und Steuerung des Temperaturverlaufs beim Abschrecken von Stahl in Wasser und Öl, *HTM 36*(5): 231–241 (1981).
62. M.A. Grossmann, M.A. Asimov, and S.F. Urban, Hardenability, its relationship to quenching and some quantitative data, in *Hardenability of Alloy Steels*, ASM International, Cleveland, OH, 1939, 237–249.
63. J.L. Lamont, How to estimate hardening depth in bars, *Iron Age 142*(14): 64–70 (1943).
64. J. Wünning and D. Liedtke, Versuche zum Ermitteln der Wärmestromdichte beim Abschrecken von Stahl in flüssigen Abschreckmitteln nach der QTA-Methode, *HTM 38*(5): 149–155 (1993).
65. B. Liscic, Predetermination of hardness results—the QTA method, in *Theory and Technology of Quenching*, B. Liscic, H.M. Tensi, W. Luty, Eds., Springer-Verlag, New York, 1992, pp. 409–419.
66. T. Lübben, H. Bomas, H.P. Hougardy and P. Mayr, Beschreibung der Abschreckwirkung flüssiger Abschreckmittel am Beispiel zweier Härteöle, *HTM 46*(1): 24–34 (1991); *HTM 46*(3): 155–170 (1991).
67. H.M. Tensi and P. Stitzelberger-Jakob, Bedeutung des H-Wertes für die Bestimmung der Härteverteilung, *HTM 44*: 99–106 (1989).
68. H.P. Hougardy and K. Yamazaki, An improved calculation of the transformation of steels, *Steel Res. 57*(9): 466–471 (1986).
69. M. Umemeto, N. Nishioka, and I. Tamura, Prediction of hardenability from isothermal transformation diagrams, *J. Heat Treat. 2*: 130–138 (1981).
70. I. Tzitzelkov, Eine mathematische Methode zur Beschreibung des Umwandlungsverhaltens eutektoider Stähle, Doctoral Thesis, RWTH Aachen, 1973.
71. I. Tzitzelkov, H.P. Hougardy, and H.P. Rose, Mathematische Beschreibung des ZTU-Schaubildes für isotherme Umwandlung und kontinuierliche Abkühlung, *Arch. Eisenhüttenwesen 45*: 525–532 (1974).
72. S. Somogyi and M. Gergely, Prediction of macrohardness by the help of the individual hardness of the microstructural elements, *Proceedings of the 4th International Conference on Heat Treatment of Materials*, Berlin, 1985, pp. 84–90.

10 Distortion of Heat-Treated Components

Michiharu Narazaki and George E. Totten

CONTENTS

10.1 Introduction 614
10.2 Basic Distortion Mechanisms 609
10.2.1 Relief of Residual Stresses 609
10.2.2 Material Movement Due to Temperature Gradients during Heating and Cooling 610
10.2.3 Volume Changes during Phase Transformations 610
10.3 Residual Stresses 612
10.3.1 Residual Stress in Components 612
10.3.2 Residual Stresses Prior to Heat Treatment 612
10.3.3 Heat Treatment after Work-Hardening Process 612
10.4 Distortion during Manufacturing 613
10.4.1 Manufacturing and Design Factors Prior to Heat Treatment That Affect Distortion 613
10.4.1.1 Material Properties 614
10.4.1.2 Homogeneity of Material 614
10.4.1.3 Distribution of Residual Stress System 614
10.4.1.4 Part Geometry 614
10.4.2 Distortion during Component Heating 615
10.4.2.1 Shape Change Due to Relief of Residual Stress 615
10.4.2.2 Shape Change Due to Thermal Stresses 615
10.4.2.3 Volume Change Due to Phase Change on Heating 615
10.4.3 Distortion during High-Temperature Processing 616
10.4.3.1 Volume Expansion during Case Diffusion 616
10.4.3.2 Distortion Caused by Metal Creep 616
10.4.4 Distortion during Quenching Process 617
10.4.4.1 Effect of Cooling Characteristics on Residual Stress and Distortion from Quenching 617
10.4.4.2 Effect of Surface Condition of Components 624
10.4.4.3 Minimizing Quench Distortion 625
10.4.4.4 Quench Uniformity 629
10.4.4.5 Quenching Methods 630
10.5 Distortion during Post Quench Processing 631
10.5.1 Straightening 631
10.5.2 Tempering 631
10.5.3 Stabilization with Tempering and Subzero Treatment 632
10.5.4 Metal Removal after Heat Treatment 633

10.6 Measurement of Residual Stresses 633
10.6.1 X-Ray Diffraction Method 634
10.6.2 Hole-Drilling Methods 635
10.6.3 Bending and Deflection Methods 636
10.6.4 Other Residual Stress Measurement Methods 636
10.7 Tests for Propensity for Distortion and Cracking 636
10.7.1 Navy C-Ring and Slotted Disk Test 637
10.7.2 Cylindrical Specimens 637
10.7.3 Stepped Bar Test 638
10.7.4 Key-Slotted Cylindrical Bar Test 638
10.7.5 Disk with an Eccentric-Positioned Hole 638
10.7.6 Finned Tubes 639
10.8 Prediction of Distortion and Residual Stresses 640
10.8.1 Governing Equations 642
10.8.1.1 Mixture Rule 642
10.8.1.2 Heat Conduction Equations and Diffusion Equation 642
10.8.1.3 Constitutive Equation 643
10.8.1.4 Kinetics of Quenching Process 643
10.8.1.5 Transformation Plasticity 644
10.8.2 Coupling Algorithm in Simulation by Finite-Element Analysis 644
10.8.3 Example of Simulation Results 645
10.8.3.1 Prediction of Warpage of Steel Shafts with Keyway 645
10.8.3.2 Prediction of Distortion during Carburized Quenching Process of Cr–Mo Steel Ring 645
10.9 Summary 648
References 648

10.1 INTRODUCTION

In various manufacturing processes of steel components, heat treatment is the most sensitive and least controllable operation because it involves unexpected and uncontrollable distortion. To assure high quality and reliability of steel components, manufacturers perform heat treatments. As long as parts have been heat-treated, distortion has been a concern. As greater dimensional accuracy is required for components, distortion becomes even more of a problem. The main industrial concern is therefore to account for distortion during design and manufacturing. Recent studies and contacts with industry have often highlighted the frustrations experienced by manufacturers trying to control dimensions consistently.

It is known that almost every step in the manufacturing process can affect the final shape of the part. If it could be accurately predicted what the new shape of a part would be after heat treatment, then this could be included in the design during manufacturing. However, there are so many variables interacting in so many ways that the problem is often beyond the present capacity for analysis, and thus distortion cannot be accurately predicted. This leads to a definition of heat treatment distortion: Distortion is an unexpected or an inconsistent change in size or shape caused by variations in manufacturing process conditions.

Although distortion of parts may become noticeable after heat treatment, the root cause may lie in another manufacturing process that is contributing to variability, such as variable residual stress, due to differences in machining. However, heat treatment of steel often requires that the steel be heated to high temperatures, held at that temperature for long periods, and then rapidly cooled by quenching. These processes are necessary to generate

high mechanical properties but they can also cause parts to change shape in unpredictable ways unless conditions are closely controlled.

This chapter will provide an overview of the effects of various factors on distortion, residual stress, and cracking of steel components. The subjects that will be discussed include:

- Basic distortion mechanisms
- Residual stresses
- Distortion during manufacturing
- Distortion during postquenching processing
- Measurement of residual stresses
- Tests for propensity for distortion and cracking
- Prediction of residual stress and distortion

10.2 BASIC DISTORTION MECHANISMS

The shape and size changes of a part during heat treating can be attributed to three fundamental causes:

- Residual stresses that cause shape change when they exceed the material yield strength. This will occur on heating when the strength properties decline.
- Stresses caused by differential expansion due to thermal gradients. These stresses will increase with the thermal gradient and will cause plastic deformation as the yield strength is exceeded.
- Volume changes due to transformational phase change. These volume changes will be contained as residual stress systems until the yield strength is exceeded.

10.2.1 Relief of Residual Stresses

If a part has locked-in residual stresses, these stresses can be relieved by heating the part until the locked-in stresses exceed the strength of the material. A typical stress–strain curve obtained from a tension test is shown in Figure 10.1. Initial changes in shape are elastic but under increased stress they occur in the plastic zone and are permanent. Upon heating, the stresses are gradually relieved by changes in the shape of the part due to plastic flow. This is a continuous process and as the temperature of the part is increased, the material yield stress

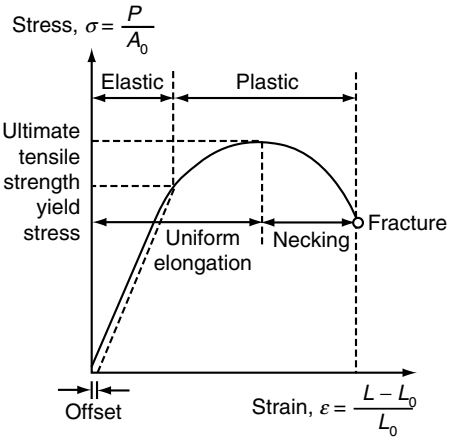

FIGURE 10.1 Various features of a typical stress–strain curve obtained from a tension test.

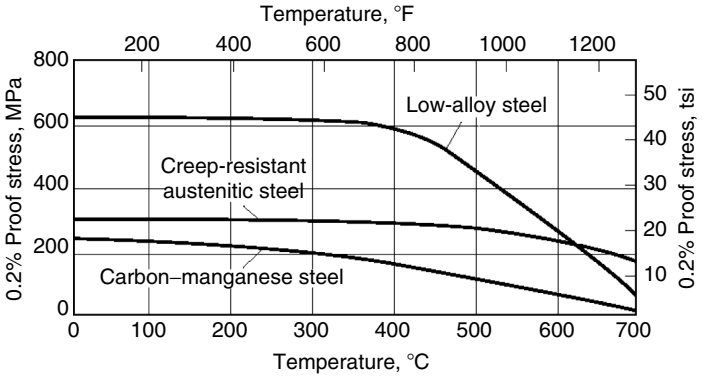

FIGURE 10.2 Variation of yield strength with temperature for three generic classes of steel. (From D.A. Canonico, in *ASM Handbook*, Vol. 4, ASM International, Materials Park, OH, 1991, pp. 33–34.)

decreases as shown in Figure 10.2 [1]. It is a function not only of temperature but also of time, because the material will creep under lower applied stresses. It is apparent that stresses can never be reduced to zero, because the material will always possess some level of yield strength below which the residual stresses cannot be reduced.

10.2.2 Material Movement Due to Temperature Gradients during Heating and Cooling

When parts are heated during heat treatment, a thermal gradient exists across the cross-section of the component. If a section is heated so that a portion of the component becomes hotter than the surrounding material, the hotter material expands and occupies a greater volume than the adjacent material and will thus be exposed to applied stresses that will cause a shape change when they exceed material strength. These movements can be related to heating rate and section thickness of the component.

10.2.3 Volume Changes during Phase Transformations

When a steel part is heated, it transforms to austenite with an accompanying reduction in volume as shown in Figure 10.3 [2]. When steel is slowly cooled, it undergoes a crystal structure (size) change as it transforms from a less densely packed austenite (face-centered cubic or fcc) to a more densely packed body-centered cubic (bcc) structure of ferrite. At faster cooling rates, the formation of ferrite is suppressed, and martensite, which is an even less densely packed body-centered tetragonal (bct) structure than austenite, is formed. This results in a volumetric expansion at the M_s temperature, as shown in Figure 10.3. If these volume changes cause stresses that are constrained within the strength of material, a residual stress system is created. If the stresses cannot be contained, then material movement will occur, which will cause cracking under extreme conditions.

The expansion is related to the composition of steel. Figure 10.4 shows that the crystal lattice of austenite expands with increasing carbon content [3]. It has been reported that, typically, when a carbide–ferrite mixture is converted to martensite, the resulting expansion due to increasing carbon content is approximately 0.002 in./in. at 0.25% C and 0.007 in./in. at 1.2%C [3]. The fractional increase in size when austenite is converted to martensite is approximately 0.014 in./in. for eutectoid compositions. This illustrates the effect of carbon structure and steel transformation on residual stresses and distortion leading to dimensional changes.

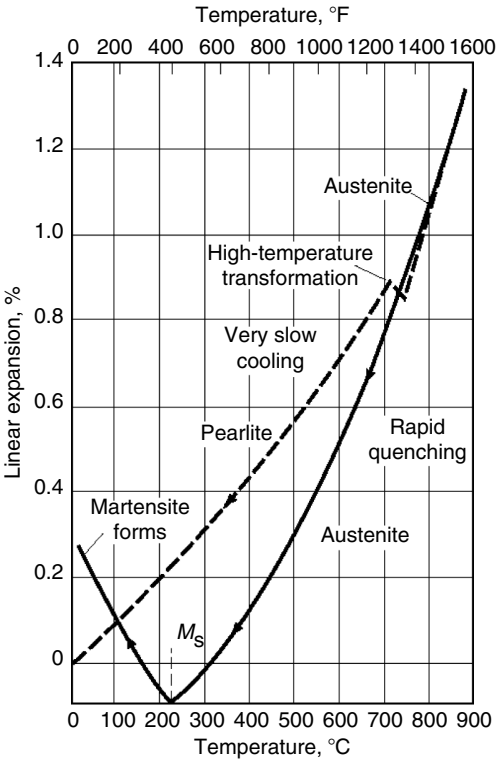

FIGURE 10.3 Steel expansion and contraction on heating and cooling. (From C.E. Bates, G.E. Totten, and R.L. Brennan, in *ASM Handbook*, Vol. 4, ASM International, Materials Park, OH, 1991, pp. 67–120.)

While these physical changes are well known, the situation is more complex when all three events occur simultaneously. In addition, other events such as heating rate, quenching, and inconsistent material composition cause further complications that are discussed later in this chapter.

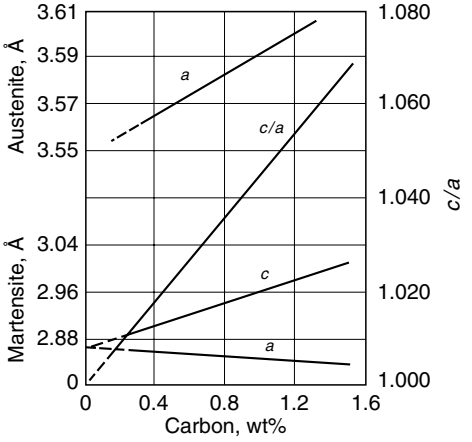

FIGURE 10.4 Carbon content versus lattice parameters of (retained) austenite and martensite at room temperature. *a* at the top of the graph is the lattice parameter of fcc austenite. *a* and *c* in the lower half of the graph are the lattice parameters for tetragonal martensite. The ratio of *c*/*a* for martensite as a function of carbon content is also given. (From S. Mocarski, *Ind. Heat*., 41(5), 1974, 58–70.)

10.3 RESIDUAL STRESSES

10.3.1 Residual Stress in Components

Residual stresses are present in parts after any process that strains the material. Heavy metal working such as forging, rolling, and extrusion causes stresses that remain in the metal if the process is performed below the hot-working temperature. If a material is hot-worked, stresses are continually removed. Processes such as cutting, grinding, and shot peening also cause residual stress formation but to much shallower depth. While compressive residual stresses are desirable in a finished component to enable it to resist applied stress systems, the stresses that exist during manufacture will be relieved during heating with consequent movement in the material as the stress system readjusts.

Residual stresses result not only from heat treatment but also from cold-working through metalworking, machining processes, and so forth. Within any steel parts there is a balanced stress system consisting of tensile and compressive residual stresses. If the finished part has the compressive stresses at the surface, these stresses increase the strength of the part under normal tensile loading and are thus beneficial. Processes like shot peening are also used to increase surface compressive stresses to improve performance and compensate for structural defects. This type of residual stress is intentional and is part of the design. The problem arises when a metal part has a residual stress system prior to heat treatment. Then an unpredictable shape change will occur.

10.3.2 Residual Stresses Prior to Heat Treatment

Parts for heat treatment should have not only correct dimensions but also a consistent residual stress pattern. Ideally, the part should be absolutely stress-free so that movement due to stress-relief can be disregarded, but in practice some final machining passes are necessary before heat treatment. The best compromise is to completely stress-relieve the part before the final machining. Several stress-relieving treatments may be necessary during initial machining to prevent dimensions from going out of control. If a part with a preexisting stress system is machined and has thus had some of the stresses removed, the system will constantly rebalance itself by changing its stress pattern.

Any forming or machining processes leave stress systems that will be relieved by a dimensional change during heat treatment. Thus, if the part is heavily stressed prior to heat treatment, the shape will change due to this factor alone. Processing should be designed so that virtually stress-free parts are heat-treated. Variations in heat treatment parameters such as case carbon level and processing temperatures will also cause final shape and size differences.

10.3.3 Heat Treatment after Work-Hardening Process

After metalworking, forgings or rolled products are often given an annealing or normalizing heat treatment to reduce hardness so that the steel may be in the best condition for machining. These processes also reduce residual stresses in the steel.

Annealing and normalizing are terms used interchangeably, but they do have specific meaning. Both terms imply heating the steel above the transformation range. The difference lies in the cooling method. Annealing requires a slow cooling rate, whereas normalized parts are cooled faster in still, room-temperature air. Annealing can be a lengthy process but produces relatively consistent results, whereas normalizing is much faster (and therefore favored from a cost point of view) but can lead to variable results depending on the position of the part in the batch and the variation of the section thickness in the part that is stress-relieved.

Normalizing always involves transforming the steel to the austenitic condition by heating to about 50°C (100°F) above the A_{C3} temperature as defined in the iron–carbon phase diagram. Cooling then usually occurs in air, and the actual cooling rate depends on the mass which is cooled.

This treatment (normalizing) have three main purposes:

- To control hardness for machinability purposes.
- To control structure. Heating to above the austenitizing temperature range will allow the material to recrystallize on cooling and to form a fine-grain structure having superior mechanical properties.
- To remove residual stresses on heating. However, if cooling is not controlled, a new stress system may result after cooling.

Stress-relief heat treating involves controlled heating to a temperature below A_{C1}, holding for the required time, and then cooling at a rate to avoid the introduction of thermal stresses. The stress relaxation involves microscopic creep and the results will be dependent on both time and temperature as correlated by the Larson–Miller equation

$$\text{Thermal effect} = T(\log t + 20)/1000$$

where T is temperature in Rankine degrees and t is time in hours [1].

Resistance of a steel to stress-relief is related to the yield strength at the treatment temperature. The temperature should be selected at the point where the material yield strength corresponds to an acceptable level of residual stress remaining in the part. After treatment, uniform cooling is absolutely necessary. Otherwise the thermal stresses can cause a new system of residual stresses.

10.4 DISTORTION DURING MANUFACTURING

The causes of distortion of steel parts will be considered during five separate stages of manufacturing and processing:

- Prior to heat treatment
- During heat-up for heat treatment
- At treatment temperature, i.e., during carburizing, nitriding, etc.
- During quenching and cooling
- During postquenching processing

10.4.1 Manufacturing and Design Factors Prior to Heat Treatment That Affect Distortion

Manufacturing and design factors that will affect distortion prior to heat treatment may be summarized as:

- Material properties
- Homogeneity of properties across the cross section of the material
- Residual stress system magnitude and distribution
- Part geometry

10.4.1.1 Material Properties

Material properties affect distortion response in several ways. As discussed above, the strength properties have important effects on the response to stress-relieving treatments, on the movement during differential thermal expansion, on the and on the residual stresses caused during quenching. The composition also is related to hardenability, which determines the phase changes during quenching. These properties can vary according to actual composition of the steel used. The composition specification allows a range for each element, which means, in practice, that each batch of steel is unique and will respond slightly differently.

10.4.1.2 Homogeneity of Material

The first variable that must be considered is the material source, starting with the steel supplier. Compositional variations across the section of the cast ingot can cause different responses during heat treatment. Processing of the steel into the form required by the manufacturing process can cause further variations and may leave high levels of residual stress, which may be removed partially by normalizing or another stress-relieving process. As these heat treatments are usually conducted on large batches, they produce variable results from part to part, which causes different responses in subsequent processing. Steel supplied to the manufacturers of precision parts is typically either forgings or rolled products, which are made from ingots or continuously cast products. In rolling and forging, the steel is heated to the 1050–1200°C (1900–2200°F) range and then worked by hammering, pressing, or rolling to break down the cast structure and produce a homogeneous cross section in both composition and structure. However, the effects of earlier processing are never totally eradicated, and they cause variable responses in hardenability, microstructure after heat treatment, residual stress levels, and consequently distortion.

10.4.1.3 Distribution of Residual Stress System

If the source of steel supply is consistent and the steel is processed under the same way every time, these effects cause consistent, predictable residual stress behavior that is acceptable. However, if the steel is coming from different melt shops, rolling mills, and forgers with different processing schedules, heat treatment and residual stress responses can vary, often without apparent explanation. Most steel is hot-rolled, and after rolling, it is allowed to cool in air on a hot bed. This causes a difference in cooling due to conduction of heat from the bottom of the bar and convection cooling from the top. If the bar is allowed to cool completely in this position, the top of the bar will have residual tensile stresses that will tend to bend the bar and make straightening necessary. Straightening can produce very high levels of residual stresses, and further stress-relieving treatment must be performed.

10.4.1.4 Part Geometry

Nonuniform heating and quenching can be caused by changes in section thickness in the same component. When a part is designed, most designers recognize the need to keep section sizes as uniform as possible to minimize temperature gradients and the tendency to produce high stresses due to differential expansion and contraction during heating and quenching. If a part is made with features such as gear teeth, however, it is unavoidable that these areas will have higher surface-to-volume ratios than the rest of the parts and that gear teeth will often tend to heat and cool faster than the rest of the section. As a result, the base of the tooth will be

restrained by the rim, and this area will tend to go into compression during heating and into tension during cooling. Similar effects will take place elsewhere in the part wherever there is a change of section.

10.4.2 Distortion during Component Heating

The major effects during heat-up are initiated by three distortion-causing mechanisms acting at the same time:

1. Shape change due to relief of residual stress
2. Shape change due to thermal stresses causing plastic flow
3. Volume change due to phase change on heating

10.4.2.1 Shape Change Due to Relief of Residual Stress

As discussed earlier, the presence of residual stresses from prior operations will cause shape changes if the stresses are relieved by heating the part to a point where the yield strength of the material decreases below the residual stress level in the material. The extent of the resulting plastic deformation will therefore depend on the magnitude and distribution of the stress fields in the part.

10.4.2.2 Shape Change Due to Thermal Stresses

If a part could be heated at the same rate throughout the section, it would expand uniformly at a rate determined by thermal expansion coefficient but maintain the same shape. In actual practice, as the part heats up, the surface will heat first and expand or try to occupy a greater volume than the colder internal material. Expansion of the outer layers is therefore constrained by the colder, stronger inner layers of the material. Compressive stresses will be present in the outer layers on heating, balanced by tensile stresses in the interior of the component. Furthermore, shape changes will occur if these stresses result in the plastic deformation when the yield strength of the heated material decreases below the stress level in the material. Therefore, shape change depends on the geometry of the part, heating rate, the coefficient of thermal expansion, material properties, and fixturing of the part.

10.4.2.3 Volume Change Due to Phase Change on Heating

When a steel is heated from room temperature, thermal expansion occurs continuously up to A_{c1}, and then steel contracts as pearlite (or pearlite–ferrite mixture) transforms to austenite (i.e., the pearlite-to-austenite phase change causes approximately 4% contraction; see Figure 10.3). The extent of decrease in volumetric contraction is related to the carbon content in the steel composition. Further heating expands the newly formed austenite. The shape and volume changes as transformation occurs depend on the heating rate, the part geometry, and the phase volume change.

The major source of control of distortion during heat-up is the heating rate. Differences in heat-up rate (due, for example, to position in load) will lead to inconsistent distortion. Rapid heating or nonuniform heating causes severe shape changes. Slow heating and preheating of parts prior to heating to the austenitizing temperature yield the most satisfactory result. Unfortunately slow heating is in direct conflict with normal practice, since to increase production rate, parts are usually heated as fast as possible to the treatment temperature.

10.4.3 Distortion during High-Temperature Processing

Once the parts are at a constant temperature there are some minor factors that will cause shape change, but the major changes will occur on further cooling. Carburized parts can be directly quenched from carburizing temperature or just below the carburizing temperature, or they can be slowly cooled, given an optional temper, reheated to austenitizing temperature, and quenched. The latter treatment is used to give optimum case properties. The factors to be considered during and after high-temperature processing are

- Volume expansion during diffusion treatments
- Distortion due to creep

10.4.3.1 Volume Expansion during Case Diffusion

The major heat treatment used for high-quality parts is a case hardening process designed to form a hard surface layer on the gear surface. This layer not only gives the part a hard, wear-resistant finish but also sets up a compressive stress system at the surface that helps to resist fatigue failures. There is a measurable volume expansion during diffusion treatments depending on the diffused element (carbon, nitrogen, etc.), the depth of diffusion, the concentration profile, the furnace temperature, and the atmosphere uniformity. The volume expansion in the case causes a stretching of the core, which results in tensile stresses that are balanced by compressive stresses in the case. Distortion due to the expansion will occur when these stresses exceed the yield stress of the material.

Carburizing involves the diffusion of carbon from a gaseous atmosphere while the part is heated in an atmosphere or vacuum furnace. Carbon is introduced to a level of 0.70–1.00% at the surface. After carburizing, the part is quenched, usually in oil to produce a hard martensitic layer on the surface. Diffusion times are usually in the range of 4–20 h depending on the temperature of treatment and the case depth required. The case depth required by the designer is related to the size of the part and is often greater for the larger part to produce the correct residual stress pattern.

Nitriding involves the diffusion of nitrogen from a gaseous atmosphere in the temperature range of 495–565°C (925–1050°F). It may be performed in an atmosphere furnace or in vacuum ion nitriding equipment. After nitriding, the parts are hard without quenching, and the increase in volume in the case causes a stretching of the core, which results in tensile stresses that are balanced by compressive stresses in the case. The magnitude of stresses in the core and the case is affected by yield strength of the material, thickness of the case, and amount and properties of nitrides formed.

Nitriding takes everywhere from one day to one week because of the slow diffusion rates. As nitriding is performed at relatively low temperatures and quenching is unnecessary, distortion is a minor problem. Another diffusion process sometimes used is carbonitriding, the simultaneous diffusion of carbon and nitrogen, generally for lower cost parts. Carbonitriding is a modified form of gas carburizing, rather than a form of nitriding.

10.4.3.2 Distortion Caused by Metal Creep

Distortion due to creep will depend on the geometry of the part, the support during processing, the temperature and time of treatment, and the creep strength of the material. A part subjected to elevated temperatures for extended times (as in carburizing) could creep under its own weight unless it is properly fixtured and supported. Long slender parts are best suspended vertically. If this is not practical, the support should have the same contour as the component rests on it.

10.4.4 Distortion during Quenching Process

Among the various processes involved in heat treatment, quenching is one of the most important processes related to distortion, cracking, and residual stress in quenched steel parts. Although quench cracking can be eliminated, quench distortion cannot be. Instead, the issue is distortion control, not elimination. Both quenching-related distortion control and quench cracking will be discussed here.

One form of distortion that may occur upon quenching is defined as shape distortion such as bending, warpage, and twisting. A second form of distortion is size distortion that includes dimensional changes observable as elongation, shrinkage, thickening, and thinning. Size distortion is due to volumetric variation that accompanies each of the transformational phases formed upon quenching [4].

Distortion during quench hardening is related to following factors:

- Cooling characteristics in quenching—quenchant selection and agitation
- Quenching uniformity
- Parts shape and size—component design
- Surface condition of parts
- Steel grade selection

10.4.4.1 Effect of Cooling Characteristics on Residual Stress and Distortion from Quenching

Steel quenching requires a wide variation in cooling rates to achieve the required hardness and strength, which is dependent on the hardenability of the steel and section size of the workpiece. At the same time, distortion and crack formation must be minimized. However, these are often contradictory objectives. For example, although increasing cooling rates increases hardness, they often increase the potential for distortion, stress, and cracking. Similarly, distortion and stress during quenching are affected by many factors, such as quenchant, bath temperature, and agitation. The dimensions, shape, and material of the workpiece also influence the distortion, stress, and cracking.

10.4.4.1.1 Effect of Quenchant Selection

The selection of quenchant is the most basic factor affecting the cooling characteristics of workpieces. Therefore, it is the basic factor to be considered for stress and distortion control during quenching. The selection of a particular quenchant depends on the quench severity desired. For example, water, brine, or lower concentrations of aqueous polymer solutions are used for plain carbon steels. Accelerated oils are used for low-alloy steels. Conventional oils or higher concentrations of polymers are used for high-alloy steels. Molten salts or liquid metals are often used for martempering (marquenching) and austempering processes.

Dimensions and shape of the workpiece that is quenched should also be considered in selecting a quenchant. In general, the thicker the workpiece, the more severe the quenchant. However, severe quenching often increases stress and distortion of the quenched workpiece. For steel parts with thick and thin cross sections, the selection of a quenchant is more difficult. Many such shapes increase the nonuniformity of cooling, and therefore increase the potential for stress, cracking, and distortion.

Wetting behavior during quenching in a volatile quenchant, such as water, oil, or aqueous polymer solutions, results in nonuniform (uneven) cooling of the workpieces producing high surface thermal gradients and often increasing distortion and stress. Many aqueous polymer

quenchants will provide more uniform wetting properties, which will result in substantial reductions in cracking and distortion [5].

Figure 10.5 and Figure 10.6 show the distortion and residual stress of 30 mm diameter and 10-mm thick carbon steel disk specimens quenched in various quenchants without agitation. Different stress distributions and distortions were obtained for each quenchant. This is a result of the difference of the cooling power of each quenchant, which dominates the cooling path on the continuous cooling transformation (CCT) curve and therefore the internal distribution of martensite and ferrite–pearlite. The wetting process on the surface of the specimen during water, polymer, and oil quenching also affects the stress and distortion. After vapor blanket cooling, a collapse of the vapor blanket (i.e., wetting) occurs progressively during water quenching (WQ). This results in nonuniform cooling of a steel specimen and increases stress and distortion. However, if the vapor blanket collapses simultaneously or explosively, as in polymer quenching, the simultaneous collapse provides uniform quenching that is effective for reducing stress and distortion. The results shown in Figure 10.5 and Figure 10.6 illustrate the effectiveness of uniform quenching by using a polymer quenchant.

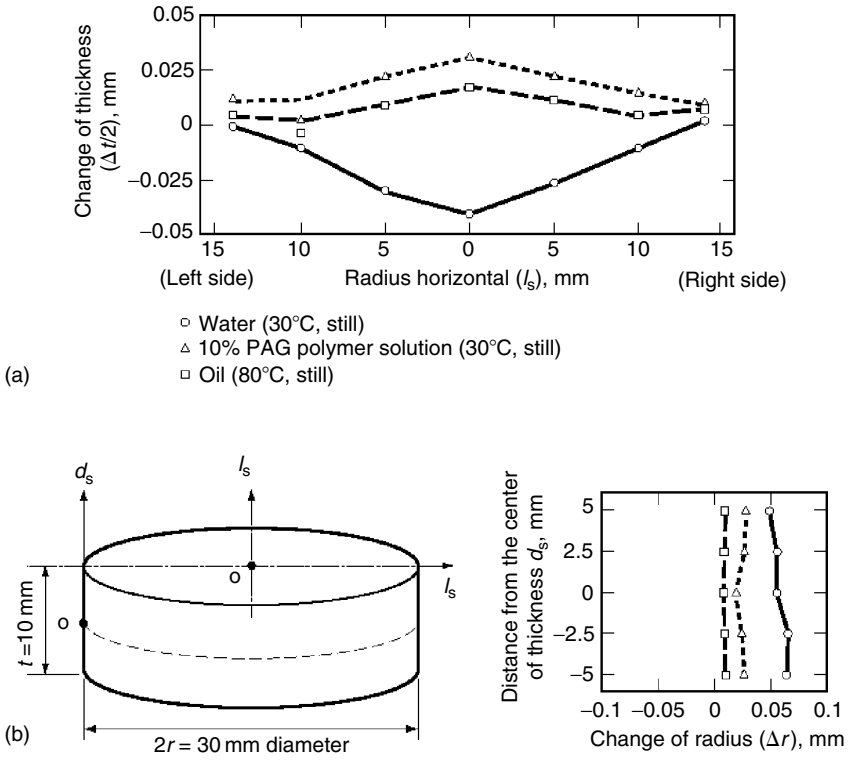

FIGURE 10.5 Effect of quenchants on quench distortion of JIS S45C carbon steel disk quenched in still quenchants. Specimen dimensions were 30 mm in diameter by 10 mm thick. (a) Distribution of axial distortion. (b) Distribution of radial distortion. (From M. Narazaki, M. Kogawara, A. Shirayoria, and S. Fuchizawa, *Proceedings of the Third International Conference on Quenching and Control of Distortion*, 24–26 March, 1999, Prague, Czech Republic, pp. 112–120; M. Narazaki, G.E. Totten, and G.M. Webster, in *Handbook of Residual Stress and Deformation of Steel*, G.E. Totten, M.A.H. Howes, and T. Inoue, Eds., ASM International, Materials Park, OH, 2002, pp. 248–295.)

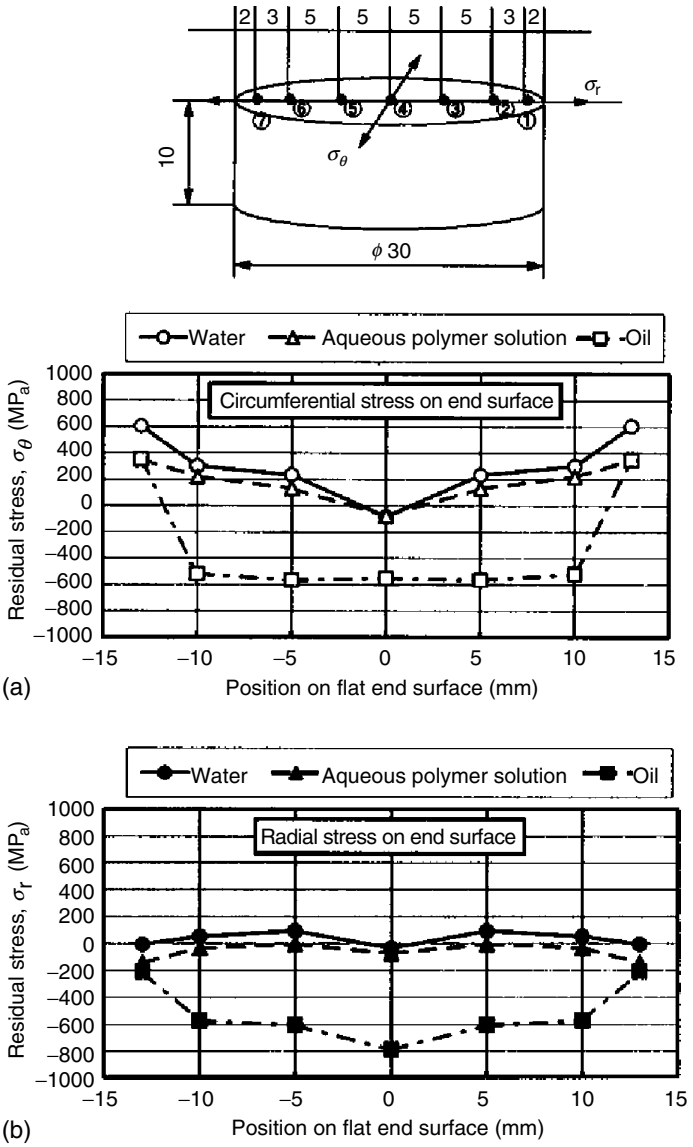

FIGURE 10.6 Effect of quenchants on residual stresses on side surface of JIS S45C carbon steel disk quenched in still quenchants. Specimen dimensions were 30 mm in diameter by 10 mm thick. (a) Circumferential stress on end surface. (b) Radial stress on end surface. (From M. Narazaki, G.E. Totten, and G.M. Webster, in *Handbook of Residual Stress and Deformation of Steel*, G.E. Totten, M.A.H. Howes, and T. Inoue, Eds., ASM International, Materials Park, OH, 2002, pp. 248–295.)

Molten salt and liquid metal quenching also provide uniform quenching, decreased cooling rate, and nonuniformity of the temperature of a steel part because of the high quenchant temperature. These characteristics are effective for the reduction of stress, distortion, and cracking.

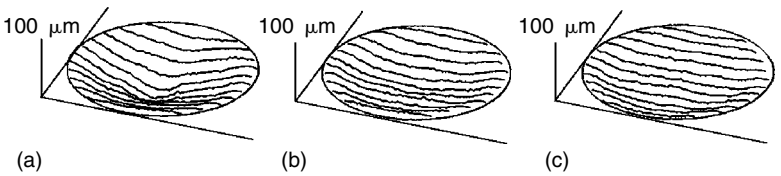

FIGURE 10.7 Effect of agitation of water on quench distortion of JIS S45C carbon steel disk. Specimen dimensions were 30 mm in diameter by 10 mm thick. Quenchant was 30°C city water. Flow velocity: (a) still water, (b) 0.3 m/s, and (c) 0.7 m/s. (From Ref. M. Narazaki, M. Kogawara, A. Shirayoria, and S. Fuchizawa, *Proceedings of the Third International Conference on Quenching and Control of Distortion*, 24–26 March, 1999, Prague, Czech Republic, pp. 112–120; M. Narazaki, G.E. Totten, and G.M. Webster, in *Handbook of Residual Stress and Deformation of Steel*, G.E. Totten, M.A.H. Howes, and T. Inoue, Eds., ASM International, Materials Park, OH, 2002, pp. 248–295.)

10.4.4.1.2 Effect of Agitation

Quench nonuniformity may arise from nonuniform flow fields around the part surface during the quench or nonuniform wetting of the surface. In addition, poor agitation design is a major source of quench nonuniformity. The purpose of the agitation is not only to increase cooling power of quenchant, but also to provide uniform cooling to suppress excessive distortion and stress of quenched steel parts.

Figure 10.7 and Figure 10.8 show the effect of agitation of quenchants on the profile of the flat surface of the steel disk after quenching [5,6]. Figure 10.7 shows that nonuniform surface cooling in still-water quenching on a concave surface of the steel disk test specimen and that agitation of the water significantly decreases quench distortion in WQ. This occurs because agitation reduces the nonuniformity of the surface cooling of the steel disk because agitation accelerates the propagation of the vapor blanket collapse on the surface. However, agitation of a polymer quenchant does not decrease quench distortion (see Figure 10.8) because the instantaneous and explosive collapse of the vapor blanket on the surface occurs with or without the agitation.

Figure 10.9 and Figure 10.10 show the effect of agitation methods of a quenchant on quench distortion of a 20 mm diameter and 60 mm long 0.45% carbon steel bars quenched in water and a polymer quenchant [6]. Figure 10.9a shows that nonuniform surface cooling in still-water quenching results in an uneven diameter of the steel bar. The increases of diameter near the ends of bars were observed, which are attributable to heat extraction from the edges

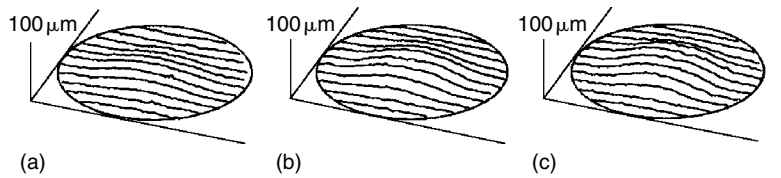

FIGURE 10.8 Effect of agitation of polymer quenchant on quench distortion of JIS S45C carbon steel disk. Specimen dimensions were 30 mm in diameter by 10 mm thick. Quenchant was 30°C 10% polymer (PAG) quenchant. Flow velocity: (a) still water, (b) 0.3 m/s, and (c) 0.7 m/s. (From M. Narazaki, M. Kogawara, A. Shirayoria, and S. Fuchizawa, *Proceedings of the Third International Conference on Quenching and Control of Distortion*, 24–26 March, 1999, Prague, Czech Republic, pp. 112–120; M. Narazaki, G.E. Totten, and G.M. Webster, in *Handbook of Residual Stress and Deformation of Steel*, G.E. Totten, M.A.H. Howes, and T. Inoue, Eds., ASM International, Materials Park, OH, 2002, pp. 248–295.)

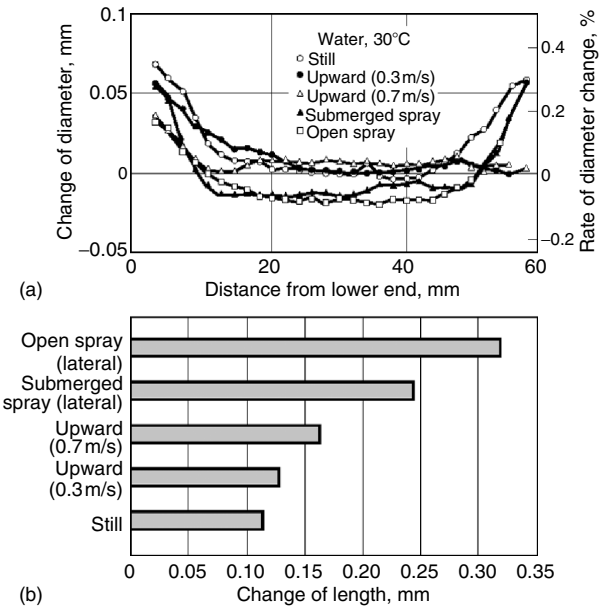

FIGURE 10.9 Effect of agitation methods on distortion of JIS S45C steel rod (20-mm diameter by 60 mm long). Quenchant was 30°C city water. Agitation methods were still, 0.3 m/s upward flow, 0.7 m/s upward flow, and lateral submerge in immersion quenching, and lateral open spray quenching in air. (a) Change of diameter, (b) change of length. (From M. Narazaki, G.E. Totten, and G.M. Webster, in *Handbook of Residual Stress and Deformation of Steel*, G.E. Totten, M.A.H. Howes, and T. Inoue, Eds., ASM International, Materials Park, OH, 2002, pp. 248–295.)

of the bar by an edge-effect. Upward flow of water decreases the edge-effect, because agitation reduces the nonuniformity of surface cooling of the steel bar. However, the diameter near the bottom end is larger than that near the top end because upward agitation produces greater heat loss at the bottom end than at the top end.

Lateral submerged and open spray decrease the diameter and increase the length of the steel bars, because the lateral flow causes fast cooling of the side-surface and thermal shrinkage of the diameter which also results in elongation of the length of the steel bar (Figure 10.9b). On the other hand, agitation of the polymer quenchant hardly affects quench distortion (see Figure 10.10) because the instantaneous and explosive collapse of the vapor blanket on the surface of specimen will occur with or without agitation.

Figure 10.11 and Figure 10.12 show the effect of agitation of a quenchant on the residual stresses on the side surface of 20-mm in diameter and 60 mm long carbon steel bars quenched in water and a polymer quenchant [6]. Figure 10.11 shows that nonuniform surface cooling in still-water quenching results in nonuniform residual stress distribution on the surface of the steel bar. Agitation of water results in ununiform stress distributions except near the both ends. In addition, submerged and open spray cooling result in high compression stresses. Figure 10.12 shows the effect of agitation on stress distribution after polymer quenching. Agitation of the polymer quenchant results in uniform stress distribution and high compression stresses except near both the ends. However, still-polymer quenching may result in uniform and high compression stress because uniform cooling occurs with or without the agitation.

Table 10.1 shows the effect of agitation on the frequency of quench cracking in water and polymer quenching of steel disks with respect to geometry and dimensional variation is

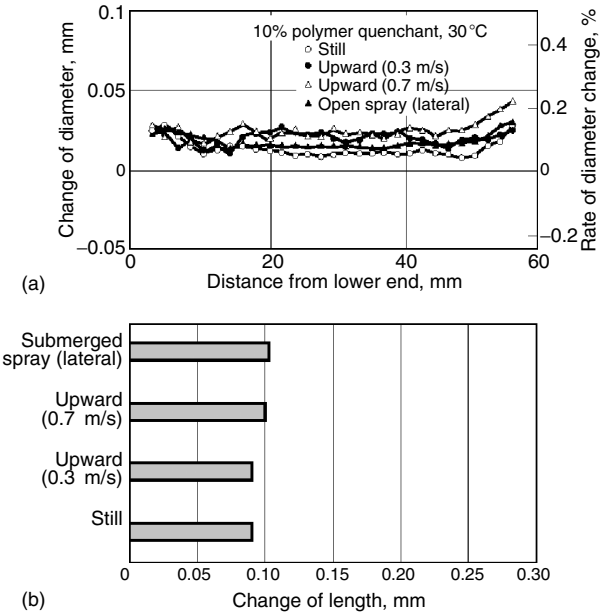

FIGURE 10.10 Effect of agitation methods on distortion in polymer quenching of JIS S45C steel rod (20-mm diameter by 60 mm long). Quenchant was 30°C 10% polymer (PAG) quenchant. Agitation methods were still, 0.3 m/s upward flow, and 0.7 m/s upward flow in immersion quenching. (a) Change of diameter, (b) change of length. (From M. Narazaki, G.E. Totten, and G.M. Webster, in *Handbook of Residual Stress and Deformation of Steel*, G.E. Totten, M.A.H. Howes, and T. Inoue, Eds., ASM International, Materials Park, OH, 2002, pp. 248–295.)

shown in Figure 10.13 [6]. The test specimen (30 mm diameter by 10-mm thick) contains an eccentrically located 10-mm-diameter hole. This specimen, was used in the work of Owaku [4] and was adopted by the Quench Cracking Working Group of the Japan Heat Treatment Society. The steel materials that were used were Japanese standard S45C, SK4, and SCM435. These results show that agitation of water largely suppresses the occurrence of quench cracking. On the other hand, quench-cracking susceptibility to agitation of the polymer quenchant is not clear because there is no crack on polymer-quenched specimen with or without agitation.

10.4.4.1.3 Workpiece Size Effects

The cooling rate of a quenched workpiece caused by a shows an inverse relationship with increasing thickness caused by a mass effect. In addition, cooling rates of the core are limited by thermal diffusion in the workpiece. Therefore, stress and distortion during quenching are affected by the dimensions, shape, and material of the workpiece that is quenched.

Figure 10.14 [7] shows the axial stress development during WQ of AISI 1045 solid steel cylinders. The 10-mm (0.4 in.) diameter cylinder starts to transform to martensite at the surface and the transformation front moves gradually inward, resulting in a typical tensile stress at the surface. Large diameter cylinders first transform to ferrite–pearlite at intermediate radii and then to martensite at the surface. This causes two stress minima as seen in the dashed curves in Figure 10.14a through Figure 11.14c. The final residual stress is compressive at the surface and tensile in the core. The relationship of stress to specimen diameter and quenching medium is summarized in Figure 10.15 [7,8]. The difference between oil and water quenching decreases with increasing diameter.

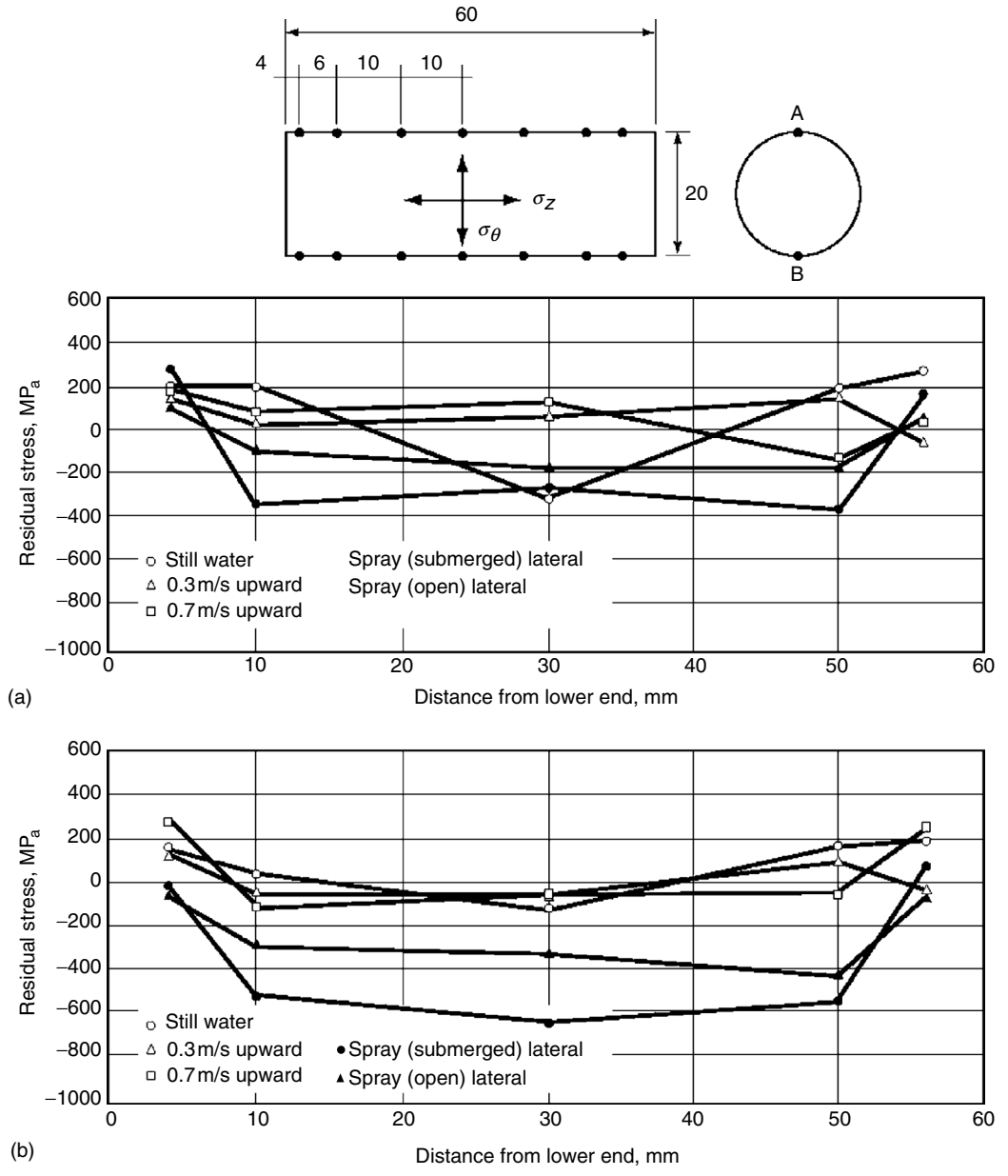

FIGURE 10.11 Effect of agitation methods on residual stress after water quenching of JIS S45C steel rod (20-mm diameter by 60 mm long). Quenchant was 30°C city water. Agitation methods were still, 0.3 m/s upward flow, 0.7 m/s upward flow, and lateral submerge in immersion quenching, and lateral open spray quenching in air. (a) Axial stress on surface, (b) tangential stress on surface. (From M. Narazaki, G.E. Totten, and G.M. Webster, in *Handbook of Residual Stress and Deformation of Steel*, G.E. Totten, M.A.H. Howes, and T. Inoue, Eds., ASM International, Materials Park, OH, 2002, pp. 248–295.)

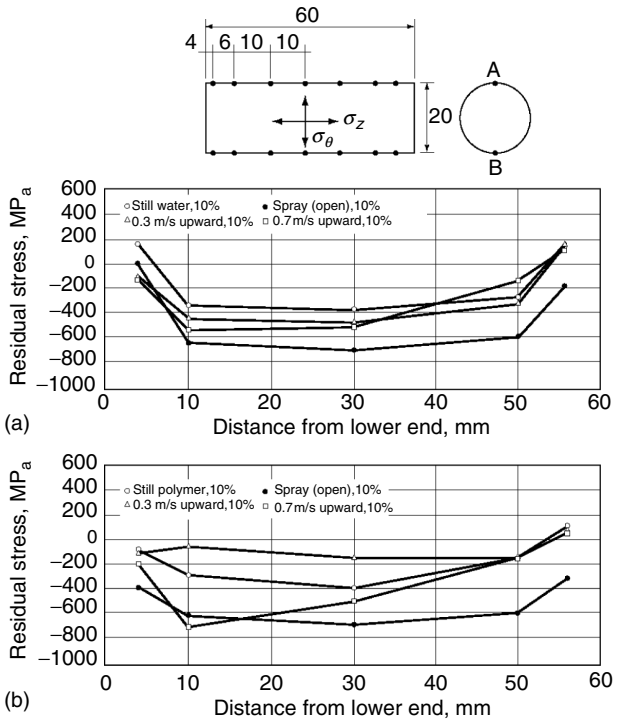

FIGURE 10.12 Effect of agitation methods on residual in polymer quenching of JIS S45C steel rod (20-mm diameter by 60 mm long). Quenchant was 30°C 10% polymer (PAG) quenchant. Agitation methods were still, 0.3 m/s upward flow, and 0.7 m/s upward flow in immersion quenching. (a) Axial stress on surface, (b) tangential stress on surface. (From M. Narazaki, G.E. Totten, and G.M. Webster, in *Handbook of Residual Stress and Deformation of Steel*, G.E. Totten, M.A.H. Howes, and T. Inoue, Eds., ASM International, Materials Park, OH, 2002, pp. 248–295.)

10.4.4.2 Effect of Surface Condition of Components

10.4.4.2.1 Effect of Surface Roughness

Surface texture and roughness are very important factors for quench cracking because the microscopic geometry and roughness of the surface affect the tendency for cracking. Narazaki et al. have shown an example of such a case [6,9]. The results were as follows:

- Surface roughness increases the tendency for quench cracking of steel if surface roughness (maximum height of irregularities R_y, or ten points height of irregularities R_z) is larger than approximately 1 μm.
- Surface texture made by lapping tends to cause a higher occurrence of quench cracking than by grinding or emery-polishing when the surface roughness is approximately the same.

This phenomenon is caused mainly by the stress concentration at the surface of the steel workpieces. The geometric shapes on the surface such as polishing marks, lapping marks, grinding marks, cutting tool marks, and micronotches act as stress riser, providing a trigger for inducing quench cracking.

10.4.4.2.2 Effect of Oxide or Coating Layer

The presence of a thin layer such as oxide scale and or a coating may cause a cooling acceleration effect by suppression of vapor blanket formation or by acceleration of the

TABLE 10.1
Effect of Agitation on Quench Cracking in Water and Polymer Quenching of Steel Disks Shown in Figure 10.13. Steel Materials Are Japanese Standard S45C, SK45 and SCM435

	Frequency of Occurrence of Quench Cracking		
Quenchants and their Agitation	**S45C 0.45%C–0.67%Mn**	**SK4 0.98%C–0.77%Mn**	**SCM435 0.35%C–0.76%Mn–1.06%Cr–0.20%Mo**
City water (30°C)			
Still (non-agitated)	100%	100% (flat surface)	100%
0.3m/s upward	70%	30% (flat surface) 70% (hole surface)	100%
0.7m/s upward	0%	0% (flat surface) 100% (hole surface)	60%
5m/s open spray	0%	10% (flat surface) 90% (hole surface)	0%
10% polymer quenchant (30°C, PAG)			
Still (non-agitated)	0%	0%	0%
0.3m/s upward	0%	—	—
0.7m/s upward	0%	0%	0%

Source: From M. Narazaki, G.E. Totten, and G.M. Webster, in *Handbook of Residual Stress and Deformation of Steel*, G.E. Totten, M.A.H. Howes, and T. Inoue, Eds., ASM International, Materials Park, OH, 2002, pp. 248–295.

collapse [6]. In addition, uniform cooling is caused by the existence of such a thin layer. Therefore, the existence of an oxide scale or clay coating largely suppresses the occurrence of quench cracking. However, a heavy oxide scale of the steel workpiece often causes unstable cooling and decarburization [6].

10.4.4.3 Minimizing Quench Distortion

10.4.4.3.1 Component Design

One of the causes of unacceptable distortion and cracking of steel parts is component design. Poor component design promotes distortion and cracking by accentuating nonuniform and nonsymmetrical heat transfer during quenching. The basic principle of successful design is to

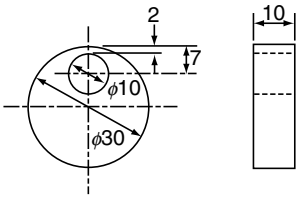

FIGURE 10.13 Disk specimen for quench-cracking test. Specimen dimensions were 30-mm diameter by 10 mm thick; specimen contains an eccentrically located 10-mm-diameter hole. (From M. Narazaki, G.E. Totten, and G.M. Webster, in *Handbook of Residual Stress and Deformation of Steel*, G.E. Totten, M.A.H. Howes, and T. Inoue, Eds., ASM International, Materials Park, OH, 2002, pp. 248–295.)

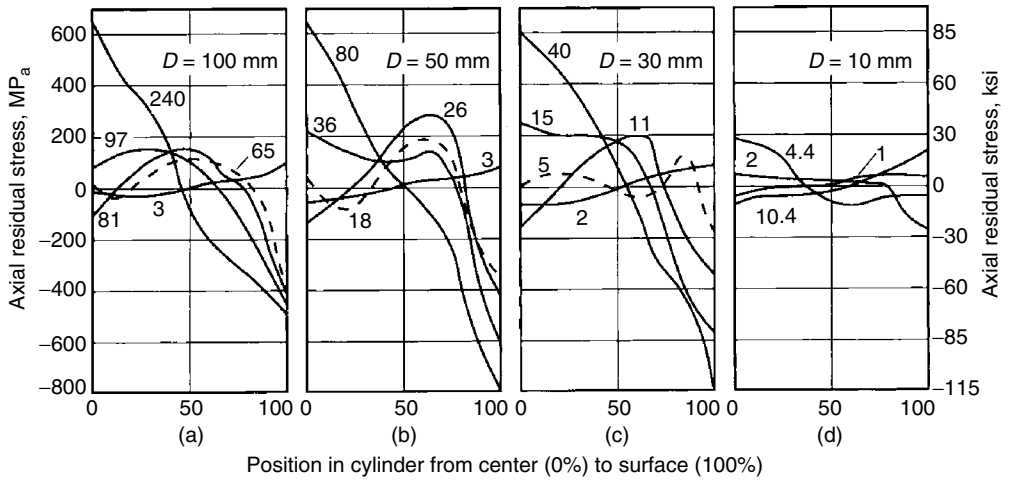

FIGURE 10.14 Axial stress distribution during water quenching for various AISI 1045 steel cylinders with diameter D, at selected times (in seconds) after the start of quenching from 850°C (1560°F) in 20°C (70 °F) water. The final microstructure of the 10-mm (0.4 in.) diameter cylinder is completely martensite, while the others have a ferritic–pearlitic core. (From T. Ericsson, *ASM Handbook*, Vol. 4, *Heat Treating*, ASM International, Materials Park, OH, 1991, p. 16; H.J. Yu, U. Wolfstieg, and E. Macherauch, *Arch. Eisenhüttenwes*., 51, 1980, 195.)

select shapes that will minimize the temperature gradient through the part during quenching. Component designs that minimize distortion and cracking are as follows:

- Design symmetry: It is important to provide greater symmetry. One of techniques for design symmetry is to add dummy holes, key grooves, or other shapes to steel parts.
- Balance of cross-sectional area: The difference between large cross-sectional area and thin one should be decreased by using several techniques as follows:
  - Avoiding abrupt cross-sectional size changes by using large radii
  - Adding dummy holes to large cross-sectional areas
  - Changing from blind holes to through-type holes
  - Changing from thick solid shapes to thin hollow shapes
  - Dividing a complicated shape to sectional components
- Avoiding sharp corners and edges: Distortion and cracking encountered when quenching a part with sharp corners and edges that increase cooling nonuniformity and act as stress risers. Therefore, it is effective to round corners and edges or to employ a tapered shape.

10.4.4.3.2 Steel Grade Selection

Although quench distortion and cracking are most often due to nonuniform cooling, material selection can be an important factor. Some attention should be paid to select a material as follows:

- The compositional tolerances should be checked to assure that the alloy is within the specification.
- It is often better to choose a low-carbon content, because the high-carbon content often causes the higher susceptibility for distortion and cracking.
- If possible, it is better to choose a combination of a high-alloy steel and a very slow cooling. As a matter of course, the selection of high-alloy steels markedly rises the material cost.

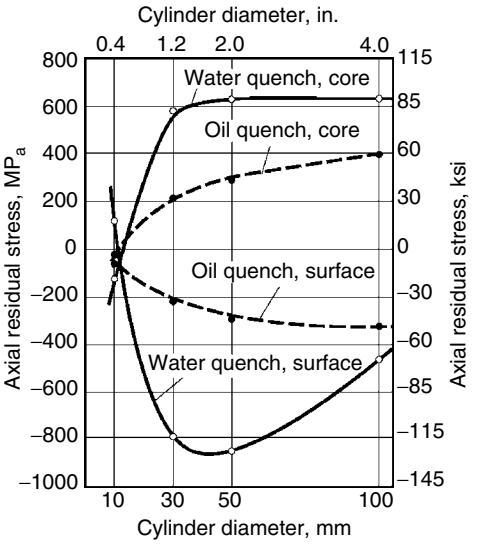

FIGURE 10.15 Dependence of axial residual stresses on cylinder diameter. Same steel as in Figure 10.14. The core is martensite for 10-mm (0.4 in.) diameter, but is ferrite–pearlite for larger diameters. (From T. Ericsson, *ASM Handbook*, Vol. 4, *Heat Treating*, ASM International, Materials Park, OH, 1991, p. 16; H.J. Yu, U. Wolfstieg, and E. Macherauch, *Arch. Eisenhüttenwes*., 51, 1980, 195.)

Cracking propensity increases as the M_s temperature and the carbon equivalent (CE) increase. Quench cracks were prevalent at carbon equivalent values above 0.525, as illustrated in Figure 10.16 [2].

10.4.4.3.3 Selection of Quenchant and Agitation

Quenchants must be selected to provide cooling rates capable of producing an acceptable microstructure in the section thickness of interest. However, it is not desirable to use quenchants with excessively high heat-removal rates. Typically, the greater the quench severity, the greater the propensity for increased distortion or cracking. Although a reduction of quench severity leads to reduced distortion, it may also be accompanied by undesirable microstructures. Therefore, it is difficult to select an optimal quenchant and agitation. Cooling power (quench severity) of quenchant should be as low as possible while maintaining a sufficiently high cooling rate to ensure the required microstructure, hardness, and strength in critical sections of the steel parts.

Quench severity is defined as the ability of a quenching medium to extract heat from a hot steel workpieces expressed in terms of the Grossmann number (H) [10]. A typical range of Grossmann H-values (numbers) for commonly used quench media are provided in Table 10.2, and Figure 10.17 provides a correlation between the H-value and the ability to harden steel, as indicated by the Jominy distance (J-distance) [11]. Although Table 10.2 is useful to obtain a relative measure of the quench severity offered by different quench media, it is difficult to apply in practice, because the actual flow rates for moderate, good, strong, and violent agitation are unknown.

Alternatively, the measurement of actual cooling rates or heat fluxes provided by a specific quenching medium does provide a quantitative meaning to the quench severity provided. Some illustrative values are provided in Table 10.3 [12].

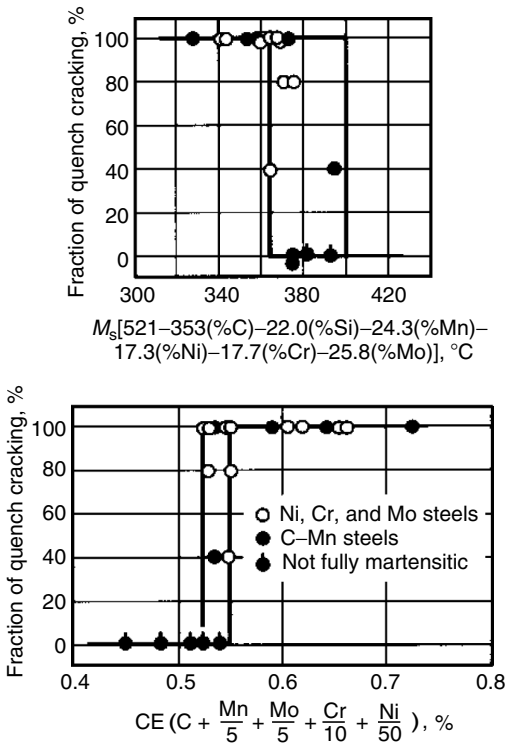

FIGURE 10.16 Effect of M_S temperature and carbon equivalent on the quench cracking of selected steel. (From C.E. Bates, G.E. Totten, and R.L. Brennan, in *ASM Handbook*, Vol. 4, ASM International, Materials Park, OH, 1991, pp. 67–120.)

Typically, the greater the quench severity, the greater the propensity of a given quenching medium to cause distortion or cracking. This usually is the result of increased thermal stress, not transformational stresses. Specific recommendations for quench media selection for use with various steel alloys is provided by standards such as Aerospace Material Specification (AMS) 2759.

TABLE 10.2
Grossmann *H*-Values for Typical Quenching Conditions

Quenching Medium	Grossmann *H*-Value
Poor (slow) oil quench—no agitation	0.20
Good oil quench—moderate agitation	0.35
Very good oil quench—good agitation	0.50
Strong oil quench—violent agitation	0.70
Poor water quench—no agitation	1.00
Very good water quench—strong agitation	1.50
Brine quench—no agitation	2.00
Brine quench violent agitation	5.00
Ideal quench	

It is possible with high-pressure impingement to achieve *H*-values greater than 5.00.

Source: From R. Kern, *Heat Treat.*, 1985, 41–45.

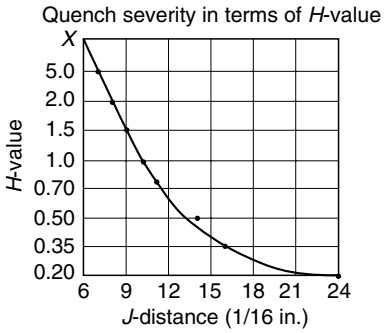

FIGURE 10.17 Quench severity in terms of Grossman (H) values. Jominy distance (J-distance). (From R. Kern, *Heat Treat.*, 1985, 41–45.)

10.4.4.4 Quench Uniformity

Quench nonuniformity is perhaps the greatest contributor to quench distortion and cracking. Nonuniform cooling can arise from nonuniform flow fields around the part surface during quenching or nonuniform wetting of the surface [4,11,13,14]. Both lead to nonuniform heat transfer during quenching. Nonuniform quenching creates large thermal gradients between the core and the surface of a steel part, or among the surfaces of the parts.

Poor agitation design is a major source of quench nonuniformity. The purpose of the agitation system is not only to take hot fluid away from the surface to the heat exchanger but also to provide uniform heat removal over the entire cooling surface of all of the parts throughout the load that is being quenched.

In the batch quench system where vertical quenchant flow occurs throughout a load, the bottom surfaces of the parts experience greater agitation than the top surfaces. Agitation produces greater heat loss at the bottom, creating a large thermal gradient between the top and the bottom surfaces.

TABLE 10.3
Comparison of Typical Heat Transfer Rates for Various Quenching Media

Quench Medium	Heat Transfer Rate, W/m^2 K
Still air	50–80
Nitrogen (1 bar)	100–150
Salt bath or fluidized bed	350–500
Nitrogen (10 bar)	400–500
Helium (10 bar)	550–600
Helium (20 bar)	900–1000
Still oil	1000–1500
Hydrogen (20 bar)	1250–1350
Circulated oil	1800–2200
Hydrogen (40 bar)	2100–2300
Circulated water	3000–3500

Source: From P.F. Stratton, N. Saxena, and R. Jain, *Heat Treat. Met.*, 24(3), 1997, 60–63.

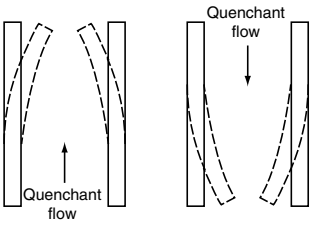

FIGURE 10.18 Effect of quenchant flow direction on distortion. (From R.T. Von Bergen, in *Quenching and Distortion Control*, G.E. Totten, Ed., ASM International, Materials Park, OH, 1992, pp. 275–282.)

If a submerged spray manifold is used to facilitate more uniform heat removal, the following design guidelines are recommended:

- The total surface of the part should experience uniform quenchant impingement.
- The sufficiently large holes and proper spacing between holes should be used.
- The manifold face should be at least 13 mm (0.5 in.) from the surface of the part that is quenched.
- The repeated removal of hot quenchant and vapor should be possible.

Excessive distortion was also obtained with an agitation system illustrated in Figure 10.18 when the quenchant flow was either in the same direction relative to the direction of part immersion or in the opposite direction [14]. The solution to this problem was to minimize the quenchant flow to that required for adequate heat transfer during the quench and to provide agitation by mechanically moving the part up and down in the quenchant. Identifying sources of nonuniform fluid flow during quenching continues to be an important design goal for optimizing distortion control and minimizing quench cracking.

Nonuniform thermal gradients during quenching are also related to interfacial wetting kinematics which is of particular interest with vaporizable liquid quenchants including: water, oil, and aqueous polymer solutions [15]. Most liquid vaporizable quenchants exhibit boiling temperatures between 100 and 300°C (210 and 570°F) at atmospheric pressure. When parts are quenched in these fluids, surface wetting is usually time-dependent which influences the cooling process and the achievable hardness.

Another major source of nonuniform quenching is foaming and contamination. Contaminants include sludge, carbon, and other insoluble materials. It includes water in oil, oil in water, and aqueous polymer quenchants. Foaming and contamination lead to soft spotting, increased distortion, and cracking.

10.4.4.5 Quenching Methods

Part design, material and quenchant selection, agitation, etc. are the most important factors to suppress quench distortion and cracking of steel parts. In addition, several methods for minimizing distortion and eliminating cracking are employed; for example, interrupted quenching, time quenching, marquenching, austempering, press quenching, and plug quenching. These quenching methods are based on the improvement of cooling uniformity by controlling of cooling, or restraint of distortion by using restraint fixtures. For the detailed description of these methods, the reader is referred to Ref. [2,6].

10.5 DISTORTION DURING POST QUENCH PROCESSING

There are many possible treatments that can be carried out after quenching. The typical operations are:

- Straightening
- Tempering
- Stabilization with tempering and subzero treatment
- Metal removal by grinding, etc.

10.5.1 STRAIGHTENING

If it is necessary to reduce the distortion of quench-hardened parts, straightening is done by flexing or selective peening the parts. Flexing or peening results in the change of the stress distribution and poses a risk of cracking. Therefore, it is the usual practice to straighten after tempering. Straightening while parts are still hot from the tempering furnace is often performed to avoid cracking.

10.5.2 TEMPERING

Steel parts are often tempered by reheating after quench-hardening to obtain specific values of mechanical properties. Tempering of steel increases ductility and toughness of quench-hardened steel, relieves quench stresses, and ensures dimensional stability. The tempering process is divided into four stages:

1. Tempering of martensite structure
2. Transformation of retained austenite to martensite
3. Tempering of the decomposition products of martensite
4. Decomposition of retained austenite to martensite

Microstructural variation during tempering results in volume changes during the tempering of hardened steel [16]. In addition to dimensional change by microstructural variation, tempering may also lead to dimensional variation due to relaxation of residual stresses and plastic distortion which is due to the temperature dependence of yield strength.

Figure 10.19 shows the distortion of round steel bars (200 mm diameter and 500 mm in length) by quenching and by stress relieving during tempering [17]. A medium-carbon steel bar (upper diagrams) and a hardenable steel bar (lower diagrams) were used in this experiment. Figure 10.19a and d shows the results of quenching from 650°C without phase transformation. The distortion in each case is almost the same regardless of the different quenchants and the different steel chemical composition. These convex distortions are caused by nonuniform thermal contraction and resultant thermal stress during cooling. Figure 10.19b and Figure 10.19e shows the results of quenching from 850°C with phase transformation. The distortion in Figure 10.19e (hardenable steel) shows a convex configuration, but the distortion in Figure 10.19b (medium-carbon steel of poor hardenability) shows a configuration that combines convex and concave distortions. In addition, WQ has a greater effect on distortion than oil quenching (OQ). Figure 10.19c and Figure 10.19f shows the configurations after tempering. These results show that tempering after quenching results in not only volumetric changes but also convex distortions. Such distortions seem to be related to relieving of residual stresses by tempering.

Figure 10.20 and Figure 10.21 [18] show the examples of stress-relief by tempering. A solid cylinder with 40 mm diameter and 100 mm length was examined for analyses

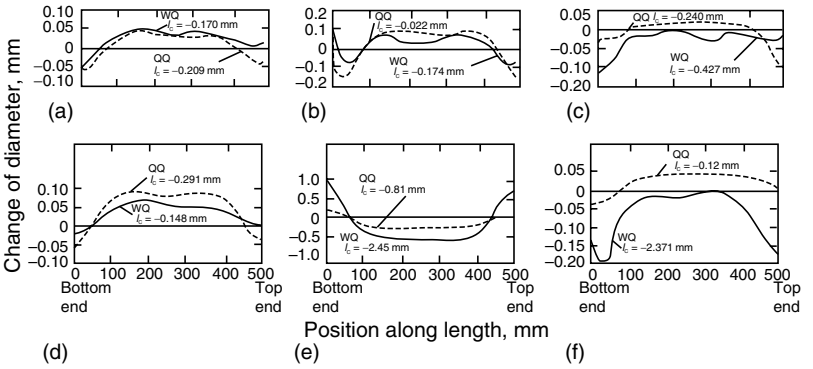

FIGURE 10.19 Deformation of medium-carbon and hardenable steel bars by quenching from below and above transformation temperature and by stress-relieving. l_C, change of length. (a) and (d) quenched from 650°C. (b) and (e) quenched from 850°C. (c) and (f) tempered at 680°C. (a) to (c) JIS S38C steel (0.38%C). (d) to (f) JIS SNCM 439 steel (0.39C–1.80Ni–0.80Cr–0.20Mo). (From Y. Toshioka, *Mater. Sci. Technol.*, 1, 1985, 883–892.)

and experiments of tempering performed after WQ. Calculated residual stress distributions after WQ are illustrated in Figure 10.20. Open and solid circles in the figure correspond to measured stresses on the surface of the cylinder by x-ray diffraction. Residual stress distributions after tempering at 400°C is shown in Figure 10.21a and Figure 10.21b for typical elapsed times of 2 and 50 h with measured values on the surface. These results show that the stresses in all directions decrease with elapsed tempering time.

10.5.3 Stabilization with Tempering and Subzero Treatment

To achieve dimensional stability over long periods, the amount of retained austenite in quenched parts should be reduced. Dimensional stability is a vital requirement for gauges and test blocks.

Stabilization can be obtained by multiple tempering and subzero treatment (cold treatment). It is the usual practice to conduct a single or repeated subzero treatment after the initial tempering. Subzero treatment is normally accomplished in a refrigerator at temperature of −60 to −90°C (−75 to −130°F). Subzero treatment may cause a size change by further austenite-to-martensite transformation resulting in further expansion. If the size change is restrained, then additional stresses will be locked in. This effect depends on the M_s–M_f

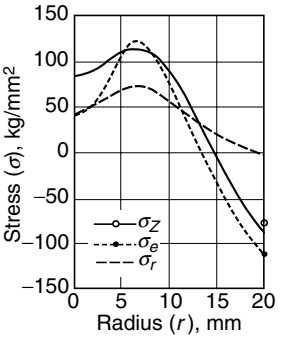

FIGURE 10.20 Stress distribution in steel cylinder after quenching. (From T. Inoue, K. Haraguchi, and S. Kimura, *Trans. ISIJ*, 18, 1978, 11–15.)

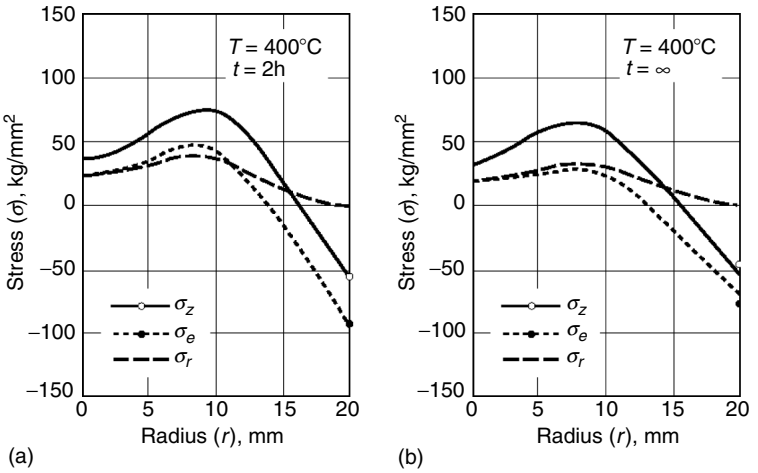

FIGURE 10.21 Stress distribution in steel cylinder during tempering. (From T. Inoue, K. Haraguchi, and S. Kimura, *Trans. ISIJ*, 18, 1978, 11–15.)

temperature range, the temperature and time of subzero treatment, and the creep strength of the material. Tools must be retempered immediately after returning to room temperature following subzero treatment to reduce internal stress and increase toughness of the fresh martensite [19].

10.5.4 Metal Removal after Heat Treatment

A finishing process such as grinding is often required to correct dimensional changes caused by heat treatment. The tendency is to try to use parts as heat-treated without touching the surface again because in this condition the part may exhibit a much greater fatigue strength [20]. This is particularly true for parts loaded under concentrated contact such as bearings or gears.

For parts with close tolerances, however, the component size must be brought under control in the finish grinding. This leads to a dilemma: if excess material is left on the part prior to heat treatment, there will be enough stock to enable the size to be brought under control. However, if too much is taken off, the most effective regions of the carburized (or nitrided) case are removed.

Figure 10.22 shows a gear with excessive material removed from a tooth after case hardening treatment [21]. In the example shown in Figure 10.22, if the tooth has distorted to the right, more material has to be ground from the right side of the tooth. This has several serious consequences. First, the lack of uniformity in case depth leads to uneven residual stress distribution. Second, its mechanical strength will be less than optimum performance. Third, a considerable thickness of material has to be removed during grinding, increasing the probability of grinding burns and cracking.

10.6 MEASUREMENT OF RESIDUAL STRESSES

In the previous discussion, it was shown that propensity for distortion and cracking is dependent on thermally-induced and transformation-induced stresses. X-ray diffraction methods are usually used for these stresses. There are, however, applicable measurement methods. Detailed description on various measurement methods of residual stress are provided in Refs. [22–24].

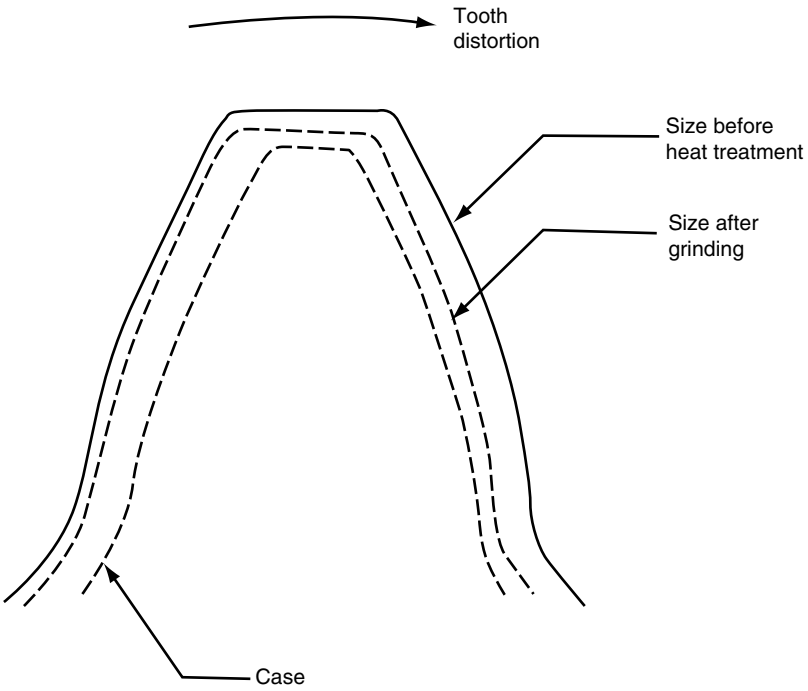

FIGURE 10.22 Schematic of material ground from a distorted gear tooth after case hardening treatment. (From M.A.H. Howes, in *Quenching and Control Distortion*, G.E. Totten, Ed., ASM International, Materials Park, OH, 1992, pp. 251–258.)

10.6.1 X-Ray Diffraction Method

X-ray diffraction is the most common method for measurement of stresses [25]. This procedure involves irradiating a sample with x-rays. When steel is irradiated with x-ray, a characteristic diffraction pattern that is dependent on the crystal structure of the iron and alloying elements is present. The spacing between the lattice points, or *d*-spacing, can be calculated from the diffraction pattern.

The interplanar *d*-spacing for any set of parallel planes is calculated from the x-ray diffraction data using Bragg's equation:

$$n\lambda = 2d \sin\theta,$$

where n is an integer, λ is the wavelength of the x-ray beam, d is the spacing between reflecting planes, and θ is the angle of incidence of the beam with sample. This relationship is illustrated in Figure 10.23.

When a load is applied to the sample, there will be a perturbation in the *d*-spacing. Thus, changes in the measured diffraction patterns (Δd) are related to the lattice strain ($\Delta d/d$). The strain ($\Delta d/d$) is calculated from the diffraction data:

$$\frac{\Delta d}{d} = -\cot\left(\frac{\Delta 2\theta}{2}\right),$$

There are a number of experimental procedures for calculating stress from the diffraction data. The most common method is the $\sin^2 \Psi$ mehtod, in which the sample is irradiated and

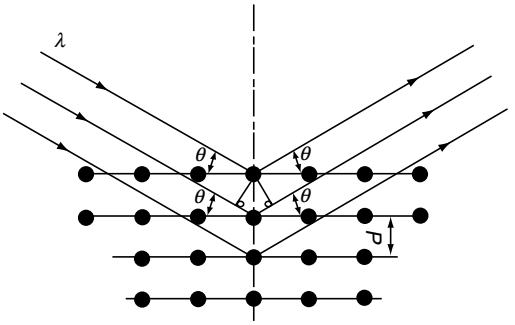

FIGURE 10.23 Illustration of the Bragg relation.

changes in the diffraction angle Ψ are related to the interplanar spacing d and to strain $\Delta d/d$. The change in interplanar spacing is determined by measuring d with different applied stresses. The stress σ is calculated from

$$\sigma = \frac{d - d_0}{d_0}\left(\frac{E}{1+\nu}\right)\left(\frac{1}{\sin^2 \psi}\right),$$

where ν is Poisson's ratio. The d-spacing is determined from the Bragg equation. If a $\Delta d/d$ versus $\sin^2 \Psi$ plot is constructed, the stress can be calculated from the slope of the straight line as follows:

$$\text{Slope} = \frac{\sigma(1+\nu)}{E},$$

which can be rearranged to solve for σ:

$$\sigma = \text{slope} \times \frac{E}{(1+\nu)},$$

Because Poisson's ratio ν is known and the (or preferably measured) modulus E is also known, the stress σ can be readily calculated.

Possible sources of x-ray measurement errors include [26]:

- Error in peak position
- Stress-relief by aging
- Sample anisotropy
- Grain size
- Round surfaces (flat surfaces are preferable)

10.6.2 Hole-Drilling Methods

Residual stress may be measured by a method in which a hole is drilled into the material tested and the change in strain is measured, usually with strain gauges. Residual stress is then calculated from the magnitude and direction of this strain, hole size, and material properties. There are many hole-drilling methods. However, one of the most commonly used methods is the classical Sachs bore-out method [27]. Changes in residual stress with depth can be determined by incrementally drilling the hole and measuring the changes in stress with depth.

The Sachs bore-out method involves following assumptions [28]:

- The metal is effectively isotropic and has a constant Young's modulus and Poisson's ratio.
- The residual stresses are distributed with rotational symmetry about the axis of the bar.
- The tube formed by boring the bar is circular in cross section, and its inner and outer walls are concentric.
- The specimen is sufficiently long (or thick) to prevent bending.

The Sachs bore-out procedure, while one of the best-known methods for the determination of residual stresses, has a number of disadvantages [28,29]:

- It is slow and relatively expensive.
- Care must be taken to ensure that plastic deformation does not occur during hole-drilling process.
- Strain gauge corrections for drift measurement must be made.
- It can only measure final stress thus cannot be readily applied to stress during cooling.
- It results in damage to test specimen.

10.6.3 Bending and Deflection Methods

Bending and deflection methods involve the measurement of a change in the diameter of a slit tube or the curvature of a flat plate [30]. The use of such methods requires knowledge of the interrelationship of stress and the amount of deflection observed. Although these methods are not applicable to the determination of radial stresses, with appropriate procedural adaptation they may be low-cost options for the determination of a systematic distribution of residual stress and uniform biaxial stresses in bars, tubes, sheets, and plates [28].

For best results, to properly account for material variation, the elastic modulus should be determined experimentally instead of using reference book values. The modulus is determined by attaching a strain gauge to the test specimen and then measuring the corresponding deflection with the application of different loads.

10.6.4 Other Residual Stress Measurement Methods

There are a number of other less commonly used but valuable experimental methods that have been used for residual stress measurement. These include magnetic method [31,32], ultrasonic method [33–35], and neutron diffraction method [36].

The magnetic method is based on the stress dependence of the Barkhausen noise amplitude. As Barkhausen noise depends on composition, texture, and work hardening, it is necessary to do calibration for each application. In addition, the use of this method is limited to only ferromagnetic materials. Ultrasonic method has the potential for greater capability and usefulness in the future, but has the disadvantage that it requires transducers shaped to match the inspected surface. Neutron diffraction method has a much deeper penetration than x-ray, but has the disadvantages of safety and cost of the apparatus.

10.7 TESTS FOR PROPENSITY FOR DISTORTION AND CRACKING

Numerous tests have been applied to evaluate the potential of a steel to undergo distortion or cracking upon heat treatment. In most cases, the test specimens are manufactured specifically for these test procedures. One of the most difficult challenges is to devise a testing procedure

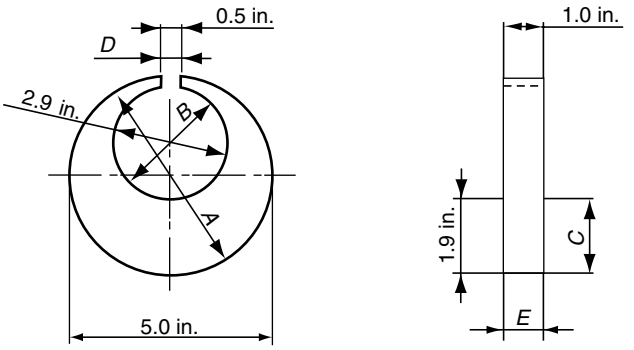

FIGURE 10.24 Example of C-ring test specimen used for quench distortion studies. (From H. Webster and W.J. Laird, *ASM Handbook*, Vol. 4, ASM International, Materials Park, OH, 1991, p. 144.)

that accounts for the statistical nature of the occurrence of cracking, because it is seldom that 100% of all parts actually undergo cracking in the heat treatment process.

10.7.1 Navy C-Ring and Slotted Disk Test

One of the oldest standard tests for evaluating quench distortion is the so-called Navy C-ring test (see Figure 10.24) [37]. A modified Navy C-ring test specimen (see Figure 10.25) has also been reported [38]. This notched test specimen has greater crack sensitivity to evaluate propensity for cracking in addition to distortion.

10.7.2 Cylindrical Specimens

Many workers have simply quenched cylindrical specimens and observed them for cracking and volumetric changes. For example, Moreaux [39] used round bar test specimens of 0.60% C, 1.6% Si, and 0.5% Cr steel whose length was three times their diameter. These studies showed that the transition temperature from film to nucleate boiling contributes primarily to thermal stress. The nucleate boiling to convective cooling transition will primarily affect the

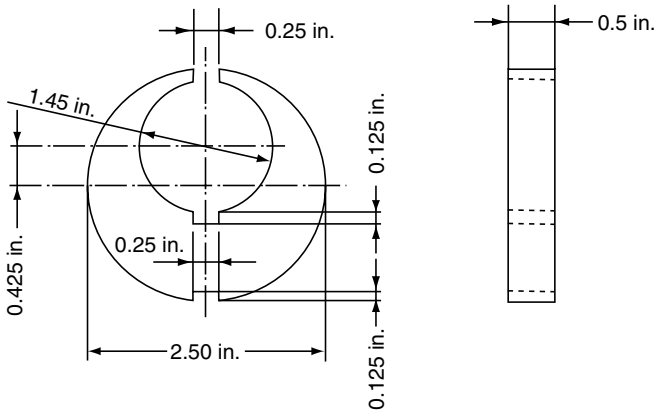

FIGURE 10.25 Modified Navy C-ring distortion test specimen. (From C.E. Bates, G.E. Totten, and R.L. Brennan, *ASM Handbook*, Vol. 4, ASM International, Materials Park, OH, 1991, p. 100.)

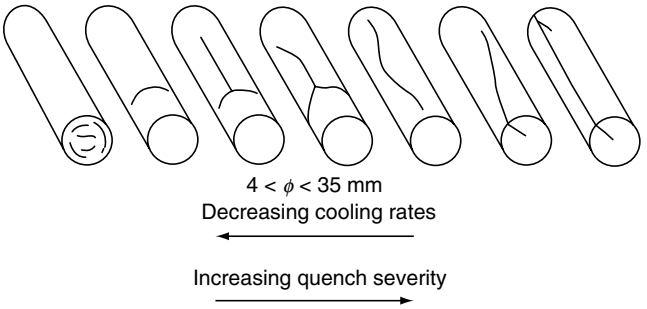

FIGURE 10.26 Quench-cracking pattern in a 34-mm-diameter cylinder of 60SC7 steel quenched in water. (From G. Beck, *Mem. Etud. Sci. Rev. Metall.*, July 1985, pp. 269–282.)

formation of transformational stresses. Beck [40] studied the effect of the interrelationship between quench severity and average cooling rates on the severity of crack formation. The work was performed using 34-mm (1.3 in.) diameter 60SC7 steel cylindrical test specimens, and the results are shown in Figure 10.26.

10.7.3 Stepped Bar Test

A stepped bar test using the test specimen shown in Figure 10.27 has been used to measure the effect of cross-sectional size on distortion [41]. In this test, the running distortion of a long bar per unit length is measured.

10.7.4 Key-Slotted Cylindrical Bar Test

Narazaki and Ninomiya used a key-slotted cylindrical bar specimen shown in Figure 10.28 to measure the effect of quenchants on distortion [42]. Furthermore, they evaluated quench simulation accuracy to compare simulated distortion and measured distortion of the key-slotted cylindrical bar specimen [43].

10.7.5 Disk with an Eccentric-Positioned Hole

Owaku [44] used steel cylinders and disk plates with eccentric-position and holes totally examine cracking mechanisms. Narazaki et al. [6] also used a disk plate with an eccentrically-positioned hole (see Figure 10.13) to examine the effects of surface condition, steel materials, and quenchants [6,9]. Several cracking patterns shown in Figure 10.29 were observed after quenching of steel disk specimens (30-mm diameter by 10-mm thick) with an eccentrically located 10-mm-diameter hole. The cracking susceptibility and patterns depended on surface condition and materials of the steel disk specimen in addition to the quenchant and agitation used [6,45].

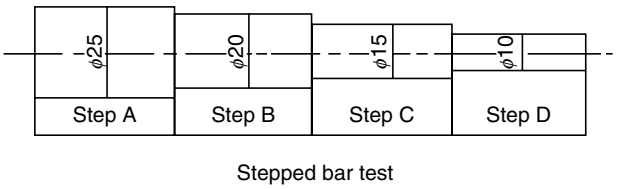

FIGURE 10.27 Stepped bar test. (From W.A.J. Moerdijk, *Adv. Mater. Process.*, 137(3), 1990, 19–28.)

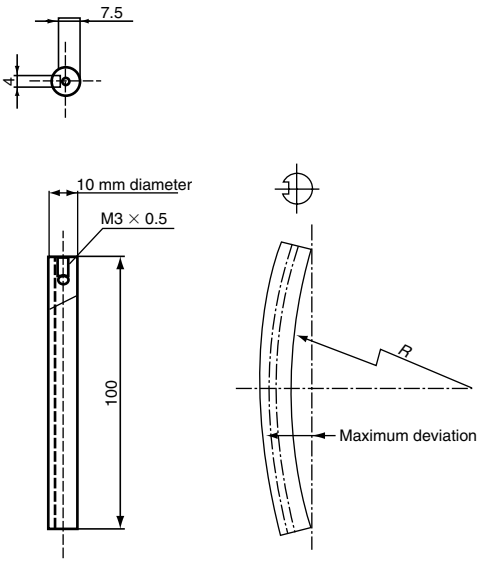

FIGURE 10.28 Key-slotted cylindrical bar specimen. (From Narazaki and S. Ninomiya, *Proceedings of the 13th International Federation for Heat Treatment & Surface Engineering* & ASM Surface Engineering Congress, Columbus, OH, October 2002, pp. 464–470.)

10.7.6 Finned Tubes

The distortion of hollow tubes has been studied by Mikita and coworkers [46,47] using the finned tube test specimen shown in Figure 10.30, where a large hole is drilled into a solid block, effectively creating a fin on one end. In this test, two types of cracks, fin and vertical, were quantified. The susceptibility for fin-cracking can be increased by cutting a V-notch in the fin [46]. Mikita and Nakabayashi [47] determined the relative cracking frequency using a limited number n of test specimens by quenching each specimen repeatedly until a crack appeared. Sensitivity for quench cracking was designated as the $1/n$ value.

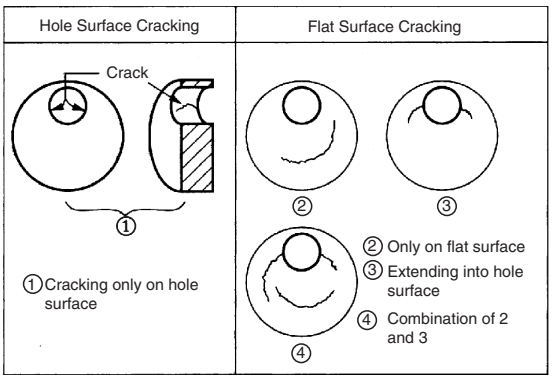

FIGURE 10.29 Cracking patterns observed on steel disk specimen (Figure 10.13). 1: cracking only on hole surface, 2: cracking only on flat surface, 3: combination of 1 and 2, 4: combination of 2 and 3. (From K. Arimoto, D. Lambert, K. Lee, W.T. Wu, and M. Narazaki, *Heat Treating: Proceedings of the 19th Conference*, S.J. Midea and G.D. Pfaffmann, Eds., ASM International, Materials Park, OH, 1999, pp. 435–440.)

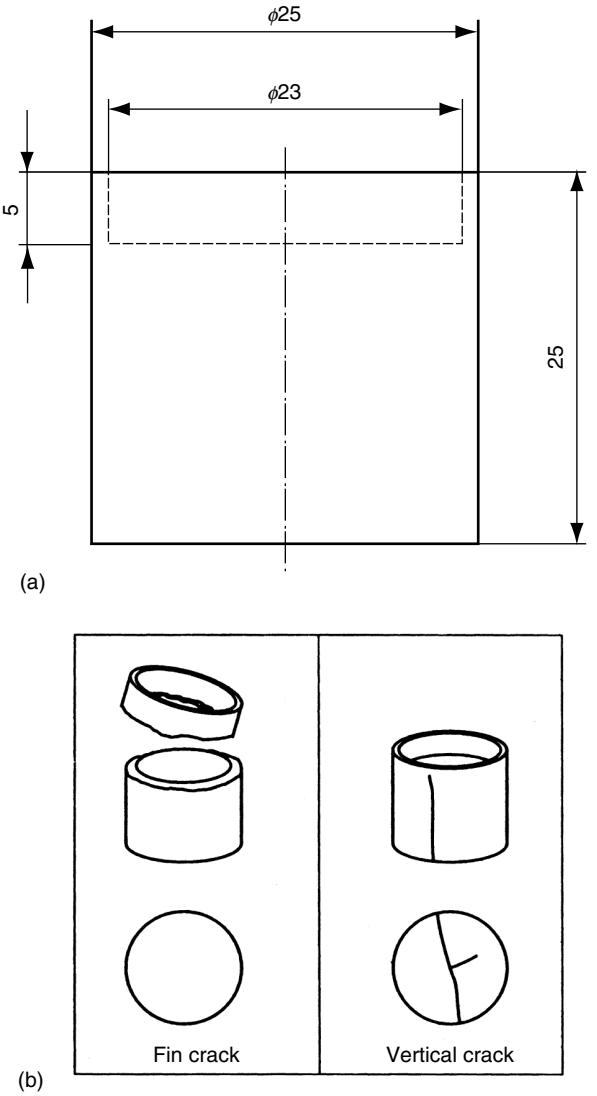

FIGURE 10.30 Finned tube specimen and types of cracks. (From Y. Mikita, I. Nakabayashki, and K. Sakamaki, *Heat Treat*., 1989, 21–24; Y. Mikita and I. Nakabayashi, *Nipon Kikai Gakkai, Ronbunshu* (A-hen), 53(489), 1987, 884–889.)

10.8 PREDICTION OF DISTORTION AND RESIDUAL STRESSES

The computer prediction of thermo-mechanical behavior in the heat-treating process is useful for determining a heat-treating condition because it is possible to predict the microstructure, hardness, distortion, and stress of steel parts after heat treating. To predict thermo-mechanical behavior, residual stresses, and distortion in the heat-treating process of steel parts, a simulation method based on metallo-thermo-mechanical theory [48,49] and finite-element analysis is often applied.

Usual procedures for numerical analysis of the heat-treating process of steel parts would be as follows:

- Define the shape. The dimensions of the part can be defined, preferably as a three dimensional CAD (computer-aided design) presentation of the part as a solid model.
- Construct a finite-element model. The solid model can be translated into a finite-element network, the complexity of which will be determined by the size, shape, and form of the part. Experience will show the optimum number of mesh elements to be used. This will also be related to the available computer power and the desired accuracy.
- Perform quenching calculations. The cooling of every network cell during the quench can be calculated based on the known characteristics of the quenching medium and the part. These will include the heat transfer coefficient of the quenchant under the conditions specified by the designer and those naturally present in the quenching system, as well as the following items: initial temperature of the part, temperature of the quenchant, cooling characteristics of the quenchant, agitation of the quench medium, orientation of quenchant flow to surface that is cooled, complexity of surface features, conductivity of the part, specific heat and latent heat data.
- Calculate the phase transformations. Phase transformations can be calculated using time–temperature–transformation (TTT) data available on the source material for the part. For carburized and nitrided steels the differences in composition and thus hardenability and phase boundary temperatures must be allowed for. Continuous cooling Transformation (CCT) data will be the preferred source.
- Calculate deformation and stress. These calculations can be made with available data on the Poisson's ratio, modulus of elasticity yield strength, work-hardening modulus, linear thermal expansion coefficient and density changes due to phase changes. All these data are obviously temperature-dependent.

The metallo-thermo-mechanical theory is coupled with temperature, phase transformation, and stress–strain fields. In the heat-treating process, the fields of metallic structures and stress–strain as well as temperature are affected by each other. The triangular diagram illustrated in Figure 10.31 shows such coupling effects [50]. In carburizing–quenching process, the effect of carbon content on the three fields is also represented by the dashed lines in the figure. A series of theoretical models with consideration of the effect of carbon diffusion and distribution is introduced.

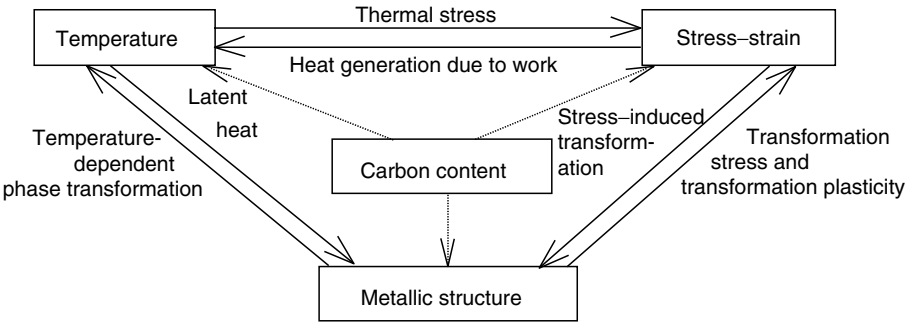

FIGURE 10.31 Coupling effects of temperature, stress–strain and metallic structure in heat treatment process. (From T. Inoue, D.Y. Ju, and Y. Arimoto, *Proceedings of the First International Conference on Quenching and Distortion Control* (Chicago), 1992, pp. 205–212.)

10.8.1 Governing Equations

An example of introducing the governing equations in the framework of thermo-mechanical behavior for describing temperature and stress–strain fields incorporating metallic structures in the quenching process is summarized as follows [50–53].

10.8.1.1 Mixture Rule

When a material point undergoing a heat treatment process is assumed to be composed of a multiphase structure, an assumption is made that a material parameter χ is described by the mixture law:

$$\chi = \sum_{I=1}^{N} \chi_I \xi_I \quad \text{and} \quad \sum_{I=1}^{N} \xi_I = 1, \tag{10.1}$$

where ξ_I denotes the volume fraction for the I-th phase.

10.8.1.2 Heat Conduction Equations and Diffusion Equation

The temperature field is governed by a special heat conduction equation coupled stress work and latent heat due to phase transformation during quenching process is given as

$$\rho c \dot{T} - \frac{\partial}{\partial x_i}\left(k \frac{\partial T}{\partial x_i}\right) - \sigma_{ij} \dot{\varepsilon}_{ij}^{p} + \sum \rho_I l_I \dot{\xi}_I = 0, \tag{10.2}$$

where k and l_I denote the coefficient of heat conduction and the latent heat produced by the progressive I-th constituent.

The boundary conditions of heat transfer on the outer surface is assumed to be

$$-k \frac{\partial T}{\partial x_i} n_i = h(T - T_{\mathrm{w}}), \tag{10.3}$$

where h is a function that depends on temperature. h and T_{w} denote the heat transfer coefficient and the temperature of coolant on heat transfer boundary with unit normal n_i, respectively.

Carbon content during carburizing process is solved by the diffusion equation

$$\dot{C} = \frac{\partial}{\partial x_i}\left(-D \frac{\partial C}{\partial x_i}\right), \tag{10.4}$$

where C is content in the position x_i -direction, D is the diffusion constant determined by the boundary condition, which is specified by the reaction across the surface layer

$$D \frac{\partial C}{\partial x_i} n_i = h_{\mathrm{c}}(C_{\mathrm{e}} - C_{\mathrm{s}}), \tag{10.5}$$

where h_{c} and C_{e} are the surface reaction rate coefficient and the known content of the external environment, respectively.

10.8.1.3 Constitutive Equation

Total strain rate $\dot{\varepsilon}_{ij}$ is assumed to be divided into elastic, plastic, thermal strain rates and those by structural dilatation due to phase transformation and transformation plasticity such that

$$\dot{\varepsilon}_{ij} = \dot{\varepsilon}^{\mathrm{e}}_{ij} + \dot{\varepsilon}_{ij}{}^{\mathrm{p}} + \dot{\varepsilon}^{\mathrm{T}}_{ij} + \dot{\varepsilon}^{\mathrm{m}}_{ij} + \dot{\varepsilon}^{\mathrm{tp}}_{ij}. \tag{10.6}$$

Here, the elastic strain

$$\varepsilon^{\mathrm{e}}_{ij} = \frac{1+\nu}{E}\sigma_{ij} - \frac{\nu}{E}(\sigma_{kk})\delta_{ij}, \tag{10.7}$$

with Young's modulus E and Poisson's ratio ν.

The thermal strain is the function of initial temperature of material T_0 and thermal expansion coefficient α as follows:

$$\varepsilon^{\mathrm{T}}_{ij} = \alpha(T - T_0)\delta_{ij}. \tag{10.8}$$

The plastic strain rate is reduced to the form by employing temperature-dependent material parameters

$$\dot{\varepsilon}^{\mathrm{p}}_{ij} = \lambda \frac{\partial F}{\partial \sigma_{ij}}, \tag{10.9}$$

$$\lambda = \hat{G}\left\{\frac{\partial F}{\partial \sigma_{kl}}\dot{\sigma}_{kl} + \frac{\partial F}{\partial T}\dot{T} + \sum_{I=1}^{N}\frac{\partial F}{\partial \xi_I}\dot{\xi}_I + \frac{\partial F}{\partial C}\dot{C}\right\}, \tag{10.10}$$

$$\frac{1}{\hat{G}} = -\left(\frac{\partial F}{\partial \varepsilon^{\mathrm{p}}_{mn}} + \frac{\partial F}{\partial \kappa}\sigma_{mn}\right)\frac{\partial F}{\partial \sigma_{mn}}, \tag{10.11}$$

with a temperature-dependent yield function

$$F = F(T,\ C,\ \sigma_{ij},\ \varepsilon^{\mathrm{p}},\ \xi_I,\ \kappa), \tag{10.12}$$

where κ is the hardening parameter.

Strain rates due to structural dilatation and transformation plasticity depending on the I-th constituent are as follows:

$$\dot{\varepsilon}^{\mathrm{m}}_{ij} = \sum_{I=1}^{N}\beta_I\dot{\xi}_I\delta_{ij} \quad \text{and} \quad \dot{\varepsilon}^{\mathrm{tp}}_{ij} = \frac{3}{2}\sum_{I=1}^{N}K_I h(\xi_I)\dot{\xi}_I s_{ij}, \tag{10.13}$$

where β and K_I stand for the dilatation due to structural change and parameter due to transformation plasticity depending on the I-th constituent.

10.8.1.4 Kinetics of Quenching Process

In the case of quenching, two kinds of phase transformation are anticipated: One is governed by the diffusionless or martensite mechanism. From thermodynamic consideration, the formula for this type of reaction from austenite is often assumed to be governed by the modified Magee's rule [54] as

$$\xi_{\mathrm{M}} = 1 - \exp\left\{\psi_1 T + \psi_2(C - C_0) + \psi_{31}\sigma_{ij} + \psi_{32}J_2^{1/2} + \psi_4\right\}, \tag{10.14}$$

where ξ_{M} is the volume fraction of martensite which is the function of carbon content, temperature, and stress. Here J_2 is the second invariant of deviatory stress. ϕ_1, ϕ_2, ϕ_3, and ϕ_4 are all coefficients obtained from experiments.

The other type of phase transformation is controlled by diffusion mechanism, and the volume fraction of developing phase such as pearlite may be expressed by modifying the Johnson–Mehl relation [55] as

$$\xi_p = 1 - \exp\left\{-\int_0^t f_t(T) f_s(\sigma_{ij}) f_c(C)(t-\tau)^3 \, \mathrm{d}\tau\right\}. \tag{10.15}$$

In this equation, $f_t(T)$, $f_s(\sigma_{ij})$, and $f_c(C)$ are the function of temperature T, stress σ_{ij}, and carbon content C, respectively. Because the TTT diagram under the applied mean stress σ_m in logarithmic scale deviates from the one without stress, which is represented by the function $f(T)$, the kinetic equation of diffusion type is often applied to the variations of pearlite or ferrite structure in quenching processes. An identification of the function $f(T)$ can be made possible by the use of some experimental data of the structure change.

10.8.1.5 Transformation Plasticity

Transformation plasticity is known as the phenomenon of accelerated plastic deformation caused by a low level of applied stress during the phase transformation. In addition to the coupling effects between stress and phase transformation, this phenomenon is also expected to influence the stress and strain distribution during quenching. Following Desalos et al. [56], the transformation plastic strain rate $\dot{\varepsilon}_{ij}^{\mathrm{tp}}$ is determined by

$$\dot{\varepsilon}_{ij}^{tp} = \sum_{I}^{N-1} \left\{\frac{3}{2} K_I h(\xi_I) \dot{\xi}_I s_{ij}\right\} \quad \text{and} \quad h(\xi_I) = 2(1 - \xi_I). \tag{10.16}$$

Here, K_I the transformation plasticity coefficient for martensitic or pearlitic transformation, in this case, may be identified by the experimental results' dependence on dilatation–temperature diagrams.

10.8.2 Coupling Algorithm in Simulation by Finite-Element Analysis

Based on the metallo-thermo-mechanical theory [50,51], The formulated finite-element equation system considering the coupling between increment of nodal displacement $\{\Delta u\}$ and temperature $\{T\}$ as well as volume fraction of structure ξ_I can be expressed as

$$[P]\{T\} + [H]\{T\} = \{Q(\xi_I), \sigma_{ij}\} \tag{10.17}$$

and

$$[K(u_i)]\{\Delta u_i\} = \{\Delta F(T, \xi_I)\}. \tag{10.18}$$

Here, matrices $[P]$, $[H]$, and $[K]$ represent the matrices of heat capacity, heat conduction, and stiffness, respectively, and the vectors $\{Q\}$ and $\{\Delta F\}$ are heat flux and increments of thermal

load. These equations are strong nonlinear equations, which are derived by the use of the expression of stress increment vector as

$$\{\mathrm{d}\sigma\} = [D]\left(\{\mathrm{d}\varepsilon\} - \frac{3\mathrm{d}\bar{\varepsilon}^{\mathrm{c}}}{2\bar{\sigma}}\{s\} - \sum_{I=1}^{N}\{\bar{\alpha}\}\,\mathrm{d}T - \sum_{I=1}^{N}\{\bar{\beta}\}\,\mathrm{d}\xi_I\right) - \sum_{I}^{N-1}\frac{3}{2}K_I h(\xi_I)\,\mathrm{d}\xi_i\{s\} + \frac{1}{S_0}\left(\frac{\partial\bar{\sigma}^2}{\partial T}\mathrm{d}T + \sum_{I=1}^{N}\frac{\partial\bar{\sigma}^2}{\partial\xi_I}\mathrm{d}\xi_I\right)\{s\}, \tag{10.19}$$

where $\bar{\varepsilon}^{c}$ and $\{s\}$ are equivalent creep strain and deviatoric stress vector. $[D]$ denotes an elastic–plastic matrix based on Mises' type yield function. Here, the functions depending on temperature and phase transformation $\bar{\alpha}$ and $\bar{\beta}$ can be written as

$$\{\bar{\alpha}\} = \frac{\partial}{\partial T}([D^{\mathrm{e}}]^{-1}\{\sigma\}) + \sum_{I=1}^{N}\left(\alpha_I\xi_I\{1\} + \frac{\partial\alpha_I}{\partial T}\xi_I\,\mathrm{d}T\{1\}\right) \tag{10.20}$$

and

$$\{\bar{\beta}\} = \frac{\partial}{\partial\xi_I}\left([D^{\mathrm{e}}]^{-1}\{\sigma\}\right) + \beta_I\{1\}, \tag{10.21}$$

α_I and β_I are the coefficients of thermal expansion and dilatation due to I-th phase transformation, respectively. $[D^{\mathrm{e}}]$ denotes the elastic matrix of materials.

In order to treat unsteady coupled equations depending on time, a time integration scheme step-by-step time integration method and Newton–Raphson method are introduced in numerical calculation, while an incremental method is used for deformation and stress analysis. Because heat transfer coefficient is dependent on the variation of the temperature on the boundary of heat transfer, we also use the time step of nonuniform to calculate temperature, phase transformation, and deformation fields [51].

10.8.3 Example of Simulation Results

10.8.3.1 Prediction of Warpage of Steel Shafts with Keyway

The finite-element method system DEFORM-HT [57] was used for simulating quenching of a JIS S45C (0.45% C) steel shaft with keyway [43]. A cylinder, 10 mm in diameter and 100 mm long, was with a keyway, 2.5 mm deep and 4 mm wide (see Figure 10.28). A tetrahedral mesh containing approximately 33,000 elements was applied to one half of the specimen; symmetry conditions were applied to the center surface. The results were evaluated against the experimental data. The simulated quench distortion history was compared against its real counterpart. Excellent resemblance was found between them as shown in Figure 10.32. In both reality and simulation, the shaft bent toward the keyway side in the beginning 1.7 s and bent to the other direction after 1.7 s. This phenomenon was believed to be caused by the combination of thermal stress, deformation, and transformation-induced volume changes.

10.8.3.2 Prediction of Distortion during Carburized Quenching Process of Cr–Mo Steel Ring

Yamanaka et al. [58] conducted a coupled metallo-thermo-mechanical analysis by using the heat-treatment simulation code HEARTS for a ring-shaped model (see Figure 10.33) of Cr–Mo

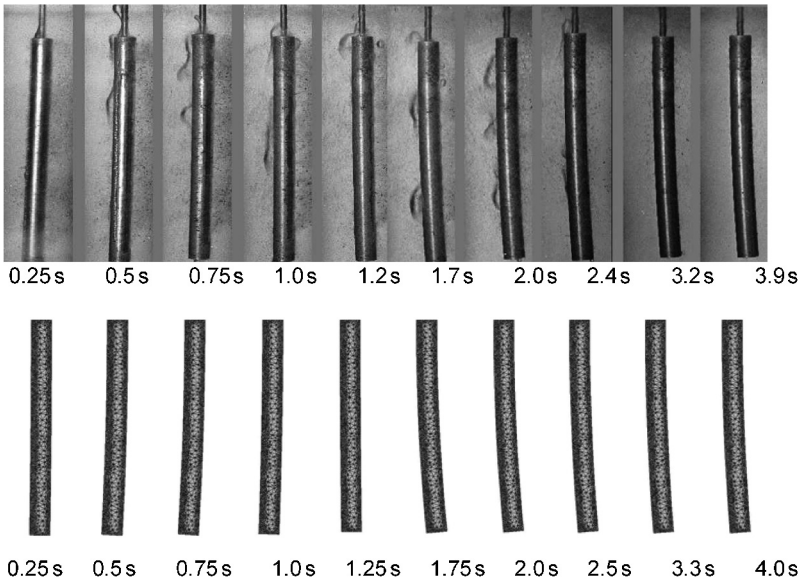

FIGURE 10.32 Distortion behavior of S45C steel shaft (10 mm in diameter and 100 mm long, was with a keyway, 2.5 mm deep and 4 mm wide, see Figure 10.28) during 30°C still-water quenching, and simulation result by using DEFORM-HT. (From T. Inoue, D.Y. Ju, and Y. Arimoto, *Proceedings of the First International Conference on Quenching and Distortion Control* (Chicago), 1992, pp. 205–212.)

steel under carburized quenching. Diffusion equation for carbon content was solved and coupled with metallo-thermo-mechanical analysis. The results were compared with the experimental data to verify and evaluate the influence of transformation plasticity on simulation results.

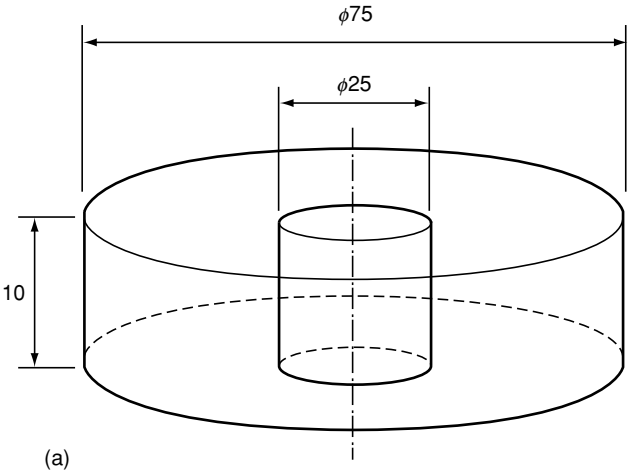

FIGURE 10.33 Dimension of ring-shaped specimen of chromium–molybdenum steel and mesh division near an edge of a ring-shaped model. (From S. Yamanaka, T. Sakanoue, T. Yoshii, T. Kozuka, and T. Inoue, in *Heat Treating Including the Liu Dai Memorial Symposium, Proceedings of the 18th Conference*, R.A. Wallis and H.W. Walton, Eds., ASM International, Materials Park, OH, 1998, pp. 657–665.)

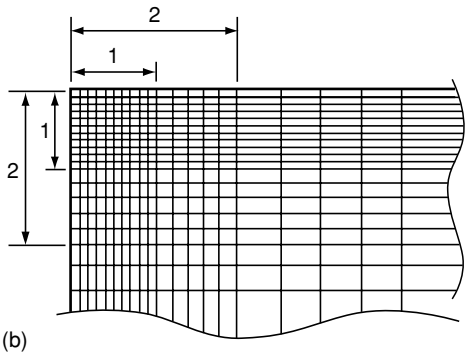

FIGURE 10.33 (Continued)

Figure 10.34 shows the simulated distortion of cross section of the ring at final step. Experimental results of distortion are plotted as solid marks in the figure. Changes in the distortion with time and without transformation plasticity are shown in Figure 10.35. The most remarkable difference between with and without effects of transformation plasticity carburized quenching lies in the mode of distortion. Transformation plasticity gives convex shape on all the surfaces, but concave without the effect. Experimental data agree well with simulated distortion with the effect in both cases of carburized and normal quenching.

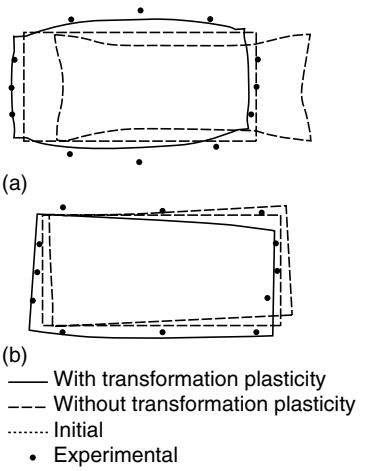

FIGURE 10.34 Simulated distortion after quenching with measured data. Distortion is enlarged by 100 times. Central axis is the left side. (a) Carburized quenching, (b) normal quenching. (From S. Yamanaka, T. Sakanoue, T. Yoshii, T. Kozuka, and T. Inoue, in *Heat Treating Including the Liu Dai Memorial Symposium, Proceedings of the 18th Conference*, R.A. Wallis and H.W. Walton, Eds., ASM International, Materials Park, OH, 1998, pp. 657–665.)

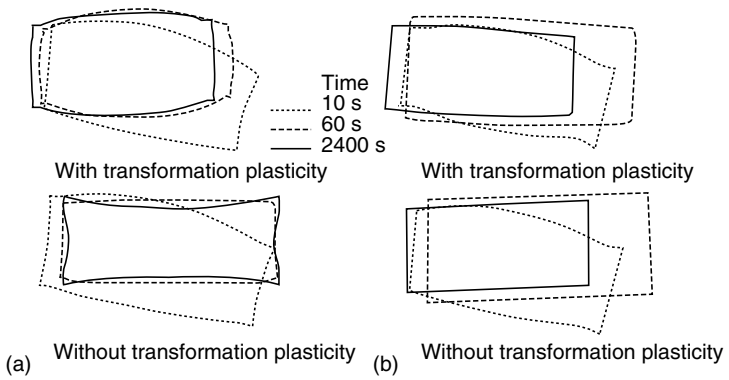

FIGURE 10.35 Comparison of simulated results depending on the effect of transformation plasticity in course of quenching. Distortion is enlarged by 100 times. Central axis is the left side. (a) Carburized quenching, (b) normal quenching. (From S. Yamanaka, T. Sakanoue, T. Yoshii, T. Kozuka, and T. Inoue, in *Heat Treating Including the Liu Dai Memorial Symposium, Proceedings of the 18th Conference*, R.A. Wallis and H.W. Walton, Eds., ASM International, Materials Park, OH, 1998, pp. 657–665.)

10.9 SUMMARY

This article provides a detailed explanation of the contributing factors affecting distortion, residual stress, and cracking of heat-treated steel components. Although mechanism of distortion and stress in heat treating is complex, an understanding of these factors allows the engineer to keep the heat-treating process under control.

REFERENCES

1. D.A. Canonico, Stress-relief in heat treating of steel, in *ASM Handbook*, Vol. 4, ASM International, Materials Park, OH, 1991, pp. 33–34.
2. C.E. Bates, G.E. Totten, and R.L. Brennan, Quenching of steel, in *ASM Handbook*, Vol. 4, ASM International, Materials Park, OH, 1991, pp. 67–120.
3. S. Mocarski, Carburizing and its Control—I. Basic Considerations, *Ind. Heat*., 41(5), 1974, 58–70.
4. S. Owaku, Quench distortion of steel parts, *Netsu Shori* (*J. Jpn. Soc. Heat Treat.*), 32(4), 1992, 198–202.
5. M. Narazaki, M. Kogawara, A. Shirayori, and S. Fuchizawa, Influence of wetting behaviour on cooling characteristics during quenching of hot metal, *Proceedings of the Third International Conference on Quenching and Control of Distortion*, 24–26 March, 1999, Prague, Czech Republic, pp. 112–120.
6. M. Narazaki, G.E. Totten, and G.M. Webster, Hardening by reheating and quenching, in *Handbook of Residual Stress and Deformation of Steel*, G.E. Totten, M.A.H. Howes, and T. Inoue, Eds., ASM International, Materials Park, OH, 2002, pp. 248–295.
7. T. Ericsson, Principles of heat treating of steels, in *ASM Handbook*, Vol. 4, *Heat Treating*, ASM International, Materials Park, OH, 1991, p. 16.
8. H.J. Yu, U. Wolfstieg, and E. Macherauch, Zum durch messereinfluss auf die Eigenspannungen in öl-und Wasserabgeschreckten Stahlzylindern, *Arch. Eisenhüttenwes*., 51, 1980, 195.
9. M. Narazaki, S. Fuchizawa, and M. Kogawara, Effect of surface roughness and surface texture on quench cracking of steel, *Netsu Shori* (*J. Jpn. Soc. Heat Treat.*), 33, 1993, 56–63.
10. J.R. Davis, Ed., *ASM Materials Engineering Dictionary*, ASM International, Materials Park, OH, 1992, p. 407.

11. R. Kern, Distortion and cracking, Part II: distortion from quenching, *Heat Treat*., 1985, 41–45.
12. P.F. Stratton, N. Saxena, and R. Jain, Requirements for gas quenching systems, *Heat Treat. Met*., 24(3), 1997, 60–63.
13. H.M. Tensi, G.E. Totten, and G.M.Webster, Proposal to monitor agitation of production quench tanks, in *Heat Treating: Proceedings of the 17th Conference*, D.L. Milam, D.A. Poteet, G.D. Pfaffmann, V. Rudnev, A. Muehlbauer, and W.B. Albert, Eds., ASM International, Materials Park, OH, 1997, pp. 423–441.
14. R.T. Von Bergen, The effects of quenchant media selection on the distortion of engineered steel parts, in *Quenching and Distortion Control*, G.E. Totten, Ed., ASM International, Materials Park, OH, 1992, pp. 275–282.
15. H.M. Tensi, A. Stich, and G.E. Totten, Fundamentals of quenching, *Met. Heat Treat*., 1995, pp. 20–28.
16. M. Wisti and M. Hingwe, Tempering of steel, in *ASM Handbook*, Vol. 4, ASM International, Materials Park, OH, 1991, pp. 121–136.
17. Y. Toshioka, Heat treatment deformation of steel products, *Mater. Sci. Technol*., 1, 1985, pp. 883–892.
18. T. Inoue, K. Haraguchi, and S. Kimura, Analysis of stresses due to quenching and tempering of steel, *Trans. ISIJ*, 18, 1978, 11–15.
19. A.B.A. Becherer and L. Ryan, Control of distortion in tool steels, in *ASM Handbook*, Vol. 4, ASM International, Materials Park, OH, 1991, pp. 761–766.
20. M.A.H. Howes and J.P. Sheehan, SAE (Society of Automotive Engineers) Technical Paper 740222, 1974.
21. M.A.H. Howes, Factors affecting distortion in hardened steel components, in *Quenching and Control Distortion*, G.E. Totten, Ed., ASM International, Materials Park, OH, 1992, pp. 251–258.
22. H.W. Walton, Deflection methods to estimate residual stress, in *Handbook of Residual Stress and Deformation of Steel*, G.E. Totten, M.A.H. Howes, and T. Inoue, Eds., ASM International, Materials Park, OH, 2002, pp. 89–98.
23. C. Ruud, Measurement of residual stresses, in *Handbook of Residual Stress and Deformation of Steel*, G.E. Totten, M.A.H. Howes, and T. Inoue, Eds., ASM International, Materials Park, OH, 2002, pp. 99–117.
24. L.A. Razumovsky, M.V. Medvedv, and A.V. Fomin, Methods for determination of inhomogeneous residual stress fields, in *Handbook of Residual Stress and Deformation of Steel*, G.E. Totten, M.A.H. Howes, and T. Inoue, Eds., ASM International, Materials Park, OH, 2002, pp. 125–138.
25. SAE, Residual Stress Measurement by X-Ray Diffraction, SAE J784a, 1971.
26. G.E. Totten, C.E. Bates, and N.A. Clinton, *Handbook of Quenchants and Quenching Technology*, ASM International, Materials Park, OH, 1993, pp. 483–486.
27. G. Sachs, The determination of internal stresses in rods and tube, *Z. Metalk*., 19(9), 1927, 352–357.
28. A.A. Denton, Determination of residual stress, *Metall. Rev*., 11, 1966, 1–23.
29. S. Nishimura, Y. Morita, and K. Tokimasa, *Bull. Jpn. Soc. Mech. Eng*., 18(116), 1975, 116–122.
30. G.E. Dieter, *Mechanical Metallurgy*, McGraw-Hill, New York, 1961, pp. 405–407.
31. T. Piech and K. Pomorski, Barkhausen noise method for estimation of direction of residual stresses in surface layers, in *Residual Stress*, (V. Hauk, H.P. Hougardy, E. Macherauck, and H.-D. Tietz, Eds.) DGM Informations Gmbh, 1993, pp. 333–340.
32. K. Titto, Use of Barkhausen effect in testing for residual stresses and material defects, in *Residual Stress in Design, Process and Material Selection*, W.B. Young, Ed., ASM International, Materials Park, OH, 1978, pp. 27–36.
33. R.E. Schromm, A.V. Clock, D.V. Mitrakovic, and S.R. Schaps, Ultrasonic measurements of residual stress in railroad wheels, in *Practical Application of Residual Stress Technology*, C. Ruud, Ed., ASM International, Materials Park, OH, 1991, pp. 61–68.
34. R.B. Thompson, An overview of ultrasonic measurement techniques, *Proceedings of Fourth International Conference on Residual Stresses*, Soc. Exp. Mech., Bethel, CT, 1994, pp. 97–110.
35. D.R. Allen and C.M. Sayers, The measurements of residual stress in textured steel using ultrasonic velocity combination technique, *Ultrasonics*, 22, 1984, 179–188.

36. H.J. Praskard and C.S. Choi, Residual stress measurements in system components by means of neutron diffraction, in *Residual Stress in Design Process and Materials*, W.B. Young, Ed., ASM International, Materials Park, OH, 1987, pp. 21–26.
37. H. Webster and W.J. Laird, Martempering of steel, in *ASM Handbook*, Vol. 4, ASM International, Materials Park, OH, 1991, p. 144.
38. C.E. Bates, G.E. Totten, and R.L. Brennan, Quenching of steel, in *ASM Handbook*, Vol. 4, ASM International, Materials Park, OH, 1991, p. 100.
39. F. Moreaux, A. Simon, and G. Beck, *J. Heat Treat*., 1(3),1980, 50–56.
40. G. Beck, *Mem. Etud. Sci. Rev. Metall*., July 1985, 269–282.
41. W.A.J. Moerdijk, *Adv. Mater. Process*., 137(3), 1990, 19–28.
42. M. Narazaki and S. Ninomiya, Molten sodium quenching of steel parts, *Proceedings of the 13th International Federation for Heat Treatment & Surface Engineering & ASM Surface Engineering Congress*, Columbus, OH, October 2002, pp. 464–470.
43. D. Huang, K. Arimoto, K. Lee, D. Lambert, and M. Narazaki, Prediction quench distortion on steel shaft with keyway by computer simulation, *Proceedings of 20th ASM Heat Treating Society Conference*, 9–12 October 2000, St. Louis, USA, ASM International, Materials Park, OH, 2000, pp. 708–712.
44. K. Arimoto, D. Lambert, K. Lee, W.T. Wu, and M. Narazaki, Prediction of quench cracking by computer simulation, *Heat Treating: Proceedings of the 19th Conference*, S.J. Midea and G.D. Pfaffmann, Eds., ASM International, Materials Park, OH, 1999, pp. 435–440.
45. S. Owaku, Criterion of quench cracking: its sources and prevention, *Netsu Shori* (*J. Jpn. Soc. Heat Treat*.), 30(2), 1990, 63–67.
46. Y. Mikita, I. Nakabayashi, and K. Sakamaki, *Heat Treat*., December 1989, 21–24.
47. Y. Mikita and I. Nakabayashi, *Nipon Kikai Gakkai, Ronbunshu* (A-hen), 53(489), 1987, 884–889.
48. T. Inoue, K. Haraguchi, and S. Kimura, Analysis of stresses due to quenching and tempering of steel, *Trans. ISIJ*, 18, 1978, 11–15.
49. T. Inoue and B. Raniecki, Determination of thermal-hardening stress in steels by use of thermo-plasticity, *J. Mech. Phys. Solids*, 26, 1978, 187–212.
50. T. Inoue, D.Y. Ju, and Y. Arimoto, Metallo-thermo-mechanical simulation of quenching process—theory and implementation of computer code HEARTS, *Proceedings of the First International Conference on Quenching and Distortion Control* (Chicago), 1992, pp. 205–212.
51. D.Y. Ju, M. Sahashi, T. Omori, and T. Inoue, Residual stresses and distortion of a ring in quenching–tempering process based on metallo-thermo-mechanics, *Proceedings of the Second International Conference on Quenching and Distortion Control* (Cleveland), 1996, pp. 249–257.
52. M. Narazaki and D.Y. Ju, Simulation of distortion during quenching of steel effect of heat transfer in quenching, *Heat Treating Including the Liu Dai Memorial Symposium, Proceedings of the 18th Conference*, R.A. Wallis and H.W. Walton, Eds., ASM International, Materials Park, OH, 1998, pp. 629–638.
53. D.Y. Ju, M. Narazaki, H. Kamisugi, and H. Hirano, Computer predictions and experimental verification of residual stresses and distortion in carburizing–quenching of steel, *Proceedings of the First International Conference on Thermal Process Modeling and Computer Simulation* (Shanghai), 2000, pp. 165–172.
54. C.L. Magee, *Nucleation of Martensite*, American Society for Metals, Materials Park, OH, 1968.
55. W.A. Johnson and R.F. Mehl, *Trans. AIME*, 135, 1939, 416–458.
56. Y. Desalos et al., Deformations et Contrainslers du Traitement Thermique de Pieces en Acier, IRSID Re 902, 1982.
57. K. Arimoto, G. Li, A. Arvind, and W.T. Wu, The modeling of heat treating process, *Heat Treating Including the Liu Dai Memorial Symposium, Proceedings of the 18th Conference*, R.A. Wallis and H.W. Walton, Eds., ASM International, Materials Park, OH, 1998, pp. 23–30.
58. S. Yamanaka, T. Sakanoue, T. Yoshii, T. Kozuka, and T. Inoue, Influence of transformation plasticity on the distortion of carburized quenching process of Cr–Mo steel, in *Heat Treating Including the Liu Dai Memorial Symposium, Proceedings of the 18th Conference*, R.A. Wallis and H.W. Walton, Eds., ASM International, Materials Park, OH, 1998, pp. 657–665.

11 Tool Steels

Elhachmi Essadiqi

CONTENTS

11.1 Introduction 651
11.2 Classification and Selection of Tool Steels 652
11.2.1 Selection of Tool Steels 652
11.2.2 Manufacturing Characteristics Are Related to Heat-Treatment Response 661
11.3 Manufacturing of Tool Steels 661
11.3.1 Steelmaking 661
11.3.2 Thermomechanical Processing 666
11.4 Important Steel Properties Relevant to the Manufacture of Tools 666
11.4.1 Dimensional Accuracy during Heat Treatment 666
11.4.2 Hot Formability 667
11.4.3 Cold Formability 667
11.4.4 Machinability 667
11.4.5 Grindability 667
11.4.6 Polishability 668
11.5 Important Properties Required for Various Applications 668
11.5.1 Hardness 668
11.5.2 Hardenability 670
11.5.3 Toughness at Operational Temperature 673
11.5.4 Resistance to Thermal Fatigue 674
11.6 Heat Treatment 674
11.6.1 Normalizing 676
11.6.2 Stress-Relief Heat Treatments 676
11.6.3 Annealing 678
11.6.4 Spheroidizing 680
11.6.5 Carbides in Tool Steels 681
11.6.6 Hardening 682
11.6.6.1 Austenitizing 682
11.6.6.2 Quenching 684
11.6.6.3 Retained Austenite 685
11.6.6.4 Tempering 685
11.7 Characteristic Steel Grades for the Different Field of Tool Application 687
Bibliography 693

11.1 INTRODUCTION

Tool steels are very special steels used to shape, cut, and form an extremely wide variety of metals and other materials under demanding conditions. The first known tool made of iron date back 60 centuries. The heat treatment to harden tool iron, consisting of heating and water

quenching, was known 30 centuries ago. The earliest tool steels were based on plain carbon steel. In the mid-19th century and early in the 20th century, highly alloyed tool steels were developed to meet very stringent requirements for specific applications. This evolution was taking place in parallel with the understanding of the benefit of the alloying elements such as manganese, tungsten, molybdenum, vanadium, and chromium, and their availability. In parallel to this evolution, steelmaking evolved toward more controlled conditions to improve the quality and cleanliness of the tool steels. This advance in technology and knowledge allows designing specialized tool steels for cold and hot working of metals, molding plastics, as well as for many other special purposes. This chapter reviews manufacturing and heat treatment of various types of tool steels to achieve the required properties for specific applications.

11.2 CLASSIFICATION AND SELECTION OF TOOL STEELS

Tool steels have been organized into groups that have evolved to perform specific functions, such as forging, cold working, die casting, and high-speed machining, in a variety of operating conditions. Within each group may be many grades that differ slightly from one another to accommodate somewhat different processing requirements, operating conditions, or work materials.

Various systems are used to classify tool steels. The most widely used system was developed by the American Iron and Steel Institute (AISI). It arranges tool steels into groups that are based on prominent characteristics such as alloying, application, or heat treatment. Table 11.1 lists nine main groups of tool steels and their identifying letter symbols [1,2]. Table 11.2 presents the AISI classification and the nominal compositions of the most widely used tool steels [1,2]. These steels are also identified by designation in the United Numbering System (UNS) for metals and alloys. Other independent classification systems for tool steels from other countries such as Germany, Japan, Great Britain, and France, exist, and are listed in Table 11.3 [1,3,4].

11.2.1 Selection of Tool Steels

The selection of tool steel for a specific operation is based on two major criteria: (1) the performance of the steel for a given application; and (2) analysis of the limitation associated

TABLE 11.1
Main Groups of Tool Steels and AISI Letter Symbols

Group	Identifying Symbol
Water-hardening tool steels	W
Shock-resisting tool steels	S
Oil-hardening cold-working tool steels	O
Air-hardening, medium-alloy cold-working tool steels	A
High-carbon, high-chromium cold-working tool steels	D
Mold steels	P
Hot-working tool steels, chromium, tungsten, and molybdenum	H
Tungsten high-speed tool steels	T
Molybdenum high-speed tool steels	M

Source: From G. Roberts, G. Krauss, and R. Kennedy, *Tool Steels*, 5th ed., ASM International, Materials Park, OH, 1998, p. 7; Tool steels, *Heat Treater's Guide: Practices and Procedures for Irons and Steels*, H. Chandler, Ed., ASM International, Materials Park, OH, 1995, pp. 517–669.

TABLE 11.2
AISI Classification and Nominal Compositions of Major Tool Steels

		Identifying Elements, %								
AISI	**UNS No.**	**C**	**Mn**	**Si**	**Cr**	**V**	**W**	**Mo**	**Co**	**Ni**
Water-hardening tool steels										
W1	T72301	0.60–1.40 (a)	—	—	—	—	—	—	—	—
W2	T72302	0.60–1.40 (a)	—	—	—	0.25	—	—	—	—
W5	T72305	1.10	—	—	0.50	—	—	—	—	—
Shock-resisting tool steels										
S1	T41901	0.50	—	—	1.50	—	2.50	—	—	—
S2	T41902	0.50	—	1.00	—	—	—	0.50	—	—
S5	T41905	0.55	0.80	2.00	—	—	—	0.40	—	—
S6	T41906	0.45	1.40	2.25	1.50	—	—	0.40	—	—
S7	T41907	0.50	—	—	0.75	—	1.75	—	—	—
Oil-hardening cold-work tool steels										
01	T31501	0.90	1.00	—	0.50	—	0.50	—	—	—
02	T31502	0.90	1.60	—	—	—	—	—	—	—
0.6 (b)	T31506	1.45	0.80	1.00	—	—	—	0.25	—	—
07	T31507	1.20	—	—	0.75	—	1.75	—	—	
Air-hardening, medium-alloy cold-work tool steels										
A2	T30102	1.00	—	—	5.00	—	—	1.00	—	—
A3	T30103	1.25	—	—	5.00	1.00	—	1.00	—	—
A4	T30104	1.00	2.00	—	1.00	—	—	1.00	—	—
A6	T30106	0.70	2.00	—	1.00	—	—	1.25	—	—
A7	T30107	2.25	—	—	5.25	4.75	1.00 (c)	1.00	—	—
A8	T30108	0.55	—	—	5.00	—	1.25	1.25	—	—
A9	T30109	0.50	—	—	5.00	1.00	—	1.40	—	1.50
A10 (b)	T30110	1.35	1.80	1.25	—	—	—	1.50	—	1.80
High-carbon, high-chromium cold-work steels										
D2	T30402	1.50	—	—	12.00	1.00	—	1.00	—	—

Continued

TABLE 11.2 (Continued)
AISI Classification and Nominal Compositions of Major Tool Steels

		Identifying Elements, %								
AISI	**UNS No.**	**C**	**Mn**	**Si**	**Cr**	**V**	**W**	**Mo**	**Co**	**Ni**
D3	T30403	2.25	—	—	12.00	—	—	—	—	—
D4	T30404	2.25	—	—	12.00	—	—	1.00	—	—
D5	T30405	1.50	—	—	12.00	—	—	1.00	—	—
D7	T30407	2.35	—	—	12.00	4.00	—	1.00	—	—
Low-alloy special-purpose tool steels										
L2	T61202	0.50–1.10 (a)	—	—	1.00	0.20	—	—	—	—
L6	T61206	0.70	—	—	0.75	—	—	0.25 (c)	—	1.50
Mold steel										
P2	T51602	0.07	—	—	2.00	—	—	0.20	—	0.50
P3	T51603	0.10	—	—	0.50	—	—	—	—	1.25
P4	T51604	0.07	—	—	5.00	—	—	0.75	—	—
P5	T51605	0.10	—	—	2.25	—	—	—	—	—
P6	T51606	0.10	—	—	1.50	—	—	—	—	—
P20	T51620	0.35	—	—	1.70	—	—	0.40	—	3.50
P21	T51621	0.20	1.20 (Al)	—	—	—	—	—	—	4.00
Chromium hot-work tool steels										
H10	T20810	0.40	—	—	3.25	0.40	—	2.50	—	—
H11	T20811	0.35	—	—	5.00	0.40	—	1.50	—	—
H12	T20812	0.35	—	—	5.00	0.40	1.50	1.50	—	—
H13	T20813	0.35	—	—	5.00	1.00	—	1.50	—	—
H14	T20814	0.40	—	—	5.00	—	5.00	—	—	—
H19	T20819	0.40	—	—	4.25	2.00	4.25	—	4.25	—
Tungsten hot-work tool steels										
H21	T20821	0.35	—	—	3.50	—	9.00	—	—	—
H22	T20822	0.35	—	—	2.00	—	11.00	—	—	—
H23	T20823	0.30	—	—	12.00	—	12.00	—	—	—
H24	T20824	0.45	—	—	3.00	—	15.00	—	—	—
H25	T20825	0.25	—	—	4.00	—	15.00	—	—	—
H26	T20826	0.50	—	—	4.00	1.00	18.00	—	—	—

Molybdenum hot-work tool steels										
H42	T20842	0.60	—	—	4.00	2.00	6.00	5.00	—	—
Tungsten high-speed tool steels										
T1	T12001	0.75 (a)	—	4.00	1.00	18.00	—	—	—	—
T2	T12002	0.80	—	—	4.00	2.00	18.00	—	—	—
T4	T12004	0.75	—	—	4.00	1.00	18.00	—	5.00	—
T5	T12005	0.80	—	—	4.00	2.00	18.00	—	8.00	—
T6	T12006	0.80	—	—	4.00	1.50	20.00	—	12.00	—
T8	T12008	0.75	—	—	4.00	2.00	14.00	—	5.00	—
T15	T12015	1.50	—	—	4.00	5.00	12.00	—	5.00	—
Molybdenum high-speed tool steels										
M1	T11301	0.80 (a)	—	—	4.00	1.00	1.50	8.00	—	—
M2	T11302	0.85–1.00 (a)	—	—	4.00	2.00	6.00	5.00	—	—
M3, class 1	T11313	1.05	—	—	4.00	2.40	6.00	5.00	—	—
M3, class 2	T11323	1.20	—	—	4.00	3.00	6.00	5.00	—	—
M4	T11304	1.30	—	—	4.00	4.00	5.50	4.50	12.00	—
M6	T11306	0.80	—	—	4.00	2.00	4.00	5.00	—	—
M7	T11307	1.00	—	—	4.00	2.00	1.75	8.75	—	—
M10	T11310	0.85–1.00 (a)	—	—	4.00	2.00	—	8.00	5.00	—
M30	T11330	8.00	—	—	4.00	1.25	2.00	8.00	8.00	—
M33	T11333	0.90	—	—	4.00	1.15	1.50	9.50	8.00	—
M34	T11334	0.90	—	—	4.00	2.00	2.00	8.00	8.00	—
M36	T11336	0.80	—	—	4.00	2.00	6.00	5.00	8.00	—
Ultra hard high-speed tool steels										
M41	T11341	1.10	—	—	4.25	2.00	6.75	3.75	5.00	—
M42	T11342	1.10	—	—	3.75	1.15	1.50	9.50	8.00	—
M43	T11343	1.20	—	—	3.75	1.60	2.75	8.00	8.25	—
M44	T11344	1.15	—	—	4.25	2.00	5.25	6.25	12.00	—
M46	T11346	1.25	—	—	4.00	3.20	2.00	8.25	8.25	—
M47	T11347	1.10	—	—	3.75	1.25	1.50	9.50	5.00	—

(a) Available with different carbon contents. (b) Contains graphite. (c) Optional.

Source: From G. Roberts, G. Krauss, and R. Kennedy, *Tool Steels*, 5th ed., ASM International, Materials Park, OH, 1998, p. 8; Tool steels, *Heat Treater's Guide: Practices and Procedures for Irons and Steels*, H. Chandler, Ed., ASM International, Materials Park, OH, 1995, pp. 517–669.

TABLE 11.3
Cross-References of AISI Tool Steels Designations to Designations in Other National Systems

United States (AISI)	West Germany (DIN)[a]	Japan (JIS)[b]	Great Britain (B.S.)[c]	France (AFNOR)[d]	Sweden (SS_{14})
Molybdenum high-speed steels (ASTM A600)					
M1	1.3346	—	4659 BMI	A35-590 4441 Z85DCWV08-04-02-10	2715
M2, reg C	1.3341, 1.3343, 1.3345, 1.3553, 1.3554	G4403 SKH51 (SKH9)	4659 BM2	A35-590 4301 Z85WDCV06-05-04-10	2722
M2, high C	1.3340, 1.3342	—	—	A35-590 4302 Z90WDCV06-05-04-02	—
M3, class 1	—	G4403 SKH52	—	—	—
M3, class 2	1.3344	G4403 SKH53	—	A35-590 4360 Z120WDCV06-05-04-03	(USA M3 class 2)
M4	—	G4403 SKH54	4659 BM4	A35-590 4361 Z130WDCV06-05-04-04	—
M7	1.3348	G4403 SKH58	—	A35-590 4442 Z100DCWV09-04-02-02	2782
M10, reg C	—	—	—	—	—
M10, high C	—	—	—	—	—
M30	1.3249	—	4659 BM34	—	—
M33	1.3249	—	4659 BM34	—	—
M34	1.3249	—	4659 BM34	—	—
M35	1.3243	G4403 SKH55	—	A35-590 4371 Z85WDKCV06-05-05-04-02 A35-590 4372 Z90WDKCV06-05-05-04-02	—
M36	1.3243	G4403 SKH55, G4403 SKH56	—	A35-590 4371 Z85WDKCV06-05-05-04	—
M41	1.3245, 1.3246	G4403 SKH55	—	A35-590 4374 Z110WDKCDV07-05-04-04	2723
M42	1.3247	G4403 SKH59	4659 BM42	A35-590 4475 Z110DKCWV09-08-04-02	2736
M43	—	—	—	A35-590 4475	—

				Z110DKCWV09-08-04-02-01	
M44	1.3207	G4403 SKH57	4659 (USA M44)	A35-590 4376	—
				Z130KWDCV12-07-06-04-03	
M46	1.3247	—	—	—	—
M47	1.3247	—	—	—	—
Intermediate high-speed steels					
M50	1.2369, 1.3551	—	—	A35-590 3551 Y80DCV42.16	(USA M50)
M52	—	—	—	—	—
Tungsten high-speed steels (ASTM A600)					
T1	1.3355, 1.3558	G4403 SKH2	4659 BT1	A33-590 4201	—
				Z80WCV18-04-01	
T2	—	—	4659 BY2, 4659 BT20	4203 18-02	—
T4	1.3255	G4403 SKH3	4659 BT4	A35-590 4271	—
				Z80WKCV18-05-04-01	
T5	1.3265	G4403 SKH4B	4659 BT5	A35-590 4275	(USA T5)
				Z80WKCV18-10-04-02	
T6	1.3257	—	4659 BT6	—	—
T8	—	G4403 SKH10	—	—	—
T15	1.3202		4659 BT15	A35-590 4171	(USA T15)
				Z160WKVC12-05-05-04	
Chromium hot-work steels (ASTM A681)					
H10	1.2365, 1.2367	G4404 SKD7	4659 BH10	A35-590 3451 32DCV28	—
H11	1.2343, 1.7783, 1.7784	G4404 SKD6	4659 BH11	A35-590 3431 FZ38CDV5	—
H12	1.2606	G4404 SKD62	4659 BH12	A35-590 3432 Z35CWDV5	—
H13	1.2344	G4404 SKD61	4659 BH13, 4659 H13	A35-590 3433 Z40CDV5	2242
H14	1.2567	G4404 SKD4	—	3541 Z40WCV3	—
H19	1.2678	G4404 SKD8	4659 BH19	—	—
Tungsten hot-work steels (ASTM A681)					
H21	1.2581	G4404 SKD5	4659 BH21, 4659 H21A	A35-590 3543	2730
				Z30WCV9	
H22	1.2581	G4404 SKD5	—	—	—
H23	1.2625	—	—	—	—
H24	—	—	—	—	—
H25	—	—	—	—	—
H26	—	—	4659 BH26	—	—

Continued

TABLE 11.3 (Continued)
Cross-References of AISI Tool Steels Designations to Designations in Other National Systems

United States (AISI)	West Germany (DIN)[a]	Japan (JIS)[b]	Great Britain (B.S.)[c]	France (AFNOR)[d]	Sweden (SS_{14})
Molybdenum hot-work steels (ASTM A681)					
H42	—	—	—	3548 Z65WDCV6.05	—
Air-hardening, medium-alloy cold-work steels (ASTM A 681)					
A2	1.2363	G4404 SKD12	4659 BA2	A35-590 2231 Z100CDV5	2260
A3	—	—	—	—	—
A4	—	—	—	—	—
A5	—	—	—	—	—
A6	—	—	4659 BA6	—	—
A7	—	—	—	—	—
A8	1.2606	G4404 SKD62	—	3432Z38CDWV5	—
A9	—	—	—	—	—
A10	—	—	—	—	—
High-carbon, high-chromium cold-work steels (ASTM A681)					
D2	1.2201, 1.2379, 1.2601	G4404 SKD11	4659 (USA D2), 4659 BD2 4659 BD2A	A35-590 2231 Z100CFV5	—
D3	1.2080, 1.2436, 1.2884	G4404 SKD1, G4404 SKD2	4659 BD3	A35-590-2233 Z200C12	—
D4	1.2080, 1.2436, 1.2884	G4404 SK1, G4404 SKD2	4659 BD3	A35-590 2233 Z200C12	—
D5	1.2880	—	—	A35-590 2234 Z200CD12	2312
D7	1.2378	—	—	2237 ZC30CVA12.04	—
Oil-hardening cold-work steels (ASTM A681)					
O1	1.2510	G4404 SKS21, G4404 SKS3, G4404 SKS93, G4404 SKS94, G4404 SKS95	4659 BO1	A35-590 2212 90 MWCV5	2140
O2	1.2842	—	4659 (USA 02) 4659 BO2		

O6	1.2206	—	—	A35-5902132 130C3	—
O7	1.214, 1.2419, 1.2442, 1.2516, 1.2519	G4404 SKS2	—	A35-590 2141 105WC13	—
Shock-resisting steels (ASTM A681)					
S1	1.2542, 1.2550	G4404 SKS 41	4659 BS1	A35-590 2341 55WC20	2710
S2	1.2103	—	4659 BS2	A35-590 2334 Y45SCD6	—
S5	1.2823	—	4659 BS5	—	—
S6	—	—	—	—	—
S7	—	—	—	—	
Low-alloy special-purpose steels (ASTM A681)					
L2	1.2235, 1.2241, 1.2242, 1.2243	G4404 SKT3, G4410 SKC11	—	A35-590 3355 55CNDV4	—
L6	1.2713, 1.2714	G4404 SKS51, G4404 SKT4	—	A35-590 3381 55NCDV7	—
Low-carbon mold steels (ASTM A681)					
L2	1.2235, 1.2241, 1.2242, 1.2243, 1.2713, 1.2714	G4404 SKT3, G4410 SKC11	—	A35-590 33335 55CNDV4	—
L6	1.2713, 1.2714	G4404 SKS51, G4404 SKT4	—	A35-590 3381 55NCDV7	—
Low-carbon mold steels (ASTM A681)					
P2	—	—	—	—	—
P3	1.5713	—	—	2881 Y10NC6	—
P4	1.2341	—	—	—	(USA P4)
P5	—	—	—	—	—
P6	1.2735, 1.2745	G4410 SKC31	—	2882 10NC12	—
P20	1.2311, 1.2328, 1.2330	—	4659 (USA P20)	A35-590 2333 35CMD7	(USA P20)
P21	—	—	—	—	—

Continued

TABLE 11.3 (Continued)
Cross-References of AISI Tool Steels Designations to Designations in Other National Systems

United States (AISI)	West Germany (DIN)[a]	Japan (JIS)[b]	Great Britain (B.S.)[c]	France (AFNOR)[d]	Sweden (SS_{14})
Water-hardening steels (ASTM A686)					
W1	1.1525, 1.1545, 1.1625, 1.1654, 1.1663, 1.1673, 1.1744, 1.1750, 1.1820, 1.1830	G4401 SK1, G4401 SK2, G4401 SK3, G4401 SK4, G4401 SK5, G4401 SK6, G4401 SK7, G4410 SKC3	4659 (USA WI), 4659 BW1A, 4659 BW1B, 4659 BW1C	A35-590 1102 Y(1) 105, A35-590 1103 Y(1) 90, A35-590 1104 Y(1) 80, A-35-590 1105 Y(1) 70, A35-590 1200 Y(2) 140, A35-590 1201 Y(2) 120, A35-596 Y75, A35-596 Y90	—
W2	1.1645, 1.2206, 1.283	G4404 SKS43, G4404 SKS44	4659 BW2	A35-590 1161 Y120V, A35-590 1162 Y105V, A35-590 1163 Y90V, A35-590 1164 Y75V, A35-590 1230 Y(2) 140C, A35-590 2130 Y100C2	(USA W2A) (USA W2B) (USA W2C)
W5	1.2002, 1.2004, 1.2056	—	—	A35-590 1232 Y105C	—

[a]Deutsche Industries Normen (German Industrial Standards).

[b]Japanese Industrial Standard.

[c]British Standard.

[d]L'Association Française de Normalization (French Standards Association).

(a) Available with different carbon contents. (b) Contains graphite. (c) Optional.

Source: From G. Roberts, G. Krauss, and R. Kennedy, *Tool Steels*, 5th ed., ASM International, Materials Park, OH, 1998, pp. 10–12; J.G. Gensure and D.L. Potts, *International Metallic Materials Cross-Reference*, 3rd ed., Genium Publishing, New York, 1988; C.W. Wegst, J.C. Hamaker, Jr., and A.R. Johnson, *Tool Steels*, 3rd ed., American Society for Metals, Materials Park, OH, 1962.

with the manufacture of the tool die or mold. After the preliminary selection based on the above two criteria, the final selection will be based on the final cost per unit part produced by the tool [1].

11.2.2 Manufacturing Characteristics Are Related to Heat-Treatment Response

Service characteristics are related to toughness, resistance to softening, and wear resistance. An overview and comparison of the most important manufacturing and service characteristics of tool steels are given in Table 11.4. This qualitative ranking helps assessing various tool steels.

11.3 MANUFACTURING OF TOOL STEELS

Tool steels are prepared using various processes such as steelmaking and casting, powder metallurgy (P/M), and the Ospray process. A summary of these manufacturing processes is presented along with their benefits and limitations in terms of improved quality and lower cost.

11.3.1 Steelmaking

Tool steels are processed through an electrical arc furnace (EAF); secondary refining processes have been introduced recently such as argon–oxygen decarburization (AOD), vacuum–oxygen decarburization (VOD), and the use of ladle furnaces [7]. The principle benefits associated with secondary refining are reduced furnace time, increased overall capacity, improved yield quality, consistency, and reproducibility.

Most tool steels are processed using EAFs. The cleanliness of the liquid steel and the control of the chemistry are performed in ladle furnace, the AOD process, and vacuum arc degassing process (VAD) [8,9]. In the latter process, optimum temperatures for vacuum degassing, refining, as well as final alloy composition and subsequent ingot teeming can be accurately controlled. In addition, stirring the argon under vacuum provides melt uniformity and maximizes the removal of undesirable gases and nonmetallic inclusions from the steel. Next to vacuum arc melting, the VAD process improves cleanliness and hence, mechanical properties in the final product. This process is required when higher levels of polishability and improving toughness of tool steels are required. If more cleanliness and improved properties are required, vacuum arc remelting (VAR) is employed. In this process, the molten steel from the VAD is teemed into a cylindrical ingot. The ingot is then remelted under vacuum into a water-cooled copper mold. The resultant VAR ingot is forged into intermediate billets or to the final product. To improve cleanliness by reducing nonmetallic inclusions of the steel and to reduce segregation of other processes such as electroslag remelting, P/M, and spray forming are used.

Electroslag remelting, which is employed in the production of a relatively small percentage of tool steels, involves passing an electrical current through a consumable electrode of similar chemistry as that desired in the final ingot, that resistance melts under a protective, refining slag, and is then solidified into an ingot. The electrode is usually of the similar chemistry as the final ingot [10]. The cleanliness of ESR-melted product is superior to that of air-melted EAF product due to the reduction of sulfur and the removal of inclusions by the ESR slag, which results in better properties such as fatigue resistance, as illustrated in Figure 11.1, and improved hot workability.

P/M has been used in the past to produce high-alloy tool steels. It is now a major manufacturing process for various types of tool steels such as cold-work and hot-work tool steels. The powder process involves melting the steel to the desired chemistry and then producing the powder by impinging a thin stream of molten steel with jets of water or gas. The powder is then processed through a series of operations such as drying, screening,

TABLE 11.4
Manufacturing and Service Characteristics of Tool Steels

	Hardening and Tempering					Fabrication and Service			
AISI Designation	Resistance to Decarburization	Hardening Response	Amount of Distortion (a)	Resistance to Cracking	Approximate Hardness (b), HRC	Machinability	Toughness	Resistance to Softening	Resistance to Wear
Molybdenum high-speed steels									
M1	Low	Deep	A or S, low, O, medium	Medium	60–65	Medium	Low	Very high	Very high
M2	Medium	Deep	A or S, low, O, medium	Medium	60–65	Medium	Low	Very high	Very high
M3 (class 1 and class 2)	Medium	Deep	A or S, low, O, medium	Medium	61–66	Medium	Low	Very high	Very high
M4	Medium	Deep	A or S, low, O, medium	Medium	61–66	Medium	Low	Very high	Very high
M6	Low	Deep	A or S, low, O, medium	Medium	61–66	Medium	Low	Highest	Very high
M7	Low	Deep	A or S, low, O, medium	Medium	61–66	Medium	Low	Very high	Very high
M10	Low	Deep	A or S, low, O, medium	Medium	60–65	Medium	Low	Very high	Very high
M30	Low	Deep	A or S, low, O, medium	Medium	60–65	Medium	Low	Highest	Very high
M33	Low	Deep	A or S, low, O, medium	Medium	60–65	Medium	Low	Highest	Very high
M34	Low	Deep	A or S, low, O, medium	Medium	60–65	Medium	Low	Highest	Very high
M36	Low	Deep	A or S, low, O, medium	Medium	60–65	Medium	Low	Highest	Very high
M41	Low	Deep	A or S, low, O, medium	Medium	65–70	Medium	Low	Highest	Very high
M42	Low	Deep	A or S, low, O, medium	Medium	65–70	Medium	Low	Highest	Very high
M43	Low	Deep	A or S, low, O, medium	Medium	65–70	Medium	Low	Highest	Very high
M44	Low	Deep	A or S, low, O, medium	Medium	65–70	Medium	Low	Highest	Very high
M46	Low	Deep	A or S, low, O, medium	Medium	67–69	Medium	Low	Highest	Very high
M47	Low	Deep	A or S, low, O, medium	Medium	65–70	Medium	Low	Highest	Very high
Tungsten high-speed steels									
T1	High	Deep	A or S, low, O, medium	High	60–65	Medium	Low	Very high	Very high
T2	High	Deep	A or S, low, O, medium	High	61–65	Medium	Low	Very high	Very high
T4	Medium	Deep	A or S, low, O, medium	Medium	62–66	Medium	Low	Highest	Very high
T5	Low	Deep	A or S, low, O, medium	Medium	60–65	Medium	Low	Highest	Very high
T6	Low	Deep	A or S, low, O, medium	Medium	60–65	Low to medium	Low	Highest	Very high
T8	Medium	Deep	A or S, low, O, medium	Medium	60–65	Medium	Low	Highest	Very high
T15	Medium	Deep	A or S, low, O, medium	Medium	63–68	Low to medium	Low	Highest	Highest
Chromium hot-work steels									
H10	Medium	Deep	Very low	Highest	39–56	Medium to high	High	High	Medium
H11	Medium	Deep	Very low	Highest	38–54	Medium to high	Very high	High	Medium

H12	Medium	Deep	Very low	Highest	38–55	Medium to high	Very high	High	Medium
H13	Medium	Deep	Very low	Highest	38–53	Medium to high	Very high	High	Medium
H14	Medium	Deep	Low	Highest	40–47	High	High	High	Medium
H19	Medium	Deep	A or S, low, O, medium	High	40–57	High	High	High	Medium to high
Tungsten hot-work steels									
H21	Medium	Deep	A or S, low, O, medium	High	36–54	Medium	High	High	Medium to high
H22	Medium	Deep	A or S, low, O, medium	High	39–52	Medium	High	High	Medium to high
H23	Medium	Deep	A or S, low, O, medium	High	34–37	Medium	Medium	Very high	Medium to high
H24	Medium	Deep	A or S, low, O, medium	High	45–55	Medium	Medium	Very high	High
H25	Medium	Deep	A or S, low, O, medium	High	35–44	Medium	High	Very high	Medium
H26	Medium	Deep	A or S, low, O, medium	High	43–48	Medium	Medium	Very high	High
Molybdenum hot-work steels									
H42	Medium	Deep	A or S, low, O, medium	Medium	50–60	Medium	Medium	Very high	High
Air-hardening medium-alloy cold-work steels									
A2	Medium	Deep	Lowest	Highest	57–62	Medium	Medium	High	High
A3	Medium	Deep	Lowest	Highest	57–65	Medium	Medium	High	Very high
A4	Medium to high	Deep	Lowest	Highest	54–62	Low to medium	Low to medium	Medium	Medium to high
A6	Medium to high	Deep	Lowest	Highest	54–60	Low to medium	Low to medium	Medium	Medium to high
A7	Medium to high	Deep	Lowest	Highest	57–67	Low	Low	High	Highest
A8	Medium to high	Deep	Lowest	Highest	50–60	Medium	Medium	High	Medium to high
A9	Medium to high	Deep	Lowest	Highest	35–56	Medium	Medium	High	Medium to high
A10	Medium to high	Deep	Lowest	Highest	55–62	Medium to high	Medium to high	Medium	High
High-carbon, high-chromium cold-work steels									
D2	Medium	Deep	Lowest	Highest	54–61	Low	Low	High	High to very high
D3	Medium	Deep	Lowest	High	54–61	Low	Low	High	Very high
D4	Medium	Deep	Lowest	Highest	54–61	Low	Low	High	Very high
D5	Medium	Deep	Lowest	Highest	54–61	Low	Low	High	High to very high
D7	Medium	Deep	Lowest	Highest	58–65	Low	Low	High	Highest
Oil-hardening cold-work steels									
O1	High	Medium	Very low	Very high	57–62	High	Medium	Low	Medium
O2	High	Medium	Very low	Very high	57–62	High	Medium	Low	Medium
O6	High	Medium	Very low	Very high	58–53	Highest	Medium	Low	Medium
O7	High	Medium	W, high, O, very low	W, high, O, very low	58–64	High	Medium	Low	Medium

Continued

TABLE 11.4 (Continued)
Manufacturing and Service Characteristics of Tool Steels

	Hardening and Tempering					Fabrication and Service			
AISI Designation	Resistance to Decarburization	Hardening Response	Amount of Distortion (a)	Resistance to Cracking	Approximate Hardness (b), HRC	Machinability	Toughness	Resistance to Softening	Resistance to Wear
Shock-resisting steels									
S1	Medium	Medium	Medium	High	40–68	Medium	Very high	Very high	Medium
S2	Low	Medium	High	Low	50–60	Medium to high	Highest	Highest	Low
S5	Low	Medium	Medium	High	50–60	Medium to high	Highest	Highest	Low
S6	Low	Medium	Medium	High	54–56	Medium	Medium	Very high	Low
S7	Medium	Deep	A, lowest, O, low	A, highest, O, high	47–57	Medium	Very high	High	Low to medium
Low-alloy special-purpose steels									
L2	High	Medium	W, low, O, medium	W, high, O, medium	45–63	High	Very high (c)	Low	Low to medium
L6	High	Medium	Low	High	45–62	Medium	Very high	Low	Medium
Low-alloy special-purpose steels									
P2	High	Medium	Low	High	58–64 (c)	Medium to high	High	Low	Medium
P3	High	Medium	Low	High	58–64 (c)	Medium to low	High	Low	Medium
P4	High	High	Very low	High	58–64 (c)	Medium	High	Medium	High
P5	High	—	W, high, O, low	High	58–64 (c)	Medium	High	Low	Medium
P6	High	—	A, very low, O, low	High	58–64 (c)	Medium	High	Low	Medium
P20	High	Medium	Low	High	28–37	Medium to high	High	Low	Low to medium
P21	High	Deep	Lowest	High	30–40 (d)	Medium	Medium	Medium	Medium
Water-hardening steels									
W1	Highest	Shallow	High	Medium	50–64	Highest	High (e)	Low	Low to medium
W2	Highest	Shallow	High	Medium	50–64	Highest	High (e)	Low	Low to medium
W5	Highest	Shallow	High	Medium	50–64	Highest	High (e)	Low	Low to medium

A, Air cool; B, brine quench; O, oil quench; S, salt bath quench; W, water quench. (b) After tempering in temperature range normally recommended for this steel. (c) Carburized case hardness. (d) After aging at 510 to 550°C. (e) Toughness decreases with increasing carbon content and depth of hardening.

Source: From A.M. Bayer, T. Vasco, and L.R. Walton, Wrought tool steels, in *ASM Handbook*, Vol. 1, *Properties and Selection: Iron, Steels, and High-Performance Alloys*, 10th ed., 1990, p. 772 *Tool Steels, Products Manual*, American Iron and Steel Institute, Washington, D.C., 1978.

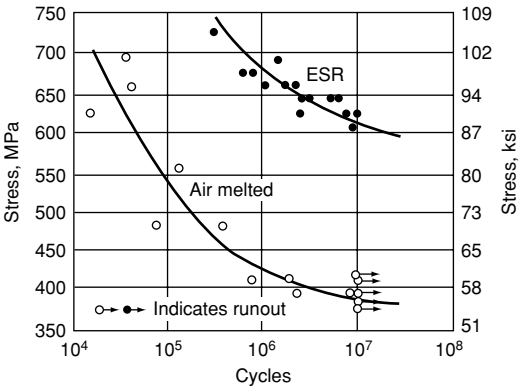

FIGURE 11.1 S–N curves for tension–compression fatigue testing of transverse air-melted and ESR A2 specimen. (From G. Roberts, G. Krauss, and R. Kennedy, *Tool Steels*, 5th ed., ASM International, Materials Park, OH, 1998, p. 33; T.V. Philip, *Met. Technol.*, 1975, 554–564.)

annealing, sintering, and pressing into billets that are conventionally forged or rolled into bars. This process is more suitable for the production of more highly alloyed tool steels such as high-carbon, high-chromium, and high-speed steels. These steels are very difficult to produce by cast ingot process due to slow cooling rates, resulting in macrosegregation and the formation of eutectic-carbide structure that are difficult to be broken down during hot working [12]. Rapid solidification associated with P/M process reduces segregation and produces uniform and fine microstructure of an atomized powder. High-speed steels produced by P/M have better grindability than the same steel produced by casting due to their fine and uniformly distributed carbides. Figure 11.2 illustrates the finer and uniformly distributed carbides and homogeneous microstructure in bars produced by P/M compared to that in ingot casting [13].

The spray forming process [1] is attracting more attention because of its economy and capability of producing dense, preformed products of metals of different shapes. This process consists of gas atomization of molten metal by nitrogen or argon into small droplets. These droplets are deposited into a rotating collector that can produce products with different

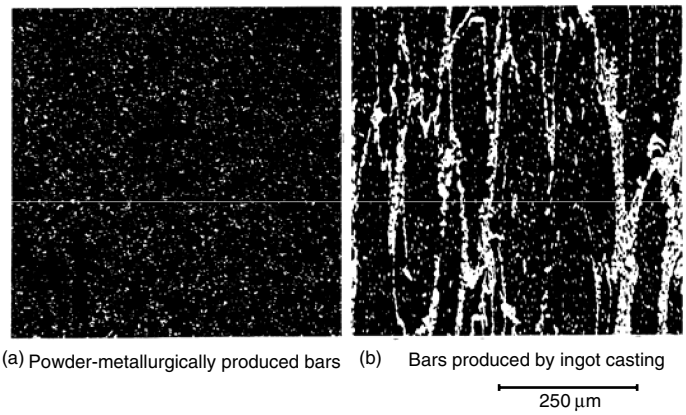

FIGURE 11.2 Microstructure in 100-mm diameter. Bars of high-speed steel M3 produced by (a) P/M and (b) ingot casting. (From S. Wilmes, H-J. Becker, and R. Krumpholz, "Tool Steels", *A Handbook for Materials Research and Engineering*, Vol. 2, Applications, ed., Verein Deurscher Eisenhuttenleute, 1993, p. 327.)

shapes such as billet, hollows, and sheet. Tool steels have been produced in Japan using the Ospray process since 1986. High-carbon, high-speed steel, and high-chromium cast iron are the alloy sprayed [8,14]. High-alloy steels made using Ospray have uniform and fine carbides of a size close to P/M products. A comparison of properties of high-speed steel tools manufactured by Ospray, powder metallurgy, and ingot metallurgy, is given in Table 11.5. It shows that the performance of tools produced by the Ospray process is equivalent to that produced by P/M.

11.3.2 Thermomechanical Processing

The purpose of hot working such as hot forging and hot rolling is to produce tool steels close to the final shape and dimension and to improve the properties and performance of the final tool through grain refinement and uniform carbide distribution. After hot working, the forged or rolled bars must be annealed usually to avoid cracking during machining, grinding, or reheating for further work. The typical hot working start temperature range is about 1190 to 1090°C and the finish temperature range is about 955 to 1010°C, depending on the steel grade and the process used to produce it.

Usually, in finish rolling after forging, a rapid heating of a 135-mm diameter billet from room temperature to the hot rolling temperature of approximately 1150°C in 10 min is used to prevent decarburization. Hot workability of tool steels depends on their chemistry and high alloying reduces it. It improves with grain refinement and reduction of segregation. Hot working of a cast structure is lower than that of the forged or rolled billet because of the coarser grain size and carbides, as well as higher segregation degree of the former microstructure.

11.4 IMPORTANT STEEL PROPERTIES RELEVANT TO THE MANUFACTURE OF TOOLS

The properties of steels that are important in the manufacturing of tools include dimensional accuracy, hot ductility, cold formability, machinability, grindability, polishability, and resistance to decarburization.

11.4.1 Dimensional Accuracy during Heat Treatment

Distortion, which is the sum of all changes in dimension and shape that appear after heat treatment, is a common concern in tool steel manufacturing. Usually it is difficult and

TABLE 11.5
Comparison of Properties (Relative Values) of High-Speed Tool Steel Made by Various Processes

Property	Ospray Metallurgy	Powder Metallurgy	Ingot Metallurgy
Carbide size, μm	5–6	2–3	15–20
Bend strength	90	100	60
Wear resistance	100	90	100
Grindability	80	100	25
Toughness	90	100	60

Source: From G. Roberts, G. Krauss, and R. Kennedy, *Tool Steels*, 5th ed., ASM International, Materials Park, OH, 1998, p. 41.

expensive to machine tool steels in the hardened condition. The final shape of some tool steels is produced by machining in the soft-annealed condition [13]. To prevent distortion that cannot be avoided during heat treatment, this process is carried out prior to manufacturing of tool steel. The factors that affect dimensional accuracy are (1) specific volume differences of phases existing before and after heat treatment; (2) thermal stresses caused by temperature differences between the surface and the core of heat-treated tool; and (3) stresses that are caused by phase transformation.

Segregation affects distortion through its influence on transformation. Segregation can be reduced by homogenization heat treatment.

11.4.2 Hot Formability

The hot ductility of tool steels is important because it prevents cracking during hot rolling or forging. Hot ductility is reduced by the presence of carbides along grain boundaries, inclusions, sulfur, and tramp elements such as Cu, Sn, and Sb. Improving steel cleanliness by remelting process is beneficial in preventing transverse cracking during hot forming of highly alloyed tool steels, such as ledeburitic steels that have poor hot ductility. Crack initiation could be prevented by improving the surface quality.

11.4.3 Cold Formability

Soft annealing that produces microstructure with large and spheroidized carbides improves cold forming such as hobbing and lowers hardness. Tool steels with very high-carbide content such as ledeburitic carbides, that cannot be influenced strongly by soft annealing, are rarely manufactured by cold forming.

11.4.4 Machinability

Machinability is characterized by all the properties of a material that play a role in shaping steels by the use of cutting tools. Soft steels such as low-carbon tool steels with high-ferrite content are difficult to machine due to adhesion between the tool and workpiece. In this case, tool steel is machined in the normalized condition with a ferrite–pearlite microstructure, and not in the soft-annealed condition. Steels with a high-carbon content are machined under soft-annealing condition with spheroidized carbides [13]. The best machining results are obtained with a hardness between about 180 and 230 HB.

Machinability is reduced by the presence of hard particles such as alumina and silica and special carbides, which increase cratering on the cut surface and abrasion on the top surface. It is well known that sulfur improves machinability through its influence on chip formation. Sulfur is generally limited to 0.1% to avoid high anisotropy of properties, such as toughness.

11.4.5 Grindability

Grindability is the ability to remove a large amount of material by grinding in a short period of time without damaging the tool surface. The grindability index is the volume of metal removed per volume of wheel wear. Usually, tools, that are heat treated after machining, are shaped by grinding after heat treatment. Surface damaging can be caused by the accumulation of heat in the surface, which may cause surface tempering or hardening. Stresses developed during such heating through volumetric changes may create grinding check defects. Grindability, which can be measured by abrasion, decreases with increasing hardness, carbide content, hardness of carbides, and carbide size.

11.4.6 Polishability

Tool steels with polished surfaces are used in stamping, forming, and plastic processing. Ledeburitic tool steels are more difficult to polish due to the presence of hard carbides. Microstructure inhomogeneities result in poor response to polishing. Clean steels with fewer nonmetallic inclusions and reduced segregation have excellent polishability. Hard inclusions such as alumina or silicates are detrimental to the quality of polished tool steels. Polishability increases with the hardness, but this is not the only factor to take into account for designing tool steels with high hardness.

11.5 IMPORTANT PROPERTIES REQUIRED FOR VARIOUS APPLICATIONS

Tool steels are high-quality steels as opposed to construction steels, for which new steel grades are developed more economically with mechanical properties obtained directly from forging or rolling. The Mechanical property of tool steels requires very highly controlled heat treatment. The microstructure and properties of tool steels resulting from heat treatment depend on the chemical composition for a given grade, on the annealing conditions.

Tool steels are used for many applications dealing with manufacturing. Their field of application includes machining, cutting, forming by stamping, pressing or forging, forming of shapes from the molten state in glass, plastics, or metals, and die casting. All tool steels are characterized and identified on the basis of their use for a particular application. Their characteristics cannot be found in the chemical composition or the properties.

The important properties of tool steels are constant hardness at low and high temperatures, hardenability, retention of hardness, high compression strength and pressure resistance, fatigue strength, toughness at operational temperatures, wear resistance at room and high temperatures, thermal fatigue resistance, and corrosion resistance.

Tool steels are associated with high hardness. However, the hardness of a tool must only be high in relation to the hardness of the material to be machined or processed. It is generally an order of magnitude related to quenched and tempered structural steels. Normal hardness values vary between about 200 HV for glass-mold steels at the lower level, and 900 HV for forming and machining tools at the upper level [13]. Hardness is the most important characteristic of steels from which their potential application can be recognized. The wear resistance of tool steels increases with increasing hardness, and toughness is reduced with increasing hardness.

11.5.1 Hardness

The hardness of tool steels is related to the material to be processed. It varies between about 200 HV for glass-mold steels at the lower level and 900 HV for forming and machining tools at the upper level. Obtaining high hardness and microstructures that have high hardness are the major objectives of final heat treatment applied to tool steels.

Carbon content is the dominant factor controlling the strength of martensite through its interaction with other structural elements of a martensitic microstructure [15–17]. Figure 11.3 illustrates hardness as a function of carbon for various microstructures obtained from the austenite transformation and heat treatment of carbon steels. Martensite transformation from austenite is never complete. At the end of the transformation corresponding to the temperature M_f a certain amount of austenite is untransformed (retained austenite [RA]) [18]. This amount of RA depends on the martensite temperature range M_s–M_f; it increases as the range narrows, and this range narrows as M_s is lowered.

Hardness is the most important characteristic of a tool steels that indicates their potential application. The hardness also allows to draw a conclusion on the working stress limit and

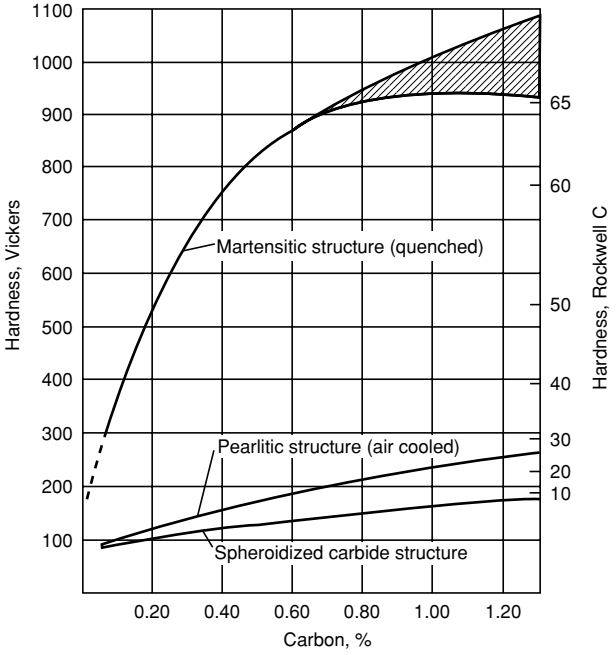

FIGURE 11.3 Hardness of three microstructures as a function of carbon content. The high-carbon region of the martensitic structure curve is broad due to retained austenite. (From E.C. Bain and H.W. Paxton, *Alloying Elements in Steel*, 2nd ed., American Society for Metals, Metals Park, OH, 1961, p. 37.)

thus, on the shape stability of a tool. Due to this shape stability, hardness must be sufficiently high that the yield stress is above the highest load stress on the tool. The relationship between hardness and flow stress in the case of tool steels is shown in Figure 11.4. However, increasing the hardness for shape stability could affect other properties such as toughness, which is usually reduced, and thus, the susceptibility to fracture of the tool steel is increased. Wear resistance increases with increasing hardness.

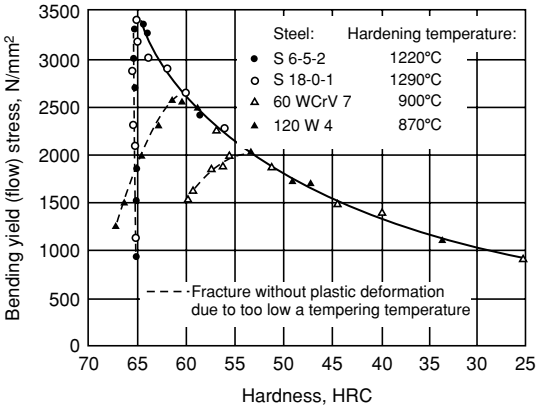

FIGURE 11.4 Relationship between hardness and bending yield stress of hardened tool steels. (From S. Wilmes, H.-J. Becker, and R. Krumpholz, "Tool steels,"*A Handbook for Materials Research and Engineering*, Vol. 2, Applications, ed., Verein Deurscher Eisenhuttenleute, 1993, p. 306; J.C. Hamaker Jr., V.C. Stang, and G.A. Roberts, *Trans. Amer. Soc. Metals*, 49, 1957, S. 550/75.)

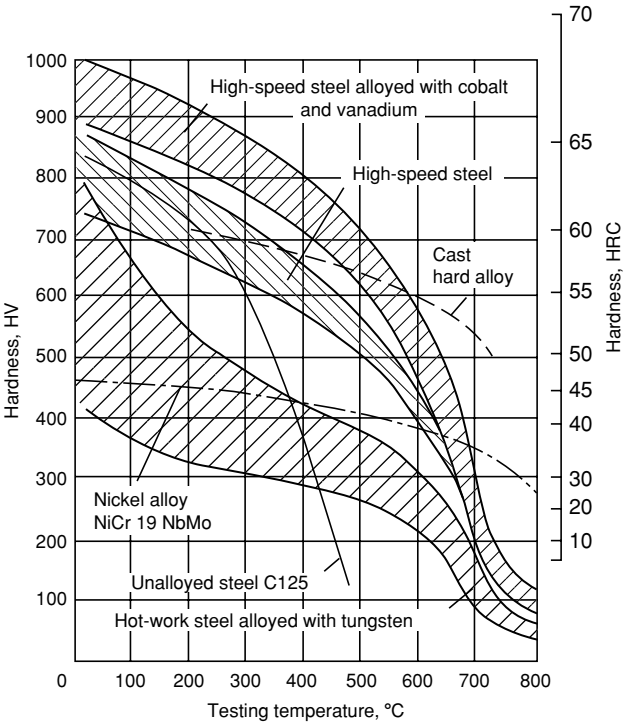

FIGURE 11.5 Hardness at elevated temperatures of different types of tool steels. (From S. Wilmes, H-J. Becker, and R. Krumpholz, "Tool steels," *A Handbook for Materials Research and Engineering*, Vol. 2, Applications, ed., Verein Deurscher Eisenhuttenleute, 1993, p. 307; G.A. Roberts, *Trans. Metallurg. Soc. AIME*, 236, 1966, S. 950/63.)

The hardness of tool steels decreases with increasing temperature. Figure 11.5 illustrates the variation with temperature of hardness of various types of tool steels. Tools that operate above 200°C must have high hardness as possible at elevated temperatures to ensure the shape stability and an adequate value of wear resistance of the tool steel at the operating conditions. At temperatures higher than 600°C the hardness of martensitic tool steels is no longer sufficient to cope with the stress. Reliable hardness is to be found in some austenitic steel and in nickel and cobalt alloys that on the other hand are not suitable for tools at low operating temperatures due to their low hardness. In tool steels, martensite formation is the most efficient method of improving hardness.

Hardness is usually measured with various loads on the Rockwell C scale (HRC), which uses a diamond cone indenter, and on the Vickers scale (HV), which uses a diamond pyramid indenter. The equivalent hardness numbers between HRC and HV are given in Table 11.6.

Soft annealing, which produces ferrite matrix with interstitial carbides, could reduce hardness. Cr is the element that has less influence on the solid solution strengthening as illustrated in Figure 11.6.

The most effective way of improving hardness in tool steels is through martensite formation during quenching and precipitation of fine carbides of Mo, Cr, and V.

11.5.2 Hardenability

Hardenability, which is of equal importance as hardness, includes maximum achievable hardness during quenching, and the depth of hardening obtained by quenching in a specific

TABLE 11.6
Approximate Conversion of Hardness Values and Tensile Strengths for Steels

		Rockwell Hardness C				
Vickers Hardness No. HV	Brinell Hardness No. 3000 kg Load 10 mm Ball	C Scale 150 kg Load Diamond Cone HRC	A Scale 60 kg Load Diamond Cone HRA	Superficial 30-N 10 kg Load Diamond Cone	Scleroscope Hardness No.	Tensile Strength (Approx.)[a]
100	95	—	43		—	—
120	115	—	46		—	393
140	135	—	50		21	455
160	155		53		24	517
180	175		56		27	
						579
200	195		58		30	634
220	215		60		31	696
240	235	20.3	60.6	41.7	34	765
260	255	24.0	62.4	45.0	37	827
280	275	27.1	63.8	47.8	40	
						889
300	295	29.8	65.2	50.2	42	952
320	311	32.2	66.4	52.3	45	1007
340	328	34.4	67.6	54.4	47	1069
360	345	36.6	68.7	56.4	50	1131
380	360	38.8	69.8	58.4	52	
						1207
400	379	40.8	70.8	60.2	55	1289
420	397	42.7	71.8	61.4	57	1372
440	415	44.5	72.8	63.5	59	1461
460	433	46.1	73.6	64.9	62	1537
480	452	47.7	74.5	66.4	64	1620
500	471	49.1	75.3	67.7	66	1703
520	487	50.5	76.1	69.0	67	1793
540	507	51.7	76.7	70.0	69	1862
560	525	53.0	77.4	71.2	71	1951

Continued

TABLE 11.6 (Continued)
Approximate Conversion of Hardness Values and Tensile Strengths for Steels

		Rockwell Hardness C				
Vickers Hardness No. HV	Brinell Hardness No. 3000 kg Load 10 mm Ball	C Scale 150 kg Load Diamond Cone HRC	A Scale 60 kg Load Diamond Cone HRA	Superficial 30-N 10 kg Load Diamond Cone	Scleroscope Hardness No.	Tensile Strength (Approx.)[a]
580	545	54.1	78.0	72.1	72	2020
600	564	55.2	78.6	73.2	74	2089
620	582	56.3	79.2	74.2	75	2186
640	601	57.3	79.8	75.1	77	2262
660	620	58.3	80.3	75.9	79	2358
680	638	59.2	80.8	76.8	80	2448
700	656	60.1	81.3	77.6	81	
720	670	61.0	81.8	78.4	83	
740	684	61.8	82.2	79.1	84	
760	698	62.5	82.6	79.7	86	
780	710	63.3	83.0	80.4	87	
800	722	64.0	83.4	81.1	88	
820	733	64.7	83.8	81.7	90	
840	745	65.3	84.1	82.2	91	
860	—	65.9	84.4	82.7	92	
880	—	66.4	84.7	83.1	93	
900	—	67.0	85.0	83.6	95	
920	—	67.5	85.3	84.0	96	
940	—	68.0	85.6	84.4	97	

[a]These values are substracted from Ref. [15] and converted to MPa.

Source: From G. Roberts, G. Krauss, and R. Kennedy, *Tool Steels*, 5th ed., ASM International, Materials Park, OH, 1998, p. 83; *Smithells Metals Reference Book*, 9th ed., pp. 21-4, and 21-5.

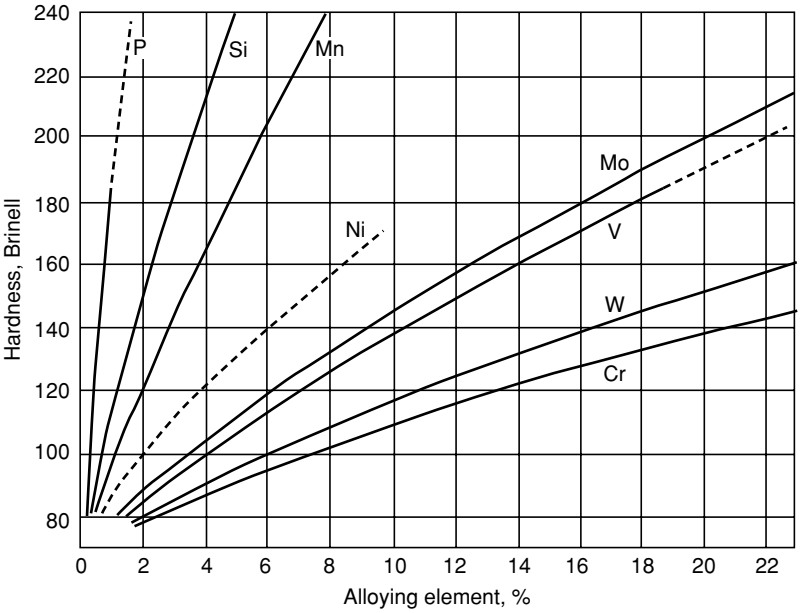

FIGURE 11.6 Influence of alloying elements on solid solution strengthening of ferrite. (From E.C. Bain and H.W. Paxton, *Alloying Elements in Steel*, 2nd ed., American Society for Metals, Metals Park, OH, 1961, p. 62.)

manner. With the same hardness, a tempered martensite has better toughness than a bainitic or pearlitic microstructure.

Steels for forging and pressing dies and for cutting tools need a thin surface zone with very high surface-hardness but with a soft core. These steels are used in tools subjected to bending or impact, due to their lack of susceptibility to cracking. Jominy tests for hardenability assessment used for structural steels are not suitable for tool steels due to their high degree of hardenability. Depth hardening of the tool steels is assessed using time–temperature–transformation (TTT) curves.

Alloying elements that stabilize austenite increase hardenability. However, with tool steels the choice of alloying elements depends on many other properties such as carbide formation, carbide hardness, decarburization tendency, nitridability, and deformability. The following examples illustrate the effects of some alloying elements: (1) adding Ni gives good hardenability without carbide formation but with lower transformation temperature; (2) Si increases the tendency of decarburization; and (3) Cr, Mo, W, and V result in carbide formation and make the steels easy to nitride.

In tool steels, carbide quantities are up to 5 vol.% in hot-work tool steels, up to 20% in high-speed tool steels, and up to 25 vol.% in ledeburitic steel with 12%Cr. With C content above 0.7%, the result of increasing the hardening temperature produces a more stable austenite, which results in large quantities of retained austenite, and therefore the hardness is decreased.

11.5.3 Toughness at Operational Temperature

The toughness of tool steels that are subjected to dynamic stresses is the ability to release stress peaks by a small local plastic deformation that prevents a crack formation. Toughness is a generic term for all influences which concern the resistance of a tool to fracture [13]. The toughness of tool steels that are used with service hardness below about 55 HRC is better assessed by impact energy on notched and unnotched specimens. In the case of tool steels with hardness in service higher than

55 HRC, static bending tests and the static torsion tests have been shown to be reliable. When comparing materials having the same hardness, only plastic bending energy or torsional energy needs to be considered in assessing toughness. Toughness properties are influenced strongly by the microstructure, and they show improvement with a more homogeneous microstructure. Finer spheroidized carbides also improve toughness. It is improved by segregation reduction, cleanliness, and reduction of inclusions such as oxides, sulfides, and carbides. To reduce toughness anisotropy, producing clean steel is not enough; there is a need for additional homogenizing which reduces the degree of segregation. In the case of alloyed steels, a reduction of segregation can be achieved by P/M, which also produces very fine carbides. Toughness properties deteriorate with the presence of an upper bainite microstructure due to carbide precipitation.

11.5.4 Resistance to Thermal Fatigue

The failure of material by heat checking is caused by the creep behavior of tool steels. Steels that are used for forging tools, pressure casting dies, glass forming, and plastic molds are subjected to thermal cycling during which heat checking is caused. The formation of these cracks is delayed by the use of materials with a high yield strength and high toughness at elevated temperatures [13]. The propagation of heat checking is connected with oxidation processes. It is then important to use chromium-alloyed steels because chromium improves the scaling resistance. At higher tool temperatures, such as those sustained by a glass forming molds, the chromium content should be higher. The resistance to heat checking can be improved by using steels with high thermal conductivity. It is advantageous to use steels with a homogeneous quenched, and tempered microstructure.

11.6 HEAT TREATMENT

The properties of tool steels depend strongly on heat treatment processing, which depends on their chemical composition and their application. The heat treatment of tool steels consists of a three-stage process: (1) heating the steel to the austenite region to form austenite; (2) cooling the steel from the austenitization temperature to transform the austenite to martensite; and (3) tempering to eliminate RA and to form carbides within the martensite.

The schematic diagrams of heat treatment steps required for producing tool steels are illustrated in Figure 11.7 and Figure 11.8 [8,23,24].

After casting or powder manufacturing and hot working, heat treatment processing steps include normalizing, annealing, machining, and stress relief followed by hardening. The final shaping of tool steels by forming and machining is performed before the final hardening heat treatment step, due to the very high as-heat treated hardness that makes tool steels very difficult to shape. However, final dimensions can be adjusted by grinding with highly abrasive materials or by electrodischarge machining [25].

Two aspects are of importance to tool steels; the first is homogenization or reduction of microstructure heterogeneity that is produced by segregation phenomenon during solidification and the second is the refinement of grains, which improves the required mechanical properties. Annealing to homogenize the microstructure is based on diffusion phenomenon. This heat treatment consists of maintaining the tool steel at a given temperature for a period of time followed by a controlled cooling rate. A coarse grain size may result from this. The homogenizing treatment is followed by a grain refinement step. This treatment is carried out at a temperature 50°C above Ac_3 for hypoeutectic steels, and above Ac_1 for hypereutectic steels. This cycle consists of reheating the steel at the required temperature for a minimum period of time required, followed by cooling in a manner to prevent the formation of bainite [28].

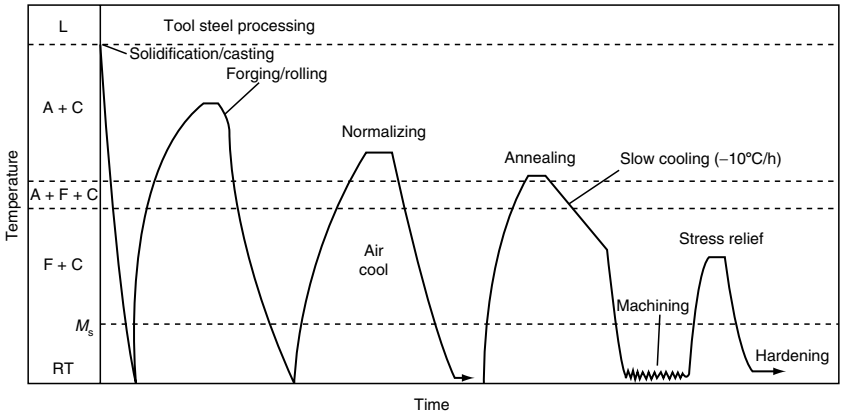

FIGURE 11.7 Schematic diagram of tool steel processing and heat treatment prior to final hardening heat treatment. A, austenite; C, carbides; F, ferrite; M, martensite. (From G. Roberts, G. Krauss, and R. Kennedy, *Tool Steels*, 5th ed., ASM International, Materials Park, OH, 1998, p. 67; G. Krauss, *Steels: Heat Treatment and Processing Principles*, ASM International, Materials Park, OH, 1990.)

The heat treatment of tool steels is implemented to achieve one of the following targets:

1. To obtain a desired microstructure and properties suitable for machining or cold deformation
2. To release residual stresses accumulated during previous thermal and mechanical treatments
3. To homogenize the microstructure with globular carbides by a spheroidization treatment
4. To dissolve by a normalizing treatment the intergranular carbides that are detrimental to the mechanical properties of tool steels

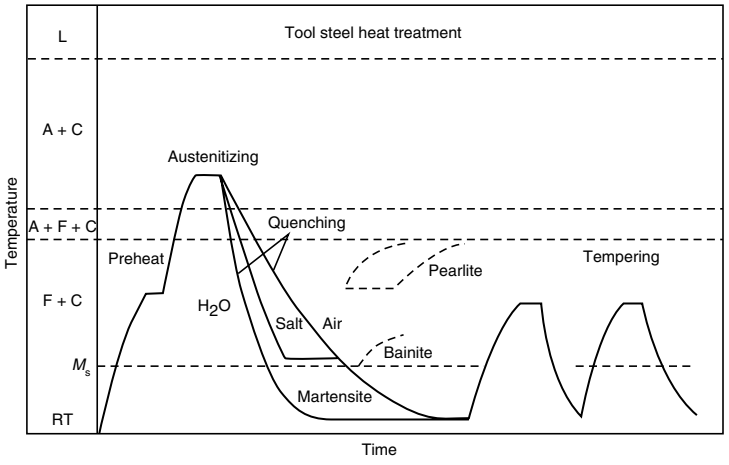

FIGURE 11.8 Schematic diagram of tool steel heat treatment steps for final hardening. (From G. Roberts, G. Krauss, and R. Kennedy, *Tool Steels*, 5th ed., ASM International, Materials Park, OH, 1998, p. 68.)

11.6.1 Normalizing

Normalizing is a heat treatment that is performed in hot forged or hot-rolled tool steels to produce more uniform, fine-grained microstructures for subsequent annealing and hardening heat treatments. The normalizing treatment helps to produce a more uniform distribution of precipitates. In tool steels with more stable carbides such as Cr and W carbides, the precipitates may be preferentially aligned in the hot-working direction, or present at grain boundaries.

The normalizing process consists of heating the steel to the temperature region indicated in Figure 11.9 by the crosshatched area, followed by air-cooling. During heating and holding at the normalizing temperature, the initial ferrite–carbide structure that is stable at low temperatures transforms to austenite. The dissolution of carbides during heating depends on the alloy content of the tool steels. During cooling austenite transforms to ferrite and cementite. In the case of the low-alloy tool steels, cementite and pearlite will form during air-cooling. The carbides in this structure will be spheroidized in subsequent annealing treatments. In high-alloy tool steels, due to their high hardenability, martensite may form during air-cooling, which may cause cracking, and thus, a normalizing treatment should be avoided for these tool steel grades. Table 11.7 lists normalizing and annealing temperatures for different tool steel grades [5,26]. As previously indicated, high-alloy steels should not be normalized.

11.6.2 Stress-Relief Heat Treatments

Heat treatment usually causes residual stresses, quench cracks, and distortion. Residual tensile surface stresses may cause cracking during manufacturing, or fracture in service, whereas compressive surface stresses are generally beneficial, they prevent cracking during manufacturing and service and hence improve fatigue strength and resistance to stress corrosion cracking. The objective of a stress-relief heat treatment is to reduce residual stresses

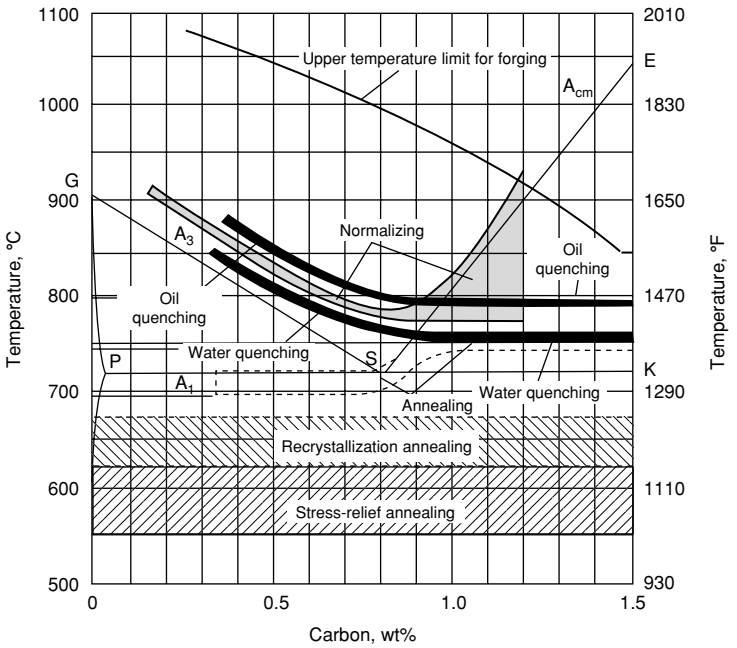

FIGURE 11.9 Schematic diagram of heat treatment temperature ranges for carbon and tool steels. (From G. Roberts, G. Krauss, and P. Kennedy, *Tool Steels*, 5th ed., ASM International, Materials Park, OH, 1998, p. 68; K.E. Thelning, *Stell and its Hert Treatment*, 2nd ed., Butterworths, London, 1984.)

TABLE 11.7
Normalizing and Annealing Temperatures of Tool Steels

Type	Normalizing Temperature, °C	Annealing		
		Temperature, °C	Rate of Cooling, °C/h	Hardness, HB
Molybdenum high-speed steels				
M1, M10	Do not normalize	815–870	22	207–235
M2	Do not normalize	870–900	22	212–241
M3, M4	Do not normalize	870–900	22	223–255
M7	Do not normalize	815–870	22	217–255
M30, M33, M34, M35, M36, M41, M42, M46, M47	Do not normalize	870–900	22	235–269
M43	Do not normalize	870–900	22	248–269
M44	Do not normalize	870–900	22	248–293
M48	Do not normalize	870–900	22	285–311
M62	Do not normalize	870–900	22	262–285
Tungsten high-speed steels				
T1	Do not normalize	870–900		217–255
T2	Do not normalize	870–900		223–255
T4	Do not normalize	870–900		229–269
T5	Do not normalize	870–900		235–277
T6	Do not normalize	870–900		248–293
T8	Do not normalize	870–900		229–255
T15	Do not normalize	870–900		241–277
Intermediate high-speed steels				
M50	Do not normalize	830–845	22	197–235
M52	Do not normalize	830–845	22	197–235
Chromium hot-work steels				
H10, H11, H12, H13	Do not normalize	845–900	22	192–229
H14	Do not normalize	870–900	22	207–235
H19	Do not normalize	870–900	22	207–241
Tungsten hot-work steels				
H21, H22, H25	Do not normalize	870–900	22	207–235
H23	Do not normalize	870–900		212–255
H24, H26	Do not normalize	870–900		217–241
Molybdenum hot-work steels				
H41, H43		815–870	22	207–235
H42	Do not normalize	845–900	22	207–235
High-carbon, high-chromium cold-work steels				
D2, D3, D4	Do not normalize	870–900	22	217–255
D5	Do not normalize	870–900	22	223–255
D7	Do not normalize	870–900	22	235–262
Medium-alloy, air-hardening, cold-work steels				
A2	Do not normalize	845–870	22	201–229
A3	Do not normalize	845–870	22	207–229
A4	Do not normalize	740–760	14	200–241
A6	Do not normalize	730–745	14	217–248
A7	Do not normalize	870–900	14	235–262
A8	Do not normalize	845–870	22	192–223
A9	Do not normalize	845–870	14	212–248
A10	Do not normalize	765–795	8	235–269

Continued

TABLE 11.7 (Continued)
Normalizing and Annealing Temperatures of Tool Steels

Type	Normalizing Temperature, °C	Annealing		
		Temperature, °C	Rate of Cooling, °C/h	Hardness, HB
Oil-hardening cold-work steels				
O1	870	760–790	22	183–212
O2	845	745–775	22	183–212
O6	870	765–790	11	183–217
O7	900	790–815	22	192–217
Shock-resisting steels				
S1	Do not normalize	790–815	22	183–229 (c)
S2	Do not normalize	760–790	22	192–217
S5	Do not normalize	775–800	14	192–229
S7	Do not normalize	815–845	14	187–223
Mold steels				
P2	Not required	730–815	22	103–123
P3	Not required	730–815	22	109–137
P4	Do not normalize	870–900	14	116–128
P5	Not required	845–870	22	105–116
P6	Not required	845	8	183–217
P20	900	760–790	22	149–179
P21	900	Do not anneal		
Low-alloy special-purpose steels				
L2	871–900	760–790	22	163–197
L3	900	790–815	22	174–201
L6	870	760–790	22	183–212
Carbon–tungsten special-purpose steels				
F1	900	760–800	22	183–207
F2	900	790–815	22	207–235
Water-hardened steels				
W1, W2	790–925 (d)	740–790 (e)	22	156–201
W5	870–925	760–790	22	163–201

Source: From A.M. Bayer, T. Vasco, and L.R. Walton, Wrought tool steels, in *ASM Handbook*, Vol. 1, *Properties and Selection: Iron, Steels, and High-Performance Alloys*, 10th ed., 1990, p. 769.

caused by phase transformation during thermomechanical processing, machining or grinding. There is no microstructural change during this process, which should be performed at temperatures below Ac_1 as shown in Figure 11.9. Stress relief is accomplished by a recovery mechanism. The duration of such a treatment is short and is in the range of 1 to 2 h depending on the section thickness. Stress relieving is performed in air furnaces or salt baths. In this process heating and cooling rates are not critical; however, cooling rates should be slow enough (300°C/h maximum) to prevent the introduction of new residual stress.

11.6.3 Annealing

Annealing is a heat treatment process consisting of heating the tool steel above a certain temperature and holding at this temperature for a given length of time. This is followed by cooling at a predetermined rate, usually in the furnace, to room temperature in order to produce a microstructure that is stable at or below room temperature. The stable structure consists of a mixture of

ferrite and carbides, the distribution of which depends on thermomechanical history of the tool steels. Tool steels subjected to an annealing treatment are soft and thus, easily machined and heat treated. If the tool steel is cold or hot rolled, it must be annealed again before subsequent operations. Annealing is also needed before a hardening operation, particularly in the case of high-alloy steels, to produce a homogeneous microstructure needed for subsequent heat treatment.

The required annealing conditions depend on tool steel application and its alloy content. Hypoeutectoid and hypereutectoid steels are annealed to just above the upper critical temperature Ac_3, and the lower critical temperature A_{cm1}, respectively. The range of these temperatures is indicated schematically in Figure 11.10.

There are various types of annealing such as full annealing, isothermal annealing, and spheroidizing.

Full annealing consists of heating the steel above the transformation temperature Ac_3 into the single-phase austenite for hypoeutectoid steel, and above A_1 in the two-phase field of austenite and carbides, in the case of hypereutectoid steels. If the hypereutectoid steels are heated above A_{cm}, carbides will form during slow cooling at grain boundaries of austenite and may cause fracture during forming or in service. The holding time at the reheating temperature is about 1 h per 25-mm thickness to dissolve the carbides present in steel and to form austenite [28]. The holding step is followed by very slow cooling rate in the furnace. The cooling rates are lower than 25°C/h to allow transformation of austenite to ferrite and the formation of globular carbides. The annealing temperatures are in the range of 730 to 900°C depending on the chemical composition of the steel, as indicated in Table 11.8.

Isothermal annealing is another variant of full annealing. The reheating and holding steps are similar to that of full annealing, followed by cooling the workpiece very rapidly to a temperature just below the transformation range and holding it at this temperature for 1 h or more, to allow complete transformation of the austenite to ferrite–pearlite or pearlite–cementite. Air-cooling follows this holding step. The isothermal process is useful for small parts where the cooling rate from the homogenization temperature can be achieved.

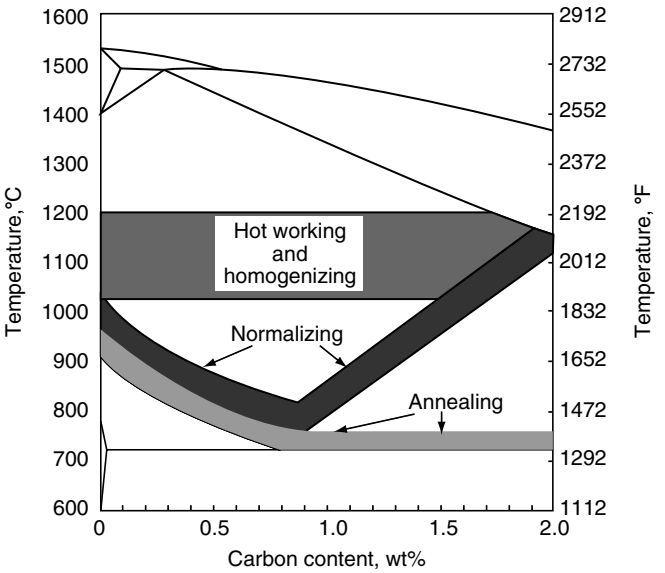

FIGURE 11.10 Temperature range of normalizing, annealing, hot working, and homogenizing hypoeutectoid and hypereutectoid steels. (From G. Krauss, *Steels: Heat Treatment and Processing Principles*, ASM International, Materials Park, OH, 1990, p. 108.)

TABLE 11.8
Effect of Alloying Elements in Tool Steels

Ferrite-Stabilizing Elements	Austenite-Stabilizing Elements
Chromium	Carbon
Molybdenum	Cobalt
Niobium	Copper
Silicon	Manganese
Tantalum	Nickel
Titanium	Nitrogen
Tungsten	
Vanadium	
Zirconium	

Source: From G. Roberts, G. Krauss, and R. Kennedy, *Tool Steels*, 5th ed., ASM International, Materials Park, OH, 1998, p. 50.

11.6.4 Spheroidizing

There are many heat treatment approaches for producing spheroidized microstructures. The spheroidizing method used for tool steels consists of heating the steel just below Ac_1, maintaining it for a period of time, with cyclic heating and cooling above A_1 and below Ar_1, followed by slow cooling rates, lower than 150°C/h. The temperature range for spheroidizing treatment is indicated in Figure 11.11.

The microstructure produced by spheroidization consists of spherical carbides uniformly distributed in a matrix of ferrite. It is the most stable microstructure and has a good machinability compared to other microstructures formed in tool steels. Figure 11.12 shows a spheroidized microstructure of 1.0% carbon steel.

The first step of spheroidization will produce a distribution of very fine-spheroidized particles from the pearlitic, bainitic, or martensitic start microstructure. In the case of highly alloyed steel coarser alloy carbide particles are produced.

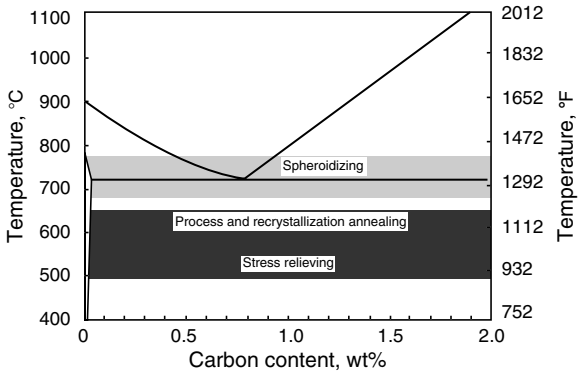

FIGURE 11.11 Temperature range around A_1 used for spheroidization. (From G. Krauss, *Steels: Heat Treatment and Processing Principles*, ASM International, Materials Park, OH, 1990 p. 118.)

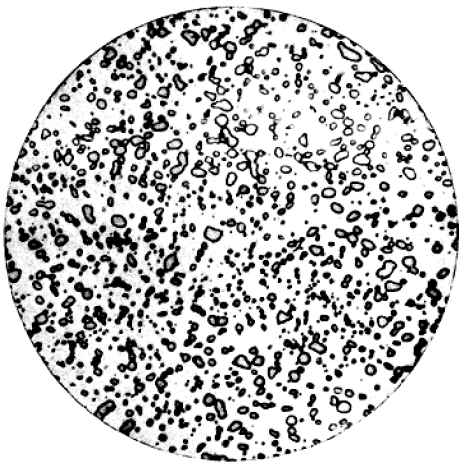

FIGURE 11.12 Spheroidized microstructure 1.0% C steel, 2000× magnification. (From E.C. Bain and H.W. Paxton, *Alloying Elements in Steel*, 2nd ed., American Society for Metals, Metals Park, OH, 1961, p. 101.)

Another key microstructural change associated with the development of spheroidized carbide–ferrite microstructures concerns the transformation of austenite on cooling from the annealing temperature. In the absence of carbide particles, the austenite on slow cooling will transform to pearlite, a lamellar mixture of ferrite and cementite. However, if dispersed undissolved carbides are present, pearlite does not nucleate and grow; instead, further spheroidization and growth of carbides take place as the austenite transforms to ferrite and additional carbides. This is why the annealing temperature has to be kept low enough to ensure that sufficient undissolved carbides are present in the austenite at the start of cooling to promote nucleation and growth of additional spherical carbide on furnace cooling [8].

11.6.5 Carbides in Tool Steels

The microstructure of annealed tool steels consists of ferrite and carbides. The nature of these carbides depends on the chemical composition of the steel. The types of carbides and some of their characteristics are listed below [8,28]:

1. M_3C, which is an orthorhombic carbide of cementite type. M could be iron, manganese, or chromium with a minor substitution of W, Mo, or V. They are present in low-alloy tool steels for cold-working applications and in high-alloy steels for hot-working applications.
2. M_7C_3 is a hexagonal-type carbide mostly present in Cr steels. They are resistant to dissolution at high temperature and are hard and abrasion resistant; these carbides are found in tempered high-speed steels.
3. $M_{23}C_6$ is a face-centered cubic (fcc)-type carbides found in high-Cr steels and all high-speed steels. The Cr can be replaced with Fe to yield carbide with W and Mo.
4. M_6C is fcc-type carbide; W or Mo-rich carbides may contain amounts of Cr, V, and Co present in all high-speed steels. They are extremely resistant to abrasion.

MC is fcc-type carbide. These carbides are vanadium-rich carbides that resist dissolution. The small amount that dissolves plays a role on secondary hardening by reprecipitation.

In hypoeutectoid steels and cold-working tool steels, the most favorable annealed structure for machining is pearlite with a fine-lamellar structure. In hypereutectoid C steels used for cold-working tool steel, the favorable structure for machining is globularized cementite.

All alloy steels have a globularized carbide structure in the annealed state. Fine-globular carbides uniformly distributed have better properties in service. This is obtained by reducing segregation through appropriate steelmaking practices, large reductions during hot working, and appropriate cooling conditions after hot-transformation cycles.

During the annealing operations, the formation of proeutectoid carbides at grain boundaries should be avoided. These carbides are not soluble during austenitization [28].

11.6.6 Hardening

The hardening operation of tool steels consists of three heat treatment steps: austenitization, quenching to obtain martensite, and finally tempering [8,19,28]. These steps are discussed below.

11.6.6.1 Austenitizing

The austenitizing heat treatment is the most critical step performed on tool steels. The following precautions have to be observed during austenitizing: to prevent abnormal grain growth, distortion or loss of ductility, excessive carbide solution that will affect austenite chemistry and hence hardenability, and decarburization that may modify surface chemistry, the austenitizing temperature and holding time should be very well controlled. The austenitizing temperature is particularly important for high-alloy steels such as high-speed steels where the austenitizing temperatures are close to the solidus temperature [19].

Figure 11.13 illustrates the austenite-phase field and the associated critical transformation temperatures [8,19] including the eutectoid temperature, Ac_1, which corresponds to the transformation during heating of ferrite and carbide to austenite. The effect of alloying elements on eutectoid temperature and eutectoid composition is given in Figure 11.14a

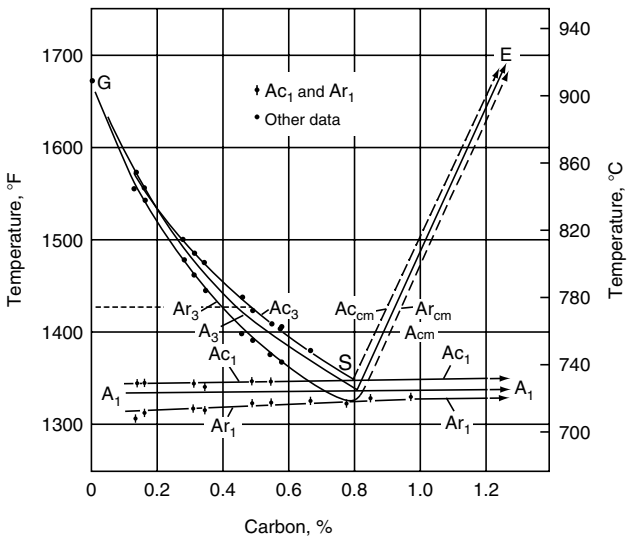

FIGURE 11.13 The transformation temperature on cooling, heating, and equilibrium for Fe–C alloys as influenced by heating and cooling at 0.125°C/min. (From G. Roberts, G. Krauss, and R. Kennedy, *Tool Steels*, 5th ed., ASM International, Materials Park, OH, 1998, p. 52; E.C. Bain and H.W. Paxton, *Alloying Elements in Steel*, 2nd ed., American Society for Metals, Metals Park, OH, 1961, p. 20.)

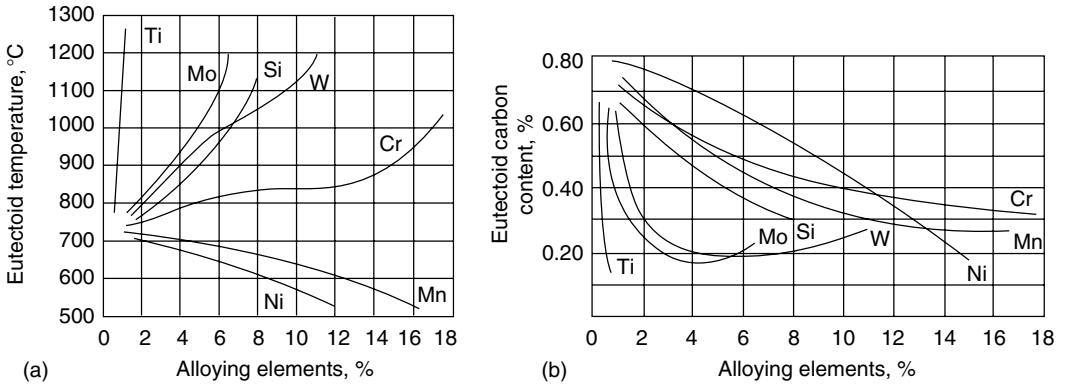

FIGURE 11.14 Effect of alloying elements on (a) the eutectoid transformation temperature Ac_1 and (b) the concentration of carbon eutectoid. (From *Steel Heat Treatment Handbook*, G.E. Totten and M.A.H. Howes, Eds., Marcel Dekker, New York, 1997, pp. 48–51.)

and Figure 11.14b, respectively. Alloying elements used in tool steels are categorized either as ferrite-stabilizing elements that reduce austenite-phase domain, or austenite-stabilizing elements that extend it. They are indicated in Table 11.7 [8]. Figure 11.15 through Figure 11.17 show the effect of Mn, Cr, and Mo on the extend of the phase field of pure austenite at elevated temperature [18].

During reheating in the austenite region, the ferritic structure with carbides transforms into austenite with or without carbides, depending on the chemical composition of the tool steels. In low-alloy steel, a homogeneous austenitic microstructure without carbides may form during austenitization treatment. In high-alloy tool steel, the resultant microstructure consists of austenite and carbides that are not dissolved. In ledeburitic steels, not all carbides are dissolved during reheating, even at the liquidus temperature [28]. It is of interest to note that in high-speed tool steels made by P/M in which the carbides are finer than that in the same steels made by conventional methods, carbide dissolution occurs more readily, particularly if these carbides are of MC type [28].

The microstructure of annealed low-alloy tool steels consists of ferrite and M_3C type carbides, which are easily dissolved in the austenite region. Generally, the quenching temperature is 50°C above Ac_3. These temperatures are a good compromise between dissol-

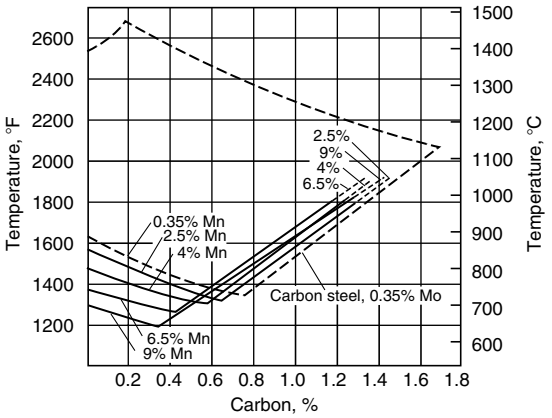

FIGURE 11.15 Effect of Mn on the austenite-phase field in Fe–Mn–C alloys. (From E.C. Bain and H.W. Paxton, *Alloying Elements in Steel*, 2nd ed., American Society for Metals, Metals Park, OH, 1961, p. 104.)

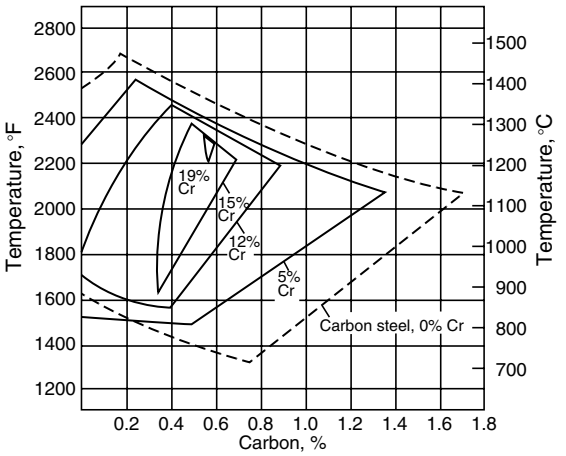

FIGURE 11.16 Effect of Cr on the austenite-phase field in Fe–Cr–C alloys. (From E.C. Bain and H.W. Paxton, *Alloying Elements in Steel*, 2nd ed., American Society for Metals, Metals Park, OH, 1961, p. 105.)

ution of carbides and minimizing austenite gain growth. The austenitizing treatment, 30 min per 25-mm thickness of the heat-treated tool in the temperature range of 750 to 900°C, is sufficient for homogenization.

In highly alloyed steels and ledeburitic steels, the austenitizing temperatures are higher than the low-alloy steels, due to the difficulty of dissolution of carbides of the type M_7C_3, $M_{23}C_6$, M_6C, and MC present in the annealed microstructure. The dissolution of these carbides depends on the annealing temperature, austenitizing temperature, and the holding time at this temperature.

11.6.6.2 Quenching

During quenching from the austenitizing temperature, austenite may transform to martensite with some volume fraction of RA. This is possible when the austenite to ferrite–carbide transformation is suppressed by high cooling rates [8] or alloying elements that retard

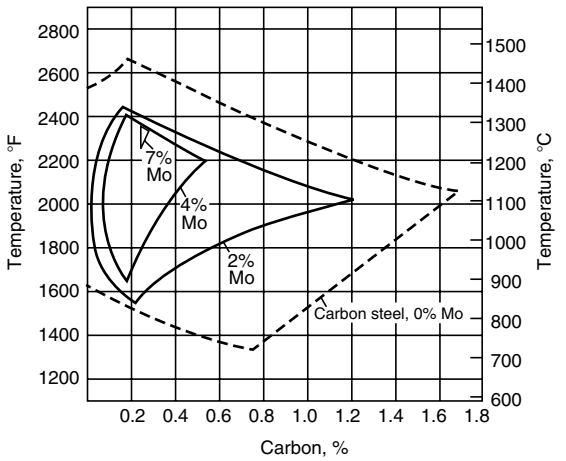

FIGURE 11.17 Effect of Mo on the austenite-phase field in Fe–Mo–C alloys. (From E.C. Bain and H.W. Paxton, *Alloying Elements in Steel*, 2nd ed., American Society for Metals, Metals Park, OH, 1961, p. 106.)

this transformation. Quenching media are typically water, brine, oil, salt, inert gas, or air depending on the composition and the thickness of the tool steel [26].

11.6.6.3 Retained Austenite

After quenching, the microstructure of tool steels consists of martensite and RA. The latter reduces the hardness of the steel and affects the properties of tools in service. During work hardening RA transforms to martensite. The quantity of RA that is related to the reduction of M_f depends on the chemical composition, austenitizing temperature, and cooling rate. RA increases with increasing austenitizing temperature due to the increase of carbon content and other alloying elements by the dissolution of carbides present in the annealed structure [28].

All of the alloying elements, except cobalt, lower M_s. Carbon has the most powerful effect on M_s temperature. The higher the alloy content of austenite, the lower the M_s temperature and the greater the amount of RA at room temperature [8].

For a given tool steel alloy and austenitizing conditions, the content of RA varies with cooling rate and is maximum around the critical cooling rate for martensite.

11.6.6.4 Tempering

Tempering, which is the final step of the heat treatment of tool steels, consists of heating the as-quenched microstructure to temperatures below the transformation temperature Ac_1. It is a very complex phenomenon originating from the as-quenched microstructure of tool steels, which consists primarily of martensite with RA and carbides. The microstructure and tempering reactions are reviewed in more detail in Refs. [8,29,34]. During tempering there are three or five transformation steps that occur depending, on the alloying of tool steels:

1. In the first step between 50 and 200°C, there is precipitation of epsilon carbides, which delays softening of the as-quenched structure. During this step a volumetric contraction occurs.
2. The second step is between 200 and 350°C, during which dissolution of epsilon carbide and precipitation of cementite are occurring along with a reduction in hardness.
3. The temperature range of the third step depends on the chemical composition of the steel and corresponds to a reduction in the stability of RA. This instability is produced by carbide precipitation, which reduces the alloy content in solution in the austenite, the and hence increases M_s. This instability starts at 150 and 450°C, for carbon steels and high-alloy tool steels, respectively. The transformation of RA to martensite or bainite during cooling results in a volume increase. This expansion increases with increasing volume fraction of RA.
4. The fourth stage corresponds to highly alloyed tool steels containing carbide-forming elements. There is an exchange of carbon between cementite and other carbides; this phenomenon is associated a large volumetric expansion.
5. The fifth stage, which is also associated with highly alloyed tool steels, starts at 600°C and continues until Ac_1. It corresponds to the coalescence of carbides and results in an annealed microstructure. This phenomenon is associated with a volumetric contraction.

It is necessary that the person designing the heat treatment be familiar with the nature of the dilatations that occur during the tempering operations in order to arrive at the proper final dimensions prior to heat treatment.

The variation of the hardness of tool and die steels with respect to the tempering temperature could have one of the four principal behaviors given in Figure 11.18. Class 1 is typical of carbon and low-alloy tool steels in which the hardness is decreasing progressively

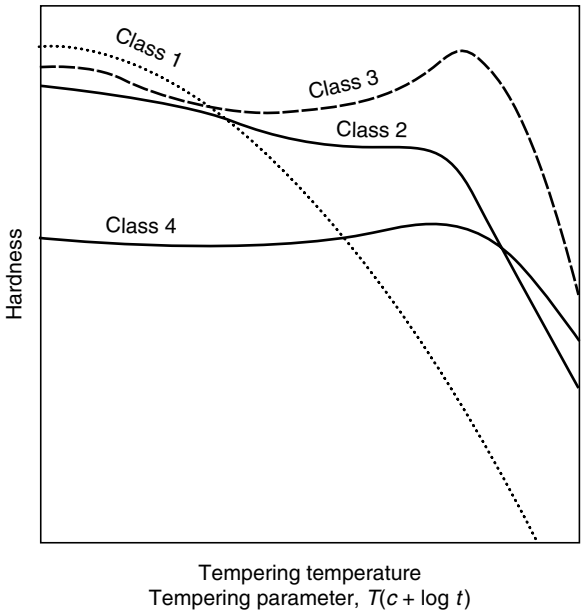

FIGURE 11.18 Four major types of hardness versus tempering temperature in tool steels. (From G. Roberts, G. Krauss, and R. Kennedy, *Tool Steels*, 5th ed., ASM International, Materials Park, OH, 1998, p. 100.)

with increasing temperature due to the precipitation and coarsening of cementite, or of other low-alloy carbides. Class 2 is characteristic of medium- to high-alloy cold-working die steels in which the alloying addition retards carbide precipitation and related softening. Curves between Class 1 and Class 2 could be obtained for low- to medium-alloy steels. Class 3 is representative of highly alloyed high-speed steels in which secondary hardening occurs at high-tempering temperatures. The final hardness of these steels could exceed that in the untempered condition. Class 4 is representative of the medium- to high-alloy hot-working tool steels that exhibit a secondary hardening, as is the case with Class 3. In Class 4, the as-quenched hardness is lower than that of class 3 due to its lower carbon content.

Secondary hardening is a result of the transformation of RA to martensite on cooling from the tempering temperature, and of precipitation of an ultrafine dispersion of alloy carbides [30].

Tungsten, vanadium, chromium, and molybdenum that are the strong carbide-forming elements are most commonly used to achieve secondary hardening. To take advantage of their precipitation characteristics, they must be dissolved in austenite during the austenitizing treatment in order to be incorporated into the martensite formed during quenching with sufficient supersaturation for secondary hardening during tempering. Figure 11.19 through Figure 11.22 show the effect of strong carbide-forming elements on the secondary hardening of 0.5% C tool steel [8].

The recommended tempering conditions for optimum performance with recommended austenitizing temperatures of each of the tool steels are given in Table 11.9. The tempering treatment should be performed as soon as possible after quenching, and heating to tempering temperatures should be slow to ensure temperature homogenization within the tool steel and the prevention of cracking. Slow cooling in still air is also recommended to minimize the development of residual stresses [8].

In carbon and low-alloy steels, tempering increases the toughness of hardened steels from the low value characteristic of as-quenched martensite. In high-alloy tool steels, tempering

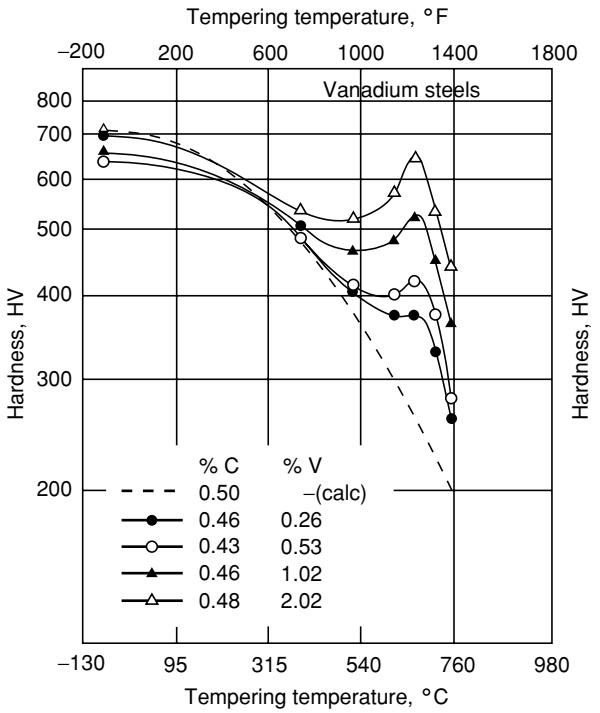

FIGURE 11.19 Secondary hardening caused by alloy carbide precipitation produced by V additions. (From G. Roberts, G. Krauss, and R. Kennedy, *Tool Steels*, 5th ed., ASM International, Materials Park, OH, 1998, p. 104.)

increases the hardness in addition to producing a dispersion of stable alloy carbides resistant to coarsening during exposure to heating. Such coarsening would lower hardness and limit tool life during high-speed machining or high-temperature forging.

11.7 CHARACTERISTIC STEEL GRADES FOR THE DIFFERENT FIELD OF TOOL APPLICATION

For more information on the selection of tool steels the reader could consult Refs. [1,6,8,13]. The selection of tool steels for some applications is presented below.

1. *Steels for plastic molds*
   During the formation of plastics, dies are subjected to heat and pressure. The temperature of the dies is as high as 250°C and the strength of about 100 MPa. In this case, hardness retention and strength requirements are of minor importance. However, good machining properties and a low degree of distortion in hardening of plastic molds are very important. P20 steel is a good choice for molds due to its low degree of distortion and good machinability. In the case of abrasive plastics, the molds are made of steels O2 and D2. During processing of aggressive plastics, which decompose into a chemically reactive products, molds are made of corrosion-resistant steel containing 0.38% C, 16% Cr, 1.2% Mo. For operating temperatures higher than 300°C, the use of H11 steels is an excellent material choice.

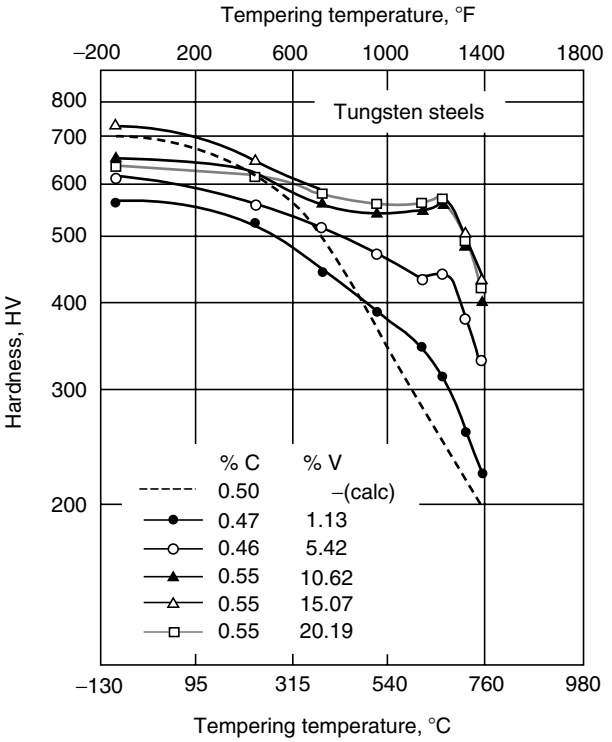

FIGURE 11.20 Secondary hardening caused by alloy carbide precipitation produced by tungsten additions. (From G. Roberts, G. Krauss, and R. Kennedy, *Tool Steels*, 5th ed., ASM International, Materials Park, OH, 1998, p. 104.)

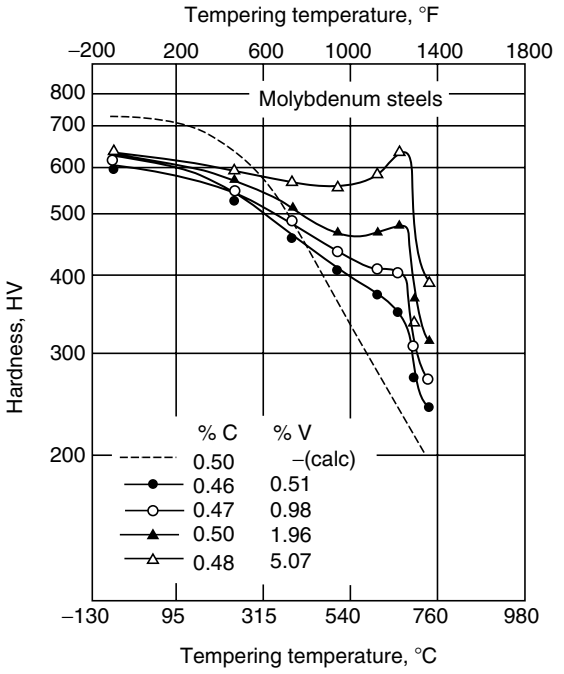

FIGURE 11.21 Secondary hardening caused by alloy carbide precipitation produced by Mo additions. (From G. Roberts, G. Krauss, and R. Kennedy, *Tool Steels*, 5th ed., ASM International, Materials Park, OH, 1998, p. 104.)

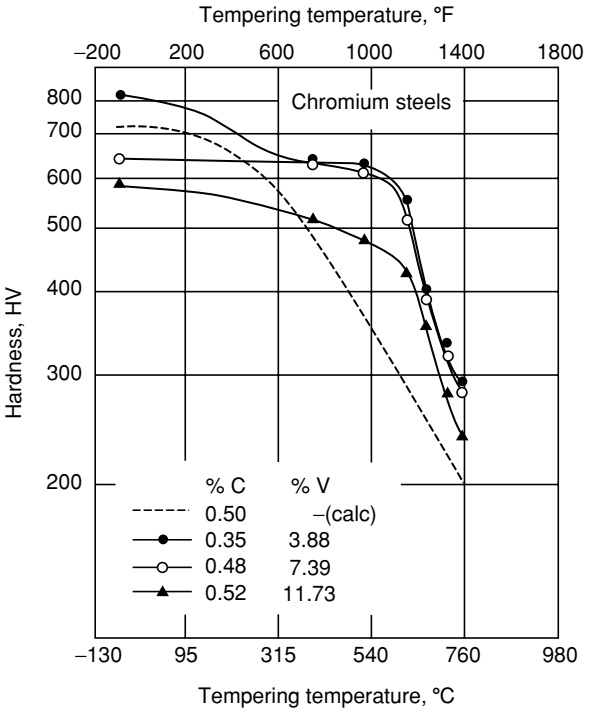

FIGURE 11.22 Secondary hardening caused by alloy carbide precipitation produced by chromium additions. (From G. Roberts, G. Krauss, and R. Kennedy, *Tool Steels*, 5th ed., ASM International, Materials Park, OH, 1998, p. 104.)

2. *Steels for high-pressure die casting molds*
   In die casting, tools are heated to about 500°C and are subjected to high mechanical forces and erosion. Molds in this process are subjected to temperature changes that may lead to a heat checking defect. The occurrence of this defect could be delayed by increasing the steel hardness of the molds that should be adapted to thermal stresses of the tool surface, which in turn depends on the wall thickness of the cast. The relationship between hardness and wall thickness of the cast is given by the following formula [13]:

$$\mathrm{HRC} = 56 \cdot \mathrm{S}^{-(0.14)}$$

   HRC is in the Rockwell C hardening and S is the wall thickness of the cast in mm.

Dies used for light metal casting are commonly made of H11 and H13 steels. The steel H10, due to its hardness retention and its higher hardness at high temperature, is used for copper casting. Die parts that are subjected to high thermal stresses are made of tool steels with high retention of hardness such as H19 and H21.

3. *Steels for cold-forming tools*
   Cold-forming processes such as cold rolling, stamping, deep drawing, extrusion, and bending have the advantage of making parts with high-dimension accuracy and good surface quality that does not need machining. In these processes, tools are subjected to high stresses from pressure and friction. Tool steels with a high hardness are used in these applications. Dies for extrusion are made of tool steels such as M2, M48, and H11 that are good for compressive stresses higher than 300 MPa. Other steels are suitable

TABLE 11.9
Hardening and Tempering of Tool Steels

Type	Rate of Heating	Hardening				
		Preheat Temperature, °C	Hardening Temperature, °C	Holding Time, min	Quenching Medium (a)	Tempering Temperature, °C
Molybdenum high-speed steels						
M1, M7, M10	Rapidly from preheat	730–845	1175–1220	2–5	O, A, or S	540–595 (c)
M2	Rapidly from preheat	730–845	1190–1230	2–5	O, A, or S	540–595 (c)
M3, M4, M30, M33, M34	Rapidly from preheat	730–845	1205–1230 (b)	2–5	O, A, or S	540–595 (c)
M6	Rapidly from preheat	790	1175–1205 (b)	2–5	O, A, or S	540–595 (c)
M36	Rapidly from preheat	730–845	1220–1245 (b)	2–5	O, A, or S	540–595 (c)
M41	Rapidly from preheat	730–845	1190–1215 (b)	2–5	O, A, or S	540–595 (d)
M42	Rapidly from preheat	730–845	1190–1210 (b)	2–5	O, A, or S	510–595 (d)
M43	Rapidly from preheat	730–845	1190–1215 (b)	2–5	O, A, or S	510–595 (d)
M44	Rapidly from preheat	730–845	1200–1225 (b)	2–5	O, A, or S	540–625 (d)
M46	Rapidly from preheat	730–845	1190–1220 (b)	2–5	O, A, or S	525–565 (d)
M47	Rapidly from preheat	730 845	1180–1205 (b)	2–5	O, A, or S	525–595 (d)
Tungsten high-speed steels						
T1, T2, T4, T8	Rapidly from preheat	815–870	1260–1300 (b)	2–5	O, A, or S	540–595 (c)
T5, T6	Rapidly from preheat	815–870	1275–1300 (b)	2–5	O, A, or S	540–595 (c)
T15	Rapidly from preheat	815–870	1205–1260 (b)	2–5	O, A, or S	540–650 (d)
Chromium hot-work steels						
H10	Moderately from preheat	815	1010–1040	15–40 (e)	A	540–650
H11, H12	Moderately from preheat	815	995–1025	15–40 (e)	A	540–650
H13	Moderately from preheat	815	995–1040	15–40 (e)	A	540–650
H14	Moderately from preheat	815	1010–1065	15–40 (e)	A	540–650
H19	Moderately from preheat	815	1095–1205	2–5	A or O	540–705
Molybdenum hot-work steels						
H41, H43	Rapidly from preheat	730–845	1095–1190	2–5	O, A, or S	565–650
H42	Rapidly from preheat	730–845	1120–1220	2–5	O, A, or S	565–650
Tungsten hot-work steels						
H21, H22	Rapidly from preheat	815	1095–1205	2–5	A or O	595–675
H23	Rapidly from preheat	845	1205–1260	2–5	O	650–815

H24	Rapidly from preheat	815	1095–1230	2–5	O	565–650
H25	Rapidly from preheat	815	1150–1260	2–5	A or O	565–675
H26	Rapidly from preheat	870	1175–1260	2–5	O, A, or S	565–675
High-carbon, high-chromium, cold-work steels						
D1, D5	Very slowly	815	980–1025	15–45	A	205–540
D3	Very slowly	815	925–980	15–45	O	205–540
D4	Very slowly	815	970–1010	15–45	A	205–540
D7	Very slowly	815	1010–1065	30–60	A	150–540
Medium-alloy air-hardening cold-work steels						
A2	Slowly	790	925–980	20–45	A	175–540
A3	Slowly	790	955–980	25–60	A	175–540
A4	Slowly	675	815–870	20–45	A	175–425
A6	Slowly	650	830–870	20–45	A	150–525
A7	Very slowly	815	955–980	30–60	A	150–540
A8	Slowly	790	980–1010	20–45	A	175–595
A9	Slowly	790	980–1025	20–45	A	510–620
A10	Slowly	650	790–815	30–60	A	175–425
Oil-hardening cold-work steels						
O1	Slowly	650	790–815	10–30	O	175–260
O2	Slowly	650	760–800	5–20	O	175–260
O6	Slowly	—	790–815	10–30	O	175–315
O7	Slowly	650	O: 790–830 W: 845–885	10–30	O or W	175–290
Shock-resisting steels						
S1	Slowly	—	900–955	15–45	O	205–650
S2	Slowly	650 (f)	845–900	5–20	B or W	175–425
S5	Slowly	760	870–925	5–20	O	175–425
S7	Slowly	650–705	925–955	15–45	A or O	205–620
Mold steels						
P2	—	900–925 (g)	830–845 (h)	15	O	175–260
P3	—	900–925 (g)	800–830 (h)	15	O	175–260
P4	—	970–995 (g)	970–995 (h)	15	A	175–480
P5	—	900–925 (g)	845–870 (h)	15	O or W	175–260
P6	—	900–925 (g)	790–815 (h)	15	A or W	175–230
P20	—	870–900 (h)	815–870	15	O	480–595 (i)

Continued

TABLE 11.9 (Continued)
Hardening and Tempering of Tool Steels

		Hardening				
Type	Rate of Heating	Preheat Temperature, °C	Hardening Temperature, °C	Holding Time, min	Quenching Medium (a)	Tempering Temperature, °C
P21(j)	Slowly	Do not preheat	705–730	60–180	A or O	510–550
Low-alloy special-purpose steels						
L2	Slowly	—	W: 790–845 O: 845–925	10–30	O or W	175–540
L3	Slowly	—	W: 775–815 O: 815–870	10–30	O or W	175–315
L6	Slowly	—	790–845	10–30	O	175–540
Carbon–tungsten special-purpose steels						
F1, F2	Slowly	650	790–870	15	W or B	175–260
Water-hardening steels						
W1, W2, W3	Slowly	565–650 (k)	760–815	10–30	B or W	175–345

(a) O, oil quench; A, air cool; S, salt bath quench; W, water quench; B, brine quench. (b) When the high temperature heating is carried out in a salt bath, the range of temperatures should be about 14°C lower than given here. (c) Double tempering recommended for not less than 1 h at temperature each time. (d) Triple tempering recommended for not less than 1 h at temperature each time. (e) Times apply to open furnace heat treatment. For pack hardening, a common rule is to heat 1.2 min per mm (30 min per in.) of cross section of the pack. (f) Preferable for large tools to minimize decarburization. (g) Carburizing temperature. (h) After carburizing. (i) carburized per case hardness. (j) P21 is a precipitation-hardening steel having a thermal treatment that involves solution treating and aging rather than hardening and tempering. (k) Recommended for large tools and tools with intricate sections.

Source: From A.M. Bayer, T. Vasco, and L.R. Walton, Wrought tool steels, in *ASM Handbook*, Vol. 1, *Properties and Selection: Iron, Steels, and High-Performance Alloys*, 10th ed., 1990, pp. 770–771.

for lower compressive stresses such as the ledeburitic chromium steel D2. In the case of deep drawing dies subject to friction forces, steel D2 is suitable for drawing punches and drawing rings and steel O2 is used for ejectors and blank holders. Nitriding could be applied to avoid cold welding.

Stamping tools that are subject to pressure and friction stresses lower than those encountered in extrusion can be made from O2 for blank holders and S1 for tools to produce coins. In rolling, suitable tool materials for cold rolls are steels L3, O, A2, D2, and M4 for thread rolls and multiroll stands.

4. *Steels for hot forging*
   In the case of hammer forging that is characterized by impact loading between the tool and the forged part, there is no need for a die material with hardness retention. The L6 family of tool steels is a good material for massive dies. Also, high-carbon (1.45%) steel with 3.3% vanadium due to its wear resistance and its hardness is suitable for dies with flat cutting. Wear resistance on the surface of these steels can be increased by nitriding or chromium plating for flat cuts.

   The hot-working steels H10, H11, and H13 are suitable for press forging dies that are heated during forging process due to the longer time contact between forged parts and die. Martensitic-hardened microstructure is suitable for delaying heat checking in dies for forging copper alloys. For hot-rolling steels H11, H20, and H21 are suitable.
5. *Steel alloys for hot extrusion*
   Hot extrusion is a hot-forming process used to produce long, straight, semifinished metal products such as bar, solid, and hollow sections, tubes, wires, and strips. The forming temperature depends on the alloys to be extruded. Tool steels used in extrusion must have high-temperature strength due to the high pressing forces involved in this process. Hot-working steels are generally adequate except in the isothermal extrusion of titanium, for which superalloys are more appropriate [35]. The tool steels H11 and H13 are suitable for the extrusion of light metals; while in the case of extrusion of heavy metals such as copper and steels Ni-base super alloy tool steels H26 and T15 are more suitable. For tube extrusion the mandrel steels H10 and H19 are more appropriate.
6. *Steels for machining*
   In machining operations, tools for turning are made of high-speed steels. Abrasive wear resistance and hardness at high temperature are the two important properties for machining tool steels. Cobalt addition in the range of 5 to 12% to the base alloy M2 improves the hardness at higher temperatures. Steel M41 which contains 4.8% Co, is used for milling cutters and screw taps. The addition of V in the range of 3 to 5% increases wear resistance. The alloy M3 with 3% V is used for countersinks, broaches, and threading taps. More information on high-speed steels is to be found in Ref. [8]. M40 type steels are used for machining aerospace materials such as Ti and nickel-base alloys. Due to its high wear resistance T15 tool steels are used for lathe tools and machining materials with high-tensile strength.

BIBLIOGRAPHY

1. G. Roberts, G. Krauss, and R. Kennedy, *Tool Steels*, 5th ed., ASM International, Materials Park, OH, 1998, pp. 7–28.
2. Tool steels, *Heat Treater's Guide: Practices and Procedures for Irons and Steels*, H. Chandler, Ed., ASM International, Materials Park, OH, 1995, pp. 517–669.
3. J.G. Gensure and D.L. Potts, *International Metallic Materials Cross-Reference*, 3rd ed., Genium Publishing, New York, 1988.
4. C.W. Wegst, J.C. Hamaker, Jr., and A.R. Johnson, *Tool Steels*, 3rd ed., American Society for Metals, Materials Park, OH, 1962.

5. A.M. Bayer, T. Vasco, and L.R. Walton, Wrought tool steels, in *ASM Handbook*, Vol. 1, *Properties and Selection: Iron, Steels, and High-Performance Alloys*, 10th ed., 1990, pp. 757–779.
6. *Tool Steels, Products Manual*, American Iron and Steel Institute, Washington, D.C., 1978.
7. K.W. Lange, Thermodynamic and kinetic aspect of secondary steelmaking processes, *Int. Mater. Rev.*, 3 (2), 1988, 53–89.
8. G. Roberts, G. Krauss, and R. Kennedy, *Tool Steels*, 5th ed., ASM International, Materials Park, OH, 1998, pp. 30–43.
9. Atlas Specialty Steels Division, Rio Algom Limited, Edmonton.
10. G. Hoyle, *Electroslag Processes, Principles and Practices*, Applied Science, Essex, U.K., 1983.
11. T.V. Philip, ESR: a means of improving transverse mechanical properties in tool and die steels, *Met. Technol.*, 1975, 554–564.
12. G.A. Roberts and R. Cary, *Tool Steels*, 4th ed., ASM International, Materials Park, OH, 1998.
13. S. Wilmes, H-J. Becker, and R. Krumpholz,"Tool steels," *A Handbook for Materials Research and Engineering*, Vol. 2, Applications, ed., Verein Deurscher Eisenhuttenleute, 1993, pp. 302–373.
11. T. Itami and Y. Kawashima, *The Production of Rolling Mill Rolls and High Speed Cutting Tools at Sumitomo Heavy Industries, Spray Forming: Science, Technology and Application*, Metal Powder Industries Federation, Princeton, NJ, 1992, pp. 77–91.
15. G. Roberts, G. Krauss, and R. Kennedy, *Tool Steels*, 5th ed., ASM International, Materials Park, OH, 1998, pp. 67–107.
16. W.C. Leslie and R.J. Sober, The strength of ferrite and of martensite as functions of composition, temperature and strain rate, *Trans. ASM*, 60, 1967, 459–484.
17. G. Krauss, Heat treated martensitic steels: microstructural systems for advanced manufacture, *Iron Steel Inst. Jpn.*, 35 (4), 1995, 349–359.
18. *Steel Heat Treatment Handbook*, G.E. Totten and M.A.H. Howes, Eds., Marcel Dekker, New York, 1997.
19. E.C. Bain and H.W. Paxton, *Alloying Elements in Steel*, 2nd ed., American Society for Metals, Metals Park, OH, 1961.
20. J.C. Hamaker Jr., V.C. Stang, and G.A. Roberts, *Trans. Amer. Soc. Metals*, 49, 1957, S. 550/75.
21. G.A. Roberts, *Trans. Metallurg. Soc. AIME*, 236, 1966, S. 950/63.
22. *Smithells Metals Reference Book*, 8th ed., Elsevier Butterworth, Heinemann, 2004, pp. 21-4 and 21-5.
23. J.R.T. Branco and G. Krauss, Heat treatment and microstructure of tool steels for molds and dies, in *Tool materials for Molds and Dies*, G. Krauss and H. Nordberg, Eds., Colorado School of Mines Press, Golden, CO, 1987, pp. 94–117.
24. G. Krauss, *Steels: Heat Treatment and Processing Principles*, ASM International, Materials Park, OH, 1990.
25. Abrasives for grinding operations, *ASM, Specialty Handbook: Tool Materials*, J.R. Davis, Ed., ASM International, Materials Park, OH, 1995, pp. 101–115.
26. B.A. Becherer and T.J. Witheford, Introduction to heat treating of tool steels, *Heat Treating*, Vol. 4, ASM International, Materials Park, OH, 1991, pp. 711–725.
27. K.E. Thelning, *Steel and its Heat Treatment*, 2nd ed., Butterworths, London, 1984.
28. R. Lévéque, Traitement Thermiques des Aciers À Outils, Technique de l'Ingenieur, Traité Métallurgie, M 1134, 1997.
29. G.R. Speich and W.C. Leslie, Tempering of steel, *Metall. Trans.*, 3, 1972, 1043–1054.
30. Y. Imai, Phases in quenched and tempered steels, *Trans. Jpn. Inst. Met.*, 16, 1975, 721–734.
31. G. Peter, Winchell symposium on the tempering of steel, *Metall. Trans. A*, 14A, 1983, 991–1145.
32. G. Krauss, Tempering and structural change in ferrous martensitic structures, in *Phase Transformation in Ferrous Alloys*, A.R. Marder and J.J. Goldstein, Eds., TMS-AIME, Warrendale, PA, 1984, pp. 101–123.
33. G. Krauss and P.E. Repas, Eds., *Fundamentals of Aging and Tempering in Bainitic and Martensitic Steel Products*, Iron and Steel Society, Warrendale, PA, 1992.
34. G.R. Speich and K.A. Taylor, Tempering of ferrous martensites, in *Martensite*, G.B. Olson and W.S. Owen, Eds., ASM International, Materials Park, OH, 1992, pp. 243–275.
35. *Handbook of Workability and Process Design*, G. Dieter, H.A. Kuhn, and S.L. Semiatin, Eds., ASM International, Materials Park, OH, 2003, pp. 291–315.

12 Stainless Steel Heat Treatment

Angelo Fernando Padilha, Ronald Lesley Plaut, and Paulo Rangel Rios

CONTENTS

12.1 Historical Background 695
12.2 Phase Diagrams and Stainless Steel Typical Phases 698
12.2.1 Equilibrium Diagrams 698
12.2.2 Schaeffler, Delong, and Other Nonequilibrium Diagrams 700
12.3 Austenitic Stainless Steels 703
12.3.1 Solution Annealing 706
12.3.2 Stabilize Annealing 707
12.3.3 Stress-Relief Annealing 708
12.3.4 Bright Annealing 708
12.3.5 Martensite Formation 708
12.3.5.1 Transformation during Cooling 709
12.3.5.2 Strain-Induced Transformation 709
12.4 Ferritic Stainless Steels 709
12.4.1 The 475°C (885°F) Embrittlement 710
12.4.2 Sigma (σ)-Phase Embrittlement 713
12.4.3 The Chi (χ) Phase 714
12.4.4 Other Phases 714
12.4.5 Processing and Heat Treatment 716
12.5 Duplex Stainless Steels 716
12.5.1 Three Types of Embrittlement in Duplex Stainless Steels 718
12.5.2 Processing and Heat Treatment 722
12.6 Martensitic Stainless Steels 723
12.6.1 Processing and Heat Treatment 728
12.7 Precipitation-Hardenable Stainless Steels 728
12.7.1 Processing and Heat Treatment of Martensitic PH Stainless Steels 733
12.8 Final Remarks 734
References 735

12.1 HISTORICAL BACKGROUND

Stainless steels are frequently classified according to their microstructure into five types: austenitic, ferritic, martensitic, duplex (ferritic–austenitic), and precipitation-hardenable (PH). More common types, such as the austenitic, ferritic, and martensitic stainless steels, have been discovered in the first decade of the 20th century. This brief historical introduction [1–4] initially deals with the century before the actual discovery of stainless steel and the following section will describe the discovery of each of the five types of stainless steels.

Chromium, which is the main alloying element in stainless steels, has been isolated chemically some 200 years ago initially from crocoite ($PbCrO_4$), known as the red lead ore of Siberia. In 1797, L.N. Vauquelin, a Frenchman, demonstrated that this material contained a new element, unknown until then. He produced chromic acid by reacting potassium carbonate with the crocoite, removing the lead. This chromic acid was further heated in graphite crucibles, which resulted in some colored chromium compounds. Following the suggestion given by R.J. Hardy, Vauquelin named the new metal chromium, derived from the Greek word meaning color. Later, in 1798, T. Lowitz, a German chemist, isolated chromium from an iron ore of the Urals, the chromite ($FeCr_2O_4$), which is nowadays the main source of chromium.

In 1821, P. Berthier, a Frenchman, observed that when chromium (1 to 1.5 wt%) was added to iron, it would give an improved resistance against acid attack and increase with chromium content. He was also the first to produce ferrochromium and use it in steel production. His ferrochromium contained high carbon and 17 to 60 wt% chromium. In 1891, H. Goldschmidt patented in Germany an aluminothermic production process to obtain low-carbon metallic chromium. In 1906, L.B. Guillet published in France a study on the constitution and properties of ternary steels, containing chromium and nickel. A.M. Portevin, a Frenchman, published in 1909 in England, a study on martensitic and ferritic steels, containing 17.4 wt% chromium and 0.12 wt% carbon, which is in other terms AISI 430. In 1909, the German W. Giesen published, in England, a long and interesting work on austenitic chromium–nickel steels. In 1911, P. Monnartz published his classical work "A study on iron–chromium alloys with emphasis on its chemical resistance to acids" [5]. This work clearly showed that starting from about 12 wt% chromium, the steels became resistant to the chemical attack of nitric acid and a series of other corrosive media. He explained his results based on the passivation theory, recognized the deleterious effect of carbon, studied the stabilization through the addition of carbide-forming elements that were more stable than chromium carbide, and recognized the positive effect of molybdenum. Monnartz, Guillet, Portevin, and Giesen established the scientific foundations that lead to the discovery and utilization of stainless steels.

Despite the effort of metallurgists, a problem remained unsolved until early 20th century: steel products were not sufficiently resistant to corrosive attack. At the beginning of this century, the problem began to be solved in different countries simultaneously.

In England, Harry Brearley, in two articles, described his experiences with corrosion-resistant alloys containing 12.8 wt% chromium and 0.24 wt% carbon. "When microscopic observation of these steels were being made, one of the first things noticeable was that reagents would not etch, or etched very slowly, those steels containing low carbon and high chromium." (H. Brearley, *Daily Independent* of Sheffield, 2.2.1924.) The martensitic stainless steels have been discovered. (Brearley's patent covered the 9 to 16 wt% chromium and less than 0.7 wt% carbon alloys.) Inventiveness frequently comes with modesty, as shown by Brearley's declaration to the *Daily Independent* in 2.2.1924: "The reader will observe that my early work on high-chromium steels was not inspired by any intention or hope on my part of discovering a stainless steel." Brearley's feat was not fully understood immediately to its full extent: "Nobody was impressed with my suggestion, perhaps the idea of producing on a commercial scale a steel which should not corrode sounded ridiculous, at least my directors failed to grasp the significance of it."

In the United Steels, in 1911, Christian Dantsizen and Frederick Becket started their experiences with alloys containing 14 to 16 wt% chromium and low-carbon contents (from 0.007 to 0.015 wt%), using ferrochromium obtained via the aluminothermical method. Ferritic stainless steels were discovered. Early as 1915 they suggested using these alloys in turbines, a procedure which is still used by project engineers.

In 1896, the Physical Chemistry Laboratory of Krupp (Chemisch-Physikalischen Versuchsanstalt der Firma Friedrich Krupp AG), in Essen, Germany, had a new head, namely

Dr. Brenno Strauss. In 1909, Dr. Eduard Maurer, the first metallurgist, started to work in this sector, following the experimental work he started in Paris under the supervision of Osmond, in the area of steel heat treatment, obtaining his doctorate in 1908 in Aachen. Between 1908 and 1910 both Strauss and Maurer worked with chromium and nickel–chromium-containing steels and by 1910 they introduced the 35 wt% nickel and 13 to 14 wt% chromium (Nichrotherm 4) steels.

In October 1912, F. Krupp (a German company) entered the German Patent Office (Reichspatentamt), in Berlin, with the patent requests DRP 304126 and 304159: "Herstellung von Gegenstanden, die hohe Widerstandskraft gegen Korrosion erfordern . . . " ("Fabrication of objects that require high corrosion resistance . . ."). Both patent requests did not mention the true inventors and they were registered in the name of the company's patent bureaucrat called Pasel. From the initial work of Strauss and Maurer, two classes of stainless steels have been developed: the martensitic VM steels (containing 0.15 wt% carbon, 14 wt% chromium, and 1.8 wt% nickel) and the austenitic VA steels (containing 0.25 wt% carbon, 20 wt% chromium, and 7 wt% nickel). V stands for Versuch that in German means trial. The products manufactured from these steels have been exhibited in 1914 Fair of Malmoe in Sweden.

F. Krupp was the first firm to commercialize these stainless steels. By the end of the first semester of 1914, some 18 tons of the V2A (austenitic) steel have been supplied to Badisch Anilin-und Sodafabrik (BASF) in Ludwigshafen. Thomas Firth & Sons Ltd. of Sheffield produced about 50 tons of the martensitic type in 1914. In 1915, in the United States, Firth-Sterling near Pittsburgh started its production. Ferritic stainless steels usage and commercialization started later on, probably around 1920, when Brown Bayley's Steel Works Ltd. of Sheffield made its first 5 to 6 tons of a 11.7 wt% chromium and 0.07 wt% carbon steel.

Duplex ferritic–austenitic stainless steels have been developed later and presented an interesting combination of properties: a yield strength (YS) twice higher than the one for the austenitic and ferritic common types, greater plasticity and toughness than the martensitic and precipitation-hardening ones, excellent intergranular, pitting and stress corrosion resistance.

In 1927, Bain and Griffiths [6] reported their results on the Fe–Cr–Ni-system and mentioned the existence of a two-phase field comprising austenite and ferrite. This was probably the first mention of the duplex-type stainless steels. Few years later the first tons have been produced and studied [7,8]. By 1930, AVESTA of Sweden started the development of two duplex alloys, namely the 453 E (25 wt% Cr–wt% Ni) and the 453 S (27 wt% Cr–5 wt% Ni–1.5 wt% Mo). The values with seawater corrosion tests, reported in 1930, showed excellent results in terms of intergranular corrosion resistance. From thereon these two compositions have been included in AVESTA's product list. The first forged axel in the 453S duplex alloy was supplied in 1932 for a Brobeck heat exchanger, i.e., only some 70 years ago.

In 1947, a new duplex alloy, the UR50 containing 21 wt% Cr–7 wt% Ni–2.5 wt% Mo–1.5 wt% Cu–0.07 wt% N, became a standard in the French Navy [7,8]. YS was higher than 400 MPa and cast or mechanically worked components were produced. At that time, control of oxygen, sulfur, and carbon was not satisfactory and products made out of UR50 frequently presented cracks and were fragile. Nevertheless, some producers fabricated small quantities of the duplex steel for the chemical, salt extraction, petroleum refining, food, paper, pharmacy, and diving instrument industries.

An interesting application of duplex steels back in the 1960s was the first submarine employing UR50, by the French company Comex. In 1970, some tons of UR50 plate have been used in three oil tankers (Zambese, Zelande e Zeebrugge) in the Dunkerque Shipyards [7,8].

Until 1940, the available stainless steels presented an excellent corrosion resistance, yet had poor mechanical properties. PH steels have been developed in the 1940s, initially by the United States Steel (USS) Corporation (Stainless W), to overcome this deficiency. Three classes have been developed: austenitic (with YS in the range of 600 to 700 MPa. Ex: A286,

17-10P), martensitic (with YS in the range of 1100 to 1600 MPa. Ex: 17-4 PH, 15-5 PH, Custom 450, Stainless W, PH 13-8 Mo, Custom 455), and semiaustenitic (with YS between 1200 and 1800 MPa. Ex: 17-7 PH, PH 15-7 Mo, AM-350, and AM-355).

With the discovery of the stainless steels the chemical industry and the high-temperature applications had a new class of materials available, more adequate to their aggressive media in their installations. The production numbers clearly show the impact these materials caused. In 1934, some 56,000 tons were produced whereas in 1953 world production was over 1 million tons.

The development of the AOD process (argon–oxygen decarburization) made possible the large-scale production of stainless steels that we know today. The first AOD plant started operation in Fort Wayne in 1968, resulting from the joint development of Linde Division of Union Carbide Corporation and the Stainless Steel Division of Joslyn Manufacturing and Supply Company. In 1985, the world stainless steel consumption was over 5 metric tons. In 1991, stainless steel production was about 10 metric tons and in 2004 it was about 22 metric tons. Stainless steel plays an important role in the modern world, even if its tonnage represents only 2.2% of the total steel production. Austenitic stainless steels represent about 60% whereas ferritic stainless steels represent about 30% of the world's total stainless steel production.

12.2 PHASE DIAGRAMS AND STAINLESS STEEL TYPICAL PHASES

Phase diagrams are important to predict the phases that are present in the stainless steels; therefore, they are also very important as a guide to their heat treatments. However, they do have limitations due to the complexity of the multicomponent thermodynamic calculations and also due to the transformation kinetics that may prevent the attainment of the equilibrium phases. Regarding the first limitation, the number of relevant components is often more than five and published diagrams are rarely found to contain more than four components. As to the second limitation, the diffusion of alloying elements in the solid state can be very slow, especially in the case of austenitic stainless steels, where the precipitation of certain intermetallic compounds can take thousands of hours.

12.2.1 Equilibrium Diagrams

In this section the most relevant features of the binary diagrams [9–13] Fe–Cr, Fe–Ni, Cr–Ni, Fe–Mo, Fe–Ti, Ni–Ti, Fe–Nb, Fe–Mn, and Fe–Si are considered. Next the Fe–Cr–Ni and Fe–Cr–Mo ternary diagrams and the quaternary Fe–Cr–Ni–Mo diagram will be discussed briefly.

The three main features of the Fe–Cr diagram [9–13], shown in Figure 12.1, which are relevant to stainless steels, are the ferrite-stabilizing character of Cr and the presence of sigma (σ) and alpha prime (α') phases. The reader should be cautioned that in the stainless steel technical literature the alpha prime (α') designation is unfortunately used for both deformation-induced martensite in austenitic stainless and for the phase formed in ferrite of stainless steels (mainly in ferritic and duplex types) around 475°C (885°F).

The Fe–Ni diagram [9–13] clearly shows the strong austenite-stabilizing effect of Ni. The intermetallic compound Ni_3Fe is not normally observed in stainless steels. Also the $CrNi_2$ compound present in the Cr–Ni diagram does not form in stainless steels. The Fe–Mo diagram [9–13] shows that Mo is a strong ferrite stabilizer and also that it forms four intermetallic compounds with iron. Of these, the sigma (σ) phase and the Laves phase, Fe_2Mo, often occur in stainless steels. The mu (μ) phase, Fe_7Mo_6, occurs less frequently in stainless steels. In the Fe–Ti diagram [9–13] one can also see the very strong ferrite-stabilizing character of the Ti and also the presence of a Laves phase, Fe_2Ti, that can occur in stainless steels, particularly in those in which the relationship Ti:C is high, the so-called over-stabilized

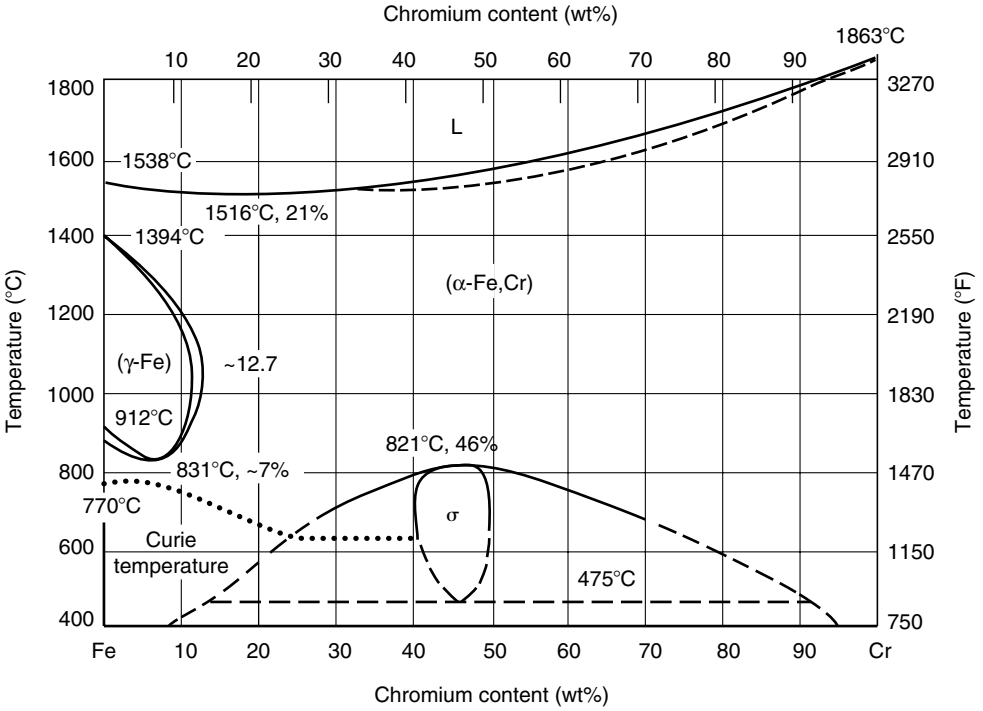

FIGURE 12.1 Binary iron–chromium equilibrium diagram. (From J.R. Davis (Ed.): *ASM Speciality Handbook: Stainless Steels*, ASM International, Materials Park, OH, 1994. Reprinted with permission of ASM International®. All rights reserved www.asminternational.org.)

steels. The Ni–Ti diagram [9–13] shows the presence of the Ni_3Ti that can be used to produce precipitation strengthening in Ni-containing stainless steels.

The Fe–Nb diagram [9–13] shows the ferrite-stabilizing character of the Nb and also the presence of a Laves phase, Fe_2Nb. Fe_2Nb, similar to Fe_2Ti, can occur in stainless steels in which the relationship Nb:C is high, which are also called over-stabilized steels.

As to the Fe–Mn diagram [9–13] the most relevant characteristic is the austenite-stabilizing character of Mn. Finally, the Fe–Si diagram [9–13] shows a strong ferrite-stabilizing effect of Si but none of the five intermetallic compounds is found in commercial stainless steels.

The ternary Fe–Cr–Ni diagram is the basic diagram for stainless steels (see Figure 12.2). It shows the presence of only three solid phases: austenite, ferrite, and sigma phase. For a high Cr/Ni ratio delta ferrite may occur during solidification and sigma phase may occur during aging at temperatures between 550°C (1020°F) and 900°C (1650°F). The compositional range of the sigma-phase field increases as the temperature is below 900°C as shown in Figure 12.2.

The Fe–Cr–Mo diagram (see Figure 12.3) shows the presence of six phases: (Fe,Cr) = solid solution; (Cr,Mo) = solid solution; Fe_7Mo_6 = mu (μ) phase; σ = sigma phase; χ = chi phase; the Laves phase η-Fe_2Mo.

The three intermetallic phases most frequently found in stainless steels are the sigma (σ), chi (χ), and Laves (η) phases. Other intermetallic phases can also be occasionally found such as the G, R, mu (μ), gamma prime (γ′), gamma double prime (γ″), η-Ni_3Ti, and δ-Ni_3Nb. The precipitation of intermetallic phases is normally associated with undesirable consequences like matrix depleting of alloying elements such as chromium, molybdenum, and niobium as well as loss of ductility, toughness, and corrosion resistance. Exceptions to this pattern are the phases causing PH such as γ′-Ni_3(Al,Ti) and β-NiAl.

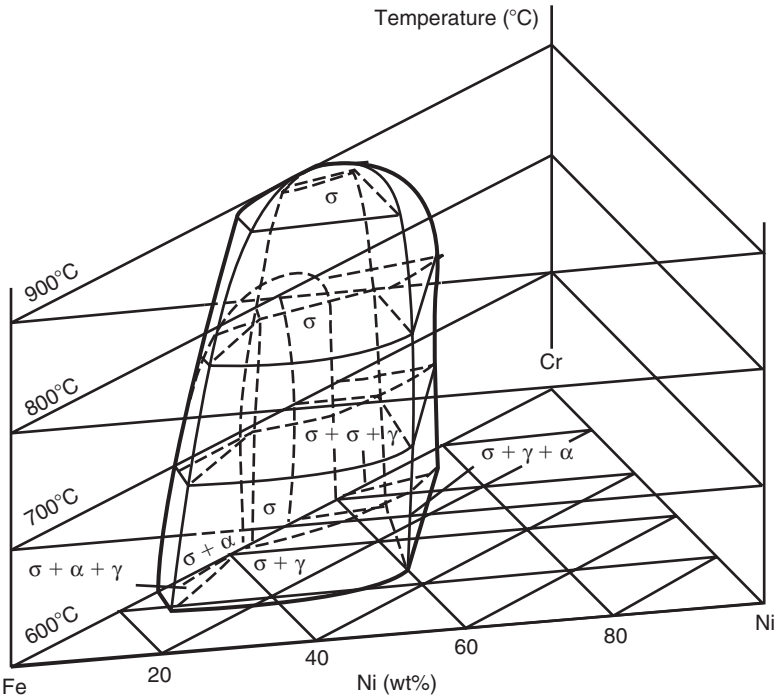

FIGURE 12.2 Three-dimensional view of the Fe–Cr–Ni equilibrium diagram. (From H.-J. Eckstein: *Korrosionsbeständige Stähle*, Deutscher Verlag für Grundstoffindustrie GmbH, Leipzig, 1990. With permission.)

Intermetallic phases that occur in stainless steels (see Table 12.1) can be classified into two groups: (i) topologically close-packed (TCP) phases, like σ, χ, Laves (η), G, R, and Mu (μ) and (ii) geometrically close-packed phases, like γ′, γ″, η-Ni_3Ti, and δ-Ni_3Nb. TCP phases are characterized by close-packed layers of atoms separated from each other by relatively large interatomic distances. The layers of close-packed atoms are displaced from one to the other by sandwiched large atoms, developing a characteristic topology. In contrast, the GCP phases are close packed in all directions. GCP phases have been observed to form mainly in nickel-base alloys whereas the TCP phases have been observed mainly in the iron-base alloys. The precipitation of these phases in the stainless steels will be discussed in more detail.

The nonmetallic elements carbon, nitrogen, boron, and sulfur are usually present in relatively small quantities but their effect can be extremely important. Table 12.1 presents information on the main carbides, nitrides, borides, and sulfides that may occur in stainless steels.

12.2.2 Schaeffler, Delong, and Other Nonequilibrium Diagrams

However useful equilibrium-phase diagrams might be, they are rarely sufficient to predict the resulting microstructure after solidification. As a result practical methods were developed. Of these, the best-known is the Schaeffler diagram. Schaeffler [15–17] divided the alloying elements into two groups: ferrite and austenite stabilizers. He also developed a formula by means of which the elements of each group could be expressed as a chromium equivalent and as a nickel equivalent. An example of such a diagram is presented in Figure 12.4. The regions of the diagram represent the microstructures that can be observed for each class of stainless steels. Schaeffler's method therefore allows a rough evaluation of the microstructure as a function of the steel composition, however it does not take into consideration the influence of

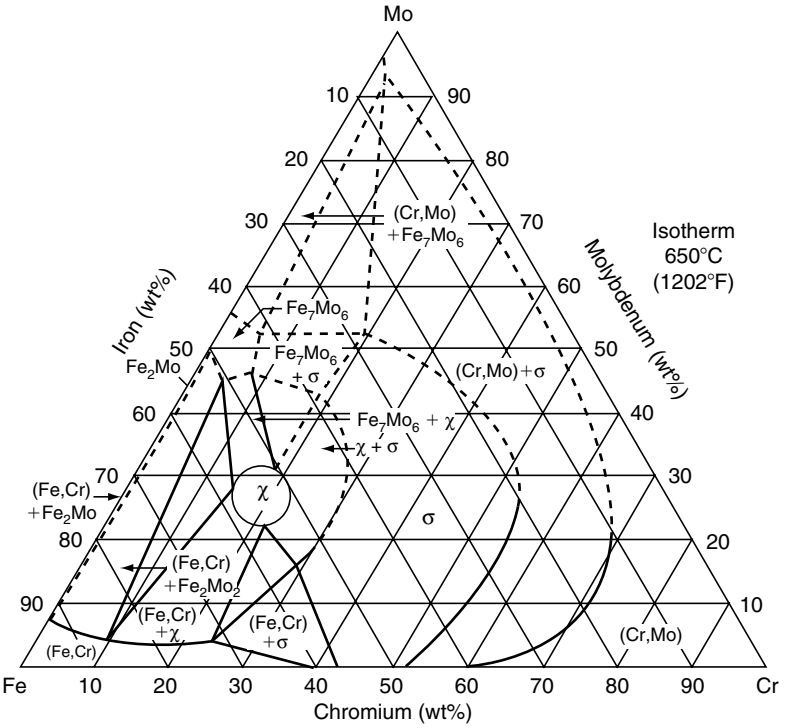

FIGURE 12.3 650°C isotherm of Fe–Cr–Mo equilibrium diagram.) (Fe,Cr) = solid solution, (Cr,Mo) = solid solution, Fe_7Mo_6 = mu (μ) phase, σ = sigma phase, χ = chi phase, Fe_2Mo = Laves phase. (From *Metals Handbook*, 8th ed.: *Metallography, Structures and Phase Diagrams*, Vol. 8, ASM International, Materials Park, OH, 1973; W. Reick, M. Pohl, and A.F. Padilha: *Metalurgia International*, 3, 46–50, 1990; M. Pohl, A.F. Padilha, and O. Fossmark: Bruchvorgänge in ferritisch-austenitischen Duplexstählen mit 475°-Versprödund. *Materialkundlieh-Technische Reihe*, Vol. 9 (Gefüge und Bruch), K.L. Maurer and M. Pohl (Eds.), Gebrüder Borntraeger. Berlin, pp. 305–314, 1990. With permission.)

the cooling rate and aging heat treatments. These diagrams have also been used to estimate the microstructure of the weld metal. The empirical formulas and the experiments present a considerable scatter with regard to the determination of the amount of delta ferrite in austenitic weld metal. DeLong [18] suggested a comparative method for delta-ferrite determination that has been adopted as a standard procedure by the International Welding Institute.

Other researchers adopted a similar methodology, such as Hull [19], who analyzed as much as 1400 specimens in order to determine the effect of 14 alloying elements (Al, C, Cu, Co, Cu, Mn, Mo, N, Nb, Si, Ti, Ta, V, and W) in addition to chromium and nickel in order to predict the occurrence of delta ferrite and intermetallic phases. Espy [20] proposed an extended Schaeffler diagram based on his study of the effects of Cu, N, V, and Al. An interesting historical discussion, especially about the diagrams that preceded Schaeffler work, can be found in Ref. [21].

These diagrams although lacking the sound thermodynamical basis of the equilibrium diagrams are nevertheless technological charts of practical importance.

Stainless steels can solidify by several mechanisms or modes: ferritic or mode A ($L \rightarrow L + \delta \rightarrow \delta$); ferritic–austenitic or mode B ($L \rightarrow L + \delta \rightarrow L + \delta + \gamma \rightarrow \gamma + \delta$); austenitic–ferritic or mode C ($L \rightarrow L + \gamma \rightarrow L + \gamma + \delta \rightarrow \gamma + \delta$); and austenitic or mode D ($L \rightarrow L + \gamma \rightarrow \gamma$). The prediction of their solidification mode and sequence can also be successfully evaluated beforehand using chromium and nickel equivalent ratios [22].

TABLE 12.1
Crystal Structures and Compositions of Phases That May Occur in Stainless Steels

Phase	Unit Cell	Atoms per Cell	Space Group	Lattice Parameters (nm)	Composition
Intermetallic phases					
Sigma (σ)	bct	30	$P4_2/mnm$	$a = 0.87–0.92$; $c = 0.4554–0.48$	$(Fe,Ni)_x(Cr,Mo)_y$
Chi (χ)	bcc	58	I43m	$a = 0.881–0.895$	$Fe_{36}Cr_{12}Mo_{10}$; $(Fe,Ni)_{36}Cr_{18}Mo_4$
Laves (η)	hex.	12	$P6_3/mmc$	$a = 0.473–0.483$; $c = 0.772–0.786$	Fe_2Mo; Fe_2Nb; Fe_2Ta; Fe_2Ti; Fe_2W
G	fcc	116	Fd3m	$a = 1.115–1.120$	$Ni_{16}Nb_6Si_7$; $Ni_{16}Ti_6Si_7$; $(Ni,Fe,Cr)_{16}(Nb,Ti)_6Si_7$
R	hex.	53 (159)	R3	$a = 1.090$; $c = 1.934$	$Fe_{22}Mo_{18}Cr_{13}$; $(Fe,Ni)_{10}Cr_5Mo_3Si_2$
Mu (μ)	rhombohedral	13	R3m	$a = 0.4762$; $c = 2.5015$	$(Fe,Co)_7(Mo,W)_6$; $(Cr,Fe)_7(Mo)_2$ $(Cr, Fe,Mo)_4$
γ′	fcc	4	Pm3m	$a = 0.3565–0.3601$;	$(Ni,Co,Fe,Cr)_3(Al,Ti)$
γ″mnm	$a = 0.3624$	Ni_3Nb		$c = 0.7406$	
			I4/mmm		
η	hex.	8	$P6_3/mmc$	$a = 0.5109$; $c = 0.8299$	Ni_3Ti
δ	orthorhombic	8	Pmmn	$a = 0.5116$; $b = 0.4259$; $c = 0.4565$	Ni_3Nb
β	ord bcc	2	Pm3m	$a = 0.2865–0.2887$	NiAl
Carbides					
$M_{23}C_6$	fcc	116	Fm3m	$a = 1.057–1.068$	$(Cr,Fe,Mo)_{23}C_6$; $(Cr_{16}Fe_5\ Mo_2)C_6$
MC	ord fcc	8	Fm3m	$a = 0.4131–0.4698$	(Ti,Nb,V)C
M_6C	fcc	112	Fd3*m*	$a = 1.085–1.128$	$(Fe,Mo,Nb,Cr)_6C$
M_7C_3	pseudo hex.	40	Pnma	$a = 1.398$; $c = 0.4523$	$(Cr,Fe)_7C_3$
Nitrides					
MN	ord fcc	8	Fm3*m*	$a = 0.4097–0.4577$	ZrN; TiN; NbN; VN
M_2N	hexagonal	9	P31m	$a = 0.478–0.480$; $c = 0.444–0.447$	$(Cr,Fe)_2N$
Z-phase	tetragonal	6	P4/nmm	$a = 0.3037$; $c = 0.7391$	CrNNb
Borides					
M_2B	orthorhombic	48	Fddd	$a = 1.4585$; $b = 0.7331$; $c = 0.4223$	$Cr_{1.04}Fe_{0.96}B$
M_3B_2	tetragonal	10	P4/mbm	$a = 0.5807$; $c = 0.3142$	$FeMo_2B_2$
Sulfides					
$M_4C_2S_2$	hexagonal	8	$P6_3/mmc$	$a = 0.320–3.39$; $c = 1.118–1.210$	$Ti_4C_2S_2$ $Zr_4C_2S_2$

Source: From A.F. Padilha and P.R. Rios: *ISIJ International (Japan)*, 42, 325–337, 2002.

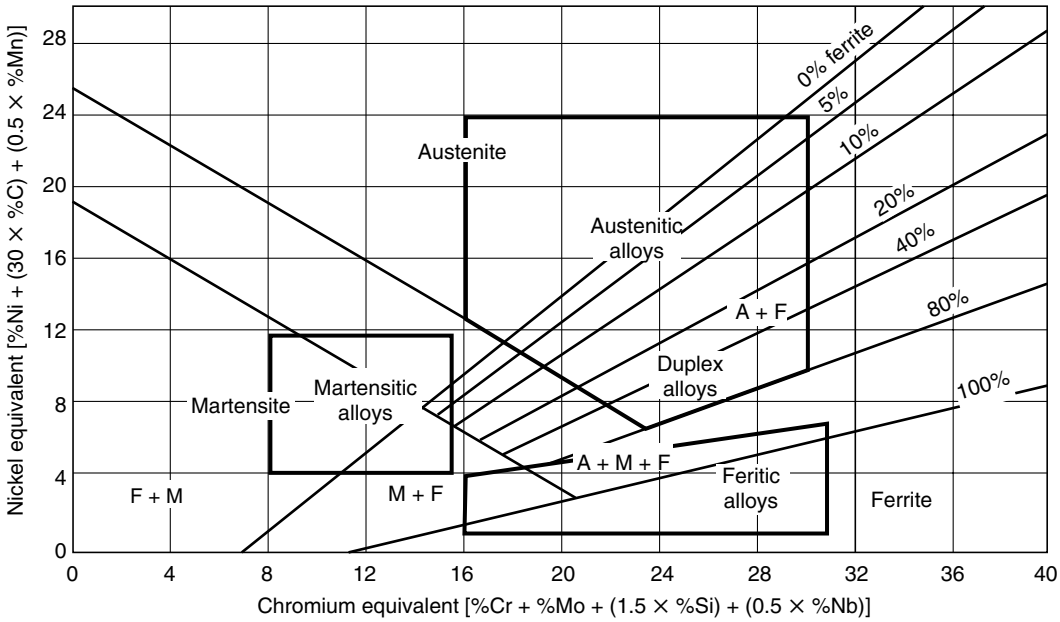

FIGURE 12.4 Schaeffler's constitution diagram for stainless steels. The typical compositional ranges of the ferritic, martensitic, austenitic, and duplex alloys have been superimposed on this diagram. (From J.R. Davis (Ed.): *ASM Speciality Handbook: Stainless Steels*, ASM International, Materials Park, OH, 1994; W. Reick, M. Pohl, and A.F. Padilha: *Metalurgia International*, 3, 46–50, 1990; M. Pohl, A.F. Padilha, and O. Fossmark: Bruchvorgänge in ferritisch-austenitischen Duplexstählen mit 475°-Versprödund. *Materialkundlieh-Technische Reihe*, Vol. 9 (Gefüge und Bruch, K.L. Maurer and M. Pohl (Eds.), Gebrüder Borntraeger, Berlin, pp. 305–314, 1990. With permission.)

12.3 AUSTENITIC STAINLESS STEELS

The discovery of stainless steels could be linked to a significant advance in the development of corrosion- and oxidation-resistant materials. At the time of their discovery, however, the austenitic stainless steels were frequently susceptible to intergranular corrosion, also called sensitization, caused by chromium depleting in the areas next to grain boundaries, due to the precipitation of the $M_{23}C_6$ carbide, known at the time as Cr_4C. (Westgren [23] in 1933 has shown that the correct formula was $Cr_{23}C_6$ and not Cr_4C.) Two approaches have been attempted, around 1930, to solve this problem: reduction of the carbon content (that resulted in the low carbon, or L-type, such as the AISI 304L and 316L types), and the addition of alloying elements that had more affinity with carbon as compared to Cr, such as Ti and Nb (that resulted in the stabilized types, such as the AISI 321 and the 347, respectively). Another important alloying modification in the austenitic stainless steels was the addition of Mo aiming at the resistance to pitting corrosion, with additions usually about 2 to 3 wt%, such as the AISI 316 and 316L types, although higher contents, such as 3 to 4 wt%, are present in the AISI 317 and 317L types. Table 12.2 presents the most frequently used types of austenitic stainless steels.

The austenitic stainless steels usually present an excellent combination of corrosion resistance, ductility, toughness, and weldability. However, for the common types their strength level, particularly the YS in the annealed condition, is relatively low, around 200 to 250 MPa. Higher levels of nitrogen additions can increase their YS to over 400 MPa. These steels, called superaustenitic, can contain up to about 0.9 wt% N, however their usual N content is about 0.2 wt%. To increase the weldability of the nitrogen-containing steels, an addition of Mn can be made. Furthermore Mn also partially replaces Ni as an austenite stabilizer and increases nitrogen solubility. Superaustenitic steels can contain up to 8 wt% Mo. One of the best-known

TABLE 12.2
Chemical Compositions (in wt%) of Some Typical Austenitic Stainless Steels

Type	UNS Designation	C	Mn	Si	Cr	Ni	Mo	N	Others
AISI 201	S20100	≤0.15	5.50–7.50	≤1.00	16.00–18.00	3.50–5.50	—	0.25	—
AISI 202	S20200	≤0.15	7.50–10.0	≤1.00	17.00–19.00	4.0–6.0	—	0.25	—
AISI 205	S20500	0.12–0.25	14.00–12.50	≤1.00	16.50–18.00	1.0–1.75	—	0.32–0.40	—
AISI 301	S30100	≤0.15	≤2.00	≤1.00	16.00–18.00	6.0–8.0	—	—	—
AISI 302	S30200	≤0.15	≤2.00	≤1.00	17.00–19.00	8.0–10.0	—	—	—
AISI 303	S30300	≤0.15	≤2.00	≤1.00	17.00–19.00	8.0–10.0	0.6	—	—
AISI 304	S30400	≤0.08	≤2.00	≤1.00	18.00–20.00	8.0–10.5	—	—	—
AISI 304H	S30409	0.04–0.10	≤2.00	≤1.00	18.00–20.00	8.0–10.5	—	—	—
AISI 304L	S30403	≤0.03	≤2.00	≤1.00	18.00–20.00	8.0–12.0	—	—	—
AISI 304N	S30400	≤0.08	≤2.00	≤1.00	18.00–20.00	8.0–10.5	—	0.10–0.16	—
AISI 304LN	S30451	≤0.03	≤2.00	≤1.00	18.00–20.00	8.0–12.0	—	0.10–0.16	—
AISI 308	S30800	≤0.08	≤2.00	≤1.00	19.00–21.00	10.0–12.0	—	—	—
AISI 309	S30900	≤0.20	≤2.00	≤1.00	22.00–24.00	12.0–12.0	—	—	—
AISI 310	S31000	≤0.25	≤2.00	≤1.00	24.00–26.00	19.0–22.0	—	—	—
AISI 316	S31600	≤0.08	≤2.00	≤1.00	16.00–18.00	10.0–14.0	2.0–3.0	—	—
AISI 316H	S31609	≤0.08	≤2.00	≤1.00	16.00–18.00	10.0–14.0	2.0–3.0	—	—
AISI 316L	S31603	≤0.03	≤2.00	≤1.00	16.00–18.00	10.0–14.0	2.0–3.0	—	—
AISI 316LN	S31653	≤0.03	≤2.00	≤1.00	16.00–18.00	10.0–14.0	2.0–3.0	0.10–0.16	—
AISI 316N	S31651	≤0.08	≤2.00	≤1.00	16.00–18.00	10.0–14.0	2.0–3.0	0.10–0.16	—
AISI 317	S31700	≤0.08	≤2.00	≤1.00	18.00–20.00	11.0–12.0	3.0–4.0	—	—
AISI 317L	S31703	≤0.03	≤2.00	≤1.00	18.00–20.00	11.0–12.0	3.0–4.0	—	—
AISI 321	S32100	≤0.08	≤2.00	≤1.00	17.00–19.00	9.0–12.0	—	—	$Ti \geq 5 \times \%C$
AISI 321H	S32109	0.04–0.10	≤2.00	≤1.00	17.00–19.00	9.0–12.0	—	—	$Ti \geq 5 \times \%C$
AISI 347	S34700	≤0.08	≤2.00	≤1.00	17.00–19.00	9.0–13.0	—	—	$Nb \geq 10 \times \%C$
AISI 347H	S34709	0.04–0.10	≤2.00	≤1.00	17.00–19.00	9.0–13.0	—	—	$1.0 \geq Nb \geq 10 \times \%C$
654 SMO®	S32654	≤0.02	2.00–4.00	≤0.50	24.00–25.00	21.0–23.0	7.0–8.0	0.45–0.55	Cu = 0.30–0.60

AISI = American Iron and Steel Institute; UNS = Unified Numbering System.

superaustenitic stainless steels is the UNS S32654 (see Table 12.2), also known as 654 SMO®. This steel offers a very interesting combination of mechanical and corrosion properties: high pitting corrosion resistance (pitting resistance equivalent [PRE] ≈ 55) combined with a YS of about 450 MPa, tensile strength of about 750 MPa, and 40% elongation.

Another very efficient alternative to increase the strength of the austenitic stainless steels is work hardening. The low stacking fault energy and the formation of deformation-induced martensite give rise to high strain-hardening, leading to a YS higher than 1200 MPa, even in the common AISI 304 type. Heating up of work-hardened material during weld processing or usage can cause recovery, martensite reversion, and even recrystallization, with a consequent loss in mechanical strength. Figure 12.5, with the help of a time–temperature–transformation (TTT) diagram, schematically presents the main transformations that occur in austenitic stainless steels during processing or utilization.

Before going into the different heat treatments for austenitic stainless steels, it is important to remember two particularly important properties of these steels, namely their low thermal

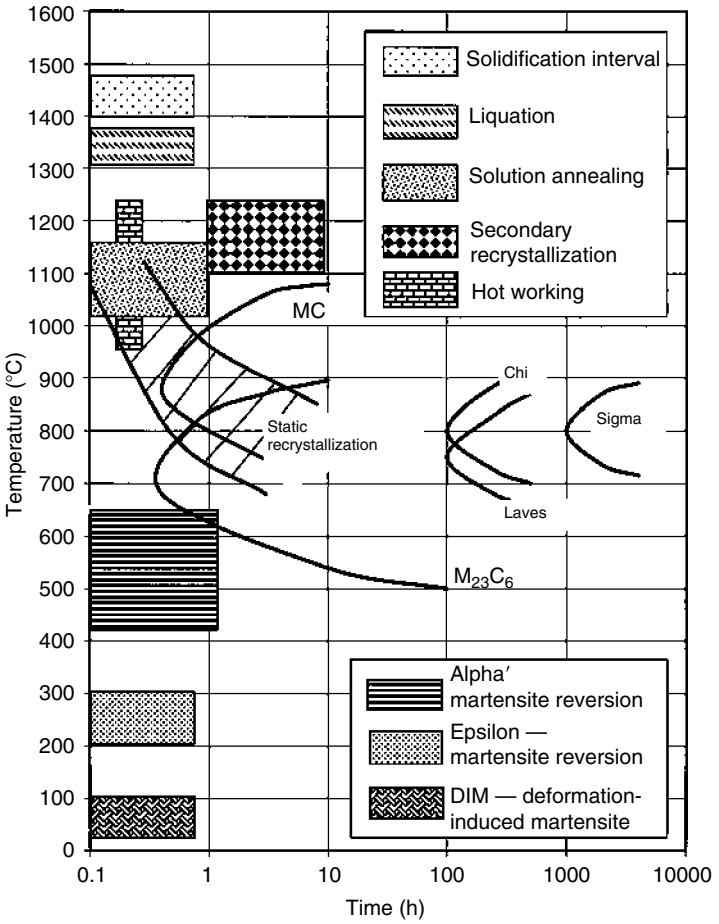

FIGURE 12.5 Main thermal treatments and transformations that occur in austenitic stainless steels between room temperature and the liquid state. (From A.F. Padilha, R.L. Plaut, and P.R. Rios: *ISIJ International (Japan)*, 43, 135–143, 2003. With permission.)

conductivity and high thermal expansion coefficient. The thermal conductivity of the austenitic stainless steels is low; about one fifth of the value for pure iron and one third of the conductivity of an AISI 1025 carbon steel. The thermal expansion coefficient of the stainless steels is about 50% higher than for pure iron or of an AISI 1025 carbon steel. While the low thermal conductivity limits the heating up and cooling speeds, the high thermal expansion coefficient requires special care concerning the spacing between pieces to be treated.

12.3.1 Solution Annealing

Solution annealing is the heat treatment most frequently specified for austenitic stainless steels, before their actual usage. The main objective of this treatment, as the name implies, is to dissolve the phases that have precipitated during the thermomechanical processing of the material, especially the chromium-rich carbides of the $M_{23}C_6$-type (see Figure 12.6), where M = Cr, Fe, Mo. As the precipitation of $M_{23}C_6$ occurs in the 450 to 900°C (840 to 1650°F) temperature range, the lower temperature limit for solution annealing should be over 900°C. Carbides should be completely dissolved but they dissolve slowly. Grain growth limits the maximum solution-annealing temperature. In particular, abnormal grain growth, also known as secondary recrystallization, must be avoided.

For the more conventional stainless steels, such as AISI 201, 202, 301, 302, 303, 304, 304L, 305, and 308, recommended solution-annealing temperatures are around 1010 to 1120°C (1850 to 2050°F). For higher carbon-containing steels such as the AISI 309 and 310 or steels containing molybdenum such as AISI 316, 316L, 317, and 317L, the minimum temperature should be increased to 1040°C whereas the maximum should be kept at 1120°C (1900 to 2050°F). In the case of the stabilized steels (see Figure 12.7), which are more prone to secondary recrystallization or abnormal grain growth [25], as compared to the nonstabilized steels, the solution-annealing temperature range should be at a lower level, between 955 and 1065°C (1750 and 1950°F), for titanium-stabilized AISI 321 type, and narrower, between 980 and 1065°C (1800 and 1950°F), for the niobium-stabilized AISI 347 and 348 (nuclear grade) types.

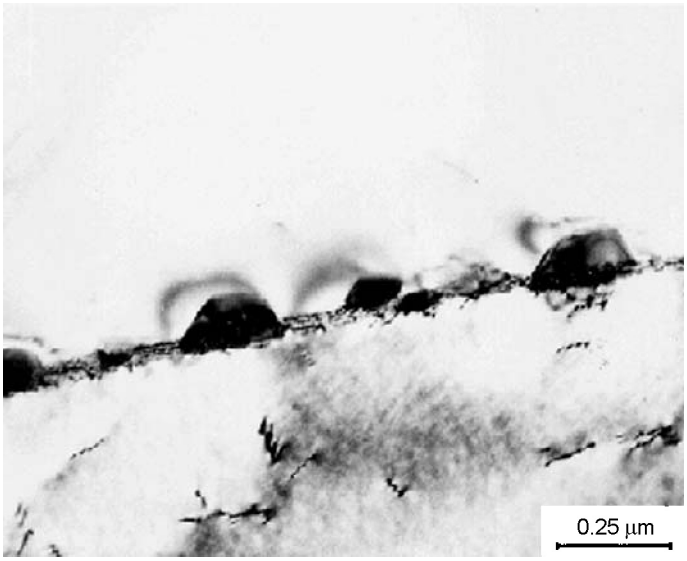

FIGURE 12.6 Grain boundary $M_{23}C_6$ precipitates in an austenitic stainless steel observed using transmission electron microscopy. (From A.F. Padilha and P.R. Rios: *ISIJ International (Japan)*, 42, 325–337, 2002. With permission.)

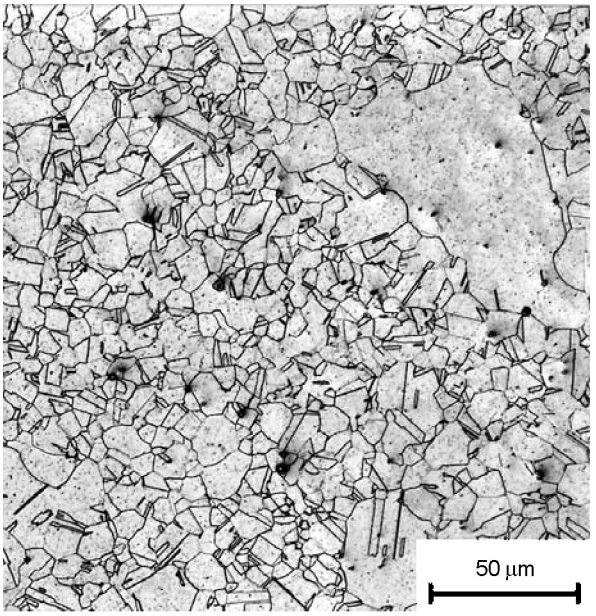

FIGURE 12.7 Optical micrograph showing secondary recrystallization start in a titanium-stabilized austenitic stainless steel after solution annealing. Etched with V2A-Beize. (From A.F. Padilha, R.L. Plaut, and P.R. Rios: *ISIJ International (Japan)*, 43, 135–143, 2003. With permission.)

Cooling from heat treatment temperatures should be sufficiently fast to avoid chromium-carbide precipitation. On the other hand, too fast cooling rates cause component distortions. In the case of nonstabilized grades such as AISI 201, 202, 301, 302, 303, 304, 305, 308, 309, 316, and 317, if distortion considerations permit, water quenching may be utilized. In the case of the AISI 309 and 310 types that contain maximum allowed carbon content and are susceptible to carbide precipitation, water cooling is mandatory. In the case of stabilized AISI 321, 347, and 348 types, water cooling is not needed and air cooling is sufficient to avoid sensitization. Molybdenum-containing steels, such as AISI 316, 316L, 317, and 317L, present an intermediate tendency toward sensitization when compared to nonstabilized conventional and the stabilized types, i.e., they do not require water cooling from the solution-annealing temperature, however their usage in the 540 to 760°C (1000 to 1400°F) temperature range should be avoided. In the case of molybdenum-containing steels, such as AISI 316, 316L, 317, and 317L types, long exposure times at temperatures in the 650 to 870°C (1200 to 1600°F) temperature range should be avoided, to avoid the precipitation of intermetallic phases (see Figure 12.5), such as sigma (σ), chi (χ), and Laves (Fe_2Mo) phases.

During solidification or welding, the formation of δ-ferrite may occur, which may be difficult to eliminate completely during the thermomechanical treatment and it may be present before the solution-annealing heat treatment or even may survive it. If the material has δ-ferrite it may be even more susceptible to the precipitation of the intermetallic phases mentioned previously [26].

12.3.2 Stabilize Annealing

Stabilize annealing is used for stabilized austenitic stainless steels in order to assure maximum intergranular corrosion resistance. After the solution-annealing treatment, only part of the carbon is bound in the form of primary phases, such as carbides, MC, carbonitrides, M(C,N), nitrides MN, or carbosulfides $M_4C_2S_2$, where M = Ti, Nb, or V. The remaining carbon stays in solid solution and may precipitate as secondary carbides MC or $M_{23}C_6$ at lower temper-

atures, since the carbon solubility in austenite under 900°C (1650°F) is very low. Careful observation of Figure 12.5 reveals that the precipitation start temperature of the thermodynamically more stable MC carbides is displaced to higher temperatures if compared to the precipitation start temperature of the less stable Cr-rich carbides of the $M_{23}C_6$ type. Therefore, exposing the steel, after solution annealing, to temperatures in the 845 to 955°C (1550 to 1750°F) temperature range for up to 5 h (depending on component size), favors MC precipitation in detriment to $M_{23}C_6$. Furnace atmosphere control, avoiding carburizing or excessively oxidizing conditions, should be employed and the sulfur content in oil- or gas-fired furnaces should be kept at low levels.

12.3.3 Stress-Relief Annealing

The most effective way to relieve stresses is to cool the component slowly from the solution-annealing temperature. During slow cooling, some $M_{23}C_6$ precipitation may occur with consequent sensitization. On the other hand, fast cooling may reintroduce residual stresses and make the component susceptible to stress-corrosion cracking (SCC). In general, a small amount of intergranular corrosion is preferable to a failure in few weeks due to SCC. Moreover, the selection of a low carbon or of a stabilized steel would be a more appropriate solution. The selection of a lower working temperature range, say in the 925 to 1010°C (1700 to 1850°F) range, would allow longer time exposure without significant grain growth.

Another alternative would be to stress relieve at a lower temperature range, between 425 and 550°C (800 and 1000°F), where $M_{23}C_6$ precipitation is very slow, allowing the material to be exposed for some hours without sensitization occurrence. This treatment may not be very efficient to reduce residual stresses, nevertheless it may be sufficient to reduce residual stresses sufficiently to significantly reduce the risk of SCC. In the case of low-carbon steels, such as AISI 304L, 316L, and 317L, the sensitization risk is even smaller.

12.3.4 Bright Annealing

All austenitic stainless steel types can be bright annealed in a pure hydrogen or dissociated ammonia atmosphere, provided that its dew point is kept below −50°C (−60°F) and that the components are dry and clean before entering the furnace. If the dew point is not kept sufficiently low, some thin green oxide film may be formed, which will be difficult to remove.

12.3.5 Martensite Formation

Austenite in stainless steels in general and the austenite in the 300 steels series in particular is not a stable phase. In the solution-annealed condition, the M_s temperature is normally below room temperature. For the majority of these steels, the M_d temperature (the temperature below which martensite will form under deformation) is above room temperature.

Two kinds of martensite can occur in stainless steels: α' (bcc, ferromagnetic) and ε (hcp, nonferromagnetic). The transformation of austenite to martensite can be also induced in austenitic stainless steels by cathodic charging with hydrogen [27]. The lattice parameters are typically:

$$a_{\alpha'} = 0.2872\,\text{nm}$$

and

$$a_{\varepsilon} = 0.2532\,\text{nm}; \qquad c_{\varepsilon} = 0.4114\,\text{nm}$$

Assuming [28] $a_\gamma = 0.3585\,\text{nm}$, we may estimate that the $\gamma \rightarrow \alpha'$ transformation causes a volume increase of 2.57%, while the $\gamma \rightarrow \varepsilon$ transformation causes a volume decrease of 0.81%.

12.3.5.1 Transformation during Cooling

There are several empirical equations that relate the M_s temperature to the chemical composition. Eichelman and Hull's [29] is one of the most widely used:

$$M_s\,(^\circ\text{C}) = 1302 - 42\,(\%\ \text{Cr}) - 61\,(\%\ \text{Ni}) - 33\,(\%\ \text{Mn}) - 28\,(\%\ \text{Si}) - 1667\,(\%\ [\text{C} + \text{N}]) \quad (12.1)$$

where compositions are in wt%.

Equation 12.1 suggests that many steels in Table 12.2, when cooled to cryogenic temperatures, will form alpha prime (α') martensite. The ability to form alpha prime (α') martensite becomes more significant during cooling after sensitization. $M_{23}C_6$ precipitation at grain boundaries causes depletion of chromium, carbon, and other alloying elements in the vicinity of the grain boundaries. This leads to a higher M_s temperature, making the material more susceptible to the formation of alpha prime (α') martensite close to grain boundaries during cooling [30]. For epsilon (ε) martensite no equations like Equation 12.1 are reported. However, it is reasonable to expect that the formation of epsilon (ε) martensite increases with a decrease in the stacking fault energy of austenite [31,32].

12.3.5.2 Strain-Induced Transformation

The most frequent case of martensite formation at room temperature in stainless steels is that of strain-induced martensite.

The formation and the amount of alpha prime (α') and epsilon (ε) depend on steel composition, on its stacking fault energy, and on the temperature, amount, and rate of deformation. According to Kaieda and Oguchi [33], the amount of α' depends also on the stress state during deformation.

There are several empirical equations that relate the M_d temperature with the chemical composition. One of the most often employed is due to Angel [34]:

$$M_d(30/50)(^\circ\text{C}) = 413 - 13.7\,(\%\ \text{Cr}) - 9.5\,(\%\ \text{Ni}) - 8.1\,(\%\ \text{Mn}) - 18.5\,(\%\ \text{Mo}) - 9.2\,(\%\ \text{Si}) - 462\,(\%\ [\text{C} + \text{N}]) \quad (12.2)$$

where compositions are in wt%. $M_d(30/50)(^\circ\text{C})$ is the temperature at which 50 vol% α' is formed after a true tensile strain of 30%.

For the majority of austenitic stainless steels, the M_d temperature is above room temperature. For epsilon (ε) martensite such empirical equations are not available. Susceptibility of the austenite to form martensite and the amount of martensite formed increases with decreasing deformation temperature.

When stainless steels containing deformation-induced martensite are annealed, the martensite may revert to austenite. This reversion usually occurs at temperatures about 100°C lower and for shorter times than those required for the recrystallization of the deformed stainless steel [35]. The formability of the austenitic alloys is influenced greatly by martensitic transformation during straining [36,37].

12.4 FERRITIC STAINLESS STEELS

It is common to classify ferritic stainless steels according to their generation [11]. The first generation of ferritic stainless steels was developed during the 20th century, when the

decarburization processes were quite inefficient and, therefore, the carbon and consequently chromium contents were relatively high. The main representatives of this generation were the AISI 430 and 446 steels (see Table 12.3). Steels of this generation were not fully ferritic in their composition and temperature range. The second generation of ferritic stainless steels had lower carbon and nitrogen contents with carbon and nitrogen getter elements, such as titanium and niobium. Moreover, we must remember that titanium, eventually in excess in solid solution, is a ferrite-forming element. Therefore, this generation presented a fully ferritic microstructure. The AISI 409 steel is a typical representative of this generation, which represents about two thirds of the total ferritic stainless steel production. The third generation of ferritic stainless steels came into scene about 1970 and possessed all the benefits of a more efficient decarburization. Carbon and nitrogen contents were typically in the order of 0.02 wt% or even lower, they were titanium- or niobium-stabilized and frequently contained molybdenum. Their typical representative is the AISI 444 steel. The development of the VOD and the AOD processes (carbon-reducing metallurgical processes) opened up new perspectives for steels, among them the ferritic stainless steels. Raising the chromium content to levels higher than 25 wt%, as well as additions of molybdenum, a strong ferrite-forming elements leads to the development of the superferritic steels. Further raising of chromium, molybdenum, and lowering of carbon levels, allowed nickel to be added, without ferrite destabilization. The main effect of nickel is to increase toughness. Nickel also has a positive effect on corrosion resistance under reducing conditions and it increases the pitting and crevice corrosion resistance. The 28Cr–4Ni–2Mo–Nb (in wt%) and 29Cr–4Mo–2Ni (in wt%) steels shown in Table 12.3 are typical representatives of this generation.

Ferritic stainless steels have a high brittle-ductile transition temperature compared to duplex ferritic–austenitic stainless steels. The transition temperature strongly depends on the amount of interstitials, mainly the carbon and nitrogen levels in the steel. Ferritic steels have only reasonable mechanical properties relative to the other types of stainless steels. The ferritic steels are not hardenable by heat treatment and have a low strain-hardening coefficient when compared to the austenitic types. Ferritic steels, specially the superferritic ones, are selected for numerous applications because of their corrosion resistance. They have an excellent resistance to generalized corrosion, pitting and crevice stress corrosion in media containing chloride ions. Their major application is in the chemical, petrochemical, pulp and paper industries, and in desalinization installations. The high levels of alloying elements that are typical in ferritic stainless steels have some negative consequences when it comes to microstructural stability [38–40]. High chromium- and molybdenum-containing steels, such as in the case of the 28 wt% Cr–4 wt% Ni–2 wt% Mo–Nb and 29 wt% Cr–4 wt% Mo–2 wt%Ni superferritic types, are susceptible to sigma- (σ) and chi (χ)-phase precipitation. Ferrites containing more than 18 wt% chromium are susceptible to the so-called 475°C embrittlement, caused by the alpha prime (α') phase. The presence of these phases in the microstructure has negative effects both on toughness and on corrosion resistance. The dissolution of phases during solution-annealing treatments may lead [25] to excessive grain coarsening (secondary recrystallization), which in turn is associated with loss in toughness. The much faster diffusion in ferrite than in austenite leads to the fact that the phenomena mentioned above are more critical in the ferritic steels than in the austenitic steels.

12.4.1 The 475°C (885°F) Embrittlement

Ferritic stainless steel embrittlement caused by their exposure to temperatures around 475°C (885°F) has been discussed in the literature for more than half a century [41,42]. It is caused by the presence of the alpha prime (α') phase in the 300 to 550°C temperature range. This phase contains mainly chromium and iron, richer in chromium than in iron, as shown in the Fe–Cr

TABLE 12.3
Chemical Composition (in wt %) of Some Typical Ferritic Stainless Steels

Type	UNS Designation	C	Mn	Si	Cr	Mo	Ni	Other Elements
AISI 430	S43000	≤0.12	≤1.00	≤1.00	16.0–18.0	—	≤0.75	
AISI 446	S44600	≤0.20	≤1.50	≤1.00	23.0–27.0	—	—	$N \leq 0.25$
AISI 409	S40900	≤0.08	≤1.00	≤1.00	10.6–11.75	—	≤0.5	$6\times \%C \leq Ti \leq 0.75$
AISI 444	S44400	≤0.025	≤1.00	≤1.00	17.5–19.5	1.75–2.50	≤1.0	$Nb + Ti \geq 0.20 + 4(C + N)$
AISI 448	S44800	≤0.01	≤0.30	≤0.20	28.0–30.0	3.50–4.20	2.00–2.50	$C + N \leq 0.025$
W. Nr. 1.4575		≤0.015	≤1.00	≤1.00	26.0–30.0	1.80–2.50	3.00–4.50	$12 \times \%C \leq Nb \leq 1.20$

diagram in Figure 12.1. The alpha prime (α′) phase has a bcc structure and is coherent with ferrite. The alpha prime (α′) precipitates are small, in the range of 20 to 200 Å. They have a high coarsening resistance, even for long exposure times. The alpha prime (α′) precipitates contain essentially chromium and iron. These two atoms show very similar atomic sizes, x-ray, and electron scattering amplitudes, which along with the small precipitate size, make their direct observation difficult even using transmission electron microscopy. Structural analysis by electron or x-ray diffractions presents similar difficulties. For the same reasons, it is also difficult to analyze them through chemical microanalysis techniques. Some special techniques, such as low-angle neutron scattering [43,44] and Mössbauer spectroscopy [45–47], are frequently employed in their study. The presence of the α′-phase has an important effect on the mechanical and corrosion properties. Significant changes in electric properties in specific weight and in the coercive force were also observed. These changes in physical properties can be removed by annealing at about 600°C (1100°F) for 1 h [42].

Hardness, yield, and tensile strength are increased, while elongation and impact resistance are decreased by the presence of alpha prime (α′). Ferrite without alpha prime (α′) presents wavy glide lines because of the numerous gliding systems in the bcc structure and its high stacking fault energy facilitating dislocation cross-slip. The presence of alpha prime (α′) changes this situation, it makes the dislocation movement difficult, restricting slip to a few crystal planes. This causes some straight slip lines, typical of fcc and low stacking fault energy alloys, such as in austenitic stainless steels or brass. Some authors consider that alpha prime (α′) containing ferrite predominantly deforms by twinning [43,44,48,49] and that the straight deformation lines mentioned above are, in reality, deformation twins. Ferrite embrittled due to the presence of alpha prime (α′), in general, presents a cleavage type brittle fracture at room temperature.

Corrosion resistance is also affected by the presence of alpha prime (α′). Bandel and Tofaute [41] observed that the presence of alpha prime (α′) significantly reduced the corrosion resistance in a solution of boiling nitric acid. Pitting corrosion resistance, determined by cyclic polarization tests, in a solution of 3.5 wt% NaCl, is also significantly reduced by the presence of alpha prime (α′) [50]. It is important to remember that superferritic stainless steels have as one of their main features an excellent resistance to pitting corrosion in seawater.

The magnitude of the effects of alpha prime (α′) on the properties depends chiefly on the chromium content of the alloy and it increases with an increase in chromium content. For example, in alloys containing 25 to 30 wt% chromium, aging at temperatures around 475°C for long times may lead to doubling its hardness [41,51]. Its maximum hardness may reach values higher than 350 HV. In an alloy containing 21 wt% chromium, the increase in maximum hardness was about 80% and its maximum hardness was 298 HV [49]. For a still lower Cr content, in an alloy containing 18 wt% chromium, the increase in maximum hardness was about 50% [41,52,53].

If, on the one hand, there is large agreement with regard to the effect of the alpha prime (α′) precipitation on properties, on the other hand, there is an ongoing dispute [43–53] on the mechanism of the precipitation of the alpha prime (α′) phase. It is not yet fully established whether it is by spinodal decomposition or by nucleation and growth. The kinetics of formation of alpha prime (α′) and of the consequent 475°C embrittlement is generally presented in the form of TTT (temperature, time, transformation) curves, with their nose around 475°C. Folkhard [12] compares TTT curves for the formation of α′ in several ferritic and duplex stainless steels. He mentions that for steels containing only 12 wt% chromium 10^5 h are needed for this phenomenon to show up. As the chromium content increases, incubation time is reduced, i.e., the C-type TTT curves are displaced to shorter times and the temperature range for this transformation to occur is enlarged. Cold working performed prior to aging in 18 wt% Cr–2 wt% Mo steels has a minor effect on the 475°C embrittlement, at least when the phenomena are followed by hardness measurements, impact and tensile testing [54]. Literature analysis shows that alpha prime (α′) formation through spinodal decomposition

seems to be concentrated in alloys containing more than 20 wt% chromium [43–45]. In alloys containing chromium in the 14 to 18 wt% range, there is evidence that ferrite embrittlement occurred due to α' precipitation on dislocations [52,53]. Kuwano and coauthors [47], using results from Mössbauer spectroscopy, suggest that the addition of 5 wt% nickel to an alloy containing 28 wt% chromium caused a modification in the precipitation mode from nucleation and growth toward spinodal.

12.4.2 Sigma (σ)-Phase Embrittlement

Sigma phase is probably the most studied intermetallic compound. Already in 1907, even before the discovery of the stainless steels, Treischke and Tamman [55] studied the Fe–Cr system and proposed the existence of an intermetallic compound containing chromium in the 30 to 50 wt% range. In 1927, Bain and Griffiths [6] studied the Fe–Cr–Ni system and observed a hard and fragile phase, which they called constituent B, from brittle. In 1936, Jett and Foote [56] called it sigma (σ) phase and in 1951, Bergmann and Shoemaker [57] determined through crystallography its structure in the Fe–Cr system.

The precipitation of sigma phase in stainless steels can occur in the austenitic, ferritic, and ferritic–austenitic phases with duplex structure types. The precipitation of this Fe–Cr–Mo intermetallic, of tetragonal structure with 30 atoms per unit cell, causes loss in toughness and results in the matrix becoming depleted of chromium and molybdenum.

In the austenitic steels, precipitation generally requires hundreds or even thousands of hours and the precipitated volumetric fraction is generally smaller than 5 vol% [58]. Precipitation can be represented by a common precipitation reaction: $\gamma \rightarrow \gamma^* + \sigma$, where γ^* is a chromium- and molybdenum-depleted austenite, if compared to the original austenite. Precipitation occurs predominantly at grain boundaries, especially at triple points.

In the case of duplex stainless steels, precipitation can be complete in a few hours and consumes all ferrite of the microstructure [59]. Precipitation in this case can be represented by a eutectoid-type reaction: $\alpha \rightarrow \gamma^* + \sigma$, where γ^* is a chromium- and molybdenum-depleted austenite if compared to a nontransformed austenite. Precipitation starts at the α–γ interface and moves into the ferrite grain.

The quantity, speed, and probably the mode of the sigma-phase precipitation in ferritic stainless steels strongly depend on the steel composition, especially on the chromium and molybdenum contents. Increasing chromium and molybdenum levels displace precipitation start to shorter times and to higher temperatures. For example, a steel containing 18 wt% chromium, sigma precipitation occurs around 550°C and demands 1,000 to 10,000 h [60]. In a steel containing 17 wt% chromium and 2 wt% molybdenum sigma precipitation occurs at 600°C in just 200 h [61]. In steels containing 28 wt% chromium and 5 wt% molybdenum [39], large quantities of sigma precipitate in a few minutes at 900°C. Molybdenum additions can also cause chi (χ)-phase precipitation, which will be discussed in the next section. Streicher [62] studied the relationship between microstructure and properties, especially corrosion resistance, in the Fe–28 wt% Cr–4 wt% Mo and Fe–28 wt% Cr–4 wt% Mo–2 wt% Ni alloys. He detected the sigma- (and chi-) phase precipitation at grain boundaries in the 704 (1300°F) to 927°C (1700°F) temperature range, after exposure for 1 h. The temperature for maximum precipitation was around 816°C (1500°F) and heat treatments at 1038°C (1900°F) caused dissolution of the previously precipitated phases. Nana and Cortie [63] observed that sigma- and chi-phase precipitations were delayed by aluminum additions and could be eliminated if additions were sufficiently high. Copper has a similar effect on the formation of these two phases [63]. For a Fe–39 wt% Cr–2 wt% Mo–2 wt% Ni superferritic steel it has been observed [64] that while aluminum and niobium additions delay the sigma (σ)-phase formation, titanium and zirconium may favor its formation. Recent studies [40,65] on a X 1

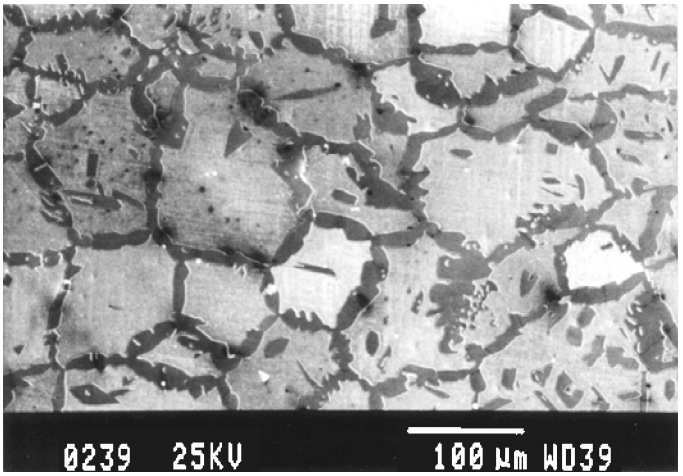

FIGURE 12.8 Sigma-phase precipitation in aged samples (850°C for 30 h) of a superferritic stainless steel X 1 CrNiMoNb 28 4 2 (W. Nr. 1.4575). Etched with V2A-Beize. (From A.F. Padilha, F.C. Pimenta Jr., and W. Reick: *Zeitschrift für Metallkunde*, 92, 351–354, 2001; F.C. Pimenta Jr, A.F. Padilha, and R.L. Plaut: *Materials Science Forum*, 426–432, 1319–1324, 2003. With permission.)

CrNiMoNb 28 4 2 (DIN W. Nr. 1.4575) steel showed that the kinetics of sigma (σ)-phase precipitation is faster than for the austenitic stainless steels, however slower than for the duplex stainless steels. The micrograph shown in Figure 12.8 illustrates the copious precipitation of sigma phase in the DIN W. Nr. 1.4575 superferritic stainless steel.

12.4.3 The Chi (χ) Phase

Chi (χ) phase was identified, for the first time, by Andrews [66] in 1949 in residues extracted from the Cr–Ni–Mo steel. Later, Kasper [67] synthetically produced the chi (χ) phase with the $Fe_{36}Cr_{12}Mo_{10}$ composition and studied its crystal structure in detail.

Chi (χ) phase, for example, may occur also in austenitic, ferritic, and duplex (ferritic–austenitic) stainless steels and its precipitation is associated with negative effects on properties. While sigma phase is present in the binary Fe–Cr system, chi phase appears only in the Fe–Cr–Mo ternary and in the Fe–Cr–Ni–Mo and Fe–Cr–Ni–Ti quaternary systems [67–69]. Still in comparison with the sigma phase, chi (χ) phase is richer in molybdenum and poorer in chromium [39].

The occurrence of (χ)-phase in ferritic stainless steels is conditioned to a minimum in the molybdenum content. For example, around 600°C, about 2 wt% of molybdenum is, in principle, sufficient for the χ-phase formation [70]. The same work [70] points out that at 700°C, some 10,000 h of aging is insufficient to attain equilibrium. Therefore, it is most probable that in various reports in which χ-phase has not been mentioned, the aging time was not sufficient to reach equilibrium. The effect of molybdenum, as a promoter of the sigma σ- and χ-phase formation becomes very clear if we compare the various TTT diagrams for precipitation start, as shown in Figure 12.9. It is interesting to observe in Figure 12.9, the appearance of χ-phase may precede the appearance of σ-phase.

12.4.4 Other Phases

Intergranular corrosion is a much less important phenomenon in ferritic than in austenitic stainless steels. Several reasons may contribute for this difference: (i) diffusion in ferrite is

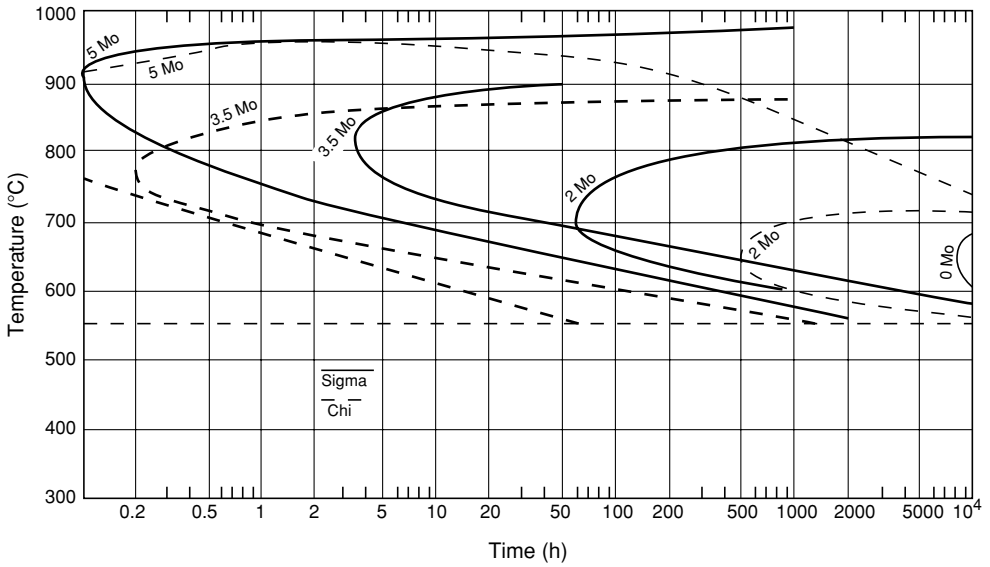

FIGURE 12.9 Effect of molybdenum on the sigma (σ)- and chi (χ)-phase formation in the Fe–28 wt% Cr–Mo system. (From R.D. Campbell: *Key Engineering Materials*, 69, 70, 167–216, 1992; H. Brandis, H. Kiesheyer, and G. Lennartz: *Archiv für das Eisenhüttenwesen*, 46, 799–804, 1976. With permission.)

about two orders of magnitude faster than in austenite, reducing the possibility of the occurrence of composition gradients; (ii) carbon content in the ferritic stainless steels is normally kept at levels that are lower than those for the austenitic ones, due to its negative effect on toughness; (iii) some ferritic stainless steels, such as the superferritic, present chromium levels over 25 wt%. Carbide precipitation at grain boundaries and the consequent chromium depleting in the surroundings are the preferred mechanism used to explain intergranular corrosion in ferritic steels [72]. The carbide formed is the $M_{23}C_6$ [73,74]. Bäumel [73] compared in a TTT diagram the intergranular corrosion behavior of two stainless steels containing similar carbon and chromium contents, with one of them ferritic without nickel and the other austenitic containing 8 wt% nickel. The intergranular corrosion (due to $M_{23}C_6$) region of the ferritic steel was displaced to shorter times and lower temperatures, when compared to the austenitic steel. The precipitation of $M_{23}C_6$ occurred so fast in the ferritic steels, which it is unavoidable for some compositions, thicknesses, and processes. The higher diffusivity in ferrite (as compared to austenite) leads to a faster $M_{23}C_6$ precipitation. On the other hand, chromium gradients around these grain boundary precipitates in ferritic stainless steels probably are less pronounced (hence less susceptible to intergranular corrosion) than the gradients adjacent to grain boundaries in austenitic stainless steels.

Titanium and niobium additions used as stabilizers are also common in ferritic stainless steels. According to Steigerwald and coauthors [75], effective titanium and niobium contents are given by Equation 12.3 and Equation 12.4, respectively:

$$\mathrm{Ti} = 0.15 + 3.7(\mathrm{C} + \mathrm{N}) \tag{12.3}$$

$$\mathrm{Nb} = 7(\mathrm{C} + \mathrm{N}) \tag{12.4}$$

where Ti, Nb, C, and N are in wt%.

The presence of titanium in stainless steels invariably leads to the appearance of three phases: $Ti_4C_2S_2$, TiN, and TiC. The carbosulfide and nitride are primary phases that form during solidification. The carbide may be present as a primary or secondary phase. Zirconium has the same effect as titanium. The presence of niobium produces Nb(C,N), which may be present either as primary coarse particles or as fine secondary particles.

If the contents of titanium and niobium used are much higher than those given by Equation 12.3 and Equation 12.4, some Laves-phase precipitation of the Fe_2M (M = Ti, Nb, and Mo) type may occur. Sawatani and coauthors [76] studied a steel containing (in wt%) 0.008% C, 0.0079% N, 18.64% Cr, 1.97% Mo, 0.32% Ti, and 0.30% Nb, and were able to detect some fine Laves $(Fe,Cr)_2(Mo,Nb,Ti)$ phase particles after aging at 700°C.

12.4.5 Processing and Heat Treatment

Ferritic stainless steel ingots have a coarse grain size, are relatively brittle, and should not be submitted to thermal shocks. Cast plates are ground, slowly heated, and hot rolled into strips. The hot-rolled coils are then annealed, slit, and pickled. Cold rolling, used to obtain intermediate gages, is followed by recrystallization-annealing.

Ferritic stainless steels are normally used only after solution annealing. The solution-annealing temperature varies substantially according to the steel type. The first-generation steels are treated at lower temperatures, for example, AISI 430 steel is treated in the 705 to 790°C (1300 to 1450°F) temperature range and the AISI 446 in the 760 to 830°C (1400 to 1525°F) range. The second-generation steels are treated at somewhat higher temperatures, for example, AISI 409 is treated in the 870 to 925°C (1600 to 1700°F) range. The third-generation steels, such as the AISI 444, are treated at even higher temperatures, in the 955 to 1010°C (1750 to 1850°F) range. Steels with higher chromium contents, such as the superferritic, should be water cooled in order to avoid the 475°C embrittlement due to alpha prime (α') formation.

Ferritic stainless steels can be cold worked by most of the mechanical working processes. In comparison with the austenitic stainless steels, the ferritic steels have higher YS before work hardening, lower ductility and therefore considered to be less workable than the austenitic steels. Moreover, the ferritic stainless steels work harden less and may show, after mechanical working, a typical defect known as roping or ridging, which is associated with the crystallographic texture [77]. Despite the mentioned disadvantages, ferritic stainless steels can be cold formed adequately and are easily hot formed.

12.5 DUPLEX STAINLESS STEELS

One of the most frequently used duplex stainless steels in the 1960s was the AISI 329 type. At that time, nitrogen additions were still not intentionally added (see Table 12.4) and the AISI 329 type was predominantly ferritic. At the end of the 1960s, metallurgists had already a reasonable idea of the aimed austenitic–ferritic relationship as well as the maximum residual impurities acceptable levels in stainless steels. However, this could not be achieved owing to the unavailability of fabrication processes. Only with the introduction of the VOD and the AOD processes it has been possible to produce duplex steels with low sulfur, oxygen, and other elements, with controlled properties. One of the first steels produced using this process was the AVESTA 3RE 60 (see Table 12.4). It was introduced into the market around 1972 and had about 40 vol% austenite [8]. In 1974, its composition was slightly changed and since then it has been produced continuously. Another development of that time was the DIN W. Nr. 1.4460 steel, standardized in Germany in 1973 [78]. Some time later, the DIN W. Nr. 1.4462, having high corrosion resistance, was developed, which is the duplex composition most frequently employed nowadays.

TABLE 12.4
Chemical Composition (in wt%) of Some Typical Duplex Stainless Steels

Type	UNS Designation	C	Mn	Si	Cr	Ni	Mo	N	Others	PRE-Range
AISI 329	S32900	≤0.20	≤1.00	≤0.75	23.0–28.0	2.50–5.00	1.00–2.00			26.3–34.6
Avesta 3RE60	S31500	≤0.03	1.2–2.0	1.4–2.0	18.0–19.0	4.25–5.25	2.5–3.0	0.05–0.10		27.1–30.5
W. Nr. 1.4460		≤0.07	≤2.0	≤1.0	25.0–28.0	4.5–6.0	1.3–2.0	0.05–0.20		30.1–37.8
W. Nr. 1.4462	S31803	≤0.03	≤2.00	≤1.00	21.0–23.0	4.50–6.50	2.50–3.50	0.08–0.20		30.5–37.8
	S31200	≤0.03	≤2.0	≤1.0	24.0–26.0	5.5–6.5	1.2–2.0	0.14–0.20		30.2–35.8
	S32550	≤0.04	≤1.50	≤1.00	24.0–27.0	4.50–6.50	2.00–4.00	0.10–0.25	Cu = 1.50–2.50	35.2–43.0
	S32950	≤0.03	≤2.0	≤0.60	26.0–29.0	3.50–5.20	1.00–2.50	0.15–0.35		31.7–42.8
SAF 2507	S32750	≤0.03	≤1.2	≤1.0	24.0–26.0	6.0–8.0	3.0–5.0	0.24–0.32	Cu = 0.50	37.7–47.6
W. Nr. 1.4464		0.30–0.50	≤1.50	≤2.0	26.0–28.0	4.0–6.0	2.0–2.50			
W. Nr. 1.4822		0.30–0.50	≤1.50	1.0–2.0	23.0–25.0	3.50–5.50				

Duplex stainless steels present high levels of alloying elements, such as chromium, nickel, molybdenum, and nitrogen, which should be properly balanced in order to achieve similar volumetric fractions of both phases and to give, both ferrite and austenite, a proper corrosion and mechanical resistance. YS in these steels is more than twice that of the single-phase stainless steels either ferritic or austenitic. They also have superior toughness and ductility when compared to the ferritic and martensitic types, in addition to superior intergranular and stress corrosion resistance in comparison to the austenitic type. This favorable combination of properties makes this class of stainless steels widely employed in oil and gas, petrochemical, pulp and paper, and pollution control industries. They are frequently used in aqueous solutions containing chlorides, where they have substituted with advantage (major reductions in weight and welding time) the austenitic stainless steels that are more susceptible to stress and pitting corrosion.

Pitting corrosion resistance in stainless steels is mainly linked to the chromium, molybdenum, and nitrogen contents. At the end of the 1960s, some relationships [79,80] were suggested relating pitting corrosion resistance (PRE) to the content of these three elements:

$$\text{PRE} = \%\,\text{Cr} + 3.3\%\,\text{Mo} + (16 \text{ or } 30)\%\,\text{N} \tag{12.5}$$

where compositions are in wt%.

The value of 30 for nitrogen in Equation 12.5 is valid for austenitic steels, while 16 is used for duplex steels. Chromium and molybdenum are ferrite formers and they concentrate mainly in ferrite, and nitrogen goes mainly to austenite. In the initial development steps, duplex steels had low nitrogen levels and were quite susceptible to pitting corrosion. Some modern duplex steels have higher nitrogen levels (0.2 to 0.32 wt%), which give a higher pitting corrosion resistance to austenite, comparable to ferrite. Here it should be mentioned that an exaggerated increase in the nitrogen level leads to an increase in the austenite level beyond the level adequate for mechanical resistance. For long exposure times in chloride-rich environments, such as seawater, a level of $\text{PRE} > 40$ is nowadays considered satisfactory. Alloys containing $\text{PRE} > 40$ are known as superduplex. Duplex stainless steels are practically immune to stress corrosion, when compared to austenitic stainless steels. They are also, in general, more resistant to intergranular corrosion.

Numerous duplex compositions having different combinations of mechanical properties, corrosion, and wear resistance are produced with continuous improvements in composition and secondary metallurgy. Due to all these developments, numerous alloys have been introduced into the market. Some had their production discontinued owing to insufficient performance for long exposure time applications. Today, about 20 major world producers supply nearly 80 different compositions.

12.5.1 Three Types of Embrittlement in Duplex Stainless Steels

Ferritic–austenitic stainless steels with a duplex microstructure can be classified into two subgroups (see Table 12.4):

1. Alloys with low-carbon content ($0.01\,\text{wt\%} \leq \text{C} \leq 0.08\,\text{wt\%}$), frequently mechanically worked and heat treatable
2. Alloys with high-carbon content ($0.3\,\text{wt\%} \leq \text{C} \leq 0.5\,\text{wt\%}$), used in the as-cast condition or after solution annealing

Duplex steels of higher carbon content show lower toughness and ductility but have an excellent wear resistance [81]. Duplex steels of lower carbon content have better formability and weldability compared to ferritic stainless steels.

Duplex stainless steels are susceptible to three types of embrittlement [82,83]:

1. Embrittlement caused by the presence of a carbide network, particularly in the austenite, in alloys with higher carbon content
2. Embrittlement caused by precipitation of the α′-phase, 475°C embrittlement of ferrite
3. Embrittlement caused by precipitation of the σ-phase, particularly in the ferrite

Duplex steels of lower carbon content solidify in a ferritic structure and the austenite forms in the solid state (see phase diagram of Figure 12.10). During hot working, between 900 (1650°F) and 1200°C (2200°F), a microstructure forms with alternating ferrite and austenite lamellae. The lamellar microstructure (see micrograph of Figure 12.11) forms because the interface energy of the α–γ interface is lower than the energies of the α–α and the γ–γ grain boundaries.

After solidification, the volume fraction of austenite and ferriteis is almost the same. Below 1000°C (1830°F) the proportion of ferrite to austenite can be only slightly modified. Ferrite strengthening occurs by solid solution hardening with preferential participation of chromium, molybdenum, and silicon, whereas austenite is stabilized and strengthened by nitrogen.

In the case of duplex steels with higher carbon content, the first phase that solidifies is also ferrite. The residual liquid enriched in carbon solidifies forming austenite and a chromium-rich $M_{23}C_6$-type carbide network. This carbide network within the austenite leads to an improved wear resistance. During cooling, austenite islands can also form in the ferrite grains. Some secondary carbide may also precipitate in austenite in the solid state. With the application of mechanical stresses, these carbides initiate fractures and cracks that propagate along the carbide network (see micrograph of Figure 12.12).

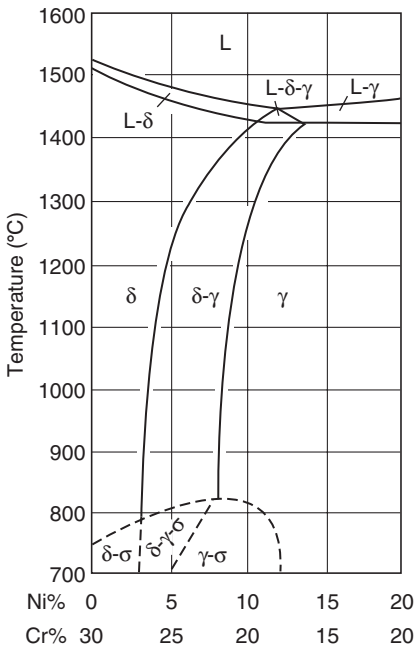

FIGURE 12.10 Section of the ternary Fe–Cr–Ni (in wt%) diagram at 65 wt% Fe. (From W. Reick, M. Pohl, and A.F. Padilha: *Metalurgia International*, 3, 46–50, 1990. With permission.)

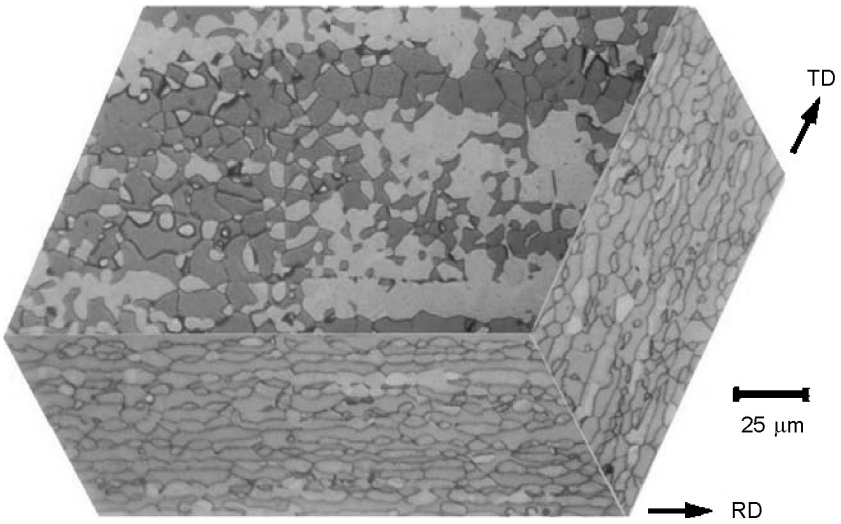

FIGURE 12.11 Three-dimensional composed micrograph of rolled duplex stainless steel. Optical microscopy. Ferrite is the darker phase. Etched with Behara II. (From W. Reick, M. Pohl, and A.F. Padilha: *ISIJ International (Japan)*, 38, 567–571, 1998. With permission.)

The schematic TTT diagram (Figure 12.13) shows the regions in which alpha prime (α') and sigma (σ) precipitation can occur. These precipitates increase the hardness and decrease ductility and the toughness. It must be pointed out that σ-phase precipitates within the ferrite [82–85]. In comparison to austenitic and ferritic stainless steels, precipitation of σ-phase in duplex alloys occurs at shorter times, at higher temperatures and larger volume fractions may be formed (see micrograph of Figure 12.14). For example, an aging treatment

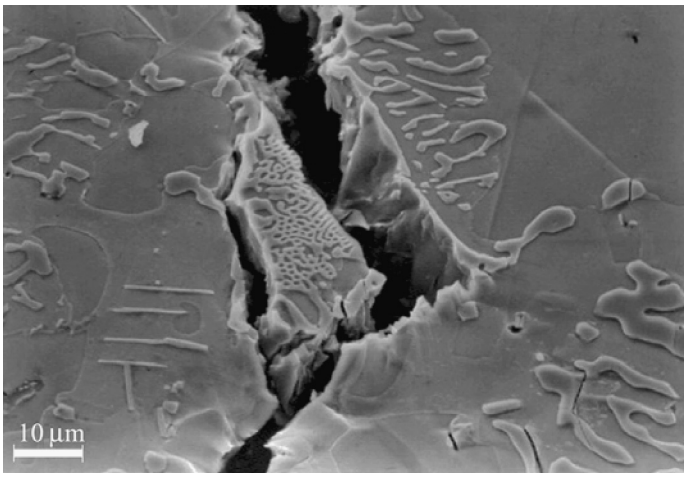

FIGURE 12.12 Crack propagation along carbide network in the high-carbon duplex stainless steel W. Nr. 1.4464. Scanning electron microscopy with secondary electrons. Etched with V2A-Beize. (From W. Reick, M. Pohl, and A.F. Padilha: *Metalurgia International*, 3, 46–50, 1990; M. Pohl, A.F. Padilha, and O. Fossmark: Bruchvorgänge in ferritisch-austenitischen Duplexstählen mit 475°-Versprödund. *Materialkundlich-Technische Reihe*, Vol. 9 (Gefüge und Bruch), K.L. Maurer and M. Pohl (Eds.), Gebrüder Borntraeger, Berlin, pp. 305–314, 1990. With permission.)

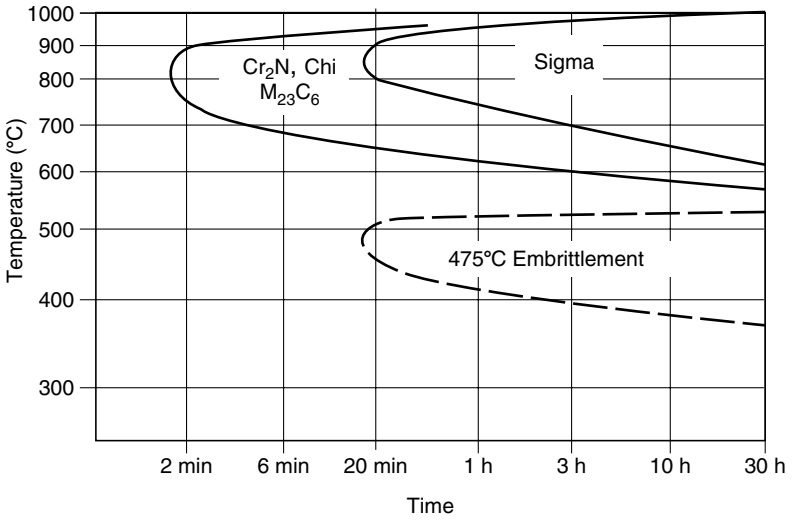

FIGURE 12.13 Schematic TTT diagram showing precipitation of sigma (σ), alpha prime (α′), and other phases in duplex stainless steels. (From W. Reick, M. Pohl, and A.F. Padilha: *Metalurgia International*, 3, 46–50, 1990. With permission.)

of the alloy DIN W. Nr.1.4462 for 200 min in the 800 to 850°C temperature range is sufficient for the formation of 15 to 20% of σ-phase [85]. In contrast to the carbides that form an almost continuous network in the austenitic regions, σ-phase is finely distributed within the ferrite. Applying mechanical stresses, σ-phase particles suffer brittle fracture. Once again, residual ductility can be linked to the austenitic regions.

The precipitation of α′ in ferritic and duplex stainless steels has been frequently discussed in the literature [80–83]. These precipitates are rich in chromium, have a cubic structure, are coherent with ferrite, and have an enormous coalescence resistance, even for very long exposure times at the 350 to 550°C (660 to 1020°F) temperature range. This renders their detection more difficult, even by transmission electron microscopy. This type of embrittlement leads to a cleavage fracture in the ferritic regions (see micrograph of Figure 12.15). Ductility is determined by the austenitic regions and is portrayed by the dimple-like fracture. Austenite volume fraction also plays an important role. Increasing chromium content in the alloy (and thereby the ferrite volume fraction) raises the sensitivity of the material to this type of embrittlement. The extent of embrittlement increases with aging time in the 350 to 550°C (660 to 1020°F) temperature range, while a maximum occurs at about 475°C (885°F).

In conclusion, ferritic–austenitic duplex stainless steels are susceptible to three types of embrittlement: carbides can form an almost continuous network in the austenitic regions, thereby offering a path for crack propagation; σ-phase particles, dispersed in the ferritic regions that suffer brittle fracture, and embrittle the material; and the α′-phase also causing embrittlement in the ferrite, leading to cleavage fracture. For all three embrittlement types, material residual ductility is given by the austenitic areas that undergo ductile dimple-like fracture. Owing to the σ-phase and α′-phase embrittlement, the upper application temperature is about 280°C (535°F) for nonwelded material and 250°C (480°F) for welded structures. Duplex alloys maintain excellent toughness at low temperatures and can be used down to −50°C (−58°F) or even lower temperatures, however the weld-metal behavior is not as good as the base metal.

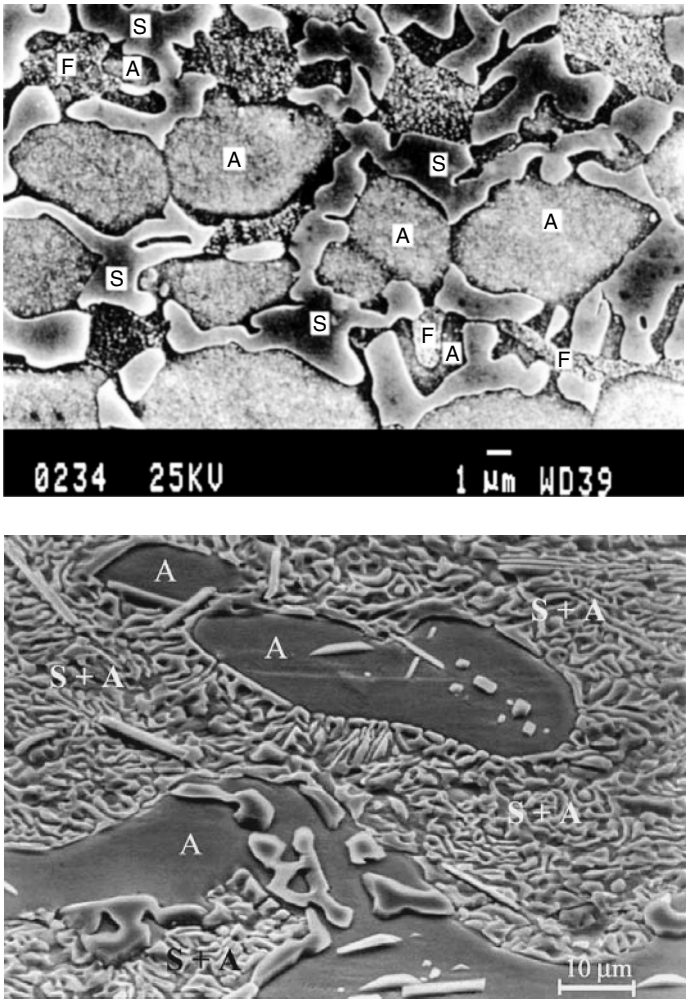

FIGURE 12.14 Sigma phase precipitation in duplex stainless steels observed using scanning electron microscopy with secondary electrons. Etched with V2A-Beize. A = austenite; F = ferrite; S = sigma phase. (a) Low-carbon duplex stainless steel W. Nr. 1.4462. (From A.F. Padilha, F.C. Pimenta Jr., and W. Reick: *Zeitschrift für Metallkunde*, 92, 351–354, 2001. With permission.) (b) High-carbon duplex stainless steel W. Nr. 1.4464. (From M. Pohl, A.F. Padilha, and O. Fossmark: Bruchvorgänge in ferritisch-austenitischen Duplexstählen mit 475°-Versprödund. *Materialkundlich-Technische Reihe*, Vol. 9 (Gefüge und Bruch), K.L. Maurer and M. Pohl (Eds.), Gebrüder Borntraeger, Berlin, pp. 305–314, 1990. With permission.)

12.5.2 Processing and Heat Treatment

The favorable combination of properties of duplex steels is intrinsically related to its microstructure. These steels solidify with ferritic structure and the austenite is formed in the solid state. Austenite nucleates at about 1300°C (2370°F) and grows first at the ferrite grain boundaries and later within the ferrite grains. Solidification cracks are rare and castability is excellent. Recrystallization kinetics are faster in ferrite than in austenite, despite the higher driving force for the recrystallization in austenite [84]. During hot deformation, at temperatures between 1000 (1830°F) and 1200°C (2190°F), alternate layers of ferrite and austenite are

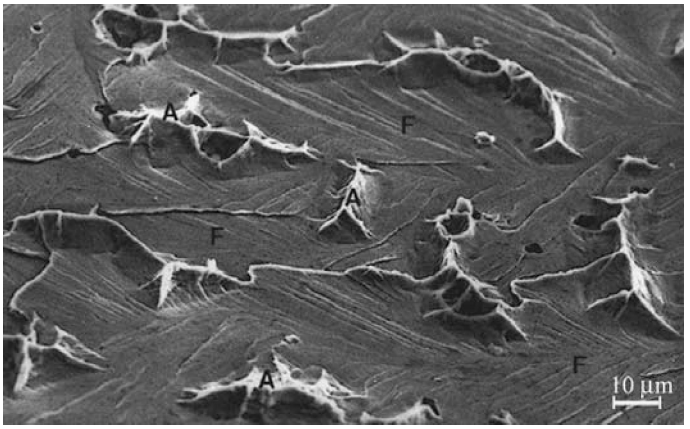

FIGURE 12.15 Ferrite brittle cleavage fracture (475°C embrittlement) caused by alpha prime (α′) in a duplex stainless steel. Scanning electron microscopy with secondary electrons. A = austenite; F = ferrite. (From W. Reick, M. Pohl and A.F. Padilha: *Metalurgia International*, 3, 46–50, 1990; M. Pohl, A.F. Padilha, and O. Fossmark: Bruchvorgänge in ferritisch-austenitischen Duplexstählen mit 475°-Versprödund. *Materialkundlich-Technische Reihe*, Vol. 9 (Gefüge und Bruch), K.L. Maurer and M. Pohl (Eds.), Gebrüder Borntraeger, Berlin, pp. 305–314, 1990. With permission.)

developed in the microstructure. Phase volumetric fractions must be nearly equal and the volumetric fraction of the minor phase should not be lower than 30% [86]. It must be remembered that the volume fraction of each phase is a function of composition and heat treatment. Furthermore, alloy compositions are adjusted to obtain equal amounts of ferrite and austenite after solution annealing at about 1050°C (1900°F). Cooling from the solution-annealing temperature should be sufficiently fast, generally into water, in order to avoid precipitation (see schematic TTT diagram of Figure 12.13), especially the 475°C (885°F) embrittlement due to alpha prime (α′). After welding, the solution-annealing treatment is recommended, followed by proper cooling.

12.6 MARTENSITIC STAINLESS STEELS

Martensitic stainless steels (see Table 12.5) are essentially Fe–Cr–C alloys, containing chromium in the range of 11.5 to 18 wt% and carbon in range of the 0.1 to 1.2 wt%. As chromium level is increased, carbon level has to increase also in order to stabilize austenite (see Figure 12.16). For the martensitic steels, it is, of course, essential to form austenite from which martensite is obtained on cooling. For example, for a complete austenitization, steels containing 13 wt% chromium need to have carbon content in excess of 0.15 wt% carbon and to be heated to at least 950°C (1740°F). Steels containing more chromium, say 17 wt%, need to have carbon content higher than 0.3 wt% carbon and to be heated to at least 1100°C (2000°F). As mentioned previously, both nitrogen and nickel expand the γ-loop, as shown in Figure 12.17 and Figure 12.18, respectively.

Other alloying elements frequently observed in martensitic stainless steels are nickel and molybdenum. Nickel entitles the usage of lower carbon contents and, as a consequence, higher toughness and corrosion resistance may be obtained. For soft but tougher martensitic steels containing lower carbon levels, nickel content may reach 5 wt%. These soft martensitic steels are frequently precipitation hardened as will be discussed in the next item. Molybdenum also improves corrosion resistance, in addition to improvement in toughness. It must be remembered that corrosion resistance in martensitic stainless steels is significantly lower if

TABLE 12.5
Chemical Composition (in wt%) of Some Typical Martensitic Stainless Steels

Type	UNS Designation	C	Mn	Si	Cr	Others	Austenitizing (°C)	Tempering (°C)	Tensile Strength (MPa)
AISI 403	S40300	≤0.15	≤1.00	≤0.50	11.50–13.00	Mo ≤ 0.60	925–1010	150–370	1105–1515
AISI 410	S41000	≤0.15	≤1.00	≤1.00	11.50–13.00	S ≥ 0.15	925–1010	150–370	1105–1515
AISI 416	S41600	≤0.15	≤1.25	≤1.0	12.0–14.0	Ni = 1.25–2.50	925–1010	150–370	1105–1515
AISI 420	S42000	≥0.15	≤1.00	≤1.00	12.0–14.0	Mo ≤ 0.75	980–1065	205–370	1550–1930
AISI 431	S43100	≤0.20	≤1.00	≤1.00	12.0–17.0	Mo ≤ 0.75	980–1065	205–370	1210–1515
AISI 440A	S44002	0.60–0.75	≤1.00	≤1.00	16.0–18.0	Mo ≤ 0.75	1010–1065	150–370	HRC = 49–57
AISI 440B	S44003	0.75–0.95	≤1.00	≤1.00	16.0–18.0	Ni = 0.40–0.60	1010–1065	150–370	HRC = 53–59
AISI 440C	S44004	0.95–1.20	≤1.00	≤1.00	16.0–18.0	Mo ≤ 0.75	1010–1065	150–370	HRC ≥ 60
AISI 440F	S44004	0.95–1.20	≤1.25	≤1.00	16.0–18.0	S = 0.10–0.35 N ≤ 0.08	1010–1065	150–370	HRC ≥ 60

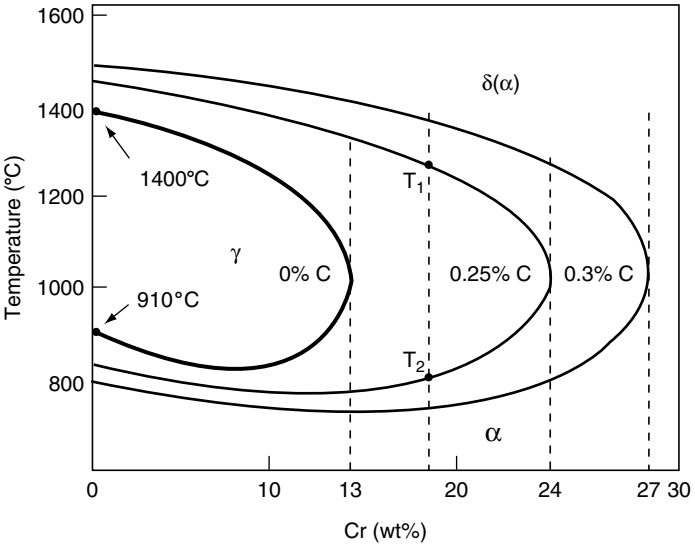

FIGURE 12.16 Projection of the ternary Fe–Cr–C diagram on the temperature x% Cr (in wt%) plane. (From P. Lacombe and G. Béranger: Structure and equilibrium diagrams of various stainless steel grades (Chapter 2). In: *Stainless steels*. P. Lacombe, B. Baroux, and G. Beranger (Eds.), les editions de physique, Les Ulis, France, pp. 13–58, 1993. With permission.)

compared to other stainless steels discussed previously in this chapter. They are inadequate for usage in more aggressive media [87–89].

The most popular composition (AISI 410) contains about 12.5 wt% chromium and 0.1 wt% carbon. In the hardened condition, its YS may reach about 1300 MPa, however upon tempering at higher temperatures its strength decreases significantly. The YS attained

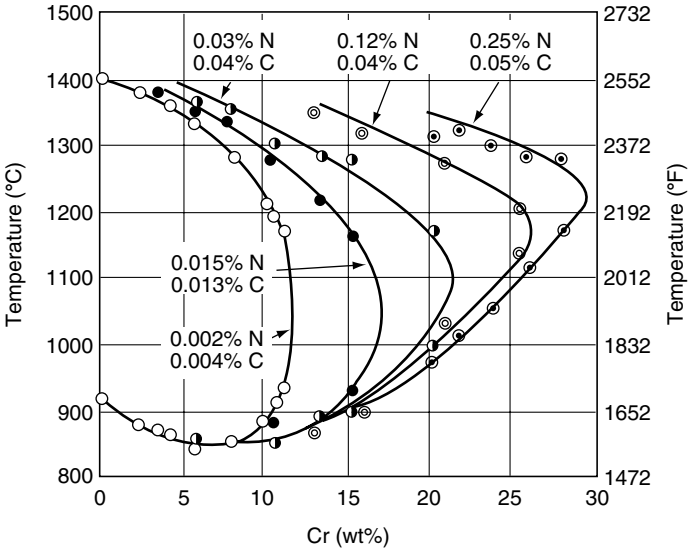

FIGURE 12.17 Shift of the γ-loop with nitrogen content (in wt%). (From P.T. Lovejoy: Structure and constitution of wrought martensitic stainless steels (Chapter 6). In: *Handbook of stainless steels*. D. Peckner and I.M. Bernstein (Eds.), McGraw-Hill, New York, pp. 6-1–6-23, 1977. With permission.)

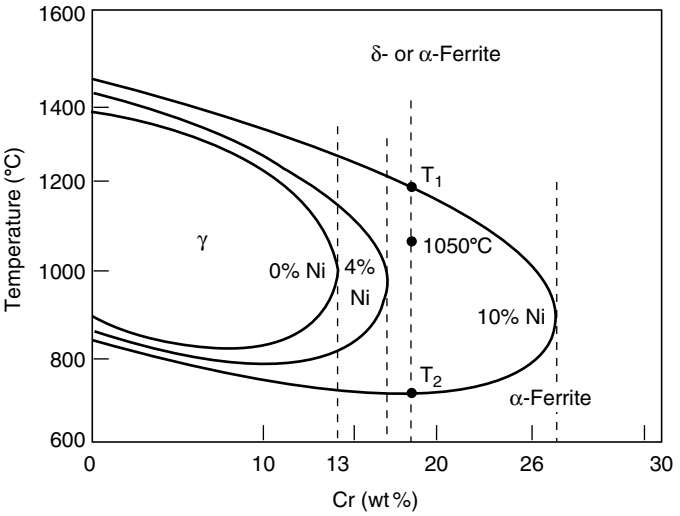

FIGURE 12.18 Influence of nickel on the extent of the γ-loop in ternary Fe–Cr–Ni alloys (in wt%). (From P. Lacombe and G. Béranger: Structure and equilibrium diagrams of various stainless steel grades (Chapter 2). In: *Stainless steels*. P. Lacombe, B. Baroux, and G. Beranger (Eds.), les editions de physique, Les Ulis, France, pp. 13–58, 1993. With permission.)

by a martensitic stainless steel depends mainly on its carbon level and some compositions may reach a YS of the order of 1900 MPa. The maximum chromium level is about 18 wt% and some compositions have up to 1 wt% molybdenum. As mentioned previously, both chromium and molybdenum shrink the austenitic field, which may be expanded by carbon and nickel. For example, a steel containing 17 wt% chromium and 0.2 wt% carbon will require 2 wt% nickel to avoid delta-ferrite formation.

Martensitic stainless steels may be subdivided (see Table 12.5) into three subgroups: (a) low-carbon steels for turbines; (b) medium-carbon steels for cutlery; and (c) high-carbon wear-resistant steels. The microstructure of each group is also characteristic: (a) martensitic needle-like microstructure; (b) very fine martensitic microstructure; and (c) ultrafine martensitic microstructure containing primary carbides, respectively. Moreover, higher carbon steels, such as the 440C, or nickel containing, such as the AISI 431, may present large amounts (more than 30% in volume) of retained austenite after quenching. Sigma-phase precipitation is of minor importance in this class of steels [88]. Depending on tempering temperature and chemical composition, especially the Cr/C ratio, several carbides may precipitate (see micrographs of Figure 12.19 and Figure 12.20), such as the M_2X, M_3C, M_7C_3, $M_{23}C_6$, and MC types [87–89].

Low-carbon martensitic stainless steels containing up to 12 wt% chromium are the most commonly used in this class. Carbon content is low because the main application of these steels is for structural purposes where high mechanical strength as well as weldability, workability, and toughness are required. They are employed in blades or other components in steam turbines, pump shafts, axels, and other components for the chemical, petrochemical and oil industries, railway axles, components for the pulp and paper industry, and oven parts that operate under 400°C (750°F).

A typical representative of the medium-carbon martensitic stainless steels is the AISI 420, containing 13 wt% chromium and 0.35 wt% carbon. Increasing the carbon content in martensitic steels leads to higher hardness and mechanical resistance with a corresponding loss in toughness and weldability. Furthermore, the higher austenitizing temperature leads to the

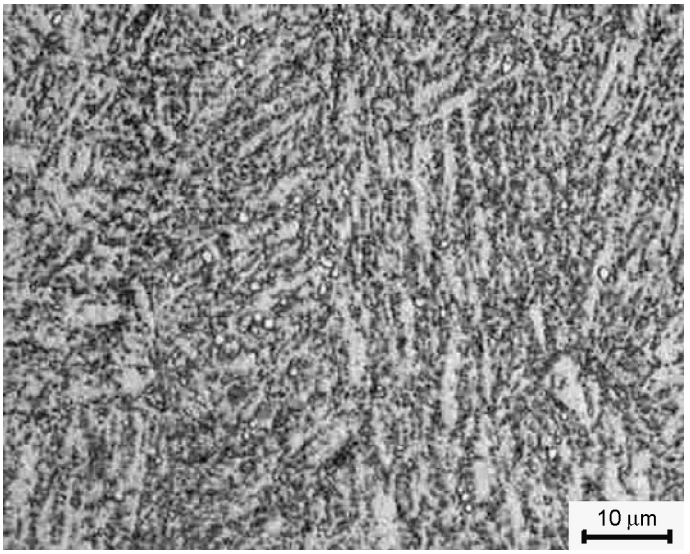

FIGURE 12.19 AISI 410 martensitic stainless steel, quenched and tempered to 20 HRC. Microstructure of tempered martensite with fine-carbide precipitates. Optical microscopy. Etched with Villela. (Courtesy of José Belotti Neto, IPT, S. Paulo, Brazil.)

possibility of $M_{23}C_6$ grain boundary precipitation (see micrograph shown in Figure 12.20). These steels are employed in cutlery, surgical and dental instrumentation, axles, valves, pumps, steam turbine blades and other components, plastic molds, and in the glass industry.

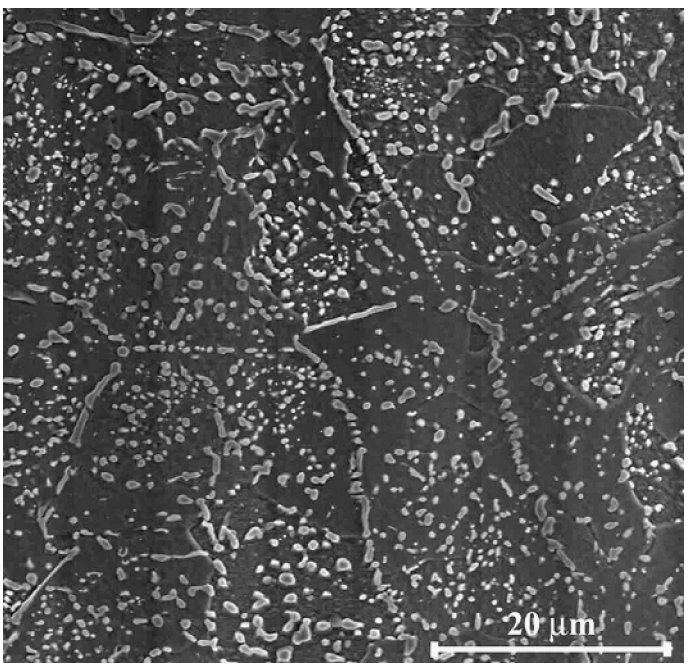

FIGURE 12.20 AISI 420 martensitic stainless steel. Microstructure of tempered martensite with intergranular and intragranular precipitates. Scanning electron microscopy using secondary electrons. Etched with Villela. (Courtesy of José Belotti Neto, IPT, S. Paulo, Brazil.)

The main representative of the higher carbon martensitic stainless steels is the AISI 440 series. The high-chromium levels make adequate their usage in marine atmospheres or in seawater. High-carbon content stabilizes austenite, increases hardness, mechanical resistance, adhesive and abrasive wear resistance. While adhesive wear resistance mainly requires higher hardness, abrasive wear also requires primary carbides. Normally, these steels are not welded. Some typical applications are roller bearings, valve needles, and spray nozzles.

12.6.1 Processing and Heat Treatment

Prior to final hardening and tempering heat treatments, martensitic stainless steels are annealed in order to be machined and cold worked. For example, an AISI 410 is annealed in the 750 (1380°F) to 900°C (1650°F) temperature range for 2 to 4 h and furnace or air cooled. In such a condition, hardness is about 160 HB, YS of 300 MPa, tensile strength of 500 MPa, elongation of 20%, with an area reduction of 60%.

Prior to their final usage, martensitic stainless steels are submitted to the same heat treatment sequence as that for carbon steels, namely they are austenitized, hardened by quenching, and tempered in order to improve ductility and toughness. At high temperatures, their stable structure is austenitic and at room temperature it is a stable mixture of ferrite and carbide. Table 12.5 presents some typical austenitizing temperatures. As the stainless steels have a low thermal conductivity, depending on the cross-sectional size and complexity, preheating in the 550 to 800°C (1020 to 1470°F) temperature range, prior to final austenitizing temperature, is recommended. Air heating may cause decarburization.

The formation of a more stable (ferrite + carbides) microstructure is very sluggish (see Figure 12.21a) and the tendency toward martensite formation (high hardenability) is very high. Therefore, the majority of martensitic stainless steels form martensite on air cooling, even for sections that are up to about 300 mm in thickness. Hardening media may be air or oil. While oil cooling is preferred in order to avoid carbide precipitation, air cooling may be needed to avoid distortions in more complex sections. Martempering is also possible in this class of steels. Martensite hardness depends essentially on carbon content varying from about 35 HRC for a 0.1 wt% carbon to 60 HRC for 0.5 wt% carbon, thereon increasing little for carbon higher than 0.5 wt%. For low-carbon martensitic steels, such as the AISI 410, the M_s and M_f temperatures are relatively high, 350 (660°F) and 250°C (480°F), respectively, and decrease with increasing carbon content. High-carbon steels may present retained austenite and a subzero treatment around −75°C (−95°F), immediately after hardening, is recommended. Double tempering is also very common. Tempering temperature is determined by the required mechanical properties (see Figure 12.21b). In general, the 420 (790°F) to 600°C (1110°F) temperature range must be avoided, because within this range brittleness may be induced apart from loss in corrosion resistance.

12.7 PRECIPITATION-HARDENABLE STAINLESS STEELS

Steels of this class have been developed in order to offer high mechanical resistance and reasonable toughness, with superior corrosion resistance when compared to the martensitic steels of the Fe–Cr–C system. PH stainless steels may be classified [90,91] according their microstructure resulting from the solution-annealing heat treatment into austenitic, semiaustenitic, and martensitic stainless steels (see Table 12.6) Semiaustenitic steels will transform into martensite during subsequent heat treatments. Practically all PH steels have a low-carbon level ($\leq$0.1 wt%) with nickel additions. Molybdenum is added to increase mechanical and corrosion resistance. PH is attained through additions of aluminium, titanium, niobium, or copper.

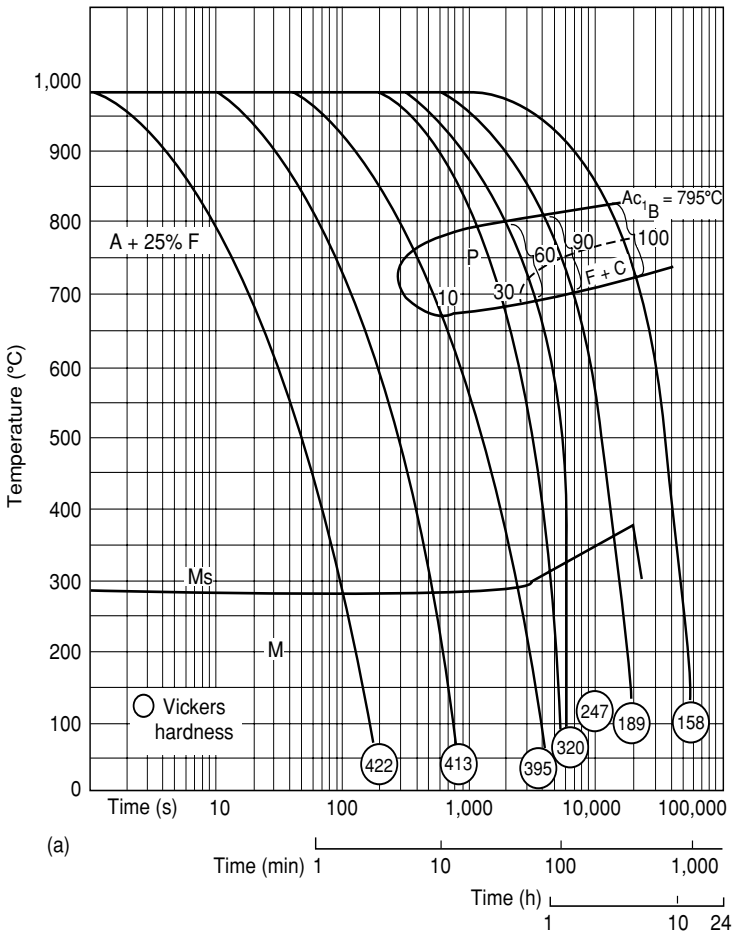

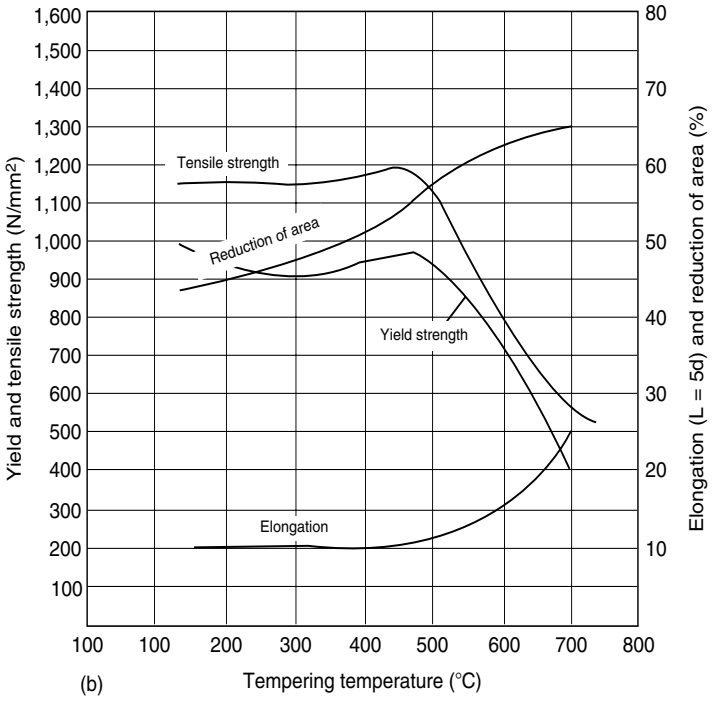

FIGURE 12.21 AISI 410 steel. (a) Continuous cooling transformation diagram and (b) tempering temperature effect on mechanical properties (After Krupp Stahl AG catalogue, Druckschriften-nr. 4.102, October, 1984, Germany.)

TABLE 12.6
Chemical Composition (in Wt%) of Some Typical Precipitation-Hardenable Stainless Steels

Type	UNS Designation	C	Mn	Si	Cr	Ni	Mo	Others
Austenitic								
A286	S66286	≤0.08	≤2.00	≤1.00	13.50–16.00	24.0–27.0	1.00–1.50	Ti = 1.90–2.35 Al = 0.35 V = 0.10–0.50 B = 10–100 ppm
17–10P		0.07	0.75	0.50	17.0	10.5		P = 0.30
Martensitic								
Stainless W	S17600	≤0.08	≤1.00	≤1.00	16.0–17.5	6.0–7.5	—	Al = 0.4 Ti = 0.4–1.2
17–4 PH	S17400	≤0.07	≤1.00	≤1.00	12.50–17.50	3.00–5.00	—	Nb = 0.15–0.45 Cu = 3.00–5.00
15–5 PH	S15500	≤0.07	≤1.00	≤1.00	14.00–12.50	3.50–5.50	—	Nb = 0.15–0.45 Cu = 2.50–4.50
Custom 450	S44000	≤0.05	≤1.00	≤1.00	14.00–16.00	5.00–7.00	0.50–1.00	Nb≥8 × %C Cu = 1.25–1.75
Custom 455	S45500	≤0.05	≤0.50	≤0.50	11.00–12.50	7.50–9.50	0.50	Nb = 0.10–0.50 Cu = 1.50–2.50
PH 13–8 Mo	S13800	≤0.05	≤0.20	≤0.10	12.25–13.25	7.50–8.50	2.00–2.50	Al = 0.90–1.35 N = 0.01
Semiaustenitic								
17–7 PH	S17700	≤0.09	≤1.00	≤1.00	16.00–18.00	6.50–7.75	—	Al = 0.75–1.50
15–7 PH	S15700	≤0.09	≤1.00	≤1.00	14.00–16.00	6.50–7.75	2.00–3.00	Al = 0.75–1.50
AM-350	S35000	0.07–0.11	0.5–1.25	≤0.5	16.0–17.0	4.0–5.0	2.5–3.25	N = 0.07–0.13
AM-355	S35500	0.10–0.15	0.5–1.25	≤0.5	12.0–16.0	4.0–5.0	2.5–3.25	

Several precipitates lead to hardening effects, according to the alloy type and the heat treatment procedure: nickel- and aluminium-rich intermetallic phases such as γ'-$Ni_3(Al,Ti)$, Ni_3Ti and β-NiAl, iron-, molybdenum-, and niobium-rich Laves phases such as $Fe_2(Mo,Nb)$, copper-rich or even nitrides of the Cr_2N type, may be formed. In a majority of the cases they are intermetallic phases that are rich in nickel, of the Ni_3M type, where M = Al, Ti, Nb, or Mo. Titanium and niobium are also nitride and carbonitride formers which are very stable and are of the MN and M(C,N) types, taking carbon and nitrogen out of solid solution. Copper, in addition to causing hardening through precipitation, enhances corrosion resistance when in solid solution. Seetharaman and coauthors [92] investigated the precipitation behavior of the martensitic PH 13-8 Mo stainless steel. Aging in the temperature range 450 to 575°C leads to finely distributed coherent particles of NiAl, which have a B2 of the CsCl-type crystal structure. The mean size of the particles, even after aging at 625°C (1160°F) for 4 h, was about 70 Å. Thus these precipitates were found to be highly resistant to overaging.

Compared to martensitic stainless steels of the Fe–Cr–C system, PH steels present a superior ductility and toughness. Some alloys have YS of up to 1700 MPa. Relative to other stainless steel types, PH steels have a moderate-to-good corrosion resistance.

The A-286 (UNS S66286) alloy is probably the most well-known austenitic PH type. It is an alloy containing (in wt%): Fe–15% Cr–25 % Ni–1.25% Mo–2% Ti–0.3% Al. Its matrix is very stable and even after large cold reductions no deformation-induced martensite formation or sigma-phase precipitation due to high temperature exposure may be formed. Solution-annealing heat treatment is performed at around 1050°C. Aging is done in the 700 to 760°C (1290 to 1400°F) temperature range and causes precipitation of intermetallic phases, γ'-$Ni_3(Al,Ti)$, with a fcc-ordered crystal structure, rich in nickel, titanium, and aluminium. Upon full aging, YS of about 600 MPa may be expected. If from one hand, this strength level is substantially lower when compared to the PH martensitic or semimartensitic steels, on the other hand, they present excellent toughness and corrosion resistance. Among the three types of PH steels the austenitic steels are least used.

Within the PH martensitic steels, the 17-4 PH (UNS S17400) is the most popular, containing (in wt%) 17% Cr, 4% Ni, 4% Cu, and 0.3% Nb. The M_s temperature is above room temperature. On air cooling from the solution-annealing temperature (1040°C or 1900°F) the matrix does not have any retained austenite, however it may present some delta-ferrite stringers. Aging treatment is performed in the 480 to 620°C (900 to 1150°F) temperature range and leads to very fine precipitation of copper particles. On solution annealing, YS goes up to about 750 MPa and after full aging it may reach 1200 MPa.

Within the PH semiaustenitic steels, the most well-known composition is the 17-7 PH (UNS S17700), containing (in wt%): 17% Cr, 7% Ni, and 1.2% Al. Its composition is balanced so that austenite has a low thermodynamic stability so it may be destabilized by heat treatment or cold working. When austenitized at high temperatures, practically all alloying elements are in solid solution. The M_s temperature is somewhat above room temperature. On air cooling, from solution annealing, its microstructure is predominantly austenitic. Austenite is destabilized due to the increase of the M_s temperature of the depleted matrix, through the precipitation of intermetallic phases and carbides in the 750 to 950°C (1380 to 1740°F) temperature range. Cold working or subzero cooling may also cause austenite to transform into martensite. Final aging treatment is performed in the 455 to 565°C (850 to 1050°F) temperature range and leads to precipitation in the martensitic matrix of nickel- and aluminium-rich intermetallic compounds. After heavy cold working and aging, YS is about 1600 MPa. The semiaustenitic stainless steels may have up to 20% delta ferrite, which remains practically unaltered during heat treatments.

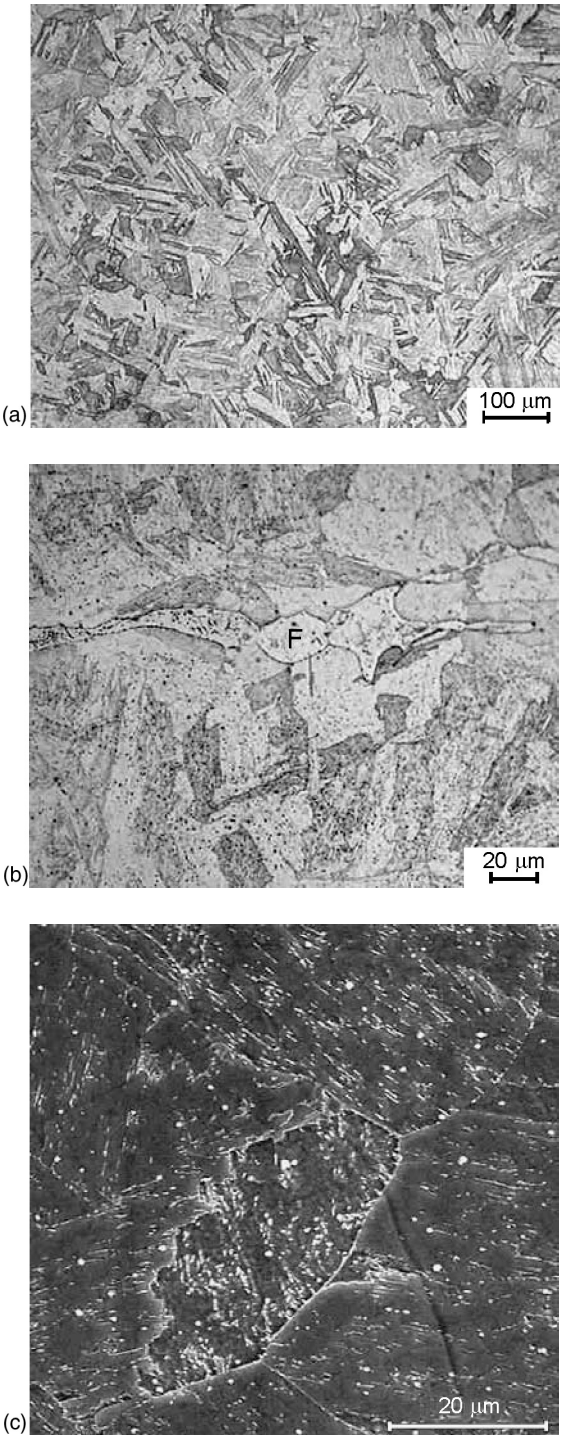

FIGURE 12.22 Stainless steel of the 15-5 PH type after hardening and tempering, hardness of 40 HRC: (a) and (b) Optical micrographs illustrating ferrite islands (F), fine-carbide precipitation in a tempered-martensite matrix; (c) Scanning electron microscopy using secondary electrons illustrating carbide precipitation. Etched with Villela. (Courtesy of José Belotti Neto, IPT, S. Paulo, Brazil.)

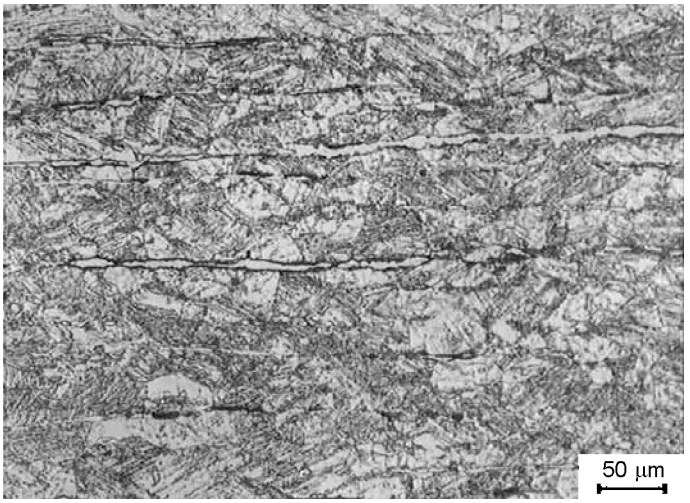

FIGURE 12.23 Stainless 17-7 PH-type steel in the RH 950 (i.e., refrigerated and tempered at 950°F or 510°C) condition, of the ASTM A 564 standard. Optical microscopy shows ferrite stringers and fine-carbide precipitates within the martensitic matrix. Etched with Villela. (Courtesy of José Belotti Neto, IPT, S. Paulo, Brazil.)

12.7.1 Processing and Heat Treatment of Martensitic PH Stainless Steels

PH steels that form martensite can be subdivided into two groups, namely single heat treatment (martensitic) stainless and double heat treatment (semiaustenitic) stainless steel.

The alloys that require a single heat treatment are solution annealed at about 1040°C (1900°F), leading to a martensitic microstructure without retained austenite at room temperature. Then these alloys are precipitation aged by intermetallic phases, through tempering in the 480 to 620°C temperature range. The properties obtained depend mainly on the alloy chemical composition and tempering treatment procedure. For example, for a 17-4 PH alloy, after aging for 1 h at 480°C (900°F), YS may reach 1310 MPa, and after 4 h aging at 620°C (1150°F), YS is only 930 MPa. Typical examples of these alloys are the 17-4 PH, 15-5 PH, and custom 450 types. Micrographs shown in Figure 12.22 illustrate the typical microstructure of a martensitic stainless steel of this type (15-5 PH) after quenching and tempering.

Alloys requiring double heat treatment are semiaustenitic, which after solution annealing, remain austenitic. A typical example of this group is the 17-7 PH, which is hardened in water from 1065°C (1950°F). Austenite conditioning is performed at about 760°C (1400°F) in order to precipitate (mainly the $M_{23}C_6$ carbides) destabilizing austenite so that it transforms into martensite on cooling under 15°C. This treatment leads to the T condition. Aging is performed in the 565 (1050°F) to 595°C (1100°F) temperature range, leading to a tensile strength from 1030 to 1240 MPa. This heat treatment cycle is known as the TH treatment. Another alternative aiming at austenite conditioning is to perform the heat treatment conditioning at a higher temperature, typically 955°C (1750°F), where less carbides precipitate, austenite destabilization is less accentuated and martensite transformation requires a subzero (−75°C) treatment. This procedure is the R condition. Austenite to martensite transformation can also be obtained by severe cold working, between 60 and 70% reduction. This procedure

TABLE 12.7
Mechanical Properties of a 17-7 PH Steel, for Several Heat Treatments

Condition	Treatment	Yield Strength (MPa)	Tensile Strength (MPa)	Elongation (%)
"A"	1040 to 1080°C, air or water cooled	<380	<1030	18
TH 1050	"A" + 90 min 955°C air cooled + 60 min at room temperature + 90 min at 565°C	960–1030	1170–1240	5–6
RH 950	"A" + 10 min at 955°C with air cooling + 8 h at –73°C + 60 min at 510°C (950°F)	1240–1310	1370–1450	4–5
"C"	"A" + 50% cold working	>1200	>1400	1
CH 900	"C" + 60 min at 480°C	>1580	>1650	1

is the C condition. After the austenite to martensite transformation, using any of these procedures, tempering follows in the 510 (950°F) to 595°C (1100°F) temperature range, leading to a tensile strength of 1035 to 1450 MPa. Typical examples of alloys of this group are the 17-7 PH and 15-7 PH. The micrograph shown in Figure 12.23 illustrates the typical microstructure of a 17-7 PH steel of this group. Table 12.7 presents the large variety in mechanical properties that can be obtained in a steel of the 17-7 PH type.

12.8 FINAL REMARKS

The world production of stainless steels, despite its greater growth rate compared to the average of all other steel types, represents only a little more than 2% of the total world steel production. However, stainless steel strip costs 5 to 10 times more than mild steel strip, despite the fact that both may offer similar YS in the annealed condition. Nevertheless, the construction of various parts and equipments and even some industrial sectors is unthinkable without the availability of stainless steel. About 70% of the stainless steel production is of the austenitic type. The almost centenary composition of the V2A or AISI 304 is the most consumed type of stainless steel in the world. Despite this fact, the standards in the industrialized countries show hundreds of different stainless steel compositions of different types, making available for the designer a vast range of properties. Stainless steels are produced in a variety of forms and geometries, with a strong predominance of flat products. During steel selection, a rule of thumb is that mechanical strength gains are linked to losses in toughness and ductility. In the case of the stainless steels this situation is even more critical because, in general, the steels that have higher mechanical properties, such as the martensitic or PH types, have low corrosion resistance when compared with the traditional austenitic or ferritic steels. Duplex stainless steels have an intermediate position between these two one-phase groups and have a superior corrosion resistance, hence their substantial growth in the last decades. The challenge is to develop a high strength stainless steel with a YS higher than 1500 MPa and with a high corrosion resistance. Nowadays, in order to achieve these levels of strength and high corrosion resistance, nitrogen additions of over 0.5 wt% and cold work hardening have been made, however these materials cannot be welded without undesirable phase transformations such as recrystallization or precipitation.

Recently, a new class of high-strength nanograin size austenitic stainless steels has been developed by combining solid solution hardening and grain-boundary hardening employing high nitrogen (ca. 1 wt%). Average grain diameters as fine as 50 to 250 nm were

achieved, and YS levels of more than 2000 MPa in the solution-annealed condition have been measured [93].

As to the martensitic stainless steels, considerable progress has been made recently [94]. Normally, martensitic stainless steels rarely attain hardness higher than 60 HRC, even for high-carbon levels, due to retained austenite. A careful combination of carbon and nitrogen contents, together with cold working and deep-freezing, can result in hardness between 61 (in this case even after tempering) and 68 HRC [94].

In summary, it may be mentioned that for austenitic, ferritic, and duplex stainless steels the solution-annealing heat treatment followed by proper cooling is the most important practice. However, caution should be exercised during actual usage of these steels because deleterious precipitation can occur, as discussed in detail in several parts (Section 12.2 through Section 12.5) of this chapter. On the other hand, martensitic and PH stainless steels demand more complex heat treatment cycles, as pointed out in Section 12.6 and Section 12.7.

REFERENCES

1. H. Krainer: 50 Jahre nichrostender Stahl. *Techn. Mitt. Krupp. Werksberichte*, 20, 165–179 (1962).
2. M.A. Streicher: Stainless steels: past, present and future. In: *Stainless Steel' 77*. R.Q. Barr (Ed.), London, Climax Molybdenum Company, London, England, pp. 1–34 (1978).
3. R. Castro: Historical background to stainless steels (Chapter 1). In: *Stainless steels*. P. Lacombe, B. Baroux, and G. Beranger (Eds.), les editions de physique, Les Ulis, France, pp. 1–12 (1993).
4. H.-J. Eckstein: *Korrosionsbeständige Stähle*, Deutscher Verlag für Grundstoffindustrie GmbH, Leipzig (1990).
5. P. Monnartz: Beitrag zum Studium der Eisenchromlegierungen unter besonderer Berücksichtigung der Säurebeständigkeit. *Metallurgie*, 8, 161–176, 193–203, (1911).
6. E.C. Bain and W.E. Griffiths: Introduction to the iron–chromium–nickel alloys. *Transactions AIME*, 75, 166–213 (1927).
7. C.V. Roscoe and K.J. Gradwell: The history and development of duplex stainless steels. In: *International Conference on Duplex Stainless Steels*. Den Haag, Holland, pp. 126–135, (1986).
8. W. Reick, M. Pohl, and A.F. Padilha: Development of ferritic–austenitic duplex stainless steels-historical and perspectives. *Metalurgia & Materiais ABM* (Brazil), 48, 551–563 (1992) (in Portuguese).
9. *Metals Handbook*, 8th ed.: *Metallography, Structures and Phase Diagrams*, Vol. 8, ASM International, Materials Park, OH (1973).
10. H. Baker (Ed.): *ASM Handbook*, Vol. 3: *Phase Diagrams*, ASM International, Materials Park, OH (1992).
11. J.R. Davis (Ed.): *ASM Speciality Handbook: Stainless Steels*, ASM International, Materials Park, OH (1994).
12. E. Folkhard: *Welding Metallurgy of Stainless Steels*, Springer-Verlag, Wien (1984).
13. V.G. Rivlin and G.V. Raynor: Phase equilibria in iron-ternary alloys. I. Critical evaluation of constitution of chromium–iron–nickel system. *International Metallurgical Reviews*, 25, 21–38 (1980).
14. A.F. Padilha and P.R. Rios: Decomposition of austenite in austenitic stainless steels. *ISIJ International (Japan)*, 42, 325–337 (2002).
15. A.L. Schaeffler: Selection of austenitic electrodes for welding dissimilar metals, *Welding Journal*, 26, Res. Suppl., 603s–620s (1947).
16. A.L. Schaeffler: Welding dissimilar metals with stainless electrodes. *Iron Age*, 162, 73–79 (1948).
17. A.L. Schaeffler: Constitution diagram for stainless steel. *Metal Progress*, 56, 680, 680B (1949).
18. W.T. DeLong: Ferrite in austenitic stainless steel weld metal. *Welding Journal*, 53, Res. Suppl., 273s–286s (1974).
19. F.C. Hull: Effects of composition on embrittlement of austenitic stainless steels. *Welding Journal*, 52, Res. Suppl., 193s–203s (1973).

20. R.H. Espy: Weldability of nitrogen-strengthened stainless steels. *Welding Journal*, 61, Res. Suppl., 149s–156s (1982).
21. M. Schirra: Die historisch-empirische Entwicklung des Gefügediagrammes der Cr-Ni-Stähle. *Stahl und Eisen*, 112(10), 117–120 (1992).
22. G.K. Allan: Solidification of austenitic stainless steels. *Ironmaking and Steelmaking*, 22, 465–477 (1995).
23. A. Westgren: Complex chromium and iron carbides. *Nature*, 132, 480 (1933).
24. A.F. Padilha, R.L. Plaut, and P.R. Rios: Annealing of cold-worked austenitic stainless steels, *ISIJ International (Japan)*, 43, 135–143 (2003).
25. F. Siciliano Jr., J.C. Dutra, F.C. Pimenta Jr., and A.F. Padilha: Abnormal grain growth in ferritic and austenitic stainless steels due to second phase dissolution, *Proceedings of the First Joint International Conference on Recrystallization and Grain Growth*, August 27–31, Springer-Verlag, Berlin, Vol. 1, pp. 471–476 (2001).
26. J. Barcik: Mechanism of sigma-phase precipitation in Cr–Ni austenitic steels. *Materials Science and Technology*, 4, 5–15 (1988).
27. P. Rozenak, L. Zevin, and D. Eliezer: Hydrogen effects on phase transformations in austenitic stainless steels. *Journal of Materials Science*, 19, 567–573 (1984).
28. D.J. Dyson and B. Holmes: Effect of alloying additions on lattice parameter of austenite. *Journal of The Iron and Steel Institute*, 208, 469–474 (1970).
29. G.J. Eichelmann and F.C. Hull: The effect of composition of spontaneous transformation of austenite to martensite in 18–8-type stainless steel. *Transactions ASM*, 45, 77–104 (1953).
30. E.P. Butler and M.G. Burke: Chromium depletion and martensite formation at grain boundaries in sensitized austenitic stainless steel. *Acta Metallurgica*, 34, 557–570 (1986).
31. M.W. Bowkett, S.R. Keown, and D.R. Harries: Quench- and deformation-induced structures in two austenitic stainless steels. *Metal Science*, 16, 499–517 (1982).
32. P. Marshall: *Austenitic Stainless Steels: Microstructure and Mechanical Properties*, Elsevier, New York, pp. 23–79 (1984).
33. Y. Kaieda and A. Oguchi: Strain-induced transformation and plastic deformation behaviour of a 17Cr-7Ni-1Al steel at high hydrostatic pressure. *Journal of Materials Science*, 20, 1847–1858, (1985).
34. T.J. Angel: Formation of martensite in austenitic stainless steels. *Journal of The Iron and Steel Institute*, 177, 165–174 (1954).
35. L.F.M. Martins, R.L. Plaut, and A.F. Padilha: Effect of carbon on the cold-worked state and annealing behaviour of two 18wt%Cr–8wt% Ni austenitic stainless steels. *ISIJ International (Japan)*, 38, 572–579 (1998).
36. S.F. Peterson, M.C. Mataya, and D.K. Matlock: The formability of austenitic stainless steels. *The Journal of the Minerals, Metals and Materials Society (JOM)*, 49(9), 54–58 (1997).
37. V. Taylan, R.H. Wagoner, and J.K. Lee: Formability of stainless steel. *Metallurgical and Materials Transactions A*, 29A, 2161–2172 (1998).
38. J.C. Bavay: The high chromium and molybdenum ferritic stainless steels. In: *Stainless steels*. P. Lacombe, B. Baroux, and G. Beranger (Eds.), les editions de physique, Les Ulis, France, pp. 535–547 (1993).
39. R.D. Campbell: Ferritic stainless steel welding metallurgy. *Key Engineering Materials*, 69, 70, 167–216 (1992).
40. A.F. Padilha, F.C. Pimenta Jr., and W. Reick: A comparative study on the precipitation of the sigma phase in a superferritic and in a duplex stainless steel. *Zeitschrift für Metallkunde*, 92, 351–354 (2001).
41. G. Bandel und W. Tofaute: Die Versprödung von hochlegierten Chromstählen im Temperaturgebiet um 500°. *Archiv für das Eisenhüttenwesen*, 14, 307–319 (1942).
42. R.M. Fischer, E.J. Dullis, and K.G. Carroll: Identification of the precipitate accompanying 885°F embrittlement in chromium steels. *Transactions of The Metallurgical Society of AIME (Journal of Metals)*, 197, 690–695 (1953).
43. M. Anglada, J. Rodriguez, and A. Isalgué: Influence of the plastic strain amplitude on the stability of the spinodal microstructure in the cyclic deformation of a Fe–28Cr–2Mo–4Ni–Nb alloy. *Scripta Metallurgica*, 23, 1633–1638 (1989).

44. A. Isalgué, M. Anglada, J. Rodriguez-Carvajal, and A. De Geyer: Study of the spinodal decomposition of an Fe–28Cr–2Mo–4Ni–Nb alloy by small-angle neutron scattering. *Journal of Materials Science*, 25, 4977–4980 (1990).
45. D. Chandra and L.H. Schwartz: Mössbauer effect study of the 475°C decomposition of Fe–Cr. *Metallurgical Transactions*, 2, 511–519 (1971).
46. H.D. Solomon and L.M. Levinson: Mössbauer effect study of 475°C embrittlement of duplex and ferritic stainless steels. *Acta Metallurgica*, 26, 429–442 (1978).
47. H. Kuwano, Y. Ishikawa, T. Yoshimura, and Y. Hamaguchi: Characterization of the spinodal decomposition of Fe–Cr alloys by Mössbauer spectroscopy. *Hyperfine Interactions*, 69, 501–504 (1991).
48. M.J. Marcinkowski, R.M. Fischer, and A. Szirmae: Effect of 500°C aging on the deformation behaviour of an iron–chromium alloy. *Transactions of The Metallurgical Society of AIME*, 230, 676–689 (1964).
49. M.J. Blackburn and J. Nutting: Metallography of an iron–21% chromium alloy subject to 475°C embrittlement. *Journal of The Iron and Steel Institute*, 202, 610–613 (1964).
50. M.M. Ura, A.F. Padilha, and N. Alonso: Influence of alpha prime (α') on pitting corrosion resistance of duplex stainless steels. *Anais do 49° Congresso Anual da ABM*, S. Paulo (Brazil), Vol. 8, pp. 337–349 (1995) (in Portuguese).
51. H.D. Newel: Properties and characteristics of 27% chromium–iron. *Metal Progress*, 50, 997–1006, 1016–1028 (1946).
52. P.J. Grobner: The 885°F (475°C) embrittlement of ferritic stainless steels. *Metallurgical Transactions*, 4A, 251–260 (1973).
53. P. Jacobsson, Y. Bergström, and B. Aronsson: Kinetics and hardening mechanism of 475°C embrittlement in 18Cr–2Mo ferritic steels. *Metallurgical Transactions*, 6A, 1577–1580 (1975).
54. P.J. Grobner and R.F. Steigerwald: Effect of cold work on the 885°F (475°C) embrittlement of 18Cr-2Mo ferritic stainless steels. *Journal of Metals (The Metallurgical Society of AIME)*, 29, 17–23 (1977).
55. W. Treitschke und G. Tammann: Über die Legierungen des Eisens mit Chrom. *Zeitschrift für Anorganische Chemie*, 55, 402–411 (1907).
56. E.R. Jett and F. Foote: The Fe–Cr alloy system. *Metals and Alloys*, 7, 207–210 (1936).
57. G. Bergman and D.P. Shoemaker: The space group of the σ-FeCr crystal structure. *Journal of Chemical Physics*, 19, 515–515 (1951).
58. B. Weiss and R. Stickler: Phase instabilities during high temperature exposure of 316 austenitic stainless steel. *Metallurgical Transactions*, 3, 851–866 (1972).
59. M.B. Cortie and E.M. Jackson: Simulation of the precipitation of sigma phase in duplex stainless steels. *Metallurgical and Materials Transactions A*, 28A, 2477–2484 (1997).
60. K. Bungardt and H. Borchers und D. Kölsch: Untersuchung der Bildung der Sigmaphase in ferritischen Chromstählen mit unterschiedlichen Gehalten an Silizium und Aluminium. *Archiv für das Eisenhüttenwesen*, 34, 465–476 (1963).
61. A. Bäumel: Vergleichende Untersuchung nichtrostender Chrom- und Chrom–Nickel–Stähle auf interkristalline Korrosion in siedender Salpetersäure und Kupfersulfat-Schwefelsäure-Lösung. *Stahl und Eisen*, 84, 798–807 (1964).
62. M.A. Streicher: Microstructures and some properties of Fe–28% Cr–4% Mo alloys. *Corrosion-NACE*, 30, 115–124 (1974).
63. S. Nana and M.B. Cortie: Retardation of intermetallic phase formation in experimental superferritic stainless steels. *Metallurgical and Materials Transactions A*, 27A, 2436–2444 (1996).
64. P. Premachandra, M.B. Cortie, and R.H. Eric: Effect of stabilising elements on formation of σ phase in experimental ferritic stainless steels containing 39% Cr. *Materials Science and Technology*, 8, 437–442 (1992).
65. F.C. Pimenta Jr, A.F. Padilha, and R.L. Plaut: Sigma phase precipitation in a superferritic stainless steel. *Materials Science Forum*, 426–432, 1319–1324 (2003).
66. K.W. Andrews: A new intermetallic phase in alloy steels. *Nature*, 164, 1015–1015 (1949).
67. J.S. Kasper: The ordering of atoms in the chi-phase of the iron–chromium–molybdenum system. *Acta Metallurgica*, 2, 456–461 (1954).

68. H. Hughes and D.T. Llewelyn: χ phase in the Fe–Cr–Ni–Ti system. *Journal of The Iron and Steel Institute*, 192, 170 (1959).
69. I.C.I. Okafor and O.N. Carlson: Equilibrium studies on chi phase-strengthened ferritic alloy. *Metallurgical Transactions A*, 9A, 1651–1657 (1978).
70. H. Kiesheyer und H. Brandis: Untersuchung von Phasengleichgewichten in Dreistoffsystem Eisen-Chrom-Molybdän im festen Zustand. *Zeitschrift für Metallkunde*, 67, 258–263 (1976).
71. H. Brandis, H. Kiesheyer und G. Lennartz: Mechanisch-technologische Eigenschaften und Ausscheidungsverhalten hochreiner ferritischer Stähle mit 20 bis 28% Cr und bis zu 5% Mo. *Archiv für das Eisenhüttenwesen*, 46, 799–804 (1976).
72. A.P. Bond: Mechanisms of intergranular corrosion in ferritic stainless steels. *Transactions of The Metallurgical Society of AIME*, 245, 2127–2134 (1969).
73. A. Bäumel: Korrosion in der Wärmeeinflußzone geschweibter chemisch beständiger Stähle und Legierungen und ihre Vergütung. *Werkstoffe und Korrosion*, 26, 433–443 (1973).
74. T. Shepard and P. Richards: Structural and substructural observations during thermomechanical processing of two ferritic stainless steels. *Journal of Materials Science*, 22, 1642–1650 (1987).
75. R.F. Steigerwald, H.J. Dundas, R.D. Redmond, and R.M. Davison: The physical metallurgy of Fe–Cr–Mo ferritic stainless steels. In: *Stainless Steel' 77*. R.Q. Barr (Ed.), Climax Molybdenum Company, London, England, pp. 57–76 (1978).
76. T. Sawatani, S. Minamino, and H. Morikawa: Effect of Laves phase on the properties of Ti and Nb stabilized low C, N–19% Cr–2% Mo stainless steels sheets. *Transactions ISIJ (Japan)*, 22, 172–180 (1982).
77. M.-Y. Huh and O. Engler: Effect of intermediate annealing on texture, formability and ridging of 17% Cr ferritic stainless steel sheet. *Materials Science Engineering A*, A308, 74–87 (2001).
78. G. Tacke und H.J. Köhler: Auscheidungsverhalten von nichtrostenden, ferritisch-austenitischen Stählen mit höherem Mo-Gehalt, *Steel Research*, 58, 123–128 (1987).
79. K. Lorenz und G. Medawar: Über das Korrosionverhalten austenitischer Chrom–Nickel–(Molybdän) Stähle mit und ohne Stickstoffzusatz unter besonderer Berücksichtigung ihrer Beanspruchbarkeit in chloridhaltigen Lösungen. *Thyssenforschung*, 1, 97–108 (1969).
80. A. Desestret and J. Charles: The duplex stainless steels. In: *Stainless steels*. P. Lacombe, B. Baroux, and G. Beranger (Eds.), les editions de physique, Les Ulis, France, pp. 612–658, (1993).
81. A. Ibach: *Verschleißverhalten von nichtrostenden ferritisch-austenitischen Duplex-Stählen: Abrasion und Erosion*. Ph.D. Thesis (Doktorarbeit), Ruhr-Universität Bochum, Fakultät für Maschinenbau, Bochum, Germany (1994).
82. W. Reick, M. Pohl, and A.F. Padilha: Three types of embrittlement in ferritic–austenitic duplex stainless steels. *Metalurgia International*, 3, 46–50 (1990).
83. M. Pohl, A.F. Padilha, and O. Fossmark: Bruchvorgänge in ferritisch-austenitischen Duplexstählen mit 475°-Versprödund. *Materialkundlich-Technische Reihe*, Vol. 9 (Gefüge und Bruch), K.L. Maurer and M. Pohl (Eds.), Gebrüder Borntraeger, Berlin, pp. 305–314 (1990).
84. W. Reick, M. Pohl, and A.F. Padilha: Recrystallization-transformation combined reactions during annealing of a cold rolled ferritic–austenitic duplex stainless steel. *ISIJ International (Japan)*, 38, 567–571 (1998).
85. L.A. Norström, S. Pettersson, and S. Nordin: Sigma-phase embrittlement in some ferritic–austenitic stainless steels. *Zeitschrift für Werkstofftechnik*, 12, 229–234 (1981).
86. R.M. Davison and J.D. Redmond: Practical guide to using duplex stainless steels. *Materials Performance*, 29, 57–62 (1990).
87. P. Lacombe and G. Béranger: Structure and equilibrium diagrams of various stainless steel grades (Chapter 2). In: *Stainless steels*. P. Lacombe, B. Baroux, and G. Beranger (Eds.), les editions de physique, Les Ulis, France, pp. 13–58 (1993).
88. P.T. Lovejoy: Structure and constitution of wrought martensitic stainless steels (Chapter 6). In: *Handbook of stainless steels*. D. Peckner and I.M. Bernstein (Eds.), McGraw-Hill, New York, pp. 6–1–6–23 (1977).
89. O. Bletton: The martensitic stainless steels (Chapter 13). In: *Stainless steels*. P. Lacombe, B. Baroux and G. Beranger (Eds.), les editions de physique, Les Ulis, France, pp. 477–504 (1993).

90. D.C. Perry and J.C. Jasper: Structure and constitution of wrought precipitation-hardenable stainless steels (Chapter 7). In: *Handbook of stainless steels*. D. Peckner and I.M. Bernstein (Eds.), McGraw-Hill, New York, pp. 7-1–7-18 (1977).
91. J. Bourrat and C. Goux: Precipitation hardened stainless steels (Chapter 19). In: *Stainless steels*. P. Lacombe, B. Baroux, and G. Beranger (Eds.), les editions de physique, Les Ulis, France, pp. 659–692 (1993).
92. V. Seetharaman, M. Sundaraman, and R. Krishnan: Precipitation hardening in a PH 13–8 Mo stainless steel. *Materials Science and Engineering*, 47, 1–11 (1981).
93. M.O. Speidel: Nanograin size, high-nitrogen austenitic stainless steels. *Zeitschrift für Metallkunde*, 94, 719–722 (2003).
94. M. Berns, M. Karlsohn, F. Schmalt und W. Trojahn: Steigerung der Härte nichtrostender martensitischer Stähle. *Zeitschrift für Werkstoffe Wärmebehandlung Fertigung*, 59, 87–97 (2004).

13 Heat Treatment of Powder Metallurgy Steel Components

Joseph W. Newkirk and Sanjay N. Thakur

CONTENTS

13.1 Introduction 741
13.2 Overview of P/M Processing 742
13.2.1 Press and Sintering 743
13.2.2 Metal Injection Molding 748
13.2.3 Powder Forging 749
13.3 Designation System for P/M Steels 750
13.4 Overview of Heat Treatment 751
13.5 Effect of Porosity on the Heat Treatment of P/M Steels 754
13.6 Effect of Alloy Content on P/M Hardenability 758
13.6.1 Copper Content 760
13.6.2 Nickel Content 760
13.6.3 Nickel–Copper Content 760
13.6.4 Molybdenum Content 762
13.7 Effect of Starting Material on Homogenization 764
13.8 Quench and Tempering 769
13.9 Sinter Hardening 772
13.10 Warm Compaction 774
13.11 Powder Forging 775
13.12 Case Hardening 778
13.12.1 Carburizing 778
13.12.2 Carbonitriding 780
13.12.3 Induction Hardening 781
13.12.4 Nitrocarburizing 781
13.12.5 Nitriding 783
13.12.6 Steam Treating 784
13.12.7 Black Oxiding 785
References 786

13.1 INTRODUCTION

While the heat treatment of powder metallurgy (P/M) parts can be exactly the same as other parts produced by other methods, majority of time, there are significant differences that must be taken into account. Porosity, composition, and homogeneity are usually the causes for these differences. Understanding the process of P/M is necessary to allow the heat-treatment professional to anticipate these differences and adjust for them. In addition, many P/M compositions exist that do not have wrought analogs, and hence can only be properly treated

with a knowledge of the specific system. Finally, there are also differences in the measurement of some mechanical properties and the manner of proof tests.

P/M is increasingly used to produce near-net-shaped parts inexpensively. In 2000, almost 80% of all powders produced were of iron or steel [1]. Iron and steel powder shipments increased 55% from 1993 to 2000. This amounted to 445,000 short tons; 93.5% is made into P/M parts. While shipments are relatively unchanged in the last few years due to the economic conditions, this growth is expected to continue over the long run as more and more P/M parts are specified in automotives, appliances, lawn and garden equipments, recreational products, power tools and hardware, business equipments, and electronics. The typical U.S. passenger car contains more than 41 lb of P/M parts, a figure that will go higher within the next several years. More than 500 million P/M hot forged connecting rods have been made for cars produced in the United States, Europe, and Japan. Commercial aircraft engines contain 1,500–4,400 lb of P/M superalloy extruded forgings per engine. It is likely that the heat-treatment supplier will continue to see more P/M parts in the future.

P/M itself is not a single process but an umbrella of processes that includes, but is not limited to press and sinter, metal injection molding (MIM), powder forging, hot isostatic pressing, powder rolling, spray forming, and more. The common theme among these processes is the use of metal powders as the feedstock for the manufacture of parts. The most likely processes to be encountered in the heat treatment of manufactured steel components are press and sinter, MIM, and powder forging.

As an example of just how different a P/M part can be to apply a required heat treatment, let us consider a case where a part is received that is made from wrought 4620 steel. A check of the standards for 4620 shows the composition limits for this material, including the carbon, which varies from 0.17 to 0.22%. For many heat treatments, this along with part dimensions may be the only information necessary to determine the proper parameters. Future experiences with 4620 will usually require the same conditions. Combining different parts of 4620 into a single furnace load can often be done without any adjustments.

A contrast to P/M parts made of a close equivalent is FL-4605. Not only has the nomenclature changed with 05 indicating a nominal 0.5% C but many other things as well. A check of the standards indicates that the FL-4605 may have anywhere from 0.4 to 0.7% C. This means that the part can have over 40% greater or lesser carbon content than nominal. While the Ni contents have similar ranges, the Mo can range from 0.4 to 1.10% as compared to 0.2 to 0.3% for wrought. Adding to this is the possibility that the original powders used for creating the P/M part may have used admixed Ni powder, which may lead to inhomogeneities in composition and altered hardening response.

Finally, the physical properties of the part are dependent on density and will change depending on the requirements for that part. Many times, the lower densities of P/M parts can be such that the surface has connected pores, which absorb quenchant or lead to larger than expected case depths.

All of these things means that different batches of P/M parts can behave very differently and special furnace loads may be required to meet the unique parameters of the parts. No wonder some commercial heat-treatment shops shudder when asked to heat-treat P/M parts. Despite all of these problems, P/M parts can be properly heat-treated, given an understanding of the differences in P/M steel and prior knowledge of the parts fabrication details.

13.2 OVERVIEW OF P/M PROCESSING

Different P/M processing methods will cause different effects during heat treatment. The high porosity of press and sinter parts has a large effect on the heat-treatment response. Metal injection molded parts have less porosity than sand-cast parts, but a very fine grain size.

Powder-forged parts have a greater homogeneity than many wrought parts. In order to properly heat-treat P/M parts, greater knowledge of the specifics of the fabrication of the part is needed than for traditional steel parts. Therefore, an overview of the different methods is helpful when discussing the differences in various P/M parts. A side-by-side comparison of these methods is given in Table 13.1.

13.2.1 Press and Sintering

Press and sintering is the P/M process that is most commonly encountered by heat treaters. Parts that have two-dimensional complexity, but have a limited number of flat surfaces in the third dimension, are especially suitable to be produced by this method. A power transmission gear is an ideal part to be made by press and sinter with its complicated outline, but simple shaped along the axis of the gear. The most important attribute of a press and sinter part is its dimensions. If the dimensions of each part can be controlled, then press and sintering is an extremely cost-effective way to manufacture metallic parts. The general steps in the press and sinter process are shown in Figure 13.1.

Compaction is probably the most critical step in the P/M process since it sets both the density of the powder and the uniformity of that density throughout the product. It is also where almost all of the shaping of the part occurs. A typical compaction sequence using a mechanical press would start with the bottom punch in its fully raised position with the powder feed in position over the die. The bottom punch then descends to a preset fill depth and the powder-feed retracts, leveling the powder. Next, the upper punch descends into the die and compacts the powder. The upper punch then retracts, and the bottom punch rises to eject the powder compact. As the powder feed advances to the next cycle, its forward edge clears the compacted part from the press, and the cycle repeats.

The objective of compaction is to produce a high-density compact with sufficient green strength for in-process handling and transport to the sintering furnace. Since final properties strongly depend on density, uniform properties require uniform density. Most compaction is performed with mechanical or hydraulic presses and rigid tooling. Compacting pressures range from 3 to 120 t/in.^{2}, with 10 to 50 t/in.^{2} as the most common. Because of press capacity limitations, most P/M products have pressing areas less than 10 in.^{2}.

TABLE 13.1
Comparison of Powder Metallurgy Techniques Discussed

Characteristic	Conventional Press and Sinter	Metal Injection Molding	Hot Isostatic Pressing	P/M Forging
Size of workpiece	Intermediate (<5 lb)	Smallest (<1/4 lb)	Largest (1–1,000 lb)	Intermediate (<5 lb)
Shape complexity	Good	Excellent	Very good	Good
Production rate	Excellent	Good	Poor	Excellent
Production quantity	>5,000	>5,000	1–1,000	>10,000
Dimensional precision	Excellent (±0.001 in./in.)	Good (±0.003 in./in.)	Poor (±0.020 in./in.)	Very good (±0.0015 in./in.)
Density	Fair	Very good	Excellent	Excellent
Mechanical properties	80–90% of wrought	90–95% of wrought	Greater than wrought	Equal to wrought
Cost	Low $0.50–5.00/lb	Intermediate $1.00–10.00/lb	High >$100.00/lb	Somewhat low $1.00–5.00/lb

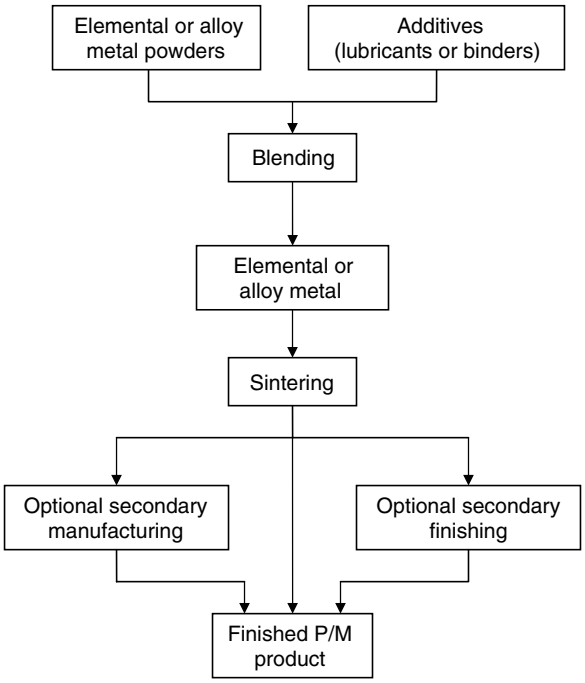

FIGURE 13.1 Simplified flowchart of the press and sinter process.

Another important consideration in the compaction of P/M parts is the ability of the green part to survive the ejection process and subsequent handling prior to sintering. Since the greatest stress is usually seen during ejection from the die, and die wall friction also leads to greater bending moments on the part, surviving ejection typically means the part will survive until sintering. The green strength of the part is critical to this step and impacts design considerations for compaction, even at the expense of final properties. Ejection forces are reduced by adding a dry lubricant to the powder mix. This also aids in compaction, but reduces green strength to a small extent. The amount of admixed lubricant is balanced to provide the best combination of attributes.

The properties of P/M parts are strongly dependent upon the density of the part, and part density in turn depends upon the amount of pressure that is applied and the characteristics of the powder (including size, shape, surface texture, and mechanical properties). When the powder particles are pressurized, density can increase for a variety of reasons, including the bulk movement and rearranging of particles, the deformation of individual particles, and particle fracture or fragmentation. The characteristics of the powdered material controls which of these mechanisms dominates. For examples, Elemental metal powders are usually highly deformable and a great deal of deformation can occur during compaction. Ceramic powders are usually brittle and will fracture. Metal powders that are cold-worked or highly alloyed will be between the two extremes.

Densities are usually reported as a pure value (such as grams per cubic centimeter) or as a percentage of the theoretical value, where the difference between this number and 100% is the amount of void space left within the compact. Adjectives before the word density define the conditions of the part when the density was determined. Apparent density refers to the density of the loose, uncompacted powder. Green density provides the value after compaction, but before sintering. Final density is determined after sintering.

Since uniform, high density is a common objective of compaction, various means have been developed to assist the densification. As mentioned above, lubricants are frequently added to reduce die wall friction and promote transmittance of the compacting pressure. Unfortunately, lubricants also reduce the green strength, and too much lubricant can actually reduce mechanical properties because of the voids produced when the lubricant is removed from the compact.

Another technique that is having an expanded use, particularly in automotive applications, is warm compaction. The powder is preheated prior to pressing, i.e., softening the metal for better response to the applied pressure. Heated dies are typically used to prevent cooling of the powder during application of the pressure. The advantages of warm compaction are higher green and sintered densities, higher green and final mechanical properties, and greater uniformity of density in the sintered part.

With good mechanical compaction practice, the density of loose powder can be raised to about 80% of an equivalent cast or forged material. At this stage, the parts generally have sufficient strength (green strength) to hold the shape and permit a reasonable amount of handling. In addition, the compaction operation determines both the nature and distribution of the remaining porosity.

In the sintering operation, the pressed compacts are placed in a controlled atmosphere environment and heated. A burn off or purge is first conducted to combust any air, volatilize and remove lubricants or binders, and raise the temperature of the compacts in a controlled manner. The temperature is then increased to a level where solid-state diffusion occurs (typically 70 to 80% of the melting point for metals and near 90% for refractory materials), and sufficient time is provided to form bridging bonds between the particles. The mechanical bonds of compaction become metallurgical bonds.

With additional time, diffusion acts to decrease the size of the remaining pores, with a parallel improvement in properties. However, pore reduction is strongly affected by the driving force for densification, the reduction in surface area, and the ability to transport atoms to pores. As densification reduces the driving force, the process slows down. In addition, at densities exceeding 90%, grain growth leads to the separation of grain boundaries from the pores and the transport of atoms slows significantly. The closer to full density, the harder it is to fully densify by sintering alone. So, the additional cost of maintaining the temperature and protective atmosphere is weighed against the ever-increasing level of properties, and an acceptable compromise is determined. The protective atmosphere is then maintained while the product is cooled to room temperature.

Atmosphere control is critical to successful sintering. Compacted powder typically contains between 10 and 25% residual porosity, and some of these voids are interconnected to exposed surfaces. If the material were heated in air, rapid oxidation would occur, and this would severely impair the bond formation and resultant properties. Reducing atmospheres break down any oxide that may be present on particle surfaces, and combust any harmful gases that may enter the furnace or be generated during the sintering. Inert gases cannot perform these tasks, but serve to prevent the formation of any additional contaminants. Vacuum sintering is often performed and nitrogen atmospheres are also common.

Ferrous alloys are often produced by mixing graphite with iron powder to form steel or stainless steel. While the high mobility of carbon allows for good homogeneity of the interstitial element, this mobility also means that carbon is free to interact with the atmosphere. This situation is similar to that found in heat-treating wrought or cast steel parts and has similar answers. The control of the carbon potential of the atmosphere may be necessary to maintain correct carbon levels. A typical microstructure of a press and sintered plain carbon steel is shown in Figure 13.2.

During the sintering operation, metallurgical bonds form between the powder particles. With the increase in density, strength, ductility, toughness, and electrical and thermal

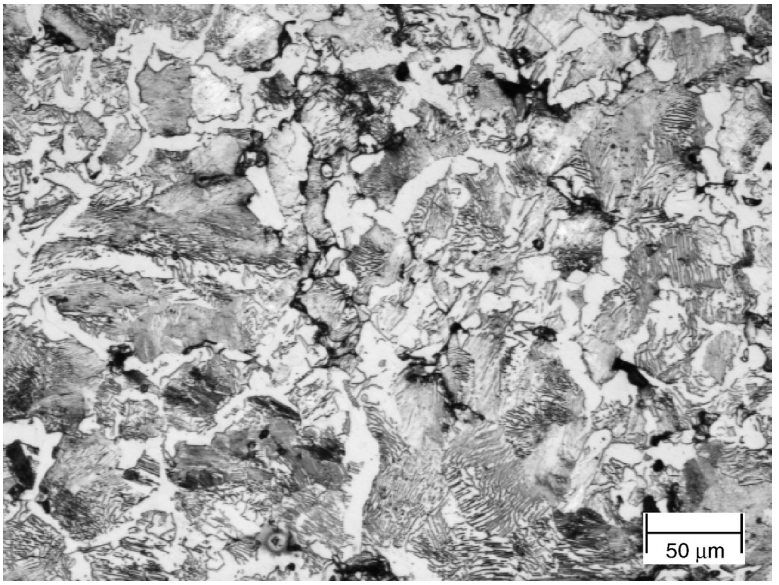

FIGURE 13.2 F-0008, compacted 50 tsi and sintered 980°C in Argon. Etched with 2/5 Nital.

conductivities also increase. If different materials were blended together, interdiffusion may promote the formation of alloys or intermetallic phases. As a consequence of the density increase, size decreases. To meet the desired tolerances, the compacted shape must be appropriately oversize. Not all of the porosity is removed, however, final-pressed and -sintered P/M products generally retain between 5 and 25% residual porosity. A typical pore structure from a press and sintered part is shown in Figure 13.3.

Higher densities along with greater homogenization can also be achieved by the use of high-temperature sintering. High-temperature sintering will result in improved pore rounding and uniformity in alloying, which allows better heat-treating response for the same alloy content. Most of the oxides are reduced during the conventional sintering at 1150°C (2100°F) but oxides of certain elements like manganese and chromium are reduced at higher temperatures in a reducing atmosphere. These oxides not only deteriorate the mechanical properties but also interfere with the heat-treatment response of the alloy. High-temperature sintering not only results in better mechanical properties, but also the benefits, which extend even in the heat-treatment stage of P/M part.

Sintering of P/M steel compacts is usually performed in mesh belt furnaces with a maximum operating temperature of about 1150°C (2100°F). Furnaces are now readily available, which overcome the temperature limitations of a mesh belt. Pusher furnaces are widely used when the sintering temperature is greater than 2100°F. One of the issues while using higher temperatures 1150 to 1315°C (2100 to 2400°F) is the increased cost of maintenance.

An alternative route for achieving higher densities with press and sintered parts is with double pressing and sintering (DPDS). The difficulty here is that normally, after the sintering operation, die P/M steel is too hard to compress, primarily because of the dissolved carbon. By lowering the initial sintering temperature until the solution of graphite is minimized, the presintered compacts can be more easily densified by repressing. After a second sintering treatment at or above the normal temperature, an alloyed steel can be produced with densities up to 95% of the theoretical value.

In a conventional press and sinter operation, the compaction operation sets dimensions, but these dimensions then change as the part shrinks during the densification of sintering. In

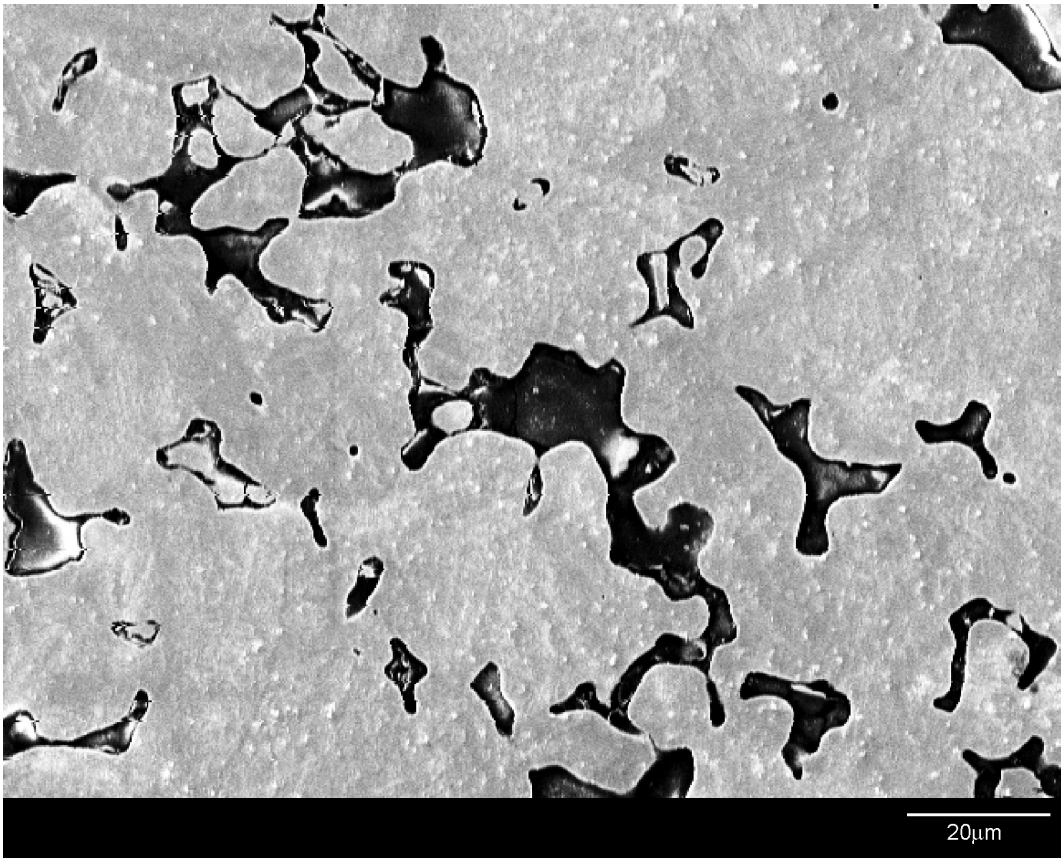

FIGURE 13.3 737SH sinter-hardened. Unetched.

addition, warping or distortion may occur as a result of nonuniform heating and cooling. Repressing, coining, or sizing may be employed to restore or improve dimensional precision. The accompanying cold working and further increase in density can combine to provide a 25 to 50% increase in product strength.

Conventional finishing operations, such as heat treatment, machining, and surface treatment, can also be performed. High-density parts, those with less than 10% porosity, can be treated as conventional parts. Parts with lower density usually require some form of special precautions, such as protective atmospheres, special coolants or quenchants, or adjusted processing conditions. This is due to the fact that the porosity will most likely be connected throughout the part when the porosity exceeds 10%, allowing the atmosphere to penetrate to the internal surfaces of the part.

P/M steel parts can be quenched and tempered to achieve high strength or hardness as required. However, the hardenability of steels depends in part on the density of the parts since the thermal conductivity of the metals is affected by the density. In addition, the homogeneity of the parts, prepared from mixed powders, will be affected by sintering conditions and can result in changes in hardenability due to composition variations. In addition to these problems, hardness measurements on a P/M sample will result in a lower hardness value due to residual porosity. If a certain heat-treated hardness is expected and used to measure the formation of martensite, the resulting lower measured hardness, called the effective hardness, due to porosity will make the steel appear not to be fully hardened. Microhardness tests, which do

not interact with the pores in the material, do give a true reading of the state of the part. These factors must be taken into account when specifying the heat treatment of the sintered steel parts.

Sinter hardening is a process where normal sintering provides the austenization treatment of steel compacts. Then quenching must be done in the furnace before removal of the part and the subsequent tempering. This process provides a significant economic benefit by the elimination of reheating to the austenite temperature. However, materials with very good hardenability are required to allow for sufficient depth of martensite formation at relatively slow cooling rates possible in the sintering furnace.

The presence of porosity and permeability also opens up the possibility of unique secondary processing, such as impregnation and infiltration. During impregnation, oil or other liquid, such as polymeric resin, is introduced into the porous network. The most common application is the oil-impregnated bearing, which contains between 10 and 40% oil by volume. Parts impregnated with Teflon offer the combined properties of high strength and low friction. If the pores are filled with a solid material, such as a lower melting point metal, the process is called infiltration. Strength and toughness improve due to the absence of pores. Components can be made gas- or liquid-tight, machinability and corrosion resistance improve, and smooth surface platings are now possible.

13.2.2 Metal Injection Molding

MIM is similar to conventional P/M process in several ways and different in other important areas. This leads to new considerations for the design of MIM parts when compared to conventional P/M. It also offers many new advantages that can be utilized to produce cost-effective, high-performance parts.

Like conventional P/M, MIM uses powdered metals as the starting material, and properties are controlled by the density produced during sintering. Every other aspect of the process is different. An overview of the process is shown in Figure 13.4. The metal powder is mixed with a specially designed plastic binder, often with thermoplastic properties. This mixture is often produced in the form of pellets, which makes for ease of handling and uniformity of composition. The mixture is called the feedstock and can contain up to 50 vol% binder. The feedstock is heated to the plastic range and injected into a mold under pressure. The mold temperature is such that the part becomes harder and can then be ejected from the mold with excellent green strength. The part is now treated to remove the plastic binder. Techniques such as solvent extraction, controlled heating to volatilize the binder, or catalytic debinding using acids are used to remove the binder. The resulting part is very fragile and must be treated carefully before sintering. The part is sintered similarly to conventional P/M parts, except that the lower density of the part before sintering leads to large amounts of shrinkage, often up to 25% or more.

In conventional P/M, the powder is often chosen to flow well during filling and compaction, as well as to result in low shrinkages so that dimensions are closely held. Since in MIM the powder is carried by the plastic binder, flow characteristics are not the major attributes of the powder chosen, and instead the powders are often chosen on the basis of sinterability instead. The powders are very fine, usually in the range of 2 to 20 μm in diameter. The fine powder sinters to high densities. Densities of 99% of the theoretical value are common. This has a significant effect on the properties of MIM parts usually making them superior to other fabrication techniques.

While the size of conventional P/M products is generally limited by press capacity, the size of MIM is more limited by two factors: the cost of the fine powders and the ability to completely remove the binder from all areas of the part. Typically, MIM parts are complex-shaped metal parts with thicknesses as large as 6.3 mm (1/4 in.) and weights under 60 g (2 oz). Section thicknesses as small as 0.25 mm (0.010 in.) are possible because of the fineness of the powder. Special binders are now available, which allows much larger parts to be successfully debound [2].

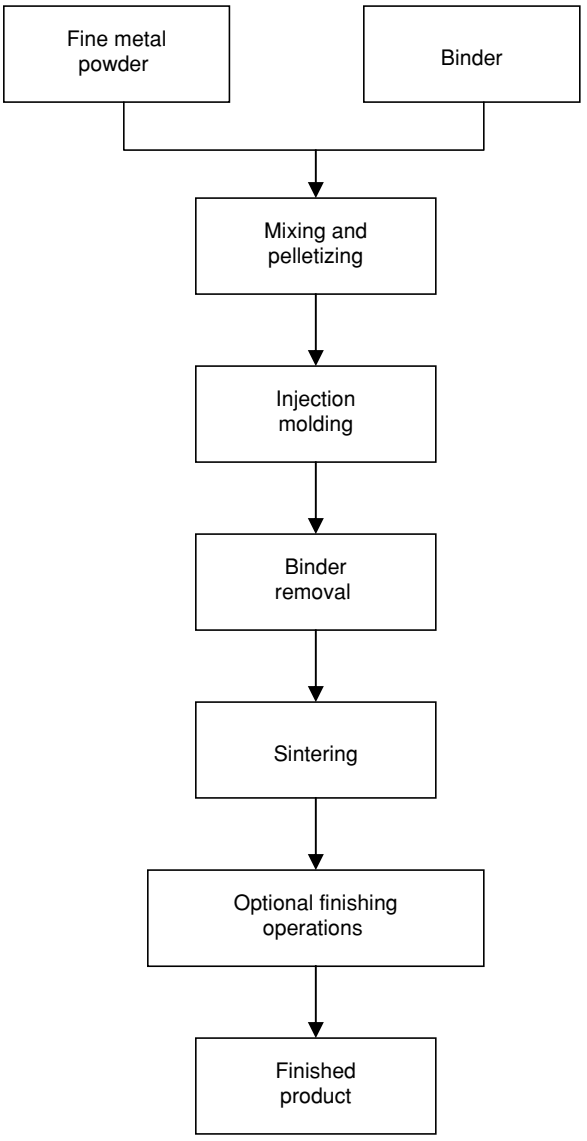

FIGURE 13.4 Simplified flowchart of the metal injection molding process.

The heat treatment of MIM parts is much like that of wrought parts. Their small size means that they heat up fast and cool down quicker. The only difference is that there is usually a smaller grain size, sometimes the composition does not have an exact wrought equivalent, and sometimes admixed additives, such as nickel, are used. The heat treatment of MIM will not be covered separately as there are no special treatments involved.

13.2.3 Powder Forging

Forging can be used to form complex shapes from canned powder or simple-shaped sintered preforms. One approach for making a complex-shaped product that would be difficult to compact is to first produce a simple-shaped preform by conventional press and sinter manufacture. Subsequent hot forging converts this material to the desired final shape, while

adding the benefits of both metal flow and further densification as a result of the shear under compression that occurs during forging. By starting with P/M, forged products that can be produced and are free of segregation, have uniform fine grain size throughout, and utilize the novel alloys and unique combinations that are possible through the blending of powders. Because of the initial porosity and permeability, protective atmospheres may be required during heating and forging operation. Powder-forged properties can be exceptionally good.

13.3 DESIGNATION SYSTEM FOR P/M STEELS

P/M steels are designated according to a system adopted by the Metal Powder Industry Federation (MPIF) [3]. This system uses a combination of letters indicating alloying elements and numbers, which give the nominal compositions. In addition, another set of numbers is attached, which indicates a minimum strength value to which the part was made. When the powder is prealloyed, there is a modified system that is used. This occurs for a number of alloyed steels or stainless steels.

Table 13.2 gives the entire list of letter codes used in designation system for P/M steels. The first letter in the code gives the base metal for the alloys, so C in the first position is for copper-based alloys such as brass and N would be for nickel-based alloys, etc. Since the topic is P/M steels, then the operative letter is F for iron. If the P/M steel contains any alloying elements of significance besides carbon, they are then added after the iron designation. The fact that an alloying element is not represented in the designation does not mean that it is not included in the alloy, so the standard composition needs to be checked. Still this system does identify the more important elements, making it easier to keep track off.

The letter code is usually followed by four digits. Unfortunately, there are differences in the significance of these four digits. For nonferrous alloys, the first two digits are the percentage by weight of the major alloying element and the second two digits are the percentage of the minor or second alloying element. For ferrous alloys, the first two digits have the same meaning, but the second two digits represent the carbon content in tens of percent. Typical American Iron and Steel Institute (AISI) designations for wrought steel would use 80 to represent 0.8% C, while the Metal Powder Industries Federation (MPIF) designation would use 08 for the same amount of carbon.

The last digits following the four alloying digits is the minimum tensile strength of the material. Once again, there are two different significances to these numbers depending on

TABLE 13.2
Letter Code for Designating P/M Alloys

A	Aluminum	G	Free graphite
C	Copper	M	Manganese
CT	Bronze	N	Nickel
CNZ	Nickel silver	P	Lead
CZ	Brass	S	Silicon
F	Iron	SS	Stainless steel (prealloyed)
FC	Iron–copper or copper steel	T	Tin
FD	Diffusion-alloyed steel	U	Sulfur
FL	Prealloyed ferrous (not SS)	Y	Phosphorous
FN	Iron–nickel or nickel steel	Z	Zinc
FX	Copper-infiltrated iron or steel		

whether the steel was heat-treated or not. Parts that have not been heat-treated will always give the minimum yield strength here. Heat-treated parts are given with the ultimate tensile strength. The reason for this is that heat-treated (hardened) P/M steels usually do not have sufficient ductility to measure with a standard tensile test, resulting in the yield strength and the ultimate tensile strength, which are essentially the same.

Exceptions to each of these sets of digits occur. One set of exceptions is for soft magnetic materials and steels with phosphorus additions. These materials are not usually subjected to heat treatments other than annealing and are not included here. The reader should consult the MPIF standards for the codes for these materials.

Another exception is for the use of prealloyed powders. Powder blends, which have a prealloyed steel powder as one of the components, have a designation that begins with FL. If the steel powder is mixed with graphite only the designation is usually modified from the AISI alloy codes. FL-4605 is a 4600 steel powder or near equivalent with 0.5% C nominally. This designation may or may not be followed by more digits giving the strength, as discussed above, and the letters HT, if it is heat-treated.

Elemental alloying additions to the prealloyed powder other than graphite are designated with one or two more letters following the FL. If additional Ni is blended with the FL-4605, it becomes FLN-4605. There may also be Ni and Cu additives for alloys designated as FLNC-4405. When Ni is added to a steel normally not containing Ni, the amount is sometimes given directly after the letter code, such as FLN2-4408.

Diffusion-alloyed powders lead to designations of FD, followed by the Ni amount and graphite, such as FD-0208, which contains nominally 2% Ni. A check of the compositions for this material reminds us that there is also 1.5% Cu.

Finally, copper-infiltrated steels will have the FX designation. The first digit is the approximate amount of copper, which has been infiltrated into the open porosity, not the copper added to the powder blend or prealloyed powder. Thus FX-1005 is approximately 10% copper-infiltrated and 0.5% graphite.

Table 13.3 lists many commonly used P/M steels and their composition ranges. Depending on the starting powders used, there may also be up to 0.5% Mn. Other possible tramp elements include P, S, and O. The O_2 content of the powder is typically reduced during sintering in a reducing atmosphere and can vary depending on processing.

13.4 OVERVIEW OF HEAT TREATMENT

There are a number of considerations when heat-treating P/M parts depending upon the chosen heat treatment. The following suggestions act as a guide to general considerations for heat treatment of P/M parts:

1. Since the cost benefit of P/M often involves avoiding machining, most parts are not machined after heat treatment. This means that any type of surface damage, dent, or scratch created during handling can reduce the functionality of the parts. Therefore, extra care must be exercised in loading parts for heat treatment and any subsequent handling.
2. Parts that have seen some sort of secondary operation (sizing, coining, machining, or rolling) prior to heat treatment probably contain residual oils. These substances, partially entrapped inside the open porosity, may adversely affect the properties that could be achieved on heat-treating and may also reduce the life of some part of the furnace. In this case, a suitable washing operation, with a proper choice of solvent, should be carried out prior to heat treatment.
3. Loading patterns of parts to be heat-treated must permit a free flow of a carburizing gas or quenching fluid. When parts are small, closely spaced parts may have little

TABLE 13.3
Compositions of Common P/M Steels

MPIF Designation	C	Ni	Cu	Mo
F-0000	0.0–0.3			
F-0005	0.3–0.6			
F-0008	0.6–0.9			
FC-0200	0.0–0.3		1.5–3.9	
FC-0205	0.3–0.6		1.5–3.9	
FC-0208	0.6–0.9		1.5–3.9	
FC-0505	0.3–0.6		4.0–6.0	
FC-0508	0.6–0.9		4.0–6.0	
FC-0808	0.6–0.9		7.0–9.0	
FC-1000	0.0–0.3		9.5–10.5	
FN-0200	0.0–0.3	1.0–3.0		
FN-0205	0.3–0.6	1.0–3.0		
FN-0208	0.6–0.9	1.0–3.0		
FN-0405	0.3–0.6	3.0–5.5		
FN-0408	0.6–0.9	3.0–5.5		
FL-4205	0.4–0.7	0.35–0.55		0.50–0.85
FL-4405	0.4–0.7	—		0.75–0.95
FL-4605	0.4–0.7	1.70–2.00		0.40–1.10
FLN-4205	0.4–0.7	1.35–2.50		0.49–0.85
FLN2-4405	0.4–0.7	1.00–3.00		0.65–0.95
FLN4-4405	0.4–0.7	3.00–5.00		0.65–0.95
FLN6-4405	0.4–0.7	5.00–7.00		0.65–0.95
FLNC-4405	0.4–0.7	1.00–3.00	1.00–3.00	0.65–0.95
FLN2-4408	0.6–0.9	1.00–3.00		0.65–0.95
FLN4-4408	0.6–0.9	3.00–5.00		0.65–0.95
FLN6-4408	0.6–0.9	5.00–7.00		0.65–0.95
FLN-4608	0.6–0.9	3.6–5.0		0.39–1.10
FLC-4608	0.6–0.9	1.60–2.00	1.00–3.00	0.39–1.10
FLC-4908	0.6–0.9	—	1.00–3.00	1.30–1.70
FLNC-4408	0.6–0.9	1.00–3.00	1.00–3.00	0.65–0.95
FD-0200	0.0–0.3	1.55–1.95	1.3–1.7	0.4–0.6
FD-0205	0.3–0.6	1.55–1.95	1.3–1.7	0.4–0.6
FD-0208	0.6–0.9	1.55–1.95	1.3–1.7	0.4–0.6
FD-0405	0.3–0.6		1.3–1.7	0.4–0.6
FD-0408	0.6–0.9		1.3–1.7	0.4–0.6
FX-1000	0.0–0.3		8.0–14.9	
FX-1005	0.3–0.6		8.0–14.9	
FX-1008	0.6–0.9		8.0–14.9	
FX-2000	0.0–0.3		15.0–25.0	
FX-2005	0.3–0.6		15.0–25.0	
FX-2008	0.6–0.9		15.0–25.0	

Up to 0.5% Mn may be present depending on starting powder.

permeability of the gas or fluid. This low permeability may cause uneven flow of active form of both carburizing gas and quenching fluid. A controlled pattern loading, using wide mesh supports and choice of suitable spacers between layers of parts, decrease the unevenness of active fluids. For best results, parts should be single-spaced in layers.

4. Care should be exercised in stacking parts with flat faces in an orderly way so that there are no dead zones, where the carburizing gas and the quenching medium cannot reach, leading to insufficient carbon enrichment and low-quenching speed. The final result is typically a low hardness.
5. As mentioned above, P/M parts do not typically undergo finishing operations after heat treatment, so exposing the parts to air before oil quenching, even for very short times, should be avoided.
6. Due to open porosity in the P/M parts, the amount of quenching oil, which penetrates into the open and interconnected porosity, cannot be neglected. Also, if the part is going to be immersed in oil during normal service, all of the quenching oil should be removed, to avoid any dangerous pollution of the suitable lubricant. A specific solvent extraction operation may become unavoidable after quenching and before stress relieving. More than one washing step is likely to be required to completely remove the oil from the pores.
7. In the case of induction hardening, a preliminary washing operation may be needed. This cleaning operation is aimed at removing residuals of cutting fluids or sizing lubricants.
8. Also in the case of induction hardening, the use of water as a quenchant may lead to rust formation on the interior of the parts, if the density is low enough to still have significant open porosity. A mild stress relieving, carried out immediately after water quenching, can be used to avoid this problem.
9. The heat-treatment conditions for a P/M part, which is replacing a full density part must be altered from those previously used, especially when case hardening. In the case where the chemical compositions are comparable, there does not usually need to be a change in temperature. However, there is almost always a need to use a faster quenching medium to account for the reduced hardenability.
10. Unless the part density exceeds 7.4 g/cm, gaseous or liquid nitriding must be preceded by a suitable pore closure treatment. Steam treatment is an effective treatment that gives consistent results. On the contrary, plasma (or ion) nitriding does not require any pore closure pretreatment. However, if the parts are not adequately cleaned prior to plasma nitriding, the remaining contaminants may deleteriously affect the results.

While these general rules do not cover all of the differences in the heat treatment of P/M steels, they do give an introduction to many of them. Many of these rules are covered in this chapter. The two basic differences are the large amount of porosity and the typically inhomogeneous microstructure. Each of these has several effects on the heat treatment of P/M steels. Also, there are often subtle to considerable differences in the starting compositions picked for a given part.

The most common problem in heat-treating P/M parts is overloading. Most commercial heat treaters base their pricing on the amount of furnace hours required to process the load and the capacity of their furnace baskets. This tendency is contrary to good practice in the heat treatment of P/M parts. Once a critical loading is reached, adding more parts is going to increase the variability in hardening. The critical load for typical P/M parts is lower than for comparable wrought materials.

Heat treatment of P/M parts is most widely done in endothermic gas with additions of methane and air to control the carbon potential. Heat treaters of P/M parts have the liberty to select from a variety of atmospheres. Endothermic gas, nitrogen–methanol blends, or any nitrogen-based atmosphere can be used if the carbon potential of the atmosphere is controlled to prevent oxidation or reduction.

During case hardening, additives like methane or propane and ammonia are added to the atmosphere. The amount of additions added depends on the part density and surface

porosity. For example, a low-density part or a part having open-surface morphology will result in greater nonuniformity of case depth. This variation can be minimized by close control of the atmosphere gas composition and case hardening at lower austenizing temperatures.

13.5 EFFECT OF POROSITY ON THE HEAT TREATMENT OF P/M STEELS

As mentioned, several factors change the response of P/M steels to heat treatment when compared to conventional steels, however, porosity probably has the greatest single effect. While it is possible to achieve very high densities in P/M steel materials, the increased difficulty, and hence cost, combined with the decreased dimensional control mean that few P/M steels are made to be fully dense. The majority of parts have porosities between 5 and 15 vol%, far more than is found in a typical casting. Every mechanism in press and sinter is subjected to diminishing returns. Compact density has a decreasing dependence on compaction pressure, as does sintering and homogenization.

Porosity can influence the heat-treatment process through its effect on:

- Density
- Thermal conductivity
- Proof testing (particularly hardness)
- Permeability (to gases and liquids)
- Electrical resistivity (in induction hardening)

The first two factors have an effect on the hardenability of P/M steels. The third affects the perception of the results of heat treatment, potentially leading to an unexpectedly low result. These factors are talked about next in greater detail.

Maximum hardness in steels is achieved when the available austenite fully transforms into martensite. Sufficiently rapid cooling is required to suppress the eutectoid reaction and subsequently to form martensite. Hardenability for a wrought steel can then be defined as the depth below the surface, where the cooling rate is just adequate to transform the austenite into martensite. Hardenability depends directly on the thermal conductivity of the steel and the composition. Since the hardenability of steel is much more sensitive to changes in composition than it is to the relatively small changes in the thermal conductivity, we generally consider only the composition changes when designing a heat treatment.

The effect of porosity on the hardenability of a P/M steel is given in Figure 13.5, where the results of a series of Jominy tests on sintered carbon steel test pieces are compared with those for wrought steel [8]. The P/M specimens were prepared from iron powder, mixed with 0.8% graphite, pressed, and sintered to various densities from 6.0 to 7.1 g/cm^3. These corresponded to porosity levels ranging from 9 to 24%. The P/M test specimens and wrought C1080 steel specimen were austenitized at 870°C (1600°F) for 30 min in a protective neutral atmosphere. The test specimens were then quenched in a Jominy end quench and the hardness was measured.

Figure 13.5 graphically points out two important differences of P/M heat treatment: Not only hardenability is reduced by porosity through its influence on thermal conductivity, but the porosity also reduced the apparent hardness of the P/M materials. This is seen in the lower hardness readings at the first Jominy distance with succeeding lower densities.

As evidenced above, the hardenability of P/M steels depends on both the composition and the porosity of part. The thermal conductivity of P/M parts has been shown to be strongly influenced by porosity, which acts as an insulator in slowing heat transfer. One model of the effect of porosity on the thermal conductivity is:

$$\lambda = \lambda_m(1 - 2\varepsilon)$$

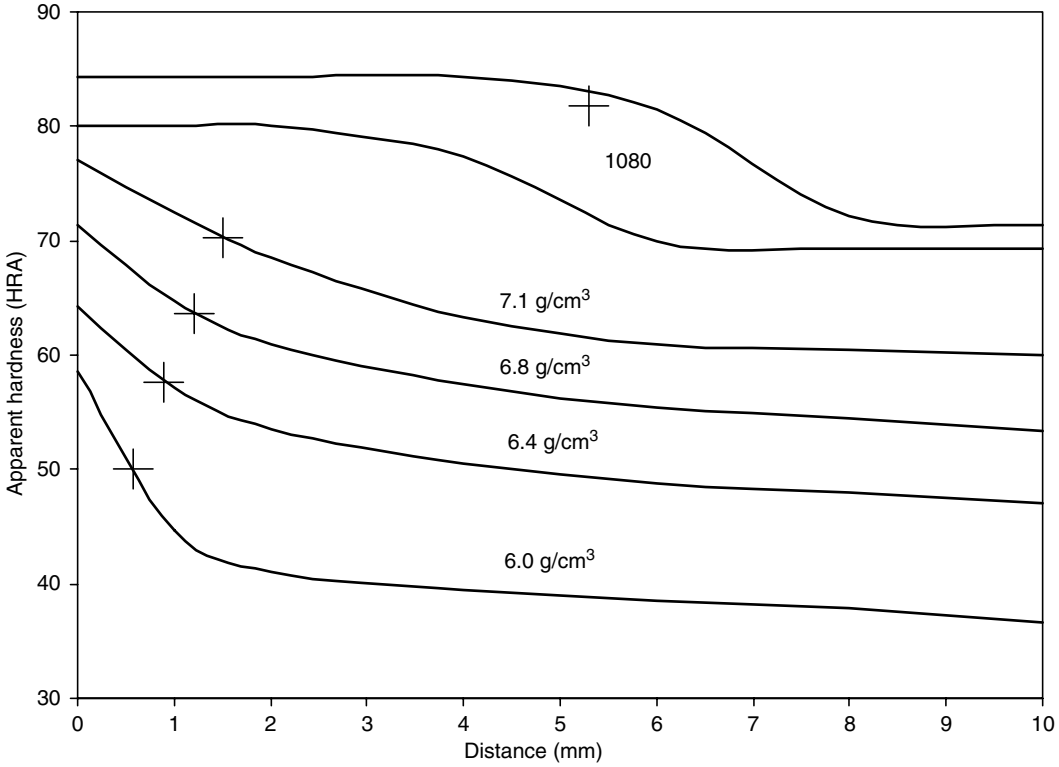

FIGURE 13.5 Hardenability curves for F-0008 compared to wrought 1080 steel. The wrought alloy has higher manganese content. The plus signs indicate the depth at which at least 50% martensite was observed in the microstructure. (Data from H. Ferguson, *Metal Progress*, ASM, 107(6), 81–83, June 1975; 108(2), 66–69, July 1975.)

where λ is the thermal conductivity of the P/M part, λ_m is the theoretical conductivity of the fully dense material, and ε is the fractional porosity (% porosity/100) of the part.

A study using simulation and experimental data resulted in a confirmation of the above equation for porosity levels between 0.1 and 10% [4]. For porosity levels greater than 12% the water-quenched samples showed higher cooling rate than expected. This was attributed to water entering the pores and cooling the samples faster.

The flow of heat from the center of a P/M part has been estimated by Bocchini [11]. The heat quantity to be removed on quenching can be given by the following relation:

$$H = M(1 - \varepsilon)c_m \Delta T \tag{13.1}$$

where H is the heat quantity to be removed, M is the mass of a fully dense body having the same shape of the sintered component, c_m is the average heat capacity of the constituting metal, and ΔT is the temperature difference between the part and the quenching medium.

One estimate of the relative cooling speed of a porous P/M part to a fully dense part is given by

$$\text{Relative cooling speed} = \frac{\lambda_m}{c_m} \times \frac{1 - 3\varepsilon}{1 - 2\varepsilon}$$

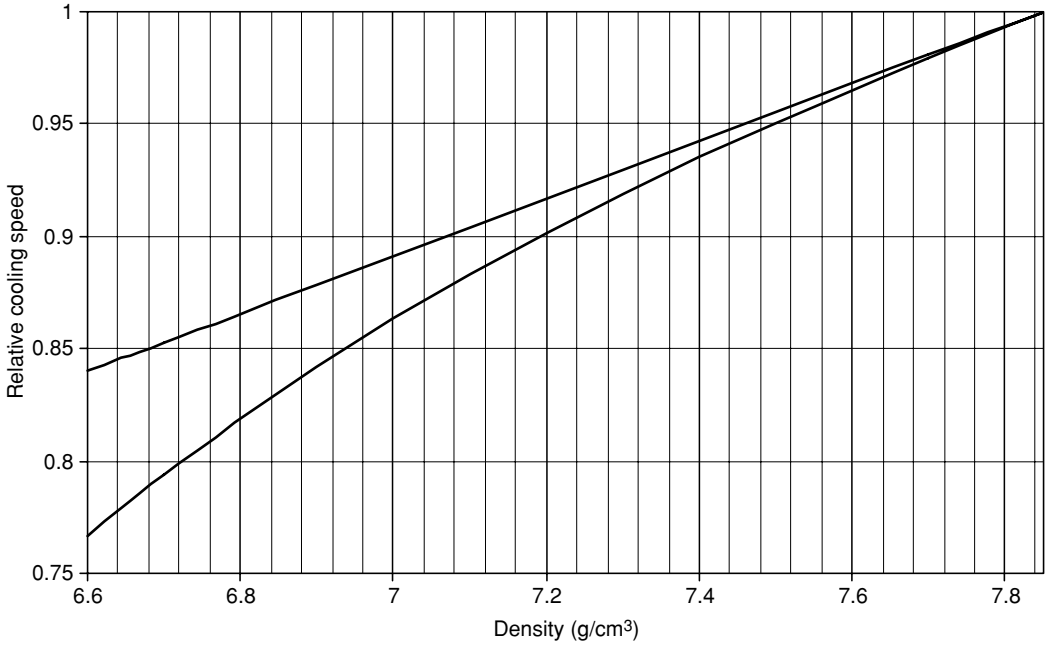

FIGURE 13.6 The relative cooling speeds of a porous steel part compared to a fully dense as predicted by two different theoretical treatments. The lower curve ignores fluid flow inside the pores. (From Bocchini., G.F., *Advances in Powder Metallurgy and Particulate Materials—2001*, Vol. 6, Metals Powder Industries Federation, Princeton, NJ, 2001, pp. 56–86.)

This approximated formula indicates, as expected, that the internal cooling speed of a part, made of porous steel, is lower than the internal cooling speed of a comparable part, made of fully dense steel. The deviation from the cooling speed of an equivalent fully dense steel increases as the porosity increases. The curve showing the decrease of internal cooling speed on quenching versus density, calculated by means of this formula, is plotted in Figure 13.6.

The flow of fluids inside pores may influence the heat exchange. A second relation gives the relative cooling speed taking this factor into account:

$$\text{Relative cooling speed} = \frac{\lambda_m}{c_m}(1 - \varepsilon)$$

The straight line corresponding to this formula is also plotted in Figure 13.6. The difference between the curves is insignificant above $7.4\,g/cm^3$, but nearly attains 6% at $6.8\,g/cm^3$. Unfortunately, no experimental results are available to eliminate the curve (or the line), which does not correspond to the practical results.

Considering the heat release at the part surfaces, two different factors should be taken into account:

- The surface porosity, which may be thought of as an increase of the roughness, consequently slowing down the speed of the cooling medium, which is removing heat from the part surfaces
- The suction effect exerted by the hot gas present inside porosity, which, by contracting itself during cooling, tends to stop and suction the vapor bubbles, originating from the quenching liquid

Since the coefficient of external heat exchange—sometimes defined as the coefficient of adduction—is linked with the state or microgeometry of the surfaces through a constant coefficient, usually between 1 and 2.5, the stage of the whole cooling process corresponding to heat removal from the external surfaces of a porous part may be considered to be slowed down to about half the typical speed of fully dense materials. In other words, the cooling of a PM component during quenching, internally and from the surface, may be visualized as a slow-motion version of the same succession of mechanisms, occurring during quenching of a nonporous body of material. Soak time is as much as 50% longer for P/M steels [5].

Usually the porosity of sintered materials is completely closed when the relative density exceeds 97%. On the contrary, porosity is completely opened, when the relative density is lower than 75 to 80%. Altogether, between porosity levels of 3 and 20%, which is typical of most mechanical components, there is a combination of opened and closed porosity. The relative amount is difficult to measure and depends on the starting material and processing conditions.

Additionally the porosity in most compacts is not uniform. This is particularly important on the upper and lower faces, which were in contact with the press punches. On these faces, the porosity is higher at the surface in press and sinter parts [6]. Figure 13.7 illustrates this effect for a F-0000 compact, which had either admixed lubricant or the die wall was lubricated. The overall porosity was approximately 8.5%, but rises to almost 15% within 0.2 mm of the surface. This creates a higher degree of open porosity on these surfaces.

While the effect of porosity on the measured hardness, called the apparent hardness, is easy to observe, it is hard to take into account. Hardness deviations from the expected values caused by porosity are generally greater, the lower the density. The relationship is generally exponential, but varies with the pore shape and dimensions, which change with the processing

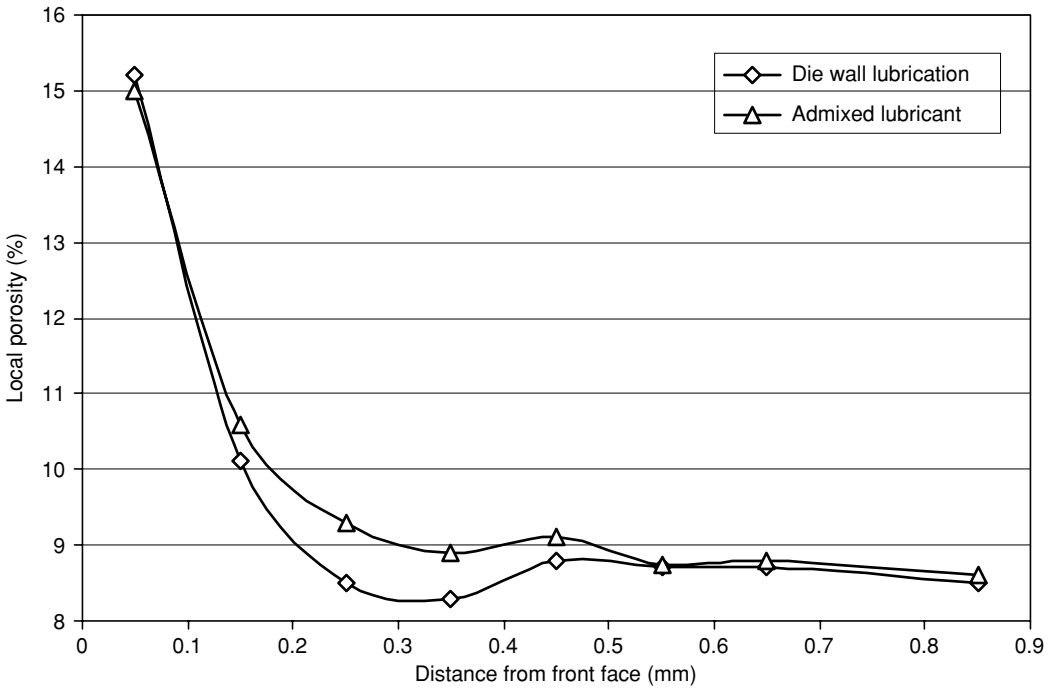

FIGURE 13.7 Local porosity variation with distance from the punch face of press and sintered F-0000 compact with eithor die wall or admixed lubricant. (From Bocchini, G.F., Fontanari, V., Molinari, A., *International Conference on Powder Metallurgy and Particulate Materials*, Metals Powder Industries Federation, Princeton, NJ, 1995.)

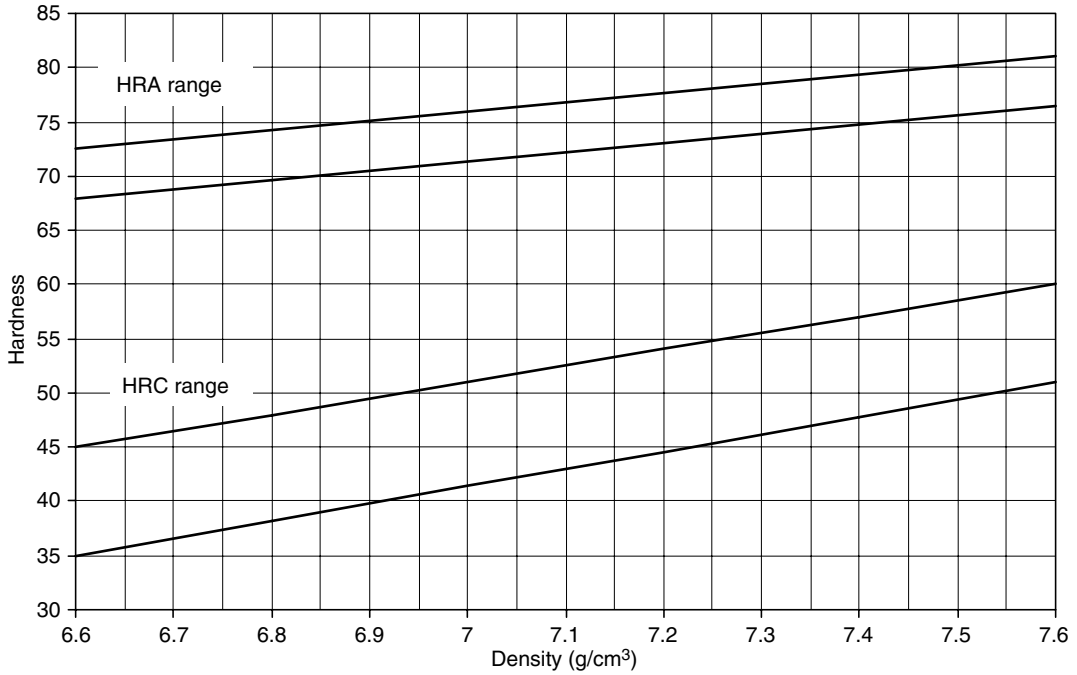

FIGURE 13.8 Dependence of hardness on density derived from experimental data. Variations in pore morphology and microstructure result in large bands. (From Bocchini, G.F., *Advances in Powder Metallurgy and Particulate Materials*—2001, Vol. 6, Metals Powder Industries Federation, Princeton, NJ, 2001. pp. 56–86.)

and starting powder. One general trend derived from experimental data is shown in Figure 13.8. The trend is shown as linear, but the resulting dependence is shown as bands, rather than exact numbers.

The difference between apparent hardness and actual hardness is clearly seen in Figure 13.9. The figure shows the standard Vickers hardness for loads greater than 1 kg compared to the microhardness, also measured by Vickers using loads less than 100 g. In the lower set of data, the Vickers indenter is producing an indent that covers large regions of the microstructure, essentially averaging the hardness of the material with the hardness of air (the pores). The upper set of data shows that the microhardness is essentially unchanged with density. The difference that can occur from simply changing the load is obvious. A plot of the change in Vickers hardness number with density is shown in Figure 13.10, which emphasizes the difference.

13.6 EFFECT OF ALLOY CONTENT ON P/M HARDENABILITY

The most important function of alloying element in heat-treatable steel is to increase hardenability, whether for quenching and tempering or sinter hardening. This increase in hardenability makes possible the hardening of larger sections and the use of oil rather than water quench to minimize distortion and to avoid quench cracking. It is known that increasing the carbon content of steel raises the tensile strength and hardness levels in proportion to the added carbon. In wrought steel, this ratio is maintained to about 1.2% C. In sintered P/M steels, the maximum tensile strength is reached at the eutectoid composition of 0.8% C. When carbon content is increased above this level, carbide networks begin to form at grain

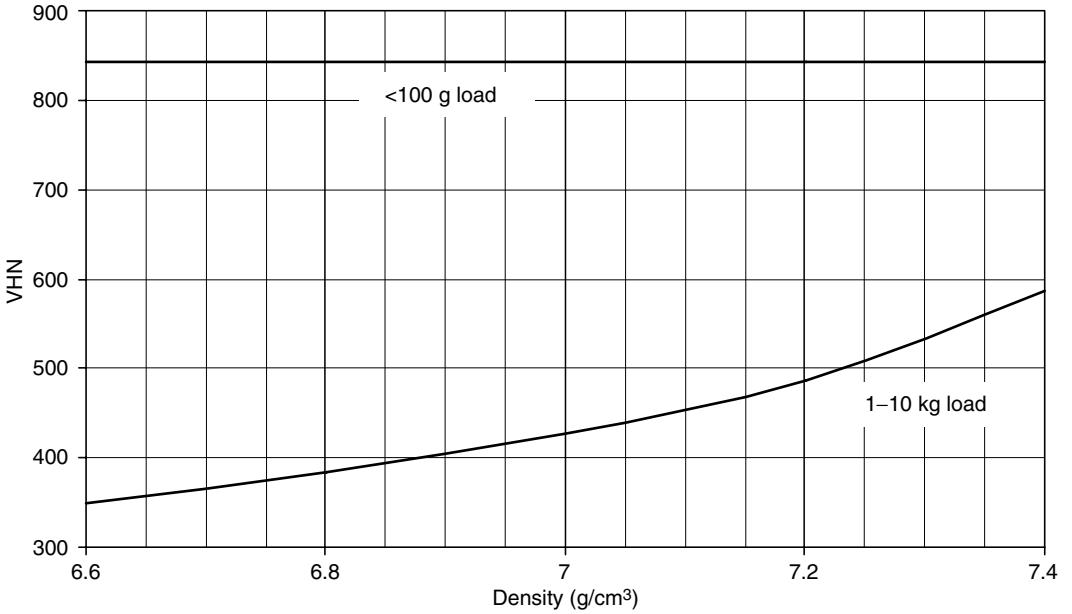

FIGURE 13.9 Difference in Vickers hardness of a P/M steel as a function of load and density. Low load corresponds to micro hardness and high load to apparent hardness. (Data from Bocchini, G.F., *Advances in Powder Metallurgy and Particulate Materials—2001*, Vol. 6, Metals Powder Industries Federation, Princeton, NJ, 2001, pp. 56–86.)

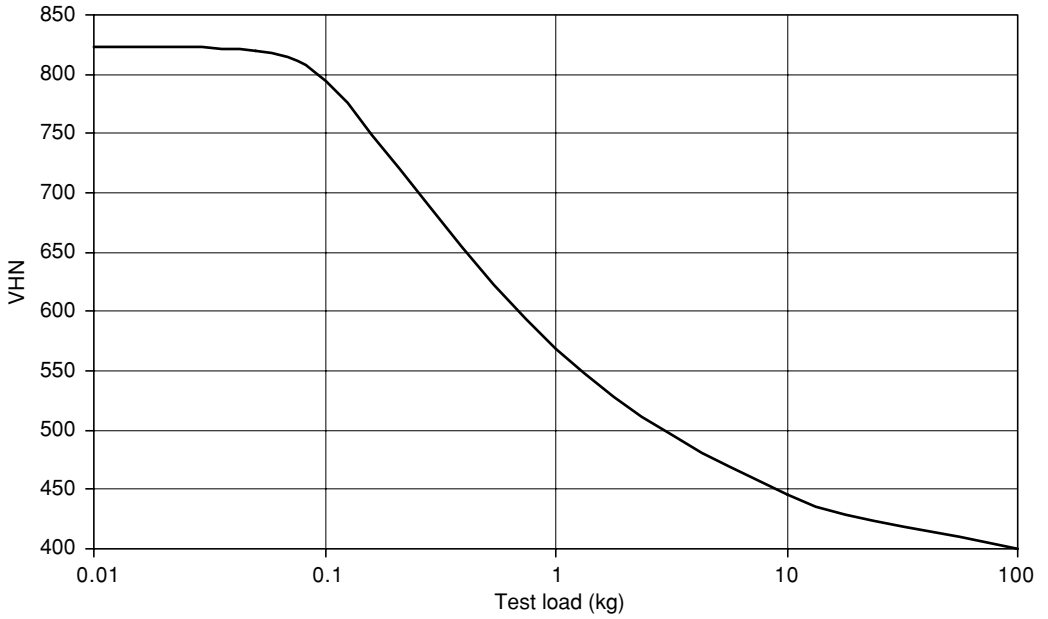

FIGURE 13.10 Dependence of Vickers hardness on applied load of heat treated P/M steels with densities between 6.8 and 7.0 g/cc. (Data from Ferguson, H., *Metal Progress*, ASM, 107(6), 81–83, June 1975; 108(2), 66–69, July 1975.)

boundaries and along porosity channels, which cause embrittlement and loss of strength. As alloying elements such as nickel, molybdenum, chromium, and copper are added, the optimum carbon level content is lowered. In sintered steels, the most common alloying elements are copper and nickel.

13.6.1 Copper Content

The addition of copper increases both hardness and tensile strength in the sintered condition. On heat treatment, they increase depth of hardness but reduce toughness and elongation. As copper content increases, rupture strength rises to an optimum level and then declines.

In the plain iron–carbon compositions, peak strength occurs near the euctectoid composition in the as-sintered condition and at approximately 0.65% C in the heat-treated condition. Fe–C systems soften progressively as the tempering temperature is raised whereas Fe–C–Cu systems show significant temper resistance of up to 371°C (700°F) [7]. Figure 13.11 shows the effect of tempering temperature and composition on hardness for Fe–C and Fe–C–Cu compositions.

The variations in the apparent hardness can be due to the effect of composition on the martensite percentage formed along with the effect of tempering. Figure 13.12 and Figure 13.13 illustrate plots showing variation of hardness and transverse rupture strength in the as-sintered and heat-treated condition. From the above figures, it is clear that for Fe–C–Cu composition, the best heat-treated properties are obtained at around 2% copper. Heat-treated strength overlaps with the sintered strength at higher copper levels as shown in Figure 13.13.

13.6.2 Nickel Content

Nickel increases tensile properties of as-sintered P/M steels approximately one half as much as copper but provides significantly higher strengths after heat treatment. This is because of the heterogeneous nature of nickel alloy steels made from blended elemental powders. Copper melts at 1083°C (1980°F) and forms a liquid phase on sintering at 1120°C (2050°F), creating a more homogeneous iron–copper alloy. Nickel has a higher melting point than the sintering temperature, and it alloys by solid-state diffusion. This produces a duplex microstructure consisting of partially alloyed iron-surrounding nickel-rich islands. On quenching, the matrix transforms to martensite but the nickel-rich areas remain austenitic. This combination results in a stronger matrix with some toughness and ductility retained.

13.6.3 Nickel–Copper Content

The effect of increasing nickel and copper contents on the hardenability of P/M steels is illustrated in Figure 13.14. Jominy bars were pressed to a density of 6.7 g/cm^3 with increasing levels of copper and nickel, while carbon content was maintained at 0.5% C. After sintering, all the Jominy bars were austenitized at 850°C (1560°F) for 2 h and quenching. The addition of 2.5% copper produced only a relatively small increase in hardenability compared to the iron–carbon alloy. However, the surface hardness increased dramatically. Adding 1% nickel to the iron–copper–carbon alloy produced little change in the surface hardness but a significant improvement in hardenability, while a 2.5% nickel addition improved surface hardness slightly, but dramatically increased the hardenability.

Many P/M components that require optimum heat-treated properties contain both nickel and copper. Figure 13.15 shows Jominy curves for FLC-4608 at different density values [8]. It shows that there is no significant drop in the hardness through Jominy position 36, which indicates its relatively high hardenability.

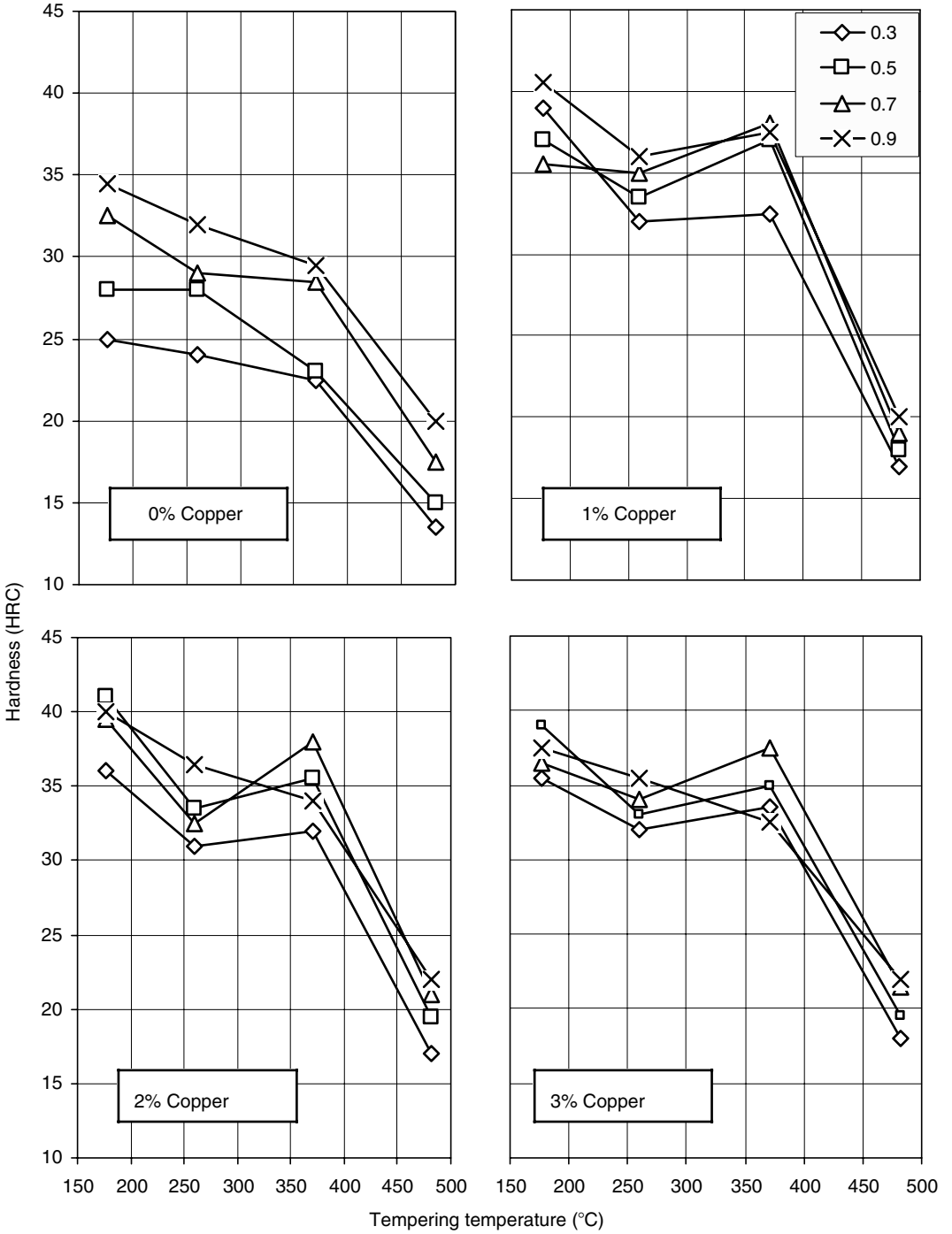

FIGURE 13.11 Variation of hardness with tempering temperature and composition. (Data from Capus, J.M. and Maaref, A., *Proceedings of the 1973 International Powder Metallurgy Conference*, Vol. 8, 1974, pp. 61–73.)

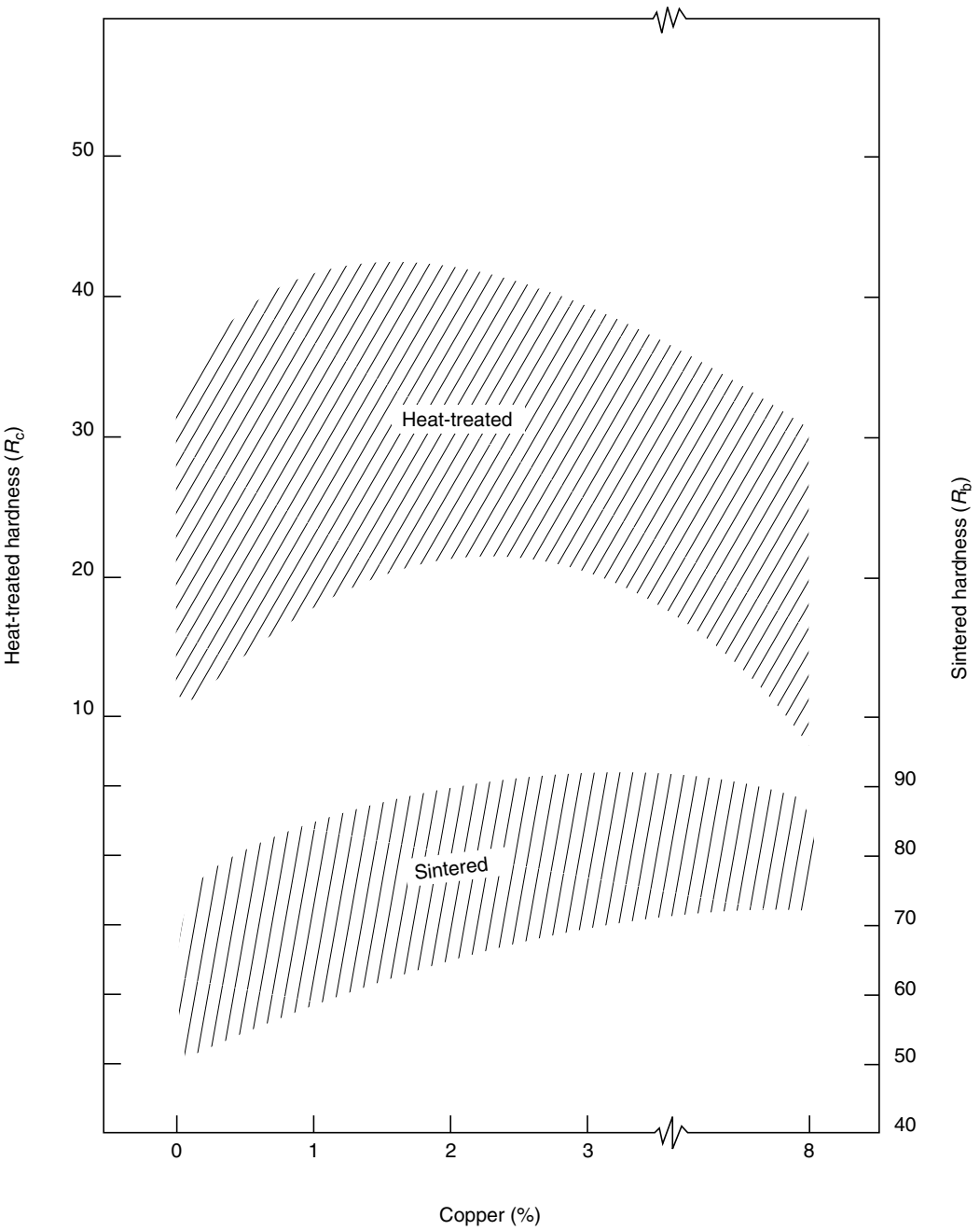

FIGURE 13.12 Variation of apparent hardness with copper content in as-sintered and heat-treated condition. (From Capus, J.M. and Maaref, A., *Proceedings of the 1973 International Powder Metallurgy Conference*, Vol. 8, 1974, pp. 61–73.)

13.6.4 Molybdenum Content

Molybdenum is a more effective alloying element than nickel for enhancing hardenability. Also it has lower affinity for oxygen and lower effect on compressibility as compared to nickel. Typical additions range from 0.5 to 1.5%. The addition of molybdenum promotes

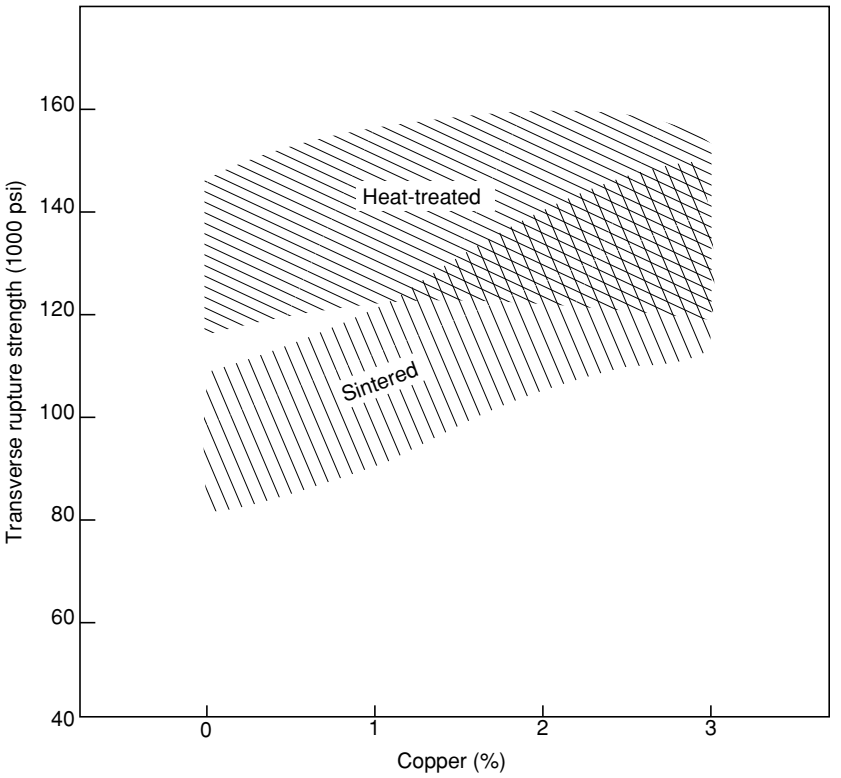

FIGURE 13.13 Variation of transverse rupture strength with copper content in as-sintered and heat-treated condition. (From Capus, J.M. and Maaref, A., *Proceedings of the 1973 International Powder Metallurgy Conference*, Vol. 8, 1974, pp. 61–73.)

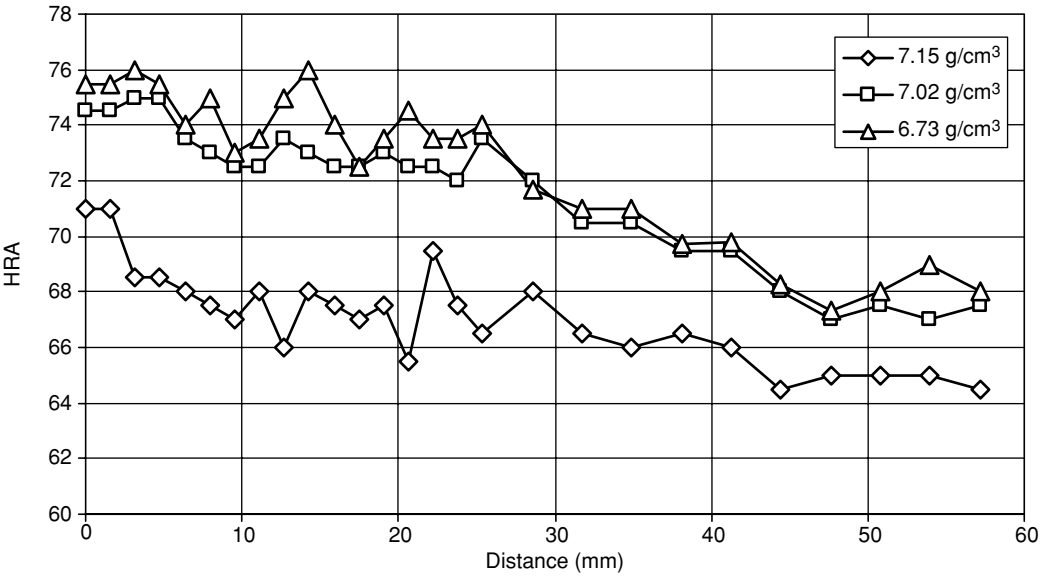

FIGURE 13.14 Jominey end-quench results on FLC-4608. (From Pershing, M.A. and Nandi, H., *Advances in Powder Metallurgy and Particulate Materials—2001*, Vol. 5, Metals Powder Industries Federation, Princeton, NJ, 2001, pp. 26–30.)

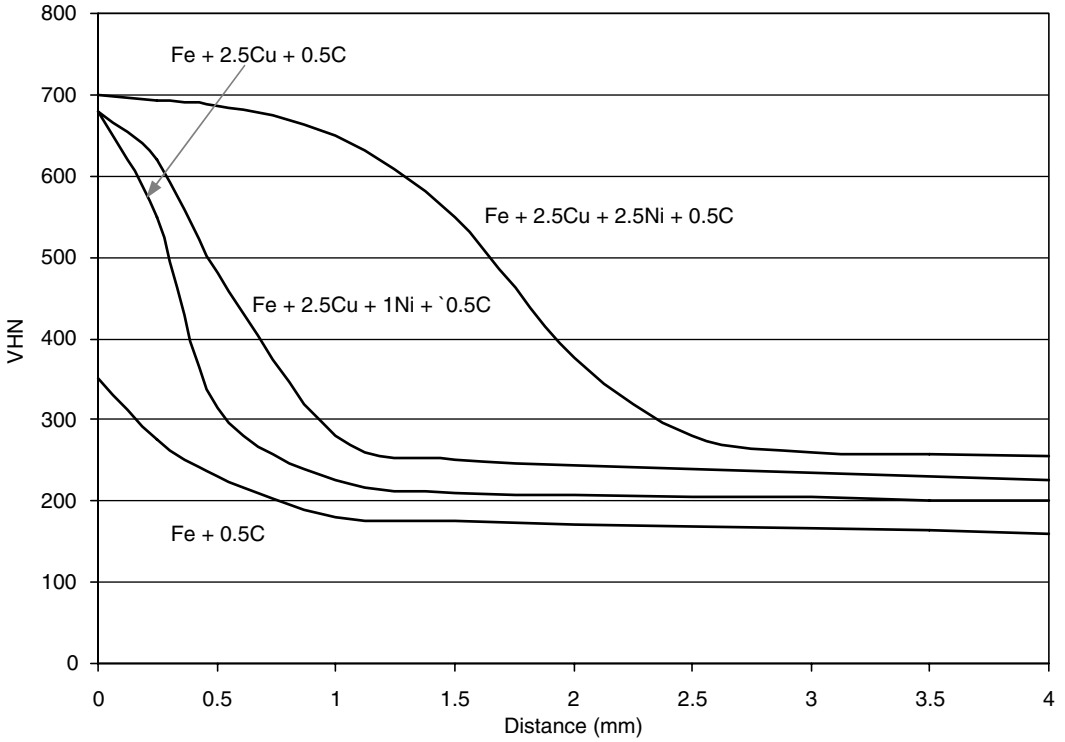

FIGURE 13.15 Effect of copper and nickel addition on the hardenability of P/M steels. Austenitizing condition was 2 h at 850°C (1560°F) and the parts were oil quenched. (From Ferguson, H., *International Journal of Powder Metallurgy*, 39(7), 33–38, 2003.)

response to heat treatment, and increases hardness, wear resistance, and strength to the required level for highly loaded P/M applications such as helical gears.

A comparison of the effect of cooling rate on properties for P/M steels containing nickel, copper, and molybdenum is shown in Figure 13.15 through Figure 13.18. Figure 13.16 shows the increase in hardenability with higher nickel and copper of up to 4% Ni and 2.25% Cu. The effect of these alloying additions is particularly apparent in the tensile strength results (Figure 13.17). The ductility is also improved significantly at all cooling rates tested (Figure 13.18). Figure 13.19 shows the effect of alloying and cooling rate on the dimensional change in the alloys. The highest addition likewise results in the smallest change in dimensions, which is the optimum result. Also, the small changes in dimensions at all cooling rates should result in lower quenching stresses and residual stresses.

13.7 EFFECT OF STARTING MATERIAL ON HOMOGENIZATION

Another difference between P/M steels and wrought steels is the degree of inhomogeneity, which is common in P/M parts. The alloying additions, discussed above, typically are added by blending powders, called admixed, of the alloying elements with iron powder. The most important reason that the alloying is done this way, rather than melting the elements together and producing the powder, called prealloyed, is to have a soft powder mixture that can be easily compacted. It is possible that a given P/M steel part could have one of four different powders as its starting material, which affects the properties and heat treatment of the steel.

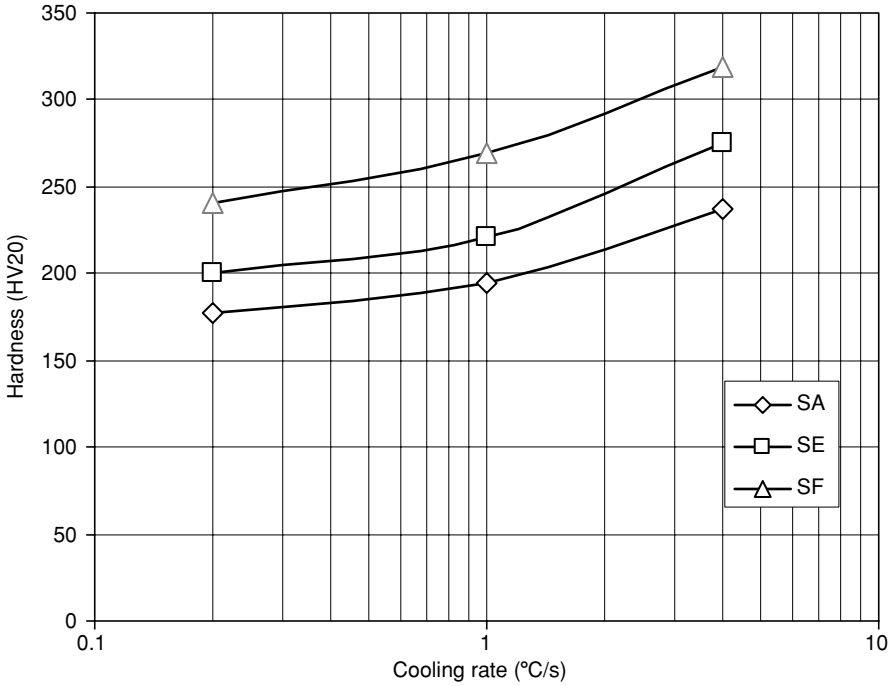

FIGURE 13.16 Effect of cooling rate of the hardness of three diffusion-alloyed P/M steels with 0.45% C. Sintered for 30 min at 1100°C in endogas. SA, Fe–1.75Ni–1.5Cu–0.5Mo; SE, Fe–4Ni–1.5Cu–0.5Mo; and SF, Fe–4Ni–2.25Cu–0.5Mo. (From Lindskog, P. and Tornblad, O., *5th European Symposium on Powder Metallurgy*, Vol. 1, 1978, p. 98; Lindskog, P. and Thornblad, O., *Powder Metallurgy International*, No. 1, 1979, p. 10; and Exner, H.E. and Danninger, H., *Powder Metallurgy of Steel, Metallurgy of Iron*, Vol. 10a,b, Springer-Verlag, Heidelberg, 1993, pp. 129a–209a, 72b–141b.)

The four types are as follows:

- *Admixed*—Elemental or master alloy powders are added to a base iron powder [9]. This method is used widely and has the lowest cost. Due to the high fraction of the mix exists as compressible (easy to compact) iron powder, it usually retains most of the compressibility. Elements that form intermetallic alloys with a low-diffusion rate are not included and the degree of alloying is limited by the mutual diffusivity of the other components. This precursor material typically has the higher degree of inhomogeneity and is particularly prone to powder segregation during handling.
- *Diffusion alloyed*—The alloying elements are diffusion-bonded to the base iron powder particles such that the core iron retains its high compressibility. Segregation of the powder during handling is essentially eliminated, but the powder still produces a very inhomogeneous microstructure with an alloying gradient varying between the center of the former powder particles and the highly alloyed interparticle boundaries.
- *Prealloyed*—All alloying elements, except carbon, are added to the melt, which is atomized to produce the powder. The sintered powder has homogeneous microstructures and compositions. However, the compressibility suffers with most alloying elements compared to admixed- and diffusion-alloyed powders and hence prealloyed powders are often considered undesirable for many turnkey operations.
- *Hybrid alloys*—Molybdenum is one alloying element, which can be in solution in iron and still be very compressible. Prealloyed- or diffusion-alloyed powders of molybdenum

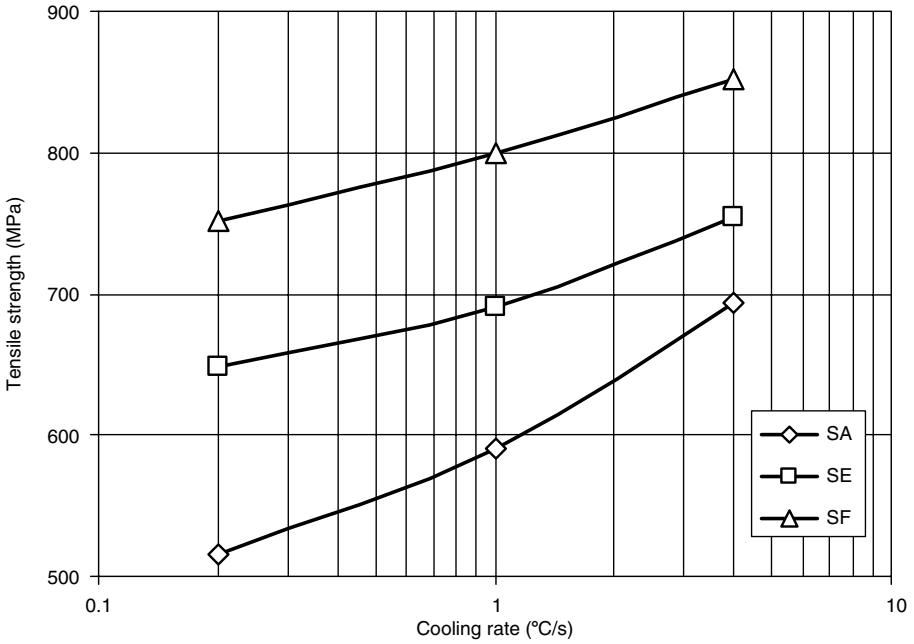

FIGURE 13.17 Effect of cooling rate on the tensile strength of three diffusion-alloyed P/M steels with 0.45% C. Sintered for 30 min at 1100°C in endogas. SA, Fe–1.75Ni–1.5Cu–0.5Mo; SE, Fe–4Ni–1.5Cu–0.5Mo; and SF, Fe–4Ni–2.25Cu–0.5Mo. (From Lindskog, P. and Tornblad, O., *5th European Symposium on Powder Metallurgy*, Vol. 1, 1978, p. 98; Lindskog, P. and Thornblad, O., *Powder Metallurgy International*, No. 1, 1979, p. 10; and Exner, H.E. and Danninger, H., *Powder Metallurgy of Steel, Metallurgy of Iron*, Vol. 10a,b, Springer-Verlag, Heidelberg, 1993, pp. 129a–209a, 72b–141b.)

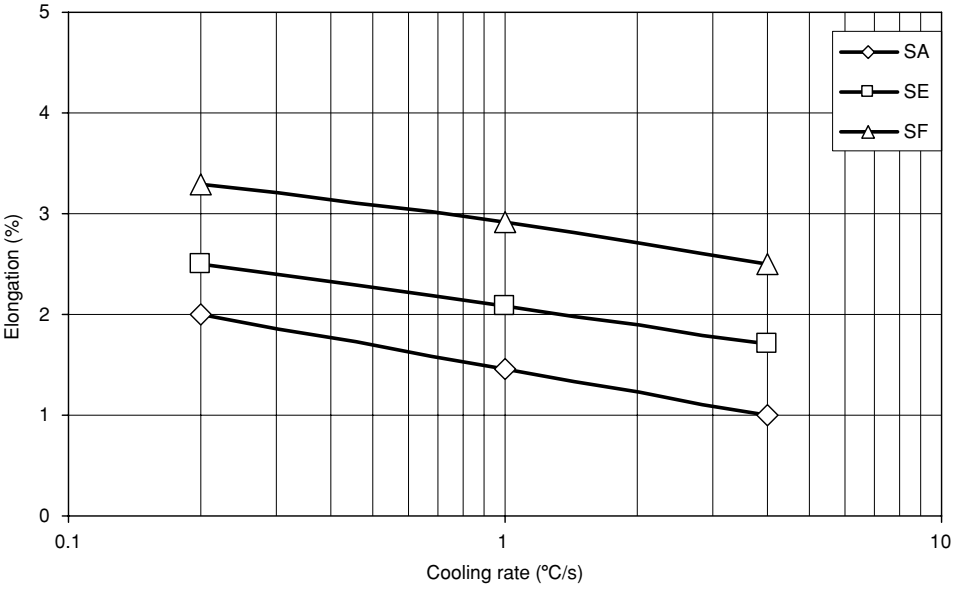

FIGURE 13.18 Effect of cooling rate on the elongation (%) of three diffusion-alloyed P/M steels with 0.45% C. Sintered for 30 min at 1100°C in endogas. SA, Fe–1.75Ni–1.5Cu–0.5Mo; SE, Fe–4Ni–1.5Cu–0.5Mo; and SF, Fe–4Ni–2.25Cu–0.5Mo. (From Lindskog, P. and Tornblad, O., *5th European Symposium on Powder Metallurgy*, Vol. 1, 1978, p. 98; Lindskog, P. and Thornblad, O., *Powder Metallurgy International*, No. 1, 1979, p. 10; and Exner, H.E. and Danninger, H., *Powder Metallurgy of Steel, Metallurgy of Iron*, Vol. 10a,b, Springer-Verlag, Heidelberg, 1993, pp. 129a–209a, 72b–141b.)

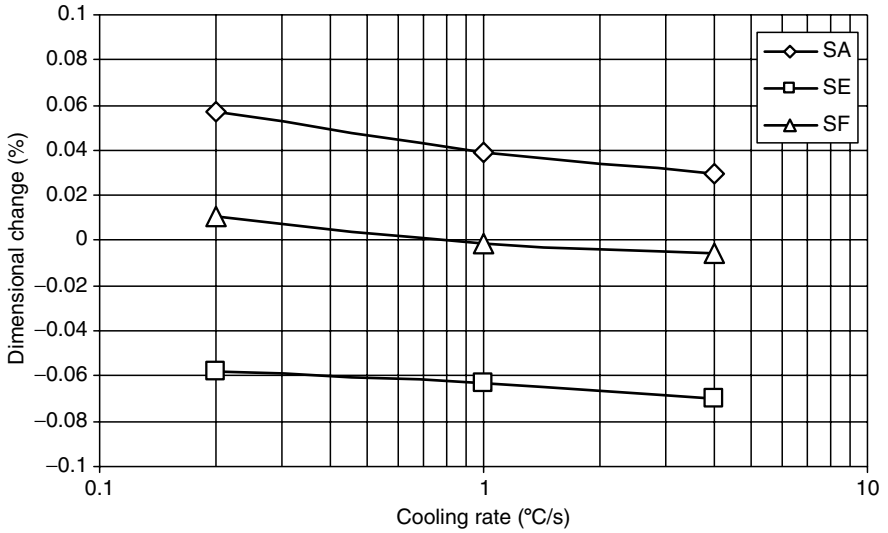

FIGURE 13.19 Effect of cooling rate on the dimensional change of three diffusion-alloyed P/M steels with 0.45% C. Sintered for 30 min at 1100°C in endogas. SA, Fe–1.75Ni–1.5Cu–0.5Mo; SE, Fe–4Ni–1.5Cu–0.5Mo; and SF, Fe–4Ni–2.25Cu–0.5Mo. (From Lindskog, P. and Tornblad, O., *5th European Symposium on Powder Metallurgy*, Vol. 1, 1978, p. 98; Lindskog, P. and Thornblad, O., *Powder Metallurgy International*, No. 1, 1979, p. 10; and Exner, H.E. and Danninger, H., *Powder Metallurgy of Steel, Metallurgy of Iron*, Vol. 10a, b, Springer-Verlag, Heidelberg 1993, pp. 129a–209a, 72b–141b.)

in iron have master alloy additions to create a series of hybrid alloy steel powders. The sintered powder typically has a less heterogeneous microstructure but retains most of the compressibility.

Carbon is also typically added in the form of graphite powder. However, carbon diffusivity is high at the sintering temperatures. The easy diffusion of carbon leads to homogenous distributions and uniform microhardness values when no other alloying additions are present.

The beneficial effects of nickel additions have been shown above. However, nickel diffuses slower than other elements, making homogenization more difficult. Consequently, it is common for the nickel composition to have a greater degree of nonuniformity than other elements [11]. Figure 13.20 illustrates a plot of the diffusivity of nickel in austenite compared to those for molybdenum and chromium [10]. The diffusion of nickel in iron between 900 and 950°C (1650 to 1790°F), common austenization temperatures, is only 1% of the rate at sintering temperatures.

A rise from 1100 to 1150°C (2010 to 2100°F) produces a doubling of the diffusivity. In this temperature range, an error of only 25°C can cause a 50% difference in nickel diffusion rate. This makes the control of temperature uniformity in the furnace very important and affects loading of parts in the furnace.

Figure 13.21 shows the effect of composition and starting powder on the hardenability. The prealloyed FL-4605 is similar in composition to the FN-0205, but has a much greater hardenability, although the surface hardness is only slightly better. The addition of nickel to F-0005 to make F-0205 also increases hardenability and surface hardness.

As a consequence of the variety of local chemical compositions, which are present after sintering, unless completely prealloyed powders are used, different microstructures will be formed on cooling. As the degree of difference in compositions locally can be very significant, it is better to look at the concept of critical cooling speed in terms of these local variations [11]. Figure 13.22 shows the conditions of maximum and minimum hardenability, and assuming that some carbon is present, it can be pointed out that [12]

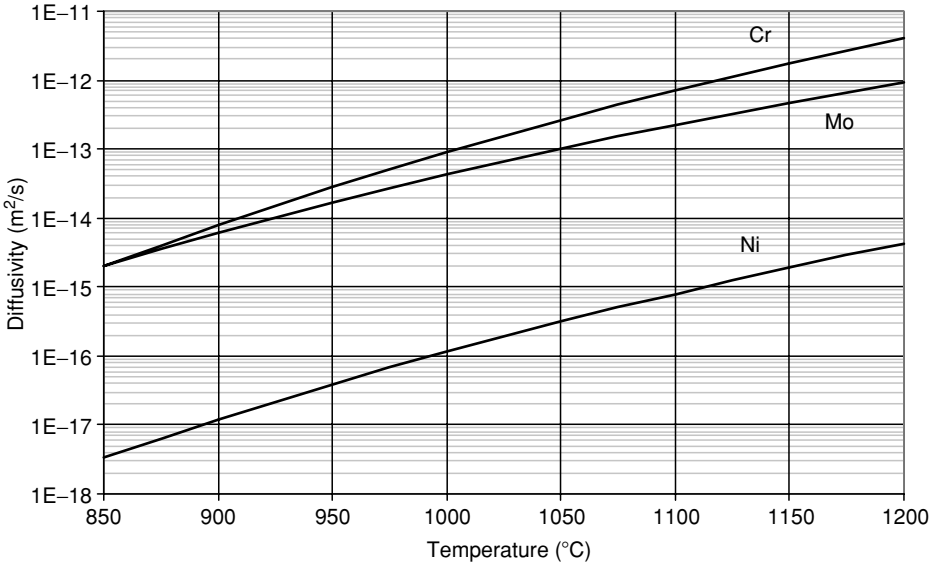

FIGURE 13.20 Difficulty of Cr, Mo, and Ni in Fe at sintering temperatures calculated from data from *Smithels Metals Reference Book*, 7th ed., Brandes, E.A., and Brook, G.B., Butterworth-Heinemann, Oxford, 1999, pp. 13–70 to 13–97

- When cooling speeds are lower than V_p, only pearlitic structures are formed. The V'_p would be the critical speed to form only pearlite in the regions richest in alloying elements.
- When cooling speeds are higher than V_m, the structure becomes completely martensitic on cooling. Likewise, V'_m would be the critical speed to form only martensite in the regions, richest in alloying elements.

The cooling speeds used in typical industrial practice after sintering are generally between V'_p and V_m. This situation typically occurs when materials based on admixed- or diffusion-bonded powders containing Ni and Mo are used. Consequently, even without a specific

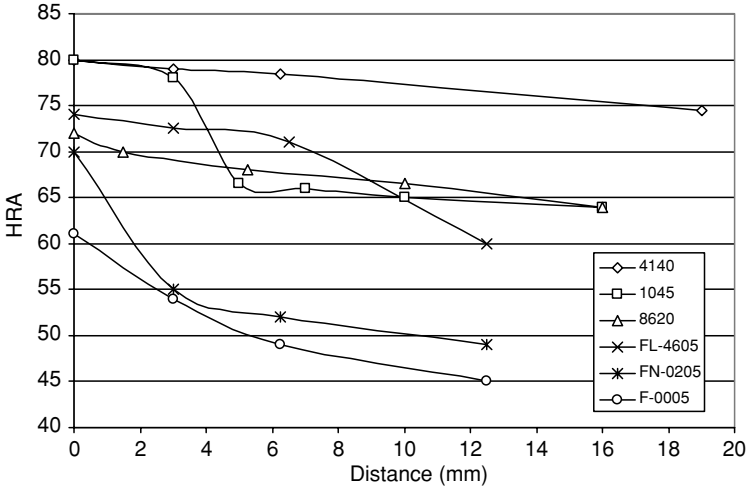

FIGURE 13.21 The effect of composition and starting powder on hardenability. See text for explanation. (From Ferguson, H., *International Journal of Powder Metallurgy*, 39(7), 33–38, 2003.)

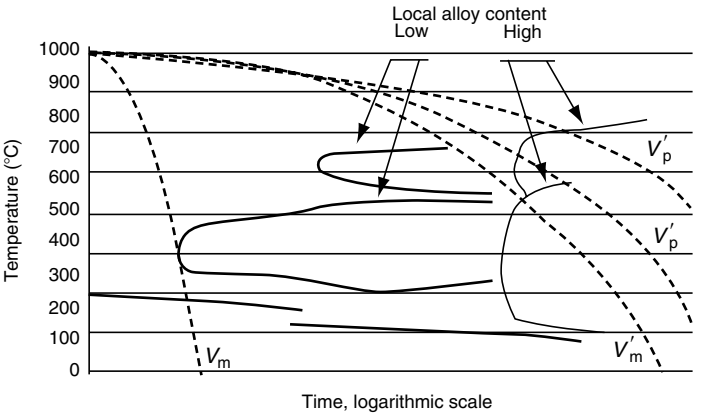

FIGURE 13.22 The effect of local variations in alloying elements on transformations in P/M steels. The inhomogenears composition leads to a variety of responses during heat treatment. (From Bocchini, G.F., *Advances in Powder Metallurgy and Particulate Materials—2001* Vol. 6, Metals Powder Industries Federation, Princeton, NJ, 2001, pp. 56–86.)

heat treatment, it is possible to observe some martensite (or possibly bainite) islands in the as-sintered state. In sintered steels, many small areas of hard phases—regularly distributed—are surrounded by softer microconstituents, which can plastically deform, through a self-adapting mechanism in case of high-applied stresses, by a cushion or damper effect [11].

Moreover, the slow diffusion of nickel results in high local concentrations in many points. When the local concentration exceeds a given threshold, austenite will survive independently of the cooling speed.

This austenite should be clearly differentiated with respect to retained or residual austenite, because it is stable or incoercible. The areas of soft austenite increase the resistance to stresses when the part is put in operation by means of local plastic-yielding and self-adapting. Lindskog and Boccini [13] explained in more detail the favorable combination of properties, typical of steels obtained from diffusion-bonded powders.

According to Boyer [14], in many instances, finely dispersed residual austenite of amount up to 30% is not detrimental to pitting fatigue strength of fully dense steels. This is partly because small amounts of retained austenite apparently allow mating surfaces to conform slightly faster and to spread the load more evenly, thus reducing the local area of high stress. This is similar to running-in bearings at low load to prolong their life at high loads. As demonstrated by repeated experiences, P/M steels from Ni-containing diffusion-bonded powders frequently exhibit randomly distributed (or finely dispersed) austenite areas. Following Boyer, this peculiarity should be seen as a favorable factor explaining several positive results of P/M parts, which have undergone demanding stress conditions. However, much lower amounts of austenite can be harmful if the austenite is not finely dispersed.

13.8 QUENCH AND TEMPERING

The as-quench properties of P/M steels depend on the cooling medium (severity of quench) and the P/M steel's hardenability. Quenching in water, salt, brine, or water-based polymer solution improves the rate of heat transfer, leading to a faster quench, but in many cases, it accelerates corrosion due to the residual quenchant trapped in surface pores. Oil quenching, although less severe than cooling in water or brine, is favored due to minimized distortion and cracking. Control of oil temperature is a must for achieving consistent results from

load-to-load. A fast oil (9 to 11 s in the magnetic quenchometer test) can be used to improve the heat transfer characteristics and is therefore recommended.

The P/M parts can absorb nearly 2 to 3% oil (by weight), which can cause problems during postquench treatment. If the oil is not completely removed, it results in heavy smoke during the tempering operation. This can not only lead to health hazard but also poses safety concerns due to the large amount of oil in the tempering furnace. Also, the much higher amount of drag out of the oil needs to be considered during processing. Most sealed quench furnaces are designed to quench out 0.5 kg (1 lb) of parts per gallon of quench oil. For P/M parts, it is recommended that 11 to 15 l (3 to 4 gal) of quench oil be used per 0.5 kg (1 lb) of parts.

Usually parts having densities greater than 6.7 g/cm^3 should be tempered after hardening. Recommended tempering temperatures for P/M parts range from 150 to 200°C (300 to 392°F) with 177°C as very common. The effect of tempering temperature on impact properties is shown in Figure 13.23 for FL-4205 at various densities. Tempering above 200°C (390°F) results in improved toughness and fatigue properties of the hardened part, while making a compromise in tensile strength and impact resistance. However, when tempering at temperatures higher than 200°C (392°F), care should be exercised as entrapped oil can ignite.

Tempering is also done to reduce the effects of retained austenite formed in low-alloy steels when rapidly quenched. Freezing by cryogenic treatment (below −100°C or −148°F) transforms the retained austenite (not the stable austenite in some nickel steels) to martensite. Following the cryogenic treatment, a second temper is done at 200°C (390°F) to relieve the stresses in newly formed martensite.

Table 13.4 shows the heat-treat properties of four different low-alloy steels tempered at 176°C (350°F) for 1 h [15]. The sintered carbon contents for the nominal 0.5% carbon level alloys varied from 0.47 to 0.53% carbon for all the listed alloys. The effect of varying carbon content on the mechanical properties of FL-42XX and FL-46XX alloy system is listed in Table 13.5.

Table 13.6 lists some recommended quench and temper parameters to achieve good wear resistance and core strength based on different ranges of porosity. These are of course general conditions and should be used only for a starting point in deciding how to heat-treat P/M steels.

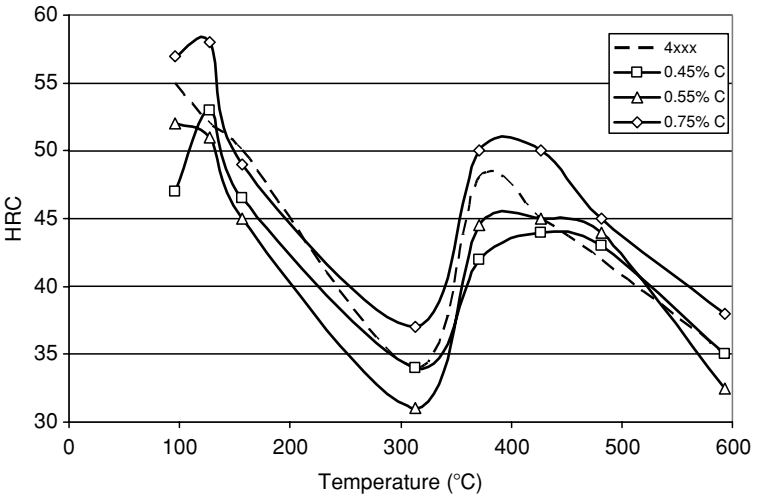

FIGURE 13.23 True hardness (VHN_{100} converted to Rockwell C) of several P/M steels vs. tempering temperature. With porosity effect removed the response during tempering is close to wrought. (From Moyer, K.H. and Jones, W.R., *Heat Treating Progress*, 2(4), 65–69, 2002.)

TABLE 13.4
Heat-Treated Properties of Low-Alloy Steels

	Density (g/cm^3)								
Alloy Grade	**TRS**	**Tensile**	**Impact**	**TRS (psi)**	**UTS (psi)**	**YS (psi)**	**Elongation (%)**	**Impact Energy (ft-lbf)**	**Hardness (HRC)**
FL-4205	6.72	6.78	6.72	190,100	129,700	—	<1	6.0	28.9
	6.95	6.97	6.95	(232,000)	150,700	—	<1	(9.0)	34.8
	7.17	7.15	7.17	270,100	179,600	159,400	<1	10.5	40.5
FL-4405	6.76	6.75	6.75	185,900	121,900	—	<1	6.3	28.2
	7.00	6.94	6.94	227,100	155,900	—	<1	8.7	35.0
	7.29	7.31	7.31	299,700	202,200	—	<1	13.2	41.4
FL-4605	6.61	6.73	6.61	168,700	125,000	—	<1	5.7	27.6
	6.95	6.96	6.95	(240,000)	147,900	—	<1	(8.5)	33.5
	7.17	7.19	7.17	280,600	175,300	—	<1	11.5	37.8
FL-4205 + 1.5 Ni	6.70	6.72	6.72	177,100	115,100	—	<1	7.0	31.6
	7.06	7.01	7.01	255,200	159,900	146,700	<1	10.2	39.7
	7.32	7.33	7.33	336,000	202,600	179,900	1	17.3	45.2

Note: Values in parentheses estimated from density carbon content data.

Source: From Sanderow, H.I. and Prucher, T., *Advances in Powder Metallurgy and Particulate Materials—1994*, Vol. 7, Metals Powder Industries Federation, Princeton, NJ, 1994, pp. 355–366.

TABLE 13.5
The Effect of Varying the Carbon Content on Heat-Treated Properties of Low-Alloy Steels

Alloy Grade	% Carbon	UTS (psi)	TRS (psi)	Impact Energy (ft-lb_f)	Hardness (HRC)
FL-42XX	0.12	88,200	147,600	18.2	8.5
	0.38	180,300	270,100	10.5	39.8
	0.50	179,600	—	—	40.5
	0.67	151,300	255,400	9.7	45.5
FL-46XX	0.16	121,200	202,800	13.5	19.8
	0.44	175,600	280,600	11.5	40.3
	0.50	175,300	—	—	37.8
	0.68	141,700	249,400	12.2	43.3

Note: All samples tempered at 176°C (350°F) for 1 h with sintered density range of 7.15–7.20 g/cm^3.
Source: From Sanderow, H.I. and Prucher, T., *Advances in Powder Metallurgy and Particulate Materials—1994*, Vol. 7, Metals Powder Industries Federation, Princeton, NJ, 1994, pp. 355–366.

Other special consideration for quench and tempering P/M parts is the large amount of surface area associated with the porosity. The significance of this effect can be seen in Table 13.7. A steel P/M part with a density of 6.81 g/cm^3 could have approximately 100 times the active surface area than expected based on part size and loading. This has important effects on the uniformity of the load, as the atmosphere composition will have a greater change from the inlet to the exhaust. Very good circulation of gases must be maintained to achieve a higher degree of uniformity.

Table 13.8 lists a number of P/M steel alloys and their hardenabilities. The hardenabilities are in terms of the depth in Jominy distance (1/16 in.) to which the Jominy bar was hardened to a minimum of 65 HRA (~29.5 HRC). The effects of density and alloy content can be readily seen.

13.9 SINTER HARDENING

It is common to have a separate, postsintering heat-treatment unit, but in some cases, it is possible to incorporate the heat treatment in the cooling portion of the sintering cycle, as done in sinter hardening. The term sinter hardening refers to a process in which the cooling rate, experienced in the cooling zone of the sintering furnace, is fast enough to transform a

TABLE 13.6
Recommended Heat Treatment Conditions for Best Wear Resistance and Core Strength at Different Densities

	Quenching				
Density (g/cm^3)	Austenizing Temperature (°C [°F])	Soak Time (min)	Transfer Time (s)	Transfer Medium	Tempering (°C [°F])
6.4–6.8	870–890 (1600–1635)	30–45	<8	Fast oil	—
6.8–7.2	850–870 (1560–1600)	45–60	<12	Fast oil	150–180 (300–355)
>7.2	820–850 (1510–1560)	60–75	<25	Medium to fast oil	170–220 (340–430)

Source: From Ferguson, H.A., *Metals Handbook*, 10th ed., *Heat Treating*, 10th ed., Vol 4, ASM, Materials Park, OH, 1991, p. 229.

TABLE 13.7
Extra Surface Area Associated with Porosity in P/M Parts

Density (g/cm^3)	5.71	6.81	7.22
Total porosity	27.4%	13.5%	8.3%
Open porosity	26.8%	10.4%	4%
Ratio open–total porosity	97.8%	77%	48%
Total pore surface (mm^2)	451,000	274,000	209,000
Total surface of open pores (mm^2)	440,000	211,000	100,000
Ratio open porosity/external area	220x	105x	50x

Source: From Rudnayova, E., Salak, A., and Zabavnik, V., *Zbornik Vedeckych Prac VST, Kosice*, No. 1, 1975, p. 177.

TABLE 13.8
Hardenability of P/M Steels vs. Density

		Depth to 65 HRA			
Material Designation	**Density (g/cm^3)**	**Depth (1/16 in.)**	**Material Designation**	**Density (g/cm^3)**	**Depth (1/16 in.)**
	6.65	<1.0		6.72	8.5
F-0005	6.87	1.0	FLN4-4405	7.10	14.5
	7.03	1.0		7.23	17.5
	6.78	1.5		6.79	13.0
F-0008	6.91	2.0	FLN6-4405	7.15	18.0
	7.06	2.0		7.30	26.0
	6.50	<1.0		6.63	26.0
FC-0205	6.82	1.5	FLC-4608	7.06	36.0
	6.96	1.5		7.14	36.0
	6.40	1.5		6.72	8.5
FC-0208	6.81	2.0	FLC-4908	7.08	9.5
	7.15	2.5		7.16	10.5
FN-0205	6.90	1.5	FLN-4608	6.82	22.5
	7.10	1.5		7.08	36.0
	7.38	2.5		7.27	36.0
	6.88	2.0		6.65	9.0
FN-0208	6.97	2.0	FLNC-4408	7.06	11.0
	7.37	3.0		7.22	15.5
	6.75	2.5		6.98	2.5
FL-4205	7.00	3.5	FD-0205	7.24	2.5
	7.20	3.5		7.32	4.5
	6.64	2.0		6.78	4.0
FL-4405	6.94	3.0	FD-0208	6.97	9.5
	7.20	4.5		7.29	12.0
	6.76	2.5		6.70	2.0
FL-4605	6.99	5.0	FD-0405	7.13	4.0
	7.12	7.0		7.26	10.0
	6.68	2.0		6.70	3.0
FLN-4205	7.00	5.0	FD-0408	7.08	8.0
	7.29	6.0		7.21	15.0
	6.71	7.5	FX-1005	7.40	2.0
FLN2-4405	7.11	10.5	FX-1008	7.39	2.5
	7.22	10.5	FX-2005	7.38	<1.0

significant portion of the material matrix into martensite. The sinter-hardening route has become increasingly popular due to its cost-effectiveness.

Advantages of sinter hardening:

- Secondary quench-hardening treatment is eliminated.
- Less severe quench leads to better dimensional control.
- Retention of quench oil in pores eliminated is leading to fewer steps during tempering.
- Oil does not have to be removed to perform secondary operations such as plating

Disadvantages of sinter hardening:

- Sinter hardened parts may not be able to be machined due to high hardness.
- Sinter hardened parts need tempering to relieve stresses and improve dynamic mechanical properties.
- High apparent hardness of sinter-hardened parts may make sizing or other secondary operations impractical

Cooling rate during sinter hardening can have a significant effect on the final properties. While there are compositions, which do not require any form of accelerated cooling to harden, there is still a gain in properties with faster cooling rates. Fans, which circulate the atmosphere in the cooling zone of the furnace, can increase the cooling rate, while even faster cooling rates can be achieved with a pressure gas quench.

Figure 13.17 through Figure 13.20 show the effect of cooling rate during sinter hardening on the mechanical properties and dimensional change of three 0.45% C diffusion prealloyed steels. As discussed earlier, composition control can lead to very good hardenability upon cooling from the sintering temperature.

Pressurized gas quenching is also effective in producing higher hardness when sinter hardening. However, this requires that the sintering furnace be equipped with an integral gas quench chamber. Since this process is of more batches than continuous, there is usually a reduction in throughput.

Vacuum sinter hardening and gas quenching show some promise for another method to achieve higher hardness. A comparison of vacuum sinter-hardened materials to wrought 4600 steel is shown in Figure 13.24. The P/M steels were sintered for 2 h at 1260°C (2300°F) in H_2, followed by a 2-bar helium gas quench. The time maintained at each temperature is 1 h. As shown, the hardness is very comparable with the wrought equivalent.

13.10 WARM COMPACTION

A major advance in P/M technology has been the warm compaction process, which yields higher density levels along with uniform density distribution. The process is applicable to both ferrous and stainless steels (still in developmental stage). The raw material consists of conventional powder mixed with a special lubricant. The lubricant system has excellent flowability and filling behavior at increased temperatures. The equipment consists of a slot heater filled with powder and fitted with oil-heated elements. The heated powder from the slot heater flows freely through electrically heated insulated hose to the filling shoe and the die assembly, which are also heated. The die assembly consists of the die, upper punch, and the adaptor table. The temperature range is 100 to 150°C (212 to 302°F). The lubricant begins to

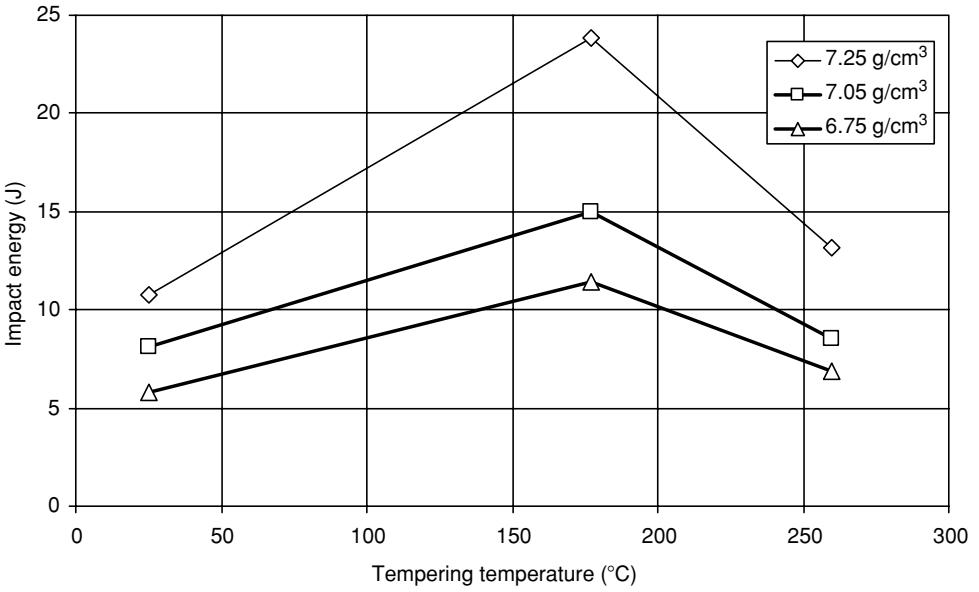

FIGURE 13.24 Effect of tempering temperature and density on the impact properties of FL-4205. (From ASM Handbook, *Powder Metal Technologies and Applications*, Vol. 7, ASM International, Metals Park, OH, 1998, p. 650.)

break down at temperatures higher than 150°C (302°F). The apparent density is decreased and the flow rate increases, which limits the working temperatures for warm compaction. Green machining of warm compacted parts is possible partly due to the increased green strength of the compact.

The mechanical properties for warm-compacted, heat-treated single press single sinter (SPSS) FLN2-4405 are given in Table 13.9 [16]. The specimens were sintered in a belt furnace at 1120°C (2050°F) for 20 min in a 90–10 N_2–H_2 atmosphere. Hardening was performed in an integral quench furnace at 870°C (1600°F) at a 0.8% carbon potential with a subsequent oil quench. Tempering was done at 175°C (350°F) for 1.5 h.

13.11 POWDER FORGING

The heat treatment of powder-forged parts is simpler in that there is a relatively small amount of porosity. Therefore concerns with low thermal conductivity and open surface porosity are practically nonexistent. The preform can be made from prealloyed powders or diffusion-bonded powders. Given sufficient forging strain and temperature, the chemical inhomogeneity of the diffusion-bonded preform can be reduced significantly. Properties depend on the forging design, as it controls porosity and homogeneity. Part surfaces tend to have somewhat higher porosity than the bulk, however, proper design eliminates most of these from consideration when the parts are heat-treated.

The difference of forged parts from typical wrought parts is the composition used. Powders tend to have lower Mn contents than wrought steels and a few other differences in minor alloying elements. These changes are relatively small. Figures 13.25 through Figure 13.27 show Jominy curves for several powder-forged steels.

TABLE 13.9
Heat-Treat Mechanical Properties for SPSS Warm-Compacted FLN2-4405 at Different Compaction Pressures

Compaction Pressure (tsi) (MPa)	Green Density (g/cm^3)	Quench and Tempering Density (g/cm^3)	TRS (10^3 psi) (Mpa)	Apparent Hardness HRA	Tensile Strength (10^3 psi) (MPa)	0.2% Yield Strength (10^3 psi) (MPa)	Elongation (%)	Impact Energy ($ft\text{-}lb_f$) (J)
30	6.92	6.95	184	72	102	—	0.7	5
(415)			(1270)		(572)			(7)
40	7.17	7.19	242	75	145	143	0.9	7
(550)			(1670)		(690)	(490)		(9)
50	7.29	7.33	270	76	165	160	0.9	8
(690)			(1860)		(779)	(538)		(10)
60	7.32	7.39	287	77	163	161	0.9	9
(825)			(1980)		(759)	(587)		(12)

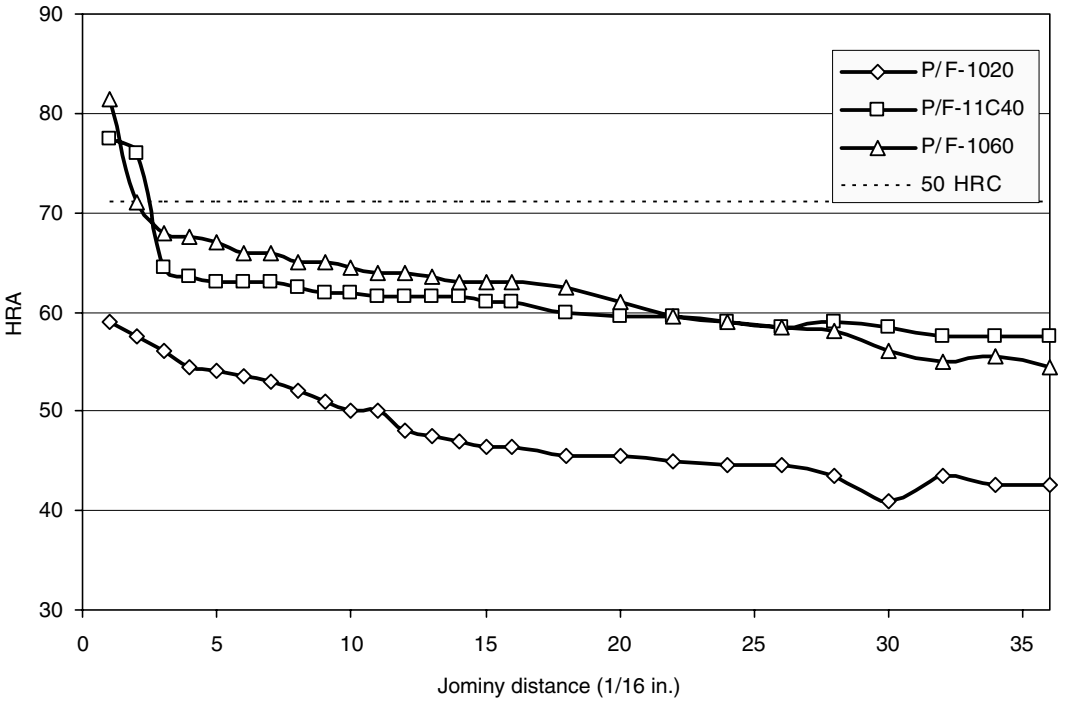

FIGURE 13.25 Jominy curves for various powder-forged P/M steels.

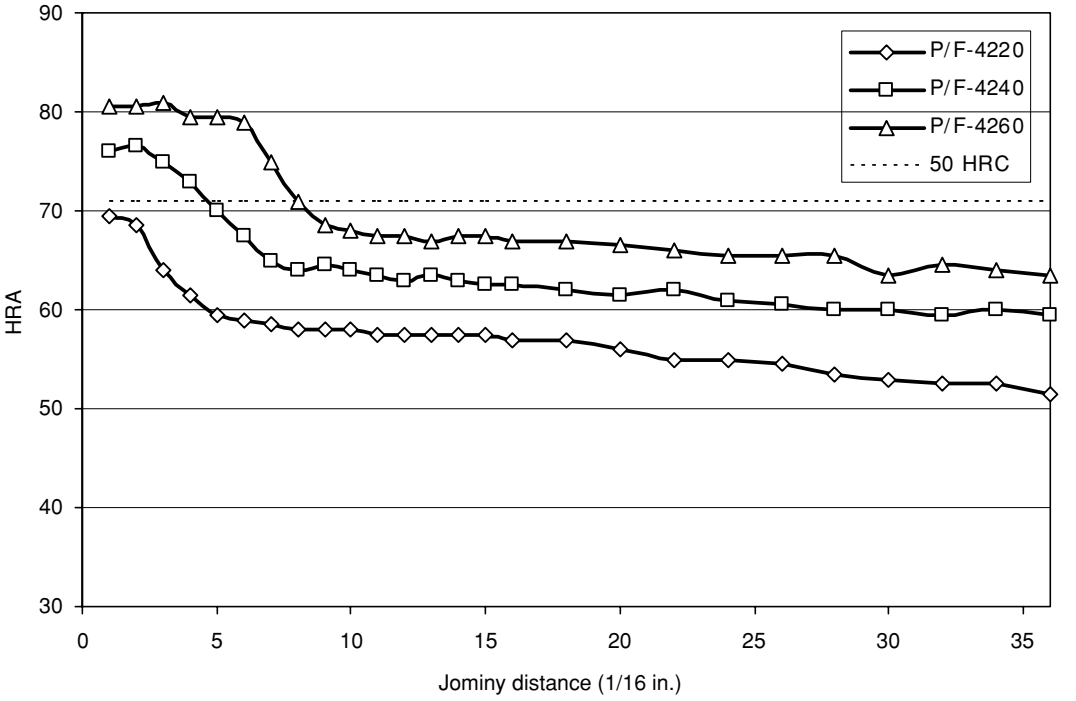

FIGURE 13.26 Jominy curves for various powder-forged P/M steels.

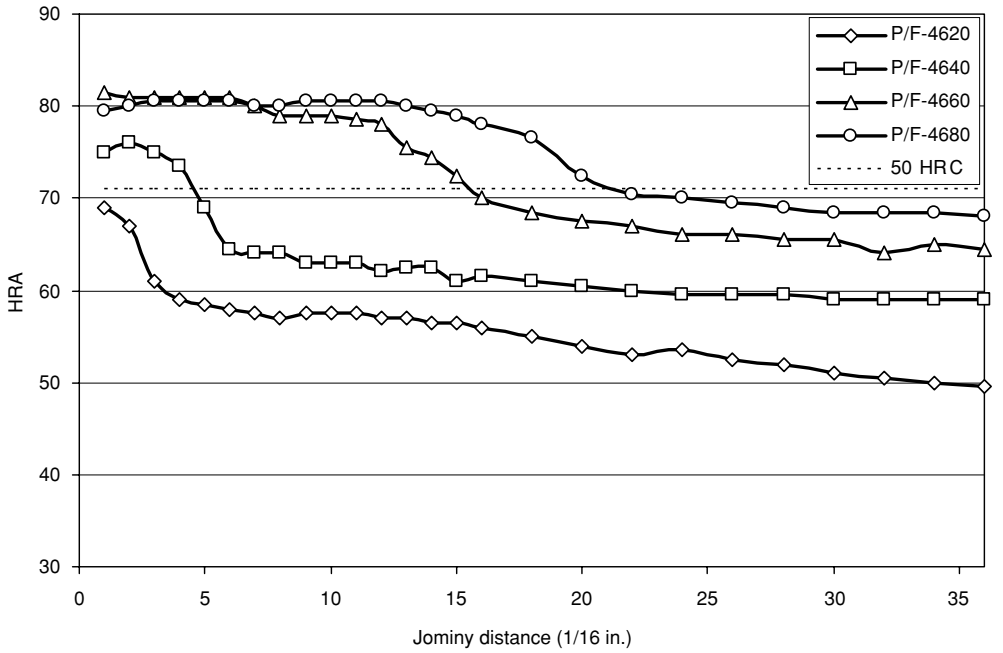

FIGURE 13.27 Jominy curves for various powder-forged P/M steels.

13.12 CASE HARDENING

As mentioned earlier, when porosity levels are such that there is significant open porosity, the pores are interconnected by small channels. This allows gases to penetrate with little hindrance. When case-hardening P/M parts contain gases with a high-carbon potential, this interconnected porosity allows diffusion of carbon into the internal pore surfaces as well as to the external surfaces of the part. This can result in carburization to a significant depth and consequent loss of any sharply defined case-hardening effect. The same condition can also be applied to other gaseous surface-hardening procedures such as nitriding or carbonitriding. In fact, the swelling, which occurs during nitriding, can be very detrimental if it occurs internally due to open porosity.

Figure 13.28 shows the effect of density on the case depth during vacuum carburizing of an iron–copper alloy. Lower densities produce much higher case depth. The line for 50 HRC indicates the effective case.

P/M parts are case-hardened to obtain higher hardness, wear, fatigue, or impact properties. The primary purpose of case hardening low-carbon steels is to provide a hard, wear-resistant surface while maintaining a soft-ductile core. This combination imparts optimum wear resistance and toughness properties to these materials.

13.12.1 CARBURIZING

The material usually specified for carburizing contains allowing elements such as nickel, molybdenum, and copper to increase hardenability, but with relatively low-carbon content. To develop optimum dynamic properties at porosity levels between 10 and 15%, a combined carbon level of 0.30 to 0.35% is recommended. As porosity is reduced below 10%, combined carbon can be reduced to 0.15 to 0.25%. As improved dynamic properties are also associated with high densities, it is recommended that combined carbon can be adjusted to a level best suited to repressing after sintering. Parts with porosity levels much higher than 15% are not

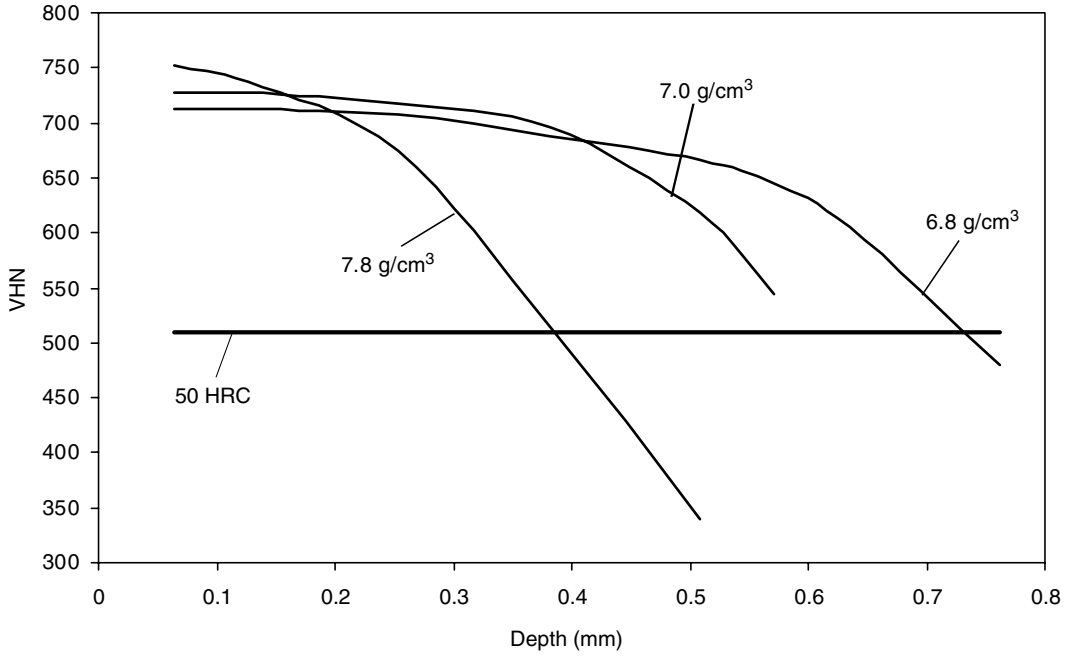

FIGURE 13.28 Effect of porosity on carbon penetration and effective case depth during vacuum Carburizing. Ferguson, H.A., *Metals Progress*, 7(6), 1975, 81–83.

recommended for carburizing because of the penetration of the pores by the carburizing gas. As already mentioned, liquid carburizing is not suitable for P/M parts because of the problem of washing the parts free of salt after the treatment. Table 13.10 gives some expected results from carburizing for different ranges of porosity.

In wrought steel, carburization is normally characterized by a surface-hardness range and an effective case depth. Microhardness measurements can accurately show the hardness profile in a cross section of wrought steel but can be erratic when used on P/M steels, where subsurface porosity can influence the hardness readings. It is recommended that at

TABLE 13.10
Effect of Density on Features of Carburized Layers on P/M Steels

Density, g/cc	Typical Properties of Carburized Layers
>7.1	Definite thickness, repeatable with precision, analogously to the one, which occurs when carburizing fully dense steels
7.1 to >6.9	The thickness may exhibit a certain scattering, which is fairly controllable through careful control of the carburizing process, carried out in a reliable equipment
6.9 to >6.6	The thickness may exhibit nonnegligible scattering, not withstanding the care and the precision in conducting the carburizing process
<6.6	The thickness may exhibit very high variations, from lot to lot, from part to part, and below differently oriented part surfaces

Source: From Bocchini, G.F., *Advances in Powder Metallurgy and Particulate Materials—2001*, Vol. 6, Metals Powder Industries Federation, Princeton, NJ, 2001, pp. 56–86.

least three readings be taken at each level below the surface and averaged to determine effective case depth (a detailed review of this procedure can be found in Ref. [13]).

P/M steels are usually gas-carburized at temperatures between 900 and 930°C (1650 and 1705°F). Time cycles are normally short because of the rapid diffusion of carbon through the interconnected porosity. Therefore, atmospheric carbon potentials for P/M steels need to be somewhat higher than those required for wrought steels of similar composition.

The rate of carbon penetration into steel is controlled by the diffusion of carbon in austenite and not by the kinetics of the chemical reactions at the surface [17,18]. As a general guideline, the carburizing of ferrous P/M components can be achieved with a lower carbon potential and in a shorter time compared to their wrought and cast counterparts. For an 86% dense P/M alloy, the carbon can be raised from 0.04 to 0.5% at a depth of 2 mm (0.08 in.) in just 2 h at 0.90% carbon potential. Figure 13.29 shows the effects of density and atmosphere on the case depth achieved at 870°C (1600°F).

13.12.2 Carbonitriding

Carbonitriding is a modified form of gas carburizing, which uses additions of up to 10% ammonia into the gas-carburizing atmosphere, and results in the addition of nitrogen to the carburized case. Dissociated nitrogen forms at the workpiece surface from the ammonia in the furnace atmosphere. Nitrogen diffuses into the steel surface simultaneously with the carbon, retarding the critical cooling rate on quenching and leading to a more consistent martensite transformation. It also produces a more consistent surface hardness profile, which improves wear resistance and toughness of the P/M steel. Process temperatures for carbonitriding are lower (800 to 850°C (1470 to 1560°F)), providing better control of distortion than carburizing.

Carbonitriding is a shallow case-hardening treatment. Case depths greater than 0.5 mm (0.02 in.) are seldom specified. For this reason, cycle times are relatively short, usually on the

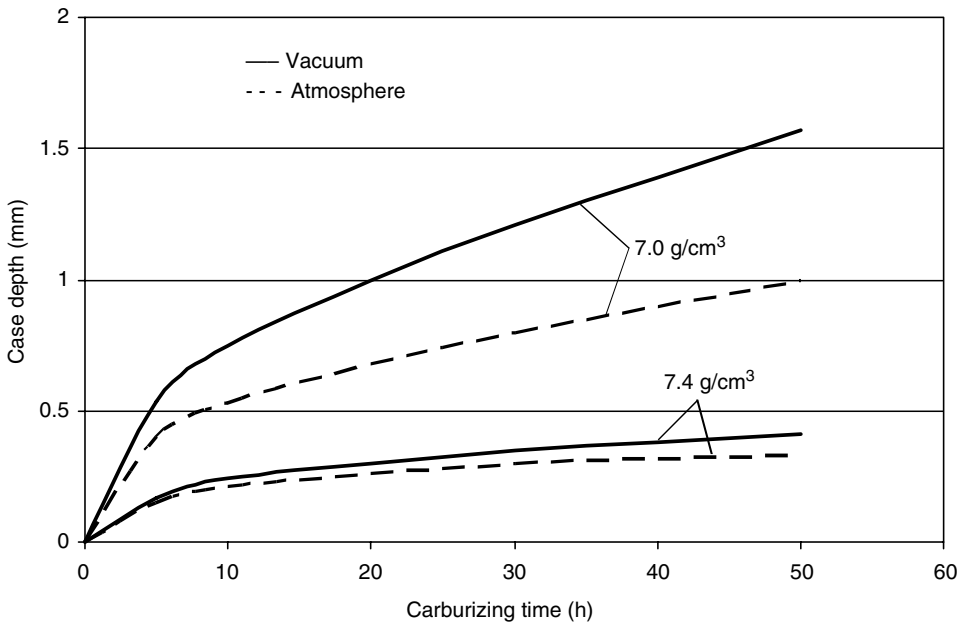

FIGURE 13.29 Dependence of case depth after carburizing P/M parts at 870°C to microhardness of 700 HV (10 g) on carburizing time and density. (From Jansson, P., *Powder Metallurgy*, No. 1, 1992, p. 63.)

order of 30 to 60 min. As in neutral hardening, carbon control is a critical aspect of the treatment. Normally, carbon potentials of 1.0 to 1.2% are specified to maintain the carbon profile in the part.

13.12.3 Induction Hardening

Spur gears, bevel gears, splined hubs, and cams are ideal components for the production using P/M. These parts usually require hard, wear-resistant surfaces at some location, and a more tougher ductile matrix. Locally hardening the piece helps to maintain dimensions. Induction hardening is commonly specified for these applications. The inductance of P/M materials is typically less than that of a wrought material of similar composition due to porosity; a higher power setting is normally required to reach a given depth of hardening. Furthermore, as the heat is rapidly dissipated, a rapid transfer to the quench is mandatory.

As with wrought steels, the response to hardening by induction is dependent on combined carbon content, alloy content, and surface decarburization. This latter variable can be a major concern with P/M parts. With today's conventional belt-type sintering furnaces using an endogas atmosphere, decarburization can occur as the parts leave the hot zone and cool slowly through the 1100 to 800°C (2010 to 1470°F) temperature range.

In most instances, induction-heated P/M parts are quenched in a water-based solution, containing some type of rust preventative to forestall internal corrosion. In those applications, where induction hardening is considered, densities above 90% should be specified. With a decrease in density, the resistivity of the steel increases and permeability decreases. For this reason, integral quench coils using a high-velocity spray quench are generally used to attain maximum surface hardness in the P/M part. Drag out of the quenchant will depend on the open surface porosity as discussed with oil quenchants.

The effect of porosity on the induction-hardening process is dependent on the material, as mentioned above. The magnetic properties of P/M steels are not all known, so predicting behavior is somewhat difficult. One study considered some measured parameters and calculated the relative penetration depth as a function of porosity and is shown in Figure 13.30 [11].

Recently, progress has been made in using induction-hardening techniques, which combine two frequencies at the same time. The high frequency helps to achieve the desired level of surface hardness, while a mid-frequency helps to provide the desired depth of hardening.

13.12.4 Nitrocarburizing

Nitrocarburizing is increasingly performed on P/M parts. Gaseous nitrocarburizing is a diffusion heat treatment that involves the addition of nitrogen and carbon to the surfaces of steel parts. It differs from carbonitriding mainly in that the temperatures used are lower, within the ferritic phase region, typically 570 to 600°C (1060 to 1110°F). Since no phase transformations occur, the dimensional changes and distortion are significantly reduced. Nitrogen is diffused into the surfaces of the steel in sufficient concentration to form a thin layer of ε-iron nitride on the surface of the part, producing a thin, hard, wear-resistant case. The effect of nitrocarburization on improving the fatigue strength of two P/M steels is shown in Figure 13.31.

The nitrocarburizing process can be carried out in a conventional integral quench atmosphere furnace. The atmosphere usually consists of a 50:50 mixture of endothermic gas and anhydrous ammonia. The control of the nitrided layer thickness, as with other treatments, is dependent on density. If the nitrided layer is allowed to form on the internal pore surfaces to any significant extent, a volume expansion can occur. For this reason, density of the P/M part should be above 90% of the pore-free density. This nitrided layer can reduce the coefficient of friction and improve the wear resistance better than conventional quench-hardening treatments. The process is best used in applications where sliding wear and fretting are involved.

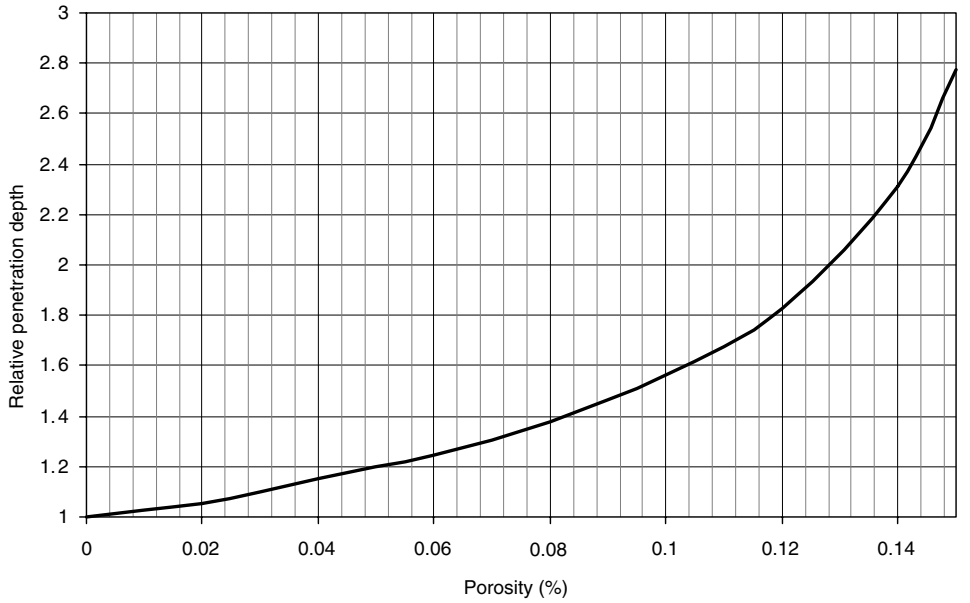

FIGURE 13.30 Porosity can increase penetration depth during induction hardening. One calculation of the relative penetration depth with porosity is shown. (From Bocchini, G.F., *Advances in Powder Metallurgy and Particulate Materials—2001*, Vol. 6, Metals Powder Industries Federation, Princeton, NJ, 2001, pp. 56–86; Bocchini, G.F., *International Seminar on Principles and Methods of Engineering Design*, Naples, Italy, 1–3 October 1997, pp. 239–266.)

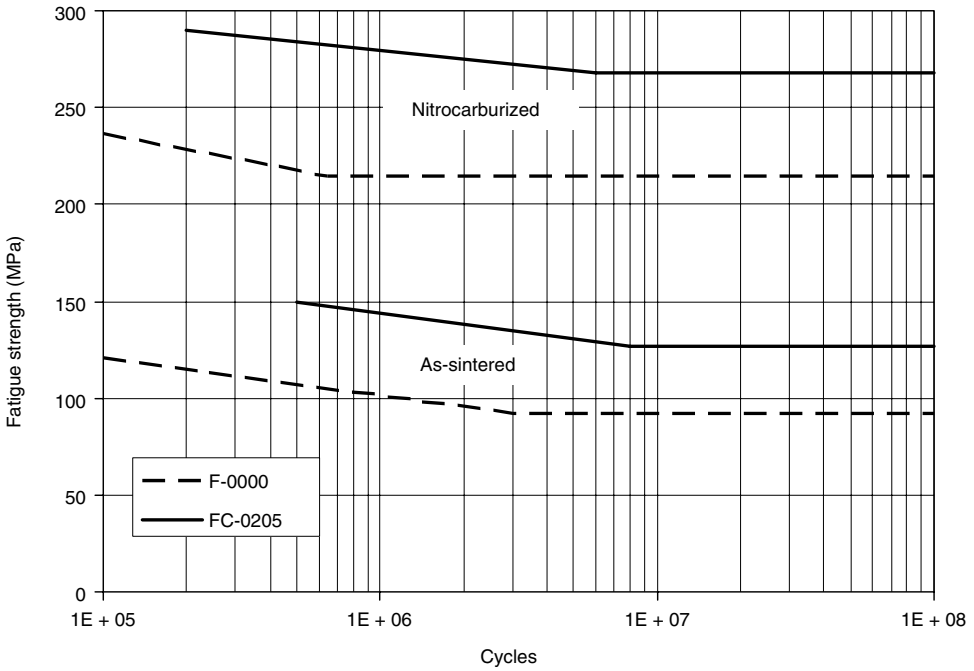

FIGURE 13.31 Effect of nitrocarburization on the notched fatigue strength of two low-carbon P/M steels (7.0 g/cm^3). (From Ferguson, H.A., *Metals Progress*, 7(6), 1975, 81–83.)

As the hard-nitrided layer is relatively thin, the process should not be applied where high indentation or impact loading is involved. The ε-nitride layer that is formed can attain a surface hardness in excess of HRC 60, depending on the alloy content of the steel. Indentation hardness testing is also not recommended when evaluating this process. Since no transformation occurs, the P/M parts can be air-cooled without loss of surface hardness. Also no oil absorption occurs, which leaves the porosity open for impregnation if desired.

13.12.5 Nitriding

P/M parts can be nitrided using alkali salts, gases, or plasmas, with the majority of applications using gases. Alkali salts can be used in some applications, as the trapped salts may not be detrimental if the part is constantly immersed in oil during service. This disadvantage can be negated and increase in fatigue strength of 100% can be achieved [19].

Gas nitriding is most often done in ammonia or nitrogen-containing ammonia. Dissociation of ammonia in the presence of iron at temperatures above 450°C (840°F) can be used to nitride up to ~950°C (~1740°F). However, normally gas nitriding is performed at temperatures below 590°C (1095°F)as higher temperatures can lead to complete nitriding of the iron. Depths of 0.5 to 1 mm are achieved in the range of 540 to 560°C (1005°F to 1040°F) [20].

The change from closed porosity to open porosity that occurs when density drops below 92% dramatically changes the nitriding behavior of P/M parts. The ε-phase can form internally if open porosity is present. Figure 13.32 [23] shows the fraction of ε-phase formed with nitriding time at 540°C (1005°F) with different densities. Open porosity can lead to nearly complete transformation to ε-phase at these temperatures. Typically, lower density

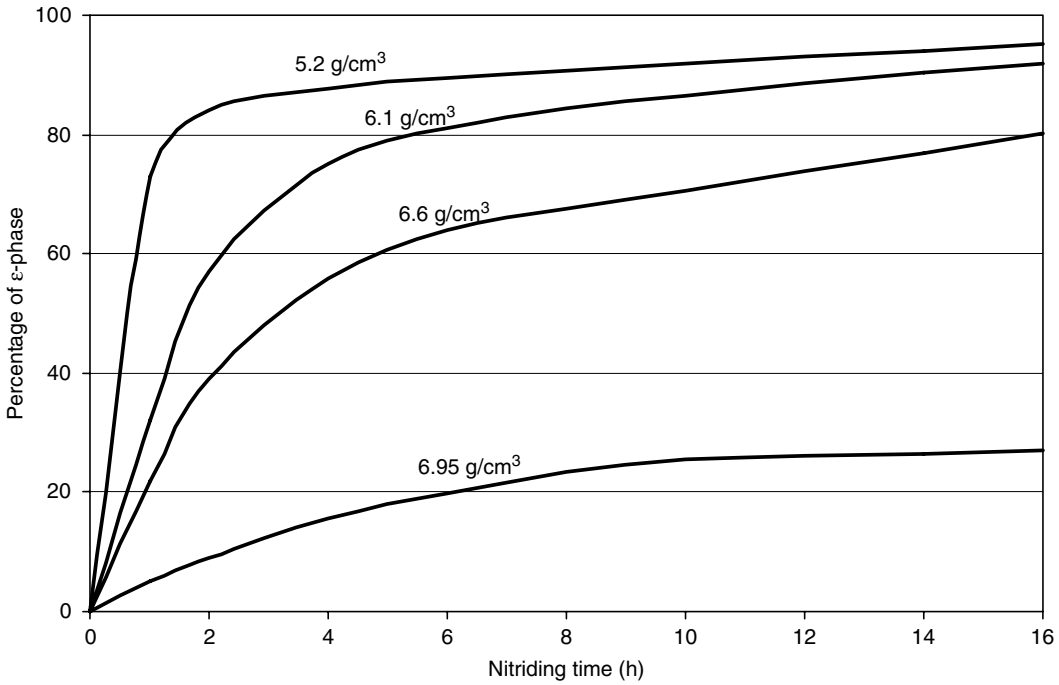

FIGURE 13.32 Effect of nitriding time of sintered sponge iron specimens of different porosity in ammonia at 540°C on the percentage of ε-phase. (From Rudnayova, E., Salak, A., and Zabavnik, V., *Zbornik Vedeckych Prac VST, Kosice*, No. 1, 1975, p. 177.)

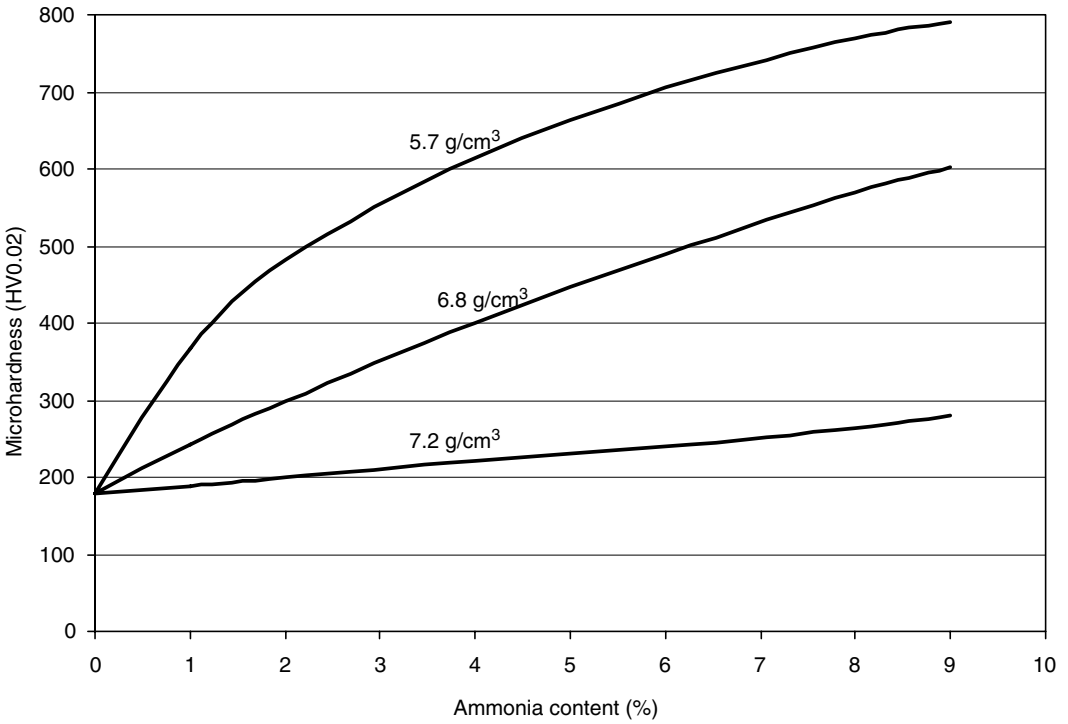

FIGURE 13.33 Effect of density on gas nitrided hardness of sponge iron specimens in ammonia at 540°C. (From Rudnayova, E., Salak, A., and Zabavniks, V., *Zbornik Vedeckych Prac VST, Kosice*, No.1, 1975, p. 177.)

parts will have higher nitrided hardness, as shown in Figure 13.33. The formation of ε-phase inside pores can cause significant swelling, with the effect increasing with time and porosity (Figure 13.34). In order to nitride parts with densities below 92%, some form of pore-closing treatment is recommended.

13.12.6 Steam Treating

Steam treating is often done on P/M parts to both seal surface porosity and to increase the hardness of the surface. This tends to improve the corrosion resistance, pressure tightness, and wear resistance. Unfortunately, it also tends to reduce the tensile strength and ductility from 10 to 20%, depending on conditions and the steel chosen. Steam treatment usually consists of heating P/M parts in a steam atmosphere at elevated temperatures to form a layer of iron oxide, most often Fe_3O_4 at temperatures between 510 and 570°C (950 to 1060°F). The oxide is formed inside the surface porosity as well, pinching off the opening due to the volume expansion associated with the conversion of the iron. In addition to sealing the surface the hardness of the surface is raised, as magnetite has a hardness equivalent to HRC 50.

The recommended procedure for steam treating is as follows [21]:

1. Wash parts to remove any fluids that may have been absorbed from prior operations.
2. Load onto a fixture and place in a furnace preheated to 315°C (600°F).
3. Heat parts in air until the center of the load has stabilized as the set temperature

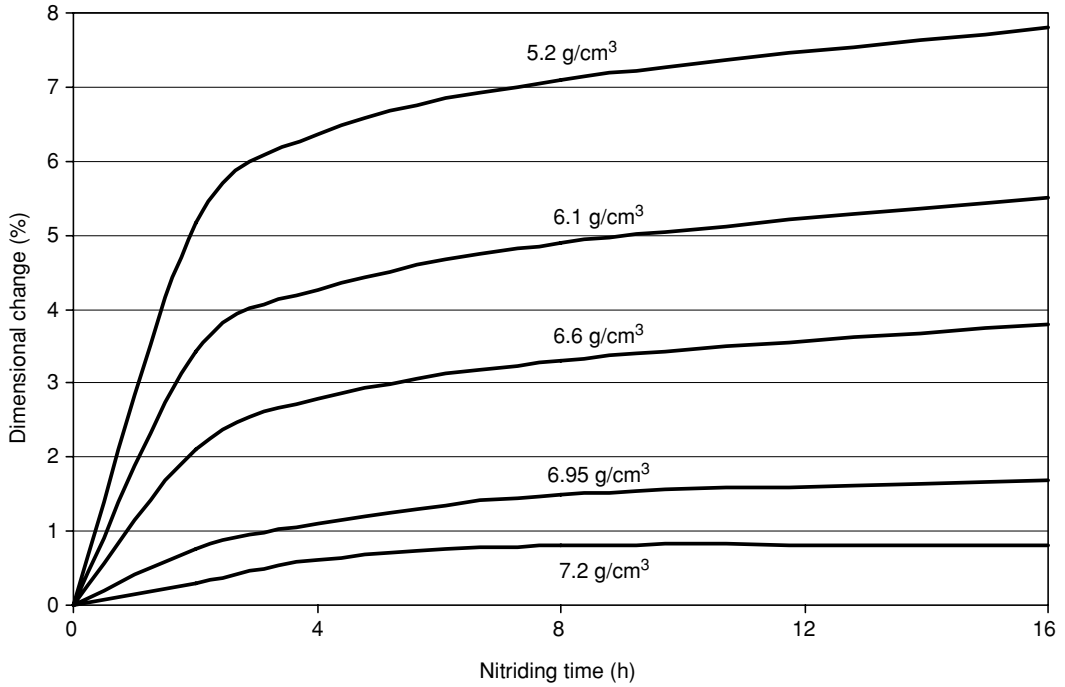

FIGURE 13.34 Dimensional change of sponge iron specimens exposed to Ammonia at 540°C (1000°F). Swelling increases with increasing porosity. (From Rudnayova, E. Salak, A., and Zabavnik, V., *Zbornik Vedeckych Prac VST, Kosice*, No.1, 1975, p. 177.)

4. Introduce superheated steam at a line pressure of 35 to 105 kPa (5 to 15 psi) and purge for at least 15 min
5. Increase furnace temperature to desired steam treatment temperature (between 510 and 595°C (950 to 1100°F) and hold for no longer than 4 h at heat.
6. On completion of treatment, reduce furnace temperature to 315°C (600°F). When parts reach this temperature, the steam can be shutoff and the parts unloaded

Caution should be exercised when opening the furnace after the treatment, as hydrogen gas, produced during the process, can ignite. It is recommended that a nitrogen purge be applied prior to unloading. The increase in density and apparent hardness produced by steam treating on various P/M steels is shown in Table 13.11 [10,22].

In steam-treated P/M steels, the ductility is significantly reduced due to the internal stresses created by the formation of the iron oxide. It is not recommended to steam treat steels with more than 0.5% carbon, due to the high internal stresses, initiating microcracks and causing extremely low ductility.

13.12.7 Black Oxiding

Black oxiding is used to improve the hardness of steel parts and provide an oxidation-resistant coating that improves the appearance of the steel. It is used with parts for firearms, auto parts, turbines, bearings, and electrical parts.

Black oxidizing is a chemical process, which uses a heated alkaline nitrate solution, typically 140°C. The black-oxidizing solution can become trapped in the pores in the steel

TABLE 13.11
Effects of Steam Treatment on Density and Hardness of P/M Steels

	Density (g/cm^3)		Apparent Hardness	
Material	**Sintered**	**Steam-Treated**	**Sintered**	**Steam-Treated**
F-0000-N	5.8	6.2	7HRF	75HRB
F-0000-P	6.2	6.4	32HRF	61HRB
F-0000-R	6.5	6.6	45HRF	51HRB
F-0008-M	5.8	6.1	44HRB	100HRB
F-0008-P	6.2	6.4	58HRB	98HRB
F-0008-R	6.5	6.6	60HRB	97HRB
FC-0700-N	5.7	6.0	14HRB	73HRB
FC-0700-P	6.35	6.5	49HRB	78HRB
FC-0700-R	6.6	6.6	58HRB	77HRB
FC-0708-N	5.7	6.0	52HRB	97HRB
FC-0708-P	6.3	6.4	72HRB	94HRB
FC-0708-R	6.6	6.6	79HRB	93HRB

Source: From Pease, III, L.F., Collette, J.P., and Pease, D.A., *Modern Developments in P/M*, Vol. 21, Metals Powder Industries Federation, Princeton, NJ, 1988, p. 275.

part if the density is low enough. In addition, copper-containing steel parts do not black oxide well, leading to poor-quality surfaces.

REFERENCES

1. D.G. White, State of the North American P/M Industry—2002, in *Advances in Powder Metallurgy & Particulate Materials—2002*, Metals Powder Industries Federation, Princeton, NJ, 2002, part 1, pp. 1–12.
2. K. Barton, S. Das, J. Lu, M. Goldenberg, D. Olsen, and J. LaSalle, *Advances in Powder Metallurgy and Particulate Materials—2001*, Vol. 4, Metals Powder Industries Federation, Princeton, NJ, 2001, pp. 159–165.
3. MPIF Standard 35, *Materials Standards for P/M Structural Parts*, Metals Powder Industries Federation, Princeton, NJ, 2000.
4. S. Saritas, R.D. Doherty, and A. Lawley, *Advances in Powder Metallurgy and Particulate Materials—2001*, Vol. 10, Metals Powder Industries Federation, Princeton, NJ, 2001, pp. 112–130.
5. D.H. Herring and P.T. Hansen, Key consideration in the heat treatment of ferrous P/M materials, in *Proceedings of the 17th Heat Treating Conference*, ASM International, Metals Park, OH, 1998, p. 213.
6. G.F. Bocchini, V. Fontanari, and A. Molinari, Friction effects in metal powder compaction; part one: theoretical aspects, in *International Conference on Powder Metallurgy and Particulate Materials*, Metals Powder Industries Federation, Princeton, NJ, 1995.
7. J.M. Capus and A. Maaref, Modern developments in powder metallurgy, in *Proceedings of the 1973 International Powder Metallurgy Conference*, Vol. 8, 1974, pp. 61–73.
8. M.A. Pershing and H. Nandi, *Advances in Powder Metallurgy and Particulate Materials—2001*, Vol. 5, Metals Powder Industries Federation, Princeton, NJ, 2001, pp. 26–30.
9. W.B. James, *Advances in Powder Metallurgy and Particulate Materials—1998*, Metals Powder Industries Federation, Princeton, NJ, pp. 1–25, 1998.
10. E.A. Brandes and G.B. Brook, Eds., *Smithells Metals Reference Book*, 7th ed., Butterworth-Heinemann, Oxford, 1999.

11. G.F. Bocchini, Overview of surface treatment methods for PM parts, in *Advances in Powder Metallurgy and Particulate Materials—2001*, Vol. 6, Metals Powder Industries Federation, Princeton, NJ, 2001, pp. 56–86.
12. G.F. Bocchini, How to design sintered steels for advanced applications, in *International Seminar on Principles and Methods of Engineering Design*, Naples, Italy, 1–3 October 1997, pp. 239–266.
13. P.F. Lindskog and G.F. Bocchini, Development of high strength P/M precision components in Europe, *International Journal of Powder Metallurgy & Powder Technology*, 15(3), 199, 1979.
14. H.E. Boyer, Ed., *Case Hardening of Steels*, ASM International, Metals Park, OH, 1985.
15. H.I. Sanderow and T. Prucher, *Advances in Powder Metallurgy and Particulate Materials—1994*, Vol. 7, Metals Powder Industries Federation, Princeton, NJ, 1994, pp. 355–366.
13. I.W. Donaldson and M.L. Marucci, *Advances in Powder Metallurgy and Particulate Materials — 2003*, Vol. 7, Metals Powder Industries Federation, Princeton, NJ, 2003, pp. 230–245.
17. G. Krauss, *Microstructure, Residual Stresses, and Fatigue of Carburized Steels*, *3 rd International Seminar on Quenching and Carburizing IFHTSE and IMM*, 1991, pp. 201–217.
18. C.R. Brooks, *Principles of the Surface Treatment of Steels*, Technomic Publications, Lancaster, PA, 1984, pp. 78–80.
19. H. Krzyminski, *Harterei Technische Mitteiluugen*., No. 1, 1971, p. 2.
20. A. Salek, *Ferrous Powder Metallurgy*, Cambridge International, Cambridge, 1995, p. 300.
21. H. Ferguson, Heat treatment of ferrous powder metallurgy parts, in *Powder Metal Technologies and Applications*, ASM International, Metals Park, OH, 1998, pp. 645–655.
22. L.F. Pease, III, J.P. Collette, and D.A. Pease, Mechanical properties of steam-blackened P/M materials, in *Modern Developments in P/M*, Vol. 21, Metals Powder Industries Federation, Princeton, NJ, 1988, p. 275.
23. E. Rudnayova, A. Salak, and V. *Zabavnik, Zbornik Vedeckych Prac VST, Kosice*, No. 1, 1975, p. 177.
24. H. Ferguson, Heat treatment of P/M parts, *Metal Progress*, ASM, 107(6), 81–83, June 1975; 108(2), 66–69, July 1975.

Appendix 1
Common Conversion Constants

Quantity	Traditional Units	SI Equivalent
1 atmosphere	$1\,\text{atm} = 760\,\text{mmHg}$	$101{,}325\,\text{N/m}^2$
Avogadro's constant	$N_A = 6.0225 \times 10^{23}$	$6.0225 \times 10^{23}\ \text{mol}^{-1}$
1 angstrom	$1\ \text{Å} = 10^{-8}$ cm	1×10^{-10} m
1 bar	$1\ \text{bar} = 1\,\text{dyn/cm}^2$	10^5N/m^2
Boltzmann's constant	$k = 1.380 \times 10^{-16}\,\text{erg/°C}$	1.380×10^{-23} J/K
1 calorie	$1\ \text{cal} = 2.61 \times 10^{19}$ eV	4.184 J
1 dyne	$1\ \text{dyn} = 2.25 \times 10^{-6}$ lb	1×10^{-5} N
1 dyne/cm^2	$1.45 \times 10^{-5}\,\text{lb/in.}^2$	10^1N/m^2
1 day	86,400 s	86.4 ks
1 degree (angle)	$1° = 0.017$ rad	17 mrad
1 erg	6.24×10^{11}eV 2.39×10^{-8} cal	10^{-7}J
1 erg/cm^2	6.24×10^{11} eV/cm^2	10^{-3} J/m^2
Gas constant	R 8.3143 $\times 10^7$ erg-atom^{-1} 1.987 cal (deg^{-1}g-atom^{-1})	8.3143 J/mol/K
Electronic charge	e$^-$4.8 $\times 10^{-10}$esu	1.6021×10^{-19}C
1 electron volt	eV 3.83×10^{-20}cal 1.6021×10^{-12}erg	1.6021×10^{-19}J
Faraday constant	$F = N_{Ae}$	9.648×10^4C/mol
1 inch	1 in. = 2.54 cm	2.54×10^{-2}m
1 kilocalorie	$1\,\text{kcal} = 4.186 \times 10^{10}$erg	
1 kilogram	1 kg = 2.21 lb	1 kg
1 kilogram/cm^2	1 kg = 2.21 lb	1 kg
1 kilogram/cm^2	$1\ \text{kg/cm}^2 = 14.22\,\text{lb/in.}^2$	10^4 kg/m^2
1 liter	1 L = 1.057 qt	1 dm^3
1 micron	$\mu\text{m} = 10^4\text{Å}$	10^{-4} cm 10^{-6} M
1 minute (angle)	$\text{min} = 2.91 \times 10^{-4}$ rad	2.91×10^{-4}rad
Planck's constant	$\text{h} = 6.6256 \times 10^{-27}$erg	6.6256×10^{-34}Js
1 pound	lb = 453.59 g	0.45359 kg
Mass of electron	$m^e = 9.1091 \times 10^{-28}$g	9.1091×10^{-31}kg
1 pound (force)	$1\,\text{lb}_f$	4.4482 N
1 psi	$1\,\text{lb}_f/\text{in.}^2$	$6.895 \times 10^3\ \text{N/m}^2$
1 radian	1 rad = 57.296°	1 rad
1 ton (force)	$1\ \text{ton}_f$	9.96402 kN
1 tsi	$1\ \text{ton}_f/\text{in.}^2 = 1.5749\,\text{kg/mm}^2$	15.4443 MN/m^2 15.443 MPa
1 tonne (metric ton)	1 t = 2200 lb = 1.1 tons	10^3 kg
1 torr	1 torr = 1 mmHg	133.322N/m^2
Velocity of light	$c = 2.997925 \times 10^{10}$ cm/s	2.997925×10^8 m/s

Appendix 2
Temperature Conversion Table

°C	°F/°C[a]	°F
−273	−459.4	—
−268	−450	—
−262	−440	—
−257	−430	—
−251	−420	—
−246	−410	—
−240	−400	—
−234	−390	—
−229	−380	—
−223	−370	—
−218	−360	—
−212	−350	—
−207	−340	—
−201	−330	—
−196	−320	—
−190	−310	—
−184	−300	—
−179	−290	—
−173	−280	—
−169	−273	−459.4
−168	−270	−454
−162	−260	−436
−157	−250	−418
−151	−240	−400
−146	−230	−382
−140	−220	−364
−134	−210	−346
−129	−200	−328
−123	−190	−310
−118	−180	−292
−112	−170	−274
−107	−160	−256
−101	−150	−238
−95.6	−140	−220
−90.0	−130	−202
−84.4	−120	−184
−78.9	−110	−166
−73.3	−100	−148
−67.8	−90	−130

Continued

(Continued)

°C	°F/°C[a]	°F
−62.2	−80	−112
−56.7	−70	−94
−51.1	−60	−76
−45.6	−50	−58
−40.0	−40	−40
−34.4	−30	−22
−28.9	−20	−4
−27.8	−18	−0.4
−26.7	−16	1.8
−25.6	−14	5.4
−24.4	−12	9
−23.3	−10	14
−17.8	0	32
−17.2	1	33.8
−16.7	2	35.6
−16.1	3	37.4
−15.6	4	39.2
−15.0	5	41.0
−14.4	6	42.8
−13.9	7	44.6
−13.3	8	46.4
−12.8	9	48.2
−12.2	10	50.0
−11.7	11	51.8
−11.1	12	53.6
−10.6	13	55.4
−10.0	14	57.2
−9.4	15	59.0
−8.89	16	60.8
−8.33	17	62.6
−7.78	18	64.4
−7.22	19	66.2
−6.67	20	68.0
−6.11	21	69.8
−5.56	22	71.6
−5.00	23	73.4
−4.44	24	75.2
−3.89	25	77.0
−3.33	26	78.8
−2.78	27	80.6
−2.22	28	82.4
−1.67	29	84.2
−1.11	30	86.0
−0.56	31	87.8
0	32	89.6
0.56	38	91.4
1.11	34	93.2
1.67	35	95.0
2.22	36	96.8
1.67	35	95.0
2.22	36	96.8
2.78	37	98.6

Continued

°C	°F/°C[a]	°F
3.33	38	100.4
3.89	39	102.2
4.44	40	104.0
5.00	41	105.8
5.56	42	107.6
6.11	43	109.4
6.67	44	111.2
7.22	45	113.0
7.78	46	114.8
8.33	47	116.6
8.89	48	118.4
9.44	49	120.2
10.0	50	120.0
10.6	51	123.8
11.1	52	125.6
11.7	53	127.4
12.2	54	129.2
12.8	55	131.0
13.3	56	132.8
13.9	57	134.6
14.4	58	136.4
15.0	59	138.2
15.6	60	140.0
16.1	61	141.8
16.7	62	143.6
17.2	63	145.4
17.8	64	147.2
18.3	65	149.0
18.9	66	150.8
19.4	67	152.6
20.0	68	154.4
20.6	69	156.2
21.2	70	158.0
21.7	71	159.8
22.2	72	161.6
22.8	73	163.4
23.3	74	165.2
23.9	75	167.0
24.4	76	168.8
25.0	77	170.6
25.6	78	172.4
26.1	79	174.2
26.7	80	176.0
27.2	81	177.8
27.8	82	179.6
28.3	83	181.4
28.9	84	183.2
29.4	85	185.0
30.0	86	186.8
30.6	87	188.6

Continued

(Continued)

°C	°F/°C[a]	°F
31.1	88	190.4
31.7	89	192.2
32.2	90	194.0
32.8	91	195.8
33.3	92	197.6
33.9	93	199.4
34.4	94	201.1
35.0	95	203.0
35.6	96	204.8
36.1	97	206.6
36.7	98	208.4
37.2	99	210.2
37.8	100	212.0
38	100	212
43	110	230
49	120	248
54	130	266
60	140	284
66	150	302
71	160	320
82	180	356
88	190	374
93	200	392
99	210	410
100	212	413
104	220	428
110	230	446
116	240	464
121	250	482
127	260	500
132	270	518
138	280	536
143	290	554
149	300	572
154	310	590
160	320	608
166	330	626
171	340	644
177	350	662
182	360	680
188	370	698
193	380	716
199	390	734
204	400	752
210	410	770
216	420	788
208	430	806
227	440	824
232	450	842
238	460	860
243	470	878
249	480	896

Continued

°C	°F/°C[a]	°F
254	490	914
260	500	932
266	510	950
271	520	968
282	540	1004
288	550	1022
293	560	1040
299	570	1058
304	580	1076
310	590	1094
316	600	1112
321	610	1130
327	620	1148
332	630	1166
338	640	1184
343	650	1202
349	660	1220
354	670	1238
360	680	1256
366	690	1274
371	700	1292
377	710	1310
382	720	1328
388	730	1346
393	740	1364
399	750	1382
404	760	1400
410	770	1418
416	780	1436
421	790	1454
427	800	1472
432	810	1490
438	820	1508
443	830	1526
449	840	1544
454	850	1562
460	860	1580
446	870	1598
471	880	1616
477	890	1634
482	900	1652
488	910	1670
493	920	1688
499	930	1706
504	940	1724
510	950	1742
516	960	1760
521	970	1778
527	980	1796
532	990	1814
538	1000	1832

Continued

(Continued)

°C	°F/°C[a]	°F
543	1010	1850
549	1020	1868
554	1030	1886
560	1040	1904
566	1050	1922
571	1060	1940
577	1070	1958
582	1080	1976
588	1090	1994
593	1100	2012
599	1110	2030
604	1120	2048
610	1130	2066
616	1140	2084
621	1150	2102
627	1160	2120
632	1170	2138
638	1180	2156
643	1190	2174
649	1200	2192
654	1210	2210
660	1220	2228
666	1230	2246
671	1240	2264
677	1250	2282
682	1260	2300
688	1270	2318
693	1280	2336
699	1290	2354
704	1300	2372
710	1310	2390
716	1320	2408
721	1330	2426
727	1340	2444
732	1350	2462
738	1360	2480
743	1370	2498
749	1380	2516
754	1390	2534
760	1400	2552
766	1410	2570
771	1420	2588
777	1480	2606
782	1440	2624
788	1450	2642
793	1460	2660
799	1470	2678
804	1480	2696
810	1490	2714
816	1500	2732
821	1510	2750
827	1520	2768

Continued

°C	°F/°C[a]	°F
832	1530	2786
838	1540	2804
843	1550	2822
849	1560	2840
854	1570	2858
860	1580	2876
866	1590	2894
871	1600	2912
877	1610	2930
882	1620	2948
888	1630	2966
893	1640	2984
899	1650	3002
904	1660	3020
910	1670	3038
916	1680	3056
921	1690	3074
927	1700	3092
932	1710	3110
938	1720	3128
949	1730	3146
949	1740	3164
954	1750	3182
960	1760	3200
966	1770	3218
971	1780	3236
977	1790	3254
982	1800	3272
988	1810	3290
993	1820	3308
999	1830	3326
1004	1840	3340
1010	1850	3362
1016	1860	3380
1021	1870	3398
1027	1880	3416
1032	1890	3434
1038	1900	3452
1043	1910	3470
1049	1920	3488
1054	1930	3506
1060	1940	3524
1066	1950	3542
1071	1960	3560
1077	1970	3578
1082	1980	3596
1088	1990	3614
1093	2000	3632
1099	2010	3650
1104	2020	3668
1110	2030	3686

Continued

(Continued)

°C	°F/°C[a]	°F
1116	2040	3704
1121	2050	3722
1127	2060	3740
1132	2070	3758
1138	2080	3776
1143	2090	3794
1149	2100	3812
1154	2110	3830
1160	2120	3848
1166	2130	3866
1171	2140	3884
1177	2150	3902
1182	2160	3920
1188	2170	3938
1193	2180	3956
1199	2190	3974
1204	2200	3992
1210	2210	4010
1216	2220	4028
1221	2230	4046
1227	2240	4064
1232	2250	4082
1238	2260	4100
1243	2270	4118
1249	2280	4136
1254	2290	4154
1260	2300	4172
1266	2310	4190
1271	2320	4208
1277	2330	4226
1282	2340	4244
1288	2350	4262
1293	2360	4280
1299	2370	4298
1304	2380	4316
1310	2390	4334
1316	2400	4352
1321	2410	4370
1327	2420	4388
1332	2430	4406
1338	2440	4424
1343	2450	4442
1349	2460	4460
1354	2470	4478
1360	2480	4496
1366	2490	4514
1371	2500	4532
1377	2510	4550
1382	2520	4568
1388	2530	4586
1393	2540	4604
1399	2550	4622

Continued

°C	°F/°C[a]	°F
1404	2560	4640
1410	2570	4658
1416	2580	4676
1421	2590	4694
1427	2600	4712
1432	2610	4730
1438	2620	4748
1443	2630	4766
1449	2640	4784
1454	2650	4802
1460	2660	4820
1466	2670	4838
1471	2680	4856
1477	2690	4874
1482	2700	4892
1488	2710	4910
1493	2720	4928
1499	2730	4946
1504	2740	4964
1510	2750	4972
1516	2760	5000
1521	2770	5018
1527	2780	5036
1532	2790	5054
1538	2800	5072
1543	2810	5090
1549	2820	5108
1554	2830	5126
1560	2840	5144
1566	2850	5162
1571	2860	5180
1577	2870	5198
1582	2880	5216
1588	2890	5234
1593	2900	5252
1599	2910	5270
1604	2920	5288
1610	2930	5306
1616	2940	5324
1621	2950	5342
1627	2960	5360
1632	2970	5378
1638	2980	5396
1643	2990	5414
1649	3000	5432

[a]Identify the desired value to be converted in the°F/°C column and then look to either the°C column or the°F column for the conversion. For example, if the −200 in the°F/°C column is read as −200°F, then look to the°C column to find the value converted to −129°C, but if the −200 in the°F/°C column is read as −200°C, then look to the°F column to find the value converted to −328°F.

Appendix 3
Volume Conversion Table

Cubic Feet (ft^3)	Cubic Meters /Cubic Feet (m^3/ft^3)	Cubic Meters (m^3)
35.3	1	0.0283
70.6	2	0.0566
105.9	3	0.0850
141.3	4	0.113
176.6	5	0.142
211.9	6	0.170
247.2	7	0.198
282.5	8	0.227
317.8	9	0.255
353.2	10	0.283
388.5	11	0.312
423.8	12	0.340
459.1	13	0.368
494.4	14	0.396
529.7	15	0.425
565.1	16	0.453
600.4	17	4.481
635.7	18	0.510
671.0	19	0.538
706.3	20	0.566
741.6	21	0.595
777.0	22	0.623
812.3	23	0.651
847.6	24	0.680
882.9	25	0.708
918.2	26	0.736
953.5	27	0.765
988.9	28	0.793
1024	29	0.821
1059	30	0.850
1095	31	0.878
1130	32	0.906
1165	33	0.935
1201	34	0.963
1236	35	0.991
1271	36	1.02
1307	37	1.05
1342	38	1.08

Continued

(Continued)

Cubic Feet (ft^3)	Cubic Meters/Cubic Feet (m^3/ft^3)	Cubic Meters (m^3)
1377	39	1.10
1413	40	1.13
1448	41	1.16
1483	42	1.19
1519	43	1.22
1554	44	1.25
1589	45	1.27
1625	46	1.30
1660	47	1.33
1695	48	1.36
1730	49	1.39
1766	50	1.42
1801	51	1.44
1836	52	1.47
1872	53	1.50
1907	54	1.53
1942	55	1.56
1978	56	1.59
2013	57	1.61
2048	58	1.64
2084	59	1.67
2119	60	1.70
2154	61	1.73
2190	62	1.76
2225	63	1.78
2260	64	1.81
2296	65	1.84
2331	66	1.87
2366	67	1.90
2402	68	1.93
2437	69	1.95
2472	70	1.98
2507	71	2.01
2543	72	2.04
2578	73	2.07
2613	74	2.10

[a]Identify the desired value to be converted to the m^3/ft^3 column and then look to either the ft^3 column or the m^3 for the conversion. For example, if the 1 in the m^3/ft^3 column is read as 1 m^3, then look to the ft^3 column to find the value converted to 35.3 ft^3, but if the 1 in the m^3/ft^3 column is being read as 1 ft^3, then look to the m^3 column to find the value converted to 0.0283 m^3.

Appendix 4
Hardness Conversion Tables: Hardened Steel and Hard Alloys

Rockwell Scale							DPH	KHN[a] 500 g	BHN	Tensile Strength
C	A	D	15 m	30 m	45 m	g	10 kg	and Over	3000 kg	10^3 psi (Approx.)
80	92.0	86.5	96.5	92.0	87.0	—	1865	—	—	—
79	91.5	85.5	—	91.5	86.5	—	1787	—	—	—
78	91.0	84.5	96.0	91.0	85.5	—	1710	—	—	—
77	90.5	84.0	—	90.5	84.5	—	1633	—	—	—
76	90.0	83.0	95.5	90.0	83.5	—	1556	—	—	—
75	89.5	82.5	—	89.0	82.5	—	1478	—	—	—
74	89.0	81.5	95.0	88.5	81.5	—	1400	—	—	—
73	88.5	81.0	—	88.0	80.5	—	1323	—	—	—
72	88.0	80.0	94.5	87.0	79.5	—	1245	—	—	—
71	87.0	79.5	—	86.5	78.5	—	1160	—	—	—
70	86.5	78.5	94.0	86.0	77.5	—	1076	972	—	—
69	86.0	78.0	93.5	85.0	76.5	—	1004	946		
68	85.5	77.0	—	84.5	75.5	—	942	920	—	—
67	85.0	76.0	83.0	83.5	74.5	—	894	895	—	—
66	84.5	75.5	92.5	83.0	73.0	—	854	870	—	—
65	84.0	74.5	92.0	82.0	72.0	—	820	846	—	—
64	83.5	74.0	—	81.0	71.0	—	789	822	—	—
63	83.0	73.0	91.5	80.0	70.0	—	763	799	—	—
62	82.5	72.5	91.0	79.0	69.0	—	739	776	—	—
61	81.5	71.5	90.5	78.5	67.5	—	716	754	—	—
60	81.0	71.0	90.0	77.5	66.5	—	695	732	614	—
59	80.5	70.0	89.5	76.5	65.5	—	675	710	600	—
58	80.0	69.0	—	75.5	64.0	—	655	690	587	—
57	79.5	68.5	89.0	75.0	63.0	—	636	670	573	—
56	79.0	67.5	88.5	74.0	62.0	—	617	650	560	—
55	78.5	67.0	88.0	73.0	61.0	—	598	630	547	301
54	78.0	66.0	87.5	72.0	59.5	—	580	612	534	291
53	77.5	65.5	87.0	71.0	58.5	—	562	594	522	282
52	77.0	64.5	86.5	70.5	57.5	—	545	576	509	273
51	76.5	64.0	86.0	69.5	56.0	—	528	558	496	264
50	76.0	63.0	85.5	68.5	55.0	—	513	542	484	255
49	75.5	62.0	85.0	67.5	54.0	—	498	526	472	246
48	74.5	61.5	84.5	66.5	52.5	—	485	510	460	237
47	74.0	60.5	84.0	66.0	51.5	—	471	495	448	229

Continued

Rockwell Scale							DPH	KHN[a] 500 g	BHN	Tensile Strength
C	A	D	15 m	30 m	45 m	g	10 kg	and Over	3000 kg	10^3 psi (Approx.)
46	73.5	60.0	83.5	65.0	50.0	—	458	480	237	221
45	73.0	59.0	83.0	64.0	49.0	—	446	466	426	214
44	72.5	58.5	82.5	63.0	48.0	—	435	452	415	207
43	72.0	57.5	82.0	62.0	46.5	—	424	438	404	200
42	71.5	57.0	81.5	61.5	45.5	—	413	426	393	194
41	71.0	56.0	81.0	60.5	44.5	—	403	414	382	188
40	70.5	55.5	80.5	59.5	43.0	—	393	402	372	182
39	70.0	54.5	80.0	58.5	42.0	—	383	391	362	177
38	69.5	54.0	79.5	57.5	41.0	—	373	380	352	171
37	69.0	53.0	79.0	56.5	39.5	—	363	370	342	166
36	68.5	52.5	78.5	56.0	38.5	—	353	360	332	162
35	68.0	51.5	78.0	55.0	37.0	—	343	351	322	157
34	67.5	50.5	77.0	54.0	36.0	—	334	342	313	153
33	67.0	50.0	76.5	53.0	35.0	—	325	334	305	148
32	66.5	49.0	76.0	52.0	33.5	—	317	326	297	144
31	66.0	48.5	75.5	51.5	32.5	—	309	318	290	140
30	65.5	47.5	75.0	50.5	31.5	—	301	311	283	136
29	65.0	47.0	74.5	49.5	30.0	91.0	293	304	276	132
28	64.5	46.0	74.0	48.5	29.0	90.0	285	297	270	129
27	64.0	45.5	73.5	47.5	28.0	89.0	278	290	265	126
26	63.5	44.5	72.5	47.0	26.5	88.0	271	284	260	123
25	63.0	44.0	72.0	46.0	25.5	87.0	264	278	255	120
24	62.5	43.0	71.5	45.0	24.0	86.0	257	272	250	117
23	62.0	42.5	71.0	44.0	23.0	84.5	251	266	245	115
22	61.5	41.5	70.5	43.0	22.0	83.5	246	261	240	112
21	61.0	41.0	70.0	42.5	20.5	82.5	241	256	235	110
20	60.5	40.0	69.5	41.5	19.5	81.0	236	251	230	108

Note: Although conversion tables dealing with hardness can be only approximate and never mathematically exact, it is of considerable value to be able to compare different hardness scales in a general way.

[a]Knoop Hardness Conversion: the values of the Knoop hardness number are approximate only, since they were determined on a limited number of tests and samples. These values are only for loads of 500 g or heavier.

Source: From *Hardness Testing Handbook*, by Vincent E. Lysaght and Anthony DeVellis, American Chain & Cable Co, PA, 1969.

Appendix 5
Recommended MIL 6875 Specification Steel Heat Treatment Conditions

TABLE A5.1
Heat Treatment Procedure for Class A (Carbon and Low-Alloy) Steel

Heating and Cooling Requirements					Approximate Tempering Temperature °F									
					Tensile Strength Range—ksi[e]									
SAE,[a] AISI, or Producer's Designation	Normalizing Temperature Range[b]	Annealing Temperature Range[c,d]	Austenitizing Temperature Range	Approved Quenchant	90–125	125–150	150–170	160–180	180–200	200–220	220–240	240–260	260–280	280–300
1025	1600/1700	1575/1650	1575/1650	Water or polymer	700	—	—	—	—	—	—	—	—	—
1035	1600/1700	1575/1650	1525/1575	Oil, water, polymer	900	—	—	—	—	—	—	—	—	—
1045	1600/1700	1550/1600	1450/1525	Oil, water, polymer	—	—	100	850	750	[f]	—	—	—	—
3140	1600/1700	1450/1525	1475/1525	Oil, polymer	1250	1100	100	825	700	—	—	—	—	—
4037	1600/1700	1525/1575	1525/1575	Oil, water, polymer	1200	1100	925	—	—	—	—	—	—	—
4130	1600/1700	1500/1600	1550/1600	Oil, water, polymer	1250	1050	925	850	725	—	—	—	—	—
4135	1600/1700	1525/1575	1550/1600	Oil, polymer	—	1125	1025	900	800	—	—	—	—	—
4140	1600/1700	1525/1575	1550/1600	Oil, polymer	1300	1175	1075	950	850	725	—	—	—	—
4150	1525/1650	1500/1550	1500/1550	Oil	—	1200	1100	975	800	—	—	—	—	—
4330V	1600/1700	1525/1600	1550/1650	Oil	—	—	—	—	1000	800	500	—	—	—
4335V	1600/1700	1525/1600	1550/1650	Oil	—	—	—	—	1000	800	—	—	—	—
4340	1600/1700	1525/1575	2500/1550	Oil	—	1200	1100	1050	925	850	—	—	—	—
4640	1600/1700	1525/1575	2500/1550	Oil	1200	1100	1000	900	750	—	—	—	—	—
6150	1600/1700	1525/1575	1550/1625	Oil	—	—	—	—	—	[g]	—	—	—	—
8630	1600/1700	1525/1575	1525/1600	Oil, water, polymer	1250	1050	925	850	725	—	—	—	—	—
8735	1600/1700	1525/1575	1525/1600	Oil, polymer	—	1125	1025	800	785	—	—	—	—	—
8740	1600/1700	1500/1575	1525/1575	Oil	—	1175	1075	950	850	725	—	—	—	—
Hy-Tul[h]	1700/1750	1375/1425	1575/1625	Oil	—	—	—	—	—	—	550	—	—	—
300m[h]	1675/1725	1525/1575	1575/1625	Oil	—	—	—	—	—	—	—	—	—	575
H-11[i]	—	1550/1650	1825/1875	Air, oil, polymer	—	—	—	—	1150	1100	1025	—	[j]	—
98BV40	1550/1650	1525/1575	1540/1560	Oil	—	—	—	—	—	—	—	—	—	500
D6AC	1700/1750	1525/1575	1675/1725	Oil	—	—	—	—	1150	1100	1025	—	600	—

9nl-4cO-.20c	1600/1700	1250/1150[k]	1525/1575	Oil, water, polymer[l]	—	—	—	—	1050	—	—	—	—	—
9Ni-4Co-.30C	1625/1675	1250/1150[k]	1475/1525	Oil[l]	—	—	—	—	—	1000	—	—	—	—
52100	1600/1700[m]	1400/1450[n]	1500/1575[o]	Oil	—	—	—	—	—	—	—	—	—	[p]
AF1410	1625/1675[q]	—	1500/1550	Oil[l]	—	—	—	—	—	—	950	—	—	—

[a]Steel alloys listed are the most frequently used. Alloys not listed should be heat treated as recommended by their manufacturers.

[b]For the purpose of this specification, normalizing describes a metallurgical process rather than a set of properties. All steels are air quenched from temperature range.

[c]Furnace cool to 1000°F or below, except furnace cool 4330, 4335V to 800°F, 4640 to 750°F, 4340 to 800°F and 300M to 600°F. Rate of furnace cool for alloy steels, except 4130, 8630, 4037, and 8735 should be 50°F per hour or slower.

[d]Recommended subcritical anneal temperature is 1250°F.

[e]Absence of values indicates the respective steel is not recommended for this tensile strength range.

[f]In general, for spring temper, temper at 700–800°F for RC 40–45.

[g]In general, for spring temper, temper at 725–900°F fir Rc 43–47.

[h]a. 4340, 260–280 tempering must be between 425 and 500°F. b. 300M and Hy Tuf—tempering is mandatory.

[i]Multiple cyclic annealing temper, temper at 725–900°F fir Rc 43–47.

[j]Final tempering shall be at or above 1000°F. Neither tempering temperature shall be less than that of previous temper nor more than 25°F higher than the previous temper.

[k]Duplex anneal—hold 4 ± 0.25 h at $1250 + 25$°F, air cool to room temperature, then reheat to $1150 + 25$°F and hold for 8 ± 0.25 h and air cool to room temperature.

[l]Cool to −100°F for 1 h minimum within 2 h after quenching and before tempering.

[m]Normalizing is not recommended practice for 52100 steel.

[n]The following annealing treatment for 52100 steel should be used: Heat to 1430°F, hold for 20 min, and cool at controlled rates as follows: 1430 to 1370°F at a rate not to exceed 20°F per hour; 1370 to 1320°F at a rate not to exceed 10°F per hour; 1320 to 1250°F at a rate not to exceed 20°F per hour.

[o]Size stability may be enhanced by refrigeration. When required, cool to −100°F for 1 h within 2 h after quenching and before tempering.

[p]For antifriction bearings, temper to Rc 58 to 65 at 300–450°F.

[q]Overage to facilitate machining by normalizing plus $1250 + 25$°F for not less than 6 h and air cool.

TABLE A5.2
Heat-Treatment Procedure for Class B (Martensitic Corrosion-Resistant) Steel

SAE, AISI, or Producer's Designation	Annealing °F		Transformation Hardening Cycle °F		Approximate Tempering Temperature °F for Tensile Strength—ksi					
	Temperature	Furnace Cool to Approx. Temp. Shown or Below	Austenitizing Temp.	Quenchant[a]	Recommended Subcritical Anneal	100 (minimum)	120 (minimum)	Avoid Tempering of Holding Within Range From[b]	180 (minimum)	200 (minimum)
403	1500 to 1600	Furnace cool 25 to 50° per hour to 1100	1750 to 1850	Oil	1200 to 1450, air cool	1300	1100	700 to 1100	500	
410	1500 to 1600	Furnace cool 25 to 50° per hour to 1100	1750 to 1850	Air Polymer Oil	1200 to 1450, air cool	1300	1100	700 to 1100	500	
416	1500 to 1650	Furnace cool 25 to 50° per hour to 1100	1750 to 1850	Air Polymer Oil	1200 to 1450, air cool	1300	1075	700 to 1075	500	
420	1550 to 1650 for 6 h	Furnace cool 25 to 50° per h to 100 followed by water quenching	1750 to 1850	Air Polymer Oil	1350 to 1450, air cool	1300[c]	1075	700 to 1075		600

440C	1550 to 1600 for 6 h, or 1650 for 2 h, +1300 for 4 h	Furnace cool 25 to 50° per hour to 1100	1900 to 1950	Air Polymer Oil Air Polymer	1250 to 1350, air cool	Temper at 325 for Rockwell C 58 minimum 1375 for Rockwell C 57 minimum 450 for Rockwell C 55 minimum

[a]When approved by the cognizant engineering organization, parts may be tempered in 1000–1050°F range when 135–145 ksi tensile strength is required, providing the parts are not subject to substantial impact loading or stress-corrosion conditions. Tempering these alloys in the range listed results in decreased impact strength and also reduced corrosion resistance. However, tempering in this range is sometimes necessary to obtain the strength and ductility required. When approved by the purchaser, material may be tempered in this range.

[b]Controlled atmosphere quench is optional for small parts. The quench for 440C shall be followed by refrigeration to –100°F or lower for 2 h. Double temper to remove retained austenite.

[c]Temper 420 steel: 300°F for Rc 52 minimum; 400°F for Rc 50 minimum; 600°F for Rc 48 minimum.

TABLE A5.3
Annealing Procedure for Class C (Austenitic Corrosion-Resistant) Steel

SAE, AISI, or Producer's Designation	Annealing Treatment Heating °F	Cooling[a]
201 and 202[b]	1850 to 2050	Water quench
301, 302, and 303[b]	1850 to 2050	Water quench
304, 304L, and 308[b]	1850 to 2050	Water quench
309[b]	1900 to 2050	Water quench
310, 316, and 316L[b]	1900 to 2050	Water quench
321[c]	1750 to 2050	Air or water quench
347[c] and 348	1800 to 2050	Air or water quench

[a]Other means of cooling permitted provided it is substantiated by tests that the rate is rapid enough to prevent carbide precipitation.
[b]Stress relieving of unstabilized grades, except 304L and 316L between $875 + 25$ and 1500°F is prohibited. Stress relieving of stabilized grades should be at 1650°F for 1 h.
[c]When stress relieving after welding is specified, hold for $\frac{1}{2}$ h minimum at temperature specified in table or holding for 2 h at 1650 ± 25°F.

TABLE A5.4
Heat Treatment Procedure for Class D (Precipitation-Hardening and Maraging) of Steel

Solution Treatment				Austenite Conditioning				Transformation treatment			
Steel	[a]	Temp.°F	Hold[b]	Quench[c]	[a]	Max Temp°F	Hold min[d]	Quench[c]	Temp. F°	Minimum min	Min. Time hr
Wrought	A	1900	[g,h]	Air							4
17–4 PH[c]				polymer							
15.5 PH[t]				Oil[i]							1
Cast											
17–4 PH[b]	HC	2100	[h]	Air[i]							$1\frac{1}{2}$
15–5 PH	A	1900		Air[i]							
PH	A	1700	[h]	Air or Oil[j]							4
13–8 Mo											
17–7 PH[k,g]	A	1950		Water, polymer, or air[l]	T	1450	90	Air[m]	+ 60	30	$1\frac{1}{2}$
					R	1750	10	Air[m]	−100	480	1
PH	A	1950		Water	T	1400	90	Air[m]	+ 60	30	$1\frac{1}{2}$
15–7Mo			[g]		R	1750	10	Air[m]	−100	480	1
			[h]		R	1750	10	Air[m]	−100	480	1
PH	A	1825	[g]	Water	SR	1700	60	Air[m]	−100	480	1
14–8 Mo											
AM-350	A	1925	[h]	Water oil or polymer	SCT	1710	[n]	Water	−100[m]	180	3
AM-355	A	1900	[p]	Water, Oil or	T	1710	[q]	Air	1400	180[j]	3
				polymer	SCT	1800	[f]	Air	−100	180	2
					SCT	1710		Water	−100[o]	180	3
A-286	A	1800	[h]	Air-blast, oil, water				or oil			16
Custom	A										
450		1700	60	Water,							4
455[r]		1525		polymer or oil							4
200[s]	A	1500	[h]	Air							3
250[s,t]	A	1500	[h]	Air							3
300[s,t]	A	1500	[h]	Air							3

Continued

TABLE A5.4 (Continued)
Heat Treatment Procedure for Class D (Precipitation-Hardening and Maraging) of Steel

Aging temperature (°F) For minimum tensile strength—Ksi															
130	135	140	145	150	155	165	170	175	180	185	190	200	205	210	220
	1150	1100	1075	1050	1025		925								
									900						
1100				1000			925		900						
							935								
1150				1100				1050		1025			1000		950
									1050			950			
				1100	1080		1060		1050						
											1050		1000		
															950
															950
														1050	950
						1000	950			850					
						850				(for castings only)					
									850						
							1000			(For wrought products only)					
1325 (Air Cool)															
1100			1050	1025			950		900			1000			950
												900			

[a]For the purpose of this specification, normalizing describes a metallurgical process rather than a set of properties. All steels are air quenched from temperature range.
[b]Recommended subcritical anneal temperature is 1250°F.

[c]Size stability may be enhanced by refrigeration. When required, cool to −100°F for 1 h within 2 h after quenching and before tempering.
[d]Stress relieving of unstabilized grades, except 304L and 316L between 875 + 25 and 1500°F is prohibited. Stress relieving of stabilized grades should be at 1650°F for 1 h.
[e]Furnace cool to 1000°F or below, except furnace cool 4330, 4335V to 800°F, 4640 to 750°F, 4340 to 800°F, and 300M to 600°F. rate of furnace cool for alloy steels, except 4130, 8630, 4037, and 8735 should be 50°F per hour or slower.
[f]Normalizing is not recommended practice for 52100 steel.
[g]Cool to −100°F for 1 h minimum within 2 h after quenching and before tempering.
[h]For antifriction bearings, temper to Rc 58 to 65 at 300–450°F.
[i]The following annealing treatment for 52100 steel should be used:
Heat to 1430°F, hold for 20 min, and cool at controlled rates as follows:
1430 to 1370°F at a rate not to exceed 20°F per hour; 1370 to 1320°F at a rate not to exceed 10°F per hour; 1320 to 1250°F at a rate not to exceed 20°F per hour.
[j]Absence of values indicates the respective steel is not recommended for this tensile strength range.
[k]When stress relieving after welding is specified, hold for $\frac{1}{2}$ h minimum at temperature specified in Table 1C or holding for 2 h at 1650 ± 25°F.
[l]Multiple cyclic annealing may be permitted to prevent grain growth.
[m]Temper 420 steel: 300°F for Rc 52 minimum; 400°F for Rc 50 minimum; 600°F for Rc 48 minimum.
[n]In general, for spring temper, temper at 700–800°F for Rc 40–45.
[o]Controlled atmosphere quench is optional for small parts. The quench for 440C shall be followed by refrigeration to −100°F or lower for 2 h. Double temper to remove retained austenite.
[p]Steel alloys listed are the most frequently used. Alloys not listed should be heat treated as recommended by their manufacturers.
[q]In general, for spring temper at 725–900°F for Rc 43–47.
[r]a. 4340, 260–280 tempering must be between 425 and 500°F. b. 300M and Hy Tuf—tempering temperature is mandatory.
[s]Final tempering shall be at or above 1000°F. Neither tempering temperature shall be less than that of previous temper nor more than 25°F higher than the previous temper.
[t]Other means of cooling permitted provided it is substantiated by tests that the rate is rapid enough to prevent carbide precipitation.

Appendix 6
Colors of Hardening and Tempering Heats

TABLE A6.1
Correlation of Hot Steel Color with Temperature

Temperature		
°F	°C	Hot Steel Color
752	400	Red; visible in the dark
885	474	Red; visible in twilight
975	525	Red; visible in daylight
1077	581	Red; visible in sunlight
1292	700	Dull red
1472	800	Turning to cherry red
1652	900	Cherry proper
1832	1000	Bright cherry red
2012	1100	Orange red
2192	1200	Orange yellow
2372	1300	White
2552	1400	Brilliant white
2732	1500	Dazzling white
2912	1600	Bluish white

TABLE A6.2
Correlation of Tempering Temperature with Heated Steel Color

Temperature Held for 1 h			Temperature Held for 8 min	
°F	°C	Color of Oxide	°F	°C
370	188	Faint yellow	460	238
390	199	Light straw	510	265
410	210	Dark straw	560	293
430	221	Brown	610	321
450	232	Purple	640	337
490	254	Dark blue	660	349
510	265	Light blue	710	376

Appendix 7
Weight Tables for Steel Bars

TABLE A7.1
Round and Square Bars, Specific Gravity 7.85

	Weight (kg/m)	
Size[a]	**Round Bars**	**Square Bars**
5	0.15	0.20
6	0.22	0.28
7	0.30	0.38
8	0.39	0.50
9	0.50	0.64
10	0.62	0.79
11	0.75	0.95
12	0.89	1.13
13	1.04	1.33
14	1.21	1.54
15	1.39	1.77
16	1.58	2.01
17	1.78	2.27
18	2.00	2.54
19	2.23	2.83
20	2.47	3.14
21	2.72	3.46
22	2.98	3.80
23	3.26	4.15
24	3.55	4.52
25	3.85	4.91
26	4.17	5.31
27	4.49	5.72
28	4.83	6.15
29	5.19	6.60
30	5.55	7.07
31	5.92	7.54
32	6.31	8.04
33	6.71	8.55
34	7.13	9.07
35	7.55	9.62
36	7.99	10.2
37	8.44	10.8
38	8.90	11.3
39	9.38	11.9

Continued

(Continued)

	Weight (kg/m)	
Size[a]	**Round Bars**	**Square Bars**
40	9.86	12.6
41	10.4	13.2
42	10.9	13.9
43	11.4	14.5
44	11.9	15.2
45	12.5	15.9
46	13.1	16.6
47	13.6	17.3
48	14.2	18.1
49	14.8	18.9
50	15.4	19.6
51	16.0	20.4
52	16.7	21.2
53	17.3	22.1
54	18.0	22.9
55	18.7	23.8
56	19.3	24.6
57	20.0	25.5
58	20.7	26.4
59	21.5	27.3
60	22.2	28.3
61	22.9	29.2
62	23.7	30.2
63	24.5	31.2
64	25.3	32.2
65	26.1	33.2
66	26.9	34.2
67	27.7	35.2
68	28.5	36.3
69	29.4	37.4
70	30.2	38.5
71	31.1	39.6
72	32.0	40.7
73	32.8	41.8
74	33.8	43.0
75	34.7	44.2
76	35.6	45.3
77	36.6	46.5
78	37.5	47.8
79	38.5	49.0
80	39.5	50.2
81	40.5	51.5
82	41.5	52.8
83	42.5	54.1
84	43.5	55.4
85	44.5	56.7
86	45.6	58.1
87	46.7	59.4
88	47.7	60.8
89	48.8	62.2
90	49.9	63.6

Continued

(Continued)

	Weight (kg/m)	
Size[a]	**Round Bars**	**Square Bars**
91	51.1	65.0
92	52.2	66.4
93	53.3	67.9
94	54.5	69.4
95	55.6	70.9
96	56.8	72.4
97	58.0	73.9
98	59.2	75.4
99	60.4	76.9
100	61.7	78.5
105	68.9	86.6
110	74.6	95.0
115	81.5	104
120	88.8	113
125	96.3	123
130	104	133
135	112	143
140	121	154
145	130	165
150	139	177
155	148	189
160	158	201
165	168	214
170	178	227
175	189	240
180	200	254
185	211	269
190	223	283
195	234	299
200	247	314
210	272	346
220	298	380
230	326	415
240	355	452
250	386	491
260	417	531
270	449	572
280	483	615
290	518	660
300	555	707

Molybdenum high-speed steels weigh approximately 3% more. High-speed steels of 18–4 type weigh approximately 10% more.

[a]Size is diameter of circular cross section, side of square cross section.

Continued

TABLE A7.2
Hexagonal and Octagonal Bars, Specific Gravity 7.85

	Weight (kg/m)	
Size[a]	Round Bars	Square Bars
5	0.17	0.16
6	0.25	0.23
7	0.33	0.32
8	0.44	0.42
9	0.55	0.53
10	0.68	0.65
11	0.82	0.79
12	0.98	0.94
13	1.15	1.10
14	1.33	1.27
15	1.53	1.46
16	1.74	1.66
17	1.97	1.88
18	2.20	2.11
19	2.45	2.35
20	2.72	2.60
21	3.00	2.87
22	3.29	3.15
23	3.60	3.44
24	3.92	3.74
25	4.25	4.06
26	4.60	4.40
27	4.96	4.74
28	5.33	5.09
29	5.72	5.47
30	6.12	5.85
31	6.53	6.25
32	6.96	6.66
33	7.41	7.08
34	7.86	7.52
35	8.33	7.97
37	9.31	8.90
39	10.3	9.89
41	11.4	10.9
43	12.6	12.0
45	13.8	13.2
47	15.0	14.4
50	17.0	16.3
53	19.1	18.3
56	21.3	20.4

[a]Dimensions are the length between opposite sides of the bar.